



ASTRONOMY AND ASTROPHYSICS LIBRARY

Series Editors:

- G. Börner, Garching, Germany
A. Burkert, München, Germany
W. B. Burton, Charlottesville, VA, USA and
Leiden, The Netherlands
M. A. Dopita, Canberra, Australia
A. Eckart, Köln, Germany
T. Encrenaz, Meudon, France
E. K. Grebel, Heidelberg, Germany
B. Leibundgut, Garching, Germany
J. Lequeux, Paris, France
A. Maeder, Sauverny, Switzerland
V. Trimble, College Park, MD, and Irvine, CA, USA

Malcolm S. Longair

Galaxy Formation

Second Edition

With 202 Figures and 20 Tables



Springer

Malcolm S. Longair

Jacksonian Professor of Natural Philosophy
Cavendish Laboratory
J. J. Thomson Avenue
Cambridge CH3 0HE
England, UK
e-mail: msl1000@cam.ac.uk

Cover image: Galaxies NGC 2207 and IC 2163. Credit: NASA and The Hubble Heritage Team (STScI); Hubble Space Telescope WFPC2; STScI-PRC99-41; Source: <http://heritage.stsci.edu/1999/41/index.html>

Library of Congress Control Number: 2007935444

ISSN 0941-7834

ISBN 978-3-540-73477-2 Springer Berlin Heidelberg New York

This work is subject to copyright. All rights are reserved, whether the whole or part of the material is concerned, specifically the rights of translation, reprinting, reuse of illustrations, recitation, broadcasting, reproduction on microfilm or in any other way, and storage in data banks. Duplication of this publication or parts thereof is permitted only under the provisions of the German Copyright Law of September 9, 1965, in its current version, and permission for use must always be obtained from Springer. Violations are liable to prosecution under the German Copyright Law.

Springer is a part of Springer Science+Business Media

springer.com

© Springer-Verlag Berlin Heidelberg 1998, 2008

The use of general descriptive names, registered names, trademarks, etc. in this publication does not imply, even in the absence of a specific statement, that such names are exempt from the relevant protective laws and regulations and therefore free for general use.

Typesetting and production: LE-TeX Jelonek, Schmidt & Vöckler GbR, Leipzig, Germany
Cover design: eStudio Calamar S.L., F. Steinen-Broo, Girona, Spain

SPIN: 11394105 55/3180/YL - 5 4 3 2 1 0 Printed on acid-free paper

For Deborah, Mark and Sarah

Preface

This is the second edition of my book *Galaxy Formation*. Many people liked the first edition which appeared in 1998, just before the explosion of magnificent new data which have completely changed the face of astrophysical cosmology. Many of the agonies which had to be gone through in the first edition have disappeared and, to many people's amazement, including mine, there is now a *concordance model* for cosmology, the cosmologist's equivalent of the particle physicist's *standard model*. Just like the standard model, however, the concordance model creates as many problems as it solves. This is not a cause for concern, but rather one for celebration because we are now able to ask much better and deeper questions than in the past. These questions indicate clearly the need for physics and astrophysics 'Beyond the Concordance Model'.

The object of this new edition is to bring this amazing story up-to-date, very much in the spirit of the first edition. To recapitulate some of the points made in the previous preface about the origin of the book, I was asked by Springer-Verlag to expand the set of lecture notes that I prepared in 1988 for the First Astrophysics School organised by the European Astrophysics Doctoral Network into a full-length book. The set of notes was entitled *Galaxy Formation* and was published as a chapter of the volume *Evolution of Galaxies: Astronomical Observations* (eds. I. Appenzeller, H.J. Habing and P. Lena, pages 1 to 93, Springer-Verlag Berlin, Heidelberg, 1989). In that chapter, I attempted to bridge the gap between elementary cosmology and the technical papers appearing in the literature which can seem quite daunting on first encounter. The objective was to present the physical ideas and key results as clearly as possible as an introduction and guide to the technical literature.

In 1993, more lecture notes on *The Physics of Background Radiation* were prepared for the 23rd Advanced Course of the Swiss Society of Astrophysics and Astronomy, the topic being *The Deep Universe* (A.R. Sandage, R.G. Kron and M.S. Longair, Springer-Verlag Berlin, Heidelberg, 1995). Then, also in 1993, I completed a history of twentieth century astrophysics and cosmology, which was published as Chap. 23 of a three-volume work entitled *Twentieth Century Physics* (eds. L.M. Brown, A. Pais and A.B. Pippard, IOP Publications, AIP Press Bristol, and New York 1995). A much enlarged full-length book on this topic entitled *The Cosmic Century: A History of Astrophysics and Cosmology* was published by Cambridge University Press in 2006. That book brought the story of the origin of

galaxies and the large-scale structure of the Universe up-to-date as of October 2005 and it has been further updated and expanded in the present book. Just as in the first edition, the present volume is much more than a recycled and concatenated version of previously published works. I have rewritten and rethought the original versions, expanded some parts, brought everything up-to-date and included new material.

I often find that I understand things best, and present them most clearly, when I have to prepare them for students, at either the undergraduate or the post-graduate level, and so I have adopted the same form of presentation here. I have intentionally presented the material in an informal, pedagogical manner, and attempted to avoid getting bogged down in formalities and technicalities. If the material becomes too difficult, I simply summarise the key points, give some appropriate references and pass on. My approach is to reduce the problems to their simplest form and rationalise from these examples the results of more complete analyses. Wherever it is feasible without excessive effort, we will attempt to derive exact results. The level of presentation is intended to be appropriate for a final-year undergraduate or first-year post-graduate course of lectures. In other words, it is assumed that the reader has a good grasp of basic physics but does not necessarily have the appropriate background in astronomy, astrophysics or cosmology. My aim has been to write a user-friendly book, taking particular care to expound carefully areas where I have found students have difficulty.

When I wrote the original set of lecture notes on galaxy formation, my objective was to tell the story of modern astrophysical cosmology from the perspective of one of its most important and fundamental problems of cosmology – how did the galaxies come about? I enjoy this approach to the exposition of modern cosmology because, to do the problem justice, it is essential to introduce the whole of what I call *classical cosmology*, as the framework for the discussion. This approach has, for me, the great advantage of concentrating upon a crucial problem of astrophysical cosmology rather than regarding the objective of cosmology as being simply the delineation of a preferred cosmological model, however interesting that is in its own right. As we will show, the origin of galaxies and larger-scale structures in the Universe is one of the great cosmological problems and has provided us with unique and direct information about the physics of the very early Universe.

This new understanding brings with it the question of whether or not the old structure of the book is really appropriate – do we really need to grind through all the old story in order to understand the problems raised by the concordance model? My decision has been to maintain much of the original structure of the book, largely because the approach was very strongly physics-motivated and the old story reveals much of the essential physics of the concordance model.

One final warning is in order. I make no claim that this presentation is complete, unbiased or objective. You should regard the book as my own impressions and opinions of what I consider to be the important issues of modern astrophysical cosmology. Others would tell the story in a completely different way and put

emphasis upon different parts of what is unquestionably a multi-dimensional story. I will endeavour to include as wide a spectrum of ideas and opinions as possible, but the text will inevitably be incomplete. I do not worry about this – it should encourage you to read as widely as possible in order to neutralise my prejudices and biases.

Good Luck!

Venice and Cambridge,
July 2007

Malcolm Longair

Acknowledgements

Many people have contributed directly, or indirectly, to my understanding of the contents of this book. Perhaps the most important influence has been the late Peter Scheuer, who first introduced me to the physics of astrophysical cosmology. His approach and methods have very strongly influenced the way I have understood and taught this material over the years. I am very grateful to Immo Appenzeller, Harm Habing and Pierre Lena for the opportunity to give the lecture course in Les Houches in 1988. In preparing that set of lecture notes, I greatly benefitted from the advice of John Peacock and Alan Heavens who read parts of the typescript of the first edition and offered very helpful comments. John Peacock very kindly allowed me to use part of his lecture notes in preparing some of the material for the original chapter. John has now written up his notes in his book *Cosmological Physics* (Cambridge University Press, 2000). In my view, John's book is a brilliant achievement and I urge all interested readers to become familiar with his deep insights. Some of the text of the present book is based upon joint work with Rashid Sunyaev, which dates from the period 1968 to 1980. I fully acknowledge Rashid's contributions to clarifying my own understanding.

The invitation to deliver the 1993 course of lectures on the background radiation, as part of the 23rd Course of the Swiss Society of Astrophysics and Astronomy, came from Gustav Tammann, Bruno Binggeli and Hermann Buser and I am grateful for their kindness and hospitality at Les Diablerets. My history of twentieth century astrophysics and cosmology was commissioned by Brian Pippard on behalf of the editors of *Twentieth Century Physics* and I am grateful to him for his perceptive comments on that article.

I am particularly grateful to Bob Williams and his colleagues at the Space Telescope Science Institute at Baltimore, where I was a Visiting Fellow from September to December 1997. Without that sabbatical term at the Institute, the completion of the first edition would have been impossible. Special thanks are due to the staff, graduate students and research fellows at the Institute and at Johns Hopkins University, who kindly acted as guinea pigs on whom I 'battle-tested' portions of the book. Many of the research workers at the Institute gave generously of their time in discussing many of the topics in the book; the discussions with Ron Allen, Michael Fall, Harry Ferguson, Mario Livio, Duccio Macchetto and Piero Madau were especially helpful. The writing was enormously aided by access to the excellent library facilities at the Institute. Martin Harwit kindly read the first edition of the book very carefully and made a number of helpful suggestions.

Since the first edition was published, many colleagues have pointed out minor errors and suggested further topics for discussion. The preparation of the present edition began in December 2005, at the beginning of a two-year period of sabbatical leave kindly granted by the University of Cambridge. So much had changed in the matter of just a few years that essentially everything had to be rewritten in the light of this new understanding.

From February to May 2006, I was Adjunct Professor of Astronomy at the Astronomy Department of the University of Massachusetts at Amherst. I am most grateful to Ronald Snell and his colleagues for their warm welcome and the many helpful discussions we had about galaxies. Martin Weinberg, Neal Katz and Hou-Jun Mo were very stimulating colleagues. A special thank you goes to Dan McIntosh who introduced me to the red and blue sequences of galaxies and showed how our perception of what galaxies are has changed.

From October to December 2006, I was Visiting Professor at the Max Planck Institute for Astrophysics at Garching at the invitation of Rashid Sunyaev. The discussions with Rashid, Simon White and their colleagues were very helpful indeed in sharpening my understanding of many of the issues of astrophysical cosmology. I was back in Garching from February to April 2007 at the invitation of Catherine Cesarsky as a Visiting Scientist at the European Southern Observatory. This also proved to be a very stimulating visit. The wealth of expertise at ESO and the nearby Institutes made Garching a ideal haven in which to complete much of the final chapters of the new edition. I am most grateful to Bruno Leibundgut and all the staff members, visitors, post-docs and graduate students on whom I tried out some of the new sections of the book. The very final sections of the book were completed while I was a guest at the Osservatorio Astrofisico di Arcetri in Florence. I am most grateful to Francesco Palla and his colleagues for their kindness and hospitality.

Four colleagues are worthy of special thanks. Paul Schechter used the first edition of the book as a text for his courses on cosmology and kindly set up a web-site with corrections to it. He also made helpful suggestions for the present edition. Megan Donahue also used the first edition as a class text and provided a very helpful list of corrections and suggested improvements. She then ‘battle-tested’ Parts 2 and 3 of the new edition on her students and made helpful comments. I am most grateful to Megan and her students for this invaluable help which will undoubtedly have improved the book. Luigi Guzzo kindly read a number of sections of the book very careful and provided helpful suggestions and corrections. Peter Schneider reviewed the draft text at the invitation of Springer-Verlag and suggested a number of very helpful improvements.

Finally, the book is dedicated to my family, Deborah, Mark and Sarah, whose constant love, support and patience have made it possible.

Contents

Part I Preliminaries

1	A Brief History of Cosmology and Galaxy Formation	3
1.1	Pre-History	3
1.2	The Galaxies and the Structure of our Galaxy	5
1.3	The Theory of the Expanding Universe	10
1.4	The Big Bang	14
1.5	Galaxy and Structure Formation	16
1.6	Hot and Cold Dark Matter	19
1.7	The Very Early Universe	22
2	The Large-Scale Structure of the Universe	27
2.1	The Spectrum and Isotropy of the Cosmic Microwave Background Radiation	27
2.1.1	The Spectrum of the Cosmic Microwave Background Radiation	28
2.1.2	The Isotropy of the Cosmic Microwave Background Radiation	29
2.2	The Large-Scale Distribution of Galaxies	33
2.2.1	Two-Point Correlation Functions	34
2.2.2	Walls and Voids in the Distribution of Galaxies on Large Scales	38
2.3	Hubble's Law and the Expansion of the Universe	44
2.4	Conclusion	48
3	Galaxies	49
3.1	Introduction	49
3.2	The Revised Hubble Sequence for Galaxies	50
3.3	Peculiar and Interacting Galaxies	56
3.4	The Light Distribution in Galaxies	59
3.4.1	Elliptical Galaxies	61
3.4.2	Spiral and Lenticular Galaxies	61
3.4.3	Putting the Light Distributions Together	62
3.5	The Masses of Galaxies	63

3.5.1	The Virial Theorem for Clusters of Stars, Galaxies and Clusters of Galaxies	63
3.5.2	The Rotation Curves of Spiral Galaxies	66
3.5.3	The Velocity Dispersions of Elliptical Galaxies	69
3.6	The Properties of Spiral and Elliptical Galaxies	70
3.6.1	The Faber–Jackson Relation and the Fundamental Plane . . .	70
3.6.2	Ellipticals Galaxies as Triaxial Systems	71
3.6.3	The Tully–Fisher Relation for Spiral Galaxies	73
3.6.4	Luminosity–Metallicity Relations	74
3.7	The Luminosity Function of Galaxies	77
3.7.1	Aspects of the Luminosity Function of Galaxies	79
3.7.2	The Integrated Luminosity and the Mean Mass-to-Luminosity Ratio for Visible Matter in the Universe	83
3.8	The Properties of Galaxies: Correlations Along the Hubble Sequence	84
3.9	The Red and Blue Sequences	88
3.9.1	Colour Versus Absolute Magnitude	89
3.9.2	Sérsic Index and Colour	91
3.9.3	Mean Stellar Age and Concentration Index C	91
3.9.4	The Effect of the Galaxy Environment	92
3.9.5	The New Perspective	93
3.10	Concluding Remark	94
4	Clusters of Galaxies	95
4.1	The Large-Scale Distribution of Clusters of Galaxies	95
4.1.1	The Abell Catalogues of Rich Clusters of Galaxies	96
4.1.2	Comparison with Clusters Selected from the Sloan Digital Sky Survey	98
4.1.3	Abell Clusters and the Large-Scale Distribution of Galaxies	99
4.2	The Distribution of Galaxies in Clusters of Galaxies	101
4.2.1	The Galaxy Content and Spatial Distribution of Galaxies in Clusters	101
4.2.2	Clusters of Galaxies and Isothermal Gas Spheres	103
4.2.3	The Luminosity Function for Cluster Galaxies	108
4.2.4	Summary of the Properties of Rich Clusters of Galaxies . .	109
4.3	Dynamical Estimates of the Masses of Clusters of Galaxies . .	110
4.4	X-Ray Observations of Hot Gas in Clusters of Galaxies	114
4.5	The Sunyaev–Zeldovich Effect in Hot Intracluster Gas	125
4.6	Gravitational Lensing by Galaxies and Clusters of Galaxies . .	128
4.6.1	Basic Theory of Gravitational Deflections	128
4.6.2	Magnification of Images by Gravitational Lensing	130
4.6.3	Extended Deflectors	133
4.6.4	Gravitational Lensing and the Astrophysics of Galaxies . .	136
4.7	Forms of Dark Matter	139

4.7.1	Baryonic Dark Matter	139
4.7.2	Non-Baryonic Dark Matter	142
4.7.3	Astrophysical and Experimental Limits	144

Part II The Basic Framework

5	The Theoretical Framework	149
5.1	The Cosmological Principle	149
5.2	Isotropic Curved Spaces	150
5.3	The Space–Time Metric for Isotropic Curved Spaces	155
5.4	The Robertson–Walker Metric	158
5.5	Observations in Cosmology	162
5.5.1	The Cosmological Redshift	162
5.5.2	Hubble’s Law	165
5.5.3	Angular Diameters	167
5.5.4	Apparent Intensities	168
5.5.5	Number Densities	170
5.5.6	The Age of the Universe	171
5.6	Summary	171
6	An Introduction to Relativistic Gravity	173
6.1	The Principle of Equivalence	173
6.2	The Gravitational Redshift	176
6.3	The Bending of Light Rays	179
6.4	Further Complications	181
6.5	The Route to General Relativity	184
6.5.1	Four-Tensors in Relativity	184
6.5.2	What Einstein Did	187
6.6	Experimental and Observational Tests of General Relativity	189
6.6.1	The Four Tests of General Relativity	189
6.6.2	Pulsars and General Relativity	192
6.6.3	Parameterised Post-Newtonian Models	195
6.6.4	Variation of the Gravitational Constant with Cosmic Epoch	197
6.7	Summary	198
7	The Friedman World Models	199
7.1	Einstein’s Field Equations	199
7.2	The Standard Friedman World Models with $\Lambda = 0$	202
7.2.1	The Newtonian Analogue of the Friedman World Models ..	202
7.2.2	The Critical Density and the Density Parameter	204
7.2.3	The Dynamics of the Friedman Models with $\Lambda = 0$..	205
7.3	Friedman Models with Non-Zero Cosmological Constant	207
7.3.1	The Cosmological Constant and the Vacuum Energy Density	208

7.3.2	Varying the Equation of State of the Vacuum Energy	210
7.3.3	The Dynamics of World Models with $\Lambda \neq 0$: General Considerations	211
7.4	Observations in Cosmology	215
7.4.1	The Deceleration Parameter	216
7.4.2	The Cosmic Time–Redshift Relation	217
7.4.3	Distance Measures as a Function of Redshift	218
7.4.4	Angular Diameter–Redshift Relations	221
7.4.5	Flux Density–Redshift Relations	223
7.4.6	The Comoving Volume Within Redshift z	226
7.5	Angular Diameter Distances Between Any Two Redshifts	228
7.6	The Flatness Problem	230
7.7	Inhomogeneous World Models	231
A7	The Robertson–Walker Metric for an Empty Universe	237
8	The Determination of Cosmological Parameters	241
8.1	The Cosmological Parameters	241
8.2	Testing the Friedman Models	242
8.3	Hubble’s Constant H_0	246
8.4	The Age of the Universe T_0	250
8.5	The Deceleration Parameter q_0	252
8.5.1	The Redshift–Magnitude Relation for the Brightest Galaxies in Clusters	252
8.5.2	The Redshift–Magnitude Relation for Radio Galaxies	254
8.5.3	The Redshift–Magnitude Relation for Type 1a Supernovae .	256
8.5.4	The Number Counts of Galaxies	259
8.5.5	The Angular Diameter–Redshift Test	261
8.6	Ω_A and the Statistics of Gravitational Lenses	263
8.7	The Density Parameter Ω_0	267
8.8	Summary	270
9	The Thermal History of the Universe	271
9.1	Radiation-Dominated Universes	271
9.2	The Matter and Radiation Content of the Universe	273
9.3	The Epoch of Recombination	277
9.4	The Radiation-Dominated Era	281
9.5	The Speed of Sound as a Function of Cosmic Epoch	285
9.6	Early Epochs	286
10	Nucleosynthesis in the Early Universe	289
10.1	Equilibrium Abundances in the Early Universe	289
10.2	The Decoupling of Neutrinos and the Neutrino Barrier	290
10.3	The Synthesis of the Light Elements	292
10.4	The Abundances of the Light Elements	295

10.4.1	Determinations of the Observed Abundances of the Light Elements	296
10.4.2	Comparison of Theory and Observations	299
10.5	The Neutrino Background Temperature and the Value of χ	301
10.6	Baryon-Symmetric Universes	303

Part III The Development of Primordial Fluctuations Under Gravity

11	The Evolution of Perturbations in the Standard Big Bang	311
11.1	What the Theorists Are Trying to Do	311
11.1.1	Why this Programme Is Feasible	312
11.1.2	A Warning	312
11.2	The Non-Relativistic Wave Equation for the Growth of Small Perturbations in the Expanding Universe	313
11.3	The Jeans' Instability	317
11.4	The Jeans' Instability in an Expanding Medium	319
11.4.1	Small Perturbation Analysis	319
11.4.2	Perturbing the Friedman Solutions	321
11.4.3	Falling Poles	322
11.4.4	The General Solution	324
11.5	The Evolution of Peculiar Velocities in the Expanding Universe	327
11.6	The Relativistic Case	331
11.7	The Basic Problem	332
12	More Tools and Problems	335
12.1	Horizons and the Horizon Problem	335
12.2	Pedagogical Interlude – Space–Time Diagrams for the Standard World Models	339
12.2.1	Distance and Times	339
12.2.2	The Past Light Cone	340
12.2.3	The Critical World Model $\Omega_0 = 1, \Omega_A = 0$	342
12.2.4	The Reference World Model $\Omega_0 = 0.3, \Omega_A = 0.7$	344
12.3	Superhorizon Scales	347
12.4	The Adiabatic Baryonic Fluctuations in the Standard Big Bang	350
12.4.1	The Radiation-Dominated Era	352
12.4.2	The Matter-Dominated Era	353
12.5	Dissipation Processes in the Pre-Recombination Era	355
12.6	Isothermal Perturbations	357
12.7	Baryonic Theories of Galaxy Formation	360
12.7.1	The Adiabatic Scenario	361
12.7.2	The Isothermal Scenario	363
12.8	What Went Wrong?	364

13 Dark Matter and Galaxy Formation	367
13.1 Introduction	367
13.2 Forms of Non-Baryonic Dark Matter	369
13.3 WIMPs as Dark Matter Particles	370
13.4 Metric Perturbations and Hot and Cold Dark Matter	374
13.5 Free Streaming and the Damping of Hot Dark Matter Perturbations	375
13.6 Instabilities in the Presence of Dark Matter	377
13.7 The Evolution of Hot and Cold Dark Matter Perturbations	380
13.7.1 Hot Dark Matter Scenario	380
13.7.2 Cold Dark Matter Scenario	381
13.8 Conclusion	384
14 Correlation Functions and the Spectrum of the Initial Fluctuations	385
14.1 The Two-Point Correlation Function for Galaxies	385
14.2 The Perturbation Spectrum	388
14.2.1 The Relation Between $\xi(r)$ and the Power Spectrum of the Fluctuations	388
14.2.2 The Initial Power Spectrum	390
14.2.3 The Harrison-Zeldovich Power Spectrum	391
14.3 Evolution of the Initial Perturbation Spectrum – Transfer Functions	393
14.3.1 Adiabatic Cold Dark Matter	393
14.3.2 Adiabatic Hot Dark Matter	396
14.3.3 Isocurvature Cold Dark Matter	396
14.3.4 The Subsequent Evolution	399
14.4 Biasing	401
14.5 Reconstructing the Processed Initial Power Spectrum	405
14.5.1 Redshift Biases	406
14.5.2 Non-Linear Development of Density Perturbations	407
14.5.3 The Role of Baryon Perturbations	409
14.6 The Acoustic Peaks in the Power Spectrum of Galaxies	411
14.6.1 The 2dF Galaxy Redshift Survey	412
14.6.2 Sloan Digital Sky Survey	412
14.7 Variations on a Theme of Cold Dark Matter	415
15 Fluctuations in the Cosmic Microwave Background Radiation	421
15.1 The Ionisation of the Intergalactic Gas Through the Epoch of Recombination	422
15.2 The Physical and Angular Scales of the Fluctuations	424
15.2.1 The Last Scattering Layer	425
15.2.2 The Silk Damping Scale	426
15.2.3 The Sound Horizon at the Last Scattering Layer	427
15.2.4 The Particle Horizon Scales	429
15.2.5 Summary	430
15.3 The Power Spectrum of Fluctuations in the Cosmic Microwave Background Radiation	431

15.3.1	The Statistical Description of the Temperature Fluctuations	431
15.3.2	The Power Spectrum of Fluctuations in the Intensity of the Cosmic Microwave Background Radiation	434
15.4	Large Angular Scales	436
15.4.1	The Sachs–Wolfe Effect – Physical Arguments	436
15.4.2	The Integrated Sachs–Wolfe and Rees–Sciama Effects	440
15.4.3	Primordial Gravitational Waves	440
15.5	Intermediate Angular Scales – the Acoustic Peaks	443
15.6	Small Angular Scales	450
15.6.1	Statistical and Silk Damping	450
15.6.2	The Sunyaev–Zeldovich Effect in Clusters of Galaxies	450
15.6.3	Confusion Due to Discrete Sources	451
15.7	The Reionised Intergalactic Gas	452
15.8	The Polarisation of the Cosmic Microwave Background Radiation	454
15.8.1	The Polarisation Mechanism for the Cosmic Microwave Background Radiation	454
15.8.2	Polarisation from the Last Scattering Layer	455
15.8.3	Polarisation from the Epoch of Reionisation	458
15.8.4	Primordial Gravitational Waves	459
15.8.5	Weak Gravitational Lensing	460
15.9	Determination of Cosmological Parameters	463
15.10	Other Sources of Primordial Fluctuations	465
15.11	Reflections	466

Part IV The Post-Recombination Universe

16	The Post-Recombination Era	471
16.1	The Non-Linear Collapse of Density Perturbations	472
16.1.1	Isotropic Top-Hat Collapse	473
16.1.2	The Zeldovich Approximation	475
16.2	The Role of Dissipation	477
16.3	The Press–Schechter Mass Function	482
16.3.1	Exposition – Elementary Theory	482
16.3.2	Development and Recapitulation	485
17	The Evolution of Galaxies and Active Galaxies with Cosmic Epoch	491
17.1	Introduction	491
17.2	Counts of Galaxies and Active Galaxies	492
17.2.1	Euclidean Source Counts	493
17.2.2	Source Counts for the Standard World Models	494
17.2.3	Submillimetre Counts of Dusty Galaxies	500
17.2.4	Number Counts in Models with Finite Ω_A	501
17.2.5	Fluctuations in the Background Radiation due to Discrete Sources	504

17.3	The V/V_{\max} or Luminosity-Volume Test	507
17.4	Background Radiation	510
17.4.1	Background Radiation and Source Counts	510
17.4.2	Evaluating the Background due to Discrete Sources	510
17.4.3	The Effects of Evolution – the Case of the Radio Background Emission	512
17.5	The Evolution of Active Galaxies with Cosmic Epoch	514
17.5.1	Number Counts and V/V_{\max} Tests for Extragalactic Radio Sources	514
17.5.2	Radio Quiet Quasars	518
17.5.3	X-Ray Source Counts	524
17.5.4	X-Ray Clusters of Galaxies	529
17.6	Infrared and Submillimetre Number Counts	532
17.7	Counts of Galaxies	537
17.8	Clusters of Galaxies	543
18	The Intergalactic Medium	547
18.1	The Background Emission of and Absorption by the Intergalactic Gas	548
18.2	The Gunn–Peterson Test	549
18.3	The Lyman- α Absorption Clouds	552
18.3.1	The Properties of the Lyman- α Absorption Clouds	552
18.3.2	The Nature of the Clouds in the Lyman- α Forest	554
18.3.3	The Evolution of Lyman- α Absorption Clouds with Cosmic Epoch	556
18.3.4	The Power Spectrum of the Lyman- α Forest	557
18.4	The Lukewarm Intergalactic Gas	560
18.4.1	The X-Ray Background and a Cosmic Conspiracy	561
18.4.2	The Collisional Excitation of the Intergalactic Gas	562
18.4.3	The Emission and Absorption of Diffuse Lukewarm Intergalactic Gas	564
18.4.4	The Proximity Effect and the Diffuse Ultraviolet Background Radiation at Large Redshifts	567
18.5	The Lyman Continuum Opacity of the Intergalactic Gas	569
18.6	Modelling the Evolution of the Intergalactic Medium	571
18.7	The Epoch of Reionisation	574
18.8	The Origin of Magnetic Fields	577
19	Making Real Galaxies	583
19.1	Star and Element Formation in Galaxies	583
19.1.1	The Background Radiation and Element Formation	584
19.1.2	The Global Star Formation Rate from Optical and Ultraviolet Observations of Star-Forming Galaxies	587
19.1.3	The Lyman-Break Galaxies	590
19.1.4	The Hubble Deep and Ultra Deep Fields	590

19.1.5 Submillimetre Determinations of the Cosmic Star-Formation Rate	596
19.2 The Abundances of Elements in Lyman- α Absorption Systems	598
19.3 The Equations of Cosmic Chemical Evolution	604
19.4 The Old Red Galaxies	607
19.5 The Origin of Rotation	610
19.6 Putting It All Together – Semi-Analytic Models of Galaxy Formation	613
20 The Very Early Universe	621
20.1 The Big Problems	621
20.1.1 The Horizon Problem	621
20.1.2 The Flatness Problem	622
20.1.3 The Baryon-Asymmetry Problem	622
20.1.4 The Primordial Fluctuation Problem	623
20.1.5 The Values of the Cosmological Parameters	623
20.1.6 The Way Ahead	624
20.2 The Limits of Observation	624
20.3 The Anthropic Cosmological Principle	625
20.4 The Inflationary Universe – Historical Background	626
20.5 The Origin of the Spectrum of Primordial Perturbations	629
20.5.1 The Equation of State	630
20.5.2 The Duration of the Inflationary Phase	630
20.5.3 The Shrinking Hubble Sphere	631
20.5.4 Scalar Fields	634
20.5.5 The Quantised Harmonic Oscillator	635
20.5.6 The Spectrum of Fluctuations in the Scalar Field	637
20.6 Baryogenesis	641
20.7 The Planck Era	642
References	645
Name Index	695
Index	701

1 A Brief History of Cosmology and Galaxy Formation

We begin with a broad-brush historical overview of the development of ideas and concepts concerning galaxies, cosmology and galaxy formation from the time of Tycho Brahe and Newton to the present day. This chapter therefore summarises qualitatively many of the key topics to be dealt with in quantitative detail in the rest of this book.¹ If you do not need this gentle introduction, or misguidedly think that history is boring, you may pass straightaway to Chap. 2.

1.1 Pre-History

It always comes as a surprise to me to realise how recent our understanding of galaxies, cosmology and galaxy formation really is. The motions of the Sun, Moon and planets against the background of the ‘fixed stars’ had been studied from ancient times, but the scientific study of their motions in the modern sense only began in the sixteenth century.

The developments which led to the Newtonian revolution can be traced to the technological and observational achievements of Tycho Brahe in the final decades of the sixteenth century. I have told this remarkable story elsewhere (Longair, 2003). Tycho Brahe measured the positions of the Sun, Moon, planets and 777 stars over a period of 20 years, resulting in an order of magnitude improvement in the accuracy with which their orbits were determined over all previous measurements. In the year before his death, he employed Johannes Kepler as his assistant and assigned him the task of working out the orbits of the planets from his magnificent data sets. In the period 1601 to 1619, Kepler succeeded in interpreting the mass of Tycho’s data in terms of elliptical planetary orbits about the Sun, which was located in one of the foci of each ellipse. Kepler’s discovery of his three laws of planetary motion was a miracle of geometrical analysis. The three laws embody not only the elliptical orbits of the planets (the first law), but also the areal law – that equal areas are swept out by the radius vector from the Sun to the planet in equal times (the second law) – and the dependence of the period T of the planet’s orbit about the Sun upon the three-halves power of its mean distance r from the Sun, $T \propto r^{3/2}$, (the third law).

¹ Comprehensive references to the original papers discussed in this chapter can be found in my book *The Cosmic Century: A History of Astrophysics and Cosmology* (Longair, 2006).

In 1664, at the age of only 21, Isaac Newton first derived his law of gravity from Kepler's third law. Writing *Newton's law of gravity* in modern vector notation,

$$\mathbf{f} = -G \frac{M_1 M_2}{r^2} \mathbf{i}_r , \quad (1.1)$$

where \mathbf{f} is the gravitational force acting between two point masses M_1 and M_2 separated by a distance r and \mathbf{i}_r is the unit vector in the direction from one mass to the other. Newton's achievement was to unify the terrestrial law of gravity with celestial dynamics by showing that (1.1) could explain the acceleration of falling apples on Earth and the orbits of the planets. It is no exaggeration to say that astronomy, astrophysics and cosmology are the *sciences of gravity* – all the systems we study in astronomy and cosmology are attempting to counteract the omnipresent attractive force of gravity by one means or another.

In 1692 Richard Bentley gave the first series of Boyle Lectures which Robert Boyle had founded 'to combat atheism'. Bentley took as his theme Newton's 'sublime discoveries' and entered into a short but profound correspondence with Newton about the nature of our physical Universe. The question at issue was the stability of a finite or infinite Universe filled with stars under the attractive force of gravity. The conclusion of the correspondence was that the Universe must be infinite because, if it were not, it would collapse to its centre under gravity. With remarkable insight, they recognised, however, that an infinite Universe filled with stars is gravitationally unstable. If a star is displaced from its equilibrium position, it continues to accelerate in that direction. To quote Harrison:

(Newton) agreed with Bentley that providence had designed a universe of infinite extent in which uniformly distributed stars stand poised in unstable equilibrium like needles on their points (Harrison, 1987).

It was only in the twentieth century that the nature of this instability was fully appreciated. For a static medium, the instability criterion and the growth rate of the instability were derived by James Jeans in 1902 and the corresponding results for an expanding medium by Georges Lemaître, Howard Robertson and Evgenii Lifshitz in the 1930s and 1940s. Their results are central to the understanding of the problems of the formation of structure in the Universe and the modern working out of their basic insights will dominate much of the discussion throughout this book.

As part of the dialogue with Bentley, Newton proposed that the stars are objects like the Sun and he made star counts in an attempt to show that the stars are indeed uniformly distributed in space. From the seventeenth century onwards, most astronomers assumed that the stars are objects similar to the Sun, but at vastly greater distances. The problem was to find means of measuring their distances. If they were assumed to have the same intrinsic luminosities as the Sun, the inverse square law could be used to estimate distances by comparing the relative brightnesses of the Sun and the distant stars. The technical problem was that the Sun is so much brighter than the brightest stars that it was difficult to make good estimates of the ratio of their observed flux densities, or apparent magnitudes. An ingenious solution was discovered in 1668 by James Gregory, who used Jupiter as an intermediate

luminosity calibrator, assuming that its light was entirely sunlight reflected from the disc of the planet and that its surface was a perfect reflector. Then, the apparent magnitudes of Jupiter and the bright star Sirius could be compared and the distance of Sirius was found to be about 83,190 astronomical units (Gregory, 1668). The same method was used by John Michell in 1767 using Saturn as an intermediary to estimate of a distance of 460,000 astronomical units for Vega, or α Lyrae.

The method of Gregory and Michell depended upon the assumption that all the stars have the same absolute luminosities. The first direct measurements of stellar distances were made by the technique of stellar parallaxes, the first successful measurement being announced in 1838 by Friedrich Bessel for the star 61 Cygni. The measurement of stellar parallaxes was however difficult and demanding technically and by 1900 only about 100 parallaxes were known for stars in the vicinity of the Sun.

1.2 The Galaxies and the Structure of our Galaxy

In his extraordinary text of 1610, the *Sidereus Nuncius* or *The Sidereal Messenger*, Galileo Galilei demonstrated that the Milky Way can be resolved into stars when observed through the telescope. These observations led to the earliest speculative cosmologies of the modern era. The ‘island universe’ model of René Descartes, published in *The World* of 1636, involved an interlocking jig-saw puzzle of solar systems. In 1750, Thomas Wright of Durham published *An Original Theory or New Hypothesis of the Universe*, in which the Sun was one of many stars which orbit the ‘Divine Centre’ of the star system. Immanuel Kant in 1755 and Johann Lambert in 1761 took these ideas further and developed the first hierarchical, or fractal, models of the Universe. Kant also made the prescient suggestion that the flattening of these ‘island universes’ was due to their rotation. The problem with these early cosmologies was that they lacked observational validation.

Towards the end of the eighteenth century, William Herschel was one of the first astronomers to attempt to define the distribution of stars in the Universe in some detail on the basis of careful astronomical observation. To determine the structure of the Milky Way, he counted the numbers of stars in different directions. Then, assuming that they all have the same intrinsic luminosities, he derived his famous picture for the structure of our Galaxy which consisting of a flattened disc of stars with diameter about five times its thickness, the Sun being located close to its centre (Fig. 1.1) (Herschel, 1785).

John Michell had already warned Herschel that the assumption that the stars have a fixed luminosity was a poor approximation. In his remarkable pioneering paper of 1767, Michell introduced statistical methods into astronomy in order to show that binary and star clusters must be real physical systems and not random associations of stars on the sky (Michell, 1767). Consequently, there must be a dispersion in the absolute luminosities of the stars from their observed range of apparent magnitudes in bright star clusters, such as the Pleiades. Despite this warning, Herschel proceeded to produce a number of different versions of his model for the structure of our Galaxy,

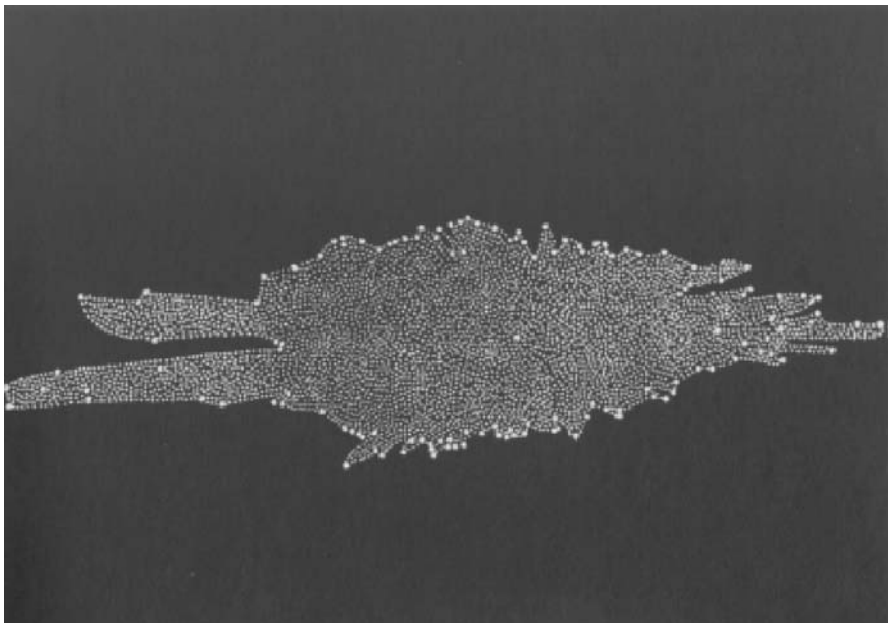


Fig. 1.1. William Herschel’s model of the Galaxy based upon star counts in different directions. The Sun is located close to the centre of the disc of stars (Herschel, 1785)

adding appendages to account for various features of the star counts in different directions.

In 1802, Herschel measured the magnitudes of visual binary stars and was forced to agree with Michell’s conclusion about the wide dispersion in the luminosities of the stars (Herschel, 1802). Equally troubling was the fact that observations with his magnificent 40-foot telescope showed that, the fainter he looked, the more stars he continued to find. There seemed to be no edge to the Galaxy and Herschel gradually lost faith in his model. In addition, the importance of interstellar extinction by dust was not appreciated – it was only in the 1930s that its central importance for studies of our own and other galaxies was fully appreciated.

Even before the discovery of the telescope, it had been realised that there exist ‘nebulous’ objects which differ from the stars in having a diffuse or fuzzy appearance. Kant, Lambert, Swedenborg and Wright argued that these objects were ‘island universes’ similar to the Milky Way, but too distant to be resolved into stars. There was, however, no observational basis for this hypothesis. Herschel also inferred that the nebulae were island universes similar to our Galaxy. A test of this picture was to show that the nebulae could be resolved into stars and he believed that this had been achieved in a number of cases. In others, he assumed that the nebulae were too distant to be resolved into individual stars. This picture came into question, however, when he discovered that, among the nebulae were the planetary nebulae, which consist of a central star surrounded by a shell of gas. Herschel recognised

that these nebulae were unlikely to be resolved into stars but rather consisted of ‘luminous fluid’ surrounding the central star.

The cataloguing of the bright nebulae was begun by Charles Messier whose catalogue of 109 objects was compiled during the years 1771 to 1784. Messier’s interest was primarily in comets and his objective in compiling the catalogue was to enable him to distinguish between diffuse nebulae and comets. The catalogue contains a mixture of what we now know are the brightest Galactic and extra-galactic nebulae and they are still commonly referred to by their Messier, or M, numbers.

The systematic cataloguing of the nebulae was begun by William Herschel and his sister Caroline and was continued through the first half of the nineteenth century by his son John Herschel. The results of these huge endeavours was the publication by John Herschel in 1864 of the *General Catalogue of Nebulae and Clusters of Stars* containing 5079 objects. These catalogues were based upon visual observations long before photography became a standard tool of the astronomer. In 1888, John Dreyer published an expanded catalogue which was known as the *New General Catalogue of Nebulae and Clusters of Stars* which, together with the two supplementary *Index Catalogues* of 1895 and 1908, contain some 15,000 objects. Objects in these catalogues are still commonly referred to by their NGC or IC numbers.

While the cataloguing of the nebulae proceeded apace, their nature remained a mystery. Undoubtedly, some of them were gas clouds, as demonstrated by William Huggins’ pioneering spectroscopic observations of diffuse nebulae in the 1860s (Huggins and Miller, 1864). The big question was whether or not the ‘spiral nebulae’ were objects within our own Galaxy or were more distant systems. These nebulae were beyond the distances at which conventional techniques of distance measurement could be used. This problem culminated in what became known as ‘The Great Debate’ and concerned two related issues. Firstly, what is the size of our own Galaxy and, secondly, are the spiral nebulae members of our Galaxy or are they separate ‘island universes’, well beyond the confines of our Galaxy? This key episode in the history of modern astronomy should be required reading for all observers and theorists (Sandage, 1961b; Hoskin, 1976; Smith, 1982; Trimble, 1995).

To illustrate the nature of the problem, by 1920, Jacobus Kapteyn had determined the luminosity function of stars near the Sun and so, from star counts in different directions, determined the structure of the Galaxy which he found to be highly flattened with dimensions 1500 pc perpendicular to the plane and about 8 times that size in the Galactic plane (Fig. 1.2) (Kapteyn, 1922).

Meanwhile, Harlow Shapley had adopted a quite different approach to the determination of Galactic structure. In 1912, Henrietta Leavitt had discovered the remarkable period–luminosity relation for Cepheid variable stars in the Magellanic Clouds (Fig. 1.3). This discovery provided a powerful means of measuring astronomical distances because the Cepheid variables are intrinsically luminous stars and their distinctive light curves can be recognised in stars in distant systems. The Cepheid variables were the tools used by Harlow Shapley to determine the structure of the Galaxy through his studies of globular clusters. He found the scale of the

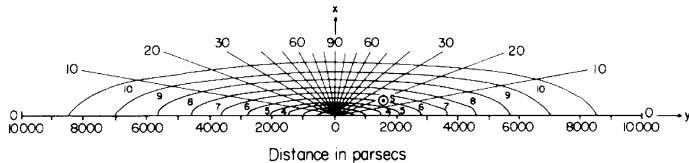


Fig. 1.2. Kapteyn's model for the distribution of stars in the Galaxy (Kapteyn, 1922). The diagram shows the distribution of stars in a plane perpendicular to the Galactic plane. The curves are lines of constant number density of stars and are in equal logarithmic steps. The Sun S is slightly displaced from the centre of the system

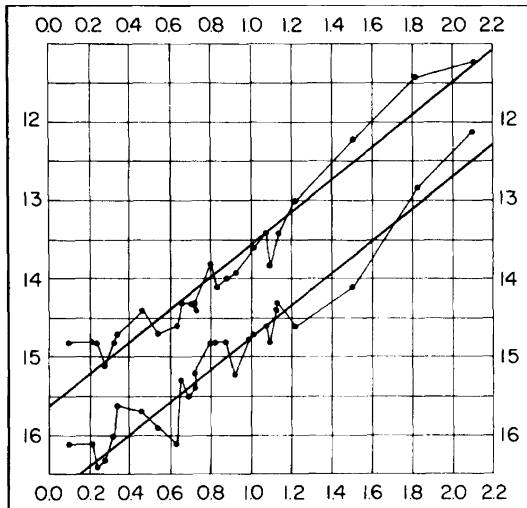


Fig. 1.3. A plot of the period-luminosity relation for the 25 Cepheid variables discovered by Leavitt in the Small Magellanic Cloud (Leavitt, 1912). The *upper locus* is found for the maximum light of the Cepheid variables and the *lower line* for their minimum brightnesses

globular cluster system to be enormous, the most distant globular cluster having a distance of 67 kpc. Furthermore, the globular cluster system was not centred upon the Solar System, but rather most of the globular clusters were found in a direction centred upon the constellation of Sagittarius (Fig. 1.4) (Shapley, 1918).

The course of the debate was complex, but the issues were resolved finally and conclusively in 1925 by Edwin Hubble's observations of Cepheid variables in the Andromeda Nebula. Using the period-luminosity relation for Cepheid variables, he established to everyone's satisfaction that the spiral nebulae are distant extragalactic systems.

Within a year, Hubble had published the first major survey of the properties of galaxies as extragalactic systems. In his remarkable paper (Hubble, 1926), he introduced an early version of his classification of galaxies into ellipticals, spirals and irregulars, estimated mass-to-light ratios for these different types of galaxies, used number counts of galaxies to show that they are uniformly distributed in space and hence estimated the mean density of matter in the Universe in the form of galaxies. Adopting Einstein's static model of the Universe, he found that the radius of curvature of its spherical geometry was 27,000 Mpc. He estimated that, with the

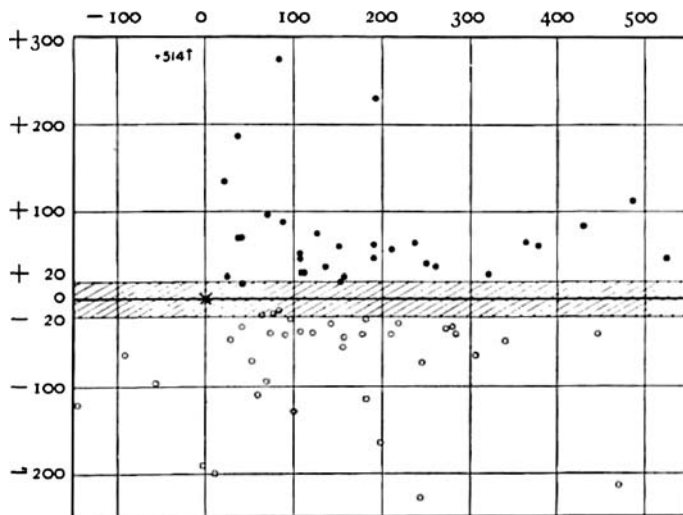


Fig. 1.4. The distribution of globular clusters in the Galaxy according to Shapley's distance measurements (Shapley, 1918). The scales on the abscissa and ordinate are in units of 100 pc and correspond to distances in and perpendicular to the Galactic plane respectively. The Sun, located at zero coordinates on the abscissa and ordinate, lies towards one edge of the globular cluster system

100-inch Hooker telescope, he could observe typical galaxies to about 1/600 of the radius of the Universe. He concluded with the remark that

... with reasonable increases in the speed of plates and sizes of telescopes, it may become possible to observe an appreciable fraction of the Einstein universe.

This paper marked the beginning of extragalactic astronomy. It comes as no surprise to learn that George Ellery Hale began his campaign to raise funds for the Palomar 200-inch telescope in 1928 – before the year was out, he had secured a grant of \$6 million from the Rockefeller Foundation for the telescope, the construction of which was completed in 1949.

In 1929, Hubble made his second fundamental contribution to cosmology. He showed that the extragalactic nebulae are all moving away from our own Galaxy and that their recessional velocities v are proportional to their distances r from our Galaxy (Fig. 1.5a) (Hubble, 1929). It is remarkable that he was able to deduce this key result from such a small sample of nearby galaxies but, within five years, he and Humason had extended the relation to very much greater velocities and distances using the apparent magnitudes of the fifth brightest members of clusters of galaxies as distance indicators (Fig. 1.5b). The velocity-distance relation $v = H_0 r$ is commonly referred to as *Hubble's law* and H_0 as *Hubble's constant*. The significance of this discovery was that, combined with the isotropy of the Universe, Hubble's law demonstrates that the whole system of galaxies is partaking in a uniform expansion.

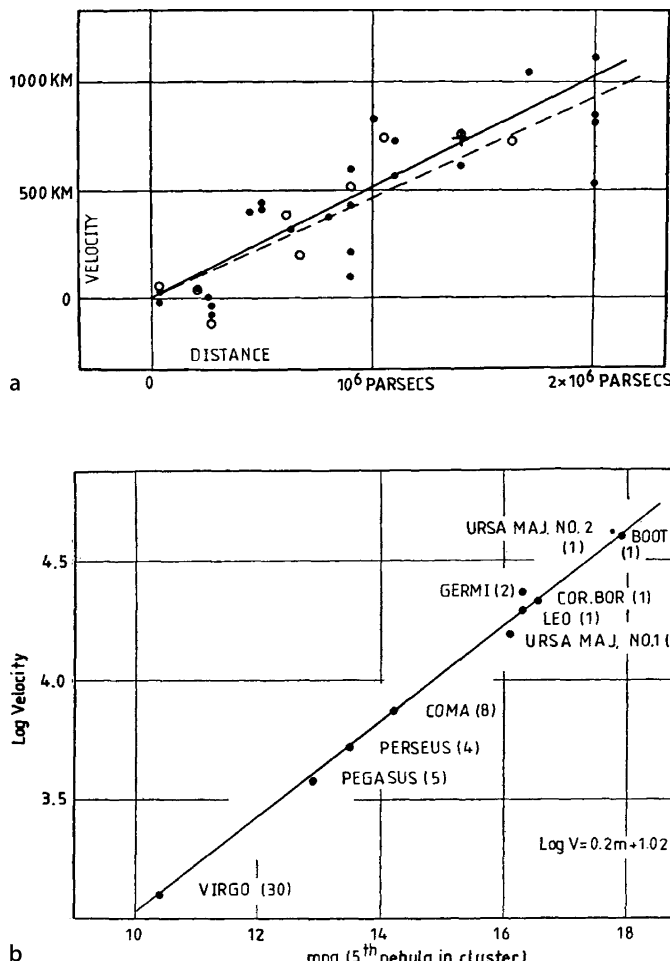


Fig. 1.5. **a** Hubble's first velocity–distance relation for nearby galaxies (Hubble, 1929). The *filled circles* and the *full line* represent a solution for the solar motion using the nebulae individually; the *open circles* and the *dashed line* represent a solution combining the nebulae into groups. The *cross* is an estimate of the mean distance of the other 20 galaxies for which radial velocities were available. **b** The velocity–apparent magnitude relation for the fifth brightest member of clusters of galaxies, corrected for galactic obscuration (Hubble and Humason, 1934). Each cluster velocity is the mean of the various individual velocities observed in the cluster, the number being indicated by the figure in brackets.

1.3 The Theory of the Expanding Universe

In Newton's *Principia Mathematica*, he emphatically took the position that all motion takes place with respect to a system of absolute space and time. He fiercely rejected the idea that the motion of a body could only be described relative to those of

other bodies. This position was challenged by Bishop Berkeley, Christiaan Huygens and others but, at least until the late nineteenth century, Newton's view prevailed. The issue was revived by Ernst Mach who argued that motion can only be defined relative to other bodies. Specifically, he took the view that the local inertial frame of reference is determined by the frame of the distant stars, or galaxies in modern parlance. Thus, a freely swinging Foucault pendulum swings in a reference frame which is fixed relative to the distant galaxies. Albert Einstein gave the name *Mach's principle* to this idea.

During the late eighteenth century, non-Euclidean geometries began to be taken seriously by mathematicians who realised that the fifth postulate of Euclid, that parallel lines meet only at infinity, might not be essential for the construction of a self-consistent geometry. Proposals that the global geometry of space might not be Euclidean were discussed by Girolamo Saccheri and Johann Lambert. In 1816, Carl Friedrich Gauss repeated this proposal in a letter to Christian Gerling and was aware of the fact that a test of the local geometry of space could be carried out by measuring the sum of the angles of a triangle between three high peaks, the Brocken, Hoherhagen and Inselberg. In 1818, Gauss was asked to carry out a geodetic survey of the state of Hanover and he devoted a large effort to carrying out and reducing the data himself. He was certainly aware of the fact that the sum of the angles of the triangle was 180° within the limits of geodetic measurements.

The fathers of non-Euclidean geometry were Nikolai Lobachevsky, who became rector of Kazan University in Russia in 1827, and János Bolyai in Transylvania, then part of Hungary. In the 1820s, they independently solved the problem of the existence of non-Euclidean geometries and showed that Euclid's fifth postulate could not be deduced from the other postulates (Lobachevsky, 1829, 1830; Bolyai, 1832). In his papers entitled *On the Principles of Geometry*, Lobachevsky also proposed an astronomical test of the geometry of space. If the geometry were hyperbolic, the minimum parallax of any object would be

$$\theta = \arctan\left(\frac{a}{\mathcal{R}}\right), \quad (1.2)$$

where a is the radius of the Earth's orbit and \mathcal{R} the radius of curvature of the geometry. He found a minimum value of $\mathcal{R} \geq 1.66 \times 10^5$ AU = 2.6 light years, using an observational upper limit of 1 arcsec for the parallax of bright stars. In a prescient statement which will warm the hearts of observational astronomers, he remarked:

There is no means other than astronomical observations for judging the exactness which attaches to the calculations of ordinary geometry.

Non-Euclidean geometries were placed on a firm theoretical basis by Bernhard Riemann, who also discovered closed spherical geometries. The English-speaking world was introduced these ideas through the works of William Clifford and Arthur Cayley. Until Albert Einstein's discovery of the General Theory of Relativity, considerations of the geometry of space and the role of gravity in defining the large-scale structure of the Universe were separate questions. After 1915, they were inextricably linked.

In that year, after a titanic intellectual struggle, Einstein discovered the definitive version of his General Theory of Relativity which describes how space–time is distorted by the presence of matter and how, in turn, matter moves along trajectories in bent space–time (Einstein, 1915, 1916). For the first time, a relativistic theory of gravity was available which enabled self-consistent models of the Universe as a whole to be constructed and, characteristically, Einstein did not hesitate to do so.

In seeking a solution of his field equations for the Universe as a whole, Einstein had explicitly in mind that Mach's principle should be incorporated into any model of the large-scale structure of the Universe. He had, however, a major problem. Without modification, the field equations predicted that the Universe was unstable. He could only find static solutions by introducing what is now known as the *cosmical* or *cosmological constant* λ , which appears as a constant in Einstein's field equations. In his great paper of 1917, Einstein showed that the introduction of the cosmological constant resulted in static solutions for the Universe as a whole which had closed, spherical geometry and a finite size (Einstein, 1917). He also believed that he had incorporated Mach's principle into General Relativity, in the sense that no solution of the equations would exist if there were no matter present. In the same year, this was, however, shown to be incorrect by Willem de Sitter, who found solutions of the equations even if there were no matter present in the Universe (de Sitter, 1917).

For many decades, the status of the cosmological constant was the subject of debate. In 1919, Einstein realised that a term involving the cosmological constant would appear in the field equations of General Relativity, quite independent of its cosmological significance (Einstein, 1919). In the derivation of the field equations, the λ -term appears as a constant of integration which is normally set equal to zero in the development of standard General Relativity. Einstein was not enthusiastic about the term, remarking that it 'detracts from the formal beauty of the theory'. Willem de Sitter wrote in 1919 that the term

... detracts from the symmetry and elegance of Einstein's original theory, one of whose chief attractions was that it explained so much without introducing any new hypotheses or empirical constant.

Others regarded it as a constant which appears in the development of the General Relativity and its value should be determined by astronomical observation.

The irony of the situation is that this debate took place *before* it was realised that the Universe is in fact non-stationary. In 1922, Aleksander Friedman published the first of two classic papers in which he discovered both static and expanding solutions of Einstein's field equations. In the first paper, Friedman found solutions for expanding universes with closed spatial geometries, including those which expand to a maximum radius and eventually collapse to a singularity (Friedman, 1922). In the second paper of 1924, he showed that there exist expanding solutions which are unbounded and which have hyperbolic geometry (Friedman, 1924). These solutions correspond exactly to the standard world models of general relativity and are known as the *Friedman world models*.

In 1925, Friedman died of typhoid in Leningrad before the fundamental significance of his work was appreciated. The neglect of Friedman's work in these early days is somewhat surprising since Einstein had commented, incorrectly as he admitted, on the first of the two papers in 1923. It was not until Georges Lemaître independently rediscovered the same solutions in 1927, and then became aware of Friedman's papers, that the pioneering nature of Friedman's contributions was appreciated (Lemaître, 1927).

Einstein's field equations without the cosmological constant contain perfectly satisfactory solutions in which the Universe is uniformly expanding. According to George Gamow, when the expansion of the Universe was discovered, Einstein regarded the introduction of the cosmological constant as 'the biggest blunder of my life' (Gamow, 1970). The cosmological constant was not consigned to oblivion for long however. As Yakov Zeldovich remarked:

The genie is out of the bottle and, once he is out, he is very difficult to put back in again.

The cosmological constant immediately found a rôle in reconciling the age of the Earth with the expansion age of the Universe as given by the inverse of Hubble's constant H_0^{-1} . If the cosmological constant is zero, all Friedman models of the Universe have ages less than H_0^{-1} . At that time, Hubble's estimate of H_0 was about $500 \text{ km s}^{-1} \text{ Mpc}^{-1}$, corresponding to $H_0^{-1} = 2 \times 10^9 \text{ years}$. This time-scale was less than the age of the Earth as determined by nucleocosmochronology, that is, from dating using long-lived radioactive isotopes. A positive value of the cosmological constant can resolve this discrepancy since its effect is to stretch out the expansion time-scale of the Universe, a picture advocated by Arthur Eddington and Lemaître. It turned out that Hubble's estimate of H_0 was seriously overestimated and, following revisions in the 1950s by Walter Baade and Allan Sandage, this conflict was eliminated. Despite the fact that the cosmological constant appeared to be no longer necessary, it made regular appearances in the literature to account for various features of cosmological data, but these pieces of evidence were not compelling. Then, during the period 1995 to 2005, convincing evidence for a positive value of the cosmological constant was found from studies of very distant Type 1a supernovae and from determinations of the power spectrum of fluctuations in the Cosmic Microwave Background Radiation.

As the standard models of General Relativity became better understood, a major thrust of cosmological research became the determination of the large-scale dynamical and geometrical properties of the Universe – its rate of expansion, its deceleration, its mean density, its geometry and its age. These remained among the most difficult programmes of modern observational cosmology until, in the first years of the twenty-first century, precise estimates became available using techniques undreamt of by the pioneers of geometrical cosmology.

1.4 The Big Bang

The next major advance occurred soon after the Second World War when George Gamow realised that, in an expanding Universe, the early stages must have been very hot indeed – the temperature was so high that the dynamics of the expansion were dominated by the energy density of thermal radiation rather than by its matter content, in other words, the Universe was radiation-dominated. Following an earlier suggestion of Lemaître, he attempted to explain the origin of the chemical elements by *primordial nucleosynthesis*, that is, by nuclear fusion processes as the Universe cooled down from its very hot initial stages. The reasons for adopting this picture were twofold. Firstly, following the work of Cecilia Payne, the abundances of the chemical elements in stars seemed to be remarkably uniform and secondly it was thought that the central temperatures of the stars were not high enough for nucleosynthesis to take place. Gamow's programme was not successful because of the problem of synthesising elements heavier than helium – there are no stable isotopes with atomic mass numbers 5 and 8. Therefore, in the short time-scales available in the hot early phases of the expansion, there was not time to synthesis elements heavier than helium. Gamow's coworkers Ralph Alpher and Robert Herman showed that only deuterium, helium-3 and helium-4 were created in significant quantities (Fig. 1.6) (Alpher and Herman, 1950).

In the course of their calculations, Alpher and Herman worked out the thermal history of the Universe in some detail and predicted that there should be present in the Universe today a diffuse background of black-body radiation with temperature about 5 K, the cooled remnant of its very hot early phases (Alpher and Herman, 1948). The detection of this background radiation was far beyond the capabilities of the technology of the 1940s and the lack of success of Gamow's programme of primordial nucleosynthesis resulted in the neglect of this key prediction for many years. Furthermore, in the 1950s, Fred Hoyle discovered the triple- α resonance, which leads to the formation of carbon from three helium nuclei (Hoyle, 1954). Soon after, he and his colleagues, Margaret Burbidge, Geoffrey Burbidge and William Fowler, showed how the heavy elements could be accounted for by nucleosynthesis in stars (Burbidge et al., 1957).

Interest in what is now referred to as the *Big Bang* model of the Universe grew steadily through the 1950s and early 1960s as evidence was found for cosmological evolutionary effects in the distribution of faint radio sources (Ryle, 1955, 1958). On the theoretical side, interest was rekindled in the question of the synthesis of elements in the early Universe, not now with a view to creating all the elements, but rather to account for the cosmic abundance of helium. By 1964, it was appreciated that, wherever helium could be observed in the Universe, it is present with a very high chemical abundance, about 24% by mass. This figure far exceeded what could be explained by stellar nucleosynthesis. I remember vividly attending a course of post-graduate lectures given by Fred Hoyle in Cambridge in 1964 entitled *Problems of Extragalactic Astrophysics* in which this problem was discussed. During the lecture course, Hoyle, Roger Tayler, and John Faulkner carried out detailed computations of the expected abundance of helium produced by primordial nucleosynthesis. Within

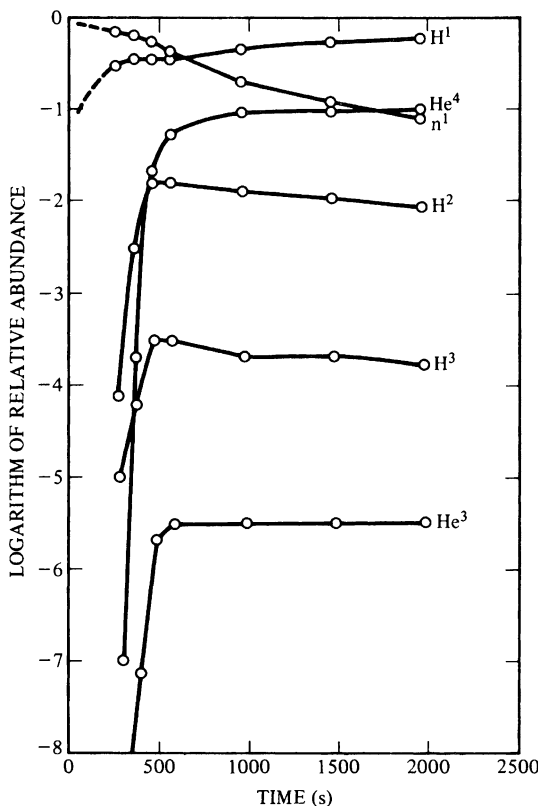


Fig. 1.6. The evolution of the fraction (by number) of the light nuclei in a radiation-dominated Universe, according to calculations by Fermi and Turkevich and published by Alpher and Herman in 1950 (Alpher and Herman, 1950). The models began with 100% of the material in the form of neutrons. The tritium 3H and neutrons shown surviving to 2000 seconds decay radioactively with half-lives of 12.46 years and 10.25 minutes respectively

a week of the topic being raised, they had shown that about 23 to 25% of helium by mass is created by this process and that the percentage is remarkably independent of the precise initial conditions. The paper by Hoyle and Tayler was published in *Nature* in 1964 (Hoyle and Tayler, 1964). Subsequent more detailed calculations by Robert Wagoner, Fowler and Hoyle confirmed these conclusions and suggested that other elements which are difficult to account for by stellar nucleosynthesis, the light isotope of helium, 3He , deuterium, D, and lithium, 7Li , could also be accounted for in this way (Wagoner et al., 1967). Equally important, the success of these computations resulted in an upper limit to the mean baryon mass density of the Universe of about one tenth the critical density – if the density were any higher, less than the observed abundances of deuterium and helium-3 would be created primordially.

By the early 1960s, as the sensitivity of receivers for centimetre wavelengths improved, it became feasible to search for the cool background radiation left over from the early stages of the Big Bang. The predicted remnant of the Big Bang was discovered, more or less by accident, by Arno Penzias and Robert Wilson in 1965 (Penzias and Wilson, 1965). The *Cosmic Microwave Background Radiation* was the second key discovery of twentieth century observational cosmology. Observations by the Cosmic Background Explorer (COBE), launched in 1989, showed that, away

from the Galactic plane, the radiation is uniform over the sky to better than one part in 100,000 on angular scales greater than 7° and that its spectrum is of black-body form with a quite remarkable precision (Smoot et al., 1992; Fixsen et al., 1996). These observations provided compelling evidence that our Universe went through a very hot, dense phase when the matter and radiation were in thermal equilibrium in its early stages.

The upshot of these discoveries was that there were four independent pieces of evidence for the Big Bang picture of the origin and evolution of our Universe. Firstly, the expansion of the distribution of galaxies discovered by Hubble; secondly, the black-body spectrum and isotropy of the Cosmic Microwave Background Radiation; thirdly, the formation of the light elements by primordial nucleosynthesis; and fourthly, the fact that the ages of the oldest stars and nucleochronology ages were of the same order as the expansion age of the Universe. Thus, the Big Bang provided a natural framework within which to tackle the problems of galaxy and structure formation.

1.5 Galaxy and Structure Formation

The Friedman world models are isotropic and homogeneous and so the enormous diversity of structure we observe in the Universe today is absent. The next step in developing more realistic models of the Universe is to include small density perturbations into the homogeneous, isotropic models and study their development under gravity. For the case of a stationary medium, this problem was solved by James Jeans in 1902 (Jeans, 1902). The criterion for collapse is that the size of the perturbation should exceed the *Jeans' length* $\lambda_J = c_s/(G\varrho_0/\pi)^{1/2}$, where c_s is the speed of sound in the medium and ϱ_0 its density. On scales greater than the Jeans' length, the instability grows exponentially. The physical meaning of the instability criterion is that, on large enough scales, the gravitational force of attraction by the matter of the perturbation exceeds the pressure gradients which resist collapse.

The analysis was repeated for the case of an expanding medium in the 1930s by Lemaître and by Richard Tolman for the case of spherically symmetric perturbations (Lemaître, 1933; Tolman, 1934) and the solution for the general case was found by Evgenii Lifshitz in 1946 (Lifshitz, 1946). Lifshitz found that the condition for gravitational collapse is exactly the same as the Jeans' criterion at any epoch but, crucially, the growth-rate of the density perturbations is no longer exponential but only algebraic. For a Universe with the critical density, $\Omega_0 = 1$ or $\varrho_0 = 3H_0^2/8\pi G$, the density contrast $\Delta = \delta\varrho/\varrho$ grows with time as $\Delta \propto t^{2/3}$. The implication of this result is that the fluctuations from which the large-scale structure of the Universe formed cannot have grown from infinitesimal random perturbations. For this reason, Lemaître, Tolman and Lifshitz inferred that galaxies could not have formed by gravitational collapse.

From the early 1960s onwards, other authors took the point of view that the solution to the problem was to include finite perturbations into the model of the early Universe and then follow in detail how their mass spectrum would evolve with time.

The Moscow school led by Yakov Zeldovich, Igor Novikov and their colleagues and James Peebles at Princeton pioneered this approach to the study of the development of structure in the Universe. If perturbations on a particular physical scale are tracked backwards into the past, at some large redshift, the scale of the perturbation is equal to the *horizon scale*, that is $r \approx ct$, where t is the age of the Universe. In 1964, Novikov showed that, to form structures on the scales of galaxies and clusters of galaxies, the density perturbations on the scale of the horizon had to have amplitude $\Delta = \delta\varrho/\varrho \sim 10^{-4}$ in order to guarantee the formation of galaxies by the present epoch (Novikov, 1964). These were certainly *not* infinitesimal perturbations and their origin had to be ascribed to processes occurring in the very early Universe.

The discovery of the Cosmic Microwave Background Radiation in 1965 had an immediate impact upon these studies since the thermal history of the pre-galactic gas could be worked out in detail and this was essential in order to determine how the speed of sound, and hence the Jeans' length, varied with cosmic epoch. If there is no energy input into the background radiation, the temperature of the thermal background radiation changes with scale factor a as $T = T_0/a = T_0(1+z)$, where z is redshift, exactly as in the adiabatic expansion of a photon gas. Therefore, at redshifts $z \sim 1500$, the temperature of the radiation was about 4000 K, at which temperature there were sufficient photons in the Wien region of the Planck distribution to ionise all the intergalactic hydrogen. This epoch is referred to as the *epoch of recombination* and at earlier epochs the hydrogen was fully ionised; at a correspondingly earlier epoch, the primordial helium was ionised as well. Somewhat earlier than the epoch of recombination, the inertial mass density of the radiation was equal to the mass density of the matter, $\varrho c^2 = aT^4$, and so, at times earlier than the *epoch of matter and radiation equality*, the dynamics of the Universe were radiation-dominated.

The coupling of matter and radiation by electron scattering was worked out by Ray Weymann in 1966 and in much more detail by Zeldovich and Rashid Sunyaev in 1969 (Weymann, 1966; Zeldovich and Sunyaev, 1969). The pioneering papers by Zeldovich and Sunyaev were based upon the theory of induced Compton scattering which had been published by Aleksander Kompaneets in 1956, long after this remarkable classified work had been completed (Kompaneets, 1956). What these papers showed was that, during the radiation-dominated epochs, the matter and radiation were maintained in very close thermal contact by Compton scattering as long as the intergalactic gas remained ionised. This enabled the speed of sound to be determined at all epochs before the epoch of recombination. Therefore, the evolution of the Jeans' length and the mass of baryonic matter within this length, what is known as the *Jeans' mass*, could be evaluated.

In 1968, Joseph Silk showed that, during the pre-recombination epochs, sound waves in the radiation-dominated plasma were damped by repeated electron scatterings (Silk, 1968). The effect of this damping was to dissipate fluctuations with masses less than about $10^{12} M_\odot$, a mass known as the *Silk mass*, by the epoch of recombination. Consequently, all fine-scale structure would be wiped out and only large-scale structures on the scale of large galaxies and clusters of galaxies could form after recombination. In the early 1970s, Zeldovich and Edward Harrison independently put together information about the spectrum of the initial fluctuations on

different physical scales and showed that observed structures in the Universe could be accounted for if the mass fluctuation spectrum had the form $\Delta(M) \propto M^{-2/3}$ in the very early Universe, corresponding to a power spectrum of initial fluctuations of the form $|\Delta_k|^2 \propto k^n$ with $n = 1$. The amplitude of this scale-free power spectrum, known as the *Harrison–Zeldovich spectrum of initial perturbations*, was inferred to be $\sim 10^{-4}$ (Harrison, 1970; Zeldovich, 1972).

A key test of these models was provided by the fact that density fluctuations at the epoch of recombination should leave some imprint upon the intensity distribution of the Cosmic Microwave Background Radiation on the sky. In the simplest picture, if the process of recombination were instantaneous, adiabatic perturbations would be expected to result in temperature fluctuations $\Delta T/T = \frac{1}{3}\Delta\phi/c^2 = \frac{1}{3}\Delta\rho/\rho$ on large physical scales associated with large-scale gravitational perturbations, an effect known as the *Sachs–Wolfe effect* (Sachs and Wolfe, 1967). In fact, the problem is somewhat more complicated than this, partly because the process of recombination is not instantaneous and because other physical processes come into play on angular scales of about 1° and less. These include the adiabatic compression of the perturbations and first-order Doppler scattering due to the collapse of the primordial perturbations. These predictions provided a challenge for the observers since the amplitudes of the temperature fluctuations in these early theories were in the range $\Delta T/T \sim 10^{-3} - 10^{-4}$, well within the capability of sensitive anisotropy measurements of the Cosmic Microwave Background Radiation.

In the 1970s, these concepts gave rise to two principal scenarios for the formation of structure in the Universe. The first, known as the *adiabatic* model, was based upon a picture in which the perturbations were adiabatic sound waves before the epoch of recombination and structure in the Universe formed by the fragmentation of large-scale structures which reached amplitude $\delta\rho/\rho \sim 1$ at relatively late epochs. A realisation of this scenario was described by Andrei Doroshkevich, Sunyaev and Zeldovich in 1974 (Doroshkevich et al., 1974).

An alternative picture was one in which the perturbations were not sound waves but *isothermal* perturbations in pressure balance with the background radiation in the pre-recombination plasma. Small mass perturbations were not damped in this picture and so perturbations on all scales survived to the recombination epoch. After that epoch, the Jeans' mass dropped to about $10^6 M_\odot$, corresponding roughly to the masses of globular clusters. Galaxies and clusters of galaxies then formed by the process of *hierarchical clustering* under the influence of perturbations on larger physical scales.

Both models predicted similar amplitudes for the density perturbations at the epoch of recombination on large physical scales and consequently similar temperature perturbations in the Cosmic Microwave Background Radiation. Their subsequent behaviour was, however, quite different. The adiabatic picture could be thought of as a ‘top-down’ process of galaxy formation in which the largest scale structures formed first and then smaller scale structures formed by a process of fragmentation. In contrast, the isothermal picture corresponded to a ‘bottom-up’ process in which small-scale objects came together to form larger structures by hierarchical clustering. In the adiabatic picture, galaxies, stars and the chemical elements all formed at

relatively late epochs, whereas in the isothermal picture, they could begin to form at very much earlier cosmic epochs.

Throughout the 1970s increasingly sensitive searches were made for temperature fluctuations in the Cosmic Microwave Background Radiation, these observations being analysed critically by Bruce Partridge in his review of 1980 (Partridge, 1980a). His own observations had reached sensitivities of $\Delta T/T \approx 10^{-4}$ or slightly better by that time (Partridge, 1980b). Models with low density parameters were in serious conflict with these upper limits because, in these, there is relatively little growth of the perturbations after the epoch of recombination. Thus, by the early 1980s, the upper limits to the intensity fluctuations in the Cosmic Microwave Background Radiation were beginning to constrain severely purely baryonic theories of structure formation. Furthermore, the limits to the density parameter in the form of baryons from primordial nucleosynthesis arguments showed that, if the density of matter in the Universe were close to the critical density, most of the matter in the Universe would have to be in some non-baryonic form.

1.6 Hot and Cold Dark Matter

A solution to these problems appeared in 1980 when Valentin Lyubimov and his collaborators reported experiments which suggested that the electron neutrino had a finite rest mass of about 30 eV (Lyubimov et al., 1980). In 1966, Semion Gershtein and Zeldovich had noted that relic neutrinos of finite rest mass could make an appreciable contribution to the mass density of the Universe (Gershtein and Zeldovich, 1966) and, in the 1970s, Györgi Marx and Alex Szalay had considered the role of neutrinos of finite rest mass as candidates for the dark matter, as well as studying their role in galaxy formation (Marx and Szalay, 1972). The intriguing aspect of Lyubimov's result was that, if the relic neutrinos had this rest mass, the Universe would just be closed, $\Omega_0 = 1$.

Zeldovich and his colleagues developed a new version of the adiabatic model in which the Universe was dominated by neutrinos with finite rest mass (Doroshkevich et al., 1980). Neutrino fluctuations would begin to grow as soon as they became non-relativistic but, since the neutrinos are very weakly interacting particles, they would stream freely out of the perturbations and so small-scale density perturbations would be quickly damped out. The closely coupled matter and radiation density fluctuations would oscillate at a low level during the pre-recombination era but, after recombination, the baryonic matter would fall into the larger amplitude neutrino fluctuations and then evolve more or less as in the standard adiabatic scenario. Because of the free-streaming of the neutrinos, however, only the very largest scale perturbations with masses $M \geq 10^{16} M_\odot$ would survive to the epoch of recombination and so, just as in the adiabatic model, the largest scale perturbations would form first and then smaller scale structures form by the process of fragmentation. This model had the great advantage of reducing very significantly the expected amplitude of temperature fluctuations in the Cosmic Microwave Background Radiation since the perturbations

in the baryonic matter would be of low amplitude during the critical phases when the background photons were last scattered.

In 1970, Zeldovich discovered a solution for the non-linear development of a collapsing cloud and used it to show that large-scale perturbations would collapse into sheets and pancakes which resemble the large-scale filamentary structure seen in the distribution of galaxies (Zeldovich, 1970). This scenario for galaxy formation became known as the *Hot Dark Matter* picture since the neutrinos were relativistic when they decoupled from the primordial plasma.

There were, however, concerns about this picture. First of all, there were reservations about the experiments which claimed to have measured the rest mass of the electron neutrino and it appears that Lyubimov's results were erroneous – the present upper limit to the rest mass of the electron neutrino is a few electronvolts. Secondly, constraints could be set to the masses of the neutrinos if they were to constitute the dark matter in galaxies, groups and clusters of galaxies. In 1979, James Gunn and Scott Tremaine showed how the phase space constraints associated with fermions such as neutrinos could be used to set lower limits to their masses (Tremaine and Gunn, 1979). While 30 eV neutrinos could bind clusters and the haloes of giant galaxies, those needed to bind dwarf galaxies would have to have masses much greater than 30 eV. This was not necessarily a fatal flaw because it could be that some other form of dark matter was present in the haloes of the dwarf galaxies.

There was also the realisation about this time that there were several alternative possibilities for the dark matter which came from theories of elementary particles. Examples included the axions, supersymmetric particles such as the gravitino or photino and ultraweakly interacting neutrino-like particles, all of which would be relics of the very early Universe. The period 1980 to 1982 marked the period when the particle physicists began to take the early Universe very seriously as a laboratory for particle physics. According to James Peebles, Richard Bond introduced the term *Cold Dark Matter* in 1982 to encompass many of the exotic types of particle suggested by particle physicists. The matter was ‘cold’ in the sense that these particles decoupled from the thermal background after they had become non-relativistic.

The Cold Dark Matter scenario is similar in many ways to the isothermal model. Since the matter is very cold, perturbations are not destroyed by free streaming. Fluctuations on all scales can survive and so, when the pre-recombination Universe became matter dominated, these perturbations began to grow, decoupled from the matter and radiation. As in the Hot Dark Matter scenario, after the epoch of recombination, the baryonic matter collapsed into the growing potential wells in the dark matter and galaxies, groups and clusters formed by hierarchical clustering. In 1982, Peebles demonstrated how the presence of such particles could reduce the amplitude of the predicted fluctuations in the Cosmic Microwave Background Radiation to levels consistent with the observational upper limits (Peebles, 1982). A remarkably useful formalism for the process of hierarchical clustering was described by William Press and Paul Schechter in 1974 which gives a good description of how the mass function of objects of different masses evolves with time (Press and Schechter, 1974).

These alternative dark matter scenarios for galaxy formation were the subject of a great deal of analysis and computer simulation during the 1980s. The Hot Dark Matter picture tended to predict too much power in large-scale structures, while the Cold Dark Matter models predicted too little (Frenk, 1986). One of the most important predictions of these models was that temperature fluctuations in the Cosmic Microwave Background Radiation should be detected at the level of about one part in 10^5 and these were detected in 1992 by the COBE satellite. Fluctuations on angular scales $\theta \geq 7^\circ$ were discovered with amplitude $\Delta I/I \approx 10^{-5}$ by George Smoot and his colleagues (Smoot et al., 1992). These fluctuations correspond to physical dimensions about ten times the size of the largest holes and voids observed in the distribution of galaxies. On these large angular scales, the source of intensity fluctuations is the Sachs–Wolfe effect, that is, the gravitational redshift associated with photons originating from within the density fluctuations at the last scattering surface (Sachs and Wolfe, 1967). It can be shown that the Harrison–Zeldovich spectrum with $n = 1$ results in temperature fluctuations which are independent of angular scale for all scales greater than a few degrees, consistent with the COBE observations.

The Cold Dark Matter model became the preferred picture for galaxy and structure formation, but it needed patching up to achieve consistency with all the observations. Viable models were constructed which include a tilted power spectrum of the initial fluctuations as compared with the standard Harrison–Zeldovich spectrum, others included the cosmological constant or decaying neutrinos, yet others considered a mixture of Hot and Cold Dark Matter and others considered that the Universe might be open. All the models included *biasing* of the distribution of visible matter relative to that of the dominant dark matter, which defined the large-scale structure of the distribution of galaxies (Turok, 1997).

The picture changed dramatically in the final years of the twentieth century and the first few years of the twenty-first. Firstly, the Type 1a supernovae were found to be excellent ‘standard candles’ for the estimation of cosmological distances. The redshift–magnitude relation for these supernovae strongly suggested that the cosmological constant was not zero, but had a large positive value, the best-fitting value corresponding to a density parameter of what became known as the *dark energy* of $\Omega_A \approx 0.7$ (Knop et al., 2003; Tonry et al., 2003).

Equally important were experiments to determine the detailed power spectrum of temperature fluctuations in the Cosmic Microwave Background Radiation which were predicted to display prominent maxima on angular scales less than 1° . The predictions were refined in the context of the baryonic adiabatic and isothermal models by Sunyaev and Zeldovich in 1970 (Sunyaev and Zeldovich, 1970). It was realised that these *acoustic* fluctuations contain a great deal of information about the large-scale properties of the Universe and a number of experimental groups made very large efforts to pin down the exact shape of their power spectrum. Strong evidence for these oscillations were found in these experiments, but these endeavours were largely superseded by the first-year results of the Wilkinson Microwave Anisotropy Probe (Bennett et al., 2003). These defined in exquisite detail the power spectrum of the fluctuations in the Cosmic Microwave Background Radiation and

enabled remarkably precise estimates of cosmological parameters to be made, particularly when combined with the results of large-scale galaxy surveys such as the Anglo-Australian Telescope 2dF Survey and the Sloan Digital Sky Survey. These observations demonstrated beyond doubt that the large-scale geometry of the Universe is very close to flat, that the density parameter in dark and baryonic matter is close to 0.28 and that the density parameter in the dark energy is close to 0.72 (Tegmark et al., 2004). What is particularly impressive about these results is that they are entirely consistent with many independent astronomical estimates of the cosmological parameters. This has given rise to the concept of the *concordance values* of the cosmological parameters, a set of parameters which, within the quoted uncertainties, are in agreement with all the best estimates of their values.

From the perspective of galaxy and structure formation, the good news was that these achievements incorporate naturally the formation of structure according to the standard Λ CDM model with no biasing. Equally impressive was the fact that the determination of the two-point correlation function for galaxies determined from the large-scale galaxy surveys now overlapped the corresponding angular scales in the Cosmic Microwave Background Radiation and that these were in excellent agreement. In the most recent analyses, evidence has been found for a maximum in the two-point correlation function for galaxies corresponding to the first peak in the power spectrum of perturbations in the Cosmic Microwave Background Radiation.

The upshot of these remarkable developments is that we have now entered the era of precision cosmology in which cosmological parameters can be estimated with confidence to better than 5% and much deeper cosmological questions can be addressed by the present and future generations of observations and experiments.

1.7 The Very Early Universe

Despite the undoubted success of the concordance model, it raises as many problems as it solves. The picture is incomplete in the sense that, within the context of the standard world models, the initial conditions have to be put in by hand in order to create the Universe as we observe it today. How did these initial conditions arise? The resolution of these problems will undoubtedly give insight into the laws of physics under physical conditions which at the moment can only be studied by cosmological observations.

- *The horizon problem.* This problem can be restated, ‘Why is the Universe so isotropic?’ (Dicke, 1961). At earlier cosmological epochs, the particle horizon $r \sim ct$ encompassed less and less mass and so the scale over which particles could be causally connected became smaller and smaller. A vivid example of this problem is to work out how far light could have travelled along the last scattering layer at $z = 1000$ since the Big Bang. Regions of the sky separated by angular distances greater than 2° could not have been in causal communication. Why then is the Cosmic Microwave Background Radiation so isotropic?

- *The flatness problem.* This problem arises from the fact that, according to the standard world models, if the Universe were set up with a value of the density parameter differing even slightly from the critical value $\Omega_0 = 1$, it would diverge very rapidly from $\Omega_0 = 1$ at later epochs (Dicke, 1961; Dicke and Peebles, 1979). There is nothing in the standard world models that would lead us to prefer any particular value of Ω_0 . Why then in the density parameter close to one today? This is sometimes referred to as the *fine-tuning problem*.
- *The baryon asymmetry problem.* The baryon asymmetry problem arises from the fact that the photon-to-baryon ratio today is $N_\gamma/N_B \approx 10^9$. If photons were neither created or destroyed, this ratio is conserved as the Universe expands. At temperature $T \approx 10^{10}$ K, electron–positron pair production takes place from the photon field. At a correspondingly higher temperature, baryon–antibaryon pair production takes place with the result that there must have been a very small asymmetry in the baryon–antibaryon ratio in the very early Universe if we are to end up with the correct photon-to-baryon ratio at the present day. If the Universe had been symmetric with respect to matter and antimatter, the photon-to-baryon ratio would now be about 10^{18} , in gross contradiction with the observed value (Zeldovich, 1965). Therefore, there must be some mechanism in the early Universe which results in a slight asymmetry between matter and antimatter.
- *The primordial fluctuation problem.* What was the origin of the density fluctuations from which galaxies and large-scale structures formed? The amplitudes of the density perturbations when they came through the horizon had to be of finite amplitude, $\Delta = \delta\varrho/\varrho \sim 10^{-4}$, on a very wide range of mass scales. These cannot have originated as statistical fluctuations in the numbers of particles on, say, the scales of superclusters of galaxies. There must have been some physical mechanism which generated finite amplitude perturbations with power spectrum close to $P(k) \propto k$ in the early Universe.
- *The values of the cosmological parameters.* The horizon and flatness problems were recognised before compelling evidence was found for the finite value of the cosmological constant, or in modern parlance, the density parameter of the dark energy Ω_Λ . The Universe seems to be geometrically flat and so the sum of the density parameters in the matter and the dark energy must sum to unity, $\Omega_\Lambda + \Omega_m = 0.72 + 0.28 = 1$. Even if the sum of these two parameters were not precisely unity, it is a surprise that the two parameters are of the same order of magnitude at the present epoch because the matter density evolves with redshift as $(1+z)^3$, while the dark energy density parameter is unchanging with cosmic epoch. Why then do we live at an epoch when they have more or less the same value?

A further problem concerns the present value of the density parameter of the dark energy Ω_Λ which can be estimated using simple concepts from quantum field theory. The value found is about 10^{120} times greater than permissible values at the present epoch. This is quite a problem, but it should not be passed over lightly. If the inflationary picture of the very early Universe is taken seriously, this is exactly the type of force which drove the inflationary expansion.

- *The nature of dark matter and dark energy.* As if these problems were not serious enough, they are compounded by the fact that the nature of the dark matter and the dark energy are unknown. One of the consequences of precision cosmology is the troubling result that we do not understand the nature of about 95% of the material which drives the large-scale dynamics of the Universe.

The first suggestion that some of these problems might be resolved by appeal to particle physics was made by Sakharov in 1967 who suggested that the baryon–antibaryon asymmetry might be associated with the type of symmetry-breaking observed in the decays of the K mesons, in other words, that the asymmetry is associated with the type of symmetry-breaking which occurs in Grand Unified Theories of elementary particles in the early Universe (Sakharov, 1967).

The most important conceptual development for contemporary cosmology came in 1981 with Alan Guth's proposal of the *inflationary model* for the very early Universe (Guth, 1981). There had been earlier suggestions foreshadowing his proposal. For example, Zeldovich had noted in 1968 that there is a physical interpretation of the cosmological constant Λ associated with the zero-point fluctuations of a vacuum. Andrei Linde in 1974 and Sydney Bludman and Malvin Ruderman in 1977 had shown that the scalar Higgs fields, which had been introduced to give the W^\pm and Z^0 particles mass, have similar properties to those which would result in a positive cosmological constant.

In Guth's paper of 1981, he realised that if the Universe went through an early exponential expansion phase, this would solve both the problem of the isotropy of the Universe on a large scale and would also drive the Universe towards a flat spatial geometry. The effects of the exponential expansion is to drive neighbouring particles apart at an exponentially increasing rate so that, although they were in causal contact in the very early Universe, the exponential inflation quickly moves them far beyond their local horizons and can account for the large-scale isotropy of the Universe by the end of the inflation epoch. The exponential expansion also straightens out the geometry of the Universe, however curved it may have been in its initial stages. At the end of this phase of exponential inflation, the Universe transforms into the standard Friedman world model, which, since it has very precisely flat geometry, must have $\Omega_0 = 1$. In Guth's original picture, the transformation to the Friedman solution took place through a first-order phase transition but this created too many magnetic monopoles. The model was revised in 1982 by Linde and by Andreas Albrecht and Paul Steinhardt who showed how the transition to the Friedman solutions could be smooth and continuous and so avoid many of the problems associated with Guth's proposal (Linde, 1982, 1983; Albrecht and Steinhardt, 1982).

The original hope that a physical realisation for the inflationary expansion could be found within the context of particle physics beyond the standard model has not been achieved, but the underlying concepts of the inflationary picture have been used to define the necessary properties of the *inflaton* potential needed to create the Universe as we know it.

Since 1982, the inflationary scenario for the early evolution of the Universe between the epochs when it was only 10^{-34} to 10^{-32} seconds old has been studied

very intensively. Among the further successes claimed for the theory has been the realisation that quantum fluctuations in the fields which drive the inflation are also amplified during the inflationary era. In 1977, Stephen Hawking and Gary Gibbons worked out the important result that quantum fluctuations in expanding de Sitter space produce thermal radiation with a well-defined temperature (Gibbons and Hawking, 1977). This acted as a stimulus to apply similar ideas to the new inflationary picture with a view to estimating the perturbation spectrum. Following the 1982 Nuffield Workshop held in Cambridge, the key result was established that the spectrum of quantum fluctuations of the vacuum Higgs fields were scale-free and result naturally in adiabatic curvature perturbations with spectrum strikingly similar to the Harrison–Zeldovich spectrum with $n \approx 1$ (Gibbons et al., 1983). According to Andrew Liddle and David Lyth:

Although introduced to resolve problems associated with the initial conditions needed for the Big Bang cosmology, inflation's lasting prominence is owed to a property discovered soon after its introduction. It provides a possible explanation for the initial inhomogeneities in the Universe that are believed to have led to all the structures we see, from the earliest objects formed to the clustering of galaxies to the observed irregularities in the microwave background (Liddle and Lyth, 2000).

2 The Large-Scale Structure of the Universe

Our current picture of how matter and radiation are distributed in the Universe on a large scale is derived from a wide variety of different types of observation. In this chapter, we concentrate upon the large-scale distribution of matter and radiation in the Universe and discuss galaxies and clusters of galaxies in Chaps. 3 and 4 respectively. The observations described in this chapter provide much of the essential underpinning of modern cosmological research.

2.1 The Spectrum and Isotropy of the Cosmic Microwave Background Radiation

On the very largest scales, the best evidence for the overall isotropy of the Universe is provided by observations of the *Cosmic Microwave Background Radiation*. This intense diffuse background radiation in the centimetre, millimetre and submillimetre wavebands was discovered in 1965 by Penzias and Wilson whilst commissioning a sensitive maser receiver system for centimetre wavelengths at the Bell Telephone Laboratories (Penzias and Wilson, 1965). It was soon established that this radiation is remarkably uniform over the sky and that, in the wavelength range $1\text{ m} > \lambda > 1\text{ cm}$, the intensity spectrum had the form $I_\nu \propto \nu^2$, corresponding to the Rayleigh–Jeans region of a black-body spectrum at a radiation temperature of about 2.7 K.

The maximum intensity of a black-body spectrum at a radiation temperature of 2.7 K occurs at a wavelength of about 1 mm at which atmospheric emission makes precise absolute measurements of the background spectrum from the surface of the Earth very difficult indeed. During the 1970s and 1980s several high-altitude balloon experiments carrying millimetre and submillimetre spectrometers were flown and evidence found for the expected turn-over in the Wien region of the spectrum, but there were discrepancies between the experiments (Weiss, 1980). The only satisfactory approach for determining the detailed spectrum and isotropy of the Cosmic Background Radiation over the whole sky was to place the receiver system in a satellite above the Earth's atmosphere and this was achieved by the Cosmic Background Explorer (COBE) of NASA which was launched in November 1989. This mission was dedicated to studies of the background radiation, not only in the millimetre and submillimetre wavebands, but also throughout the infrared waveband from 2 to 1000 μm .

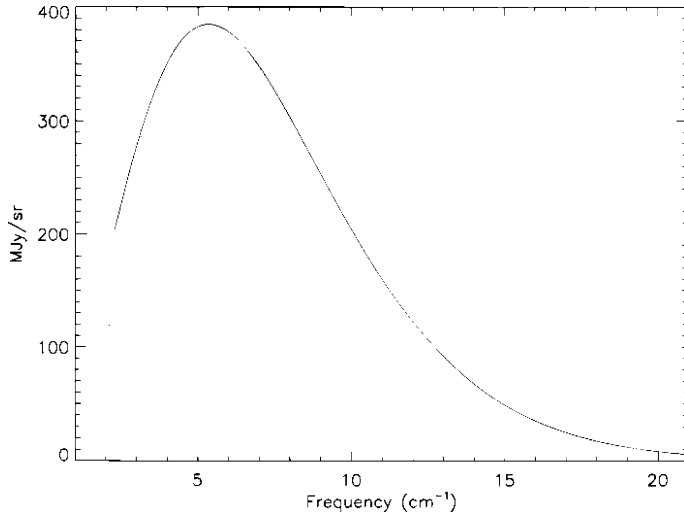


Fig. 2.1. The final spectrum of the Cosmic Microwave Background Radiation as measured by the COBE satellite (Fixsen et al., 1996). The units of the abscissa are inverse centimetres, so that 10 units corresponds to 1 mm and 5 to 2 mm. Uncertainties are a small fraction of the line thickness. Within the quoted errors, the spectrum is precisely that of a perfect black-body at radiation temperature $T = 2.728 \pm 0.002$ K

2.1.1 The Spectrum of the Cosmic Microwave Background Radiation

The Far Infrared Absolute Spectrophotometer (FIRAS) of COBE measured the *spectrum* of the Cosmic Microwave Background Radiation in the wavelength range 0.5 to 2.5 mm with very high precision during the first year of the mission. The FIRAS detectors and a reference black-body source were cooled to liquid helium temperatures and there was sufficient liquid cryogen for only one year of observation. Particular care was taken over the thermometry involved in making such absolute temperature measurements. The final spectrum shown in Fig. 2.1 is that of a perfect black-body with a radiation temperature $T = 2.728 \pm 0.002$ K (Fixsen et al., 1996). More quantitatively, the deviations from a perfect black-body spectrum in the wavelength interval $2.5 > \lambda > 0.5$ mm amounted to less than 0.03% of the maximum intensity. This is the most beautiful example I know of a naturally occurring black-body radiation spectrum.

There are two convenient ways of describing the degree to which the observed spectrum differs from that of a perfect black-body spectrum, both of them pioneered by Zeldovich and Sunyaev in the late 1960s (for details of their work, see their review of 1980 (Sunyaev and Zeldovich, 1980a)). They showed that the injection of large amounts of thermal energy in the form of hot gas into the intergalactic medium can produce various types of distortion of the black-body radiation spectrum because of Compton scattering of the background photons by hot electrons. We will not go into

the physics of these processes at this point, except to note the forms of distortion and the limits which can be set to certain characteristic parameters.

If there were early injection of thermal energy prior to the epoch when the primordial plasma recombined at a redshift of about 1000, and if the number of photons was conserved, the spectrum would relax to an equilibrium Bose–Einstein spectrum with a finite dimensionless chemical potential μ ,

$$I_\nu = \frac{2h\nu^3}{c^2} \left[\exp\left(\frac{h\nu}{kT_r} + \mu\right) - 1 \right]^{-1}. \quad (2.1)$$

The simplest way of understanding this result is to note that the Bose–Einstein distribution is the equilibrium distribution for photons when there is a mismatch between the total energy and the number of photons over which this energy is to be distributed. In the case of a black-body spectrum, both the energy density and number density of photons are determined solely by the temperature T_r . In contrast, the Bose–Einstein distribution is determined by two parameters, the temperature T_r and the dimensionless chemical potential μ .

In the case of Compton scattering by hot electrons at late epochs, the energies of the photons are redistributed about their initial values and, to second order, there is an increase in their mean energies so that the spectrum is shifted to slightly greater frequencies.¹ In 1969, Zeldovich and Sunyaev showed that the distortion of the black-body spectrum takes the form

$$\frac{\Delta I_\nu}{I_\nu} = y \frac{x e^x}{(e^x - 1)} \left[x \left(\frac{e^x + 1}{e^x - 1} \right) - 4 \right], \quad (2.2)$$

where y is the Compton scattering optical depth $y = \int (kT_e/m_e c^2) \sigma_T N_e dl$, $x = h\nu/kT_r$ and σ_T is the Thomson scattering cross-section (Zeldovich and Sunyaev, 1969). In the limit of small distortions, $y \ll 1$, the intensity in the Rayleigh–Jeans region decreases as $\Delta I_\nu/I_\nu = -2y$ and the total energy under the spectrum increases as $\varepsilon = \varepsilon_0 e^{4y}$.

Limits to the parameters y and μ have been derived from the very precise spectral measurements made by the FIRAS instrument. The results quoted by Page are as follows (Page, 1997):

$$|y| \leq 1.5 \times 10^{-5}, \quad |\mu| \leq 10^{-4}. \quad (2.3)$$

These are very strong limits indeed and will prove to be of astrophysical importance in the study of the physics of the intergalactic gas, as well as constraining the amount of star and metal formation which could have taken place in young galaxies.

2.1.2 The Isotropy of the Cosmic Microwave Background Radiation

Equally remarkable were the COBE observations of the *isotropy* of the distribution of the Cosmic Microwave Background Radiation over the sky. The prime instruments

¹ I have given a derivation of this result in my book *High Energy Astrophysics, Vol. I* (Longair, 1997b).

for these studies were the Differential Microwave Radiometers which operated at frequencies of 31.5, 53 and 90 GHz, thus sampling the Rayleigh–Jeans region of the background spectrum. The angular resolution of the radiometers was 7° . The choice of observing frequency was crucial in these observations. At higher frequencies, the millimetre and submillimetre emission of diffuse Galactic dust at high galactic latitudes, often referred to as ‘cirrus’, confuses the picture, whilst at lower frequencies the radio synchrotron radiation of ultrarelativistic electrons gyrating in the Galactic magnetic field becomes important. The final results of the four-year mission are shown in Fig. 2.2 at increasing levels of sensitivity (Bennett et al., 1996).

Figure 2.2a illustrates the stunning result that the Cosmic Microwave Background Radiation is extraordinarily uniform over the whole sky with radiation temperature 2.728 K.

At a sensitivity level of about one part in 1000 of the total intensity, a large-scale anisotropy of dipolar form was observed over the whole sky (Fig. 2.2b). The plane of our Galaxy can also be observed as a faint band of emission along the Galactic equator. The global dipole anisotropy is naturally attributed to aberration effects associated with the Earth’s motion through an isotropic radiation field. Excluding regions close to the Galactic plane, the temperature distribution was found to have precisely the expected dipole distribution, $T = T_0[1 + (v/c) \cos \theta]$, where θ is the angle with respect to the direction of maximum intensity and v is the Earth’s velocity through the isotropic background radiation. The amplitude of the cosmic microwave dipole was 3.353 ± 0.024 mK with the maximum intensity in the direction towards galactic coordinates $l = 264.25^\circ \pm 0.33^\circ$; $b = 48.22^\circ \pm 0.13^\circ$ (Bennett et al., 1996). It was inferred that the Earth is moving at about 350 km s^{-1} with respect to the frame of reference in which the radiation would be 100% isotropic. It is significant that, although not designed to undertake this task, exactly the same form of large-scale dipole anisotropy was observed by the FIRAS instrument.

The measurement of the velocity of the Sun relative to the Cosmic Microwave Background Radiation is an important result for understanding the large-scale distribution of mass in the Universe. Once allowance is made for the motion of the Sun about the centre of our Galaxy, an estimate of the peculiar velocity of our Galaxy and the local group of galaxies relative to the frame of reference in which the background radiation would be perfectly isotropic can be found. This motion can be attributed to perturbations in the distribution of mass on very large scales in the relatively nearby Universe (Kolatt et al., 1995).

On angular scales of 7° and greater, Bennett and his colleagues achieved sensitivity levels better than one part in 100,000 of the total intensity from analyses of the complete microwave data set obtained over the four years of the COBE mission (Fig. 2.2c). At this sensitivity level, the radiation from the plane of the Galaxy is intense, but is confined to a broad strip lying along the Galactic equator. Away from this region, the sky appears quite smooth on a large scale, but there are significant fluctuations in intensity from beamwidth to beamwidth over the sky. These fluctuations are present at the level of only about 1 part in 100,000 of the total intensity and, when averaged over the clear region of sky at $|b| > 20^\circ$ amount to a root-mean-square amplitude of $35 \pm 2 \mu\text{K}$ on an angular scale of 7° , or to $29 \pm 1 \mu\text{K}$ when

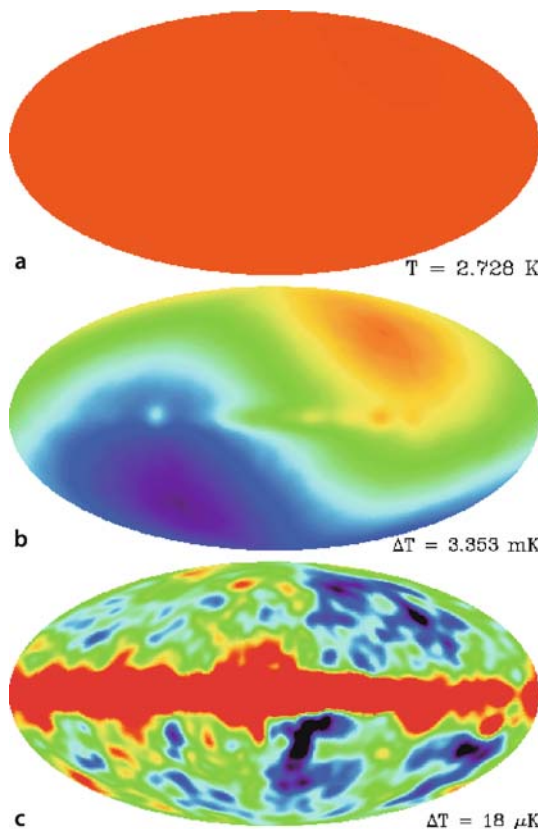


Fig. 2.2a–c. Maps of the whole sky in galactic coordinates as observed at a wavelength of 5.7 mm (53 GHz) by the COBE satellite at different sensitivity levels. **a** The distribution of total intensity over the sky. **b** Once the uniform component was removed, the dipole component associated with the motion of the Earth through the background radiation was observed, as well as a weak signal from the Galactic plane. **c** Once the dipole component was removed, radiation from the plane of the Galaxy was seen as a bright band across the centre of the picture. The fluctuations seen at high galactic latitudes were a combination of noise from the telescope and the instruments and a genuine cosmological signal. The rms value of the fluctuations at each point away from the Galactic equator amounted to $36 \mu\text{K}$. When averaged statistically over the whole sky at high latitudes, an excess sky noise signal of cosmological origin of $30 \pm 5 \mu\text{K}$ was detected (Bennett et al., 1996)

smoothed to 10° angular scale. These values were found to be frequency independent for the three COBE frequency channels at 31.5, 53 and 90 GHz. The detection of these fluctuations is a crucial result for understanding the origin of the large-scale structure of the Universe. The COBE observations allow information to be obtained about the angular spectrum of the intensity fluctuations on all scales $\theta \geq 7^\circ$. In Chap. 15, we will deal with the important cosmological information which can be

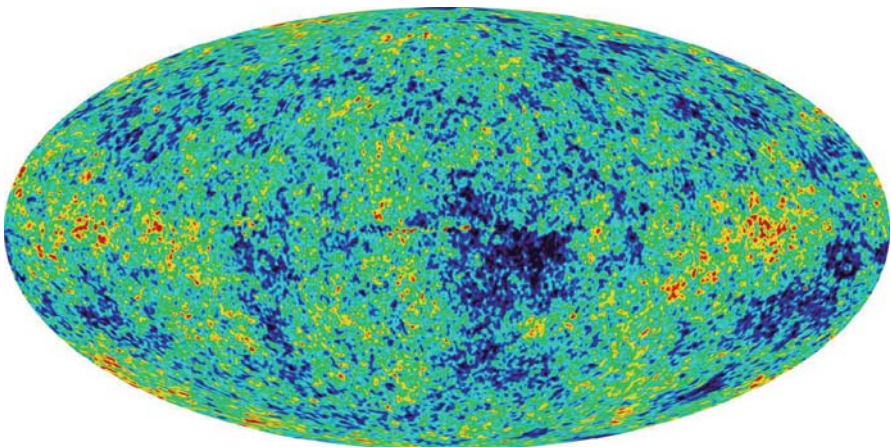


Fig. 2.3. A map of the whole sky in galactic coordinates as observed by the WMAP satellite at millimetre wavelengths (Bennett et al., 2003). The angular resolution of the map is about 20 times higher than that of Fig. 2.2c. The emissions due to Galactic dust and synchrotron radiation have been subtracted from this map

derived from observations of temperature fluctuations in the Cosmic Microwave Background Radiation on smaller angular scales.

It is interesting to compare the COBE map (Fig. 2.2c) with the more recent WMAP observations of 2003 made with about 20 times higher angular resolution (Bennett et al., 2003) (Fig. 2.3). It can be seen that the same large scale features are present on both maps. In particular, regions of strong positive and negative fluctuations agree rather well. We will have a lot more to say about Fig. 2.3 in due course.

The COBE observations are crucial for cosmology. From the point of view of the structure of the Universe on the very largest angular scales, they show that the Cosmic Microwave Background Radiation is isotropic to better than one part in 100,000. Whatever its origin, this observation in itself shows that the Universe must be extraordinarily isotropic on the large scale. As we will show, it is wholly convincing that this radiation is the cooled remnant of the very hot early phases of the Big Bang.

How is the distribution of radiation related to the distribution of matter in the Universe? We will take up this topic in much more detail in Chap. 9, but it is useful to outline here how they are related. In the standard Big Bang picture, when the Universe was squashed to only about one thousandth of its present size, the temperature of the Cosmic Microwave Background Radiation was about one thousand times greater than it is now. The temperature of the background radiation varies with redshift z as $T_r = 2.728(1 + z)$ K and so, at a redshift $z = 1500$, the temperature of the radiation field was about 4000 K. At this temperature, there were sufficient Lyman continuum photons in the Wien region of the background spectrum to photoionise all the neutral hydrogen in the Universe. At this early epoch, known as the *epoch*

of recombination, galaxies had not formed and all the ordinary baryonic matter, which was eventually to become the visible matter of galaxies as we know them, was still in the form of remarkably smooth, partially ionised pre-galactic gas. At earlier epochs, the pre-galactic gas was fully ionised and was very strongly coupled to the background radiation by Thomson scattering.

Therefore, when we look back to these epochs, it is as if we were looking at the surface of a star surrounding us in all directions, but the temperature of the radiation we observe has been cooled by a cosmological redshift factor of 1500, so that what we observe is redshifted into the millimetre waveband. This analogy makes it clear that, because of Thomson scattering of the background radiation, we can only observe the very surface layers of our ‘star’. We cannot obtain any direct information about what was going on at earlier epochs. This ‘surface’ at which the Universe became opaque to radiation is known as the *last scattering surface* and the fluctuations observed by COBE are interpreted as the very low intensity ripples present on that surface on angular scales of 7° and greater. These ripples grow under gravity and will eventually define some of the very largest scale structures in the local Universe.

In the interpretation of the COBE observations described in the last paragraph, it was assumed that the intergalactic gas was transparent to radiation from the epoch of recombination onwards and was not reionised and heated at some later epoch. If that were to occur, the perturbations would be further damped by Thomson scattering and this has now been detected in the WMAP observations. However, the damping is not so great that features in the power spectrum of the fluctuations are wiped out.

One important aspect of these studies is that the energy density of the Cosmic Microwave Background Radiation amounts to $\varepsilon_{\text{rad}} = aT_r^4 = 4.2 \times 10^{-14} \text{ J m}^{-3} = 2.64 \times 10^5 \text{ eV m}^{-3}$. This energy density of radiation pervades the whole Universe at the present epoch and provides by far the greatest contribution to the average energy density of the universal background radiation.

2.2 The Large-Scale Distribution of Galaxies

The visible Universe of galaxies is highly inhomogeneous, consisting of structures from the scale of isolated galaxies, through groups and clusters of galaxies to superclusters and giant voids in the distribution of galaxies. As we progress to larger and larger scales, the distribution of galaxies becomes smoother, but still contains significant non-random features. For many purposes, it is convenient to think of the galaxies as the *building blocks of the Universe* which define its large-scale structure.

An excellent representation of the large-scale distribution of galaxies on the sky is shown in Fig. 2.4. This remarkable picture was created from scans of 185 contiguous UK Schmidt plates, each of which covers an area of $6^\circ \times 6^\circ$ on the sky, the scanning being carried out by the Cambridge APM high-speed measuring machine (Maddox et al., 1990). The image is centred on the South Galactic pole and so the effect of Galactic obscuration by dust on the distribution of galaxies is negligible. Each plate was carefully calibrated and stars distinguished from galaxies by their different image profiles. Figure 2.4 contains over two million galaxies with

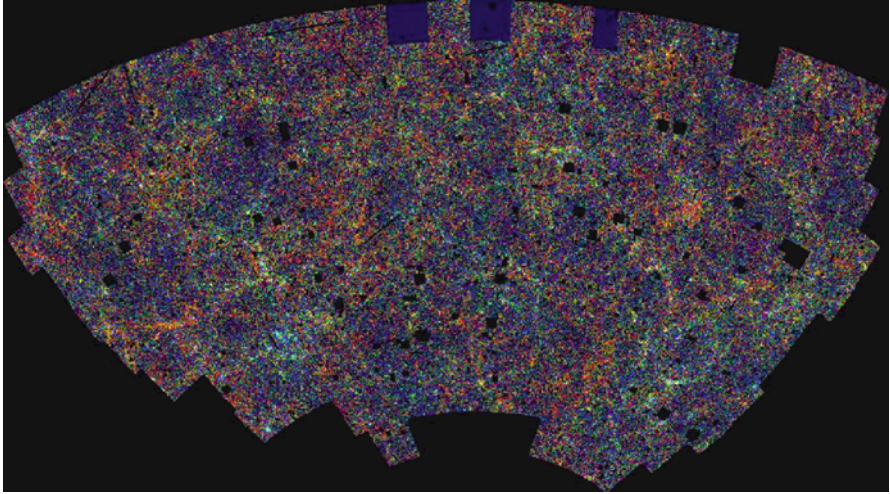


Fig. 2.4. The distribution of galaxies with $17 \leq b_j \leq 20.5$ shown in an equal area projection centred on the South Galactic pole. This image was reconstructed from machine scans of 185 UK Schmidt plates by the Cambridge APM measuring machine. There are over two million galaxies in this image. The small empty patches in the map are regions that have been excluded about bright stars, nearby dwarf galaxies, globular clusters and step wedges (Maddox et al., 1990)

apparent magnitudes in the range $17 \leq b_j \leq 20.5$ and so represents the distribution of galaxies on the sky on the grandest scale.

It is apparent that, although one bit of Fig. 2.4 does not look too different from another on a large enough scale, the distribution of galaxies is far from uniform on a small scale. There appear to be clumps of galaxies, stringy structures and holes but, of course, the eye is expert at finding such structures in random data. Despite this concern, much of the obvious clumping, the clusters, holes and stringy structures are real features of our Universe. To demonstrate the reality of these features, the three-dimensional distribution of galaxies needs to be determined and so distances have to be measured for very large samples of galaxies. Although this is a really huge task, this has now been achieved thanks to the efforts of many astronomers.

2.2.1 Two-Point Correlation Functions

We need statistical methods appropriate for describing the clustering properties of galaxies on a wide range of scales and the simplest approach is to use *two-point correlation functions*. In the cosmological case, these can be described either in terms of the distribution of galaxies on the sky, or in terms of spatial two-point correlation functions in three dimensions. On the sky, we define the *angular two-point correlation function*, $w(\theta)$, by

$$N(\theta) d\Omega = n_g [1 + w(\theta)] d\Omega , \quad (2.4)$$

where $w(\theta)$ describes the excess probability of finding a galaxy at an angular distance θ from any given galaxy. The term $d\Omega$ is the element of solid angle and n_g is a suitable average surface density of galaxies. The term $w(\theta)$ contains information about the clustering properties of galaxies to a given limiting apparent magnitude and can be measured with some precision from large statistical surveys of galaxies such as the Cambridge APM surveys which contain over two million galaxies (Fig. 2.4). Notice the important point that two-point correlation functions take circularly symmetric averages about each galaxy and so throw away all information about the ‘stringiness’ of the distribution of galaxies. Some of this more detailed structural information can be recovered using three- and four-point correlation functions, but let us begin with the two-point correlation functions.

The homogeneity of the distribution of galaxies with increasing distance can be studied by measuring the angular two-point correlation function as a function of increasing apparent magnitude. If the galaxies are sampled from a homogeneous, but clustered, distribution, the angular two-point correlation function scales with increasing limiting distance D in local Euclidean space as

$$w(\theta, D) = \frac{D_0}{D} w_0 \left(\theta \frac{D}{D_0} \right), \quad (2.5)$$

where the function $w_0(\theta)$ has been determined to distance D_0 . The factor $\theta(D/D_0)$ in the argument of w_0 takes account of the fact that a fixed scale subtends a smaller angle at a greater distance D and the factor (D_0/D) in front of w_0 takes account of the fact that there are more background galaxies ($\propto D^3$), but that the surface density of galaxies about any galaxy to a fixed physical scale increases only as D^2 . If the galaxies extend to distances D such that redshift effects need to be taken into account, it is necessary to integrate over the luminosity function of the galaxies counted and to use a Friedman world model to determine the spatial and surface number densities of galaxies (Groth and Peebles, 1977; Scranton et al., 2002).

Such scaling analyses were carried out by Groth and Peebles who showed that the two-point correlation functions determined from a bright sample of Zwicky galaxies, from the Lick counts of galaxies and from a deep sky survey plate in an area known as the Jagellonian field scaled exactly as expected if the distribution of the galaxies displayed the same degree of spatial correlation throughout the local Universe out to $z \sim 0.1$ (Groth and Peebles, 1977, 1986). A similar result was found by comparing the two-point correlation functions found at increasing apparent magnitude limits in the machine-scanned surveys carried out by the APM group at Cambridge (Maddox et al., 1990). Figure 2.5a shows the angular two-point correlation functions $w(\theta)$ measured at increasing apparent magnitude limits in the magnitude range $17.5 < m < 20.5$. In Fig. 2.5b, these functions are scaled to the angular correlation function found from the Lick survey.

More recently, the same type of analysis has been carried out for a large sample of galaxies from the Sloan Digital Sky Survey (SDSS) which extends to apparent magnitude $r^* = 23$ by Connolly, Scranton and their colleagues. According to their estimates, the mean redshift in the magnitude interval $21 \leq r^* \leq 22$ is 0.43. Using the same scaling procedures with a proper Friedman cosmological model, they

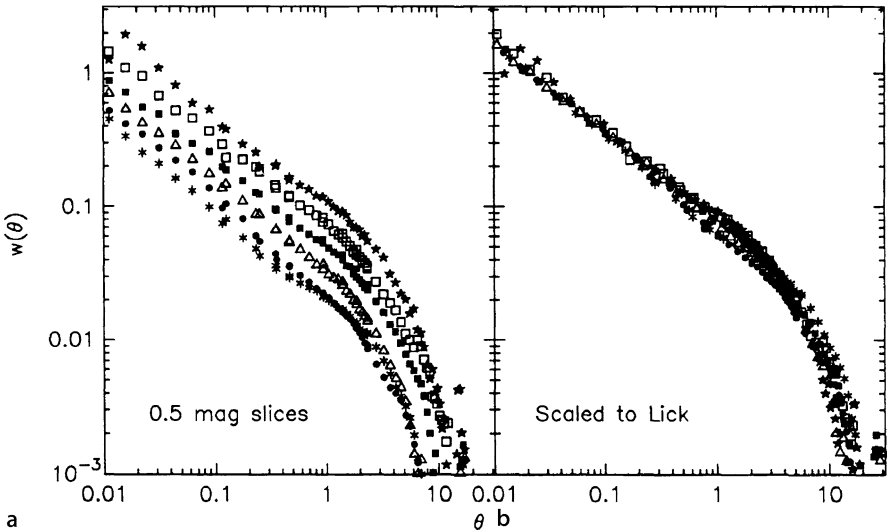


Fig. 2.5a,b. The two-point correlation function for galaxies over a wide range of angular scales. **a** The scaling test for the homogeneity of the distribution of galaxies can be performed using the correlation functions for galaxies derived from the APM surveys at increasing limiting apparent magnitudes in the range $17.5 < m < 20.5$. The correlation functions are displayed in intervals of 0.5 magnitudes. **b** The two-point correlation functions scaled to the correlation function derived from the Lick counts of galaxies (Maddox et al., 1990)

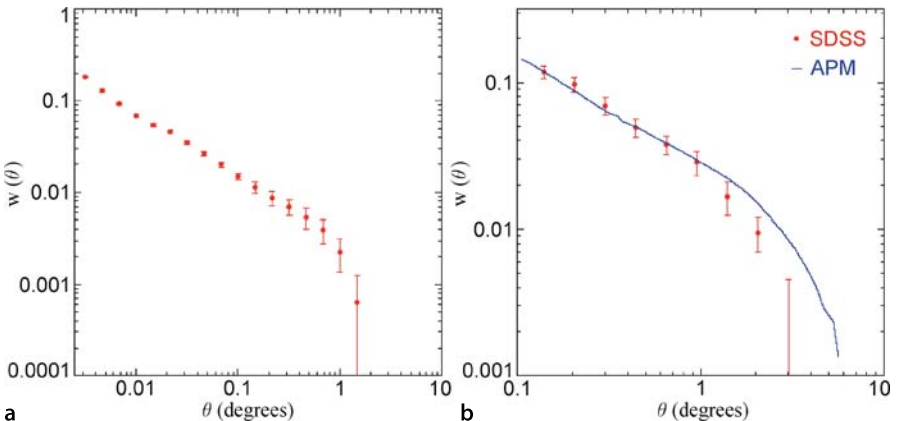


Fig. 2.6a,b. The two-point correlation function for galaxies determined from the Sloan Digital Sky Survey (SDSS) (Connolly et al., 2002; Scranton et al., 2002). **a** The angular two-point correlation function determined in a preliminary analysis of 2% of the galaxy data contained in the Sloan Digital Sky Survey. **b** Comparison of the scaled angular two-point correlation functions found by Maddox and his colleagues from the APM galaxy survey (solid line) with that found from the SDSS analysis

find excellent agreement with the angular two-point correlation function determined by Maddox and his colleagues (Fig. 2.6) (Connolly et al., 2002; Scranton et al., 2002). It is noteworthy that a better match of the correlation functions is found for a concordance world model with $\Omega_0 = 0.3$ and $\Omega_\Lambda = 0.7$ than for the critical model with $\Omega_0 = 1$ and $\Omega_\Lambda = 0$.

These are important results for the construction of cosmological models. As expressed by Peebles (Peebles, 1993):

... the correlation function analyses have yielded a new and positive test of the assumption that the galaxy space distribution is a stationary (statistically homogeneous) random process.

Figures 2.5b and 2.6b illustrate the important point that the correlation function for galaxies is smooth, meaning that clustering is found on all angular scales with no prominent features on the scales of clusters or superclusters of galaxies. Of course, it needs to be remembered that the two-point correlation function is circularly symmetric about each galaxy and so wipes out a lot of detailed information. In Figs. 2.5b and 2.6b, $w(\theta)$ can be characterised by a power law of the form

$$w(\theta) \propto \theta^{-(0.7-0.8)} \quad (2.6)$$

with a cut-off on large angular scales.

It is more meaningful physically to work in terms of the *spatial two-point correlation function* $\xi(r)$ which describes the clustering properties of galaxies in three dimensions about any galaxy:

$$N(r) dV = N_0[1 + \xi(r)] dV, \quad (2.7)$$

where $N(r) dV$ is the number of galaxies in the volume element dV at distance r from any galaxy and N_0 is a suitable average space density. $\xi(r)$ describes the excess number of galaxies at distance r from any given galaxy.

In order to derive $\xi(r)$ directly from observation, we need to know the distribution of galaxies in space. If, however, we make a number of reasonable assumptions, we can derive a simple formula which relates $w(\theta)$ to $\xi(r)$. Suppose a cluster of galaxies has radial number density distribution $n(r) = n_0[1 + \xi(r)]$. Then, it is a simple calculation to show that the projected distribution is given by the integral

$$N(a) = 2 \int_a^{a_{\max}} \frac{n(r) r}{(r^2 - a^2)^{1/2}} dr = 2 \int_a^{a_{\max}} \frac{n_0[1 + \xi(r)] r}{(r^2 - a^2)^{1/2}} dr, \quad (2.8)$$

where a is the projected radial distance from the centre of the cluster and a_{\max} is the tidal radius of the cluster. The first term in the second integral for $n(a)$ is just a constant. If we adopt a power law dependence for $\xi(r)$, $\xi(r) \propto r^{-\gamma}$, the second term in the integral can be written in dimensionless form using the substitution $r = ax$ as follows:

$$N(a) = 2n_0 a^{-(\gamma-1)} \int_1^{a_{\max}/a} \frac{x^{-(\gamma-1)}}{(x^2 - 1)^{1/2}} dx. \quad (2.9)$$

Allowing the upper limit of the integral to go to infinity, we see that the integral is a constant and that $N(a)$ and $\xi(r)$ are related by

$$N(a) \propto a^{-(\gamma-1)}. \quad (2.10)$$

Consequently, in the region in which the angular two-point correlation function can be described by the power law relation (2.6), the function $\xi(r)$ can be well represented by a power law of the form

$$\xi(r) = \left(\frac{r}{r_0}\right)^{-\gamma}, \quad (2.11)$$

where $\gamma = 1.7 - 1.8$. More detailed analyses of the relation between $\xi(r)$ and $w(\theta)$ show that the correlation function (2.11) is a good match to the data on physical scales from about $100h^{-1}$ kpc to $10h^{-1}$ Mpc in which the scale $r_0 = 5h^{-1}$ Mpc and the exponent $\gamma = 1.7 - 1.8$.² On scales greater than about $10h^{-1}$ Mpc the two-point correlation function decreases more rapidly than the power law (2.11). Thus, on large enough scales, the amplitude of the clustering decreases dramatically and the Universe becomes isotropic on the very largest physical scales.

We also obtain the important result that on physical scales $r \gg 5h^{-1}$ Mpc, the mean amplitude of the density perturbations is less than one and consequently density perturbations on larger scales are on average still in the linear regime $\delta\rho/\rho \ll 1$ at the present epoch.

2.2.2 Walls and Voids in the Distribution of Galaxies on Large Scales

The analysis of Sect. 2.2.1 provides the simplest description of the distribution of galaxies on large scales, but it cannot describe the walls and voids in the distribution of galaxies seen in Fig. 2.4. The nature of these structures has been well defined by a number of large-scale redshift surveys for galaxies.

One of the earliest complete samples of nearby galaxies is presented in Fig. 2.7 which shows the local three-dimensional distribution of galaxies derived from the Harvard-Smithsonian Astrophysical Observatory survey of over 14,000 bright galaxies (Geller and Huchra, 1989). Our own Galaxy is located at the centre of the diagram and, if the galaxies were uniformly distributed in the local Universe, the points would be uniformly distributed over the diagram, which is certainly very far from the case. There are gross inhomogeneities and irregularities in the local Universe including large ‘holes’ or ‘voids’ in which the local number density of galaxies is significantly lower than the mean, and long ‘filaments’ or ‘walls’ of galaxies, including the feature known as the ‘Great Wall’, which extends from right ascensions 9^{h} to 17^{h}

² The use of $h = H_0/(100 \text{ km s}^{-1} \text{ Mpc}^{-1})$ is a convenient device for adjusting the dimensions and luminosities of extragalactic objects to the reader’s preferred value of Hubble’s constant. If a value of $H_0 = 100 \text{ km s}^{-1} \text{ Mpc}^{-1}$ is preferred, $h = 1$; if the value $H_0 = 50 \text{ km s}^{-1} \text{ Mpc}^{-1}$ is adopted, $h = 0.5$ and so on. It is now known that the value of h is $h = 0.72 \pm 0.07$.

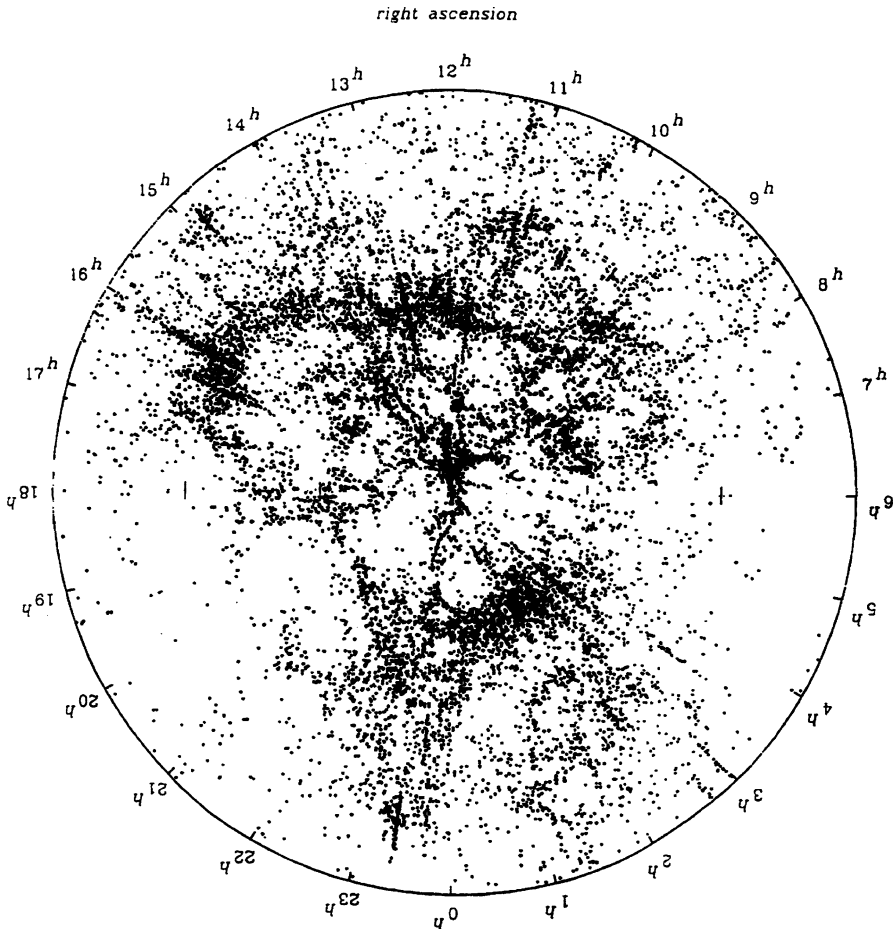


Fig. 2.7. The distribution of galaxies in the nearby Universe as derived from the Harvard-Smithsonian Center for Astrophysics survey of galaxies. The map contains over 14,000 galaxies which form a complete statistical sample around the sky between declinations $\delta = 8.5^\circ$ and 44.5° . All the galaxies have recession velocities less than $15,000 \text{ km s}^{-1}$. Our Galaxy is located at the centre of the map and the radius of the bounding circle is $150h^{-1} \text{ Mpc}$. The galaxies within this slice have been projected onto a plane to show the large-scale features in the distribution of galaxies. Rich clusters of galaxies which are gravitationally bound systems with internal velocity dispersions of about 10^3 km s^{-1} appear as ‘fingers’ pointing radially towards our Galaxy at the centre of the diagram. The distribution of galaxies is highly irregular with huge holes, filaments and clusters of galaxies throughout the local Universe (Geller and Huchra, 1989)

about half-way to the limit of the survey. There are a number of ‘streaks’ or ‘fingers’ pointing towards our own Galaxy and these correspond to clusters of galaxies, the lengths of the ‘streaks’ corresponding to the components of the velocity dispersion of the galaxies in the clusters along the line of sight.

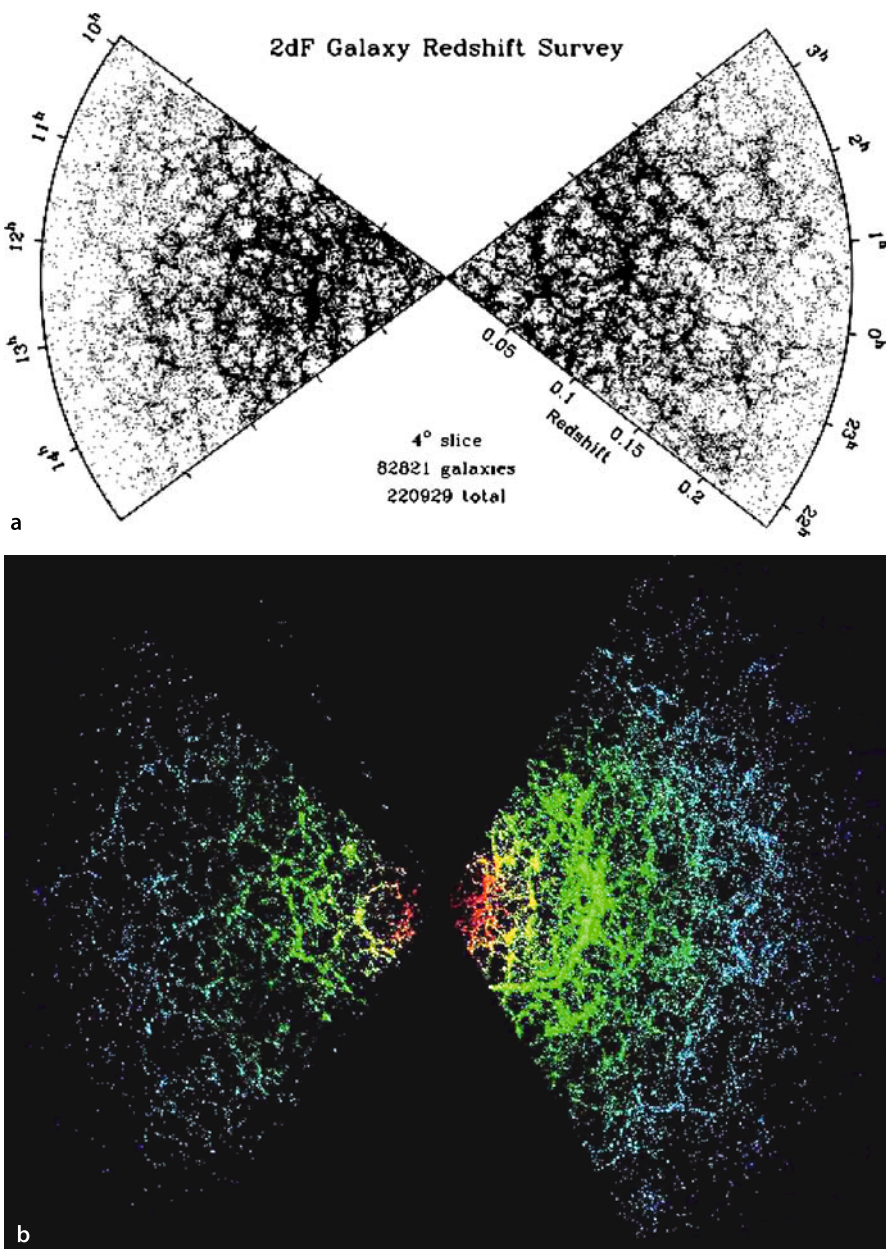


Fig. 2.8a,b. The spatial distribution of galaxies on a large-scale. In both diagrams, the distribution extends to a redshift $z \approx 0.25$. **a** A slice through the Anglo-Australian Telescope 2dF Galaxy Survey (Colless et al., 2001) showing the pronounced ‘cellular’ structure of the distribution of galaxies on the large scale (image courtesy of the 2dFGRS Team). **b** The distribution of galaxies in the Sloan Digital Sky Survey, showing the same ‘cellular’ structure observed in the AAT 2dF survey (Stoughton et al., 2002)

These surveys have now been extended to much greater distances and the same overall picture emerges. Among the first of these surveys, the Las Campanas Redshift Survey sampled the distribution of galaxies to a distance about four times that of the Harvard–Smithsonian survey and included 26,418 galaxies (Lin et al., 1996). The sizes of the voids in the galaxy distribution were on roughly the same physical scale as those in Fig. 2.7, indicating that the Universe is homogeneous on a large enough scale, consistent with the scaling arguments from the angular two-point correlation functions.

More recently, the statistics of such surveys has been increased by an order of magnitude by the Anglo-Australian Telescope Two-degree Field (2dF) survey of galaxies and the first results of the Sloan Digital Sky Galaxy Survey (Fig. 2.8a and b). In the 2dF survey, the redshifts of over 200,000 galaxies were measured. To reveal the ‘cellular’ structure more clearly, only a narrow wedge 4° wide is shown in Fig. 2.8a which includes 56,237 galaxies (Colless et al., 2001). The map shown in Fig. 2.8b from the Sloan galaxy survey also includes over 200,000 galaxies (Stoughton et al., 2002). In both cases, the surveys extend to redshifts of about 0.25 and it can be seen that the ‘cellular structure persists out to the limits of the surveys. Notice that this means that these surveys have already mapped out a large fraction of the distribution of galaxies at the present epoch.

In Figs. 2.7 and 2.8a and b, the scales of the largest holes are about 30–50 times the scale of a cluster of galaxies, that is, up to about $50h^{-1}$ Mpc. These are the largest known structures in the Universe and one of the major cosmological challenges is to reconcile this gross irregularity in the large-scale spatial distribution of galaxies with the remarkable smoothness of the Cosmic Microwave Background Radiation seen in Fig. 2.2c. Despite the presence of the huge voids however, the amplitude of these irregularities decreases with increasing scale so that on the very largest scales, one bit of Universe looks very much like another.

It is important to have a quantitative description of the large-scale topology of the galaxy distributions shown in Figs. 2.7 and 2.8a and b. In the 1980s, Gott and his colleagues developed techniques for evaluating the topology of the distribution of voids and galaxies from large redshift surveys (Gott et al., 1986; Melott et al., 1988). As they expressed the issue delightfully in their paper:

We would like to know whether the distribution of galaxies on large scales is best described as a hierarchy of clusters, an irregular lattice of cells or ‘bubbles’, a network of filaments, or a set of non-intersecting filaments. Loosely speaking, one might describe the topology of these models as respectively a ‘meatball’ topology, a ‘swiss-cheese’ topology, a ‘sponge’ topology and a ‘spaghetti’ topology.

The importance of these studies is that the topology of the distribution of galaxies is intimately related to the initial conditions from which the large-scale structure formed, in particular, to the common assumption that the perturbations were Gaussian fluctuations with random phases.

From an analysis of the CfA galaxy survey, Gott and his colleagues found that the distribution of the galaxies on the large scale is ‘sponge-like’, the material of

the sponge representing the location of the galaxies and the holes in the sponge corresponding to the large voids (Gott et al., 1986; Melott et al., 1988). Both the holes and the distribution of galaxies are continuously connected throughout the local Universe. This topology is possible in three dimensions but not in two. Just like a sponge, overall the distribution of material of the sponge and the holes is homogeneous, but, on a small scale, it is highly inhomogeneous.

Similar analyses have been carried out for the large AAT 2dF and SDSS Galaxy surveys by Hoyle, Vogeley, Gott and their colleagues (Hoyle et al., 2002a,b). They find that the overall topology of the two independent surveys are in remarkable agreement and similar to that of a Gaussian random field. They go further and show how further astrophysically important issues can be addressed by considering the topologies of red and blue galaxies separately and comparing these with simulations of the formation of structure in the concordance Λ CDM model. We will return to these issues in Part IV.

Another way of investigating the large-scale distribution of discrete objects in the Universe is to study the distribution of extragalactic radio sources over the sky. Unlike the optical waveband, it turns out that, when a survey of the radio sky is made, the objects which are easiest to observe are extragalactic radio sources associated with certain rare classes of active galaxy, the radio quasars and radio galaxies, at very great distances. Because they are rare objects, they sample the isotropy of the Universe on a very large scale. Figure 2.9 shows the distribution of the brightest 54,579 extragalactic radio sources at a wavelength of 6 cm in the Greenbank Catalogue of radio sources which spans most of the northern hemisphere (Gregory and Condon, 1991; Kooiman et al., 1995). Besides the hole about the North Celestial pole, there are holes in the vicinity of a few intense radio sources. There is also a small excess of sources lying along the Galactic plane but otherwise the distribution is entirely consistent with the sources being distributed uniformly at random over the sky on the large scale.

Kooiman and his colleagues report weak clustering on angular scales $1\text{--}2^\circ$, consistent with an angular two-point correlation function of the form $w(\theta) \propto \theta^{-0.8}$. A much stronger angular two-point correlation signal was found in the much deeper FIRST survey carried out with the VLA by Helfand and his colleagues (Cress et al., 1996). At a limiting flux density of 1 mJy at 1.4 GHz, 138,665 radio sources were detected and an angular two-point correlation function of the form $w(\theta) \propto \theta^{-1.1}$ measured down to angular separations of a tenth of a degree.

The radio sources are ideal for probing the large-scale distribution of discrete objects since they are readily observed at large distances. The bulk of the radio sources plotted in Fig. 2.9 lie at redshifts $z \geq 1$ and so they sample the distribution of discrete sources on the largest physical scales accessible to us at the present epoch. Notice that the extragalactic radio sources provide complementary information to that provided by the Cosmic Microwave Background Radiation, in that they refer to the large-scale distribution of discrete objects, such as galaxies, once they have formed.

On fine scales, the clustering of galaxies takes place on a very wide variety of scales from pairs and small groups of galaxies, such as the Local Group of galaxies, to giant *clusters* of galaxies, such as the Coma and Pavo clusters which can

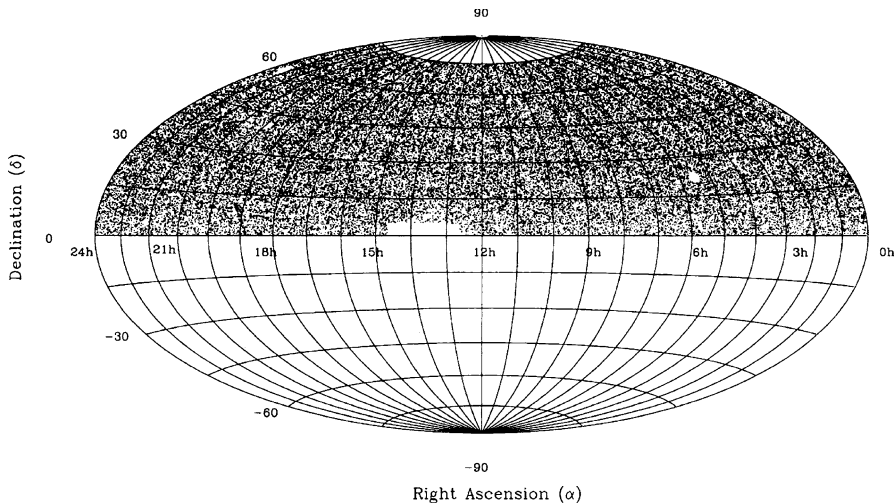


Fig. 2.9. The distribution of radio sources in the Greenbank Catalogue of radio sources at 6 cm (Gregory and Condon, 1991). The picture includes 54,579 radio sources with angular sizes less than 10.5 arcmin and flux densities $S \geq 25$ mJy. The area about the North Celestial pole was not surveyed. There are ‘holes’ in the distribution about a few bright radio sources and a small excess of sources associated with the Galactic plane. Otherwise, the distribution does not display any significant departure from a random distribution on a large scale, although there is evidence for clustering on the scale of 1° (Kooiman et al., 1995)

contain thousands of members – we discuss some of their properties in Chap. 4. The rich regular clusters are self-gravitating bound systems, but there are also irregular clusters which have an irregular, extended appearance and it is not so clear that these are bound systems.

The term *supercluster* is used to describe structures on scales larger than those of clusters of galaxies. They may consist of associations of clusters of galaxies, or a rich cluster with associated groups and an extended distribution of galaxies. Some authors would classify the ‘stringy’ structures seen in Figs. 2.7 and 2.8 as superclusters, or supercluster cells. From the physical point of view, the distinction between the clusters and the superclusters is whether or not they are gravitationally bound. Even in the rich, regular clusters of galaxies, which have had time to relax to a state of dynamical equilibrium, there has only been time for individual galaxies to cross the cluster up to about 10 times in the age of the Universe and so, on larger scales, there is scarcely time for the systems to become gravitationally bound. Our own Galaxy and the Local Group of galaxies are members of what is known as the *Local Supercluster*. This is the huge flattened distribution of galaxies centred on the Virgo cluster, which lies at a distance of about 15–20 Mpc from our own Galaxy. It can be seen very prominently in maps of the distribution of bright galaxies running more or less perpendicular to the plane of the Galaxy and is outlined by filled circles in Fig. 2.10 (Kolatt et al., 1995).

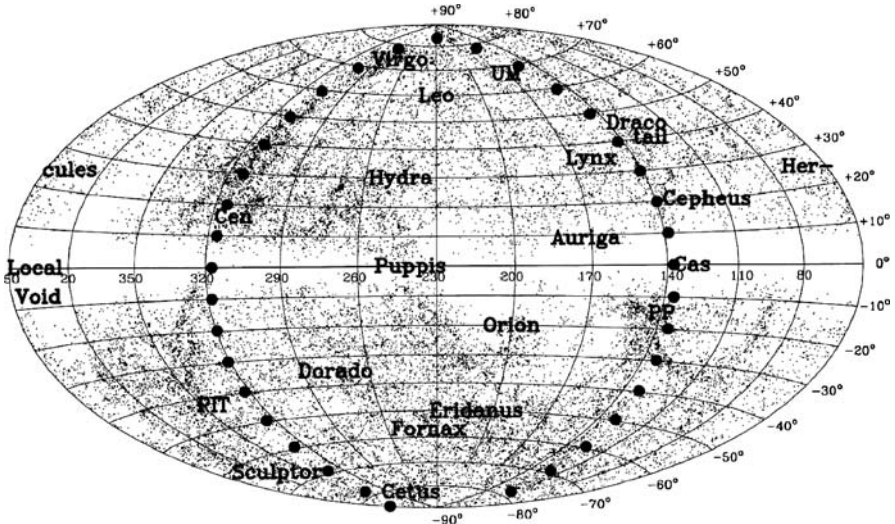


Fig. 2.10. An equal area projection drawn in galactic coordinates of the distribution of bright galaxies over the whole sky. In the north, the galaxies are taken from the UGC catalogue and, in the south, from the ESO, UGC and MCG catalogues. There is an absence of galaxies at low galactic latitudes because of extinction by interstellar dust. The prominent band of galaxies intersecting the Galactic plane at right angles at $l \sim 320^\circ$ is the Local Supercluster of Galaxies and the Supergalactic plane is delineated by the filled circles. Some regions in which prominent clustering of galaxies is found are labelled by the constellations in which these lie (Kolatt et al., 1995)

We conclude that, on the very largest scales, the distribution of matter and radiation is remarkably isotropic and homogeneous. This greatly simplifies the construction of cosmological models.

2.3 Hubble's Law and the Expansion of the Universe

Hubble made his great discovery of the velocity–distance relation for galaxies in 1929 (Hubble, 1929). A modern version of Hubble's law, in the form of an redshift–apparent magnitude relation or Hubble diagram, is shown in Fig. 2.11 for the brightest galaxies in clusters (Sandage, 1968). It is found empirically that the brightest galaxies in nearby clusters all have more or less the same intrinsic luminosities and so their apparent magnitudes can be used to estimate relative distances by application of the inverse square law.

For a class of galaxy of fixed intrinsic luminosity L , the observed flux density S is given by the inverse square law, $S = L/4\pi r^2$ and so, converting this relation into astronomical apparent magnitudes m using the standard relation $m = \text{constant} - 2.5 \log_{10} S$, it follows that

$$m = 5 \log_{10} r + \text{constant} . \quad (2.12)$$

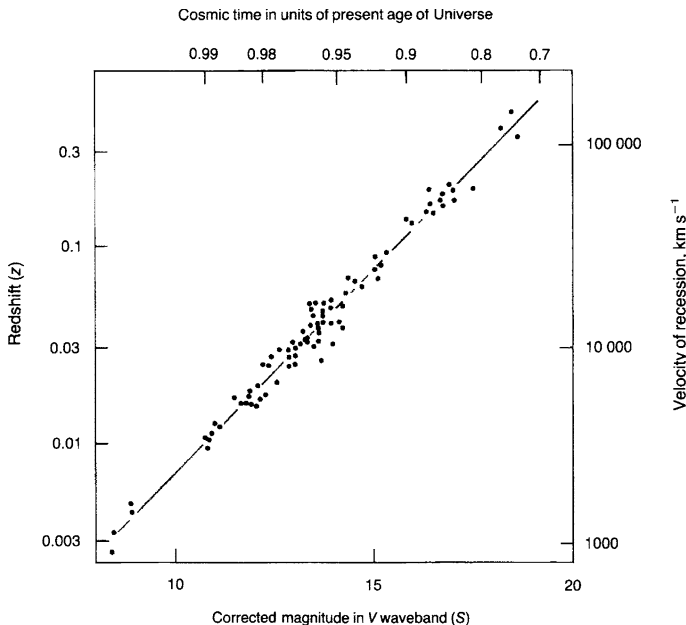


Fig. 2.11. A modern version of the velocity–distance relation for galaxies for the brightest galaxies in rich clusters of galaxies. This correlation indicates that the brightest galaxies in clusters have remarkably standard properties and that their velocities of recession from our own Galaxy are proportional to their distances (Sandage, 1968)

This was the approach adopted by Hubble and Humason in their pioneering analysis of 1934 (Hubble and Humason, 1934) – they assumed that the 5th brightest galaxy in a cluster would have more or less the same intrinsic luminosity (Fig. 1.5b). In Fig. 2.11, the corrected apparent magnitude in the V waveband is plotted against the logarithm of the redshift of the brightest galaxies in a number of rich clusters of galaxies which span a wide range of redshifts. The *redshift* z is defined by the formula

$$z = \frac{\lambda_{\text{obs}} - \lambda_{\text{em}}}{\lambda_{\text{em}}} , \quad (2.13)$$

where λ_{em} is the emitted wavelength of some spectral feature and λ_{obs} is the wavelength at which it is observed. In the limit of small velocities, $v \ll c$, if the redshift is interpreted in terms of a recessional velocity v of the galaxy, $v = cz$ and this is the type of velocity plotted in the velocity–distance relation. It is an unfortunate tradition in optical astronomy that the splendidly dimensionless quantity, the redshift z , is converted into a velocity by multiplying it by the speed of light. As we will see below, interpreting the redshift in terms of a recessional velocity leads to confusion and misunderstanding of its real meaning in cosmology. It is best if all mention of recessional velocities are expunged in developing the framework of cosmological models.

The solid line shown in Fig. 2.11 is $m = 5 \log_{10} z + \text{constant}$, corresponding to $v \propto r$, and it runs precisely through the observed points – correlations do not come any better than this in cosmology. The velocity–distance relation is normally written $v = H_0 r$, where H_0 is known as *Hubble's constant*. The velocity–distance relation appears to hold good for all classes of extragalactic system, including the active galaxies and quasars.

We discussed in detail recent evidence for the homogeneity of the distribution of galaxies in space in Sect. 2.2. In fact, Hubble realised in the 1930s that a simple test of the homogeneity of the Universe is provided by the number counts of galaxies. As we will show in Sect. 17.2.1, in a homogeneous Universe it is expected that the number counts of galaxies follow the law $N(\geq S) \propto S^{-3/2}$, where S is the observed flux density of the galaxy. This result is independent of the luminosity function of the sources so long as the counts do not extend to such large distances that the effects of the cosmological redshift have to be taken into account. In terms of apparent magnitudes, this relation becomes $N(\leq m) \propto 10^{0.6m}$.

Hubble found that the counts of galaxies to about 20th magnitude more or less followed this relation, although they showed some convergence at the faintest apparent magnitudes, which Hubble interpreted as evidence for the effects of space curvature at large distances (Hubble, 1936). More recent counts of galaxies are shown in Fig. 2.12 which extend to very faint apparent magnitudes (Metcalfe et al., 1996). The results are similar to those of Hubble at $m \leq 20$; the counts are slightly flatter than the Euclidean predictions, but are entirely consistent with the expectations of uniform world models once the effects of observing the populations at significant cosmological distances are taken into account. Divergences from the expectations of the uniform models occur at much fainter blue apparent magnitudes ($B \geq 22$), in the sense that there is an excess of faint blue galaxies; we will take up the origin of this excess in detail in Chap. 17.

The combination of the observed large-scale isotropy and homogeneity of the Universe with Hubble's law shows that the Universe as a whole is expanding uniformly at the present time. Let us show this formally by the following simple calculation. Consider a uniformly expanding system of points (Fig. 2.13). The definition of a uniform expansion is that the distances between any two points should increase by the same factor in a given time interval, that is, we require

$$\frac{r_1(t_2)}{r_1(t_1)} = \frac{r_2(t_2)}{r_2(t_1)} = \cdots = \frac{r_n(t_2)}{r_n(t_1)} = \cdots = \alpha = \text{constant} , \quad (2.14)$$

for any set of points. Let us select some galaxy at random and take the distances of the other galaxies from it to be r_1, r_2, \dots . Then, the recession velocity of galaxy 1 relative to the chosen origin is

$$\begin{aligned} v_1 &= \frac{r_1(t_2) - r_1(t_1)}{t_2 - t_1} = \frac{r_1(t_1)}{t_2 - t_1} \left[\frac{r_1(t_2)}{r_1(t_1)} - 1 \right] \\ &= \frac{r_1(t_1)}{t_2 - t_1} (\alpha - 1) = H_0 r_1(t_1) . \end{aligned} \quad (2.15)$$

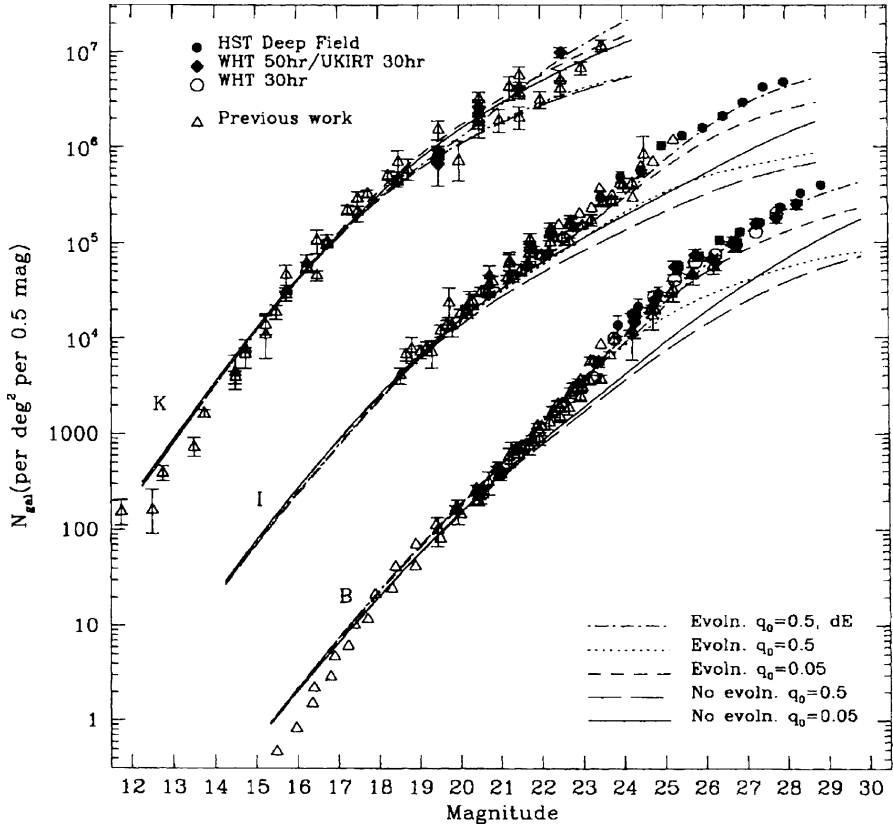


Fig. 2.12. The counts of faint galaxies observed in the B, I and K wavebands compared with the expectations of various uniform world models, as well as other models in which various forms of the evolution of the luminosity function of galaxies with redshift are assumed (Metcalfe et al., 1996). The galaxy counts follow closely the expectations of uniform world models at magnitudes less than about 22, but there is a excess of galaxies in the B and I wavebands at fainter magnitudes

Similarly, for the n th galaxy,

$$v_n = \frac{r_n(t_1)}{t_2 - t_1}(\alpha - 1) = H_0 r_n(t_1) . \quad (2.16)$$

Thus, a uniformly expanding distribution of galaxies automatically results in a velocity-distance relation of the form $v \propto r$.

This analysis is, however, much deeper than simply an explanation of the local velocity-distance relation. Notice that the above analysis applies to galaxies at all distances in a uniformly expanding universe. The requirements of isotropy and homogeneity mean that the same linear velocity-distance relation must hold true *at all distances*, including at distances at which the recession velocities exceed the

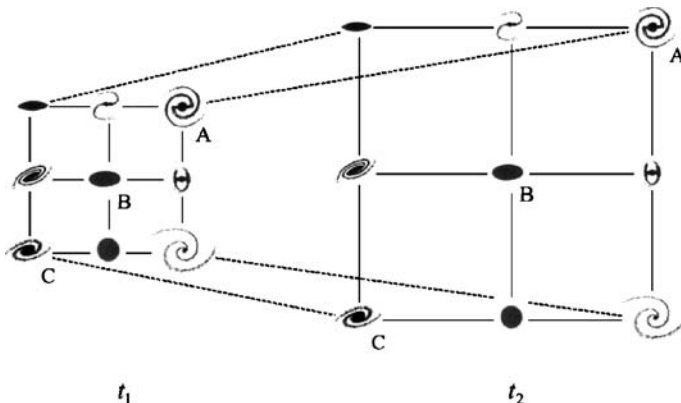


Fig. 2.13. Illustrating the origin of the velocity–distance relation for an isotropically expanding distribution of galaxies. The distribution of galaxies expands uniformly between the epochs t_1 and t_2 . If, for example, we consider the motions of the galaxies relative to the galaxy A, it can be seen that galaxy C travels twice as far as galaxy B between the epochs t_1 and t_2 and so has twice the recession velocity of galaxy B relative to A. Since C is always twice the distance of B from A, it can be seen that the velocity–distance relation is a general property of isotropically expanding universes

speed of light. A good way of understanding this assertion is to consider the familiar example of the surface of an expanding balloon as an analogue for the kinematics of an expanding universe. As the balloon is blown up, the distances between points on the sphere increase and everywhere a velocity–distance relation is obtained locally. When the balloon is blown up to a huge size, widely separated points on the sphere separate at speeds which can be greater than the speed of light. There is, however, nothing unphysical about this since there is no causal connection between the points. The points are simply partaking in a geometrically uniformly expansion which takes place over enormous distances. We will return to this important point in Chap. 12.

2.4 Conclusion

The upshot of the considerations of this chapter is that the correct starting point for the construction of models for the large-scale dynamics of the Universe is that they should be isotropic and homogenous on the large scale and that they should be uniformly expanding. These are enormous simplifications and, taken in conjunction with the General Theory of Relativity, provide a set of simple world models which provide the framework within which we can study the problems of the origin of galaxies and the other large-scale structures we observe in the Universe today.

3 Galaxies

3.1 Introduction

‘Galaxy formation’ is the title of this book and so we should summarise what is known about the properties of galaxies. This is not a trivial business because normal galaxies are complex, many-body systems. Typically, a galaxy can consist of hundreds of millions or billions of stars, it can contain considerable quantities of interstellar gas and dust and can be subject to environmental influences through interactions with other galaxies and with the intergalactic gas. Star formation takes place in dense regions of the interstellar gas. To complicate matters further, it is certain that dark matter is present in galaxies and in clusters of galaxies and the dynamics of galaxies are largely dominated by this invisible dark component. Its nature is, however, unknown.

Until the advent of the massive surveys of galaxies, the 2dF Galaxy Survey undertaken by the Anglo-Australian Telescope and the Sloan Digital Sky Survey (SDSS), the typical properties of galaxies were defined by meticulous morphological studies of large samples of bright galaxies. Being bright and relatively nearby, the morphological classification schemes had to encompass a vast amount of detail and this was reflected in Hubble’s pioneering studies as elaborated by de Vaucouleurs, Kormendy, Sandage, van den Bergh and others. In contrast, the sheer size of the new galaxy samples, which each encompass about 200,000 galaxies, has meant that classification schemes had to be based upon parameters which could be derived from computer analysis of the galaxy images and spectra. What the new approach loses in detail, it more than makes up for in the huge statistics involved and in the objective nature of the classification procedures.

These recent developments have changed the complexion of the description of the properties of galaxies. While the new samples provide basic global information about the properties of galaxies, the old schemes describe many features which need to be incorporated into the understanding of the detailed evolution and internal dynamics of particular classes of galaxy. The upshot is that, we need to develop in parallel both the traditional and more recent approaches to the classification of galaxies. We will summarise some of their more important properties, as well as elucidating some of the essential physics. In the next chapter, we will perform a similar exercise for clusters of galaxies. The books *Galaxies in the Universe: an Introduction* by Sparke and Gallagher, *Galactic Astronomy* by Binney and Merrifield and *Galactic Dynamics* by Binney and Tremaine can be thoroughly recommended

as much more thorough introductions to these topics (Sparke and Gallagher, 2000; Binney and Merrifield, 1998; Binney and Tremaine, 1987). The results of the 2dF Galaxy Survey and the Sloan Digital Sky Survey (SDSS) are too recent to have entered the textbooks. We begin with the traditional approach and then relate these studies to the more global approach adopted in recent analyses.

3.2 The Revised Hubble Sequence for Galaxies

Let us first describe the traditional approach to the classification of galaxies, noting points of contact with more recent statistical approaches. Galaxies come in a bewildering variety of different shapes and forms. In order to put some order into this diversity, classification schemes were devised on the basis of their visual appearances, or morphologies, originally on photographic plates but nowadays from digital images taken with CCD cameras. The basis of the traditional morphological schemes remains the *Hubble Sequence of Galaxies*, described in Hubble's monograph *The Realm of the Nebulae* (Hubble, 1936). The Hubble sequence, sometimes referred to as a 'tuning-fork' diagram, arranges galaxies into a continuous sequence of types with elliptical galaxies at the left-hand end and spirals at the right-hand end (Fig. 3.1). The spiral galaxies are ordered into two branches named 'normal' and 'barred' spirals. Conventionally, galaxies towards the left-hand end of the sequence are referred to as 'early-type' galaxies and those towards the right as 'late-type' galaxies, reflecting Hubble's original prejudice concerning their evolution from one type to another. Despite the fact that these ideas have long outlived their usefulness, the terms are still in common use, even in the era of the massive surveys of galaxies.

Morphological classification schemes such as the Hubble sequence become an integral part of astrophysics when independent properties of galaxies are found to correlate with the morphological classes. This has been found to be the case for

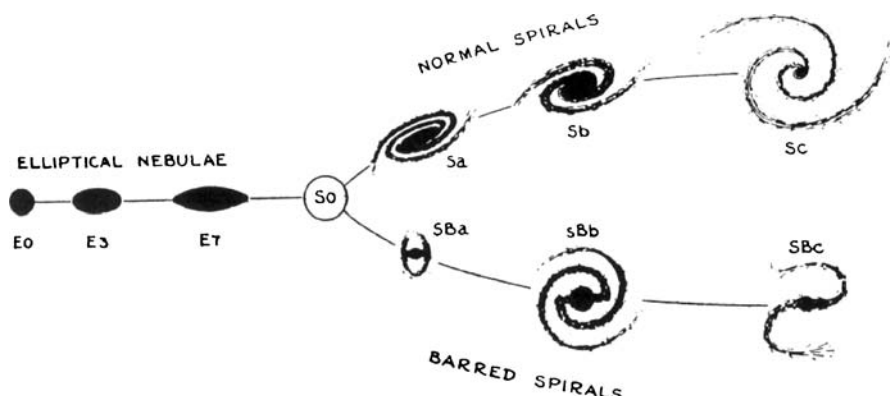


Fig. 3.1. The Hubble sequence of galaxies as presented in *The Realm of the Nebulae* (Hubble, 1936)

a number of the overall properties of galaxies such as their integrated colours, the fraction of the mass of the galaxy in the form of neutral and molecular gas, and so on (Sect. 3.8). The vast majority of galaxies can be accommodated within the *revised Hubble Sequence of Galaxies*, which is described in detail by de Vaucouleurs, Sandage, Kormendy and van den Bergh (de Vaucouleurs, 1974; Sandage, 1975; Kormendy, 1982; van den Bergh, 1998). Van den Bergh emphasised that the classical Hubble types refer primarily to intrinsically luminous galaxies and that, in addition, there exists a large population of intrinsically low luminosity *dwarf galaxies* which can only be observed relatively nearby. There are also various other categories of galaxies with special characteristics, for example, the Seyfert galaxies, cD galaxies, N galaxies, radio galaxies, starburst galaxies and so on. Many of these types of galaxy contain *active galactic nuclei*.

Elliptical galaxies E. These galaxies show no structural features in their brightness distributions but have an elliptical appearance, as if they were spheroids or ellipsoids of revolution (Fig. 3.2a). In absolute magnitude, elliptical galaxies range from among the most luminous galaxies known, having $M_B \approx -24$, to dwarf ellipticals (dE), which are found in the Local Group of galaxies. In Hubble's notation, the observed ellipticity of the galaxy is included in the morphological designation according to the rule that the number $10 \times (a - b)/a$ was written after the letter E, where a and b are the observed major and minor axes of the ellipse. Thus E0 galaxies are circular and E7 galaxies, the most extreme ellipticities found in elliptical galaxies, have $b/a = 0.3$. Galaxies flatter than E7 all show a distinct disc and bulge structure and hence are classified as lenticular (S0) rather than E galaxies.

Spiral galaxies S, SA, SB. The characteristic feature of spiral galaxies is their disk-like appearance with well-defined spiral arms emanating from their central regions (Fig. 3.2b and 3.3a). Very often the spiral pattern is double with a remarkable degree of symmetry with respect to the centre of the galaxy, but many more complicated configurations of spiral structure are known. The light distribution of what Hubble termed 'normal' spiral galaxies (or SA galaxies) can be decomposed into a *central bulge* or *spheroidal component*, similar in character to an elliptical galaxy, and a *disk component*, within which the spiral arms lie. In the case of the *barred spirals* (or SB galaxies), the central bulge has an elongated or ellipsoidal appearance, the spiral arms originating from the ends of the bar (Fig. 3.3a). There are as many 'barred' spiral galaxies as 'normal' spirals and, furthermore, there are just as many spirals intermediate between these two classes.

Spiral galaxies are classified as Sa, Sb, Sc according to the following criteria, in decreasing order of importance: (1) the openness of the winding of the spiral arms, (2) the degree of resolution of the arms into stars and (3) the size of the spheroidal component or central bar relative to the disk component. Thus,

- *Sa galaxies* have tightly wound spiral arms which are smooth showing no resolution into stars. The central bulge or bar is dominant, shows no structure and is unresolved into star clusters.
- *Sb galaxies* have more open spiral arms, which show resolution into stars. The central spheroidal component or bar is generally smaller than in Sa galaxies.



Fig. 3.2a,b. Examples of different types of normal galaxy. **a** The elliptical galaxy M87 (NGC 4486), one of the most luminous galaxies in the nearly Virgo cluster of galaxies. This image shows its famous optical jet originating in the bright nucleus of the galaxy which contains a black hole of mass $M \sim 10^9 M_\odot$

- *Sc galaxies* have very open spiral arms which are patchy and are resolved into star clusters and regions of ionised hydrogen. The spheroidal component is very small. In barred spiral galaxies, the bar is resolved into clusters and HII regions and is not as prominent as in classes Sa or Sb.
- The revised Hubble scheme extends this classification beyond Sc to include ‘nearly chaotic’ structures which would have been classified as very late Sc spirals in the standard sequence but are now as classified Sd spirals.

These morphological classes are rather broad and intermediate stages along the sequence are defined as Sab, Sbc and Scd. It is found that, within a given class of spiral galaxy, the importance of the bulge can vary considerably. It is interesting to compare this approach with the more recent statistical approach in which the bulge-to-disc ratio is one of the key measurable parameters.



Fig. 3.2. (continued) **b** The spiral galaxy M51 (NGC 5194) and its nearby dusty companion (NGC 5195). (Images courtesy of NASA, ESA and the Hubble Heritage Team (STScI/AURA))

Lenticular galaxies S0 or L. All galaxies with smooth light distributions and axial ratios $b/a < 0.3$ show evidence of a disk-like component and these are called *lenticular* (lens-like) or S0 galaxies (Fig. 3.3b). They are similar to spiral galaxies in that their light distributions can be decomposed into a central bulge, similar in properties to elliptical galaxies, and an extensive disk. The lenticular galaxies appear intermediate in morphological type between elliptical and spiral galaxies.

In many cases, the central bulges of the S0 galaxies have a bar-like appearance and hence, as in the case of the spirals, they can be divided into ‘ordinary’ and ‘barred’ lenticulars as well as intermediate types. In a number of lenticular galaxies, there is evidence for obscuring matter, often in the form of rings as can be seen in the example of NGC 1300 in Fig. 3.3b. In the revised Hubble classification, lenticular galaxies which are free of obscuring matter are termed ‘early’ S0[−] with stages S0⁰ and S0⁺ representing ‘later’ stages with increasing amounts of obscuring material. By the intermediate stage between lenticular and spiral galaxies, S0/a, the obscuring matter begins to show what is referred to as ‘incipient spiral structure’.

Irregular galaxies. In Hubble’s original classification, irregular galaxies were systems ‘lacking both dominating nuclei and rotational symmetry’ and the class included everything which could not be readily incorporated into the standard Hubble



Fig. 3.3a,b. Examples of different types of normal galaxy. **a** The barred spiral galaxy NGC 1300

sequence. Many of these irregulars were similar to the companion galaxies of our own Galaxy, the Magellanic Clouds, and these were designated Irr I or Magellanic irregulars. There remained a small class of irregulars consisting of galaxies such as M82 , NGC 520 and NGC 3077, in which there was no evidence of resolution into stars; these galaxies were classified Irr II galaxies.

Evidence that the Irr I galaxies form a natural extension of the Hubble sequence was provided by de Vaucouleurs' discovery of weak but definite spiral structure in the Large Magellanic Cloud (LMC). Galaxies like the LMC can be considered to belong to stages in the Hubble sequence later than Sd and are denoted Sm. Thus, the late stages of the sequence reads: Scd, Sd, Sdm, Sm, Im. The Irr II systems find no natural place in the revised sequence and are designated I0 by de Vaucouleurs. The characteristics of the I0 irregular galaxies are that they are very rich in interstellar matter and contain young stars and active regions of star formation; a number of these would be classified as starburst galaxies.

In the revised Hubble sequence, shown in tabular form in Table 3.1, the various stages along the sequence are assigned numbers ranging from -6 to 11. All transitions along the sequence are smooth and continuous. The frequencies with which different types of galaxy are found among catalogues of bright galaxies are shown in Tables 3.2 and 3.3 (de Vaucouleurs 1963). Striking features of this table are the large percentage of lenticular galaxies and the roughly equal proportions of normal, barred and intermediate spiral galaxies. The latter statistics indicate that, in well over half the known examples of spiral galaxies, there are bar-like structures

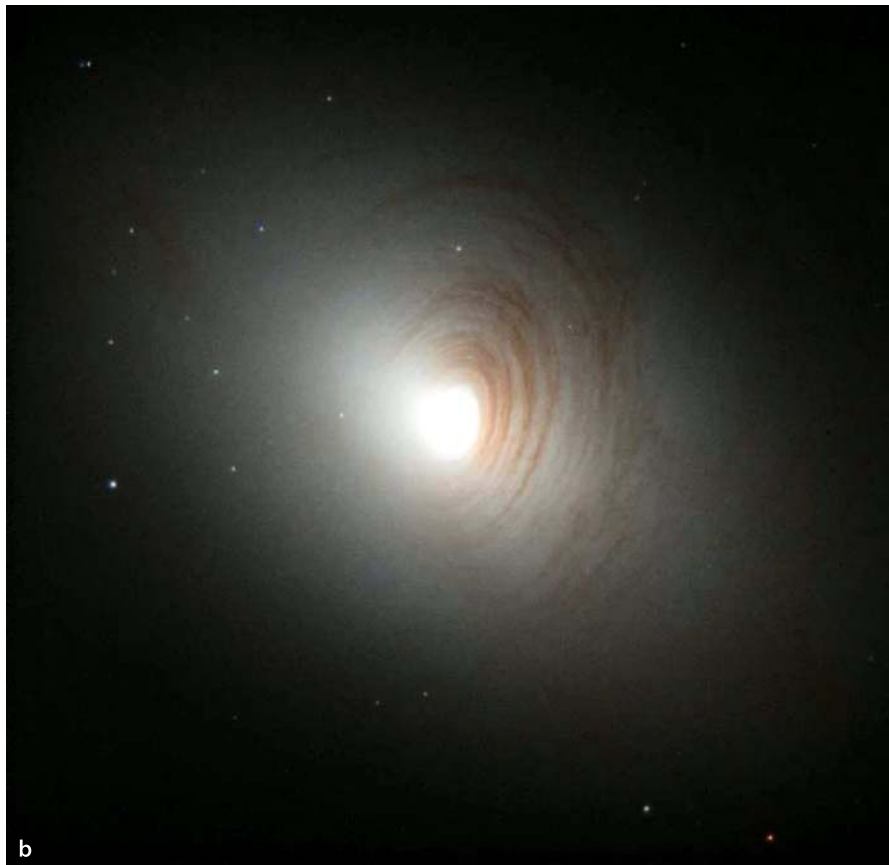


Fig. 3.3. (continued) b The SB0 or lenticular galaxy NGC 2787. (Images courtesy of NASA, ESA and the Hubble Heritage Team (STScI/AURA))

Table 3.1. The revised Hubble sequence of galaxies according to de Vaucouleurs' classification (de Vaucouleurs, 1974)

-6	-5	-4	-3	-2	-1	0	1	2	3	4	5	6	7	8	9	10	11
E ⁻	E ⁰	E ⁺	S0 ⁻	S0 ⁰	S0 ⁺	S0a	Sa	Sab	Sb	Sbc	Sc	Scd	Sd	Sdm	Sm	Im	Io

in their central regions and this has important implications for the origin of spiral structure.

The figures given in Tables 3.2 and 3.3 must be treated with considerable caution. First of all, the galaxies included in the above statistics are those present in bright galaxy catalogues. They therefore refer to objects of a very wide range of intrinsic luminosities, from among the most luminous galaxies known, such as M87, to nearby dwarf galaxies. Secondly, as mentioned above, the classical Hubble types refer

Table 3.2. The frequencies with which galaxies of different morphological types are found among samples of bright galaxies (de Vaucouleurs, 1963)

Class of Galaxy	E	L	S	Im	I0	Pec	Total
Number	199	329	934	39	13	14	1528
Percentage	13.0	21.5	61.1	2.55	0.85	0.9	100

Table 3.3. The frequencies of different subtypes among 994 spiral galaxies (de Vaucouleurs, 1963)

Class of Galaxy	0/a	a	ab	b	bc	c	cd	d	dm	m	?	Total	Percentage
SA	17	25	25	57	57	82	30	9	3	4	2	311	31.3
SAB	13	15	23	45	50	71	35	11	3	7	1	274	27.6
SB	26	43	33	83	27	55	27	28	9	30	10	366	36.8
S	4	1	0	6	1	13	1	10	0	0	7	43	4.3

almost exclusively to intrinsically luminous galaxies. Thirdly, the above statistics include galaxies belonging to the general field, to weak groups and to rich clusters of galaxies, but the fractions of the different morphological types vary with the local galaxy number density. In an important paper, Dressler plotted the frequency of different galaxy types as a function of the number density of galaxies in which they are found (Fig. 3.4) (Dressler, 1980). Field galaxies, that is, galaxies which are not members of groups or clusters of galaxies, are located towards the left of the diagram, while rich clusters of galaxies are towards the right. It can be seen that, in rich clusters, the elliptical and S0 galaxies are much more common than the spiral galaxies, whereas in the general field, the majority of galaxies are spirals. Evidently, the environment in which a galaxy finds itself is correlated with its morphological characteristics. These relations will be quantified in more detail in Sect. 3.9.4.

3.3 Peculiar and Interacting Galaxies

The revised Hubble classification can encompass the forms of virtually all galaxies. There are, however, a number of galaxies with very strange appearances and these are referred to collectively as *peculiar galaxies*. Arp published his *Atlas of Peculiar Galaxies* in 1966 and a corresponding catalogue for the Southern Hemisphere 1987 (Arp, 1966; Arp et al., 1987). As he remarked in the introduction to the first Atlas:

The greatest deviations from the normal are emphasised in this atlas.

A few galaxies are known, for example, in which the stellar component is in the form of a ring rather than a disc or spheroid, the Cartwheel being a beautiful example of this type of galaxy (Fig. 3.5); these are known as *ring galaxies*.

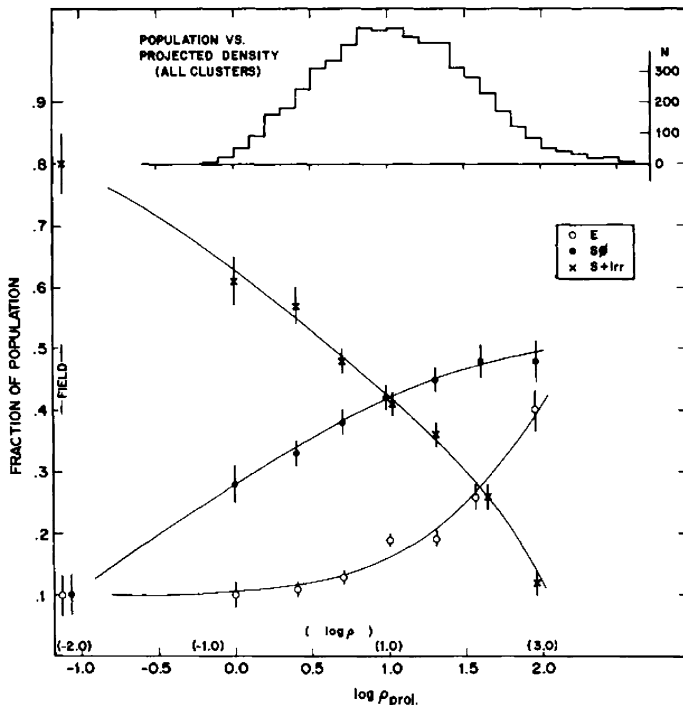


Fig. 3.4. The fractions of different morphological types of galaxy found in different galaxy environments. The local number density of galaxies is given as a projected surface density, ρ_{proj} of galaxies, that is, numbers Mpc^{-2} (Dressler, 1980)

Most of these remarkable structures are due to strong gravitational interactions, or collisions, between galaxies. In the early 1970s, Toomre and Toomre carried out pioneering computer simulations of close encounters between galaxies which showed how such events could give rise to remarkable asymmetric structures (Toomre and Toomre, 1972). In Fig. 3.6, a deep image of the pair of interacting galaxies known as the Antennae is shown, revealing the extraordinary long ‘tails’ which seem to be emanating from a pair of closely interacting spiral galaxies in which a great deal of recent star formation has occurred.

The Toomres showed how such elongated ‘tails’ could be accounted for by a gravitational interaction between two spiral galaxies. In the simulation shown in Fig. 3.7, the two spiral galaxies pass close to each other on prograde orbits, that is, the rotational axes of the two discs are parallel and also parallel to the rotational axis of the two galaxies about their common centre of mass. The spiral galaxies are represented by differentially rotating discs of stars and, while they are at their distance of closest approach, the stars in the outermost rings feel the same mutual force acting upon them for a very much longer time than if the passage had been in, say, the retrograde direction. As a result, the outer rings of stars feel

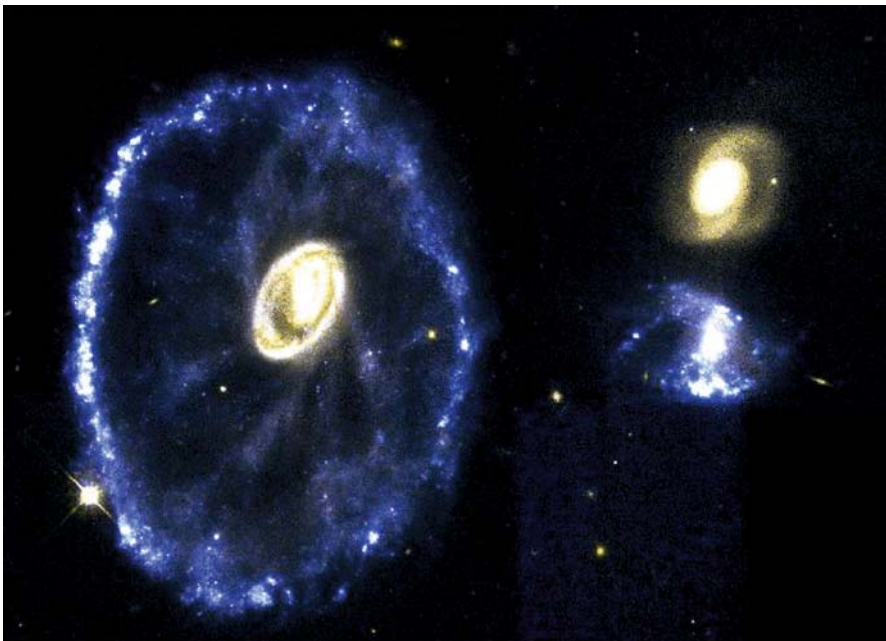


Fig. 3.5. The peculiar galaxy known as the Cartwheel as observed by the Hubble Space Telescope. (Image courtesy of NASA, ESA and the Hubble Heritage Team (STScI/AURA)) Its strange appearance is almost certainly due to a recent collision, or strong interaction, with one of its nearby companions. The simulations by Toomre and Toomre show that such a ‘tidal wave’ is expected if a compact mass had passed through a spiral galaxy close to its centre (Toomre, 1974)

a coherent force for an extended period and are stripped off to form the types of extended structure observed in the Antennae. Many of the features of strong gravitational interactions are described in the pioneering papers by the Toomres. Similar structures are found in more recent supercomputer simulations of colliding and interacting galaxies which can include millions of stars, as well as incorporating the dynamics of the interstellar gas in the collision (Barnes and Hernquist, 1996; Mihos and Hernquist, 1996; Springel, 2005). The compression of the interstellar media in the collision results in regions of intense star formation.

Interactions between galaxies play a central role in many aspects of galactic evolution. From the observational point of view, the IRAS satellite showed that colliding galaxies are among the most luminous extragalactic far-infrared sources. The inference is that, when galaxies collide, their interstellar media are compressed to high densities and the rate of star formation is greatly enhanced, resulting in intense far-infrared emission.

Collisions between galaxies have also assumed a central role in models of galaxy formation. In the preferred scenarios of structure formation, galaxies are built up

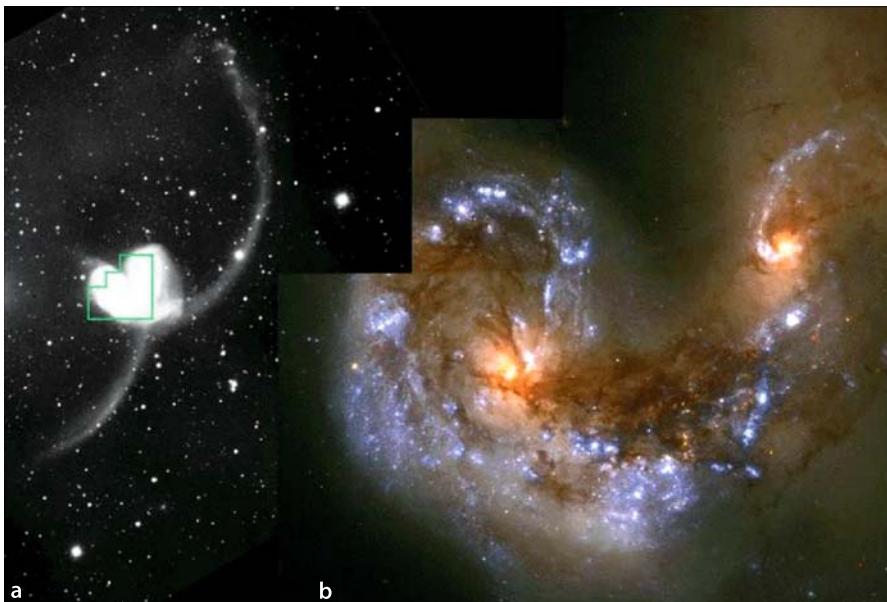


Fig. 3.6a,b. The strange pair of interacting galaxies known as the Antennae, named after the elongated structures apparently torn off in a collisions between the galaxies. **a** A wide field image showing the extended ‘tails’ produced in the encounter. **b** A ‘true colour’ Hubble Space Telescope image of the colliding galaxies. The many blue regions in the diagram contain young luminous stars, indicating that a large amount of star formation has been induced by the collision between the interstellar media of the interacting galaxies. (Image courtesy of NASA, ESA and the Hubble Heritage Team (STScI/AURA))

by the process of hierarchical clustering in which larger galaxies are formed by the coalescence of smaller galaxies. In this picture, strong gravitational encounters between galaxies are essential in forming the structures we observe today. Reference to Table 3.2 shows that the percentage of peculiar and interacting systems among the present population of galaxies is only about 1%. We will find that this percentage increases dramatically as we look further and further back in time, consistent with the hierarchical picture of structure formation.

3.4 The Light Distribution in Galaxies

Another approach to the classification of galaxies is to use their light distributions since it is found that these are somewhat different for bulge-dominated and disc-dominated systems. Let us first summarise the results of studies of bright galaxies and then show how these can be adapted for the study of large samples of galaxies.

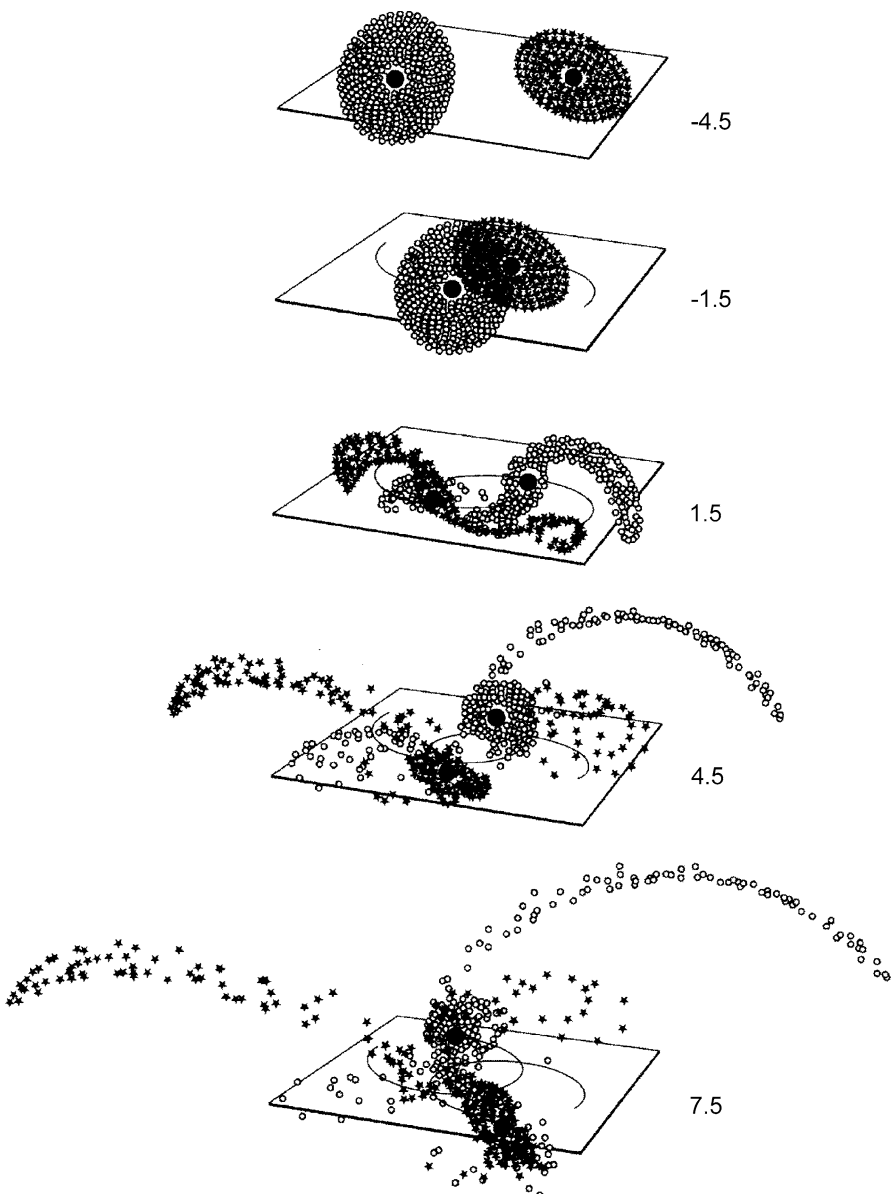


Fig. 3.7. A simulation of a close encounter between two disc galaxies which approach each other on prograde orbits. It can be seen that the outer rings of stars are torn off each galaxy, forming the remarkable ‘Antenna’ structures (Toomre and Toomre, 1972)

3.4.1 Elliptical Galaxies

The earliest expression for the observed surface brightness distribution of elliptical galaxies as a function of radius r is commonly referred to as *Hubble's law*

$$I(r) = I_0 \left(\frac{r}{r_c} + 1 \right)^{-2}, \quad (3.1)$$

where r_c is the *core radius* of the galaxy. This expression provides a reasonable description of the intensity distribution in the central regions of elliptical galaxies but is a poor fit in the outer regions.

A much better description of the surface brightness distribution of elliptical galaxies and the bulges of spiral galaxies is the empirical law proposed by de Vaucouleurs which is usually referred to as the $r^{1/4}$ law (de Vaucouleurs, 1948)

$$\log_{10} \left[\frac{I(r)}{I(r_e)} \right] = -3.3307 \left[\left(\frac{r}{r_e} \right)^{1/4} - 1 \right], \quad (3.2)$$

or

$$\log_e \left[\frac{I(r)}{I(r_e)} \right] = -7.6692 \left[\left(\frac{r}{r_e} \right)^{1/4} - 1 \right]. \quad (3.3)$$

This expression provides a good representation of the luminosity profile over many decades of surface brightness. The expression has been normalised so that r_e is the radius within which half the total luminosity is emitted and $I(r_e)$ is the surface brightness at that radius. The corresponding total luminosity of the galaxy is

$$L = 7.215\pi I_e r_e^2 \left(\frac{b}{a} \right), \quad (3.4)$$

where b/a is the apparent axis ratio of the elliptical galaxy (Gilmore et al., 1989).

3.4.2 Spiral and Lenticular Galaxies

The light distributions in most spiral and lenticular galaxies can be decomposed into two components, a spheroidal component associated with the central bulge and a disc component. The luminosity profile of the spheroidal component is the same as that of an elliptical galaxy and may be described by the de Vaucouleurs $r^{1/4}$ law discussed above.

In almost all galaxies in which there is evidence of a disc component, including spirals, barred spirals and lenticulars, the luminosity profile of the disc may be represented by an exponential light distribution

$$I(r) = I_0 \exp(-r/h), \quad (3.5)$$

where h is called the *disc scale length*; for our own Galaxy $h \approx 3$ kpc. I_0 is the central surface brightness. The total luminosity of the disc is then $L = 4\pi h^2 I_0$. According to Freeman, this luminosity profile is also found in very late-type galaxies, such as the Magellanic irregulars which show evidence of a disc in rotation.

In 1970, Freeman discovered the remarkable result that, although the disc components of large disc galaxies have a wide range of luminosities, there is remarkably little scatter in the value of the central surface brightness I_0 (Freeman, 1970). A mean value of $I_0 = 21.67 \pm 0.3$ B magnitudes arcsec $^{-2}$ was found for the galaxies in the sample studied by Freeman, the differences in total luminosity being due to variations in the scale length of the light distribution h from galaxy to galaxy. There has been considerable debate about the validity of this result because the samples of galaxies studied are strongly influenced by selection effects, in particular, the galaxies have to be bright enough and large enough for precise surface photometric observations to be possible. Disney suggested that the constancy of the central surface brightness of the discs of spiral galaxies could be largely attributed to these selection effects (Disney, 1976). Van der Kruit surveyed a number of attempts to remove the effects of observational selection from the samples studied and concluded that ‘non-dwarf galaxies do have a relatively narrow dispersion of central surface brightnesses, and this is not the result of selection effects’ (Gilmore et al., 1989). It is certainly the case that, for low luminosity spiral galaxies, the values of central surface brightness are smaller Freeman’s standard value, the most extreme cases being the low surface brightness disc galaxies which can have I_0 as low as 25.5 B magnitudes arcsec $^{-2}$.

3.4.3 Putting the Light Distributions Together

A convenient way of combining the light distributions of elliptical and spiral galaxies is to adopt the formulation proposed by Sérsic which can be thought of as a generalisation of de Vaucouleurs’ $r^{1/4}$ law (Sérsic, 1968)

$$\log_{10} \left[\frac{I(r)}{I(r_e)} \right] = -b_n \left[\left(\frac{r}{r_e} \right)^{1/n} - 1 \right]. \quad (3.6)$$

where r_e is the radius within which half of the total light is emitted and the b_n is a normalisation constant to ensure that the total light sums to L_{tot} for a given value of n . It can be seen that the value $n = 4$ results in de Vaucouleurs’ $r^{1/4}$ law and $n = 1$ in the exponential law found in the discs of spiral galaxies.

This formalism can be used to discriminate between disc-dominated and bulge-dominated galaxies. A beautiful example of the application of Sérsic’s formula to a large sample of galaxies is shown in Fig. 3.8a which shows the distribution of n among 10,095 galaxies selected from the Millennium Galaxy Catalogue (Driver et al., 2006). It can be seen that the galaxy sample splits very beautifully into two populations, one centred on the value $n = 4$, corresponding to the elliptical galaxies and the bulges of spiral galaxies and the other the value $n = 1$, corresponding to the light distribution of disc galaxies. In the analysis by Driver and his colleagues, the morphological categories were checked by visual inspection of the images of the

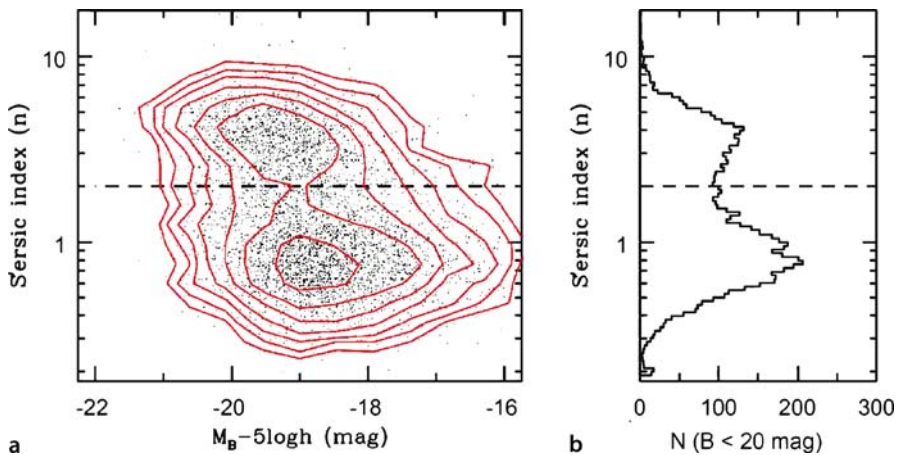


Fig. 3.8. **a** A plot of the observed value of the Sérsic index n as a function of the absolute blue magnitude in a sample of 10,095 galaxies from the Millennium Galaxy Catalogue. **b** The histogram showing the number of galaxies in equal logarithmic bins of Sérsic index n (Driver et al., 2006)

galaxies. The distinction between the bulge-dominated and disc-dominated systems occurs at about $n \approx 2$. As we will see, these structural parameters are strongly correlated with other properties of the galaxies, in particular, with the red and blue galaxy sequences described in Sect. 3.9.2. This procedure is particularly valuable in distinguishing the structural properties of large samples of galaxies by computer analyses.

3.5 The Masses of Galaxies

All direct methods of measuring masses in astronomy are dynamical. For systems such as star clusters, galaxies and clusters of galaxies, it can generally be assumed that they have reached some form of dynamical equilibrium and then, by measuring the velocities of the objects which make up the system and knowing its dimensions, mass estimates can be made. A key result for determining the masses of galaxies and clusters of galaxies is the *virial theorem*, first derived for star clusters by Eddington in 1916 (Eddington, 1916).

3.5.1 The Virial Theorem for Clusters of Stars, Galaxies and Clusters of Galaxies

Star clusters, galaxies and clusters of galaxies can generally be considered to be gravitationally bound configurations, meaning that the stars or galaxies have come into *dynamical equilibrium* under gravity. This assertion is supported by comparison of the *crossing time* of an object within the system with its age. The crossing time is

defined to be $t_{\text{cr}} = R/\langle v \rangle$ where R is the size of the system and $\langle v \rangle$ is the typical speed, or velocity dispersion, of the objects of which it is composed. For example, the orbital speed of the stars in our Galaxy at our distance from its centre, 8.5 kpc, is about 220 km s⁻¹. Therefore, the time it takes the stars to make one complete revolution about the centre of our Galaxy is $t = 2\pi R/v \approx 2.5 \times 10^8$ years. This is very much less than the age of the Galaxy, which is about 1.3×10^{10} years, and so the system must be gravitationally bound. Similarly, in the Coma cluster of galaxies, the crossing time is less than about one-tenth the age of the Universe, indicating that the cluster must be gravitationally bound, or else the galaxies would have dispersed long ago.

The *virial* was introduced by Rudolph Clausius in 1870 in connection with the thermal energy of gases. The virial was defined to be the quantity $\mathcal{E}_i = -\frac{1}{2}\langle \mathbf{r}_i \cdot \mathbf{F}_i \rangle$ where the force \mathbf{F}_i acts on the particle i located at position vector \mathbf{r}_i . The angle brackets represent the time average of the force acting on the particle and Clausius showed that \mathcal{E}_i is the system's average kinetic energy (see p. 105 in (Sparke and Gallagher, 2000)). In the astronomical context, the theorem refers to the energy balance in systems in equilibrium under gravity and it is found in a variety of different guises. In its application to the internal properties of stars, the virial theorem describes the relation between the thermal energy of the gas and its gravitational potential energy. The theorem can be extend to include rotational energy, magnetic energy, the energy in the form of convective motions or turbulence, and so on. In stellar dynamics, in which the ‘gas’ of stars may be taken to be collisionless, the *tensor virial theorem* relates the equilibrium state to the energies associated with the velocity distribution of the stars at each point, which will in general be anisotropic (Binney and Tremaine, 1987). In this section, we will only consider the simplest form of virial theorem for a self-gravitating system of point masses.

Suppose a system of particles (stars or galaxies), each of mass m_i , interact with each other only through their mutual forces of gravitational attraction. Then, the acceleration of the i th particle due to all other particles can be written vectorially

$$\ddot{\mathbf{r}}_i = \sum_{j \neq i} \frac{Gm_j(\mathbf{r}_j - \mathbf{r}_i)}{|\mathbf{r}_i - \mathbf{r}_j|^3}. \quad (3.7)$$

Now, take the scalar product of both sides with $m_i \mathbf{r}_i$.

$$m_i(\mathbf{r}_i \cdot \ddot{\mathbf{r}}_i) = \sum_{j \neq i} Gm_i m_j \frac{\mathbf{r}_i \cdot (\mathbf{r}_j - \mathbf{r}_i)}{|\mathbf{r}_i - \mathbf{r}_j|^3}. \quad (3.8)$$

Differentiating $(\mathbf{r}_i \cdot \mathbf{r}_i)$ with respect to time

$$\frac{d}{dt}(\mathbf{r}_i \cdot \mathbf{r}_i) = 2\dot{\mathbf{r}}_i \cdot \mathbf{r}_i, \quad (3.9)$$

and then, taking the next derivative,

$$\frac{1}{2} \frac{d^2}{dt^2}(\mathbf{r}_i^2) = \frac{d}{dt}(\dot{\mathbf{r}}_i \cdot \mathbf{r}_i) = (\ddot{\mathbf{r}}_i \cdot \mathbf{r}_i + \dot{\mathbf{r}}_i \cdot \dot{\mathbf{r}}_i) = (\ddot{\mathbf{r}}_i \cdot \mathbf{r}_i + \dot{\mathbf{r}}_i^2). \quad (3.10)$$

Therefore, (3.8) can be rewritten

$$\frac{1}{2} \frac{d^2}{dt^2} (m_i \mathbf{r}_i^2) - m_i \dot{\mathbf{r}}_i^2 = \sum_{j \neq i} G m_i m_j \frac{\mathbf{r}_i \cdot (\mathbf{r}_j - \mathbf{r}_i)}{|\mathbf{r}_i - \mathbf{r}_j|^3}. \quad (3.11)$$

Now we sum over all the particles in the system,

$$\frac{1}{2} \frac{d^2}{dt^2} \sum_i m_i \mathbf{r}_i^2 - \sum_i m_i \dot{\mathbf{r}}_i^2 = \sum_i \sum_{j \neq i} G m_i m_j \frac{\mathbf{r}_i \cdot (\mathbf{r}_j - \mathbf{r}_i)}{|\mathbf{r}_i - \mathbf{r}_j|^3}. \quad (3.12)$$

Now the double sum on the right-hand side represents the sum over all the elements of a square $n \times n$ matrix with all the diagonal terms zero. If we sum the elements ij and ji of the matrix, we find

$$G m_i m_j \left[\frac{\mathbf{r}_i \cdot (\mathbf{r}_j - \mathbf{r}_i)}{|\mathbf{r}_i - \mathbf{r}_j|^3} + \frac{\mathbf{r}_j \cdot (\mathbf{r}_i - \mathbf{r}_j)}{|\mathbf{r}_j - \mathbf{r}_i|^3} \right] = -\frac{G m_i m_j}{|\mathbf{r}_i - \mathbf{r}_j|}. \quad (3.13)$$

Therefore,

$$\frac{1}{2} \frac{d^2}{dt^2} \sum_i m_i \mathbf{r}_i^2 - \sum_i m_i \dot{\mathbf{r}}_i^2 = -\frac{1}{2} \sum_{\substack{j \neq i \\ i,j}} \frac{G m_i m_j}{|\mathbf{r}_i - \mathbf{r}_j|}, \quad (3.14)$$

where the factor $\frac{1}{2}$ on the right-hand side is included because the sum is still over all elements of the array and so the sum of each pair would be counted twice.

Now, $\sum_i m_i \dot{\mathbf{r}}_i^2$ is twice the total kinetic energy, T , of all the particles in the system, that is,

$$T = \frac{1}{2} \sum_i m_i \dot{\mathbf{r}}_i^2. \quad (3.15)$$

The gravitational potential energy of the system is

$$U = -\frac{1}{2} \sum_{\substack{j \neq i \\ i,j}} \frac{G m_i m_j}{|\mathbf{r}_i - \mathbf{r}_j|}. \quad (3.16)$$

Therefore,

$$\frac{1}{2} \frac{d^2}{dt^2} \sum_i m_i \mathbf{r}_i^2 = 2T - |U|. \quad (3.17)$$

If the system is in statistical equilibrium

$$\frac{d^2}{dt^2} \sum_i m_i \mathbf{r}_i^2 = 0, \quad (3.18)$$

and therefore

$$T = \frac{1}{2}|U|. \quad (3.19)$$

This is the equality known as the *virial theorem* in stellar dynamics.

Notice that, at no point, have we made any assumption about the orbits or velocity distributions of the particles. The velocities might be random, as is often assumed to be the case for globular clusters or spherical elliptical galaxies, but they might also have highly elongated orbits about the centre of the galaxy. In the case of the discs of spiral galaxies, the velocity vectors are highly ordered and the mean rotational speed about the centre is much greater than the random velocities of the stars. In all these cases, the virial theorem must hold if the system is to remain in dynamical equilibrium. In its simplest form, the expression (3.19) tells us nothing about the velocity distribution of the stars or galaxies within the system.

Despite the elegance of the theorem, its application to astronomical systems is not straightforward. In most cases, we can only measure directly radial velocities from the Doppler shifts of spectral lines and positions on the sky. In some cases, independent distance measures of the stars or galaxies within the system are available, but generally, within star clusters and clusters of galaxies, it is not possible to distinguish whether the objects are on the near or far side of the cluster. In some cases, the proper motions of the objects can be measured and then their three-dimensional space motions can be found. Generally, for clusters of galaxies, we need to make assumptions about the spatial and velocity distributions of galaxies in the cluster. For example, if we assume that the velocity distribution of the galaxies is isotropic, the same velocity dispersion is expected in the two perpendicular directions as along the line of sight and so $\langle v^2 \rangle = 3\langle v_{\parallel}^2 \rangle$, where v_{\parallel} is the radial velocity. If the velocity dispersion is independent of the masses of the stars or galaxies, we can find the total kinetic energy $T = (1/2) \sum_i m_i \dot{r}_i^2 = (3/2)M\langle v_{\parallel}^2 \rangle$, where M is the total mass of the system. If the velocity dispersion varies with mass, then $\langle v_{\parallel}^2 \rangle$ is a mass-weighted velocity dispersion. If the system is spherically symmetric, we can work out from the observed surface distribution of stars or galaxies a suitably weighted mean separation R_{cl} , so that the gravitational potential energy can be written $|U| = GM^2/R_{\text{cl}}$. Thus, the mass of the system can be found from the virial theorem

$$T = \frac{1}{2}|U| \quad M = 3\langle v_{\parallel}^2 \rangle R_{\text{cl}}/G. \quad (3.20)$$

Notice that, in general, we have to estimate some characteristic velocity, or velocity dispersion, and the size of the system in order to find its mass. This general result is widely applicable in astrophysics.

3.5.2 The Rotation Curves of Spiral Galaxies

In the case of spiral galaxies, masses can be estimated from their *rotation curves*, that is, the variation of the orbital, or rotational, speed $v_{\text{rot}}(r)$ about the centre of the galaxy with distance r from its centre. Examples of the rotation curves of spiral

galaxies derived from optical and radio 21-cm line studies are shown Fig. 3.9b (Bosma, 1981). In a few galaxies, there is a well-defined maximum in the rotation curve and the velocity of rotation decreases monotonically with increasing distance from the centre. If this decrease continues to infinite distance, the total mass of the galaxy converges and is similar to that derived from the rotation curve in the central regions. In many cases, however, the rotational velocities in the outer regions of galaxies are remarkably constant with increasing distance from the centre. It is apparent from Fig. 3.9a that the flat rotation curve of our spiral neighbour M31 extends far beyond the optical image of the galaxy.

The significance of these flat rotation curves can be appreciated from application of Gauss's theorem to Newton's law of gravity. For simplicity, let us assume that the distribution of mass in the galaxy is spherically symmetric, so that we can write the mass within radius r as $M(\leq r)$. According to Gauss's law for gravity, for any spherically symmetric variation of mass with radius, we can find the radial acceleration at radius r by placing the mass within radius r , $M(\leq r)$, at the centre of the galaxy. Then, equating the centripetal acceleration at radius r to the gravitational acceleration, we find

$$\frac{GM(\leq r)}{r^2} = \frac{v_{\text{rot}}^2(r)}{r} \quad M(\leq r) = \frac{v_{\text{rot}}^2(r)r}{G}. \quad (3.21)$$

For a point mass, say the Sun, $M(\leq r) = M_{\odot}$, and we recover Kepler's third law of planetary motion, the orbital period T being equal to $2\pi r/v_{\text{rot}} \propto r^{3/2}$. This result can also be written $v_{\text{rot}} \propto r^{-1/2}$ and is the variation of the circular rotational velocity expected in the outer regions of a galaxy if most of the mass is concentrated within the central regions.

If the rotation curve of the spiral galaxy is flat, $v_{\text{rot}} = \text{constant}$, $M(\leq r) \propto r$ and so the mass within radius r increases linearly with distance from the centre. This contrasts dramatically with the distribution of light in the discs, bulges and haloes of spiral galaxies which decrease exponentially with increasing distance from the centre

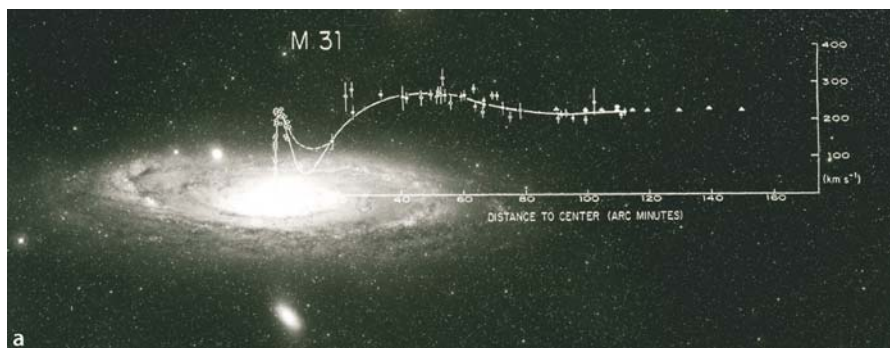


Fig. 3.9. a The rotation curve for the nearby giant spiral galaxy M31, showing the flat rotation curve extending well beyond the optical image of the galaxy (Courtesy of Dr. Vera Rubin)

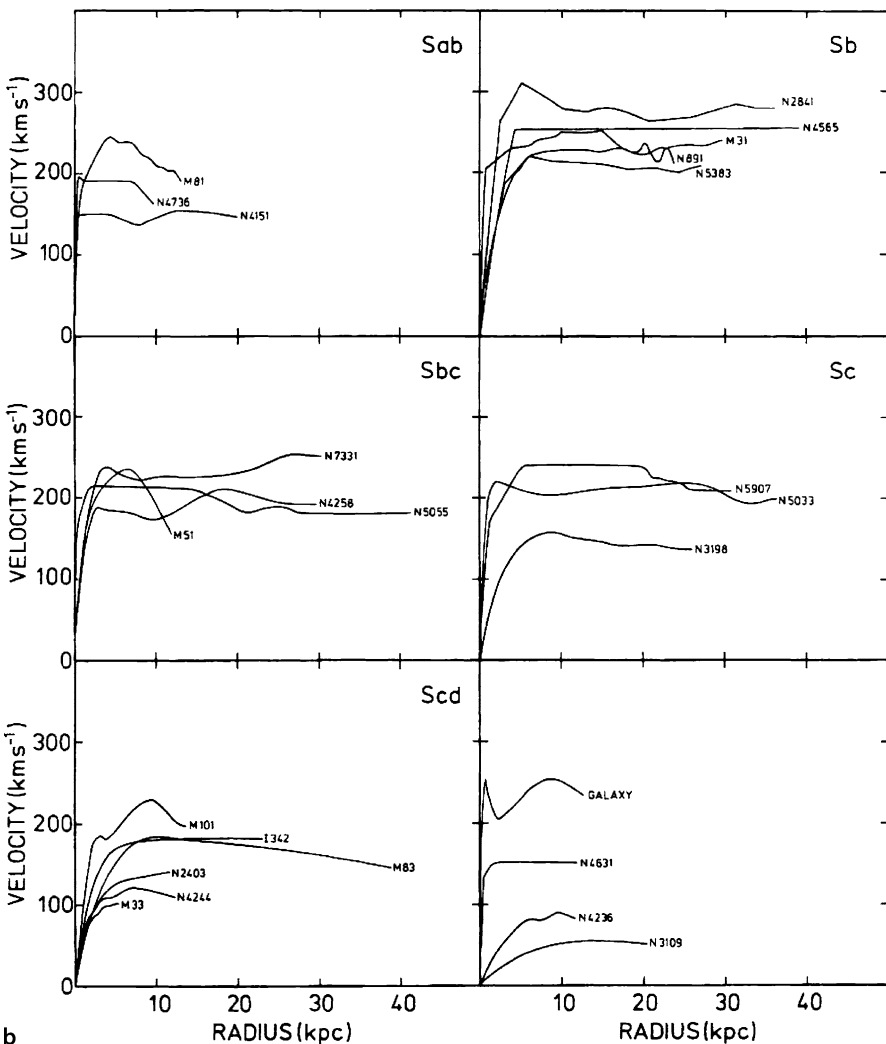


Fig. 3.9. (continued) **b** Examples of the rotation curves of spiral galaxies from optical and neutral hydrogen observations (Bosma, 1981)

(see Sect. 3.4.2). Consequently, the local mass-to-luminosity ratio must increase in the outer regions of spiral galaxies.

It is most convenient to quote the results in terms of mass-to-luminosity ratios relative to that of the Sun. For the visible parts of spiral galaxies, for which the rotation curves are well-determined, mean mass-to-light ratios in the B waveband in the range 1–10 are found. This is similar to the value found in the solar neighbourhood; averaging over the masses and luminosities of the local stellar populations, a value of $M/L \approx 3$ is found. The M/L ratio must however increase to much larger values at large values of r . Values of $M/L \approx 10\text{--}20 M_{\odot}/L_{\odot}$ are found in the outer regions of

spiral galaxies, similar to the values found for elliptical galaxies. These data provide crucial evidence for the presence of dark matter in galaxies.

There are theoretical reasons why spiral galaxies should possess dark haloes. Ostriker and Peebles showed that, without such a halo, a differentially rotating disc of stars is subject to a bar instability (Ostriker and Peebles, 1973). Their argument has been confirmed by subsequent computer simulations and suggests that dark haloes can stabilise the discs of spiral galaxies. We will return to the thorny question of the nature of the dark matter in Chap. 4.

3.5.3 The Velocity Dispersions of Elliptical Galaxies

Expression (3.20) can be used to estimate the masses of elliptical galaxies. Doppler broadening of the widths of stellar absorption lines in galaxies can be used to estimate the velocity dispersion $\langle \Delta v_{\parallel}^2 \rangle$ of stars along the line of sight through the galaxy. Typical mass-to-luminosity ratios for elliptical galaxies are about $10-20 M_{\odot}/L_{\odot}$. The trouble with this argument is that it has to be assumed that the velocity distribution of the stars in the elliptical galaxy is isotropic. As will be discussed in Sect. 3.6.3, there is compelling evidence that in general elliptical galaxies are triaxial systems and so the isotropy of the stellar velocity distribution needs to be tested directly by observation.

Evidence that there must indeed be considerable amounts of dark matter in the haloes about two of the giant elliptical galaxies in the Virgo cluster, M49 and M87, has been presented by Côté and his colleagues (Côté et al., 2001, 2003). They measured the radial velocities of a large sample of globular clusters in the haloes of these galaxies and so were able to extend the range of radii over which the velocity dispersion in these galaxies could be measured. A beautiful example of the quality of their data for M49 is shown in Fig. 3.10. Their measurements are shown by the filled circles at radii $R \geq 10$ kpc, the dotted and solid lines bracketing them showing the one and two sigma ranges of their estimates of the velocity dispersion. The points at radii less than 10 kpc show the velocity dispersion measured by other authors and it can be seen that the data are consistent with the velocity dispersion remaining remarkably constant out to radii up to 40 kpc from the centre.

Various attempts to account for the variation of the velocity dispersion with radius are indicated by the different lines on the diagram. These assume that the mass distribution follows the radial optical intensity distribution, but with various extreme assumptions about the anisotropy of the stellar velocity distribution. Even models in which the stars (or globular clusters) are on radial orbits cannot account for the fact that the line-of-sight velocity dispersion is independent of radius out to 40 kpc. Côté and his colleagues conclude that these data provide evidence that the velocity dispersion is isotropic and that there must be dark matter haloes about these galaxies. Similar conclusions can be drawn from X-ray observations of these galaxies, using the technique described in the context of clusters of galaxies in Sect. 4.4.

Physically, the fact that the velocity dispersion remains constant out to large radii has exactly the same explanation as the flatness of the rotation curves of spiral galaxies (see expression 3.21). To bind globular clusters to these massive galaxies

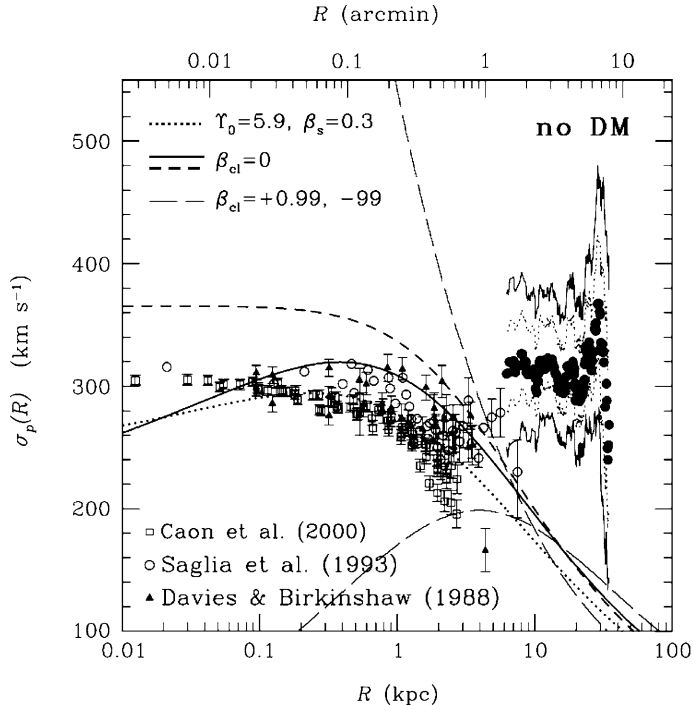


Fig. 3.10. The velocity dispersion of stars and globular clusters in the nearby giant elliptical galaxy M49 (NGC 4472). The data points at $R < 10$ kpc are obtained from the velocity width of the stellar absorption lines. The filled circles at radii $R > 10$ kpc are derived from the velocity dispersion of globular clusters. Various models for the velocity dispersion as a function of radius R , assuming that the mass follows the light are shown (Côté et al., 2003)

with these large velocity dispersions at large radii means that the mass within radius R must increase proportional to R .

3.6 The Properties of Spiral and Elliptical Galaxies

At first glance, it would seem that the elliptical galaxies should be among the simpler stellar systems to interpret theoretically because they can be approximated as single spheroidal stellar distributions. This turns out to be an overoptimistic expectation.

3.6.1 The Faber–Jackson Relation and the Fundamental Plane

Extensive studies have been made of correlations between various properties of elliptical galaxies, specifically, their luminosities, their sizes, as described by the de Vaucouleurs radius r_e , their central velocity dispersions, their surface brightnesses, the abundance of heavy elements, and so on. Of these, two studies are of particular

importance. The first is the analysis of Faber and Jackson who found a strong correlation between luminosity L and central velocity dispersion σ of the form $L \propto \sigma^x$ where $x \approx 4$ (Faber and Jackson, 1976). This correlation has been studied by other authors who have found values of x ranging from about 3 to 5. The significance of this relation is that, if the velocity dispersion σ is measured for an elliptical galaxy, its intrinsic luminosity can be found from the Faber–Jackson relation and hence, by measuring its observed flux density, its distance can be found.

This procedure for measuring distances was refined by Dressler and his colleagues and by Djorgovski and Davis who introduced the concept of the *fundamental plane* for elliptical galaxies (Dressler et al., 1987; Djorgovski and Davis, 1987). The fundamental plane lies in a three-dimensional space in which luminosity L is plotted against the central velocity dispersion σ and the mean surface brightness Σ_e within the half-light radius r_e , that is, $\Sigma_e = L(\leq r_e)/\pi r_e^2$. Dressler and his colleagues found an even stronger correlation than the Faber–Jackson relation when the surface brightness was included,

$$L \propto \sigma^{8/3} \Sigma_e^{-3/5}. \quad (3.22)$$

Various expressions for the fundamental plane appear in the literature, for example

$$r_e \propto \sigma^{1.4} I_e^{-0.9} \quad (3.23)$$

which is remarkably similar to (3.22).

Dressler and his colleagues found just as good a correlation if they introduced a new diameter D_n , which was defined as the circular diameter within which the total mean surface brightness of the galaxy exceeded a particular value. The surface brightness was chosen to be 20.75 B magnitudes arcsec $^{-2}$. The correlation found was $\sigma \propto D_n^{3/4}$, thus incorporating the dependence of both L and Σ_e into the new variable D_n .

The origin of these empirical correlations is not understood. The argument can be inverted to determine under what conditions relations such as the Faber–Jackson relation would be found. For example, since the mass of the galaxy is given by $M \propto \sigma^2 r_e$ and $L \propto I_e r_e^2$, it follows that $L \propto \sigma^4 / I_e (M/L)^2$. Thus, if I_e and M/L were constant for all elliptical galaxies, we would obtain $L \propto \sigma^4$. It is not at all clear, however, why I_e and M/L should be constant for elliptical galaxies.

Despite the lack of theoretical underpinning of these correlations, Dressler and his colleagues estimate that they enable the distances of individual galaxies to be determined to about 25% and for clusters of galaxies to about 10%.

3.6.2 Ellipticals Galaxies as Triaxial Systems

It might be thought that the internal dynamics of elliptical galaxies would be relatively straightforward. Their surface brightness distributions appear to be ellipsoidal, the ratio of the major to minor axes ranging from 1:1 to about 3:1. It is natural to attribute the flattening of the elliptical galaxies to the rotation of these stellar systems and this

can be tested by observations of the mean velocities and velocity dispersions of the stars throughout the body of the galaxy. These measurements can be compared with the rotation and internal velocity dispersions expected if the flattening of the elliptical galaxies were wholly attributed to the rotation of an axisymmetric distribution of stars. In the simplest picture, it is assumed that the velocity distribution is isotropic at each point within the galaxy.

Bertola and Capaccioli in 1975 and Illingworth in 1977 first showed that elliptical galaxies rotate too slowly for centrifugal forces to be the cause of their observed flattening; in other words, the ratio of rotational to random kinetic energy is too small (Bertola and Capaccioli, 1975; Illingworth, 1977). This analysis was repeated in 1983 for a larger sample of elliptical galaxies and for the bulges of spiral galaxies by Davies and his colleagues with the results shown in Fig. 3.11 (Davies et al., 1983). The solid lines show the amount of rotation v_m necessary to account for the observed ellipticity of the elliptical galaxy relative to the velocity dispersion σ of the stars. It can be seen that, for low luminosity elliptical galaxies and for the bulges of spiral galaxies, the ellipticity of the stellar distribution can be attributed to rotation. The most luminous ellipticals with $M_B < -20.5$ generally do not possess enough rotation to account for the observed flattening of the galaxies. This means that the assumptions of an axisymmetric spatial distribution and/or an isotropic velocity distribution of stars at all points within the galaxy must be wrong. As a consequence, these massive elliptical galaxies must be *triaxial* systems, that is, systems with three unequal axes and consequently with anisotropic stellar velocity distributions. There is no reason why the velocity distribution should be isotropic because the time-scale for the exchange of energy between stars through gravitational encounters is generally greater than the age of the galaxy. Therefore, if the velocity distribution began by being anisotropic, it would not have been isotropised by now.

Further evidence for the triaxial nature of massive elliptical galaxies has come from studies of their light distributions. In many systems not only does the ellipticity of the isophotes of the surface brightness distribution vary with radius, but also the position angle of the major axis of the isophotes can change as well. All types of variation of ellipticity with radius are known. In some cases there is a monotonic change with radius but in others there can be maxima and minima in the radial variation of the ellipticity (Bertola and Galletta, 1979). The dynamics of such galaxies must be much more complicated than those of a rotating isothermal gas sphere. Another piece of evidence for the complexity of the shapes and velocity distributions within elliptical galaxies comes from the observation that, in some ellipticals, rotation takes place along the minor as well as along the major axis (Bertola et al., 1991). Thus, despite their simple appearances, some elliptical galaxies may be triaxial systems.

The theoretical position has been clarified by an elegant and original analysis by Martin Schwarzschild (Schwarzschild, 1979). By applying linear programming techniques to the determination of orbits in general self-gravitating systems, he showed that there exist stable triaxial configurations not dissimilar from those necessary to explain some of the internal dynamical properties of what appear on the surface to be simple ellipsoidal stellar distributions. His analysis showed that there exist stable orbits about the major and minor axes but not about the immediate axis of the

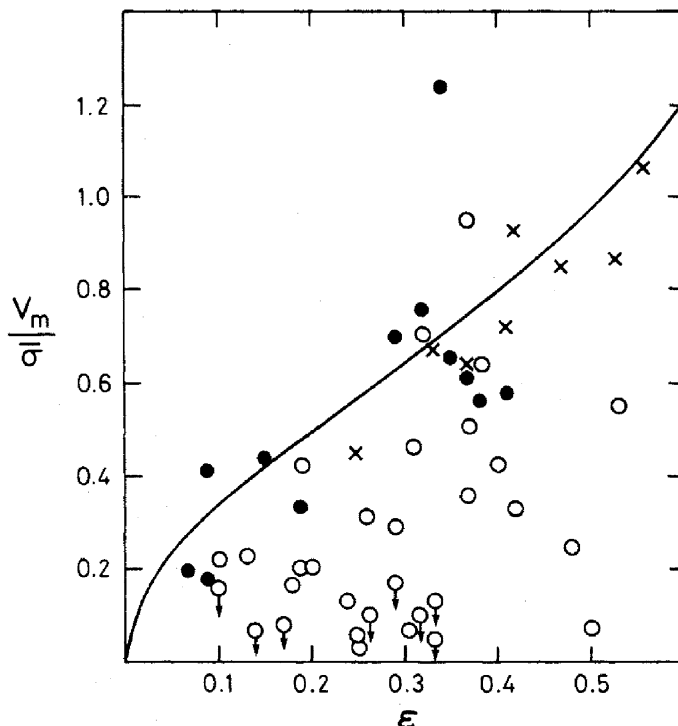


Fig. 3.11. A diagram showing the flattening of elliptical galaxies as a function of their rotational velocities. The *open circles* are luminous elliptical galaxies, the *filled circles* are lower luminosity ellipticals and the *crosses* are the bulges of spiral galaxies. If the ellipticity were entirely due to rotation with an isotropic stellar velocity distribution at each point, the galaxies would be expected to lie along the *solid line*. This diagram shows that, at least for massive ellipticals, this simple picture of rotational flattening cannot be correct (Davies et al., 1983)

triaxial figure. With this new understanding of the stellar motions in elliptical galaxies, galaxies can be characterised as oblate-axisymmetric, prolate-axisymmetric, oblate-triaxial, prolate-triaxial and so on.

3.6.3 The Tully–Fisher Relation for Spiral Galaxies

The masses of spiral galaxies can be estimated from their rotation curves as described in Sect. 3.5.2. In 1975, Tully and Fisher discovered that, for spiral galaxies, the widths of the profiles of the 21-cm line of neutral hydrogen, once corrected for the effects of inclination, are strongly correlated with their intrinsic luminosities (Tully and Fisher, 1977). In their studies, they correlated the total B luminosities with the corrected velocity width ΔV of the 21-cm line and found the relation

$$L_B \propto \Delta V^\alpha, \quad (3.24)$$

where $\alpha = 2.5$. A much larger survey carried out by Aaronson and Mould found a somewhat steeper slope, $\alpha = 3.5$, for luminosities measured in the optical B waveband and an even steeper slope, $\alpha = 4.3$ in the near-infrared H waveband at $1.65\text{ }\mu\text{m}$ (Aaronson and Mould, 1983). The correlation was found to be much tighter in the infrared as compared with the blue waveband, because the luminosities of spiral galaxies in the blue waveband are significantly influenced by interstellar extinction within the galaxies themselves, whereas, in the infrared waveband the dust becomes transparent. What has come to be called the *infrared Tully–Fisher relation* is very tight indeed. As a result, measurement of the 21-cm velocity width of a spiral galaxy can be used to infer its absolute H magnitude and hence, by measuring its flux density in the H waveband, its distance can be estimated. This procedure has resulted in some of the best distance estimates for spiral galaxies and has been used in programmes to measure the value of Hubble's constant.

There is an interesting interpretation of the Tully–Fisher relation for exponential discs. Suppose that the mass distribution follows the same distribution as the optical surface brightness with radius, $I = I_0 \exp(-r/h)$. Then, the total mass of the disc is

$$M = \int_0^\infty 2\pi r I_0 e^{-r/h} dr = 2\pi I_0 h^2 \int_0^\infty x e^{-x} dx = 2\pi I_0 h^2. \quad (3.25)$$

Thus, most of the mass of the disc lies within radius $r \sim h$. The maximum of the rotation curve therefore corresponds roughly to the Keplerian velocity at distance h from the centre. Placing all the mass at the centre of the disc and equating the centripetal and gravitational accelerations, the maximum of the rotation curve is expected to correspond to V_{\max} where

$$\frac{V_{\max}^2}{h} \approx \frac{2\pi G I_0 h^2}{h^2}; \quad V_{\max} \propto (I_0 h)^{1/2}. \quad (3.26)$$

Eliminating h from (3.25) and (3.26), we find that $M \propto V_{\max}^4$. If we now adopt Freeman's result that the central surface brightnesses of bright spiral galaxies have a roughly constant value and assume that the mass-to-luminosity ratio is constant within the discs of spiral galaxies, we expect $L \propto V_{\max}^4$, roughly the observed Tully–Fisher relation.

3.6.4 Luminosity–Metallicity Relations

An important aspect of the physics of galaxies which will play an important role in understanding their formation is the relation between their luminosities, masses, colours and the abundances of the heavy elements, the last being referred to as their *metallicities*. The observations are well-understood, but their interpretation is subject to many caveats and uncertainties.

For elliptical galaxies, Faber showed in 1973 showed that there is a correlation between their luminosities and the strength of the magnesium absorption lines (Faber, 1973). In subsequent analyses, a similar relation was established over a wide range of luminosities and between the central velocity dispersion of the elliptical galaxy

and the strength of the Mg₂ index (Bender et al., 1993). They also showed that the Mg₂ index was strongly correlated with the (B – V) colours of the bulges of these galaxies and so the correlation referred to the properties of the galaxy as a whole. The result was a strong correlation between luminosity, colour and metallicity spanning almost a factor of 1000 in luminosity (Fig. 3.12).

A similar relation was found by Visvanathan and Sandage for elliptical galaxies in groups and clusters of galaxies in the sense that the more luminous the galaxy, the redder they were observed to be (Visvanathan and Sandage, 1977). Their prime interest was in using this correlation in groups and clusters of galaxies to estimate their distances, but the sense of the correlation is the same as that found by Faber and her colleagues since galaxies with greater metallicities have greater line blanketing in the blue and ultraviolet regions of the spectrum and hence are redder than their lower metallicity counterparts.

A similar correlation was first established for late-type and star forming galaxies by Lequeux and his colleagues (Lequeux et al., 1979). These pioneering studies involved determining the gas-phase metallicities of the galaxies and were followed by a number of studies which extended the luminosity–metallicity correlation to a range of 11 magnitudes in absolute luminosity and a factor of 100 in metallicity (Zaritsky et al., 1994). These studies laid the foundation for the analyses of the huge databases of galaxies available from the Sloan Digital Sky Survey.

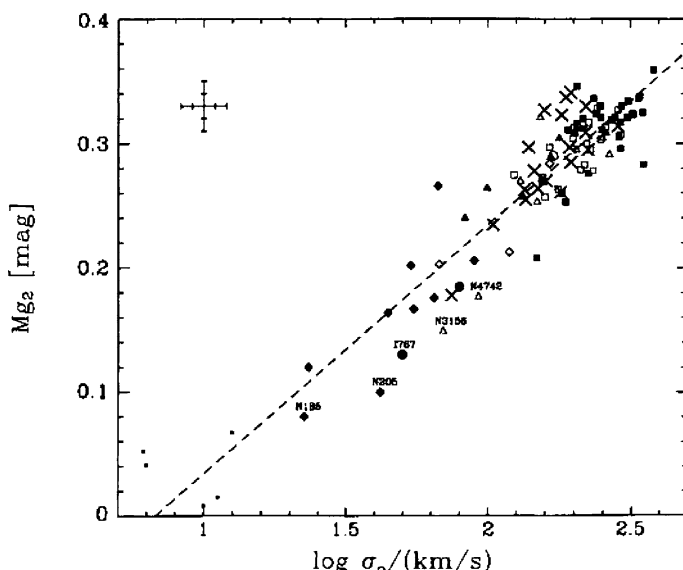


Fig. 3.12. The correlation between the luminosity of the bulges or spheroids of elliptical galaxies, what Faber and her colleagues refer to as ‘Dynamically Hot Galaxies’, and the strength of their absorption lines due to heavy elements, as measured by the Mg₂ index (Bender et al., 1993)

In the analysis of Tremonti and her colleagues, rather than using luminosity, they work directly with the stellar mass of the galaxy (Tremonti et al., 2004). This approach has become feasible thanks to the development of efficient and reliable codes for determining the stellar and gaseous masses of galaxies from their optical spectra (Bruzual and Charlot, 2003; Charlot and Longhetti, 2001). It turns out that the correlation with stellar mass is stronger than that with luminosity. Figure 3.13 shows the strong correlation between metallicity and the total stellar mass of star-forming galaxies. These observations provide important constraints on the physics of the evolution of galaxies. With the advent of 8–10-metre class telescopes, these studies have been extended to samples of galaxies at large redshifts and so constrain directly the evolution of the stellar and gaseous content of galaxies of different masses (Savaglio et al., 2005). These topics will be taken up in much more detail in Chaps. 17 to 19.

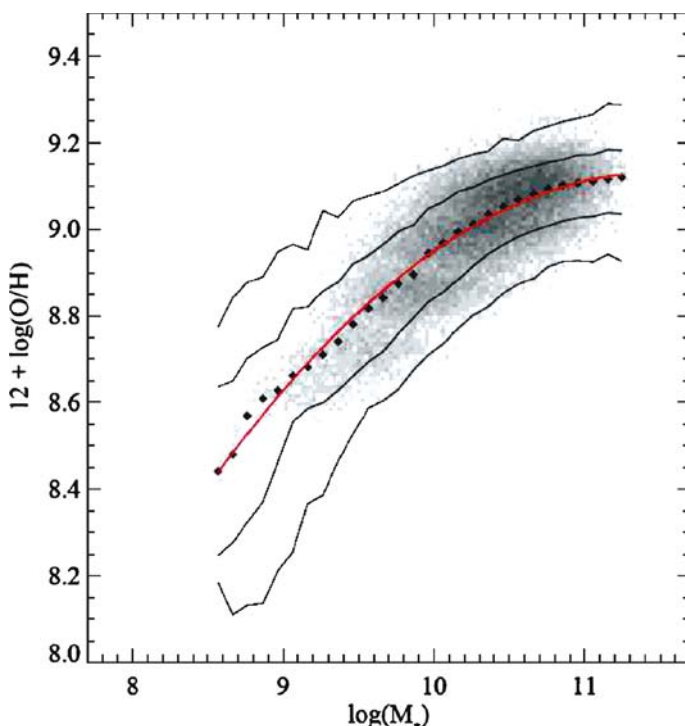


Fig. 3.13. The stellar mass–gas phase metallicity relation for 53,400 star-forming galaxies from the SDSS. The large *black points* represent the median in bins of 0.1 dex in mass which include at least 100 data points. The *thin line* through the data is a best-fitting smooth curve and the *solid lines* are the contours which enclose 68% and 95% of the data (Tremonti et al., 2004)

3.7 The Luminosity Function of Galaxies

The frequency with which galaxies of different intrinsic luminosities are found in space is described by the *luminosity function* of galaxies. The luminosity function of galaxies $\phi(L) dL$ is defined to be the space density of galaxies with intrinsic luminosities in the range L to $L + dL$. If S is the flux density (in $\text{W m}^{-1} \text{Hz}^{-1}$) of a nearby galaxy, for which redshift corrections can be neglected, the luminosity of the galaxy is $L = 4\pi r^2 S$ (in W Hz^{-1}), where r is the distance of the galaxy. In optical astronomy, it is traditional to work in terms of absolute magnitudes, M , rather than luminosities and so, in terms of absolute magnitudes, the luminosity function $\phi(L) dL = \Phi(M) dM$. The important difference between these two forms of the luminosity function is that, in terms of magnitudes, the luminosity function is presented on a logarithmic scale of luminosity. The absolute magnitude M and the luminosity L are related by the expression

$$\log\left(\frac{L}{L^*}\right) = -0.4(M - M^*) . \quad (3.27)$$

where the absolute magnitude M^* and the luminosity L^* are corresponding reference values of these quantities.

In 1977, Felten made a careful comparison of nine different determinations of the local luminosity function for nearby galaxies, reducing them all to the same value of Hubble's constant, the same magnitude system and the same corrections for Galactic extinction. In this heroic analysis, he found that the independent determinations were in remarkably good agreement (Felten, 1977). Felten's analysis is summarised in Fig. 3.14, using reduced absolute magnitudes, $M_{B_T^0}$ in de Vaucouleurs' B_T^0 magnitude system and using a Galactic extinction law $A_B = 0.25 \operatorname{cosec}|b|$. The solid line shows a best-fit to the data of the form of luminosity function proposed by Schechter

$$\phi(x) dx = \phi^* x^\alpha e^{-x} dx , \quad (3.28)$$

or,

$$\phi(L) dL = \phi^* \left(\frac{L}{L^*}\right)^\alpha \exp\left(-\frac{L}{L^*}\right) \frac{dL}{L^*} , \quad (3.29)$$

where $x = L/L^*$ and L^* is the luminosity which characterises the 'break' in the luminosity function seen in Fig. 3.14 (Schechter, 1976). The form of the Schechter luminosity function is as simple as it could be: a power law with a high luminosity exponential cut-off. Its shape is characterised by two parameters, the slope of the power law α at low luminosities and the 'break' luminosity L^* .

It is traditional in optical astronomy to write the luminosity function in terms of astronomical magnitudes rather than luminosities and then the beautiful simplicity of the Schechter function is somewhat spoiled:

$$\begin{aligned} \Phi(M) dM &= \frac{2}{5} \phi^* \ln 10 \left\{ \operatorname{dex}[0.4(M^* - M)] \right\}^{\alpha+1} \\ &\times \exp\left\{-\operatorname{dex}[0.4(M^* - M)]\right\} dM , \end{aligned} \quad (3.30)$$

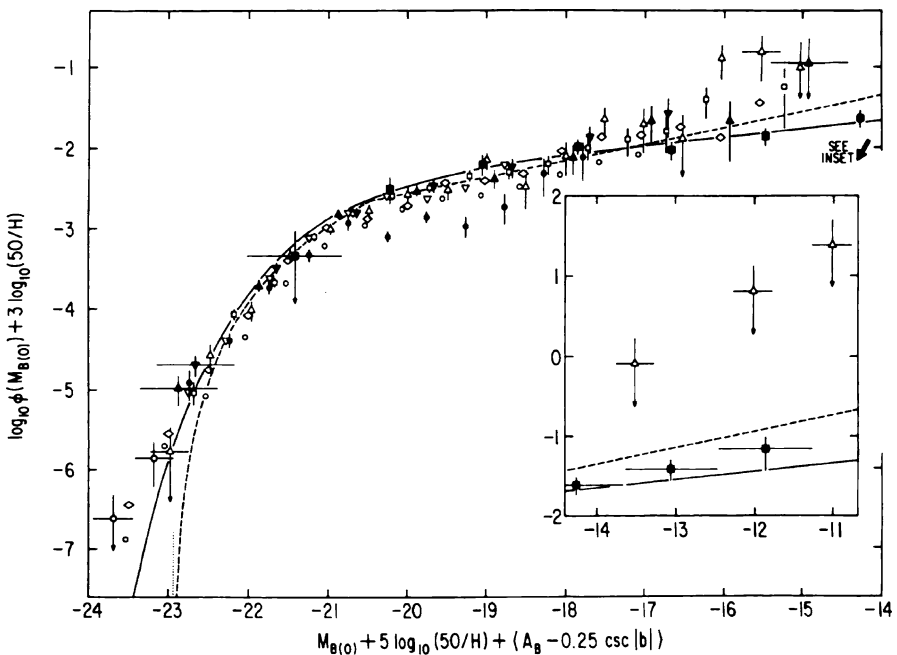


Fig. 3.14. The local luminosity function of galaxies from nine independent estimates considered by Felten fitted by a Schechter luminosity function of the form $n(x) dx \propto x^\alpha e^{-x} dx$, where $x = L/L^*$ (Felten, 1977)

where M^* is the absolute magnitude corresponding to the luminosity L^* . We have used the notation $\text{dex } y$ to mean 10^y . In his reassessment of the luminosity function for galaxies in 1985, Felten preferred the following best-fit values: $\alpha = -1.25$ and $M_{B(0)}^* = -20.05 + 5 \log_{10} h$ (Felten, 1985).

The normalisation factor ϕ^* determines the space density of galaxies and allowance has to be made for the fact that the galaxies used in the determination mostly lie within the local supercluster. Hence, the value of ϕ^* is an overestimate as compared with what would be found for a sample of field galaxies. Felten's preferred value of ϕ^* for the general field was $1.20 \times 10^{-2} h^3 \text{ Mpc}^{-3}$.

These pioneering efforts by Felten were followed by careful studies of larger and larger samples of galaxies (see, for example, the review by Binggeli, Sandage and Tammann (Binggeli et al., 1988)), culminating in the analyses of very large samples of galaxies observed in the 2dF and Sloan Digital Sky Survey (SDSS) galaxy surveys. These very large surveys sample such large volumes of the Universe that the problems of correcting for the presence of the local supercluster are not relevant. Recent determinations of the luminosity function of galaxies from these surveys are shown in Fig. 3.15. The 2dF galaxy survey included 221,414 galaxies for all of which spectroscopic redshifts and colours were available (Fig. 3.15a). The overall luminosity function, as well as the functions for red and blue galaxies are shown on

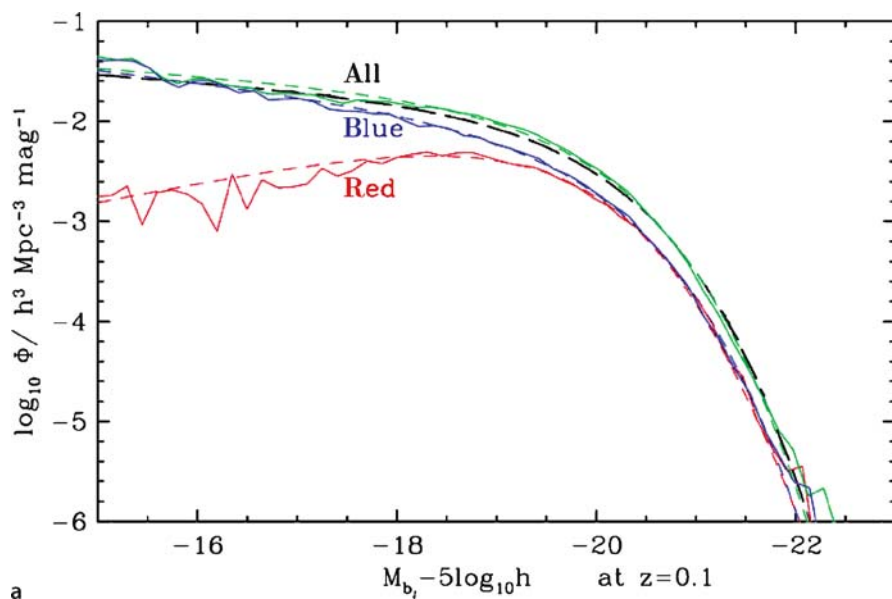


Fig. 3.15. a The luminosity function of galaxies derived from a sample of 221,414 galaxies observed in the 2dF galaxy survey. The overall luminosity function and those of the red and blue galaxies in the sample have been fitted by Schechter luminosity functions (Cole et al., 2005)

Table 3.4. Parameters describing the overall luminosity function of galaxies from the 2dF and SDSS surveys. The functions are determined at a redshift of 0.1 and include K-corrections and evolutionary corrections for the observed change in form of the luminosity functions over the redshift interval $0 < z < 0.3$

Galaxy survey	Waveband	$\phi^*/h^3 \text{Mpc}^{-3}$	$M^* - 5 \log_{10} h$	α
2dF galaxy survey	b _J	0.0156	-19.52	-1.18
SDSS galaxy survey	r	0.0149 ± 0.0004	-20.44 ± 0.01	-1.05 ± 0.01

the diagram. In the case of the SDSS survey, redshifts were determined for 147,986 galaxies (Fig. 3.15b) (Blanton et al., 2003). The best-fit parameters describing the overall luminosity function for these two large surveys are listed in Table 3.4. It can be seen that the form of these functions are in good agreement.

3.7.1 Aspects of the Luminosity Function of Galaxies

A number of features of the luminosity function of galaxies should be noted.

Dependence upon galactic environment. With the availability of large unbiased samples of galaxies, it is possible to determine the luminosity function for galaxies of different morphological types in different environments, such as clusters, groups and void regions. The evidence of Fig. 3.15a shows that there is a clear difference in

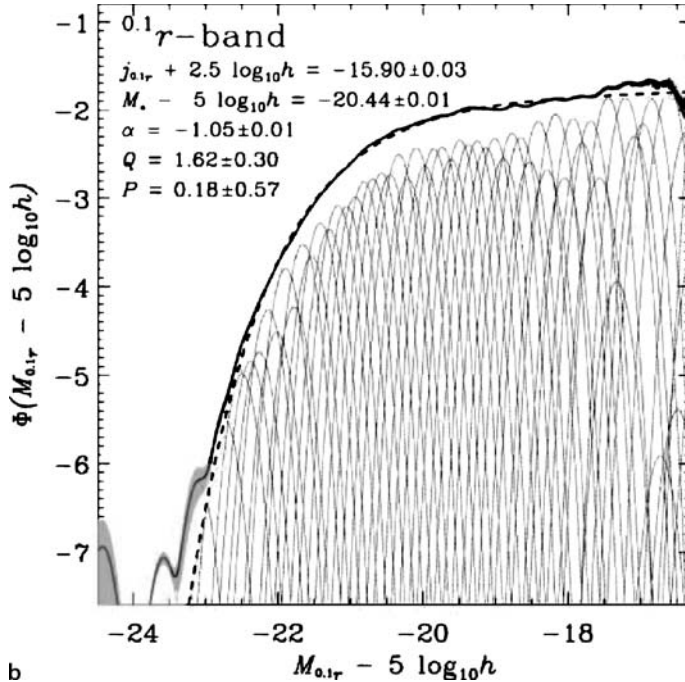


Fig. 3.15. (continued) **b** The luminosity function of galaxies derived from a sample of 147,986 galaxies observed in the Sloan Digital Sky Survey. The magnitudes are measured in the r^* waveband as observed at a redshift $z = 0.1$. The observations are very well-fitted by a Schechter luminosity function with the parameters given on the diagram and in Table 3.4 (Blanton et al., 2003)

the luminosity functions of red and blue selected galaxies, corresponding to early and late-type galaxies respectively in the Hubble sequence. In addition, there is evidence that the luminosity function of galaxies in rich clusters differs from that of galaxies in underdense regions of the Universe, the void regions. Using data from the 2dF galaxy survey, Croton and his colleagues showed clear differences in the forms of the luminosity functions for early and late-type galaxies as a function of the over or underdensity of the region relative to the mean density of galaxies (Fig. 3.16) (Croton et al., 2005). The population in the voids is dominated by late-type galaxies and shows, relative to the mean, a deficit of early-type galaxies that becomes increasingly pronounced at magnitudes fainter than $M_{\text{bj}} - 5 \log_{10} h = -18.5$. In contrast, clusters show a relative excess of very bright early-type galaxies with $M_{\text{bj}} - 5 \log_{10} h < -19$.

These facts combined with the differences in the relative numbers of galaxies of different morphological types as a function of galaxy density indicate that the approximation of a universal luminosity function for all galaxies wherever they are found in the Universe is, at best, a rough approximation.

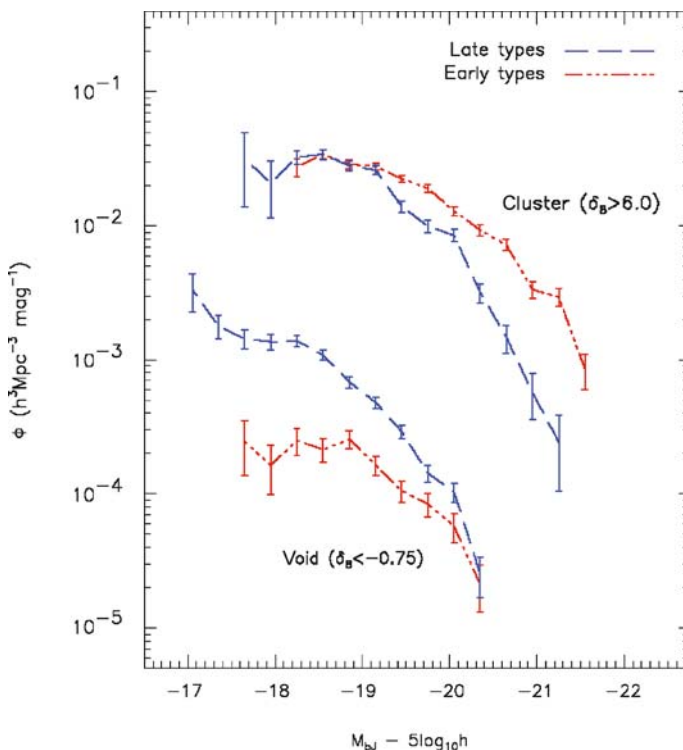


Fig. 3.16. The luminosity functions for early and late-type galaxies in rich clusters of galaxies and in large voids (Croton et al., 2005). As they express this result, the void population is composed almost exclusively of faint late-type galaxies, while in the clusters the galaxy population brighter than $M_{\text{BJ}} - 5 \log_{10} h = -19$ consists predominantly of early types

Is L^* a standard candle? In 1962, Abell suggested that the luminosity of the break in the luminosity function of rich clusters L^* , corresponding to M^* , could be used as a ‘standard candle’ in the redshift–apparent magnitude relation (Abell, 1962). He found excellent agreement with the expected slope of the redshift–magnitude relation using this technique. Subsequent studies of the luminosity functions of individual clusters of galaxies have shown that they are similar in form to the standard Schechter function with more or less the same parameters as those described above. Schechter found that, if only those clusters for which good fits to his proposed function were included, the dispersion in the absolute magnitude of M^* was only 0.25 magnitudes, as good a result as has been obtained from studies of the brightest galaxies in clusters (Schechter, 1976).

With the availability of the large surveys of galaxies, this proposal has to be treated with some caution since there is evidence for the evolution of the form the luminosity function, even over remarkably small redshift intervals. As shown in

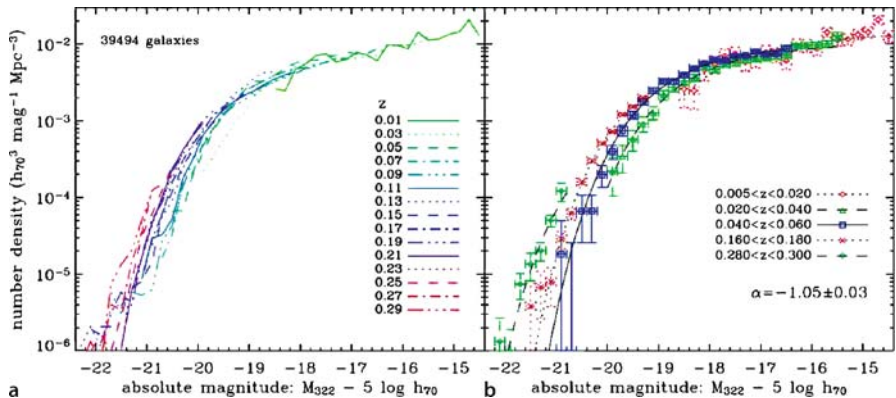


Fig. 3.17. The evolution of the luminosity function of galaxies at small redshifts. Over the redshift interval 0 to 0.3, the value of M^* becomes more positive by (0.8 ± 0.1) magnitudes, that is, the break in the luminosity function moves to fainter intrinsic luminosities as the Universe grows older (Baldry et al., 2005)

Fig. 3.17, the luminosity function as observed in the u -waveband shows significant changes over the small redshift interval $0.3 > z > 0.02$ (Baldry et al., 2005). Specifically, they find that M^* decreases by 0.8 ± 0.1 magnitudes between redshifts 0.3 and zero.

The brightest galaxies in clusters. At the very highest luminosities, the brightest galaxies in clusters do not fit smoothly onto an extrapolation of the Schechter luminosity function. These massive galaxies, a splendid example of which can be seen in Fig. 4.1, are known as *cD galaxies*, their characteristic being that they are similar to giant elliptical galaxies but in addition possess extensive stellar envelopes. They are the most luminous galaxies found in rich clusters and groups of galaxies. It appears that these are very special galaxies and not just the most luminous members of the luminosity function of galaxies, as was shown statistically by Tremaine and Richstone (Tremaine and Richstone, 1977). Evidently, there must be some physical reason why the first ranked cluster galaxies have these unique properties; we will return to this issue in Chap. 4.

The luminosity function for low luminosity galaxies. The luminosity function is quite poorly known at low luminosities, because these galaxies can only be observed in relatively nearby groups and clusters. According to Binggeli and his colleagues, the lowest luminosity regions of the luminosity function are exclusively associated with irregular and dwarf elliptical galaxies (Binggeli et al., 1988). These conclusions are confirmed by analyses of the SDSS, in particular, the analysis of a large sample of galaxies with distances in the range $10 < r < 150$ Mpc so that galaxies as faint as $M = -12.5$ can be included (Blanton et al., 2005). These data show an upturn in the slope of the luminosity function at very low luminosities, the best-fitting value of α being about -1.3 . As the authors comment, however, a large number of galaxies at very low luminosities may be missing because of their low surface brightnesses

and so the true low luminosity slope may be -1.5 or even steeper. In agreement with Bingelli and his colleagues, they find that extremely low luminosity galaxies are predominantly blue, low surface brightness, exponential disks.

3.7.2 The Integrated Luminosity and the Mean Mass-to-Luminosity Ratio for Visible Matter in the Universe

An important calculation is the integrated luminosity of all the galaxies within a given volume of space. For a cluster of galaxies, the result would be the integrated optical luminosity of the cluster; if this were a typical unit volume of space, the result would be the luminosity density of the radiation due to all the galaxies in the Universe. Although the number of galaxies in the luminosity function diverges at low luminosities, the total background light remains finite. The luminosity density is

$$\begin{aligned}\varepsilon_{B(0)} &= \int_0^\infty L \phi(L) dL = \phi^* L^* \int_0^\infty x^{a+1} e^{-x} dx \\ &= \phi^* L^* \Gamma(a+2),\end{aligned}\quad (3.31)$$

where Γ is the gamma-function. For a cluster of galaxies, ϕ^* is the normalisation factor in the luminosity function. To estimate the luminosity density of a typical volume of space, we can use the values determined by Felten for the field luminosity function quoted above, $a = -1.25$, $\phi^* = 1.2 \times 10^{-3} h^3 \text{ Mpc}^{-3}$ and $M^* = -20.05 + 5 \log_{10} h$, corresponding to $1.24 \times 10^{10} h^{-2} L_\odot$. Then,

$$\varepsilon_{B(0)} = 1.8 \times 10^8 h L_\odot \text{ Mpc}^{-3}. \quad (3.32)$$

The value found from the SDSS luminosity function (Blanton et al., 2003) in the $^{0.1}r$ waveband is

$$(1.84 \pm 0.04) \times 10^8 h L_\odot \text{ Mpc}^{-3}. \quad (3.33)$$

These results are consistent with other estimates of the luminosity density, for example from the 2dF Galaxy Redshift Survey (Fig. 3.15a) and the Millennium Galaxy Catalogue.

A useful reference value for cosmological studies is the average mass-to-luminosity ratio for the Universe, if it is assumed to have the critical cosmological density, $\varrho_c = 3H_0^2/8\pi G = 2.0 \times 10^{-26} h^2 \text{ kg m}^{-3}$. In terms of solar units, the mass-to-luminosity ratio would be

$$\frac{\varrho_c}{\varepsilon_B} = \left(\frac{M}{L} \right)_B = 1600 h \left(\frac{M_\odot}{L_\odot} \right)_B. \quad (3.34)$$

Although there is some variation about this estimate, its importance lies in the fact that it is significantly greater than the typical mass-to-luminosity ratios of galaxies and clusters of galaxies, even when account is taken of the dark matter which must

be present. This result indicates that the mass present in galaxies and clusters of galaxies is not sufficient to close the Universe.

It is useful to work out typical values for the mean space density and luminosity of galaxies. Using the mean luminosity of galaxies for Felten's best estimate of the luminosity function with $a = -1.25$, we find $\langle L \rangle = 1.25L^* = 1.55 \times 10^{10}h^{-2}L_\odot$. Adopting the mean luminosity density of the Universe given by (3.32), the typical number density of galaxies $\bar{n} = \varepsilon_{B(0)}/\langle L \rangle = 10^{-2}h^3 \text{ Mpc}^{-3}$. In other words, the typical galaxies which contribute most of the integrated light of galaxies are separated by a distance of about $5h^{-1} \text{ Mpc}$, if they were uniformly distributed in space, which we know to be very far from the truth. For reference, galaxies such as our own and M31 have luminosities $L_{\text{Gal}}(\text{B}) \approx 10^{10}L_\odot$. Evidently, if the ratio of mass-to-luminosity were the same for all galaxies, the 'mean' galaxies would also contribute most of the visible mass in the Universe.

These data also enable limits to be placed upon the average mass density in stars at the present epoch. In the simplest estimate, we can adopt a typical mass-to-luminosity ratio for the *visible* parts of galaxies of $M/L \approx 3$ and then the density parameter in stars at the present epoch would be $\Omega_*h = 2 \times 10^{-3}$. A very much more careful analysis has been carried out by Bell and his collaborators who used the combined SDSS and *Two Micron All Sky Survey* (2MASS) catalogues of galaxies (Bell et al., 2003). The benefit of including the 2MASS data is that the luminosity functions can be determined in the relatively unobscured $2 \mu\text{m}$ waveband. Their upper limit to the stellar mass density in the local Universe is

$$\Omega_*h = (2 \pm 0.6) \times 10^{-3}, \quad (3.35)$$

assuming the initial mass function of stars is as rich in low mass stars as is allowed by galaxy dynamics in the local Universe. This is a key result for many aspects of galaxy formation.

3.8 The Properties of Galaxies: Correlations Along the Hubble Sequence

What gives the Hubble classification physical significance is the fact that a number of physical properties are correlated with position along the sequence. Many of these were reviewed by Roberts and Haynes in an important analysis of the properties of a large sample of bright galaxies selected primarily from the Third Reference Catalogue of Bright Galaxies (de Vaucouleurs et al., 1991; Roberts and Haynes, 1994). They emphasised that, although there are clear trends, there is a wide dispersion about these correlations at any point along the sequence (Fig. 3.18).

Some of the more important findings of Roberts and Haynes' survey are as follows:

- *Total masses and luminosities.* The average masses and range of masses are roughly constant for galaxies in classes S0 to Scd. At later stages beyond Scd,

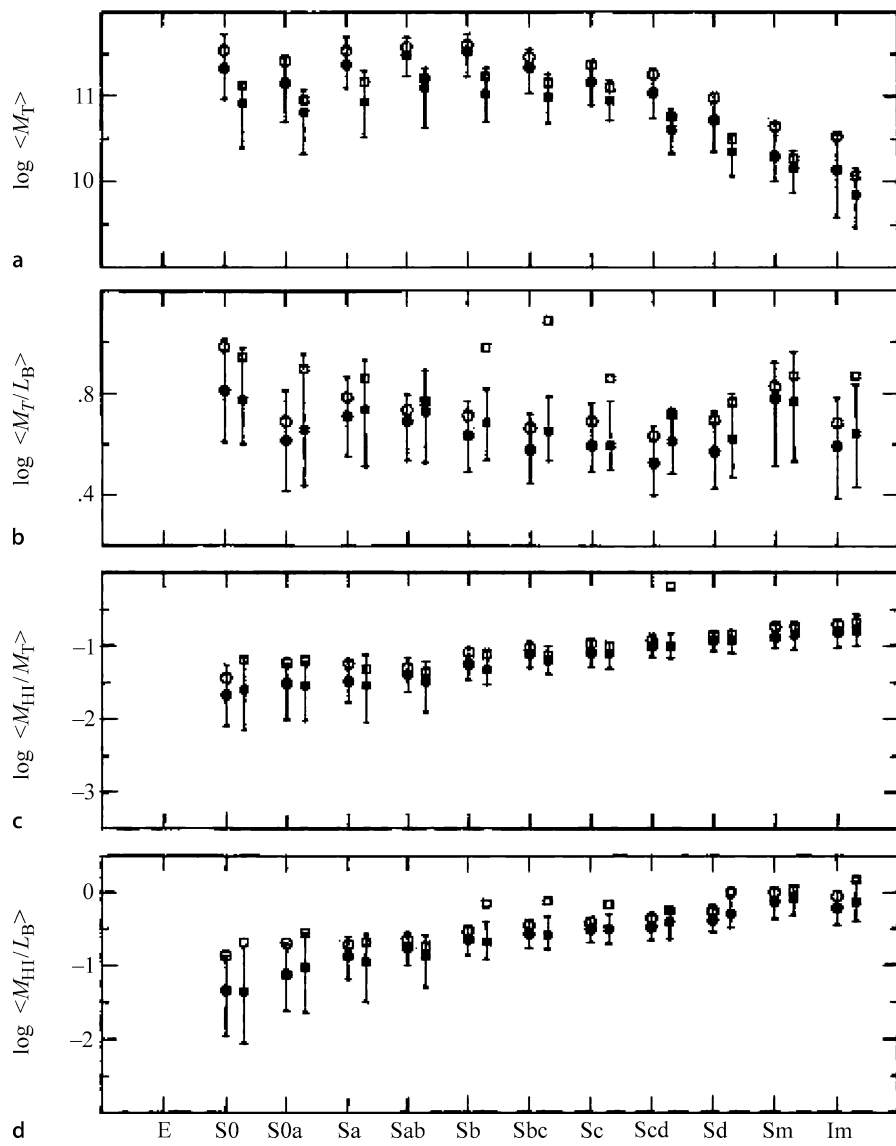


Fig. 3.18a–g. Global galaxy parameters as a function of stage along the Hubble sequence (Roberts and Haynes, 1994). The *circles* represent the galaxies in the RC3-UGC sample and the *squares* those within the local supercluster of galaxies. The *filled circles* are medians; the *open symbols* are mean values. The *error bars* represent the 25 and 75 percentiles of the distributions. **a** Total masses, M_T ; **b** Total mass-to-luminosity ratio (M_T / L_B); **c** Neutral hydrogen mass to total mass (M_{HI} / M_T); **d** Neutral hydrogen mass to blue luminosity (M_{HI} / L_B)

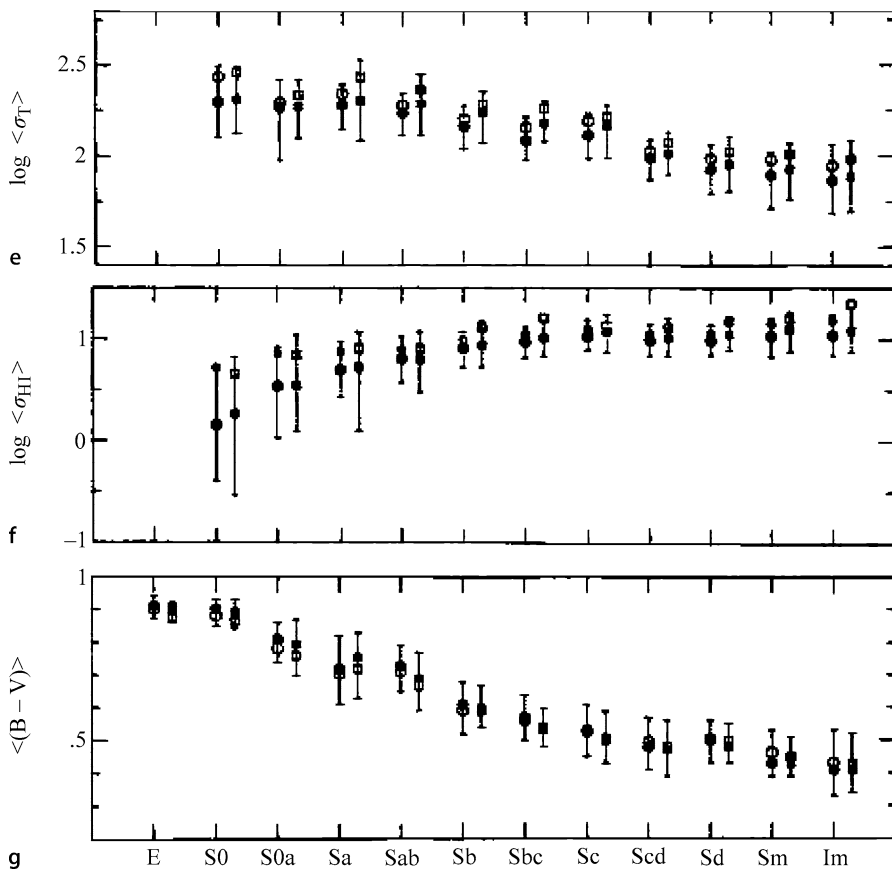


Fig. 3.18. (continued) **e** Total mass surface density (σ_T); **f** Surface mass density of neutral hydrogen (σ_{HI}); **g** Integrated ($B - V$) colour

the masses of the galaxies decrease monotonically (Fig. 3.18a). The mass-to-luminosity ratios of the galaxies in the sample are roughly constant (Fig. 3.18b) and so it is no surprise that the average luminosity for the S0 to Scd galaxies is roughly constant, whilst it decreases monotonically beyond Scd. These relations again quantify van den Bergh's remark that the classical Hubble types refer primarily to luminous, and consequently, massive galaxies.

- *Neutral hydrogen.* There is a clear distinction between elliptical and spiral galaxies in that very rarely is neutral hydrogen observed in ellipticals while all spiral and late-type galaxies have significant gaseous masses. The upper limit to the mass of neutral hydrogen in elliptical galaxies corresponds to $M_{HI}/M_{\text{tot}} \leq 10^{-4}$. For spiral galaxies, the fractional mass of the galaxy in the form of neutral hydrogen ranges from about 0.01 for Sa galaxies to about 0.15 at Sm, the increase being monotonic along the revised Hubble sequence (Fig. 3.18c). The fractional

hydrogen mass is more or less independent of the mass of the galaxy at a particular point along the Hubble sequence. A consequence of the constancy of the M_{tot}/L_B ratio for the galaxies in the sample is that there is also a significant trend for the ratio M_{HI}/L_B to increase along the sequence (Fig. 3.18d).

- *Total surface density and surface density of neutral hydrogen.* These quantities change in opposite senses along the Hubble sequence. The total surface density, as determined by the total mass of the galaxy and its characteristic radius, decreases monotonically along the sequence (Fig. 3.18e), whereas the surface density of neutral hydrogen increases along the sequence (Fig. 3.18f).
- *Integrated colour.* There is a strong correlation in the sense that elliptical galaxies are red whereas late-type galaxies are blue. This relation is shown quantitatively in Fig. 3.18g. Despite the systematic trend, there is a significant dispersion about the relation at each point in the sequence. For example, there are Sc galaxies which are red. As we will see, the analysis of the very large samples of galaxies provided by the SDSS and 2dF Galaxy Surveys have quantified the central importance of colour in understanding the astrophysics of galaxies (Sect. 3.9).
- *Luminosity function of HII regions.* In a pioneering study, Kennicutt and his colleagues determined the luminosity function of HII regions in different galaxy types (Kennicutt et al., 1989). Normalising to the same fiducial mass, it was found that there is a much greater frequency of HII regions in the late-type galaxies as compared with early-type galaxies and that the relation is monotonic along the sequence.

Morton and Haynes pointed out that an obvious interpretation of these correlations is that there are different rates of star formation in different types of galaxy. As they express it, the various correlations provide information about the past, current and future star formation rates in galaxies. The correlation with colour along the sequence is related to the past star formation history of the galaxy; the changes in the luminosity function of HII regions refer to star formation rates at the present epoch; the large fraction of the mass of neutral hydrogen and its large surface density at late stages in the sequence show that these galaxies may continue to have high star formation rates in the future.

To put more flesh on this argument, the integrated colours of galaxies of different Hubble types can be plotted on a $(U - B, B - V)$ colour–colour diagram, the colours being corrected for internal and external reddening. Such a colour–colour diagram for a sample of galaxies selected from the Hubble Atlas of Galaxies is shown in Fig. 3.19 in which it can be seen that the colours of galaxies occupy a remarkably narrow region of the $(U - B, B - V)$ plane (Larson and Tinsley, 1978). There is a monotonic variation of Hubble types along this locus, the bluest galaxies being the Sc and Sd galaxies and the reddest the elliptical galaxies, as can be seen from comparison with Fig. 3.18g. The colours of the galaxies cannot be represented by those of any single class of star which is hardly surprising since different classes of star make the dominant contribution at different wavelengths.

The integrated light of galaxies is principally the sum of the light of main sequence stars plus red giant stars, in particular, the K and M giants. To a rough

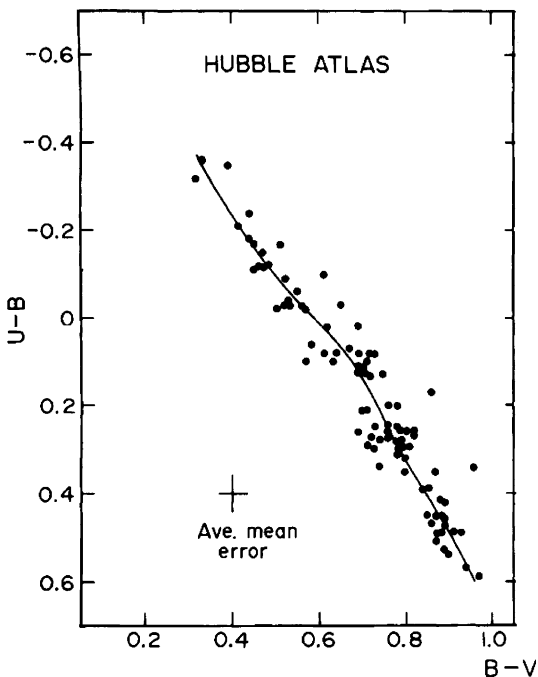


Fig. 3.19. The colour–colour ($U-B$, $B-V$) diagram for the integrated colours of galaxies of different morphological types for galaxies selected from the Hubble Atlas of Galaxies (Larson and Tinsley, 1978)

approximation, the colours of galaxies can be represented by the sum of the numbers of luminous blue stars on the main sequence and of luminous giants on the giant branch. If all the stars in galaxies formed 10^{10} years ago, the main sequence termination point would now have reached roughly the mass of the Sun, $M \approx M_{\odot}$, and the brightest main-sequence stars would have spectral properties similar to that of the Sun, that is, a G2 star. There would therefore be no bright blue stars on the main sequence and the integrated light of the galaxy would be dominated by red giants. On the other hand, if star formation has continued over 10^{10} years, or if there were a burst of star formation in the recent past, there would be a significant population of hot blue stars on the main sequence giving the galaxy a significantly bluer colour.

3.9 The Red and Blue Sequences

With the availability of the large samples of galaxies from the SDSS and the 2dF Galaxy Survey, a more quantitative approach to the classification of galaxies has had to be developed, necessitated by the need to analyse these huge samples by computer algorithms. What is lost in detail in these computer-based classifications is more than compensated for by the huge statistics of galaxies with different properties. The upshot of these studies is that what are traditionally referred to as early and late-

type galaxies are found to form two distinct sequences which are known as the *red* and *blue sequences*. In summary:

- The *red sequence* consists of non-star-forming, high mass spheroidal galaxies, or, more colloquially ‘old, red and dead’ galaxies.
- The *blue sequence* consists of star-forming, low mass galaxies which are disc-dominated.

These two sequences are defined by a number of the characteristic properties which have already been introduced.

3.9.1 Colour Versus Absolute Magnitude

Perhaps the most striking distinction between the two sequences appears in the plot of the colour $^{0.1}(g - r)$ against absolute magnitude M . Figure 3.20a shows the distribution of these properties for 144,000 galaxies from the SDSS catalogue (Blanton et al., 2003). Superimposed on the diagram are isodensity contours, the bulk of the galaxies lying within the heavy white contours. The separation into two sequences is clearly defined, the oval region at the top of the diagram being the red sequence and the broader region towards the bottom right the blue sequence.

Baldry and his colleagues have shown that the colour distribution of these galaxies can be separated into red and blue sequences which can be very well-described by Gaussian distributions over the magnitude range $-23.5 \leq M_r \leq -15.75$ (Baldry et al., 2004). It is striking how precisely the overall colour distribution in each bin of absolute magnitude over this wide magnitude range can be decomposed into two Gaussian distributions (Fig. 3.21). The red galaxies are the

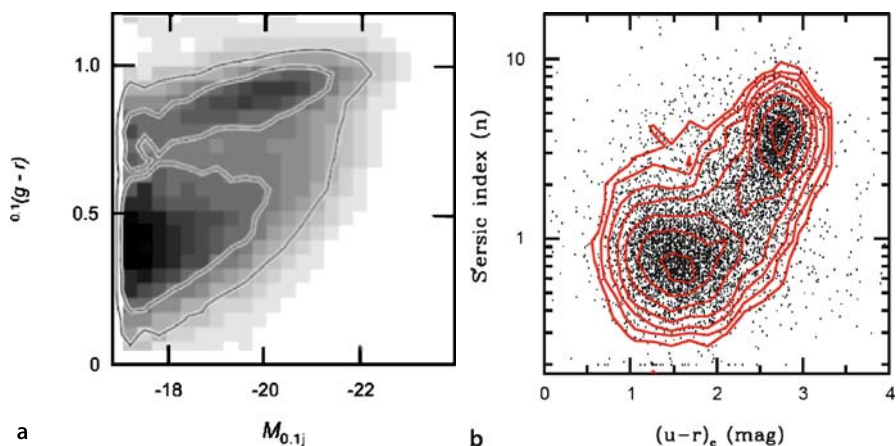


Fig. 3.20. **a** Illustrating the bimodality in the distribution of colour $^{0.1}(g - r)$ of galaxies as a function of optical absolute magnitude (Blanton et al., 2003). **b** A plot of Sérsic index against colour for 10,095 galaxies selected from the Millennium Galaxy Catalogue (Driver et al., 2006)

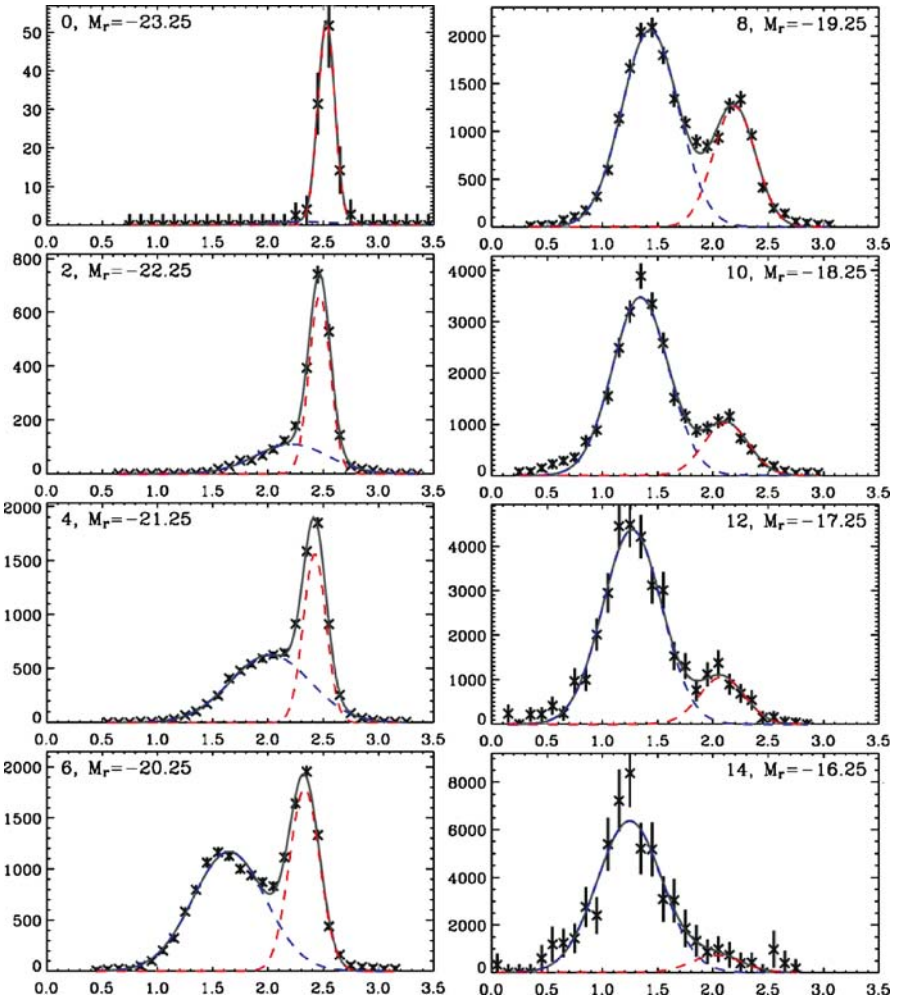


Fig. 3.21. Illustrating the bimodality in the distribution of the colours of galaxies as a function of optical absolute magnitude for a sample of 66,848 galaxies selected from the Sloan Digital Sky Survey (SDSS). The distributions of colours have been fitted by pairs of Gaussians. The data have been binned in intervals of 0.1 in the rest frame ($u - r$) colour. The galaxy distributions are binned in 0.5 magnitude intervals. Only half of the histograms presented by the authors are shown (Baldry et al., 2004)

most luminous, while the blue galaxies form the dominant population at low absolute magnitudes, as is reflected in the different luminosity functions for red and blue galaxies (Fig. 3.15a).

3.9.2 Sérsic Index and Colour

Bimodality is also present in the structural properties of the galaxies. As seen in Fig. 3.8a, the Sérsic index n can be used to divide galaxies into spheroidal-dominated and disc-dominated galaxies and this shows up even more dramatically in a plot of colour against Sérsic index (Fig. 3.20b) (Driver et al., 2006). As discussed in Sect. 3.4.3, the spheroid-dominated systems are most commonly found with Sérsic parameter $n = 4$, whereas the disc-dominated systems typically have $n = 1$. There is a clear separation between these systems in Fig. 3.8a, but it is even more pronounced in Fig. 3.20b in which the red and blue sequences occupy quite separate regions of the diagram. The dividing line between the two sequences occurs about $n = 2$.

3.9.3 Mean Stellar Age and Concentration Index C

Another approach to separating galaxies into two sequences is to use measures of the age of their stellar populations and the degree of concentration of the light towards their centres. Kauffmann and her colleagues have used sample of 122,808 galaxies from the SDSS to study the average age of their stellar populations using the amplitude of the Balmer break, or discontinuity, at 400 nm, $D_n(4000)$, and the Balmer absorption line index $H\delta_A$. The latter measures the strengths of the Balmer absorption line which are particularly strong in galaxies which have undergone a recent burst of star formation (Kauffmann et al., 2003). They have shown that these indices provide good measures of star formation activity over the last 10^9 and $(1-10) \times 10^9$ years respectively.

The concentration index C is defined to be the ratio $C = (R90/R50)$, where $R90$ and $R50$ are the radii enclosing 90% and 50% of the Petrosian r-band luminosity of the galaxy. The concentration parameter C is strongly correlated with Hubble type, $C = 2.6$ separating early from late-type galaxies. Those galaxies with concentration indices $C \geq 2.6$ are early-type galaxies, reflecting the fact that the light is more concentrated towards their centres.

$D_n(4000)$ and $H\delta_A$ are plotted against the concentration index C and the mean stellar mass density within the half light radius μ_* in Fig. 3.22. The panels of that diagram show that the galaxy populations are divided into two distinct sequences. Kauffmann and her colleagues show that the dividing line between the two sequences occurs at a stellar mass $M \approx 3 \times 10^{10} M_\odot$. Lower mass galaxies have young stellar populations, low surface mass densities and the low concentration indices typical of disks. They infer that a significant fraction of the lowest mass galaxies have experienced recent starbursts. For stellar masses $M \geq 3 \times 10^{10} M_\odot$, the fraction of galaxies with old stellar populations increases rapidly. These also have the high surface mass densities and high concentration indices typical of spheroids or bulges.

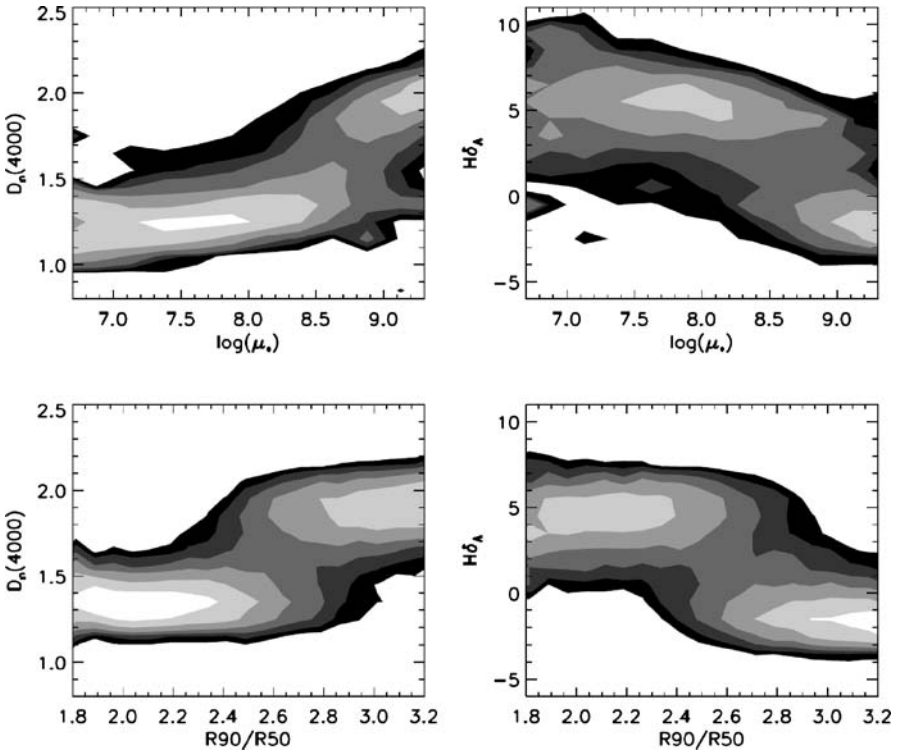


Fig. 3.22. Density distributions showing the trends of the stellar age indicators $D_n(4000)$ and $H\delta_A$ with concentration index $C = (R90/R50)$ and surface mass density μ_* (Kauffmann et al., 2003)

3.9.4 The Effect of the Galaxy Environment

The differences in morphological types of galaxies found in different galactic environments has already been illustrated in Figs. 3.4 and 3.16. Another way of presenting these data emphasising the distinction between the galaxies in the red and blue sequences was carried out by Hogg and his colleagues (Hogg et al., 2004). The sample consisted of 55,158 galaxies in the redshift interval $0.08 \leq z \leq 0.12$. The local galaxy density about any given galaxy was defined by the quantity $\delta_{1\times 8}$, meaning the overdensity about any galaxy in a cylindrical volume with transverse comoving radius $1 h^{-1}$ Mpc and comoving half-length along the line of sight of $8 h^{-1}$ Mpc. Thus, a galaxy in an environment with the average density of galaxies has $\delta_{1\times 8} = 0$. Values of $\delta_{1\times 8} \geq 50$ are found in the cores of rich clusters.

The top row of Fig. 3.23 shows contour plots of the number density of galaxies in the colour–absolute magnitude diagram of Fig. 3.21a, but now shown separately for different overdensity environments, ranging from low excess number densities, $\delta_{1\times 8} \leq 3$, to very high density environments $\delta_{1\times 8} \geq 50$. These data quantify the statement that red galaxies are found preferentially in rich galaxy environments. The

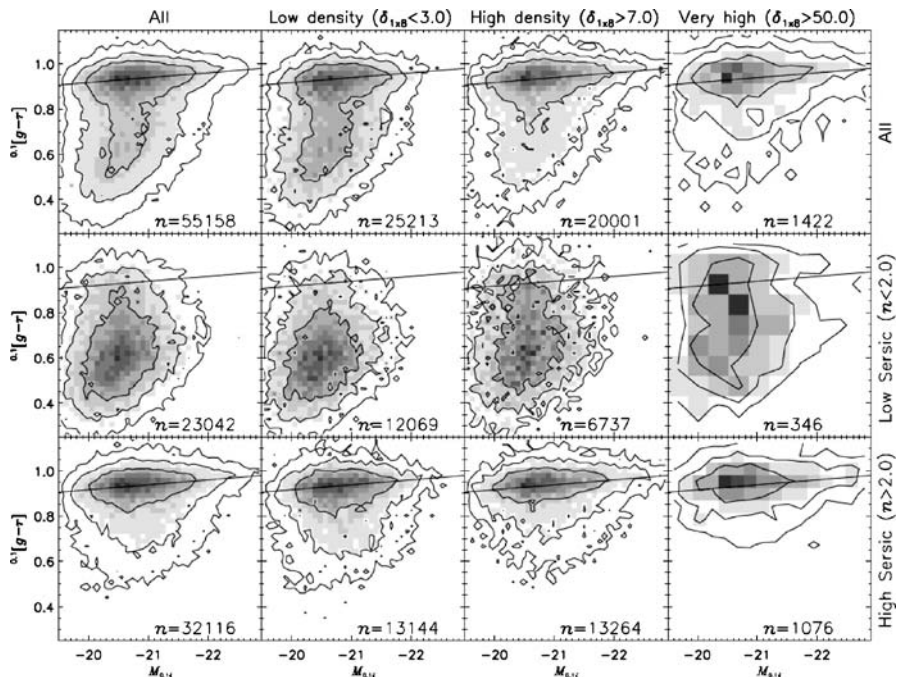


Fig. 3.23. Illustrating the bimodality in the distribution of the colours of galaxies as a function of the density of galaxies in which the galaxy is observed and as a function of their structures as parameterised by the Sérsic index n (Hogg et al., 2004)

second and third rows further split the sample of galaxies into those with Sérsic parameters greater and less than 2. These diagrams quantify the statement that red spheroidal galaxies are found in the richest cluster regions and these are avoided by the blue disc-like galaxies.

3.9.5 The New Perspective

The new way of quantifying the physical properties of galaxies developed in this section illustrates a profound difference of approach to the study of galaxies as compared with, say, ten years ago when the first edition of this book was written. The advent of the huge galaxy surveys as represented by the SDSS and 2dF galaxy surveys have provided the opportunity to quantify by computer algorithm the properties of galaxies which in the past relied somewhat upon the eye of the experienced observer. The division of galaxies into members of the blue and red sequences parallels in many ways the division into early and late-type galaxies. To a good approximation, galaxies earlier than Sa in the Hubble sequence, stage $T = 1$ in de Vaucouleurs' classification (Table 3.1), are members of the red sequence and galaxies later than $T = 1$ belong to the blue sequence.

Of particular importance is the fact that the relative number densities of galaxies of different types are now well-established with large statistics and so are ripe for comparison with the predictions of theories of galaxy formation. As an example of the usefulness of the new statistics, an important result is how the average number, luminosity and mass densities of the stellar component of galaxies in the local Universe are made up. Bell and his colleagues have shown, for example, that while the red sequence contains only 20% of the galaxies by number, these contribute 40% of the stellar luminosity density and 60% of the average stellar mass density at the present epoch (Bell et al., 2003).

3.10 Concluding Remark

This exposition has focussed upon understanding the properties of galaxies *at the present epoch* and has refrained from consideration of the vast amount of data now available on samples of galaxies at earlier epochs, or large redshifts, which provide clues to their origin and evolution. These topics will be taken up in much more detail in Chaps. 17 to 19 once the origin of large-scale structures in the Universe has been established.

4 Clusters of Galaxies

Associations of galaxies range from pairs and small groups, through the giant clusters containing over a thousand galaxies, to the vast structures on scales much greater than clusters such as the vast ‘walls’ seen in Figs. 2.7 and 2.8. Clustering occurs on all scales, as is demonstrated by the two-point correlation function for galaxies (Figs. 2.5 and 2.6). Few galaxies can be considered truly isolated. Rich clusters of galaxies are of particular interest because they are the largest gravitationally bound systems we know of in the Universe. They possess correspondingly deep gravitational potential wells which can be observed through the bremsstrahlung X-ray emission of hot gas which forms an atmosphere within the cluster. The hot gas can also be detected through the decrements which it causes in the Cosmic Microwave Background Radiation as a result of the Sunyaev–Zeldovich effect.

Clusters, therefore, provide laboratories for studying many different aspects of galactic evolution within rather well-defined astrophysical environments. Interactions of galaxies with each other and with the intergalactic medium in the cluster can be studied, as well as the distribution and nature of the dark matter, which dominates their dynamics. Radio source events can strongly perturb the distribution of hot gas. From the perspective of the formation of large-scale structure, the mass function for clusters of galaxies provides constraints on the development of structure on large scales and on cosmological parameters.

4.1 The Large-Scale Distribution of Clusters of Galaxies

Until relatively recently, the surveys of rich clusters of galaxies which have been the focus of most attention resulted from the pioneering efforts of George Abell. More recently, clusters have been detected by analysing the distribution of galaxies found in machine-scanned surveys of 48-inch Schmidt telescope plates, such as the APM and COSMOS cluster surveys. Most recently, rich clusters have been identified in the large catalogues of galaxies provided by the Sloan Digital Sky Survey. Another approach is to identify clusters of galaxies as extended X-ray sources at high galactic latitudes and this has proved to be an effective procedure which is independent of the need to identify the individual cluster members (Sect. 4.4).

4.1.1 The Abell Catalogues of Rich Clusters of Galaxies

It is worthwhile recounting the heroic efforts of Abell and his colleagues in creating the Abell catalogue of rich clusters of galaxies and its southern counterpart. The 48-inch Schmidt telescope was constructed on Palomar mountain during the late 1940s as a wide-field telescope to support and complement observations made with the 200-inch telescope. The Palomar Sky Survey took seven years to complete and comprised 879 pairs of 14-inch plates, each providing roughly $6^\circ \times 6^\circ$ sky coverage and having limiting magnitudes of 21.1 in the blue and 20.0 in the red wavebands. Abell was one of the principal observers for the Palomar Sky Survey and, while the plates were being taken, he systematically catalogued the rich clusters of galaxies appearing on the plates. The word ‘rich’ meant that there was no doubt as to the reality of the associations of galaxies appearing on the plates (Abell, 1958). A typical example of a rich, regular cluster of galaxies, Abell 2218, is shown in Fig. 4.1. A corresponding catalogue for the southern hemisphere was created with the completion of the ESO-SERC Southern Sky Survey, which was made with the 48-inch UK Schmidt Telescope at the Siding Spring Observatory in New South Wales (Abell et al., 1989). In both cases, the clusters were found by visual inspection of the Sky Survey plates.

Crucial to the success of Abell’s programme was adherence to the strict set of criteria he established for the inclusion of clusters in the catalogue. The 4073 clusters in the combined northern and southern catalogue of Abell, Corwin and Olowin fulfil the following selection criteria:

- *Richness criterion.* The clusters must have 50 members brighter than 2 magnitudes ($m_3 + 2$) fainter than the third brightest member (m_3). *Richness classes* are defined by the number of galaxies with magnitudes between m_3 and $m_3 + 2$,

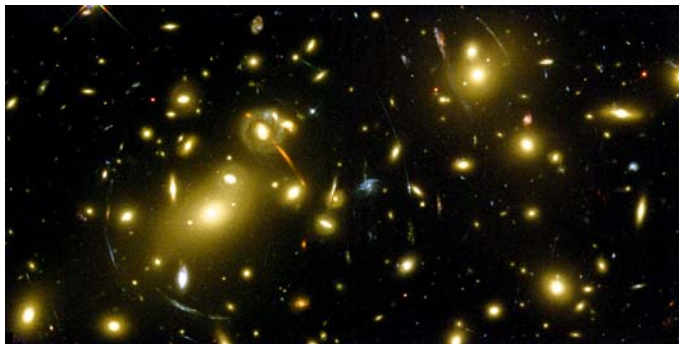


Fig. 4.1. The rich, regular cluster of galaxies Abell 2218. Abell classified this cluster as richness class 4. The central galaxy is a supergiant or cD galaxy, which is very much brighter than all the other galaxies in the cluster. It is located close to the dynamical centre of the cluster. The image also shows a number of arcs which are the gravitationally lensed images of very distant background galaxies (Courtesy NASA, ESA and the Space Telescope Science Institute)

as described in Table 4.1. A richness class 0 is included for clusters which have between 30 and 50 members within the same magnitude interval, but the catalogues are not complete for this class. Studies of a number of nearby clusters of different richness classes have shown that richness is proportional to the total number of galaxies in the cluster.

- *Compactness criterion.* Galaxies are only counted within a radius of $1.5 h^{-1}$ Mpc of the cluster centre. This radius corresponds to an angular radius of $1.7/z$ arcmin, the redshift of the cluster being estimated from the apparent magnitude of its tenth brightest member, m_{10} .
- *Distance criteria.* Abell clusters with redshifts less than 0.02 span more than one Sky Survey plate and hence this lower redshift limit was adopted. The upper redshift limit is set by the fact that galaxies could not be counted to magnitudes fainter than $m_r = 20$ in the northern survey and therefore the third brightest galaxy must be brighter than $m_3 = 17.5$. This redshift limit corresponds to $z \approx 0.2$. From redshift measurements of a number of clusters, it was found that m_{10} , the apparent magnitude of the tenth brightest cluster member, is a reliable distance indicator. The clusters were then divided into *distance classes* in such a way that there was a small probability of the class assigned to the cluster being more than one class wrong.

Within the northern sample, Abell defined a *complete statistical sample* of 1682 clusters which fulfilled distance criteria 1 to 6 and richness criteria 1 to 5. The numbers of clusters in each richness class in this sample and the total numbers in the southern sample are included in Table 4.1. The number density distribution of clusters with increasing distance, equivalent to the number counts of clusters, is shown in Fig. 4.2 (Batuski et al., 1989). It can be seen that serious incompleteness sets in at distances greater than about $600h^{-1}$ Mpc, corresponding to redshift $z = 0.2$, but at smaller distances, there is reasonable agreement between the samples of clusters

Table 4.1. Definitions of the richness classes R of Abell clusters and the numbers of clusters within Abell's complete northern sample of 1682 clusters and the total sample of southern clusters. N is the number of galaxies in the cluster between magnitudes m_3 and $m_3 + 2$ (Abell, 1958; Bahcall, 1988; Abell et al., 1989)

Richness Class R	N	Number of clusters in the complete northern sample	Total number of clusters in the southern sample
(0) ^a	(30 – 49)	($\geq 10^3$)	(664)
1	50 – 79	1224	656
2	80 – 129	383	273
3	130 – 199	68	41
4	200 – 299	6	1
5	300 or more	1	0

^a The sample is not complete for richness class zero

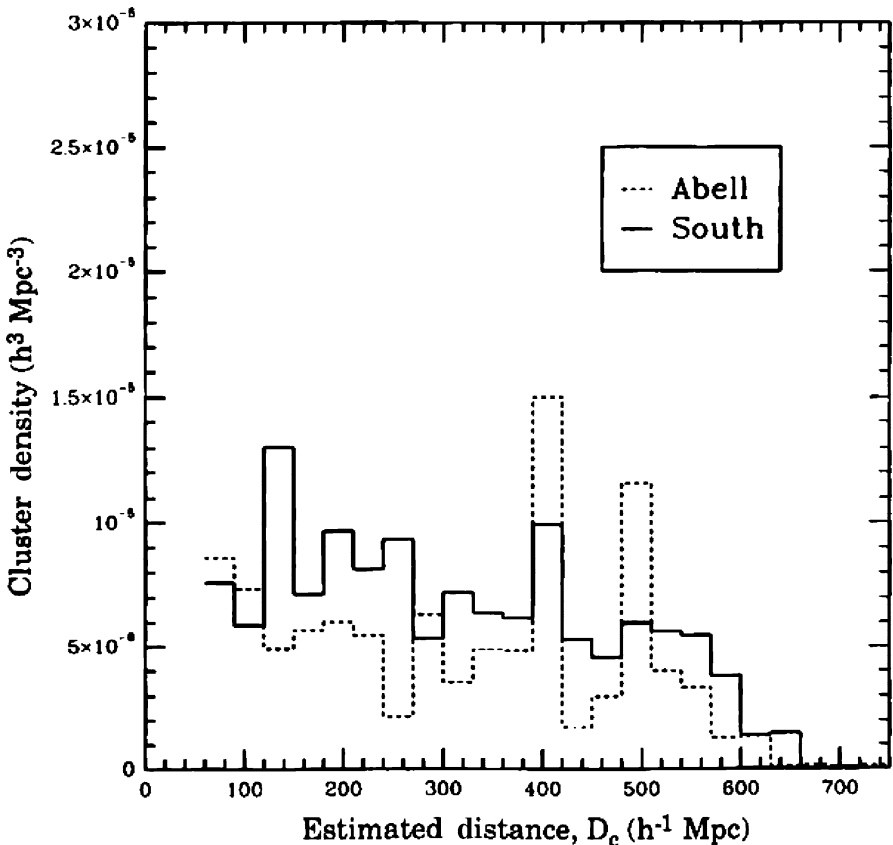


Fig. 4.2. The average estimated space densities of Abell clusters in the Northern and Southern catalogues for richness classes $R \geq 1$ as a function of estimated distance D_c (Batuski et al., 1989)

in the northern and southern hemispheres. The space density of Abell clusters with richness classes greater than or equal to 1 is, to a good approximation,

$$N_{\text{cl}}(R \geq 1) \approx 10^{-5} h^3 \text{ Mpc}^{-3}, \quad (4.1)$$

so that the typical distance between cluster centres, if they were uniformly distributed in space, would be $\sim 50 h^{-1} \text{ Mpc}$. These figures can be compared with the space density of ‘mean galaxies’ of $10^{-2} h^3 \text{ Mpc}^{-3}$ and their typical separations of $5 h^{-1} \text{ Mpc}$ (see Sect. 3.7.2).

4.1.2 Comparison with Clusters Selected from the Sloan Digital Sky Survey

The studies of Abell and his colleagues were entirely based upon visual inspection of the plates and film copies of the Northern and Southern 48-inch Schmidt

Telescope Sky Surveys. Great care was taken to ensure the consistency of the cluster identifications and classifications over many years. The advent of high speed measuring machines with powerful procedures for star-galaxy separation enabled more objective approaches to the identification of rich clusters to be developed. It is perhaps most instructive to compare Abell's results with those of the Bahcall and her colleagues who have identified the clusters present in the early release commissioning data of the Sloan Digital Sky Survey (SDSS) (Bahcall et al., 2003b). The SDSS has the great advantages of having images in five different wavebands as well as redshifts for very large samples of galaxies at $z \leq 0.1$. As a result, velocity dispersions are available for many of the clusters studied, enabling masses to be estimated.

The analyses described by Bahcall and her colleagues do not use all these data but employ two of the various algorithms available to isolate clusters of galaxies which satisfy criteria similar to Abell's, but which extend to slightly lower richness classes. They find that 53 of the 58 Abell clusters in the area of sky studied are included in their merged catalogue of clusters, the remaining five clusters being detected just below the richness limits of their catalogue. This is a remarkable testament to the quality of the visual approach of Abell and his colleagues.

An advantage of the procedures adopted by Bahcall and her colleagues is that the limits of the catalogue can be expressed in terms of the velocity dispersions and masses of the clusters. Thus, the threshold for the inclusion of clusters in the catalogue corresponds to typical velocity dispersions $\sigma_v \geq 400 \text{ km s}^{-1}$ and to masses M within radius $0.6 h^{-1} \text{ Mpc}$ of their centres of $M \geq 5 \times 10^{13} h^{-1} M_\odot$. This threshold corresponds to richness classes below Abell's richness class 0. The average space density of these rich clusters is $2 \times 10^{-5} h^3 \text{ Mpc}^{-3}$, in excellent agreement with Abell's estimate when account is taken of the fact that the sample extends to somewhat lower richness limits.

Bahcall and her colleagues provide a useful table showing the velocity dispersions, masses and luminosities for the samples of clusters of different richnesses in their catalogue (Table 4.2). These data provide estimates of the mass-to-luminosity ratios for clusters of different richnesses. It can be seen from Table 4.2 that these range from $\sim 170 h$ to $\sim 250 h$ with increasing richness. In turn, these data can be used to determine the mass functions of rich clusters of galaxies and to provide constraints on the mass density parameter Ω_0 and the amplitude of the mass fluctuations σ_8 (Sects. 8.7 and 14.4).

4.1.3 Abell Clusters and the Large-Scale Distribution of Galaxies

Abell clusters are strongly correlated in space, both with each other and with the distribution of galaxies in general. These associations were originally described in terms of the superclustering of galaxies, but it is preferable nowadays to express the clustering in terms of the correlation functions introduced in Sect. 2.2.1. It is simplest to quote the results of the SDSS survey of rich clusters by Bahcall and her colleagues who include extensive references to earlier work (Bahcall et al., 2003a).

Table 4.2. An example of the scaling relations for clusters of galaxies of different richnesses from analysis of the commissioning data from the SDSS (Bahcall et al., 2003b). N_{gal} is the number of red E/S0 galaxies one magnitude fainter than L^* in the i band within a radius of $1 h^{-1}$ Mpc of the brightest cluster galaxy where $L^* = 10^{10} h^2 L_\odot$. Λ is a measure of the richness of the cluster and is derived from the best-fit cluster model which has total luminosity $L_{\text{cl}} = \Lambda L^*$, where the luminosity is measured within a radius of $1 h^{-1}$ Mpc

N_{gal}	Λ	σ_v (km s $^{-1}$)	L_{tot} ($10^{11} h^{-2} L_\odot$)	M ($10^{14} h^{-1} M_\odot$)
10	35	350	2.1	0.35
15	43	430	3.2	0.6
20	50	500	4.4	0.9
25	56	560	5.5	1.2
30	61	620	6.6	1.5
40	70	730	8.7	2.2

The correlation functions for the different richness classes described in Table 4.2 are shown in Fig. 4.3. The best-fit two-point correlation function has the form

$$n(r) dV = n_0 [1 + \xi(r)] dV , \quad \text{where} \quad \xi(r) = \left(\frac{r}{r_0} \right)^{-2} , \quad (4.2)$$

which is slightly steeper than the value found on smaller physical scales for galaxies in general. The data included in Fig. 4.3 show that the correlation length r_0 is much greater than that for galaxies in general. Bahcall and her colleagues find that the variation can be described by the relation $r_0 = 2.6\sqrt{d}$ for $(20 \leq d \leq 90)h^{-1}$ Mpc, where d is the mean comoving separation distance of the clusters belonging to different richness classes. Thus, the correlation lengths for these rich clusters are large, on the scale of the huge voids seen in the distribution of galaxies in general.

The rich clusters are generally found in the densest regions in the ‘cosmic web’ seen in Figs. 2.7 and 2.8. Some measure of the association of Abell clusters with galaxies in general has been provided by the analysis of Seldner and Peebles (Seldner and Peebles, 1977). They cross-correlated the counts of galaxies in the Shane–Wirtanen catalogue, which extended to apparent magnitude $m \approx 19$, with the positions of Abell clusters of distance class 5. The cross-correlation function was found to be of the form

$$\xi_{\text{gc}} = Ar^{-2.4} ,$$

out at a distance of $15h^{-1}$ Mpc from the cluster centres. This function represents the correlation of the Abell clusters with galaxies in the vicinity of the cluster, but outside what would normally be considered to be the cluster boundary; Seldner and Peebles refer to this phenomenon as the superclustering of galaxies about Abell clusters. This result is in agreement with the visual impression of the distribution of galaxies seen in Figs. 2.7 and 2.8.

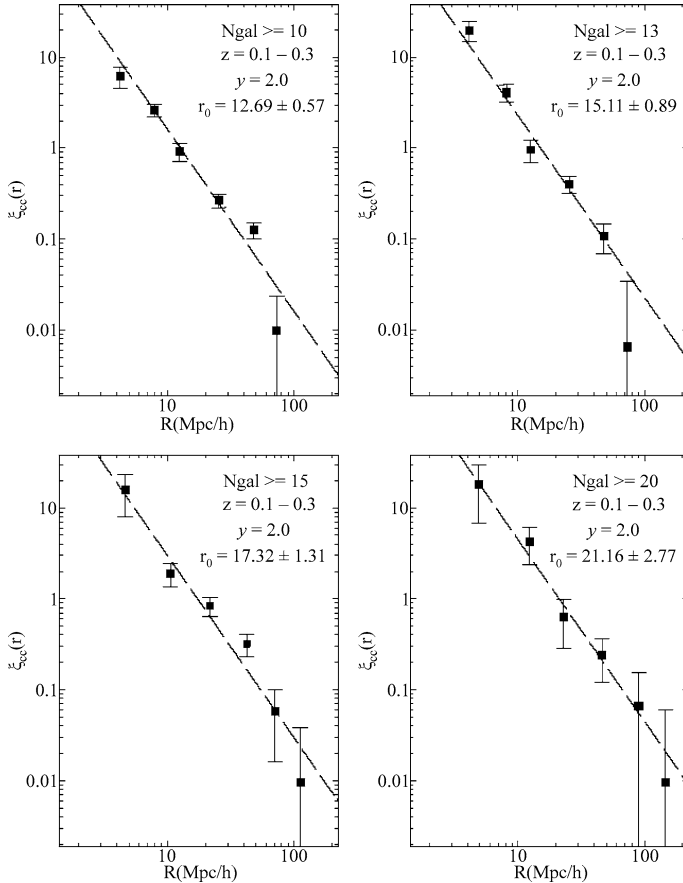


Fig. 4.3. The two-point spatial correlation function for four richness thresholds ($N_{\text{gal}} \geq 10$, ≥ 13 , ≥ 15 , ≥ 20) for clusters selected from the SDSS (Bahcall et al., 2003a). Best-fit functions with slope 2 and correlation-scale r_0 are shown by the *dashed lines*. The *error bars* show the 1σ uncertainties in the estimates. The values of d for the four panels are 26.2, 35.6, 41.5 and 58.1 Mpc with increasing richness

4.2 The Distribution of Galaxies in Clusters of Galaxies

Clusters of galaxies come in a variety of shapes and forms and various schemes have been developed to put some order into this diversity. Just as in the case of galaxies, modern computer-based systems of classification bring new, quantitative insights into the wealth of detail contained in the visual classification of clusters.

4.2.1 The Galaxy Content and Spatial Distribution of Galaxies in Clusters

Abell classified clusters as *regular* if they are more or less circularly symmetrical with a central concentration, similar in structure to globular clusters (Abell, 1962). These

are among the richest clusters, generally containing over 1000 members. Examples include the Coma cluster. The galaxies are predominantly elliptical and S0 galaxies as has been indicated by the results shown in Figs. 3.4 and 3.16. Abell called all the other clusters in which there is much less well-defined structure *irregular* clusters. In his words, the irregular clusters

... have a more nearly amorphous appearance, and possess little or no spherical symmetry or central concentration. The irregular clusters sometimes, however, have several small subcondensations or nuclei and resemble loose swarms of small clusters.

Examples of the latter include the Hercules and Virgo clusters.

Oemler studied systematically a representative sample of fifteen Abell clusters of different richness classes and morphological types and distinguished three principal types of cluster according to their *galaxy content* (Oemler, 1974):

- *cD clusters* have a unique and dominant cD galaxy and the ratio of elliptical (E) to lenticular (S0) to spiral (S) galaxies is roughly 3 : 4 : 2, that is, only about 20% are spirals. These clusters are very rich in E and S0 galaxies.
- *Spiral-rich clusters* have galaxy-type ratios E : S0 : S roughly 1 : 2 : 3, that is, about 50% spirals, a distribution similar to the proportions of types found in the general field.
- The remaining clusters are called *spiral-poor clusters*. They have no dominant cD galaxy and have galaxy type ratios E : S0 : S roughly 1 : 2 : 1.

Abell noted that there is a correlation between the structure of clusters and galaxy content and this result was quantified by Oemler who established the following relations:

- In *cD clusters* or *regular clusters*, the spatial distribution of galaxies resembles the distribution of stars in a globular cluster (see Sect. 4.2.2). The space density of galaxies increases rapidly towards the centre of the cluster. The *spiral-rich clusters* and *irregular clusters* are not symmetric and there is little central concentration; the spatial density of galaxies is roughly uniform towards the central regions and is lower than that in cD clusters. The *spiral-poor clusters* are intermediate between these two extremes.
- In the case of *spiral-rich clusters*, the radial distribution of elliptical, lenticular and spiral galaxies is more or less the same. In *cD* and *spiral-poor clusters*, however, the relative space density of spiral galaxies decreases markedly towards the central regions, reflecting Dressler's correlation of galaxy type with galaxy number density (Dressler, 1984). In these clusters, the spiral galaxies form a halo around a central core of elliptical and S0 galaxies. There is therefore *segregation by galaxy type* in cD and spiral-poor clusters.
- In addition to evidence for segregation by galaxy type, there is some evidence for *mass segregation* as a function of cluster type. Adopting apparent magnitude as a measure of mass, Oemler found that, in *cD* and *spiral-poor clusters*, the massive galaxies are located closer to the centre than less massive galaxies.

However, this mass segregation is only important for the brightest members of clusters, $m \leq m_1 + 2$, where m_1 is the apparent magnitude of the brightest galaxy; galaxies fainter than $m_1 + 2$ appear to be uniformly distributed throughout the clusters. No such mass segregation is found in *spiral-rich clusters*.

As discussed in Sects. 3.7.1 and 4.2.3, the cD galaxies found in the centres of cD clusters have a number of features which distinguish them from giant elliptical galaxies (Kormendy, 1982). Their most distinctive features are their extensive stellar envelopes which can be as large as 100 kpc. In addition to being found in rich clusters, examples of cD galaxies are known in small groups of galaxies but, in all cases, they are found in regions of significantly enhanced galaxy density relative to the general field. Dressler found that cD galaxies are only found in regions in which the galaxy density exceeds $1 h^{-3}$ galaxy Mpc $^{-3}$, compared with an average galaxy density of $10^{-2} h^{-3}$ Mpc $^{-3}$ (Dressler, 1984). According to Dressler, the local galaxy density rather than the richness of the cluster determines whether or not a cD galaxy is present in a group or cluster. Some of the central cD galaxies in rich clusters are also distinctive in having multiple nuclei which are found in about 25–50% of all cD galaxies. In contrast, multiple nuclei are an order of magnitude less common in second and third ranked cluster members.

These results are important in understanding the dynamical evolution of clusters. Regular, cD clusters are systems which have had time to relax to dynamical equilibrium, whereas the other systems are still in the process of relaxation.

4.2.2 Clusters of Galaxies and Isothermal Gas Spheres

In regular clusters, the space density of galaxies increases towards the central regions, which are referred to as the *cores* of the clusters. Outside the core, the space density of galaxies decreases steadily until it disappears into the background of unrelated objects. The regular structures of these clusters suggests that they have relaxed to a stationary dynamical state similar to that found in the distribution of stars in globular clusters. The spatial distribution of galaxies in a regular cluster can be modelled by the distribution of mass in an *isothermal gas sphere*. These distributions are important in the discussion which follows and so let us derive the relevant expressions for the density distribution of an isothermal gas sphere.

The term *isothermal* means that the temperature, or mean kinetic energy of the particles, is constant throughout the cluster. In physical terms, this means that the velocity distribution of the galaxies is Maxwellian with the same velocity dispersion (or temperature) throughout the cluster. If all the galaxies had the same mass, the velocity dispersion would be the same at all locations within the cluster. This is a rather sweeping approximation since it would mean that there had been enough time for the galaxies to have exchanged kinetic energy and come to a thermal equilibrium velocity distribution. Although a good case can be made that the galaxies have had time to ‘virialise’, that is, to satisfy the virial theorem when the cluster formed, it takes much longer for energy exchange to take place, except for the most massive galaxies in the cluster. Nonetheless, let us work out the density distribution of an isothermal gas sphere as a reference model for comparison with the observations.

We need the *Lane–Emden equation*, which describes the structure of a spherically symmetric object, such as a star, in hydrostatic equilibrium. The requirement of hydrostatic equilibrium is that, at all points in the system, the attractive gravitational force acting on a mass element $\varrho \, dV$ at radial distance r from the centre of the system is balanced by the pressure gradient at that point,

$$\nabla p = \frac{dp}{dr} = -\frac{GM\varrho}{r^2}, \quad (4.3)$$

where M is the mass contained within radius r ,

$$M = \int_0^r 4\pi r^2 \varrho(r) dr \quad dM = 4\pi r^2 \varrho(r) dr. \quad (4.4)$$

Reordering (4.3) and differentiating, we find

$$\begin{aligned} \frac{r^2}{\varrho} \frac{dp}{dr} &= -GM \quad \frac{d}{dr} \left(\frac{r^2}{\varrho} \frac{dp}{dr} \right) = -G \frac{dM}{dr} \\ \frac{d}{dr} \left(\frac{r^2}{\varrho} \frac{dp}{dr} \right) + 4\pi Gr^2 \varrho &= 0. \end{aligned} \quad (4.5)$$

Equation (4.5) is the *Lane–Emden equation*. We are interested in the case in which the pressure p and the density ϱ are related by the perfect gas law at all radii r , $p = \varrho kT/\mu$, where μ is the mass of an atom, molecule or galaxy. In thermal equilibrium, $\frac{3}{2}kT = \frac{1}{2}\mu\langle v^2 \rangle$, where $\langle v^2 \rangle$ is the mean square velocity of the atoms, molecules or galaxies. Therefore, substituting for p ,

$$\frac{d}{dr} \left(\frac{r^2}{\varrho} \frac{d\varrho}{dr} \right) + \frac{4\pi G\mu}{kT} r^2 \varrho = 0. \quad (4.6)$$

Equation (4.6) is a non-linear differential equation and, in general, must be solved numerically. There is, however, an analytic solution for large values of r . If $\varrho(r)$ is expressed as a power series in r , $\varrho(r) = \sum A_n r^{-n}$, there is a solution for large r with $n = 2$,

$$\varrho(r) = \frac{2}{Ar^2} \quad \text{where} \quad A = \left(\frac{4\pi G\mu}{kT} \right). \quad (4.7)$$

This mass distribution has the unfortunate property that the total mass of the cluster diverges at large values of r ,

$$\int_0^\infty 4\pi r^2 \varrho(r) dr = \int_0^\infty \frac{8\pi}{A} dr \rightarrow \infty. \quad (4.8)$$

There are, however, at least two reasons why there should be a cut-off at large radii. First of all, at very large distances, the particle densities become so low that the mean free path between collisions is very long. The thermalisation time-scales consequently become greater than the time-scale of the system. The radius at which this

occurs is known as *Smoluchowski's envelope*. Secondly, in astrophysical systems, the outermost stars or galaxies are stripped from the system by tidal interactions with neighbouring systems. This process defines a *tidal radius* r_t for the cluster. Therefore, if clusters are modelled by isothermal gas spheres, it is perfectly permissible to introduce a cut-off at some suitably large radius, resulting in a finite total mass.

It is convenient to rewrite (4.6) in dimensionless form by writing $\varrho = \varrho_0 y$, where ϱ_0 is the central mass density, and introducing a *structural index* or *structural length* α , where α is defined by the relation

$$\alpha = \frac{1}{(A\varrho_0)^{1/2}}. \quad (4.9)$$

Distances from the centre can then be measured in terms of the dimensionless distance $x = r/\alpha$. Then, (4.6) becomes

$$\frac{d}{dx} \left[x^2 \frac{d(\log y)}{dx} \right] + x^2 y = 0. \quad (4.10)$$

Two versions of the solution of (4.10) are listed in Table 4.3 and illustrated in Fig. 4.4. In column 2, the solution of y as a function of distance x is given; in the third column, the projected distribution onto a plane is given, this being the observed distribution of a cluster of stars or galaxies on the sky. It is a simple calculation to show that, if q is the projected distance from the centre of the cluster, the surface density $N(q)$ is related to $y(x)$ by the integral

$$N(q) = 2 \int_q^\infty \frac{y(x)x}{(x^2 - q^2)^{1/2}} dx. \quad (4.11)$$

Inspection of Table 4.3 and Fig. 4.4, shows that α is a measure of the size of the *core* of the cluster. It is convenient to fit the projected distribution $N(q)$ to the distribution of stars or galaxies in a cluster and then a *core radius* for the cluster can be defined. It can be seen that the projected density falls to the value $N(q) = 1/2$ at $q = 3$, that is, at a core radius $R_{1/2} = 3\alpha$. $R_{1/2}$ is a convenient measure of the core radius of the cluster.

Having measured $R_{1/2}$, the central mass density of the cluster can be found if the velocity dispersion of the galaxies in this region is also known. From Maxwell's equipartition theorem, $\frac{1}{2}\mu\langle v^2 \rangle = \frac{3}{2}kT$ and therefore, from the definition of α ,

$$\alpha^2 = \frac{1}{A\varrho_0} = \frac{kT}{4\pi G\mu\varrho_0} = \frac{\langle v^2 \rangle}{12\pi G\varrho_0}. \quad (4.12)$$

Observationally, we can only measure the radial component of the galaxies' velocities $v_{||}$. Assuming the velocity distribution of the galaxies in the cluster is isotropic,

$$\langle v^2 \rangle = \langle v_x^2 \rangle + \langle v_y^2 \rangle + \langle v_z^2 \rangle = 3\langle v_{||}^2 \rangle. \quad (4.13)$$

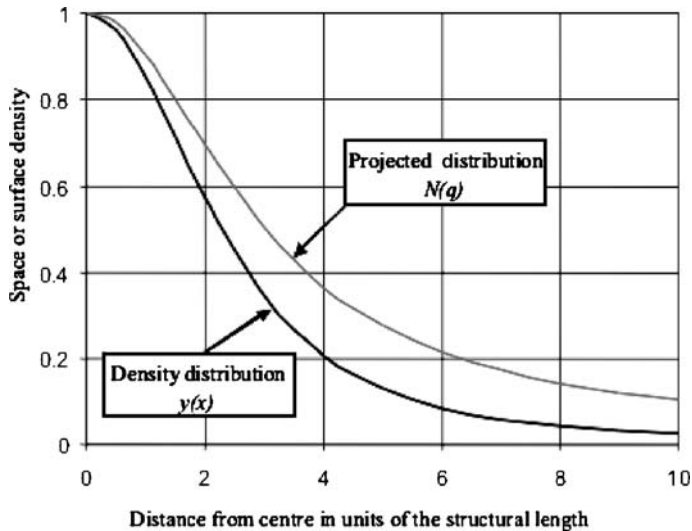


Fig. 4.4. The density distribution $y(x)$ and the projected density distribution $N(q)$ for an isothermal gas sphere

Table 4.3. The density distribution $y(x)$ and the projected density distribution $N(q)$ for an isothermal gas sphere

x, q	$y(x)$	$N(q)$	x, q	$y(x)$	$N(q)$
0	1.0	1.0	12	0.0151	0.0839
0.5	0.9597	0.9782	14	0.0104	0.0694
1.0	0.8529	0.9013	16	0.0075	0.0591
1.5	0.7129	0.8025	20	0.0045	0.0457
2	0.5714	0.6955	30	0.0019	0.0313
3	0.3454	0.5033	40	0.0010	0.0229
4	0.2079	0.3643	50	0.0007	0.0188
5	0.1297	0.2748	100	1.75×10^{-4}	0.0101
6	0.0849	0.2143	200	5.08×10^{-5}	0.0053
7	0.0583	0.1724	300	2.32×10^{-5}	0.0036
8	0.0418	0.1420	500	8.40×10^{-6}	0.0021
9	0.0311	0.1209	1000	2.0×10^{-6}	0.0010
10	0.0238	0.1050			

Expressing the central density ϱ_0 in terms of $R_{1/2}$ and $\langle v_{\parallel}^2 \rangle$, we find

$$\varrho_0 = \frac{9 \langle v_{\parallel}^2 \rangle}{4\pi G R_{1/2}^2}. \quad (4.14)$$

Thus, assuming the central density distribution of a cluster can be represented by an isothermal gas sphere, we can find the central mass density of the cluster by measuring $\langle v_{\parallel}^2 \rangle$ and $R_{1/2}$.

Improved versions of the isothermal sphere model were evaluated by King and these have provided good fits to the light distributions of globular clusters and galaxies (King, 1966, 1981). The models were originally derived from studies of the solutions of the Fokker–Planck equation which describes the distribution function $f(v, r)$ for the stars in a cluster under the condition that there should be no particles present with velocities which enable them to escape from the cluster. This might occur for two reasons. Either the stars have velocities which exceed the escape velocity from the cluster, or the stars travel to distances greater than the tidal radius of the cluster when they are lost from the cluster because of tidal forces. In either case, the cluster can be modelled as a truncated isothermal gas sphere in which none of the stars can have velocities exceeding some value v_e . This is implemented by truncating the Maxwell velocity distribution at this velocity which in turn results in models with finite tidal radii r_t . The luminosity profiles for such clusters are shown in Fig. 4.5, the models being parameterised by the quantity $\log r_t/r_c$, the logarithm of the ratio of the tidal and core radii. In the limit $r_t/r_c \rightarrow \infty$, the models become isothermal gas spheres.

The models which best represent elliptical galaxies are not too dissimilar from isothermal gas spheres. In terms of King's models, the giant elliptical galaxies

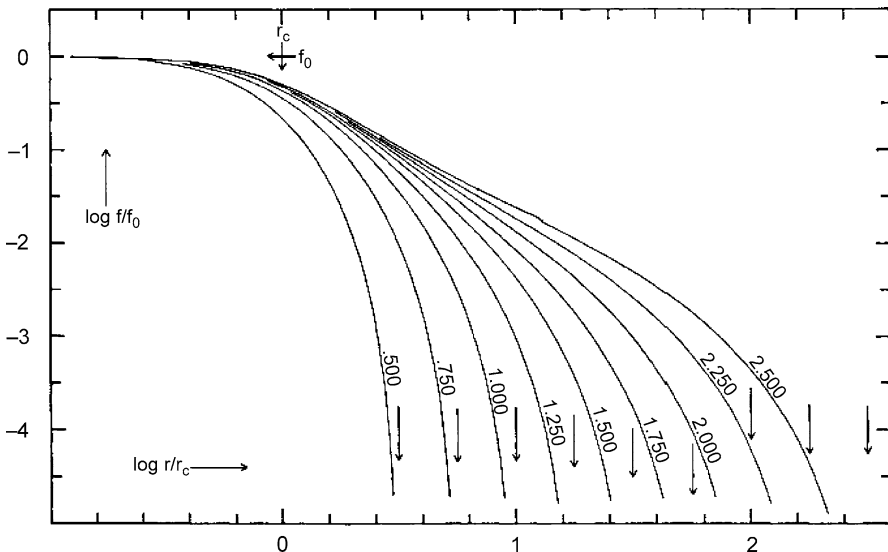


Fig. 4.5. King models for the distribution of stars in globular clusters, galaxies or of galaxies in clusters of galaxies (King, 1966, 1981). The curves show the projected distribution of stars or galaxies, equivalent to $N(q)$ in Table 4.3, and are parameterised by the quantity $\log(r_t/r_c)$ where r_t is the tidal radius and r_c the core radius. The arrows indicate $\log r_t$

have $\log r_t/r_c \approx 2.2$; for dwarf elliptical galaxies, the surface brightness decreases somewhat more rapidly in the outer regions and King models having small values of $\log r_t/r_c$ can give a good representation of the data. These profiles have also been found to provide a good description of the distribution of galaxies in clusters.

According to Bahcall, the observed distribution of galaxies in regular clusters can be described by truncated isothermal distributions $N(r)$ of the form

$$N(r) = N_0[f(r) - C], \quad (4.15)$$

where $f(r)$ is the projected isothermal distribution normalised to $f(r) = 1$ at $r = 0$ and C is a constant which reduces the value of $N(r)$ to zero at some radius R_h such that $f(R_h) = C$ (Bahcall, 1977). For regular clusters core radii lie in the range $R_{1/2} = 150 - 400$ kpc, the Coma cluster having $R_{1/2} = 220$ kpc. Bahcall found that there is a relatively small dispersion in the values of C required to provide a satisfactory fit to the profiles of many regular clusters, typically the value of C corresponding to about 1.5% of the isothermal central density.

Many different density distributions have been proposed to describe the space density distribution of galaxies in clusters in addition to the above examples. These include models such as de Vaucouleurs' law for elliptical galaxies (equations 3.2 or 3.3) as well other possibilities such as the Plummer model which is derived from a gravitational potential with a core radius b of the form

$$\phi = -\frac{GM}{(r^2 + b^2)^{1/2}}, \quad (4.16)$$

where M is the total mass of the system. Using Poisson's law for gravity in spherical polar coordinates, we find the density distribution from

$$\nabla^2\phi = \frac{1}{r^2} \frac{\partial}{\partial r} \left(r^2 \frac{\partial \phi}{\partial r} \right) = 4\pi G \varrho. \quad (4.17)$$

Then,

$$\varrho(r) = \frac{3M}{4\pi b^3} \left(1 + \frac{r^2}{b^2} \right)^{-5/2}. \quad (4.18)$$

Binney and Tremaine discuss these and other possibilities (Binney and Tremaine, 1987).

4.2.3 The Luminosity Function for Cluster Galaxies

The luminosity functions for cluster galaxies can be represented by the Schechter function introduced in Sect. 3.7, but, as indicated by Fig. 3.16, there are significant differences in the shapes of the luminosity functions for early and late-type galaxies as compared with the general field, or the even more extreme case of the void regions. These functions are another way of presenting Dressler's results concerning the

different types of galactic populations found in environments of different densities (Fig. 3.4).

In Sandage's analysis of the redshift-apparent magnitude relation, he demonstrated that there is remarkably little scatter in the absolute magnitudes of the brightest members of rich clusters of galaxies, the standard deviation of the brightest cluster galaxies amounting to $\sigma_M = 0.28$ (Sandage, 1988) (see Fig. 2.11). There was some controversy about whether or not the constancy of the absolute magnitude of the first-ranked cluster galaxy could be explained by randomly sampling the high luminosity region of the luminosity function, or whether they possess some special property which is independent of the cluster richness.

Tremaine and Richstone compared the dispersion in absolute magnitudes of the first-ranked members $\sigma(M_1)$ with the mean value of the difference in magnitude between the first and second ranked members $\Delta M_{12} = \langle M_1 - M_2 \rangle$ (Tremaine and Richstone, 1977). They showed that for any statistical luminosity function $\sigma(M_1)/\Delta M_{12} = t_1 > 1$ must hold. For example, using Schechter's function, $t_1 = 1.20$. For Sandage's data on rich clusters, $t_1 = 0.48 \pm 0.10$, supporting his point of view that there is much less dispersion in the absolute magnitudes of first ranking cluster galaxies than would be expected if they were simply randomly sampled from the luminosity function. Geller and Postman failed to confirm this result (Geller and Postman, 1983). Nonetheless, as discussed in Sect. 4.2.1, the cD galaxies are quite distinct from normal giant elliptical galaxies (Kormendy, 1982).

A further classification scheme, due to Bautz and Morgan also bears upon the issue of the origins of the brightest galaxies in clusters (Bautz and Morgan, 1970). In the *Bautz–Morgan classification* scheme, clusters are classified according to the presence or absence of a dominant D or cD galaxy at the centre of the cluster. Bautz–Morgan class I clusters contain a dominant centrally located cD galaxy (for example Abell 2199); class II clusters have a central galaxy intermediate between a cD and giant elliptical galaxy (for example, the Coma cluster); class III clusters have no dominant central galaxy. Intermediate classes between classes I, II and III have been defined. A number of properties of clusters depend upon Bautz–Morgan class. For example, Sandage has found that there is a weak correlation between Bautz–Morgan class and the absolute magnitude of the brightest cluster member which cannot account for all the difference between the Bautz–Morgan classes. There must in addition be an inverse correlation between Bautz–Morgan class and the absolute magnitudes of the second and third brightest members in the sense that they are relatively brighter in Bautz–Morgan class III clusters. This phenomenon is illustrated by the data in Table 4.4 which lists the mean absolute magnitudes of the first, second and third brightest galaxies in a large sample of rich clusters studied by Sandage and Hardy (Sandage and Hardy, 1973).

4.2.4 Summary of the Properties of Rich Clusters of Galaxies

There are some clear trends in the overall properties of clusters of galaxies. A sequence of types can be defined based on Abell's distinction between *regular* and *irregular* clusters with the addition of an *intermediate* class. Table 4.5 is adapted

Table 4.4. The absolute magnitudes of the first, second and third ranked cluster galaxies as a function of Bautz–Morgan type (Sandage 1976). It is assumed that $h = 0.5$

Bautz–Morgan Class	M_1	M_2	M_3
I	-23.09 ± 0.051	-22.72 ± 0.077	-22.47 ± 0.091
I-II	-23.30 ± 0.068	-22.83 ± 0.091	-22.56 ± 0.121
II	-23.37 ± 0.130	-22.60 ± 0.217	-22.34 ± 0.212
II-III	-23.46 ± 0.092	-22.18 ± 0.247	-21.96 ± 0.233
III	-23.68 ± 0.102	-22.22 ± 0.157	-21.82 ± 0.187

Table 4.5. A summary of the typical properties of rich cluster of galaxies of different types (Bahcall, 1977)

Property/Class	Regular	Intermediate	Irregular
Bautz–Morgan type	I, I-II, II	(II), II-III	(II-III), III
Galaxy content	Elliptical/S0-rich	Spiral-poor	Spiral-rich
E : S0 : S ratio	3 : 4 : 2	1 : 4 : 2	1 : 2 : 3
Symmetry	Spherical	Intermediate	Irregular shape
Central concentration	High	Moderate	Very little
Central profile	Steep gradient	Intermediate	Flat gradient
Mass segregation	Marginal evidence for $m - m(1) < 2$	Marginal evidence for $m - m(1) < 2$	No segregation
Examples	Abell 2199, Coma	Abell 194, 539	Virgo, Abell 1228

from Bahcall's review of 1977 and summarises many of the properties described above as a function of cluster type (Bahcall, 1977). Like the Hubble sequence for galaxies, these types are only part of a continuous sequence and there is considerable overlap in some of the properties.

4.3 Dynamical Estimates of the Masses of Clusters of Galaxies

It might seem that the measurement of the masses of clusters of galaxies is relatively straightforward. The virial theorem (3.20) provides a simple relation between the mass of the cluster, the radial velocity dispersion of the galaxies $\langle v_{\parallel}^2 \rangle$ and the characteristic radius R_{cl} of the galaxy distribution. The problems arise in ensuring that the galaxies really belong to the cluster and are not random coincidences of foreground or background objects and also that large enough samples of radial velocities are available. These problems are now being addressed by projects such as the Sloan Digital Sky Survey in which radial velocities, colours and structural data are available for large samples of clusters. The results presented in Table 4.2 give some impression of the wealth of data which will become available for many clusters over the coming years.



Fig. 4.6. An optical image of the central region of the Coma cluster of galaxies, Abell 1656, showing the two central massive galaxies NGC 4889 and NGC 4874. North is to the right of this image. (Courtesy of Dr. Robert Lupton and the SDSS consortium)

As a case study, let us consider the Coma cluster (Fig. 4.6) which has always been regarded as the archetype of a rich regular cluster of galaxies; we will find that this is an overoptimistic assertion. The surface density distribution of galaxies in the Coma cluster and the variation of their velocity dispersion with radius were determined in a classic paper by Kent and Gunn who assembled radial velocities for about 300 cluster members (Kent and Gunn, 1982). The projected surface density of galaxies increases smoothly towards the centre and can be described by a King profile with tidal radius $r_t = 16h^{-1}$ Mpc (Fig. 4.7a). The inference is that the cluster has relaxed to a bound equilibrium configuration, as is confirmed by comparing the *crossing time* of a typical galaxy in the cluster with the age of the Universe. The crossing time is $t_{\text{cr}} = R/\langle v \rangle$ where R is the size of the cluster and $\langle v \rangle$ is the mean random velocity of galaxies. For the Coma cluster, taking $\langle v \rangle = 10^3$ km s $^{-1}$ and $R = 2$ Mpc, the crossing time is about 2×10^9 years, roughly a tenth the age of the Universe and so the cluster must be gravitationally bound.

These data were further analysed in detail by Merritt who considered a wide range of possible models for the mass distribution within the cluster (Merritt, 1987). In the simplest reference model, with which the others can be compared, it is assumed that the mass distribution in the cluster follows the galaxy distribution, that is, the mass-to-luminosity ratio is a constant throughout the cluster, and that the velocity distribution is isotropic at each point in the cluster. With these assumptions, Merritt derived a mass for the Coma cluster of $1.79 \times 10^{15}h^{-1} M_\odot$, assuming that the cluster extends to $16h^{-1}$ Mpc. The mass within a radius of $1h^{-1}$ Mpc of the cluster centre is $6.1 \times 10^{14} M_\odot$. The corresponding value of the mass-to-blue luminosity ratio for the central regions of the Coma cluster is about $350h M_\odot/L_\odot$. The population of

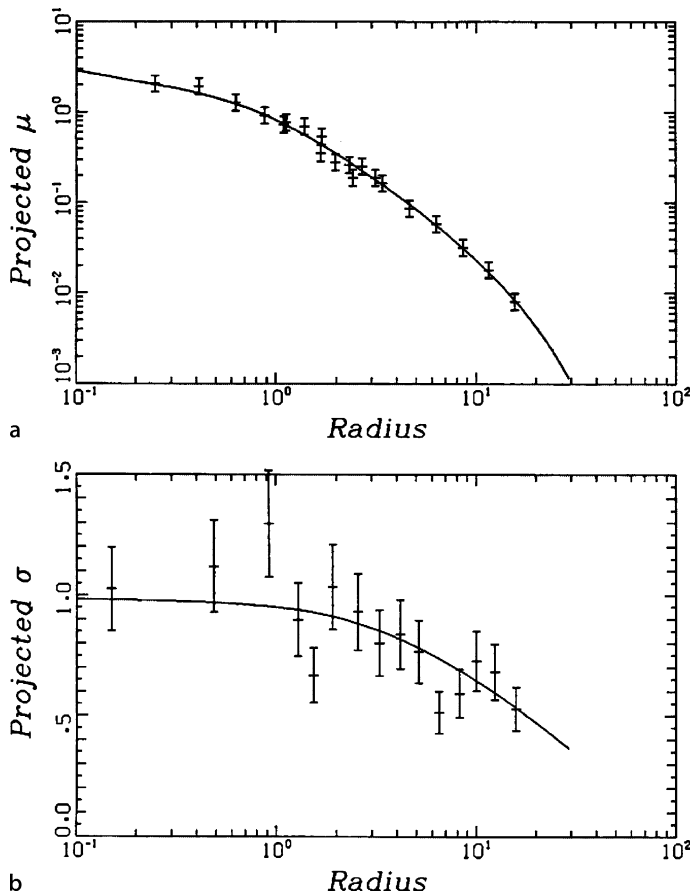


Fig. 4.7. **a** The surface density profile for the distribution of galaxies in the Coma cluster according to Kent and Gunn. **b** The projected velocity dispersion as a function of radius for galaxies in the Coma cluster (Kent and Gunn, 1982)

galaxies in the central region of the Coma cluster is dominated by elliptical and S0 galaxies for which the typical mass-to-luminosity ratios are about $10 - 20 M_{\odot}/L_{\odot}$. There is therefore a discrepancy of about a factor of 20 between the mass which can be attributed to galaxies and the total mass which must be present. This is the result which was discovered by Zwicky (Zwicky, 1937).

This is also where the trouble begins. *Dark matter* dominates the mass of the cluster but there is no reason why it should have the same distribution as the visible matter. Likewise, there is no reason *a priori* why the velocity distribution of the galaxies should be isotropic. This is most simply expressed in terms of the velocity dispersion of the galaxies in the radial and circumferential directions, $\sigma_r^2(r)$, $\sigma_{\theta}^2(r)$ and $\sigma_{\phi}^2(r)$ within the cluster. The assumption of isotropy is that $\sigma_r^2(r) = \sigma_{\theta}^2(r) = \sigma_{\phi}^2(r)$. If, however, the galaxies were on circular orbits about the

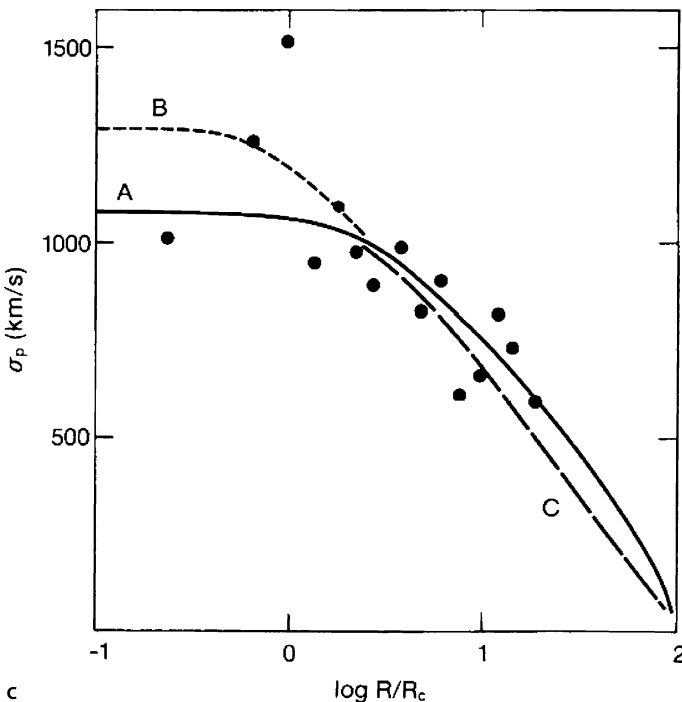


Fig. 4.7. (continued) c Three possible velocity dispersion profiles which are consistent with the data of Gunn and Kent, A corresponding to an isotropic velocity distribution, while B and C involve velocity anisotropies (Merritt, 1987)

centre, $\sigma_r^2(r) = 0$, or, if they were purely radial, $\sigma_\theta^2(r) = \sigma_\phi^2(r) = 0$. Kent and Gunn pointed out that the extreme radial models are inconsistent with the variation of velocity dispersion with radius shown in Fig. 4.7. Merritt carried out a careful study of how the inferred mass-to-luminosity ratio would change for a wide range of different assumptions about the relative distributions of the visible and dark matter and the anisotropy of the velocity distribution (Fig. 4.7c) (Merritt, 1987). For the cluster as a whole, the mass-to-luminosity ratio varied from about 0.4 to at least three times the reference value, while the mass-to-luminosity ratio within the core of the cluster at $1 h^{-1}$ Mpc was always very close to $350 h M_\odot / L_\odot$. There can be no doubt that the dynamics of the cluster are dominated by dark matter.

Perhaps the most remarkable result of recent times has been the finding that the Coma cluster is probably not the quiescent regular cluster it appears to be. Colless and Dunn have added 243 more radial velocities to the sample, bringing the total number of cluster members with radial velocities to 450 (Colless and Dunn, 1996). They find compelling evidence that, in addition to the main body of the cluster, there is a distinct subcluster whose brightest member is NGC 4839. The main cluster has mass $0.9 \times 10^{15} h^{-1} M_\odot$, while the less massive cluster has mass $0.6 \times 10^{14} h^{-1} M_\odot$.

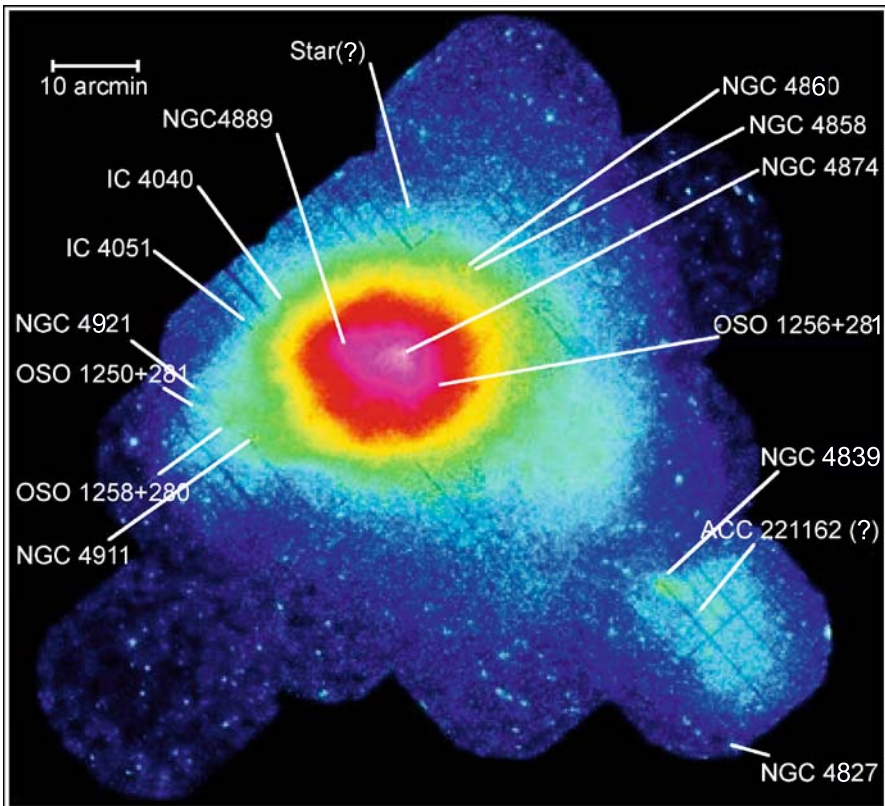


Fig. 4.8. An X-ray image of the Coma cluster of galaxies obtained by the XMM-Newton Observatory, showing the X-ray emission associated with the main body of the Coma cluster and the smaller cluster associated with NGC 4839 (Courtesy of the Max Planck Institute for Extraterrestrial Physics and ESA)

These clusters are clearly seen in the XMM-Newton X-ray image of the Coma cluster and the total masses derived from the X-ray observations agree with those derived by Colless and Dunn (Fig. 4.8). In addition, Colless and Dunn inferred that there is subclustering of galaxies about the two brightest members NGC4889 and NGC4874 and that these are in the process of coalescing in the central regions of the cluster. The moral of this story is that appearances can be deceptive.

4.4 X-Ray Observations of Hot Gas in Clusters of Galaxies

The X-ray image of the Coma cluster (Fig. 4.8) provides an excellent demonstration of the power of X-ray astronomy in the study of clusters of galaxies. One of the most important discoveries made by the UHURU X-ray Observatory was the detection of intense X-ray emission from rich clusters of galaxies. The nature of the emission was

soon identified as the bremsstrahlung of hot intracluster gas, the key observations being the extended nature of the emission and the subsequent detection of the highly ionised iron line FeXXVI by the Ariel-V satellite (Mitchell et al., 1976). It was quickly appreciated that the X-ray emission of the gas provides a very powerful probe of the gravitational potential within the cluster enabling the distribution of hot gas and the total gravitating mass to be determined. Let us repeat the calculation presented by Fabricant, Lecar and Gorenstein which shows how this can be done (Fabricant et al., 1980).

For simplicity, we assume that the cluster is spherically symmetric so that the total gravitating mass within radius r is $M(\leq r)$. The gas is assumed to be in hydrostatic equilibrium within the gravitational potential defined by the total mass distribution in the cluster, that is, by the sum of the visible and dark matter as well as the gaseous mass. If p is the pressure of the gas and ϱ its density, both of which vary with position within the cluster, the requirement of hydrostatic equilibrium is

$$\frac{dp}{dr} = -\frac{GM(\leq r)\varrho}{r^2}. \quad (4.19)$$

The pressure is related to the local gas density ϱ and temperature T by the perfect gas law

$$p = \frac{\varrho kT}{\mu m_H}, \quad (4.20)$$

where m_H is the mass of the hydrogen atom and μ is the mean molecular weight of the gas. For a fully ionised gas with the standard cosmic abundance of the elements, a suitable value is $\mu = 0.6$. Differentiating (4.20) with respect to r and substituting into (4.19), we find

$$\frac{\varrho kT}{\mu m_H} \left(\frac{1}{\varrho} \frac{d\varrho}{dr} + \frac{1}{T} \frac{dT}{dr} \right) = -\frac{GM(\leq r)\varrho}{r^2}. \quad (4.21)$$

Reorganising (4.21),

$$M(\leq r) = -\frac{kTr^2}{G\mu m_H} \left[\frac{d(\log \varrho)}{dr} + \frac{d(\log T)}{dr} \right]. \quad (4.22)$$

Thus, the mass distribution within the cluster can be determined if the variation of the gas density and temperature with radius are known. Assuming the cluster is spherically symmetric, these can be derived from high sensitivity X-ray intensity and spectral observations. A suitable form for the bremsstrahlung spectral emissivity of a plasma is

$$\kappa_\nu = \frac{1}{3\pi^2} \frac{Z^2 e^6}{\varepsilon_0^3 c^3 m_e^2} \left(\frac{m_e}{kT} \right)^{1/2} g(\nu, T) N N_e \exp \left(-\frac{h\nu}{kT} \right), \quad (4.23)$$

where N_e and N are the number densities of electrons and nuclei respectively, Z is the charge of the nuclei and $g(v, T)$ is the Gaunt factor, which can be approximated by

$$g(v, T) = \frac{\sqrt{3}}{\pi} \ln \left(\frac{kT}{hv} \right). \quad (4.24)$$

The spectrum of thermal bremsstrahlung is roughly flat up to X-ray energies $\varepsilon = hv \sim kT$, above which it cuts off exponentially (Longair, 1997b). Thus, by making precise spectral measurements, it is possible to determine the temperature of the gas from the location of the spectral cut-off and the column density of the hot gas from the X-ray surface brightness. In practice, the spectral emissivity has to be integrated along the line of sight through the cluster. Performing this integration and converting it into an intensity, the observed surface brightness at projected radius a from the cluster centre is

$$I_v(a) = \frac{1}{2\pi} \int_a^\infty \frac{\kappa_v(r)r}{(r^2 - a^2)^{1/2}} dr. \quad (4.25)$$

Cavaliere noted that this is an Abel integral which can be inverted to find the emissivity of the gas as a function of radius (Cavaliere, 1980)

$$\kappa_v(r) = \frac{4}{r} \frac{d}{dr} \int_r^\infty \frac{I_v(a)a}{(a^2 - r^2)^{1/2}} da. \quad (4.26)$$

X-rays maps of about 200 clusters were made by the Einstein X-ray Observatory (Forman and Jones, 1982) and more recently analyses of the ROSAT All Sky Survey have resulted in the NORAS and REFLEX catalogues of clusters of galaxies identified solely through the requirement that the extragalactic X-ray sources have extended structures (Böhringer et al., 2000, 2001). In the northern NORAS sample, it was found that 76% of the extended X-ray sources were indeed associated with clusters of galaxies. In addition, the ROSAT, Chandra and XMM-Newton X-ray Observatories have produced beautiful X-ray maps and spectroscopic studies of the hot gas in clusters.

An example of the quality of data now available is illustrated by the X-ray map of the central regions of the Virgo cluster as observed in the ROSAT All Sky Survey (Fig. 4.9a). A number of galaxies belonging to the Virgo cluster have been detected as X-ray sources, as well as a few background clusters and active galaxies. In addition, the X-ray emission of the diffuse intergalactic gas is roughly centred on the massive galaxy M87. Evidence that the intergalactic gas traces the mass distribution of the cluster is provided by comparison of the contours of the X-ray surface brightness distribution with the surface distribution of galaxies as determined by the photometric survey of the Virgo cluster by Binggeli, Tammann and Sandage (Binggeli et al., 1987; Schindler et al., 1999). The distribution of galaxies in the cluster and the diffuse X-ray emission are remarkably similar (Fig. 4.9b). In both wavebands the irregular structure of the Virgo cluster can be decomposed into three major subclusters centred on M87, M49, and M86. In the M87 subcluster the gas

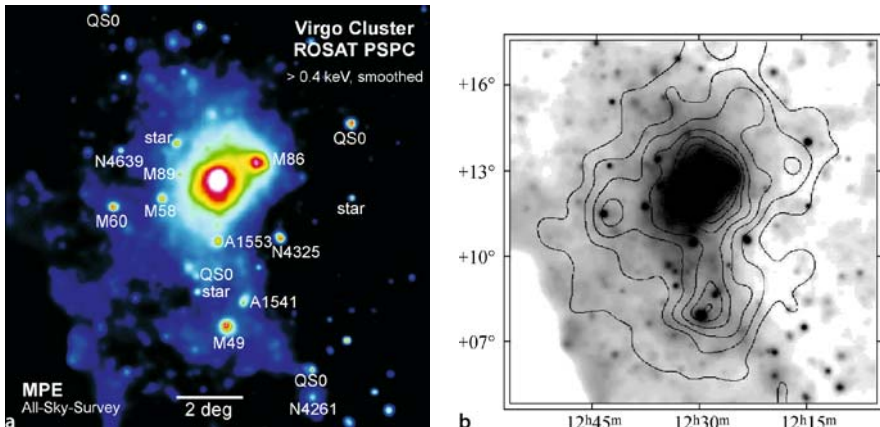


Fig. 4.9a,b. Comparison of the X-ray surface brightness distribution and the surface density of luminous matter in galaxies in the Virgo cluster. **a** The X-ray image of the Virgo cluster from the ROSAT All Sky Survey in the X-ray energy band 0.4 – 2 keV. The image has been smoothed with a Gaussian filter with $\sigma = 24$ arcmin at the faintest levels and with decreasing filter size with increasing surface brightness. Some galaxies in the Virgo cluster have been detected as well as a few distant clusters and active galaxies. (Courtesy of the Max Planck Institute for Extraterrestrial Physics, Garching.) **b** The *contours* show the number density of the 1292 member galaxies in the Virgo Cluster Catalogue smoothed with a Gaussian filter with $\sigma = 24$ arcmin. The spacing of the contours is linear (Schindler et al., 1999)

mass is about three times the visible mass in galaxies, assuming $M/L = 20$ for the galaxies), while it accounts only for 8% to 14% of the total mass at 0.4 and 1 Mpc, respectively. The projected mass-to-light ratio has a roughly constant value of about $500 M_{\odot}/L_{\odot}$. Thus, the dark matter, which defines the gravitational potential in the cluster and which is traced by the distribution of hot gas, must have a similar distribution to that of the visible matter.

Another beautiful example of the combined use of X-ray imaging and spectroscopy is provided by the observations and analysis of the rich cluster Abell 1413 by Pratt and Arnaud (Pratt and Arnaud, 2002). The observations by the XMM-Newton X-ray Observatory included spatially resolved X-ray spectroscopy of the cluster X-ray emission and so the projected temperature variation with radius in the cluster could be determined. Their results are shown in Fig. 4.10. First, the average X-ray surface brightness distribution as a function of radius is fitted by an empirical model (Fig. 4.10a). Then, the projected average temperature of the gas is estimated in annuli at different radial distances from the centre of the cluster (Fig. 4.10b). These are deprojected to derive the variation of the total mass within radius r using (4.22) (Fig. 4.10c). Finally, the ratio of gas density to total density as a function of radius, or in the case of Fig. 4.10d, the overdensity relative to the critical cosmological density, can be found.

These data are typical of what is found in rich clusters of galaxies. The dominant form of mass is the dark matter the nature of which is unknown. About 20% of the

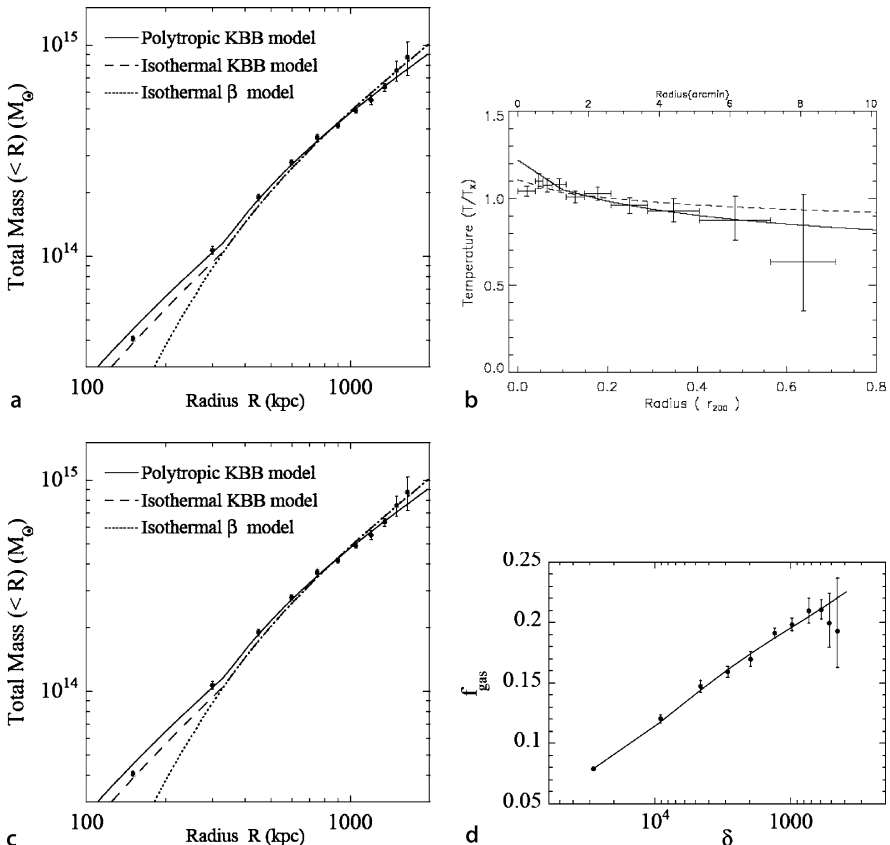


Fig. 4.10a–d. Illustrating the determination of the physical properties of the cluster A1413 from X-ray imaging and spectroscopy by the XMM-Newton X-ray Observatory. **a** The X-ray brightness distribution as a function of distance from the centre of the cluster. **b** The projected radial distribution of temperature of the gas. **c** The integrated mass distribution as a function of distance from the centre. **d** The fraction of gas density to total mass density f_{gas} within the cluster as a function of overdensity δ relative to the critical cosmological density (Pratt and Arnaud, 2002)

mass is in the form of hot intergalactic and this is typically about five times the mass in the visible parts of galaxies. The spectroscopic observations also enable the mass of iron in the intracluster medium to be determined and this is typically found to be between about 20 and 50% of the solar value, indicating that the intergalactic gas has been enriched by the products of stellar nucleosynthesis.

The wealth of data from the recent generation of X-ray satellites has enabled important insights into their origin and evolution of clusters to be obtained. It is convenient to adopt a simple reference model for understanding the various correlations between the properties of clusters, what is referred to as the *self-similar model* for cluster formation; this will be discussed in more detail in Chap. 16.

The simplest picture of cluster formation is to suppose that clusters developed from small perturbations in the distribution of the dark matter by gravitational collapse (see Part II). The amplitude of the perturbations grew from values $\delta\varrho/\varrho \sim 10^{-3}$ at the epoch of recombination to large amplitudes $\delta\varrho/\varrho \gg 1$ at late epochs. The considerations of Sect. 16.1 suggest that clusters became virialised bound systems when $(\delta\varrho/\varrho)_v \approx 200$. In the standard self-similar model, it is supposed that clusters of all masses virialised at the same epoch with the same values of $(\delta\varrho/\varrho)_v$. As a result, their masses are simply proportional to $\varrho_v R^3$, where ϱ_v was the mean density of the Universe at the epoch of virialisation. When the clusters virialised, they satisfied the virial theorem, $GM^2/R = M\sigma_v^2$. Since $M \propto R^3$, it follows that $\sigma_v \propto R$, where R can be taken to be the characteristic radius of the cluster.

The bolometric X-ray luminosity of the intracluster gas due to thermal bremsstrahlung is given by the relation

$$L_x \propto VN_e^2 T^{1/2}, \quad (4.27)$$

where $V \sim R^3$ is the volume of emitting gas, N_e is the electron density and T the temperature of the gas (Longair, 1997b). The gas forms an atmosphere within the gravitational potential of the cluster as a whole, the latter being defined by the distribution of the dark matter. Equation (4.19) can be written to order of magnitude as

$$\frac{p}{R} \sim \frac{GM\varrho}{R^2} \quad \text{and so} \quad 3N_e kT \sim \frac{GM}{R}\varrho, \quad (4.28)$$

where it is assumed that the ions and electrons both contribute to the pressure of the gas. According to the virial theorem (3.19), the velocity dispersion of the galaxies is related to the gravitational potential by $GM/R \approx \sigma_v^2$ and so

$$kT \sim m_p \sigma_v^2, \quad (4.29)$$

that is, $T \propto \sigma_v^2$. If the fraction of the total mass of the cluster in hot intracluster gas is η , it follows that the X-ray luminosity of the cluster is

$$L_x \propto \eta^2 \frac{M^2}{R^3} T^{1/2} \propto R\sigma_v^2 T^{1/2} \propto \sigma_v^4, \quad (4.30)$$

where it has been assumed that η takes the same value for clusters of different masses. Then, since $M \propto R^3 \propto \sigma^3$, this model results in the prediction that the X-ray luminosity and the mass of the cluster are related by

$$L_x \propto M^{4/3}. \quad (4.31)$$

The scaling relations (4.30) and (4.31) have been the subject of considerable study. Figure 4.11 shows the results of a major study of X-ray clusters discovered in the ROSAT All Sky Survey (Reiprich and Böhringer, 2002). It can be seen that the best-fit relation is slightly steeper than the predictions of the scaling model, but it is interesting that the general trend is not so different from the simple picture.

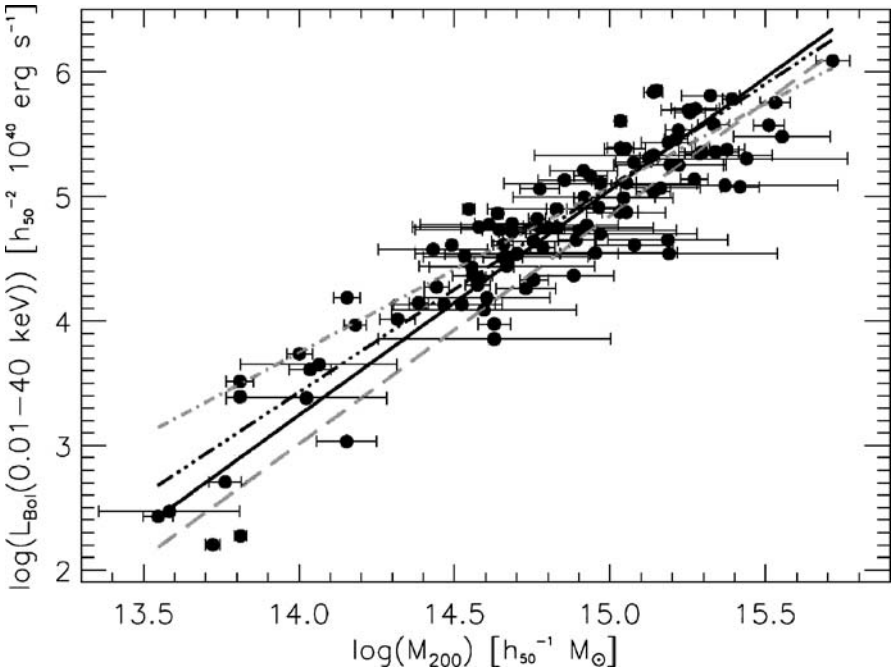


Fig. 4.11. The correlation between the X-ray luminosity of a cluster of galaxies and its total mass for the brightest X-ray clusters of galaxies in the ROSAT All Sky Survey (Reiprich and Böhringer, 2002). The mass was determined to the virial radius which was taken to be a density 200 greater than the critical cosmological density. The best-fit relation for their sample of 106 clusters is shown by the *solid line*. The best-fit relation for a smaller sample of 63 clusters which form a better complete sample is shown by the *tripledot-dashed line*. The *dot-dashed line* shows the expectation of the simple self-similar relation $L_x \propto M^{4/3}$. The *dashed line* is the prediction of a model with preheating of the intracluster gas

Another test of this model is the X-ray luminosity–velocity dispersion relation which has been analysed in some detail by Ortiz-Gil and her colleagues (Ortiz-Gil et al., 2004). For a large sample of clusters from the REFLEX catalogue derived from the ROSAT All Sky Survey, they found a correlation of the form $L_x \propto \sigma_v^{(4.1 \pm 0.3)}$, in good agreement with the correlation (4.30) predicted by the self-similar model (Fig. 4.12). A similar result was found for a smaller sample of clusters which formed a more complete statistical sample. Although this result is encouraging, their results for the $L_x - T$ and $\sigma_v - T$ relations differ from the expectations of the self-similar model. They found $L_x \propto T^{3.1 \pm 0.2}$ compared with the expected relation $L_x \propto T^2$ and $\sigma_v \propto T^{1.00 \pm 0.16}$ compared with the predicted $\sigma_v \propto T^{0.5}$. They noted that these last two relations are compatible with the X-ray luminosity–velocity dispersion relation. They inferred that there must be other contributions to the thermal heating and cooling of the intracluster gas than simply the thermal energy which resulted from the initial process of virialisation. There is now considerable evidence that such

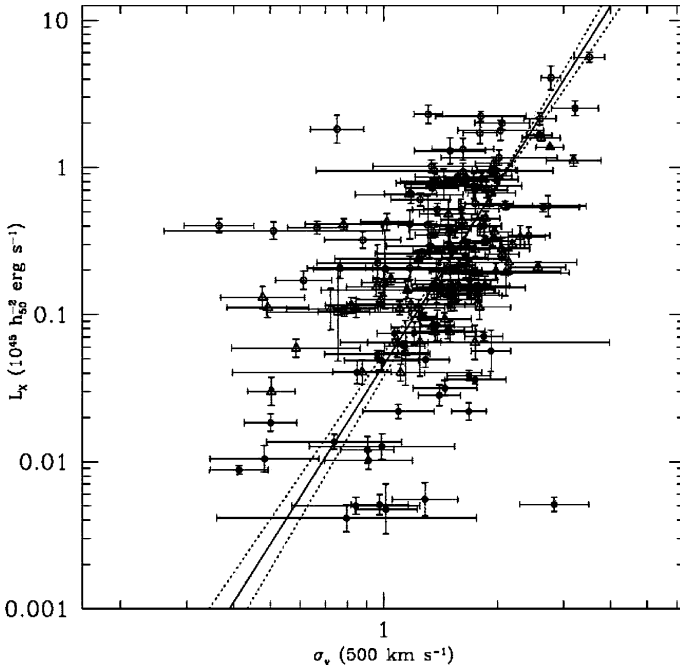


Fig. 4.12. A plot of bolometric X-ray luminosity L_x versus radial velocity dispersion σ_v for the REFLEX sample of 171 clusters. The linear fit has logarithmic slope of (4.1 ± 0.3) . The dashed lines are the 1σ errors. Filled circles correspond to clusters at redshift $z \leq 0.05$, open triangles are clusters with $0.05 < z \leq 0.1$ and open circles are clusters at $z > 0.1$ (Ortiz-Gil et al., 2004)

additional sources of heating and cooling are important in understanding the state of the intracluster gas.

If the density of the hot intracluster gas is large enough, its cooling rate can be sufficiently great for it to cool over cosmological time-scales. At high enough temperatures, the principal energy loss mechanism for the gas is the same thermal bremsstrahlung process which is responsible for the X-ray emission. The total energy loss rate per unit volume due to thermal bremsstrahlung is

$$-\left(\frac{dE}{dt}\right) = 1.435 \times 10^{-40} Z^2 T^{1/2} \bar{g} N N_e \quad \text{W m}^{-3}, \quad (4.32)$$

where Z is the charge of the ions, N and N_e are the number densities of ions and electrons respectively and \bar{g} is a mean Gaunt factor which has value roughly 1 – we assume $Z = 1$ and $N = N_e$. The thermal energy density of the fully ionised plasma is $\epsilon = 3NkT$ and so the characteristic cooling time for the gas is

$$t_{\text{cool}} = \frac{3NkT}{\left|\frac{dE}{dt}\right|} = 10^{10} \frac{T^{1/2}}{N} \quad \text{years}, \quad (4.33)$$

where the temperature is measured in kelvins and the number density of ions or electrons is measured in particles m⁻³. Thus, if the typical temperature of the gas is 10⁷ to 10⁸ K, the cooling time is less than 10¹⁰ years if the electron density is greater than about 3 × 10³ to 10⁴ m⁻³. These conditions are indeed found in many of the clusters of galaxies which are intense X-ray emitters. As a result, the central regions of these hot gas clouds cool and, to preserve pressure balance, the gas density increases, resulting in the formation of a *cooling flow*.

Evidence for these cooling flows and their role in the evolution of clusters of galaxies was reviewed by Fabian (Fabian, 1994). An example of the cooling flow in the cluster Abell 478 is illustrated by the diagrams shown in Fig. 4.13. The ROSAT observations have been deprojected to determine mean values of the density and temperature of the gas as a function of radial distance from the centre. The temperature decreases towards the central regions while the electron density increases to values greater than 10⁴ m⁻³ in the very centre. At a radius of 200 kpc, the electron temperature is $T = 7 \times 10^7$ K and the electron density $N_e = 8 \times 10^3$ m⁻³. Inserting these values into (4.33), we find that the cooling time is 10¹⁰ years. It can be seen that, outside this radius, the temperature of the gas is constant, whilst at smaller radii the gas temperature decreases towards the central regions.

As a result, matter drifts slowly in through the surface at radius r_{cool} , at which the cooling time of the gas is equal to the age of the cluster. The X-ray luminosity of

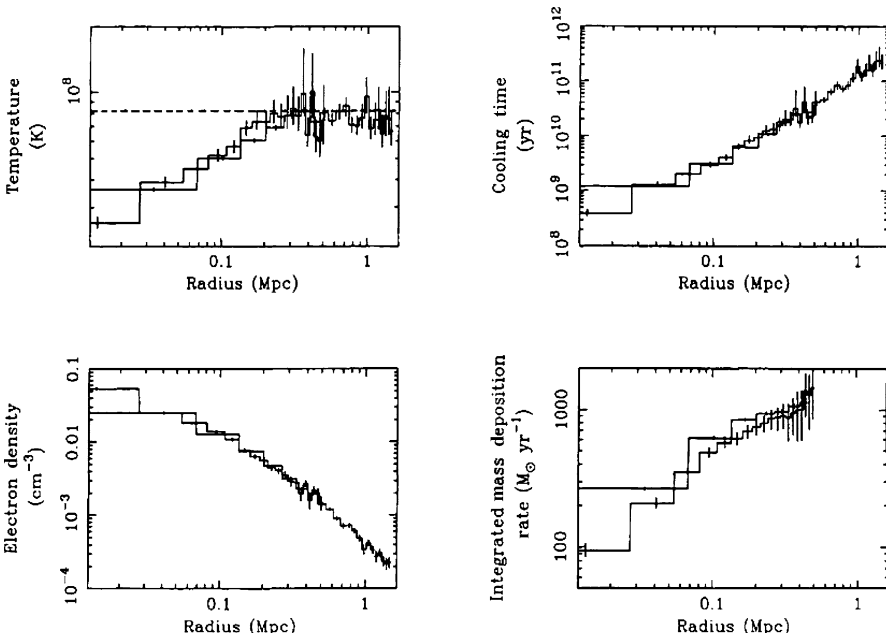


Fig. 4.13. The properties of the intracluster gas in the cluster Abell 478 obtained by deprojecting images taken by the ROSAT X-ray Observatory (White et al., 1994). The cooling time of the gas is less than 10¹⁰ years within a radius of 200 kpc (Fabian, 1994)

the cooling flow results from the internal energy of each element of the gas as well as the work done as it drifts slowly in towards the central regions whilst maintaining hydrostatic equilibrium. The appropriate conserved quantity is

$$\varrho v^2 (\frac{1}{2} v^2 + w) , \quad (4.34)$$

where ϱ , v and w are the density, velocity and enthalpy of the gas flow. Note that the relevant quantity which describes the energy content of the flow is the enthalpy $w = \epsilon + pV$, where ϵ is the internal energy of the gas and p and V are its pressure and specific volume. This is because, in addition to its internal thermal energy, work is done on the volume element by the pressure of the gas. When the volume element drifts within the cooling radius r_{cool} , all of the energy associated with the enthalpy is available for heating the gas and so the energy deposited per unit mass is $w = \epsilon + pV = \frac{5}{2} n k T$ for a perfect gas, where n is the number density of particles in the flow. It follows that the total energy input to the gas is determined by the rate at which mass drifts inwards through any radius, \dot{N} . In the steady state, this energy is reradiated by the gas as X-rays and so the cooling luminosity of the flow L_{cool} is

$$L_{\text{cool}} = \frac{5}{2} \dot{N} k T = \frac{5}{2} \frac{\dot{M}}{\mu m} k T , \quad (4.35)$$

where m is the mass of the hydrogen atom and μ is the mean molecular weight of the gas. Thus, knowing the total X-ray luminosity due to cooling, and the temperature of the gas, (4.35) can be used to work out the mass flow rate \dot{M} through any radius. The result of this calculation for the cluster Abell 478 is shown in Fig. 4.13. The cooling flow results in a mass inflow rate of about 600 to $800 M_{\odot} \text{ y}^{-1}$ and so over a period of 10^{10} years, such cooling flows can contribute significantly to the baryonic mass in the central regions of the cluster.

According to Fabian, about half of the clusters detected by the Einstein X-ray Observatory have high central X-ray surface brightnesses and cooling times less than 10^{10} years (Fabian, 1994). Abell 478 has a particularly massive flow. Typically, the inferred mass flow rates are about 100 to $300 M_{\odot} \text{ y}^{-1}$.

This cannot be the whole story, however, since X-ray spectroscopic observations of the cores of clusters have shown that there is an absence of cool gas which would be expected if there were no other energy sources. This is most vividly demonstrated by observations by the ESA XMM-Newton satellite, for example, the observations of the cluster Sérsic 159-03 which has a cool core (de Plaa et al., 2005). Figure 4.14 shows the X-ray spectrum of the cluster, the solid line showing the wealth of X-ray emission lines expected according to standard models of cooling flows. It can be seen that the observed spectrum differs dramatically from the expectations of the cooling flow models, because of the absence of strong lines associated with ions such as FeXVII. This lack of cool gas seems to be a feature of many of the cooling flows observed in rich clusters of galaxies (Kaastra et al., 2004). The inference is that there must be some further heating source within the cluster to reheat the cooling gas.

Many models have been proposed to resolve this problem, some of these being listed by Kaastra and his colleagues (Kaastra et al., 2004). These models include

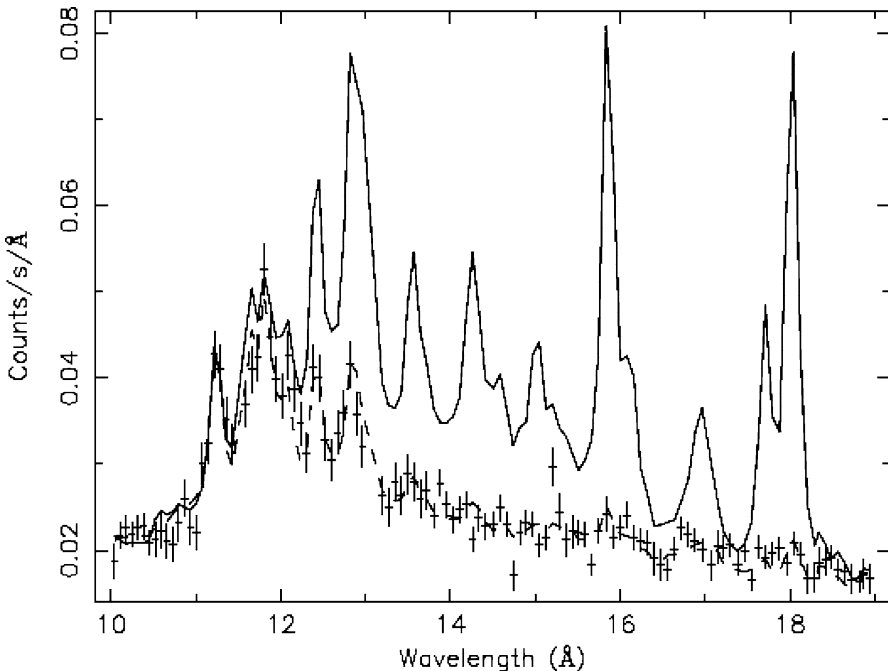


Fig. 4.14. Comparison of the observed high resolution X-ray spectrum of the cluster of galaxies Sérsic 159-03 observed by the ESA XMM-Newton satellite with the predicted spectrum of a standard cooling flow model without heating. The strong lower excitation lines from ions such as Fe XVII are absent, indicating the lack of cool gas in the cluster (de Plaa et al., 2005)

metallicity inhomogeneities, buoyantly rising radio bubbles transporting cool gas outwards, halo-in-halo structures, turbulent mixing due to rising and falling hot gas bubbles, heating by AGN activity, contamination due to non-thermal X-ray emission, heating by dead radio galaxies, rapid cooling due to mixing with cold gas and heat conduction by electrons. They also propose heating by coronal loops, similar to those observed in the corona of the Sun, but on the scale of the cores of clusters of galaxies.

A highly suggestive set of observations made by the Chandra X-ray Observatory shows that the cooling gas in the central regions of a number of clusters is perturbed by the presence of radio lobes of recent radio source events. One of the most compelling examples is the central region of the Perseus cluster of galaxies in which the buoyant lobes of relativistic plasma have pushed back the intracluster gas, forming ‘holes’ in the X-ray brightness distribution (Fig. 4.15a) (Fabian et al., 2000). In a very long X-ray exposure with the Chandra X-ray Observatory, Fabian and his colleagues identify what they interpret as isothermal sound waves produced by the weak shock wave associated with the expanding lobes (Fig. 4.15b). They show that the energy injected into the intracluster gas by these sound waves can balance the radiative cooling of the cooling flow (Fabian et al., 2006).

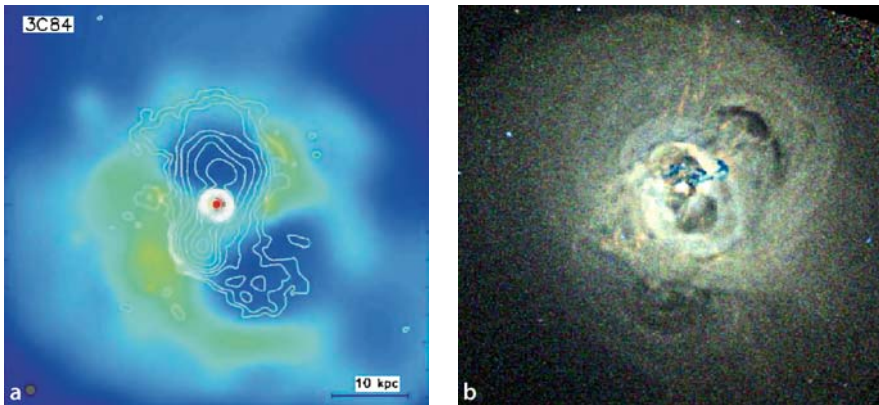


Fig. 4.15a,b. The central regions of the Perseus cluster of galaxies as observed by the Chandra X-ray Observatory. **a** The central regions of the cluster showing the cavities evacuated by the radio lobes which are shown by the *white contour lines* (Fabian et al., 2000). **b** An unsharp-mask image of the central regions of the cluster showing the various features caused by the expanding radio lobes. Many of the features are interpreted as sound waves caused by the weak shock wave associated with the expansion of the radio lobes (Fabian et al., 2006)

4.5 The Sunyaev–Zeldovich Effect in Hot Intracluster Gas

An independent method of studying hot gas in clusters of galaxies and elsewhere in the Universe is through the search for decrements in the intensity of the Cosmic Microwave Background Radiation. As the photons of the background radiation pass through the gas cloud, a few of them suffer Compton scattering by the hot electrons. Although to first order the photons are just as likely to gain as lose energy in these scatterings, to second order there is a net statistical gain of energy and so the spectrum of the Cosmic Microwave Background Radiation is shifted to slightly higher energies. As a result, there is expected to be a decrease in the intensity of the background radiation in the Rayleigh–Jeans region of the spectrum, that is, at energies $h\nu \ll kT_r$, while in the Wien region, $h\nu \gg kT_r$, there should be a slight excess – T_r is the temperature of the background radiation. These predictions were made by Sunyaev and Zeldovich as long ago as 1969 (Sunyaev and Zeldovich, 1970) and it was almost 20 years before the *Sunyaev–Zeldovich effect* was observed with confidence in the directions of clusters of galaxies (Birkinshaw, 1990).

The magnitude of the distortion is determined by the *Compton scattering optical depth* y through the region of hot gas,

$$y = \int \left(\frac{kT_e}{m_e c^2} \right) \sigma_T N_e \, dl . \quad (4.36)$$

The resulting decrement in the Rayleigh–Jeans region of the spectrum is

$$\frac{\Delta I_\nu}{I_\nu} = -2y . \quad (4.37)$$

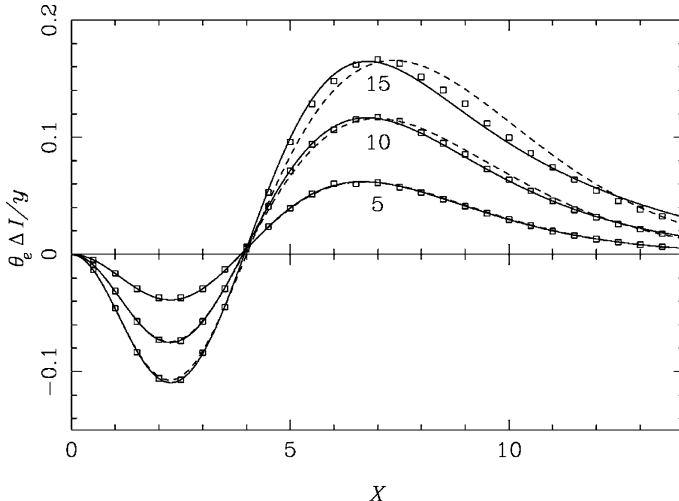


Fig. 4.16. Intensity changes due to the Sunyaev–Zeldovich effect in units of $2(kT_0)^3/(hc)^2$, plotted against $X = h\nu/kT_0$ for three values of kT_e (in keV), where $\theta_e = kT_e/m_ec^2$. The solid curves are calculated using the second-order correction to the Kompaneets equation, while the dashed lines are calculated from the first-order correction. The points are the result of a Monte Carlo evaluation of the Boltzmann collision integral by Garrett and Gull (Challinor and Lasenby, 1998)

Thus, the magnitude of the decrement along any line of sight through the cluster provides a measure of the quantity $\int N_e T_e dl$, in other words, the integral of the pressure of the hot gas along the line of sight.¹ For the typical parameters of hot intracluster gas, the predicted decrement amounts to $\Delta I/I \approx 10^{-4}$. The spectral signature of the effect is quite distinctive over the peak of the spectrum of the Cosmic Microwave Background Radiation (Fig. 4.16) and has been worked out in detail by Challinor and Lasenby (Challinor and Lasenby, 1998). This form of distortion has been measured in 15 Abell clusters in the SuZIE experiment carried out at the CalTech Submillimetre Observatory on Mauna Kea (Benson et al., 2004).

An important feature of the Sunyaev–Zeldovich effect is that, if the hot gas clouds have the same properties at all redshifts, the observed decrement is independent of redshift since the scattering results in only a *fractional* change in the temperature of the background radiation. This prediction is beautifully illustrated by the maps of decrements in the Cosmic Microwave Background Radiation obtained by the OVRO and BIMA millimetre arrays which span a range of redshift from 0.1 to 0.8 (Fig. 4.17)(Carlstrom et al., 2000). All these clusters were known to be X-ray sources and there is good agreement between the sizes of the X-ray images and the Sunyaev–Zeldovich decrements.

¹ I have given a discussion of the physical process involved in the Sunyaev–Zeldovich effect in *High Energy Astrophysics, Vol. 1* (Longair, 1997b).

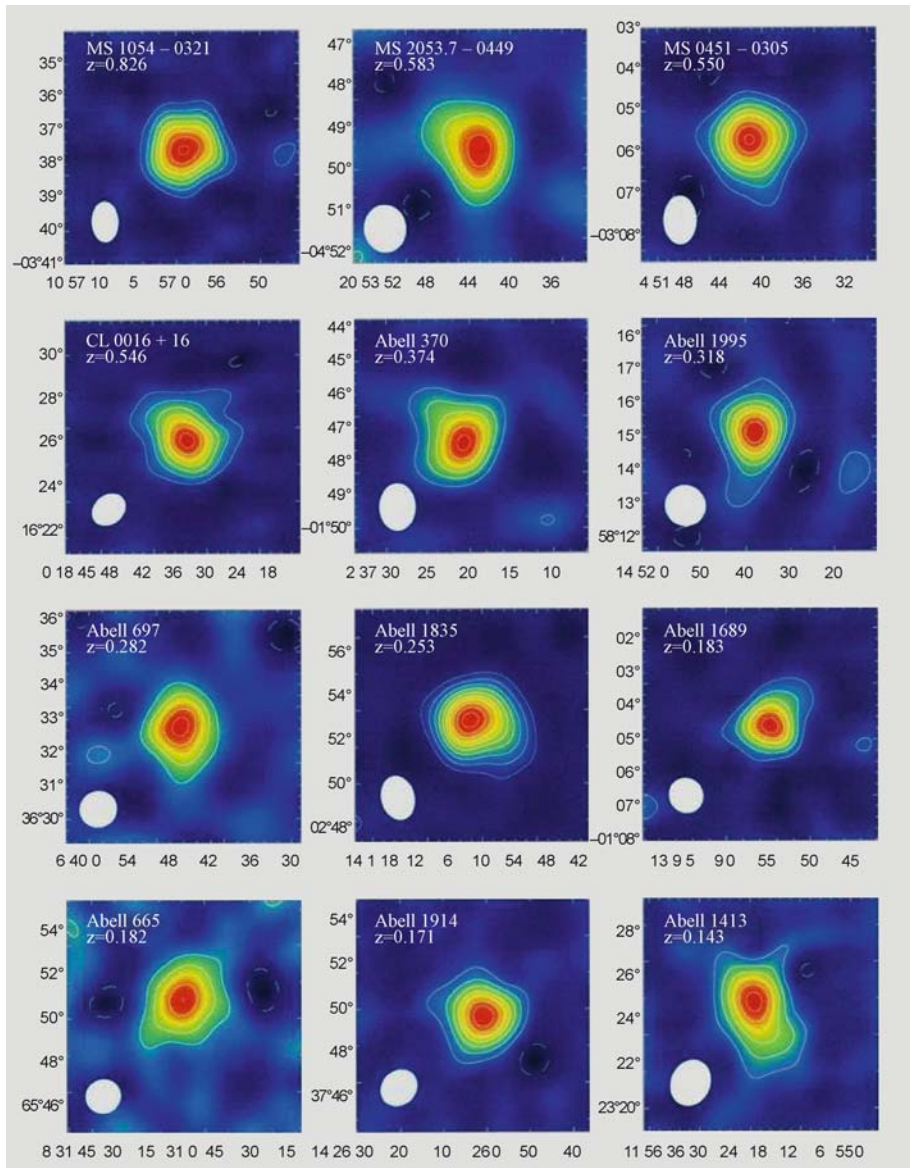


Fig. 4.17. Images of the Sunyaev–Zeldovich decrement in 12 distant clusters with redshifts in the range 0.14 to 0.89 (Carlstrom et al., 2000). Each of the images is plotted on the same intensity scale. The data were taken with the OVRO and BIMA millimetre arrays. The *filled ellipse* at the bottom left of each image shows the full-width half-maximum of the effective resolution used in reconstructing the images

The combination of the Sunyaev–Zeldovich and thermal bremsstrahlung observations of the intracluster gas enable the dimensions of the hot gas cloud to be determined independently of knowledge of the redshift of the cluster. Using order of magnitude arguments, the Sunyaev–Zeldovich effect determines the quantity $N_e T_e L$, where L is the dimension of the volume of hot gas. The bremsstrahlung emission of the cluster determines the quantity $L^3 N_e^2 T^{1/2}$. The temperature T can be estimated from the shape of the bremsstrahlung spectrum and so N_e can be eliminated between these two relations so that an estimate of L can be found. By measuring the angular size θ of the emitting volume, the distance of the cluster can be found from $D = L/\theta$. Once the redshift of the cluster has been measured, Hubble's constant can be estimated (Sect. 8.3). This is one of the more promising physical methods of estimating Hubble's constant without the necessity of using a hierarchy of distance indicators.

4.6 Gravitational Lensing by Galaxies and Clusters of Galaxies

A beautiful method for determining the mass distribution in galaxies and clusters of galaxies has been provided by the observation of gravitationally lensed images of background galaxies. In the case of clusters of galaxies, these consist of spectacular arcs about the central core of the cluster as well as distorted images of background galaxies caused by the individual galaxies in the cluster. Gravitational lensing has the potential to provide information about many key problems in the astrophysics of galaxies, clusters and larger-scale structures. It is therefore worthwhile studying some simple aspects of gravitational lensing and its applications.

4.6.1 Basic Theory of Gravitational Deflections

Many of the most important results can be derived from the formula for the gravitational deflection of light rays by the Sun, first derived by Einstein in his great paper of 1915 on the General Theory of Relativity (Einstein, 1915). He showed that the deflection of light by a point mass M due to the bending of space–time amounts to precisely twice that predicted by a Newtonian calculation,

$$\tilde{\alpha} = \frac{4GM}{\xi c^2}, \quad (4.38)$$

where ξ is the ‘collision parameter’ (Fig. 4.18a). The angles in Fig. 4.18a have been exaggerated to illustrate the geometry of the deflection. For the very small deflections involved in the gravitational lens effect, ξ is almost exactly the distance of closest approach of the light ray to the deflector.

Chwolson in 1924 and Einstein in 1936 realised that, if a background star were precisely aligned with a deflecting point object, the gravitational deflection of the light rays would result in a circular ring, centred upon the deflector (Fig. 4.18c)

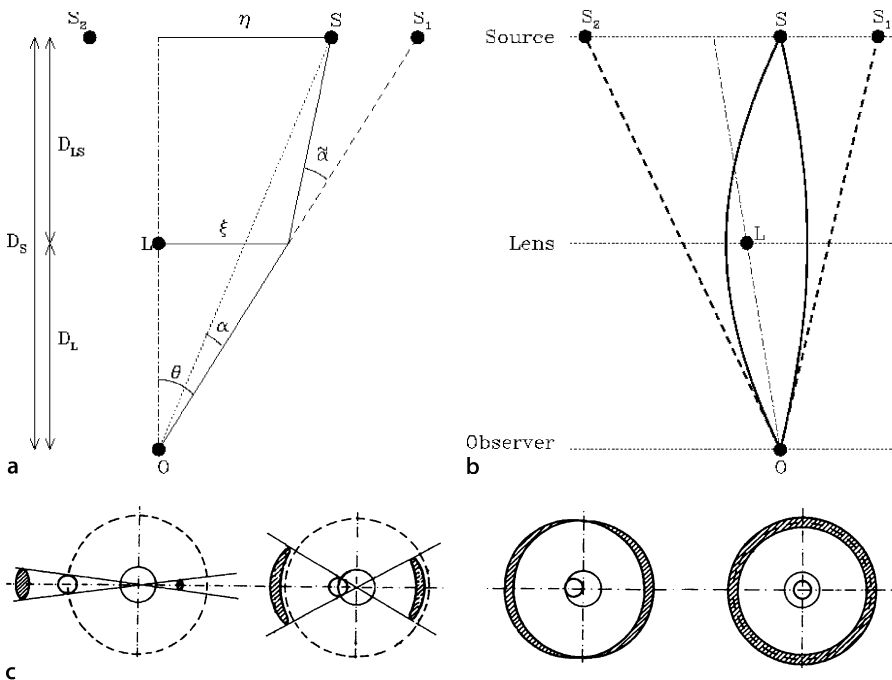


Fig. 4.18. **a** Illustrating the geometry of the deflection of light by a deflector, or lens, of mass M (Wambsganss, 1998). **b** Illustrating the two light paths from the source to the observer for a point mass (Wambsganss, 1998). **c** Illustrating the changes of the appearance of a compact background source as it passes behind a point mass. The *dashed circles* correspond to the Einstein radius. When the lens and the background source are precisely aligned, an Einstein ring is formed with radius equal to the Einstein radius θ_E

(Chwolson, 1924; Einstein, 1936). It is a straightforward calculation to work out the radius of what came to be known as an ‘Einstein ring’, although it should perhaps be known as a ‘Chwolson ring’. In the following analysis, we adopt the notation used by Wambsganss in his excellent online introduction to many aspects of gravitational lensing (Wambsganss, 1998). In Fig. 4.18a, the distance of the background source is D_S and that of the deflector, or lens, D_L , the distance between them being D_{LS} . Suppose the observed angular radius of the Einstein ring is θ_E . Then, for a point source on-axis, since all the angles are small,

$$\theta_E = \tilde{\alpha} \left(\frac{D_{LS}}{D_S} \right) = \frac{4GM}{\xi c^2} \left(\frac{D_{LS}}{D_S} \right), \quad (4.39)$$

where $\tilde{\alpha}$ is the deflection given by (4.38). Since $\xi = \theta_E D_L$,

$$\theta_E^2 = \frac{4GM}{c^2} \left(\frac{D_{LS}}{D_S D_L} \right) = \frac{4GM}{c^2} \frac{1}{D}, \quad (4.40)$$

where $D = (D_S D_L / D_{LS})$. Thus, the *Einstein angle* θ_E , the angle subtended by the Einstein ring at the observer, is given by the relation

$$\theta_E = \left(\frac{4GM}{c^2} \right)^{1/2} \frac{1}{D^{1/2}} . \quad (4.41)$$

We have worked out this expression assuming the geometry of space is Euclidean. The above relation is also correct if the sources are at cosmological distances, provided the D_s are *angular diameter distances* (Blandford and Narayan, 1992).²

Expressing the mass of the deflector in solar masses M_\odot and the distance D in Gpc ($= 10^9$ pc $= 3.056 \times 10^{25}$ m), we find

$$\theta_E = 3 \times 10^{-6} \left(\frac{M}{M_\odot} \right)^{1/2} \frac{1}{D_{\text{Gpc}}^{1/2}} \text{ arcsec} . \quad (4.42)$$

Thus, clusters of galaxies with masses $M \sim 10^{15} M_\odot$ at cosmological distances can result in Einstein rings with angular radii tens of arcseconds. Such rings were first reported by Soucail and his colleagues and by Lynds and Petrosian (Lynds and Petrosian, 1986; Soucail et al., 1987). Beautiful examples of partial Einstein rings about the centre of the cluster Abell 2218 have been observed with the Hubble Space Telescope by Kneib, Ellis and their colleagues (Figs. 4.1 and 4.19). The rings are not complete and are elliptical rather than circular. The ellipticity and the incompleteness of the rings reflect the facts that the gravitational potential of the cluster is not precisely spherically symmetric and that the background galaxy and the cluster are not perfectly aligned.

4.6.2 Magnification of Images by Gravitational Lensing

It is worth developing the theme of gravitational lensing a little further since the technique provides some of the most important information about the distribution of dark matter in the Universe is proving to be a powerful cosmological tool. In addition to the very accessible review by Wambsganss, the comprehensive discussion of all aspects of gravitational lensing presented in the volume *Gravitational Lensing: Strong, Weak and Micro* by Schneider, Kochanek and Wambsganss can be thoroughly recommended (Wambsganss, 1998; Schneider et al., 2006).

Let us first continue the analysis of the images of a background point source formed by a point mass deflector. We can first relate the angle of the observed image to its position in the absence of the deflector. From Fig. 4.18a, recalling that all the angles are very small,

$$\theta D_S = \beta D_S + \tilde{\alpha} D_{LS} . \quad (4.43)$$

Next, it is useful to introduce the *reduced deflection angle* $\alpha(\theta)$ which is the deflection of the image of the background object because of the presence of the deflector as

² Angular diameter distances are introduced in Sect. 5.5.3. The formula for angular diameter distances between any two redshifts is derived in Sect. 7.5.

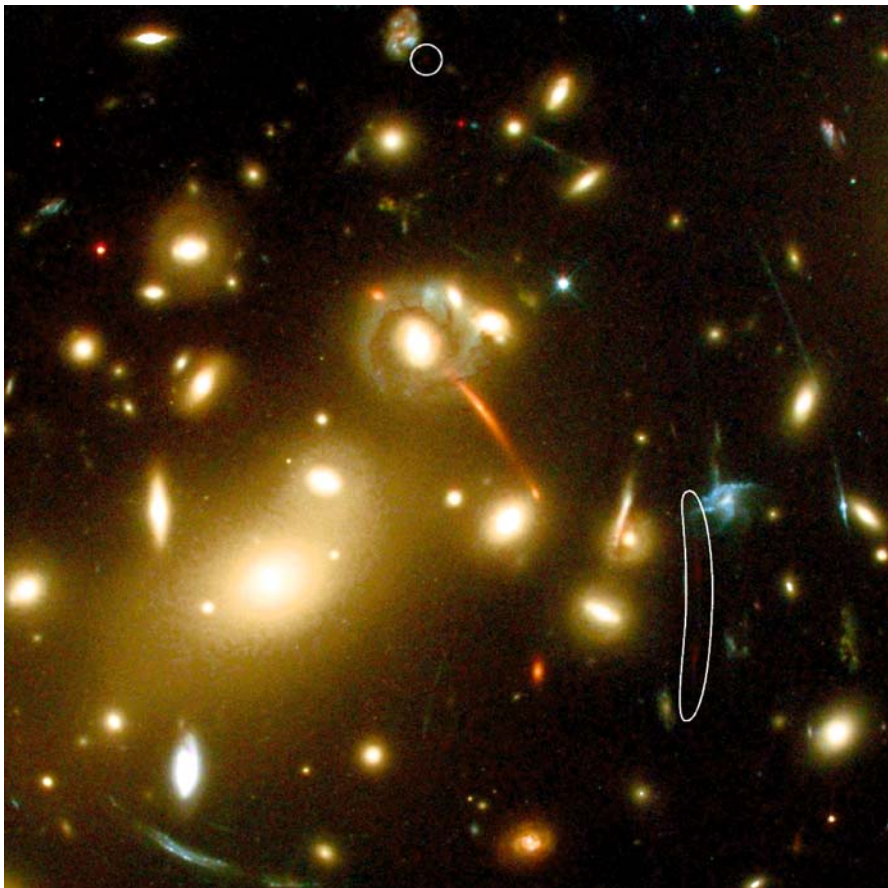


Fig. 4.19. The central region of the rich cluster of galaxies Abell 2218 observed by the Hubble Space Telescope at a wavelength of 840 nm. Several arcs can be observed more or less centred on the core of the Abell cluster. These are the gravitationally lensed images of background galaxies more or less perfectly aligned with the centre of the cluster. The *circled segments* of rings are the images of an extremely distant red galaxy (Courtesy of NASA, J.-P. Kneib, R. Ellis, and the Space Telescope Science Institute)

measured by the observer. From the geometry of Fig. 4.18a,

$$\beta = \theta - \alpha(\theta) . \quad (4.44)$$

Inserting the value of $\tilde{\alpha}$ into the expression $\alpha(\theta) = (D_{\text{LS}}/D_{\text{S}})\tilde{\alpha}$, we find

$$\alpha(\theta) = (D_{\text{LS}}/D_{\text{S}})\tilde{\alpha} = \left(\frac{D_{\text{LS}}}{D_{\text{S}}} \right) \frac{4GM}{\xi c^2} = \left(\frac{D_{\text{LS}}}{D_{\text{S}} D_{\text{L}}} \right) \frac{4GM}{\theta c^2} = \frac{\theta_{\text{E}}^2}{\theta} , \quad (4.45)$$

where we have used the expression (4.41) for the Einstein angle θ_E . As a result, the *lens equation* (4.44) can be written

$$\beta = \theta - \frac{\theta_E^2}{\theta}. \quad (4.46)$$

The solutions of this quadratic equation give the two possible routes from the source to the observer:

$$\theta = \frac{\beta \pm \sqrt{\beta^2 + 4\theta_E^2}}{2}. \quad (4.47)$$

These light paths are illustrated in Fig. 4.18b. Notice that one of the angles is positive and the other negative, the small negative value corresponding to the longer route. The negative sign means that, if the object were extended, it would be mirror-inverted relative to the other image. Notice also that the images lie on opposite sides of the Einstein angle θ_E .

As in the case of geometric optics, surface brightness is conserved on passing through a gravitational lens and so the images are magnified because of the changes in solid angle. Consider a small angular segment of an arc of azimuthal angle $d\phi$. In the absence of the lens, the solid angle subtended at the observer would be $d\phi \beta d\theta$. Because of the effect of gravitational lensing, the angle β becomes θ and $d\beta$ becomes $d\theta$ and so the solid angle becomes $d\phi \theta d\theta$. Consequently, the magnification of the lensed images is

$$\mu = \frac{\theta}{\beta} \frac{d\theta}{d\theta}. \quad (4.48)$$

Finally, it is convenient to introduce a normalised impact parameter u in terms of the Einstein radius θ_E , $u = \beta/\theta_E$. After a little algebra, the magnifications of the two images can be written

$$\mu_i = \left(1 - \frac{\theta_E^4}{\theta_i^4}\right)^{-1} = \frac{1}{2} \pm \frac{u^2 + 2}{2u\sqrt{u^2 + 4}}. \quad (4.49)$$

Again, the magnification of the image outside the Einstein radius is positive and the other, inside the Einstein radius, is negative because of mirror-imaging. The sum of the magnitudes of the two image magnifications is the total magnification of the background point source:

$$\mu = |\mu_1| + |\mu_2| = \frac{u^2 + 2}{u\sqrt{u^2 + 4}}. \quad (4.50)$$

The reason for carrying out this calculation is that it is the expression which describes the characteristic signature of microlensing of background stars by objects in the halo of our Galaxy (see Sect. 4.7.1). A sketch of the gravitational deflections of a star of finite diameter by a point deflector is shown in Fig. 4.18c.

4.6.3 Extended Deflectors

The simplest generalisation of the above result is to consider the deflection due to a lens with an axially symmetric mass distribution along the line of sight. In that case, Schneider and his colleagues show that the deflection is given by the expression

$$\tilde{\alpha} = \frac{4GM(\leq \xi)}{\xi c^2}, \quad (4.51)$$

where $M(\leq \xi)$ is the total projected mass within the radius ξ at the lens, a result corresponding to Gauss's theorem for Newtonian gravity.

We can derive from this result the necessary condition for the formation of a gravitationally lensed image about an object of mass M and radius R . For simplicity, let us suppose that the lens is a uniform disc of radius R and mass M . Then, using the result (4.51), the deflection for rays grazing the edge of the disc is

$$\tilde{\alpha} = \frac{4GM(< R)}{Rc^2} = \frac{4\pi G \Sigma}{c^2} R, \quad (4.52)$$

where we have introduced the surface density of the lens is $\Sigma = M/\pi R^2$. The deflection measured by the observer at the origin is, as before,

$$\alpha(\theta) = \frac{D_{LS}}{D_S} \tilde{\alpha} = \frac{D_{LS}}{D_S} \frac{4\pi G \Sigma}{c^2} R. \quad (4.53)$$

Let us now introduce a *critical surface density* defined by

$$\Sigma_{\text{crit}} = \frac{c^2}{4\pi G} \frac{D_S}{D_{LS} D_L} = \frac{c^2}{4\pi G} \frac{1}{D} \quad (4.54)$$

Then,

$$\alpha(\theta) = \frac{\Sigma}{\Sigma_{\text{crit}}} \frac{R}{D_L} = \frac{\Sigma}{\Sigma_{\text{crit}}} \theta. \quad (4.55)$$

Thus, if the surface density of the deflector is of the same order as the critical surface density, multiple images will be observed. The significance of the critical surface density can be appreciated by rewriting it in terms of the critical cosmological density which will be introduced in Sect. 7.2.2, $\varrho_c = 3H_0^2/8\pi G = 3H_0^2/8\pi G = 2 \times 10^{-26} h^2 \text{ kg m}^{-3}$. Then,

$$\Sigma_{\text{crit}} \sim \varrho_c \frac{c^2}{H_0^2} \frac{1}{D}. \quad (4.56)$$

If the sources are at cosmological distances $D \sim c/H_0$, the critical surface density is

$$\Sigma_{\text{crit}} \sim \varrho_c \frac{c}{H_0}. \quad (4.57)$$

Thus, for sources at cosmological distances, the critical surface density is roughly $2h \text{ kg m}^{-2}$. In fact, the Universe as a whole can be thought of as acting as a giant gravitational lens in understanding the effects of inhomogeneities upon the cosmological

redshift–angular diameter relation³ (Dyer and Roeder, 1972, 1973; Dashevsky and Zeldovich, 1964; Zeldovich, 1964).

Let us apply the result (4.51) to the case of an isothermal gas sphere, which provides a reasonable description of the mass distribution in clusters of galaxies. We consider the simple analytic solution (4.7), which has the unpleasant features of being singular at the origin and of having infinite mass when integrated to an infinite distance, but these are unimportant for our present analysis. For this reason, this analysis is often referred to as the case of a *singular isothermal sphere*. Assuming that the velocity dispersion is isotropic and that $\langle v_{\parallel}^2 \rangle$ is the observed velocity dispersion along the line of sight,

$$\varrho(r) = \frac{2}{Ar^2} \quad \text{where} \quad A = \frac{4\pi G \mu}{kT} = \frac{4\pi G}{\langle v_{\parallel}^2 \rangle}. \quad (4.58)$$

We now work out the projected mass density, or the surface density $\Sigma(\xi)$, at projected distance ξ by integrating along the line of sight, say, in the z -direction

$$\Sigma(\xi) = 2 \int_0^\infty \varrho(r) dz = 2 \int_0^{\pi/2} \varrho(r) \xi \sec^2 \theta d\theta \quad (4.59)$$

$$= \frac{\langle v_{\parallel}^2 \rangle}{\pi G} \frac{1}{\xi} \int_0^{\pi/2} d\theta = \frac{\langle v_{\parallel}^2 \rangle}{2G} \frac{1}{\xi}. \quad (4.60)$$

Therefore, the total mass within the distance ξ perpendicular to the line of sight at the deflector is

$$\int_0^\xi \Sigma(\xi) 2\pi \xi d\xi = \frac{\pi \langle v_{\parallel}^2 \rangle \xi}{G}. \quad (4.61)$$

The gravitational deflection of the light rays is therefore

$$\tilde{\alpha} = \frac{4GM(<\xi)}{\xi c^2} = \frac{4\pi \langle v_{\parallel}^2 \rangle}{c^2}. \quad (4.62)$$

This is the remarkable result we have been seeking. For a singular isothermal gas sphere, the gravitational deflection is *independent* of the distance at which the light rays pass by the lens. We can therefore find the Einstein radius θ_E directly from (4.39)

$$\theta_E = \frac{4\pi \langle v_{\parallel}^2 \rangle}{c^2} \frac{D_{LS}}{D_S} = 28.8 \langle v_{3\parallel}^2 \rangle \frac{D_{LS}}{D_S} \text{ arcsec}, \quad (4.63)$$

where $\langle v_{3\parallel}^2 \rangle$ means the observed velocity dispersion of the galaxies in the cluster measured in units of 10^3 km s^{-1} . Fort and Mellier note that this is a rather robust expression for estimating the masses of clusters of galaxies (Fort and Mellier, 1994). They find that for a variety of plausible mass distributions the estimates agree to within about 10%.

³ These relations are developed in Sect. 7.7.

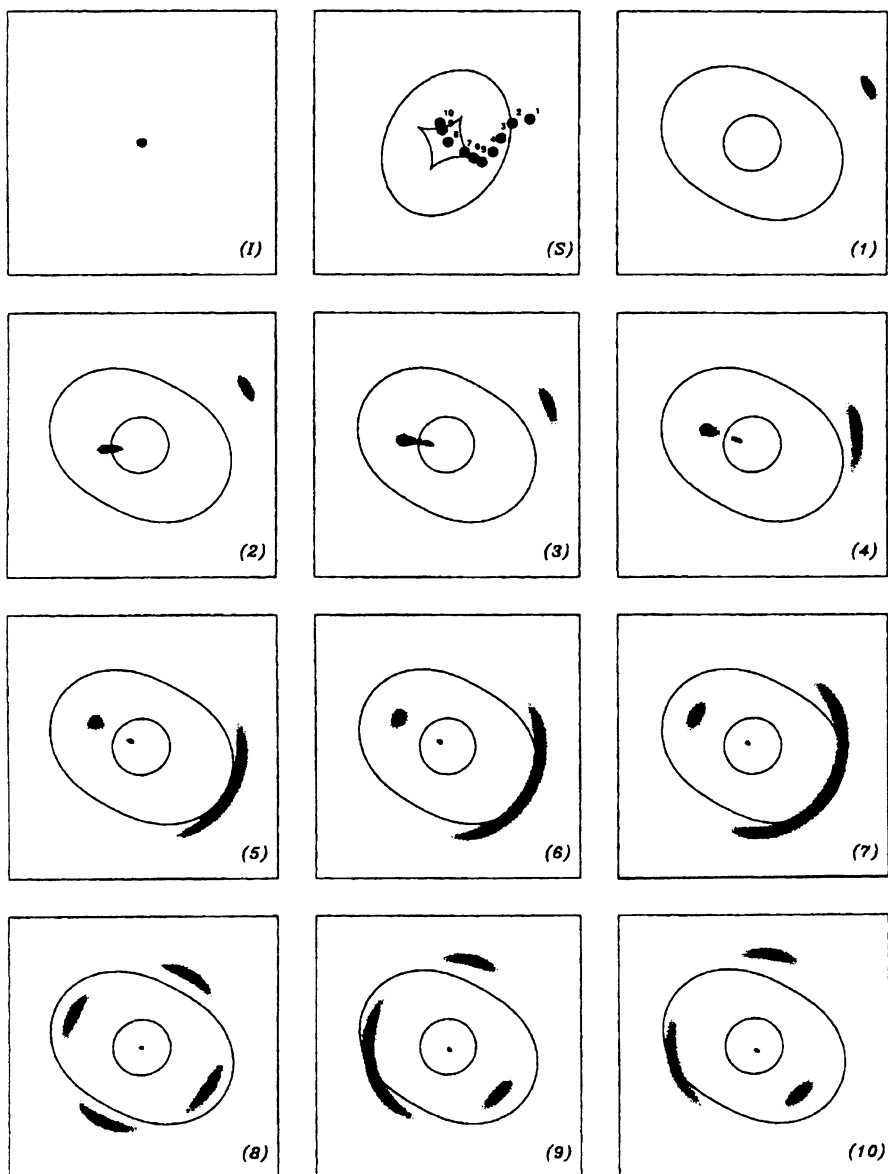


Fig. 4.20. The gravitational distortions of a background source (*Panel I*) when it is located at different positions with respect to the axis of the gravitational lens. In this example, the lens is an ellipsoidal non-singular squeezed isothermal sphere. The ten positions of the source with respect to the critical inner and outer caustics are shown in the panel (*S*). The panels labelled (*I*) to (*10*) show the shapes of the images of the lensed source (Kneib, 1993). Note the shapes of the images when the source crosses the critical caustics. Positions (*6*) and (*7*) correspond to cusp catastrophes and position (*9*) to a fold catastrophe (Fort and Mellier, 1994)

Strong lensing of background sources only occurs if they lie within the Einstein angle θ_E of the axis of the lens. An excellent discussion of the shapes and intensities of the gravitationally distorted images of background sources for more general mass distributions is given by Fort and Mellier (Fort and Mellier, 1994). The gravitational lensing is not true lensing in the sense of geometric optics but rather the light rays come together to form caustics and cusps. Figure 4.20 shows the types of images expected for gravitational lensing by an ellipsoidal gravitational potential. The background source is shown in panel (I) and, in the second panel labelled (S), different positions of the background source with respect to the critical inner and outer caustic lines associated with the gravitational lens are shown. These are lines along which the lensed intensity of the image is infinite. The images labelled (1) to (10) show the observed images of the background source when it is located at the positions labelled on the second panel (S). The numbers and shapes of the images depend upon the location of the source with respect to the caustic surfaces. It can be seen that the predicted images resemble the arcs seen in Figs. 4.1 and 4.19.

For clusters of galaxies, these inferred masses are in good agreement with the values obtained by measuring the velocity dispersion of the cluster galaxies and with the X-ray methods of measuring total masses. An important aspect of the gravitational lensing approach to the determination of cluster masses is that it is possible to determine the details of the gravitational potential within the cluster. These studies show, for example, that the distribution of mass in Abell 2218 is more complex than a simple spherically symmetric distribution (Kneib et al., 1996). Another example of the power of the gravitational lensing technique is shown in Fig. 4.21 which was created by Tyson and his colleagues using a parametric inversion technique to analyse a very deep HST image of the cluster Cl 0024+1654 (Tyson et al., 1998). They find that, excluding mass concentrations centered on visible galaxies, more than 98% of the remaining mass is represented by a smooth concentration of dark matter centered on the brightest galaxies in the core of the cluster. With the availability of very deep cluster images in a number of wavebands taken with the Advanced Camera for Surveys (ACS) on the Hubble Space Telescope, the distortions of background objects by many galaxies in the clusters can be used to define detailed mass distributions (Zekser et al., 2006).

The extension of these techniques to the weak gravitational lensing of large samples of distant galaxies by large-scale structures has been developed by Kaiser who has shown how the distorted images can be used to determine the large-scale two-point correlation function for galaxies (Kaiser, 1992).

4.6.4 Gravitational Lensing and the Astrophysics of Galaxies

The above discussion barely scratches the surface of what will undoubtedly be a major growth area in the physics of galaxies and clusters in the coming years. Gravitational lensing probes directly the total mass distribution, independent of the distribution of baryonic matter and so can be used to address a number of key

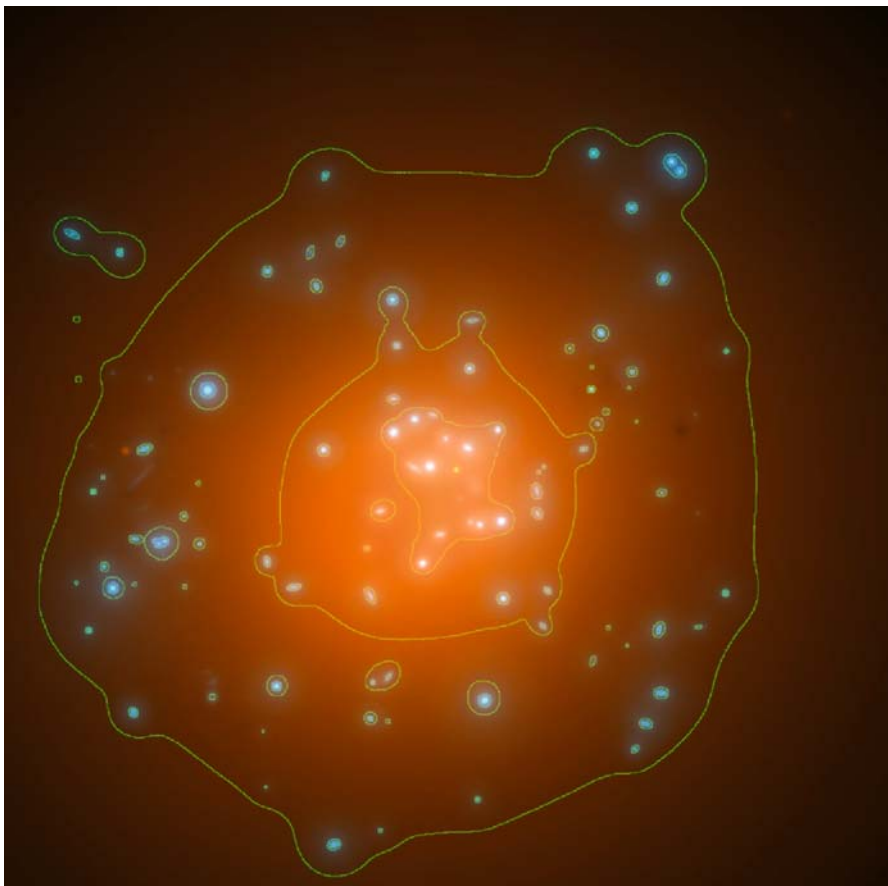


Fig. 4.21. The reconstructed mass distribution in the cluster Cl 0024+1654 which is dominated by the underlying dark matter distribution shown in orange. Mass associated with the galaxies is shown in blue. The contours show 0.5, 1 and 1.5 times the critical lensing column density. Tyson and his colleagues find the mass distribution is remarkably smooth once the mass associated with the galaxies is removed. They find a mass-to-luminosity ratio for the cluster of $M/L = (276 \pm 40)h(M_\odot/L_\odot)$ (Tyson et al., 1998)

astrophysical questions. For example:

- What is the distribution of mass in the dark matter haloes of galaxies and clusters?
- What are the tidal radii of the mass distributions for galaxies, both in the general field and in the cores of clusters?
- What is the bias parameter for galaxies, meaning the ratio between the clustering amplitudes for the baryonic and dark matter?
- Is there structure in the distribution of dark matter within galaxies and clusters, or is it smooth?

These and many other issues are addressed in the comprehensive survey *Gravitational Lensing: Strong, Weak and Micro* by Schneider, Kochanek and Wambsganss (Schneider et al., 2006). Strong lensing effects such as those illustrated in Fig. 4.20 enable the mass distribution to be determined on the scale of the inner caustic surfaces but, in addition, weak lensing can be detected statistically to much larger radii. As can be seen from panels 1, 2 and 3 of Fig. 4.20, the gravitationally lensed images are predicted to be stretched tangentially to the line joining the lens to the background galaxy. Therefore, by measuring the orientations of the images of large numbers of background galaxies, the effects of weak gravitational lensing can be distinguished statistically from the intrinsic ellipticities of galaxies. Convincing evidence for the detection of a statistical weak lensing signature for galaxies was first discovered by Brainerd and her colleagues (Brainerd et al., 1996) and has since been repeated for very much larger samples of galaxies.

As Schneider emphasises in his review, galaxy-galaxy imaging may well provide the best constraints statistically on the dimensions of dark matter haloes. A good example of what has been achieved is provided by the Red-Sequence Cluster Survey which involved $\sim 1.2 \times 10^5$ lensing galaxies and $\sim 1.5 \times 10^6$ fainter background galaxies in an area of 45.5 square degrees (Hoekstra et al., 2004). The lensing galaxies had medium redshift $z \approx 0.35$ and the background galaxies $z \approx 0.53$. These data showed that the dark matter haloes were somewhat rounder than the light distribution of the galaxies. Interestingly, the analysis of the shear data on larger angular scales provided evidence for truncation of the isothermal density distribution at a radius of $(185 \pm 30) h^{-1}$ kpc, one of the few direct estimates of the scale of the dark matter haloes.

A good example of the power of this technique is the determination of the mass distribution in a sample of 22 early-type galaxies which were imaged by the Advanced Camera for Surveys (ACS) of the Hubble Space Telescope (Gavazzi et al., 2007). In the central regions, the mass distributions were determined by optical spectroscopy and by strong gravitational lensing. In the outer regions, the statistical weak gravitational lensing technique enabled the mass profile to be determined out to about 300 kpc. Gavazzi and his colleagues found that the total mass density profile was consistent with that of an isothermal sphere, $\varrho \propto r^{-2}$, over two decades in radius from $(3\text{--}300) h^{-1}$ kpc, despite the fact that the inner regions are dominated by baryonic matter whilst the outer regions are dominated by dark matter. They found that the average stellar mass-to-light ratio was $M_*/L_V = 4.48 \pm 0.46 h M_\odot/L_\odot$ while the overall average virial mass-to-light ratio was $M_{\text{vir}}/L_V = 246^{+101}_{-87} h M_\odot/L_\odot$.

An example of the use of weak gravitational lensing to estimate the bias parameter for large samples of galaxies has been carried out by Simon and his colleagues using the data from the Garching-Bonn Deep Survey (Simon et al., 2007). Typically, about 10^5 lensing galaxies were studied in three redshift intervals centred on $z = 0.35, 0.47, 0.61$ and for each sample typically $(1 - 3) \times 10^6$ background galaxies were observed. Similar bias parameters were found in the three redshift intervals, each about $b = 0.8 \pm 0.1$ (see Sect. 14.4).

Another example of the power of gravitational lensing techniques is provided by the remarkable simulations of Wambsganss, which are contained in his online re-

view of gravitational lensing (Wambsganss, 1998). While the deflection data provide strong geometric constraints on the overall distribution of dark matter, the observed intensities of the multiple images of background quasars are more difficult to reconcile with the simplest smooth models. Wambsganss's splendid simulations illustrate the expected fluctuations in the observed intensities of the multiple images if the dark matter in the lensing galaxy consisted of large numbers moving lenses. Such fluctuations are observed in the relative brightnesses of the four components of the quadruple quasar Q2237+0305.

4.7 Forms of Dark Matter

One of the fundamental problems of cosmology is the unknown nature of the dark matter which is the dominant form of gravitating mass in the outer regions of large galaxies, in clusters of galaxies and other large-scale systems. This problem will haunt much of this book.

We are certain that the dark matter is present on the basis of the various arguments presented in Sects. 4.3 to 4.6, but we can only identify what it might be by standard astronomical techniques if it emits radiation or absorbs the radiation of background sources. An illustrative toy model is to suppose that the dark matter is in the form of standard bricks. There would have to be only one kilogram brick per cube of side roughly 500 million kilometres to attain the critical cosmological density $\varrho_c = 3H_0^2/8\pi G$. If the bricks were uniformly distributed throughout the Universe, they would not obscure the most distant objects we can observe and they would be so cold that they would emit negligible amounts of far-infrared radiation. This example illustrates the point that there could be many forms of ordinary baryonic dark matter present in the Universe which would be very difficult to detect, even before we consider more exotic possibilities. Let us consider first the case of baryonic dark matter.

4.7.1 Baryonic Dark Matter

By *baryonic matter*, we mean ordinary matter composed of protons, neutrons and electrons and for convenience we will include the black holes in this discussion. As illustrated by the example of the bricks, certain forms of baryonic matter are very difficult to detect because they are very weak emitters of electromagnetic radiation. Important examples of such weak emitters are stars with masses $M \leq 0.08M_\odot$, in which the central temperatures are not hot enough to burn hydrogen into helium – they are referred to collectively as *brown dwarfs*. They have no internal energy source and so the source of their luminosity is the thermal energy with which they were endowed at birth. There could be a small contribution from deuterium burning, but even this is not possible for stars with masses $M \leq 0.01M_\odot$. Brown dwarfs are normally classified as inert stars with masses in the range $0.08 \geq M \geq 0.01M_\odot$. Below that mass, they are normally referred to as planets, $0.01M_\odot$ corresponding to ten times the mass of Jupiter.

Until recently, brown dwarfs proved to be very difficult to detect. The situation has changed dramatically with a number technical advances in optical and infrared astronomy. The 2MASS infrared sky survey, which was conducted at a wavelength of $2\text{ }\mu\text{m}$, has discovered many cool brown dwarfs. The NICMOS infrared camera on the HST has discovered numerous brown dwarfs in nearby star clusters. The same techniques of high precision optical spectroscopy which has been spectacularly successful in discovering extrasolar system planets, has also been used to discover a number of brown dwarfs orbiting normal stars. Although the brown dwarfs are estimated to be about twice as common as stars with masses $M \geq 0.08M_{\odot}$, they contribute very little to the mass density in baryonic matter as compared with normal stars because of their low masses. The consensus of opinion is that brown dwarfs could only make a very small contribution to the dark matter problem.

A strong limit to the total amount of baryonic matter in the Universe is provided by considerations of primordial nucleosynthesis. As will be shown in Sect. 10.4, the standard Big Bang model is remarkably successful in accounting for the observed abundances of light elements such as helium-4, helium-3, deuterium and probably lithium-7 through the process of *primordial nucleosynthesis*. An important consequence of that success story is that the primordial abundances of the light elements, particularly of deuterium and helium-3, are sensitive tracers of the mean baryon density of the Universe. Steigman has reviewed recent observational evidence on the primordial abundances of the light elements and compared these with the predictions of standard Big Bang nucleosynthesis (Steigman, 2006). He finds a best estimate of the mean baryon density of the Universe of $\Omega_B h^2 = (0.0223 \pm 0.002)$. Adopting a value of $h = 0.7$ (see Sect. 8.3), the density parameter in baryonic matter is $\Omega_B = 0.0455$, compared with a mean density of matter in the Universe of $\Omega_0 \approx 0.3$ (see Sect. 8.7). Thus, ordinary baryonic matter is only about one tenth of the total mass density of the Universe, most of which must therefore be in some non-baryonic form.

Black holes are another possible candidate for the dark matter. The supermassive black holes in the nuclei of galaxies have masses which are typically only about 0.1% of the mass of the bulges of their host galaxies and so they contribute negligibly to the mass density of the Universe. There might, however, be an invisible intergalactic population of massive black holes. Limits to the number density of such black holes can be set in certain mass ranges from studies of the numbers of gravitational lenses observed in large samples of extragalactic radio sources. In their VLA survey of a very large sample of extragalactic radio sources, designed specifically to search for gravitationally lensed structures, Hewitt and her colleagues set limits to the number density of massive black holes with masses in the range $10^{10} \leq M \leq 10^{12} M_{\odot}$. They found that the numbers corresponded to $\Omega_{BH} \ll 1$ (Hewitt et al., 1987). The same technique can be used to study the mass density of lower mass black holes by searching for the gravitationally lensed images on an angular scale of a milliarcsecond, corresponding to masses in the range $10^6 \leq M \leq 10^8 M_{\odot}$ (Kassiola et al., 1991). Wilkinson and his colleagues searched a sample of 300 compact radio sources studied by VLBI techniques for examples of multiple gravitationally lensed images but none were found. The upper limit to the cosmological mass density of

intergalactic supermassive compact objects in the mass range $10^6 \leq M \leq 10^8 M_\odot$ corresponded to less than 1% of the critical cosmological density (Wilkinson et al., 2001).

It cannot be excluded that the dark matter might consist of a very large population of very low mass black holes but these would have to be produced by a rather special initial perturbation spectrum in the very early Universe before the epoch of primordial nucleosynthesis. The fact that black holes of mass less than about 10^{12} kg evaporate by Hawking radiation on a cosmological time-scale sets a firm lower limit to the possible masses of mini-black holes which could contribute to the dark matter at the present epoch (Hawking, 1975).

An impressive approach to setting limits to the contribution which discrete low mass objects, collectively known as MAssive Compact Halo Objects, or MACHOs, could make to the dark matter in the halo of our own Galaxy, has been the search for gravitational microlensing signatures of such objects as they pass in front of background stars. The MACHOs include low mass stars, white dwarfs, brown dwarfs, planets and black holes. These events are very rare and so very large numbers of background stars have to be monitored. The beauty of this technique is that it is sensitive to MACHOs with a very wide range of masses, from 10^{-7} to $100 M_\odot$, and so the contributions of a very wide range of candidates for the dark matter can be constrained. In addition, the expected light curve of such gravitational lensing events has a characteristic form which is given by the magnification relation (4.50) and which is independent of wavelength. The time-scale of the brightening is roughly the time it takes the MACHO to cross the Einstein radius of the dark deflector which is why a very wide range of masses can be constrained by this technique. Two very large projects, the MACHO and the EROS projects, have made systematic surveys over a number of years to search for these events. The MACHO project, which ran from 1992 to 1999 used stars in the Magellanic Clouds and in the Galactic bulge as background stars and millions stars were monitored regularly (Alcock et al., 1993b). The first example of a microlensing event was discovered in October 1993 (Fig. 4.22), the mass of the invisible lensing object being estimated to lie in the range $0.03 < M < 0.5 M_\odot$ (Alcock et al., 1993a).

By the end of the MACHO project, many lensing events had been observed, including over 100 in the direction towards the Galactic bulge, about three times more than expected. In addition, 13 definite and 4 possible events were observed in the direction of the Large Magellanic Cloud (Alcock et al., 2000). The numbers are significantly greater than the 2–4 detections expected from known types of star. The technique does not provide distances and masses for individual objects, but, interpreted as a Galactic halo population, the best statistical estimates suggest that the mean mass of these MACHOs is between $0.15\text{--}0.9 M_\odot$. The statistics are consistent with MACHOs making up about 20% of the necessary halo mass, the 95% confidence limits being 8–50%. Somewhat fewer microlensing events were detected in the EROS project which found that less than 25% of the mass of the standard dark matter halo could consist of dark objects with masses in the range 2×10^{-7} to $1 M_\odot$ at the 95% confidence level (Afonso et al., 2003). The most likely candidates for the MACHOs observed by the MACHO project would appear to be white dwarfs which

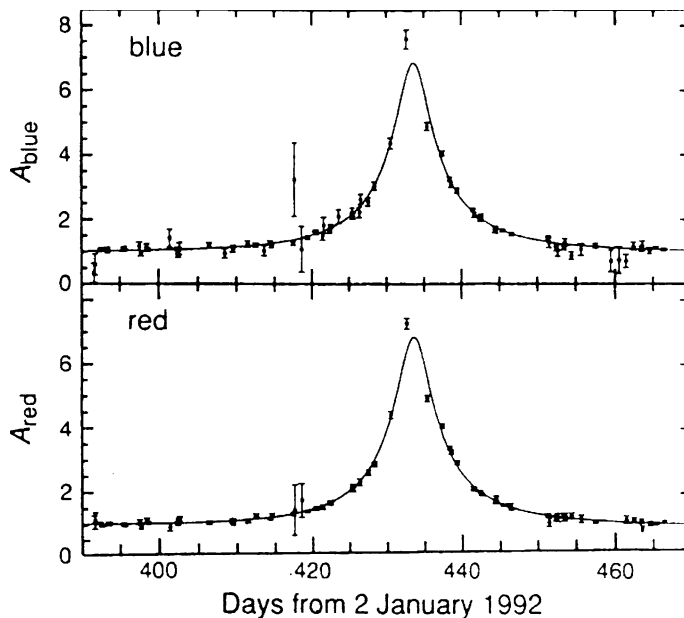


Fig. 4.22. The gravitational microlensing event recorded by the MACHO project in February and March 1993. The *horizontal axis* shows the date in days measured from day zero on 2 January 1992. The *vertical axis* shows the amplification of the brightness of the lensed star relative to the unlensed intensity in blue and red wavebands. The *solid lines* show the expected variations of brightness of a lensed star with time (Eq. 4.50). The same characteristic light curve is observed in both wavebands, as expected for a gravitational microlensing event (Alcock et al., 1993b)

would have to be produced in large numbers in the early evolution of the Galaxy, but other more exotic possibilities cannot be excluded. The consensus view is that MACHOs alone cannot account for all the dark matter in the halo of our Galaxy and so some form of non-baryonic matter must make up the difference.

4.7.2 Non-Baryonic Dark Matter

The general consensus is that the dark matter is most likely to be some non-baryonic form and so is of the greatest interest for particle physicists since it may consist of the types of particles predicted by theories of elementary particles but not yet detected experimentally. Three of the most popular possibilities are discussed in the following paragraphs.

Axions. The smallest mass candidates are the *axions* which were invented by particle theorists in order to ‘save quantum chromodynamics from strong CP violation’. If they exist, they must have been created when the thermal temperature of the Universe was about 10^{12} K but they were out of equilibrium and never acquired thermal

velocities – they remained ‘cold’. Their rest mass energies are expected to lie in the range 10^{-2} to 10^{-5} eV. The role of such particles in cosmology and galaxy formation is discussed by Efstathiou and Kolb and Turner (Efstathiou, 1990; Kolb and Turner, 1990).

Neutrinos with finite rest mass. A second possibility is that the three known types of neutrino have finite rest masses. Laboratory tritium β -decay experiments have provided an upper limit to the rest mass of the electron antineutrino of $m_\nu \leq 2$ eV (Weinheimer, 2001), although the particle data book suggests a conservative upper limit of 3 eV (see <http://www-pdg.lbl.gov/pdg.html>). This measurement does not exclude the possibility that the two other types of neutrino, the μ and τ neutrinos, could have greater masses. However, the discovery of neutrino oscillations has provided a measurement of the mass difference between the μ and τ neutrinos of $\Delta m_\nu^2 \sim 3 \times 10^{-3}$ (Eguchi et al., 2003; Aliu et al., 2005). Thus, although their masses are not measured directly, they probably have masses of the order of 0.1 eV.

The reason that these values are of interest is that neutrinos of rest mass about 10–20 eV would be enough to provide the critical density, as may be appreciated from the following calculation. The number density of neutrinos of a single type in thermal equilibrium at temperature T is

$$N = \overline{N} = \frac{4\pi g}{h^3} \int_0^\infty \frac{p^2 dp}{e^{E/kT} + 1} = 0.091 \left(\frac{2\pi kT}{hc} \right)^3 m^{-3}, \quad (4.64)$$

where the statistical weight g for the neutrinos is $g = 1$. If there are N_ν neutrino types present, each with rest mass m_ν , the present mass density of neutrinos in the Universe would be

$$\varrho_\nu = N N_\nu m_\nu. \quad (4.65)$$

The present temperature of the neutrino background radiation, which was in equilibrium with the matter prior to the epoch when the neutrinos decoupled, is $(4/11)^{1/3}$ of the temperature of the Cosmic Microwave Background Radiation, that is, $T_\nu = 1.94$ K, and so the value of N is rather precisely known (see Sect. 10.5). Therefore, if ϱ_ν is to equal the critical density of the Universe $\varrho_c = 1.88 \times 10^{-26} h^2 \text{ kg m}^{-3}$, the necessary rest mass energy of the neutrino is $m_\nu = 184 h^2 / N_\nu$ eV. Since there are three neutrino species, each with its antiparticle, $N_\nu = 6$ and hence the necessary rest mass of the neutrino is $31 h^2$ eV. Taking $h = 0.7$, it follows that, if the neutrino rest mass were about 15 eV, known types of neutrino could close the Universe. However, if the mass of the neutrinos is of the order 0.1 eV, they certainly could not account for the amount of dark matter present in the Universe.

WIMPs. A third possibility is that the dark matter is in some form of *Weakly Interacting Massive Particle*, or WIMP. This might be the gravitino, the supersymmetric partner of the graviton, or the photino, the supersymmetric partner of the photon, or some form of as yet unknown massive neutrino-like particle. The possible existence of these types of unknown particles represents theoretical extrapolations beyond the

range of energies which have been explored experimentally, but these ideas are sufficiently compelling on theoretical grounds that many particle theorists take seriously the possibility that cosmological studies will prove to be important in constraining theories of elementary processes at very high energies.

In fact, there is the real possibility that clues will be found from experiments to be carried out in the TeV energy range with the Large Hadron Collider (LHC) and the next generation International Linear Collider (ILC). An understanding of TeV physics will undoubtedly impact our understanding of the Universe back to epochs $t \sim 10^{-8}$ seconds. But there are even more exciting possibilities. To paraphrase the generic arguments given by Trodden, physics beyond the standard model of particles physics is essential and almost any model involves new particles at the TeV scale (Trodden, 2006). These particles are related to the particles of the standard model through an extra new symmetry which is necessary to avoid proton decay and the violation of precision tests of electro-weak theory. This new symmetry leads to the expectation of some new stable particle at the weak energy scale. It is particularly intriguing that the weak interaction cross-section is of exactly the right order of magnitude at the decoupling mass-scale to provide sufficient mass density in WIMPs to account for the dark matter (see Sect. 10.6).

4.7.3 Astrophysical and Experimental Limits

Useful astrophysical limits can be set to the number densities of different types of neutrino-like particles in the outer regions of giant galaxies and in clusters of galaxies. The WIMPs and massive neutrinos are collisionless fermions and therefore there are constraints on the phase space density of these particles, which translate into a lower limit to their masses. This is because, for a given momentum, only a finite number of particles within a given volume is allowed. Let us give a simple derivation of this result. More details of this calculation are given by Tremaine and Gunn, who provide a slightly tighter constraint on the masses of these hypothetical particles (Tremaine and Gunn, 1979).

Being fermions, neutrino-like particles are subject to the Pauli exclusion principle according to which there is a maximum number of particle states in phase space for a given momentum p_{\max} . The elementary phase volume is \hbar^3 and, recalling that there can be two particles of opposite spin per state, the maximum number of particles with momenta up to p_{\max} is

$$N \leq 2 \frac{g}{\hbar^3} \frac{4\pi}{3} p_{\max}^3 , \quad (4.66)$$

per unit volume, where g is the statistical weight of the neutrino species. If there is more than one neutrino species present, we multiply this number by N_ν . Bound gravitating systems such as galaxies and clusters of galaxies are subject to the virial theorem according to which the kinetic energy of the particles which make up the system is equal to half of its gravitational potential energy (Sect. 3.5.1). If σ is the root-mean-square velocity dispersion of the objects which bind the system,

$\sigma^2 = GM/R$, and the maximum velocity which particles within the system can have is the escape velocity from the cluster, $v_{\max} = (2GM/R)^{1/2} = \sqrt{2}\sigma$. The neutrino-like particles bind the system and so its total mass is $M = NN_\nu m_\nu$ where m_ν is the rest mass of the particle. We therefore find the following lower limit to the rest mass of the particle from (4.66) in terms of observable quantities:

$$m_\nu^4 \geq \left(\frac{9\pi}{8\sqrt{2}g} \right) \frac{\hbar^3}{N_\nu G \sigma R^2} \quad m_\nu \geq \frac{1.5}{(N_\nu \sigma_3 R_{\text{Mpc}}^2)^{1/4}} \text{ eV}, \quad (4.67)$$

where the velocity dispersion σ_3 is measured in units of 10^3 km s^{-1} and R is measured in Mpc.

Let us insert typical values for the velocity dispersions and radii of the systems in which there is known to be a dark matter problem. In clusters of galaxies, typical values are $\sigma = 1000 \text{ km s}^{-1}$ and $R = 1 \text{ Mpc}$. If there is only one neutrino species, $N_\nu = 1$, we find $m_\nu \geq 1.5 \text{ eV}$. If there were six neutrino species, namely, electron, muon, tau neutrinos and their antiparticles, $N_\nu = 6$ and then $m_\nu \geq 0.9 \text{ eV}$. For giant galaxies, for which $\sigma = 300 \text{ km s}^{-1}$ and $R = 10 \text{ kpc}$, $m_\nu \geq 20 \text{ eV}$ if $N_\nu = 1$ and $m_\nu \geq 13 \text{ eV}$ if $N_\nu = 6$. For small galaxies, for which $\sigma = 100 \text{ km s}^{-1}$ and $R = 1 \text{ kpc}$, the corresponding figures are $m_\nu \geq 80 \text{ eV}$ and $m_\nu \geq 50 \text{ eV}$ respectively. Thus, particles with rest masses $m_\nu \sim 1 \text{ eV}$ could bind clusters of galaxies but they could not bind the haloes of giant or small galaxies.

There is a further constraint on the possible masses WIMPs. Studies of the decay of the W^\pm and Z^0 bosons at CERN have shown that the width of the decay spectrum is consistent with there being only three neutrino species with rest mass energies less than about 40 GeV. Therefore, if the dark matter is in some form of ultraweakly interacting particle, its rest mass energy must be greater than 40 GeV.

Another important constraint is that, if the masses of the particles were greater than 15 eV and they are as common as neutrinos and photons, as expected in the standard Big Bang model, the present density of the Universe would exceed the critical mass density ρ_c (see Sect. 4.7.2). Therefore there would have to be some suppression mechanism to ensure that, if $m \geq 40 \text{ GeV}$, these particles are very much less common than the photons and electrons neutrinos at the present day. This could take place by the mechanism described in Sect. 10.6.

The search for evidence for different types of dark matter particles has developed into one of the major areas of the discipline known as *astroparticle physics*. An important class of experiments involves the search for weakly interacting particles with masses $m \geq 1 \text{ GeV}$, which could make up the dark halo of our Galaxy. In order to form a bound dark halo about our Galaxy, the particles would have to have velocity dispersion $\langle v^2 \rangle^{1/2} \sim 230 \text{ km s}^{-1}$ and their total mass is known. Therefore, the number of WIMPs passing through a terrestrial laboratory each day is a straightforward calculation. When these massive particles interact with the sensitive volume of the detector, the collision results in the transfer of momentum to the nuclei of the atoms of the material of the detector and this recoil can be measured in various ways. There is a small temperature increase which can be measured in a cryogenically cooled detector, or the ionisation caused by the recoiling nucleus

can be measured in an ionisation chamber, or the light emitted by the passage of the recoil nucleus through the material detected by a scintillation detector. The challenge is to detect the very small number of events expected because of the very small cross-section for the interaction of WIMPs with the nuclei of atoms. A typical estimate is that less than one WIMP per day would be detectable by 1 kilogram of detector material. These are very demanding experiments and they have to be located deep underground to avoid contamination by cosmic rays and must be heavily shielded against natural radioactivity in the surrounding rocks. Such experiments have been carried out in deep underground laboratories such as those at Gran Sasso in Italy, the Soudan Underground Laboratory in Minnesota, USA and the Boulby Underground Laboratory in Yorkshire, England.

A good example of the quality of the data now available is provided by the results of the Cryogenic Dark Matter Search (CDMS) at the Soudan Laboratory. The CDMS experiment has set a 90% confidence upper limit to the spin-independent WIMP–nucleon interaction cross-section at its most sensitive mass of $60 \text{ GeV}/c^2$ of $\sigma_w \leq 1.6 \times 10^{-47} \text{ m}^2$ (Akerib et al., 2006). This cross-section can be compared with the weak interaction cross-section for neutrino–electron scattering, $\sigma = 3 \times 10^{-49} (E/m_e c^2) \text{ m}^2$. Already the CDMS result constrains the predictions of supersymmetric models. The sensitivity of these experiments should improve by an order of magnitude with the CDMSII experiment planned for 2007 and then by successive order of magnitude improvements through the different phases of the SuperCDMS proposal.

5 The Theoretical Framework

5.1 The Cosmological Principle

The observational evidence discussed in Chap. 2, particularly the isotropy of the Cosmic Microwave Background Radiation, indicates that the natural starting point for the construction of cosmological models is to assume that, to first approximation, the Universe is isotropic and homogeneous at the present epoch. This is precisely what Einstein assumed in developing his static model of 1917, the first fully self-consistent model of the Universe, derived long before the large-scale isotropy of our Universe was established (Einstein, 1917). Likewise, Friedman's discovery of what were to become the standard models for the large-scale dynamics of the Universe predated the discovery of the expansion of the Universe. The Friedman models were based upon expanding solutions of Einstein's equations, following clues provided by de Sitter and Lanczos.¹

One of the problems facing the pioneers of relativistic cosmology was the interpretation of the space and time coordinates to be used in these calculations. For example, de Sitter's solution for an empty universe could be written in apparently stationary form, or as an exponentially expanding solution. By 1935, the problem was solved independently by Robertson and Walker (Robertson, 1935; Walker, 1936). They derived the metric of space–time for *all* isotropic, homogeneous, uniformly expanding models of the Universe. This form of the metric is independent of the assumption that the large-scale dynamics of the Universe are described by Einstein's General Theory of Relativity – whatever the physics of the expansion, the space–time metric must be of *Robertson–Walker* form, because of the assumptions of isotropy and homogeneity.

A key step in the development of these models was the introduction by Hermann Weyl in 1923 of what is known as *Weyl's postulate* (Weyl, 1923). To eliminate the arbitrariness in the choice of coordinate frames, Weyl introduced the idea that, in the words of Hermann Bondi (Bondi, 1960):

The particles of the substratum (representing the nebulae) lie in space–time on a bundle of geodesics diverging from a point in the (finite or infinite) past.

¹ For details of the historical development of the standard world models, see my book *The Cosmic Century* (Longair, 2006)

The most important aspect of this statement is the postulate that the geodesics, which represent the world lines of galaxies, do not intersect, except at a singular point in the finite, or infinite, past. Again, it is remarkable that Weyl introduced this postulate *before* Hubble's discovery of the recession of the nebulae. By the term 'substratum', Bondi meant an imaginary medium which can be thought of as a fluid which defines the overall kinematics of the system of galaxies. A consequence of Weyl's postulate is that there is only one geodesic passing through each point in space–time, except at the origin. Once this postulate is adopted, it becomes possible to assign a notional observer to each world line and these are known as *fundamental observers*. Each fundamental observer carries a standard clock and time measured on that clock from the singular point is called *cosmic time*.

One further assumption is needed before we can derive the framework for the standard models. This is the assumption known as the *cosmological principle* and it can be stated:

We are not located at any special location in the Universe.

A corollary of this statement is that we are located at a *typical* position in the Universe and that any other fundamental observer located anywhere in the Universe at the same cosmic epoch would observe the same large-scale features which we observe. Thus, we assert that every fundamental observer at the same cosmic epoch observes the same Hubble expansion of the distribution of galaxies, the same isotropic Cosmic Microwave Background Radiation, the same large-scale spongy structure in the distribution of galaxies and voids, and so on. As we showed in Sect. 2.3, the combination of Hubble's law and the isotropy of the Universe implies that the system of galaxies as a whole is expanding uniformly and every observer on every galaxy partaking in the uniform expansion observes the same Hubble flow at the same epoch – all of them correctly believe that they are at the centre of a uniformly expanding Universe. The isotropy of the background radiation, the evidence of the scaling of the two-point correlation function with apparent magnitude and the ubiquity of the sponge-like structure of the distribution of galaxies suggest that the cosmological principle is a sensible starting point for the construction of cosmological models.

The specific features of the observable Universe we need in what follows are its overall isotropy and homogeneity, as well as Hubble's law. The combination of these with the Minkowski metric of special relativity results in the *Robertson–Walker metric* for any isotropic, uniformly expanding world model.

5.2 Isotropic Curved Spaces

During the late eighteenth century, non-Euclidean spaces began to be taken seriously by mathematicians who realised that Euclid's fifth postulate, that parallel lines meet only at infinity, might not be essential for the construction of self-consistent geometries. The first suggestions that the global geometry of space might not be Euclidean were discussed by Lambert and Saccheri. In 1786, Lambert noted that, if space were hyperbolic rather than flat, the radius of curvature of space could be used

as an absolute measure of distance. In 1816, Gauss repeated this proposal in a letter to Gerling and was well aware of the fact that a test of the local geometry of space could be carried out by measuring the sum of the angles of a triangle between three high mountain peaks (Longair, 2006).

The fathers of non-Euclidean geometry were Nikolai Ivanovich Lobachevsky in Russia and János Bolyai in Transylvania (Lobachevsky, 1829, 1830; Bolyai, 1832). In his papers, *On the Principles of Geometry* of 1829 and 1930, Lobachevsky at last solved the problem of the existence of non-Euclidean geometries and showed that Euclid's fifth postulate could not be deduced from the other postulates. Non-Euclidean geometry was placed on a firm theoretical basis by the studies of Bernhard Riemann and the English-speaking world was introduced to these ideas through the works of Clifford and Cayley.

Einstein's monumental achievement was to combine special relativity and the theory of gravity through the use of Riemannian geometry and tensor calculus to create the General Theory of Relativity (see Chap. 6). Within a couple of years of formulating the theory, Einstein realised that he now had the tools with which fully self-consistent models for the Universe as a whole could be constructed. In Einstein's model, which we discuss in Sect. 7.3, the Universe is static, closed and has isotropic, spherical geometry. The Friedman solutions, published in 1922 and 1924, were also isotropic models but they were expanding solutions and included geometries that were both spherical and hyperbolic (Friedman, 1922, 1924).

It turns out that it is not necessary to become enmeshed in the details of Riemannian geometry to appreciate the geometrical properties of isotropic curved spaces. We can demonstrate simply why the only isotropic curved spaces are those in which the two-dimensional curvature of any space section κ is constant throughout the space and can only take positive, zero or negative values. The essence of the following argument was first shown to me by my colleague, the late Peter Scheuer.

Let us consider first of all the simplest two-dimensional curved geometry, the surface of a sphere (Fig. 5.1). In the diagram, a triangle is shown consisting of two lines drawn from the north pole down to the equator, the angle between them being 90° ; the triangle is completed by the line drawn along the equator of the sphere. The three sides of this triangle are all segments of great circles on the sphere and so are the shortest distances between the three corners of the triangle. The three lines are *geodesics* in the curved geometry.

We need a procedure for working out how non-Euclidean the curved geometry is. The way this is done in general is by the procedure known as the *parallel displacement* or *parallel transport* of a vector on making a complete circuit around a closed figure such as the triangle in Fig. 5.1. Suppose we start with a little vector perpendicular to AC at the pole and lying in the surface of the sphere. We then transport that vector from A to C, keeping it perpendicular to AC. At C, we rotate the vector through 90° so that it is now perpendicular to CB. We then transport the vector, keeping it perpendicular to CB to the corner B. We make a further rotation through 90° to rotate the vector perpendicular to BA and then transport it back to A. At that point, we make a final rotation through 90° to bring the vector back to its original direction. Thus, the total rotation of the vector is 270° . Clearly, the surface

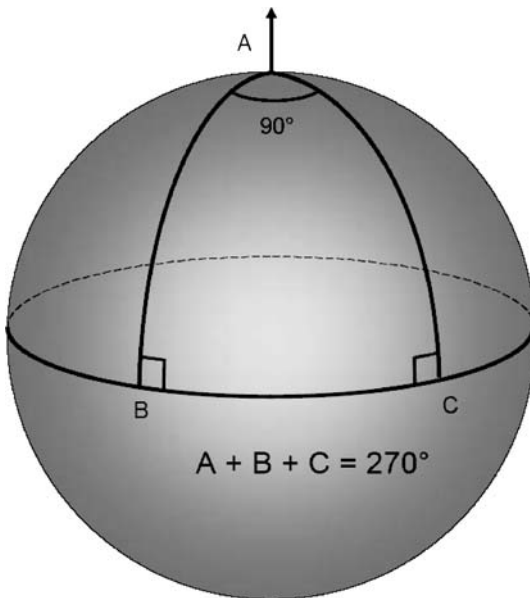


Fig. 5.1. Illustrating the sum of the angles of a triangle on the surface of a sphere.

of the sphere is a non-Euclidean space. This procedure illustrates how we can work out the geometrical properties of any two-space, entirely by making measurements within the two-space, in this case, on the surface of the sphere.

Another simple calculation illustrates an important feature of parallel transport on the surface of a sphere. Suppose the angle at A is not 90° but some arbitrary angle θ . Then, if the radius of the sphere is R_c , the surface area of the triangle ABC is $A = \theta R_c^2$. Thus, if $\theta = 90^\circ$, the area is $\pi R_c^2/2$ and the sum of the angles of the triangle is 270° ; if $\theta = 0^\circ$, the area is zero and the sum of the angles of the triangle is 180° . Evidently, the difference of the sum of the angles of the triangle from 180° is proportional to the area of the triangle, that is

$$(\text{Sum of angles of triangle} - 180^\circ) \propto (\text{Area of triangle}) . \quad (5.1)$$

This result is a general property of isotropic curved spaces.

Let us now work out the sum of the angles round a closed figure in an isotropic curved space. The procedure is shown schematically in Fig. 5.2a which shows two geodesics from the origin at O being crossed by another pair of geodesics at distances r and $r + \Delta x$ from the origin. The angle $d\theta$ between the geodesics at O is assumed to be small. In Euclidean space, the length of the segment of the geodesic AB would be $\xi = r d\theta$. However, this is no longer true in non-Euclidean space and instead, we write

$$\xi(r) = f(r) d\theta . \quad (5.2)$$

It is straightforward to work out the angle between the diverging geodesics at distance r from the origin. From Fig. 5.2a, it can be seen that the angle between the geo-

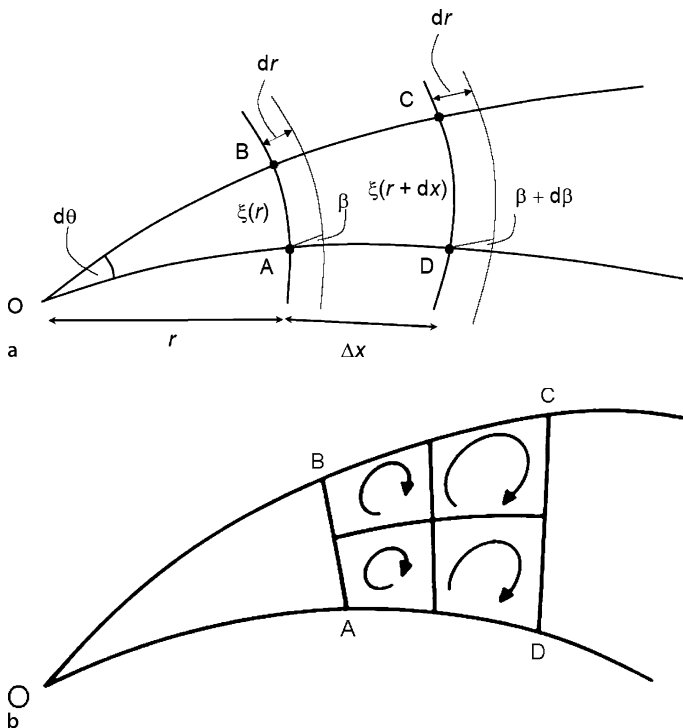


Fig. 5.2. **a** A schematic diagram illustrating the change in angle β between the geodesics from O over the distance interval Δx . **b** Illustrating how the sum of the rotations around the subloops add up linearly to the total rotation $d\beta$ round the large loop and hence that the total rotation is proportional to the area enclosed by the loop

desics is

$$\beta = \frac{\xi(r + dr) - \xi(r)}{dr} = \frac{d\xi(r)}{dr} = d\theta \frac{df(r)}{dr}. \quad (5.3)$$

Let us now move a distance Δx further along the geodesics. The change in the angle β , $\Delta\beta$ is

$$\Delta\beta = \frac{d\xi(r + \Delta x)}{dr} - \frac{d\xi(r)}{dr} = \frac{d^2\xi(r)}{dr^2} \Delta x = \frac{d^2f(r)}{dr^2} \Delta x d\theta. \quad (5.4)$$

Let us check that this result makes sense. In Euclidean space, $\xi(r) = f(r) d\theta = r d\theta$, $f(r) = r$ and hence (5.3) becomes $\beta = d\theta$. Furthermore, in Euclidean space, $d^2f(r)/dr^2 = 0$ and so $\Delta\beta = 0$, in other words, $\beta = d\theta$ remains true for all values of r .

Now, the rotation of the vector $d\beta$ depends upon the area of the quadrilateral ABCD. In the case of an isotropic space, we should obtain the same rotation wherever we place the loop in the two-space. Furthermore, if we were to split the loop up into a number of subloops, the rotations around the separate subloops must add

up linearly to the total rotation $d\beta$ (Fig. 5.2b). Thus, in an isotropic two-space, the rotation $d\beta$ should be proportional to the area of the loop ABCD and must be a constant everywhere in the two-space, just as we found in the particular case of a spherical surface in Fig. 5.1.

The area of the loop is $dA = \xi(r)\Delta x = f(r)\Delta x d\theta$, and so we can write

$$\frac{d^2 f(r)}{dr^2} = -\kappa f(r) , \quad (5.5)$$

where κ is a constant, the minus sign being chosen for convenience. This is the equation of simple harmonic motion which has solution

$$f(r) = A \sin \kappa^{1/2} r . \quad (5.6)$$

We can find the value of A from the expression for $\xi(r)$ for very small values of r , which must reduce to the Euclidean expression $d\theta = \xi/r$. Therefore, $A = \kappa^{-1/2}$ and

$$f(r) = \frac{\sin \kappa^{1/2} r}{\kappa^{1/2}} . \quad (5.7)$$

κ is the *curvature* of the two-space and can be positive, negative or zero. If it is negative, we can write $\kappa = -\kappa'$, where κ' is positive and then the circular functions become hyperbolic functions

$$f(r) = \frac{\sinh \kappa'^{1/2} r}{\kappa'^{1/2}} . \quad (5.8)$$

As we showed above, in the Euclidean case, $d^2 f(r)/dr^2 = 0$ and so $\kappa = 0$.

The results we have derived include all possible isotropic curved two-spaces. The constant κ can be positive, negative or zero corresponding to spherical, hyperbolic and flat spaces respectively. In geometric terms, $R_c = \kappa^{-1/2}$ is the radius of curvature of a two-dimensional section through the isotropic curved space and has the same value at all points and in all orientations within the plane. It is often convenient to write the expression for $f(r)$ in the form

$$f(r) = R_c \sin \frac{r}{R_c} , \quad (5.9)$$

where R_c is real for closed spherical geometries, imaginary for open hyperbolic geometries and infinite for the case of Euclidean geometry.

The simplest examples of such spaces are the spherical geometries in which R_c is just the radius of the sphere as illustrated in Fig. 5.1. The hyperbolic spaces are more difficult to envisage. The fact that R_c is imaginary can be interpreted in terms of the principal radii of curvature of the surface having opposite sign. The geometry of a hyperbolic two-sphere can be represented by a saddle-shaped figure (Fig. 5.3), just as a two-sphere provides an visualisation of the properties of a spherical two-space.

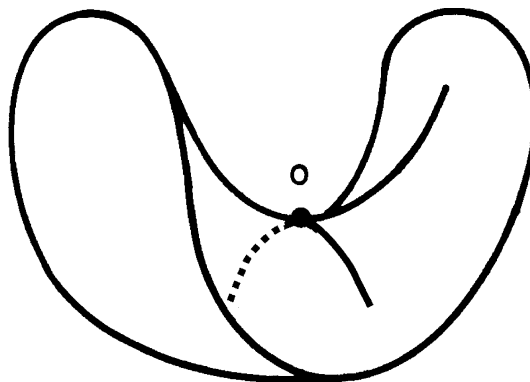


Fig. 5.3. Illustrating the geometry of an isotropic hyperbolic two-space. The principal radii of curvature of the surface are equal in magnitude but have opposite signs in orthogonal directions

5.3 The Space–Time Metric for Isotropic Curved Spaces

In flat space, the distance between two points separated by dx, dy, dz is

$$dl^2 = dx^2 + dy^2 + dz^2. \quad (5.10)$$

Let us now consider the simplest example of an isotropic *two-dimensional* curved space, namely the surface of a sphere which we discussed in Sect. 5.2. We can set up an orthogonal frame of reference at each point locally on the surface of the sphere. It is convenient to work in spherical polar coordinates to describe positions on the surface of the sphere as indicated in Fig. 5.4. In this case, the orthogonal coordinates are the angular coordinates θ and ϕ , and the expression for the increment of distance dl between two neighbouring points on the surface can be written

$$dl^2 = R_c^2 d\theta^2 + R_c^2 \sin^2 \theta d\phi^2, \quad (5.11)$$

where R_c is the radius of curvature of the two-space, which in this case is just the radius of the sphere.

The expression (5.11) is known as the *metric* of the two-dimensional surface and can be written more generally in tensor form

$$dl^2 = g_{\mu\nu} dx^\mu dx^\nu. \quad (5.12)$$

It is a fundamental result of differential geometry that the *metric tensor* $g_{\mu\nu}$ contains all the information about the intrinsic geometry of the space. The problem is that we can set up a variety of different coordinate systems to define the coordinates of a point on any two-dimensional surface. For example, in the case of a Euclidean plane, we could use rectangular *Cartesian coordinates* so that

$$dl^2 = dx^2 + dy^2, \quad (5.13)$$

or we could use *polar coordinates* in which

$$dl^2 = dr^2 + r^2 d\phi^2. \quad (5.14)$$

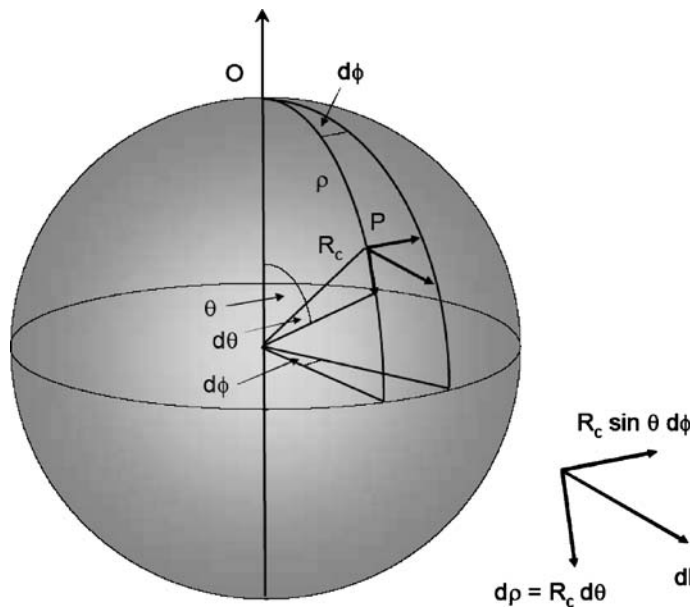


Fig. 5.4. The surface of a sphere as the simplest example of a two-dimensional curved space

How can we determine the *intrinsic curvature* of the space simply in terms of the $g_{\mu\nu}$ of the metric tensor? Gauss first showed how it is possible to do this (Weinberg, 1972; Berry, 1989). For the case of two-dimensional metric tensors which can be reduced to diagonal form, as in the cases of the metrics (5.11), (5.13) and (5.14), the intrinsic curvature of the space is given by the quantity

$$\kappa = \frac{1}{2g_{11}g_{22}} \left\{ -\frac{\partial^2 g_{11}}{\partial x_2^2} - \frac{\partial^2 g_{22}}{\partial x_1^2} + \frac{1}{2g_{11}} \left[\frac{\partial g_{11}}{\partial x_1} \frac{\partial g_{22}}{\partial x_1} + \left(\frac{\partial g_{11}}{\partial x_2} \right)^2 \right] + \frac{1}{2g_{22}} \left[\frac{\partial g_{11}}{\partial x_2} \frac{\partial g_{22}}{\partial x_2} + \left(\frac{\partial g_{22}}{\partial x_1} \right)^2 \right] \right\}. \quad (5.15)$$

It is a useful exercise to use (5.15) to show that both metrics (5.13) and (5.14) have zero curvature and that, for the surface of a sphere, the metric (5.11) corresponds to a space of positive curvature with $\kappa = R_c^{-2}$ at all points on the sphere. κ is known as the *Gaussian curvature* of the two-space and is the same as the definition of the curvature introduced in Sect. 5.2. In general curved spaces, the curvature κ varies from point to point in the space. The extension to isotropic three-spaces is straightforward if we remember that any two-dimensional section through an isotropic three-space must be an isotropic two-space and we already know the metric tensor for this case.

We have already worked out the length of the distance increment dl (5.11). The natural system of coordinates for an isotropic two-space is a spherical polar system in which a radial distance ϱ round the sphere is measured from the pole and the angle ϕ measures angular displacements at the pole. From Fig. 5.4, the distance ϱ round the arc of a great circle from the point O to P is $\varrho = \theta R_c$ and so the metric can be written

$$dl^2 = d\varrho^2 + R_c^2 \sin^2 \left(\frac{\varrho}{R_c} \right) d\phi^2. \quad (5.16)$$

The distance ϱ is the shortest distance between O and P on the surface of the sphere since it is part of a great circle and is therefore the *geodesic distance* between O and P in the isotropic curved space. Geodesics play the role of straight lines in curved space.

We can write the metric in an alternative form if we introduce a distance measure

$$x = R_c \sin \left(\frac{\varrho}{R_c} \right). \quad (5.17)$$

Differentiating and squaring, we find

$$dx^2 = \left[1 - \sin^2 \left(\frac{\varrho}{R_c} \right) \right] d\varrho^2 \quad d\varrho^2 = \frac{dx^2}{1 - \kappa x^2}, \quad (5.18)$$

where $\kappa = 1/R_c^2$ is the curvature of the two-space.

Therefore, we can rewrite the metric in the form

$$dl^2 = \frac{dx^2}{1 - \kappa x^2} + x^2 d\phi^2. \quad (5.19)$$

Notice the interpretation of the distance measure x . It can be seen from the metric (5.19) that $dl = x d\phi$ is a *proper dimension* perpendicular to the radial coordinate ϱ and that it is the correct expression for the length of a line segment which subtends the angle $d\phi$ at geodesic distance ϱ from O. It is therefore what is known as an *angular diameter distance* since it is guaranteed to give the correct answer for the length of a line segment perpendicular to the line of sight. We can use either ϱ or x in our metric but notice that, if we use x , the increment of geodesic distance is $d\varrho = dx/(1 - \kappa x^2)^{1/2}$. We recall that the curvature $\kappa = 1/R_c^2$ can be *positive* as in the spherical two-space discussed above, *zero* in which case we recover flat Euclidean space ($R_c \rightarrow \infty$) and *negative* in which case the geometry becomes *hyperbolic* rather than spherical.

We can now write down the expression for the spatial increment in any isotropic, three-dimensional curved space. As mentioned above, the trick is that any two-dimensional section through an isotropic three-space must be an isotropic two-space for which the metric is (5.16) or (5.19). We note that, in spherical polar coordinates, the general angular displacement perpendicular to the radial direction is

$$d\Phi^2 = d\theta^2 + \sin^2 \theta d\phi^2, \quad (5.20)$$

and can be found by rotating the coordinate system about the radial direction. Note that the θ s and ϕ s in (5.20) are different from those used in Fig. 5.4. Thus, by a straightforward extension of the formalism we have derived already, we can write the spatial increment

$$dl^2 = d\varrho^2 + R_c^2 \sin^2 \left(\frac{\varrho}{R_c} \right) [d\theta^2 + \sin^2 \theta \, d\phi^2] , \quad (5.21)$$

in terms of the three-dimensional spherical polar coordinates (ϱ, θ, ϕ) . An exactly equivalent form is obtained if we write the spatial increment in terms of x, θ, ϕ in which case we find

$$dl^2 = \frac{dx^2}{1 - \kappa x^2} + x^2 [d\theta^2 + \sin^2 \theta \, d\phi^2] . \quad (5.22)$$

We are now in a position to write down the *Minkowski metric* in any isotropic three-space. It is given by

$$ds^2 = dt^2 - \frac{1}{c^2} dl^2 , \quad (5.23)$$

where dl is given by either of the above forms of the spatial increment, (5.21) or (5.22). Notice that we have to be careful about the meanings of the distance coordinates $-x$ and ϱ are equivalent but physically quite distinct distance measures. We can now proceed to derive from this metric the *Robertson–Walker metric*.

5.4 The Robertson–Walker Metric

In order to apply the metric (5.23) to isotropic, homogeneous world models, we need the *cosmological principle* and the concepts of *fundamental observers* and *cosmic time* which were introduced in Sect. 5.1. For uniform, isotropic world models, we define a set of *fundamental observers*, who move in such a way that the Universe always appears to be isotropic to them. Each of them has a clock and proper time measured by that clock is called *cosmic time*. There are no problems of synchronisation of the clocks carried by the fundamental observers because, according to Weyl's postulate, the geodesics of all observers meet at one point in the past and cosmic time can be measured from that reference epoch.

We can now write down the metric for such Universes from the considerations of Sect. 5.3. From (5.21) and (5.23), the metric can be written in the form

$$ds^2 = dt^2 - \frac{1}{c^2} [d\varrho^2 + R_c^2 \sin^2(\varrho/R_c) (d\theta^2 + \sin^2 \theta \, d\phi^2)] . \quad (5.24)$$

t is cosmic time and $d\varrho$ is an increment of proper distance in the radial direction.

There is a problem in applying this metric to the expanding Universe as is illustrated by the space–time diagram shown in Fig. 5.5. Since light travels at a finite

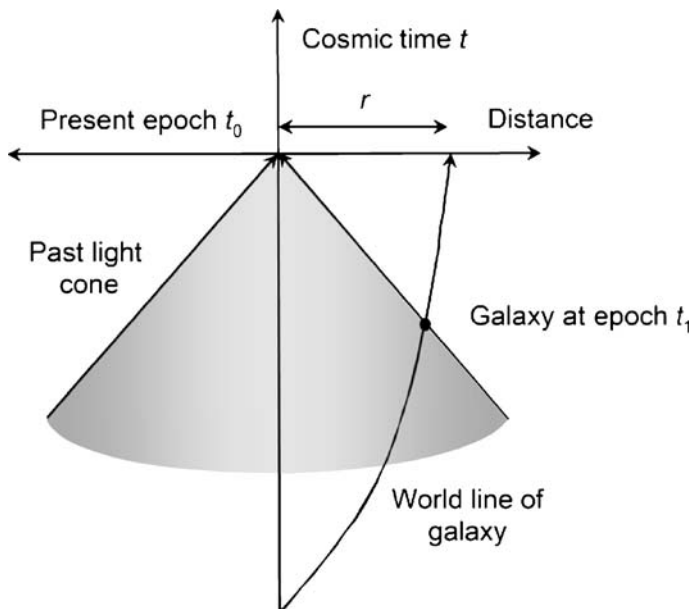


Fig. 5.5. A simple space–time diagram illustrating the definition of the comoving radial coordinate distance

speed, we observe all astronomical objects along a *past light cone* which is centred on the Earth at the present epoch t_0 . Therefore, when we observe distant objects, we do not observe them at the present epoch but rather at an earlier epoch t_1 when the Universe was still homogeneous and isotropic but the distances between fundamental observers were smaller and the spatial curvature different. The problem is that we can only apply the metric (5.24) to an isotropic curved space defined *at a single epoch*.

To resolve this problem, we perform the following thought experiment. To measure a proper distance which can be included in the metric (5.24), we line up a set of fundamental observers between the Earth and the galaxy whose distance we wish to measure. The observers are all instructed to measure the distance $d\varrho$ to the next fundamental observer at a particular cosmic time t which they read on their own clocks. By adding together all the $d\varrho$ s, we can find a proper distance ϱ which is measured *at a single epoch* and which can be used in the metric (5.24). Notice that ϱ is a *fictitious distance* in that we cannot actually measure distances in this way. We observe distant galaxies as they were at some epoch earlier than the present and we do not know how to project their positions relative to us forward to the present epoch until we know the kinematics of the expanding Universe. Thus, *the distance measure ϱ depends upon the choice of cosmological model*.

Let us work out how the ϱ coordinates of galaxies change in a uniformly expanding Universe. The definition of a uniform expansion is that between two cosmic

epochs, t_1 and t_2 , the distances of any two fundamental observers, i and j , change such that

$$\frac{\varrho_i(t_1)}{\varrho_j(t_1)} = \frac{\varrho_i(t_2)}{\varrho_j(t_2)} = \text{constant} , \quad (5.25)$$

that is,

$$\frac{\varrho_i(t_1)}{\varrho_i(t_2)} = \frac{\varrho_j(t_1)}{\varrho_j(t_2)} = \dots = \text{constant} = \frac{a(t_1)}{a(t_2)} . \quad (5.26)$$

For isotropic world models, $a(t)$ is a universal function known as the *scale factor* which describes how the relative distances between *any* two fundamental observers change with cosmic time t . Let us therefore adopt the following definitions. We set $a(t)$ equal to 1 at the present epoch t_0 and let the value of ϱ at the present epoch be r , that is, we can rewrite (5.26) as

$$\varrho(t) = a(t)r . \quad (5.27)$$

The term r thus becomes a *distance label* which is attached to a galaxy or fundamental observer for all time and the variation in proper distance in the expanding Universe is taken care of by the scale factor $a(t)$; r is called the *comoving radial distance coordinate*.

Proper distances perpendicular to the line of sight must also change by a factor a between the epochs t and t_0 because of the isotropy and homogeneity of the world model,

$$\frac{\Delta l(t)}{\Delta l(t_0)} = a(t) . \quad (5.28)$$

From the metric (5.24),

$$a(t) = \frac{R_c(t) \sin [\varrho/R_c(t)] d\theta}{R_c(t_0) \sin [r/R_c(t_0)] d\theta} . \quad (5.29)$$

Reorganising this equation and using (5.27), we see that

$$\frac{R_c(t)}{a(t)} \sin \left[\frac{a(t)r}{R_c(t)} \right] = R_c(t_0) \sin \left[\frac{r}{R_c(t_0)} \right] . \quad (5.30)$$

This is only true if

$$R_c(t) = a(t) R_c(t_0) , \quad (5.31)$$

that is, the radius of curvature of the spatial sections is proportional to the scale factor $a(t)$. Thus, in order to preserve isotropy and homogeneity, *the curvature of space changes as the Universe expands as $\kappa = R_c^{-2} \propto a^{-2}$* . Notice that κ cannot change sign and so, if the geometry of the Universe was once, say, hyperbolic, it will always remain so.

Let us call the value of $R_c(t_0)$, that is, the radius of curvature of the spatial geometry at the present epoch, \mathfrak{N} . Then

$$R_c(t) = a(t) \mathfrak{N}. \quad (5.32)$$

Substituting (5.27) and (5.32) into the metric (5.24), we obtain

$$ds^2 = dt^2 - \frac{a^2(t)}{c^2} [dr^2 + \mathfrak{N}^2 \sin^2(r/\mathfrak{N})(d\theta^2 + \sin^2 \theta d\phi^2)]. \quad (5.33)$$

This is the *Robertson–Walker metric* in the form we will use in much of our future analysis. Notice that it contains one unknown function $a(t)$, the scale factor, which describes the dynamics of the Universe and an unknown constant \mathfrak{N} which describes the spatial curvature of the Universe at the present epoch.

It is possible to rewrite this metric in different ways. For example, if we use a *comoving angular diameter distance* $r_1 = \mathfrak{N} \sin(r/\mathfrak{N})$, the metric becomes

$$ds^2 = dt^2 - \frac{a^2(t)}{c^2} \left[\frac{dr_1^2}{1 - kr_1^2} + r_1^2(d\theta^2 + \sin^2 \theta d\phi^2) \right], \quad (5.34)$$

where $\kappa = 1/\mathfrak{N}^2$. By a suitable rescaling of the r_1 coordinate $\kappa r_1^2 = r_2^2$, the metric can equally well be written

$$ds^2 = dt^2 - \frac{R_1^2(t)}{c^2} \left[\frac{dr_2^2}{1 - kr_2^2} + r_2^2(d\theta^2 + \sin^2 \theta d\phi^2) \right], \quad (5.35)$$

with $k = +1, 0$ and -1 for universes with spherical, flat and hyperbolic geometries respectively. Notice that, in this rescaling, the value of $R_1(t) = R_c(t_0)a = \mathfrak{N}a$ and so the value of $R_1(t)$ at the present epoch is \mathfrak{N} rather than unity. This is a popular form for the metric, but I will normally use (5.33) because the r coordinate has an obvious and important physical meaning.

The importance of the metrics (5.33), (5.34) and (5.35) is that they enable us to define the invariant interval ds^2 between events at any epoch or location in the expanding Universe. Let us recall the meanings of the various components and variables in the metric (5.33):

- The term t is cosmic time, that is, time as measured by a clock carried by a fundamental observer.
- The term r is the *comoving radial distance coordinate* which is fixed to a galaxy for all time and which is the proper distance the galaxy would have if its world line were projected forward to the present epoch t_0 and its distance measured at that time.
- The term $a(t) dr$ is the element of proper (or geodesic) distance in the radial direction at the epoch t .
- The term $a(t) [\mathfrak{N} \sin(r/\mathfrak{N})] d\theta = a(t) r_1 d\theta$ is the element of proper distance perpendicular to the radial direction subtended by the angle $d\theta$ at the origin.

- Similarly, $a(t) [\mathfrak{R} \sin(r/\mathfrak{R})] \sin \theta d\phi = a(t) r_1 \sin \theta d\phi$ is the element of proper distance in the ϕ -direction.

Notice that so far we have specified nothing about the physics which determines the rate of expansion of the Universe; this has all been absorbed into the function $a(t)$. Note the key point that, whatever the physics which determines the function $a(t)$, only the three types of isotropic geometry described by the Robertson–Walker metric are allowed and these types are fixed for all time, although the curvature changes as $a^{-2}(t)$.

5.5 Observations in Cosmology

Many of the most important results which relate the intrinsic properties of distant objects to their observed properties are independent of the specific cosmological model. It is therefore useful to produce a catalogue of results which describe how the observed properties of objects are related to their intrinsic properties and which are independent of the particular form of $a(t)$. First of all, let us elucidate the real meaning of redshift in cosmology.

5.5.1 The Cosmological Redshift

By cosmological redshift, we mean the shift of spectral lines to longer wavelengths associated with the isotropic expansion of the system of galaxies. If λ_e is the wavelength of the line as emitted and λ_0 the observed wavelength, the redshift z is defined to be

$$z = \frac{\lambda_0 - \lambda_e}{\lambda_e}. \quad (5.36)$$

If the redshift z were interpreted as the recession velocity v of a galaxy, these would be related by the Newtonian Doppler shift formula

$$v = cz. \quad (5.37)$$

This is the type of velocity which Hubble used in deriving the velocity–distance relation, $v = H_0 r$. As discussed in Sect. 2.3 and elaborated in Chap. 12, it is incorrect to use the special relativistic Doppler shift formula

$$1 + z = \left(\frac{1 + v/c}{1 - v/c} \right)^{1/2}, \quad (5.38)$$

at large redshifts. Rather, because of the requirements of isotropy and homogeneity, the relation $v \propto r$ applies at all comoving radial distances, including those at which the recession velocity would exceed the speed of light.

The key point is that the redshift has a much deeper meaning in cosmology, which we can demonstrate from an analysis of the Robertson–Walker metric. Consider a wave packet of frequency ν_1 emitted between cosmic times t_1 and $t_1 + \Delta t_1$ from a distant galaxy. This wave packet is received by an observer at the present epoch in the interval of cosmic time t_0 to $t_0 + \Delta t_0$. The signal propagates along null cones, $ds^2 = 0$, and so, considering radial propagation from source to observer, $d\theta = 0$ and $d\phi = 0$, the metric (5.33) gives us the relation

$$dt = -\frac{a(t)}{c} dr \quad \frac{c dt}{a(t)} = -dr . \quad (5.39)$$

Notice that $a(t) dr$ is simply the interval of proper distance at cosmic time t . The minus sign appears because the origin of the r coordinate is the observer at $t = t_0$. Considering first the leading edge of the wave packet, the integral of (5.39) is

$$\int_{t_1}^{t_0} \frac{c dt}{a(t)} = - \int_r^0 dr . \quad (5.40)$$

The end of the wave packet must travel the same distance in units of comoving distance coordinate since the r coordinate is fixed to the galaxy for all time. Therefore,

$$\int_{t_1 + \Delta t_1}^{t_0 + \Delta t_0} \frac{c dt}{a(t)} = - \int_r^0 dr , \quad (5.41)$$

that is,

$$\int_{t_1}^{t_0} \frac{c dt}{a(t)} + \frac{c \Delta t_0}{a(t_0)} - \frac{c \Delta t_1}{a(t_1)} = \int_{t_1}^{t_0} \frac{c dt}{a(t)} . \quad (5.42)$$

Since $a(t_0) = 1$, we find that

$$\Delta t_0 = \frac{\Delta t_1}{a(t_1)} . \quad (5.43)$$

This is the cosmological expression for the phenomenon of *time dilation*. Distant galaxies are observed at some earlier cosmic time t_1 when $a(t_1) < 1$ and so phenomena are observed to take longer in our frame of reference than they do in that of the source. The phenomenon is precisely the same as time dilation in special relativity, whereby, for example, relativistic muons, created at the top of the atmosphere, are observed to have longer lifetimes in the observer's frame as compared with their proper lifetimes.

The result (5.43) provides us with an expression for *redshift*. If $\Delta t_1 = \nu_1^{-1}$ is the period of the emitted waves and $\Delta t_0 = \nu_0^{-1}$ the observed period, then

$$\nu_0 = \nu_1 a(t_1) . \quad (5.44)$$

Rewriting this result in terms of redshift z ,

$$z = \frac{\lambda_0 - \lambda_e}{\lambda_e} = \frac{\lambda_0}{\lambda_e} - 1 = \frac{v_1}{v_0} - 1, \quad (5.45)$$

that is,

$$a(t_1) = \frac{1}{1+z}. \quad (5.46)$$

This is one of the most important relations in cosmology and displays the real meaning of the redshifts of galaxies. *Redshift is a measure of the scale factor of the Universe when the radiation was emitted by the source.* When we observe a galaxy with redshift $z = 1$, the scale factor of the Universe when the light was emitted was $a(t) = 0.5$, that is, the distances between fundamental observers (or galaxies) were half their present values. Note, however, that we obtain no information about *when* the light was emitted. If we did, we could determine directly from observation the function $a(t)$. Understanding of the astrophysical evolution of galaxies is improving all the time and it may eventually be possible to determine $a(t)$ in this way.

One important consequence of this calculation is that we can now derive an expression for the comoving radial distance coordinate r . Equation (5.40) can be written

$$r = \int_{t_1}^{t_0} \frac{c dt}{a(t)}. \quad (5.47)$$

Thus, once we know $a(t)$, we can immediately find r by integration. This integral emphasises the point that r is an artificial distance which depends upon how the Universe has expanded between the emission and reception of the radiation.

The expression (5.43) for the time dilation as a function of redshift provides a direct test of the Robertson–Walker formalism. The discovery that supernovae of Type Ia have a narrow dispersion in their absolute magnitudes and have exactly the same light curves, that is, the time-variation of their luminosities throughout the supernova outburst, has made these objects particularly important cosmological tools. Their properties and their use in determining cosmological parameters are described in more detail in Sect. 8.5.3. These standard properties become even more precisely defined when account is taken of a correlation between the maximum luminosity and the width of the light curve (Fig. 5.6). These supernovae have such great luminosities at maximum light that they can be observed at large redshifts. Figure 5.7a shows a plot of the width w of the light curves for a large sample of supernovae from the Calán-Tololo and Supernova Cosmology Program projects as a function of redshift z , or, more precisely, $(1+z)$ (Goldhaber et al., 2001). In the lower panel (Fig. 5.7b), the observed light curve width w has been divided by $(1+z)$ for each supernova. It can be seen that the observations are in excellent agreement with the expectations of (5.43).

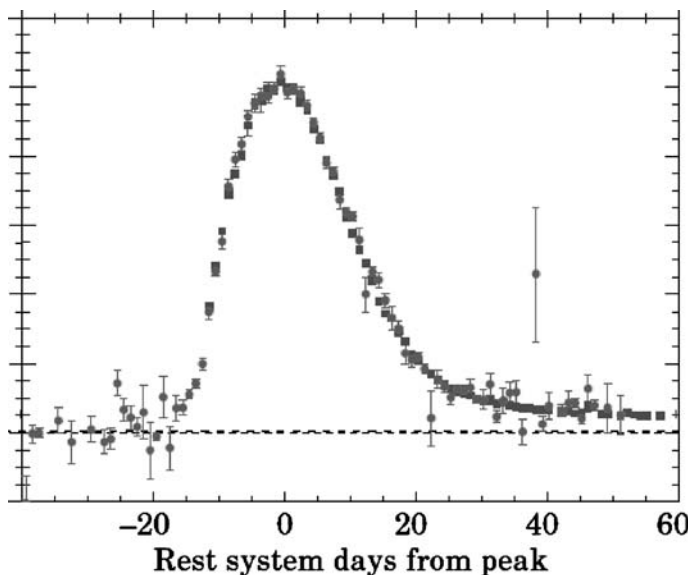


Fig. 5.6. The average time variation of the brightness of a Type Ia supernova from a large sample of supernovae observed in the Calán-Tololo and Supernova Cosmology Program projects. The light curves have been corrected for the effects of time dilation and the luminosity–width correlation (Goldhaber et al., 2001)

Another way of testing the time dilation relation using the remarkably standard properties of the Type Ia supernovae is to use their spectral evolution as a clock to compare the time evolution of low and high redshift supernovae. This test has been carried out for the supernova SN 1997ex, which had redshift 0.361, by members of the Supernova Cosmology Program team (Foley et al., 2005). The time between the first two spectra was 24.88 days and between the first and third spectra 30.95 days. The amount of aging in the supernova rest frame should be a factor of $1/(1+z)$ smaller corresponding to ages of 18.28 and 22.74 days. The spectral feature age technique applied to the Keck spectra observed for the supernova showed that the corresponding elapsed times in the supernova rest frame were 16.97 ± 2.75 and 18.01 ± 3.14 days, respectively, in excellent agreement with the expectations of cosmological time dilation. Similar results are found from the ESSENCE programme which involves a large consortium of the key players in the Type Ia supernova area (Wood-Vasey et al., 2007).

5.5.2 Hubble's Law

In terms of proper distances, Hubble's law can be written $v = H\varrho$ and so

$$\frac{d\varrho}{dt} = H\varrho . \quad (5.48)$$

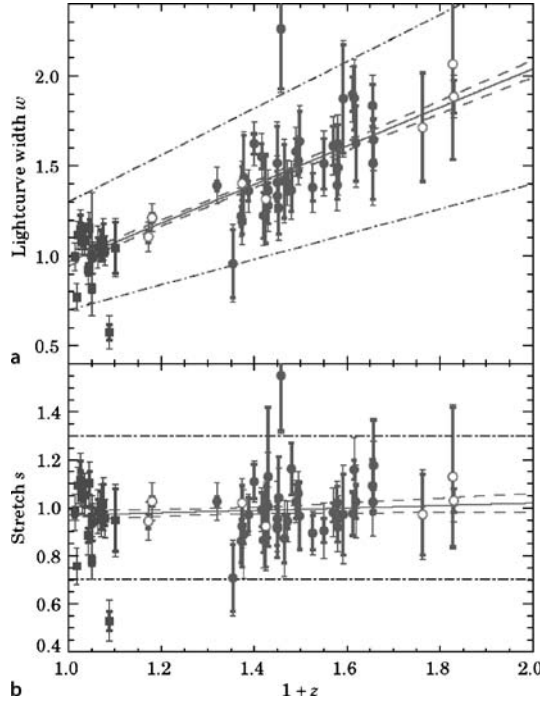


Fig. 5.7. **a** The observed width w of the light curves of Type 1a supernovae plotted against $(1+z)$. The *low redshift squares* are from the Calán-Tololo supernova programme and the *high redshift circles* are for a subset of 35 supernovae from the Supernova Cosmology Program (SCP). The *open circles* are for the remainder of the 42 SCP fully analyzed supernovae. The band delineated by the *dash-dotted lines* corresponds to stretch values 0.7 to 1.3 which encompass the bulk of the data, except for two outliers. The best-fitting linear relation and the 1σ limits are also shown. **b** The stretch s plotted against $(1+z)$. Stretch is defined as the observed light curve width w divided by $(1+z)$ for each supernova. The notation is the same as in **a** (Goldhaber et al., 2001)

We have written H rather than H_0 in Hubble's law since a 'Hubble's constant' H can be defined at any epoch as we show below. Substituting $\varrho = a(t)r$, we find that

$$r \frac{da(t)}{dt} = Ha(t)r , \quad (5.49)$$

that is,

$$H = \dot{a}/a . \quad (5.50)$$

Since we measure Hubble's constant H_0 at the present epoch, $t = t_0$, $a = 1$, we find

$$H_0 = (\dot{a})_{t_0} . \quad (5.51)$$

Thus, Hubble's constant H_0 defines the present expansion rate of the Universe. Notice that we can define a value of Hubble's constant at any epoch through the more general relation

$$H(t) = \dot{a}/a . \quad (5.52)$$

5.5.3 Angular Diameters

The great simplification which results from the use of the Robertson–Walker metric in the form (5.33) is apparent in working out the angular size of an object of proper length d perpendicular to the radial coordinate at redshift z . The relevant spatial component of the metric (5.33) is the term in $d\theta$. The proper length d of an object at redshift z , corresponding to scale factor $a(t)$, is given by the increment of proper length perpendicular to the radial direction in the metric (5.33), that is,

$$d = a(t) \mathfrak{N} \sin \left(\frac{r}{\mathfrak{N}} \right) \Delta\theta = a(t) D \Delta\theta = \frac{D \Delta\theta}{(1+z)} ; \quad (5.53)$$

$$\Delta\theta = \frac{d(1+z)}{D} , \quad (5.54)$$

where we have introduced a *distance measure* $D = \mathfrak{N} \sin(r/\mathfrak{N})$. For small redshifts, $z \ll 1$, $r \ll \mathfrak{N}$, (5.54) reduces to the Euclidean relation $d = r\Delta\theta$.

The expression (5.54) can also be written in the form

$$\Delta\theta = \frac{d}{D_A} , \quad (5.55)$$

so that the relation between d and $\Delta\theta$ looks like the standard Euclidean relation. To achieve this, we have to introduce another distance measure $D_A = D/(1+z)$ which is known as the *angular diameter distance* and which is often used in the literature.

Another useful calculation is the angular diameter of an object which continues to partake in the expansion of the Universe. This is the case for infinitesimal perturbations in the expanding Universe. A good example is the angular diameter which large-scale structures present in the Universe today would have subtended at an earlier epoch, say, the epoch of recombination, if they had simply expanded with the Universe. This calculation is used to work out physical sizes today corresponding to the angular scales of the fluctuations observed in the Cosmic Microwave Background Radiation. If the physical size of the object is $d(t_0)$ now and it expanded with the Universe, its physical size at redshift z was $d(t_0)a(t) = d(t_0)/(1+z)$. Therefore, the object subtended an angle

$$\Delta\theta = \frac{d(t_0)}{D} . \quad (5.56)$$

Notice that in this case the $(1+z)$ factor has disappeared from (5.53).

5.5.4 Apparent Intensities

Suppose a source at redshift z has luminosity $L(\nu_1)$ (measured in W Hz^{-1}), that is, the total energy emitted over 4π steradians per unit time per unit frequency interval. What is the flux density $S(\nu_0)$ of the source at the observing frequency ν_0 , that is, the energy received per unit time, per unit area and per unit bandwidth ($\text{W m}^{-2} \text{Hz}^{-1}$) where $\nu_0 = a(t_1)\nu_1 = \nu_1/(1+z)$? Suppose the source emits $N(\nu_1)$ photons of energy $h\nu_1$ in the bandwidth ν_1 to $\nu_1 + \Delta\nu_1$ in the proper time interval Δt_1 . Then the luminosity $L(\nu_1)$ of the source is

$$L(\nu_1) = \frac{N(\nu_1) h\nu_1}{\Delta\nu_1 \Delta t_1}. \quad (5.57)$$

These photons are distributed over a ‘sphere’ centred on the source at epoch t_1 and, when the ‘shell’ of photons arrives at the observer at the epoch t_0 , a certain fraction of them is intercepted by the telescope. The photons are observed at the present epoch t_0 with frequency $\nu_0 = a(t_1)\nu_1$, in a proper time interval $\Delta t_0 = \Delta t_1/a(t_1)$ and in the waveband $\Delta\nu_0 = a(t_1)\Delta\nu_1$.

We also need to know how the photons spread out over a sphere between the epochs t_1 and t_0 , that is, we must relate the diameter of our telescope Δl to the angular diameter $\Delta\theta$ which it subtends at the source at epoch t_1 . The metric (5.33) provides an elegant answer. The proper distance Δl refers to the present epoch at which $R(t) = 1$ and hence

$$\Delta l = D\Delta\theta, \quad (5.58)$$

where $\Delta\theta$ is the angle measured by a fundamental observer, located at the source.

We can also understand this result by considering how the photons emitted by the source spread out over solid angle $d\Omega$, as observed from the source in the curved geometry. If the Universe were not expanding, the surface area over which the photons would be observed at a time t after their emission would be

$$dA = R_c^2 \sin^2 \frac{x}{R_c} d\Omega, \quad (5.59)$$

where $x = ct$. In the expanding Universe, R_c changes as the Universe expands and so, in place of the expression x/R_c , we should write

$$\frac{1}{\mathfrak{R}} \int_{t_1}^{t_0} \frac{c dt}{a} = \frac{r}{\mathfrak{R}}, \quad (5.60)$$

where r is the comoving radial distance coordinate. Thus,

$$dA = \mathfrak{R}^2 \sin^2 \frac{r}{\mathfrak{R}} d\Omega. \quad (5.61)$$

Therefore, the diameter of the telescope as observed from the source is $\Delta l = D\Delta\theta$. Notice how the use of the comoving radial distance coordinate takes account of the

changing geometry of the Universe in this calculation. Notice also the difference between (5.54) and (5.58). They correspond to angular diameters measured in opposite directions along the light cone. The factor of $(1+z)$ difference between them is part of a more general relation concerning angular diameter measures along light cones which is known as the *reciprocity theorem*.

Therefore, the surface area of the telescope is $\pi \Delta l^2/4$ and the solid angle subtended by this area at the source is $\Delta\Omega = \pi \Delta\theta^2/4$. The number of photons incident upon the telescope in time Δt_0 is therefore

$$N(\nu_1) \Delta\Omega / 4\pi , \quad (5.62)$$

but they are now observed with frequency ν_0 . Therefore, the flux density of the source, that is, the energy received per unit time, per unit area and per unit bandwidth is

$$S(\nu_0) = \frac{N(\nu_1) h \nu_0 \Delta\Omega}{4\pi \Delta t_0 \Delta \nu_0 (\pi/4) \Delta l^2} . \quad (5.63)$$

We can now relate the quantities in (5.63) to the properties of the source, using (5.43) and (5.44)

$$S(\nu_0) = \frac{L(\nu_1) a(t_1)}{4\pi D^2} = \frac{L(\nu_1)}{4\pi D^2(1+z)} . \quad (5.64)$$

If the spectra of the sources are of power law form, $L(\nu) \propto \nu^{-\alpha}$, this relation becomes

$$S(\nu_0) = \frac{L(\nu_0)}{4\pi D^2(1+z)^{1+\alpha}} . \quad (5.65)$$

We can repeat the analysis for *bolometric* luminosities and flux densities. In this case, we consider the total energy emitted in a finite bandwidth $\Delta\nu_1$ which is received in the bandwidth $\Delta\nu_0$, that is

$$\begin{aligned} L_{\text{bol}} &= L(\nu_1) \Delta\nu_1 = 4\pi D^2 S(\nu_0) (1+z) \times \Delta\nu_0 (1+z) \\ &= 4\pi D^2 (1+z)^2 S_{\text{bol}} , \end{aligned} \quad (5.66)$$

where the bolometric flux density is $S_{\text{bol}} = S(\nu_0) \Delta\nu_0$. Therefore,

$$S_{\text{bol}} = \frac{L_{\text{bol}}}{4\pi D^2 (1+z)^2} = \frac{L_{\text{bol}}}{4\pi D_L^2} . \quad (5.67)$$

The quantity $D_L = D(1+z)$ is called the *luminosity distance* of the source since this definition makes the relation between S_{bol} and L_{bol} look like an inverse square law. The bolometric luminosity can be integrated over any suitable bandwidth so long as the corresponding redshifted bandwidth is used to measure the bolometric flux density at the present epoch,

$$\sum_{\nu_0} S(\nu_0) \Delta\nu_0 = \frac{\sum_{\nu_1} L(\nu_1) \Delta\nu_1}{4\pi D^2 (1+z)^2} = \frac{\sum_{\nu_1} L(\nu_1) \Delta\nu_1}{4\pi D_L^2} . \quad (5.68)$$

The formula (5.64) is the best expression for relating the observed intensity $S(\nu_0)$ to the intrinsic luminosity of the source $L(\nu_1)$. We can also write (5.67) in terms of the luminosity of the source at the observing frequency ν_0 as

$$S(\nu_0) = \frac{L(\nu_0)}{4\pi D_L^2} \left[\frac{L(\nu_1)}{L(\nu_0)}(1+z) \right], \quad (5.69)$$

but this now requires knowledge of the spectrum of the source $L(\nu)$. The last term in square brackets is a form of what is known as the *K-correction*. K-corrections were introduced by the pioneer optical cosmologists in the 1930s in order to ‘correct’ the apparent magnitude of distant galaxies for the effects of redshifting their spectra when observations are made through standard filters with a fixed mean observing frequency ν_0 (Sandage, 1961b). Taking logarithms and multiplying by -2.5 , we can write (5.69) in terms of absolute (M) and apparent (m) magnitudes through the relations $M = \text{constant} - 2.5 \log_{10} L(\nu_0)$ and $m = \text{constant} - 2.5 \log_{10} S(\nu_0)$. We find

$$M = m - 5 \log_{10}(D_L) - K(z) - 2.5 \log_{10}(4\pi), \quad (5.70)$$

where

$$K(z) = -2.5 \log_{10} \left[\frac{L(\nu_1)}{L(\nu_0)}(1+z) \right]. \quad (5.71)$$

This form of K-correction is correct for *monochromatic* flux densities and luminosities. In the case of observations in the optical waveband, apparent magnitudes are measured through standard filters which usually have quite wide pass-bands. Therefore, to determine the appropriate K-corrections, the spectral energy distribution of the galaxy has to be convolved with the transmission function of the filter in the rest frame and at the redshift of the galaxy. This is a straightforward calculation once the spectrum of the object is known.

Although I prefer to work directly with (5.64) and take appropriate averages, K-corrections are rather firmly established in the literature and it is often convenient to use the term to describe the effects of shifting the emitted spectrum into the observing wavelength window.

5.5.5 Number Densities

We often need to know the number of objects in a particular redshift interval, z to $z + dz$. Since there is a one-to-one relation between r and z , the problem is straightforward because, by definition, r is a radial proper distance coordinate defined *at the present epoch*. Therefore, the number of objects in the interval of comoving radial coordinate distance r to $r + dr$ is given by results already obtained in Sect. 5.3. The space–time diagram shown in Fig. 5.5 illustrates how we can evaluate the numbers of objects in the comoving distance interval r to $r + dr$ entirely by working in terms of *comoving volumes* at the present epoch. At the present epoch,

the radius of curvature of the spatial geometry is \mathfrak{N} and so the volume of a spherical shell of thickness dr at comoving distance coordinate r is

$$dV = 4\pi \mathfrak{N}^2 \sin^2(r/\mathfrak{N}) dr = 4\pi D^2 dr . \quad (5.72)$$

Therefore, if N_0 is the present space density of objects and their number is conserved as the Universe expands,

$$dN = N(z) dz = 4\pi N_0 D^2 dr . \quad (5.73)$$

The definition of comoving coordinates automatically takes care of the expansion of the Universe. Another way of expressing this result is to state that (5.73) gives the number density of objects in the redshift interval z to $z + dz$, assuming the *comoving number density* of the objects is unchanged with cosmic epoch. If, for some reason, the comoving number density of objects changes with cosmic epoch as, say, $f(z)$ with $f(z = 0) = 1$, then the number of objects expected in the redshift interval dz is

$$dN = N(z) dz = 4\pi N_0 f(z) D^2 dr . \quad (5.74)$$

5.5.6 The Age of the Universe

Finally, let us work out an expression for the age of the Universe, T_0 , from a rearranged version of (5.39). The basic differential relation is

$$-\frac{c dt}{a(t)} = dr , \quad (5.75)$$

and hence

$$T_0 = \int_0^{t_0} dt = \int_0^{r_{\max}} \frac{a(t) dr}{c} , \quad (5.76)$$

where r_{\max} is the comoving distance coordinate corresponding to $a = 0, z = \infty$.

5.6 Summary

The results we have derived can be used to work out the relations between intrinsic properties of objects and observables for any isotropic, homogeneous world model. Let us summarise the procedures described above:

1. First work out from theory, or otherwise, the function $a(t)$ and the curvature of space at the present epoch $\kappa = \mathfrak{N}^{-2}$. Once we know $a(t)$, we know the redshift–cosmic time relation.

2. Now work out the *comoving radial distance coordinate* r from the integral

$$r = \int_{t_1}^{t_0} \frac{c dt}{a(t)}. \quad (5.77)$$

Recall what this expression means: the proper distance interval $c dt$ at epoch t is projected forward to the present epoch t_0 by the scale factor $a(t)$. This integration yields an expression for r as a function of redshift z .

3. Next, work out the *distance measure* D from

$$D = \mathfrak{R} \sin \frac{r}{\mathfrak{R}}. \quad (5.78)$$

This relation determines D as a function of redshift z .

4. If so desired, the *angular diameter distance* $D_A = D/(1+z)$ and the *luminosity distance* $D_L = D(1+z)$ can be introduced to relate physical sizes and luminosities to angular diameters and flux densities respectively.
5. The number of objects dN in the redshift interval dz and solid angle Ω can be found from the expression

$$dN = \Omega N_0 D^2 dr, \quad (5.79)$$

where N_0 is the number density of objects at the present epoch which are assumed to be conserved as the Universe expands.

We will develop some explicit solutions for these functions in Chap. 7.

6 An Introduction to Relativistic Gravity

The standard world models which are used as the framework for astrophysical cosmology and for studying the problems of galaxy formation are based upon Einstein's General Theory of Relativity. General Relativity is a beautiful theory but it requires a thorough understanding of tensor calculus in four-dimensional non-Euclidean spaces to appreciate fully Einstein's epoch-making achievement. This is beyond the scope of the present text and so Sects. 6.1 to 6.5 are intended to provide some flavour of the full theory and to introduce some key ideas which will be needed later.¹ In Sect. 6.6, the experimental and observational status of General Relativity is reviewed and it is shown that it has triumphantly survived the many critical tests of the theory which have been devised since its inception in 1915.² If you are happy to accept General Relativity at its face value, you may advance to Chap. 7.

6.1 The Principle of Equivalence

As Einstein expressed it many years later:

I was sitting in a chair in the patent office in Bern when all of a sudden a thought occurred to me: 'If a person falls freely he will not feel his own weight'. I was startled. This simple thought made a deep impression upon me. It impelled me towards a theory of gravitation.

Expressed in more technical terms, a key consideration which led Einstein to the General Theory was the null result of the Eötvös experiment, which showed rather precisely that gravitational mass m_g is proportional to inertial mass m_I . Following Will's exposition (Will, 2006), the deviations from linearity can be written

$$m_g = m_I + \sum_A \frac{\eta^A E^A}{c^2}. \quad (6.1)$$

¹ I have given a more extended introduction to the theory in Chap. 17 of my book *Theoretical Concepts in Physics* (Longair, 2003). For an up-to-date physical exposition of General Relativity, the book *General Relativity: An Introduction for Physicists* by Hobson, Efstathiou and Lasenby can be recommended (Hobson et al., 2006).

² This assessment is based upon the superb article by Will published in *Living Reviews in Relativity* (Will, 2006).

E^A is the internal energy of the body generated by interaction A, η is a dimensionless parameter that measures the strength of the violation of the linearity of the relation between m_g and m_I induced by that interaction, and c is the speed of light. The internal energy terms include all the mass-energy terms which can contribute to the inertial mass of the body, for example, the body's rest energy, its kinetic energy, its electromagnetic energy, weak-interaction energy, binding energy and so on. If the inertial and gravitational masses were not exactly linearly proportional to each other, there would be a finite value η^A which would be exhibited as a difference in the accelerations of bodies of the same inertial mass composed of different materials. A measurement of, or limit to, the fractional difference in accelerations between two bodies yields the quantity known as the 'Eötvös ratio',

$$\eta = 2 \frac{|a_1 - a_2|}{a_1 + a_2} = \sum_A \eta^A \left(\frac{E_1^A}{m_1 c^2} - \frac{E_2^A}{m_2 c^2} \right), \quad (6.2)$$

where the subscript 'I' has been dropped from the inertial masses.

A summary of the limits to η from the time of Eötvös to the present day is shown in Fig. 6.1 which includes the famous torsion balance experiments of Eötvös, Dicke, Braginsky and their collaborators. From the late 1980s onwards, numerous experiments were carried out primarily to search for a "fifth force" but their null results also provided limits to the Eötvös ratio. For example, as discussed by Will, the "Eöt-Wash" experiments carried out at the University of Washington used a sophisticated torsion balance tray to compare the accelerations of various materials toward local topographical features on Earth, movable laboratory masses, the Sun and the Galaxy and provided limits of $\eta \leq 3 \times 10^{-13}$. Thus, gravitational mass m_g is proportional to inertial mass m_I to better than one part in 3×10^{12} .

The principle of equivalence asserts that the gravitational field \mathbf{g} at any point in space can be precisely replaced by an accelerated frame of reference \mathbf{a} . In Newton's terminology, 'mass' is proportional to 'weight'. The statement that, locally inertial and gravitational mass are the same is known as the *weak equivalence principle*. Einstein's version of the principle is much stronger. In his own words:

All local, freely falling, non-rotating laboratories are fully equivalent for the performance of all physical experiments.

By *free-fall*, we mean a frame of reference which is accelerated at the local gravitational acceleration at that point in space, $\mathbf{a} = \mathbf{g}$. This statement formally identifies inertial and gravitational mass, since the force acting on a particle in a gravitational field depends upon the particle's *gravitational mass*, whereas the acceleration depends upon its *inertial mass*.

A more transparent statement of the principle is given by Will who clarifies exactly what is assumed in what he calls the *Einstein equivalence principle*. In Will's words:

The Einstein equivalence principle (EEP) is a more powerful and far-reaching concept; it states that:

1. The weak equivalence principle is valid.

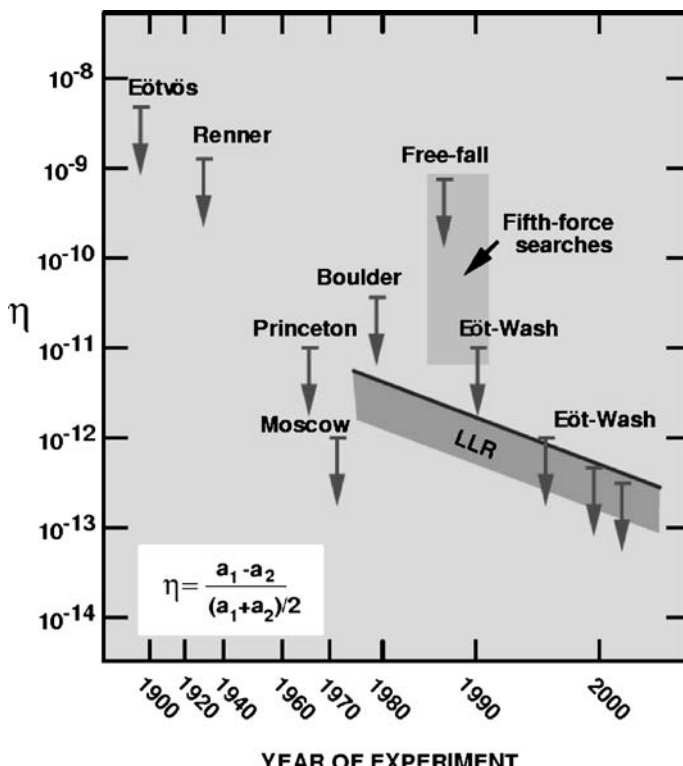


Fig. 6.1. Selected tests of the weak equivalence principle, showing bounds on η , which measures the fractional differences in accelerations of different materials or bodies. The free-fall and Eöt-Wash experiments were originally performed to search for a fifth force (*light grey region*, representing many experiments). The *dark grey band* shows bounds on η for gravitating bodies from lunar laser ranging (LLR) (Will, 2006)

2. The outcome of any local non-gravitational experiment is independent of the velocity of the freely falling reference frame in which it is performed.
3. The outcome of any local non-gravitational experiment is independent of where and when in the universe it is performed.

The second piece of EEP is called local Lorentz invariance (LLI), and the third piece is called local position invariance (LPI).

The importance of this description of the assumptions behind the General Theory of Relativity is that it makes clear the scope for developing alternative theories of relativistic gravity. Thus, if either (2) or (3) were to be relaxed, a much wider range of possible theories of relativistic gravity could be developed and these are illustrated by the range of additional parameters listed in Table 6.1. For our modest ambitions in this chapter, we simply use the parameterised post-Newtonian (PPN) coefficients listed in Table 6.1 as measures of the success of standard General Relativity.

Table 6.1. The PPN parameters and their significance (note that α_3 has been shown twice to indicate that it is a measure of two effects)

Parameter	What it measures relative to General Relativity	Value in General Relativity	Value in semi-conservative theories	Value in fully conservative theories
γ	How much space-curvature is produced by unit rest mass?	1	γ	γ
β	How much ‘non-linearity’ in the superposition law for gravity?	1	β	β
ξ	Preferred-location effects?	0	ξ	ξ
α_1	Preferred-frame effects?	0	α_1	0
α_2		0	α_2	0
α_3		0	0	0
α_3	Violation of conservation of total momentum?	0	0	0
ζ_1		0	0	0
ζ_2		0	0	0
ζ_3		0	0	0
ζ_4		0	0	0

The principle of equivalence has profound consequences for our understanding of the nature of space and time in a gravitational field. Let us illustrate some of these by two elementary examples.

6.2 The Gravitational Redshift

In the first example, we replace a stationary frame of reference located in a uniform gravitational field \mathbf{g} by a frame of reference which is accelerated in the opposite direction. Consider a light wave of frequency ν propagating from the ceiling to the floor of a lift in a gravitational field $\mathbf{g} = -\mathbf{a}$ (Fig. 6.2).

We assume that the acceleration is small. If the height of the lift is h , a light signal travels from the ceiling to the floor in a time $t = h/c$. According to the principle of equivalence, we can replace the gravitational field by an accelerated frame of reference and so, after time t , the floor is accelerated to a speed $u = at = |\mathbf{g}|t$. Hence,

$$u = \frac{|\mathbf{g}|h}{c}. \quad (6.3)$$

Therefore, the light wave is observed with a higher frequency when it arrives at the floor of the lift because of the Doppler effect. To first order in u/c , the observed frequency ν' is

$$\nu' = \nu \left(1 + \frac{u}{c} \right) = \nu \left(1 + \frac{|\mathbf{g}|h}{c^2} \right). \quad (6.4)$$

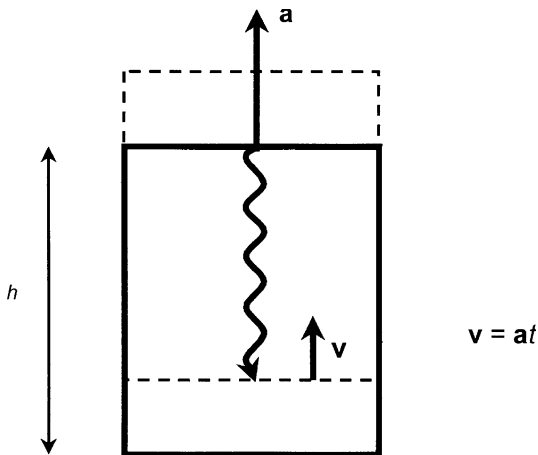


Fig. 6.2. Illustrating the gravitational redshift/blueshift of an electromagnetic wave propagating from the ceiling to the floor of a stationary lift in a gravitational field according to the principle of equivalence

Let us now express this result in terms of the change in gravitational potential between the ceiling and floor of the lift. Since $\mathbf{g} = -\text{grad } \phi$

$$|\mathbf{g}| = -\frac{\Delta\phi}{h}. \quad (6.5)$$

Notice that, because of the attractive nature of the gravitational force, ϕ is more negative at $h = 0$ than at the ceiling. Therefore,

$$v' = v \left(1 - \frac{\Delta\phi}{c^2}\right). \quad (6.6)$$

This is the formula for the *gravitational redshift* z_g in the ‘Newtonian’ limit. Recalling the definition of redshift,

$$z = \frac{\lambda_{\text{obs}} - \lambda_{\text{em}}}{\lambda_{\text{em}}} = \frac{v - v'}{v}, \quad (6.7)$$

we find that

$$z_g = \frac{\Delta\phi}{c^2}. \quad (6.8)$$

In this simple example, since $\Delta\phi$ is negative, z_g is also negative corresponding to a gravitational blueshift rather than redshift. If the light waves propagated from the floor to the ceiling, we would obtain a redshift of the same magnitude. Thus, the frequency of the waves depends upon to the *gravitational potential* in which the light waves are propagated.

A test of the expression (6.8) for the gravitational redshift was proposed by Eddington in 1924. He estimated that the gravitational redshift of the lines in the spectrum of the white dwarf star Sirius B should be $cz_g = 20 \text{ km s}^{-1}$. The value measured by Adams in 1925 was 19 km s^{-1} . Eddington was jubilant (Eddington, 1926):

Prof. Adams has thus killed two birds with one stone. He has carried out a new test of Einstein's theory of General Relativity, and has shown that matter at least 2000 times denser than platinum is not only possible, but actually exists in the stellar universe.

Laboratory experiments to measure the gravitational redshift were carried out by Pound, Rebka and Snider who measured the difference in redshift of γ -ray photons moving up then down a tower 22.5 m high at Harvard University using the Mössbauer effect (Pound and Rebka, 1960; Pound and Snider, 1965). In this effect, the recoil effects of the emission and absorption of the γ -ray photons are zero since the momentum is absorbed by the whole atomic lattice. The γ -ray resonance is therefore very sharp indeed and only tiny Doppler shifts are needed to move off resonance absorption. In the Harvard experiment, the difference in redshifts for γ -ray photons moving up and down the tower was:

$$z_{\text{up}} - z_{\text{down}} = \frac{2gh}{c^2} = 4.905 \times 10^{-15}. \quad (6.9)$$

The measured value was $(4.900 \pm 0.037) \times 10^{-15}$, a precision of about 1%. Notice the key point that the gravitational redshift is incompatible with special relativity, according to which the observers at the top and bottom of the tower are at rest in the same inertial frame of reference.

Suppose we now write (6.6) in terms of the period of the waves T . Then,

$$T' = T \left(1 + \frac{\Delta\phi}{c^2} \right). \quad (6.10)$$

This expression is exactly the same as the time dilation formula between inertial frames of reference in special relativity, only now the expression refers to different locations in the gravitational field. This expression for time dilation is exactly what would be evaluated for any time interval and so we can write in general

$$dt' = dt \left(1 + \frac{\Delta\phi}{c^2} \right). \quad (6.11)$$

Let us now take the gravitational potential to be zero at infinity and measure the gravitational potential at any point in the field relative to that value. We assume that we are in the weak field limit in which changes in the gravitational potential are small. Then, at any point in the gravitational field, we can write

$$dt'^2 = dt^2 \left[1 + \frac{\phi(r)}{c^2} \right]^2, \quad (6.12)$$

where dt is the time interval measured at $\phi = 0$, that is, at $r = \infty$. Since $\phi(r)/c^2$ is small, we can write this expression as

$$dt'^2 = dt^2 \left[1 + \frac{2\phi(r)}{c^2} \right]. \quad (6.13)$$

If we now adopt the Newtonian expression for the gravitational potential for a point mass M ,

$$\phi(r) = -\frac{GM}{r}, \quad (6.14)$$

we find

$$dt'^2 = dt^2 \left(1 - \frac{2GM}{rc^2}\right). \quad (6.15)$$

Let us now introduce this expression for the time interval into the standard Minkowski metric of special relativity,

$$ds^2 = dt'^2 - \frac{1}{c^2} dl^2, \quad (6.16)$$

where dl is the differential element of proper distance. The metric of space–time about the point mass can therefore be written as

$$ds^2 = dt^2 \left(1 - \frac{2GM}{rc^2}\right) - \frac{1}{c^2} dl^2. \quad (6.17)$$

This calculation shows how the metric coefficients become more complicated than those of Minkowski space–time when we attempt to derive a relativistic theory of gravity. Notice how careful we have to be about keeping track of time in General Relativity. The time interval measured by an observer at a point in the gravitational field is dt' ; the interval dt is a time interval at infinity. The gravitational redshift relates these differences in time keeping. Notice further that both of these are different from the time measured by an observer in free-fall in the gravitational field.

6.3 The Bending of Light Rays

Let us show how the expression for dl has to be changed as well. Consider the propagation of light rays in our lift but now travelling perpendicular to the gravitational acceleration. We again use the principle of equivalence to replace the stationary lift in a gravitational field by an accelerated lift in free space (Fig. 6.3).

In the time the light ray propagates across the lift, a distance l , the lift moves upwards a distance $\frac{1}{2}|{\mathbf g}|t^2$. Therefore, in the frame of reference of the accelerated lift, and also in the stationary frame in the gravitational field, the light ray follows a parabolic path as illustrated in Figs. 6.3a–c. Let us approximate the light path by a circular arc of radius R . The length of the chord d across the circle is then

$$d^2 = \frac{1}{4}|{\mathbf g}|^2 t^4 + l^2. \quad (6.18)$$

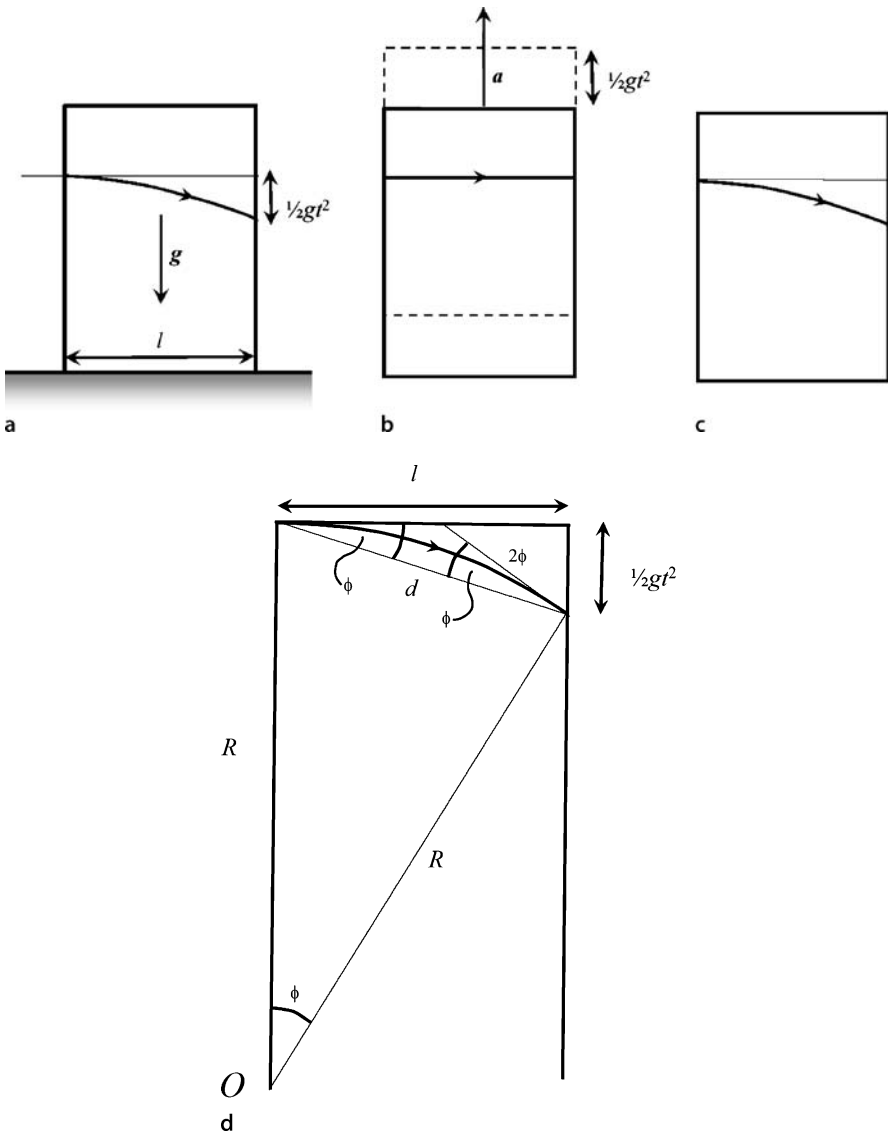


Fig. 6.3a–d. Illustrating the application of the principle of equivalence to the propagation of a light ray in a gravitational field and in a uniformly accelerated lift. In the equivalent accelerated frame of reference, the light ray travels along a curved path

Now, from the geometry of the diagram, it can be seen that $\phi = |\mathbf{g}|t^2/2l$. Hence, since $R\phi = d$,

$$R^2 = \frac{d^2}{\phi^2} = l^2 + \frac{4l^4}{|\mathbf{g}|^2 t^4}. \quad (6.19)$$

Now, $\frac{1}{2}|\mathbf{g}|t^2 \ll l$, $l = ct$ and so the second term in (6.19) is much larger than the first. Therefore,

$$R = \frac{2l^2}{|\mathbf{g}|t^2} = \frac{2c^2}{|\mathbf{g}|}. \quad (6.20)$$

Thus, the radius of curvature of the path of the light ray depends only upon the local gravitational acceleration $|\mathbf{g}|$. Since \mathbf{g} is determined by the gradient of the gravitational potential, it follows that the *curvature of the paths of light rays depends upon the mass distribution*.

6.4 Further Complications

The consequences of these two elementary calculations are that the rate at which clocks tick depends upon the gravitational potential in which they are located and the paths of light rays are bent by the gravitational influence of the mass-energy distribution. In other words, not only is space curved but, more generally, *space-time* is curved. Neither the space nor time coordinates take the simple ‘Euclidean’ values which appear in the Minkowski metric, which can be written in polar coordinates

$$ds^2 = dt^2 - \frac{1}{c^2} [dr^2 + r^2(d\theta^2 + \sin^2 \theta d\phi^2)]. \quad (6.21)$$

It must be emphasised that the arguments of Sects. 6.2 and 6.3 are *illustrative* of how Newtonian gravity has to be modified to incorporate the principle of equivalence and the rules of special relativity and many unsatisfactory steps were involved.

To complicate matters further, any relativistic theory of gravity must be non-linear. This follows from Einstein’s mass-energy relation $E = mc^2$ as applied to the gravitational field. The gravitational field due to some mass distribution has a certain local energy density at each point in space. Since $E = mc^2$, it follows that there is a certain inertial mass density in the gravitational field which is itself a source of gravitational field. This property contrasts with that of, say, an electric field distribution. This possesses a certain amount of electromagnetic field energy and a corresponding inertial mass density but this does not generate additional electrostatic charge. Thus, relativistic gravity is intrinsically a non-linear theory and this accounts for a great deal of its complexity.

This feature of relativistic gravity was recognised by Einstein in 1912. From his student days, he vaguely remembered Gauss’s theory of surfaces and consulted his old school friend, the mathematician Marcel Grossmann, about the most general forms of transformation between frames of reference for metrics of the form

$$ds^2 = g_{\mu\nu} dx^\mu dx^\nu. \quad (6.22)$$

Although outside Grossmann's field of expertise, he soon came back with the answer that the most general transformation formulae were the Riemannian geometries, but that they had the 'bad feature' that they are non-linear. Einstein instantly recognised that, on the contrary, this was a great advantage since any satisfactory theory of relativistic gravity must be non-linear.

Finally, although we can eliminate the *acceleration* due to gravity at a particular point in space, we cannot eliminate completely the effects of gravity in the vicinity of that point. This is most easily seen by considering the gravitational field at distance r from a point mass M (Fig. 6.4). It is apparent that we need different freely falling lifts at different points in space in order to eliminate gravity everywhere. Even over very limited regions of space, if we make very precise measurements, neighbouring particles will be observed to begin to move under the influence of the quadrupole field which cannot be eliminated by transforming to a single accelerated reference frame. As an example, consider a standard Euclidean (x, y, z) coordinate frame inside an orbiting Space Station, the z -coordinate being taken in the radial direction. It is a useful exercise to show that, if two test particles are released from rest, with

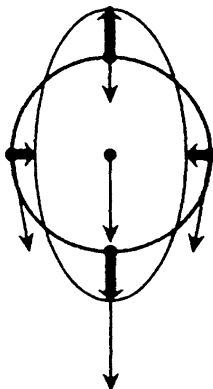


Fig. 6.4. Illustrating the 'tidal forces' which cannot be eliminated when the acceleration due to gravity \mathbf{g} is replaced by an accelerated reference frame at a particular point in space. In this example, the observer is in centrifugal equilibrium in the field of a point mass. Initially, test masses are located on a sphere about the observer. At a later time, the sphere is distorted into an ellipsoid because of the tidal forces which cannot be eliminated when transforming away the gravitational field at the observer (Penrose, 1997)

an initial separation vector ξ , this separation vector varies with time as

$$\frac{d^2}{dt^2} \begin{bmatrix} \xi^x \\ \xi^y \\ \xi^z \end{bmatrix} = \begin{bmatrix} -GM/r^3 & 0 & 0 \\ 0 & -GM/r^3 & 0 \\ 0 & 0 & +2GM/r^3 \end{bmatrix} \begin{bmatrix} \xi^x \\ \xi^y \\ \xi^z \end{bmatrix}. \quad (6.23)$$

The pleasant aspect of this analysis is that it can be seen that the uncompensated forces depend upon r^{-3} . This is the part of the gravitational field which cannot be eliminated by transforming to a single freely falling frame. Notice that it has the form of a ‘tidal force’, which depends upon r^{-3} , of exactly the same type which causes Earth–Moon and Earth–Sun tides. We therefore need a theory which reduces locally to Einstein’s special relativity in a freely falling frame and which transforms correctly into another freely falling reference frame when we move to a different point in space. There is no such thing as a global Lorentz frame in the presence of a non-uniform gravitational field.

Einstein’s General Relativity enables us to find the metric of space–time in the presence of mass-energy. The simplest example is the metric of space–time about a point mass of mass M , the *Schwarzschild metric*, which can be written

$$ds^2 = dt^2 \left(1 - \frac{2GM}{rc^2}\right) - \frac{1}{c^2} \left[\frac{dr^2}{\left(1 - \frac{2GM}{rc^2}\right)} + r^2(d\theta^2 + \sin^2\theta^2 d\phi^2) \right], \quad (6.24)$$

where the metric has been written in spherical polar coordinates. The Schwarzschild metric is *exact* for a stationary point mass in General Relativity. Some elements of the Schwarzschild metric are similar to those which were derived in our approximate analyses. For example, the increment of *proper time* is

$$dt' = dt \left(1 - \frac{2GM}{rc^2}\right)^{1/2}, \quad (6.25)$$

and has the same properties which we derived above, namely, the *coordinate time* t keeps track of how clocks measure time at infinity. Clocks closer to the origin run slower relative to clocks at infinity by the factor $(1 - 2GM/rc^2)^{1/2}$. This enables us to derive the general expression for *gravitational redshift*. The period of the light waves changes by precisely this factor as the light ray propagates from radius r from the point mass to infinity. Therefore, the change of frequency is

$$\nu' = \nu \left(1 - \frac{2GM}{rc^2}\right)^{-1/2}, \quad (6.26)$$

where ν is the frequency measured at infinity. Thus, the redshift z of the radiation is

$$z_g = \frac{\lambda_{\text{obs}} - \lambda_{\text{em}}}{\lambda_{\text{em}}} = \frac{\lambda_{\text{obs}}}{\lambda_{\text{em}}} - 1 = \left(1 - \frac{2GM}{rc^2}\right)^{-1/2} - 1, \quad (6.27)$$

or

$$1 + z_g = \left(1 - \frac{2GM}{rc^2}\right)^{-1/2}. \quad (6.28)$$

Light rays emitted from the *Schwarzschild radius* $r_g = 2GM/c^2$ are shifted to infinite wavelengths.³

6.5 The Route to General Relativity

Einstein's great achievement was to understand how the features discussed in Sects. 6.1 to 6.4 could be incorporated into a self-consistent theory of relativistic gravity. The remarkable story of Einstein's struggles to discover the theory is told in some detail by Abraham Pais in his splendid scientific biography of Einstein *Subtle is the Lord ...* (Pais, 1982). This is not the place to go into the technical details of what Einstein did. In summary, his thinking was guided by four ideas:

- The influence of gravity on light
- The principle of equivalence
- Riemannian space–time
- The principle of covariance

My recommended approach would be to begin with Rindler's excellent introductory text *Relativity: Special, General, and Cosmological* (Rindler, 2001), and then proceed to either Weinberg's *Gravitation and Cosmology* or Hobson, Efstathiou and Lasenby's *General Relativity: An Introduction for Physicists*, which both describe clearly why General Relativity has to be as complex as it is. In both books the physical content of the theory and the mathematics are elucidated at each stage (Weinberg, 1972; Hobson et al., 2006). Another useful recommendation is d'Inverno's *Introducing Einstein's Relativity* which is particularly clear on the geometric aspects of the theory (d'Inverno, 1992). The understanding of the theory requires considerable effort. Let me outline some of the key steps in its formal development.

6.5.1 Four-Tensors in Relativity

In formulating the Special Theory of Relativity, Einstein realised that all the laws of physics, with the exception of gravity, could be written in Lorentz-invariant form. By this, we mean that the equations are *form-invariant* under Lorentz transformations:

³ I have given further examples of the use of the Schwarzschild metric to derive expressions for light deflection by point masses and the advance of the perihelion of planetary orbits, as well as an introduction to Schwarzschild black holes, in Chap. 17 of my book *Theoretical Concepts in Physics* (Longair, 2003).

this is often called *Lorentz covariance*. The simplest example is the introduction of *four-vectors* into special relativity; these are designed to be objects which are form-invariant under Lorentz transformations. Just for this subsection, we use the notation used by professional relativists in which the velocity v is measured in units of the speed of light, equivalent to setting the value of $c = 1$. Then, the time coordinate $x^0 = t$ and the spatial components are $x = x^1$, $y = x^2$ and $z = x^3$. As a result, we can write the transformation of a four-vector V^α between two inertial frames of reference in standard configuration in the form

$$V^\alpha \rightarrow V'^\alpha = \Lambda_\beta^\alpha V^\beta , \quad (6.29)$$

where the matrix Λ_β^α is the standard Lorentz transformation

$$\Lambda_\beta^\alpha = \begin{bmatrix} \gamma & -\gamma v & 0 & 0 \\ -\gamma v & \gamma & 0 & 0 \\ 0 & 0 & 1 & 0 \\ 0 & 0 & 0 & 1 \end{bmatrix} , \quad (6.30)$$

and $\gamma = (1 - v^2/c^2)^{-1/2}$. The convention of summing over identical indices is adopted in (6.29). Some familiar examples of four-vectors are listed in Table 6.2, along with their translations into more familiar quantities.

Many physical quantities are naturally described in terms of tensors rather than vectors. The natural extension of the concept of four-vectors is then to *four-tensors* which are objects which transform according to the rule

$$T^{\alpha\gamma} \rightarrow T'^{\alpha\gamma} = \Lambda_\beta^\alpha \Lambda_\delta^\gamma T^{\beta\delta} . \quad (6.31)$$

For example, relativists call matter without any internal pressure ‘dust’ and the *energy-momentum tensor* for dust is $T^{\alpha\beta} = \varrho_0 u^\alpha u^\beta$, where ϱ_0 is the proper mass density of the dust, meaning the density measured by an observer moving with the flow, or a comoving observer; u^α is the velocity four-vector. Writing out the

Table 6.2. Examples of common four-vectors. The second column gives the four-vector notation used in this section. The third column translates the components of the four-vectors into more familiar quantities. In all cases, $c = 1$ and $\gamma = (1 - v^2/c^2)^{-1/2}$

Displacement four-vector	$[x^0, x^1, x^2, x^3]$	$[t, x, y, z]$
Velocity four-vector	$[v^0, v^1, v^2, v^3]$	$[\gamma, \gamma v_x, \gamma v_y, \gamma v_z]$
Momentum four-vector	$[p^0, p^1, p^2, p^3]$	$[\gamma m_0, \gamma m_0 v_x, \gamma m_0 v_y, \gamma m_0 v_z]$
Acceleration four-vector	$[a^0, a^1, a^2, a^3]$	$\left[\gamma \frac{d\gamma}{dt}, \gamma \frac{d(\gamma v_x)}{dt}, \gamma \frac{d(\gamma v_y)}{dt}, \gamma \frac{d(\gamma v_z)}{dt} \right]$
Frequency four-vector	$[k^0, k^1, k^2, k^3]$	$[\omega, k_x, k_y, k_z]$
Four-momentum of photon	$[p^0, p^1, p^2, p^3]$	$[\hbar\omega, \hbar k_x, \hbar k_y, \hbar k_z]$

components of $T^{\alpha\beta}$ in terms of the quantities in the third column of Table 6.2, we find

$$T^{\alpha\beta} = \gamma^2 \varrho_0 \begin{bmatrix} 1 & u_x & u_y & u_z \\ u_x & u_x^2 & u_y u_x & u_z u_x \\ u_y & u_x u_y & u_y^2 & u_z u_y \\ u_z & u_x u_z & u_y u_z & u_z^2 \end{bmatrix}, \quad (6.32)$$

where (u_x, u_y, u_z) are the components of the three-velocity measured in the chosen reference frame. It is instructive to note the form of the T^{00} component of this four-tensor, $T^{00} = \gamma^2 \varrho_0$, which corresponds to the total energy density. This quantity has a natural interpretation in special relativity. The observed density of the dust ϱ as it moves with the flow is increased by two powers of the Lorentz factor γ over the proper value ϱ_0 . One of these is associated with the formula for the relativistic three-momentum of the dust, $p = \gamma m \mathbf{u}$, and the other with length contraction in the direction of motion of the dust, $l = l_0/\gamma$.

When the pressure cannot be neglected, the energy-momentum tensor becomes

$$T^{\alpha\beta} = (\varrho_0 + p)u^\alpha u^\beta - pg^{\alpha\beta}, \quad (6.33)$$

where $g^{\alpha\beta}$ is the metric tensor, which in the case of special relativity is the matrix

$$g^{\alpha\beta} = \begin{bmatrix} 1 & 0 & 0 & 0 \\ 0 & -1 & 0 & 0 \\ 0 & 0 & -1 & 0 \\ 0 & 0 & 0 & -1 \end{bmatrix}. \quad (6.34)$$

Then, it is a pleasant exercise to show that the equation

$$\partial_\beta T^{\alpha\beta} = 0, \quad (6.35)$$

expresses the laws of conservation of momentum and energy in relativity, where ∂_β means partial differentiation of the tensor components with respect to β and so the operator ∂_β has the form

$$[\partial/\partial x_0, \partial/\partial x_1, \partial/\partial x_2, \partial/\partial x_3]. \quad (6.36)$$

Maxwell's equations in a vacuum can be written in compact form in terms of the antisymmetric electromagnetic field tensor $F^{\alpha\beta}$

$$F^{\alpha\beta} = \begin{bmatrix} 0 & E_x & E_y & E_z \\ -E_x & 0 & B_z & -B_y \\ -E_y & -B_z & 0 & B_x \\ -E_z & B_y & -B_x & 0 \end{bmatrix}, \quad (6.37)$$

and the current density four-vector $j^\alpha = [\varrho_e, \mathbf{j}]$. I apologise for deviating from my normal practice of using strictly SI units. This form of Maxwell's equations is written

in Heaviside–Lorentz units with $c = 1$. The equation of continuity becomes

$$\partial_\alpha j^\alpha = 0 . \quad (6.38)$$

Maxwell's equations for the relations between electric and magnetic fields and their sources become

$$\partial_\beta F^{\alpha\beta} = j^\alpha . \quad (6.39)$$

Thus, four-tensors provide the natural language for expressing the laws of physics in a form which guarantees that they transform correctly according to the Lorentz transformations.

6.5.2 What Einstein Did

The elementary considerations of Sects. 6.1 to 6.4 indicate that the aim of General Relativity is to incorporate the influence of the mass-energy distribution upon space–time into the metric coefficients $g_{\mu\nu}$. The metric of space–time locally has to reduce to the standard Minkowski metric

$$ds^2 = dt^2 - \frac{1}{c^2} dl^2 . \quad (6.40)$$

Therefore, the natural starting point for the development of general transformations between arbitrary four-dimensional spaces is the *Riemannian metric* of form

$$ds^2 = \sum_{\mu,\nu} g_{\mu\nu} dx^\mu dx^\nu = g_{\mu\nu} dx^\mu dx^\nu , \quad (6.41)$$

where the coordinates x^μ and x^ν define points in four-dimensional space and the interval ds^2 is given by a homogeneous quadratic differential form in these coordinates. The components of the *metric tensor* $g_{\mu\nu}$ vary from point-to-point in space–time and define its local curvature. Since the local curvature defines the properties of the gravitational field, the $g_{\mu\nu}$ can be thought of as being analogous to gravitational potentials.

We need to develop a way of relating the $g_{\mu\nu}$ to the mass-energy distribution, that is, to find the analogue of Poisson's equation in Newtonian gravity which involves second-order partial differential equations. As an illustrative example, in deriving (6.13), we rationalised that g_{00} should have the form

$$g_{00} = \left(1 + \frac{2\phi}{c^2} \right) , \quad (6.42)$$

(see also the Schwarzschild metric (6.24)). Poisson's equation for gravity is

$$\nabla^2 \phi = 4\pi G \varrho , \quad (6.43)$$

and hence, from (6.42) and (6.43), we find that

$$\nabla^2 g_{00} = \frac{8\pi G}{c^2} T_{00}. \quad (6.44)$$

This is a crude calculation but it shows why it is reasonable to expect a close relation between the derivatives of $g_{\mu\nu}$ and the corresponding components of the energy-momentum tensor $T_{\mu\nu}$.

The tensor equivalent of this analysis involves the differentiation of tensors and this is where the complications begin: partial differentiation of tensors does not generally yield other tensors. Thus, the definitions of the equivalent vector operations of grad, div and curl are correspondingly more complicated for tensors as compared with vectors. Furthermore, the analysis can no longer be carried out in Minkowski space-time since space-time is necessarily curved. How this problem was solved and the components of the metric tensor $g_{\mu\nu}$ are related to the energy-momentum tensor $T_{\mu\nu}$ was Einstein's extraordinary achievement of the years 1912 to 1915.

What is needed is a tensor which involves the metric tensor $g_{\mu\nu}$ and its first and second derivatives and which is linear in its second derivatives. It turns out that there is a unique answer to this problem: it is the fourth-rank tensor $R_{\mu\nu\lambda}^{\lambda}$ which is known as the *Riemann–Christoffel tensor*. Other tensors can be formed from this tensor by contraction, the most important of these being the *Ricci tensor*

$$R_{\mu\nu} = R_{\mu\lambda\nu}^{\lambda}, \quad (6.45)$$

and the *curvature scalar*

$$R = g^{\mu\nu} R_{\mu\nu}. \quad (6.46)$$

Einstein's stroke of genius was to propose that these tensors are related to the energy-momentum tensor in the following way

$$R_{\mu\nu} - \frac{1}{2} g_{\mu\nu} R = -\frac{8\pi G}{c^2} T_{\mu\nu}. \quad (6.47)$$

This is the key relation which shows how the components of the metric tensor $g_{\mu\nu}$ are related to the mass-energy distribution $T_{\mu\nu}$ in the Universe.

We will go no further along this route, except to note that Einstein realised that he could add an additional term to the left-hand side of (6.47). This is the origin of the famous cosmological constant Λ and was originally introduced in order to construct a static closed model for the Universe. Equation (6.47) then becomes

$$R_{\mu\nu} - \frac{1}{2} g_{\mu\nu} R + \Lambda g_{\mu\nu} = -\frac{8\pi G}{c^2} T_{\mu\nu}. \quad (6.48)$$

In the discussion of Chap. 7, we will use the Newtonian equivalents of these equations but it must be appreciated that we can only do this with the reassurance that the complete Einstein equations give fully self-consistent world models, without any need to introduce ad hoc assumptions. Our Newtonian equivalences can however provide intuitive impressions of the physical content of the theory.

6.6 Experimental and Observational Tests of General Relativity

In Einstein's exposition of the General Theory of Relativity, three tests of the theory were proposed, the gravitational redshift, the advance of the perihelion of planetary orbits and the deflection of light rays by the Sun. In 1964, Irwin Shapiro proposed a fourth test, the time delay of electromagnetic waves due to the distortion of space-time in the gravitational field of the Sun (Shapiro, 1964). The history of these tests and their status up to 1993 were comprehensively described by Will in his excellent book *Theory and Experiment in Gravitational Physics* (Will, 1993). More recently, he has updated the status of these tests and many other approaches to validating General Relativity (Will, 2006). Let us first review the four classic tests of the theory and then look briefly at the current status of possible modifications to General Relativity.

6.6.1 The Four Tests of General Relativity

Traditionally, there are four tests of the theory. The *first* is the measurement of the *gravitational redshift* of electromagnetic waves in a gravitational field which was discussed in Sect. 6.2. There, we described the use of the Mössbauer effect to measure the redshift of γ -ray photons in terrestrial experiments and the observation of the gravitational redshift of the emission lines in white dwarfs. More recent versions of the test have involved placing hydrogen masers in rocket payloads and measuring very precisely the change in frequency with altitude. These experiments have demonstrated directly the gravitational redshift of light. In the rocket experiments, the gravitational redshift was measured with a precision of about 5 parts in 10^5 . Nowadays, it is preferable to regard this as a test of the conservation of energy in a gravitational field.

The *second* and oldest test, and the first great triumph of General Relativity, was the explanation of the *perihelion shift* of the orbit of the planet Mercury. Mercury's orbit has ellipticity $e = 0.2$ and, in 1859, Le Verrier found that, once account is taken of the influence of the other planets in the Solar System, there remained a small but significant advance of the perihelion of its orbit which amounted to about $\dot{\omega} \approx 43$ arcsec per century (Le Verrier, 1859). The origin of this perihelion shift remained a mystery, possible explanations including the presence of a hitherto unknown planet close to the Sun, oblateness of the solar interior, deviations from the inverse square law of gravity near the Sun and so on. Continued observations of Mercury by radar ranging have established the advance of the perihelion of its orbit to about 0.1% precision with the result $\dot{\omega} = 42.98(1 \pm 0.001)$ arcsec per century, once the perturbing effects of the other planets had been taken into account (Shapiro, 1990). Einstein's theory of General Relativity predicts a value of $\dot{\omega} = 42.98$ arcsec per century, in remarkable agreement with the observed value.

There has been some debate as to whether or not the agreement really is as good as this comparison suggests because there might be a contribution to the perihelion advance if the core of the Sun were rapidly rotating and so possessed a finite quadrupole moment. Observations of the vibrational modes of the Sun,

or *helioseismology*, have shown that the core of the Sun is not rotating sufficiently rapidly to upset the excellent agreement between the predictions of General Relativity and the observed perihelion advance. Specifically, the quadrupole moment of the Sun has now been measured to be $J_2 = (2.2 \pm 0.1) \times 10^{-7}$ and so its contribution to the perihelion advance is less than 0.1% of the predicted advance. In Will's recent assessment, he quotes the limits in terms of the values of PPN coefficients γ and β (see Sect. 6.6.3),

$$\dot{\omega} = 42.98 \left[\frac{1}{3}(2 + 2\gamma - \beta) + 3 \times 10^{-4} \frac{J_2}{10^{-7}} \right] \text{ arcsec per century .} \quad (6.49)$$

Adopting the above value of J_2 , the limit of 0.1% accuracy for $\dot{\omega}$ corresponds to $(2\gamma - \beta - 1) < 3 \times 10^{-3}$.

The *third* test was the measurement of the deflection of light by the Sun. For light rays just grazing the limb of the Sun, the deflection amounts to $\Delta\theta_{\text{GR}} = 4GM/R_\odot c^2 = 1.75$ arcsec, where R_\odot is the radius of the Sun. Historically, this was a very important result. According to Newtonian theory, if we assume that the photon has a momentum $p = h\nu/c$ and then use the Rutherford scattering formula to work out the deviation of the light path, we find that the Newtonian deflection amounts to half the prediction of General Relativity, $\Delta\theta_{\text{Newton}} = 2GM/R_\odot c^2$. This prediction led to the famous eclipse expeditions of 1919 led by Eddington and Crommelin to measure precisely the angular deflections of the positions of stars observed close to the limb of the Sun during a solar eclipse. One expedition went to Sobral in Northern Brazil and the other to the island of Principe, off the coast of West Africa. The Sobral result was 1.98 ± 0.012 arcsec and the Principe result 1.61 ± 0.3 arcsec. These were technically demanding observations and there has been some controversy about the reliability of the results (Coles, 2001).

The modern version of the test originally involved measuring very precisely the angular separations between compact radio sources as they are observed close to the Sun. By means of Very Long Baseline Interferometry (VLBI), an angular precision of 100 microarcsec has now been achieved. In recent experiments, the VLBI technique has been used to measure deflections by the Sun over the whole sky. For example, at 90° to the direction of the Sun, the deflection of the radio waves still amounts to 4 milliarcsec, which is readily measurable by VLBI techniques.

The evolution of the precision of the light deflection test from the early optical studies to the most recent VLBI experiments is shown in the upper panel of Fig. 6.5. Transcontinental and intercontinental VLBI observations of quasars and radio galaxies have been used to monitor the Earth's rotation and these are sensitive to the deflection of light over almost the entire celestial sphere. An analysis of almost 2 million VLBI observations of 541 radio sources made by 87 VLBI sites over the period 1979 to 1999 yielded the following value for the parameter γ : $(\gamma - 1) = (-1.7 \pm 4.5) \times 10^{-4}$, or equivalently, $(1 + \gamma)/2 = 0.99992 \pm 0.00023$ (Shapiro et al., 2004). Notice also the limits shown in Fig. 6.5 obtained from the very precise positions of stars measured by the ESA *Hipparcos* astrometric satellite. General relativistic corrections had to be made for stars over the whole sky in order to obtain the quoted accuracy of about one milliarcsecond for the stars in the *Hipparcos* catalogue.

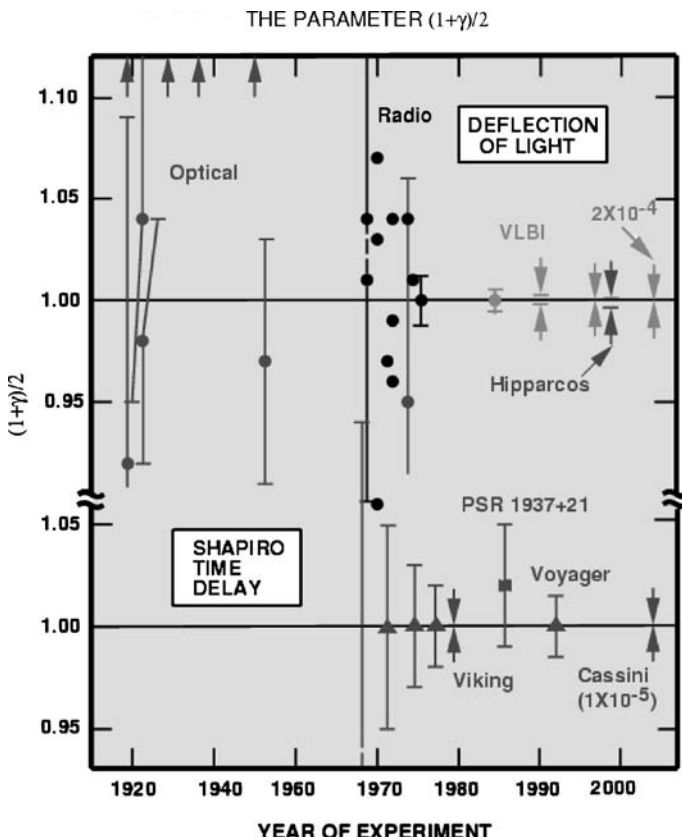


Fig. 6.5. Measurements of the quantity $(1 + \gamma)/2$ from light deflection and time delay experiments. The value of γ according to General Relativity is unity. The arrows at the top of the diagram denote anomalously large values from early eclipse expeditions. The time delay measurements from the Cassini spacecraft yielded agreement with General Relativity at the level of 10^{-3} percent. VLBI radio deflection measurements have reached 0.02 percent accuracy. The *Hipparcos* limits were derived from precise measurements of the positions stars over the whole sky and resulted in a precision of 0.1 percent in the measurement of γ (Will, 2006)

The forthcoming GAIA mission of ESA will measure the positions of about a billion stars in the Galaxy with a precision of about ten microarcsecond for stars brighter than 15th magnitude and so further estimates of the value of γ can be expected.

The fourth of the traditional tests is closely related to the deflection of light by the Sun and concerns the time delay expected when an electromagnetic wave propagates through a varying gravitational potential. In 1964, Shapiro realised that the gravitational redshift of radio signals passing close to the Sun causes a small time delay which can be measured by very precise timing of signals which are reflected from planets or space vehicles as they are about to be occulted by the Sun (Shapiro, 1964). Originally, the radio signals were reflected from the surface of the planets,

but later experiments used transponders on space vehicles which passed behind the Sun. The most accurate results from the early experiments were obtained using transponders on the *Viking* space vehicles which landed on Mars. These ‘anchored’ transponders gave results in agreement with General Relativity to within 0.1%.

A significant improvement was obtained in 2003 from Doppler tracking of the Cassini spacecraft while en route to Saturn. This experiment had the advantage of carrying out the timing measurements at two different radio frequencies and so much improved corrections could be made for the effects of the dispersion of the radio signals by the interplanetary plasma. The result of this experiment was $(\gamma - 1) = (2.1 \pm 2.3) \times 10^{-5}$. Hence the coefficient $\frac{1}{2}(1 + \gamma)$ must be within at most 0.0012 percent of unity (Bertotti et al., 2003). These results are summarised diagrammatically in the lower panel of Fig. 6.5, which is taken from Will’s review (Will, 2006).

6.6.2 Pulsars and General Relativity

Some of the most remarkable results have come from radio observations of *pulsars*. These pulsating radio sources are identified with rotating, magnetised neutron stars and they emit beams of radio emission along their magnetic poles. It is assumed that the rotational and magnetic axes are misaligned so that the distant observer normally detects one pulse per rotation period of the neutron star. A sketch of this model for a pulsar is shown schematically in Fig. 6.6 for the case of the binary pulsar PSR 1913+16. The typical parameters for a neutron star are that their masses are about $1.4M_{\odot}$, their radii about 10 km and their magnetic flux densities range from 10^4 to 10^9 T. Observations by Joseph Taylor and his colleagues using the Arecibo radio telescope have demonstrated that these are among the most stable clocks we know of in the Universe (Taylor, 1992).

The most intriguing systems are those pulsars which are members of binary systems, particularly those which are referred to as *relativistic binaries* in which both members of the binaries are neutron stars and their binary periods are less than a day. The first of these to be discovered was the binary pulsar PSR 1913+16 (Hulse and Taylor, 1975). The system has a binary period of only 7.75 hours and its orbital eccentricity is large, $e = 0.617$. This system is a pure gift for the relativist. To test General Relativity, we need a perfect clock in a rotating frame of reference and systems such as PSR 1913+16 are ideal for this purpose. The neutron stars are so inert and compact that the binary system is very ‘clean’ and so can be used for some of the most sensitive tests of General Relativity yet devised.

Precise timing of the arrival times of the pulses enables many independent parameters of the binary system to be determined and these depend upon the masses of the neutron stars. In Fig. 6.7, the most accurately determined three parameters are used to estimate the masses of the neutron stars in the binary system PSR 1913+16, assuming that General Relativity is the correct theory of gravity. It can be seen that the different loci intersect very precisely at a single point in the m_1/m_2 plane. Some measure of the precision with which the theory is known to be correct can be obtained from the accuracy with which the masses of the neutron stars are known:

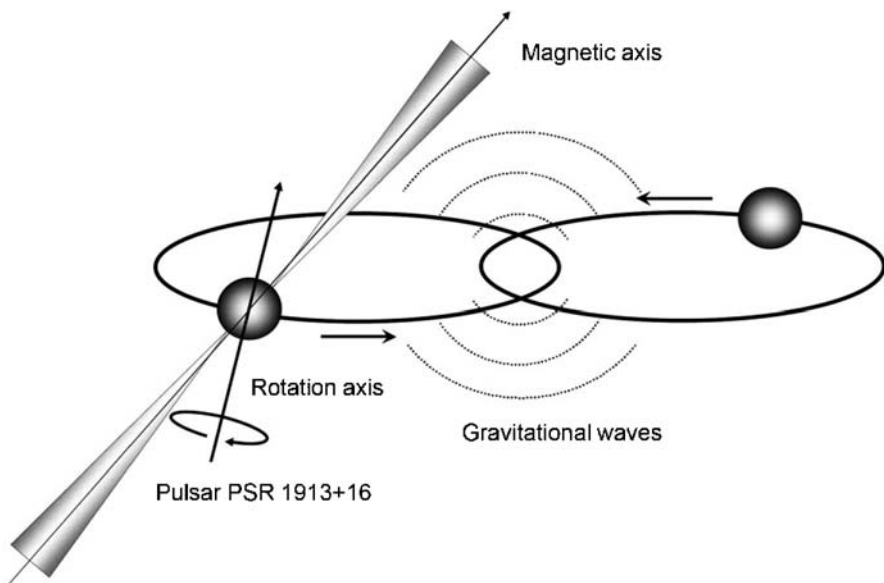


Fig. 6.6. A schematic diagram of the orbit of the binary pulsar PSR 1913+16. The pulsar is one of a pair of neutron stars in binary orbits about their common centre of mass. There is a displacement between the axis of the magnetic dipole and the rotation axis of the neutron star. The radio pulses are assumed to be due to beams of radio emission from the poles of the magnetic field distribution and are associated with the passage of the beam across the line of sight to the observer. As a result of the ability to measure precisely many parameters of the binary orbit from ultraprecise pulsar timing, the masses of the two neutron stars have been measured with very high precision (Taylor, 1992; Will, 2006)

$m_1 = 1.4414 \pm 0.0002 M_{\odot}$ and $m_2 = 1.3867 \pm 0.0002 M_{\odot}$. These are the most accurately known masses for any extrasolar system object.

Four other neutron star–neutron star binaries are known, including the system J0737-3039 in which both neutron stars are observed as pulsars (Lyne et al., 2004). This system is of the greatest interest since ultimately even better estimates of the orbital parameters of the system can be found than is the case for PSR 1913+16. It has not, however, yet been observed over as long a time period as PSR 1913+16.

A second remarkable measurement has been the rate of loss of orbital rotational energy by the *emission of gravitational waves*. A binary star system loses energy by the emission of gravitational radiation and the rate at which energy is lost can be precisely predicted once the masses of the neutron stars and the parameters of the binary orbit are known.⁴ The rate of change of the angular frequency Ω of the orbit due to the emission of gravitational radiation is precisely known, $d\Omega/dt \propto \Omega^5$.

⁴ I have given a simple heuristic derivation of the formula for the rate of loss of energy of a binary system by gravitational radiation in the Explanatory Supplement to Chap. 8 of my book *The Cosmic Century* (Longair, 2006).

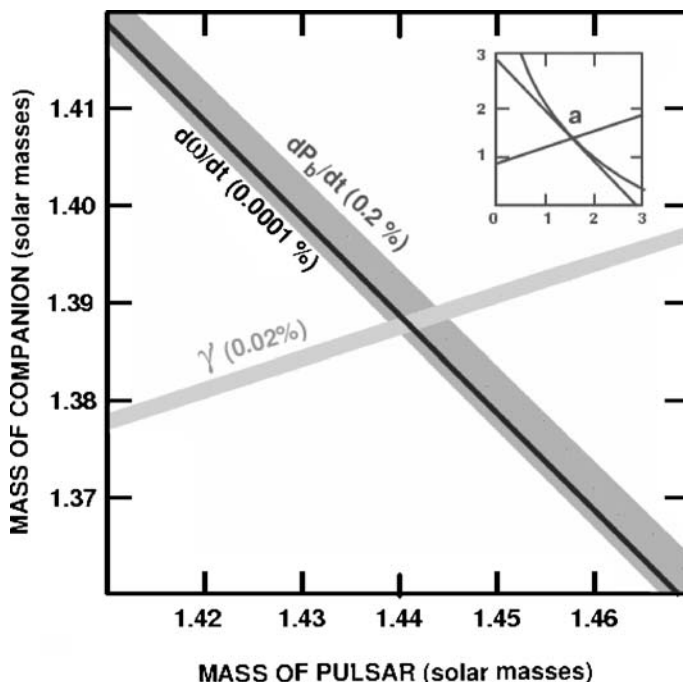


Fig. 6.7. Constraints on the masses of the pulsar PSR 1913+16 and its invisible companion from precise timing data, assuming General Relativity to be the correct theory of gravity. The width of each strip in the plane reflects the observational uncertainties, shown as a percentage. The *inset* shows the same three most accurate constraints on the full mass plane; the intersection region has been magnified 400 times in the large figure (Will, 2006)

The change in orbital phase of the binary pulsar PSR 1913+16 has been observed over a period of 30 years and General Relativity is in precise agreement with the observed changes over that period (Fig. 6.8). Thus, although the gravitational waves themselves have not been detected, exactly the correct energy loss rate from the system has been measured; it is generally assumed that this is convincing evidence for the existence of gravitational waves and this observation acts as a spur to their direct detection by future generations of gravitational wave detectors.

This is a very important result for the theory of gravitation since it enables a range of alternative theories of gravity to be excluded. For example, since General Relativity predicts only quadrupole emission of gravitational radiation, any theory which, say, involved the dipole emission of gravitational waves can potentially be excluded. The only problem with this argument for the system PSR 1913+16 is that the masses of the two neutron stars are almost exactly the same and so it possesses a rather small dipole moment. It turns out that at the moment the solar system tests provide better constraints on theories of relativistic gravity.

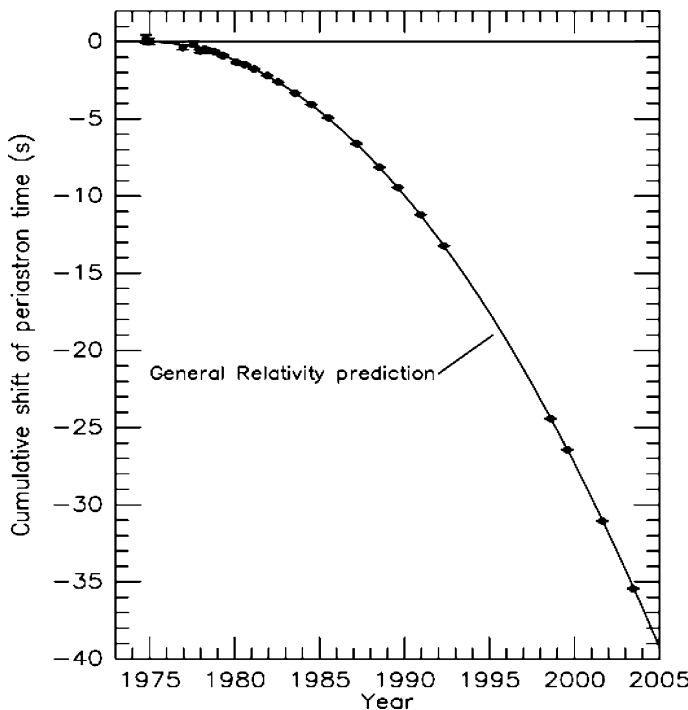


Fig. 6.8. The change of orbital phase as a function of time for the binary neutron star system PSR 1913+16 compared with the expected changes due to gravitational radiation energy loss by the binary system (Taylor, 1992; Will, 2006)

6.6.3 Parameterised Post-Newtonian Models

We have already introduced the parameters β and γ without explaining precisely what they mean. These quantities are found in what are called *parameterised post-Newtonian (PPN) models* for theories of relativistic gravity. To understand this approach to comparing the theories with observation, it is simplest to quote the words of Will (Will, 2006):

The comparison of metric theories of gravity with each other and with experiment becomes particularly simple when one takes the slow-motion, weak-field limit. This approximation, known as the post-Newtonian limit, is sufficiently accurate to encompass most solar-system tests that can be performed in the foreseeable future. It turns out that, in this limit, the space-time metric predicted by nearly every metric theory of gravity has the same structure. It can be written as an expansion about the Minkowski metric in terms of dimensionless gravitational potentials of varying degrees of smallness.

The spirit of this approach is to relax the powerful constraints implied by the Einstein equivalence principle discussed in Sect. 6.1 and so allow a wider range of possible theories of relativistic gravity. To give some impression of what is involved in this approach, Table 6.1, taken from Will's survey, shows a list of the various parameters involved in these theories. Notice that the entries for ξ and for α_1, α_2 and α_3 correspond to relaxing the second and third conditions involved in the Einstein equivalence principle.

These modifications would change the metric coefficients from the values they take in General Relativity. Thus, quoting Will, the metric coefficients would become:

$$\begin{aligned} g_{00} = & -1 + 2U - 2\beta U^2 - 2\xi\Phi_W + (2\gamma + 2 + \alpha_3 + \zeta_1 - 2\xi)\Phi_1 \\ & + 2(3\gamma - 2\beta + 1 + \zeta_2 + \xi)\Phi_2 + 2(1 + \zeta_3)\Phi_3 + 2(3\gamma + 3\zeta_4 - 2\xi)\Phi_4 \\ & - (\zeta_1 - 2\xi)\mathcal{A} - (\alpha_1 - \alpha_2 - \alpha_3)w^2U - \alpha_2 w^i w^j U_{ij} \\ & + (2\alpha_3 - \alpha_1)w^i V_i + \mathcal{O}(\epsilon^3) \end{aligned} \quad (6.50)$$

$$\begin{aligned} g_{0i} = & -\frac{1}{2}(4\gamma + 3 + \alpha_1 - \alpha_2 + \zeta_1 - 2\xi)V_i - \frac{1}{2}(1 + \alpha_2 - \zeta_1 + 2\xi)W_i \\ & - \frac{1}{2}(\alpha_1 - 2\alpha_2)w^i U - \alpha_2 w^j U_{ij} + \mathcal{O}(\epsilon^{5/2}) \end{aligned} \quad (6.51)$$

$$g_{ij} = (1 + 2\gamma U)\delta_{ij} + \mathcal{O}(\epsilon^2). \quad (6.52)$$

The quantities $U, U_{ij}, \Phi_W, \Phi_1, \Phi_2, \Phi_3, \Phi_4, \mathcal{A}, V_i, W_i$ are various metric potentials which can be interpreted in terms of Newtonian gravity. Thus, U , defined by

$$U = \int \frac{\varrho'}{|x - x'|} d^3x', \quad (6.53)$$

is just the Newtonian gravitational potential.

The expressions (6.50) to (6.52) look rather forbidding at first sight, but the important point is that it is possible to test theories in which the Einstein equivalence principle is relaxed and provide further constraints upon acceptable theories. As Will points out in his review, some of the theories may appear somewhat unphysical within the realms of known physics, but in some extensions of the Standard Model of particle physics, for example, even some of our most cherished theories, such as Lorentz invariance, might have to be sacrificed. Another example involves scalar-tensor modifications of General Relativity which are involved in unification schemes such as string theory, and in cosmological model building.

Some of these post-Newtonian ‘corrections’ have quite obvious meanings. For example, inspection of the first three terms of (6.50) shows that, for a point mass, the first two are just the familiar metric coefficient $(1 + \phi/c^2)$ in our notation and the third is a non-linear term in the square of the potential $\beta(\phi/c^2)^2$. In the same way, inspection of (6.52) shows that γ describes how much space-curvature is produced by unit mass, reducing to the standard result if $\gamma = 1$. The limits which can be set to possible deviations from the Einstein equivalence principle are listed in Table 6.3. Will's review should be consulted for more details about these possibilities.

Table 6.3. Current limits on the PPN parameters. Here η_N is a combination of other parameters given by $\eta_N = 4\beta - \gamma - 3 - 10\xi/3 - \alpha_1 + 2\alpha_2/3 - 2\xi_1/3 - \xi_2/3$

Parameter	Effect	Limit	Remarks
$\gamma - 1$	Time delay	2.3×10^{-5}	Cassini tracking
	Light deflection	4×10^{-4}	VLBI
$\beta - 1$	Perihelion shift	3×10^{-3}	$J_2 = 10^{-7}$ from helioseismology
	Nordtvedt effect	2.3×10^{-4}	$\eta_N = 4\beta - \gamma - 3$ assumed
ξ	Earth tides	10^{-3}	Gravimeter data
α_1	Orbital polarisation	10^{-4}	Lunar laser ranging
		2×10^{-4}	PSR J2317+1439
α_2	Spin precession	4×10^{-7}	Solar alignment with ecliptic
α_3	Pulsar acceleration	4×10^{-20}	Pulsar \dot{P} statistics
η_N	Nordtvedt effect	9×10^{-4}	Lunar laser ranging
ξ_1	–	2×10^{-2}	Combined PPN bounds
ξ_2	Binary acceleration	4×10^{-5}	\ddot{P}_p for PSR 1913+16
ξ_3	Newton's 3rd law	10^{-8}	Lunar acceleration
ξ_4	–	–	Not independent ($6\xi_4 = 3\alpha_3 + 2\xi_1 - 3\xi_3$)

Table 6.4. Constancy of the gravitational constant G . For binary pulsar data, the bounds are dependent upon the theory of gravity in the strong-field regime and on the neutron star equation of state. Big Bang nucleosynthesis bounds assume a specific form for the time dependence of G

Method	$(\dot{G}/G)/10^{-13} \text{ year}^{-1}$	Reference
Lunar laser ranging	4 ± 9	(Williams et al., 2004)
Binary pulsar PSR 1913+16	40 ± 50	(Kaspi et al., 1994)
Helioseismology	0 ± 16	(Guenther et al., 1998)
Big Bang nucleosynthesis	0 ± 4	(Copi et al., 2004)

6.6.4 Variation of the Gravitational Constant with Cosmic Epoch

An important question for cosmology is whether or not the gravitational constant G has varied with time. A summary of recent results is shown in Table 6.4 (Will, 2006).

- The technique of lunar laser ranging has provided the strongest limit to date. In the analysis of these data, evidence is sought for steady changes in the lunar orbit which could be attributed to changes in the gravitational constant with time.
- The techniques of accurate pulsar timing have been used to determine whether or not there is any evidence for steady changes in the pulsar's orbital period due to steady variations in the gravitational constant G with time. This test is somewhat dependent upon the equation of state used to describe the interior of the neutron star.

- The helioseismology limit is derived from the remarkable success of the standard astrophysical model of the solar interior in accounting for its internal structure. The frequency spacings between the p -modes of different azimuthal and radial order are very sensitive to the sound speed in the central regions of the star. If the gravitational constant had varied with cosmic epoch, the chemical composition and hence the speed of sound and frequency separations in the central regions would have been significantly different from the observed values.
- The primordial nucleosynthesis argument follows from the fact that, if the gravitational constant were greater in the past, the early evolution of the Universe would have been more rapid than in the standard model of its early stages and so helium would have been dramatically overproduced relative to its observed cosmic value. We will return to this argument in Chap. 10.

The sense of the data listed in Table 6.4 is that there can have been little change in the value of the gravitational constant over typical cosmological time-scales which are about 10^{10} years.

6.7 Summary

General Relativity has passed every observational and experimental test which has been made of the theory and so we can have confidence that it is the correct starting point for the development of models of the large-scale dynamical structure of our Universe.

7 The Friedman World Models

7.1 Einstein's Field Equations

Einstein realised that, in General Relativity, he had discovered a theory which enabled fully self-consistent models for the Universe as a whole to be constructed. The standard models contain three essential ingredients:

- The *cosmological principle*, which, combined with the observations that the Universe is isotropic, homogeneous and uniformly expanding on a large scale, leads to the Robertson–Walker metric (5.33).
- *Weyl's postulate*, according to which the world lines of particles meet at a singular point in the finite or infinite past. This means that there is a unique world line passing through every point in space–time. The fluid moves along streamlines in the universal expansion and so behaves like a perfect fluid for which the energy–momentum tensor is given by the $T^{\alpha\beta}$ of (6.33).
- General Relativity, which enables us to relate the energy–momentum tensor to the geometrical properties of space–time through (6.47) or (6.48).

The assumptions of isotropy and homogeneity result in enormous simplifications of Einstein's field equations which reduce to the following pair of equations:

$$\ddot{a} = -\frac{4\pi G}{3}a \left(\varrho + \frac{3p}{c^2} \right) + \frac{1}{3}\Lambda a^2; \quad (7.1)$$

$$\dot{a}^2 = \frac{8\pi G\varrho}{3}a^2 - \frac{c^2}{\mathfrak{R}^2} + \frac{1}{3}\Lambda a^2. \quad (7.2)$$

In these equations, a is the scale factor normalised to the value unity at the present epoch t_0 , ϱ is the total inertial mass density of the matter and radiation content of the Universe and p the associated total pressure. \mathfrak{R} is the radius of curvature of the geometry of the world model at the present epoch and so the term $-c^2/\mathfrak{R}^2$ is a constant of integration. The *cosmological constant* Λ was introduced by Einstein in 1917 in order to create a static Universe with closed geometry which he hoped would enable Mach's principle to be incorporated into General Relativity (Einstein, 1917).

Let us look more closely at the meanings of (7.1) and (7.2). Equation (7.2) is referred to as *Friedman's equation* and has the form of an energy equation, the

term on the left-hand side corresponding to the kinetic energy of the expanding fluid and the first term on the right-hand side to its gravitational potential energy, as we will show in Sect. 7.2. An illuminating account of Friedman's equation, its physical content and its solutions has been given by White, whose presentation can be thoroughly recommended (White, 1990). The pair of equations (7.1) and (7.2) incorporate the First Law of Thermodynamics in its full relativistic form as can be appreciated from the following analysis. We write the first law in the usual form

$$dU = -p dV . \quad (7.3)$$

We need to formulate the law so that it is applicable for relativistic and non-relativistic fluids and so we write the internal energy U as the sum of all the terms which can contribute to the total energy of the fluid in the relativistic sense. Thus, the total internal energy consists of the fluid's rest mass energy, its kinetic energy, its thermal energy and so on. If we write the sum of these energies as $\varepsilon_{\text{tot}} = \sum_i \varepsilon_i$, the internal energy is $\varepsilon_{\text{tot}} V$ and so, dividing (7.3) by da , it follows that

$$\frac{d}{da} (\varepsilon_{\text{tot}} V) = -p \frac{dV}{da} . \quad (7.4)$$

Now, $V \propto a^3$ and so, differentiating, we find

$$\frac{d\varepsilon_{\text{tot}}}{da} + 3 \frac{(\varepsilon_{\text{tot}} + p)}{a} = 0 . \quad (7.5)$$

This result can be expressed in terms of the inertial mass density associated with the total energy $\varepsilon_{\text{tot}} = \varrho c^2$; this is the type of density ϱ which should be included in (7.1) and (7.2). Therefore, (7.5) can also be written

$$\frac{d\varrho}{da} + 3 \frac{\left(\varrho + \frac{p}{c^2}\right)}{a} = 0 . \quad (7.6)$$

Let us show how (7.5) and (7.6) lead to a number of important results which we will use repeatedly in what follows. First of all, suppose the fluid is very 'cold' in the sense that $p \ll \varrho_0 c^2$, where ϱ_0 is its rest mass density. Then, setting $p = 0$ and $\varepsilon_0 = Nmc^2$, where N is the number density of particles of rest mass m , we find

$$\frac{dN}{da} + \frac{3N}{a} = 0 \quad \text{and so} \quad N = N_0 a^{-3} , \quad (7.7)$$

that is, the equation of conservation of mass for a gas of non-relativistic particles.

Next, the thermal pressure of non-relativistic matter can be included into (7.5). We will normally be dealing with monatomic gases or plasmas for which the thermal energy is $\varepsilon_{\text{th}} = \frac{3}{2} NkT$ and $p = NkT$. Then, substituting $\varepsilon_{\text{tot}} = \frac{3}{2} NkT + Nmc^2$ and $p = NkT$ into (7.5), we find

$$\begin{aligned} \frac{d}{da} \left(\frac{3}{2} NkT + Nmc^2 \right) + 3 \left(\frac{\frac{5}{2} NkT + Nmc^2}{a} \right) &= 0 , \\ \frac{d(NkT)}{da} + \frac{5NkT}{a} &= 0 \quad \text{and so} \quad NkT = N_0 k T_0 a^{-5} . \end{aligned} \quad (7.8)$$

Since $N = N_0 a^{-3}$, we find the standard result for the adiabatic expansion of a monatomic gas with ratio of specific heats $\gamma = 5/3$, $T \propto a^{-2}$. More generally, if the ratio of specific heats of the gas is γ , the energy density is $\varepsilon_{\text{tot}} = NkT/(\gamma - 1) + Nmc^2$ and so the temperature changes as $T \propto a^{-3(\gamma-1)}$.

We can deduce another important result from the expression for a monatomic gas, $T \propto a^{-2}$. If we write $\varepsilon_{\text{th}} = \frac{1}{2}Nm\langle v^2 \rangle$, where $\langle v^2 \rangle$ is the mean square velocity of the particles of the gas, we find $\langle v^2 \rangle \propto a^{-2}$. Thus, the random velocities of the particles of the gas decrease as $v \propto a^{-1}$. This result applies equally to the random motions of galaxies relative to the mean Hubble flow, what are known as the *peculiar velocities* of galaxies, v_{pec} . Therefore, as the Universe expands, we expect the peculiar velocities of galaxies to decrease as $v_{\text{pec}} \propto a^{-1}$.

Finally, in the case of a gas of ultrarelativistic particles, or a gas of photons, we can write $p = \frac{1}{3}\varepsilon_{\text{tot}}$. Therefore, from (7.5),

$$\frac{d\varepsilon_{\text{tot}}}{da} + \frac{4\varepsilon_{\text{tot}}}{a} = 0 \quad \text{and so} \quad \varepsilon_{\text{tot}} \propto a^{-4}. \quad (7.9)$$

In the case of a gas of photons, $\varepsilon_{\text{rad}} = \sum Nhv$ and, since $N \propto a^{-3}$, we find $v \propto a^{-1}$. This is an alternative derivation of the relation between the scale factor a and the cosmological redshift z . If v_0 is the frequency of the photon at the present epoch and v_{em} its frequency when the scale factor was a , $v_{\text{em}}/v_0 = a^{-1}$ and hence, from the definition of (5.45),

$$z = \frac{v_{\text{em}}}{v_0} - 1; \quad a = \frac{1}{1+z}. \quad (7.10)$$

Let us now return to the analysis of (7.2). Differentiating this equation with respect to time and dividing through by \dot{a} , we find

$$\ddot{a} = \frac{4\pi Ga^2}{3} \frac{d\varrho}{da} + \frac{8\pi G\varrho a}{3} + \frac{1}{3}\Lambda a. \quad (7.11)$$

Now, substituting the expression for $d\varrho/da$ from (7.6), we find

$$\ddot{a} = -\frac{4\pi Ga}{3} \left(\varrho + \frac{3p}{c^2} \right) + \frac{1}{3}\Lambda a, \quad (7.12)$$

that is, we recover (7.1). The purpose of these calculations has been to show how (7.1) and (7.2) correctly include the law of conservation of energy for both relativistic and non-relativistic gases.

Equation (7.1) has the form of a force equation, but, as we have shown, it contains implicitly the First Law of Thermodynamics as well. An equation of this form can be derived from Newtonian considerations, but it does not contain the pressure term $3p/c^2$. This pressure term can be considered a ‘relativistic correction’ to the inertial mass density, but it is unlike normal pressure forces which depend upon the gradient of the pressure and, for example, hold up the stars. The term $\varrho + (3p/c^2)$ can be thought of as playing the role of an *active gravitational mass density*.

The general solutions of (7.2) for expanding world models were discovered by Aleksander Aleksandrovich Friedman in two remarkable papers published in 1922 and 1924 (Friedman, 1922, 1924) (for translations, see the book *Cosmological Constants* (Bernstein and Feinberg, 1986)). In these papers, Friedman assumed that $\Lambda \neq 0$ and so it is appropriate to refer the complete set of models with and without the Λ -term as the *Friedman world models*.

As we will discuss in Chaps. 8 and 15, there is now compelling evidence for a finite value of the cosmological constant Λ . It might therefore seem best to plunge straight into the full analysis of (7.1) and (7.2) with $\Lambda \neq 0$. Rather than do this, I will develop the models with and without a finite value of Λ in parallel in what follows. There are two reasons for not discarding the models with $\Lambda = 0$ immediately. The first is that the models with $\Lambda = 0$ often have simple analytic solutions which give insight into the behaviour of the cosmological models. The second reason is that the effects of the cosmological constant only become appreciable at late cosmological epochs and so for many purposes, particularly in the early Universe, we can confidently set the cosmological constant equal to zero.

7.2 The Standard Friedman World Models with $\Lambda = 0$

By *dust*, cosmologists mean a pressureless fluid and so we set $p = 0$ in the Friedman equations. In this section, the cosmological constant Λ is also set to zero. It is convenient to refer the density of the fluid to its value at the present epoch ϱ_0 and then, because of conservation of mass, $\varrho = \varrho_0 a^{-3}$. Therefore, (7.1) and (7.2) reduce to

$$\ddot{a} = -\frac{4\pi G\varrho_0}{3a^2}; \quad \dot{a}^2 = \frac{8\pi G\varrho_0}{3a} - \frac{c^2}{\mathfrak{R}^2}. \quad (7.13)$$

7.2.1 The Newtonian Analogue of the Friedman World Models

In 1934, Milne and McCrea showed that relations of the form (7.13) can be derived using non-relativistic Newtonian dynamics (Milne and McCrea, 1934a,b). We will perform this calculation because the ideas implicit in the argument can be used to understand some of the problems which arise in the theory of galaxy formation. Consider a galaxy at distance x from the Earth and work out its deceleration due to the gravitational attraction of the matter inside the sphere of radius x centred on the Earth (Fig. 7.1). By Gauss's theorem, because of the spherical symmetry of the distribution of matter about the origin, we can replace that mass, $M = (4\pi/3)\varrho x^3$, by a point mass at the centre of the sphere and so the deceleration of the galaxy is

$$m\ddot{x} = -\frac{GMm}{x^2} = -\frac{4\pi x\varrho m}{3}. \quad (7.14)$$

The mass of the galaxy m cancels out on either side of the equation, showing that the deceleration refers to the sphere of matter as a whole rather than to any particular

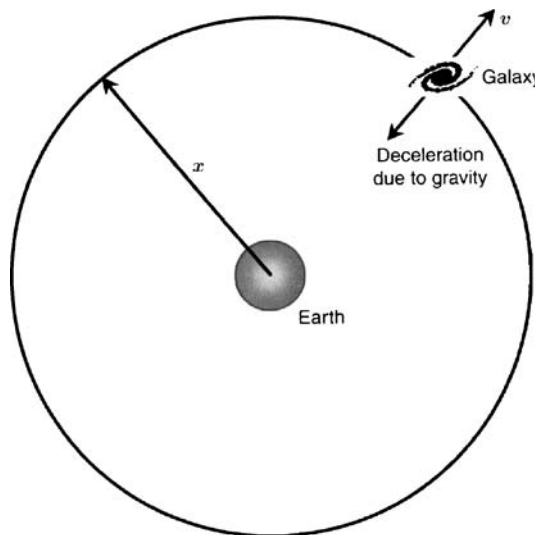


Fig. 7.1. Illustrating the dynamics of Newtonian world models

galaxy. We now replace x by the comoving radial distance coordinate r using the relation $x = ar$, and express the density in terms of its value at the present epoch, $\varrho = \varrho_0 a^{-3}$. Then,

$$\ddot{a} = -\frac{4\pi G \varrho_0}{3a^2}, \quad (7.15)$$

which is identical to (7.1) for dust models with $\Lambda = 0$. Multiplying (7.15) by \dot{a} and integrating, we find

$$\dot{a}^2 = \frac{8\pi G \varrho_0}{3a} + \text{constant}. \quad (7.16)$$

This result is identical to (7.2) if we identify the constant with $-c^2/\mathfrak{R}^2$. This Newtonian calculation illustrates why we can identify the left-hand side of (7.2) with the kinetic energy of expansion of the fluid and the first term on the right-hand side with its gravitational potential energy.

The above analysis brings out a number of important features of the Friedman world models. First of all, there is an important flaw in the Newtonian argument in that we have applied Gauss's law to an infinite distribution of matter and ignored the issue of the boundary conditions at infinity. The argument works, however, because of the assumption of isotropy and homogeneity of the matter throughout the infinite Universe: local physics is also global physics. The same physics which defines the local behaviour of matter also defines its behaviour on the largest scales. For example, the curvature of space κ within one cubic metre is exactly the same as that on the scale of the Universe itself.

Furthermore, although we might appear to have placed the Earth in a preferred position in Fig. 7.1, an observer located on any galaxy anywhere in the Universe

would perform exactly the same calculation to estimate the deceleration of any other galaxy relative to the observer's galaxy. This is a result of the cosmological principle which asserts that all fundamental observers should observe the same large-scale features of the Universe at the same epoch. In other words, the Newtonian calculation applies for all observers who move in such a way that the Universe appears isotropic to them which is, by definition, for all fundamental observers.

Notice also that at no point in the argument did we ask over what physical scale the calculation was to be valid. For strictly uniform isotropic models, this calculation describes correctly the dynamics of the Universe on scales greater than the *horizon scale* which, for the moment, we can take to be $r = ct$, that is, the maximum distance between points which can be causally connected at the epoch t . The reason for this is the same as for the first two points: local physics is also global physics and so, if the Universe were set up in such a way that it had uniform density on scales far exceeding the horizon scale, the dynamics on these very large scales would be exactly the same as the local dynamics.

Friedman died of typhoid during the civil war in Leningrad in 1925 and did not live to see what have become the standard models of the Universe bear his name (see the biography by Tropp, Frenkel and Chernin (Tropp et al., 1993)). It is perhaps surprising that these papers did not attract more widespread interest at the time. This may have been partly due to a brief note published by Einstein in 1922 criticising some steps in Friedman's first paper (Einstein, 1922). In the following year, Einstein graciously acknowledged that his criticism was based upon an error in his own calculations and that Friedman's solution was indeed correct (Einstein, 1923). Georges Lemaître rediscovered Friedman's solutions in 1927 and brought Friedman's contributions to the wider notice of astronomers and cosmologists during the 1930s (Lemaître, 1927).

7.2.2 The Critical Density and the Density Parameter

It is convenient to express the density of the world models in terms of a *critical density* ϱ_c which is defined to be

$$\varrho_c = (3H_0^2/8\pi G) = 1.88 \times 10^{-26} h^2 \text{ kg m}^{-3}. \quad (7.17)$$

Where Hubble's constant H_0 has been written $H_0 = 100h \text{ km s}^{-1} \text{ Mpc}^{-1}$ in view of uncertainty about its exact value.¹ Then, the actual density of the model at the present epoch ϱ_0 can be referred to this value through a *density parameter* $\Omega_0 = \varrho_0/\varrho_c$. Thus, the density parameter is defined to be

$$\Omega_0 = \frac{\varrho_0}{\varrho_c} = \frac{8\pi G \varrho_0}{3H_0^2}. \quad (7.18)$$

The subscript 0 has been attached to Ω because the critical density ϱ_c changes with cosmic epoch, as does Ω . It is convenient to refer any cosmic density to ϱ_c .

¹ As will be discussed in Chaps. 8 and 15, Hubble's constant is now known to better than 10% accuracy. A value of $h = 0.7$ can be used with some confidence.

For example, we will often refer to the density parameter of baryons, Ω_B , or of visible matter, Ω_{vis} , or of dark matter, Ω_D , and so on; these are convenient ways of describing the relative importance of different contributions to Ω_0 .

The dynamical equations (7.13) therefore become

$$\ddot{a} = -\frac{\Omega_0 H_0^2}{2a^2}; \quad \dot{a}^2 = \frac{\Omega_0 H_0^2}{a} - \frac{c^2}{\mathfrak{R}^2}. \quad (7.19)$$

Several important results can be deduced from these equations. If we set the quantities in the second equation of (7.19) equal to their values at the present epoch, $t = t_0$, $a = 1$ and $\dot{a} = H_0$, we find

$$\mathfrak{R} = \frac{c/H_0}{(\Omega_0 - 1)^{1/2}} \quad \text{and} \quad \kappa = \frac{(\Omega_0 - 1)}{(c/H_0)^2}. \quad (7.20)$$

This last result shows that there is a one-to-one relation between the density of the Universe Ω_0 and its spatial curvature κ , one of the most beautiful results of the Friedman world models with $\Lambda = 0$.

7.2.3 The Dynamics of the Friedman Models with $\Lambda = 0$

To understand the solutions of (7.19), we substitute (7.20) into (7.19) to find the following expression for \dot{a}

$$\dot{a}^2 = H_0^2 \left[\Omega_0 \left(\frac{1}{a} - 1 \right) + 1 \right]. \quad (7.21)$$

In the limit of large values of a , \dot{a}^2 tends to

$$\dot{a}^2 = H_0^2 (1 - \Omega_0). \quad (7.22)$$

Thus:

- The models having $\Omega_0 < 1$ have open, hyperbolic geometries and expand to $a = \infty$. They continue to expand with a finite velocity at $a = \infty$ with $\dot{a} = H_0(1 - \Omega_0)^{1/2}$.
- The models with $\Omega_0 > 1$ have closed, spherical geometry and stop expanding at some finite value of $a = a_{\max}$ – they have ‘imaginary expansion rates’ at infinity. They reach the maximum value of the scale factor after a time

$$t_{\max} = \frac{\pi \Omega_0}{2H_0(\Omega_0 - 1)^{3/2}}. \quad (7.23)$$

These models collapse to an infinite density after a finite time $t = 2t_{\max}$, an event sometimes referred to as the ‘big crunch’.

- The model with $\Omega_0 = 1$ separates the open from the closed models and the collapsing models from those which expand forever. This model is often referred to as the *Einstein-de Sitter* or the *critical model*. The velocity of expansion tends

to zero as a tends to infinity. It has a particularly simple variation of $a(t)$ with cosmic epoch,

$$a = \left(\frac{t}{t_0} \right)^{2/3} \quad \kappa = 0, \quad (7.24)$$

where the present age of the world model is $t_0 = (2/3)H_0^{-1}$.

Some solutions of (7.21) are displayed in Fig. 7.2 which shows the well-known relation between the dynamics and geometry of the Friedman world models with $\Lambda = 0$. The abscissa in Fig. 7.2 is in units of H_0^{-1} and so the slope of the relations at the present epoch, $a = 1$, is always 1. The present age of the Universe is given by the intersection of each curve with the line $a = 1$.

Another useful result is the function $a(t)$ for the empty world model, $\Omega_0 = 0$, $a(t) = H_0 t$, $\kappa = -(H_0/c)^2$. This model is sometimes referred to as the *Milne*

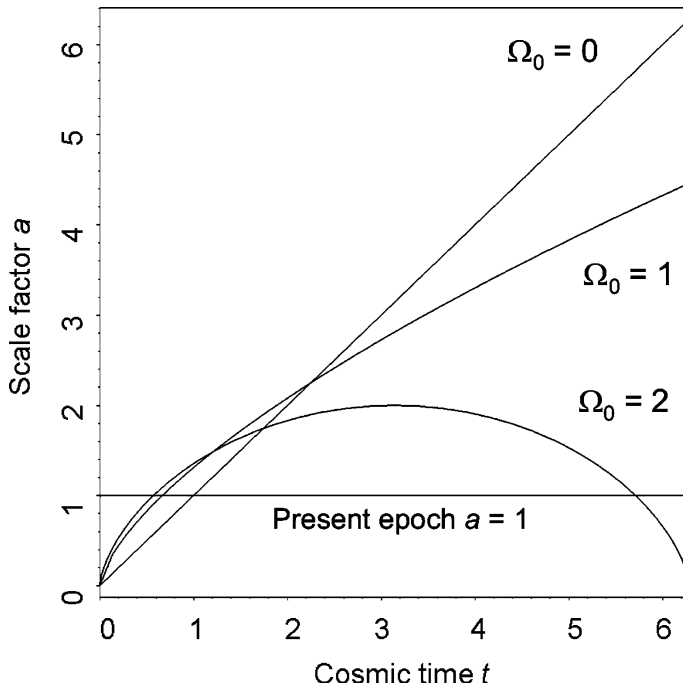


Fig. 7.2. The dynamics of the classical Friedman models with $\Omega_A = 0$ characterised by the density parameter $\Omega_0 = \rho_0/\rho_c$. If $\Omega_0 > 1$, the Universe collapses to $a = 0$ as shown; if $\Omega_0 < 1$, the Universe expands to infinity and has a finite velocity of expansion as a tends to infinity. In the case $\Omega_0 = 1$, $a = (t/t_0)^{2/3}$ where $t_0 = (2/3)H_0^{-1}$. The time axis is given in terms of the dimensionless time $H_0 t$. At the present epoch $a = 1$ and in this presentation, the three curves have the same slope of 1 at $a = 1$, corresponding to a fixed value of Hubble's constant at the present day. If t_0 is the present age of the Universe, then $H_0 t_0 = 1$ for $\Omega_0 = 0$, $H_0 t_0 = 2/3$ for $\Omega_0 = 1$ and $H_0 t_0 = 0.57$ for $\Omega_0 = 2$.

model. It is an interesting exercise to show why it is that, in the completely empty world model, the global geometry of the Universe is hyperbolic. The reason is that, in the empty model, the galaxies partaking in the universal expansion are undecelerated and any particular galaxy always has the same velocity relative to the same fundamental observer. Therefore, the cosmic times measured in different frames of reference are related by the standard Lorentz transform $t' = \gamma(t - vr/c^2)$ where $\gamma = (1 - v^2/c^2)^{-1/2}$. The key point is that the conditions of isotropy and homogeneity apply at constant cosmic time t' in the frames of reference of all fundamental observers. The Lorentz transform shows that this cannot be achieved in flat space but it is uniquely satisfied in hyperbolic space with $\kappa = -(H_0/c)^2$. A simple derivation of this result is given in the Appendix to this chapter.

The general solutions of (7.21) are most conveniently written in parametric form. For $\Omega_0 > 1$,

$$a = A(1 - \cos \theta) \quad t = B(\theta - \sin \theta), \quad (7.25)$$

$$A = \frac{\Omega_0}{2(\Omega_0 - 1)} \quad \text{and} \quad B = \frac{\Omega_0}{2H_0(\Omega_0 - 1)^{3/2}}. \quad (7.26)$$

For $\Omega_0 < 1$,

$$a = A(\cosh \phi - 1) \quad t = B(\sinh \phi - \phi), \quad (7.27)$$

$$A = \frac{\Omega_0}{2(1 - \Omega_0)} \quad \text{and} \quad B = \frac{\Omega_0}{2H_0(1 - \Omega_0)^{3/2}}. \quad (7.28)$$

All the models tend towards the dynamics of the critical model at early times but with a different constant, that is, for $\theta \ll 1$ and $\phi \ll 1$,

$$a = \Omega_0^{1/3} \left(\frac{3H_0 t}{2} \right)^{2/3}. \quad (7.29)$$

We will find these results useful in understanding the growth of small perturbations in the expanding Universe (Sect. 11.4.2).

7.3 Friedman Models with Non-Zero Cosmological Constant

The tortuous history of the cosmological constant Λ was told briefly in Chap. 1 and need not be repeated here. So far as the interpretation of the term is concerned, Einstein soon realised that the Λ -term would appear as a constant in his field equations quite independent of its cosmological significance (Einstein, 1919). In 1933, Lemaître suggested that the Λ -term could be interpreted in terms of a finite vacuum energy density (Lemaître, 1933). In his words:

Everything happens as though the energy in vacuo would be different from zero.

This insight foreshadows the present interpretation of the cosmological constant which associates it with *dark energy*, the nature of which is one of the great unsolved cosmological mysteries. Let us illustrate how this remarkable situation has come about.

7.3.1 The Cosmological Constant and the Vacuum Energy Density

Einstein's field equations with the inclusion of the cosmological constant can be written

$$\ddot{a} = -\frac{4\pi Ga}{3}\left(\varrho + \frac{3p}{c^2}\right) + \frac{1}{3}\Lambda a ; \quad (7.30)$$

$$\dot{a}^2 = \frac{8\pi G\varrho}{3}a^2 - \frac{c^2}{\mathfrak{N}^2} + \frac{1}{3}\Lambda a^2 . \quad (7.31)$$

Considering dust-filled universes as in Sect. 7.2, we set $3p/c^2 = 0$ and then (7.30) becomes

$$\ddot{a} = -\frac{4\pi Ga\varrho}{3} + \frac{1}{3}\Lambda a = -\frac{4\pi G\varrho_0}{3a^2} + \frac{1}{3}\Lambda a . \quad (7.32)$$

Inspection of (7.32) gives some insight into the physical meaning of the cosmological constant. Even in an empty universe, $\varrho = 0$, there is a net force acting on a test particle. If Λ is positive, the term may be thought of as the 'repulsive force of a vacuum', in the words of Zeldovich, the repulsion being relative to an absolute geometrical frame of reference (Zeldovich, 1968). There was no obvious interpretation of the Λ -term according to classical physics. There is, however, a natural interpretation in the context of quantum field theory.

A key development has been the introduction of Higgs fields into the theory of weak interactions. These and other ideas of quantum field theory are described by Zeldovich in an article aimed at providing enlightenment for observational astronomers (Zeldovich, 1986). The Higgs field was introduced into the electro-weak theory of elementary particles in order to eliminate singularities in the theory and to endow the W^\pm and Z^0 bosons with masses. Precise measurement of the masses of these particles at CERN has confirmed the theory very precisely, although the Higgs particles themselves have not yet been found in accelerator experiments; the particle physics community confidently expects that these elusive particles will be discovered in the first experiments carried out at the Large Hadron Collider (LHC) at CERN in 2008. As described by Zeldovich, the Higgs fields have the property of being *scalar* fields, unlike the vector fields of electromagnetism or the tensor fields of General Relativity, and have negative pressure equations of state $p = -\varrho c^2$.

In the modern picture of the vacuum, there are zero-point fluctuations associated with the zero-point energies of all quantum fields. The stress-energy tensor of a vacuum has a negative pressure equation of state, $p = -\varrho c^2$. This pressure may be thought of as a 'tension' rather than a pressure. When such a vacuum expands, the work done $p dV$ in expanding from V to $V + dV$ is just $-\varrho c^2 dV$ so that, during the expansion, the mass-energy density of the negative pressure field remains constant. We can find the same result directly from (7.6). If the vacuum energy density is to remain constant, $\varrho_{\text{vac}} = \text{constant}$, it follows from that equation that $p = -\varrho c^2$.

Since vacuum fluctuations are now an integral part of modern physics, it is straightforward to work out what the cosmological vacuum energy should be. Carroll,

Press and Turner have described how a theoretical value of Λ can be estimated using simple concepts from quantum field theory (Carroll et al., 1992). In their approach, they perform a standard analysis to estimate the energy density of the vacuum fields by integrating to a maximum wavenumber k_{\max} at which the theory breaks down. They find

$$\varrho_{\text{vac}} = \lim_{L \rightarrow \infty} \frac{E_0}{L^3} = \hbar \frac{k_{\max}^4}{16\pi^2}. \quad (7.33)$$

They take the energy at which conventional field theory breaks down due to quantum gravitational effects to occur at the Planck energy scale, $E^* \approx 10^{19}$ GeV and hence, if $k_{\max} = E^*/\hbar$, $\varrho_{\text{vac}} \approx 10^{95}$ kg m⁻³.

A similar argument is presented by Peacock in his splendid book *Cosmological Physics* (Peacock, 2000). Heisenberg's Uncertainty Principle states that a virtual pair of particles of mass m can exist for a time $t \sim \hbar/mc^2$, corresponding to a maximum separation $x \sim \hbar/mc$. Hence, the typical density of the vacuum fields is $\varrho \sim m/x^3 \approx c^3 m^4/\hbar^3$. The mass density in the vacuum fields is unchanging with cosmic epoch and so, adopting the Planck mass for $m = m_{\text{Pl}} = (hc/G)^{1/2} = 5.4 \times 10^{-8}$ kg $\equiv 3 \times 10^{19}$ GeV, the mass density corresponds to about 10^{97} kg m⁻³.

There is now compelling evidence that Λ is finite with mass density corresponding to $\varrho_v \approx 6 \times 10^{-27}$ kg m⁻³, about 10^{120} times less than the predicted value. This is quite a problem, but it should not be passed over lightly. If the inflationary picture of the very early Universe is taken seriously, this is exactly the type of field which drove the inflationary expansion. Then, we have to explain why ϱ_v decreased by a factor of about 10^{120} at the end of the inflationary era. In this context, 10^{-120} looks remarkably close to zero, which would correspond to the standard Friedman picture with $\Lambda = 0$, but this evidently cannot be the type of Universe we live in.

Thus, it is now quite natural to believe that there are indeed forces in nature which can provide Zeldovich's 'repulsion of the vacuum' and to associate a certain mass density ϱ_v with the energy density of the vacuum, or the *dark energy*, at the present epoch. It is convenient to rewrite the formalism we have developed above in terms of a density parameter Ω_Λ associated with the dark energy as follows. We begin with (7.30) in the form:

$$\ddot{a} = -\frac{4\pi G a}{3} \left(\varrho_m + \varrho_v + \frac{3p_v}{c^2} \right), \quad (7.34)$$

where, in addition to the density of 'dust' ϱ_m , we have included the mass density ϱ_v and pressure p_v of the vacuum fields. Since $p_v = -\varrho_v c^2$, it follows that

$$\ddot{a} = -\frac{4\pi G a}{3} (\varrho_m - 2\varrho_v). \quad (7.35)$$

As the Universe expands, $\varrho_m = \varrho_0/a^3$ and $\varrho_v = \text{constant}$. Therefore,

$$\ddot{a} = -\frac{4\pi G \varrho_0}{3a^2} + \frac{8\pi G \varrho_v a}{3}. \quad (7.36)$$

Equations (7.32) and (7.36) have precisely the same dependence of the ‘cosmological term’ upon the scale factor a and so we can formally identify the cosmological constant with the vacuum mass density.

$$\Lambda = 8\pi G \varrho_v . \quad (7.37)$$

At the present epoch, $a = 1$ and so

$$\ddot{a}(t_0) = -\frac{4\pi G \varrho_0}{3} + \frac{8\pi G \varrho_v}{3} . \quad (7.38)$$

A density parameter associated with ϱ_v can now be introduced, in exactly the same way as the density parameter Ω_0 was defined:

$$\Omega_\Lambda = \frac{8\pi G \varrho_v}{3H_0^2} \quad \text{and so} \quad \Lambda = 3H_0^2 \Omega_\Lambda . \quad (7.39)$$

The dynamical equations (7.30) and (7.31) can now be written

$$\ddot{a} = -\frac{\Omega_0 H_0^2}{2a^2} + \Omega_\Lambda H_0^2 a ; \quad (7.40)$$

$$\dot{a}^2 = \frac{\Omega_0 H_0^2}{a} - \frac{c^2}{\mathfrak{R}^2} + \Omega_\Lambda H_0^2 a^2 . \quad (7.41)$$

We now substitute the values of a and \dot{a} at the present epoch, $a = 1$ and $\dot{a} = H_0$, into (7.41) to find the relation between the curvature of space, Ω_0 and Ω_Λ :

$$\frac{c^2}{\mathfrak{R}^2} = H_0^2 [(\Omega_0 + \Omega_\Lambda) - 1] , \quad (7.42)$$

or

$$\kappa = \frac{1}{\mathfrak{R}^2} = \frac{[(\Omega_0 + \Omega_\Lambda) - 1]}{(c^2/H_0^2)} . \quad (7.43)$$

Thus, the condition that the spatial sections are flat Euclidean space becomes

$$(\Omega_0 + \Omega_\Lambda) = 1 . \quad (7.44)$$

We recall that the radius of curvature R_c of the spatial sections of these models change with scale factor as $R_c = a\mathfrak{R}$ and so, if the space curvature is zero now, it must have been zero at all times in the past.

7.3.2 Varying the Equation of State of the Vacuum Energy

A further generalisation of the formalism given above is to suppose that the equation of state has the generic form $p_i = w_i \varrho_i c^2$. We can then use the relativistic energy conservation equation (7.6) to find the variation of the density with scale factor a .

Equation (7.6) becomes

$$\frac{d\varrho_i}{da} + 3 \frac{\left(\varrho_i + \frac{p_i}{c^2}\right)}{a} = 0; \quad \frac{d\varrho_i}{da} = -\frac{3\varrho_i(1+w_i)}{a}. \quad (7.45)$$

Hence, integrating, the variation of the density with scale factor is

$$\varrho_i \propto a^{-3(1+w_i)}. \quad (7.46)$$

This result makes a lot of sense. In the case of cold matter, $w_i = 0$ and so $\varrho \propto a^{-3}$. For photons and ultrarelativistic matter, $w_i = 1/3$ and so $\varrho \propto a^{-4}$. For standard dark energy, $w_i = -1$ and $\varrho = \text{constant}$. It is therefore straightforward to repeat the analysis of the previous section to find the relations between the density parameter in the species i and the geometrical properties of the world models. We leave it as an exercise for the reader to show that the results of these calculations are:

$$\ddot{a} = -\frac{\Omega_0 H_0^2}{2a^2} - (1+3w_i) \frac{\Omega_{i0} H_0^2}{2a^{2+3w_i}}, \quad (7.47)$$

where the density parameter at the present epoch of the species i , Ω_{i0} , is given by

$$\Omega_{i0} = \frac{8\pi G \varrho_{i0}}{3H_0^2}. \quad (7.48)$$

The expression for \dot{a} becomes

$$\dot{a}^2 = \frac{\Omega_0 H_0^2}{a} + \frac{\Omega_{i0} H_0^2}{a^{1+3w_i}} - \frac{c^2}{\mathfrak{R}^2}. \quad (7.49)$$

Inserting the values of $a = 1$ and $\dot{a} = H_0$ at the present epoch, we find

$$\frac{c^2}{\mathfrak{R}^2} = H_0^2 [(\Omega_0 + \Omega_{i0}) - 1], \quad (7.50)$$

and so

$$\kappa = \frac{1}{\mathfrak{R}^2} = \frac{[(\Omega_0 + \Omega_{i0}) - 1]}{(c^2/H_0^2)}. \quad (7.51)$$

The reason for carrying out this extension of the standard formalism is that we can use these results to estimate w_i directly from the observations. Note also that (7.51) shows that the condition for flat spatial geometry is that all the contributions to Ω_0 and Ω_{0i} sum to unity,

$$\Omega_0 + \sum_i \Omega_{0i} = 1. \quad (7.52)$$

7.3.3 The Dynamics of World Models with $\Lambda \neq 0$: General Considerations

The dynamics of world models with $\Lambda \neq 0$ are of special importance in the light of the most recent estimates of the values of cosmological parameters. First of all, we

discuss some general considerations of the dynamics of these models and then look in more detail at the range of models which are likely to be relevant for our future studies.

Models with $\Lambda < 0$ are not of a great deal of interest because the net effect is to incorporate an attractive force in addition to gravity which slows down the expansion of the Universe. The one difference from the models with $\Lambda = 0$ is that, no matter how small the values of Ω_Λ and Ω_0 are, the universal expansion is eventually reversed, as may be seen by inspection of (7.32).

Models with $\Lambda > 0$, $\Omega_\Lambda > 0$ are much more interesting because a positive cosmological constant leads to a repulsive force which opposes the attractive force of gravity. In each of these models, there is a minimum rate of expansion \dot{a}_{\min} which is found by setting $\ddot{a} = 0$ in (7.40). The corresponding value of the scale factor and minimum rate of expansion are

$$a_{\min} = (\Omega_0/2\Omega_\Lambda)^{1/3}, \quad (7.53)$$

$$\dot{a}_{\min}^2 = \frac{3H_0^2}{2} (2\Omega_\Lambda\Omega_0^2)^{1/3} - \frac{c^2}{\mathfrak{R}^2}. \quad (7.54)$$

If the right-hand side of (7.54) is greater than zero, the dynamical behaviour shown in Fig. 7.3a is found. For large values of a , the dynamics become those of the de Sitter universe

$$a(t) \propto \exp \left[\left(\frac{\Lambda}{3} \right)^{1/2} t \right] = \exp \left(\Omega_\Lambda^{1/2} H_0 t \right). \quad (7.55)$$

If the right-hand side of (7.54) is less than zero, there exists a range of scale factors for which no solution exists and it can be shown readily that the function $a(t)$ has two branches, as illustrated in Fig. 7.3b. For the branch B, the Universe never expanded to sufficiently large values of a that the repulsive effect of the Λ -term can prevent the Universe collapsing. In the case of branch A, the dynamics are dominated by the Λ -term; the repulsive force is so strong that the Universe never contracted to such a scale that the attractive force of gravity could overcome its influence. In the latter model, there was no initial singularity – the Universe ‘bounced’ under the influence of the Λ -term. In the limiting case in which the density of matter is zero, $\Omega_0 = 0$, the dynamics of the model are described by

$$\dot{a}^2 = H_0^2 [\Omega_\Lambda a^2 - (\Omega_\Lambda - 1)], \quad (7.56)$$

which has solution

$$a = \left(\frac{\Omega_\Lambda - 1}{\Omega_\Lambda} \right)^{1/2} \cosh \Omega_\Lambda^{1/2} H_0 \tau, \quad (7.57)$$

where the time $\tau = t - t_{\min}$ is measured from the time at which the model ‘bounced’, that is, from the time at which $a = a_{\min}$. In all cases in which the models bounce, the variation of a with cosmic time is symmetrical about a_{\min} . Their asymptotic

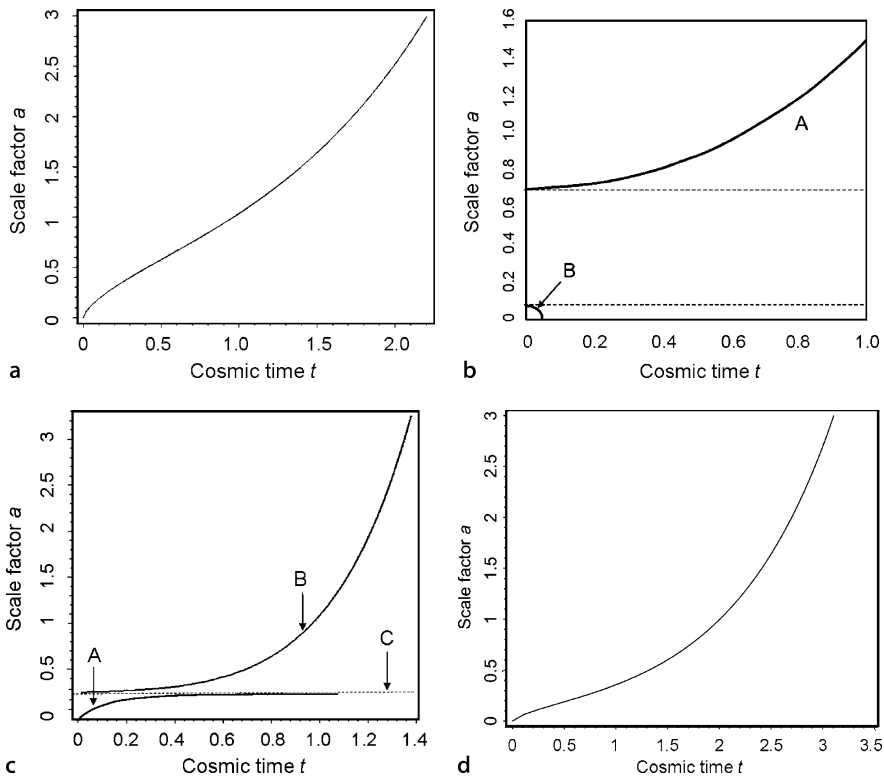


Fig. 7.3a–d. Examples of the dynamics of world models in which $\Lambda \neq 0$ (Bondi, 1960). Models **a** and **d** are referred to as Lemaître models. In **a**, the model parameters are $\Omega_0 = 0.3$ and $\Omega_\Lambda = 0.7$, a favoured model according to current best estimates of these parameters. **b** This ‘bouncing’ model has $\Omega_0 = 0.05$ and $\Omega_\Lambda = 2$. The zero of cosmic time has been set to the value when $\dot{a} = 0$. The loci are symmetrical in cosmic time with respect to this origin. **c** This model is an Eddington–Lemaître model which is stationary at redshift $z_c = 3$, corresponding to scale factor $a = 0.25$. In **d**, the model parameters are $\Omega_0 = 0.01$ and $\Omega_\Lambda = 0.99$ and the age of the Universe can far exceed H_0^{-1}

behaviour corresponds to exponentially collapsing and expanding de Sitter solutions

$$a = \left(\frac{\Omega_\Lambda - 1}{\Omega_\Lambda} \right)^{1/2} \exp(\pm \Omega_\Lambda^{1/2} H_0 \tau). \quad (7.58)$$

In these ‘bouncing’ Universes, the smallest value of a , a_{\min} , corresponds to the largest redshifts which objects could have.

The most interesting cases are those for which $\dot{a}_{\min} \approx 0$. The case where $\dot{a}_{\min} = 0$ is known as the *Eddington–Lemaître model* and is illustrated in Fig. 7.3c. The literal interpretation of these models is either: A, the Universe expanded from an origin at some finite time in the past and will eventually attain a stationary state in the infinite

future; B, the Universe is expanding away from a stationary solution in the infinite past. The stationary state C is unstable because, if it is perturbed, the Universe moves either onto branch B, or onto the collapsing variant of branch A. In Einstein's static Universe, the stationary phase occurs at the present day. From (7.53), the value of Λ corresponding to $\dot{a}_{\min} = 0$ is

$$\Lambda = \frac{3}{2}\Omega_0 H_0^2(1+z_c)^3 \quad \text{or} \quad \Omega_\Lambda = \frac{\Omega_0}{2}(1+z_c)^3, \quad (7.59)$$

where z_c is the redshift of the stationary state. The static Eddington–Lemaître models have $\dot{a} = 0$ for all time and so, setting the right-hand side of (7.41) equal to zero and substituting (7.59), we find a one-to-one relation between the mean density of matter in the Universe Ω_0 and the redshift of the stationary phase z_c ,

$$\Omega_0 = \frac{2}{(1+z_c)^3 - 3(1+z_c) + 2} = \frac{2}{z_c^2(z_c+3)}. \quad (7.60)$$

This calculation is largely of academic interest nowadays. If a stationary, or near-stationary, state had occurred, the fact that galaxies and quasars are now observed with redshifts $z > 6$ suggests that $z_c > 6$ and so $\Omega_0 \leq 0.01$, which is at least an order of magnitude less than the total mass density in dark matter at the present epoch.

The properties of the world models with non-zero cosmological constant are conveniently summarised in a plot of Ω_0 against $\Omega_0 + \Omega_\Lambda$ presented by Carroll, Press and Turner (Fig. 7.4) (Carroll et al., 1992). The world models with $\Lambda = 0$ lie along the 45° line passing through zero on both axes. As shown by (7.43), the spatial geometry of the world model depends upon the value of $\Omega_0 + \Omega_\Lambda$, the value unity separating the open from closed geometries. The models which were stationary in the past, corresponding to the dividing line between those models which had a singular past and those which ‘bounced’, are given by (7.59) and (7.60), the values of the stationary redshifts being indicated along the locus to the bottom right of the diagram – Carroll, Press and Turner call these ‘loitering’ models. Finally, the diagram also shows the dividing line between those models which will eventually recollapse to a ‘big crunch’ in the future and those which will expand forever. This dividing line can also be found from (7.59) and (7.60) by requiring the models to tend to stationary phases in the future, for which the values of a are greater than one and the redshifts less than zero. For example, using (7.60), we find that the model which is stationary at a scale factor $a = 1.5$, corresponding to $(1+z_c) = 2/3$, has $\Omega_0 = 27/16 = 1.69$. The corresponding value of Ω_Λ from (7.59) is 0.25, so that $\Omega_0 + \Omega_\Lambda = 31/16 = 1.94$, which lies on the solid line separating the models which expand to infinity from those which collapse in a finite time in Fig. 7.4.

The models with positive cosmological constant can have ages greater than H_0^{-1} . In the limiting cases of Eddington–Lemaître models with $\dot{a}_{\min} = 0$ in the infinite past, for example, the Universe is infinitely old. A closely related set of models, with ages which can be greater than H_0^{-1} , are the *Lemaître models* which have values of

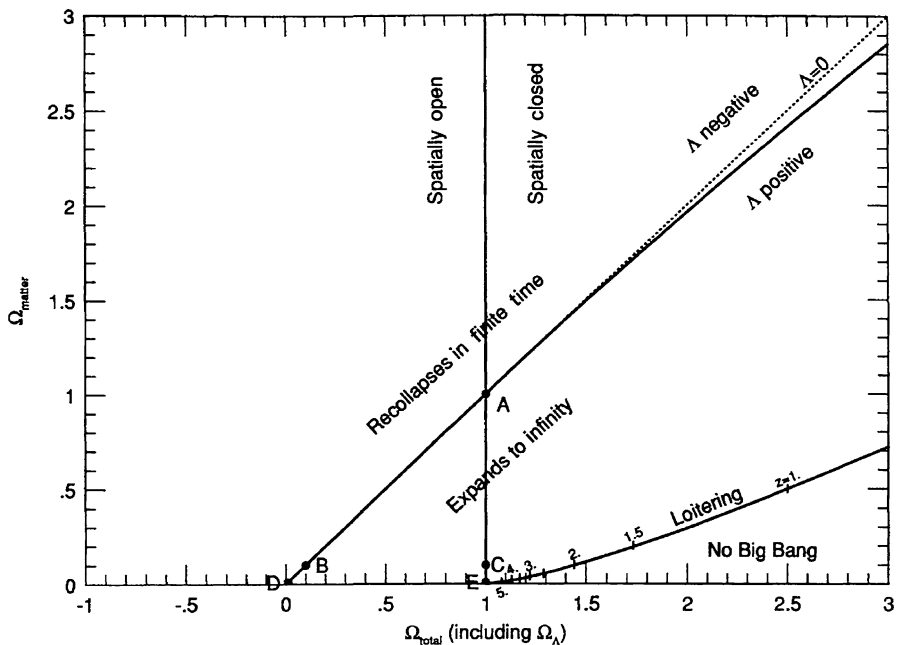


Fig. 7.4. The classification of the Friedman world models with $\Omega_\Lambda \neq 0$ in a plot of Ω_0 against $\Omega_0 + \Omega_\Lambda$ (Carroll et al., 1992). The Eddington–Lemaître models lie along the line labelled ‘loitering’

Ω_Λ such that the value of \dot{a}_{\min} is just greater than zero. An example of this type of model is shown in Fig. 7.3d.

As we will show in Chap. 15, there is now strong evidence that the spatial geometry of the Universe is flat, so that $\Omega_0 + \Omega_\Lambda$ is very close to unity. The dynamics of such spatially flat models with different combinations of Ω_0 and Ω_Λ are shown in Fig. 7.5. These models indicate how the age of the Universe can be greater than H_0^{-1} for large enough values of Ω_Λ .

7.4 Observations in Cosmology

Models with finite values of the cosmological constant dominate much of current cosmological thinking and so it is convenient to develop the expressions for the relations between observables and intrinsic properties in parallel for models with and without the Λ -term. The reason for including the results for world models with $\Omega_\Lambda = 0$ is that they can often be expressed analytically in closed form and so provide insight into the physics of the world models.

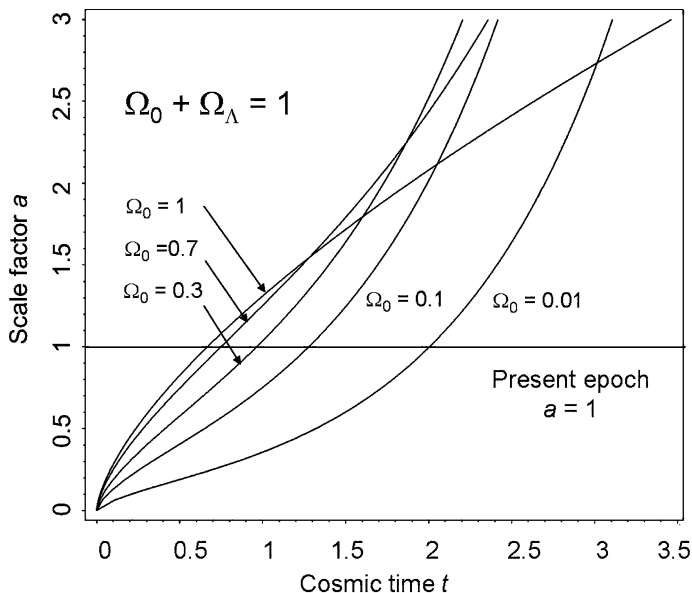


Fig. 7.5. The dynamics of spatially flat world models, $\Omega_0 + \Omega_\Lambda = 1$, with different combinations of Ω_0 and Ω_Λ . The abscissa is plotted in units of H_0^{-1} . The dynamics of these models can be compared with those shown in Fig. 7.2 which have $\Omega_\Lambda = 0$

7.4.1 The Deceleration Parameter

Just as Hubble's constant H_0 measures the expansion rate of the Universe at the present epoch, so we can define the present deceleration of the Universe $\ddot{a}(t_0)$. It is conventional to define the *deceleration parameter* q_0 to be the dimensionless deceleration at the present epoch through the expression

$$q_0 = -\left(\frac{a\ddot{a}}{\dot{a}^2}\right)_{t_0}. \quad (7.61)$$

Substituting $a = 1$, $\dot{a} = H_0$ at the present epoch into the dynamical equation (7.40), we find

$$q_0 = \frac{\Omega_0}{2} - \Omega_\Lambda. \quad (7.62)$$

Equation (7.62) represents the present competition between the decelerating effect of the attractive force of gravity and the accelerating effect of the repulsive dark energy. Substituting the favoured values of $\Omega_0 = 0.3$ and $\Omega_\Lambda = 0.7$ (see Chaps. 8 and 15), we find $q_0 = -0.55$, showing that the Universe is accelerating at the present epoch because of the dominance of the dark energy.

7.4.2 The Cosmic Time–Redshift Relation

An important result for many aspects of astrophysical cosmology is the relation between cosmic time t and redshift z . Combining (7.41) and (7.42), we find

$$\dot{a} = H_0 \left[\Omega_0 \left(\frac{1}{a} - 1 \right) + \Omega_\Lambda (a^2 - 1) + 1 \right]^{1/2}. \quad (7.63)$$

Because $a = (1+z)^{-1}$,

$$\frac{dz}{dt} = -H_0(1+z) \left[(1+z)^2(\Omega_0 z + 1) - \Omega_\Lambda z(z+2) \right]^{1/2}. \quad (7.64)$$

The cosmic time t measured from the Big Bang follows immediately by integration from $z = \infty$ to z ,

$$t = \int_0^t dt = -\frac{1}{H_0} \int_{\infty}^z \frac{dz}{(1+z)[(1+z)^2(\Omega_0 z + 1) - \Omega_\Lambda z(z+2)]^{1/2}}. \quad (7.65)$$

Let us evaluate this integral separately for models with $\Omega_\Lambda = 0$ and for finite Ω_Λ .

Models with $\Omega_\Lambda = 0$. For $\Omega_0 > 1$, we can write $x = (\Omega_0 - 1)a/\Omega_0 = (\Omega_0 - 1)/\Omega_0(1+z)$, and then the cosmic time–redshift relation becomes

$$t(z) = \frac{\Omega_0}{H_0(\Omega_0 - 1)^{3/2}} [\sin^{-1} x^{1/2} - x^{1/2}(1-x)^{1/2}]. \quad (7.66)$$

For $\Omega_0 < 1$, we write $y = (1-\Omega_0)a/\Omega_0 = (1-\Omega_0)/\Omega_0(1+z)$, and then the cosmic time–redshift relation becomes

$$t(z) = \frac{\Omega_0}{H_0(1-\Omega_0)^{3/2}} [y^{1/2}(1+y)^{1/2} + \sinh^{-1} y^{1/2}]. \quad (7.67)$$

For large redshifts, $z \gg 1$, $\Omega_0 z \gg 1$, (7.66) and (7.67) reduce to

$$t(z) = \frac{2}{3H_0\Omega_0^{1/2}} z^{-3/2}. \quad (7.68)$$

We can find the present age of the Universe for the different world models by integrating from $z = 0$ to $z = \infty$.

$$t_0 = \frac{\Omega_0}{H_0(\Omega_0 - 1)^{3/2}} \left[\sin^{-1} \left(\frac{\Omega_0 - 1}{\Omega_0} \right)^{1/2} - \frac{(\Omega_0 - 1)^{1/2}}{\Omega_0} \right] \quad \text{if } \Omega_0 > 1;$$

$$t_0 = \frac{2}{3H_0} \quad \text{if } \Omega_0 = 1;$$

$$t_0 = \frac{\Omega_0}{H_0(1-\Omega_0)^{3/2}} \left[\frac{(1-\Omega_0)^{1/2}}{\Omega_0} - \sinh^{-1} \left(\frac{1-\Omega_0}{\Omega_0} \right)^{1/2} \right] \quad \text{if } \Omega_0 < 1.$$

The age of the Universe is a monotonic function of Ω_0 . The useful simple cases are those for the critical model $\Omega_0 = 1$ for which the present age of the Universe is $(2/3)H_0^{-1}$ and the empty model, $\Omega_0 = 0$, for which it is H_0^{-1} . For $\Omega_0 = 2$, the age of the Universe is $0.571 H_0^{-1}$.

Models with $\Omega_A \neq 0$. The time–redshift relation for any of the models with finite Ω_A can be found by integration of (7.65). The models with zero curvature are of particular interest and there is a simple analytic solution for the cosmic time–redshift relation for these models. From (7.44), the condition that the curvature of space is zero, $\mathfrak{R} \rightarrow \infty$, is $\Omega_0 + \Omega_A = 1$. Then, from (7.65),

$$t = \int_0^t dt = -\frac{1}{H_0} \int_{\infty}^z \frac{dz}{(1+z)[\Omega_0(1+z)^3 + \Omega_A]^{1/2}} . \quad (7.69)$$

The cosmic time–redshift relation becomes

$$t = \frac{2}{3H_0\Omega_A^{1/2}} \ln \left(\frac{1+\cos\theta}{\sin\theta} \right) \quad \text{where} \quad \tan\theta = \left(\frac{\Omega_0}{\Omega_A} \right)^{1/2} (1+z)^{3/2} . \quad (7.70)$$

The present age of the Universe follows by setting $z = 0$

$$t_0 = \frac{2}{3H_0\Omega_A^{1/2}} \ln \left[\frac{1+\Omega_A^{1/2}}{(1-\Omega_A)^{1/2}} \right] . \quad (7.71)$$

This relation illustrates how it is possible to find a Friedman model which has age greater than H_0^{-1} and yet has flat spatial sections. For example, if $\Omega_A = 0.9$ and $\Omega_0 = 0.1$, the age of the world model would be $1.28H_0^{-1}$. For the popular world model with $\Omega_0 = 0.3$ and $\Omega_A = 0.7$, the age of the Universe is $0.964H_0^{-1}$, remarkably close to H_0^{-1} .

7.4.3 Distance Measures as a Function of Redshift

We can now complete our programme of finding expressions for the comoving radial distance coordinate r and the distance measure D . We recall that the increment of comoving radial coordinate distance is

$$dr = -\frac{c dt}{a(t)} = -c dt(1+z) . \quad (7.72)$$

From (7.64),

$$dr = -\frac{c dt}{a} = \frac{c}{H_0} \frac{dz}{[(1+z)^2(\Omega_0 z + 1) - \Omega_A z(z+2)]^{1/2}} , \quad (7.73)$$

and so, integrating from redshift 0 to z , we find the expression for r ,

$$r = \frac{c}{H_0} \int_0^z \frac{dz}{[(1+z)^2(\Omega_0 z + 1) - \Omega_A z(z+2)]^{1/2}} . \quad (7.74)$$

Then, we can find the distance measure D by evaluating $D = \mathfrak{R} \sin(r/\mathfrak{R})$, where \mathfrak{R} is given by (7.42). Let us discuss first the case $\Omega_A = 0$.

Models with $\Omega_\Lambda = 0$. Integrating (7.74) with $\Omega_\Lambda = 0$ and $\Omega_0 > 1$, we find

$$r = \frac{c}{H_0} \int_0^z \frac{dz}{(1+z)(\Omega_0 z + 1)^{1/2}} \quad (7.75)$$

$$= \frac{2c}{H_0(\Omega_0 - 1)^{1/2}} \left[\tan^{-1} \left(\frac{\Omega_0 z + 1}{\Omega_0 - 1} \right)^{1/2} - \tan^{-1} (\Omega_0 - 1)^{-1/2} \right]. \quad (7.76)$$

If $\Omega_0 < 1$, the inverse tangents are replaced by inverse hyperbolic tangents. After some further straightforward algebra, we find that

$$D = \frac{2c}{H_0 \Omega_0^2 (1+z)} \{ \Omega_0 z + (\Omega_0 - 2)[(\Omega_0 z + 1)^{1/2} - 1] \}. \quad (7.77)$$

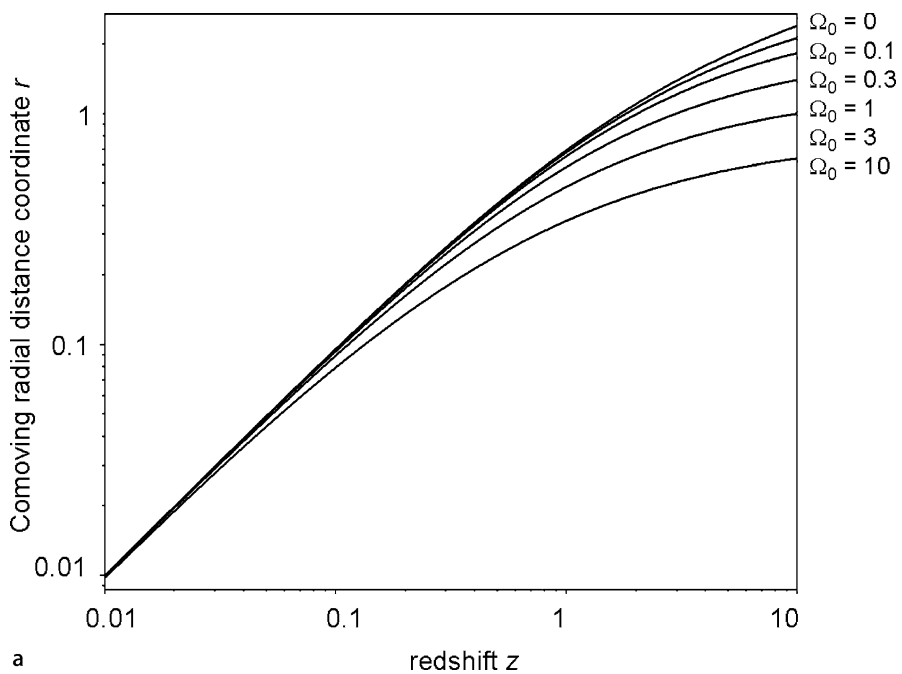
This is the famous formula first derived by Mattig (Mattig, 1959). Although the integral has been found for the case of spherical geometry, it turns out that the formula is correct for all values of Ω_0 . In the limit of the empty, or Milne, world model, $\Omega_0 = 0$, (7.77) becomes

$$D = \frac{cz}{H_0} \frac{\left(1 + \frac{z}{2}\right)}{(1+z)}. \quad (7.78)$$

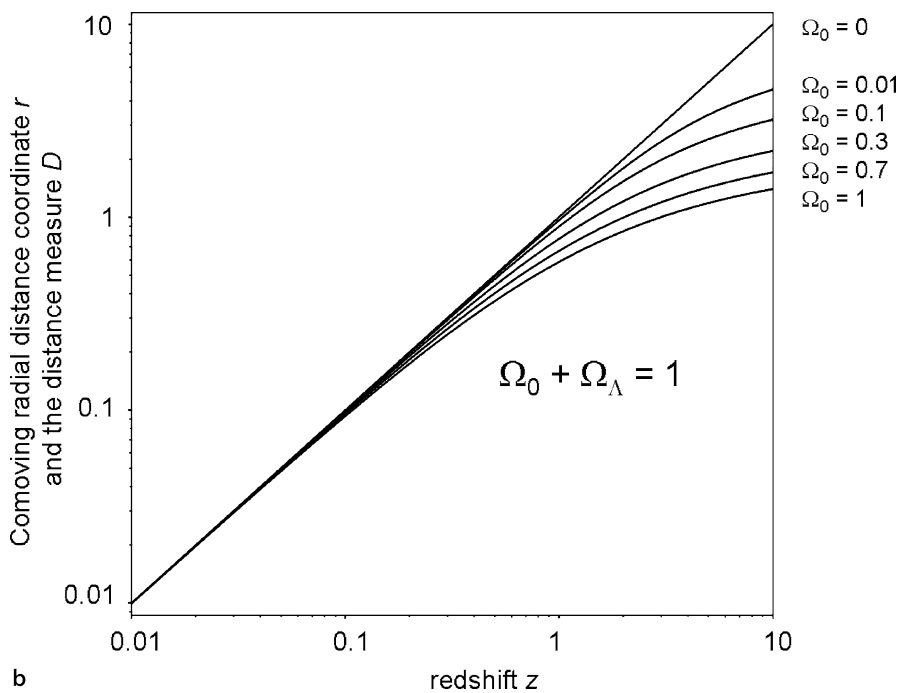
The variations of r and D with redshift for a range of standard world models are shown in Figs. 7.6a and 7.7.

Models with $\Omega_\Lambda \neq 0$. Solutions of the integral (7.74) for the case $\Omega_\Lambda \neq 0$ may be found in terms of elliptic functions but we do not wish to enter into that exercise here. It is generally easier to evaluate the comoving radial distance coordinate r and distance measure $D = \mathfrak{R} \sin(r/\mathfrak{R})$ by numerical integration. Some examples of these computations for flat world models with $\Omega_0 + \Omega_\Lambda = 1$ for different values of Ω_0 are shown in Fig. 7.6b. Notice that, because the geometry of these world models is flat $\mathfrak{R} = \infty$, $r = D$.

Figures 7.6 and 7.7 repay some study. For the models with $\Omega_\Lambda = 0$, the smaller the value of Ω_0 , the greater the comoving radial distance coordinate at a given redshift. We can interpret this result in terms of the light travel time along the radial geodesic from the source to the observer on Earth. The smaller the deceleration of the expansion, the greater the distance light has to travel to reach the Earth. Likewise, for the models with finite values of Ω_Λ , the greater the value of Ω_Λ , the greater the stretching of the cosmic time-scale and so the greater the light travel time to the Earth. The comparison of Figs. 7.6a and 7.7 shows the influence of the curved spatial geometry upon the observed properties of distant objects. For the case $\Omega_0 = 1$, D and r are the same in the two diagrams since the geometry is flat. For other values of Ω_0 , the loci of the distance measure D in Fig. 7.7 diverge with respect to this model because of their hyperbolic ($\Omega_0 < 1$) and spherical ($\Omega_0 > 1$) geometries.



a



b

Fig. 7.6a,b. The variation with redshift of **a** the radial comoving distance coordinate r for models with $\Omega_A = 0$, and **b** the comoving radial distance coordinate r for models with $\Omega_A \neq 0$. Because the geometry is flat, $\Omega_0 + \Omega_A = 1$, r is also equal to the distance measure D in Fig. 7.6b. In the case $\Omega_A = 1$, $D = r = (c/H_0)z$. In both diagrams, r and D are measured in units of c/H_0

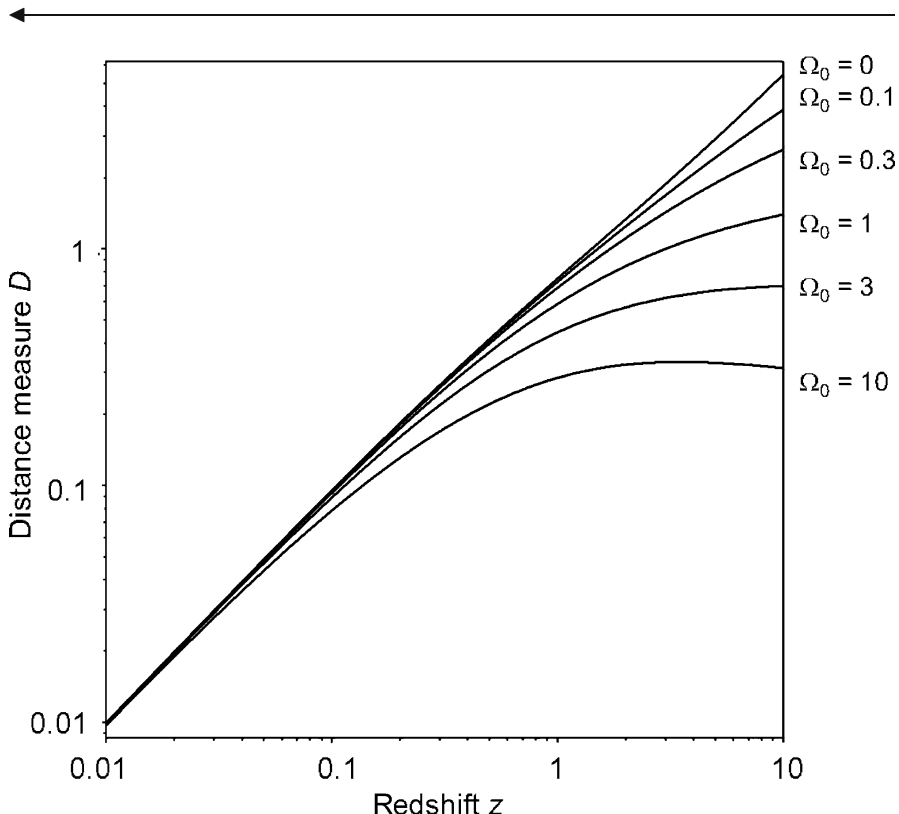


Fig. 7.7. The variation with redshift of the distance measure D for Friedman world models with $\Omega_A = 0$. D is measured in units of c/H_0

7.4.4 Angular Diameter–Redshift Relations

Models with $\Omega_A = 0$. In Fig. 7.8a, the variation of the observed angular size of a rigid rod of unit proper length is shown using the expressions (5.54) and (7.77) – this type of angular diameter is known as a *metric angular diameter*. Except for the empty world model, $\Omega_0 = 0$, there is a minimum in the angular diameter–redshift relation which occurs at $z = 1.25$ for the critical model, $\Omega_0 = 1$, and at $z = 1$ if $\Omega_0 = 2$. The reason for the minimum in the angular diameter–redshift relation is a combination of two effects. The first is the curved spatial geometry of the world models and the second, and more important, is the fact that a rigid rod occupies

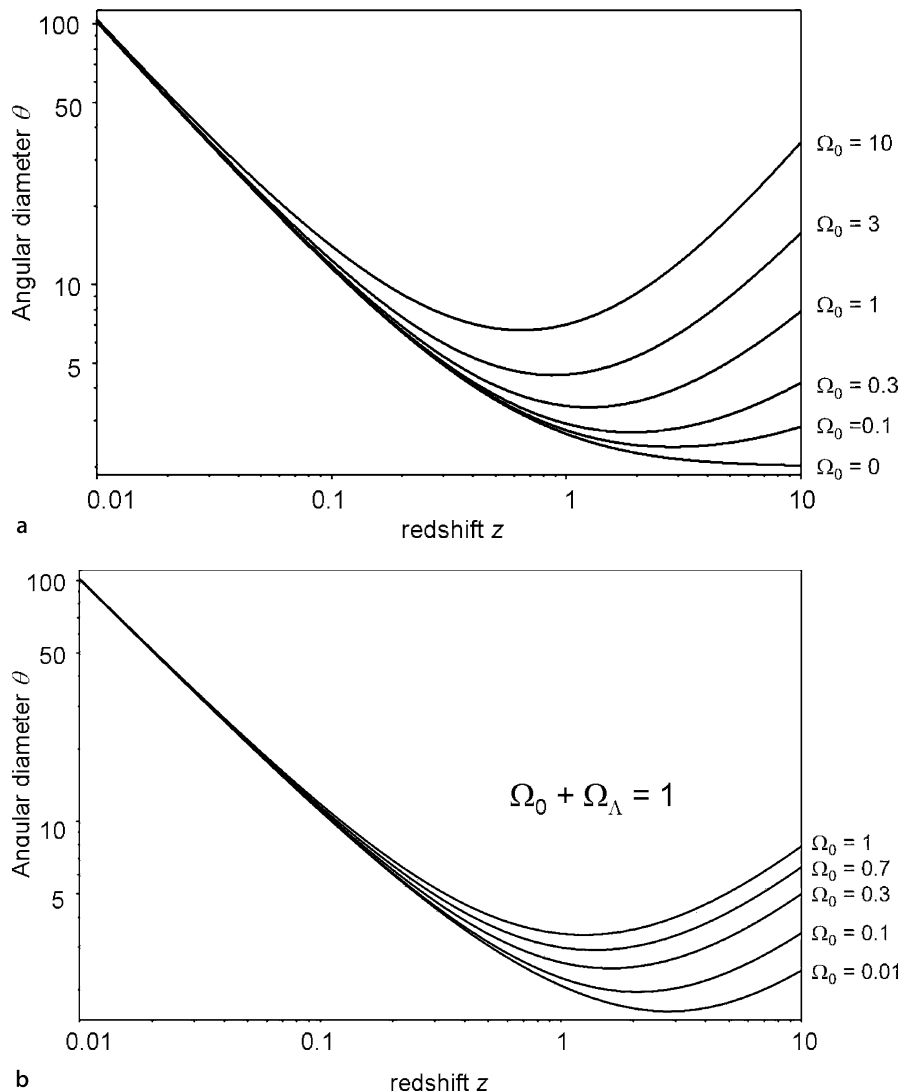


Fig. 7.8. **a** The variation of the angular diameter of a rigid rod of unit proper length with redshift for world models with $\Omega_\Lambda = 0$. **b** The variation of the angular diameter of a rigid rod of unit proper length with redshift for world models with finite values of Ω_Λ and flat spatial geometry, $\Omega_0 + \Omega_\Lambda = 1$. In both diagrams, c/H_0 has been set equal to unity

a larger fraction of the celestial sphere at a large redshift, by the factor $(1+z)$ which appears in (5.54).

Metric angular diameters are different from the types of angular diameter which are often used to measure the sizes of galaxies. The latter are often defined to some limiting surface brightness and so, since bolometric surface brightnesses vary with

redshift as $(1+z)^{-4}$, angular sizes measured to the same limiting surface brightness at a wide range of redshifts are not rigid rods of fixed proper length. The angular diameter–redshift relation can be worked out for *isophotal angular diameters*, but this requires knowledge of the K-corrections to be applied as a function of radius within the galaxy.

Models with $\Omega_\Lambda \neq 0$. The corresponding metric angular diameter–redshift relations for models with flat spatial geometry and finite values of Ω_Λ are shown in Fig. 7.8b. All these models have minima at some redshift, reflecting the fact that $r(z)$ ‘saturates’ at large redshifts (Fig. 7.6b) and the $(1+z)$ term in the expression (5.54) dominates the dependence upon redshift.

7.4.5 Flux Density–Redshift Relations

Models with $\Omega_\Lambda = 0$ and $\Omega_\Lambda \neq 0$. The observed flux density of a source of unit luminosity per unit frequency interval at frequency ν_0 with a power law spectrum $L(\nu) \propto \nu^{-1}$ is given by (5.65) with the distance measure D given by (7.77) for models with $\Omega_\Lambda = 0$ (Fig. 7.9a). The corresponding diagram for flat spatial models with $\Omega_\Lambda \neq 0$ are shown in Fig. 7.9b. Comparison of (5.65) and (5.66) shows that, because we have taken the spectral index to be $\alpha = 1$, these are also the variations of the bolometric flux density with redshift in both cases. For galaxies, the detailed form of the spectrum has to be taken into account and this is often done using the K-corrections described by (5.69), (5.70) and (5.71). Figure 7.9 illustrates the very considerable challenge involved in attempting to distinguish between world models using the redshift–apparent magnitude, or flux density–redshift, relation. Objects with remarkably standard luminosities need to be used to have a hope of making progress. Fortunately, this has been achieved with the use of the Type 1a supernovae.

Ghost images. A unique feature of the Lemaître world models is the possible appearance of *ghost images*. In the Eddington–Lemaître models, the curvature of space κ is positive, as may be seen from the location of the ‘loitering’ line in Fig. 7.4. Those models which have \dot{a}_{\min} just greater than zero also have closed spherical spatial sections, as may also be seen in Fig. 7.4. Since the expansion almost stops at redshift z_c , there is time for electromagnetic waves to propagate from the source to the observer a number of times around the closed geometry of the Universe. In principle, the same object may be observed in diametrically opposite directions, or multiply in the same position on the sky, although at different redshifts and consequently at different times in its life-history.

To illustrate this behaviour, consider the case of the Eddington–Lemaître model which is stationary at redshift $z_c = 3$. In this case, the density parameter can be found from (7.60), $\Omega_0 = 1/27$, and the value of Ω_Λ from (7.59), $\Omega_\Lambda = 32/27$. Consequently, the radius of curvature of the closed geometry is $\mathfrak{R} = (27/6)^{1/2}(c/H_0)$. Inserting these values into (7.74) and integrating, we find the relation between r/\mathfrak{R} and redshift shown in Fig. 7.10. The values of $r/\mathfrak{R} = \pi, 2\pi, 3\pi$ and 4π are shown. It can be seen that r/\mathfrak{R} tends to infinity as the redshift approaches the stationary value $z_c = 3$.

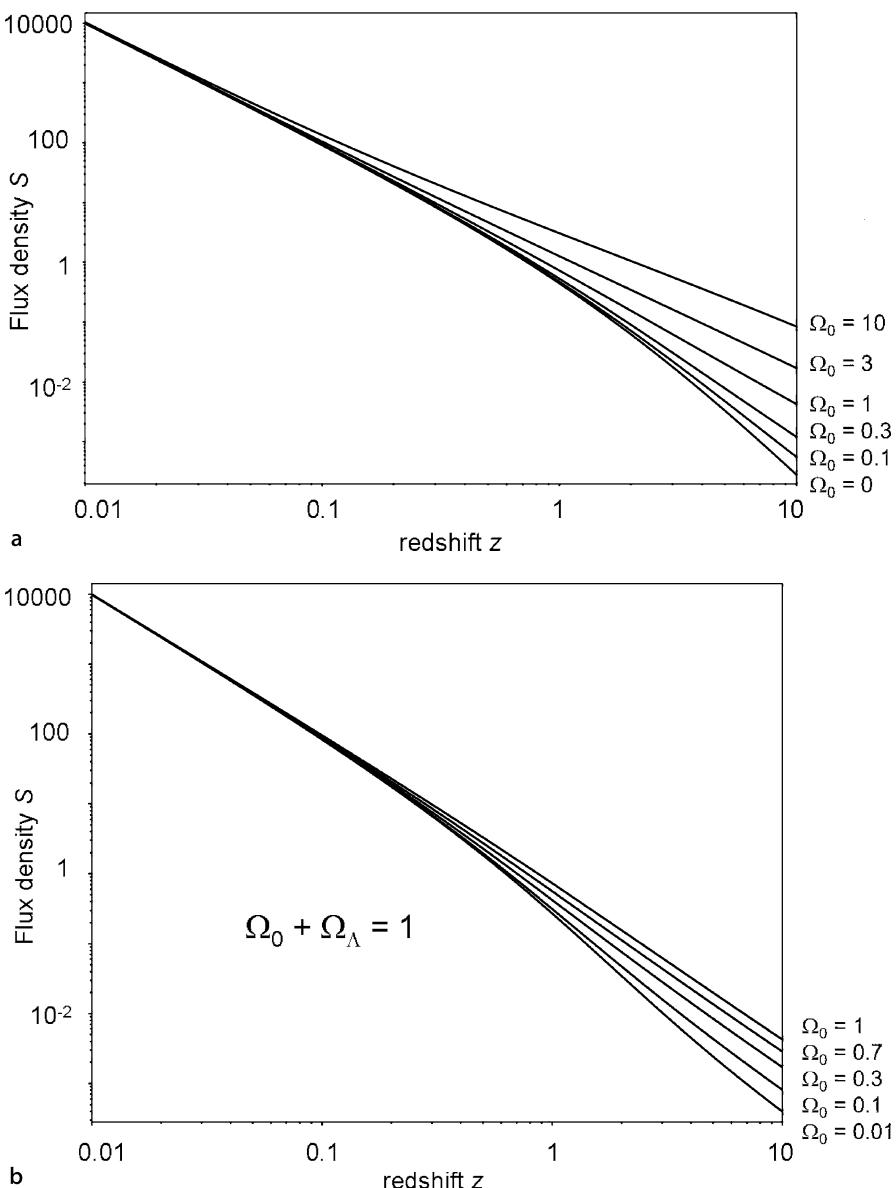


Fig. 7.9. The variation of the flux density of a source of luminosity 1 W Hz^{-1} with a power law spectrum $L(\nu) \propto \nu^{-1}$ with redshift. In both diagrams, $c/H_0 = 1$. Comparison of (5.65) and (5.66) shows that, since the spectral index $\alpha = 1$, these relations are the same as the variations of bolometric flux densities with redshift. **a** World models with $\Omega_\Lambda = 0$. **b** World models with finite values of Ω_Λ and flat spatial geometry $\Omega_0 + \Omega_\Lambda = 1$

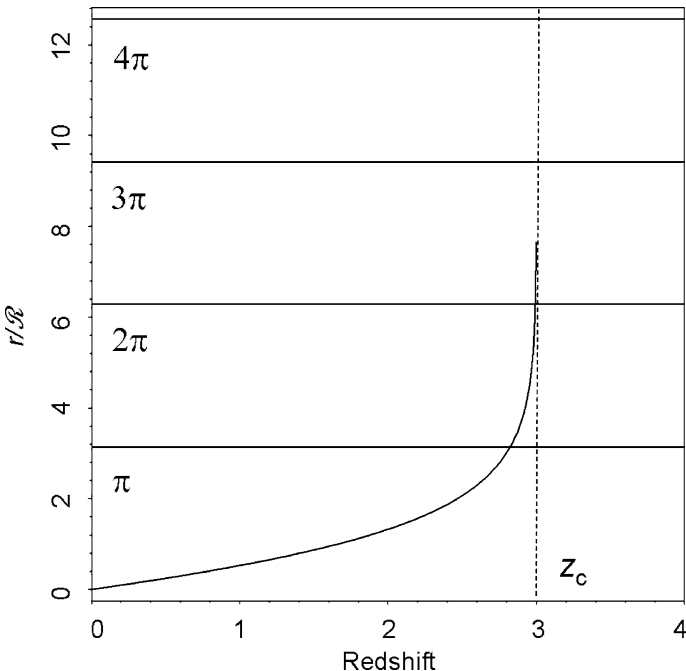


Fig. 7.10. The function r/\mathcal{R} as a function of redshift z for the Eddington–Lemaître model which is stationary at redshift $z_c = 3$

The flux density–redshift relation for a source with spectral index $\alpha = 1$, defined by $S \propto \nu^{-\alpha}$, is

$$S \propto \frac{1}{[\mathcal{R} \sin(r/\mathcal{R})]^2(1+z)^2}. \quad (7.79)$$

It can therefore be seen that there is a first minimum in the flux density–redshift relation corresponding to $r/\mathcal{R} = \pi/2$ and the observed flux density diverges at $r/\mathcal{R} = \pi$, corresponding to redshift $z = 2.825$. This behaviour is repeated in the intervals $\pi < r/\mathcal{R} < 2\pi$, $2\pi < r/\mathcal{R} < 3\pi$, $3\pi < r/\mathcal{R} < 4\pi$, . . . , the corresponding redshifts being 2.9923, 2.99967, 2.999986 and so on. The interpretation of these phenomena is that, at $r/\mathcal{R} = \pi$, we observe the antipodal point in the spherical closed geometry to our own location in the Universe. We may think of the light from a galaxy at the antipodal point being focussed on our own Galaxy at $z = 0$. In the case $r/\mathcal{R} = 2\pi$, we observe our own locality, but as it was at the redshift $z = 2.9923$. These repeated images occur indefinitely as $z \rightarrow z_c$.

A corollary of this behaviour is that we can observe the same object in opposite directions in the sky, provided it has a very long lifetime. The radiation sets off in opposite directions from the source in the closed spherical geometry. If the source is observed at the redshift corresponding to r/\mathcal{R} , there will be an image of the source at an earlier time in the opposite direction with redshift corresponding to $2\pi - r/\mathcal{R}$.

Similar results are found in Lemaître models which do not quite reach the stationary state but have slightly positive values of \dot{a}_{\min} . They would lie just slightly above the ‘loitering’ line in Fig. 7.4. These models have to be rather finely tuned for the effect to be observable.

The possibility of observing ‘ghost’ images does not occur in the Friedman models with $\Omega_A = 0$. It is left as an exercise for the reader to use (7.76) to show that in all closed Friedman models with $\Omega_A = 0$, r/\mathfrak{R} tends to $\pi/2$ as z tends to infinity. Since $r/\mathfrak{R} = \pi/2$ corresponds to light rays propagating from the minimum flux density in the closed geometry to the Earth, the possibility of observing the same source in opposite directions in the sky, or multiple images of the same object in the same direction, does not occur.

The reason for discussing this aspect of the Lemaître models is that, if such repeated ‘ghost’ images were found, this would be evidence that the Universe passed through a long quasi-stationary phase. Searches for such ghost images have been carried out using large catalogues of extragalactic radio sources, but no positive result has been reported.

7.4.6 The Comoving Volume Within Redshift z

This relation can be determined from (5.72) by integration using the familiar expressions for the element of comoving radial distance coordinate dr and the distance measure D .

Models with $\Omega_A = 0$. In these cases, there are convenient expressions for the three cases with $\kappa > 1$, $\kappa = 1$ and $\kappa < 1$. The expression (5.72) can be integrated for the case $\Omega_0 > 1$, $\mathfrak{R} = (c/H_0)(\Omega_0 - 1)^{-1/2}$ to give

$$V(z) = 2\pi\mathfrak{R}^3 \left(\frac{r}{\mathfrak{R}} - \frac{1}{2} \sin \frac{2r}{\mathfrak{R}} \right) = 2\pi\mathfrak{R}^3 \left(\sin^{-1} \frac{D}{\mathfrak{R}} - \frac{D}{\mathfrak{R}} \sqrt{1 - \frac{D^2}{\mathfrak{R}^2}} \right). \quad (7.80)$$

For the case $\Omega_0 < 1$, $\mathfrak{R} = (c/H_0)(1 - \Omega_0)^{-1/2}$,

$$V(z) = 2\pi\mathfrak{R}^3 \left(\frac{1}{2} \sinh \frac{2r}{\mathfrak{R}} - \frac{r}{\mathfrak{R}} \right) = 2\pi\mathfrak{R}^3 \left(\frac{D}{\mathfrak{R}} \sqrt{1 + \frac{D^2}{\mathfrak{R}^2}} - \sinh^{-1} \frac{D}{\mathfrak{R}} \right). \quad (7.81)$$

For the critical world model, $\Omega_0 = 1$, $\mathfrak{R} = \infty$, $r = D$ and so

$$V(z) = \frac{4\pi}{3} r^3. \quad (7.82)$$

Examples of the comoving volume within redshift z are shown in Fig. 7.11a. Notice in Fig. 7.11a the convergence of the enclosed volume at redshifts $z > 1$. One of the problems of finding large redshift objects can be appreciated from this diagram. Whereas, at small redshifts, the volume elements increase with redshift as $z^2 dz$, at large redshifts, $\Omega_0 z > 1$, $z > 1$, the volume elements decrease with increasing redshift as $z^{-3/2} dz$ and so per unit redshift interval there are fewer sources and they become rarer and rarer with increasing redshift, even if the comoving number density is constant.

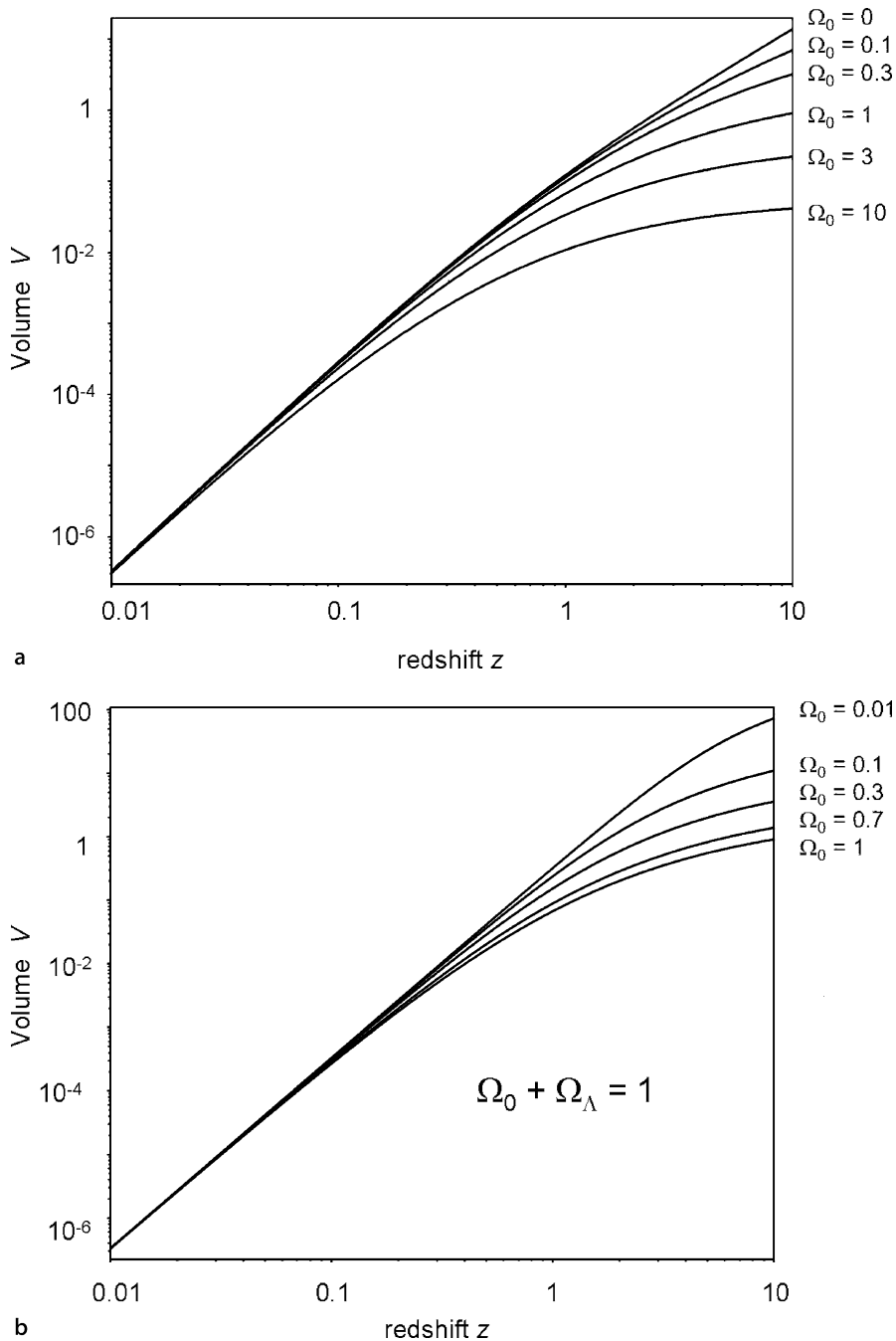


Fig. 7.11. **a** The variation of the comoving volume within redshift z for world models with $\Omega_\Lambda = 0$. **b** The variation of the comoving volume within redshift z for flat world models with finite values of Ω_Λ

Models with $\Omega_A \neq 0$. There is little alternative in general to numerical integration using the familiar expressions for the element of comoving radial distance coordinate dr and the distance measure D . The case of flat geometry, with $\Omega_0 + \Omega_A = 1$, is simpler since $D = r$. Some examples of the results for models with finite values of Ω_A are shown in Fig. 7.11b. The model with $\Omega_0 = 1$ appears on both Fig. 11a and b. It can be seen that there is greater enclosed volume in the models with finite Ω_A because of the stretching of the cosmological time-scale.

7.5 Angular Diameter Distances Between Any Two Redshifts

There are occasions when it is necessary to relate metric diameters as observed from locations other than the origin at $z = 0$. A good example is the geometry of gravitational lensing in which we need the angular diameter distance $D_A(z_i, z_j)$, meaning the angular diameter distance necessary to work out the physical size of an object which subtends an angle θ between redshifts z_i and z_j (see Sect. 4.6 and (4.40)). It is a useful exercise to derive the pleasant result presented by Blandford and Narajan for the appropriate angular diameter distance to be used for models with $\Omega_A = 0$ (Blandford and Narayan, 1992). The extension to models with $\Omega_A \neq 0$ follows the same line of development, but it is simplest to carry out these calculations by numerical integration.

Models with $\Omega_A = 0$. We begin with the expression for the comoving radial distance coordinate r_{ij} between redshifts z_i and z_j . By extension of (7.76), we find

$$\begin{aligned} r_{ij} &= \frac{2c}{H_0(\Omega_0 - 1)^{1/2}} \left[\tan^{-1} \left(\frac{\Omega_0 z_j + 1}{\Omega_0 - 1} \right)^{1/2} - \tan^{-1} \left(\frac{\Omega_0 z_i + 1}{\Omega_0 - 1} \right)^{1/2} \right] \\ &= \frac{2c}{H_0(\Omega_0 - 1)^{1/2}} \left[\tan^{-1} \frac{G_j}{(\Omega_0 - 1)^{1/2}} - \tan^{-1} \frac{G_i}{(\Omega_0 - 1)^{1/2}} \right], \end{aligned} \quad (7.83)$$

where $G_j = (\Omega_0 z_j + 1)^{1/2}$ and $G_i = (\Omega_0 z_i + 1)^{1/2}$. Using the summation formulae for inverse tangents, this can be rewritten

$$r_{ij} = \frac{2c}{H_0(\Omega_0 - 1)^{1/2}} \tan^{-1} \frac{N_1(\Omega_0 - 1)^{1/2}}{N_2}, \quad (7.84)$$

where $N_1 = (G_j - G_i)$ and $N_2 = (\Omega_0 - 1 + G_i G_j)$.

We now form the expression $\Re' \sin(r'_{ij}/\Re')$ in order to find the distance measure D_{ij} between the redshifts z_i and z_j . We need to use the radius of curvature of the spatial geometry \Re' and the comoving radial distance coordinate r'_{ij} at the redshift z_i , but these both scale as $a(t)$ and so, since $\Re = (c/H_0)/(\Omega_0 - 1)^{1/2}$,

$$\sin \frac{r'_{ij}}{\Re'} = \sin \frac{r_{ij}}{\Re} = \sin \left[2 \tan^{-1} \frac{N_1(\Omega_0 - 1)^{1/2}}{N_2} \right] \quad (7.85)$$

$$= \frac{2N_1 N_2 (\Omega_0 - 1)^{1/2}}{N_1^2 (\Omega_0 - 1) + N_2^2}. \quad (7.86)$$

Hence the distance measure $D(z_i, z_j)$ is

$$D(z_i, z_j) = \mathfrak{N}' \sin \frac{r'_{ij}}{\mathfrak{N}'} = \frac{2c}{H_0(1+z_i)} \frac{N_1 N_2}{N_1^2(\Omega_0 - 1) + N_2^2}. \quad (7.87)$$

Expanding the denominator of the second term, we find

$$N_1^2(\Omega_0 - 1) + N_2^2 = \Omega_0^2(1+z_i)(1+z_j), \quad (7.88)$$

and so the distance measure from z_i to z_j is

$$D(z_i, z_j) = \frac{2c}{H_0\Omega_0^2} \frac{(G_j - G_i)(\Omega_0 - 1 + G_i G_j)}{(1+z_i)^2(1+z_j)}. \quad (7.89)$$

Therefore, following the argument which led to (5.54), but now between the scale factors $a(z_1)$ and $a(z_2)$, we find

$$\theta = \frac{d(1+z_j)}{D(z_i, z_j)(1+z_i)} = \frac{d}{D_A(z_i, z_j)}, \quad (7.90)$$

where the angular diameter distance $D_A(z_i, z_j)$ is given by

$$D_A(z_i, z_j) = \frac{D(z_i, z_j)(1+z_i)}{(1+z_j)} \quad (7.91)$$

$$= \frac{2c}{H_0\Omega_0^2} \frac{(G_j - G_i)(\Omega_0 - 1 + G_i G_j)}{(1+z_i)(1+z_j)^2}. \quad (7.92)$$

This is the expression for the angular diameter distance between redshifts z_i and z_j quoted by Blandford and Narajan and can be used in the expressions for the gravitational lens formulae (4.39) to (4.41). Expression (7.92) has the attractive feature that it can be used in either direction along the light cone. Thus, the angular diameter distance from z_j to z_i is found by interchanging the indices i and j in (7.92),

$$D_A(z_j, z_i) = \frac{2c}{H_0\Omega_0^2} \frac{(G_i - G_j)(\Omega_0 - 1 + G_i G_j)}{(1+z_j)(1+z_i)^2}, \quad (7.93)$$

and so we find

$$\frac{D_A(z_i, z_j)}{D_A(z_j, z_i)} = \frac{(1+z_i)}{(1+z_j)}. \quad (7.94)$$

This is precisely the *reciprocity theorem* which we alluded to in Sect. 5.5.4. The angular diameter distances to be used in opposite directions along the light cone differ by the ratio of the scale factors corresponding to the redshifts z_1 and z_2 . If we set $z_i = 0$ and $z_j = z$, we find

$$\frac{D_A(0 \rightarrow z)}{D_A(z \rightarrow 0)} = \frac{1}{(1+z)}, \quad (7.95)$$

as we demonstrated in Sect. 5.5.4.

Models with $\Omega_A \neq 0$. In place of (7.84), we write

$$r_{ij} = \frac{c}{H_0} \int_{z_i}^{z_j} \frac{dz}{[(1+z)^2(\Omega_0 z + 1) - \Omega_A z(z+2)]^{1/2}} \quad (7.96)$$

and then form $D_{ij} = \Re \sin(r_{ij}/\Re)$ using the expression $\Re^2 = (c/H_0)^2/[(\Omega_0 + \Omega_A) - 1]$. In the case of the flat models, $\Re \rightarrow \infty$ and so $D_{ij} = r_{ij}$ which simplifies the further analysis. These values of D_{ij} can be used directly in (7.90) and (7.91). This is an important set of computations since the D_{ij} are needed in order to work out the statistics of gravitationally lensed images expected in deep images of the sky.

7.6 The Flatness Problem

Hubble's constant was introduced in Section 5.5.2 where it was emphasised that, in general, it changes with cosmic epoch. We can find the variation of Hubble's constant with redshift from (7.63) by setting $a = (1+z)^{-1}$. Then,

$$H(z) = \frac{\dot{a}}{a} = H_0 [(1+z)^2(\Omega_0 z + 1) - \Omega_A z(z+2)]^{1/2}. \quad (7.97)$$

In the same way, we can define a density parameter Ω at any epoch through the definition $\Omega = 8\pi G \rho / 3H^2$. For the case of 'dust' $\rho = \rho_0(1+z)^3$ and so

$$\Omega = \frac{8\pi G}{3H^2} \rho_0 (1+z)^3 \quad (7.98)$$

$$= \frac{\Omega_0}{\left[\frac{\Omega_0 z + 1}{1+z} \right] - \Omega_A \left[\frac{1}{(1+z)} - \frac{1}{(1+z)^3} \right]}. \quad (7.99)$$

Therefore at large redshifts $z \gg 1$, $\Omega_0 z \gg 1$, it can be seen that the terms in the second square bracket in the denominator of (7.99) tend to zero and the terms in the first square bracket tends to Ω_0 . Therefore, at large redshifts, $\Omega \rightarrow 1$, *whatever the value of Ω_0 at the present epoch*.

It is not surprising that the dark energy is unimportant dynamically at large redshifts because of the very different dependences of the matter and the dark energy densities upon redshift. Let us therefore set the term in Ω_A equal to zero and rewrite (7.99) as follows:

$$\left(1 - \frac{1}{\Omega}\right) = (1+z)^{-1} \left(1 - \frac{1}{\Omega_0}\right). \quad (7.100)$$

There are two ways of looking at this result. On the one hand, it reaffirms our conclusion from (7.29) that the dynamics of all the world models tend to those of the critical model in their early stages. On the other hand, it is remarkable that the Universe is as close as it is to the value $\Omega_0 = 1$ at the present day. If the value

of Ω_0 were significantly different from 1 in the distant past, then it would be very different from 1 now as can be seen from (7.100). There is nothing in the standard models which requires Ω_0 to take any particular value – it is simply a parameter which should be fixed as part of the initial conditions of our Universe.

As will be shown in Chaps. 8 and 15, the observational evidence strongly suggests that $\Omega_0 \approx 0.3$, which on its own means that the curvature of space κ must be close to zero at the present epoch. Indeed, as we will show in Chap. 15, the curvature of space as determined by the WMAP mission is quite remarkably close to zero. This is the origin of what is often referred to as the *flatness problem*, namely, that our Universe must have been very finely tuned indeed to the value $\Omega = 1$ in the distant past if it is to end up close to $\Omega_0 = 1$ now. This observation turns out to be one of the key pieces of empirical evidence for the *inflationary picture* of the early Universe.

7.7 Inhomogeneous World Models

The results derived above are exact for isotropic, homogeneous world models. The evidence discussed in Chap. 2 shows that the Universe is isotropic and homogeneous on the large scale but, on small scales, the Universe is very far from homogeneous. Matter is concentrated into stars and galaxies which are very large perturbations in the mean density. These perturbations cause deviations of the paths of light rays and it is important to understand their effect upon the results quoted above. We consider first the limiting case in which the matter distribution is so inhomogeneous that there is no matter within the light cone subtended by a distant object at the observer.

This problem was treated elegantly by Zeldovich using simple physical arguments (Zeldovich, 1964). Identical results are obtained more arduously from a general Riemannian approach to the propagation of light signals in inhomogeneous cosmological models. We consider the case of the critical Einstein–de Sitter world model, $\Omega_0 = 1$, $\Omega_A = 0$, for which the spatial geometry is flat, $\kappa = 0$, $\mathfrak{N} = \infty$.

If the Universe were so inhomogeneous that all the matter was condensed into point-like objects, there is only a small probability that there will be any matter within the light cone subtended by a distant object of small angular size. Because of the long-range nature of gravitational forces, however, the background metric remains the standard flat Einstein–de Sitter metric and the overall dynamics of the Universe are unaltered. The Robertson–Walker metric for the critical model can be written

$$ds^2 = dt^2 - \frac{a^2(t)}{c^2} [dr^2 + r^2(d\theta^2 + \sin^2 \theta d\phi^2)] \quad (7.101)$$

$$= dt^2 - \frac{a^2(t)}{c^2} [dx^2 + dy^2 + dz^2], \quad (7.102)$$

where $a(t) = (t/t_0)^{2/3}$ and $t_0 = \frac{2}{3}H_0$ is the present age of the Universe. The terms r , x , y and z are comoving coordinates referred to the present epoch t_0 .

First, we consider the homogeneous case. Consider the events A and B which correspond to the emission of light signals at cosmic time t from either end of

a standard rod of length L oriented at right angles to the line of sight at comoving radial distance coordinate r (Fig. 7.12a). Then, the interval between events is minus the square of a proper length

$$c^2 ds^2 = -a^2(t)r^2 d\theta^2 = -a^2(t) dy^2 = -L^2. \quad (7.103)$$

Since $a(t) = (1+z)^{-1}$, we recover the result of Sects. 5.5.3 and 7.4.4,

$$d\theta = \frac{L(1+z)}{r}, \quad (7.104)$$

where $r = D = (2c/H_0)[1 - (1+z)^{-1/2}]$ for the Einstein-de Sitter model. Notice that, in the homogeneous case, the angle between the light rays $d\theta$ remains a constant during propagation from the source to the observer. This fundamental result is true for all isotropic world models and is a consequence of the postulates of isotropy and homogeneity.

In the model of an inhomogeneous Universe, we consider the propagation of the light rays in this background metric, but include in addition the effect of the absence of matter within the light cone subtended by the source at the observer. As discussed in Sect. 4.6, the angular deflection of a light ray by a point mass, or by an axially symmetric distribution of mass at the same distance, is

$$\frac{4GM(< p)}{pc^2}, \quad (7.105)$$

where $M(< p)$ is the mass within ‘collision parameter’ p , that is, the distance of closest approach of the light ray to the point mass (Fig. 4.18b). Figure 7.12b shows an idealised model for the propagation of the rays along the light cone, assuming the light paths are known. Because of the principle of superposition,

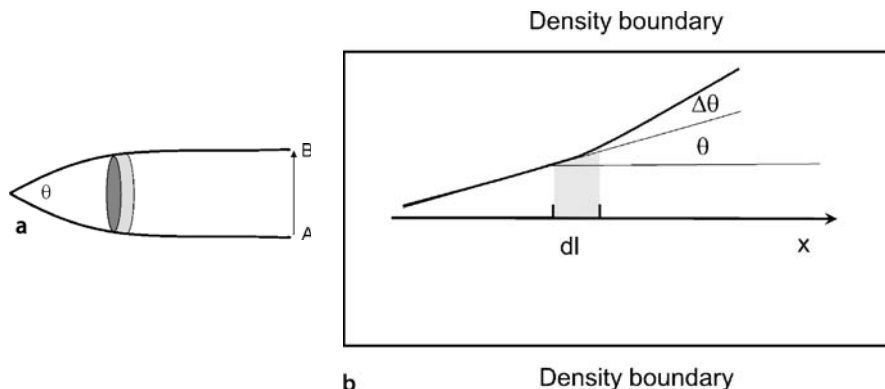


Fig. 7.12. **a** Illustrating the deflection of light rays by a disc of material within the light cone subtended by the distant object AB. **b** Illustrating the divergence of a light ray because of the ‘negative’ mass, indicated by the grey shaded area, due to the absence of a disc of material in the interval dl within the light cone (Zeldovich, 1964)

the effect of the ‘missing mass’ within the light cone may be precisely found by supposing that the distribution of mass has negative density $-\varrho(t)$ within the light cone. The deviations of the light cones from the homogeneous result, $d\theta = dy/dx = \text{constant}$, are due to the influence of the ‘negative mass’ within the light cone. As a result, the light rays bend *outwards* rather than inwards, as in the usual picture (Fig. 7.12b).

Considering a small section of the light path of proper length $dl = a(t) dx$ in the radial direction, the change in θ due to the ‘negative mass’ inside the light cone is

$$\Delta\theta = \frac{4G dM(< p)}{pc^2}. \quad (7.106)$$

Now, $dM(< p) = \pi p^2 \varrho(t) dl$ and hence

$$\frac{d\theta}{dl} = \frac{4\pi G p \varrho(t)}{c^2}. \quad (7.107)$$

We now convert to comoving coordinates $\theta = dy/dx$, $l = a(t)x$, $p = a(t)y$. For the Einstein–de Sitter model, $\varrho(t) = \varrho_0(1+z)^3$ with $\varrho_0 = 3H_0^2/8\pi G$ and

$$x = \frac{2c}{H_0} [1 - (1+z)^{-1/2}]. \quad (7.108)$$

If we write $2c/H_0 = x_0$, then $(1+z) = x_0^2/(x_0-x)^2$ and hence

$$\frac{dy}{dx^2} = \frac{6y}{(x_0-x)^2}. \quad (7.109)$$

This equation can be solved using a series trial function $y = \sum_n a_n(x_0-x)^n$, for which the solution can be written

$$y = a_3(x_0-x)^3 + a_{-2}(x_0-x)^{-2}. \quad (7.110)$$

Fitting the boundary conditions, namely that, at $x = y = 0$, the angle subtended by the source is $\Theta = dy/dx$, we find

$$y = \frac{2c\Theta}{5H_0}(1+z)[1 - (1+z)^{-5/2}]. \quad (7.111)$$

Therefore, since $L = a(t)y = y/(1+z)$, the final result is

$$L = \frac{2c\Theta}{5H_0}[1 - (1+z)^{-5/2}]. \quad (7.112)$$

Corresponding results have been obtained for Friedman models with $\Omega_0 \neq 1$ by Dashevsky and Zeldovich and by Dyer and Roeder (Dashevsky and Zeldovich,

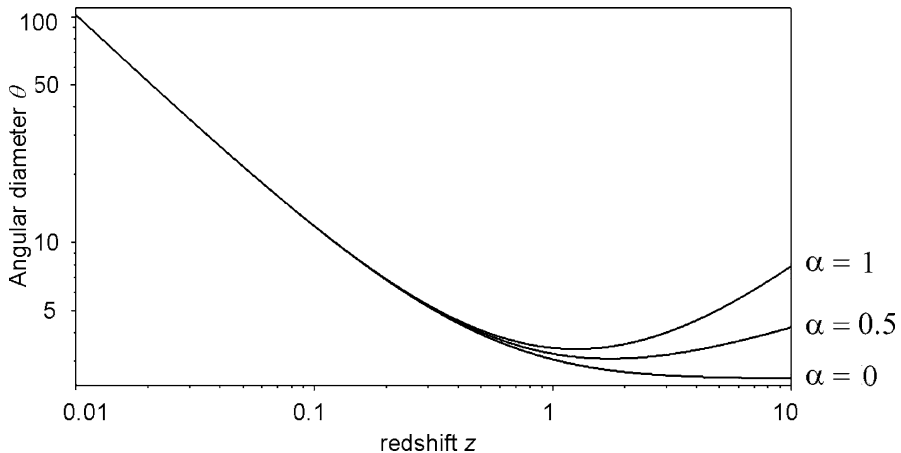


Fig. 7.13. Comparison between the angular diameter–redshift relation in the homogeneous, uniform Einstein–de Sitter world model ($\alpha = 1$), the same background model in which there is no mass within the light cone subtended by the source ($\alpha = 0$) and the case in which half of the total mass is uniformly distributed and the rest is contained in point masses ($\alpha = 0.5$)

1964; Dyer and Roeder, 1972). In these cases, if $\Omega_0 > 1$,

$$L = \frac{3c\Omega_0^2\Theta}{4H_0(\Omega_0 - 1)^{5/2}} \left[\sin^{-1} \left(\frac{\Omega_0 - 1}{\Omega_0} \right)^{1/2} - \sin^{-1} \left(\frac{\Omega_0 - 1}{\Omega_0(1+z)} \right)^{1/2} \right] \\ - \frac{3c\Omega_0\Theta}{4H_0(\Omega_0 - 1)^2} \left[1 - \frac{(1 + \Omega_0 z)^{1/2}}{(1+z)} \right] + \frac{1}{2(\Omega_0 - 1)} \left[1 - \frac{(1 + \Omega_0 z)^{1/2}}{(1+z)^2} \right]. \quad (7.113)$$

If $\Omega_0 < 1$, the inverse trigonometric functions are replaced by inverse hyperbolic functions according to the rule $\sin^{-1} ix = i \sinh^{-1} x$.

The $\theta - z$ relation (7.112) is compared with the standard result (7.104) in Fig. 7.13. It can be seen that the minimum in the standard $\theta - z$ relation disappears in the maximally inhomogeneous model. Thus, if no minimum is observed in the $\theta - z$ relation for a class of standard rods, it does not necessarily mean that the Universe must have $\Omega_0 \approx 0$. It might just mean that the Universe is of high density and is highly inhomogeneous.

Dyer and Roeder have presented the analytic results for intermediate cases in which a certain fraction of the total mass density is uniformly distributed within the light cone (Dyer and Roeder, 1973). A particularly simple result is found for the case of the Einstein–de Sitter model in which it is assumed that a fraction α of the total mass density is uniformly distributed within the light cone, the remainder being condensed into discrete point masses. It is assumed that the light cone does not pass so close to any of the point masses that strong gravitational lensing distorts the light

cones. They find the simple result:

$$L = \Theta D_A = \Theta \frac{2}{\beta} (1+z)^{(\beta-5)/4} [1 - (1+z)^{-\beta/2}] , \quad (7.114)$$

where $\beta = (25 - 24\alpha)^{1/2}$. It can be seen that (7.114) reduces to (7.104) and (7.112) in the limits $\alpha = 1$ and $\alpha = 0$ respectively. The angular diameter-redshift relation for the case $\alpha = 0.5$ is included in Fig. 7.13. Finding the minimum of (7.114), Dyer and Roeder also show that, for the Einstein-de Sitter model, the minimum in the angular diameter-redshift relation occurs at a redshift (Dyer and Roeder, 1973),

$$z_{\min} = \left(\frac{5+\beta}{5-\beta} \right)^{2/\beta} - 1 . \quad (7.115)$$

Thus, if a minimum *is* observed in the $\theta - z$ relation, there must be matter within the light cone and limits can be set to the inhomogeneity of the matter distribution in the Universe. The effects upon the observed intensities of sources may be evaluated using the same approach as in Sect. 7.4.5. The $\theta - z$ relation may be used to work out the fraction of the total luminosity of the source incident upon the observer's telescope using the reciprocity theorem. The end results are not so very different from those of the standard models.

The case of strong gravitational lensing, in which the light cone subtended by the source at the observer passes close to a massive deflector, was discussed in Sect. 4.6. As shown in that section, strong gravitational lensing causes major distortions of the images of distant background sources, if they lie within roughly the Einstein angle θ_E , given by (4.42) and (4.63), of the deflector. The types of distortion, illustrated in Fig. 4.20, have been observed in a number of gravitationally lensed sources in the optical and radio wavebands. In addition, the flux densities of the background sources can be enhanced by factors of up to about 40 over their unlensed intensities. This type of flux density enhancement has been shown to account for the extraordinary luminosity of the galaxy IRAS F10214+4724. Assuming the galaxy were unlensed, its far-infrared luminosity would be $\sim 3 \times 10^{14} L_\odot$. The image of the galaxy is, however, clearly distorted because of strong gravitational lensing and, once a best-fitting mass model has been used to determine the flux density enhancement, the far-infrared luminosity of the galaxy is found to be $\sim 10^{13} L_\odot$, still a very large value, but not as extreme as once believed (Close et al., 1995).

As mentioned in Sect. 4.6, even in the weak lensing limit, the images of background objects are distorted by the presence of mass concentrations along the line of sight. These distortions are often referred to as the effects of *cosmic shear* upon the images of galaxies and can be used to determine the distribution of dark matter in the intervening objects. An example of this technique for determining the distribution of dark matter in the rich cluster of galaxies Cl 0024+1654 was shown in Fig. 4.21.

Kaiser has also shown how the statistics of the distortions of background objects by intervening mass concentrations can be used to determine the power spectrum of density fluctuations in the large-scale distribution of matter in the Universe (Kaiser, 1992). We will return to this topic in Sect. 15.8.5.

A7 The Robertson–Walker Metric for an Empty Universe

The world model containing no matter at all, $\Omega_0 = 0$, $\Omega_A = 0$, is often referred to as the *Milne model*. We have already emphasised the contradictions inherent in using the special theory of relativity in the presence of gravitational fields. In this special case, however, there are no gravitational forces since there is no matter present. The value of this analysis is that it brings out the importance of the cosmological principle in the setting up of the framework for cosmological models. We will show how the appropriate Robertson–Walker metric can be derived for this special case.

In the empty model, test particles move apart at constant velocity from $t = 0$ to $t = \infty$. The origin of the uniform expansion is taken to be $[0, 0, 0, 0]$ and the world lines of particles diverge from this point, each point maintaining constant velocity with respect to the others. The space–time diagram for this case is shown in Fig. A7.1, our own world line being the t axis and that of particle P having constant velocity v with respect to us.

The problem becomes apparent as soon as we attempt to define a suitable *cosmic time* for ourselves and for a fundamental observer moving with the particle P . At time t , the observer P is at distance r and, since v is constant, $r = vt$. Because of the

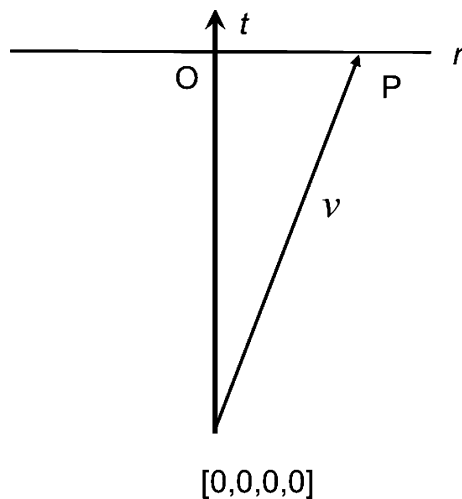


Fig. A7.1. The space–time diagram for an empty Universe

relativity of simultaneity, however, the observer P measures a different time τ from the observer O. From the Lorentz transformation,

$$\tau = \gamma \left(t - \frac{vr}{c^2} \right); \quad \gamma = \left(1 - \frac{v^2}{c^2} \right)^{-1/2}.$$

Since $r = vt$,

$$\tau = t \left(1 - \frac{r^2}{c^2 t^2} \right)^{1/2}. \quad (\text{A7.1})$$

The problem is that t is only proper time for the observer at O and for nobody else. We need to be able to define surfaces of constant cosmic time τ , because it is only on these surfaces that we can impose conditions of isotropy and homogeneity on the large-scale structure of the Universe, in accordance with the cosmological principle. Therefore, the surface of constant cosmic time τ is

$$\tau = t \left(1 - \frac{r^2}{c^2 t^2} \right)^{1/2} = \text{constant}. \quad (\text{A7.2})$$

Locally, at each point in the space, this surface must be normal to the world line of the fundamental observer.

Next we define the element of radial distance dl at the point P on the surface $\tau = \text{constant}$. The interval $ds^2 = dr^2 - (1/c^2) dt^2$ is an invariant. Over the $\tau = \text{constant}$ surface, $ds^2 = -(1/c^2) dl^2$ and hence

$$dl^2 = dr^2 - c^2 dt^2. \quad (\text{A7.3})$$

τ and dl define locally the proper time and proper distance of events at P and are exactly the elements cosmic time t and radial distance coordinate x introduced in Sects. 5.1 and 5.4. This analysis clarifies why the metric of empty space is not a simple Euclidean metric.

Let us now transform from the frame S to the frame S' at P moving at radial velocity v . Distances perpendicular to the radial coordinate remain unaltered under Lorentz transformation and therefore, if in S ,

$$ds^2 = dt^2 - \frac{1}{c^2} (dr^2 + r^2 d\theta^2), \quad (\text{A7.4})$$

the invariance of ds^2 means that

$$dt^2 - \frac{1}{c^2} dr^2 = d\tau^2 - \frac{1}{c^2} dl^2, \quad (\text{A7.5})$$

the perpendicular distance increment $r^2 d\theta^2$ remaining unaltered. Therefore, in S' ,

$$ds^2 = d\tau^2 - \frac{1}{c^2} (dl^2 + r^2 d\theta^2). \quad (\text{A7.6})$$

Now we need to express r in terms of l and τ to complete the transformation to the (τ, l) coordinate system.

Along the surface of constant τ ,

$$dl^2 = dr^2 - c^2 dt^2. \quad (\text{A7.7})$$

The Lorentz transform of $d\tau$ is

$$d\tau = \gamma \left(dt - \frac{v}{c^2} dr \right) = 0,$$

and hence,

$$dt^2 = \frac{v^2}{c^4} dr^2, \quad (\text{A7.8})$$

that is, from (A7.7)

$$dl^2 = dr^2 \left(1 - \frac{v^2}{c^2} \right) = dr^2 \left(1 - \frac{r^2}{c^2 t^2} \right). \quad (\text{A7.9})$$

Hence we need only replace t by τ using (A7.1) to find a differential expression for dr in terms of dl and τ ,

$$dl = \frac{dr}{\left(1 + \frac{r^2}{c^2 \tau^2} \right)^{1/2}}. \quad (\text{A7.10})$$

Integrating using the substitution $r = c\tau \sinh x$, the solution is

$$r = c\tau \sinh(l/c\tau). \quad (\text{A7.11})$$

The metric (A7.6) can therefore be written

$$ds^2 = d\tau^2 - \frac{1}{c^2} [dl^2 + c^2 \tau^2 \sinh^2(l/c\tau) d\theta^2]. \quad (\text{A7.12})$$

This corresponds precisely to the Robertson–Walker metric for an empty Universe. The geometry is an isotropic curved space with hyperbolic geometry, the radius of curvature of the geometry \mathfrak{R} being $c\tau$. This explains why an empty universe has hyperbolic spatial sections. The conditions (A7.1) and (A7.10) are the key relations which indicate why we can only define a consistent cosmic time and radial distance coordinate in hyperbolic rather than flat space.

8 The Determination of Cosmological Parameters

In this chapter, we summarise the results of programmes to determine the cosmological parameters discussed in Chap. 7 by the observation of distant objects, such as galaxies, clusters of galaxies and quasars. The information which can be derived from observations of the Cosmic Microwave Background Radiation and the large-scale distribution of galaxies will be described in Chap. 15, once the tools necessary to interpret these data have been developed. Therefore, the discussion presented in this chapter is *necessarily incomplete*. All the information will be synthesised into a consistent picture, what is often referred to as the *concordance model*, in Sect. 15.9.

8.1 The Cosmological Parameters

We can summarise the results of the calculations of Chap. 7 for observational cosmology as follows. The standard uniform world models can be described by a small number of parameters:

- *Hubble’s constant*, H_0 , describes the present rate of expansion of the Universe,

$$H_0 = \left(\frac{\dot{a}}{a} \right)_{t_0} = \dot{a}(t_0). \quad (8.1)$$

- The *deceleration parameter*, q_0 , describes the present dimensionless deceleration of the Universe

$$q_0 = - \left(\frac{\ddot{a}a}{\dot{a}^2} \right)_{t_0} = - \frac{\ddot{a}(t_0)}{H_0^2}. \quad (8.2)$$

- The *density parameter* Ω_0 , is defined to be the ratio of the present mass-energy density of the Universe ϱ_0 to the critical density $\varrho_c = 3H_0^2/8\pi G$,

$$\Omega_0 = \frac{\varrho_0}{\varrho_c} = \frac{8\pi G \varrho_0}{3H_0^2}. \quad (8.3)$$

For many aspects of astrophysical cosmology, it is important to determine separately the density parameter in baryonic matter Ω_B and the overall density parameter Ω_0 , which includes all forms of baryonic and non-baryonic dark matter.

- The density parameter of the vacuum fields, or the dark energy,

$$\Omega_\Lambda = 8\pi G \rho_v / 3H_0^2 = \Lambda / 3H_0^2 , \quad (8.4)$$

where Λ is the cosmological constant.

- The curvature of space is given by $\kappa = c^2 / \mathfrak{R}^2$.
- The age of the Universe T_0 is given by

$$T_0 = \int_0^1 \frac{da}{\dot{a}} . \quad (8.5)$$

As discussed in the Chap. 7, within the context of the Friedman world models, these are not independent parameters. Specifically, (7.51) and (7.62) show that

$$\kappa \left(\frac{c}{H_0} \right)^2 = (\Omega_0 + \Omega_\Lambda) - 1 , \quad (8.6)$$

and

$$q_0 = \frac{\Omega_0}{2} - \Omega_\Lambda . \quad (8.7)$$

Other parameters will be introduced in Chap. 15 in relation to the formation of structure in the Universe.

The observational approach to the determination of these parameters can be appreciated from the relations presented in Sect. 7.4, specifically, Figs. 7.6 to 7.9 and 7.11. The basic point is that the variation of the different distance measures with redshift are determined by the dynamics and geometry of the Universe. Thus, if precise measurements of any of these relations could be made, the parameters Ω_0 and Ω_Λ could be estimated directly. The best approach would be to estimate precisely some distance measure, for example r , D , D_A or D_L , for some class of object by a technique which is *independent* of redshift and then plot the results on relations such as (7.6) or (7.7). This procedure is now possible in some of cosmological tests, as we will discuss.

A traditional approach has been to select objects which are believed to possess the same intrinsic properties at different redshifts and then determine how their observed properties vary with redshift; then, the angular diameter-redshift or flux density-redshift relations can be compared with the expectations of Figs. 7.8 and 7.9 respectively. This procedure is critically dependent upon our ability to identify reliably the same types of ‘standard candle’ or ‘rigid rod’ at different redshifts.

8.2 Testing the Friedman Models

Let us first investigate in a little more detail the relation between the cosmological parameters and how we might disentangle them. To repeat the Einstein equations,

which are the basis of the standard models,

$$\ddot{a} = -\frac{\Omega_0 H_0^2}{2a^2} + \Omega_\Lambda H_0^2 a, \quad (8.8)$$

$$\dot{a}^2 = \frac{\Omega_0 H_0^2}{a} + \Omega_\Lambda H_0^2 a^2 - \frac{c^2}{\mathfrak{R}^2}. \quad (8.9)$$

These equations describe two different aspects of the cosmological models. Equation (8.8) describes the deceleration, or acceleration, of the Universe under the competing influences of gravity and the dark energy. Expression (8.7) shows that the deceleration parameter provides a measure of the difference between half the density parameter Ω_0 and the density parameter in the vacuum fields Ω_Λ .

In contrast, (8.9) describes how the curvature of space, $\kappa = \mathfrak{R}^{-2}$, depends upon the total energy density in both the matter and the dark energy, as well as the kinetic energy of the expansion. The expression (8.9) describes the basic feature of the isotropic, homogeneous world models of General Relativity that the curvature of space at any epoch is determined by the total mass-energy density at any epoch. Furthermore, (5.32) shows that the space curvature changes as $\kappa = R_c^{-2}(t) = (\mathfrak{R}a)^{-2} \propto a^{-2}$, that is, its variation with cosmic epoch is independent of the details of the dynamics of the Universe. Let us look in a little more detail into how we can distinguish between these parameters observationally.

The deceleration of the Universe and its present mass density are separately measurable quantities. The density parameter Ω_0 can be found from the virial theorem in its various guises (Sect. 8.7). Inspection of the expressions for the comoving radial distance coordinate r and the distance measure D shows that the dynamical and geometrical properties of the models become entangled when we relate the intrinsic properties of objects at large redshifts to observables. It turns out, however, that at small redshifts the differences between the world models depend only upon the deceleration parameter and *not* upon the density parameter and the curvature of space. Let us demonstrate this by a simple argument given by Gunn (Gunn, 1978).

In order to relate observables to intrinsic properties, we need to know how the distance measure D depends upon redshift and this involved two steps. First, we worked out the dependence of the comoving radial distance coordinate r upon redshift z and then formed the distance measure $D = \mathfrak{R} \sin(r/\mathfrak{R})$. Let us first carry out this calculation in terms of the *kinematics* of a world model decelerating with deceleration parameter q_0 . We can write the variation of the scale factor a with cosmic epoch in terms of a Taylor series as follows:

$$\begin{aligned} a &= a(t_0) + \dot{a}(t_0) \Delta t + \frac{1}{2}\ddot{a}(t_0)(\Delta t)^2 + \dots \\ &= 1 - H_0\tau - \frac{1}{2}q_0 H_0^2 \tau^2 + \dots, \end{aligned} \quad (8.10)$$

where we have introduced H_0 , q_0 and the look-back time $\tau = t_0 - t = -\Delta t$; t_0 is the present epoch and t is some earlier epoch. The above expansion can be written in terms of $x = H_0\tau$ and so, since $a = (1+z)^{-1}$,

$$\frac{1}{1+z} = 1 - x - \frac{q_0}{2}x^2 + \dots. \quad (8.11)$$

Now, we express the redshift z to second order in $x = H_0\tau$. This is achieved by making a further Taylor expansion of $[1 - x - (1/2)q_0x^2]^{-1}$ to second order in x . Carrying out this expansion, we find

$$z = x + \left(1 + \frac{q_0}{2}\right)x^2 + \dots . \quad (8.12)$$

We can now find the expression for the comoving radial distance coordinate r by taking the integral

$$\begin{aligned} r &= \int_0^\tau \frac{c d\tau}{a} = \int_0^\tau c(1+z) d\tau \\ &= \frac{c}{H_0} \left[x + \frac{x^2}{2} + \left(1 + \frac{q_0}{2}\right) \frac{x^3}{3} \dots \right]. \end{aligned} \quad (8.13)$$

Finally, we can express r to second order in z by dividing (8.13) successively through by (8.12). We find

$$r = \left(\frac{c}{H_0}\right) \left[z - \frac{z^2}{2}(1+q_0) + \dots \right]. \quad (8.14)$$

The last step is to evaluate $D = \mathfrak{R} \sin(r/\mathfrak{R})$ but, since the expansion for small values of r/\mathfrak{R} is

$$D = r \left(1 - \frac{1}{6} \frac{r^2}{\mathfrak{R}^2}\right), \quad (8.15)$$

the dependence upon the curvature only appears in third order in z and so to second order, we find the kinematic result

$$D = \left(\frac{c}{H_0}\right) \left[z - \frac{z^2}{2}(1+q_0) \right]. \quad (8.16)$$

Let us now evaluate the comoving radial distance coordinate r and the distance measure D to third order in redshift starting from the full solution of the dynamical field equations, that is, starting from the general result (7.74) for r

$$r = \frac{c}{H_0} \int_0^z \frac{dz}{[(1+z)^2(\Omega_0 z + 1) - \Omega_A z(z+2)]^{1/2}}.$$

The denominator of the integral can be reorganised to show explicitly the dependence upon the deceleration parameter q_0 and the present matter density parameter Ω_0 using (8.7)

$$\begin{aligned} r &= \frac{c}{H_0} \int_0^z \frac{dz}{[1 + (2 + \Omega_0 - 2\Omega_A)z + (1 + 2\Omega_0 - \Omega_A)z^2 + \Omega_0 z^3]^{1/2}} \\ &= \frac{c}{H_0} \int_0^z \frac{dz}{[1 + 2(1 + q_0)z + (1 + \frac{3}{2}\Omega_0 + q_0)z^2 + \Omega_0 z^3]^{1/2}}. \end{aligned} \quad (8.17)$$

Now expand the denominator to second order for small values of z

$$\begin{aligned} r &= \frac{c}{H_0} \int_0^z \left[1 - z(1 + q_0) + \frac{z^2}{2} (2 + 5q_0 + 3q_0^2 - \frac{3}{2}\Omega_0) \right] dz \\ &= \frac{c}{H_0} \left[z - \frac{z^2}{2}(1 + q_0) + \frac{z^3}{6} (2 + 5q_0 + 3q_0^2 - \frac{3}{2}\Omega_0) \right]. \end{aligned} \quad (8.18)$$

As before, we form $D = \mathfrak{R} \sin(r/\mathfrak{R})$, where

$$\mathfrak{R} = \frac{c/H_0}{[(\Omega_0 + \Omega_\Lambda) - 1]^{1/2}} = \frac{c/H_0}{(\frac{3}{2}\Omega_0 - q_0 - 1)^{1/2}}. \quad (8.19)$$

Preserving quantities to third order in z , we find

$$D = \frac{c}{H_0} \left[z - \frac{z^2}{2}(1 + q_0) + \frac{z^3}{6} (3 + 6q_0 + 3q_0^2 - 3\Omega_0) \right]. \quad (8.20)$$

This is the result we have been seeking.

To second order in the redshift, we obtain exactly the same result as that obtained from the kinematic argument (8.16). What this means is that, to second order in redshift, the distance measure D does not depend upon the density parameter Ω_0 at small redshifts, $z \ll 1$; it only depends upon the deceleration, or acceleration, whatever its cause. The physical meaning of this result is that the greater the deceleration, the closer the source of the radiation is to us and so the smaller the look-back time and the comoving radial distance coordinate of the source. Conversely, if the Universe accelerated between the redshift z and the present epoch, the look-back time τ would be greater and so would the comoving radial distance coordinate r . The negative sign in front of the terms in z^2 in (8.20) formalises these qualitative arguments. It can also be seen from (8.20) that, even to third order in the redshift, the dependence upon the density parameter is quite weak.

One approach to the determination of the kinematics of the Universe is therefore to estimate the deceleration of the Universe by determining the distance measures D for objects at small redshifts, say $z \leq 0.3$, at which there are small but appreciable differences between the world models. This is a very demanding programme, but it may well become feasible with the huge surveys of nearby galaxies undertaken by the AAT 2dF and SDSS teams.

As discussed above, the standard procedure is to determine the $D - z$ relation very precisely to large redshifts and then estimate the parameters Ω_0 and Ω_Λ from the detailed shape of that relation. As an example, the variations of the comoving radial distance coordinate r and the distance measure D are shown as a function of redshift in Fig. 7.6 for a range of flat world models. It can be seen that these relations are of quite different shapes.

The importance of these analyses is that they provide tests of General Relativity and the laws of physics on the largest scales accessible to us at the present epoch. To express this thought less cryptically, is the present deceleration or acceleration of the Universe entirely due to the amount of gravitating matter and dark energy present in the Universe today?

8.3 Hubble's Constant H_0

Hubble's constant H_0 appears ubiquitously in cosmological formulae and its value was the subject of considerable controversy for many years. The use of the redshift-magnitude relation for brightest cluster galaxies had the advantage that Hubble's law is defined well beyond distances at which there might have been deviations associated with the peculiar motions of clusters and superclusters of galaxies (Fig. 2.11). Therefore, Hubble's constant could be found if the distances to the nearest rich clusters of galaxies could be estimated accurately.

The traditional approach to this calibration involved a hierarchy of distance indicators to extend the local distance scale from the vicinity of the Solar System to the nearest giant cluster of galaxies, the Virgo cluster. The only direct methods of distance measurement involve stellar parallaxes and can only be used for stars in the neighbourhood of the Sun. To extend the distance scale further, it is assumed that objects of the same intrinsic types can be identified at greater distances. Then, their relative brightnesses provide estimates of their distances. Examples of the different techniques used are summarised in Fig. 8.1. The period-luminosity relation for Cepheid variables provides one of the best means of extending the distance scale from our own Galaxy to nearby galaxies. Other techniques were used to extend the distance scale from the neighbourhood of our Galaxy to the Virgo cluster, including the luminosity functions of globular clusters, the brightest stars in galaxies and the luminosities of Type 1a supernovae at maximum light. In 1977, Tully and Fisher discovered the relation between the absolute magnitudes of spiral galaxies and the velocity widths of their 21-cm line emission (Tully and Fisher, 1977). This relation could be determined for a number of spiral galaxies in a nearby group or cluster and then relative distances found by assuming that the same correlation between their intrinsic properties is found in more distant groups and clusters (see Sect. 3.6.3).

From the 1970s until the 1990s, there was an ongoing controversy concerning the value of Hubble's constant. A detailed discussion of the different approaches to the determination of Hubble's constant during the 1970s and 1980s was provided by Rowan-Robinson, his conclusions being updated in 1988 (Rowan-Robinson, 1985, 1988). In a long series of papers, Sandage and Tammann found values of Hubble's constant of about $50 \text{ km s}^{-1} \text{ Mpc}^{-1}$, whereas de Vaucouleurs, Aaronson, Mould and their collaborators consistently found values of about $80 \text{ km s}^{-1} \text{ Mpc}^{-1}$. The nature of the discrepancy can be appreciated from their estimates of the distance to the Virgo cluster. If its distance is 15 Mpc, the higher estimate of H_0 is found, whereas if the distance is 22 Mpc, values close to $50 \text{ km s}^{-1} \text{ Mpc}^{-1}$ are obtained. Sandage and Tammann repeatedly emphasised how sensitive the distance estimates are to observational selection effects, such as the Malmquist effect, namely that intrinsically more luminous galaxies are selected in faint samples of galaxies than in brighter samples, and systematic errors.

During the 1990s, a major effort was made to resolve these differences, much of it stimulated by the capability of the Hubble Space Telescope (HST) to measure Cepheid variable stars in the Virgo cluster of galaxies. When the HST project was approved in 1977, one of its major scientific objectives was to use its superb

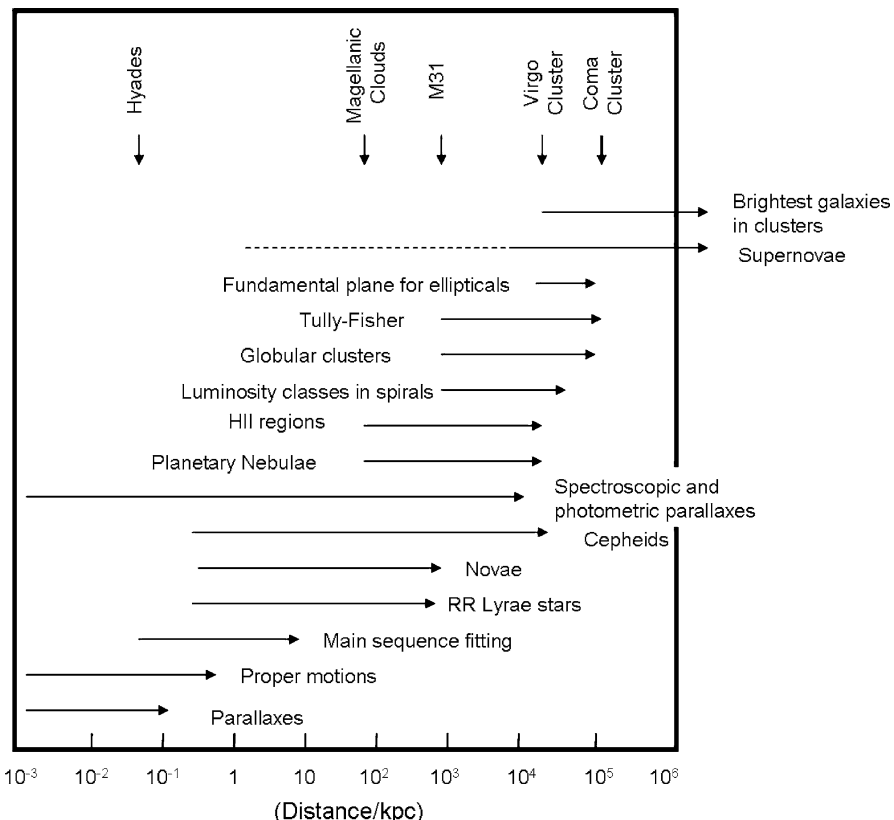


Fig. 8.1. Illustrating the ‘cosmological distance ladder’ (Rowan-Robinson, 1985, 1988). The diagram shows roughly the range of distances over which different classes of object can be used to estimate astronomical distances. The diagram has been redrawn and updated from Rowan-Robinson’s presentation

sensitivity for faint star-like objects to enable the light curves of Cepheid variables in the Virgo cluster to be determined precisely and so estimate the value of Hubble’s constant to 10% accuracy. This programme was raised to the status of an HST Key Project in the 1990s with a guaranteed share of observing time to enable a reliable result to be obtained.

The Key Project team, led by Freedman, carried out an outstanding programme of observations and analysis of these data. Equally important was the fact that the team used not only HST data, but also all the other distance measurement techniques to ensure internal self-consistency of the distance estimates. For example, the improved determination of the local distance scale in our own Galaxy from the parallax programmes of the *Hipparcos* astrometric satellite improved significantly the reliability of the calibration of the local Cepheid distance scale. The great advance of the 1990s was that the distances of many nearby galaxies became known very

much more precisely than they were previously. As a result, by 2000, there was relatively little disagreement among the experts about the distances of those galaxies which had been studied out to the distance of the Virgo cluster. If there were differences, they arose from how the data were to be analysed once the distances were known, in particular, in the elimination of systematic errors and biases in the observed samples of galaxies. The final result of the HST Key Project published in 2001 was $72 \pm 8 \text{ km s}^{-1} \text{ Mpc}^{-1}$, where the errors are $1 - \sigma$ errors (Freedman et al., 2001).

In addition to this approach, new *physical methods* of measuring H_0 became available which have the advantage of eliminating many of the steps involved in the traditional cosmological distance ladder. They are based upon measuring a physical dimension l of a distant object, independent of its redshift, and its angular size θ , so that an angular diameter distance D_A can be found from $D_A = l/\theta$ at a known redshift z . A beautiful example of the use of this technique was described by Panagia and his colleagues who combined IUE observations of the time-variability of the emission lines from the supernova SN 1987A in the Large Magellanic Cloud with Hubble Space Telescope observations of the emission-line ring observed about the site of the explosion to measure the physical size of the ring (Panagia et al., 1991). The distance found for the Large Magellanic Cloud was as accurate as that found by the traditional procedures.

Another promising method, suggested originally by Baade in 1926 and modified by Wesselink in 1947, involves measuring the properties of an expanding stellar photosphere (Baade, 1926; Wesselink, 1947). If the velocity of expansion can be measured from the Doppler shifts of the spectral lines and the increase in size estimated from the change in luminosity and temperature of the photosphere, the distance of the star can be found. The *Baade–Wesselink method* was first applied to supernovae by Branch and Patchett and by Kirshner and Kwan in the 1970s (Branch and Patchett, 1973; Kirshner and Kwan, 1974). It was successfully applied to the supernovae SN 1987A in the Large Magellanic Cloud by Eastman and Kirshner, resulting in a distance consistent with other precise distance measurement techniques (Eastman and Kirshner, 1989). Extending the Baade–Wesselink technique to 10 Type II supernovae with distances ranging from 50 kpc to 120 Mpc, Schmidt and his colleagues found a value of H_0 of $60 \pm 10 \text{ km s}^{-1} \text{ Mpc}^{-1}$ (Schmidt et al., 1992).

Another approach which has produced promising results involves the use of the hot gaseous atmospheres in clusters of galaxies, the properties of which can be measured from their X-ray emission and from the Sunyaev–Zeldovich decrement in the Cosmic Microwave Background Radiation due to inverse Compton scattering. As discussed in Sect. 4.5, clusters of galaxies contain vast quantities of hot gas which is detected by its X-ray bremsstrahlung. The X-ray surface brightness depends upon the electron density N_e and the electron temperature T_e through the relation $I_\nu \propto \int N_e^2 T_e^{-1/2} dl$. The electron temperature T_e can be found from the shape of the bremsstrahlung spectrum. Furthermore, the decrement in the background due to the Sunyaev–Zeldovich effect is proportional to the Compton optical depth $y = \int (kT_e/m_e c^2) \sigma_T N_e dl \propto \int N_e T_e dl$. Thus, the physical properties of the hot gas are

overdetermined and the physical dimensions of the X-ray emitting volume can be found. Bonamente and his colleagues studied 38 clusters of galaxies in the redshift interval $0.14 \leq z \leq 0.89$ using X-ray data from the Chandra X-ray Observatory and measurements of the corresponding Sunyaev–Zeldovich decrements from the Owens Valley Radio Observatory and the Berkeley–Illinois–Maryland Association interferometric arrays (Bonamente et al., 2006). An estimate of Hubble's constant of $H_0 = 76.9^{+3.9}_{-3.4}$ (stat) $^{+10.0}_{-8.0}$ (syst) $\text{km s}^{-1} \text{Mpc}^{-1}$ was found assuming $\Omega_0 = 0.3$ and $\Omega_A = 0.7$.

Another example of a physical method of measuring H_0 is to use gravitational lensing of distant objects by intervening galaxies or clusters. The first gravitationally lensed quasar 0957+561 was discovered by Walsh, Carswell and Weymann in 1979 (Walsh et al., 1979). The gravitational deflection of the light from the quasar by the intervening galaxy splits its image into a number of separate components, in the case of 0957+561 into two almost identical quasar images (Fig. 8.2). If the background quasar is variable, a time delay is observed between the variability of the different images because of the different path lengths from the quasar to the observer on Earth. For example, a time delay of 418 days has been measured for the two components of the double quasar 0957+561 (Kundic et al., 1997). This observation enables physical scales at the lensing galaxy to be determined, the main uncertainty resulting from the modelling of the mass distribution in the lensing galaxy. In the case of the double quasar 0957+561, Kundic and his colleagues claim

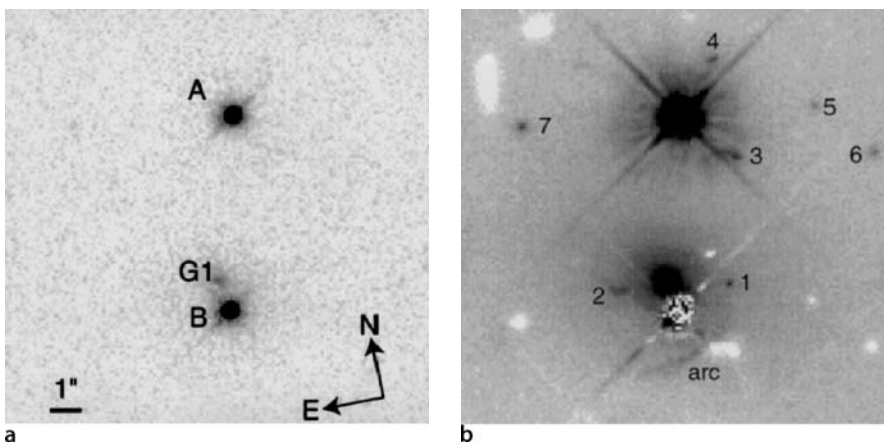


Fig. 8.2a,b. Optical images of the double quasar 0957+561. **a** The system observed in a 80 second exposure made with the WFPC2 camera of the Hubble Space Telescope. The A and B quasar images and the primary lensing galaxy G1 are apparent. **b** A 39,000 second image made with the same camera. A shifted version of the image has been subtracted so that quasar A acts as a template for quasar B. White objects are negative 'ghosts' resulting from the subtraction process. The lensing galaxy is now clearly visible, as are other faint features including the arc to the south of the lensing galaxy (Bernstein et al., 1997)

that the mass distribution in the galaxy is sufficiently well-constrained for the model dependent uncertainties to be small. They derived a value of Hubble's constant of $H_0 = 64 \pm 13 \text{ km s}^{-1} \text{ Mpc}^{-1}$ at the 95% confidence level. A statistical analysis of 16 multiply imaged quasars by Oguri found a value of Hubble's constant of $H_0 = 68 \pm 6 \text{ (stat)} \pm 8 \text{ (syst) } \text{km s}^{-1} \text{ Mpc}^{-1}$ (Oguri, 2007).

The estimates of Hubble's constant found by these physical methods, as well as the value determined from studies of the fluctuation spectrum of the Cosmic Microwave Background Radiation (Chap. 15), are consistent with the value of $H_0 = 72 \pm 8 \text{ km s}^{-1} \text{ Mpc}^{-1}$ found by Freedman and her colleagues.

8.4 The Age of the Universe T_0

Globular clusters are among the oldest systems in our Galaxy and so their ages provide lower limits to the age of the Universe. The determination of their ages was pioneered by Sandage and Schwarzschild and involved the comparison of the Hertzsprung–Russell diagrams of the oldest, metal-poor, globular clusters with the expectations of the theory of stellar evolution from the main sequence onto the giant branch (Sandage and Schwarzschild, 1952).

The feature of these diagrams which is particularly sensitive to the age of the cluster is the *main sequence termination point*. In the oldest globular clusters, the main sequence termination point has reached a mass of about $0.9 M_\odot$ and in the most metal-poor, and presumably oldest, clusters the abundances of the elements with $Z \geq 3$ are about 150 times lower than their Solar System values. These facts make the determination of stellar ages much simpler than might be imagined. As Bolte has pointed out, low mass, metal-poor stars have radiative cores and so are unaffected by the convective mixing of unprocessed material from their envelopes into their cores (Bolte, 1997). Furthermore, the corrections to the perfect gas law equation of state are relatively small throughout most solar mass stars. Finally, the surface temperatures of these stars are high enough for molecules to be rare in their atmospheres, simplifying the conversion of their effective temperatures into predicted colours. Taking account of the various sources of uncertainty, Chaboyer demonstrated that the absolute magnitude of the main sequence termination point is the best indicator of the age of the cluster (Chaboyer, 1998).

As understanding of the theory of stellar evolution has advanced, improved estimates of the ages of the oldest globular clusters have become available. A good example of what can be achieved is illustrated in Fig. 8.3 which shows a comparison of the Hertzsprung–Russell diagram for the old globular cluster 47 Tucanae with the predicted isochrones for various assumed ages for the cluster. In this case the abundance of the heavy elements is only 20% of the Solar abundance and the age of the cluster is estimated to be between $(12 - 14) \times 10^9$ years (Hesser et al., 1987).

In 1994, Maeder reported evidence that the ages of the oldest globular clusters are about 16×10^9 years (Maeder, 1994) and similar results were reported by Sandage

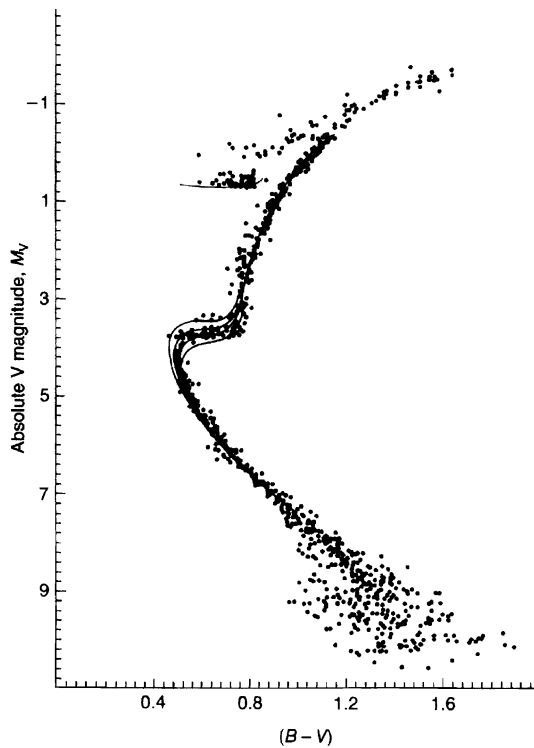


Fig. 8.3. The Hertzsprung–Russell diagram for the globular cluster 47 Tucanae (Hesser et al., 1987). The solid lines show fits to the data using theoretical models of the evolution of stars of different masses from the main sequence to the giant branch due to VandenBerg. The isochrones shown have ages of 10, 12, 14 and 16×10^9 years, the best-fitting values lying in the range $(12\text{--}14) \times 10^9$ years. The cluster is metal-rich relative to other globular clusters, the metal abundance corresponding to about 20% of the solar value

in 1995 (Sandage, 1995). In 1997, Bolte argued that the ages of the oldest globular clusters were

$$T_0 = 15 \pm 2.4 \text{ (stat)} \begin{array}{l} +4 \\ -1 \end{array} \text{ (syst) Gy.} \quad (8.21)$$

The first results of the *Hipparcos* astrometric survey relating to the determination of the local distance scale were announced in 1997, with the result that it increased by about 10% (Feast and Catchpole, 1997). This result meant that the stars in globular clusters were more luminous than previously thought and so their main sequence lifetimes were reduced. In Chaboyer's review of 1998, the ages of globular clusters were estimated to be $T_0 = (11.5 \pm 1.3)$ Gy (Chaboyer, 1998).

Constraints on the age of the Galaxy can also be obtained from estimates of the cooling times for white dwarfs. According to Chaboyer, these provide a firm lower limit of 8 Gyr. The numbers of white dwarfs observed in the vicinity of the Solar System enable an estimate of $(9.5 \begin{array}{l} +1.1 \\ -0.8 \end{array})$ Gy to be made for the age of the disc of our Galaxy (Oswalt et al., 1996).

In 1904, Rutherford used the relative abundances of radioactive species to set a lower limit to the age of the Earth of 700 million years, in the process demolishing the Kelvin–Helmholtz picture of stellar evolution (Rutherford, 1907). Using similar techniques, lower limits to the age of the Universe can be derived from the discipline

of *nucleocosmochronology*. A secure lower limit to the age of the Universe can be derived from the abundances of long-lived radioactive species. In 1963 Anders used these to determine an accurate age for the Earth of 4.6×10^9 years (Anders, 1963). Some pairs of long-lived radioactive species, such as ^{232}Th – ^{238}U , ^{235}U – ^{238}U and ^{187}Re – ^{187}Os can provide information about nucleosynthetic time-scales before the formation of the Solar System (Schramm and Wasserburg, 1970). These pairs of elements are all produced by the r-process in which the time-scale for neutron capture is less than the β -decay lifetime. The production abundances of these elements can be predicted and compared with their present observed ratios (Cowan et al., 1991).

The best astronomical application of this technique has been carried out by Sneden, Cowan and their colleagues for the ultrametal-poor K giant star CS 22892-052 in which the iron abundance is 1000 times less than the solar value (Sneden et al., 1992). A number of species never previously observed in such metal-poor stars were detected, for example, Tb (terbium, $Z = 65$), Ho (holmium, $Z = 67$), Tm (thulium, $Z = 69$), Hf (hafnium, $Z = 72$) and Os (osmium, $Z = 76$), as well a single line of Th (thorium, $Z = 90$). The thorium abundance is significant smaller than its scaled solar system abundance and so the star must have been formed much earlier than the Solar System. A lower limit to the age of CS 22892-052 of $(15.2 \pm 3.7) \times 10^9$ years was found.

A conservative lower bound to the cosmological time-scale can be found by assuming that all the elements were formed promptly at the beginning of the Universe. From this line of reasoning, Schramm found a lower limit to the age of the Galaxy of 9.6×10^9 years (Schramm, 1997). The best estimates of the age of the Galaxy are somewhat model-dependent, but typically ages of about $(12\text{--}14) \times 10^9$ years are found (Cowan et al., 1991).

8.5 The Deceleration Parameter q_0

The hope of the pioneers of observational cosmology was that the value of q_0 could be found from studies of distant galaxies through the redshift–apparent magnitude relation, the angular diameter–redshift relation or the number counts of galaxies. This programme proved to be very much more difficult than the pioneers had expected. By the beginning of the twenty-first century, however, real progress was made by two rather different routes, one involving the use of supernovae of Type 1a and the other observations of the spectrum of fluctuations in the Cosmic Microwave Background Radiation.

The major problem encountered by many of the traditional approaches concerned the evolution with cosmic time of the properties of the objects studied and it is salutary to review exactly what went wrong.

8.5.1 The Redshift–Magnitude Relation for the Brightest Galaxies in Clusters

The redshift–apparent magnitude relation for the brightest galaxies in clusters shows an impressive linear relation (Fig. 2.11), but it only extends to redshifts $z \sim 0.5$ at which the differences between the world models are still relatively small (Sandage,

1968). Sandage was well aware of the many effects which needed to be considered before a convincing estimate of q_0 could be found. Some of these were straightforward, such as the need to determine the luminosities of galaxies within a given metric diameter, but others were more complex. For example, as discussed in Sect. 4.2.3, Sandage and Hardy discovered that the brightest galaxy in a cluster is more luminous, the greater the difference in magnitude between the brightest and next brightest galaxies in the cluster (Sandage and Hardy, 1973). In what they termed the *Bautz–Morgan effect*, the second and third ranked members of the cluster were intrinsically fainter than the corresponding galaxies in other clusters with less dominant first ranked galaxies. It seemed as though the brightest galaxy became brighter at the expense of the next brightest members, a phenomenon which could plausibly be attributed to the effects of galactic cannibalism (Hausman and Ostriker, 1977). Sandage adopted an empirical correction to reduce the clusters to a standard Bautz–Morgan type.

Sandage was also well aware of the need to take account of the evolution of the stellar populations of the galaxies with cosmic time. These corrections followed naturally from his work on the Hertzsprung–Russell diagrams of globular clusters of different ages which mimic the cosmic evolution of the old stellar populations of galaxies. He included evolutionary corrections in the K-corrections to the absolute magnitudes of the galaxies. There were, however, other worrying pieces of evidence which did not fit easily into a picture of the passive evolution of galaxies in clusters. Dramatic evidence for the evolution of galaxies in rich, regular clusters at relatively small redshifts was first described in the pioneering analyses of Butcher and Oemler. They found that the fraction of blue galaxies in such clusters increased from less than 5% in a nearby sample to percentages as large as 50% at redshift $z \sim 0.4$ (Butcher and Oemler, 1978, 1984). The Butcher–Oemler effect has been the subject of a great deal of study and debate, the major observational problems concerning the contamination of the cluster populations by foreground and background galaxies, as well as bias in the selection criteria for the clusters selected for observation (Dressler, 1984).

The determination of q_0 might seem to be easier if the samples of galaxies extended to larger redshifts, but it proved far from trivial to find suitable clusters at redshifts greater than 0.5. Those in which the brightest galaxies were observed often turned out to be bluer than expected. This finding reflects a basic problem with this approach to measuring the deceleration parameter: the differences between the expectations of the world models only become appreciable at large redshifts at which the Universe was significantly younger than it is now. Consequently careful account has to be taken of the evolutionary changes of the objects which are assumed to have ‘standard’ properties.

By the time of Sandage’s review of the problem in 1993, the uncertainties in the value of q_0 had not decreased, his estimate being $q_0 = 1 \pm 1$ (Sandage, 1995). In fact, by that time, Aragón-Salamanca , Ellis and their colleagues had extended the infrared redshift–apparent magnitude relation for the brightest galaxies in clusters to redshift $z = 0.9$ (Aragón-Salamanca et al., 1993). They found evidence that the galaxies were bluer at the larger redshifts, but, perhaps surprisingly, that their redshift–apparent magnitude relation followed closely a model with $q_0 = 1$ with no

corrections for the evolution of the stellar populations of the galaxies, for cluster richness or for Bautz–Morgan type.

8.5.2 The Redshift–Magnitude Relation for Radio Galaxies

Another approach to extending the redshift–apparent magnitude relation to large redshifts became possible in the early 1980s when the use of the first generation of CCD cameras enabled complete samples of bright 3CR radio sources to be identified with very faint galaxies. These galaxies turned out to have very strong, narrow emission line spectra and spectroscopy by Hyron Spinrad and his colleagues showed that many of these radio galaxies had very large redshifts. These observations showed that the 3CR radio galaxies are among the most luminous galaxies known.

At about the same time, infrared photometry of these galaxies in the 1–2.2 μm waveband became feasible with the development of sensitive indium antimonide detectors. There were several advantages in defining the redshift–apparent magnitude relation in the K waveband at 2.2 μm , one of them being that dust becomes transparent in the near-infrared waveband and so extinction corrections to the luminosities of the galaxies are very small. A second advantage is that the stars which contribute most of the luminosity at these wavelengths belong to the old red giant population of the galaxy. As a result, the magnitudes are not affected by bursts of star formation which can profoundly influence the optical magnitudes of the galaxies and which is largely responsible for the fact that the galaxies at redshifts greater than 0.5 are significantly bluer than those observed at lower redshifts (see Sect. 17.2.2).

In 1984, Lilly and I determined the redshift–apparent magnitude relation for a complete sample of 3CR radio galaxies at an infrared wavelength of 2.2 μm (Fig. 8.4) (Lilly and Longair, 1984). We found that there is a remarkably well-defined K magnitude–redshift relation which extended to redshifts of 1.5. It was also clear that the galaxies at large redshifts were more luminous than expected for world models with $q_0 \sim 0\text{--}0.5$. When simple evolutionary corrections were made for the increased rate at which stars evolved onto the giant branch at earlier epochs (Sect. 17.2.2), values of q_0 in the range 0 to 1 were found. This appeared to be evidence for the evolution of the stellar populations of these galaxies over cosmological time-scales.

There were, however, problems with this simple picture. In the late 1980s, Chambers, Miley, McCarthy and their collaborators discovered the alignment of the radio structures with the optical images of the 3CR galaxies and this complicated the interpretation of these data (Chambers et al., 1987; McCarthy et al., 1987). Optical images taken with the Hubble Space Telescope and ground-based infrared images taken with the UK Infrared Telescope of five of the 3CR radio galaxies in the redshift interval $1 < z < 1.3$ are shown in Fig. 8.5 (Best et al., 1996). The infrared images in the right-hand column look exactly like the classic picture of a double radio source associated with a giant elliptical galaxy. In the HST images in the left-hand column, however, a wide variety of high surface brightness structures is observed aligned with the radio structures – the optical images of the radio galaxies are quite unlike the symmetric structure of giant elliptical galaxies. Our optical spectroscopic observations of the aligned structures seen in the five radio galaxies in Fig. 8.5

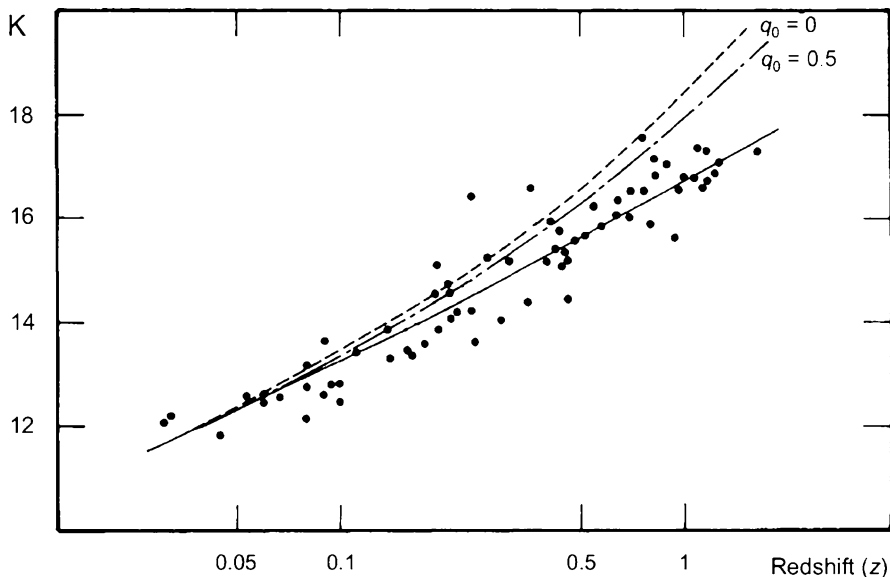


Fig. 8.4. The K magnitude–redshift relation for a complete sample of narrow line radio galaxies from the 3CR catalogue. The infrared apparent magnitudes were measured at a wavelength of $2.2\text{ }\mu\text{m}$. The *dashed lines* show the expectations of world models with $q_0 = 0$ and $\frac{1}{2}$. The *solid line* is a best-fitting line for standard world models with $\Omega_A = 0$ and includes the effects of stellar evolution of the old stellar population of the galaxies (Lilly and Longair, 1984)

showed that they are shock-excited gas clouds, probably associated with the strong shocks created by the passage of the radio jets through the intergalactic medium surrounding the radio galaxy (Best et al., 2000).

Using a combination of surface photometry of these galaxies in the optical and infrared wavebands, we were able to show that the alignment effect does not have a strong influence upon the K magnitude–redshift relationships (Best et al., 1998). More serious was the fact that surveys of fainter samples of 6C radio galaxies by Eales, Rawlings and their colleagues found that, although the K magnitude–redshift relation agreed with our relation at redshifts less than 0.6, their sample of radio galaxies at redshifts $z \sim 1$ were significantly less luminous than the 3CR galaxies by about 0.6 magnitudes (Eales et al., 1997). Our most recent analysis of these data for a preferred cosmological model with $\Omega_0 = 0.3$ and $\Omega_A = 0.7$, including corrections for the evolution of their stellar populations, have demonstrated that 3CR radio galaxies at redshifts $z \geq 0.6$ are indeed significantly more luminous than their nearby counterparts (Inskip et al., 2002). Our apparent success in accounting for the K magnitude–redshift relation for 3CR radio galaxies in the 1980s was an unfortunate cosmic conspiracy.

The lesson of this story is that the selection of galaxies as standard objects at large redshifts is a hazardous business; we generally learn more about the astrophysics and astrophysical evolution of the galaxies rather than about cosmological parameters.

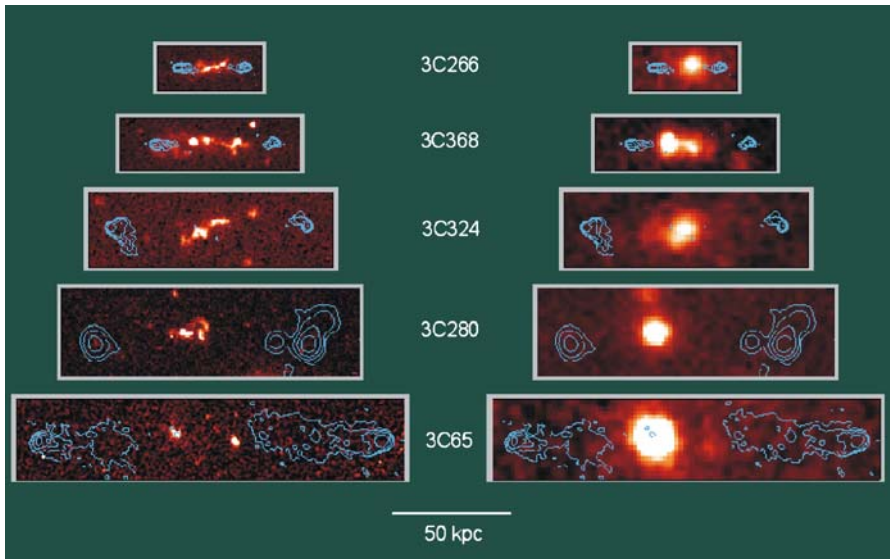


Fig. 8.5. HST (left) and UKIRT (right) images of the radio galaxies 3C 266, 368, 324, 280 and 65 with the VLA radio contours superimposed (Best et al., 1996). The images are drawn on the same physical scale. The angular resolution of the HST images is 0.1 arcsec while that of the ground-based infrared images is about 1 arcsec

8.5.3 The Redshift–Magnitude Relation for Type 1a Supernovae

The discussion of Sect. 7.4.5 makes it clear that what is required is a set of standard objects which are not susceptible to poorly understood evolutionary changes with cosmic epoch. The use of supernovae of Type 1a to extend the redshift–apparent magnitude relation to redshifts $z > 0.5$ has a number of attractive features. First of all, it is found empirically that these supernovae have a very small dispersion in absolute luminosity at maximum light (Branch and Tammann, 1992). This dispersion can be further reduced if account is taken of the correlation between the maximum luminosity of Type 1a supernovae and the duration of the initial outburst. This correlation, referred to as the *luminosity–width relation*, is in the sense that the supernovae with the slower decline rates from maximum light are more luminous than those which decline more rapidly (Phillips, 1993). Secondly, there are good astrophysical reasons to suppose that these objects are likely to be good standard candles, despite the fact that they are observed at earlier cosmological epochs. The preferred picture is that these supernovae result from the explosion of white dwarfs which are members of binary systems which accrete mass from the other member of the binary. Although the precise mechanism which initiates the explosion has not been established, the favoured picture is that mass accreted onto the surface of the white dwarf raises the temperature of the surface layers to such a high temperature that nuclear burning is initiated and a deflagration front propagates into the interior of

the star, causing the explosion which results in its destruction. It is entirely plausible that these types of explosion should have uniform properties.

In 1995 Ariel Goobar and Saul Perlmutter discussed the feasibility of observing Type 1a supernova out to redshift $z \approx 1$ in order to estimate the values of Ω_0 and Ω_A (Goobar and Perlmutter, 1995). In 1996, they and their colleagues described the first results of systematic searches for Type 1a supernovae at redshifts $z \sim 0.5$ using an ingenious approach to detect them before they reached maximum light (Perlmutter et al., 1996). Deep images of selected fields, including a number which contain distant clusters of galaxies, were taken during one period of new moon and the fields were then imaged in precisely the same way during the next new moon. Using rapid image analysis techniques, any supernovae which appeared between the first and second epoch observations were quickly identified and reobserved photometrically and spectroscopically over the succeeding weeks to determine their types and light curves.

Using this search technique, Perlmutter and his colleagues discovered 27 supernovae of Type 1a between redshifts 0.4 and 0.6 in three campaigns in 1995 and 1996 (Perlmutter et al., 1996, 1997). The team used these and subsequent data to demonstrate convincingly the effects of cosmological time dilation by comparing the light curves of Type 1a supernovae at redshifts $z \sim 0.4\text{--}0.8$ with those of the same type at the present epoch, thus testing directly the cosmological time dilation–redshift relation (Goldhaber et al., 2001) (see Fig. 5.7). The same peak luminosity–width correlation was found as that observed at small redshifts. When account was taken of this relation, the intrinsic spread in the luminosities of the Type 1a supernovae was only 0.21 magnitudes.

This same technique has been used to discover Type 1a supernovae at redshifts greater than $z = 0.8$ as a result of observations with the Hubble Space Telescope. In two independent programmes, Garnavich, Perlmutter and their colleagues discovered the Type 1a supernovae SN1997ck at redshift $z = 0.97$ and SN1997ap at redshift $z = 0.83$ respectively (Garnavich et al., 1998; Perlmutter et al., 1998). The great advantage of the HST observations is that their high angular resolution enables very accurate photometry to be carried out on stellar objects in distant galaxies.

The redshift–apparent magnitude relation presented by Wood-Vasey and his colleagues was derived from the combined ESSENCE and Supernova Legacy Survey data (Fig. 8.6). This compilation has resulted in a redshift–apparent magnitude relation similar to that found by Perlmutter, Garnavich and their colleagues, but with much larger statistics (Wood-Vasey et al., 2007). The solid line shows a best-fitting theoretical curve (solid line) which has cosmological parameters $\Omega_0 = 0.27$ and $\Omega_A = 0.73$. The major result of these observations, which has been found by the independent groups, is that the data favour cosmological models in which Ω_A is non-zero. This was the first time in the history of observational cosmology that compelling evidence for a finite value of the cosmological constant has been found. The groups have continued to extend this technique to large redshifts through the discovery of Type 1a supernovae at very large redshifts (Knop et al., 2003; Tonry et al., 2003). The best presentation of these results is in terms of a diagram in which

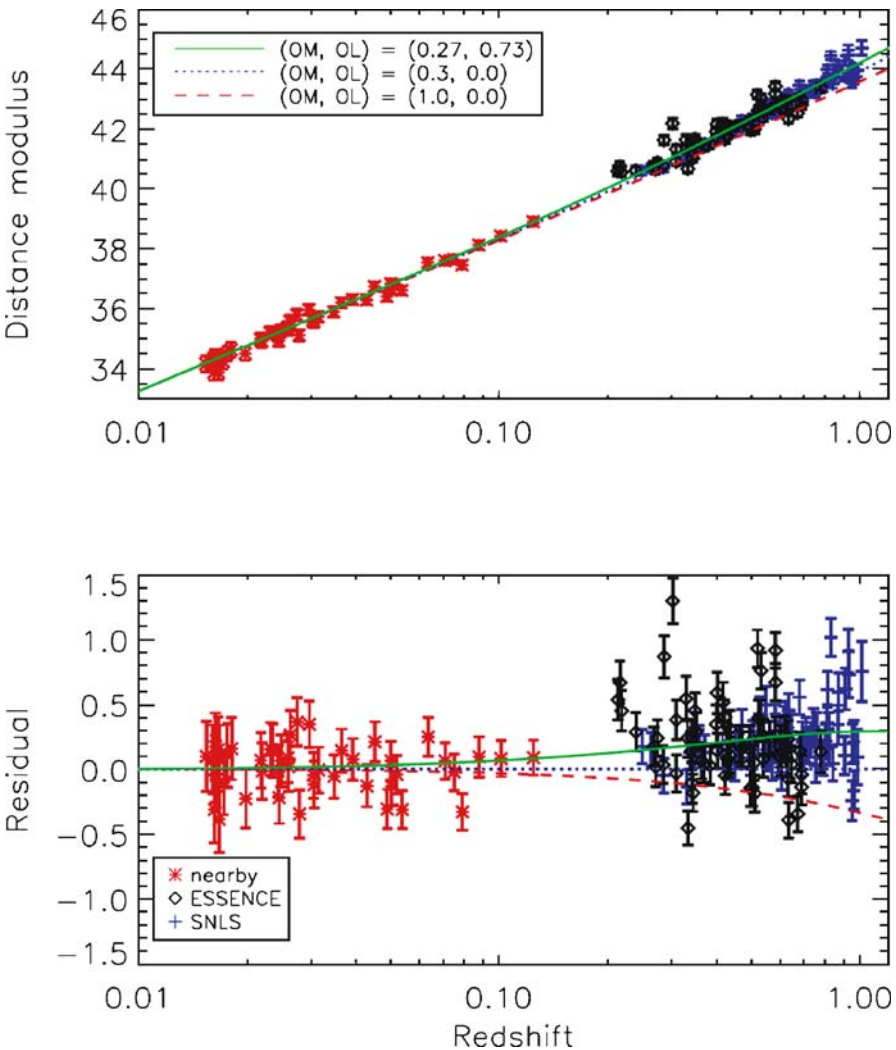


Fig. 8.6. The luminosity–redshift relation for supernovae of Type 1a from the combined ESSENCE and Supernova Legacy Survey data. For comparison the overplotted *solid* line and *residuals* are for a Λ CDM model with $w = -1$, $\Omega_0 = 0.27$ and $\Omega_A = 0.73$. The *dotted* and *dashed* lines are for models with $\Omega_A = 0$, as indicated in the figure legend (Wood-Vasey et al., 2007)

the density parameter of the matter content of the Universe Ω_0 is plotted against Ω_A . The results of the Supernova Cosmology Project are shown in Fig. 8.7.

There are various ways of interpreting Fig. 8.7, particularly when taken in conjunction with independent evidence on the mean mass density of the Universe and the evidence from the spectrum of fluctuations in the Cosmic Microwave Background

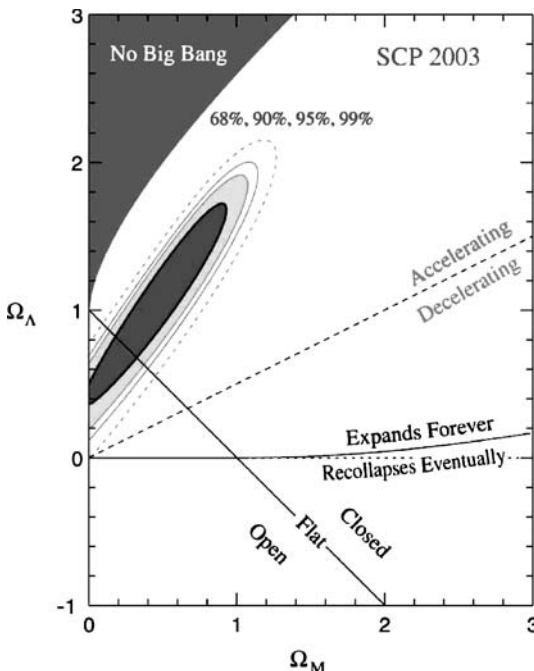


Fig. 8.7. The 68%, 90%, 95% and 99% confidence limits for the values of Ω_0 and Ω_Λ determined by the Supernova Cosmology Project. Also shown the diagram is the condition $\Omega_0 + \Omega_\Lambda = 1$ which corresponds to flat geometry (Knop et al., 2003)

Radiation. Perhaps the most conservative approach is to note that the matter density in the Universe must be greater than 0 and, as discussed in Sect. 8.7, all the data are consistent with values of $\Omega_0 \approx 0.25 - 0.3$. Consequently, Ω_Λ must be non-zero. The data would be consistent with $\Omega_0 + \Omega_\Lambda = 1$ if $\Omega_0 \approx 0.25 - 0.3$. We will come back to these results in Chap. 15.

8.5.4 The Number Counts of Galaxies

In his assessment of approaches to the determination of cosmological parameters, Sandage was not optimistic about the use of the number counts of galaxies (Sandage, 1961a):

Galaxy counts are insensitive to the model . . . There seems to be no hope of finding q_0 from the $N(m)$ counts because the predicted differences between the models are too small compared with the known fluctuations of the distribution.

These concerns have been fully justified by subsequent studies. The determination of precise counts of galaxies has proved to be one of the more difficult areas of observational cosmology. Ellis has provided an excellent account of the problems of determining and interpreting the counts of faint galaxies (Ellis, 1997). The reasons for these complications are multifold. First of all, galaxies are extended objects, often with complex brightness distributions, and great care must be taken to ensure that

the same types of object are compared at different magnitude limits and redshifts. Furthermore, the distribution of galaxies is far from uniform on scales less than about $50 h^{-1}$ Mpc, as illustrated by the large voids and walls seen in Figs. 2.7 and 2.8. Even at the faintest magnitudes, this ‘cellular’ structure in the distribution of galaxies results in fluctuations in the number counts of galaxies which exceed the statistical fluctuations expected in a random distribution (see Sect. 17.7). In addition, the probability of finding galaxies of different morphological types depends upon the galaxy environment. Finally, the luminosity function of galaxies is quite broad (Figs. 3.14 to 3.16) and so the differences between models are masked by the convolution of the predictions of the world models with this function.

Up till about 1980, the deepest counts extended to apparent magnitudes of about 22 to 23 and, although there were disagreements between the results of different observers, there was no strong evidence that the counts of galaxies departed from the expectations of uniform world models. Since that time, much deeper number counts have been determined thanks to the use of large area CCD cameras on large telescopes, as well as the spectacular images obtained from the Hubble Deep Field

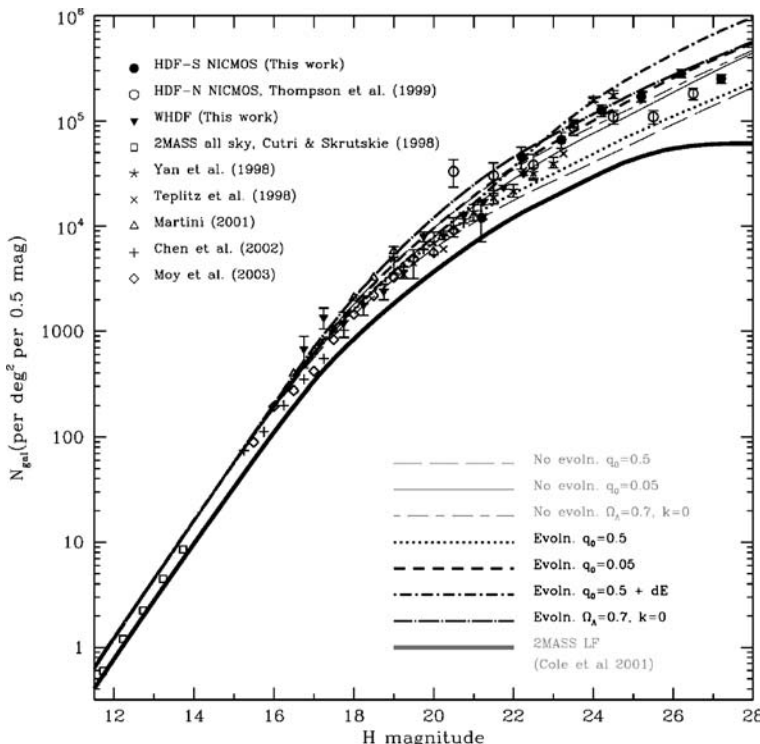


Fig. 8.8. Galaxy number counts in the infrared H waveband ($1.65 \mu\text{m}$) to $H = 28$ magnitude compiled by Metcalfe and his colleagues. The predictions of the various evolving and non-evolving models discussed by them are also shown (Metcalfe et al., 2006)

and the Hubble Ultra-Deep Field. An example of a compilation of deep counts of galaxies in the blue (B), red (I) and infrared (K) wavebands is shown in Fig. 2.12 (Metcalfe et al., 1996). It can be seen that there is a large excess of faint galaxies at blue magnitudes greater than about 22 while the counts of galaxies at red and infrared wavelengths show rather more modest evolution. The counts in the infrared H waveband in particular show little evidence for evolution, but various predictions for models with evolving and non-evolving galaxy populations indicate the real difficulties of determining cosmological parameters by this means (Fig. 8.8). While there is little prospect of using these observations to determine cosmological parameters, they are of the greatest interest in studying the astrophysical evolution of galaxies with cosmic epoch and this topic will be taken up in Chaps. 17 and 19.

8.5.5 The Angular Diameter–Redshift Test

The angular diameter–redshift relation provides an attractive route for the determination of cosmological parameters if accurate proper distances l of astronomical objects can be measured at large redshifts and their corresponding angular sizes θ measured. Then, the angular diameter distance $D_A = l/\theta$ can be determined as a function of redshift and compared with the predictions of the standard world models. The physical methods of measuring proper distances at large redshifts described in Sect. 8.3, involving the Sunyaev–Zeldovich effect in conjunction with X-ray observations of the hot gas in clusters, gravitational lenses and the various versions of the Baade–Wesselink method, all provide means of undertaking this test. A possible problem with this programme is the extent to which the predicted angular diameter–redshift relations are modified by inhomogeneities in the distribution of mass along the line of sight, which can significantly change the predicted relations (Sect. 7.7).

The alternative approach is to use objects which may be considered to be ‘rigid rods’, but the problem is to find suitable metric sizes which can be used in the test. A distinctive feature of this test is the predicted minimum angular diameter as the objects are observed at large redshifts (Fig. 7.8). A good example is the use of the separation of the radio components of double radio sources, such as those illustrated in Fig. 8.5. Large samples of these objects can be found spanning a wide range of redshifts. This test was first carried out by Miley who used the largest angular size of the radio structures of radio galaxies and quasars as a ‘rigid rod’ (Miley, 1968, 1971), but no minimum was found in the observed relation. Kapahi confirmed this result using instead the median angular separation θ_m of the radio source components as a function of redshift (Kapahi, 1987), but again no minimum was found (Fig. 8.9a). The median angular separation of the source components is observed to be roughly inversely proportional to redshift and this was interpreted as evidence that the median physical separation of the source components l_m was smaller at large redshifts. Examples of fits to the observational data using evolution functions of the form $l_m \propto (1+z)^{-n}$ are shown in Fig. 8.9a for world models with $q_0 = 0$ and 0.5; values of $n \approx 1.5\text{--}2.0$ can provide good fits to the data. There are many reasons why the separation of the radio source components might be smaller

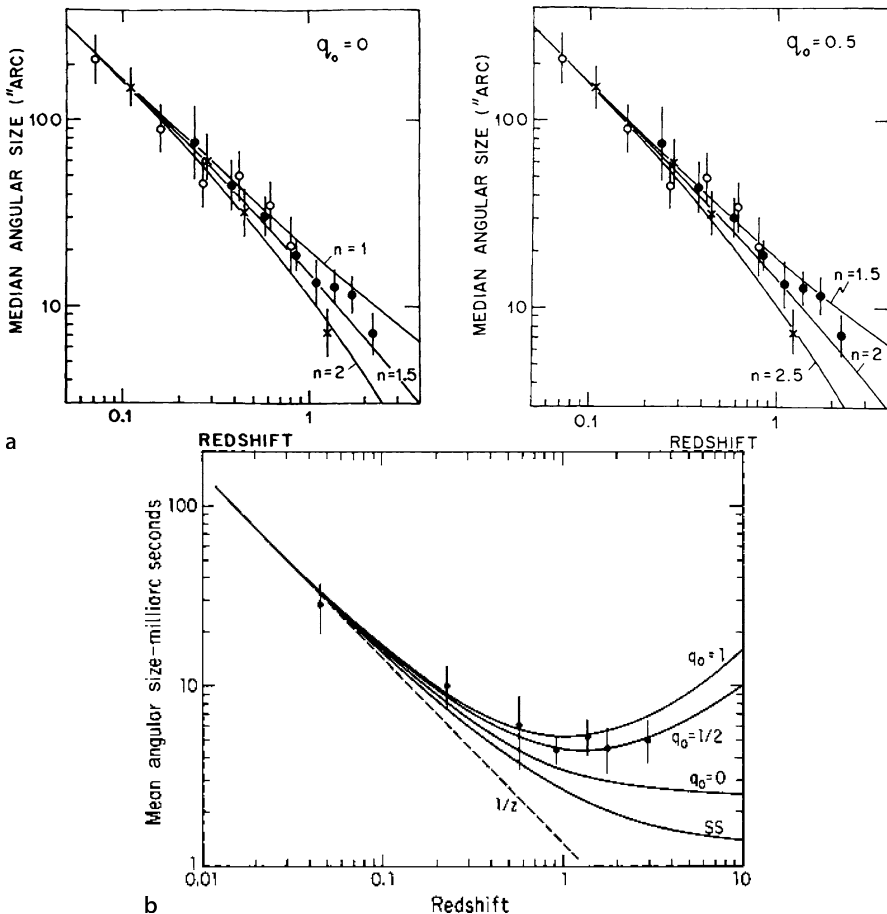


Fig. 8.9. **a** The angular diameter-redshift relation for double radio sources, in which the median angular separation of the double radio source components θ_m is plotted against redshift (Kapahi, 1987). The observed relation follows closely the relation $\theta_m \propto z^{-1}$. The left-hand panel shows fits to the observations for a world model with $q_0 = 0$ and the right-hand panel for a model with $q_0 = 0.5$, in both cases, the median separation of the components being assumed to change with redshift as $\theta_m \propto (1+z)^{-n}$. **b** The mean angular diameter-redshift relation for 82 compact radio sources observed by VLBI (Kellermann, 1993). In addition to the standard Friedman models, the relation for steady state cosmology (SS) as well as the relation $\theta \propto z^{-1}$ (dashed line) are shown

in the past, for example, the ambient interstellar and intergalactic gas may well have been greater in the past and so the source components could not penetrate so far through the surrounding gas. Again, we learn more about astrophysical changes with cosmic epoch of the objects studied rather than about cosmological parameters.

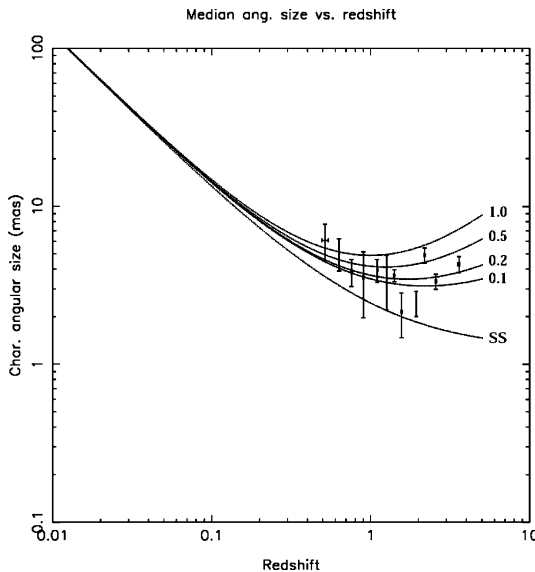


Fig. 8.10. The median angular diameter-redshift relation for 145 high luminosity compact radio sources observed by VLBI (Gurvits et al., 1999). The notation is the same as Fig. 8.9b

Another version of the same test was described by Kellermann and involved using only compact double radio structures studied by Very Long Baseline Interferometry (Kellermann, 1993). He argued that these sources are likely to be less influenced by changes in the properties of the intergalactic and interstellar gas, since the components are deeply embedded within the central regions of the host galaxy. In his angular diameter–redshift relation, there is evidence for a minimum in the relation, which would be consistent with a value of $q_0 \sim 0.5$ (Fig. 8.9b). A problem with this analysis is that the sources at small redshifts are less luminous than those at large redshift. Gurvits and his colleagues repeated the analysis with a much larger sample of 330 compact radio quasars from which they selected a subsample of 145 high luminosity quasars with $L \geq 10^{26} \text{ W Hz}^{-1}$ (Gurvits et al., 1999). The resulting angular diameter–redshift relation shown in Fig. 8.10 shows the large scatter when the data were binned into 12 bins, each with 12–13 sources. As they comment:

None of the solid lines represents the best fit.

Presumably, the properties of the sources are determined by local physical conditions close to the quasar nucleus. In addition, there is a clear lack of high luminosity sources at small redshifts which would ‘anchor’ the relation.

8.6 Ω_A and the Statistics of Gravitational Lenses

One way of testing models with finite values of Ω_A is to make use of the fact that the volume enclosed by redshift z increases as Ω_A increases, as illustrated by Fig. 7.11b for the case $\Omega_0 + \Omega_A = 1$. The statistics of gravitationally lensed images by intervening galaxies therefore provides an important test of models with finite Ω_A .

The power of this approach is illustrated by the following calculation (Fukugita et al., 1992). We assume, for simplicity, that we can represent the population of lensing galaxies by identical isothermal spheres which have constant comoving space density N_0 . We can then use the calculation which resulted in (4.63) for the Einstein radius θ_E , within which strong distortions of the image of a background object are expected,

$$\theta_E = \frac{4\pi \langle v_{\parallel}^2 \rangle}{c^2} \frac{D_{LS}}{D_S},$$

where $\langle v_{\parallel}^2 \rangle$ is the mean square velocity dispersion along the line of sight of the particles which make up each isothermal sphere, D_S is the angular diameter distance of the background quasar and D_{LS} the angular diameter distance from the lens to the background source. We can therefore write the cross-section σ_E of the isothermal sphere for strong lensing as

$$\sigma_E = \pi D_L^2 \theta_E^2 = A \left(\frac{D_L D_{LS}}{D_S} \right)^2, \quad (8.22)$$

where D_L is the angular diameter distance of the isothermal sphere, or lens. We now work out the probability that a background quasar at redshift z_S is observed to be strongly lensed. From (5.73), the number of isothermal spheres in the redshift interval z to $z + dz$ per steradian is

$$dN = N_0 D^2 dr, \quad (8.23)$$

where D is the distance measure which is related to the angular diameter distance by $D_A = D/(1+z)$. Therefore, the probability of strong lensing in the redshift interval dz is given by the total solid angle subtended by all the isothermal spheres in the increment of comoving radial distance coordinate dr

$$p(z) dz = \frac{N_0 \sigma_E D^2}{D_A^2} dr = \frac{N_0 \sigma_E D^2}{[D/(1+z)]^2} dr = N_0 \sigma_E (1+z)^2 dr. \quad (8.24)$$

We integrate this result from $z = 0$ to z_S to obtain the desired probability:

$$p(z_S) = AN_0 \int_0^{z_S} \left(\frac{D_L D_{LS}}{D_S} \right)^2 (1+z)^2 dr. \quad (8.25)$$

In general, dr is given by the expression

$$dr = \frac{c dz}{H_0 [(1+z)^2 (\Omega_0 z + 1) - \Omega_A z (z+2)]^{1/2}}, \quad (8.26)$$

and so

$$p(z_S) = A N_0 \int_0^{z_S} \left(\frac{D_L D_{LS}}{D_S} \right)^2 \frac{c(1+z)^2 dz}{H_0 [(1+z)^2(\Omega_0 z + 1) - \Omega_A z(z+2)]^{1/2}}. \quad (8.27)$$

To integrate this expression we need to evaluate D_{LS} , the angular diameter distance from the lens to the source. Following the reasoning of Sect. 7.5, the appropriate comoving distance coordinate between the epochs corresponding to z_L and z_S is

$$r(z_L, z_S) = - \int_{z_L}^{z_S} \frac{c dt}{a(t)}, \quad (8.28)$$

and then we form the distance measure $D(z_L, z_S)$ and the angular diameter distance $D_A(z_L, z_S)$,

$$D_A(z_L, z_S) = D(z_L, z_S) \frac{1+z_L}{1+z_S} = \frac{\mathfrak{R}}{(1+z_S)} \sin \int_{z_L}^{z_S} \frac{dr}{\mathfrak{R}}. \quad (8.29)$$

Carroll and his colleagues present the results of the integral (8.27) in a pleasant format. They normalise the integral to the probability of lensing in the case of the Einstein-de Sitter model, $\Omega_0 = 1$, $\Omega_A = 0$ in which case, it is straightforward to show that the probability for any other model becomes

$$p(z_S) = \frac{15 H_0^2}{4c^2} \left[1 - \frac{1}{(1+z_S)} \right]^{-3} \int_0^{z_S} \left(\frac{D_L D_{LS}}{D_S} \right)^2 \times \frac{(1+z)^2 dz}{[(1+z)^2(\Omega_0 z + 1) - \Omega_A z(z+2)]^{1/2}}. \quad (8.30)$$

This function is plotted in Fig. 8.11 in the same format as Fig. 7.4, the contours showing the relative lensing probabilities for a quasar at a typical redshift $z_S = 2$. It can be seen that, if $\Omega_A = 0$, as represented by the solid diagonal line, there are only small changes in the probability of lensing. For low values of Ω_0 , the probability increases by about a factor of 2 as compared with the $\Omega_0 = 1$ model. In contrast, the probability of lensing is very strongly dependent upon the value of Ω_A . For example, for the flat world models with $\Omega_0 + \Omega_A = 1$, the probability of lensing increases by almost a factor of ten as Ω_0 changes from 1 to 0.1. This dramatic increase occurs for a number of reasons. First of all, the distance measure D increases with increasing redshift more rapidly in models with low Ω_0 than in models with high Ω_0 and so much greater volumes are encompassed at a given redshift (Fig. 7.11). Second, the combination of parameters $D_L D_{LS}/D_S$ is sensitive to the presence of the cosmological constant which stretches out the angular diameter distance at a given redshift.

To obtain limits to the value of Ω_A from the frequency and properties of gravitational lenses in complete samples of quasars and radio galaxies, modelling of the lens and background source populations needs to be carried out. The probabilities

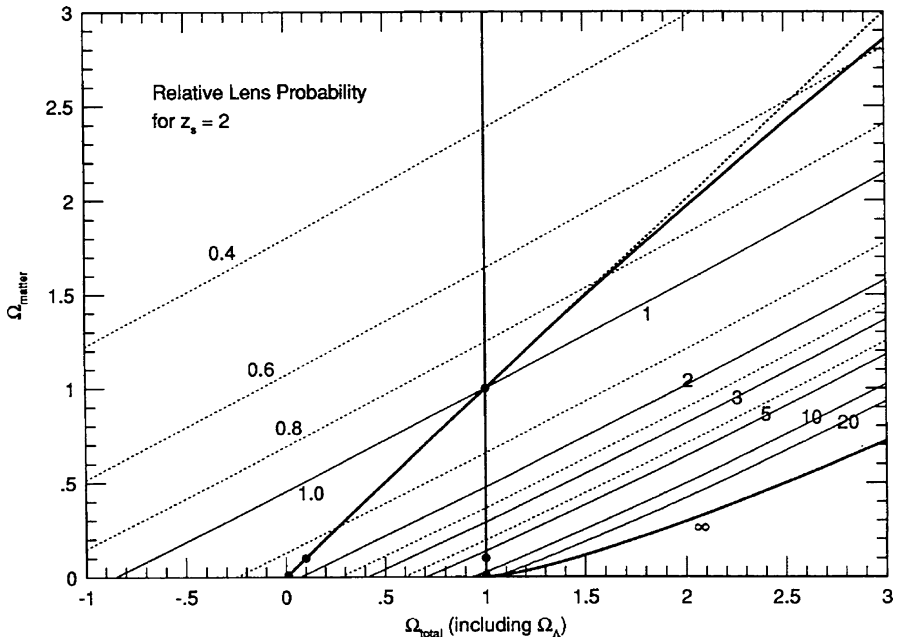


Fig. 8.11. The probability of observing strong gravitational lensing relative to that of the critical Einstein-de Sitter model, $\Omega_0 = 1$, $\Omega_\Lambda = 0$ for a quasar at redshift $z_S = 2$ (Carroll et al., 1992). The contours show the relative probabilities derived from the integral (8.30) and are presented in the same format as in Fig. 7.4

have to be averaged over the luminosity functions of lensing galaxies and the distribution of background sources. Models have to be adopted for the lenses which can account for the observed structures of the lensed images. The amplification of the brightness of the images as well as the detectability of the distorted structures need to be included in the computations. These complications are considered in some detail in the review by Carroll and his colleagues and by Kochanek (Carroll et al., 1992; Kochanek, 1996).

The largest survey to date designed specifically to address this problem has been the Cosmic Lens All Sky Survey (CLASS) in which a very large sample of flat spectrum radio sources was imaged by the Very Large Array (VLA), the Very Long Baseline Array (VLBA) and the MERLIN long baseline interferometer. The sources were selected according to strict selection criteria and resulted in the detection of 13 sources which were multiply imaged out of a total sample of 8958 radio sources (Chae et al., 2002). More recently, the CLASS collaboration has reported the point-source lensing rate to be one per 690 ± 190 targets (Mitchell et al., 2005). The analysis of these data used the luminosity functions for different galaxy types found in the AAT 2dF survey as well as models for the evolution of the population of flat-spectrum radio sources. The CLASS collaboration found that the observed fraction of multiply lensed sources was consistent with flat world models, $\Omega_0 + \Omega_\Lambda = 1$, in

which density parameter in the matter Ω_0 was

$$\Omega_0 = 0.31 \begin{array}{l} +0.27 \\ -0.14 \end{array} \text{(68\%)} \begin{array}{l} +0.12 \\ -0.10 \end{array} \text{(syst).} \quad (8.31)$$

Alternatively, for a flat universe with an equation of state for the dark energy of the form $p = w\varrho c^2$, they found an upper limit to w ,

$$w < -0.55 \begin{array}{l} +0.18 \\ -0.11 \end{array} \text{(68\%),} \quad (8.32)$$

consistent with the standard value for the cosmological constant $w = -1$ (Chae et al., 2002).

8.7 The Density Parameter Ω_0

Estimates of the average cosmological density of matter in galaxies were included in Hubble's first paper on the extragalactic nature of the diffuse nebulae. He used his estimates of their average mass-to-light ratios to estimate a mean cosmological density of $\varrho_0 = 1.5 \times 10^{-28} \text{ kg m}^{-3}$ (Hubble, 1926). A similar analysis was carried out in 1958 by Oort who found that the average mass density was $3.1 \times 10^{-28} \text{ kg m}^{-3}$ assuming that Hubble's constant was $180 \text{ km s}^{-1} \text{ Mpc}^{-1}$ (Oort, 1958).

In 1978, Gunn expressed the same result in terms of the mass-to-light ratio which would be needed if the Universe were to attain the critical density (Gunn, 1978). He found $(M/L)_{\text{crit}} = 2600h$, very much greater than the values found in our vicinity in the plane of the Galaxy. As described in Sects. 3.5, 4.3 and 4.4, the mass of dark matter in galaxies and clusters of galaxies far exceeds that in the visible parts of galaxies. If account is taken of the dark matter, the overall mass-to-luminosity ratio attains values of $M/L \sim 100\text{--}150$. In well-studied rich clusters, such as the Coma cluster, the value of M/L is of the order of 250, but this value is biased towards elliptical and S0 galaxies which have three times larger values of M/L than the spiral galaxies, the latter contributing most of the light per unit volume in the Universe at large. These values of M/L are significantly less than the value needed to close the Universe. Gunn's best estimate of the density parameter for bound systems such as galaxies, groups and clusters of galaxies was about 0.1 and was independent of the value of h .

In 2000, Bahcall reviewed the many different approaches which can be taken to derive values of M/L for clusters of galaxies – cluster mass-to-light ratios, the baryon fraction in clusters and studies of cluster evolution (Bahcall, 2000). These have all found the same consistent result that the mass density of the universe corresponds to $\Omega_0 \approx 0.25$ and furthermore that the mass approximately traces light on large scales. These results reflect the generally accepted view that, if mass densities are determined for bound systems, the total mass density in the Universe is about a factor of 4 less than that needed to close the Universe.

On scales greater than those of clusters of galaxies, estimates of the mass density in the general field can be found from the *cosmic virial theorem* (Peebles, 1976). In this procedure, the random velocities of galaxies with respect to the mean Hubble flow are compared with the varying component of the gravitational acceleration due to large-scale inhomogeneities in the distribution of galaxies. As in the other methods of mass determination, the mass density is found by comparing the random kinetic energy of galaxies with their gravitational potential energy, this comparison being carried out in terms of two-point correlation functions for both the velocities and positions of galaxies selected from the general field. Application to the random velocities of field galaxies suggested that Ω_0 might be larger than 0.2 (Davis et al., 1978; Davis and Peebles, 1983).

A similar argument involves studies of the infall of galaxies into superclusters of galaxies. Galaxies in the vicinity of a supercluster are accelerated towards it, thus providing a measure of the mean density of gravitating matter within the system. The velocities induced by large-scale density perturbations depend upon the *density contrast* $\delta\varrho/\varrho$ between the system studied and the mean background density. A typical formula for the infall velocity u of test particles into a density perturbation is (Gunn, 1978):

$$u \propto H_0 r \Omega_0^{0.6} \left(\frac{\delta\varrho}{\varrho} \right)_0 . \quad (8.33)$$

In Gunn's analysis, this method resulted in values of Ω_0 about 0.2 to 0.3. In the case of small spherical perturbations, a result correct to second order in the density perturbation was presented by Lightman and Schechter (Lightman and Schechter, 1990).

$$\frac{\delta v}{v} = -\frac{1}{3} \Omega_0^{4/7} \left(\frac{\delta\varrho}{\varrho} \right)_0 + \frac{4}{63} \Omega_0^{13/21} \left(\frac{\delta\varrho}{\varrho} \right)_0^2 . \quad (8.34)$$

In an ambitious programme, Dekel and his colleagues devised numerical procedures for deriving the distribution of mass in the local Universe entirely from the measured velocities and distances of complete samples of nearby galaxies, the objective being to determine a three-dimensional map of velocity deviations from the mean Hubble flow. Then, applying Poisson's equation, the mass distribution responsible for the observed peculiar velocity distribution can be reconstructed numerically. Figure 8.12 shows an example of a reconstruction of the local density distribution using this procedure (Hudson et al., 1995). Despite using only the velocities and distances, and *not* their number densities, many of the familiar features of our local Universe are recovered – the Virgo supercluster and the ‘Great Attractor’ can be seen as well as voids in the mean mass distribution. These procedures tended to produce somewhat larger values of Ω_0 , Dekel stating that the density parameter is greater than 0.3 at the 95% confidence level.

The issue of the total amount of dark matter present in the Universe was the subject of heated debate throughout the 1990s. Some flavour of the points of contention among the experts in the field can be gained from the discussions at the 1996

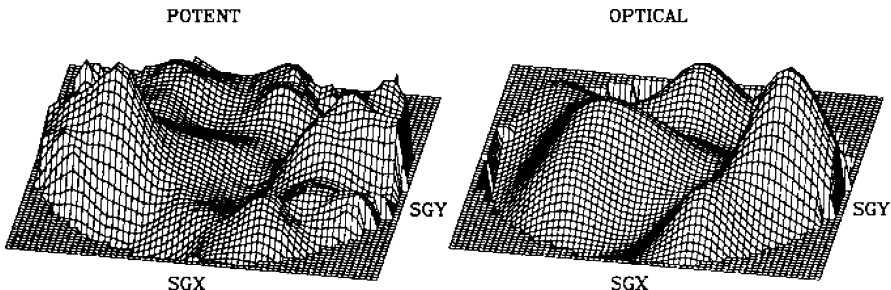


Fig. 8.12. Surface density plots of the density field in the local Supergalactic plane. The *left-hand panel* shows the mass distribution reconstructed from the peculiar velocity and distance information for the galaxies in this region using the POTENT numerical procedure. The *right-hand panel* shows the density field of optical galaxies, both images smoothed with a Gaussian filter of radius 1200 km s^{-1} . The density contrast is proportional to the height of the surface above (or below) the plane of the plot (Hudson et al., 1995)

Princeton meeting *Critical Dialogues in Cosmology* between Burstein and Dekel, White acting as moderator (Dekel et al., 1997). The upshot of these considerations was that there was agreement that the value of Ω_0 is greater than 0.1 and a value of 0.2 to 0.3 would be consistent with most of the data.

The infall test became feasible on very large scales following the completion of the Two-Degree Field (2dF) survey of galaxy redshifts carried out at the Anglo-Australian Telescope. The survey involved measuring redshifts for almost 200,000 galaxies randomly selected from the Cambridge APM galaxy survey. A cut from that survey was shown in Fig. 2.8a. The concept behind the test was that superclusters of galaxies generate a systematic infall of other galaxies in their vicinities and this would be evident in the pattern of recessional velocities, resulting in anisotropy in the inferred spatial clustering of galaxies. Using the redshifts of more than 141,000 galaxies from the 2dF galaxy redshift survey, Peacock and his colleagues discovered convincing statistical evidence for infall and estimated the overall density parameter to be $\Omega_0^{0.6} = 0.43b \pm 0.07$, where b is the bias parameter, the factor by which visible matter is more clustered than the dominant dark matter. When this result was combined with data on the anisotropy of the Cosmic Microwave Background, their result favoured a low density Universe with $\Omega_0 \approx 0.3$ (Peacock et al., 2001).

When taken in conjunction with the results derived from the power spectrum of fluctuations in the Cosmic Microwave Background Radiation discussed in Sect. 15.9, the consensus view is that the best estimate of the overall density parameter for the Universe is $\Omega_0 \approx 0.25 - 0.3$. An immediate consequence of this result is that most of the mass in the Universe cannot be in baryonic matter, which is constrained by the production of the light elements in the early stages of the Big Bang. As will be discussed in Sect. 10.4, the best estimate of the density parameter in baryons is $\Omega_{\text{bar}} = (0.0223 \pm 0.002)h^{-2}$, consistent with the results of analyses of the power spectrum of fluctuations in the Cosmic Microwave Background Radiation. Adopting $h = 0.7$, $\Omega_{\text{bar}} = 0.0455$ and so there cannot be sufficient baryons to account for

the observed total mass density. Most of the mass in the Universe must be in some non-baryonic form.

8.8 Summary

From a subject dogged by controversy and strong feeling for most of the twentieth century, classical cosmology saw a dramatic change in perspective during the last decade. New methods were developed which eliminated many of the problems of the pioneering efforts of previous decades. Whilst the emphasis in this chapter has been upon the traditional route to the determination of cosmological parameters, the consensus picture received a remarkable boost from analyses of the fluctuation spectrum of the Cosmic Microwave Background Radiation, a story which is told in the context of the understanding of the formation of large-scale structures in the Universe in Chap. 15. Indeed, many cosmologists would now look first to these observations as providing the key to unlocking many of the problems of the determination of cosmological parameters.

9 The Thermal History of the Universe

We are now well on our way to setting the scene for our attack on the problems of understanding the origin and evolution of galaxies and the large-scale structure of our Universe. Before we can do that, however, we need to work out in some detail the thermal history of the matter and radiation content of the Universe according to the standard Big Bang picture. In this chapter and Chap. 10, we develop a number of concepts which are essential for understanding the problems of galaxy formation. We first consider the dynamics of radiation-dominated universes.

9.1 Radiation-Dominated Universes

For a gas of photons, massless particles or a relativistic gas in the ultrarelativistic limit $E \gg mc^2$, pressure p is related to energy density ε by $p = \frac{1}{3}\varepsilon$ and the inertial mass density of the radiation ϱ_r is related to its energy density ε by $\varepsilon = \varrho_r c^2$. If $N(\nu)$ is the number density of photons of energy $h\nu$, then the energy density of radiation is found by summing over all frequencies

$$\varepsilon = \sum_{\nu} h\nu N(\nu) . \quad (9.1)$$

If the number of photons is conserved, their number density varies with scale factor a as $N = N_0 a^{-3} = N_0(1+z)^3$ and the energy of each photon changes with redshift by the usual redshift factor $\nu = \nu_0(1+z)$. Therefore, the variation of the energy density of radiation with redshift is

$$\varepsilon = \sum_{\nu_0} h\nu_0 N_0(\nu_0)(1+z)^4 = \varepsilon_0(1+z)^4 = \varepsilon_0 a^{-4} . \quad (9.2)$$

This is exactly the same expression as (7.9) which was deduced from a more thermodynamic perspective. In the case of black-body radiation, the energy density of the radiation is described by the Stefan–Boltzmann law¹

$$\varepsilon = \frac{4\sigma}{c} T^4 , \quad (9.3)$$

and its spectral energy density, that is, its energy density per unit frequency range, by the Planck distribution

$$\varepsilon(\nu) d\nu = \frac{8\pi h\nu^3}{c^3} \frac{1}{e^{h\nu/kT} - 1} d\nu . \quad (9.4)$$

It immediately follows that, for black-body radiation, the radiation temperature T_r varies with redshift as $T_r = T_0(1+z)$ and the spectrum of the radiation changes as

$$\begin{aligned} \varepsilon(\nu_1) d\nu_1 &= \frac{8\pi h\nu_1^3}{c^3} \frac{1}{e^{h\nu_1/kT_1} - 1} d\nu_1 \\ &= \frac{8\pi h\nu_0^3}{c^3} \frac{1}{e^{h\nu_0/kT_0} - 1} (1+z)^4 d\nu_0 \\ &= (1+z)^4 \varepsilon(\nu_0) d\nu_0 , \end{aligned} \quad (9.5)$$

where $T_1 = T_0(1+z)$. Thus, a black-body spectrum preserves its form as the Universe expands, but the radiation temperature changes as $T_r = T_0(1+z)$ and the frequency of each photon as $\nu = \nu_0(1+z)$. Another way of looking at these results is in terms of the adiabatic expansion of a gas of photons. The ratio of specific heats γ for radiation and a relativistic gas in the ultrarelativistic limit is $\gamma = 4/3$. It is a simple exercise to show that, in an adiabatic expansion, $T \propto V^{-(\gamma-1)} = V^{-1/3} \propto a^{-1}$, which is exactly the same as the above result.

A key test of the standard Big Bang picture is whether or not the temperature of the Cosmic Microwave Background Radiation has followed the predicted relation $T_r = T_0(1+z)$. The fine-structure splittings of the ground state of neutral carbon atoms CI enable this test to be carried out. The photons of the background radiation excite the fine-structure levels of the ground state of the neutral carbon atoms and the relative strengths of the absorption lines originating from the ground and first excited states are determined by the energy density and temperature of the background radiation. The test has been carried out using the absorption lines observed in damped Lyman- α clouds in the spectra of quasars (see Sect. 18.3). This is a difficult experiment since the lines are weak, but successful observations were carried out with the Keck 10-metre Telescope in the 1990s. Cowie and his colleagues observed the CI absorption lines in a damped Lyman- α cloud at redshift $z = 1.776$ in the spectrum of the quasar Q1331+170 and derived a background temperature $T_{\text{rad}} = 7.4 \pm 0.8$ K, consistent with expected temperature, $T(z) = T_0(1+z) = 7.58$ K (Songaila et al.,

¹ I have written the Stefan–Boltzmann law in terms of the Stefan–Boltzmann constant $\sigma = 5.670 \times 10^{-8} \text{ W m}^{-2} \text{ K}^{-4}$. The pre-factor $4/c$ converts this intensity into an energy density.

1994). The experiment was repeated by Ge and his colleagues who studied the CI absorption lines in a damped Lyman- α cloud at redshift $z = 1.9731$ in the spectrum of the quasar QSO 0013-004 and found $T_{\text{rad}} = 7.9 \pm 1.0$ K, consistent with the predicted temperature of $T(z) = T_0(1 + z) = 8.105$ K (Ge et al., 1997). Most recently, the observation has been repeated by Ledoux and his colleagues for the quasar PSS J1443+2724 in which there is an absorption system at redshift $z_{\text{abs}} = 4.224$ (Ledoux et al., 2006). The expected radiation temperature of the background radiation at this redshift is 14.2 K, consistent with the observed excitation of the ground and first fine-structure excited states of CI. Strictly speaking, these are only upper limits to the temperature of the background radiation, since there might be other local sources of excitation of the fine-structure lines, but this is regarded as unlikely. The results of these experiments provide evidence that the radiation temperature of the background radiation has followed the expected dependence upon redshift.

The variations of p and ϱ with a can now be substituted into Einstein's field equations with the results:

$$\ddot{a} = -\frac{8\pi G \varrho_0}{3a^3} + \frac{1}{3}\Lambda a; \quad \dot{a}^2 = \frac{8\pi G \varrho_0}{3a^2} - \frac{c^2}{3t^2} + \frac{1}{3}\Lambda a^2.$$

In the early Universe, $a \ll 1$ and so the terms associated with the cosmological constant and the space curvature become negligible. Therefore,

$$\ddot{a} = -\frac{8\pi G \varepsilon_0}{3c^2} \frac{1}{a^3}; \quad \dot{a}^2 = \frac{8\pi G \varepsilon_0}{3c^2} \frac{1}{a^2}. \quad (9.6)$$

Integrating

$$a = \left(\frac{32\pi G \varepsilon_0}{3c^2} \right)^{1/4} t^{1/2} \quad \text{or} \quad \varepsilon = \varepsilon_0 a^{-4} = \left(\frac{3c^2}{32\pi G} \right) t^{-2}. \quad (9.7)$$

Thus, the dynamics of the radiation-dominated models, $a \propto t^{1/2}$, depend only upon the *total inertial mass density in relativistic and massless forms*. Therefore, to determine the dynamics of the early Universe, we have to include in all the massless and relativistic components into the total energy density, ε_0 or ϱ_0 . The force of gravity acting upon the sum of these determines the rate of deceleration of the early Universe.

9.2 The Matter and Radiation Content of the Universe

A schematic representation of the intensity I_ν of the extragalactic background radiation from radio to γ -ray wavelengths is shown in Fig. 9.1a (Longair and Sunyaev, 1971). This is a rather old picture, but I still like it since it gives a good representation of the intensity of the background radiation in those regions in which it has been measured (solid lines) and those regions in which only upper limits to the extragalactic background had been made (dashed lines).

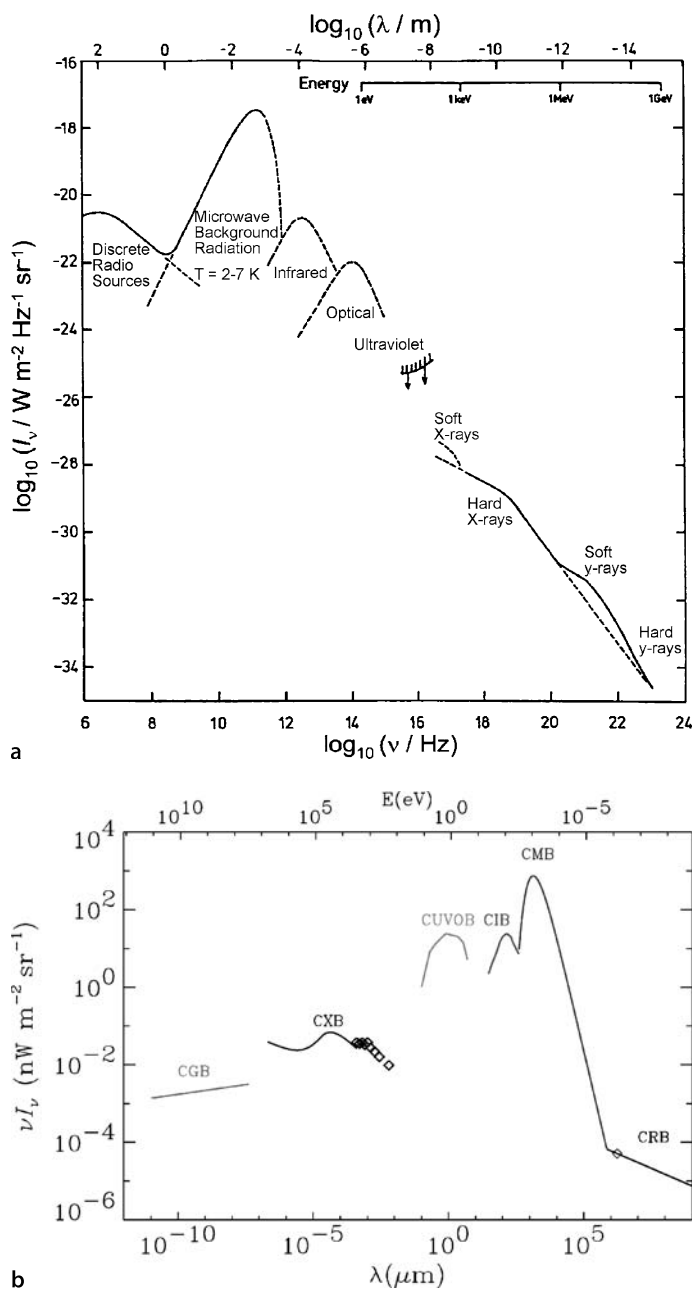


Fig. 9.1. **a** The spectrum of the extragalactic background radiation as it was known in 1969 (Longair and Sunyaev, 1971). This figure still provides a good indication of the overall spectral energy distribution of the background radiation. The *solid lines* indicate regions of the spectrum in which extragalactic background radiation had been detected. The *dashed lines* were theoretical estimates of the background intensity due to discrete sources and should not be taken too seriously. **b** The spectrum of the extragalactic background radiation plotted as $I = \nu I_\nu = \lambda I_\lambda$ (Hauser and Dwek, 2001). The *acronyms* used in this diagram stand for: *CRB* = cosmic radio background; *CMB* = cosmic microwave background; *CIB* = cosmic infrared background; *CUVOB* = cosmic ultraviolet and optical background; *CXB* = cosmic X-ray background; *CGB* = cosmic γ -ray background

Figure 9.1a has the virtue of representing the spectral shape of the background over an enormous range of energies, but, since it is presented in units per unit frequency interval, it does not provide a good representation of the energy density of radiation in each waveband. To obtain the integrated intensity, we need $I = \int I_\nu d\nu$. For rough estimates, this is often approximated by $I \sim \nu I_\nu$. A version of this form of presentation is shown in Fig. 9.1b which enables the main contributors to the energy density of the extragalactic background radiation to be identified (Hauser and Dwek, 2001).

I surveyed the background radiation in all wavebands in 1995 and refer the interested reader to that review (Longair, 1995). Since that time, new estimates of the ultraviolet, optical and infrared background have become available and these are shown in Fig. 9.2, which is presented in the same units as in Fig. 9.1b. The filled symbols show upper limits to the background radiation. The open symbols show the background intensity due to galaxies which are observed in very deep surveys in these wavebands. The solid and dashed lines show estimates of the background intensity from analyses of the spectra of ultrahigh energy γ -ray sources in which the effects of $\gamma\gamma$ absorption attenuates the high energy spectrum (Aharonian et al., 2006).

In summary, diffuse background radiation of cosmological origin has been detected in the radio, centimetre, millimetre, far-infrared, X- and γ -ray wavebands. Background radiation in the ultraviolet, optical and near-infrared wavebands has not been detected with certainty, but is now strongly constrained by the observational upper limits and the number counts of faint galaxies shown in Fig. 9.2.

It is useful to have estimates of the typical energy densities and number densities of the photons in each waveband and these are summarised in Table 9.1. It must be emphasised that these are very rough estimates and, for precise calculations, integrations should to be taken over the appropriate regions of the spectrum.

To anticipate the discussion of Chap. 17, the bulk of the diffuse extragalactic background in the radio, far-infrared, infrared, optical, ultraviolet, X-ray and γ -ray waveband is due to the integrated emission of discrete sources (Longair, 1995; Hauser and Dwek, 2001). The one exception is the Cosmic Microwave Background Radiation which cannot be associated with discrete sources and is convincingly

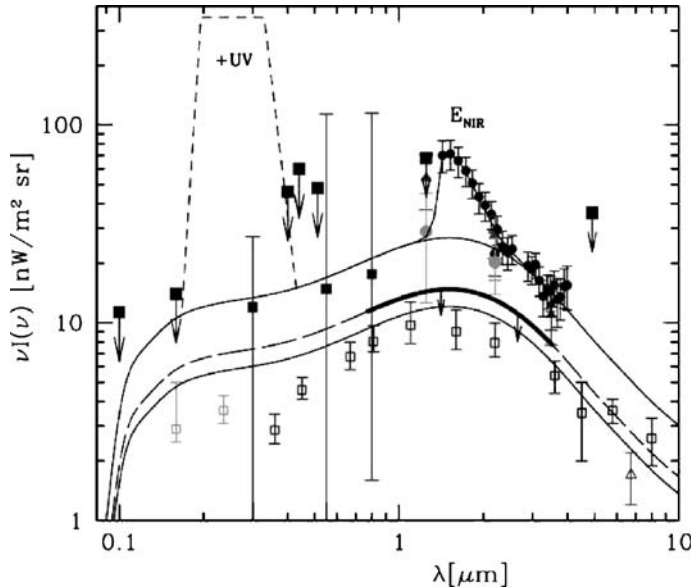


Fig. 9.2. The spectrum of the extragalactic background radiation plotted as $I = \nu I_\nu = \lambda I_\lambda$ in the ultraviolet, optical and infrared wavebands. The *filled symbols* show upper limits to the background radiation. The *open symbols* show the background due to known types of sources. The *solid lines* show the range of limits to the background intensity from analysis of the spectra of ultrahigh energy γ -ray sources in which the effects of $\gamma\gamma$ absorption attenuates the high energy spectrum (Aharonian et al., 2006). The *dashed line* with the *thicker solid line* shows the best estimate of the upper limit to the background intensity

identified with the cooled remnant of the hot early phases of the Big Bang, as we will show.

It can be seen from Fig. 9.1b and Table 9.1 that the Cosmic Microwave Background Radiation provides by far the largest contribution to the energy density of radiation in intergalactic space. Adopting a radiation temperature of 2.728 K, the energy density of radiation is $2.616 \times 10^5 \text{ eV m}^{-3}$. Comparing the inertial mass density in the radiation and the matter, we find

$$\frac{\varrho_r}{\varrho_m} = \frac{4\sigma T^4(z)}{\varrho_0 \varrho_c (1+z)^3 c^3} = \frac{2.48 \times 10^{-5} (1+z)}{\varrho_0 h^2}. \quad (9.8)$$

Thus, at redshifts $z \geq 4 \times 10^4 \varrho_0 h^2$, the Universe was certainly *radiation-dominated*, even before we take account of the contribution of the three types of neutrino to the inertial mass density. During the radiation-dominated phase, the dynamics are described by the relation, $a \propto t^{1/2}$. Adopting the reference values $h = 0.7$, $\varrho_0 = 0.3$, the transition to the radiation-dominated era would take place at redshift $z \approx 6000$. At redshifts less than this value, the Universe was *matter-dominated* and the dynamics were described by the standard Friedman models, $a \propto t^{2/3}$ provided $\varrho_0 z \gg 1$. We

Table 9.1. The energy densities and photon number densities of the extragalactic background radiation in different regions of electromagnetic spectrum. These estimates are based on the data provided by Hauser and Dwek (Hauser and Dwek, 2001). Note that these are generally rough estimates which are intended only to be used for making order of magnitude calculations

Waveband	Energy density of radiation (eV m ⁻³)	Number density of photons (m ⁻³)
Radio (300 MHz)	10 ⁻²	~ 10 ⁴
Cosmic Microwave Background	2.6 × 10 ⁵	4 × 10 ⁸
Infrared (140–1000 μm)	4 × 10 ³	3 × 10 ⁵
UV-optical-near IR (0.16–3.5 μm)	~ 10 ⁴	~ 10 ⁴
X-ray (~ 10 keV)	20	3 × 10 ⁻³
γ-ray (~ 1 MeV)	10	~ 10 ⁻⁵
γ-ray (≥ 10 MeV)	0.5	~ 3 × 10 ⁻⁸

will provide a more precise estimate of the epoch at which the inertial mass densities in the massless particles and non-relativistic matter were equal in Sect. 10.5.

The present *photon-to-baryon number ratio* is another key cosmological parameter. The number density of photons associated with the Cosmic Microwave Background Radiation is

$$N = 0.244 \left(\frac{2\pi kT}{hc} \right)^3 = 4.13 \times 10^8 \text{ m}^{-3}, \quad (9.9)$$

assuming $T = 2.728$ K. Therefore, the photon-to-baryon number ratio is

$$\frac{N_\gamma}{N_B} = \frac{3.7 \times 10^7}{\Omega_B h^2}. \quad (9.10)$$

Adopting the reference values $\Omega_B = 0.05$, $h = 0.7$, we find $N_\gamma/N_B = 1.5 \times 10^9$. Thus, the number density of photons is overwhelmingly greater than that of baryons at the present epoch. If photons were neither created nor destroyed during the expansion of the Universe, this number is an invariant. This ratio is also proportional to the specific entropy per baryon during the radiation-dominated phases of the expansion (see Sect. 10.5).

The resulting thermal history of the Universe is summarised in Fig. 9.3. Certain epochs are of special significance for structure formation and we now deal with some of these in more detail.

9.3 The Epoch of Recombination

At redshifts $z \approx 1500$, the radiation temperature of the Cosmic Microwave Background Radiation was $T \approx 4000$ K and then there were sufficient photons with

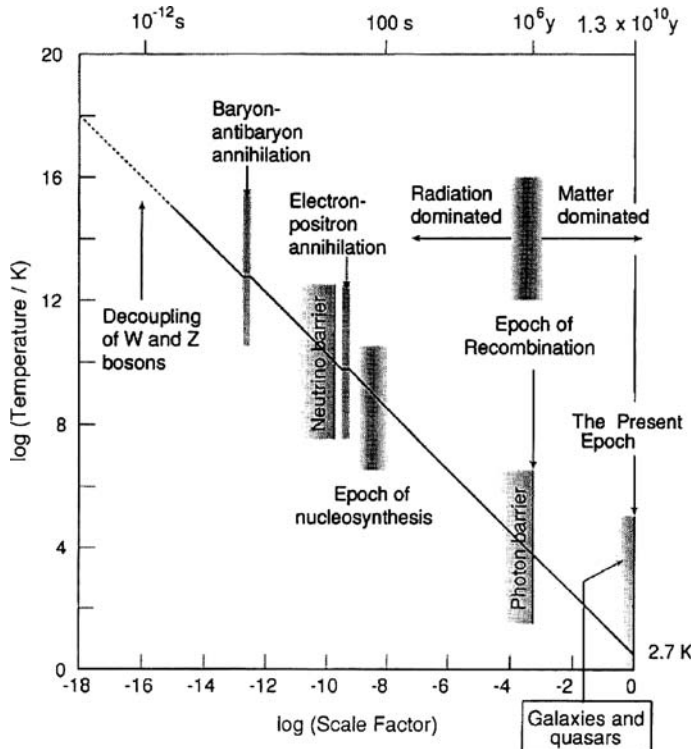


Fig. 9.3. The thermal history of the Cosmic Microwave Background Radiation according to the standard Big Bang picture. The radiation temperature decreases as $T_r \propto a^{-1}$ except for small discontinuities as different particle-antiparticle pairs annihilate at $kT \approx mc^2$. Various important epochs in the standard picture are indicated, including the neutrino and photon barriers. In the standard model, the Universe is optically thick to neutrinos and photons prior to these epochs. An approximate time-scale is indicated along the top of the diagram

energies $h\nu \geq 13.6$ eV in the high energy region of the Planck distribution to ionise all the neutral hydrogen present in the intergalactic medium. We will often refer to the region of the Planck spectrum with photon energies $E = h\nu \gg kT$ as the *Wien region*. It may at first appear strange that the temperature is not closer to 150,000 K, the temperature at which $\langle h\nu \rangle = kT = 13.6$ eV, the ionisation potential of neutral hydrogen. The important points to note are that the photons far outnumber the baryons in the intergalactic medium and that there is a broad range of photon energies present in the Planck distribution.

It is a useful calculation to work out the fraction of photons in the Wien region of the Planck distribution with energies $h\nu \geq E$ in the limit $h\nu \gg kT$. Their number density is

$$n(\geq E) = \int_{E/h}^{\infty} \frac{8\pi\nu^2}{c^3} \frac{d\nu}{e^{h\nu/kT}} = \frac{1}{\pi^2} \left(\frac{2\pi kT}{hc} \right)^3 e^{-x} (x^2 + 2x + 2), \quad (9.11)$$

where $x = h\nu/kT$. Now, the total number density of photons in a black-body spectrum at temperature T is

$$N = 0.244 \left(\frac{2\pi kT}{hc} \right)^3 \text{ m}^{-3}. \quad (9.12)$$

Therefore, the fraction of the photons of the black-body spectrum with energies greater than E is

$$\frac{n(\geq E)}{n_{\text{ph}}} = \frac{e^{-x}(x^2 + 2x + 2)}{0.244\pi^2}. \quad (9.13)$$

Roughly speaking, the intergalactic gas will be ionised if there are as many ionising photons with $h\nu \geq 13.6$ eV as there are hydrogen atoms, that is, we need only one photon in $3.6 \times 10^7/\Omega_B h^2 \sim 10^9$ of the photons of the Cosmic Microwave Background Radiation to have energy greater than 13.6 eV to ionise the gas. For illustrative purposes, let us take the ratio to be one part in 10^9 . Then, to find x , we need to solve

$$\frac{1}{10^9} = \frac{e^{-x}(x^2 + 2x + 2)}{0.244\pi^2}. \quad (9.14)$$

The solution is $x = E/kT \approx 26.5$. This is a very important result. There are so many photons relative to hydrogen atoms that the temperature of the radiation can be 26.5 times less than that found by setting $E = kT$ and there are still sufficient photons with energy $E \geq 13.6$ eV to ionise the gas. Therefore, the intergalactic gas was largely ionised at a temperature $T \sim 150,000/26.5 = 5600$ K. Since the present temperature of the Cosmic Microwave Background Radiation is 2.728 K, this means that the Universe became ionised at a scale factor $a \sim 2.728/5600 = 5 \times 10^{-4}$ or at a redshift $z \sim 2000$.

It is interesting to note that this type of calculation appears in a number of different guises in astrophysics. For example, the nuclear reactions which power the Sun take place at a much lower temperature than expected, the temperature at which regions of ionised hydrogen become fully ionised is only about 10,000 K and light nuclei are destroyed in the early Universe at much lower temperatures than would be expected. In all these cases, the Wien region of the Planck and the high energy tail of the Maxwell distributions contain large numbers of photons and particles respectively with energies very much greater than the mean.

Detailed calculations show that the pre-galactic gas was 50% ionised at a redshift $z_r \approx 1500$ and this epoch is referred to as the *epoch of recombination*, since the pre-galactic gas was ionised prior to this epoch. When we run the clocks forward, the universal plasma recombined at this time. At earlier epochs, $z \approx 6000$, helium was 50% ionised and rapidly became fully ionised at earlier times. The most important consequence of these considerations is that, at redshifts greater than about 1000, the Universe became optically thick to *Thomson scattering*. This is the simplest of the scattering processes which impede the propagation of photons from their sources

to the Earth through an ionised plasma (Longair, 1997b). The photons are scattered without any loss of energy by free electrons. The increment of optical depth of the intergalactic gas to Thomson scattering is

$$d\tau_T = \sigma_T N_e(z) dx = \sigma_T N_e(z) c \frac{dt}{dz} dz, \quad (9.15)$$

where σ_T is the Thomson scattering cross-section $\sigma_T = 6.653 \times 10^{-29} \text{ m}^2$ and dx is the increment of proper distance at redshift z . Let us evaluate this integral in the limit of large redshifts, assuming that the Universe was matter-dominated through the epoch of recombination. Then, from (7.64), the cosmic time-redshift relation can be written in the limit $\Omega_0 z \gg 1, z \gg 1$

$$\frac{dz}{dt} = -H_0(1+z) [(1+z)^2(\Omega_0 z + 1) - \Omega_A z(z+2)]^{1/2} = -H_0 \Omega_0^{1/2} z^{5/2}. \quad (9.16)$$

It is important to distinguish between the total mass density ϱ_0 and the mass density in baryons ϱ_B . Assuming that 25% of the primordial material by mass is helium (see Sect. 10.4), $N_H = (3/4)\varrho_B/m_p$ and so we can write the density parameter in baryons $\Omega_B = 8\pi G \varrho_B / 3H_0^2 = 32\pi G m_p N_H / 9H_0^2$. Then, if $x(z)$ is the fractional ionisation of hydrogen, the number density of electrons is $N_H x(z)(1+z)^3$ and so the optical depth for Thomson scattering in the limit $z \gg 1$ is

$$\tau_T = \frac{9\sigma_T H_0 c}{32\pi G m_p} \frac{\Omega_B}{\Omega_0^{1/2}} \int \frac{z^3 x(z)}{z^{5/2}} dz = 0.052 \frac{\Omega_B}{\Omega_0^{1/2}} h \int x(z) z^{1/2} dz. \quad (9.17)$$

It can be seen that, as soon as the pre-galactic hydrogen was fully ionised, $x(z) \approx 1$, at $z \approx 1500$, the optical depth to Thomson scattering became very large. For example, if we assume the intergalactic gas was more or less fully ionised at $z > 1,000$, the optical depth at larger redshifts was

$$\tau_T = 0.035 \frac{\Omega_B}{\Omega_0^{1/2}} h z^{3/2}. \quad (9.18)$$

For our reference values $\Omega_B = 0.05$, $\Omega_0 = 0.3$ and $h = 0.7$, $\tau_T = 2.23 \times 10^{-3} z^{3/2} = 130$ at a redshift of 1,500. Detailed calculations of the ionisation state of the intergalactic gas with redshift are discussed in Sect. 15.1 where it is shown that the optical depth of the intergalactic gas became unity at a redshift very close to 1,000. Therefore, the Universe beyond a redshift of 1,000 is unobservable. Any photons originating from larger redshifts were scattered many times before they propagated to the Earth and consequently all the information they carry about their origin is rapidly lost. Exactly the same process prevents us observing inside the Sun. There is therefore a *photon barrier* at a redshift of 1000 beyond which we cannot obtain information directly using photons.

We will return to the process of recombination and the variation of the optical depth to Thomson scattering with redshift in Sect. 15.1 because this is a crucial topic

in evaluating the observability of fluctuations in the Cosmic Microwave Background Radiation. If there is no further scattering of the photons of the background radiation, the redshift of 1000 becomes the *last scattering surface* and therefore the fluctuations imprinted on the radiation at this epoch determine the spatial fluctuations in the intensity of the background radiation observed today.

9.4 The Radiation-Dominated Era

At redshifts $z \gg 4 \times 10^4 \Omega_0 h^2 \approx 6000$, the Universe was radiation-dominated. If the matter and radiation were not thermally coupled, they would cool independently, the hot gas having ratio of specific heats $\gamma = 5/3$ and the radiation $\gamma = 4/3$. These result in adiabatic cooling which depends upon the scale factor a as $T_B \propto a^{-2}$ and $T_r \propto a^{-1}$ for the diffuse baryonic matter and radiation respectively. We therefore expect the matter to cool more rapidly than the radiation and this is indeed what is expected to take place during the post-recombination era. This is not the case, however, during the pre-recombination and immediate post-recombination eras because the matter and radiation are strongly coupled by *Compton scattering*. As shown in the last section, the optical depth of the pre-recombination plasma for Thomson scattering is very large, so large that we can no longer ignore the small energy transfers which take place between the photons and the electrons in Compton collisions. It turns out that these Compton scatterings are sufficient to maintain the matter at the same temperature as the radiation.

The exchange of energy between photons and electrons is an enormous subject and has been treated by Weymann, by Sunyaev and Zeldovich and by Pozdnyakov and his colleagues (Weymann, 1966; Sunyaev and Zeldovich, 1980a; Pozdnyakov et al., 1983). The equation for the rate of exchange of energy between a thermal radiation field at radiation temperature T_r and a plasma with electron temperature T_e interacting solely by Compton scattering was derived by Weymann in 1965,

$$\frac{d\varepsilon_r}{dt} = -\frac{d\varepsilon_m}{dt} = 4N_e \sigma_{TC} c \varepsilon_r \left(\frac{kT_e - kT_r}{m_e c^2} \right), \quad (9.19)$$

where ε_r and ε_m are the energy densities of radiation and matter. We can understand the form of this equation by considering the case in which the temperature of the electrons is greater than that of the radiation. The number of collisions per electron per second with the photon field is $N_\gamma \sigma_{TC}$, where N_γ is the number density of photons. In each collision, the average energy transfer to the photon field is $(4/3) (v^2/c^2) h\bar{v}$, where $h\bar{v}$ is the mean energy of the photons (Longair, 1997b). Since the average energy of the electrons is $\frac{1}{2}m_e v^2 = \frac{3}{2}kT_e$, the rate of loss of energy per electron is

$$-\frac{dE}{dt} = 4\sigma_{TC} N_\gamma h\bar{v} \left(\frac{kT_e}{m_e c^2} \right) = 4\sigma_{TC} c \varepsilon_r \left(\frac{kT_e}{m_e c^2} \right). \quad (9.20)$$

Equation (9.19) expresses the fact that, if the electrons are hotter than the radiation, the radiation is heated up by the matter and, conversely, if the radiation is hotter

than the matter, the matter is heated by the radiation. The astrophysical difference between the two cases arises from the enormous difference in the number densities of the photons and electrons $N_\gamma/N_e \approx 10^9$. Let us look at this difference from the point of view of the optical depths for the interaction of an electron with the radiation field and of a photon with the electrons of the intergalactic gas. In the first case, the optical depth for interaction of an electron with the radiation field is $\tau_e = \sigma_T c N_\gamma t$, whereas that of the photon with the electrons is $\tau_\gamma = \sigma_T c N_e t$ where σ_T is the Thomson cross-section and t is the age of the Universe. Thus, because $N_\gamma \gg N_e$, it is much more difficult to modify the spectrum of the photons as compared with the energy distribution of the electrons because, in the time any one photon is scattered by an electron, the electron has been scattered $\approx 10^9$ times by the photons. Another way of expressing this is to say that the heat capacity of the radiation is very much greater than that of the matter.

We consider two important applications of these results. In the first, we consider the heating of the electrons by Compton scattering of the photons of the Microwave Background Radiation. The collision times between electrons, protons and atoms are always much shorter than the age of the Universe and hence, when energy is transferred from the radiation field to the electrons, it is rapidly communicated to the matter as a whole. This is the process by which the matter and radiation are maintained at the same temperature in the early Universe. Let us work out the redshift to which Compton scattering can maintain the matter and radiation at the same temperature.

We rewrite (9.19) for the case in which the plasma is heated by the radiation field. The thermal energy density of the plasma is $\varepsilon_m = 3N_e k T_e$, since both the electrons and protons are maintained at the same temperature, and then

$$\frac{dT_e}{dt} = \frac{4}{3}\sigma_T \varepsilon_r \left(\frac{T_r - T_e}{m_e c} \right). \quad (9.21)$$

As pointed out above, because of the enormous heat capacity of the radiation, T_r scarcely changes at all and so (9.21) defines the characteristic exponential time-scale τ_{ex} for the exchange of energy between the radiation and the plasma. Assuming $z \gg 1$,

$$\tau_{\text{ex}} = \frac{T_e}{dT_e/dt} = \frac{3m_e c}{4\sigma_T \varepsilon_r} = \frac{3m_e c^2}{16\sigma_T \sigma T_0^4} (1+z)^{-4} = 7.4 \times 10^{19} z^{-4} \text{ s}. \quad (9.22)$$

Thus, when the plasma was fully ionised at $z \gg 1000$, the time-scale τ_{ex} was $7.4 \times 10^7 \text{ s} = 2.7 \text{ years}$, that is, very much shorter than the age of the Universe and so the matter and radiation were maintained at the same temperature throughout the radiation-dominated era.

As the temperature fell below 4000 K, most of the protons recombined with electrons to form neutral hydrogen, but there remained a small, but finite, fraction of free electrons which did not recombine, $x \approx 2.5 \times 10^{-5}$, at redshifts $z < 700$ (see Sect. 15.1). These enabled energy to be transferred from the photons to the gas even in the post-recombination era. The energy density of the gas was predominantly

associated with the kinetic energy of hydrogen atoms, $\varepsilon_H = \frac{3}{2} N_H kT$, and the number density of free electrons was $x(z)N_H$. Repeating the above calculation for the post-recombination era, the rate of change of the temperature of the neutral hydrogen was

$$\frac{dT_H}{dt} = \frac{8}{3} \sigma_T \varepsilon_r x(z) \left(\frac{T_r - T_H}{m_e c} \right), \quad (9.23)$$

and the characteristic time-scale τ_{ex} for the exchange of energy was

$$\tau_{\text{ex}} = \frac{3m_e c^2}{32\sigma_T x(z)\sigma T_r^4} = \frac{3m_e c^2}{32\sigma_T x(z)\sigma T_0^4} (1+z)^{-4} = 1.47 \times 10^{24} z^{-4} \text{ s}. \quad (9.24)$$

During the matter-dominated epochs, when $\Omega_0 z \gg 1$, the age of the Universe was

$$t = \frac{2.06 \times 10^{17}}{h\Omega_0^{1/2}} z^{-3/2} \text{ s}. \quad (9.25)$$

Therefore, equating (9.24) and (9.25), the time-scale τ_{ex} for the exchange of energy from the background radiation to the neutral hydrogen was equal to the age of the Universe at a redshift

$$z = 550 h^{2/5} \Omega_0^{1/5} \approx 375. \quad (9.26)$$

Thus, there was a period after the epoch of recombination when the matter and radiation cooled at the same rate but, at redshifts less than about 375, the matter and the radiation cooled independently, the matter temperature as $T_H \propto a^{-2}$ and the radiation temperature as $T_r \propto a^{-1}$. Peebles found the decoupling redshift to be $z \sim 150$ in his more detailed calculations (Peebles, 1993).

In the second application, we derive the necessary condition for significant distortions of the spectrum of the Microwave Background Radiation to take place. Suppose the electrons are heated to a temperature greater than the radiation temperature by some process. This might result from the dissipation of primordial sound waves or turbulence, matter–antimatter annihilation, the evaporation of primordial black holes by the Hawking mechanism or the decay of heavy unstable leptons. If no photons were created, the spectrum of the radiation would be distorted from its black-body form by Compton scattering. The interaction of the hot electrons with the photons results in an average frequency change of $\Delta\nu/\nu = 4kT_e/m_e c^2$. Thus, to obtain a significant change in the energy of the photon, $\Delta\nu/\nu \approx 1$, not only must the optical depth for Thomson scattering be very much greater than one, there must also be sufficient Compton scatterings to change the energies of the photons significantly so that $\Delta\nu/\nu \approx 1$. Evidently, the *Compton optical depth*

$$\tau_C = \int \left(\frac{kT_e}{m_e c^2} \right) \sigma_T c N_e dt, \quad (9.27)$$

should be greater or equal to one. We know that the Thomson scattering condition was satisfied during the pre-recombination era and also that the temperature of the

electrons was maintained at that of the thermal background radiation. Therefore, assuming $T_e = T_0(1 + z)$ and $N_e = N_0(1 + z)^3$, the Compton optical depth is

$$\tau_C = \left(\frac{kT_0}{m_e c^2} \right) \frac{\sigma_T c N_0}{H_0} \int \frac{(1 + z)^2}{(\Omega_0 z + 1)^{1/2}} dz . \quad (9.28)$$

For $z \gg 1$,

$$\tau_C = \left(\frac{kT_0}{m_e c^2} \right) \frac{2\sigma_T c N_0}{5\Omega_0^{1/2} H_0} z^{5/2} . \quad (9.29)$$

It is convenient to express this result in terms of the density parameter in baryons at the present epoch Ω_B . Assuming that 25% of the baryonic mass is in the form of helium and that the plasma is fully ionised in the relevant range of redshifts, we find that $\Omega_B = (64\pi G m_p / 21 H_0^2) N_e$ and so

$$\tau_C = \left(\frac{kT_0}{m_e c} \right) \frac{21\sigma_T}{160\pi G m_p} \frac{H_0 \Omega_B}{\Omega_0^{1/2}} z^{5/2} = 1.1 \times 10^{-11} \frac{h \Omega_B}{\Omega_0^{1/2}} z^{5/2} . \quad (9.30)$$

Thus, the optical depth was unity at redshift

$$z = 2.4 \times 10^4 \left(\frac{\Omega_0}{h^2 \Omega_B^2} \right)^{1/5} \approx 7 \times 10^4 , \quad (9.31)$$

for the reference values of Ω_0 , Ω_B and h . To observe a distortion of the black-body spectrum, the temperature of the electrons must be raised significantly above the temperature $T_e = T_0(1 + z)$. If this were to occur, the spectrum would relax from a Planck to a Bose–Einstein spectrum with a finite dimensionless chemical potential μ ,

$$I_\nu = \frac{2h\nu^3}{c^2} \left[\exp \left(\frac{h\nu}{kT_r} + \mu \right) - 1 \right]^{-1} .$$

This is the form of equilibrium spectrum expected when there is a mismatch between the number of photons and the energy to be distributed among them to create a Planck spectrum. In the present instance, the photon energies are redistributed by Compton scattering. At early enough epochs, $z \sim 10^7$, Compton double scattering can create additional low energy photons and so, at these very large redshifts, the black-body spectrum is re-established. As discussed in Sect. 2.1.1, there are now very good upper limits to the value of μ from the COBE spectral observations of the Cosmic Microwave Background Radiation, $|\mu| \leq 10^{-4}$. In general terms, this means that there cannot have been major injections of energy into the intergalactic gas in the redshift interval $10^7 \geq z \geq 7 \times 10^4$, thus providing important constraints on the processes listed above (Sunyaev and Zeldovich, 1980a). These authors have also surveyed the types of distortion which would result from large injections of thermal energy into the intergalactic gas during the post-recombination era.

9.5 The Speed of Sound as a Function of Cosmic Epoch

One crucial result for understanding the physics of the formation of structure in the Universe is the variation of the speed of sound with cosmic epoch, particularly through the epochs when the Universe changed from being radiation to matter-dominated. All sound speeds are proportional to the square root of the ratio of the pressure which provides the restoring force to the inertial mass density of the medium. More precisely, the speed of sound c_s is given by

$$c_s^2 = \left(\frac{\partial p}{\partial \varrho} \right)_S , \quad (9.32)$$

where the subscript S means ‘at constant entropy’, that is, we consider adiabatic sound waves. The complication is that, from the epoch when the energy densities of matter and radiation were equal to beyond the epoch of recombination the dominant contributors to p and ϱ change dramatically as the Universe changes from being radiation to matter-dominated. The key point is that the baryonic matter and radiation are closely coupled throughout the pre-recombination era and the square of the sound speed can then be written

$$c_s^2 = \frac{(\partial p / \partial T)_r}{(\partial \varrho / \partial T)_r + (\partial \varrho / \partial T)_m} , \quad (9.33)$$

where the partial derivatives are taken at constant entropy. It is straightforward to show that this reduces to the following expression:

$$c_s^2 = \frac{c^2}{3} \frac{4\varrho_r}{4\varrho_r + 3\varrho_m} . \quad (9.34)$$

Thus, in the radiation-dominated era, $z \gg 4 \times 10^4 \Omega_0 h^2 \approx 6000$, $\varrho_r \gg \varrho_m$ and the speed of sound tends to the relativistic sound speed, $c_s = c/\sqrt{3}$. At smaller redshifts, the sound speed decreases as the contribution of the inertial mass density of the matter becomes more important. Specifically, between the epoch of equality of the matter and radiation energy densities and the epoch of the recombination, the pressure of sound waves is provided by the radiation, but the inertia is provided by the matter. Thus, the speed of sound decreases from the relativistic value of $c_s = c/\sqrt{3}$ to

$$c_s = \left(\frac{4c^2}{9} \frac{\varrho_r}{\varrho_m} \right)^{1/2} = \left[\frac{16\sigma T_0^4 (1+z)}{9\Omega_m \varrho_c c} \right]^{1/2} = \frac{10^6 z^{1/2}}{(\Omega_m h^2)^{1/2}} = 6.3 \times 10^6 z^{1/2} \text{ m s}^{-1} . \quad (9.35)$$

After recombination, the sound speed becomes the thermal sound speed of the matter which, because of the close coupling between the matter and the radiation, has temperature $T_r = T_m$ at redshifts $z \geq 550 h^{2/5} \Omega_0^{1/5}$, as explained above. Thus, at a redshift of 375, the temperature of the gas was 1000 K. If nothing else happened to

the matter, we would expect it to be very cold at the present epoch, about 375 times colder than 2.728 K. In fact, whatever intergalactic gas there is at the present day must be very much hotter than this – it must have been heated up once the process of galaxy formation got underway. We will take up this intriguing story in Chap. 18.

9.6 Early Epochs

Let us complete this brief thermal history of the Universe by outlining what happens at earlier times:

- We can extrapolate back to redshifts $z \approx 3 \times 10^8$ at which the radiation temperature was about $T = 10^9$ K. This temperature is sufficiently high for the background photons to have γ -ray energies, $\varepsilon = kT = 100$ keV. At this high temperature, the high energy photons in the Wien region of the Planck distribution are energetic enough to dissociate light nuclei such as helium and deuterium. At earlier epochs, all nuclei are dissociated into protons and neutrons. When we run the clocks forward, it is at about this epoch that the process of primordial nucleosynthesis of the light elements takes place. This is a key topic for the whole of cosmology and we will discuss it in some detail in Chap. 10.
- At redshift, $z \approx 10^9$, electron–positron pair production from the thermal background radiation took place and the Universe was then flooded with electron–positron pairs, one pair for every pair of photons present in the Universe now. When we run the clocks forward from an early epoch, the electrons and positrons annihilate at about this epoch and their energy is transferred to the photon field – this accounts for the little discontinuity in the temperature history at the epoch when the electrons and positrons were annihilated (see Sect. 10.5).
- At a slightly earlier epoch the opacity of the Universe for weak interactions became unity (see Sect. 10.2). This results is a *neutrino barrier*, similar to the photon barrier at $z \sim 1000$.
- We can extrapolate even further back in time to $z \approx 10^{12}$ when the temperature of the background radiation was sufficiently high for baryon–antibaryon pair production to take place from the thermal background. Just as in the case of the epoch of electron–positron pair-production, the Universe was flooded with baryons and antibaryons, one pair for every pair of photons present in the Universe now. Again, there is a little discontinuity in the temperature history at this epoch. These considerations lead to one of the great cosmological problems, the *baryon asymmetry problem*. In order to produce the matter-dominated Universe we live in today, there must have been a tiny asymmetry between matter and antimatter in the very early Universe. For every 10^9 antibaryons, there must have been $10^9 + 1$ baryons. When we run the clocks forward, 10^9 baryons annihilate with the 10^9 antibaryons, leaving one baryon which becomes the Universe as we know it with the correct photon-to-baryon number ratio. If the early Universe were completely symmetric with respect to matter and antimatter, the photon-to-baryon ratio would be about 10^9 times greater than it is today and there would

be equal amounts of matter and antimatter in the Universe (see Sect. 10.6). The baryon asymmetry must originate in the very early Universe. Fortunately, we know that there is a slight asymmetry between matter and antimatter because of CP violation observed in the decays of K^0 mesons – the origin of the baryon asymmetry is a major industry for theorists of the early Universe.

We can carry this process of extrapolation further and further back into the mists of the early Universe, as far as we believe we understand high energy particle physics. Probably most particle physicists would agree that the standard model of elementary particles has been tried and tested to energies of at least 100 GeV and so we can probably trust laboratory physics back to epochs as early as 10^{-6} s, although those of a more conservative disposition would probably be happier to accept 10^{-3} s. How far back one is prepared to extrapolate is largely a matter of taste. The most ambitious theorists have no hesitation in extrapolating back to the very earliest Planck eras, $t_P \sim (Gh/c^5)^{1/2} = 10^{-43}$ s, when the relevant physics was certainly very different from the physics of the Universe from redshifts of about 10^{12} to the present day.

References

- Aaronson, M. and Mould, J. (1983). A distance scale from the infrared magnitude/H I velocity-width relation: IV. The morphological type dependence and scatter in the relation; the distances to nearby groups, *Astrophysical Journal*, **265**, 1–17.
- Abell, G.O. (1958). The distribution of rich clusters of galaxies, *Astrophysical Journal Supplement*, **3**, 221–288.
- Abell, G.O. (1962). Membership of clusters of galaxies, in *Problems of Extragalactic Research*, ed. McVittie, G.C., pp. 213–238. New York: Macmillan.
- Abell, G.O., Corwin Jr, H.G., and Olowin, R.P. (1989). A catalogue of rich clusters of galaxies, *Astrophysical Journal Supplement*, **70**, 1–138.
- Abraham, R.G., Tanvir, N.R., Santiago, B., Ellis, R.S., Glazebrook, K., and van den Bergh, S. (1996). Galaxy morphology to $I = 25$ mag in the Hubble Deep Field, *Monthly Notices of the Royal Astronomical Society*, **279**, L47–L52.
- Adelberger, K.L. and Steidel, C.C. (2000). Multiwavelength observations of dusty star formation at low and high redshift, *Astrophysical Journal*, **544**, 218–241.
- Afonso, C., Albert, J.N., and 40 authors (2003). Limits on galactic dark matter with 5 years of EROS SMC data, *Astronomy and Astrophysics*, **400**, 951–956.
- Aharonian, F., Akhperjanian, A.G., Bazer-Bachi, A.R., Beilicke, M., Benbow, W., Berge, D., Bernlöhr, K., Boisson, C., Bolz, O., Borrel, V., Braun, I., Breitling, F., Brown, A.M., Chadwick, P.M., Chounet, L.-M., Cornils, R., Costamante, L., Degrange, B., Dickinson, H.J., Djannati-Ataï, A., Drury, L.O., Dubus, G., Emmanoulopoulos, D., Espigat, P., Feinstein, F., Fontaine, G., Fuchs, Y., Funk, S., Gallant, Y.A., Giebels, B., Gillessen, S., Glicenstein, J.F., Goret, P., Hadjichristidis, C., Hauser, D., Hauser, M., Heinzelmann, G., Henri, G., Hermann, G., Hinton, J.A., Hofmann, W., Holleran, M., Horns, D., Jacholkowska, A., de Jager, O.C., Khélifi, B., Klages, S., Komin, N., Konopelko, A., Latham, I.J., Le Gallou, R., Lemière, A., Lemoine-Goumard, M., Leroy, N., Lohse, T., Martin, J.M., Martineau-Huynh, O., Marcowith, A., Masterson, C., McComb, T.J.L., de Naurois, M., Nolan, S.J., Noutsos, A., Orford, K.J., Osborne, J.L., Ouchrif, M., Panter, M., Pelletier, G., Pita, S., Pühlhofer, G., Punch, M., Raubenheimer, B.C., Raue, M., Raux, J., Rayner, S.M., Reimer, A., Reimer, O., Ripken, J., Rob, L., Rolland, L., Rowell, G., Sahakian, V., Saugé, L., Schlenker, S., Schlickeiser, R., Schuster, C., Schwanke, U., Siewert, M., Sol, H., Spangler, D., Steenkamp, R., Stegmann, C., Tavernet, J.-P., Terrier, R., Théoret, C.G., Tluczykont, M., van Eldik, C., Vasileiadis, G., Venter, C., Vincent, P., Völk, H.J., and Wagner, S.J.

- (2006). A low level of extragalactic background light as revealed by γ -rays from blazars, *Nature*, **440**, 1018–1021.
- Akerib, D.S., Attisha, M.J., Bailey, C.N., Baudis, L., Bauer, D.A., Brink, P.L., Brusov, P.P., Bunker, R., Cabrera, B., Caldwell, D.O., Chang, C.L., Cooley, J., Crisler, M.B., Cushman, P., Daal, M., Dixon, R., Dragowsky, M.R., Driscoll, D.D., Duong, L., Ferril, R., Filippini, J., Gaitskell, R.J., Golwala, S.R., Grant, D.R., Hennings-Yeomans, R., Holmgren, D., Huber, M.E., Kamat, S., Leclercq, S., Lu, A., Mahapatra, R., Mandic, V., Meunier, P., Mirabolfathi, N., Nelson, H., Nelson, R., Ogburn, R.W., Perera, T.A., Pyle, M., Ramberg, E., Rau, W., Reisetter, A., Ross, R.R., Sadoulet, B., Sander, J., Savage, C., Schnee, R.W., Seitz, D.N., Serfass, B., Sundqvist, K.M., Thompson, J.-P.F., Wang, G., Yellin, S., Yoo, J., and Young, B.A. (2006). Limits on spin-independent interactions of weakly interacting massive particles with nucleons from the two-tower run of the cryogenic dark matter search, *Physical Review Letters*, **96**, 011302–+.
- Albrecht, A. and Steinhardt, P. (1982). Cosmology for grand unified theories with radiatively induced symmetry breaking, *Physical Review Letters*, **48**, 1220–1223.
- Alcock, C., Akerlof, C.W., Allsman, R.A., Axelrod, T.S., Bennett, D.P., Chan, S., Cook, K.H., Freeman, K.C., Griest, K., Marshall, S.L., Park, H.-S., Perlmutter, S., Peterson, B.A., Pratt, M.R., Quinn, P.J., Rogers, A.W., Stubbs, C.W., and Sutherland, W. (1993a). Possible gravitational microlensing of a star in the Large Magellanic Cloud, *Nature*, **365**, 621–623.
- Alcock, C., Allsman, R.A., Axelrod, T.S., Bennett, D.P., Cook, K.H., Park, H.-S., Marshall, S.L., Stubbs, C.W., Griest, K., Perlmutter, S., Sutherland, W., Freeman, K.C., Peterson, B.A., Quinn, P.J., and Rogers, A.W. (1993b). The MACHO Project – a Search for the Dark Matter in the Milky-Way, in *Sky Surveys: Protostars to Protogalaxies*, ed. Soifer, T., pp. 291–296. San Francisco: Astronomical Society of the Pacific Conference Series.
- Alcock, C., Allsman, R.A., Alves, D.R., Axelrod, T.S., Becker, A.C., Bennett, D.P., Cook, K.H., Dalal, N., Drake, A.J., Freeman, K.C., Geha, M., Griest, K., Lehner, M.J., Marshall, S.L., Minniti, D., Nelson, C.A., Peterson, B.A., Popowski, P., Pratt, M.R., Quinn, P.J., Stubbs, C.W., Sutherland, W., Tomaney, A.B., Vandehei, T., and Welch, D. (2000). The MACHO Project: microlensing results from 5.7 years of Large Magellanic Cloud observations, *Astrophysical Journal*, **542**, 281–307.
- Aliu, E., Andringa, S., Aoki, S., and colleagues (2005). Evidence for muon neutrino oscillation in an accelerator-based experiment, *Physical Review Letters*, **94**(8), 081802–+.
- Alpher, R.A. and Herman, R.C. (1948). Evolution of the Universe, *Nature*, **162**, 774–775.
- Alpher, R.A. and Herman, R.C. (1950). Theory of the origin and relative distribution of the elements, *Reviews of Modern Physics*, **22**, 153–212.
- Anders, E. (1963). Meteorite ages, in *The Moon, Meteorites and Comets – The Solar System IV*, eds. Middelhurst, B.M. and Kuiper, G.P., pp. 402–495. Chicago: University of Chicago Press.

- Aragòn-Salamanca, A., Ellis, R.S., Couch, W.J., and Carter, D. (1993). Evidence for systematic evolution in the properties of galaxies in distant clusters, *Monthly Notices of the Royal Astronomical Society*, **262**, 764–794.
- Arp, H.C. (1966). *Atlas of Peculiar Galaxies*. Pasadena: California Institute of Technology.
- Arp, H.C., Madore, B.F., and Roberton, W.E. (1987). *A Catalogue of Southern Peculiar Galaxies and Associations*. Cambridge: Cambridge University Press.
- Baade, W. (1926). Über eine Möglichkeit, die Pulsationstheorie der δ -Cephei-Veränderlichen zu Prüfen (On a Possible Method of Testing the Pulsation Theory of the Variations of δ -Cephei), *Astronomische Nachrichten*, **228**, 359–362.
- Babbedge, T.S.R., Rowan-Robinson, M., Vaccari, M., Surace, J.A., Lonsdale, C.J., Clements, D.L., Fang, F., Farrah, D., Franceschini, A., Gonzalez-Solares, E., Hatziminaoglou, E., Lacey, C.G., Oliver, S., Onyett, N., Pérez-Fournon, I., Polletta, M., Pozzi, F., Rodighiero, G., Shupe, D.L., Siana, B., and Smith, H.E. (2006). Luminosity functions for galaxies and quasars in the Spitzer Wide-area Infrared Extragalactic Legacy Survey, *Monthly Notices of the Royal Astronomical Society*, **370**, 1159–1180.
- Bahcall, N. (1997). Dark matter, in *Critical Dialogues in Cosmology*, ed. Turok, N., pp. 221–232. Singapore: World Scientific.
- Bahcall, N.A. (1977). Clusters of galaxies, *Annual Review of Astronomy and Astrophysics*, **15**, 505–540.
- Bahcall, N.A. (1988). Large-scale structure in the Universe indicated by galaxy clusters, *Annual Review of Astronomy and Astrophysics*, **26**, 631–686.
- Bahcall, N.A. (2000). Clusters and cosmology, *Physics Reports*, **333**, 233–244.
- Bahcall, N.A., Dong, F., Hao, L., Bode, P., Annis, J., Gunn, J.E., and Schneider, D.P. (2003a). The richness-dependent cluster correlation function: early Sloan Digital Sky Survey Data, *Astrophysical Journal*, **599**, 814–819.
- Bahcall, N.A., McKay, T.A., Annis, J., Kim, R.S.J., Dong, F., Hansen, S., Goto, T., Gunn, J.E., Miller, C., Nichol, R.C., Postman, M., Schneider, D., Schroeder, J., Voges, W., Brinkmann, J., and Fukugita, M. (2003b). A merged catalog of clusters of galaxies from early Sloan Digital Sky Survey data, *Astrophysical Journal Supplement*, **148**, 243–274.
- Bajtlik, S., Duncan, R.C., and Ostriker, J.P. (1988). Quasar ionization of Lyman-alpha clouds – the proximity effect, a probe of the ultraviolet background at high redshift, *Astrophysical Journal*, **327**, 570–583.
- Baldry, I.K., Glazebrook, K., Brinkmann, J., Ivezić, Z., Lupton, R.H., Nichol, R.C., and Szalay, A. (2004). Quantifying the bimodal color-magnitude distribution of galaxies, *Astrophysical Journal*, **600**, 681–694.
- Baldry, I.K., Glazebrook, K., Budavári, T., Eisenstein, D.J., Annis, J., Bahcall, N.A., Blanton, M.R., Brinkmann, J., Csabai, I., Heckman, T.M., Lin, H., Loveday, J., Nichol, R.C., and Schneider, D.P. (2005). The Sloan Digital Sky Survey u-band Galaxy Survey: luminosity functions and evolution, *Monthly Notices of the Royal Astronomical Society*, **358**, 441–456.

- Barcons, X. and Fabian, A.C. (1989). The small-scale autocorrelation function of the X-ray background, *Monthly Notices of the Royal Astronomical Society*, **237**, 119–127.
- Bardeen, J.M. (1980). Gauge-invariant cosmological perturbations, *Physical Review D*, **22**, 1882–1905.
- Bardeen, J.M., Bond, J.R., Kaiser, N., and Szalay, A.S. (1986). The statistics of peaks in Gaussian random fields, *Astrophysical Journal*, **304**, 15–61.
- Barger, A.J., Cowie, L.L., Smail, I., Ivison, R.J., Blain, A.W., and Kneib, J.-P. (1999). Redshift distribution of the faint submillimeter galaxy population, *Astronomical Journal*, **117**, 2656–2665.
- Barkats, D., Bischoff, C., Farese, P., Fitzpatrick, L., Gaier, T., Gundersen, J.O., Hedman, M.M., Hyatt, L., McMahon, J.J., Samtleben, D., Staggs, S.T., Vandervlinde, K., and Winstein, B. (2005). First measurements of the polarization of the cosmic microwave background radiation at small angular scales from CAPMAP, *Astrophysical Journal Letters*, **619**, L127–L130.
- Barnes, J. and Efstathiou, G. (1987). Angular momentum from tidal torques, *Astrophysical Journal*, **319**, 575–600.
- Barnes, J. and Hernquist, L. (1996). Transformations of galaxies. II. Gasdynamics in merging disk galaxies, *Astrophysical Journal*, **471**, 115–142.
- Barrow, J. and Tipler, F. (1986). *The Anthropic Cosmological Principle*. Oxford: Oxford University Press.
- Batuski, D.J., Bahcall, N.A., Olowin, R.P., and Burns, J.O. (1989). The distribution of clusters in the Southern ACO Catalog, *Astrophysical Journal*, **341**, 599–610.
- Baugh, C.M. (2006). A primer on hierarchical galaxy formation: the semi-analytical approach, *Reports of Progress in Physics*, **69**, 3101–3156.
- Baumann, D. (2007). On the quantum origin of structure in the inflationary universe, See <http://www.princeton.edu/~dbaumann/inflation.pdf>.
- Bautz, L. and Morgan, W.W. (1970). On the classification of the forms of clusters of galaxies, *Astrophysical Journal Letters*, **162**, L149–L153.
- Beaver, E., Burbidge, M., Cohen, R., Junkkarinen, V., Lyons, R., and Rosenblatt, E. (1992). Spectroscopy of QSOs with the Faint Object Spectrograph, in *Science with the Hubble Space Telescope*, eds. Benvenuti, P. and Schreier, E.J., pp. 53–60.
- Bechtold, J., Weymann, R.J., Lin, Z., and Malkan, M.A. (1987). The integrated ultraviolet radiation field from QSOs, *Astrophysical Journal*, **315**, 180–197.
- Beck, R., Brunetti, G., and Feretti, L. (2006). The origin and evolution of cosmic magnetism, in *Astronomische Nachrichten*, eds. Beck, R., Brunetti, G., and Feretti, L., volume 327, pp. 385–639. Weinheim: Wiley Interscience.
- Becker, R., Fan, X., and 29 authors (2001). Evidence for reionisation at $Z \sim 6$: detection of a Gunn–Peterson trough in a $Z = 6.28$ quasar, *Astronomical Journal*, **122**, 2850–2857.
- Beckwith, S.V.W., Stiavelli, M., Koekemoer, A.M., Caldwell, J.A.R., Ferguson, H.C., Hook, R., Lucas, R.A., Bergeron, L.E., Corbin, M., Jogee, S., Panagia, N., Robberto, M., Royle, P., Somerville, R.S., and Sosey, M. (2006). The Hubble Ultra Deep Field, *Astronomical Journal*, **132**, 1729–1755.

- Bell, E.F., McIntosh, D.H., Katz, N., and Weinberg, M.D. (2003). The optical and near-infrared properties of galaxies: I. Luminosity and stellar mass functions, *Astrophysical Journal Supplement Series*, **149**, 289–312.
- Bender, R., Burstein, D., and Faber, S.M. (1993). Dynamically hot galaxies: II. Global stellar populations, *Astrophysical Journal*, **411**, 153–169.
- Bennett, C., Halpern, M., Hinshaw, G., Jarosik, N., Kogut, A., Limon, M., Meyer, S., Page, L., Spergel, D., Tucker, G., Wollack, E., Wright, E., Barnes, C., Greason, M., Hill, R., Komatsu, E., Nolta, M., Odegard, N., Peiris, H., Verde, L., and Weiland, J. (2003). First-year Wilkinson Microwave Anisotropy Probe (WMAP) observations: preliminary maps and basic results, *Astrophysical Journal Supplement Series*, **148**, 1–27.
- Bennett, C.L., Banday, A.J., Gorski, K.M., Hinshaw, G., Jackson, P., Koegstra, P., Kogut, A., Smoot, G.F., Wilkinson, D.T., and Wright, E.L. (1996). Four-year COBE DMR cosmic microwave background observations: maps and basic results, *Astrophysical Journal*, **464**, L1–L4.
- Benson, A.J., Frenk, C.S., Baugh, C.M., Cole, S., and Lacey, C.G. (2001). The clustering evolution of the galaxy distribution, *Monthly Notices of the Royal Astronomical Society*, **327**, 1041–1056.
- Benson, B.A., Church, S.E., Ade, P.A.R., Bock, J.J., Ganga, K.M., Henson, C.N., and Thompson, K.L. (2004). Measurements of Sunyaev–Zel'dovich effect scaling relations for clusters of galaxies, *Astrophysical Journal*, **617**, 829–846.
- Bergeron, J. (1988). Properties of the heavy-element absorption systems, in *QSO Absorption Lines: Probing the Universe*, eds. Blades, J., Turnshek, D., and Norman, C., pp. 127–143. Cambridge: Cambridge University Press.
- Bergeron, J. (2006). Cosmic star formation history: high redshift galaxies and black holes, in *Scientific Requirements for Extremely Large Telescopes: IAU Symposium No. 232*, eds. Whitelock, P., Dennefeld, M., and Leibundgut, B., pp. 159–170. Cambridge: Cambridge University Press.
- Bernstein, G., Fischer, P., Tyson, J.A., and Rhee, G. (1997). Improved parameters and new lensed features for Q0957+561 from WFPC2 imaging, *Astrophysical Journal*, **483**, L79–L82.
- Bernstein, J. and Feinberg, G. (1986). *Cosmological Constants: Papers in Modern Cosmology*. New York: Columbia University Press.
- Berry, M. (1989). *Principles of Cosmology and Gravitation*. Bristol: Adam Hilger.
- Bertola, F., Bettoni, D., Danziger, J., Sadler, E., Spark, L., and de Zeeuw, T. (1991). Testing the gravitational field in elliptical galaxies: NGC 5077, *Astrophysical Journal*, **373**, 369–390.
- Bertola, F. and Capaccioli, M. (1975). Dynamics of early type galaxies: I. The rotation curve of the elliptical galaxy NGC 4697, *Astrophysical Journal*, **200**, 439–445.
- Bertola, F. and Galletta, G. (1979). Ellipticity and twisting of isophotes in elliptical galaxies, *Astronomy and Astrophysics*, **77**, 363–365.
- Bertotti, B., Iess, L., and Tortora, P. (2003). A Test of general relativity using radio links with the Cassini spacecraft, *Nature*, **425**, 374–376.

- Bertschinger, E. (1996). Cosmological dynamics, in *Cosmology and Large Scale Structure: Proceedings of the “Les Houches Ecole d’Ete de Physique Theorique”*, eds. Schaeffer, R., Silk, J., Spiro, M., and Zinn-Justin, J., pp. 273–346. Amsterdam: Elsevier.
- Best, P.N., Longair, M.S., and Röttrung, H.J.A. (1996). Evolution of the aligned structures in $z \sim 1$ radio galaxies, *Monthly Notices of the Royal Astronomical Society*, **280**, L9–L12.
- Best, P.N., Longair, M.S., and Röttrung, H.J.A. (1998). HST, radio and infrared observations of 28 3CR radio galaxies at redshift z approximately equal to 1: II. Old stellar populations in central cluster galaxies, *Monthly Notices of the Royal Astronomical Society*, **295**, 549–567.
- Best, P.N., Longair, M.S., and Röttrung, H.J.A. (2000). Ionization, shocks and evolution of the emission-line gas of distant 3CR radio galaxies, *Monthly Notices of the Royal Astronomical Society*, **311**, 23–36.
- Biermann, L. (1950). On the Origin of Magnetic Fields on Stars and in Interstellar Space, *Zeitschrift für Naturforschung*, **5a**, 65–71.
- Binggeli, B., Sandage, A., and Tammann, A. (1988). The luminosity function of galaxies, *Annual Review of Astronomy and Astrophysics*, **26**, 509–560.
- Binggeli, B., Tammann, G.A., and Sandage, A. (1987). Studies of the Virgo Cluster: VI. Morphological and kinematical structure of the Virgo Cluster, *Astronomical Journal*, **94**, 251–277.
- Binney, J. and Merrifield, M. (1998). *Galactic Astronomy*. Princeton: Princeton University Press.
- Binney, J. and Tremaine, S. (1987). *Galactic Dynamics*. Princeton: Princeton University Press.
- Birkinshaw, M. (1990). Observations of the Sunyaev–Zeldovich effect, in *The Cosmic Microwave Background: 25 Years Later*, eds. Mandolesi, N. and Vittorio, N., pp. 77–94. Dordrecht: Kluwer.
- Blain, A.W., Ivison, R.J., and Smail, I. (1998). Observational limits to source confusion in the millimetre/submillimetre waveband, *Monthly Notices of the Royal Astronomical Society*, **296**, L29–L33.
- Blain, A.W. and Longair, M.S. (1993). Sub-millimetre cosmology, *Monthly Notices of the Royal Astronomical Society*, **264**, 509–521.
- Blain, A.W. and Longair, M.S. (1996). Observing strategies for blank-field surveys in the sub-millimetre waveband, *Monthly Notices of the Royal Astronomical Society*, **279**, 847–858.
- Blandford, R.D. and Narayan, R. (1992). Cosmological applications of gravitational lensing, *Annual Review of Astronomy and Astrophysics*, **30**, 311–358.
- Blanton, M., Hogg, D., Bahcall, N., Brinkmann, J., Britton, M., Connolly, A., Csabai, I., Fukugita, M., Loveday, J., Meiksin, A., Munn, J., Nichol, R., Okamura, S., Quinn, T., Schneider, D., Shimasaku, K., Strauss, M., Tegmark, M., Vogeley, M., and Weinberg, D. (2003). The galaxy luminosity function and luminosity density at redshift $z = 0.1$, *Astrophysical Journal*, **592**, 819–838.
- Blanton, M.R., Hogg, D.W., Bahcall, N.A., Baldry, I.K., Brinkmann, J., Csabai, I., Eisenstein, D., Fukugita, M., Gunn, J.E., Ivezić, Ž., Lamb, D.Q., Lupton, R.H.,

- Loveday, J., Munn, J.A., Nichol, R.C., Okamura, S., Schlegel, D.J., Shimasaku, K., Strauss, M.A., Vogeley, M.S., and Weinberg, D.H. (2003). The broadband optical properties of galaxies with redshifts $0.02 \leq z \leq 0.22$, *Astrophysical Journal*, **594**, 186–207.
- Blanton, M.R., Lupton, R.H., Schlegel, D.J., Strauss, M.A., Brinkmann, J., Fukugita, M., and Loveday, J. (2005). The properties and luminosity function of extremely low luminosity galaxies, *Astrophysical Journal*, **631**, 208–230.
- Bludman, S. and Ruderman, M. (1977). Induced cosmological constant expected above the phase transition restoring the broken symmetry, *Physical Review Letters*, **38**, 255–257.
- Blumenthal, G.R., Faber, S.M., Primack, J.R., and Rees, M.J. (1984). Formation of galaxies and large-scale structure with cold dark matter, *Nature*, **311**, 517–525.
- Bochkarev, N.G. and Sunyaev, R.A. (1977). Ionizing background radiation and the hydrogen at the periphery of galaxies, *Soviet Astronomy*, **21**, 542–547.
- Böhringer, H., Schuecker, P., Guzzo, L., Collins, C.A., Voges, W., Schindler, S., Neumann, D.M., Crudace, R.G., De Grandi, S., Chincarini, G., Edge, A.C., MacGillivray, H.T., and Shaver, P. (2001). The ROSAT-ESO flux limited X-ray (REFLEX) galaxy cluster survey. I. The construction of the cluster sample, *Astronomy and Astrophysics*, **369**, 826–850.
- Böhringer, H., Voges, W., Huchra, J.P., McLean, B., Giacconi, R., Rosati, P., Burg, R., Mader, J., Schuecker, P., Simić, D., Komossa, S., Reiprich, T.H., Retzlaff, J., and Trümper, J. (2000). The Northern ROSAT All-Sky (NORAS) Galaxy Cluster Survey: I. X-Ray properties of clusters detected as extended X-ray sources, *Astrophysical Journal Supplement*, **129**, 435–474.
- Boksenberg, A. (1997). Quasar absorption lines: reflections and views, in *The Hubble Space Telescope and the High Redshift Universe*, eds. Tanvir, N., Aragón-Salamanca, A., and Wall, J., pp. 283–294. Singapore: World Scientific.
- Bolte, M. (1997). Globular clusters: old, in *Critical Dialogues in Cosmology*, ed. Turok, N., pp. 156–168. Singapore: World Scientific.
- Bolyai, J. (1832). Appendix: Scientiam Spatii Absolute Veritam Exhibens (Appendix Explaining the Absolutely True Science of Space). published as an appendix to the essay by his father F. Bolyai, *An Attempt to Introduce Studious Youth to the Elements of Pure Mathematics*. Maros Vásárhely, Transylvania.
- Bonamente, M., Joy, M.K., LaRoque, S.J., Carlstrom, J.E., Reese, E.D., and Dawson, K.S. (2006). Determination of the cosmic distance scale from Sunyaev–Zel'dovich effect and Chandra X-ray measurements of high-redshift galaxy clusters, *Astrophysical Journal*, **647**, 25–54.
- Bond, J.R. and Efstathiou, G. (1984). Cosmic background radiation anisotropies in universes dominated by nonbaryonic dark matter, *Astrophysical Journal Letters*, **285**, L45–L48.
- Bond, J.R. and Efstathiou, G. (1991). The formation of cosmic structure with a 17 keV neutrino, *Physics Letters B*, **265**, 245–250.
- Bond, J.R. and Szalay, A.S. (1983). The collisionless damping of density fluctuations in the expanding Universe, *Astrophysical Journal*, **274**, 443–468.
- Bondi, H. (1960). *Cosmology*, 2nd edn. Cambridge: Cambridge University Press.

- Borgani, S. and Guzzo, L. (2001). X-ray clusters of galaxies as tracers of structure in the Universe, *Nature*, **409**, 39–45.
- Bosma, A. (1981). 21-cm line studies of spiral galaxies: II. The distribution and kinematics of neutral hydrogen in spiral galaxies of various morphological types, *Astronomical Journal*, **86**, 1825–1846.
- Bouwens, R.J., Illingworth, G.D., Blakeslee, J.P., (Broadhurst), T., and Franx, M. (2004). Galaxy size evolution at high redshift and surface brightness selection effects: constraints from the Hubble Ultra Deep Field, *Astrophysical Journal*, **611**, L1–L4.
- Bouwens, R.J., Illingworth, G.D., Blakeslee, J.P., and Franx, M. (2006). Galaxies at $z \sim 6$: the UV luminosity function and luminosity density from 506 HUDF, HUDF Parallel ACS Field, and GOODS i-Dropouts, *Astrophysical Journal*, **653**, 53–85.
- Boyle, B.J., Shanks, T., Croom, S.M., Smith, R.J., Miller, L., Loaring, N., and Heymans, C. (2000). The 2dF QSO Redshift Survey: I. The optical luminosity function of quasi-stellar objects, *Monthly Notices of the Royal Astronomical Society*, **317**, 1014–1022.
- Bracassi, A., Formiggini, L., and Gandolfi, E. (1970). Magnitudes, colours and coordinates of 175 ultraviolet excess objects in the field 13^{h} , $+36^{\circ}$, *Astronomy and Astrophysics*, **5**, 264–279. Erratum: *Astronomy and Astrophysics*, **23**, 159.
- Bracewell, R. (1986). *The Fourier Transform and Its Applications*. New York: McGraw-Hill.
- Brainerd, T.G., Blandford, R.D., and Smail, I. (1996). Weak gravitational lensing by galaxies, *Astrophysical Journal*, **466**, 623–637.
- Branch, D. and Patchett, B. (1973). Type I supernovae, *Monthly Notices of the Royal Astronomical Society*, **161**, 71–83.
- Branch, D. and Tammann, G.A. (1992). Type I supernovae as standard candles, *Annual Review of Astronomy and Astrophysics*, **30**, 359–389.
- Brandt, W.N. and Hasinger, G. (2005). Deep extragalactic X-ray surveys, *Annual Review of Astronomy and Astrophysics*, **43**, 827–859.
- Brentjens, M.A. and de Bruyn, A.G. (2006). RM-synthesis of the Perseus cluster, *Astronomische Nachrichten*, **327**, 545–551.
- Bridle, A.H. (1967). The spectrum of the radio background between 13 and 404 MHz, *Monthly Notices of the Royal Astronomical Society*, **136**, 219–240.
- Bruni, M., Dunsby, P.K.S., and Ellis, G.F.R. (1992). Cosmological perturbations and the physical meaning of gauge-invariant variables, *Astrophysical Journal*, **395**, 34–53.
- Bruzual, G. and Charlot, S. (2003). Stellar population synthesis at the resolution of 2003, *Monthly Notices of the Royal Astronomical Society*, **344**, 1000–1028.
- Burbidge, E., Burbidge, G., Fowler, W., and Hoyle, F. (1957). Synthesis of the elements in stars, *Reviews of Modern Physics*, **29**, 547–650.
- Butcher, H. and Oemler, Jr., A. (1978). The evolution of galaxies in clusters: I. ISIT Photometry of C1 0024+1654 and 3C 295, *Astrophysical Journal*, **219**, 18–30.
- Butcher, H. and Oemler, Jr., A. (1984). The evolution of galaxies in clusters: V. A study of populations since $z \approx 0.5$, *Astrophysical Journal*, **285**, 426–438.

- Cappelluti, N., Hasinger, G., Brusa, M., Comastri, A., Zamorani, G., Boehringer, H., Brunner, H., Civano, F., Finoguenov, A., Fiore, F., Gilli, R., Griffiths, R.E., Mainieri, V., Matute, I., Miyaji, T., and Silverman, J. (2007). The XMM-Newton wide-field survey in the COSMOS field II: X-ray data and the $\log N$ - $\log S$, *ArXiv Astrophysics e-prints*.
- Carlstrom, J.E., Joy, M.K., Grego, L., Holder, G.P., Holzapfel, W.L., Mohr, J.J., Patel, S., and Reese, E.D. (2000). Imaging the Sunyaev-Zel'dovich effect, in *Particle Physics and the Universe: Proceedings of Nobel Symposium 198*, eds. Bergström, L., Carlson, P., and Fransson, C., pp. 148–155. Stockholm: Physica Scripta.
- Carroll, S.M., Press, W.H., and Turner, E.L. (1992). The cosmological constant, *Annual Review of Astronomy and Astrophysics*, **30**, 499–542.
- Carswell, R.F. (1988). Properties of the Ly-alpha clouds, in *QSO Absorption Lines: Probing the Universe*, eds. Blades, J.C., Turnshek, D., and Norman, C.A., pp. 91–100. Cambridge: Cambridge University Press.
- Carswell, R.F., Whelan, J.A.J., Smith, M.G., Boksenberg, A., and Tytler, D. (1982). Observations of the spectra of Q0122-380 and Q1101-264, *Monthly Notices of the Royal Astronomical Society*, **198**, 91–110.
- Carter, B. (1974). Large number coincidences and the anthropic principle in cosmology, in *Confrontation of Cosmological Theories with Observational Data, IAU Symposium No. 63*, ed. Longair, M., pp. 291–298. Dordrecht: Reidel.
- Cavaliere, A. (1980). Models of X-ray Emission from Clusters of Galaxies, in *X-ray Astronomy*, eds. Giacconi, R. and Setti, G., pp. 217–237. Dordrecht: Reidel.
- Chaboyer, B. (1998). The age of the Universe, *Physics Reports*, **307**, 23–30.
- Chae, K.-H., Biggs, A.D., Blandford, R.D., Browne, I.W., de Bruyn, A.G., Fassnacht, C.D., Helbig, P., Jackson, N.J., King, L.J., Koopmans, L.V., Mao, S., Marlow, D.R., McKean, J.P., Myers, S.T., Norbury, M., Pearson, T.J., Phillips, P.M., Readhead, A.C., Rusin, D., Sykes, C.M., Wilkinson, P.N., Xanthopoulos, E., and York, T. (2002). Constraints on cosmological parameters from the analysis of the cosmic lens all sky survey radio-selected gravitational lens statistics, *Physical Review Letters*, **89**, 151301–.
- Challinor, A. (2005). Cosmic microwave background anisotropies, in *Lecture Notes in Physics Vol. 653: The Physics of the Early Universe*, ed. Tamvakis, K., vol. 653, pp. 71–+. Berlin: Springer.
- Challinor, A. and Lasenby, A. (1998). Relativistic corrections to the Sunyaev–Zeldovich effect, *Astrophysical Journal*, **499**, 1–6.
- Chambers, K.C., Miley, G.K., and van Breugel, W.J.M. (1987). Alignment of radio and optical orientations in high-redshift radio galaxies, *Nature*, **329**, 604–606.
- Chapman, S.C., Blain, A.W., Smail, I., and Ivison, R.J. (2005). A redshift survey of the submillimeter galaxy population, *Astrophysical Journal*, **622**, 772–796.
- Charlot, S. and Longhetti, M. (2001). Nebular emission from star-forming galaxies, *Monthly Notices of the Royal Astronomical Society*, **323**, 887–903.
- Chluba, J. and Sunyaev, R.A. (2006). Induced two-photon decay of the 2s level and the rate of cosmological hydrogen recombination, *Astronomy and Astrophysics*, **446**, 39–42.

- Chwolson, O. (1924). Über eine mögliche Form fiktiver Doppelsterne, *Astronomische Nachrichten*, **221**, 329–330.
- Cimatti, A., Daddi, E., Renzini, A., Cassata, P., Vanzella, E., Pozzetti, L., Cristiani, S., Fontana, A., Rodighiero, G., Mignoli, M., and Zamorani, G. (2004). Old galaxies in the young Universe, *Nature*, **430**, 184–187.
- Close, L.M., Hall, P.B., Liu, M.C., and Hege, E.K. (1995). Spectroscopic and morphological evidence that IRAS FSC 10214+4724 is a gravitational lens, *Astrophysical Journal*, **452**, L9–L12.
- Cole, S., Percival, W.J., Peacock, J.A., Norberg, P., Baugh, C.M., Frenk, C.S., Baldry, I., Bland-Hawthorn, J., Bridges, T., Cannon, R., Colless, M., Collins, C., Couch, W., Cross, N.J.G., Dalton, G., Eke, V.R., De Propris, R., Driver, S.P., Efstathiou, G., Ellis, R.S., Glazebrook, K., Jackson, C., Jenkins, A., Lahav, O., Lewis, I., Lumsden, S., Maddox, S., Madgwick, D., Peterson, B.A., Sutherland, W., and Taylor, K. (2005). The 2dF Galaxy Redshift Survey: power-spectrum analysis of the final data set and cosmological implications, *Monthly Notices of the Royal Astronomical Society*, **362**, 505–534.
- Coles, P. (2001). Einstein, Eddington and the 1919 Eclipse, in *Historical Development of Modern Cosmology*, eds. Martínez, V.J., Trimble, V., and Pons-Bordeña, M.J., pp. 21–41. San Francisco: ASP Conference Series, No. 252.
- Coles, P. and Lucchin, F. (1995). *Cosmology – the Origin and Evolution of Cosmic Structure*. Chichester: Wiley.
- Coles, P., Melott, A.L., and Shandarin, S.F. (1993). Testing approximations for non-linear gravitational clustering, *Monthly Notices of the Royal Astronomical Society*, **260**, 765–776.
- Colless, M., Dalton, G., Maddox, S., Sutherland, W., Norberg, P., Cole, S., Bland-Hawthorn, J., Bridges, T., Cannon, R., Collins, C., Couch, W., Cross, N., Deely, K., De Propris, R., Driver, S.P., Efstathiou, G., Ellis, R.S., Frenk, C.S., Glazebrook, K., Jackson, C., Lahav, O., Lewis, I., Lumsden, S., Madgwick, D., Peacock, J.A., Peterson, B.A., Price, I., Seaborne, M., and Taylor, K. (2001). The 2dF Galaxy Redshift Survey: spectra and redshifts, *Monthly Notices of the Royal Astronomical Society*, **328**, 1039–1063.
- Colless, M. and Dunn, A.M. (1996). Structure and dynamics of the Coma cluster, *Astrophysical Journal*, **458**, 435–454.
- Connolly, A., Scranton, R., Johnston, D., Dodelson, S., Eisenstein, D., Friedman, J., Gunn, J., Hui, L., Jain, B., Kent, S., Loveday, J., Nichol, R., O’Connell, L., Postman, M., Scoccimarro, R., Sheth, R., Stebbins, A., Strauss, M., Szalay, A., Szapudi, I., Tegmark, M., Vogeley, M., Zehavi, I., Annis, J., Bahcall, N., Brinkmann, J., Csabai, I., Doi, M., Fukugita, M., Hennessy, G., Hindsley, R., Ichikawa, T., Ivezić, Z., Kim, R., Knapp, G., Kunszt, P., Lamb, D., Lee, B., Lupton, R., McKay, T., Munn, J., Peoples, J., Pier, J., Rockosi, C., Schlegel, D., Stoughton, C., Tucker, D., Yanny, B., and York, D. (2002). The angular correlation function of galaxies from early Sloan Digital Sky Survey data, *Astrophysical Journal*, **579**, 42–47.
- Copi, C.J., Davis, A.N., and Krauss, L.M. (2004). New nucleosynthesis constraint on the variation of G, *Physical Review Letters*, **92**, 171301, 1–3.

- Corbelli, E. and Salpeter, E.E. (1993). Sharp HI edges in the outskirts of disk galaxies, *Astrophysical Journal*, **419**, 104–110.
- Costa, E., Frontera, F., Heise, J., Feroci, M., in 't Zand, J., Fiore, F., Cinti, M.N., dal Fiume, D., Nicastro, L., Orlandini, M., Palazzi, E., Rapisarda, M., Zavattini, G., Jager, R., Parmar, A., Owens, A., Molendi, S., Cusumano, G., Maccarone, M.C., Giarrusso, S., Coletta, A., Antonelli, L.A., Giommi, P., Muller, J.M., Piro, L., and Butler, R.C. (1997). Discovery of an X-ray afterglow associated with the gamma-ray burst of 28 February 1997, *Nature*, **387**, 783–785.
- Côté, P., McLaughlin, D.E., Cohen, J.G., and Blakeslee, J.P. (2003). Dynamics of the globular cluster system associated with M49 (NGC 4472): cluster orbital properties and the distribution of dark matter, *Astrophysical Journal*, **591**, 850–877.
- Côté, P., McLaughlin, D.E., Hanes, D.A., Bridges, T.J., Geisler, D., Merritt, D., Hesser, J.E., Harris, G.L.H., and Lee, M.G. (2001). Dynamics of the globular cluster system associated with M87 (NGC 4486): II. Analysis, *Astrophysical Journal*, **559**, 828–850.
- Cowan, J.J., Thielemann, F.K., and Truran, J.W. (1991). Radioactive dating of the elements, *Annual Review of Astronomy and Astrophysics*, **29**, 447–497.
- Cowie, L. (1988). Protogalaxies, in *The Post-Recombination Universe*, eds. Kaiser, N. and Lasenby, A.N., pp. 1–18. Dordrecht: Kluwer.
- Cowie, L., Lilly, S., Gardner, J., and McLean, I. (1988). A cosmologically significant population of galaxies dominated by very young star formation, *Astrophysical Journal*, **332**, L29–L32.
- Cowie, L.L., Barger, A.J., and Kneib, J.-P. (2002). Faint submillimeter counts from deep 850 micron observations of the lensing clusters A370, A851, and A2390, *Astronomical Journal*, **123**, 2197–2205.
- Cowie, L.L., Songaila, A., Hu, E.M., and Cohen, J.D. (1996). New insight on galaxy formation and evolution from Keck spectroscopy of the Hawaii deep fields, *Astronomical Journal*, **112**, 839–864.
- Cress, C., Helfand, D., Becker, R., Gregg, M., and White, R. (1996). The angular two-point correlation function for the FIRST Radio Survey, *Astrophysical Journal*, **473**, 7–14.
- Crittenden, R., Bond, R., Davis, R.L., Efstathiou, G., and Steinhardt, P.J. (1993). Imprint of gravitational waves on the cosmic microwave background, *Physical Review Letters*, **71**, 324–327.
- Croom, S.M., Boyle, B.J., Shanks, T., Smith, R.J., Miller, L., Outram, P.J., Loaring, N.S., Hoyle, F., and da Ângela, J. (2005). The 2dF QSO Redshift Survey: XIV. Structure and evolution from the two-point correlation function, *Monthly Notices of the Royal Astronomical Society*, **356**, 415–438.
- Croton, D.J., Farrar, G.R., Norberg, P., Colless, M., Peacock, J.A., Baldry, I.K., Baugh, C.M., Bland-Hawthorn, J., Bridges, T., Cannon, R., Cole, S., Collins, C., Couch, W., Dalton, G., De Propris, R., Driver, S.P., Efstathiou, G., Ellis, R.S., Frenk, C.S., Glazebrook, K., Jackson, C., Lahav, O., Lewis, I., Lumsden, S., Maddox, S., Madgwick, D., Peterson, B.A., Sutherland, W., and Taylor, K. (2005). The 2dF Galaxy Redshift Survey: luminosity functions by density environment

- and galaxy type, *Monthly Notices of the Royal Astronomical Society*, **356**, 1155–1167.
- Dashevsky, V.M. and Zeldovich, Y.B. (1964). Propagation of light in a nonhomogeneous non-flat Universe II, *Astronomicheskii Zhurnal*, **41**, 1071–1074. Translation: (1965), *Soviet Astronomy*, **8**, 854–856.
- Davidsen, A.F. (1993). Far-ultraviolet astronomy on the Astro-1 space shuttle mission, *Science*, **259**, 327–334.
- Davidsen, A.F., Kriss, G.A., and Zheng, W. (1996). Measurement of the opacity of ionized helium in the intergalactic medium, *Nature*, **380**, 47–49.
- Davidson, W. and Davies, M. (1964). Interpretation of the counts of radio sources in terms of a 4-parameter family of evolutionary universes, *Monthly Notices of the Royal Astronomical Society*, **127**, 241–255.
- Davies, R.L., Efstathiou, G., Fall, S.M., Illingworth, G., and Schechter, P.L. (1983). The kinematic properties of faint elliptical galaxies, *Astrophysical Journal*, **266**, 41–57.
- Davis, M., Efstathiou, G., Frenk, C., and White, S.D.M. (1985). The evolution of large-scale structure in a universe dominated by cold dark matter, *Astrophysical Journal*, **292**, 371–394.
- Davis, M., Efstathiou, G., Frenk, C., and White, S.D.M. (1992a). The end of cold dark matter?, *Nature*, **356**, 489–494.
- Davis, M., Geller, M.J., and Huchra, J. (1978). The local mean mass density of the Universe – new methods for studying galaxy clustering, *Astrophysical Journal*, **221**, 1–18.
- Davis, M. and Peebles, P.J.E. (1983). A survey of galaxy redshifts: V. The two-point position and velocity correlations, *Astrophysical Journal*, **267**, 465–482.
- Davis, R.L., Hodges, H.M., Smoot, G.F., Steinhardt, P.J., and Turner, M.S. (1992b). Cosmic microwave background probes models of inflation, *Physical Review Letters*, **69**, 1856–1859.
- Davis, T.M. and Lineweaver, C.H. (2004). Expanding confusion: common misconceptions of cosmological horizons and the superluminal expansion of the universe, *Publications of the Astronomical Society of Australia*, **21**, 97–109.
- de Plaa, J., Kaastra, J.S., Méndez, M., Tamura, T., Bleeker, J.A.M., Peterson, J.R., Paerels, F.B.S., Bonamente, M., and Lieu, R. (2005). The temperature structure in the core of Sérsic 159-03, *Advances in Space Research*, **36**, 601–604.
- de Sitter, W. (1917). On Einstein's theory of gravitation and its astronomical consequences, *Monthly Notices of the Royal Astronomical Society*, **78**, 3–28.
- de Vaucouleurs, G. (1948). Recherches sur les nébuleuses extragalactiques, *Annales d'Astrophysique*, **11**, 247–287.
- de Vaucouleurs, G. (1963). Revised classification of 1500 bright galaxies, *Astrophysical Journal Supplement*, **8**, 31–97.
- de Vaucouleurs, G. (1974). Structure, dynamics and statistical properties of galaxies (invited paper), in *The Formation and Dynamics of Galaxies*, IAU Symposium No. 58, ed. Shakeshaft, J.R., pp. 1–53. Dordrecht: Reidel.

- de Vaucouleurs, G., de Vaucouleurs, A., Corwin Jr., H.G., Buta, R.J., Paturel, G., and Fouque, P. (1991). *Third reference catalogue of bright galaxies: containing information on 23,024 galaxies with reference to papers published between 1913 and 1988*. Berlin: Springer.
- Dekel, A. (1986). Biased galaxy formation, *Comments on Astrophysics*, **11**, 235–256.
- Dekel, A., Burstein, D., and White, S. (1997). Measuring omega, in *Critical Dialogues in Cosmology*, ed. Turok, N., pp. 175–194. Singapore: World Scientific.
- Dekel, A. and Rees, M.J. (1987). Physical mechanisms for biased galaxy formation, *Nature*, **326**, 455–462.
- Dessauges-Zavadsky, M., Prochaska, J.X., DOdorico, S., Calura, F., and Matteucci, F. (2006). A new comprehensive set of elemental abundances in DLAs: II. Data analysis and chemical variation studies, *Astronomy and Astrophysics*, **445**, 93–113.
- Dey, A. (1997). The host galaxies of distant radio sources, in *The Hubble Space Telescope and the High Redshift Universe*, eds. Tanvir, N.R., Aragón-Salamanca, A., and Wall, J.V., pp. 373–376. Singapore: World Scientific.
- Dicke, R. (1961). Dirac's cosmology and Mach's principle, *Nature*, **192**, 440–441.
- Dicke, R. and Peebles, P. (1979). Big Bang cosmology – enigmas and nostrums, in *General Relativity: an Einstein Centenary Survey*, eds. Hawking, S. and Israel, W., pp. 504–517. Cambridge: Cambridge University Press.
- Dickinson, C., Battye, R.A., Carreira, P., Cleary, K., Davies, R.D., Davis, R.J., Genova-Santos, R., Grainge, K., Gutiérrez, C.M., Hafez, Y.A., Hobson, M.P., Jones, M.E., Kneissl, R., Lancaster, K., Lasenby, A., Leahy, J.P., Maisinger, K., Ödman, C., Pooley, G., Rajguru, N., Rebolo, R., Rubiño-Martin, J.A., Saunders, R.D.E., Savage, R.S., Scaife, A., Scott, P.F., Slosar, A., Sosa Molina, P., Taylor, A.C., Titterington, D., Waldram, E., Watson, R.A., and Wilkinson, A. (2004). High-sensitivity measurements of the cosmic microwave background power spectrum with the extended Very Small Array, *Monthly Notices of the Royal Astronomical Society*, **353**, 732–746.
- Dickinson, M. (1997). Clusters of galaxies at $z \geq 1$, in *The Hubble Space Telescope and the High Redshift Universe*, eds. Tanvir, N., Aragón-Salamanca, A., and Wall, J., pp. 207–218. Singapore: World Scientific.
- d'Inverno, R. (1992). *Introducing Einstein's Relativity*. Oxford: Clarendon.
- Disney, M.J. (1976). Visibility of galaxies, *Nature*, **263**, 573–575.
- Djorgovski, S.G. and Davis, M. (1987). Fundamental properties of elliptical galaxies, *Astrophysical Journal*, **313**, 59–68.
- Dodelson, S. (2003). *Modern Cosmolgy*. Amsterdam: Academic.
- Dodelson, S., Gates, E.I., and Turner, M.S. (1996). Cold dark matter, *Science*, **274**, 69–75.
- Doroshkevich, A., Sunyaev, R., and Zeldovich, Y. (1974). The formation of galaxies in Friedmannian universes, in *Confrontation of Cosmological Theories with Observational Data, (IAU Symposium No. 63)*, ed. Longair, M., pp. 213–225. Dordrecht: Reidel.
- Doroshkevich, A., Zeldovich, Y., Sunyaev, R., and Khlopov, M. (1980). Astrophysical Implications of the Neutrino Rest Mass: Part II. The density-perturbation

- spectrum and small-scale fluctuations in the microwave background, *Pis'ma v Astronomicheskii Zhurnal*, **6**, 457–464.
- Dressler, A. (1980). Galaxy morphology in rich clusters – implications for the formation and evolution of galaxies, *Astrophysical Journal*, **236**, 351–365.
- Dressler, A. (1984). The evolution of galaxies in clusters, *Annual Review of Astronomy and Astrophysics*, **22**, 185–222.
- Dressler, A., Lynden-Bell, D., Burstein, D., Davies, R.L., Faber, S.M., Terlevich, R., and Wegner, G. (1987). Spectroscopy and photometry of elliptical galaxies: I. A new distance estimator, *Astrophysical Journal*, **313**, 42–58.
- Dressler, A., Oemler, A.J., Couch, W.J., Smail, I., Ellis, R.G., Barger, A., Butcher, H., Poggianti, B.M., and Sharples, R.M. (1997). Evolution since $z = 0.5$ of the morphology-density relation for clusters of galaxies, *Astrophysical Journal*, **490**, 577–591.
- Dressler, A. and Smail, I. (1997). HST observations of distant clusters: implications for galaxy evolution, in *The Hubble Space Telescope and the High Redshift Universe*, eds. Tanvir, N., Aragón-Salamanca, A., and Wall, J., pp. 185–194. Singapore: World Scientific.
- Driver, S.P., Allen, P.D., Graham, A.W., Cameron, E., Liske, J., Ellis, S.C., Cross, N.J.G., De Propris, R., Phillipps, S., and Couch, W. (2006). The Millennium Galaxy Catalogue: morphological classification and bimodality in the colour-concentration plane, *Monthly Notices of the Royal Astronomical Society*, **368**, 414–434.
- Dunlop, J.S. (1998). Cosmic star-formation and radio source evolution, in *ASSL Vol. 226: Observational Cosmology with the New Radio Surveys*, eds. Bremer, M.N., Jackson, N., and Perez-Fournon, I., pp. 157–164. Dordrecht: Kluwer Academic Publishers.
- Dunlop, J.S. and Peacock, J.A. (1990). The redshift cut-off in the luminosity function of radio galaxies and quasars, *Monthly Notices of the Royal Astronomical Society*, **247**, 19–42.
- Dunlop, J.S., Peacock, J.A., Spinrad, H., Dey, A., Jimenez, R., Stern, D., and Windhorst, R. (1996). A 3.5-Gyr-old galaxy at redshift 1.55, *Nature*, **381**, 581–584.
- Dyer, C.C. and Roeder, R.C. (1972). The distance-redshift relation for universes with no intergalactic medium, *Astrophysical Journal Letters*, **174**, L115–L117.
- Dyer, C.C. and Roeder, R.C. (1973). Distance-redshift relations for universes with some intergalactic medium, *Astrophysical Journal Letters*, **180**, L31–L34.
- Eales, S.A., Rawlings, S., Law-Green, D., Cotter, G., and Lacy, M. (1997). A first sample of faint radio sources with virtually complete Redshifts: I. Infrared images, the Hubble diagram and the alignment effect, *Monthly Notices of the Royal Astronomical Society*, **291**, 593–615.
- Eastman, R.G. and Kirshner, R.P. (1989). Model atmospheres for SN 1987A and the distance to the Large Magellanic Cloud, *Astrophysical Journal*, **347**, 771–793.
- Eddington, A.S. (1916). The kinetic energy of a star cluster, *Monthly Notices of the Royal Astronomical Society*, **76**, 525–528.
- Eddington, A.S. (1926). Diffuse matter in interstellar space, *Proceedings of the Royal Society, A***111**, 424–456.

- Efstathiou, G. (1988). Effects of reionization on microwave background anisotropies, in *Large-scale Motions in the Universe*, eds. Rubin, V. and Coyne, G., pp. 299–319. Princeton: Princeton University Press.
- Efstathiou, G. (1990). Cosmological perturbations, in *Physics of the Early Universe*, eds. Peacock, J.A., Heavens, A.F., and Davies, A.T., pp. 361–463. Edinburgh: SUSSP.
- Efstathiou, G. (1995). High-redshift galaxies: problems and prospects, in *Galaxies in the Young Universe*, eds. Hippelein, H., Meissenheimer, K., and Röser, H.J., pp. 299–314. Berlin: Springer, Lecture Notes in Physics, Vol. 463.
- Efstathiou, G. and Bond, J.R. (1986). Isocurvature cold dark matter fluctuations, *Monthly Notices of the Royal Astronomical Society*, **218**, 103–121.
- Efstathiou, G., Frenk, C.S., White, S.D.M., and Davis, M. (1988). Gravitational clustering from scale-free initial conditions, *Monthly Notices of the Royal Astronomical Society*, **235**, 715–748.
- Efstathiou, G., Lawrence, C., and Tauber, J. (2005). *Planck: The Scientific Programme*. Noordwijk: European Space Agency Publications, ESA-SCI(2005)1.
- Efstathiou, G. and Rees, M.J. (1988). High-redshift quasars in the cold dark matter cosmogony, *Monthly Notices of the Royal Astronomical Society*, **230**, 5P–11P.
- Eguchi, K., Enomoto, S., and 97 authors (2003). First results from Kamland: evidence for reactor anti-neutrino disappearance, *Physical Review Letters*, **90**, id. 021802(1–6).
- Einstein, A. (1915). Die Feldgleichung der Gravitation (The field equations of gravitation), *Sitzungsberichte, Königlich Preussische Akademie der Wissenschaften (Berlin)*, **II**, 844–847.
- Einstein, A. (1916). Die Grundlage der Allgemeinen Relativitätstheorie (Foundation of the General Theory of Relativity), *Annalen der Physik*, **49**, 769–822.
- Einstein, A. (1917). Kosmologische Betrachtungen zur Allgemeinen Relativitätstheorie (Cosmological considerations in the General Theory of Relativity), *Sitzungsberichte, Königlich Preussische Akademie der Wissenschaften (Berlin)*, **I**, 142–152.
- Einstein, A. (1919). Spielen Gravitationsfelder im Aufbau der materiellen Elementarteilchen eine wesentliche Rolle? (Do gravitational fields play a significant role for the structure of elementary particles), *Sitzungsberichte, Königlich Preussische Akademie der Wissenschaften, Part 1*, 349–356.
- Einstein, A. (1922). Bemerkung zu der Arbeit von A. Friedmann “Ueber die Krümmung des Raumes” (Remark on the work of A. Friedmann “On the Curvature of Space”), *Zeitschrift für Physik*, **11**, 326.
- Einstein, A. (1923). Notiz zu der Arbeit von A. Friedmann “Über die Krümmung des Raumes” (A Note on the Work of A. Friedmann “On the Curvature of Space”), *Zeitschrift für Physik*, **16**, 228.
- Einstein, A. (1936). Lens-like action of a star by the deviation of light in the gravitational field, *Science*, **84**, 506–507.
- Eisenstein, D.J. and Hu, W. (1998). Baryonic features in the matter transfer function, *Astrophysical Journal*, **496**, 605–614.

- Eisenstein, D.J., Zehavi, I., Hogg, D.W., Scoccimarro, R., Blanton, M.R., Nichol, R.C., Scranton, R., Seo, H.-J., Tegmark, M., Zheng, Z., Anderson, S.F., Annis, J., Bahcall, N., Brinkmann, J., Burles, S., Castander, F.J., Connolly, A., Csabai, I., Doi, M., Fukugita, M., Frieman, J.A., Glazebrook, K., Gunn, J.E., Hendry, J.S., Hennessy, G., Ivezić, Z., Kent, S., Knapp, G.R., Lin, H., Loh, Y.-S., Lupton, R.H., Margon, B., McKay, T.A., Meiksin, A., Munn, J.A., Pope, A., Richmond, M.W., Schlegel, D., Schneider, D.P., Shimasaku, K., Stoughton, C., Strauss, M.A., SubbaRao, M., Szalay, A.S., Szapudi, I., Tucker, D.L., Yanny, B., and York, D.G. (2005). Detection of the baryon acoustic peak in the large-scale correlation function of SDSS luminous red galaxies, *Astrophysical Journal*, **633**, 560–574.
- Ellis, R.G. (1997). Faint blue galaxies, *Annual Review of Astronomy and Astrophysics*, **35**, 389–443.
- Ellis, R.G., Smail, I., Dressler, A., Couch, W.J., Oemler, A.J., Butcher, H., and Sharples, R.M. (1997). The homogeneity of spheroidal populations in distant clusters, *Astrophysical Journal*, **483**, 582–596.
- Ellis, S.C. and Bland-Hawthorn, J. (2006). GalaxyCount: a JAVA calculator of galaxy counts and variances in multiband wide-field surveys to 28 AB mag, *ArXiv Astrophysics e-prints*.
- Faber, S.M. (1973). Variations in spectral-energy distributions and absorption-line strengths among elliptical galaxies, *Astrophysical Journal*, **179**, 731–754.
- Faber, S.M. and Jackson, R.E. (1976). Velocity dispersions and mass-to-light ratios for elliptical galaxies, *Astrophysical Journal*, **204**, 668–683.
- Fabian, A.C. (1994). Cooling flows in clusters of galaxies, *Annual Review of Astronomy and Astrophysics*, **32**, 277–318.
- Fabian, A.C. and Barcons, X. (1992). The origin of the X-ray background, *Annual Review of Astronomy and Astrophysics*, **30**, 429–456.
- Fabian, A.C., Sanders, J.S., Ettori, S., Taylor, G.B., Allen, S.W., Crawford, C.S., Iwasawa, K., Johnstone, R.M., and Ogle, P.M. (2000). Chandra imaging of the complex X-ray core of the Perseus cluster, *Monthly Notices of the Royal Astronomical Society*, **318**, L65–L68.
- Fabian, A.C., Sanders, J.S., Taylor, G.B., Allen, S.W., Crawford, C.S., Johnstone, R.M., and Iwasawa, K. (2006). A very deep Chandra observation of the Perseus cluster: shocks, ripples and conduction, *Monthly Notices of the Royal Astronomical Society*, **366**, 417–428.
- Fabricant, D.G., Lecar, M., and Gorenstein, P. (1980). X-ray measurements of the mass of M87, *Astrophysical Journal*, **241**, 552–560.
- Fall, S. (1983). Galaxy formation – some comparisons between theory and observation, in *Internal Kinematics and Dynamics of Galaxies: IAU Symposium No. 100*, ed. Athanassoula, E., pp. 391–398. Dordrecht: Reidel.
- Fall, S. (1997). A global perspective on star formation, in *The Hubble Space Telescope and the High Redshift Universe*, eds. Tanvir, N., Aragón-Salamanca, A., and Wall, J., pp. 303–308. Singapore: World Scientific.
- Fall, S.M. and Efstathiou, G. (1980). Formation and rotation of disc galaxies with haloes, *Monthly Notices of the Royal Astronomical Society*, **193**, 189–206.

- Fall, S.M. and Pei, Y.C. (1993). Obscuration of quasars by dust in damped Lyman-alpha systems, *Astrophysical Journal*, **402**, 479–492.
- Fan, X., Hennawi, J.F., Richards, G.T., Strauss, M.A., Schneider, D.P., Donley, J.L., Young, J.E., Annis, J., Lin, H., Lampeitl, H., Lupton, R.H., Gunn, J.E., Knapp, G.R., Brandt, W.N., Anderson, S., Bahcall, N.A., Brinkmann, J., Brunner, R.J., Fukugita, M., Szalay, A.S., Szokoly, G.P., and York, D.G. (2004). A survey of $z \geq 5.7$ quasars in the Sloan Digital Sky Survey: III. Discovery of five additional quasars, *Astronomical Journal*, **128**, 515–522.
- Fan, X., Narayanan, V.K., Lupton, R.H., Strauss, M.A., Knapp, G.R., Becker, R.H., White, R.L., Pentericci, L., Leggett, S.K., Haiman, Z., Gunn, J.E., Ivezić, Ž., Schneider, D.P., Anderson, S.F., Brinkmann, J., Bahcall, N.A., Connolly, A.J., Csabai, I., Doi, M., Fukugita, M., Geballe, T., Grebel, E.K., Harbeck, D., Hennessy, G., Lamb, D.Q., Miknaitis, G., Munn, J.A., Nichol, R., Okamura, S., Pier, J.R., Prada, F., Richards, G.T., Szalay, A., and York, D.G. (2001). A survey of $z \geq 5.8$ quasars in the Sloan Digital Sky Survey: I. Discovery of three new quasars and the spatial density of luminous quasars at $z \sim 6$, *Astronomical Journal*, **122**, 2833–2849.
- Feast, M.W. and Catchpole, R.M. (1997). The cepheid period-luminosity zero-point from HIPPARCOS trigonometrical parallaxes, *Monthly Notices of the Royal Astronomical Society*, **286**, L1–L5.
- Fechner, C., Reimers, D., Kriss, G.A., Baade, R., Blair, W.P., Giroux, M.L., Green, R.F., Moos, H.W., Morton, D.C., Scott, J.E., Shull, J.M., Simcoe, R., Songaila, A., and Zheng, W. (2006). The UV spectrum of HS 1700+6416: II. FUSE observations of the HeII Lyman alpha forest, *Astrophysical Journal*, **455**, 91–106.
- Felten, J. (1977). Study of the luminosity function for field galaxies, *Astronomical Journal*, **82**, 861–878.
- Felten, J. (1985). Galaxy luminosity functions, M/L ratios, and closure of the Universe – numbers and problems, *Comments on Astrophysics*, **11**, 53–67.
- Ferguson, H.C., Dickinson, M., and Williams, R. (2000). The Hubble Deep Fields, *Annual Review of Astronomy and Astrophysics*, **38**, 667–715.
- Fixsen, D., Cheng, E., Gales, J., Mather, J., Shafer, R., and Wright, E. (1996). The cosmic microwave background spectrum from the full COBE FIRAS data set, *Astrophysical Journal*, **473**, 576–587.
- Foley, R.J., Filippenko, A.V., Leonard, D.C., Riess, A.G., Nugent, P., and Perlmutter, S. (2005). A definitive measurement of time dilation in the spectral evolution of the moderate-redshift type 1a Supernova 1997ex, *Astrophysical Journal Letters*, **626**, L11–L14.
- Fomalont, E.B., Kellermann, K.I., Anderson, M.C., Weistroop, D., Wall, J.V., Windhorst, R.A., and Kristian, J.A. (1988). New limits to fluctuations in the cosmic background radiation at 4.86 GHz between 12 and 60 arcsecond resolution, *Astrophysical Journal*, **96**, 1187–1191.
- Forman, W. and Jones, C. (1982). X-ray-imaging observations of clusters of galaxies, *Annual Review of Astronomy and Astrophysics*, **20**, 547–585.

- Fort, B. and Mellier, Y. (1994). Arc(let)s in clusters of galaxies, *Astronomy and Astrophysics Reviews*, **5**, 239–292.
- Frayer, D.T., Fadda, D., Yan, L., Marleau, F.R., Choi, P.I., Helou, G., Soifer, B.T., Appleton, P.N., Armus, L., Beck, R., Dole, H., Engelbracht, C.W., Fang, F., Gordon, K.D., Heinrichsen, I., Henderson, D., Hesselroth, T., Im, M., Kelly, D.M., Lacy, M., Laine, S., Latter, W.B., Mahoney, W., Makovoz, D., Masci, F.J., Morrison, J.E., Moshir, M., Noriega-Crespo, A., Padgett, D.L., Pesenson, M., Shupe, D.L., Squires, G.K., Storrie-Lombardi, L.J., Surace, J.A., Teplitz, H.I., and Wilson, G. (2006). Spitzer 70 and 160 μm observations of the extragalactic First Look Survey, *Astronomical Journal*, **131**, 250–260.
- Freedman, W.L., Madore, B.F., Gibson, B.K., Ferrarese, L., Kelson, D.D., Sakai, S., Mould, J.R., Kennicutt Jr., R.C., Ford, H.C., Graham, J.A., Huchra, J.P., Hughes, S.M.G., Illingworth, G.D., Macri, L.M., and Stetson, P.B. (2001). Final results from the Hubble Space Telescope key project to measure the Hubble constant, *Astrophysical Journal*, **533**, 47–72.
- Freeman, K.C. (1970). On the disks of spiral and S0 galaxies, *Astrophysical Journal*, **160**, 811–830.
- Frenk, C. (1986). Galaxy clustering and the dark-matter problem, *Philosophical Transactions of the Royal Astronomical Society*, **A320**, 517–541.
- Friedman, A.A. (1922). On the Curvature of Space, *Zeitschrift für Physik*, **10**, 377–386.
- Friedman, A.A. (1924). On the possibility of a world with constant negative curvature, *Zeitschrift für Physik*, **12**, 326–332.
- Fukugita, M., Futamase, T., Kasai, M., and Turner, E.L. (1992). Statistical properties of gravitational lenses with a nonzero cosmological constant, *Astrophysical Journal*, **393**, q3–21.
- Furlanetto, S.R., Sokasian, A., and Hernquist, L. (2004). Observing the reionization epoch through 21-centimetre radiation, *Monthly Notices of the Royal Astronomical Society*, **347**, 187–195.
- Gamow, G. (1970). *My World Line*. New York: Viking. The reference to Einstein's admission of 'the greatest blunder of my life' is on p. 44.
- Garnavich, P.M., Kirshner, R.P., Challis, P., Tonry, J., Gilliland, R.L., Smith, R.C., Clocchiatti, A., Diercks, A., Filippenko, A.V., Hamuy, M., Hogan, C.J., Leibundgut, B., Phillips, M.M., Riess, D., Riess, A.G., Schmidt, B.P., Schommer, R.A., Spyromilio, J., Stubbs, C., Suntzeff, N.B., and Wells, L. (1998). Constraints on cosmological models from Hubble Space Telescope observations of high-z supernovae, *Astrophysical Journal Letters*, **493**, L53–L58.
- Gavazzi, R., Treu, T., Rhodes, J.D., Koopmans, L.V.E., Bolton, A.S., Burles, S., Massey, R., and Moustakas, L.A. (2007). The Sloan Lens ACS Survey: IV. The mass density profile of early-type galaxies out to 100 effective radii, *ArXiv Astrophysics e-prints*.
- Ge, J., Bechtold, J., and Black, J. (1997). A new measurement of the cosmic microwave background radiation temperature at $Z = 1.97$, *Astrophysical Journal*, **474**, 67–73.
- Geller, M.J. and Huchra, J.P. (1989). Mapping the Universe, *Science*, **246**, 897–903.

- Geller, M.J. and Postman, M. (1983). First-ranked galaxies in groups, *Astrophysical Journal*, **274**, 31–38.
- Gershtein, S. and Zeldovich, Y. (1966). Rest mass of a muonic neutrino and cosmology, *Pisma v Zhurnal Eksperimentalnoi i Teoreticheskoi Fiziki*, **4**, 174–177.
- Giacconi, R., Gursky, H., Paolini, F.R., and Rossi, B.B. (1962). Evidence for X rays from sources outside the solar system, *Physical Review Letters*, **9**, 439–443.
- Giavalisco, M., Dickinson, M., Ferguson, H.C., Ravindranath, S., Kretchmer, C., Moustakas, L.A., Madau, P., Fall, S.M., Gardner, J.P., Livio, M., Papovich, C., Renzini, A., Spinrad, H., Stern, D., and Riess, A. (2004a). The rest-frame ultraviolet luminosity density of star-forming galaxies at redshifts $z \geq 3.5$, *Astrophysical Journal Letters*, **600**, L103–L106.
- Giavalisco, M., Ferguson, H.C., Koekemoer, A.M., Dickinson, M., Alexander, D.M., Bauer, F.E., Bergeron, J., Biagetti, C., Brandt, W.N., Casertano, S., Cesarsky, C., Chatzichristou, E., Conselice, C., Cristiani, S., Da Costa, L., Dahlen, T., de Mello, D., Eisenhardt, P., Erben, T., Fall, S.M., Fassnacht, C., Fosbury, R., Fruchter, A., Gardner, J.P., Grogin, N., Hook, R.N., Hornschemeier, A.E., Idzi, R., Jogee, S., Kretchmer, C., Laidler, V., Lee, K.S., Livio, M., Lucas, R., Madau, P., Mobasher, B., Moustakas, L.A., Nonino, M., Padovani, P., Papovich, C., Park, Y., Ravindranath, S., Renzini, A., Richardson, M., Riess, A., Rosati, P., Schirmer, M., Schreier, E., Somerville, R.S., Spinrad, H., Stern, D., Stiavelli, M., Strolger, L., Urry, C.M., Vandame, B., Williams, R., and Wolf, C. (2004b). The Great Observatories Origins Deep Survey: initial results from optical and near-infrared imaging, *Astrophysical Journal Letters*, **600**, L93–L98.
- eds. Gibbons, G., Shellard, E., and Rankin, S. (2003). *The Future of Theoretical Physics and Cosmology*. Cambridge: Cambridge University Press.
- Gibbons, G.W. and Hawking, S.W. (1977). Cosmological event horizons, thermodynamics, and particle creation, *Physical Review*, **D15**, 2738–2751.
- eds. Gibbons, G.W., Hawking, S.W., and Siklos, S.T.C. (1983). *The Very Early Universe: Proceedings of the Nuffield Workshop, Cambridge, UK, 21 June–9 July 1982*. Cambridge: Cambridge University Press.
- Gilli, R., Comastri, A., and Hasinger, G. (2007). The synthesis of the cosmic X-ray background in the Chandra and XMM-Newton era, *Astronomy and Astrophysics*, **463**, 79–96.
- Gilmore, G., King, I., and van der Kruit, P.C. (1989). *The Milky Way as a Galaxy: Proceedings of the 19th Advanced Course of the Swiss Society of Astronomy and Astrophysics (SSAA)*. Mill Valley, California: University Science Books. Van der Kruit's analyses of the surface brightness distributions in elliptical and spiral galaxies are contained in Sect. 5.2 (pp. 80–88) and Sect. 12.1 (pp. 257–267).
- Glazebrook, K., Abraham, R.G., McCarthy, P.J., Savaglio, S., Chen, H.-W., Crampton, D., Murowinski, R., Jørgensen, I., Roth, K., Hook, I., Marzke, R.O., and Carlberg, R.G. (2004). A high abundance of massive galaxies 3–6 billion years after the Big Bang, *Nature*, **430**, 181–184.
- Glazebrook, K., Ellis, R.S., Colless, M., Broadhurst, T.J., Allington-Smith, J.R., and Tanvir, N.R. (1995). The morphological identification of the rapidly evolving

- population of faint galaxies, *Monthly Notices of the Royal Astronomical Society*, **275**, L19–L22.
- Goldhaber, G., Groom, D.E., Kim, A., Aldering, G., Astier, P., Conley, A., Deustua, S.E., Ellis, R., Fabbro, S., Fruchter, A.S., Goobar, A., Hook, I., Irwin, M., Kim, M., Knop, R.A., Lidman, C., McMahon, R., Nugent, P.E., Pain, R., Panagia, N., Pennypacker, C.R., Perlmutter, S., Ruiz-Lapuente, P., Schaefer, B., Walton, N.A., and York, T. (2001). Timescale stretch parameterization of type 1a supernova B-band light curves, *Astrophysical Journal*, **558**, 359–368.
- Goobar, A. and Perlmutter, S. (1995). Feasibility of measuring the cosmological constant lambda and mass density omega using type IA supernovae, *Astrophysical Journal*, **450**, 14–18.
- Gott, J.R., Melott, A.L., and Dickinson, M. (1986). The sponge-like topology of large-scale structure in the Universe, *Astrophysical Journal*, **306**, 341–357.
- Govoni, F. (2006). Observations of magnetic fields in regular and irregular clusters, *Astronomische Nachrichten*, **327**, 539–544.
- Gregory, J. (1668). *Geometriae Pars Universalis*. Padua.
- Gregory, P. and Condon, J. (1991). The 87GB catalog of radio sources covering delta between 0 and +75 deg at 4.85 GHz, *Astrophysical Journal Supplement Series*, **75**, 1011–1291.
- Greve, T.R., Bertoldi, F., Smail, I., Neri, R., Chapman, S.C., Blain, A.W., Ivison, R.J., Genzel, R., Omont, A., Cox, P., Tacconi, L., and Kneib, J.-P. (2005). An interferometric CO survey of luminous submillimetre galaxies, *Monthly Notices of the Royal Astronomical Society*, **359**, 1165–1183.
- Gribben, J. and Rees, M. (1989). *Dark Matter, Mankind and Anthropic Cosmology*. New York: Bantam.
- Groth, E. and Peebles, P. (1977). Statistical Analysis of Catalogs of Extragalactic Objects. VII – Two- and Three-point correlation functions for the high-resolution Shane–Wirtanen catalog of galaxies, *Astrophysical Journal*, **217**, 385–405.
- Groth, E. and Peebles, P. (1986). The Shane–Wirtanen counts – observer and time-dependent effects, *Astrophysical Journal*, **310**, 507–517.
- Guenther, D.B., Krauss, L.M., and Demarque, P. (1998). Testing the constancy of the gravitational constant using helioseismology, *Astrophysical Journal*, **498**, 871–876.
- Gunn, J.E. (1978). The Friedmann models and optical observations in cosmology, in *Observational Cosmology: 8th Advanced Course, Swiss Society of Astronomy and Astrophysics, Saas-Fee 1978*, eds. Maeder, A., Martinet, L., and Tammann, G., pp. 1–121. Geneva: Geneva Observatory Publications.
- Gunn, J.E., Hoessel, J.G., Westphal, J.A., Perryman, M.A.C., and Longair, M.S. (1981). Investigations of the optical fields of 3CR radio sources to faint limiting magnitudes: IV. *Monthly Notices of the Royal Astronomical Society*, **194**, 111–123.
- Gunn, J.E. and Peterson, B.A. (1965). On the density of neutral hydrogen in intergalactic space, *Astrophysical Journal*, **142**, 1633–1636.
- Gurvits, L.I., Kellermann, K.I., and Frey, S. (1999). The “angular size – redshift” relation for compact radio structures in quasars and radio galaxies, *Astronomy and Astrophysics*, **342**, 378–388.

- Guth, A. (1981). Inflationary universe: a possible solution to the horizon and flatness problems, *Physical Review*, **D23**, 347–356.
- Guth, A.H. (1997). *The Inflationary Universe: The Quest for a New Theory of Cosmic Origins*. Reading, MA: Addison-Wesley.
- Guth, A.H. and Pi, S.-Y. (1982). Fluctuations in the new inflationary universe, *Physical Review Letters*, **49**, 1110–1113.
- Hamilton, A.J.S., Kumar, P., Lu, E., and Matthews, A. (1991). Reconstructing the primordial spectrum of fluctuations of the Universe from the observed nonlinear clustering of galaxies, *Astrophysical Journal*, **374**, L1–L4.
- Harrison, E. (1970). Fluctuations at the threshold of classical cosmology, *Physical Review*, **D1**, 2726–2730.
- Harrison, E.R. (1987). *Darkness at Night: A Riddle of the Universe*. Cambridge: Cambridge University Press.
- Hasinger, G., Burg, R., Giacconi, R., Hartner, G.D., Schmidt, M., Trümper, J., and Zamorani, G. (1993). A deep X-ray survey in the Lockman hole and the soft X-ray logN-logS, *Astronomy and Astrophysics*, **275**, 1–15.
- Hauser, M.G., Arendt, R.G., Kelsall, T., Dwek, E., Odegard, N., Weiland, J.L., Freudenreich, H.T., Reach, W.T., Silverberg, R.F., Moseley, S.H., Pei, Y.C., Lubin, P., Mather, J.C., Shafer, R.A., Smoot, G.F., Weiss, R., Wilkinson, D.T., and Wright, E.L. (1998). The COBE diffuse infrared background experiment search for the cosmic infrared background: I. Limits and detections, *Astrophysical Journal*, **508**, 25–43.
- Hauser, M.G. and Dwek, E. (2001). The cosmic infrared background: measurements and implications, *Annual Review of Astronomy and Astrophysics*, **39**, 249–307.
- Hausman, M.A. and Ostriker, J.P. (1977). Cannibalism among galaxies – dynamically produced evolution of cluster luminosity functions, *Astrophysical Journal*, **217**, L125–L129.
- Hausman, M.A. and Ostriker, J.P. (1978). Galactic cannibalism: III. The morphological evolution of galaxies and clusters, *Astrophysical Journal*, **224**, 320–336.
- Hawking, S.W. (1975). Particle creation by black holes, in *Quantum Gravity: Proceedings of the Oxford Symposium*, eds. Isham, C.J., Penrose, R., and Sciama, D.W., pp. 219–267. Oxford: Clarendon.
- Hawkins, M.R.S. (1986). On the nature of objects detected as faint long-term variables, *Monthly Notices of the Royal Astronomical Society*, **219**, 417–426.
- Heath, D.J. (1977). The growth of density perturbations in zero pressure Friedmann-Lemaître universes, *Monthly Notices of the Royal Astronomical Society*, **179**, 351–358.
- Helou, G., Soifer, B.T., and Rowan-Robinson, M. (1985). Thermal infrared and nonthermal radio – remarkable correlation in disks of galaxies, *Astrophysical Journal*, **298**, L7–L11.
- Hernquist, L., Katz, N., Weinberg, D.H., and Miralda-Escudé, J. (1996). The Lyman-alpha forest in the cold dark matter model, *Astrophysical Journal*, **457**, L51–L55.
- Herschel, W. (1785). On the construction of the heavens, *Philosophical Transactions of the Royal Society*, **75**, 213–268.

- Herschel, W. (1802). Catalogue of 500 new nebulae, nebulous stars, planetary nebulae, and clusters of stars; with remarks on the construction of the heavens, *Philosophical Transactions of the Royal Society*, **92**, 477–528.
- Hesser, J.E., Harris, W.E., VandenBerg, D.A., Allwright, J.W.B., Shott, P., and Stetson, P. (1987). A CCD color-magnitude study of 47 tucanae, *Publications of the Astronomical Society of the Pacific*, **99**, 739–808.
- Hewish, A. (1961). Extrapolation of the number-flux density relation of radio stars by Scheuer's statistical methods, *Monthly Notices of the Royal Astronomical Society*, **123**, 167–181.
- Hewitt, J.N., Turner, E.L., Burke, B.F., Lawrence, C.R., and Bennett, C.L. (1987). A VLA gravitational lens survey, in *Observational Cosmology: IAU Symposium No. 124*, eds. Hewitt, A., Burbidge, G., and Fang, L.Z., pp. 747–750. Dordrecht: Reidel.
- Higgs, P. (1964). Broken symmetries, massless particles and gauge fields, *Physics Letters*, **12**, 132–133.
- Hinshaw, G., Nolta, M.R., Bennett, C.L., Bean, R., Doré, O., Greason, M.R., Halpern, M., Hill, R.S., Jarosik, N., Kogut, A., Komatsu, E., Limon, M., Odegard, N., Meyer, S.S., Page, L., Peiris, H.V., Spergel, D.N., Tucker, G.S., Verde, L., Weiland, J.L., Wollack, E., and Wright, E.L. (2007). Three-year Wilkinson Microwave Anisotropy Probe (WMAP) observations: temperature analysis, *Astrophysical Journal Supplement*, **170**, 288–334.
- Hinshaw, G., Spergel, D.N., Verde, L., Hill, R.S., Meyer, S.S., Barnes, C., Bennett, C.L., Halpern, M., Jarosik, N., Kogut, A., Komatsu, E., Limon, M., Page, L., Tucker, G.S., Weiland, J.L., Wollack, E., and Wright, E.L. (2003). First-Year Wilkinson Microwave Anisotropy Probe (WMAP) observations: the angular power spectrum, *Astrophysical Journal Supplement*, **148**, 135–159.
- Hobson, M., Efstathiou, G., and Lasenby, A. (2006). *General Relativity: An Introduction for Physicists*. Cambridge: Cambridge University Press.
- Hoekstra, H., Yee, H.K.C., and Gladders, M.D. (2004). Properties of galaxy dark matter halos from weak lensing, *Astrophysical Journal*, **606**, 67–77.
- Hogan, C.J. (1997). Big Bang nucleosynthesis and the observed abundances of light elements, in *Critical Dialogues in Cosmology*, ed. Turok, N., pp. 50–62. Singapore: World Scientific.
- Hogg, D.W., Blanton, M.R., Brinchmann, J., Eisenstein, D.J., Schlegel, D.J., Gunn, J.E., McKay, T.A., Rix, H.-W., Bahcall, N.A., Brinkmann, J., and Meiksin, A. (2004). The dependence on environment of the color-magnitude relation of galaxies, *Astrophysical Journal*, **601**, L29–L32.
- Hogg, D.W., Eisenstein, D.J., Blanton, M.R., Bahcall, N.A., Brinkmann, J., Gunn, J.E., and Schneider, D.P. (2005). Cosmic homogeneity demonstrated with luminous red galaxies, *Astrophysical Journal*, **624**, 54–58.
- Holtzman, J.A. (1998). Microwave background anisotropies and large-scale structure in universes with cold dark matter, baryons, radiation and massive and massless neutrinos, *Astrophysical Journal Suppllement*, **71**, 1–24.
- Hook, I.M., McMahon, R.G., Boyle, B.J., and Irwin, M.J. (1991). The variability of a large sample of quasars, in *The Space Distribution of Quasars*, ed. Crampton, D.,

- vol. 21, pp. 67–75. San Francisco: Astronomical Society of the Pacific Conference Series.
- Hoskin, M.A. (1976). The ‘Great Debate’: what really happened, *Journal of the History of Astronomy*, **7**, 169–182.
- Hoyle, F. (1954). On nuclear reactions occurring in very hot stars: I. The synthesis of elements from carbon to nickel, *Astrophysical Journal Supplement*, **1**, 121–146.
- Hoyle, F. and Tayler, R. (1964). The mystery of the cosmic helium abundance, *Nature*, **203**, 1108–1110.
- Hoyle, F., Vogeley, M., and Gott III, J. (2002a). Two-dimensional topology of the Two-Degree Field Galaxy Redshift Survey, *Astrophysical Journal*, **570**, 44–53.
- Hoyle, F., Vogeley, M., Gott III, J., Blanton, M., Tegmark, M., Weinberg, D., Bahcall, N., Brinkmann, J., and York, D. (2002b). Two-dimensional topology of the Sloan Digital Sky Survey, *Astrophysical Journal*, **580**, 663–671.
- Hu, E.M., Kim, T.-S., Cowie, L.L., Songaila, A., and Rauch, M. (1995a). The distribution of column densities and B values in the Lyman-alpha forest, *Astronomical Journal*, **110**, 1526–1543.
- Hu, W. (1996). Concepts in CMB anisotropy formation, in *The Universe at High-z, Large-Scale Structure and the Cosmic Microwave Background*, eds. Martinez-Gonzales, E. and Sanz, J.L., pp. 207–240. Berlin: Springer.
- Hu, W. and Dodelson, S. (2002). Cosmic microwave background anisotropies, *Annual Review of Astronomy and Astrophysics*, **40**, 171–216.
- Hu, W. and Okamoto, T. (2002). Mass reconstruction with cosmic microwave background polarization, *Astrophysical Journal*, **574**, 566–574.
- Hu, W., Scott, D., Sugiyama, N., and White, M. (1995b). Effect of physical assumptions on the calculation of microwave background anisotropies, *Physical Review D*, **D52**, 5498–5515.
- Hu, W. and Sugiyama, N. (1995). Anisotropies in the cosmic microwave background: an analytic approach, *Astrophysical Journal*, **444**, 489–506.
- Hu, W., Sugiyama, N., and Silk, J. (1997). The physics of microwave background anisotropies, *Nature*, **386**, 37–43.
- Hu, W. and White, M. (1997). A CMB polarization primer, *New Astronomy*, **2**, 323–344.
- Hubble, E.P. (1926). Extra-galactic nebulae, *Astrophysical Journal*, **64**, 321–369.
- Hubble, E.P. (1929). A relation between distance and radial velocity among extra-galactic nebulae, *Proceedings of the National Academy of Sciences*, **15**, 168–173.
- Hubble, E.P. (1936). *The Realm of the Nebulae*. New Haven: Yale University Press.
- Hubble, E.P. and Humason, M. (1934). The velocity–distance relation among extra-galactic nebulae, *Astrophysical Journal*, **74**, 43–80.
- Hudson, M.J., Dekel, A., Courteau, S., Faber, S.M., and Willick, J.A. (1995). Ω and biasing from optical galaxies versus POTENT mass, *Monthly Notices of the Royal Astronomical Society*, **274**, 305–316.
- Huggins, W. and Miller, W.A. (1864). On the spectra of some of the nebulae; a supplement to the paper “On the Spectra of Some Fixed Stars”, *Philosophical Transactions of the Royal Society of London*, **154**, 437–444.

- Hulse, R.A. and Taylor, J.H. (1975). Discovery of a pulsar in a binary system, *Astrophysical Journal Letters*, **195**, L51–L53.
- Ikeuchi, S. and Ostriker, J.P. (1986). Evolution of the intergalactic medium – what happened during the epoch $Z = 3\text{--}10?$, *Astrophysical Journal*, **301**, 522–543.
- Illingworth, G. (1977). Rotation (?) in 13 elliptical galaxies, *Astrophysical Journal Letters*, **218**, L43–L47.
- Inskip, K.J., Best, P.N., Longair, M.S., and MacKay, D.J.C. (2002). Infrared magnitude-redshift relations for luminous radio galaxies, *Monthly Notices of the Royal Astronomical Society*, **329**, 277–289.
- Irwin, M., McMahon, R.G., and Hazard, C. (1991). APM optical surveys for high redshift quasars, in *ASP Conf. Ser. 21: The Space Distribution of Quasars*, ed. Crampton, D., pp. 117–126.
- Jakobsen, P. (1995). Ultraviolet background (theory), in *The Extragalactic Background Radiation*, eds. Calzetti, D., Livio, M., and Madau, P., pp. 75–101. Cambridge: Cambridge University Press.
- Jakobsen, P. (1996). Intergalactic helium absorption toward quasars, in *Science with the Hubble Space Telescope – II*, eds. Benvenuti, P., Macchetto, F.D., and Schreier, E.J., pp. 153–159. Paris: European Space Agency.
- Jakobsen, P., Boksenberg, A., Deharveng, J.M., Greenfield, P., Jedrzejewski, R., and Paresce, F. (1994). Detection of intergalactic ionized helium absorption in a high-redshift quasar, *Nature*, **370**, 35–39.
- Jeans, J. (1902). The stability of a spherical nebula, *Philosophical Transactions of the Royal Society of London*, **199**, 1–53.
- Jones, B.J.T. (1973). Cosmic turbulence and the origin of galaxies, *Astrophysical Journal*, **181**, 269–294.
- Jones, B.J.T. and Peebles, P.J.E. (1972). Chaos in cosmology, *Comments on Astrophysics and Space Physics*, **4**, 121–128.
- Jones, B.J.T. and Wyse, R.F.G. (1985). The ionisation of the primeval plasma at the time of recombination, *Astronomy and Astrophysics*, **149**, 144–150.
- Jones, W.C., Ade, P.A.R., Bock, J.J., Bond, J.R., Borrill, J., Boscaleri, A., Cabella, P., Contaldi, C.R., Crill, B.P., de Bernardis, P., De Gasperis, G., de Oliveira-Costa, A., De Troia, G., di Stefano, G., Hivon, E., Jaffe, A.H., Kisner, T.S., Lange, A.E., MacTavish, C.J., Masi, S., Mauskopf, P.D., Melchiorri, A., Montroy, T.E., Natoli, P., Netterfield, C.B., Pascale, E., Piacentini, F., Pogosyan, D., Polenta, G., Prunet, S., Ricciardi, S., Romeo, G., Ruhl, J.E., Santini, P., Tegmark, M., Veneziani, M., and Vittorio, N. (2006). A measurement of the angular power spectrum of the CMB temperature anisotropy from the 2003 flight of BOOMERANG, *Astrophysical Journal*, **647**, 823–832.
- Kaastra, J.S., Tamura, T., Peterson, J.R., Bleeker, J.A.M., Ferrigno, C., Kahn, S.M., Paerels, F.B.S., Piffaretti, R., Branduardi-Raymont, G., and Böhringer, H. (2004). Spatially resolved X-ray spectroscopy of cooling clusters of galaxies, *Astronomy and Astrophysics*, **413**, 415–439.
- Kaiser, N. (1984). On the spatial correlations of Abell clusters, *Astrophysical Journal*, **284**, L9–L12.

- Kaiser, N. (1987). Clustering in real space and in redshift space, *Monthly Notices of the Royal Astronomical Society*, **227**, 1–21.
- Kaiser, N. (1992). Weak gravitational lensing of distant galaxies, *Astrophysical Journal*, **388**, 272–286.
- Kapahi, V.K. (1987). The angular size-redshift relation as a cosmological tool, in *Observational Cosmology*, eds. Hewitt, A., Burbidge, G., and Fang, L.-Z., pp. 251–265. Dordrecht: Reidel.
- Kapteyn, J.C. (1922). First attempt at a theory of the arrangement and motion of the sidereal system, *Astrophysical Journal*, **55**, 302–328.
- Kashlinsky, A., Mather, J.C., Odenwald, S., and Hauser, M.G. (1996). Clustering of the diffuse infrared light from the COBE DIRBE maps: I. C(0) and limits on the near-infrared background, *Astrophysical Journal*, **470**, 681–705.
- Kaspi, V.M., Taylor, J.H., and Ryba, M.F. (1994). High-precision timing of millisecond pulsars: 3. Long-term monitoring of PSRs B1855+09 and B1937+21, *Astrophysical Journal*, **428**, 713–728.
- Kassiola, A., Kovner, I., and Blandford, R.D. (1991). Bounds on intergalactic compact objects from observations of compact radio sources, *Astrophysical Journal*, **381**, 6–13.
- Katz, N., Weinberg, D.H., Hernquist, L., and Miranda-Escudé, J. (1996). Damped Lyman-alpha and Lyman-limit absorbers in the cold dark matter model, *Astrophysical Journal*, **457**, L57–L60.
- Kauffmann, G., Heckman, T.M., White, S.D.M., Charlot, S., Tremonti, C., Peng, E.W., Seibert, M., Brinkmann, J., Nichol, R.C., SubbaRao, M., and York, D. (2003). The dependence of star formation history and internal structure on stellar mass for 10^5 low-redshift galaxies, *Monthly Notices of the Royal Astronomical Society*, **341**, 54–69.
- Kauffmann, G., J.M. Colberg, J.M., Diaferio, A., and White, S.D.M. (1999). Clustering of galaxies in a hierarchical universe: I. Methods and results at $z = 0$, *Monthly Notices of the Royal Astronomical Society*, **303**, 188–206.
- Kauffmann, G. and White, S.D. (1993). The merging history of dark matter haloes in a hierarchical universe, *Monthly Notices of the Royal Astronomical Society*, **261**, 921–928.
- Kellermann, K.I. (1993). The cosmological deceleration parameter estimated from the angular-size/redshift relation for compact radio sources, *Nature*, **361**, 134–136.
- Kennicutt, R. (1989). The star formation law in galactic discs, *Astrophysical Journal*, **344**, 685–703.
- Kennicutt, R.C., Edgar, B.K., and Hodge, P.W. (1989). Properties of H II region populations in galaxies: II. The H II region luminosity function, *Astrophysical Journal*, **337**, 761–781.
- Kent, S.M. and Gunn, J.E. (1982). The dynamics of rich clusters of galaxies: I. The Coma cluster, *Astronomical Journal*, **87**, 945–971.
- Kibble, T.W.B. (1976). Topology of cosmic domains and strings, *Journal of Physics A: Mathematical and General*, **9**, 1387–1398.

- King, I.R. (1966). The structure of star clusters: III. Some simple dynamical models, *Astronomical Journal*, **71**, 64–75.
- King, I.R. (1981). The dynamics of globular clusters, *Quarterly Journal of the Royal Astronomical Society*, **22**, 227–243.
- Kippenhahn, R. and Weigert, A. (1990). *Stellar Structure and Evolution*. Berlin and Heidelberg: Springer.
- Kirshner, R. and Kwan, J. (1974). Distances to extragalactic supernovae, *Astrophysical Journal*, **193**, 27–36.
- Kneib, J.P. (1993). *Ph.D. dissertation*. Université Paul Sabatier, Toulouse.
- Kneib, J.-P., Ellis, R.S., Smail, I., Couch, W.J., and Sharples, R.M. (1996). Hubble Space Telescope observations of the lensing cluster Abell 2218, *Astrophysical Journal*, **471**, 643–656.
- Knop, R., Aldering, G., Amanullah, R., Astier, P., Blanc, G., Burns, M., Conley, A., Deustua, S., Doi, M., Ellis, R., Fabbro, S., Folatelli, G., Fruchter, A., Garavini, G., Garmond, S., Garton, K., Gibbons, R., Goldhaber, G., Goobar, A., Groom, D., Hardin, D., Hook, I., Howell, D., Kim, A., Lee, B., Lidman, C., Mendez, J., Nobili, S., Nugent, P., Pain, R., Panagia, N., Pennypacker, C., Perlmutter, S., Quimby, R., Raux, J., Regnault, N., Ruiz-Lapuente, P., Sainton, G., Schaefer, B., Schahmaneche, K., Smith, E., Spadafora, A., Stanishev, V., Sullivan, M., Walton, N.A., Wang, L., Wood-Vasey, W.M., and Yasuda, N. (2003). New constraints on Ω_M , Ω_Λ , and w from an independent set of 11 high-redshift supernovae observed with the Hubble Space Telescope, *Astrophysical Journal*, **598**, 102–137.
- Kochanek, C. (1996). Is there a cosmological constant?, *Astrophysical Journal*, **466**, 638–659.
- Kogut, A., Banday, A.J., Bennett, C.L., Górski, K.M., Hinshaw, G., Smoot, G.F., and Wright, E.L. (1996). Tests for non-Gaussian statistics in the DMR four-year sky maps, *Astrophysical Journal*, **464**, L29–L33.
- Kolatt, T., Dekel, A., and Lahav, O. (1995). Large-scale mass distribution behind the galactic plane, *Monthly Notices of the Royal Astronomical Society*, **275**, 797–811.
- Kolb, E.W. and Turner, M.S. (1990). *The Early Universe*. Redwood City, CA: Addison-Wesley.
- Kompaneets, A. (1956). The establishment of thermal equilibrium between quanta and electrons, *Zhurnal Eksperimentalnoi i Teoreticheskoi Fiziki*, **31**, 876–885. (English translation: 1957 Soviet Physics, 4, 730–737).
- Koo, D.C. and Kron, R. (1982). QSO counts – a complete survey of stellar objects to $B = 23$, *Astronomy and Astrophysics*, **105**, 107–119.
- Kooiman, B.L., Burns, J.O., and Klypin, A.A. (1995). Two-point angular correlation function for the Green Bank 4.85 GHz Sky Survey, *Astrophysical Journal*, **448**, 500–509.
- Kormendy, J. (1982). Observations of galaxy structure and dynamics, in *Morphology and Dynamics of Galaxies: 12th Advanced Course of the Swiss Society of Astronomy and Astrophysics*, eds. Martinet, L. and Mayor, M., pp. 113–288. Sauverny, Switzerland: Geneva Observatory.

- Kormendy, J. and Richstone, D.O. (1995). Inward bound—the search for supermassive black holes in galactic nuclei, *Annual Review of Astronomy and Astrophysics*, **33**, 581–624.
- Kovac, J.M., Leitch, E.M., Pryke, C., Carlstrom, J.E., Halverson, N.W., and Holzapfel, W.L. (2002). Detection of polarization in the cosmic microwave background using DASI, *Nature*, **420**, 772–787.
- Kriss, G.A., Shull, J.M., Oegerle, W., Zheng, W., Davidsen, A.F., Songaila, A., Tumlinson, J., Cowie, L.L., Deharveng, J.-M., Friedman, S.D., Giroux, M.L., Green, R.F., Hutchings, J.B., Jenkins, E.B., Kruk, J.W., Moos, H.W., Morton, D.C., Sembach, K.R., and Tripp, T.M. (2001). Resolving the structure of ionized helium in the intergalactic medium with the far ultraviolet spectroscopic explorer, *Science*, **293**, 1112–1116.
- Kulkarni, V.P. and Fall, S.M. (1993). The proximity effect and the mean intensity of ionizing radiation at low redshifts, *Astrophysical Journal*, **413**, L63–L66.
- Kulkarni, V.P., Fall, S.M., Lauroesch, J.T., York, D.G., Welty, D.E., Khare, P., and Truran, J.W. (2005). Hubble space telescope observations of element abundances in low-redshift damped Ly α galaxies and implications for the global metallicity-redshift relation, *Astrophysical Journal*, **618**, 68–90.
- Kulsrud, R.M. (1997). Pregalactic model for cosmic magnetic fields, in *Critical Dialogues in Cosmology*, ed. Turok, N., pp. 328–342. Singapore: World Scientific.
- Kulsrud, R.M. (2005). *Plasma Physics for Astrophysics*. Princeton, NJ: Princeton University Press.
- Kundic, T., Turner, E.L., Colley, W.N., Gott III, J.R., Rhoads, J.E., Wang, Y., Bergeron, L.E., Gloria, K.A., Long, D.C., Malhotra, S., and Wambsganss, J. (1997). A robust determination of the time delay in 0957+561A, B and a measurement of the global value of Hubble's constant, *Astrophysical Journal*, **482**, 75–82.
- Kuo, C.L., Ade, P.A.R., Bock, J.J., Cantalupo, C., Daub, M.D., Goldstein, J., Holzapfel, W.L., Lange, A.E., Lueker, M., Newcomb, M., Peterson, J.B., Ruhl, J., Runyan, M.C., and Torbet, E. (2004). High-resolution observations of the cosmic microwave background power spectrum with ACBAR, *Astrophysical Journal*, **600**, 32–51.
- Kurt, V.G. and Sunyaev, R.A. (1967). Measurement of the ultraviolet and X-ray background outside the Earth's atmosphere and their role in the study of intergalactic gas, *Cosmical Research*, **5**, 496–512.
- Kutyrev, A.S. and Reynolds, R.J. (1989). Probable detection of H- α emission from a very high velocity cloud in Cetus, *Astrophysical Journal Letters*, **344**, L9–L11.
- Lacy, M., Miley, G., Rawlings, S., Saunders, R., Dickinson, M., Garrington, S., Maddox, S., Pooley, G., Steidel, C., Bremer, M.N., Cotter, G., van Oijk, R., Röttgering, H., and Warner, P. (1994). 8C 1435+635: a radio galaxy at $z = 4.25$, *Monthly Notices of the Royal Astronomical Society*, **271**, 504–512.
- Lagache, G., Dole, H., and Puget, J.-L. (2003). Modelling infrared galaxy evolution using a phenomenological approach, *Monthly Notices of the Royal Astronomical Society*, **338**, 555–571.
- Lagache, G., Dole, H., Puget, J.-L., Pérez-González, P.G., Le Floc'h, E., Rieke, G.H., Papovich, C., Egami, E., Alonso-Herrero, A., Engelbracht, C.W., Gordon, K.D.,

- Misselt, K.A., and Morrison, J.E. (2004). Polycyclic aromatic hydrocarbon contribution to the infrared output energy of the Universe at $z \cong 2$, *Astrophysical Journal Supplement*, **154**, 112–117.
- Laing, R.A., Riley, J.M., and Longair, M.S. (1983). Bright radio sources at 178 MHz – flux densities, optical identifications and the cosmological evolution of powerful radio galaxies, *Monthly Notices of the Royal Astronomical Society*, **204**, 151–187.
- Lanczos, K. (1922). Bemerkung zur die Sitterschen Welt (Remarks on de Sitter's World Model), *Physikalische Zeitschrift*, **23**, 539–543.
- Lanzetta, K., Wolfe, A., and Turnshek, D. (1995). The IUE Survey for damped Lyman- α and Lyman-limit absorption systems, *Astrophysical Journal*, **440**, 435–457.
- Larson, R.B. (1972). Infall of matter in the galaxies, *Nature*, **236**, 21–23.
- Larson, R.B. and Tinsley, B.M. (1978). Star formation rates in normal and peculiar galaxies, *Astrophysical Journal*, **219**, 46–59.
- Le Verrier, U.J.J. (1859). Sur la théorie de mercure et sur le mouvement du périhélie de cette planète (On the theory of mercury and the movement of the perihelion of this planet), *Comptes Rendus*, **49**, 379–383.
- Leavitt, H.S. (1912). Periods of 25 variable stars in the Small Magellanic Cloud, *Harvard College Observatory Circular*, No. **173**, 1–2.
- Ledoux, C., Petitjean, P., and Srianand, R. (2006). Molecular hydrogen in a damped Ly α system at $z_{\text{abs}} = 4.224$, *Astrophysical Journal*, **640**, L25–L28.
- Leitch, E.M., Kovac, J.M., Pryke, C., Carlstrom, J.E., Halverson, N.W., Holzapfel, W.L., Dragovan, M., Reddall, B., and Sandberg, E.S. (2002). Measurement of polarization with the Degree Angular Scale Interferometer, *Nature*, **420**, 763–771.
- Lemaître, G. (1927). A homogeneous universe of constant mass and increasing radius, accounting for the radial velocity of extra-galactic nebulae, *Annales de la Société Scientifique de Bruxelles*, **A47**, 29–39. Translation: (1931), *Monthly Notices of the Royal Astronomical Society*, **91**, 483–490.
- Lemaître, G. (1933). Spherical condensations in the expanding Universe, *Comptes Rendus de L'Academie des Sciences de Paris*, **196**, 903–904.
- Lequeux, J., Peimbert, M., Rayo, J.F., Serrano, A., and Torres-Peimbert, S. (1979). Chemical composition and evolution of irregular and blue compact galaxies, *Astronomy and Astrophysics*, **80**, 155–166.
- Liddle, A.R. and Lyth, D. (2000). *Cosmological Inflation and Large-Scale Structure*. Cambridge: Cambridge University Press.
- Lifshitz, E. (1946). On the gravitational stability of the expanding Universe, *Journal of Physics, Academy of Sciences of the USSR*, **10**, 116–129.
- Lightman, A.P. and Schechter, P.L. (1990). The omega dependence of peculiar velocities induced by spherical density perturbations, *Astrophysical Journal Supplement Series*, **74**, 831–832.
- Lilly, S. and Cowie, L. (1987). Deep infrared surveys, in *Infrared Astronomy with Arrays*, eds. Wynn-Williams, C. and Becklin, E., pp. 473–482. Honolulu: Institute for Astronomy, University of Hawaii Publications.

- Lilly, S.J. (1988). Discovery of a radio galaxy at a redshift of 3.395, *Astrophysical Journal*, **333**, L161–L167.
- Lilly, S.J. and Longair, M.S. (1984). Stellar populations in distant radio galaxies, *Monthly Notices of the Royal Astronomical Society*, **211**, 833–855.
- Lilly, S.J., Tresse, L., Hammer, F., Crampton, D., and LeFevre, O. (1995). The Canada–France Redshift Survey: VI. Evolution of the galaxy luminosity function to $z \sim 1$, *Astrophysical Journal*, **455**, 108–124.
- Lin, C.C., Mestel, L., and Shu, F. (1965). The gravitational collapse of a uniform spheroid, *Astrophysical Journal*, **142**, 1431–1446.
- Lin, H., Kirshner, R.P., Shectman, S.A., Landy, S.D., Oemler, A., and Tucker, D.L. (1996). The power spectrum of galaxy clustering in the Las Campanas Redshift Survey, *Astrophysical Journal*, **471**, 617–635.
- Linde, A. (1974). Is the Lee constant a cosmological constant?, *Zhurnal Experimentalnoi i Teoreticheskoi Fiziki (JETP) Letters*, **19**, 183–184.
- Linde, A. (1982). A new inflationary universe scenario: a possible solution of the horizon, flatness, homogeneity, isotropy and primordial monopole problems, *Physics Letters*, **108B**, 389–393.
- Linde, A. (1983). Chaotic inflation, *Physics Letters*, **129B**, 177–181.
- Lineweaver, C.H. (2005). Inflation and the cosmic microwave background, in *The New Cosmology*, ed. Colless, M., pp. 31–65.
- Linsky, J.L., Diplas, A., Savage, B., Andrusis, C., and Brown, A. (1994). Deuterium in the local interstellar medium: its cosmological Significance, in *Frontiers of Space and Ground-based Astronomy, 27th ESLAB Symposium*, eds. W. Wamsteker, W., Longair, M., and Kondo, Y., pp. 301–304.
- Lobachevsky, N.I. (1829). On the principles of geometry, *Kazanski Vestnik (Kazan Messenger)*.
- Lobachevsky, N.I. (1830). On the principles of geometry, *Kazanski Vestnik (Kazan Messenger)*.
- Longair, M. (1997a). Active galactic nuclei – the Redshift One 3CR galaxies, *Astronomy and Geophysics*, **38**, 10–15.
- Longair, M.S. (1965). Objects in the fields of 88 radio sources, *Monthly Notices of the Royal Astronomical Society*, **129**, 419–436.
- Longair, M.S. (1966). On the interpretation of radio source counts, *Monthly Notices of the Royal Astronomical Society*, **133**, 421–436.
- Longair, M.S. (1978). Radio astronomy and cosmology, in *Observational Cosmology: 8th Advanced Course, Swiss Society of Astronomy and Astrophysics, Saas-Fee 1978*, eds. Maeder, A., Martinet, L., and Tammann, G., pp. 125–257. Geneva: Geneva Observatory Publications.
- Longair, M.S. (1995). The physics of background radiation, in *The Deep Universe, by Sandage, A.R., Kron, R.G. and Longair, M.S.*, eds. Binggeli, B. and Buser, R., pp. 317–514.
- Longair, M.S. (1997b). *High Energy Astrophysics, Vol. 1 (revised 2nd edn.)*. Cambridge: Cambridge University Press.
- Longair, M.S. (1997c). *High Energy Astrophysics, Vol. 2 (revised 2nd edn.)*. Cambridge: Cambridge University Press.

- Longair, M.S. (2003). *Theoretical Concepts in Physics: An Alternative View of Theoretical Reasoning in Physics*. Cambridge: Cambridge University Press.
- Longair, M.S. (2006). *The Cosmic Century: A History of Astrophysics and Cosmology*. Cambridge: Cambridge University Press.
- Longair, M.S. and Scheuer, P.A.G. (1970). The luminosity-volume test for quasi-stellar objects, *Monthly Notices of the Royal Astronomical Society*, **151**, 45–63.
- Longair, M.S. and Sunyaev, R.A. (1969). Fluctuations in the microwave background radiation, *Nature*, **223**, 719–721.
- Longair, M.S. and Sunyaev, R.A. (1971). The electromagnetic background radiation of the Universe, *Uspekhi Fizicheskikh Nauk*, **105**, 41–96. English translation: *Soviet Physics Uspekhi*, **14**, 569–599, 1972.
- Lotz, J.M., Madau, P., Giavalisco, M., Primack, J., and Ferguson, H.C. (2006). The rest-frame far-ultraviolet morphologies of star-forming galaxies at $z \sim 1.5$ and 4, *Astrophysical Journal*, **636**, 592–609.
- Lynden-Bell, D. (1967). Statistical mechanics of violent relaxation in stellar systems, *Monthly Notices of the Royal Astronomical Society*, **136**, 101–121.
- ed. Lynden-Bell, D. (1997). *Cosmical magnetism*. Dordrecht: Kluwer.
- Lynds, R. and Petrosian, V. (1986). Giant luminous arcs in galaxy clusters, *Bulletin of the American Astronomical Society*, **18**, 1014.
- Lyne, A.G., Burgay, M., Kramer, M., Possenti, A., Manchester, R.N., Camilo, F., McLaughlin, M.A., Lorimer, D.R., D'Amico, N., Joshi, B.C., Reynolds, J., and Freire, P.C.C. (2004). A double-pulsar system: a rare laboratory for relativistic gravity and plasma physics, *Science*, **303**, 1153–1157.
- Lyubimov, V., Novikov, E., Nozik, V., Tretyakov, E., and Kozik, V. (1980). An estimate of the v_e mass from the β -spectrum of tritium in the valine molecule, *Physics Letters*, **138**, 30–56.
- Ma, C.-P. and Bertschinger, E. (1995). Cosmological perturbation theory in the synchronous and conformal Newtonian gauges, *Astrophysical Journal*, **455**, 7–25.
- Macchetto, F. and Dickinson, M. (1997). Galaxies in the young Universe, *Scientific American*, **276**, 66–73.
- Madau, P. (1995). Radiative transfer in a clumpy universe: the colors of high-redshift galaxies, *Astrophysical Journal*, **441**, 18–27.
- Madau, P., Ferguson, H., Dickinson, M., Giavalisco, M., Steidel, C., and Fruchter, A. (1996). High-redshift galaxies in the *Hubble Deep Field*: colour selection and star formation history to $z \sim 4$, *Monthly Notices of the Royal Astronomical Society*, **283**, 1388–1404.
- Maddox, S.J., Efstathiou, G., Sutherland, W.G., and Loveday, J. (1990). Galaxy correlations on large scales, *Monthly Notices of the Royal Astronomical Society*, **242**, 43P–47P.
- Maeder, A. (1994). A selection of 10 most topical stellar problems, in *Frontiers of Space and Ground-Based Astronomy*, eds. Wamsteker, W., Longair, M.S., and Kondo, Y., pp. 177–186. Dordrecht: Kluwer.
- Magorrian, J., Tremaine, S., Richstone, D., Bender, R., Bower, G., Dressler, A., Faber, S.M., Gebhardt, K., Green, R., Grillmair, C., Kormendy, J., and Lauer, T.

- (1998). The demography of massive dark objects in galaxy centers, *Astronomical Journal*, **115**, 2285–2305.
- Majewski, S.R., Munn, J.A., Kron, R.G., Bershadsky, M.A., Smetanka, J.J., and Koo, D.C. (1991). A proper motion and variability QSO survey to $B = 22.5$, in *The Space Distribution of Quasars*, ed. Crampton, D., volume 21, pp. 55–65. San Francisco: Astronomical Society of the Pacific Conference Series.
- Maloney, P. (1993). Sharp edges to neutral hydrogen disks in galaxies and the extragalactic radiation field, *Astrophysical Journal*, **414**, 41–56.
- Marleau, F.R., Fadda, D., Storrie-Lombardi, L.J., Helou, G., Makovoz, D., Frayer, D.T., Yan, L., Appleton, P.N., Armus, L., Chapman, S., Choi, P.I., Fang, F., Heinrichsen, I., Im, M., Lacy, M., Shupe, D., Soifer, B.T., Squires, G., Surace, J., Teplitz, H.I., and Wilson, G. (2004). Extragalactic source counts at 24 microns in the Spitzer First Look Survey, *Astrophysical Journal Supplement*, **154**, 66–69.
- Marshall, F.E., Boldt, E.A., Holt, S.S., Miller, R.B., Mushotzky, R.F., Rose, L.A., Rothschild, R.E., and Serlemitsos, P.J. (1980). The diffuse X-ray background spectrum from 3 to 50 keV, *Astrophysical Journal*, **235**, 4–10.
- Martin, C. and Bowyer, S. (1989). Evidence for an extragalactic component of the far-ultraviolet background and constraints on galaxy evolution for Z between 0.1 and 0.6, *Astrophysical Journal*, **338**, 677–706.
- Marx, G. and Szalay, A. (1972). Cosmological limit on neutretto mass. in *Neutrino '72*, vol. 1, pp. 191–195. Budapest: Technoinform.
- Mather, J. (1995). Microwave background radiation (observations), in *The Extragalactic Background Radiation*, eds. Calzetti, D., Livio, M., and Madau, P., pp. 169–190. Cambridge: Cambridge University Press.
- Matthews, J. and Walker, R.L. (1973). *Mathematical Methods of Physics*. New York: W.A. Benjamin.
- Mattig, W. (1959). Über den Zusammenhang Zwischen der Anzahl der Extragalaktischen Objekte und der Scheinbaren Helligkeit, *Astronomische Nachrichten*, **285**, 1–2.
- Mazzarella, J. and Balzano, V. (1986). A catalog of Markarian galaxies, *Astrophysical Journal Supplement Series*, **62**, 521–819.
- McCarthy, P.J. (2006). Galaxy formation and cosmology in the ELT era, in *Scientific Requirements for Extremely Large Telescopes: IAU Symposium No. 232*, eds. Whitelock, P., Dennefeld, M., and Leibundgut, B., pp. 119–129. Cambridge: Cambridge University Press.
- McCarthy, P.J., Le Borgne, D., Crampton, D., Chen, H.-W., Abraham, R.G., Glazebrook, K., Savaglio, S., Carlberg, R.G., Marzke, R.O., Roth, K., Jørgensen, I., Hook, I., Murowinski, R., and Juneau, S. (2004). Evolved galaxies at $z \geq 1.5$ from the Gemini Deep Deep Survey: the formation epoch of massive stellar systems, *Astrophysical Journal Letters*, **614**, L9–L12.
- McCarthy, P.J., van Breugel, W.J.M., Spinrad, H., and Djorgovski, G. (1987). A correlation between the radio and optical morphologies of distant 3CR radio galaxies, *Astrophysical Journal*, **321**, L29–L33.
- McCrea, W. (1970). A philosophy for Big Bang cosmology, *Nature*, **228**, 21–24.

- McDonald, P., Seljak, U., Burles, S., Schlegel, D.J., Weinberg, D.H., Cen, R., D., S., Schaye, J., Schneider, D.P., Bahcall, N.A., Briggs, J., Brinkmann, J., Brunner, R.J., Fukugita, M., Gunn, J.E., Ivezić, Z., Kent, S., Lupton, R.H., and Vanden Berk, D.E. (2006). The Ly- α forest power spectrum from the Sloan Digital Sky Survey, *Astrophysical Journal Supplement Series*, **163**, 80–109.
- McLure, R.J., Jarvis, M.J., Targett, T.A., Dunlop, J.S., and Best, P.N. (2006). On the evolution of the black hole: spheroid mass ratio, *Monthly Notices of the Royal Astronomical Society*, **368**, 1395–1403.
- McNally, S.J. and Peacock, J.A. (1995). The smallscale clustering power spectrum and relativistic decays, *Monthly Notices of the Royal Astronomical Society*, **277**, 143–151.
- Melott, A., Weinberg, D., and Gott, J. (1988). The topology of large-scale structure: II. Nonlinear evolution of Gaussian models, *Astrophysical Journal*, **328**, 50–68.
- Merritt, D. (1987). The distribution of dark matter in the Coma cluster, *Astrophysical Journal*, **313**, 121–135.
- Mészáros, P. (1974). The behaviour of point masses in an expanding cosmological substratum, *Astronomy and Astrophysics*, **37**, 225–228.
- Metcalfe, N., Shanks, T., Campos, A., Fong, R., and Gardner, J.P. (1996). Galaxy formation at high redshifts, *Nature*, **383**, 236–237.
- Metcalfe, N., Shanks, T., Weilbacher, P.M., McCracken, H.J., Fong, R., and Thompson, D. (2006). Galaxy number counts: VI. An H-band survey of the Herschel Deep Field, *Monthly Notices of the Royal Astronomical Society*, **370**, 1257–1273.
- ed. Meylan, G. (1995). *QSO Absorption Lines*. Berlin, Heidelberg: Springer.
- Michell, J. (1767). An inquiry into the probable parallax, and magnitude of the fixed stars, from the quantity of light which they afford us, and the particular circumstances of their situation, *Philosophical Transactions of the Royal Society*, **57**, 234–264.
- Mihos, J.C. and Hernquist, L. (1994). Triggering of starbursts in galaxies by minor mergers, *Astrophysical Journal*, **425**, L13–L16.
- Mihos, J.C. and Hernquist, L. (1996). Gasdynamics and starbursts in major mergers, *Astrophysical Journal*, **464**, 641–663.
- Miley, G.K. (1968). Variation of the angular sizes of quasars with red-shift, *Nature*, **218**, 933–934.
- Miley, G.K. (1971). The radio structure of quasars – a statistical investigation, *Monthly Notices of the Royal Astronomical Society*, **152**, 477–490.
- Milne, E.A. and McCrea, W.H. (1934a). Newtonian expanding universe, *Quarterly Journal of Mathematics*, **5**, 64–72.
- Milne, E.A. and McCrea, W.H. (1934b). Newtonian universes and the curvature of space, *Quarterly Journal of Mathematics*, **5**, 73–80.
- Miranda-Escudé, J., Cen, R., Ostriker, J.P., and Rauch, M. (1996). The Lyman alpha forest from gravitational collapse in the CDM + lambda model, *Astrophysical Journal*, **471**, 582–616.
- Mitchell, J.L., Keeton, C.R., Frieman, J.A., and Sheth, R.K. (2005). Improved cosmological constraints from gravitational lens statistics, *Astrophysical Journal*, **622**, 81–98.

- Mitchell, R.J., Culhane, J.L., Davison, P.J.N., and Ives, J.C. (1976). Ariel 5 observations of the X-ray spectrum of the Perseus cluster, *Monthly Notices of the Royal Astronomical Society*, **175**, 29P–34P.
- Møller, P. and Jakobsen, P. (1990). The Lyman continuum opacity at high redshifts – through the Lyman forest and beyond the Lyman valley, *Astronomy and Astrophysics*, **228**, 299–309.
- Monaco, P. (1998). The cosmological mass function, *Fundamentals of Cosmic Physics*, **19**, 157–317.
- Monaco, P. (1999). Dynamics in the cosmological mass function (or, why does the Press & Schechter work?), in *Observational Cosmology: The Development of Galaxy Systems*, eds. Giuricin, G., Mezzetti, M., and Salucci, P., pp. 186–197. San Francisco: Astronomical Society of the Pacific Conference Series No. 176.
- Monchaux, R., Berhanu, M., Bourgoin, M., Moulin, M., Odier, P., Pinton, J.-F., Volk, R., Fauve, S., Mordant, N., Pétrélis, F., Chiffaudel, A., Daviaud, F., Dubrulle, B., Gasquet, C., Marié, L., and Ravelet, F. (2007). Generation of a magnetic field by dynamo action in a turbulent flow of liquid sodium, *Physical Review Letters*, **98**(4), 044502.
- Montroy, T.E., Ade, P.A.R., Bock, J.J., Bond, J.R., Borrill, J., Boscaleri, A., Cambella, P., Contaldi, C.R., Crill, B.P., de Bernardis, P., De Gasperis, G., de Oliveira-Costa, A., De Troia, G., di Stefano, G., Hivon, E., Jaffe, A.H., Kisner, T.S., Jones, W.C., Lange, A.E., Masi, S., Mauskopf, P.D., MacTavish, C.J., Melchiorri, A., Natoli, P., Netterfield, C.B., Pascale, E., Piacentini, F., Pogosyan, D., Polenta, G., Prunet, S., Ricciardi, S., Romeo, G., Ruhl, J.E., Santini, P., Tegmark, M., Veneziani, M., and Vittorio, N. (2006). A measurement of the CMB (EE) spectrum from the 2003 flight of BOOMERANG, *Astrophysical Journal*, **647**, 813–822.
- Mukhanov, V. (2005). *Physical Foundations of Cosmology*. Cambridge: Cambridge University Press.
- Murdoch, H.S., Hunstead, R.W., Pettini, M., and Blades, J.C. (1986). Absorption spectrum of the $Z = 3.78$ QSO 2000-330: II. The redshift and equivalent width distributions of primordial hydrogen clouds, *Astrophysical Journal*, **309**, 19–32.
- Naselsky, P., Novikov, D., and Novikov, I. D. (2006). *The Physics of the Cosmic Microwave Background*. Cambridge: Cambridge University Press.
- Norberg, P., Baugh, C.M., Hawkins, E., Maddox, S., Madgwick, D., Lahav, O., Cole, S., Frenk, C.S., Baldry, I., Bland-Hawthorn, J., Bridges, T., Cannon, R., Colless, M., Collins, C., Couch, W., Dalton, G., De Propris, R., Driver, S.P., Efstathiou, G., Ellis, R.S., Glazebrook, K., Jackson, C., Lewis, I., Lumsden, S., Peacock, J.A., Peterson, B.A., Sutherland, W., and Taylor, K. (2002). The 2dF Galaxy Redshift Survey: the dependence of galaxy clustering on luminosity and spectral type, *Monthly Notices of the Royal Astronomical Society*, **332**, 827–838.
- Norberg, P., Baugh, C.M., Hawkins, E., Maddox, S., Peacock, J.A., Cole, S., Frenk, C.S., Bland-Hawthorn, J., Bridges, T., Cannon, R., Colless, M., Collins, C., Couch, W., Dalton, G., De Propris, R., Driver, S.P., Efstathiou, G., Ellis, R.S., Glazebrook, K., Jackson, C., Lahav, O., Lewis, I., Lumsden, S., Madgwick, D., Peterson, B.A., Sutherland, W., and Taylor, K. (2001). The 2dF Galaxy Redshift

- Survey: luminosity dependence of galaxy clustering, *Monthly Notices of the Royal Astronomical Society*, **328**, 64–70.
- Novikov, I. (1964). On the possibility of appearance of large scale inhomogeneities in the expanding Universe, *Journal of Experimental and Theoretical Physics*, **46**, 686–689.
- Oemler, A.J. (1974). The systematic properties of clusters of galaxies. Photometry of 15 clusters, *Astrophysical Journal*, **194**, 1–20.
- Oguri, M. (2007). Gravitational lens time delays: a statistical assessment of lens model dependences and implications for the global Hubble constant, *Astrophysical Journal*, **660**, 1–15.
- Ohta, K., Yamada, T., Nakanishi, K., Kohno, K., Akiyama, M., and Kawabe, R. (1996). Detection of molecular gas in the quasar BR1202-0725 at redshift $z = 4.69$, *Nature*, **382**, 426–428.
- Oliver, S.J., Rowan-Robinson, M., and Saunders, W. (1992). Infrared background constraints on the evolution of IRAS galaxies, *Monthly Notices of the Royal Astronomical Society*, **256**, 15P–22P.
- Omton, A. (1996). 1.3 mm detection and mapping of radioquiet QSOs at very high redshifts, in *Science with Large Millimetre Arrays*, ed. Shaver, P., pp. 82–85. Berlin: Springer.
- Omton, A., Petitjean, P., Guilloteau, S., McMahon, R.G., Solomon, P.M., and Pécontal, E. (1996). Molecular gas and dust around a radio-quiet quasar at redshift 4.69, *Nature*, **382**, 428–431.
- O'Neill, S.M., Jones, T.W., Tregillis, I.L., and Ryu, D. (2006). 3D MHD interactions of jets with cluster media, *Astronomische Nachrichten*, **327**, 535–536.
- Oort, J.H. (1958). Distribution of galaxies and density in the universe, in *Solvay Conference on The Structure and Evolution of the Universe*, pp. 163–181. Brussels: Institut International de Physique Solvay.
- Opal Collaboration (1990). A combined analysis of the hadronic and leptonic decays of the Z^0 , *Physics Letters*, **B240**, 497–512.
- Ortiz-Gil, A., Guzzo, L., Schuecker, P., Böhringer, H., and Collins, C.A. (2004). The X-ray luminosity-velocity dispersion relation in the REFLEX Cluster Survey, *Monthly Notices of the Royal Astronomical Society*, **348**, 325–332.
- Osmer, P.S. (1982). Evidence for a decrease in the space density of quasars at z more than about 3.5, *Astrophysical Journal*, **253**, 28–37.
- Ostriker, J.P. and Cowie, L. (1981). Galaxy formation in an intergalactic medium dominated by explosions, *Astrophysical Journal*, **243**, L127–L131.
- Ostriker, J.P. and Ikeuchi, S. (1983). Physical properties of the intergalactic medium and the Lyman-alpha absorbing clouds, *Astrophysical Journal Letters*, **268**, L63–L68.
- Ostriker, J.P. and Peebles, P.J.E. (1973). A numerical study of the stability of flattened galaxies: or, can cold galaxies survive?, *Astrophysical Journal*, **186**, 467–480.
- Oswalt, T.D., Smith, J.A., Wood, M.A., and Hintzen, P. (1996). A lower limit of 9.5 Gyr on the age of the galactic disk from the oldest white dwarf stars, *Nature*, **382**, 692–694.

- Ouchi, M., Shimasaku, K., Okamura, S., Furusawa, H., Kashikawa, N., Ota, K., Doi, M., Hamabe, M., Kimura, M., Komiyama, Y., Miyazaki, M., Miyazaki, S., Nakata, F., Sekiguchi, M., Yagi, M., and Yasuda, N. (2004). Subaru Deep Survey: V. A census of Lyman break galaxies at $z \sim 4$ and 5 in the Subaru Deep Fields: photometric properties, *Astrophysical Journal*, **611**, 660–684.
- Paciesas, W.S., Meegan, C.A., Pendleton, G.N., Briggs, M.S., Kouveliotou, C., Koshut, T.M., Lestrade, J.P., McCollough, M.L., Brainerd, J.J., Hakkila, J., Henze, W., Preece, R.D., Connaughton, V., Kippen, R.M., Mallozzi, R.S., Fishman, G.J., Richardson, G.A., and Sahi, M. (1999). The 4th BATSE Gamma-Ray Burst Catalog (revised), *Astrophysical Journal Supplement Series*, **122**, 465–495.
- Padmanabhan, T. (1993). *Structure Formation in the Universe*. Cambridge: Cambridge University Press.
- Padmanabhan, T. (1996). *Cosmology and Astrophysics through Problems*. Cambridge: Cambridge University Press. See pp. 437–440.
- Padmanabhan, T. (1997). Nonlinear gravitational clustering in the expanding Universe, in *Gravitation and Cosmology: Proc. ICGC-95 Conference, Pune*, eds. Dhurandhar, S. and Padmanabhan, T., pp. 37–52. Dordrecht: Kluwer Academic Publishers.
- Page, L. (1997). Review of observations of the cosmic microwave background, in *Critical Dialogues in Cosmology*, ed. Turok, N., pp. 343–362. Singapore: World Scientific.
- Page, L., Hinshaw, G., Komatsu, E., Nolta, M.R., Spergel, D.N., Bennett, C.L., Barnes, C., Bean, R., Doré, O., Dunkley, J., Halpern, M., Hill, R.S., Jarosik, N., Kogut, A., Limon, M., Meyer, S.S., Odegard, N., Peiris, H.V., Tucker, G.S., Verde, L., Weiland, J.L., Wollack, E., and Wright, E.L. (2007). Three-year Wilkinson Microwave Anisotropy Probe (WMAP) observations: polarization analysis, *Astrophysical Journal Supplement*, **170**, 335–376.
- Pagel, B. (1997). *Nucleosynthesis and Chemical Evolution of Galaxies*. Cambridge: Cambridge University Press.
- Pais, A. (1982). *Subtle is the Lord . . . : the Science and Life of Albert Einstein*. Oxford: Oxford University Press.
- Panagia, N., Gilmozzi, R., Macchetto, F., Adorf, H.-M., and Kirshner, R.P. (1991). Properties of the SN 1987A circumstellar ring and the distance to the Large Magellanic Cloud, *Astrophysical Journal*, **380**, L23–L26.
- Parker, E.N. (1997). Galactic dynamos and other questions on the origins of magnetic fields, in *Critical Dialogues in Cosmology*, ed. Turok, N., pp. 309–327. Singapore: World Scientific.
- Partridge, R. (1980a). Fluctuations in the cosmic microwave background radiation at small angular scales, *Physica Scripta*, **21**, 624–629.
- Partridge, R. (1980b). New limits on small-scale angular fluctuations in the cosmic microwave background, *Astrophysical Journal*, **235**, 681–687.
- Peacock, J. (2000). *Cosmological Physics*. Cambridge: Cambridge University Press.
- Peacock, J.A. (1985). The high-redshift evolution of radio galaxies and quasars, *Monthly Notices of the Royal Astronomical Society*, **217**, 601–631.

- Peacock, J.A., Cole, S., Norberg, P., Baugh, C.M., Bland-Hawthorn, J., Bridges, T., Cannon, R.D., Colless, M., Collins, C., Couch, W., Dalton, G., Deeley, K., De Propris, R., Driver, S.P., Efstathiou, G., Ellis, R.S., Frenk, C.S., Glazebrook, K., Jackson, C., Lahav, O., Lewis, I., Lumsden, S., Maddox, S., Percival, W.J., Peterson, B.A., Price, I., Sutherland, W., and Taylor, K. (2001). A measurement of the cosmological mass density from clustering in the 2dF Galaxy Redshift Survey, *Nature*, **410**, 169–173.
- Peacock, J.A. and Dodds, S.J. (1994). Reconstructing the linear power spectrum of cosmological mass fluctuations, *Monthly Notices of the Royal Astronomical Society*, **267**, 1020–1034.
- Peacock, J.A. and Heavens, A.F. (1985). The statistics of maxima in primordial density perturbations, *Monthly Notices of the Royal Astronomical Society*, **217**, 805–820.
- Peebles, P. (1981). Primeval adiabatic perturbations – constraints from the mass distribution, *Astrophysical Journal*, **248**, 885–897.
- Peebles, P. (1982). Large-scale background temperature and mass fluctuations due to scale-invariant primeval perturbations, *Astrophysical Journal*, **263**, L1–L5.
- Peebles, P.J.E. (1968). Recombination of the primeval plasma, *Astrophysical Journal*, **153**, 1–11.
- Peebles, P.J.E. (1976). A cosmic virial theorem, *Astrophysics and Space Science*, **45**, 3–19.
- Peebles, P.J.E. (1980). *The Large-Scale Structure of the Universe*. Princeton: Princeton University Press.
- Peebles, P.J.E. (1993). *Principles of Physical Cosmology*. Princeton: Princeton University Press.
- Peebles, P.J.E. and Yu, J.T. (1970). Primeval adiabatic perturbation in an expanding Universe, *Astrophysical Journal*, **162**, 815–836.
- Pei, Y. and Fall, S. (1995). Cosmic chemical evolution, *Astrophysical Journal*, **454**, 69–76.
- Penrose, R. (1997). *The Large, the Small and the Human Mind*. Cambridge: Cambridge University Press.
- Penzias, A.A. and Wilson, R.W. (1965). A measurement of excess antenna temperature at 4080 MHz, *Astrophysical Journal*, **142**, 419–421.
- Perlmutter, S., Aldering, G., della Valle, M., Deustua, S., Ellis, R.S., Fabbro, S., Fruchter, A., Goldhaber, G., Groom, D.E., Hook, I.M., Kim, A.G., Kim, M.Y., Knop, R.A., Lidman, C., McMahon, R.G., Nugent, P., Pain, R., Panagia, N., Pennypacker, C.R., Ruiz-Lapuente, P., Schaefer, B., and Walton, N. (1998). Discovery of a supernova explosion at half the age of the universe, *Nature*, **391**, 51–54.
- Perlmutter, S., Boyle, B., Bunclark, P., Carter, D., Couch, W., Deustua, S., Dopita, M., Ellis, R., Filippenko, A.V., Gabi, S., Glazebrook, K., Goldhaber, G., Goobar, A., Groom, D., Hook, I., Irwin, M., Kim, A., Kim, M., Lee, J., Matheson, T., McMahon, R., Newberg, H., Pain, R., Pennypacker, C., and Small, I. (1996). High-redshift supernova discoveries on demand: first results from a new tool for cosmology and bounds on q_0 , *Nuclear Physics B*, **51**, 20–29.

- Perlmutter, S., Gabi, S., Goldhaber, G., Goobar, A., Groom, D.E., Hook, I.M., Kim, A.G., Kim, M.Y., Lee, J.C., Pain, R., Pennypacker, C.R., Small, I.A., Ellis, R.S., McMahon, R.G., Boyle, B.J., Bunclark, P.S., Carter, D., Irwin, M.J., Glazebrook, K., Newberg, H.J.M., Filippenko, A.V., Matheson, T., Dopita, M., and Couch, W.J. (1997). Measurements of the cosmological parameters omega and lambda from the first seven supernovae at $z > 0.35$, *Astrophysical Journal*, **483**, 565–581.
- Persic, M., de Zotti, G., Boldt, E.A., Marshall, F.E., Danese, L., Franceschini, A., and Palumbo, G.G.C. (1989). The autocorrelation properties of fluctuations in the cosmic X-ray background, *Astrophysical Journal Letters*, **336**, L47–L50.
- Petrosian, V. and Salpeter, E.E. (1968). Ghost images in inhomogeneous Friedmann universes, *Astrophysical Journal*, **151**, 411–429.
- Pettini, M., Ellison, S.L., Steidel, C.C., and Bowen, D.V. (1999). Metal abundances at $z \leq 1.5$: fresh clues to the chemical enrichment history of damped Lyman- α systems, *Astrophysical Journal*, **510**, 576–589.
- Pettini, M., King, D.L., Smith, L.J., and Hunstead, R.W. (1997). The metallicity of high-redshift galaxies: the abundance of zinc in 34 damped Ly- α systems from $z = 0.7$ to 3.4, *Astrophysical Journal*, **486**, 665–680.
- Phillips, M.M. (1993). The absolute magnitudes of Type IA supernovae, *Astrophysical Journal*, **413**, L105–L108.
- Pound, R. and Rebka, G. (1960). Apparent weight of photons, *Physical Review Letters*, **4**, 337–341.
- Pound, R. and Snider, J. (1965). Effect of gravity on gamma radiation, *Physical Review*, **140**, B788–B803.
- Pozdnyakov, L.A., Sobol, I.M., and Sunyaev, R.A. (1983). Comptonization and the shaping of X-ray source spectra – Monte Carlo calculations, *Soviet Scientific Reviews, Section E: Astrophysics and Space Physics Reviews*, **2**, 189–331.
- Pratt, G.W. and Arnaud, M. (2002). The mass profile of A1413 observed with XMM-Newton: implications for the M-T relation, *Astronomy and Astrophysics*, **394**, 375–393.
- Press, W. and Schechter, P. (1974). Formation of galaxies and clusters of galaxies by self-similar gravitational condensation, *Astrophysical Journal*, **187**, 425–438.
- Primack, J.R., Seckel, D., and Sadoulet, B. (1988). Detection of cosmic dark matter, *Annual Review of Nuclear and Particle Science*, **38**, 751–807.
- Pritchard, J.R. and Furlanetto, S.R. (2007). 21-cm Fluctuations from inhomogeneous X-ray heating before reionisation, *Monthly Notices of the Royal Astronomical Society*, **376**, 1680–1694.
- Prochaska, J.X. and Wolfe, A.M. (2002). The UCSD HIRES/Keck I damped Ly α abundance database: II. The implications, *Astrophysical Journal*, **566**, 68–92.
- Prochaska, J.X., Gawiser, E., Wolfe, A.M., Castro, S. and Djorgovski, S.G. (2003). The Age-Metallicity Relation of the Universe in Neutral Gas: The First 100 Damped Ly α Systems, *Astrophysical Journal Letters*, **595**, L9–L12.
- Puget, J.-L., Abergel, A., Bernard, J.-P., Boulanger, F., Burton, W.B., Desert, F.-X., and Hartmann, D. (1996). Tentative detection of a cosmic far-infrared background with COBE, *Astronomy and Astrophysics*, **308**, L5–L8.

- Readhead, A.C.S., Mason, B.S., Contaldi, C.R., Pearson, T.J., Bond, J.R., Myers, S.T., Padin, S., Sievers, J.L., Cartwright, J.K., Shepherd, M.C., Pogosyan, D., Prunet, S., Altamirano, P., Bustos, R., Bronfman, L., Casassus, S., Holzapfel, W.L., May, J., Pen, U.-L., Torres, S., and Udomprasert, P.S. (2004). Extended mosaic observations with the cosmic background imager, *Astrophysical Journal*, **609**, 498–512.
- Rees, M.J. (1994). Origin of the seed magnetic field for a galactic dynamo, in *Cosmical Magnetism*, ed. Lynden-Bell, D., pp. 155–160. Dordrecht: Kluwer.
- Rees, M.J. (1995). *Perspectives in Astrophysical Cosmology*. Cambridge: Cambridge University Press.
- Rees, M.J. (2006). Origin of cosmic magnetic fields, *Astronomische Nachrichten*, **327**, 395–398.
- Rees, M.J. and Ostriker, J.P. (1977). Cooling, dynamics and fragmentation of massive gas clouds – clues to the masses and radii of galaxies and clusters, *Monthly Notices of the Royal Astronomical Society*, **179**, 541–559.
- Rees, M.J. and Sciama, D.W. (1968). Large-scale density inhomogeneities in the Universe, *Nature*, **217**, 511–516.
- Refregier, A. (2003). Weak gravitational lensing by large-scale structure, *Annual Review of Astronomy and Astrophysics*, **41**, 645–668.
- Reimers, D., Clavel, J., Groote, D., Engels, D., Hagen, H.J., Naylor, T., Wamsteker, W., and Hopp, U. (1989). The luminous Quasar HS1700+6416 and the shape of the ‘Big Bump’ below 500 Å, *Astronomy and Astrophysics*, **218**, 71–77.
- Reiprich, T.H. and Böhringer, H. (2002). The mass function of an X-Ray Flux-limited sample of galaxy clusters, *Astrophysical Journal*, **567**, 716–740.
- Richards, G.T., Strauss, M.A., Fan, X., Hall, P.B., Jester, S., Schneider, D.P., Vanden Berk, D.E., Stoughton, C., Anderson, S.F., Brunner, R.J., Gray, J., Gunn, J.E., Ivezić, Ž., Kirkland, M.K., Knapp, G.R., Loveday, J., Meiksin, A., Pope, A., Szalay, A.S., Thakar, A.R., Yanny, B., York, D.G., Barentine, J.C., Brewington, H.J., Brinkmann, J., Fukugita, M., Harvanek, M., Kent, S.M., Kleinman, S.J., Krzesiński, J., Long, D.C., Lupton, R.H., Nash, T., Neilsen, Jr., E.H., Nitta, A., Schlegel, D.J., and Snedden, S.A. (2006). The Sloan Digital Sky Survey Quasar Survey: quasar luminosity function from data release 3, *Astronomical Journal*, **131**, 2766–2787.
- Rindler, W. (1956). Visual horizons in world models, *Monthly Notices of the Royal Astronomical Society*, **116**, 662–677.
- Rindler, W. (2001). *Relativity: Special, General and Cosmological*. Oxford: Oxford University Press.
- Roberts, M.S. and Haynes, M.P. (1994). Physical parameters along the Hubble Sequence, *Annual Review of Astronomy and Astrophysics*, **26**, 115–152.
- Robertson, H.P. (1935). Kinematics and world structure, *Astrophysical Journal*, **82**, 284–301.
- Rosati, P., Borgani, S., and Norman, C. (2002). The evolution of X-ray clusters of galaxies, *Annual Review of Astronomy and Astrophysics*, **40**, 539–577.

- Rowan-Robinson, M. (1968). The determination of the evolutionary properties of quasars by means of the luminosity-volume test, *Monthly Notices of the Royal Astronomical Society*, **141**, 445–458.
- Rowan-Robinson, M. (1985). *The Cosmological Distance Ladder*. New York: Freeman.
- Rowan-Robinson, M. (1988). The extragalactic distance scale, *Space Science Reviews*, **48**, 1–71.
- Rowan-Robinson, M., Benn, C.R., Lawrence, A., McMahon, R.G., and Broadhurst, T.J. (1993). The evolution of faint radio sources, *Monthly Notices of the Royal Astronomical Society*, **263**, 123–130.
- Rutherford, E. (1907). Some cosmical aspects of radioactivity, *Journal of the Royal Astronomical Society of Canada*, **1**, 145–165.
- Ryle, M. (1955). Radio stars and their cosmological significance, *The Observatory*, **75**, 137–147.
- Ryle, M. (1958). The nature of the cosmic radio sources, *Proceedings of the Royal Society*, **A248**, 289–308.
- Ryle, M. and Sandage, A.R. (1964). The optical identification of three new radio objects of the 3C 48 class, *Astrophysical Journal*, **139**, 419–421.
- Sachs, R. and Wolfe, A. (1967). Perturbations of a cosmological model and angular variations in the microwave background, *Astrophysical Journal*, **147**, 73–90.
- Sahu, K.C., Livio, M., Petro, L., Macchetto, F.D., van Paradijs, J., Kouveliotou, C., Fishman, G.J., Meegan, C.A., Groot, P.J., and Galama, T. (1997). The optical counterpart to gamma-ray burst GRB 970228 observed using the Hubble Space Telescope, *Nature*, **387**, 476–478.
- Sajina, A., Scott, D., Dennefeld, M., Dole, H., Lacy, M., and Lagache, G. (2006). The 1–1000 μm spectral energy distributions of far-infrared galaxies, *Monthly Notices of the Royal Astronomical Society*, **369**, 939–957.
- Sakharov, A. (1965). The initial stage of an expanding universe and the appearance of a nonuniform distribution of matter, *Zhurnal Eksperimentalnoi i Teoreticheskoi Fiziki*, **49**, 345–358. [English translation: *Soviet Physics JETP*, **22**, 241–249, 1966.]
- Sakharov, A. (1967). Violation of CP invariance, C asymmetry, and baryon asymmetry of the Universe, *Zhurnal Experimentalnoi i Teoreticheskikh Fizika (JETP) Letters*, **5**, 32–35.
- Sandage, A.R. (1961a). The ability of the 200-inch telescope to discriminate between selected world models, *Astrophysical Journal*, **133**, 355–392.
- Sandage, A.R. (1961b). *The Hubble Atlas of Galaxies*. Washington D.C.: Carnegie Institution of Washington. Publication 618.
- Sandage, A.R. (1965). The existence of a major new constituent of the Universe: the quasistellar galaxies, *Astrophysical Journal*, **141**, 1560–1578.
- Sandage, A.R. (1968). Observational cosmology, *The Observatory*, **88**, 91–106.
- Sandage, A.R. (1975). Classification and stellar content of galaxies obtained from direct photography, in *Stars and Stellar Systems*, **9. Galaxies and the Universe**, eds. A.R. Sandage, M.S. and Kristian, J., pp. 1–35. Chicago: Chicago University Press.

- Sandage, A.R. (1988). Observational tests of world models, *Annual Review of Astronomy and Astrophysics*, **26**, 561–630.
- Sandage, A.R. (1995). Practical cosmology: inventing the past, in *The Deep Universe*, by Sandage, A.R., Kron, R.G. and Longair, M.S., eds. Binggeli, B. and Buser, R., pp. 1–232. Berlin: Springer-Verlag.
- Sandage, A.R. and Hardy, E. (1973). The redshift-distance relation: VII. Absolute magnitudes of the first three ranked cluster galaxies as function of cluster richness and Bautz–Morgan cluster type: the effect on q_0 , *Astrophysical Journal*, **183**, 743–758.
- Sandage, A.R. and Schwarzschild, M. (1952). Inhomogeneous stellar models: II. Models with exhausted cores in gravitational contraction, *Astrophysical Journal*, **116**, 463–476.
- Sanders, D.B. and Mirabel, I.F. (1996). Luminous infrared galaxies, *Annual Review of Astronomy and Astrophysics*, **34**, 749–792.
- Saunders, W., Rowan-Robinson, M., Lawrence, A., Efstathiou, G., Kaiser, N., Ellis, R.S., and Frenk, C.S. (1990). The 60-micron and far-infrared luminosity functions of IRAS galaxies, *Monthly Notices of the Royal Astronomical Society*, **242**, 318–337.
- Savaglio, S., Glazebrook, K., Le Borgne, D., Juneau, S., Abraham, R.G., Chen, H.-W., Crampton, D., McCarthy, P.J., Carlberg, R.G., Marzke, R.O., Roth, K., Jørgensen, I., and Murowinski, R. (2005). The Gemini Deep Deep Survey: VII. The redshift evolution of the mass-metallicity relation, *Astrophysical Journal*, **635**, 260–279.
- Schechter, P. (1976). An analytic expression for the luminosity function of galaxies, *Astrophysical Journal*, **203**, 297–306.
- Schechter, P.L. (2002). Tales within tales and cutoffs within cutoffs: what sets the mass scale for galaxies?, in *Lighthouses of the Universe: The Most Luminous Objects and Their Use for Cosmology*, eds. Gilfanov, M., Sunyeav, R., and Churazov, E., pp. 3–12. Berlin: Springer.
- Scheuer, P.A.G. (1957). A statistical method for analysing observations of faint radio stars, *Proceedings of the Cambridge Philosophical Society*, **53**, 764–773.
- Scheuer, P.A.G. (1965). A sensitive test for the presence of atomic hydrogen in intergalactic space, *Nature*, **207**, 963.
- Scheuer, P.A.G. (1974). Fluctuations in the X-ray background, *Monthly Notices of the Royal Astronomical Society*, **166**, 329–338.
- Scheuer, P.A.G. (1990). Radio source counts, in *Modern Cosmology in Retrospect*, eds Bertotti, B., Balbinot, R., Bergia, S., and Messina, A., pp. 331–346. Cambridge: Cambridge University Press.
- Schindler, S., Binggeli, B., and Böhringer, H. (1999). Morphology of the Virgo cluster: gas versus galaxies, *Astronomy and Astrophysics*, **343**, 420–438.
- Schmidt, B.P., Kirshner, R.P., and Eastman, R.G. (1992). Expanding photospheres of type II supernovae and the extragalactic distance scale, *Astrophysical Journal*, **395**, 366–386.
- Schmidt, M. (1968). Space distribution and luminosity functions of quasi-stellar sources, *Astrophysical Journal*, **151**, 393–409.

- Schmidt, M. and Green, R.F. (1983). Quasar evolution derived from the Palomar Bright Quasar Survey and other complete quasar surveys, *Astrophysical Journal*, **269**, 352–374.
- Schmidt, M., Schneider, D.P., and Gunn, J.E. (1995). Spectroscopic CCD Surveys for Quasars at Large Redshift. IV. Evolution of the luminosity function from quasars detected by their Lyman-alpha emission, *Astronomical Journal*, **110**, 68–77.
- Schneider, D., Schmidt, M., and Gunn, J.E. (1991). PC 1247 + 3406 - an optically selected quasar with a redshift of 4.897, *Astronomical Journal*, **102**, 837–840.
- Schneider, P., Kochanek, C.S., and Wambsganss, J. (2006). *Gravitational Lensing: Strong, Weak and Micro*. Berlin: Springer. Saas-Fee Advanced Course 33: eds. Meylan, G. and Jetzer, P. and North, P.
- Schramm, D.N. (1997). The age of the Universe, in *Critical Dialogues in Cosmology*, ed. Turok, N., pp. 81–91. Singapore: World Scientific.
- Schramm, D.N. and Wasserburg, G.T. (1970). Nucleochronologies and the mean age of the elements, *Astrophysical Journal*, **162**, 57–69.
- Schutz, B. (2001). Gravitational radiation, in *Encyclopaedia of Astronomy and Astrophysics*, ed. P. M., volume 2, pp. 1030–1042. Bristol and Philadelphia: Institute of Physics Publishing and London: Nature Publishing Group.
- Schwarzchild, M. (1979). A numerical model for a triaxial stellar system in dynamical equilibrium, *Astrophysical Journal*, **232**, 236–228.
- Scott, J., Bechtold, J., Dobrzycki, A., and Kulkarni, V.P. (2000). A uniform analysis of the Ly α forest at $z = 0 – 5$: II. Measuring the mean intensity of the extragalactic ionizing background using the proximity effect, *Astrophysical Journal Supplement*, **130**, 67–89.
- Scranton, R., Johnston, D., Dodelson, S., Frieman, J., Connolly, A., Eisenstein, D., Gunn, J., Hui, L., Jain, B., Kent, S., Loveday, J., Narayanan, V., Nichol, R., O’Connell, L., Scoccimarro, R., Sheth, R., Stebbins, A., Strauss, M., Szalay, A., Szapudi, I., Tegmark, M., Vogeley, M., Zehavi, I., Annis, J., Bahcall, N., Brinkman, J., Csabai, I., Hindsley, R., Ivezić, Z., Kim, R., Knapp, G., Lamb, D., Lee, B., Lupton, R., McKay, T., Munn, J., Peoples, J., Pier, J., Richards, G., Rockosi, C., Schlegel, D., Schneider, D., Stoughton, C., Tucker, D., Yanny, B., and York, D. (2002). Analysis of systematic effects and statistical uncertainties in angular clustering of galaxies from early Sloan Digital Sky Survey Data, *Astrophysical Journal*, **579**, 48–75.
- Seager, S., Sasselov, D.D., and Scott, D. (2000). How exactly did the Universe become neutral?, *Astrophysical Journal Supplement*, **128**, 407–430.
- Seldner, M. and Peebles, P.J.E. (1977). Statistical analysis of catalogs of extragalactic objects: VIII. Cross-correlation of the Abell and the 10-arcmin Shane–Wirtanen catalogs, *Astrophysical Journal*, **215**, 703–716.
- Seljak, U., Makarov, A., McDonald, P., Anderson, S.F., Bahcall, N.A., Brinkmann, J., Burles, S., Cen, R., Doi, M., Gunn, J.E., Ivezić, Ž., Kent, S., Loveday, J., Lupton, R.H., Munn, J.A., Nichol, R.C., Ostriker, J.P., Schlegel, D.J., Schneider, D.P., Tegmark, M., Berk, D.E., Weinberg, D.H., and York, D.G. (2005). Cosmological parameter analysis including SDSS Ly α forest and galaxy bias: constraints on the

- primordial spectrum of fluctuations, Neutrino Mass, and Dark Energy, *Physical Review D*, **71**, 103515.
- Seljak, U. and Zaldarriaga, M. (1996). A line-of-sight integration approach to cosmic microwave background anisotropies, *Astrophysical Journal*, **469**, 437–444.
- Sérsic, J.L. (1968). *Atlas de galaxias australes*. Cordoba, Argentina: Observatorio Astronomico.
- Shapiro, I. (1990). Solar system tests of General Relativity: recent results and present plans, in *General Relativity and Gravitation*, eds. Ashby, N., Bartlett, D.F., and Wyss, W., pp. 313–330. Cambridge: Cambridge University Press.
- Shapiro, I.I. (1964). Fourth test of General Relativity, *Physical Review Letters*, **13**, 789–791.
- Shapiro, S.S., Davis, J.L., Lebach, D.E., and Gregory, J.S. (2004). Measurement of the solar gravitational deflection of radio waves using geodetic very-long-baseline interferometry data, 1979–1999, *Physical Review Letters*, **92**, 121101.
- Shapley, H. (1918). Studies Based on the Colors and Magnitudes in Stellar Clusters. VII. The distances, distribution in space, and dimensions of 60 globular clusters, *Astrophysical Journal*, **48**, 154–181.
- Shectman, S.A. (1974). The small scale anisotropy of the cosmic light, *Astrophysical Journal*, **188**, 233–242.
- Shellard, P. (2003). The future of cosmology: observational and computational prospects, in *The Future of Theoretical Physics and Cosmology*, eds. Gibbons, G., Shellard, E., and Rankin, S., pp. 755–780. Cambridge: Cambridge University Press.
- Sheth, R.K., Mo, H.J., and Tormen, G. (2001). Ellipsoidal collapse and an improved model for the number and spatial distribution of dark matter haloes, *Monthly Notices of the Royal Astronomical Society*, **323**, 1–12.
- Shimasaku, K., Ouchi, M., Furusawa, H., Yoshida, M., Kashikawa, N., and Okamura, S. (2005). Number density of bright Lyman-break galaxies at $z \sim 6$ in the Subaru Deep Field, *Publications of the Astronomical Society of Japan*, **57**, 447–458.
- Silk, J. (1968). Cosmic black-body radiation and galaxy formation, *Astrophysical Journal*, **151**, 459–471.
- Silk, J. and Wyse, R.F.G. (1993). Galaxy formation and Hubble sequence, *Physics Reports*, **231**, 293–365.
- Simon, P., Hetterscheidt, M., Schirmer, M., Erben, T., Schneider, P., Wolf, C., and Meisenheimer, K. (2007). GaBoDS: The Garching–Bonn Deep Survey: VI. Probing galaxy bias using weak gravitational lensing, *Astronomy and Astrophysics*, **461**, 861–879.
- Smail, I., Ivison, R.J., and Blain, A.W. (1997). A deep sub-millimeter survey of lensing clusters: a new window on galaxy formation and evolution, *Astrophysical Journal Letters*, **490**, L5–L8.
- Smith, R.W. (1982). *The Expanding Universe: Astronomy's 'Great Debate' 1900–1931*. Cambridge: Cambridge University Press.
- Smoot, G., Bennett, C., Kogut, A., Wright, E., Aymon, J., Boggess, N., Cheng, E., de Amici, G., Gulkis, S., Hauser, M., Hinshaw, G., Jackson, P., Janssen, M.,

- Kaita, E., Kelsall, T., Keegstra, P., Lineweaver, C., Loewenstein, K., Lubin, P., Mather, J., Meyer, S., Moseley, S., Murdock, T., Rokke, L., Silverberg, R., Tenorio, L., Weiss, R., and Wilkinson, D. (1992). Structure in the COBE differential microwave radiometer first-year maps, *Astrophysical Journal*, **396**, L1–L5.
- Sneden, C., McWilliam, A., Preston, G.W., Cowan, J.J., Burris, D.L., and Armosky, B.J. (1992). The ultra-metal-poor, neutron-capture-rich giant star CS 22892-052, *Astrophysical Journal*, **467**, 819–840.
- Songaila, A., Bryant, W., and Cowie, L.L. (1989). Limits on the galactic and cosmic ionizing fluxes from measurements of H- α emission from the high-velocity neutral hydrogen clouds, *Astrophysical Journal Letters*, **345**, L71–L73.
- Songaila, A., Cowie, L.L., Vogt, S., Keane, M., Wolfe, A.M., Hu, E.M., Oren, A.L., Tytler, D.R., and Lanzetta, K.M. (1994). Measurement of the microwave background temperature at a redshift of 1.776, *Nature*, **371**, 43–45.
- Songaila, A., Hu, E.M., and Cowie, L.L. (1995). A population of very diffuse Lyman- α clouds as the origin of the He $^+$ absorption signal in the intergalactic medium, *Nature*, **375**, 124–126.
- Soucail, G., Fort, B., Mellier, Y., and Picat, J.P. (1987). A blue ring-like structure, in the center of the A370 cluster of galaxies, *Astronomy and Astrophysics*, **172**, L14–L16.
- Sparke, L. and Gallagher, J. (2000). *Galaxies in the Universe: an Introduction*. Cambridge: Cambridge University Press.
- Spergel, D.N., Bean, R., Doré, O., Nolta, M.R., Bennett, C.L., Dunkley, J., Hinshaw, G., Jarosik, N., Komatsu, E., Page, L., Peiris, H.V., Verde, L., Halpern, M., Hill, R.S., Kogut, A., Limon, M., Meyer, S.S., Odegard, N., Tucker, G.S., Weiland, J.L., Wollack, E., and Wright, E.L. (2007). Three-year Wilkinson Microwave Anisotropy Probe (WMAP) observations: implications for cosmology, *Astrophysical Journal Supplement*, **170**, 377–408.
- Spinrad, H., Dey, A., and Graham, J.R. (1995). Keck observations of the most distant galaxy: 8C 1435+63 at $z = 4.25$, *Astrophysical Journal*, **438**, L51–L54.
- Spite, F. and Spite, M. (1982). Abundance of lithium in unevolved halo stars and old disk stars – interpretation and consequences, *Astronomy and Astrophysics*, **115**, 357–366.
- Springel, V. (2005). The cosmological simulation code GADGET-2, *Monthly Notices of the Royal Astronomical Society*, **364**, 1105–1134. For access to his simulations, see <http://www.mpa-garching.mpg.de/gadget/right.html>.
- Springel, V., White, S.D.M., Jenkins, A., Frenk, C.S., Yoshida, N., Gao, L., Navarro, J., Thacker, R., Croton, D., Helly, J., Peacock, J.A., Cole, S., Thomas, P., Couchman, H., Evrard, A., Colberg, J., and Pearce, F. (2005). Simulations of the formation, evolution and clustering of galaxies and quasars, *Nature*, **435**, 629–636.
- Srianand, R. (2006). Intergalactic medium, in *The Scientific Requirements for Extremely Large Telescopes: IAU Symposium No. 232*, eds. Whitelock, P., Dennefeld, M., and Leibundgut, B., pp. 130–139.
- Starobinsky, A.A. (1985). Cosmic background anisotropy induced by isotropic flat-spectrum gravitational-wave perturbations, *Soviet Astronomy Letters*, **11**, 133–137. In Russian: 1985, *Pis'ma v Astronomicheskii Zhurnal*, **11**, 323–330.

- Steidel, C. (1998). Galaxy evolution: has the “epoch of galaxy formation” been found?, in *Eighteenth Texas Symposium on Relativistic Astrophysics and Cosmology*, eds. Olinto, A., Frieman, J., and Schramm, D., pp. 124–135. River Edge, NJ: World Scientific.
- Steidel, C. and Hamilton, D. (1992). Deep imaging of high redshift QSO fields below the Lyman limit: I. The field of Q0000-263 and galaxies at $Z = 3.4$, *Astronomical Journal*, **104**, 941–949.
- Steidel, C.C., Adelberger, K.L., Giavalisco, M., Dickinson, M., and Pettini, M. (1999). Lyman-break galaxies at $z \geq 4$ and the evolution of the ultraviolet luminosity density at high redshift, *Astrophysical Journal*, **519**, 1–17.
- Steigman, G. (1997). The crisis confronting standard Big Bang nucleosynthesis, in *Critical Dialogues in Cosmology*, ed. Turok, N., pp. 63–80. Singapore: World Scientific.
- Steigman, G. (2004). Big Bang nucleosynthesis: probing the first 20 minutes, in *Measuring and Modeling the Universe*, ed. Freedman, W.L., pp. 169–195. Cambridge: Cambridge University Press.
- Steigman, G. (2006). Primordial nucleosynthesis: successes and challenges, *International Journal of Modern Physics E*, **15**, 1–35.
- Steigman, G. (2007). Primordial nucleosynthesis, *Annual Review of Nuclear and Particle Science*, **57**, (in press).
- Storrie-Lombardi, L., McMahon, R., and Irwin, M. (1996). Evolution of neutral gas at high redshift: implications for the epoch of galaxy formation, *Monthly Notices of the Royal Astronomical Society*, **283**, L79–L83.
- Stoughton, D., Lupton, R.H., and 191 authors (2002). Sloan Digital Sky Survey: early data release, *Astronomical Journal*, **123**, 485–548.
- Strömborg, G. (1934). The origin of the galactic rotation and of the connection between physical properties of the stars and their motions, *Astrophysical Journal*, **79**, 460–474.
- Subramanian, K. (2005). The physics of CMBR anisotropies, *Current Science*, **88**, 1068–1087.
- Sullivan, III, W.T. (1990). The entry of radio astronomy into cosmology: radio stars and Martin Ryle’s 2C survey, in *Modern Cosmology in Retrospect*, eds. Bertotti, B., Balbinot, R., Bergia, S., and Messina, A., pp. 309–330. Cambridge: Cambridge University Press.
- Sunyaev, R. and Zeldovich, Y. (1970). Small-scale fluctuations of relic radiation, *Astrophysics and Space Science*, **7**, 3–19.
- Sunyaev, R.A. (1969). The interaction of the metagalactic ultraviolet background radiation with galaxies and the limit on the density of the intergalactic gas, *Astrophysical Letters*, **3**, 33–38.
- Sunyaev, R.A. and Zeldovich, Y.B. (1972). Formation of clusters of galaxies; protocluster fragmentation and intergalactic gas heating, *Astronomy and Astrophysics*, **20**, 189–200.
- Sunyaev, R.A. and Zeldovich, Y.B. (1980a). Microwave background radiation as a probe of the contemporary structure and history of the Universe, *Annual Review of Astronomy and Astrophysics*, **18**, 537–560.

- Sunyaev, R.A. and Zeldovich, Y.B. (1980b). The velocity of clusters of galaxies relative to the microwave background – the possibility of its measurement, *Monthly Notices of the Royal Astronomical Society*, **190**, 413–420.
- eds. Tanvir, N.R., Aragon-Salamanca, A., and Wall, J.V. (1997). *The Hubble Space Telescope and the High Redshift Universe*. Singapore: World Scientific.
- Taylor, R.J. (1994). *The Stars: Their Structure and Evolution*. Cambridge: Cambridge University Press.
- Taylor, G.B. and Wright, E.L. (1989). Effects of a hot intergalactic medium, *Astrophysical Journal*, **339**, 619–628.
- Taylor, J.H. (1992). Pulsar timing and relativistic gravity, *Philosophical Transactions of the Royal Society*, **341**, 117–134.
- Taylor, J.H. and Cordes, J.M. (1993). Pulsar distances and the galactic distribution of free electrons, *Astrophysical Journal*, **411**, 674–684.
- Tegmark, M., Strauss, M., and 66 authors (2004). Cosmological parameters from SDSS and WMAP, *Physical Review D*, **69**, 103501 (1–28).
- Thorne, K., Price, R., and Macdonald, D. (1986). *Black Holes: The Membrane Paradigm*. New Haven: Yale University Press.
- Tinsley, B.M. (1980). Evolution of the stars and gas in galaxies, *Fundamentals of Cosmic Physics*, **5**, 287–388.
- Tinsley, B.M. and Gunn, J.E. (1976). Luminosity functions and the evolution of low-mass population: I. Giants, *Astrophysical Journal*, **206**, 525–535.
- Toller, G.N. (1990). Optical observations of galactic and extragalactic light – implications for galactic structure, in *The Galactic and Extragalactic Background Radiation*, eds. Bowyer, S. and Leinert, C., IAU Symposium No. 139, pp. 21–34. Dordrecht: Kluwer.
- Tolman, R. (1934). Effect of inhomogeneity on cosmological models, *Proceedings of the National Academy of Sciences*, **20**, 169–176.
- Tonks, L. and Langmuir, I. (1929). Oscillations in ionized gases, *Physical Review*, **33**, 195–210.
- Tonry, J., Schmidt, B., Barris, B., Candia, P., Challis, P., Clocchiatti, A., Coil, A., Filippenko, A., Garnavich, P., Hogan, C., Holland, S., Jha, S., Kirshner, R., Krisciunas, K., Leibundgut, B., Li, W., Matheson, T., Phillips, M., Riess, A., Schommer, R., Smith, R., Sollerman, J., Spyromilio, J., Stubbs, C., and Suntzeff, N. (2003). Cosmological results from high-z supernovae, *Astrophysical Journal*, **594**, 1–24.
- Toomre, A. (1974). Gravitational interactions between galaxies, in *IAU Symposium No. 58: The Formation and Dynamics of Galaxies*, ed. Shakeshaft, J., pp. 347–365. Dordrecht: D. Reidel Publishing Company
- Toomre, A. and Toomre, J. (1972). Galactic bridges and tails, *Astrophysical Journal*, **178**, 623–666.
- Tremaine, S. and Gunn, J. (1979). Dynamical role of light neutral leptons in cosmology, *Physical Review Letters*, **42**, 407–410.
- Tremaine, S. and Richstone, D.O. (1977). A test of a statistical model for the luminosities of bright cluster galaxies, *Astrophysical Journal*, **212**, 311–316.

- Tremonti, C.A., Heckman, T.M., Kauffmann, G., Brinchmann, J., Charlot, S., White, S.D.M., Seibert, M., Peng, E.W., Schlegel, D.J., Uomoto, A., Fukugita, M., and Brinkmann, J. (2004). The origin of the mass-metallicity relation: insights from 53,000 star-forming galaxies in the Sloan Digital Sky Survey, *Astrophysical Journal*, **613**, 898–913.
- Trimble, V. (1995). The 1920 Shapley–Curtis discussion: background, issues, and aftermath, *Publications of the Astronomical Society of the Pacific*, **107**, 1133–1144.
- Trodden, M. (2006). Physics of the very early Universe: what can we learn from particle collider experiments?, *Proceedings of Science*, **CMB2006**, 1–9. This electronic publication can be found at <http://pos.sissa.it/archive/conferences/027/003/CMB2006-003.pdf>.
- Tropp, E., Frenkel, V., and Chernin, A. (1993). *Alexander A. Friedmann: the Man who Made the Universe Expand*. Cambridge: Cambridge University Press.
- Trushkin, S.A. (2003). Radio spectra of the WMAP catalog sources, *Bulletin of the Special Astrophysical Observatory*, **55**, 90–132.
- Tully, R.B. and Fisher, J.R. (1977). A new method of determining distances to galaxies, *Astronomy and Astrophysics*, **54**, 661–673.
- Turner, M. (1997). Inflationary cosmology, in *Relativistic Astrophysics*, eds Jones, B.J.T. and Markovic, D., pp. 83–102. Cambridge: Cambridge University Press.
- Turok, N. (1989). Global texture as the origin of cosmic structure, *Physical Review Letters*, **63**, 2625–2628.
- ed. Turok, N. (1997). *Critical Dialogues in Cosmology*. Singapore: World Scientific.
- Tyson, J.A., Kochanski, G.P., and dell’Antonio, I.P. (1998). Detailed mass map of CL 0024+1654 from strong lensing, *Astrophysical Journal Letters*, **498**, L107–L110.
- Vallée, J.P. (1997). Observations of the magnetic fields inside and outside the Milky Way, starting with globules (~ 1 parsec), filaments, clouds, superbubbles, spiral arms, galaxies, superclusters, and ending with the cosmological Universe’s background surface (at ~ 8 teraparsecs), *Fundamentals of Cosmic Physics*, **19**, 1–89.
- van den Bergh, S. (1998). *Galaxy Morphology and Classification*. Cambridge: Cambridge University Press.
- Verde, L., Heavens, A.F., Percival, W.J., Matarrese, S., Baugh, C.M., Bland-Hawthorn, J., Bridges, T., Cannon, R., Cole, S., Colless, M., Collins, C., Couch, W., Dalton, G., De Propris, R., Driver, S.P., Efstathiou, G., Ellis, R.S., Frenk, C.S., Glazebrook, K., Jackson, C., Lahav, O., Lewis, I., Lumsden, S., Maddox, S., Madgwick, D., Norberg, P., Peacock, J.A., Peterson, B.A., Sutherland, W., and Taylor, K. (2002). The 2dF Galaxy Redshift Survey: the bias of galaxies and the density of the Universe, *Monthly Notices of the Royal Astronomical Society*, **335**, 432–440.
- Vishniac, E.T. (1987). Reionization and small-scale fluctuations in the microwave background, *Astrophysical Journal*, **322**, 597–604.

- Visvanathan, N. and Sandage, A.R. (1977). The color-absolute magnitude relation for E and S0 galaxies: I. Calibration and tests for universality using Virgo and eight other nearby clusters, *Astrophysical Journal*, **216**, 214–226.
- Vogel, S. and Reimers, D. (1995). The ultraviolet absorption spectrum of the $Z = 2.72$ QSO HS 1700+6416: 1. Results on heavy-element absorption systems, *Astronomy and Astrophysics*, **294**, 377–410.
- von Weizsächer, C.F. (1947). Zur Kosmogonie, *Zeitschrift für Astrophysik*, **24**, 181–206.
- Waddington, I., Dunlop, J.S., Peacock, J.A., and Windhorst, R.A. (2001). The LBDS Hercules sample of mJy radio sources at 1.4 GHz – II. Redshift distribution, radio luminosity function, and the high-redshift cut-off, *Monthly Notices of the Royal Astronomical Society*, **328**, 882–896.
- Wagoner, R., Fowler, W., and Hoyle, F. (1967). On the synthesis of elements at very high temperatures, *Astrophysical Journal*, **148**, 3–49.
- Wagoner, R.V. (1973). Big-Bang nucleosynthesis revisited, *Astrophysical Journal*, **179**, 343–360.
- Walker, A.G. (1936). On Milne's theory of world structure, *Proceedings of the London Mathematical Society, Series 2*, **42**, 90–127.
- Wall, J.V. (1996). Space distribution of radio source populations, in *Extragalactic Radio Sources, IAU Symposium No. 175*, eds. Ekers, R., Fanti, C., and Padrielli, L., pp. 547–552. Dordrecht: Kluwer.
- Walsh, D., Carswell, R.F., and Weymann, R.J. (1979). 0957+561A, B – twin quasistellar objects or gravitational lens, *Nature*, **279**, 381–384.
- Wambsganss, J. (1998). Gravitational lensing in astronomy, *Living Review in Relativity*, **1**. Online article: accepted 28 August 1998; last amended 31 August 2001 <http://www.livingreviews.org/lrr-1998-12>.
- Wang, W.-H., Cowie, L.L., and Barger, A.J. (2006). A near-infrared analysis of the submillimeter background and the cosmic star-formation history, *Astrophysical Journal*, **647**, 74–85.
- Warren, S.J., Hewett, P.C., Irwin, M.J., McMahon, R.G., and Bridgeland, M.T. (1987). First observation of a quasar with a redshift of 4, *Nature*, **325**, 131–133.
- Weedman, D. (1994). Starburst galaxies at high redshift, in *First Stromlo Symposium: Physics of Active Galactic Nuclei*, eds. Bicknell, G., Dopita, M., and Quinn, P., pp. 409–415. San Francisco: Astronomical Society of the Pacific Conference Series, Vol. 34.
- Weinberg, S. (1972). *Gravitation and Cosmology*. New York: Wiley.
- Weinberg, S. (1989). The cosmological constant problem, *Reviews of Modern Physics*, **61**, 1–23.
- Weinberg, S. (1997). Theories of the cosmological constant, in *Critical Dialogues in Cosmology*, ed. Turok, N., pp. 195–203. Singapore: World Scientific.
- Weinheimer, C. (2001). Neutrino mass from tritium β -Decay, in *Dark Matter in Astro- and Particle Physics, Proceedings of the International Conference DARK 2000*, ed. Klapdor-Kleingrothaus, H.V., pp. 513–519. Berlin: Springer-Verlag.
- Weiss, R. (1980). Measurements of the cosmic background radiation, *Annual Review of Astronomy and Astrophysics*, **18**, 489–535.

- Wesselink, A.J. (1947). The Observations of Brightness, Colour and Radial Velocity of δ -Cephei and the pulsation hypothesis, *Bulletin of the Astronomical Institutes of the Netherlands*, **10**, 91–99. Errata, **10**, 258 and 310.
- Weyl, H. (1923). Zur allgemeinen Relativitätstheorie (On the Theory of General Relativity), *Physikalische Zeitschrift*, **29**, 230–232.
- Weymann, R. (1966). The energy spectrum of radiation in the expanding Universe, *Astrophysical Journal*, **145**, 560–571.
- Weymann, R. (1967). Possible thermal histories of intergalactic gas, *Astrophysical Journal*, **147**, 887–900.
- Wheeler, J. (1977). Genesis and observership, in *Foundational Problems in the Special Science*, eds. Butts, R. and Hintikka, J., pp. 3–33. Dordrecht: Reidel.
- White, D.A., Fabian, A.C., Allen, S.W., Edge, A.C., Crawford, C.S., Johnstone, R.M., Stewart, G.C., and Voges, W. (1994). A ROSAT HRI observation of the ABELL:478 cluster of galaxies, *Monthly Notices of the Royal Astronomical Society*, **269**, 589–606.
- White, S.D. (1989). Observable signatures of young galaxies, in *The Epoch of Galaxy Formation*, eds. Frenk, C.S., Ellis, R.S., Shanks, T., Heavens, A.F., and Peacock, J.A., pp. 15–30. Dordrecht: Kluwer.
- White, S.D.M. (1990). Physical cosmology, in *Physics of the Early Universe*, eds Peacock, J.A., Heavens, A.F., and Davies, A.T., pp. 1–62. Edinburgh: SUSSP.
- White, S.D.M. and Rees, M.J. (1978). Core condensation in heavy halos – a two-stage theory for galaxy formation and clustering, *Monthly Notices of the Royal Astronomical Society*, **183**, 341–358.
- Wilkinson, P.N., Henstock, D.R., Browne, I.W., Polatidis, A.G., Augusto, P., Readhead, A.C., Pearson, T.J., Xu, W., Taylor, G.B., and Vermeulen, R.C. (2001). Limits on the cosmological abundance of supermassive compact objects from a search for multiple imaging in compact radio sources, *Physical Review Letters*, **86**, 584–587.
- Will, C. (1993). *Theory and Experiment in Gravitational Physics*. Cambridge: Cambridge University Press.
- Will, C.M. (2006). The confrontation between General Relativity and experiment, *Living Reviews in Relativity*, **9**. Online article: cited on 21 June 2006 <http://www.livingreviews.org/lrr-2006-3>.
- Williams, J.G., Turyshev, S.G., and Boggs, D.H. (2004). Progress in lunar laser ranging tests of relativistic gravity, *Physical Review Letters*, **93**, 261101, 1–4.
- eds. Williams, P., Shu, C.-G., and Ménard, B. (2005). *Probing Galaxies through Quasar Absorption Lines*. Cambridge: Cambridge University Press.
- Williams, R.E., Baum, S., Bergeron, L.E., Bernstein, N., Blacker, B.S., Boyle, B.J., Brown, T.M., Carollo, C.M., Casertano, S., Covarrubias, R., de Mello, D.F., Dickinson, M.E., Espey, B.R., Ferguson, H.C., Fruchter, A., Gardner, J.P., Gonnella, A., Hayes, J., Hewett, P.C., Heyer, I., Hook, R., Irwin, M., Jones, D., Kaiser, M.E., Levay, Z., Lubenow, A., Lucas, R.A., Mack, J., MacKenty, J.W., Madau, P., Makidon, R.B., Martin, C.L., Mazzuca, L., Mutchler, M., Norris, R.P., Perriello, B., Phillips, M.M., Postman, M., Royle, P., Sahu, K., Savaglio, S., Sherwin, A., Smith, T.E., Stiavelli, M., Suntzeff, N.B., Teplitz, H.I., van der

- Marel, R.P., Walker, A.R., Weymann, R.J., Wiggs, M.S., Williger, G.M., Wilson, J., Zacharias, N., and Zurek, D.R. (2000). The Hubble Deep Field South: formulation of the observing campaign, *Astronomical Journal*, **120**, 2735–2746.
- Williams, R.E., Blacker, B., Dickenson, M., Dixon, W.V.D., Ferguson, H.C., Fruchter, A.S., Giavalisco, M., Gilliland, R.L., Heyer, I., Katsanis, R., Levay, Z., Lucas, R.A., McElroy, D.B., Petro, L., Postman, M., Adorf, H.M., and Hook, R.N. (1996). The Hubble Deep Field: observations, data reduction, and galaxy photometry, *Astronomical Journal*, **112**, 1335–1389.
- Windhorst, R.A., Dressler, A., and Koo, D.A. (1987). Ultradeep optical identifications and spectroscopy of faint radio sources, in *Observational Cosmology*, eds. Hewitt, A., Burbidge, G., and Fang, L.-Z., pp. 573–576. Dordrecht: Reidel.
- Windhorst, R.A., Fomalont, E.B., Kellermann, K.I., Partridge, R.B., Richards, E., Franklin, B.E., Pascerelle, S.M., and Griffiths, R.E. (1995). Identification of faint radio sources with optically luminous interacting disk galaxies, *Nature*, **375**, 471–474.
- Wolfe, A. (1988). Damped Ly- α absorption systems, in *QSO Absorption Lines: Probing the Universe*, eds. Blades, J., Turnshek, D., and Norman, C., pp. 306–317. Cambridge: Cambridge University Press.
- Woltjer, L. (1990). Phenomenology of active galactic nuclei, in *Saas-Fee Advanced Course 20. Active Galactic Nuclei*, eds. Courvoisier, T.J.-L. and Mayor, M., pp. 1–55. Berlin: Springer-Verlag.
- Wood-Vasey, W.M., Miknaitis, G., Stubbs, C.W., Jha, S., Riess, A.G., Garnavich, P.M., Kirshner, R.P., Aguilera, C., Becker, A.C., Blackman, J.W., Blondin, S., Challis, P., Clocchiatti, A., Conley, A., Covarrubias, R., Davis, T.M., Filippenko, A.V., Foley, R.J., Garg, A., Hicken, M., Krisciunas, K., Leibundgut, B., Li, W., Matheson, T., Miceli, A., Narayan, G., Pignata, G., Prieto, J.L., Rest, A., Salvo, M.E., Schmidt, B.P., Smith, R.C., Sollerman, J., Spyromilio, J., Tonry, J.L., Suntzeff, N.B., and Zenteno, A. (2007). Observational constraints on the nature of the dark energy: first cosmological results from the ESSENCE Supernova Survey, *Astrophysical Journal*, **666**, 294–715.
- Zaldarriaga, M. (1997). Polarization of the microwave background in reionized models, *Physical Review*, **D55**, 1822–1829.
- Zaldarriaga, M. (2004). The polarization of the cosmic microwave background, in *Measuring and Modeling the Universe*, ed. Freedman, W.L., pp. 309–329. Cambridge: Cambridge University Press.
- Zaritsky, D., Kennicutt, R.C., and Huchra, J.P. (1994). H II regions and the abundance properties of spiral galaxies, *Astrophysical Journal*, **420**, 87–109.
- Zekser, K.C., White, R.L., Broadhurst, T.J., Benítez, N., Ford, H.C., Illingworth, G.D., Blakeslee, J.P., Postman, M., Jee, M.J., and Coe, D.A. (2006). Mass modeling of Abell 1689 Advanced Camera for surveys observations with a perturbed Navarro-Frenk-White model, *Astrophysical Journal*, **640**, 639–661.
- Zeldovich, Y. (1965). Survey of modern cosmology, *Advances of Astronomy and Astrophysics*, **3**, 241–379.
- Zeldovich, Y. (1970). Gravitational instability: an approximate theory for large density perturbations, *Astronomy and Astrophysics*, **5**, 84–89.

- Zeldovich, Y. (1972). A hypothesis, unifying the structure and the entropy of the universe, *Monthly Notices of the Royal Astronomical Society*, **160**, 1P–3P.
- Zeldovich, Y. (1986). Cosmological field theory for observational astronomers, *Astrophysics and Space Physics Reviews*, **5**, 1–37.
- Zeldovich, Y. and Sunyaev, R. (1969). The interaction of matter and radiation in a hot-model universe, *Astrophysics and Space Science*, **4**, 301–316.
- Zeldovich, Y.B. (1964). Observations in a Universe homogeneous in the mean, *Astronomicheskii Zhurnal*, **41**, 19–24. [Translation: (1964), *Soviet Astronomy*, **8**, 13–16].
- Zeldovich, Y.B. (1968). The cosmological constant and the theory of elementary particles, *Uspekhi Fizicheskikh Nauk*, **95**, 209–230. [Translation: (1968) *Soviet Physics – Uspekhi*, **11**, 381–393.]
- Zeldovich, Y.B. (1993). Particles, nuclei and the Universe, in *Selected Works of Yakov Borisovich Zeldovich*, Vol. 2., eds. Ostriker, J., Barenblatt, G., and Sunyaev, R. Princeton: Princeton University Press.
- Zeldovich, Y.B., Kurt, D., and Sunyaev, R.A. (1968). Recombination of hydrogen in the hot model of the Universe, *Zhurnal Eksperimentalnoi i Teoreticheskoi Fiziki*, **55**, 278–286. Translation: (1969), *Soviet Physics – JETP*, **28**, 146–150.
- Zeldovich, Y.B. and Novikov, I.D. (1983). *Relativistic astrophysics*, Vol. 2. Chicago: Chicago University Press.
- Zeldovich, Y.B. and Sunyaev, R.A. (1980). The angular distribution of the microwave background, and its intensity in the direction of galaxy clusters, *Soviet Astronomy Letters*, **6**, 285–286.
- Zwicky, F. (1937). On the masses of nebulae and of clusters of nebulae, *Astrophysical Journal*, **86**, 217–246.

Name Index

- Aaronson, Marc 246
Abell, George 81, 95, 101, 102
Abraham, Robert 540
Adams, Walter 177, 178
Albrecht, Andreas 24, 629
Alpher, Ralph 14
Aragón-Salamanca, Alfonso 253, 544
Arnaud, Monique 117
Arp, Halton 56
- Baade, Walter 13, 248
Babbage, Thomas 536
Bahcall, John 568
Bahcall, Neta 99, 100, 108, 267, 387
Bajtlik, Stanislaw 568, 569
Balzano, Vicki 597
Barcons, Xavier 561
Bardeen, James 348, 349, 394–396, 402
Barger, Amy 597, 598
Barnes, Joshua 611
Barrow, John 625
Baugh, Carlton 615
Baumann, Daniel 630, 631, 634, 636–638, 640
Bautz, Laura 109
Becker, Robert 552
Beckwith, Steven 543, 590, 592, 593, 596
Benson, Bradford 404
Bentley, Richard 4
Bergeron, Jacqueline 479, 489, 593
Berkeley, Bishop 11
Bertschinger, Edmund 348, 349, 638
Bessel, Friedrich 5
Biermann, Ludwig 579
Binggeli, Bruno 78, 82, 116
Binney, James 108
Blain, Andrew 452, 534
Bland-Hawthorn, Jonathan 539
- Blandford, Roger 228, 229
Bludman, Sydney 24, 626
Blumenthal, George 481
Bolte, Michael 250, 251
Bolyai, János 11, 151
Bond, Richard 20, 375, 396, 398, 399
Bondi, Hermann 149, 150, 341
Borgani, Stefano 531
Bouwens, Rychard 592, 593
Bowyer, Stuart 506
Boyle, Brian 521
Boyle, Robert 4
Bracessi, Alessandro 519
Bracewell, Ronald 433
Braginsky, Vladimir 174
Brahe, Tycho 3
Brainerd, Tereasa 138
Branch, David 248
Brandt, W. Niel 524, 525, 527
Bruzual, Gustavo 498, 499, 587, 588, 594, 607–609
Burbidge, Geoffrey 14
Burbidge, Margaret 14
Burstein, David 269
Butcher, Harvey 543
- Cappelluti, Nico 529
Carroll, Sean 265, 324
Carswell, Robert 249
Carter, Brandon 625
Cayley, Arthur 11, 151
Chaboyer, Brian 250, 251
Challinor, Anthony 126, 422, 441, 449, 452, 454
Chambers, Kenneth 254
Charlot, Stéphane 498, 499, 594, 607–609
Chluba, Jens 423
Chwolson, Orest 128

- Cimatti, Andrea 542, 608, 609
 Clausius, Rudolph 64
 Clifford, William 11, 151
 Cole, Shaun 405
 Coles, Peter 331, 332, 354, 358, 360, 377,
 382, 402, 474
 Colless, Matthew 113
 Corbelli, Edvige 568
 Cowan, John 252
 Cowie, Lennox 272, 534, 542, 566, 586,
 587, 589, 590, 598
 Crommelin, Andrew 190
 Croom, Scott 387
- Dashevsky, Vladimir 233
 Davidsen, Arthur 550, 564, 566
 Davies, Roger 612
 Davis, Tamara 339, 342, 347
 de Bruyn, Ger 580
 de Sitter, Willem 12, 149
 de Vaucouleurs, Gérard 49, 51, 54, 246
 Dekel, Avni 268, 269, 402
 Descartes, René 5
 Dessauges-Zavadsky, Miroslava 603, 604
 Dicke, Robert 174, 621, 622
 Dickinson, Mark 545
 Disney, Michael 62
 Dodds, Stephen 405, 409, 415, 416, 439
 Dodelson, Scott 348, 350, 367, 368, 371,
 416, 422, 438, 440, 443, 445, 446,
 454, 614
 Doroshkevich, Andrei 18, 360
 Dressler, Alan 56, 102, 108, 404
 Dreyer, John 7
 Dunlop, James 516, 609
 Dunn, Andrew 113
 Dyer, Charles 233–235
- Eales, Stephen 255
 Eastman, Ronald 248
 Eddington, Arthur 13, 177, 178, 190
 Efstathiou, George 143, 173, 184, 313,
 358, 398, 399, 403, 408, 417, 439,
 443, 453, 484, 487, 611
 Einstein, Albert 11, 12, 128, 149, 151,
 173, 174, 181, 182, 184, 188, 199,
 204, 207
 Eisenstein, Daniel 409, 411, 412
 Ellis, George 348
- Ellis, Richard 130, 253, 259, 537, 538,
 542
 Ellis, Simon 539
 Eötvös, Lóránd 174
- Faber, Sandra 74
 Fabian, Andrew 122–124, 561
 Fabricant, Donald 115
 Fall, Michael 568, 598, 604–606, 611, 612
 Fan, Xiaohui 522, 524
 Faulkner, John 14
 Fechner, Cora 567
 Felten, James 77, 78, 509
 Fisher, Richard 73
 Fomalont, Edward 506
 Fort, Bernard 134, 136
 Fowler, William 14, 293
 Freedman, Wendy 247, 250
 Freeman, Kenneth 62, 612
 Frenk, Carlos 400, 401
 Friedman, Aleksander 12, 13, 149, 202,
 204
 Furlanetto, Steven 574, 576, 577
- Galilei, Galileo 5
 Gamow, George 13, 14
 Garnavich, Peter 257
 Gauss, Carl Friedrich 11, 151, 156
 Gavazzi, Raphaël 138
 Ge, Jian 273
 Geller, Margaret 109
 Gerling, Christian 11
 Gershtein, Semion 19
 Giacconi, Riccardo 524
 Giavalisco, Mauro 592
 Gibbons, Gary 25
 Gilli, Roberto 526, 528, 529
 Glazebrook, Karl 607
 Goobar, Ariel 257
 Gorenstein, Paul 115
 Gott, Richard 41, 42
 Govoni, Federica 580
 Green, Richard 519, 521
 Gregory, James 4
 Greve, Thomas 479
 Gribben, John 625
 Grossmann, Marcel 181, 182
 Groth, Edward 35

- Gunn, James 20, 111–113, 144, 267, 268,
499, 549
- Gurvits, Leonid 263
- Guth, Alan 24, 364, 626, 627, 639
- Guzzo, Luigi 531
- Hale, George Ellery 9
- Hamilton, Andrew 408, 409, 472
- Hardy, Eduardo 253
- Harrison, Edward 17, 392, 510
- Hasinger, Günther 506, 524, 525, 527
- Hauser, Michael 535, 587
- Hausman, Marc 544
- Hawking, Stephen 25, 643, 644
- Hawkins, Michael 521
- Haynes, Martha 84
- Heath, D. 324
- Heavens, Alan 402, 475
- Helfand, David 42
- Herman, Robert 14
- Hernquist, Lars 572
- Herschel, Caroline 7
- Herschel, John 7
- Herschel, William 5–7
- Hewish, Antony 504, 506
- Hewitt, Jacqueline 140
- Hinshaw, Gary 451
- Hogan, Craig 298
- Hoyle, Fiona 42
- Hoyle, Fred 14, 293
- Hu, Esther 555
- Hu, Wayne 409, 411, 415, 422, 426, 438,
443, 445, 447, 448, 454, 462, 463
- Hubble, Edwin 8–10, 44–46, 162, 267,
492–494
- Huggins, William 7
- Humason, Milton 9, 45
- Huygens, Christiaan 11
- Ikeuchi, Satoru 555
- Ivison, Robert 452
- Jakobsen, Peter 564, 566, 569, 571
- Jeans, James 4, 16, 313, 317
- Jones, Bernard 610
- Kaiser, Nicholas 136, 235, 402, 406, 407,
460
- Kant, Immanuel 5
- Kapahi, Vijay 261
- Kapteyn, Jacobus 7, 8
- Kashlinsky, Alexander 507
- Katz, Neal 572
- Kauffmann, Guinevere 417, 545
- Kellermann, Kenneth 263
- Kennicutt, Robert 87, 554, 616
- Kent, Stephen 111–113
- Kepler, Johannes 3
- Kibble, Thomas 628
- King, Ivan 107
- Kirshner, Robert 248
- Kneib, Jean-Pierre 130
- Kochanek, Christopher 130, 138
- Kogut, Alan 432
- Kolb, Rocky 143, 301, 303, 307, 369, 376,
397, 402, 642
- Kompaneets, Aleksander 17
- Koo, David 519
- Kooiman, Brian 42
- Kormendy, John 49, 51
- Kriss, Gerard 566
- Kron, Richard 519
- Kulkarni, Varsha 568, 601, 603
- Kulsrud, Russell 578–581
- Kundic, Tomislav 249
- Kurt, Vladimir 423, 563
- Kwan, John 248
- Lacy, Mark 610
- Lagache, Guilane 533, 536
- Lambert, Johann 5, 11, 150
- Lanczos, Cornelius 149
- Langmuir, Irving 317
- Lanzetta, Kenneth 601
- Larson, Richard 606
- Lasenby, Anthony 126
- Le Verrier, Urbain 189
- Leavitt, Henrietta 7, 8
- Lecar, Myron 115
- Ledoux, Cédric 273
- Lemaître, Georges 4, 13, 16, 204, 207,
322, 333
- Liddle, Andrew 25, 348, 349, 629, 630
- Lifshitz, Evgenii 4, 16, 313, 322, 333
- Lightman, Alan 268, 329
- Lilly, Simon 254, 587, 589, 590, 609
- Linde, Andrei 24, 626, 629

- Lineweaver, Charles 339, 342, 347, 427, 626
 Lobachevsky, Nikolai 11, 151
 Longair, Malcolm 534
 Lotz, Jennifer 594
 Lucchin, Francesco 331, 332, 354, 358, 360, 377, 382, 402, 474
 Lynden-Bell, Donald 399, 474
 Lynds, Roger 130
 Lyth, David 25, 348, 349, 629, 630
 Lyubimov, Valentin 19, 369
- Ma, Chung-Pei 349
 Mach, Ernst 11
 Madau, Piero 590, 596, 606
 Maeder, André 250
 Majewski, Steven 521
 Maloney, Philip 568
 Marshall, Francis 561
 Martin, Christopher 506
 Marx, Györgi 19
 Mather, John 561
 Mazzarella, Joseph 597
 McCarthy, Patrick 254, 607, 608
 McCrea, William 202, 624
 McDonald, Patrick 557
 Mellier, Yannick 134, 136
 Merritt, David 111–113
 Messier, Charles 7
 Metcalfe, Nigel 538
 Michell, John 5, 6
 Miley, George 254, 261
 Milne, Ernest 202
 Miralda-Escudé, Jordi 572
 Monaco, Pierluigi 485–487
 Morgan, William 109
 Mould, Jeremy 246
 Mukhanov, Vyechislav 368
 Møller, Palle 569, 571
- Narajan, Ramesh 228, 229
 Naselsky, Pavel 368
 Newton, Isaac 4, 174
 Norberg, Peder 404, 405
 Novikov, Dmitry 368
 Novikov, Igor 17, 303, 304, 362, 368
 Oemler, Augustus 102, 543
 Okamoto, Takemi 462, 463
- Olbers, Heinrich 510
 Oort, Jan 267
 Osmer, Patrick 521
 Ostriker, Jeremiah 69, 479, 481, 486, 544, 556, 612, 616
- Padmanabhan, Thanu 332, 354, 409, 438, 442
 Page, Lyman 29, 459
 Pagel, Bernard 604
 Pais, Abraham 184
 Panagia, Nino 248
 Parker, Eugene 578–581
 Partridge, Bruce 19
 Patchett, Bruce 248
 Payne, Cecilia 14
 Peacock, John 269, 348, 368, 390, 396, 398, 402, 405–407, 409, 415, 416, 439, 442, 475, 516
 Peebles, James 17, 20, 35, 37, 69, 100, 283, 357, 360, 363, 375, 386, 423, 432, 433, 439, 443, 445, 610–612, 616, 622
 Pei, Yichuan 604–606
 Penrose, Roger 644
 Penzias, Arno 15, 27
 Perlmutter, Saul 257
 Peterson, Bruce 549
 Petrosian, Vahe 130, 504
 Pettini, Max 601–603
 Pi, So-Young 639
 Postman, Marc 109
 Pound, Robert 178
 Pozdnyakov, Lev 281
 Pratt, Gabriel 117
 Press, William 363, 472, 482–485
 Pritchard, Jonathan 576, 577
 Prochaska, Jason 603, 604
 Puget, Jean-Loup 535, 587
- Rawlings, Stephen 255
 Rebka, Glen 178
 Rees, Martin 402, 479, 481, 482, 486, 487, 578, 580, 581, 611, 625
 Refregier, Alexandre 460
 Richards, Gordon 524
 Richstone, Douglas 82, 109
 Riemann, Bernhard 11, 151
 Roberts, Morton 84

- Robertson, Howard 4, 149
 Roeder, Robert 233–235
 Rosati, Piero 532
 Rowan-Robinson, Michael 246, 514
 Ruderman, Malvin 24, 626
 Rutherford, Ernest 251
 Ryle, Martin 549
 Ryu, Dongsu 580
- Saccheri, Girolamo 11, 150
 Sachs, Rainer 436, 438
 Sajina, Anna 535
 Sakharov, Andrei 24, 641
 Salpeter, Edwin 504, 568
 Sandage, Allan 13, 49, 51, 78, 109, 116,
 246, 250, 251, 253, 259, 518
 Sargent, Wallace 553
 Schechter, Paul 77, 268, 329, 363, 472,
 482–486
 Scheuer, Peter 151, 504–506, 514, 549
 Schmidt, Brian 248
 Schmidt, Maarten 508, 514, 519, 521, 522
 Schneider, Peter 130, 133, 138
 Schramm, David 252
 Schutz, Bernard 459
 Schwarzschild, Martin 250
 Scott, Douglas 433
 Scott, Jennifer 568, 569
 Seager, Sara 423
 Seldner, Michael 100
 Seljak, Uros 559
 Shapiro, Irwin 189, 191
 Shapley, Harlow 7, 9
 Shectman, Stephen 506
 Shellard, Paul 629
 Silk, Joseph 17, 364, 433, 443, 448, 479
 Smail, Ian 452, 597
 Smoot, George 21
 Sneden, Christopher 252
 Snider, Joseph 178
 Songaila, Antoinette 566
 Soucail, Geneviève 130
 Spergel, David 463, 465
 Spinrad, Hyron 254, 514, 610
 Spite, François 298
 Spite, Monique 298
 Springel, Volker 487, 615, 616
 Srianand, Raghunathan 552
 Steidel, Charles 590
- Steigman, Gary 140, 294, 296, 298–301
 Steinhardt, Paul 24, 629
 Storrie-Lombardi, Lisa 601
 Subramanian, Kandaswamy 422
 Sugiyama, Naoshi 415, 422, 426, 443,
 445, 448
 Sullivan, Woodruff 514
 Sunyaev, Rashid XI, XII, 17, 18, 21, 28,
 29, 125, 281, 360, 365, 392, 423, 443,
 451, 454, 455, 561, 563, 568
 Szalay, Alex 19, 396
- Tammann, Gustav 78, 116, 246
 Tayler, Roger 14
 Taylor, Joseph 192
 Tegmark, Max 463, 559
 Tinsley, Beatrice 499, 604
 Tipler, Frank 625
 Toller, Gary 586
 Tolman, Richard 16, 322, 333
 Tonks, Lewi 317
 Toomre, Alar 57, 58
 Toomre, Juri 57, 58
 Tremaine, Scott 20, 82, 108, 109, 144
 Trodden, Mark 144
 Tully, Brent 73
 Turner, Michael 143, 301, 303, 307, 369,
 376, 397, 402, 642
 Tyson, Anthony 136
 Tytler, David 566
- Vallée, Jacques 577
 van den Bergh, Sidney 49, 51, 542
 van der Kruit, Piet 62
 Vandenberg, Donald 251
 Verde, Licia 403, 404, 407
 Vishniac, Ethan 453
 Vogeley, Michael 42
- Waddington, Ian 517
 Wagoner, Robert 15, 292, 294
 Walker, Arthur 149
 Wall, Jasper 506, 515
 Walsh, Dennis 249
 Wambsganss, Joachim 129, 130, 138
 Wang, Wei-Hao 598
 Warren, Stephen 519
 Weedman, Daniel 597
 Weinberg, Steven 338, 355, 626

- Wesselink, Adriaan 248
Weyl, Hermann 149, 150
Weymann, Raymond 17, 249, 281, 563
Wheeler, John 625
White, Martin 433, 454
White, Simon 200, 269, 482, 486, 545,
 587
Wilkinson, David 434
Wilkinson, Peter 140
Will, Clifford 173, 174, 189, 190, 192,
 195, 196
Williams, Robert 590
Wilson, Robert 15, 27
Wolfe, Arthur 436, 438, 554, 603, 604
Woltjer, Lodewijk 519
Wright, Thomas 5
Wyse, Rosemary 479
Yu, Jer Tsang 443, 445
Zaldarriaga, Matias 422, 454, 458
Zeldovich, Yakov 13, 17–21, 24, 28, 29,
 125, 208, 231, 233, 281, 303, 304,
 360–363, 365, 375, 381, 392, 423,
 443, 451, 454, 455, 476, 561, 626

Index

Major topics and their principal references are highlighted in **bold-face** type.

- Abell 194 110
Abell 478 122, 123
Abell 1228 110
Abell 1413 117, 118
Abell 1656 *see* Coma cluster of galaxies
Abell 2199 109, 110
Abell 2218 96, 130, 131, 136
Abell Catalogues of rich clusters of galaxies 96–98
comparison with clusters selected from the Sloan Digital Sky Survey 98–99
complete statistical sample 97
selection criteria for inclusion in 96
compactness criterion 97
distance criterion 97
richness criterion and richness classes 96, 97
space density of clusters in 98
Abell clusters and the large-scale distribution of galaxies 99–100
superclustering of galaxies about 100
absolute luminosities of galaxies 77
absorption history of the Universe 604
abundances of elements in Lyman- α absorption systems 598–604
absorption, or scattering, cross-sections and 600
advantages of determining zinc abundance 601, 602, 606
chemical history of the interstellar gas and 601
depletion of heavy elements and 601
in redshift interval $0.3 \leq z \leq 3.5$ 601
density parameter $\Omega_{\text{HI}}(z)$ for neutral hydrogen 601, 606
corrected for dust extinction and systems with low column densities 601
density parameter $\Omega_x(z)$ for species x and 600, 601
determination of average 598
global metallicity ratios and 600
iron abundance in redshift interval $1.7 \leq z \leq 4.6$ 603
uniformity of relative 604
variation of neutral hydrogen abundance with redshift 602
Acbar experiment 435
acoustic oscillations in galaxy power spectrum 362, 410–415
Sloan Digital Sky Survey (SDSS) 412–415
first peak and 414
2dF galaxy redshift survey 412–413
cosmological parameters from 413
first and second peaks and 412
acoustic oscillations in the power spectrum of the cosmic microwave background radiation
as forced oscillations 446
estimation of cosmological parameters and 449
acoustic oscillations in the power spectrum of the cosmic microwave background radiation 428–430, 436, 443–449
adiabatic temperature oscillations of 446, 447
amplitudes of 444
as forced oscillations 445, 446

- 'dipole' contributions to 447, 448, 455, 456, 459
- Doppler fluctuations associated with 446, 447
- effective temperature perturbation of 447
- estimation of cosmological parameters and 444, 449
- even and odd harmonics of 444
- first maximum of 427, 443, 444, 449
- gravitational redshifting of 447
- isocurvature modes and 447
- 'monopole' contributions to 447, 448, 456, 459
- relation to adiabatic density perturbations 445
- temperature excursions of 448
- wavenumbers of maxima of 444
- active galactic nuclei 51
 - ratio of black hole to spheroid masses 610, 617
 - Type 1 528
 - unobscured 528
- active gravitational mass density 201
- adiabatic baryonic perturbations in the standard Big Bang 350–357, 361–363**
 - as a 'top-down' process 363
 - 'burning of pancakes' 363
 - formation of 'pancakes' 363
 - matter-dominated era 353–355
 - radiation-dominated era 352
- adiabatic damping of neutrino velocities 377
- adiabatic damping of the sound waves 354
- adiabatic expansion of a photon gas 272, 281
- adiabatic expansion of a thermal gas 281
- adiabatic hot dark matter 396
- adiabatic model of structure formation 18
- adiabatic sound speed 316
- Advanced Camera for Surveys (ACS) 136, 138, 538, 592
- age of the Earth 251
- age of the Universe T_0 13, 16, 242
 - globular clusters and 250, 251
 - nucleocosmochronology and 252
 - white dwarf cooling ages and 251
- alignment effect in radio galaxies 254, 256
 - shock-excitation and 255
- Andromeda Nebula 8
- Anglo-Australian Telescope 2dF Survey 22, 519
- angular diameter distance 130, 157, 264
- angular diameter distances between any two redshifts 228–230**
 - gravitational lens formulae and 229
 - models with $\Omega_A = 0$ 228–229
 - models with $\Omega_A \neq 0$ 230
 - reciprocity theorem 229
- angular two-point correlation function 34–36, 386
 - for extragalactic radio sources 42
- Antennae galaxies 57–60, 614
- anthropic cosmological principle 624–626
 - existence of sentient beings and 625
 - strong form of 625
- APM galaxy survey 33–36
- APM survey of clusters of galaxies 95
- Arecibo radio telescope 192
- Ariel-V satellite 115, 524
- ASCA Large Sky Survey 525
- Astro-2 mission 565, 566
- astroparticle physics 145
- Atacama Large Millimetre Array (ALMA) 598
- Atlas of Peculiar Galaxies (Arp) 56
- Auger cosmic ray air-shower array 625
- autocorrelation function 432, 433
- Baade–Wesselink method 261
- background radiation 510–513**
 - discrete source contribution to 510–512
 - effects of evolution 512–513
 - 'luminosity evolution' 513
 - integrated emission of galaxies and 587
 - Lyman- α emission of the intergalactic gas 562
 - origin of, in standard world models 512
 - radio emission at long radio wavelengths 513
 - source counts and 510
 - starburst galaxies and 589
 - independence of cosmological model 589
- submillimetre and far-infrared 597
- COBE observations of 587

- contribution of active galactic nuclei 598
 main contributors to 598
 metal formation and 587
ultraviolet
 decrease at large redshifts 595, 596
 decrease in intensity from $z = 1$ to present epoch 596
 from the proximity effect 568–569
 from the proximity effect at small redshifts 568
 global star formation rate and 595
 integrated emission of quasars and 569
 integrated emission of star-forming galaxies at large redshifts 569
 neutral hydrogen in the peripheries of galaxies and 568
 ultraviolet, optical and near-infrared 586
 effects of dust 587
 from spectra of ultra-high-energy γ -ray sources 587
baising
 antibiasing 402
 galactic explosions and 402
Balloon Observations Of Millimetric Extragalactic Radiation ANisotropy and Geophysics (Boomerang) 456
bar instability in differentially rotating discs 69
 barred spiral galaxies 51, 54
baryogenesis 641–642
 baryon number violation of primordial X, \overline{X} bosons 642
 baryon-asymmetry problem 641
 Sakharov's rules 641
 baryon number violation 641
 C and CP violation 641
 non-equilibrium conditions 641
 unification of quarks and leptons and 642
 baryon asymmetry problem 23, 286, 307, 622
 baryon number violation
 generic feature of grand unified theories 641
 baryon perturbations in cold dark matter models 409–410
 baryon–antibaryon pair production 23, 622
baryonic theories of galaxy formation 360–364, 383
 what went wrong 364–365
 Bautz–Morgan classification of clusters of galaxies 109, 110
 Bautz–Morgan effect 253, 254, 544
 Bayesian statistical techniques 463
 Bell Telephone Laboratories 27
bending of light rays 179–181
 by ‘negative mass’ in inhomogeneous Universe 232, 233
 dependence upon the gravitational potential 181
 Beppo-SAX satellite 498
 bias parameter 137
 gravitational lensing and 138
 biasing 21, 401–405
 bias parameter 269, 403, 404, 407, 417
 bispectrum of galaxy distribution and 403
 dependence of luminosity and spectral type 404, 405
 for different classes of galaxy 405
 two-point correlation function for galaxies and 403, 405
 Gaussian fluctuations and 402
 hot gas in voids 402
 mechanisms for 402
 non-linear bias parameter 403
 Biermann battery 579, 581
Big Bang model of the Universe, history of 14–16
 big crunch 205, 338
big problems of cosmology 466, 621–624
 BIMA Millimetre Array 126, 127, 249
 black holes 140, 586
 formation in early Universe 392
 supermassive 140, 471, 488, 492
 epoch of maximum quasar activity 517
 non-thermal radiation processes and 492
 ratio of mass to spheroid mass 488
 Bohr's theory of the hydrogen atom 623
 Boltzmann equation 368, 377, 395, 409, 411, 422, 440, 448, 614
 Boomerang experiment 435

- Bose–Einstein spectrum 29, 284
 Boulby Underground Laboratory 146
 bremsstrahlung 95, 115, 128, 248, 547,
 561
 bolometric luminosity of 119
 cooling rate 121, 479
 emissivity of 128
 spectral emissivity of 115
 spectrum of 116, 128, 248
 thermal 561
 brightest galaxies in clusters 44, 45
 brightest members of rich clusters of
 galaxies
 absolute magnitudes of 109
 brown dwarfs 139–141
 Butcher–Oemler effect 253, 543–544
 changing fractions of galaxy types with
 redshift and 543
 passive evolution of spheroidal galaxies
 and 543
 selection criteria and 543
- C and CP violation
 in decay of neutral K^0 and \bar{K}^0 mesons
 641
- Calán-Tololo supernova project 164–166
 CalTech Submillimetre Observatory 126
 CAMB computer code 422, 430, 440
 Cambridge 4C survey 506
 Cambridge APM galaxy survey 269, 386
 Canada-France Redshift Survey 590
 Cartesian coordinates 155
 Cartwheel galaxy 56, 58
 Cassini spacecraft 191, 192
 CBI experiment 435
 cD clusters of galaxies 102–103
 cD galaxies 51, 82, 96, 102, 103, 109
 in small groups 103
 central bulge of lenticular galaxies 53
 central bulge of spiral galaxies 51
 central limit theorem 487, 505, 508
 Cepheid variables 7, 246, 247
 period–luminosity relation for 7, 8, 246
 CfA galaxy survey 38, 39, 41, 400, 401,
 406
 ChaMP study 525
 Chandra Deep Fields 525
 Chandra X-ray Observatory 116, 124,
 125, 249, 491, 525
- chemical potential 284
 Chwolson ring 129
 Cl 0024+1654 235
 classification of galaxies 59
 cluster Cl 0024+1654 136, 137
clusters of galaxies 37, 42, 43, **95–146**
 Butcher–Oemler effect 543–544
 central mass density of 107
 core radius 103, 105
 counts of X-ray clusters 529–532
distribution of galaxies in **101–110**
 galaxy content and spatial distribution
 of galaxies in 101–103
dynamical estimates of masses of
110–114
gravitational lensing by *see* gravitational
 lensing by galaxies and clusters
 of galaxies
hot gas in *see* hot gas in clusters of
 galaxies
isothermal gas spheres and *see*
 isothermal gas spheres, **103–108**
large-scale distribution of **95–100**
luminosity function for galaxies in
108–110
 mass–luminosity ratios of 99, 117
 on a temperature-number density diagram
 481
 segregation by galaxy type 102
 segregation by mass 103
summary of properties of **109–110**
Sunyaev–Zeldovich effect in hot intra-
 cluster gas *see* Sunyaev–Zeldovich
 effect in hot intracluster gas
 two-point correlation functions for 100,
 101, 387, 402
 velocity dispersions of 99
 CMBfast computer code 422, 425, 430,
 440
 cold dark matter 19–21, 359, 374, 375,
 381, 382, 398, 441, 464, 476, 615
 perturbations in 367, 374, 376, 380,
 382, 396, 437, 557
 WIMPs and 375
cold dark matter model of galaxy
 formation 20, 21, 349, 380–383,
 393–395, 399, 401–403, 409–412,
 414, 415, 418, 428, 482, 487, 489
 adiabatic 395, 396, 399, 412

- as a ‘bottom-up’ picture for structure formation 382
 broken-scale-invariant 419
 concerns about 415
 hierarchical clustering in 382
 isocurvature 396, 398, 400
 mixed hot and 418
 open 400, 401, 410, 413, 416–418
 standard 401, 409, 415–418, 530, 532, 559, 572, 573
 tilted 419
 with decaying neutrinos 416–418
 with finite cosmological constant 416–418, 572, 613
 collisions between galaxies 478, 544, 613
 Coma cluster of galaxies 42, 64, 102, 109–114, 547
 core radius of 108
 mass of 111
 mass–luminosity ratio of 111, 113, 267
 Sunyaev–Zeldovich effect in 450
 X-ray image of 114
 comoving angular diameter distance 161
 comoving luminosity density 589
comoving radial distance coordinate
 159, 160, 161, 168, 170, 172, 203, 218, 219, 221, 226, 228, 232, 243, 244, 316, 336, 339, 341, 342, 424, 425, 494, 501, 507, 511, 631–633
 definition of 164
 comoving volume 171
 variation with redshift 495
 Compton double scattering 284
 Compton Gamma-ray Observatory
 BATSE instrument 498
 Compton optical depth of hot diffuse intergalactic gas 561
 Compton scattering 17, 28, 29, 125, 248, 281–284, 301, 352, 357, 359, 561
 exchange of energy between photons and electrons by 281–284
 induced 17
 inverse 492
 Compton scattering in post-recombination Universe 282, 284
 Compton scattering in radiation-dominated Universe 281–284
 Compton scattering optical depth 29, 125, 283, 284
 computer simulations
 galaxy formation and 472
 hydrodynamic, of intergalactic gas 557, 571–574
 at redshift $z = 2$ 573
 cold dark matter models and 572
 feedback processes and 572
 predicted column density distribution of Lyman- α absorption clouds 572, 615
 predicted structures of neutral hydrogen clouds and 572, 615
 Single Particle Hydrodynamics 572
 star formation and 572
 supernova explosions and 572
 hydrodynamical simulations of galaxy collisions 616
 large-scale structure and 400, 474, 477, 484, 486, 487, 489, 530
 excess of dwarf satellites 486
 Press–Schechter mass function 487, 488
 large-scale structure formation 613
 origin and evolution of cosmic structures and 614
 origin of intracluster magnetic fields by turbulence 580
 predicted spin parameter λ 611
 reionisation era 574, 575
 semi-analytic models of galaxy formation 583
 concentration index C 91, 92
 concordance Λ CDM world model 22, 37, 42, 241, 424, 560, 621, 623, 625
 conformal diagram 631
 including inflation 632
 passing through and re-entering the Hubble sphere 633
 conformal Newtonian gauge 348, 349, 445
 conformal time 317, 340, 342, 344, 346–348, 445, 458, 631–634, 637
 extension to negative values before end of inflationary era 631
 confusion 505
 confusion-limited survey 505
 systematic overestimation of flux densities in 505
 convergence κ 460

- cooling rate of astrophysical plasma 479, 480
 cooling time of astrophysical plasma 479, 481, 486
 Copernicus satellite 297
 core radius of brightness distribution 61
correlation functions and the spectrum of the initial fluctuations 385–419
 acoustic peaks in the power spectrum of galaxies 411–415
 2dF galaxy redshift survey 412–413
 Sloan digital sky survey 412–415
 biasing 401–405
 evolution of the initial perturbation spectrum – transfer functions 393–401
 adiabatic cold dark matter 393–396
 adiabatic hot dark matter 396
 isocurvature cold dark matter 396–399
 subsequent evolution 399–401
 power spectrum
 origin of maximum of 415
 reconstructing the processed initial power spectrum 405–410
 non-linear development of the density fluctuations 407–409
 redshift biases 406–407
 role of baryon perturbations 409–410
 the perturbation spectrum 388–392
 Harrison–Zeldovich power spectrum 391–392
 initial power spectrum 390–391
 relation between $\xi(r)$ and the power spectrum of the fluctuations 388–390
 two-point correlation function for galaxies 385–388
 variation on a theme of cold dark matter 415
 correlation functions for galaxies 363, 405
 correlation lengths 404
 higher order 386
 three-point correlation function 403
 Cosmic Anisotropy Polarization Mapper (CAPMAP) 456
 Cosmic Background Explorer (COBE) 15, 21, 27–33, 284, 415, 416, 419, 421, 429, 432, 434, 437, 440, 442, 507, 561, 587
 Cosmic Background Imager (CBI) 456
The Cosmic Century: A History of Astrophysics and Cosmology (Longair) 3, 149, 193, 434, 514
 cosmic chemical evolution, equations of 604–607
 closed box model 605, 606
 conservation of mass 605
 infall of material from intergalactic medium 604–607
 inflow model 606
 instantaneous recycling approximation 605
 loss of heavy elements due to star formation 605
 outflow due to supernova explosions 606
 outflow model 606
 outflow of processed material 604–607
 rate of change of mass of heavy elements 605
 rate of infall or outflow $\dot{\Omega}_f$ 605
 rate of star formation 605
 role of dust 604, 606
 yield y 605
 Cosmic Lens All Sky Survey (CLASS) 266
cosmic microwave background radiation 15, 16, 18, 22, 27–33, 241, 275, 467, 624
 dipole component of 30, 31
 discovery of 17, 362
 distortions from a perfect black-body spectrum 283–284
 causes of 283
 distortions from a perfect black-body spectrum 28, 29
 energy density of 276
 epoch of recombination and 277, 279
 estimation of cosmological parameters from 250, 252, 259, 269, 270, 300
 fluctuations in the *see* fluctuations in the cosmic microwave background radiation
 horizon problem and 621
isotropy of 29–33, 41, 42, 149, 150, 337
 last scattering surface of 325, 631
 neutrinos and 369

- number density of photons in 277, 423
 polarisation of *see* polarisation of the cosmic microwave background radiation
 prediction of 14
 specific entropy per baryon of 277
spectrum of 28–29
 Sunyaev–Zeldovich distortions of 125, 126, 561
 temperature fluctuations in the *see* fluctuations in the cosmic microwave background radiation
 temperature of 143, 356, 371, 416, 576
 observations of the variation with redshift 272, 273
 variation with redshift 272
 temperature of at epoch of recombination 279
 thermal history of 278
cosmic star-formation rate
 advantages of submillimetre waveband 597
 cosmic abundances of the elements and 598–607
 maximum at redshifts $z \sim 1\text{--}2$ 610
 optical–UV determinations of 606
 problem of dust extinction 596, 598
 problems with the simple models 606
 submillimetre determinations of 596–598, 606
 as a function of redshift 598, 599
cosmic time 150, 158–160, 161, 163, 207, 217, 231, 237–239, 252, 317, 339, 344, 438, 445
 cosmic variance 434–436, 467
 cosmic virial theorem 268, 329
Cosmical Magnetism (ed. Lynden–Bell) 577
 cosmological constant Λ 13, 21, 202, 208, 212, 214, 215, 242, 265, 267, 273, 336, 344, 414–418, 425, 630
 ‘repulsive force of a vacuum’ and 208, 209
 dark energy and 23, 24, 207, 208, 210, 626
 evidence for finite value of 257
 history of 12, 13, 24, 188, 199, 207, 623
 zero-point fluctuations of vacuum and 626
Cosmological Constants (Bernstein and Feinberg) 202
Cosmological Inflation and Large-Scale Structure (Liddle and Lyth) 313, 629
cosmological parameters, determination of 241–270, 463–465
 Ω_A and the statistics of gravitational lenses 263–267
 age of the Universe T_0 *see* age of the Universe T_0 , 250–252
 angular diameter–redshift test 261–263
 deceleration parameter q_0 *see* deceleration parameter q_0 , 252–263
 density parameter Ω_0 267–270
 Hubble’s constant H_0 *see* Hubble’s constant, 246–250
 number counts of galaxies 259–261
 infrared H waveband 260
 problems of using to determine q_0 259, 260
 parameters to be determined 463–465
 relative lensing probabilities Ω_A and the statistics of gravitational lenses 265
 relative lensing probabilities 265
see density parameter Ω_0 267
 testing the Friedman models 242–245
 the parameters and relations between them 241–242
 three-year WMAP data and 463–465
Cosmological Physics (Peacock) 209, 313
cosmological principle 149–150, 158, 199, 204, 237, 238, 625
 Cosmology Calculator of Dr. Edward Wright 425
 COSMOS survey of clusters of galaxies 95
 counts of γ -ray bursts 498
 counts of active galaxies evolution in infrared waveband 536
 counts of extragalactic radio sources 498, 508, 514–516
 excess of faint radio sources 514
 evidence for strong cosmological evolution 514
 counts of far-infrared and submillimetre sources 597
counts of galaxies 537–543
 advantages of infrared K waveband 538

- evidence for homogeneity of Universe 493
- excess of faint blue galaxies 47, 261, 540
- and starburst galaxies 542, 543
- nature of 540–543
- fluctuations in, due to large-scale clustering 538–541
- for irregular/peculiar/merger systems 542
- for spheroidal and spiral galaxies 540, 542
- Hubble's 494
- in infrared K band 540
- in infrared K waveband 542
- in U, B, R, I and K wavebands 541
- problems of determining 537–538
- counts of galaxies and active galaxies, predicted** 492–507
- at submillimetre wavelengths 500–501, 534
- normalised differential counts 501, 503
- Euclidean 493
- differential 493
- integral 493
- for standard world models 494–500
- comparison with Euclidean counts 495
- for bolometric luminosities and flux densities 495
- for sources with power-law spectra 495–496
- normalised, differential 495–496
- optical counts for galaxies 498–500
- slopes of integral and differential 496, 498
- models with finite Ω_A 501–504
- counts of infrared and submillimetre sources** 532–537
- convergence of, at mid-infrared wavelengths 537
- far-infrared wavelengths 533, 534
- IRAS galaxies 532, 533
- excess of faint sources 532
- Spitzer First Look Survey 533
- excess of faint sources 533
- submillimetre wavelengths 534
- excess of faint sources 534
- counts of radio-quiet quasars 518, 521, 522
- counts of X-ray clusters of galaxies 529–532
- counts of X-ray sources** 524–532
- evidence for evolution of the source populations 525
- hard X-ray energies, 2–10 keV 525, 527, 529
- history of 524
- problems of interpretation 525
- soft X-ray energies, 0.5–2 keV 527
- and the integrated X-ray background emission 527
- soft X-ray energies, 0.5–2 keV and 2–10 keV 525
- coupling of dark and baryonic matter by gravity 378
- coupling of electrons and protons by Coulomb collisions 367
- coupling of matter and radiation in the expanding Universe 17, 353, 355, 367
- CP violation in decays of K^0 mesons 287
- Crab Nebula
- origin of magnetic field of 580
- critical surface density for star formation in spiral galaxies 554
- critical cosmological density** 139, 145, 204
- in neutrinos with finite mass 143
- critical density 439
- critical density for star formation 616
- Critical Dialogues in Cosmology* (ed. Turok) 269, 298, 415
- crossing time 111, 474
- definition of 63
- for a cluster of galaxies 43
- Cryogenic Dark Matter Search (CDMS) 146
- Cryogenic Dark Matter Search (CDMS II) 373, 374
- curvature of space κ** 154, 156, 157, 171, 231, 242, 243, 320, 627, 638
- condition for flat Euclidean space 210, 211, 364
- effect of hyperbolic space on growth of perturbations 320, 326, 327

- radius of, at the present epoch \mathfrak{N} 161, 199, 210, 228, 239
 relation between Ω_0 , Ω_A and 210
 variation with scale factor a 160
 curvature of space–time 181
 curvature perturbations 437
 amplitude of 463
 cusp catastrophe 135
 61 Cygni 5
- damped Lyman- α systems in quasar spectra 272, 600–604, 606, 607
 dark ages 384, 471, 552, 574, 576
 observability through fluctuations in the neutral hydrogen intensity 577
dark energy 207–211, 216, 230, 243, 245, 327, 331, 335, 344, 345, 414, 623, 634
 density parameter Ω_A of the 21–23, 242, 449, 501, 503, 623
equation of state of 210–211, 267, 465, 630
 problem of the 23, 24, 365, 623
dark matter 139–146, 241, 268, 269, 367
astrophysical and experimental limits
144–146
 axions and 142, 369
baryonic 139–142
 black holes and 140, 141
 limits to mass density from gravitational lensing 140
 very low mass 141
 brown dwarfs and baryonic 140
 clusters of galaxies and 95, 112, 113, 115
 density parameter Ω_D in the 205, 214
 distribution of 235
forms of 139–146
 gravitational coupling to baryonic matter 368
 gravitational lensing and 130, 136, 137
 in clusters of galaxies 113, 117, 119, 136, 137, 267
 in early-type galaxies 138
 in elliptical galaxies 69
 in galaxies 267, 367, 368
 in spiral galaxies 69
 MACHOs and 141, 142
- gravitational microlensing and 141, 142
 masses of dark matter particles 145
 nature of 24, 301, 625
 neutrinos with finite rest mass and 143, 369
non-baryonic 142–144, 301, 335, 364, 365, 367
 nature of 368, 369
 searches for dark matter particles 145, 146
 standard bricks and 139
 structure of 137
 WIMPs and 143, 144
- dark matter and galaxy formation**
367–384, 400
 evolution of hot and cold dark matter perturbations 380–384
 cold dark matter scenario 381–384
 hot dark matter scenario 380–381
 forms of non-baryonic dark matter 369–370
 free-streaming and damping of hot dark matter perturbations 375–377
 instabilities in the presence of dark matter 377–379
 metric perturbations and hot and cold dark matter 374–375
 adiabatic curvature modes 374, 379
 curvature modes 374
 isocurvature modes 374, 375
 WIMPs as dark matter particles 370–374
- dark matter haloes
 formation according to Press-Schechter formalism 489
 dark matter haloes of galaxies and clusters 137
- dark matter particles
 collisionless 399
 nature of 384
 ultraweakly interacting 368
 dark matter problem 350, 365
Darkness at Night (Harrison) 510
 de Sitter solution 149, 213
 de Sitter world model 337, 626, 639
 de Vaucouleurs $r^{1/4}$ law for surface brightness 61, 62, 108
 de Vaucouleurs radius 70

- de Vaucouleurs' classification of galaxies 54, 55, 93
- deceleration parameter q_0 216, 241
- angular diameter-redshift test 261–263
- for compact radio sources 262, 263
 - for double radio sources 261, 262
- number counts of galaxies 259–261
- redshift-magnitude relation for brightest galaxies in clusters 252–254
- effects of stellar evolution on 253
- infrared 544–545
- problems of interpreting at large redshifts 253
- redshift-magnitude relation for radio galaxies 254–255
- advantages of determining in the K waveband 254, 255
- and the alignment effect 254, 256
- corrections for effects of stellar evolution 254
- redshift-magnitude relation for Type 1a supernovae 256–259, 464
- evidence for non-zero cosmological constant 257
- relation with Ω_0 and Ω_A 243
- decoupling of matter and radiation in the post-recombination Universe 283
- deflection D 505
- deformation tensor in Zeldovich approximation 476, 477
- Degree Angular Scale Interferometer (DASI) 456
- density contrast 268, 269, 311, 312, 315, 325, 328, 354, 358, 378, 391, 393, 402, 408, 443, 482, 573
- for curvature modes in early Universe 374
- growth of 393
- density parameter** Ω_0 204, 241, 243, 267–270, 412, 414
- cosmic virial theorem and 268
- defined at any epoch 230
- infall of galaxies into large-scale structures and 268, 269, 406, 407, 464
- density parameter in baryons** Ω_B 269, 289, 352, 362, 364, 444, 548, 561, 563, 564, 576, 586, 622
- from primordial nucleosynthesis 293, 299, 301, 357
- from WMAP power spectrum 300, 464
- density parameter in gas Ω_g 604–607
- density parameter in heavy elements Ω_m 604–607
- density parameter in intergalactic gas Ω_{IGG} 555
- density parameter in neutral hydrogen Ω_{HI} 554
- density parameter in stars Ω_s 547, 598, 604–607
- density parameter of the dark energy** Ω_A 21, 23, 209, 210, 242, 449, 464, 501, 503, 623, 626
- density parameter of the dark matter** Ω_D 464
- deuterium D
- abundance in Lyman- α absorbers 297
 - observed primordial abundance 297–298
 - as a ‘baryometer’ 299
 - solar abundance 297
- deuteron, binding energy of 292
- Differential Microwave Radiometers of COBE 30
- disc component of spiral galaxies 51
- disc scale length for spiral galaxies 62
- discs of spiral galaxies
- stability of 612
- dissipation processes and galaxy formation** 477–482
- radiative processes 478
 - star formation and 478–479
 - first generation of stars 478
 - in very large redshift objects 479
 - thermal instabilities 478, 481
- distance indicators 246, 247
- distance measure D 494, 495
- distance of the stars 4
- distortion matrix 462
- shear components of 460, 461
- Doppler shift
- Newtonian 162, 176
 - special relativistic 162
 - ‘downsizing’ 614
- ‘drop-out’ galaxies 543, 593, 594, 607
- decrease in luminosity density at large redshifts 595

- luminosity functions for 595
- properties of 593
- dust emission and star formation 478, 501
- dust extinction 538
- dust extinction of galaxy spectral energy distribution 535, 536
- dwarf elliptical galaxies 51
- dwarf galaxies 51
- dynamical equilibrium 63
- dynamical friction 399, 544

- early history of cosmology 3–5**
- early history of galaxies and the structure of our Galaxy 5–9**
- The Early Universe* (Kolb and Turner) 313
- early-type galaxies 50
 - mass distribution is 138
- eclipse expeditions of 1919 190
- Einstein angle 130, 132, 136
- Einstein radius 129, 132, 134, 264
- Einstein ring 130
- Einstein X-ray Observatory 116, 123, 507
- Einstein's field equations** 12, 13, 149,
 - 188, 199–202, 208, 243, 273, 348, 365, 368, 395, 422, 440, 448
 - conservation of energy for relativistic and non-relativistic gases 201
 - equation of conservation of mass and 200
 - first law of thermodynamics and 200, 201
 - monatomic gases and 201
 - ultrarelativistic gases and 201
- Einstein's static model of the Universe 8, 12, 149, 151, 188, 199, 214
- Einstein-de Sitter world model 205, 231–235, 265, 266, 319, 320, 322, 336, 483, 485, 496, 500
 - as only ‘stable’ model 622
- electron–positron annihilation 301
- electron–positron pair production 23, 622
- elliptical galaxies 50, 51
 - formation at large redshifts 543
- elliptical galaxies as triaxial systems 71–73**
 - linear programming techniques for 73
- ellipticities of elliptical galaxies 51
- emission history of the Universe 604

- energies of the photon and neutrino backgrounds 302
- energy density of the Cosmic Microwave Background Radiation 33
- entropies of the photon and neutrino backgrounds 301, 302
- entropy per baryon
 - fluctuations in, in isothermal picture of structure formation 357
- Eötvös experiment 173
- Eöt-Wash experiment 174, 175
- Eötvös ratio 174, 175
- epicyclic frequency 554
- epoch of baryon–antibaryon pair production 286
- epoch of decoupling of matter and radiation 574
- epoch of electron-positron pair production 286
- epoch of equality of radiation and matter
 - energy densities 17, 277, 285, 354, 358, 359, 376, 381, 393, 395, 396, 398, 410, 425, 430
 - including neutrinos 303
- epoch of formation of first stars 574
- epoch of formation of galaxies, clusters and superclusters 312, 474, 487
- epoch of maximum quasar activity 362
- epoch of nucleosynthesis 286
- epoch of recombination 17, 33, 277–281, 285, 312, 325, 355, 357, 362, 364, 378–381, 410, 440, 446
- epoch of recombination for helium 279
- epoch of reheating of the intergalactic gas 286
- epoch of reionisation of the intergalactic gas 33, 355, 452, 471, 547, 552, 574–577
- role of black holes in nuclei of galaxies 574
- equation of continuity 313
 - relativistic case 331
- equation of state
 - for photons, massless particles and ultrarelativistic gas 271, 331
- equivalence principle *see* principle of equivalence
- EROS project 141
- ESO catalogue of galaxies 44
- ESSENCE supernova project 257, 258

- Euclid's fifth postulate 150
 Euler's equation 313, 440, 448
 relativistic case 331
 Eulerian coordinate system 314, 476
 event horizon 338, 339, 342, 346, 634
 definition of 338
evolution of active galaxies with cosmic epoch 514–532, 569
 extragalactic radio sources 514–518
 ‘luminosity evolution’ 516
 cut-off of strong evolution beyond redshift $z \sim 2\text{--}3$ 516, 517
 for sources with steep and flat radio spectra 516, 517
 luminosity-dependent density evolution 516, 518
 radio-quiet quasars 518–524
evolution of galaxies and active galaxies with cosmic epoch 471, 491–545
 active galaxies 492, 514–532
 extragalactic radio sources 514–518
 radio-quiet quasars 518–524
 X-ray clusters of galaxies 529–532
 X-ray sources 524–529
 background radiation
 source counts and 510
 background radiation and 510–513
 effects of evolution and the radio background emission 512–513
 evaluation of 510–512
 brief history of evidence for 491–492
 clusters of galaxies 543–545
 co-evolution of stellar and black hole properties of galaxies 492
 counts of galaxies 537–543
 counts of galaxies and active galaxies 492–507
 euclidean source counts 493
 fluctuations in the background radiation
 due to discrete sources 504–507
 for standard world models 500
 models with finite Ω_A 501–504
 submillimetre counts of dusty galaxies 500–501
 counts of galaxies and active galaxies, predicted
 for standard world models 494
 infrared and submillimetre number counts 532–537
 stellar and gaseous components of galaxies 492
 V/V_{\max} or luminosity-volume test 507–510
 excess dwarf galaxy problem
 solution by sweeping out gas by astrophysical processes 613
 excess of faint blue galaxies 46, 591
 irregular nature of 593, 594
 extragalactic background radiation
 due to discrete sources 275
 due to galaxies 275
 energy density of, in different wavebands 275
 in the ultraviolet, optical and infrared wavebands 275, 276
 limits from $\gamma\gamma$ absorption in spectra of γ -ray sources 275
 number density of photons in different wavebands 275, 277
 spectrum of 273–277
 plotted as vI_v 275
 plotted as I_v 275, 276
 extragalactic radio sources 578
 depolarisation of 578
 luminosity function of
 evolution with cosmic epoch 514–518
 origin of magnetic fields of 580, 581
 active galactic nuclei and 581
 supermassive black holes in nuclei of 581
- Faber–Jackson Relation for elliptical galaxies 70–71**
 Faint Object Camera 564–566, 592
 Far Infrared Absolute Spectrophotometer (FIRAS) of COBE 28
 Far Ultraviolet Spectroscopic Explorer (FUSE) 566, 567
 feedback mechanisms in galaxy formation 471
 field galaxies 56
 fifth force, search for 174, 175
 fine-tuning problem 23, 622
 ‘fingers of God’ 39, 406, 407
 FIRST deep VLA survey of radio sources 42
 first generation of stars 552
 formation of interstellar dust 587

- properties of 574
 ultraviolet and X-ray emission of 574
- first law of thermodynamics 200, 201
- flat two-space, isotropic 154
- flatness problem** 23, 24, 230–231, 622
- fluctuations in the background radiation due to discrete sources 504–507
 spatial correlation technique 506
- fluctuations in the cosmic microwave background radiation 18, 19, 21, 30, 32, 33, 167, 281, 362, 364, 379, 382, 384, 410, 414–416, 419, 421–467, 614, 640
- acoustic peaks *see* acoustic oscillations in the power spectrum of the cosmic microwave background radiation
- discrete source confusion and 451, 505
- epoch of recombination and 430
- ionisation of the intergalactic gas through the epoch of recombination 422–423
- physical and angular scales of 424–430
 last scattering layer 425–426
 particle horizon scales 429–430
 Silk damping scale 426
 sound horizon at the last scattering layer 427–429
- physics of 443
- power spectrum of 13, 431–436, 439, 465
 cosmological parameters from 444, 463–465, 548
 observations of 434–436
 other sources of 465–466
 statistical description of 431–434
- power spectrum on intermediate scales – acoustic peaks 443–449
- power spectrum on large angular scales 436–443
- integrated Sachs–Wolfe and Rees–Sciama effects 440
- primordial gravitational waves 440–443
- Sachs–Wolfe effect – physical arguments 436–440
- power spectrum on small angular scales 450–452
- confusion due to discrete sources 451–452
- confusion due to submillimetre sources 452
- statistical and Silk damping 426, 450
- Sunyaev–Zeldovich effect in clusters of galaxies 450–451
- quadrupole anisotropy of 442
- reionised intergalactic gas 452–453
- Sunyaev–Zeldovich effect and 450
 detection of statistical effect from X-ray Abell clusters by WMAP 451
- Thomson scattering optical depth and 453, 574
- Fokker–Planck equation for stars in clusters 107
- fold catastrophe 135
- four-tensors in relativity 184–187**
- curvature scalar 188
 - differentiation of 188
 - electromagnetic field tensor 186
 - energy–momentum tensor 188
 - for dust 186
 - including pressure 186
 - Maxwell’s equations 186, 187
 - Ricci tensor 188
 - Riemann–Christoffel tensor 188
 - energy–momentum tensor
 - for dust 185
 - four-vectors 185
 - examples of 185
 - velocity 185
- Fourier integral 389
- Fourier series 389, 431
- Fourier transformations 431, 462
 autocorrelation theorem for 433
 of acoustic oscillations in cosmic microwave background radiation 445
- three-dimensional 388
- FR2 3CR radio sources 609
- fractal Universe 392
- free-bound and bound-bound transitions of hydrogen 479
- free-streaming of neutrinos 19
- Freeman’s law 62, 74, 612
- ‘freeze-out’ of hot dark matter particles by free-streaming 376
- ‘freeze-out’ of massive particle species in the early Universe 307

- frequencies of galaxies of different types
 54, 56, 541
 in different galactic environments 56,
 57, 404, 538
- Friedman world models** 12, 13, 16, 151,
 199–239, 621, 624
- Friedman world models with $\Lambda = 0$**
202–207
- closed, spherical geometries 205
 - critical world model 205
 - curvature–density parameter relation
 205
 - dust models 202
 - dynamics of 205–207
 - flat Einstein–de Sitter model 205
 - Newtonian analogue for 202–204
 - problems of boundary conditions 203
 - open, hyperbolic geometries 205
 - parametric solutions for 207, 321
- Friedman world models with $\Lambda \neq 0$**
207–215
- bouncing models 212–214
 - classification of 215
 - dust models 208, 209
 - dynamics of 211–216
 - Eddington–Lemaître models 213, 214,
 223, 501
 - antipodal points of 225, 501, 503, 504
 - effects of gravitational lensing at
 antipodal points 504
 - number counts in 501, 503
 - redshift–flux density relation for 501
 - stationary redshift 214, 223
 - Lemaître models 214, 501, 503
 - ghost images in 226
 - loitering models 214, 223, 226
 - minimum rate of expansion of 212
- Friedman’s equation 199, 200, 320, 326,
 638
- Friedman: the man who made the Universe expand* (Tropp, Frenkel and Chernin)
 204
- fundamental observer 150, 158–161, 164,
 168, 204, 207, 237, 238, 335, 337,
 339–341, 347
- fundamental plane for elliptical galaxies**
70–71
- The Future of Theoretical Physics* (eds.
 Gibbons, Shellard and Rankin) 643
- GADGET computer code 616
- GAIA mission, prospects for light deflection
 observations 191
- Galactic ‘cirrus’ 30
- Galactic Astronomy* (Binney and Merrifield)
 49
- Galactic bulge 141
- galactic cannibalism 253, 544
- Galactic Dynamics* (Binney and Tremaine)
 49
- galactic extinction law 77
- Galactic synchrotron radiation 30
- galaxies 49
 - characteristic masses of 480
 - dependence of types upon environment
 613
 - mean luminosity of 84
 - mean space density of 84
 - on a temperature-number density diagram
 481
 - passive evolution of 498, 499
 - importance of red giant branch 499
 - starbursts and evolution of 499
- Galaxies in the Universe: an Introduction*
 (Sparke and Gallagher) 49, 64
- galaxies, correlations along the**
Hubblesequence 84–88
- colour–colour diagram and 87, 88
 - integrated colour 87
 - luminosity function of HII regions 87
 - masses and luminosities 84
 - neutral hydrogen 86
 - star formation rates and 87
 - total surface density and surface density
 of neutral hydrogen 87
- galaxies, old red 542
- galaxies, properties of 8, 49
- galaxies, red and blue sequences of** 63,
88–94, 412
 - colour–absolute magnitude relation
 89–90
 - colour–Sérsic index relation 91
 - definitions of 89
 - effect of the galaxy environment 92–93
 - mean stellar age–concentration index
 relation 91
- Galaxy
 age of 64

- disc scale length of 62
- luminosity of 84
- structure of 7–9
- galaxy and structure formation, history of 16–19**
- galaxy formation 583–620**
 - background radiation and element formation 584–587
 - energy density of background radiation and density of metals formed 586
 - intensity of background radiation and density of metals formed 586
 - processes of element formation 584, 585
 - collisions between galaxies and 614
 - ‘downsizing’ 610
 - feedback mechanisms and 486, 583, 614
 - growth of supermassive black holes and 614
 - Lyman-break galaxies 590
 - in the general field 590
 - multicolour technique for discovering 590, 591
 - observed global star formation rate 587–590
 - as a function of redshift 583, 589
 - star-forming galaxies and 587
 - starburst galaxies at large redshift 589
- star and element formation and 583–598
 - build-up of heavy elements in galaxies 583
 - numbers of ‘drop-out’ galaxies and 584
 - numbers of blue star-forming galaxies and 584
 - numbers of far-infrared and submillimetre galaxies and 584
 - quasar absorption line systems and 584
- star formation and 614
- two-stage theory of 482, 611
 - final radius of disc 612
- γ -ray background emission
 - Comptonisation and 529
 - spectrum of 526
- Garching-Bonn Deep Survey 138
- gas dynamics
 - equations of 313
 - in Lagrangian form 314
 - Newton’s second law in 314
 - relativistic case 331, 332
 - relativistic case in Lagrangian coordinates 331
- gauge choices
 - in electrodynamics 347
 - Lorentz and Coulomb gauges 347
 - superhorizon scales and 347, 437, 438
 - gauge-invariant gravitational potential 445
 - gauge-invariant variables 348
- Gaunt factor 116, 121
- Gauss’s theorem for Newton’s law of gravity 67, 133, 202
- Gauss, Carl Friedrich
 - theory of surfaces 181
- Gaussian curvature *see* curvature
- Gaussian fluctuations 402, 432, 443, 475, 477, 482, 484, 487
- Gaussian perturbations with random phases 41, 42
- Gemini Deep Deep Survey 607, 608
- general relativity 11, 48, 149, 151**
 - introduction to 173–198**
 - further complications 181–184
 - what Einstein did 187–188
 - route to 184–188**
 - superhorizon scales and 347–350
 - general relativity, experimental and observational tests of 189–197**
 - four tests of general relativity 189–192
 - advance of perihelion of Mercury 189
 - deflection of light and radio waves by the Sun 190, 191
 - gravitational redshift 189
 - time delay in Sun’s gravitational field 191, 192
 - parameterised post-Newtonian (PPN)
 - formulation of 175, 195
 - limits to values of the parameters 197
 - metric potentials in 196
 - physical significance of 176
 - pulsars and 192–194
 - xparameterised post-Newtonian (PPN)
 - formulation of 197
 - General Relativity: An Introduction for Physicists* (Hobson, Efstathiou and Lasenby) 173, 184, 313

- general theory of relativity *see* general relativity, 614
- geodesic distance 157
- geodesics 149–153, 158, 320
- giant molecular clouds 478
- globular cluster 47 Tucanae 250, 251
- globular clusters 250, 355
- Gran Sasso underground laboratory 146
- Gravitation and Cosmology* (Weinberg) 184
- gravitational collapse
- timescale of 479
- gravitational constant, variation with cosmic epoch 197–198**
- helioseismology and 198
 - limits to 197
 - lunar laser ranging and 197
 - primordial nucleosynthesis and 198
 - pulsar timing and 197
- gravitational deflection of light rays 134
- by the Sun 128
 - collision parameter for 128
- gravitational lensing by galaxies and clusters of galaxies 128–139**
- necessary conditions for 133
 - astrophysics of galaxies and 136–139
 - basic theory of 128–131
 - caustics and cusps in 135, 136
 - cluster masses from 134
 - critical surface density for 133
 - dark matter and 130, 136, 137
 - distortion of background images by 136
 - extended deflectors and 133–136
 - galaxy-galaxy imaging and 138
 - magnification of images by 130–132
 - mirror inversion of images in 132
 - time variations of intensities of images 139
- gravitational lensing, strong 138, 235
- case of the galaxy IRAS F10214+4724 235
 - complete sample of radio sources and quasars 266
 - magnification of intensities by 235
 - probability of 264, 266
- gravitational lensing, weak 138, 235, 460–463
- and cosmic shear 235
 - shear variance distribution of 461
- power spectrum of density perturbations in the mass distribution and 462
- Gravitational Lensing: Strong, Weak and Micro* (Schneider, Kochanek and Wambsganss) 130, 138
- gravitational mass 173, 174
- gravitational potential, Newtonian limit 179
- gravitational redshift 176–179**
- dependence upon gravitational potential 177
 - in general relativity 183
 - in the Newtonian limit 177
 - incompatibility with special relativity 178
 - time dilation in a gravitational field and 178
- gravitational relaxation timescale 544
- gravitational waves 625
- and tilt of spectrum of scalar perturbations 442
 - dependence upon inflationary potential 442
 - limits to energy density of primordial 442, 460
 - polarisation signature of primordial 441
 - primordial
 - detection of as the ‘smoking gun’ for inflationary cosmologies 640
 - spectral index of primordial 441, 640
 - from WMAP power spectrum 640
 - temperature power spectrum of 441, 442 - tensor to scalar ratio of primordial 442, 460, 640
 - limits to 460
- gravitons 373
- ‘Great Attractor’ 268
- ‘Great Debate’ 7
- Great Observatories Origins Deep Survey (GOODS) 538, 540, 592, 595, 598
- ‘Great Wall’ 38
- Greenbank Catalogue of radio sources at 6 cm 42, 43
- grey-body spectrum 535
- GUT era, new physics at 643
- GUT phase transition 628
- half-light radius of light distribution 61

- Harrison–Zeldovich initial power spectrum** 18, 21, 25, **391–392**, 393–396, 399, 433, 439, 441, 465, 484, 485, 559, 560, 624, 630, 640
- Hawking radiation 141
- He^+ Lyman- α absorption clouds in intergalactic medium 566
- HEAO-1 X-ray Observatory 524
- HEAO1 A-2 experiment 507
- Heaviside–Lorentz units 187
- Heisenberg’s uncertainty principle 636
- helium abundance
- as a thermometer of the early Universe 293
- helium-3 He^3
- observed by radio hyperfine transition line 298
 - observed primordial abundance 298
- helium-4 He^4
- observed primordial abundance 296
 - in low metallicity, extragalactic HII regions 296
- Hercules cluster of galaxies 102
- Hertzsprung–Russell (H–R) diagram 250, 251, 584, 585
- main sequence termination point 250
- hierarchical clustering 18, 59
- hierarchical model of the Universe 5
- hierarchical models of galaxy formation
- old red galaxies and 607
- hierarchical scenario for cluster formation 545
- Higgs fields and Higgs particles 24, 208, 373, 623, 626, 643
- High Energy Astrophysics Vol. 1* (Longair) 126, 544
- High Energy Astrophysics, Vol. 2* (Longair) 577
- Himalayas 402
- Hipparcos* astrometric satellite 247, 251
- Hipparcos* measurements of light deflection by the Sun 191
- Hopkins Ultraviolet Telescope 565, 566
- horizon mass 352, 353, 391, 395
- horizon problem** 22, 24, 337, 631
- last scattering surface and 337
 - solution of in inflationary model of the early Universe 337, 626, 627, 631
- horizon scale 17, 204, 441, 627
- horizons and the horizon problem** 335–338, 621
- hot and cold dark matter model of galaxy formation 335, 418
- hot and cold dark matter, history of** 19–22
- hot dark matter model of galaxy formation 19–21, 375–377, 380–381, 400–402
- formation of galaxies by fragmentation of large-scale structures 381
- late formation of structure in 400
- hot gas in clusters of galaxies** 114–124
- absence of cool gas in 123
 - associated with heating by radio lobes 124
 - models to explain the 123
 - abundance of iron 118
 - characteristic cooling time for 121
 - cooling flows in 122, 478
 - enthalpy of 123
 - mass inflow rates of 123
 - cooling time of 122
 - iron line FeXXVI from 115
 - sound waves in 125
- Hubble Deep and Ultra-Deep Fields 261
- Hubble Deep Field 491, 538, 542, 590–593
- Hubble Deep Field South (HDFS) 592
- Hubble diagram 44
- Hubble sequence of galaxies 50
- Hubble Space Telescope 58, 59, 130, 131, 138, 249, 254, 257, 297, 464, 491, 538, 540, 543, 550, 552, 564, 565, 568, 590, 593, 595, 601
- The Hubble Space Telescope and the High Redshift Universe* (ed. Tanvir) 552
- Hubble Space Telescope Science Institute 590
- Hubble sphere 342–346, 632–634, 638
- definition of 342
 - distinction between particle horizon and 631
 - shrinking of 631, 633, 634
- Hubble Ultra Deep Field (HUDF) 491, 538, 540, 542, 543, 590, 592, 594–596
- filter transmission curves for 594
- Hubble’s constant 9, 13, 46, 241
- Baade–Wesselink method and 248
 - brightest stars in galaxies and 246

- Cepheid variables and 246, 247
 controversy over value of 246
 cosmological distance ladder and 246,
 247
 defined at any epoch 166, 230
 from Sunyaev–Zeldovich effect 128
 globular clusters and 246
 Hubble Space Telescope Key project and
 246, 247
 final result of 248, 464
 present expansion rate of the Universe
 and 167
 redshift–magnitude relation for brightest
 cluster galaxies and 246
 Sunyaev–Zeldovich effect and 248
 Tully–Fisher relation and 246
 Type 1a supernovae and 246
 written as $H_0 = 100h \text{ km s}^{-1} \text{ Mpc}^{-1}$
 204
- Hubble's law 9, 10, 44–46, 150, 165, 314,
 407
 comoving radial distance coordinates and
 340
 discovery of 150
 gravitational lensing and 249
 recession velocities exceeding the speed
 of light in 341
- Hubble's law and the expansion of the
 Universe 44–48, 165**
- Hubble's law for surface brightness 61
 hydrostatic equilibrium 104, 115
 hydrostatic support, equation of 318
 hyperbolic two-space, isotropic 154, 155
- i*-band drop-outs 552
 I0 galaxies 54
 inertial mass 173, 174, 181
 inflationary model of the early Universe
 24, 25, 364, 392, 621, 624
 accelerated expansion 634
 chaotic inflation 626
 exponential expansion and 626, 627,
 629
 role of scalar fields 629
 straightening of geometry 627
 violation of strong energy condition and
 630
- historical background 626–629
- formation of ‘bubbles’ in original Guth
 picture 628
 lack of physical realisation of
 inflationary picture 629
 monopole problem 628
 new inflationary model of Linde,
 Albrecht and Steinhardt 629
 slow rollover model 629
 symmetry breaking in Grand Unified
 Theories 627
 transition from false to true vacuum in
 original Guth picture 627
- necessary conditions for many e-folding
 times 635
- necessary tools from theoretical and
 particle physics 630
 release of ‘latent heat’ 627
 scale factor-temperature relation 628
 shrinking of Hubble sphere 634
 three equivalent conditions 634
 violation of the strong energy condition
 634
 transition to standard radiation-dominated
 model 627
- inflaton potential 24, 629
- infrared luminosity function of galaxies
 evolution of 536
 comparison with evolution of active
 galaxies 537
- Infrared Space Observatory (ISO) 532,
 533
- inhomogeneous world models 231–235**
- initial mass function
 modified 487
- initial power spectrum
 curvature of 463
 modifications of 409
 modified 484
 reconstruction of 474
- interacting galaxies 57, 60, 478
 fraction of 59
- intergalactic gas, optical depth for Thomson
 scattering of 280, 281
- intergalactic medium 547–582**
- absorption by 548
 absorption coefficient of 548
 background emission of 548
 emissivity of 548
 epoch of reionisation of 574–577

- Gunn–Peterson test for ionised helium in 564–567, 571
due to integrated effect of Lyman- α clouds 566–567
feasibility of, for large redshift quasars 564
Gunn–Peterson test for neutral hydrogen in 547, 549–552, 569, 574
positive detection at $z \geq 6$ 551, 552, 564, 574
upper limits to neutral hydrogen number density from 550
lukewarm gas in 555, 560–569
collisional excitation of 562–563
diffuse ultraviolet radiation at large redshifts and 567–569
emission and absorption of 564–567
proximity effect and 567–569
Lyman continuum opacity of 569–571, 574
Lyman- α absorption clouds in 547, 552–560
evolution of, with cosmic epoch 556
nature of 554–556
power spectrum of forest of 557–560
predicted evolution of, with cosmic epoch 556
properties of 552–554
modelling the evolution of 571–574
neutral hydrogen at large redshifts 574
fluctuations in observed intensity 574–577
intensity of 576
ionsation by first generation of massive stars 575
observational challenge of detecting 575
predicted brightness temperature of 576
problem of synchrotron radiation foregrounds 576
optical depth of 548
origin of magnetic fields 577–582
ultraviolet opacity of 569–571
X-ray background and a cosmic conspiracy 561
International Linear Collider (ILC) 144
International Ultraviolet Explorer (IUE) 248, 597
intrinsic curvature *see* curvature
Introducing Einstein's Relativity (d'Inverno) 184
ionisation fraction through epoch of recombination 423, 424
ionisation of intergalactic gas through the epoch of recombination 422–423
IRAS F10214+4724 235
IRAS Faint Source Survey 532
IRAS galaxies 501, 503
catalogue of 532
complete samples of 532
correlation functions for 405
ultraluminous 58
IRAS infrared observatory 478, 491, 532
IRAS Point Source Catalogue 532
Irr II galaxies 54
irregular clusters of galaxies 102–103
irregular galaxies 53
island universes 5
ISO infrared space observatory 478
isocurvature cold dark matter 396–399
fluctuations in local equation of state and 397
isophotal angular diameters 223
isothermal baryonic perturbations in the standard Big Bang 357–360
isothermal gas spheres 103–108, 134, 264, 611
projected 105, 106
singular 134
tidal radius of 107
truncated 107
isothermal model of structure formation 18, 357–360, 363–364
‘bottom-up’ picture of galaxy formation 364
‘freezing in’ of perturbations 358, 359
early enrichment of heavy elements 363
early formation of globular clusters and 363
hierarchical clustering and 363
radiation drag, effects of 359, 360
isotropic curved spaces 150–154, 159
radius of curvature of 155
three-dimensional 156, 157
two-dimensional 155, 156
isotropic two-space flat 157

- hyperbolic 157
- spherical 154, 157
- isotropy of the distribution of extragalactic radio sources 42
- isotropy of Universe on a large scale 32
- J0737-3039 (binary pulsar) 193
- Jagellonian field 35
- James Clerk Maxwell Telescope (JCMT) 452, 534, 597
- Jeans' analysis of damped harmonic oscillator 638
- Jeans' criterion in an expanding Universe 16, 319
- Jeans' instability 318, 324, 478
 - growth rate of 324, 358
 - physical nature of 318
- Jeans' instability criterion 16, 378
 - for collisionless gas 377
- Jeans' length 16, 17, 318, 332, 351–353, 379, 428, 429
 - in baryons 352
 - relativistic case 332
- Jeans' mass 17, 18, 351–355, 360, 361, 377
- Jeans' wavelength 318
- Jupiter 4, 5
- K-correction 170, 253, 495, 498, 538
 - in infrared K waveband 538
 - submillimetre 597
 - uncertainties in ultraviolet wavebands due to starbursts 538
- K20 sample of galaxies 542
- K20 Survey 607, 608
 - very red galaxies in 608
- Keck 10-metre telescope 272, 542, 555, 566, 590
- Keck-2 telescope 551, 552
- Kelvin-Helmholtz picture of stellar evolution 251
- Kepler's laws of planetary motion 3
 - third law 4, 67
- King profiles for mass distribution in clusters 107, 111
- Kolmogorov spectrum of turbulence 580
- Kompaneets equation 126
- Lagrangian and comoving coordinate systems, difference between 314
- Lagrangian coordinate system 314, 476
- Λ CDM model of galaxy and structure formation** 22, 59, 435, 440, 462, 463, 466, 472, 483, 486, 487, 530, 532, **613–620**
- problems with 613–614
 - accounting for Faber–Jackson relation and Tully–Fisher relation 614, 620
 - 'downsizing' problem 614
 - excess dwarf galaxy problem 613
 - mass-metallicity correlation 613
 - predicted cusps in central regions of galaxies 613
- Landau damping 376
- Lane–Emden equation 104
- Langmuir waves 317
- Large Electron–Positron collider (LEP) 300, 371
- Large Hadron Collider (LHC) 144, 208, 643
- Large Magellanic Cloud (LMC) 54, 141
 - distance of 248
- large-scale distribution of galaxies 33–44**
- large-scale structure of the Universe 27–48**
- The Large-Scale Structure of the Universe* (Peebles) 363
- Las Campanas redshift survey 41
- last scattering layer 444
- last scattering layer at $z = 1000$ 621
- last scattering surface 33, 333, 357
 - for neutrinos 292
- last scattering surface at the epoch of recombination 631, 632
- last scattering surface for electromagnetic radiation 624
- late-type galaxies 50
- laws of conservation of momentum and energy in relativity 186
- Legendre function
 - associated 431
- Legendre polynomials 433, 455
- Leiden–Berkeley Deep Survey (LBDS) 516, 518
- lens equation 132
- lenticular galaxies 52, 55
- lepton number L_i 301

- Lick counts of galaxies 35, 36
 Lick Observatory 550
light distribution in galaxies 59–63
 in elliptical galaxies 61
 in spiral and lenticular galaxies 61
 in spiral galaxies 68
 putting the light distributions together
 62
 light elements, primordial nucleosynthesis
 of *see* nucleosynthesis, primordial
 lightest supersymmetric particle 643
 limits of observation in cosmology
 624–625
 fundamental limitations 624
 limitations due to cosmic variance 624
 lithium ^7Li
 observed primordial abundance 298,
 299
 local group of galaxies 51
 local supercluster of galaxies 43, 44, 78
 Lockman Hole survey field 525
 LOFAR project (Netherlands) 576
 longitudinal gauge 348
 longitudinal plasma oscillations 317
 Lorentz invariance 184, 196
 form-invariance 184
 Lorentz transformations 185, 187, 207,
 238, 239
 lukewarm intergalactic gas 560–569
 collisional excitation of 562–563
 ‘thermostat’ temperatures of 563
 by shock waves 562
 emissivity of 562, 563
 HI and HeII Ly- α line emission due to
 562
 ionisation state of 563
 diffuse ultraviolet radiation at large
 redshifts and 567–569
 emission and absorption of 564–567
 detectability of redshifted Lyman- α
 emission 564
 photoexcitation and 564
 shock excitation and 564
 proximity effect and 567–569, 572
luminosity function of galaxies 77–84,
 509
luminosity–metallicity relations for
galaxies 74–76
 luminous infrared galaxies
 evolution of 536
 luminous infrared galaxy N1-015
 spectral energy distribution of 535
 lunar laser ranging 175
 Lyman limit 588, 589, 591
 ‘Lyman valley’ 570
Lyman- α absorption clouds in in-
tergalactic medium 545, 550,
552–560
 confinement of 555
 evolution of, with cosmic epoch 556,
 569
 nature of 554–556
 according to large-scale hydrodynamic
 simulations 573
 observed number density distribution of
 554, 555, 566, 600
 power spectrum of forest of 557–560
 properties of 552–554
 column densities of 554
 damped Lyman- α systems 554
 fractional ionisation of 555
 Lyman- α forest 552–554, 556–558,
 566–572, 574
 Lyman-limit systems 553, 554, 556,
 564, 569–571, 590
 masses of 555
 origin of damped Lyman- α systems
 572
 two-point correlation function of 557,
 558
 dark matter perturbations and 559
 SiIII absorption features and 557, 558
 Lyman- α emission of the intergalactic gas
 562
 Lyman- α radiation field, colour temperature
 of 576
 Lyman- α scattering, optical depth for 549
 Lyman- α transition
 oscillator strength for 549
 photo-excitation cross-section for 549
 Lyman-break galaxies 479, 607
 redshift distribution of 590, 592
 Lyman-limit galaxies, decreasing comoving
 density at large redshifts 489
 α Lyrae 5
 M31
 luminosity of 84

- rotation curve of 67
- M49 (NGC 4472) 69, 116
 - velocity dispersion of 70
- M51 (NGC 5194) 52
- M82 54
- M86 116
- M87 (NGC 4486) 52, 55, 69, 116
- Mössbauer effect 178, 189
- Mach's principle 11, 12, 199
- MACHO project 141, 142
- MACHOs 141
 - mean mass of 141
- Magellanic Clouds 7, 54, 141
- Magellanic irregular galaxies 54
- magnetic fields
 - in stars 578
 - in the interstellar and intergalactic medium 578
 - origin of 577–582
 - amplification mechanisms and 578
 - amplification of seed field by turbulence 580
 - dynamo action and 578, 580
 - emf created by Biermann battery 579
 - extragalactic radio sources and 581
 - extragalactic radio sources at large redshifts 582
 - laboratory demonstration of dynamo action 578
 - magnetic reconnection and 578
 - problems of dynamo action on large scales 578
 - seed field created by Biermann battery 579
 - seed fields 579
- power spectrum of magnetic turbulence 580
- predicted power spectrum from magnetic turbulence 580
- role in astrophysics 577
- rotation measure synthesis and 580
- making real galaxies 583–620**
 - abundances of elements in Lyman- α absorption systems 598–604
 - equations of cosmic chemical evolution 604–607
 - old red galaxies 607–610
 - origin of rotation 610–613
- putting it all together – semi-analytic models of galaxy formation 613–620
- star and element formation 583–598
 - background radiation and element formation 584–587
- Hubble Deep and Ultra Deep Fields 590–596
- Lyman-break galaxies 590
- observed global star formation rate 587–590
- submillimetre determinations of cosmic star-formation rate 596–598
- Malmquist bias 246
- Markarian ultraviolet-excess galaxies 597
- mass density of the Universe
 - in stars at the present epoch 84
- mass–luminosity ratio
 - early-type galaxies 138
 - for clusters of galaxies 267
 - for galaxies and clusters 482
 - for Universe as a whole 83, 267
 - of elliptical galaxies 69, 84
 - of spiral galaxies 68, 84
- mass–luminosity relation for stars 499
- mass–metallicity relations for galaxies at large redshifts 76
- mass–energy relation $E = mc^2$ 181
- masses of galaxies 63–70**
- massive galaxies in clusters 617
- massive ultra-weakly interacting particles 643
- matter-dominated Universe 276
- Mattig's formula 219
- MCG catalogue of galaxies 44
- 'meatball' topology 41
- Medium Deep Survey of galaxies (MDS) 542
- Mercury, advance of perihelion of 189
 - radar ranging and 189
- 'merger trees', hierarchical clustering and 615
- mergers of coalescing galaxies 614
- MERLIN long baseline interferometer 266
- Mészáros effect 358–359, 381, 393, 396, 398
- metallicity Z 74, 600, 605, 606
- metric angular diameters 221, 253

- between any two redshifts 228
- metric of isotropic two-space 155
- metric perturbations 368, 374, 392, 436
- metric tensor 155, 186–188
 - components of as gravitational potentials 187
- microlensing, gravitational 132
- Millennium Galaxy Catalogue 62, 63, 83
- Millennium Simulation 486–488, 613–615, 617–619
 - first quasar candidate 619
- Milne empty world model 207, 237
- Minkowski metric 158, 179, 181, 187, 188, 195
 - ‘missing baryon’ problem 547
- Modern Cosmology* (Dodelson) 313, 422
- Monte Carlo Markov chain methods 463
- Monte Carlo methods 506
- Moon, fluorescent X-rays from 524, 525
- morphologies of galaxies 49, 50
- Mount Wilson 100-inch telescope 492
- multipole moment 432, 433

- N galaxies 51
- nebulae
 - cataloguing of 7
 - nature of 6, 7
- ‘negative mass’ in inhomogeneous Universe 233
- negative pressure equation of state 208, 623, 630, 644
 - speed of sound for 638
- neutralinos 373
- neutrino astrophysics 625
- neutrino background temperature 301–303
- neutrino barrier 286, 292
- neutrino chemical potential 301
- neutrino interaction cross-sections 291
- neutrino oscillations 143
- neutrino perturbation
 - damping by free-streaming 376
 - free-streaming damping mass 377, 380, 381
- neutrinos
 - astrophysical limits to masses of 20
 - cosmological limits to masses of 560
 - cosmological limits to number of species of 463
 - cosmological mass density in 463, 465
- decoupling of 367
- equilibrium number density of 143, 301
- free-streaming of 380, 400
- laboratory limits to the masses of 143
- laboratory limits to the number of species of 145
- massive decaying 417
- neutrino background temperature 376
 - their role in primordial nucleosynthesis
 - see* nucleosynthesis, primordial
- time-scale for interaction in the early Universe 291
- with finite rest mass 19, 367, 375, 376, 380
- neutrinos, free-streaming of 396
- neutron decay 292, 294
- neutron stars 586
- Newton’s law of gravity 4
- Newtonian gravitational potential 348, 350, 438
- NGC 1300 53, 54
- NGC 2787 55
- NGC 3077 54
- NGC 4486 52
- NGC 4839 114
- NGC 4874 111, 114
- NGC 4889 111, 114
- NGC 5194 52
- NGC 5195 52
- NGC 520 54
- NICMOS infrared camera of Hubble Space Telescope 140
- non-Euclidean geometries 11, 150–152, 173, 492
- non-Gaussian fluctuations 432, 466
 - examples of 432
 - skewness and kurtosis 466
- non-linear collapse of spherical density perturbations 472–477
 - spherical top-hat collapse 473–475
 - maximum scale-factor for 473
 - redshift of collapse of 473
 - turn-around epoch 473
 - violent relaxation and 474
- non-linear development of density fluctuations 407–409
- self-similar solution for 408
- two-point correlation function 407–409

- NORAS catalogue of X-ray clusters of galaxies 116
- normalised impact parameter 132
- nuclear reactions in the Sun 279
- nucleocosmochronology 13, 252
- nucleosynthesis in stars 14
- nucleosynthesis, primordial** 14–16, 140, 289, 289–307, 417
- baryon-symmetric Universes 303–307
- ‘freeze-out’ of abundances in 304, 306
- equilibrium abundances in the early Universe 289–290
- equilibrium energy densities 290
- in the non-relativistic limit 290, 303
- neutron–proton ratio 290
- relativistic statistical mechanics and 289
- evolution of abundances during 293, 294
- light elements, abundances of 295–301
- comparison of theory and observation 299–301
- observations of 296–299
- massive neutrinos and 369
- neutrino background temperature 301–303
- neutrinos, decoupling of 290–292
- ‘freezing out’ of the n/p ratio and 291
- non-standard assumptions concerning 300
- lepton asymmetry 300
- limits to the number of unknown neutrino species 300
- varying gravitational constant 300
- synthesis of the light elements 292–295
- dependence upon photon-baryon ratio 294
- deuterium formation 292, 293
- epoch of nucleosynthesis 292
- helium formation 292, 293
- lithium formation 293, 294
- neutron fraction 292
- nuclear reactions involved in 292
- number counts of galaxies 46
- number counts of submillimetre sources 452
- Nyquist frequency 504, 505
- O04 survey 595
- observable Universe of galaxies 471
- observations in cosmology** 162–171
- age of the Universe** T_0 171
- angular diameter distance 167, 172
- angular diameters** 167
- apparent intensities** 168–170
- for bolometric luminosities and flux densities 169
- K-corrections 170, 223
- cosmological redshift and time dilation** 162–166
- the meaning of redshift in cosmology 164
- distance measure D 167, 172, 218, 243
- independence of Ω_0 at small redshifts 245
- Hubble’s law** 165–167
- luminosity distance 169, 172
- number densities** 170–171, 172
- comoving number density 171
- comoving volume 170
- reciprocity theorem 169
- observations in cosmology for Friedman world models** 215–228
- angular diameter–redshift relations 221–223
- for inhomogeneous Friedman world models 233, 234
- for models with $\Omega_A = 0$ 221
- for models with $\Omega_A \neq 0$ 223
- for partially inhomogeneous Friedman world models 235
- comoving volume within redshift z 226–228
- models with $\Omega_A = 0$ 226
- models with $\Omega_A \neq 0$ 228, 263
- cosmic time–redshift relation 217–218, 280
- age of Universe for flat world models with $\Omega_A \neq 0$ 218
- age of Universe for models with $\Omega_A = 0$ 217
- for flat world models with $\Omega_A \neq 0$ 218
- for models with $\Omega_A = 0$ 217
- for models with $\Omega_A \neq 0$ 218
- deceleration parameter 216
- relation to Ω_0 and Ω_A 216

- distance measures as a function of redshift 218–219
 for Milne's empty world model 219
 for models with $\Omega_A = 0$ 219
 for models with $\Omega_A \neq 0$ 219
 Mattig's formula 219
- flux density–redshift relations 223–226
 for inhomogeneous Friedman world models 235
 for starburst galaxies in the submillimetre waveband 501, 503
 ghost images 223
- Occam's razor 419
- Ohio State University 295
- Olbers' paradox 510
 in an infinite, static, Euclidean Universe 511
- resolution of, in standard world models 511, 512
- old red galaxies 607–610
 constancy of masses with redshift 607
 early formation of stellar populations of 610
 evidence for old stellar populations in 608
 evolving stellar mass density and 607
 massive 607–610
 need for early starbursts 608, 609
 selected in the K waveband 607
 star-forming galaxies at large redshift and 608
 stellar masses as a function of redshift 608
- On the Principles of Geometry* (Lobachevsky) 11, 151
- optical depth for intergalactic HeII absorption 564
- optical jet in M87 52
- The Origin and Evolution of Cosmic Magnetism* (ed. Beck, Brunetti, and Feretti) 577, 580
- origin of the spectrum of primordial perturbations 629–640**
 duration of the inflationary phase 630–631
 necessary number of e-folding times 631
 equation of state 630
- freezing of perturbations on passing through Hubble sphere 634
 shrinking Hubble sphere 631–634
- OVRO Millimetre Array 126, 127, 249
- P(D)* distribution 504–506, 514, 525
 asymptotic slope of 505
 in infrared waveband 507
 in ultraviolet waveband 506
 in X-ray waveband 507
 non-Gaussian statistics and 505
 physical meaning of 505
 shape of 505
- Palomar 200-inch telescope 514, 521
- Palomar 48-inch Schmidt telescope 96
- Palomar 48-inch Telescope Sky Survey 96
- pancakes 20, 363, 400, 402, 476, 477, 480
- parallel transport, or parallel displacement 151–153
- Parkes Selected Region (PSR) sample 517, 518
- Parseval's theorem 388
- particle horizon** 22, 335–340, 342, 344, 346–349, 351–354, 361, 362, 376, 377, 379, 380, 391–393, 415, 429, 430, 436, 441, 443, 444, 626–629, 631
 definition of 336
 radiation-dominated Universe and 337
- particle physics and cosmology 624, 625
- particle–antiparticle annihilation in the early Universe 278, 303
- collision time exceeds expansion age 306
- cross-sections for 304
- epoch of decoupling of particles and antiparticles 305
- equilibrium number densities 304
- Particles, Nuclei and the Universe, Selected Works of Yakov Borisovich Zeldovich, Vol. 2.* (Zeldovich) 381
- past light cone 159, 335, 339–344, 346, 631–633
- Pauli exclusion principle 144
- Pavo cluster of galaxies 42
- peculiar and interacting galaxies 56–59**
- peculiar velocities
 from polarisation measurements of the cosmic microwave background radiation 451

- in the local Universe 268
 of galaxies 201
 of perturbations 315, 453
 Perseus cluster of galaxies 124, 125, 547,
 617
perturbations, evolution of, in the standard cosmological models 311–333
 acoustic oscillation and 361–362
 conservation of angular momentum and 328
 for models with $\Omega_A = 0$ 325
 for models with $\Omega_A \neq 0$ 326
 in terms of conformal time τ 340
 Jeans' instability 317–318
 dispersion relation for, in a static medium 317
 growth rate for, in static medium 318
 Jeans' instability in an expanding Universe 319–327
 Einstein-de Sitter case 319
 empty Milne world model 320
 falling poles 322–324
 general solution 324–327
 linear growth of 319–327, 332, 351,
 354
 necessity of finite initial amplitudes 322, 333
 perturbing the Friedman solutions 321–323, 476
 small perturbation analysis 319–320
 spherical perturbations in standard Friedman models 321
 linear 312
 non-relativistic wave equation for 313–317
 adiabatic perturbations 316
 first-order solutions for 315
 in terms of conformal time 317
 in terms of cosmic time 317
 unperturbed solutions for 315
 peculiar velocities in the expanding Universe 327–331
 decay of in $\Omega_0 = 0$ case 329
 evolution of 329, 330
 growth of in $\Omega_0 = 1$ case 328
 potential motions 327, 328, 406
 primordial turbulence and 328
 rotational motions 328
 relativistic case 331–332
 growth rate in radiation-dominated case 332
 the basic problem 332–333
 what the theorists are trying to do 311–313
 Petrosian r-band luminosity 91
 photon barrier 280
 photon diffusion 355
 coefficients of thermal conduction and shear viscosity 355, 356
 photon-to-baryon number ratio 23, 277,
 622
 physics beyond the standard model 372
 Planck energy scale 209
 Planck era 287, 631, 642–644
 need for quantum theory of gravity 642
 new physics before reaching 643
 Planck mass 209
 Planck mission of ESA 421, 450–452,
 467, 625
 Planck spectral energy distribution
 Rayleigh-Jeans region of 455
 variation with redshift z 272
 Wien region of 278, 279
 fraction of photons in 278
 Planck time 642
 planetary nebula IC418 452
 Pleiades star cluster 5
 Plummer model for elliptical galaxies 108
 Poisson noise 392
 Poisson's equation for gravity 108, 187,
 268, 313
 linearity of 315
 relativistic case 331
 polar coordinates 155
polarisation of the cosmic microwave background radiation 454–463, 625
 anticorrelated TE cross correlation power spectrum of as evidence of adiabatic perturbations 458
 B-modes and 457, 467
 B-modes due to gravitational lensing 457
 BB power spectrum and 457
 EE power spectrum of 456, 457, 459
 from the epoch of reionisation 458–459

- angular scale of strongest polarised signal 458
 from the last scattering layer 455–458
 physics of 454–455
 necessity of quadrupole intensity distribution 455, 458
 polarised galactic radio emission and 456, 457
 primordial gravitational waves and 459–460
 B-modes 459, 460
 E-modes 459
 origin in the early Universe 460
 polarisation modes of 459
 predicted BB power spectrum of 460
 TE cross correlation power spectrum of 457–459
 TT intensity power spectrum and 456, 457
 weak gravitational lensing and 460–463
 BB-mode polarisation due to lensing of
 EE-mode polarisation 462, 463
 distortion matrix 460
 E-mode polarisation due to 462
 polycyclic aromatic hydrocarbon (PAH) molecules 535
post-recombination era 384, 471–489
 non-linear collapse of density perturbations 472–477
 isotropic top-hat collapse 473–475
 Zeldovich approximation 475–477
 Press–Schechter mass function 482–489
 development and recapitulation 485–489
 exposition – elementary theory 482–484
 role of dissipation 477–482
 POTENT reconstruction procedures 269
 power spectrum of cosmic microwave background radiation 434, 436
 power spectrum of fluctuations 388–392
 relations between different descriptions of 391
 power spectrum of initial fluctuations 17, 390–392, 405, 438
 modifications of 393–401
 power spectrum of temperature fluctuations 432, 433
 for non-Gaussian fluctuations 466
 precision cosmology 421, 466, 614, 621
Press–Schechter mass function 20, 363, 482, 482–489
 ‘peaks-within-peaks’ problem 485
 critical density contrast for structure formation 483
 evolution of number density of dark matter haloes with redshift 487, 489
 hierarchical clustering and 486, 487, 489
 mass function of clusters and 486
 problems with simple derivation 485, 486
 time evolution of 484, 485
 primordial fluctuation problem 23, 25, 472, 623
 Harrison–Zeldovich spectrum and 623
 primordial gravitational waves 440–443
 equation of state of 441
 on superhorizon scales 441
 quadrupole nature of 441
 quantum origin in the early Universe 441
 tensor to scalar ratio 441
 primordial nucleosynthesis of the light elements *see* nucleosynthesis, primordial
Principia Mathematica (Newton) 10
 principle of covariance 184
principle of equivalence 173–176, 176, 177, 179–181, 184, 196
 Einstein’s 174, 175, 196
 local Lorentz invariance (LLI) 175
 local position invariance (LPI) 175
 free-fall 174, 179
 weak 174, 175
Principles of Physical Cosmology (Peebles) 313
 probability integral 483
Probing Galaxies through Quasar Absorption Lines (eds. Williams, Shu and Ménard) 552
 problem of the values of the cosmological parameters 23
 prograde orbits 57
 projected surface brightness 116
 proper radial distance coordinate 339

- properties of spiral and elliptical galaxies** **70–76**
- proton decay
 - avoidance of 373
 - PSR 1913+16 192–195
 - pulsars and general relativity 192–194
 - emission of gravitational waves 193, 194
 - acceleration of binary pulsar due to 194, 195
 - masses of neutron stars 193, 194
- QSO Absorption Lines* (ed. Meylan) 552
- quadrupole component of the temperature power spectrum 434
 - quantised harmonic oscillator 635–637
 - angular frequency of 636
 - carrying out a proper calculation 637
 - energy levels of 635
 - Hermite polynomials and 636
 - Schrödinger's equation for 635
 - wavefunctions for 635
 - zero-point energy of 636
 - zero-point fluctuations of 636
 - quantum theory of gravity 644
 - quasar 0957+561 (double quasar) 249
 - quasar 2345+007 (double quasar) 554
 - Quasar Absorption Line key project 568
 - quasar HE 2347-4342 566, 567
 - quasar HS1700+64 566, 567, 571
 - quasar OQ 172 570
 - ultraviolet spectrum of 550
 - quasar PKS1935–692 564, 571
 - quasar PSS J1443+2724 273
 - quasar Q0302–003 564, 566, 571
 - quasar Q1331+170 272
 - quasar Q1422+2309 553
 - quasar Q2237+0305 139
 - quasar QSO 0013–004 273
 - quasar spectra
 - Lyman- α emission line 519, 520
 - prominent emission lines in 520
 - quasars
 - 3CR sample of radio 508, 509
 - cut-off at large redshifts 487, 488
 - early formation of supermassive black holes in 610
 - low-luminosity 521
 - most luminous 488
 - radio-quiet *see* radio-quiet quasars
 - ratio of black hole to spheroid masses 610, 617
 - unification scheme with radio galaxies 610
- radiation-dominated universe 14, 276
- Compton scattering in 281–284
 - dynamics of 271–273
 - including neutrinos 302, 303
 - maintenance of photons and matter at the same temperature by Compton scattering 282
 - time-scale for expansion of 291
 - total energy density of relativistic species 291
- radio galaxies 51, 479
- 3CR sample of 508, 509
 - evidence for old stellar populations in 609
 - radio galaxy 0902+34 609
 - radio galaxy LBDS 53W069 610
 - radio galaxy LBDS 53W091 609
 - radio-far-infrared correlation for galaxies 597
 - flattening of radio source counts and 537
- radio-quiet quasars
- counts of 521, 522
 - cut-off at large redshifts 519, 524, 569
 - definition of complete samples of 518–521
 - completeness of 521
 - dispersion prism-grating techniques 521
 - multicolour photometric technique 519–520
 - searches for '*i*-band drop-outs' 520–521, 524
 - searches for Lyman- α and CIV emission lines 521
 - searches for variability of 521
 - ultraviolet excess technique 519
 - discovery of 518
 - evolution of, with cosmic epoch 518, 520, 521, 610
 - luminosity function of
 - 'luminosity evolution' of 522
 - evolution of 521, 522

- ram-pressure stripping 544, 613
 Rayleigh–Jeans region of Planck spectrum 455
 Rayleigh–Jeans spectrum 27, 29, 30
The Realm of the Nebulae (Hubble) 50, 492
 reciprocity theorem 229
 reconstruction of local mass distribution 268, 269
 red and blue sequences of galaxies *see* galaxies, red and blue sequences of Red-Sequence Cluster Survey 138
 redshift biases 406–407
 redshift, definition of 45, 162
 redshift–apparent magnitude relation 44
 redshift–magnitude relation for brightest galaxies in clusters
 infrared 544–545
 cosmic conspiracy and 544, 545
 galactic cannibalism and 545
 passive evolution and 544
 reduced deflection angle 130
 Rees–Sciama effect 440
 REFLEX catalogue of X-ray clusters of galaxies 116, 120, 121
 regular clusters of galaxies 102–103
 reionisation of the intergalactic gas 382
 relation between angular and spatial two-point correlation functions 37, 38
 relativistic binary stars 192
relativistic gravity, introduction to 173–198
 non-linearity of 181, 182
 relativistic jets, heating of the interstellar gas by 617
 relativity of simultaneity 238
Relativity: Special, General, and Cosmological (Rindler) 184
revised Hubble sequence for galaxies 50–56
 Riemannian geometries 151, 182, 184
 Riemannian metric 187
 ring galaxies 56, 58
Robertson–Walker metric 149, 150, 158–162, 163, 167, 168, 340, 341
 for an empty Milne Universe 237–239
 for the critical world model 231
 invariant interval ds^2 161
 ROSAT X-ray Observatory 116, 117, 119, 120, 122, 451, 491, 506, 524, 525
 rotation curve of a centrifugally supported disc in isothermal gas sphere 612
rotation curves of spiral galaxies 66–69
 rotation of galaxies, origin of 610–613
 damping of primordial rotational velocities 610
 dissipative contraction within dark matter haloes 611
 problem of specific angular momenta 612
 problems of theories of primordial turbulence 610
 role of tidal stripping 613
 roles of dissipation and tidal stripping 612
 tidal torques 611, 612
 during linear growth of perturbations 611
 slow rotation of the spheroidal components of elliptical and spiral galaxies and 611
 Rutherford scattering 190
 S0 galaxies 52
 Sérsic 159–03 123, 124
 Sérsic index 91
 Sa galaxies 51
Sachs–Wolfe effect 18, 21, 441, 447, 456
 dependence upon angular scale 439
 gravitational redshift and 436, 437
 integrated 452, 456
 physical arguments 436–440
 SAGDP99 survey 595
 Sakharov oscillations 21, 362
 Salpeter initial mass function 500, 588
 Sb galaxies 51
 Sc galaxies 52
 scalar fields 208, 623, 629, 634–635
 density and pressure of 634
 Einstein’s field equations and 635
 fluctuations in 635
 negative pressure equation of state and 634
 not yet detected experimentally 634
 properties of 634–635
 slow-roll parameters 635, 640
 string theory and 634

- theories beyond the standard model of particle physics and 634
- scale factor** $a(t)$ 160, 161, 162, 164, 167, 171, 172
- scale factor-redshift relation** 164, 201, 271
- scaling test for homogeneity of clustering of galaxies 35–37
- Schönberg–Chandrasekhar limit 500
- Schechter luminosity function for galaxies 77, 79, 82, 108, 109, 590, 593, 595
- break absolute magnitude M^* of 78, 81
- break luminosity L^* of 77, 78, 81
- brightest galaxies in clusters 82
- dependence upon galactic environment 79, 81
- evolution with redshift 82
- for low luminosity galaxies 82
- in voids 80, 81
- L^* as a standard candle 80
- turnover luminosity L^* 607
- Schwarzschild metric 183, 187
- coordinate time in 183
- proper time in 183
- Schwarzschild radius r_g 184
- Sco X-1 524
- SCUBA submillimetre bolometer array 534, 597
- Sd galaxies 52
- secular instabilities in rotating stellar discs 616
- self-similar model for cluster formation 118, 119
- semi-analytic models of galaxy formation** 412, 472, 486, 583, 613–620
- acoustic peaks in the large-scale galaxy distribution and 620
- as ‘experimental computational astrophysics’ 615
- dust extinction and 617
- evolution of mass function of galaxies and 620
- formation of supermassive black holes and 617, 618
- in centres of rich clusters 620
- heating of the intergalactic gas in clusters and 617
- mergers of galaxies and 616
- major 616
- minor 616
- morphologies of galaxies and 616
- nuclear starbursts and 616, 617
- objectives of 615
- quasars at large redshifts and 618, 619
- radiative cooling and star formation 615
- spectrophotometric properties of galaxies and 616
- supernova explosions and 616
- the epoch of maximum quasar activity and 620
- ‘trial and error’ approach to 617
- two-point correlation function for galaxies and 617, 618
- for different luminosities and colours 617
- Sérsic index 63
- Sérsic’s law 62
- Seyfert galaxies 51, 516, 521
- counts of 521
- Shane–Wirtanen catalogue of galaxies 100
- Sidereus Nuncius or the Starry Messenger* (Galileo) 5
- σ_8
- definition of 403
- two-point correlation function and 403
- Silk damping 353, 355, 357, 360, 361, 381, 410, 426, 430, 450
- Silk mass 17, 353, 356, 357
- singularity theorems of Penrose and Hawking 644
- Sirius 5
- Sirius B 177
- 6C radio galaxies 255
- Sloan Digital Sky Survey (SDSS) 22, 35, 36, 40–42, 49, 50, 75, 76, 78, 79, 82–84, 87–91, 93, 95, 99–101, 110, 111, 245, 362, 387, 410–412, 414, 465, 491, 520, 522, 524, 552, 557, 559
- power spectrum of galaxies in 412–415
- Small Magellanic Cloud 8
- Smoluchowski’s envelope 105
- Soudan Underground Laboratory 146, 374
- sound horizon 443, 444
- sound horizon at the last scattering layer 427–429
- Space Telescope Imaging Spectrograph 567

- space–time diagram
 for an empty Universe 237
 for the expanding Universe 170
- space–time diagrams for standard world models 339–347**
- critical world model $\Omega_0 = 1, \Omega_A = 0$ 342–344
 distances and times 339–340
 past light cone 340
 reference world model
 $\Omega_0 = 0.3, \Omega_A = 0.7$ 344–347
- space–time metric for isotropic curved spaces 155–158**
- ‘spaghetti’ topology 41
 spatial two-point correlation function 37, 38, 385, 386
 special theory of relativity 183, 184, 186
 spectral energy distribution of galaxies
 evolution of 498–500
 in far infrared and submillimetre
 wavebands 500, 503
 spectrum of primordial perturbations
 spectrum of primordial gravitational waves and 640
 spectrum of primordial perturbations in the scalar field 637–640
 constant noise-power on horizon scale 639
 damping on superhorizon scales 638
 decay of scalar field at end of inflationary era 639
 growth of potential fluctuations in inflationary expansion 638
 applicability on superhorizon scales 638
 as an equation of damped harmonic oscillator 638
 damping on superhorizon scales 638
 growth of vacuum fluctuations in inflationary expansion 637
 comparison with growth of non-relativistic density perturbations 637
 differential equation for 637
 growth of zero point fluctuations 638
 relation to perturbations in post-inflationary relativistic plasma 639
- time-delay formalism for 639
 zero point fluctuations in the ground state 638
- speed of sound as a function of cosmic epoch 285–286, 354, 427, 444
 at constant entropy 285
- speed of sound, relativistic 332, 352
- spherical harmonic functions 431, 433
 addition theorem for 433
- spheroidal component of spiral galaxies 51
- spin parameter λ 611, 612, 616
 as a measure of rotational support of a galaxy 611
- spin temperature of neutral hydrogen 576
- spiral galaxies 50, 51
 rotation curves of 66
 types of 51
- spiral-poor clusters of galaxies 102–103
- spiral-rich clusters of galaxies 102–103
- Spite plateau 298, 299
- Spitzer First Look Survey 533
- Spitzer infrared space observatory 478, 491, 533
- ‘sponge’ topology 41, 42
- Square Kilometre Array (SKA) 576
- stability diagram for adiabatic baryon perturbations 361
- standard cold dark matter model of galaxy formation 403
- star formation in galaxies 472
- star-forming galaxies 452
 at redshifts $z > 3$ 591
 dust extinction and 597
 spectrum of 594
- starburst galaxies 54, 536, 537
 ultraviolet spectra of 587, 588
 rate of formation of heavy elements and 588
- statistical equilibrium 65
- statistical methods into astronomy 5
- statistical weight g 289
- Stefan–Boltzmann law 272
- stellar evolution and element formation 584, 585
 energy generation in the conversion of hydrogen into helium 584, 585
 mean stellar luminosity during main sequence evolution 586

- stellar parallaxes 5
 stellar populations, ages of 91
 structural index, or structural length 105
 sub-dwarf (sdB) stars 519
 Subaru 8-metre telescope 595
 Subaru Deep Surveys 595
 submillimetre background radiation 534
 submillimetre bolometer array (SCUBA)
 452
 submillimetre galaxies
 problems of redshift determinations 597
 redshifts measurements in CO line 479
 substratum 149, 150, 341, 354, 358
Subtle is the Lord . . . (Pais) 184
 Sun, quadrupole moment of 189
 measured by helioseismology 190
Sunyaev–Zeldovich effect in hot
 intracluster gas 95, 125–128, 261
 distance estimates using 128
 fluctuations in the cosmic microwave
 background radiation and 450–451
 in the Rayleigh–Jeans limit 126
 kinematic 451
 spectral shape of distortions 126
 SuZIE experiment and measurement of
 spectral shape of distortions 126
 Sunyaev–Zeldovich marginalisation factor
 463
 superCDMS experiment 146
 superclusters of galaxies 43
 supergalactic plane 44, 269
superhorizon scales 347–350, 367, 379,
 382, 391, 392, 397, 437
 freezing of potential fluctuations on 439
 Supernova Cosmology Program 164–166,
 258, 259
 Supernova Legacy Survey 257, 258, 465
 supernova SN1987A 369
 distance of Large Magellanic Cloud and
 248
 supernovae of Type Ia 165, 166, 252
 ESSENCE project 165
 luminosity–width correlation 164, 165,
 256, 257
 redshift–apparent magnitude relation for
 256–259
 stretch factor 166
 white dwarfs in binary systems and 256,
 257
 supersymmetric particles 373
 suppression factor 450
 SWIRE Legacy sample 536
 ‘swiss-cheese’ topology 41
 symmetry breaking 24
 fluctuations associated with 466
 synchronous gauge 349
 synchrotron radiation 492
 synchrotron radio emission in clusters of
 galaxies 578
 temperature fluctuation on the last scattering
 surface
 adiabatic 364, 365
 temperature of formation of light elements
 279
 temperature of regions of ionised hydrogen
 279
 temperature-scale factor relation in the very
 early Universe 371, 372
 temperatures of the photon and neutrino
 backgrounds 301–303
 tensor perturbations and gravitational waves
 348
 tensor virial theorem 64
*The Inflationary Universe: The Quest for
 a New Theory of Cosmic Origins*
 (Guth) 626
Theoretical Concepts in Physics (Longair)
 173, 184, 314
*Theory and Experiment in Gravitational
 Physics* (Will) 189
**theory of the expanding Universe, history
 of** 10–13
thermal history of the Universe 17, 32,
 271–287
 early epochs 286–287
 epoch of recombination 277–281
 matter and radiation content of the
 Universe 273–277
 radiation-dominated era 271–273,
 281–284
 speed of sound as a function of cosmic
 epoch 285–286
*Third Reference Catalogue of Bright
 Galaxies* (de Vaucouleurs et al) 84
 Thomson optical depth for reionisation
 459

- Thomson scattering 33, 279, 356, 422, 451–454
 conditions for creation of polarised radiation by 454, 455, 458
 cross-section 29, 356
 optical depth of intergalactic gas for 452
3CR quasars 610
 black holes masses of 609
3CR radio galaxies 254–256, 514, 609, 610
 early formation of bulk of stellar population 609
 increase in luminosity with redshift 255
 stellar masses of large redshift 609
3CR radio sources 514, 516, 518
 tidal forces 613
 tidal forces and relativistic gravity 182, 183
 tidal radius 137, 138
 tidal radius of cluster of galaxies 105
 time dilation
 cosmological 163
 test of 164–166
 in a gravitational field 178, 438
 in special relativity 163
 topological defects
 cosmic strings, monopoles and textures 466, 628, 640
 isocurvature perturbations and 466
 phase transitions in the early Universe and 466
 topology of the distribution of galaxies 41, 42
 transfer function 393
 adiabatic cold dark matter 393–396
 adiabatic hot dark matter 394, 396
 isocurvature cold dark matter 394, 396–399
 subsequent evolution of different modified power spectra 399–401
 transfer functions
 for baryons 410, 411
 triaxial velocity distribution in galaxies 69
 triple- α reaction 293, 584
 tritium, half-life of 293
Tully–Fisher relation for spiral galaxies
73–74, 612
 in the infrared waveband 74
 ‘tuning-fork’ diagram 50
 turnaround epoch 408, 409
 2C radio survey 505
 Two Micron All Sky Survey (2MASS) 84, 140
2dF galaxy redshift survey 40–42, 49, 50, 78–83, 87, 88, 93, 245, 266, 269, 362, 387, 403–407, 410–414, 465, 491, 519, 618
 final power spectrum of 412–413
2dF quasar redshift survey 387, 510, 519–522, 524
 two-dimensional isotropic curved geometry 151, 152
 two-photon process 423
 two-point correlation function 432
 angular 433
two-point correlation function for galaxies
22, 34–38, 150, 268, 362, **385–388**, 433
 features of 387–388
 relation to the density contrast 386
 relation to the power spectrum of density fluctuations 389
 Type Ia supernovae 13, 21
 types of topology of the distribution of galaxies 41
 UGC catalogue of galaxies 44
 UHURU X-ray Observatory 114, 524
 UK Schmidt telescope 33, 519
 ultraluminous infrared galaxies (ULIRGs) 479, 503, 532
 spectra of 532
 ultrametal-poor star CS 22892-052
 thrium abundance in 252
 ultraviolet astronomy
 unit used in 562
 ultraviolet opacity of the intergalactic medium 569
 V/V_{\max} or luminosity-volume test
 507–510
 banded 509
 for radio galaxies 514
 for radio quasars 514
 for radio-quiet quasars 518
 space distribution of galaxies, quasars
 active galaxies 507–510

- vacuum energy density** 207, 208–211, 625
 estimate from quantum field theory 209
 problem of the magnitude of 209, 623
 values of the cosmological parameters
 problems of 623
 vector perturbations and vortex motions 348
- velocity dispersions of elliptical galaxies** 69–70
 velocity of Solar System through the Cosmic Microwave Background Radiation 30
 velocity–distance relation for galaxies 44–46, 48
 in an expanding universe 46, 47
- very early Universe** 621–644
 anthropic cosmological principle 625–626
 baryogenesis 641–642
 big problems of cosmology 621–624
 baryon-asymmetry problem 622
 flatness problem 622
 horizon problem 621
 primordial fluctuation problem 623
 values of the cosmological parameters 623
 way ahead 624
- inflationary Universe – historical background 22–25, 626–629
 limits of observation 624–625
 origin of the spectrum of primordial perturbations 629–640
 duration of the inflationary phase 630–631
 equation of state 630
 fluctuations in the scalar field and 637–640
 quantised harmonic oscillator 635–637
 scalar fields 634–635
 shrinking Hubble sphere 631–634
 Planck era 642–644
- Very Large Array (VLA) 140, 266, 597
 Very Long Baseline Array (VLBA) 266
Viking spacecraft 191, 192
 violent relaxation 399
 Virgo Cluster Catalogue 117
 Virgo cluster of galaxies 43, 52, 102, 110, 116, 117, 246, 248
 Virgo consortium 418, 615
 Virgo supercluster 268
 virial of Clausius 64
virial theorem 63–66, 103, 110, 119, 243, 375, 399, 408, 409, 474, 475
 applied to clusters of galaxies 66
 problems of applying 66
 Vishniac effect 453
 visibility function 423, 424, 426
 visible matter in the Universe
 integrated luminosity of 83
 mean mass–luminosity ratio of 83
 VLBI measurements of deflection of radio waves by the Sun 190, 191
 voids in the distribution of galaxies 41, 381, 439, 537
 Voigt profile 554
 VSA experiment 435
- walls and voids in the distribution of galaxies** 38–44
 weak gravitational lensing 136
 Weyl's postulate 149, 150, 158, 199
 white dwarfs 519, 586
 cooling times for 251
 gravitational redshift and 189
- Wide Field Planetary Camera 2 591, 592
 Wilkinson Microwave Anisotropy Probe (WMAP) 21, 32, 33, 231, 300, 421, 429, 434–437, 440, 442, 444, 450, 451, 456–458, 460, 463, 465–467, 547, 559, 561, 615, 620, 624, 625
 point sources detected in the WMAP survey 451
 nature of 452
- William Herschel's model of the Galaxy 5
 WIMPs
 abundance of 289
 as dark matter particles 370–374
 astrophysical limits to the masses of 144
 candidates for 143
 decoupling from thermal equilibrium 370
 in very early Universe 371
 epoch of decoupling of 372
 equilibrium abundances of 370

- 'freezing out' of abundances of 370, 371
- interaction cross-section for 371–373
 - experimental limits for 374
- laboratory detection of 145
- laboratory limits to the masses of 145
- suppression mechanisms for 145, 370–372, 375
- world lines 199, 237
 - of galaxies 342, 345
- Wouthuysen-Field effect 576
- W^\pm and Z^0 bosons 145, 208
- X-ray background emission 524
 - at hard X-ray energies
 - nature of sources contributing to 529
 - at soft X-ray energies
 - nature of sources contributing to 527, 529
- a cosmic conspiracy and 561
- contributions of different classes of source to 528
- spectrum of 526
- X-ray clusters of galaxies
 - number counts as a test of cosmological models 532
- tests of cosmological models and 529–532
- X-ray emission of intracluster gas 95
- X-ray luminosity–mass relation for clusters of galaxies 119, 120
- X-ray luminosity–velocity dispersion relation for clusters of galaxies 120
- X-ray sources
 - Comptonisation and 529
 - evolution of luminosity function of, with cosmic epoch 527
 - populations at soft and hard X-ray energies 526, 528
 - strongly absorbed 529
 - template spectra for strongly absorbed sources 529
- XMM-Newton X-ray Observatory 114, 116–118, 123, 124, 491, 525
- Z^0 boson, energy width of 300
- Zeldovich solution for non-linear collapse under gravity 20, 363
 - formation of caustics 477
- zinc abundance 601, 602
- Zwicky catalogue of galaxies 35



ASTRONOMY AND ASTROPHYSICS LIBRARY

Series Editors:

G. Börner · A. Burkert · W. B. Burton · M. A. Dopita
A. Eckart · T. Encrenaz · E. K. Grebel · B. Leibundgut
J. Lequeux · A. Maeder · V. Trimble

The Stars By E. L. Schatzman and F. Praderie

Modern Astrometry 2nd Edition

By J. Kovalevsky

The Physics and Dynamics of Planetary Nebulae By G. A. Gurzadyan

Galaxies and Cosmology By F. Combes,
P. Boissé, A. Mazure and A. Blanchard

Observational Astrophysics 2nd Edition
By P. Léna, F. Lebrun and F. Mignard

Physics of Planetary Rings Celestial Mechanics of Continuous Media
By A. M. Fridman and N. N. Gorkavyi

Tools of Radio Astronomy 4th Edition,
Corr. 2nd printing
By K. Rohlfs and T. L. Wilson

Tools of Radio Astronomy Problems and Solutions 1st Edition, Corr. 2nd printing
By T. L. Wilson and S. Hüttemeister

Astrophysical Formulae 3rd Edition
(2 volumes)

Volume I: Radiation, Gas Processes and High Energy Astrophysics
Volume II: Space, Time, Matter and Cosmology
By K. R. Lang

Galaxy Formation 2nd Edition

By M. S. Longair

Astrophysical Concepts 4th Edition
By M. Harwit

Astrometry of Fundamental Catalogues
The Evolution from Optical to Radio Reference Frames

By H. G. Walter and O. J. Sovers

Compact Stars. Nuclear Physics, Particle Physics and General Relativity 2nd Edition
By N. K. Glendenning

The Sun from Space By K. R. Lang

Stellar Physics (2 volumes)

Volume 1: Fundamental Concepts and Stellar Equilibrium
By G. S. Bisnovatyi-Kogan

Stellar Physics (2 volumes)

Volume 2: Stellar Evolution and Stability
By G. S. Bisnovatyi-Kogan

Theory of Orbits (2 volumes)

Volume 1: Integrable Systems and Non-perturbative Methods
Volume 2: Perturbative and Geometrical Methods
By D. Boccaletti and G. Pucacco

Black Hole Gravitohydromagnetics

By B. Punsly

Stellar Structure and Evolution

By R. Kippenhahn and A. Weigert

Gravitational Lenses By P. Schneider,
J. Ehlers and E. E. Falco

Reflecting Telescope Optics (2 volumes)

Volume I: Basic Design Theory and its Historical Development. 2nd Edition
Volume II: Manufacture, Testing, Alignment, Modern Techniques
By R. N. Wilson

Interplanetary Dust

By E. Grün, B. Å. S. Gustafson, S. Dermott and H. Fechtig (Eds.)

The Universe in Gamma Rays

By V. Schönfelder

Astrophysics. A New Approach 2nd Edition

By W. Kundt

Cosmic Ray Astrophysics

By R. Schlickeiser

Astrophysics of the Diffuse Universe

By M. A. Dopita and R. S. Sutherland

The Sun An Introduction. 2nd Edition

By M. Stix

Order and Chaos in Dynamical Astronomy

By G. J. Contopoulos

Astronomical Image and Data Analysis

2nd Edition By J.-L. Starck and F. Murtagh

The Early Universe Facts and Fiction

4th Edition By G. Börner



ASTRONOMY AND ASTROPHYSICS LIBRARY

Series Editors:

G. Börner · A. Burkert · W. B. Burton · M. A. Dopita
A. Eckart · T. Encrenaz · E. K. Grebel · B. Leibundgut
J. Lequeux · A. Maeder · V. Trimble

The Design and Construction of Large Optical Telescopes By P. Y. Bely

The Solar System 4th Edition
By T. Encrenaz, J.-P. Bibring, M. Blanc,
M. A. Barucci, F. Roques, Ph. Zarka

General Relativity, Astrophysics, and Cosmology By A. K. Raychaudhuri,
S. Banerji, and A. Banerjee

Stellar Interiors Physical Principles,
Structure, and Evolution 2nd Edition
By C. J. Hansen, S. D. Kawaler, and V. Trimble

Asymptotic Giant Branch Stars
By H. J. Habing and H. Olofsson

The Interstellar Medium
By J. Lequeux

Methods of Celestial Mechanics (2 volumes)
Volume I: Physical, Mathematical, and
Numerical Principles
Volume II: Application to Planetary System,
Geodynamics and Satellite Geodesy
By G. Beutler

Solar-Type Activity in Main-Sequence Stars
By R. E. Gershberg

Relativistic Astrophysics and Cosmology
A Primer By P. Hoang

Magneto-Fluid Dynamics
Fundamentals and Case Studies
By P. Lorrain

Compact Objects in Astrophysics
White Dwarfs, Neutron Stars and Black Holes
By Max Camenzind

Special and General Relativity
With Applications to White Dwarfs, Neutron
Stars and Black Holes
By Norman K. Glendenning



ASTRONOMY AND ASTROPHYSICS LIBRARY

Series Editors:

- G. Börner, Garching, Germany
A. Burkert, München, Germany
W. B. Burton, Charlottesville, VA, USA and
Leiden, The Netherlands
M. A. Dopita, Canberra, Australia
A. Eckart, Köln, Germany
T. Encrenaz, Meudon, France
E. K. Grebel, Heidelberg, Germany
B. Leibundgut, Garching, Germany
J. Lequeux, Paris, France
A. Maeder, Sauverny, Switzerland
V. Trimble, College Park, MD, and Irvine, CA, USA

Malcolm S. Longair

Galaxy Formation

Second Edition

With 202 Figures and 20 Tables



Springer

Malcolm S. Longair

Jacksonian Professor of Natural Philosophy
Cavendish Laboratory
J. J. Thomson Avenue
Cambridge CH3 0HE
England, UK
e-mail: msl1000@cam.ac.uk

Cover image: Galaxies NGC 2207 and IC 2163. Credit: NASA and The Hubble Heritage Team (STScI); Hubble Space Telescope WFPC2; STScI-PRC99-41; Source: <http://heritage.stsci.edu/1999/41/index.html>

Library of Congress Control Number: 2007935444

ISSN 0941-7834

ISBN 978-3-540-73477-2 Springer Berlin Heidelberg New York

This work is subject to copyright. All rights are reserved, whether the whole or part of the material is concerned, specifically the rights of translation, reprinting, reuse of illustrations, recitation, broadcasting, reproduction on microfilm or in any other way, and storage in data banks. Duplication of this publication or parts thereof is permitted only under the provisions of the German Copyright Law of September 9, 1965, in its current version, and permission for use must always be obtained from Springer. Violations are liable to prosecution under the German Copyright Law.

Springer is a part of Springer Science+Business Media

springer.com

© Springer-Verlag Berlin Heidelberg 1998, 2008

The use of general descriptive names, registered names, trademarks, etc. in this publication does not imply, even in the absence of a specific statement, that such names are exempt from the relevant protective laws and regulations and therefore free for general use.

Typesetting and production: LE-TeX Jelonek, Schmidt & Vöckler GbR, Leipzig, Germany
Cover design: eStudio Calamar S.L., F. Steinen-Broo, Girona, Spain

SPIN: 11394105 55/3180/YL - 5 4 3 2 1 0 Printed on acid-free paper

For Deborah, Mark and Sarah

Preface

This is the second edition of my book *Galaxy Formation*. Many people liked the first edition which appeared in 1998, just before the explosion of magnificent new data which have completely changed the face of astrophysical cosmology. Many of the agonies which had to be gone through in the first edition have disappeared and, to many people's amazement, including mine, there is now a *concordance model* for cosmology, the cosmologist's equivalent of the particle physicist's *standard model*. Just like the standard model, however, the concordance model creates as many problems as it solves. This is not a cause for concern, but rather one for celebration because we are now able to ask much better and deeper questions than in the past. These questions indicate clearly the need for physics and astrophysics 'Beyond the Concordance Model'.

The object of this new edition is to bring this amazing story up-to-date, very much in the spirit of the first edition. To recapitulate some of the points made in the previous preface about the origin of the book, I was asked by Springer-Verlag to expand the set of lecture notes that I prepared in 1988 for the First Astrophysics School organised by the European Astrophysics Doctoral Network into a full-length book. The set of notes was entitled *Galaxy Formation* and was published as a chapter of the volume *Evolution of Galaxies: Astronomical Observations* (eds. I. Appenzeller, H.J. Habing and P. Lena, pages 1 to 93, Springer-Verlag Berlin, Heidelberg, 1989). In that chapter, I attempted to bridge the gap between elementary cosmology and the technical papers appearing in the literature which can seem quite daunting on first encounter. The objective was to present the physical ideas and key results as clearly as possible as an introduction and guide to the technical literature.

In 1993, more lecture notes on *The Physics of Background Radiation* were prepared for the 23rd Advanced Course of the Swiss Society of Astrophysics and Astronomy, the topic being *The Deep Universe* (A.R. Sandage, R.G. Kron and M.S. Longair, Springer-Verlag Berlin, Heidelberg, 1995). Then, also in 1993, I completed a history of twentieth century astrophysics and cosmology, which was published as Chap. 23 of a three-volume work entitled *Twentieth Century Physics* (eds. L.M. Brown, A. Pais and A.B. Pippard, IOP Publications, AIP Press Bristol, and New York 1995). A much enlarged full-length book on this topic entitled *The Cosmic Century: A History of Astrophysics and Cosmology* was published by Cambridge University Press in 2006. That book brought the story of the origin of

galaxies and the large-scale structure of the Universe up-to-date as of October 2005 and it has been further updated and expanded in the present book. Just as in the first edition, the present volume is much more than a recycled and concatenated version of previously published works. I have rewritten and rethought the original versions, expanded some parts, brought everything up-to-date and included new material.

I often find that I understand things best, and present them most clearly, when I have to prepare them for students, at either the undergraduate or the post-graduate level, and so I have adopted the same form of presentation here. I have intentionally presented the material in an informal, pedagogical manner, and attempted to avoid getting bogged down in formalities and technicalities. If the material becomes too difficult, I simply summarise the key points, give some appropriate references and pass on. My approach is to reduce the problems to their simplest form and rationalise from these examples the results of more complete analyses. Wherever it is feasible without excessive effort, we will attempt to derive exact results. The level of presentation is intended to be appropriate for a final-year undergraduate or first-year post-graduate course of lectures. In other words, it is assumed that the reader has a good grasp of basic physics but does not necessarily have the appropriate background in astronomy, astrophysics or cosmology. My aim has been to write a user-friendly book, taking particular care to expound carefully areas where I have found students have difficulty.

When I wrote the original set of lecture notes on galaxy formation, my objective was to tell the story of modern astrophysical cosmology from the perspective of one of its most important and fundamental problems of cosmology – how did the galaxies come about? I enjoy this approach to the exposition of modern cosmology because, to do the problem justice, it is essential to introduce the whole of what I call *classical cosmology*, as the framework for the discussion. This approach has, for me, the great advantage of concentrating upon a crucial problem of astrophysical cosmology rather than regarding the objective of cosmology as being simply the delineation of a preferred cosmological model, however interesting that is in its own right. As we will show, the origin of galaxies and larger-scale structures in the Universe is one of the great cosmological problems and has provided us with unique and direct information about the physics of the very early Universe.

This new understanding brings with it the question of whether or not the old structure of the book is really appropriate – do we really need to grind through all the old story in order to understand the problems raised by the concordance model? My decision has been to maintain much of the original structure of the book, largely because the approach was very strongly physics-motivated and the old story reveals much of the essential physics of the concordance model.

One final warning is in order. I make no claim that this presentation is complete, unbiased or objective. You should regard the book as my own impressions and opinions of what I consider to be the important issues of modern astrophysical cosmology. Others would tell the story in a completely different way and put

emphasis upon different parts of what is unquestionably a multi-dimensional story. I will endeavour to include as wide a spectrum of ideas and opinions as possible, but the text will inevitably be incomplete. I do not worry about this – it should encourage you to read as widely as possible in order to neutralise my prejudices and biases.

Good Luck!

Venice and Cambridge,
July 2007

Malcolm Longair

Acknowledgements

Many people have contributed directly, or indirectly, to my understanding of the contents of this book. Perhaps the most important influence has been the late Peter Scheuer, who first introduced me to the physics of astrophysical cosmology. His approach and methods have very strongly influenced the way I have understood and taught this material over the years. I am very grateful to Immo Appenzeller, Harm Habing and Pierre Lena for the opportunity to give the lecture course in Les Houches in 1988. In preparing that set of lecture notes, I greatly benefitted from the advice of John Peacock and Alan Heavens who read parts of the typescript of the first edition and offered very helpful comments. John Peacock very kindly allowed me to use part of his lecture notes in preparing some of the material for the original chapter. John has now written up his notes in his book *Cosmological Physics* (Cambridge University Press, 2000). In my view, John's book is a brilliant achievement and I urge all interested readers to become familiar with his deep insights. Some of the text of the present book is based upon joint work with Rashid Sunyaev, which dates from the period 1968 to 1980. I fully acknowledge Rashid's contributions to clarifying my own understanding.

The invitation to deliver the 1993 course of lectures on the background radiation, as part of the 23rd Course of the Swiss Society of Astrophysics and Astronomy, came from Gustav Tammann, Bruno Binggeli and Hermann Buser and I am grateful for their kindness and hospitality at Les Diablerets. My history of twentieth century astrophysics and cosmology was commissioned by Brian Pippard on behalf of the editors of *Twentieth Century Physics* and I am grateful to him for his perceptive comments on that article.

I am particularly grateful to Bob Williams and his colleagues at the Space Telescope Science Institute at Baltimore, where I was a Visiting Fellow from September to December 1997. Without that sabbatical term at the Institute, the completion of the first edition would have been impossible. Special thanks are due to the staff, graduate students and research fellows at the Institute and at Johns Hopkins University, who kindly acted as guinea pigs on whom I 'battle-tested' portions of the book. Many of the research workers at the Institute gave generously of their time in discussing many of the topics in the book; the discussions with Ron Allen, Michael Fall, Harry Ferguson, Mario Livio, Duccio Macchetto and Piero Madau were especially helpful. The writing was enormously aided by access to the excellent library facilities at the Institute. Martin Harwit kindly read the first edition of the book very carefully and made a number of helpful suggestions.

Since the first edition was published, many colleagues have pointed out minor errors and suggested further topics for discussion. The preparation of the present edition began in December 2005, at the beginning of a two-year period of sabbatical leave kindly granted by the University of Cambridge. So much had changed in the matter of just a few years that essentially everything had to be rewritten in the light of this new understanding.

From February to May 2006, I was Adjunct Professor of Astronomy at the Astronomy Department of the University of Massachusetts at Amherst. I am most grateful to Ronald Snell and his colleagues for their warm welcome and the many helpful discussions we had about galaxies. Martin Weinberg, Neal Katz and Hou-Jun Mo were very stimulating colleagues. A special thank you goes to Dan McIntosh who introduced me to the red and blue sequences of galaxies and showed how our perception of what galaxies are has changed.

From October to December 2006, I was Visiting Professor at the Max Planck Institute for Astrophysics at Garching at the invitation of Rashid Sunyaev. The discussions with Rashid, Simon White and their colleagues were very helpful indeed in sharpening my understanding of many of the issues of astrophysical cosmology. I was back in Garching from February to April 2007 at the invitation of Catherine Cesarsky as a Visiting Scientist at the European Southern Observatory. This also proved to be a very stimulating visit. The wealth of expertise at ESO and the nearby Institutes made Garching a ideal haven in which to complete much of the final chapters of the new edition. I am most grateful to Bruno Leibundgut and all the staff members, visitors, post-docs and graduate students on whom I tried out some of the new sections of the book. The very final sections of the book were completed while I was a guest at the Osservatorio Astrofisico di Arcetri in Florence. I am most grateful to Francesco Palla and his colleagues for their kindness and hospitality.

Four colleagues are worthy of special thanks. Paul Schechter used the first edition of the book as a text for his courses on cosmology and kindly set up a web-site with corrections to it. He also made helpful suggestions for the present edition. Megan Donahue also used the first edition as a class text and provided a very helpful list of corrections and suggested improvements. She then ‘battle-tested’ Parts 2 and 3 of the new edition on her students and made helpful comments. I am most grateful to Megan and her students for this invaluable help which will undoubtedly have improved the book. Luigi Guzzo kindly read a number of sections of the book very careful and provided helpful suggestions and corrections. Peter Schneider reviewed the draft text at the invitation of Springer-Verlag and suggested a number of very helpful improvements.

Finally, the book is dedicated to my family, Deborah, Mark and Sarah, whose constant love, support and patience have made it possible.

Contents

Part I Preliminaries

1	A Brief History of Cosmology and Galaxy Formation	3
1.1	Pre-History	3
1.2	The Galaxies and the Structure of our Galaxy	5
1.3	The Theory of the Expanding Universe	10
1.4	The Big Bang	14
1.5	Galaxy and Structure Formation	16
1.6	Hot and Cold Dark Matter	19
1.7	The Very Early Universe	22
2	The Large-Scale Structure of the Universe	27
2.1	The Spectrum and Isotropy of the Cosmic Microwave Background Radiation	27
2.1.1	The Spectrum of the Cosmic Microwave Background Radiation	28
2.1.2	The Isotropy of the Cosmic Microwave Background Radiation	29
2.2	The Large-Scale Distribution of Galaxies	33
2.2.1	Two-Point Correlation Functions	34
2.2.2	Walls and Voids in the Distribution of Galaxies on Large Scales	38
2.3	Hubble's Law and the Expansion of the Universe	44
2.4	Conclusion	48
3	Galaxies	49
3.1	Introduction	49
3.2	The Revised Hubble Sequence for Galaxies	50
3.3	Peculiar and Interacting Galaxies	56
3.4	The Light Distribution in Galaxies	59
3.4.1	Elliptical Galaxies	61
3.4.2	Spiral and Lenticular Galaxies	61
3.4.3	Putting the Light Distributions Together	62
3.5	The Masses of Galaxies	63

3.5.1	The Virial Theorem for Clusters of Stars, Galaxies and Clusters of Galaxies	63
3.5.2	The Rotation Curves of Spiral Galaxies	66
3.5.3	The Velocity Dispersions of Elliptical Galaxies	69
3.6	The Properties of Spiral and Elliptical Galaxies	70
3.6.1	The Faber–Jackson Relation and the Fundamental Plane . . .	70
3.6.2	Ellipticals Galaxies as Triaxial Systems	71
3.6.3	The Tully–Fisher Relation for Spiral Galaxies	73
3.6.4	Luminosity–Metallicity Relations	74
3.7	The Luminosity Function of Galaxies	77
3.7.1	Aspects of the Luminosity Function of Galaxies	79
3.7.2	The Integrated Luminosity and the Mean Mass-to-Luminosity Ratio for Visible Matter in the Universe	83
3.8	The Properties of Galaxies: Correlations Along the Hubble Sequence	84
3.9	The Red and Blue Sequences	88
3.9.1	Colour Versus Absolute Magnitude	89
3.9.2	Sérsic Index and Colour	91
3.9.3	Mean Stellar Age and Concentration Index C	91
3.9.4	The Effect of the Galaxy Environment	92
3.9.5	The New Perspective	93
3.10	Concluding Remark	94
4	Clusters of Galaxies	95
4.1	The Large-Scale Distribution of Clusters of Galaxies	95
4.1.1	The Abell Catalogues of Rich Clusters of Galaxies	96
4.1.2	Comparison with Clusters Selected from the Sloan Digital Sky Survey	98
4.1.3	Abell Clusters and the Large-Scale Distribution of Galaxies	99
4.2	The Distribution of Galaxies in Clusters of Galaxies	101
4.2.1	The Galaxy Content and Spatial Distribution of Galaxies in Clusters	101
4.2.2	Clusters of Galaxies and Isothermal Gas Spheres	103
4.2.3	The Luminosity Function for Cluster Galaxies	108
4.2.4	Summary of the Properties of Rich Clusters of Galaxies . .	109
4.3	Dynamical Estimates of the Masses of Clusters of Galaxies . .	110
4.4	X-Ray Observations of Hot Gas in Clusters of Galaxies	114
4.5	The Sunyaev–Zeldovich Effect in Hot Intracluster Gas	125
4.6	Gravitational Lensing by Galaxies and Clusters of Galaxies . .	128
4.6.1	Basic Theory of Gravitational Deflections	128
4.6.2	Magnification of Images by Gravitational Lensing	130
4.6.3	Extended Deflectors	133
4.6.4	Gravitational Lensing and the Astrophysics of Galaxies . .	136
4.7	Forms of Dark Matter	139

4.7.1	Baryonic Dark Matter	139
4.7.2	Non-Baryonic Dark Matter	142
4.7.3	Astrophysical and Experimental Limits	144

Part II The Basic Framework

5	The Theoretical Framework	149
5.1	The Cosmological Principle	149
5.2	Isotropic Curved Spaces	150
5.3	The Space–Time Metric for Isotropic Curved Spaces	155
5.4	The Robertson–Walker Metric	158
5.5	Observations in Cosmology	162
5.5.1	The Cosmological Redshift	162
5.5.2	Hubble’s Law	165
5.5.3	Angular Diameters	167
5.5.4	Apparent Intensities	168
5.5.5	Number Densities	170
5.5.6	The Age of the Universe	171
5.6	Summary	171
6	An Introduction to Relativistic Gravity	173
6.1	The Principle of Equivalence	173
6.2	The Gravitational Redshift	176
6.3	The Bending of Light Rays	179
6.4	Further Complications	181
6.5	The Route to General Relativity	184
6.5.1	Four-Tensors in Relativity	184
6.5.2	What Einstein Did	187
6.6	Experimental and Observational Tests of General Relativity	189
6.6.1	The Four Tests of General Relativity	189
6.6.2	Pulsars and General Relativity	192
6.6.3	Parameterised Post-Newtonian Models	195
6.6.4	Variation of the Gravitational Constant with Cosmic Epoch	197
6.7	Summary	198
7	The Friedman World Models	199
7.1	Einstein’s Field Equations	199
7.2	The Standard Friedman World Models with $\Lambda = 0$	202
7.2.1	The Newtonian Analogue of the Friedman World Models ..	202
7.2.2	The Critical Density and the Density Parameter	204
7.2.3	The Dynamics of the Friedman Models with $\Lambda = 0$..	205
7.3	Friedman Models with Non-Zero Cosmological Constant	207
7.3.1	The Cosmological Constant and the Vacuum Energy Density	208

7.3.2	Varying the Equation of State of the Vacuum Energy	210
7.3.3	The Dynamics of World Models with $\Lambda \neq 0$: General Considerations	211
7.4	Observations in Cosmology	215
7.4.1	The Deceleration Parameter	216
7.4.2	The Cosmic Time–Redshift Relation	217
7.4.3	Distance Measures as a Function of Redshift	218
7.4.4	Angular Diameter–Redshift Relations	221
7.4.5	Flux Density–Redshift Relations	223
7.4.6	The Comoving Volume Within Redshift z	226
7.5	Angular Diameter Distances Between Any Two Redshifts	228
7.6	The Flatness Problem	230
7.7	Inhomogeneous World Models	231
A7	The Robertson–Walker Metric for an Empty Universe	237
8	The Determination of Cosmological Parameters	241
8.1	The Cosmological Parameters	241
8.2	Testing the Friedman Models	242
8.3	Hubble’s Constant H_0	246
8.4	The Age of the Universe T_0	250
8.5	The Deceleration Parameter q_0	252
8.5.1	The Redshift–Magnitude Relation for the Brightest Galaxies in Clusters	252
8.5.2	The Redshift–Magnitude Relation for Radio Galaxies	254
8.5.3	The Redshift–Magnitude Relation for Type 1a Supernovae .	256
8.5.4	The Number Counts of Galaxies	259
8.5.5	The Angular Diameter–Redshift Test	261
8.6	Ω_A and the Statistics of Gravitational Lenses	263
8.7	The Density Parameter Ω_0	267
8.8	Summary	270
9	The Thermal History of the Universe	271
9.1	Radiation-Dominated Universes	271
9.2	The Matter and Radiation Content of the Universe	273
9.3	The Epoch of Recombination	277
9.4	The Radiation-Dominated Era	281
9.5	The Speed of Sound as a Function of Cosmic Epoch	285
9.6	Early Epochs	286
10	Nucleosynthesis in the Early Universe	289
10.1	Equilibrium Abundances in the Early Universe	289
10.2	The Decoupling of Neutrinos and the Neutrino Barrier	290
10.3	The Synthesis of the Light Elements	292
10.4	The Abundances of the Light Elements	295

10.4.1	Determinations of the Observed Abundances of the Light Elements	296
10.4.2	Comparison of Theory and Observations	299
10.5	The Neutrino Background Temperature and the Value of χ	301
10.6	Baryon-Symmetric Universes	303

Part III The Development of Primordial Fluctuations Under Gravity

11	The Evolution of Perturbations in the Standard Big Bang	311
11.1	What the Theorists Are Trying to Do	311
11.1.1	Why this Programme Is Feasible	312
11.1.2	A Warning	312
11.2	The Non-Relativistic Wave Equation for the Growth of Small Perturbations in the Expanding Universe	313
11.3	The Jeans' Instability	317
11.4	The Jeans' Instability in an Expanding Medium	319
11.4.1	Small Perturbation Analysis	319
11.4.2	Perturbing the Friedman Solutions	321
11.4.3	Falling Poles	322
11.4.4	The General Solution	324
11.5	The Evolution of Peculiar Velocities in the Expanding Universe	327
11.6	The Relativistic Case	331
11.7	The Basic Problem	332
12	More Tools and Problems	335
12.1	Horizons and the Horizon Problem	335
12.2	Pedagogical Interlude – Space–Time Diagrams for the Standard World Models	339
12.2.1	Distance and Times	339
12.2.2	The Past Light Cone	340
12.2.3	The Critical World Model $\Omega_0 = 1, \Omega_A = 0$	342
12.2.4	The Reference World Model $\Omega_0 = 0.3, \Omega_A = 0.7$	344
12.3	Superhorizon Scales	347
12.4	The Adiabatic Baryonic Fluctuations in the Standard Big Bang	350
12.4.1	The Radiation-Dominated Era	352
12.4.2	The Matter-Dominated Era	353
12.5	Dissipation Processes in the Pre-Recombination Era	355
12.6	Isothermal Perturbations	357
12.7	Baryonic Theories of Galaxy Formation	360
12.7.1	The Adiabatic Scenario	361
12.7.2	The Isothermal Scenario	363
12.8	What Went Wrong?	364

13 Dark Matter and Galaxy Formation	367
13.1 Introduction	367
13.2 Forms of Non-Baryonic Dark Matter	369
13.3 WIMPs as Dark Matter Particles	370
13.4 Metric Perturbations and Hot and Cold Dark Matter	374
13.5 Free Streaming and the Damping of Hot Dark Matter Perturbations	375
13.6 Instabilities in the Presence of Dark Matter	377
13.7 The Evolution of Hot and Cold Dark Matter Perturbations	380
13.7.1 Hot Dark Matter Scenario	380
13.7.2 Cold Dark Matter Scenario	381
13.8 Conclusion	384
14 Correlation Functions and the Spectrum of the Initial Fluctuations	385
14.1 The Two-Point Correlation Function for Galaxies	385
14.2 The Perturbation Spectrum	388
14.2.1 The Relation Between $\xi(r)$ and the Power Spectrum of the Fluctuations	388
14.2.2 The Initial Power Spectrum	390
14.2.3 The Harrison–Zeldovich Power Spectrum	391
14.3 Evolution of the Initial Perturbation Spectrum – Transfer Functions	393
14.3.1 Adiabatic Cold Dark Matter	393
14.3.2 Adiabatic Hot Dark Matter	396
14.3.3 Isocurvature Cold Dark Matter	396
14.3.4 The Subsequent Evolution	399
14.4 Biasing	401
14.5 Reconstructing the Processed Initial Power Spectrum	405
14.5.1 Redshift Biases	406
14.5.2 Non-Linear Development of Density Perturbations	407
14.5.3 The Role of Baryon Perturbations	409
14.6 The Acoustic Peaks in the Power Spectrum of Galaxies	411
14.6.1 The 2dF Galaxy Redshift Survey	412
14.6.2 Sloan Digital Sky Survey	412
14.7 Variations on a Theme of Cold Dark Matter	415
15 Fluctuations in the Cosmic Microwave Background Radiation	421
15.1 The Ionisation of the Intergalactic Gas Through the Epoch of Recombination	422
15.2 The Physical and Angular Scales of the Fluctuations	424
15.2.1 The Last Scattering Layer	425
15.2.2 The Silk Damping Scale	426
15.2.3 The Sound Horizon at the Last Scattering Layer	427
15.2.4 The Particle Horizon Scales	429
15.2.5 Summary	430
15.3 The Power Spectrum of Fluctuations in the Cosmic Microwave Background Radiation	431

15.3.1	The Statistical Description of the Temperature Fluctuations	431
15.3.2	The Power Spectrum of Fluctuations in the Intensity of the Cosmic Microwave Background Radiation	434
15.4	Large Angular Scales	436
15.4.1	The Sachs–Wolfe Effect – Physical Arguments	436
15.4.2	The Integrated Sachs–Wolfe and Rees–Sciama Effects	440
15.4.3	Primordial Gravitational Waves	440
15.5	Intermediate Angular Scales – the Acoustic Peaks	443
15.6	Small Angular Scales	450
15.6.1	Statistical and Silk Damping	450
15.6.2	The Sunyaev–Zeldovich Effect in Clusters of Galaxies	450
15.6.3	Confusion Due to Discrete Sources	451
15.7	The Reionised Intergalactic Gas	452
15.8	The Polarisation of the Cosmic Microwave Background Radiation	454
15.8.1	The Polarisation Mechanism for the Cosmic Microwave Background Radiation	454
15.8.2	Polarisation from the Last Scattering Layer	455
15.8.3	Polarisation from the Epoch of Reionisation	458
15.8.4	Primordial Gravitational Waves	459
15.8.5	Weak Gravitational Lensing	460
15.9	Determination of Cosmological Parameters	463
15.10	Other Sources of Primordial Fluctuations	465
15.11	Reflections	466

Part IV The Post-Recombination Universe

16	The Post-Recombination Era	471
16.1	The Non-Linear Collapse of Density Perturbations	472
16.1.1	Isotropic Top-Hat Collapse	473
16.1.2	The Zeldovich Approximation	475
16.2	The Role of Dissipation	477
16.3	The Press–Schechter Mass Function	482
16.3.1	Exposition – Elementary Theory	482
16.3.2	Development and Recapitulation	485
17	The Evolution of Galaxies and Active Galaxies with Cosmic Epoch	491
17.1	Introduction	491
17.2	Counts of Galaxies and Active Galaxies	492
17.2.1	Euclidean Source Counts	493
17.2.2	Source Counts for the Standard World Models	494
17.2.3	Submillimetre Counts of Dusty Galaxies	500
17.2.4	Number Counts in Models with Finite Ω_A	501
17.2.5	Fluctuations in the Background Radiation due to Discrete Sources	504

17.3	The V/V_{\max} or Luminosity-Volume Test	507
17.4	Background Radiation	510
17.4.1	Background Radiation and Source Counts	510
17.4.2	Evaluating the Background due to Discrete Sources	510
17.4.3	The Effects of Evolution – the Case of the Radio Background Emission	512
17.5	The Evolution of Active Galaxies with Cosmic Epoch	514
17.5.1	Number Counts and V/V_{\max} Tests for Extragalactic Radio Sources	514
17.5.2	Radio Quiet Quasars	518
17.5.3	X-Ray Source Counts	524
17.5.4	X-Ray Clusters of Galaxies	529
17.6	Infrared and Submillimetre Number Counts	532
17.7	Counts of Galaxies	537
17.8	Clusters of Galaxies	543
18	The Intergalactic Medium	547
18.1	The Background Emission of and Absorption by the Intergalactic Gas	548
18.2	The Gunn–Peterson Test	549
18.3	The Lyman- α Absorption Clouds	552
18.3.1	The Properties of the Lyman- α Absorption Clouds	552
18.3.2	The Nature of the Clouds in the Lyman- α Forest	554
18.3.3	The Evolution of Lyman- α Absorption Clouds with Cosmic Epoch	556
18.3.4	The Power Spectrum of the Lyman- α Forest	557
18.4	The Lukewarm Intergalactic Gas	560
18.4.1	The X-Ray Background and a Cosmic Conspiracy	561
18.4.2	The Collisional Excitation of the Intergalactic Gas	562
18.4.3	The Emission and Absorption of Diffuse Lukewarm Intergalactic Gas	564
18.4.4	The Proximity Effect and the Diffuse Ultraviolet Background Radiation at Large Redshifts	567
18.5	The Lyman Continuum Opacity of the Intergalactic Gas	569
18.6	Modelling the Evolution of the Intergalactic Medium	571
18.7	The Epoch of Reionisation	574
18.8	The Origin of Magnetic Fields	577
19	Making Real Galaxies	583
19.1	Star and Element Formation in Galaxies	583
19.1.1	The Background Radiation and Element Formation	584
19.1.2	The Global Star Formation Rate from Optical and Ultraviolet Observations of Star-Forming Galaxies	587
19.1.3	The Lyman-Break Galaxies	590
19.1.4	The Hubble Deep and Ultra Deep Fields	590

19.1.5 Submillimetre Determinations of the Cosmic Star-Formation Rate	596
19.2 The Abundances of Elements in Lyman- α Absorption Systems	598
19.3 The Equations of Cosmic Chemical Evolution	604
19.4 The Old Red Galaxies	607
19.5 The Origin of Rotation	610
19.6 Putting It All Together – Semi-Analytic Models of Galaxy Formation	613
20 The Very Early Universe	621
20.1 The Big Problems	621
20.1.1 The Horizon Problem	621
20.1.2 The Flatness Problem	622
20.1.3 The Baryon-Asymmetry Problem	622
20.1.4 The Primordial Fluctuation Problem	623
20.1.5 The Values of the Cosmological Parameters	623
20.1.6 The Way Ahead	624
20.2 The Limits of Observation	624
20.3 The Anthropic Cosmological Principle	625
20.4 The Inflationary Universe – Historical Background	626
20.5 The Origin of the Spectrum of Primordial Perturbations	629
20.5.1 The Equation of State	630
20.5.2 The Duration of the Inflationary Phase	630
20.5.3 The Shrinking Hubble Sphere	631
20.5.4 Scalar Fields	634
20.5.5 The Quantised Harmonic Oscillator	635
20.5.6 The Spectrum of Fluctuations in the Scalar Field	637
20.6 Baryogenesis	641
20.7 The Planck Era	642
References	645
Name Index	695
Index	701

10 Nucleosynthesis in the Early Universe

One of the reasons why the standard Big Bang model is taken so seriously is its remarkable success in accounting for the observed abundances of the light elements by *primordial nucleosynthesis*, meaning the nuclear processes which took place during the first ten minutes of the cosmic expansion. The results of this analysis are crucial for a number of aspects of galaxy formation. In particular, primordial nucleosynthesis provides one of the most important constraints upon the density parameter in the form of baryons Ω_B . In developing these results, we need to study in some detail the rôle of neutrinos in the early Universe, how they change the dynamics of the expansion and how they decouple from the electrons and positrons. The neutrinos provide an example of the type of decoupling process which is important for other unknown types of weakly interacting particle.

10.1 Equilibrium Abundances in the Early Universe

Consider a particle of mass m at very high temperatures such that its total energy is much greater than its rest mass energy, $kT \gg mc^2$. If the time-scales of the interactions which maintain this species in thermal equilibrium with all the other species present at temperature T are shorter than the age of the Universe at that epoch, the equilibrium number densities of the particle and its antiparticle according to relativistic statistical mechanics are

$$N = \bar{N} = \frac{4\pi g}{h^3} \int_0^\infty \frac{p^2 dp}{e^{E/kT} \pm 1}, \quad (10.1)$$

where g is the statistical weight of the particle, p its momentum and the \pm sign depends upon whether the particles are fermions (+) or bosons (-). The photons are massless bosons for which $g = 2$, nucleons, antinucleons, electrons and positrons are fermions with $g = 2$ and the electron, muon and tau neutrinos are fermions with helicity for which $g = 1$. The equilibrium number densities for these particles and their antiparticles $N = \bar{N}$ and their energy densities ε can be found from this expression. For (a) photons, (b) nucleons, electrons and their antiparticles and

(c) neutrinos and antineutrinos respectively, these are:

$$\begin{aligned}
 \text{(a)} \quad g &= 2, \quad N = 0.244 \left(\frac{2\pi kT}{hc} \right)^3 \text{m}^{-3}, \quad \varepsilon = aT^4; \\
 \text{(b)} \quad g &= 2, \quad N = \bar{N} = 0.183 \left(\frac{2\pi kT}{hc} \right)^3 \text{m}^{-3}, \quad \varepsilon = \frac{7}{8}aT^4; \\
 \text{(c)} \quad g &= 1, \quad N = \bar{N} = 0.091 \left(\frac{2\pi kT}{hc} \right)^3 \text{m}^{-3}, \quad \varepsilon = \frac{7}{16}aT^4. \quad (10.2)
 \end{aligned}$$

To find the total energy density, we add together all the equilibrium energy densities, that is,

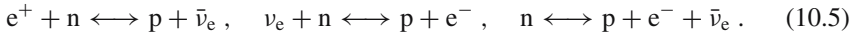
$$\text{Total energy density} = \varepsilon = \chi(T) aT^4. \quad (10.3)$$

When the particles become non-relativistic, $kT \ll mc^2$ and the abundances of the different species are maintained in equilibrium by interactions between the particles, the equilibrium number density is given by the non-relativistic limit of the integral of (10.1),

$$N = g \left(\frac{mkT}{h^2} \right)^{3/2} \exp \left(-\frac{mc^2}{kT} \right). \quad (10.4)$$

Thus, once the particles become non-relativistic, the number density of the species decreases exponentially with temperature and it no longer contributes to the inertial mass density which determines the rate of deceleration of the Universe.

Let us consider the simplest case of the abundances of protons and neutrons in the early Universe. At redshifts less than 10^{12} , the neutrons and protons are non-relativistic, $kT \ll mc^2$, and their equilibrium abundances are maintained by the weak interactions



The values of g for neutrons and protons are the same and so the relative abundances of neutrons to protons is

$$\left[\frac{n}{p} \right] = \exp \left(-\frac{\Delta mc^2}{kT} \right), \quad (10.6)$$

where Δmc^2 is the mass difference between the neutron and the proton.

10.2 The Decoupling of Neutrinos and the Neutrino Barrier

The following arguments summarise the essential physics of the process of decoupling of neutrinos and their influence upon the dynamics of the early Universe.

The abundance ratio of neutrons to protons ‘freezes out’ when the neutrino interactions can no longer maintain the equilibrium abundances of neutrons and protons. The condition for ‘freezing out’ is that the time-scale of the weak interactions becomes greater than the age of the Universe. Now, the neutrons and protons are non-relativistic during the era of primordial nucleosynthesis and so their abundances decrease exponentially, while the electrons and positrons are still relativistic and so are present with the abundances given by (10.2b). Consequently, the processes which prevent the neutrinos escaping freely are their interactions with the electrons and positrons. These interactions are:

$$e^- + e^+ \longleftrightarrow \nu_e + \bar{\nu}_e, \quad e^\pm + \nu_e \longleftrightarrow e^\pm + \bar{\nu}_e, \quad e^\pm + \bar{\nu}_e \longleftrightarrow e^\pm + \bar{\nu}_e. \quad (10.7)$$

The time-scale for these interactions is $t_{\text{weak}} = (\sigma Nc)^{-1}$, where the cross-section for the weak neutrino interactions, $\sigma \approx 3 \times 10^{-49} (E/m_e c^2)^2 \text{ m}^2$, is proportional to the square of the neutrino’s energy. N is the total number density of electrons and positrons which decreases as $R^{-3} \propto T^3$ and so, since $\bar{E} = 3kT$ for relativistic particles, it follows that the time-scale for the weak interactions changes with temperature as T^{-5} . Specifically, using (10.2b) for N and the above estimate for σ , we find

$$t_{\text{weak}} \approx \frac{3 \times 10^{40}}{\left(\frac{3k}{m_e c^2}\right)^2 \left(\frac{2\pi k}{hc}\right)^3} \frac{1}{T^5} = \left(\frac{1.7 \times 10^{10}}{T}\right)^5 \text{ s}. \quad (10.8)$$

This time-scale increases with decreasing temperature much more rapidly than the expansion time-scale of the Universe, which is given by (9.7). We have to modify (9.7) to take account of all the types of elementary particles which can contribute to the energy density ε during these early epochs, that is, we have to use (10.3). During these epochs, the particles which contribute to the total energy density are the photons, the electrons, the electron-, muon- and tau-neutrinos and their antiparticles. Adding together these contributions, we find from (10.2) that

$$\chi = 1 + 2 \times \frac{7}{8} + 2N_\nu \times \frac{7}{16}, \quad (10.9)$$

if there are N_ν neutrino species. If we adopt the known numbers of neutrino species, $N_\nu = 3$, we find that $\chi = 43/8$ and so

$$\varepsilon = \chi a T^4 = \frac{3c^2}{32\pi G} t^{-2}, \quad T = \left(\frac{3c^2}{32\pi G \chi a}\right)^{1/4} t^{-1/2} = 10^{10} t^{-1/2} \text{ K}, \quad (10.10)$$

where the time t is measured in seconds. It can be seen that the time-scales for the expansion of the Universe and the decoupling of the neutrinos were the same when the Universe had temperature $T \approx 1.2 \times 10^{10}$ K at $t = 0.7$ s; at this epoch, kT was almost precisely 1 MeV. Notice the important point that this time-scale and temperature are determined by fundamental constants of physics.

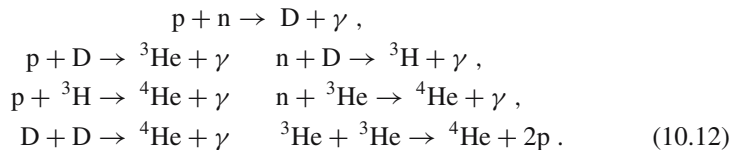
As a by-product of the above analysis, we have derived the epoch at which the Universe became transparent to neutrinos, namely, the epoch when the neutrinos could no longer maintain the neutrons and protons in thermodynamic equilibrium. Just as there was a barrier for photons at a redshift of about 1,500, so there is a *neutrino barrier* at energy $kT = 1$ MeV. This means that we would expect the background neutrinos to be last scattered at the epoch corresponding to $kT = 1$ MeV, about 1 second from the origin of the Big Bang.

10.3 The Synthesis of the Light Elements

At the epoch when the neutrinos decoupled at $kT = 1$ MeV, the neutron fraction, as determined by (10.6), froze out with a $n/(n+p)$ ratio of

$$\left[\frac{n}{n+p} \right] = 0.21 , \quad (10.11)$$

so that by this epoch, the protons were significantly more abundant than the neutrons. After this time, the neutron fraction decreased only slowly, although the process of neutron decay, which has half-life $\tau_n = 885.7 \pm 0.8$ s, needs to be taken into account. The protons and neutrons now began the process of light element formation through the following sequence of nuclear reactions:



The net result is that almost all the neutrons were combined with protons to form ${}^4\text{He}$ nuclei so that, for every pair of neutrons which survives, a helium nucleus was formed.

Most of the nucleosynthesis did not take place immediately after the neutrinos decoupled, but at a much lower temperature of about 10^9 K because, at higher temperatures, the deuterons which were formed by the crucial first interaction of (10.12) were destroyed by the γ -rays of the background radiation. We can understand this result from the following calculation. The binding energy of the deuteron is $E_B = 2.23$ MeV and so this energy is equal to kT at $T = 2.6 \times 10^{10}$ K. Just as in the case of the recombination of the intergalactic gas (Sect. 9.3), the photons far outnumbered the nucleons and it was only when the temperature of the expanding gas had decreased to about 26 times less than this temperature that the number density of dissociating photons was less than the number of nucleons. Thus, the bulk of the nucleosynthesis took place after about 100 s when the temperature of the background radiation had fallen to about 10^9 K.

The detailed temperature history and evolution of the light elements during the epoch of nucleosynthesis were worked out in a classic paper by Wagoner, following

earlier pioneering computations by Wagoner, Fowler and Hoyle (Wagoner, 1973; Wagoner et al., 1967) (Fig. 10.1). It can be seen that the bulk of the synthesis of the light elements occurred when the Universe was about 300 seconds old. Although some of the neutrons had decayed spontaneously by this time, the bulk of them survived. Detailed calculations show that after 300 s the neutron mass fraction had fallen to 0.123 (Weinberg, 1972) and so the predicted mass fraction of helium Y_p is expected to be twice the neutron fraction

$$Y_p = \left[\frac{^4\text{He}}{\text{H} + ^4\text{He}} \right] \approx 0.25 . \quad (10.13)$$

In addition to ^4He , which is always produced with an abundance of about 23 to 24%, traces of the light elements deuterium (D), helium-3 (^3He) and lithium-7 (^7Li) were created. Tritium (^3H) was also created, but it decayed with a radioactive half-life of only 12.3 years. Heavier elements were not synthesised because of the absence of stable isotopes with mass numbers 5 and 8. All the heavier elements were synthesised during the course of stellar evolution, the key step being the rare triple- α process, which enables carbon nuclei to be formed when three helium nuclei come together.

These are remarkable results. Historically, it was always a problem to understand why the abundance of helium is so high wherever it can be observed in the Universe. Its chemical abundance always appears to be greater than about 23%. In addition, it was a mystery how the deuterium in the Universe could have been synthesised. It is a very fragile nucleus and is destroyed rather than created in stellar interiors. The same argument applies to a lesser extent to the lighter isotope of helium, ^3He , and to ^7Li . Precisely these elements were synthesised in the early stages of the Big Bang model. The difference between primordial and stellar nucleosynthesis is that, in stellar interiors, nucleosynthesis takes place in roughly thermodynamic equilibrium over very long time-scales, whereas in the early stages of the Big Bang the ‘explosive’ nucleosynthesis is all over in fifteen minutes.

Note that the physics which determines the abundance of ^4He is different from that which determines the abundance of the other light elements. The above analysis shows that the synthesis of ^4He is essentially thermodynamic, in that it is fixed by the ratio of neutrons to protons when the neutrinos decoupled from the nuclear reactions which maintained them in their equilibrium abundances. In other words, the ^4He abundance is a measure of the *temperature* at which the decoupling of the neutrinos took place. On the other hand, the abundances of D, ^3He and ^7Li are determined by the extent to which the sequence of reactions (10.12) can convert all the neutrons into ^4He before the temperature falls below that at which nucleosynthesis can continue to take place. Thus, in Universes with high baryon number densities, there is time for essentially all the neutrons to be combined into deuterium nuclei which then combine to form ^4He nuclei and the predicted deuterium abundance is low. On the other hand, if the baryon number density is low, there is not time for all the intermediate stages in the synthesis of helium to be completed and the result is a much higher abundance of deuterium and ^3He . Thus, the abundances of the deuterium and ^3He are measures of the *present baryon density* of the Universe.

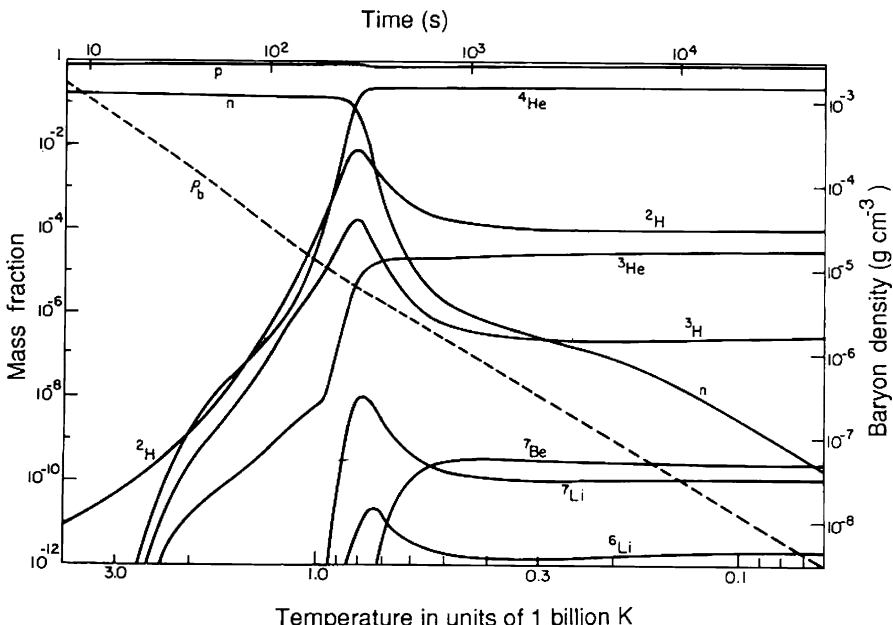


Fig. 10.1. An example of the time and temperature evolution of the abundances of the light elements according to the standard Big Bang model of the Universe from detailed computer calculations by Wagoner (Wagoner, 1973). Before about 100 s, no significant synthesis of the light elements took place because deuterium ${}^2\text{H}$ was destroyed by hard γ -ray photons in the high energy (Wien) region of the black-body spectrum. As the temperature decreased, more and more of the deuterium survived and the synthesis of heavier light elements became possible through the reactions (10.12). Notice that the synthesis of elements such as D, ${}^3\text{He}$, ${}^4\text{He}$, ${}^7\text{Li}$ and ${}^7\text{Be}$ was completed after about 15 minutes. The neutrons decayed with a half-life of 885.7 ± 0.8 s and the ${}^3\text{H}$ with a half-life of 12.3 years

The predicted abundances of the light elements and their uncertainties using the most recent values of the nuclear interaction cross-sections are shown in Fig. 10.2, which is taken from the authoritative review by Steigman (Steigman, 2004). The predicted abundances are displayed as a function of the baryon-to-photon ratio in the form $\eta = 10^{10} n_B/n_\gamma = 274 \Omega_B h^2$, which is conserved as the Universe expands from the epoch of nucleosynthesis to the present day. Y_p is the abundance of helium by mass, whereas the abundances of D, ${}^3\text{He}$ and ${}^7\text{Li}$ are plotted as ratios by number relative to hydrogen. The widths of the bands reflect the theoretical uncertainties in the predictions. It can be seen that for the standard Hot Big Bang, the ${}^4\text{He}$ abundance is relatively insensitive to the present baryon density in the Universe, in contrast to those of the other light elements.

The variations of D and ${}^3\text{He}$ can be understood in terms of the arguments given above. The ${}^7\text{Li}$ abundance decreases with increasing values of η , but then increases at the largest values of η . The reason is that, at low values of η , ${}^7\text{Li}$ is principally synthesised through the ${}^3\text{H}(\alpha, \gamma){}^7\text{Li}$ reaction but is easily destroyed in collisions with

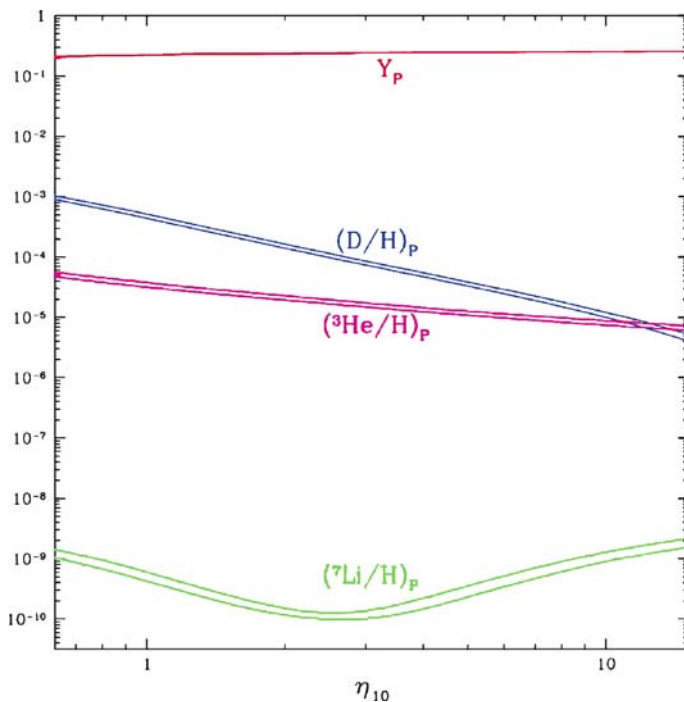


Fig. 10.2. The predicted primordial abundances of the light elements as a function of the present baryon-to-photon ratio in the form $\eta = 10^{10}n_B/n_\gamma = 274 \Omega_B h^2$. Y_p is the abundance of helium by mass, whereas the abundances for D, ${}^3\text{He}$ and ${}^7\text{Li}$ are plotted as ratios by number relative to hydrogen. The widths of the bands reflect the theoretical uncertainties in the predictions. The computations were carried out using Big Bang nucleosynthesis codes developed at Ohio State University (Steigman, 2004)

protons. Therefore, the ${}^7\text{Li}/\text{H}$ abundance decreases as the baryon density increases. At higher values of η however, ${}^7\text{Li}$ is synthesised by a different route. First, ${}^7\text{Be}$ is created through the reaction ${}^3\text{He}(\alpha, \gamma){}^7\text{Be}$, ${}^7\text{Be}$ being a more tightly bound nucleus than ${}^7\text{Li}$ and therefore more difficult to destroy. As η increases at high values, the abundance of ${}^7\text{Be}$ increases. Later in the evolution of the Universe, when neutral atoms began to form, the ${}^7\text{Be}$ nucleus can capture an s-electron and the subsequent β -decay results in the creation of ${}^7\text{Li}$.

10.4 The Abundances of the Light Elements

The predictions of the theory of primordial nucleosynthesis are of the greatest importance for astrophysical cosmology and a great deal of effort has been devoted to the observational determination of the primordial abundances of the light elements. This is a far from trivial exercise but there is now good agreement among a number

of independent estimates of these, although it would be wrong to imply that all the issues are closed. The key issue is to find means of determining the light element abundances in systems which have not been contaminated by astrophysical processes in stars and the interstellar medium. Steigman has provided an excellent summary of the theory and observations of the light elements, indicating clearly the undoubtedly quantitative successes, as well as potential problem areas (Steigman, 2004, 2006).

10.4.1 Determinations of the Observed Abundances of the Light Elements

Helium-4 (${}^4\text{He}$). Helium can only be observed in hot stars and in regions of ionised hydrogen. It is synthesised in the course of stellar evolution and so it is important to determine the helium abundance in systems which are relatively uncontaminated by the effects of stellar nucleosynthesis. This can be achieved by determining the helium abundance as a function of metallicity and then extrapolating to zero metallicity. Steigman advocates the use of helium and hydrogen recombination lines in low metallicity, extragalactic HII regions – data are now available for about 100 such systems. The ${}^4\text{He}$ mass fraction Y as a function of the oxygen abundance for these systems is shown in Fig. 10.3. It can be seen that the extrapolation to zero metallicity is rather small. Steigman adopts a mean value for the primordial helium abundance of $Y_p = 0.238 \pm 0.005$, where the errors encompass the small residual differences between independent estimates.

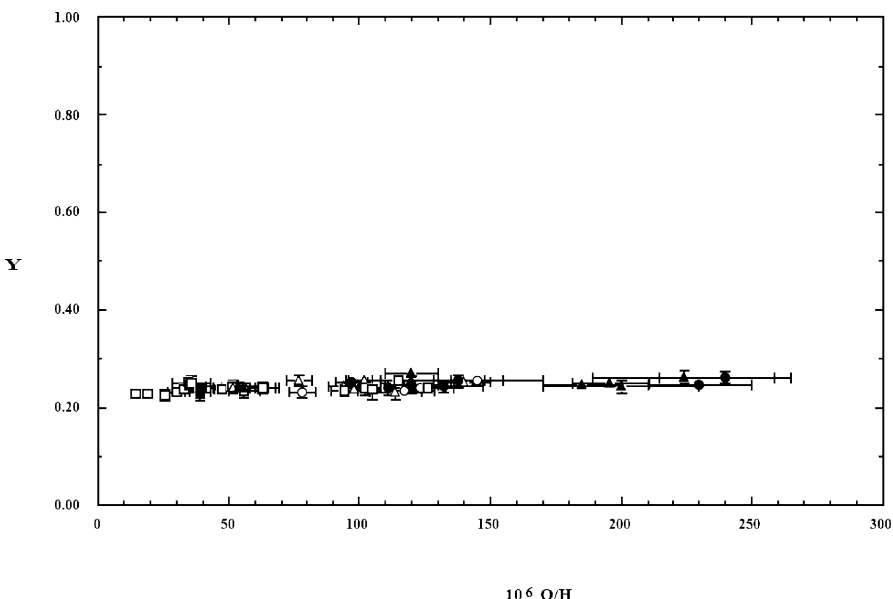


Fig. 10.3. The helium mass fraction Y as a function of oxygen abundance, derived from the same data sets, for a large sample of low metallicity extragalactic HII regions (Steigman, 2004)

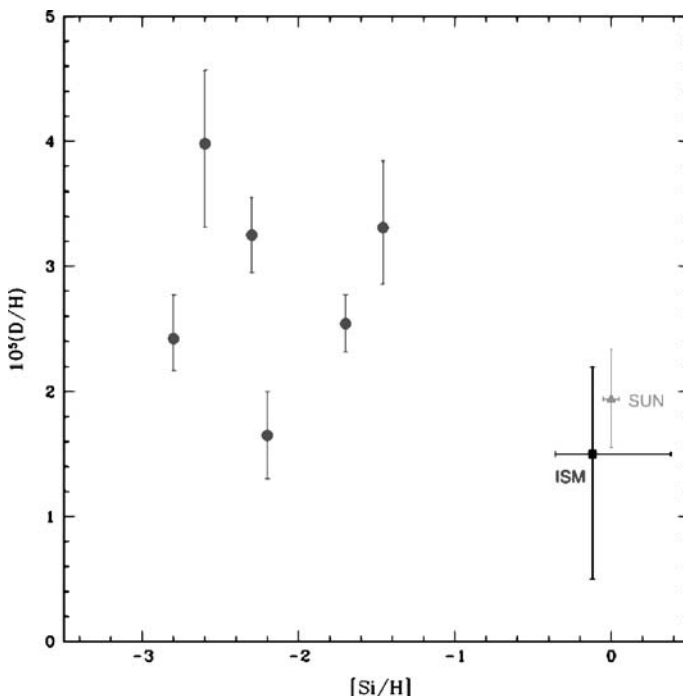


Fig. 10.4. The cosmic deuterium abundance (D/H) as a function of the silicon abundance from observations of quasar absorption line systems (filled circles). Also shown are the D abundances for the local interstellar medium (ISM, filled square) and the solar system (Sun, filled triangle) (Steigman, 2004, 2007)

Deuterium (D). The abundance of deuterium is crucial cosmologically because of its strong dependence upon the present baryon density. The local interstellar abundance of deuterium in our Galaxy has been well-determined by observations of the resonance absorption lines of deuterium in interstellar clouds by the Copernicus satellite and by the Hubble Space Telescope (Linsky et al., 1994). The values found amount to $(D/H) = (1.5 \pm 0.2) \times 10^{-5}$, the point labelled ‘ISM’ in Fig. 10.4. This is a secure lower limit to the primordial deuterium abundance since deuterium is destroyed when it is circulated through the hot central interiors of stars. It is not so different from the deuterium abundance observed in the solar atmosphere, the point labelled ‘Sun’ in Fig. 10.4. A key issue is the extent to which the process of deuterium destruction has taken place during the course of the chemical evolution of interstellar material.

The most important recent results have come from estimates of the deuterium abundance in the Lyman- α absorbers observed in the spectra of high redshift quasars. Absorption line systems in the spectra of quasars with redshifts $z \geq 2.5$ have sufficiently large redshifts for the deuterium Lyman resonance lines to be redshifted into the optical region of the spectrum and so accessible to ground-based high resolution

spectroscopy with large telescopes (see also Chap. 18). These are highly non-trivial observations and the interpretation depends upon understanding the processes responsible for line broadening and eliminating the effects of ‘confusion’ by very weak hydrogen absorbers which may be redshifted to the wavelengths of the deuterium lines. They have, however, the advantage that absorption line systems with very low metallicities can be selected, the inference being that there must have been negligible circulation of the primordial deuterium through stars.

Steigman discusses carefully the best recent determinations of the cosmic deuterium abundance and the discrepancies between them. Figure 10.4 taken from his review indicates the present level of uncertainty, the deuterium abundance being plotted against the metallicities of the systems studied. Steigman’s preferred value is $(D/H) = (2.6 \pm 0.4) \times 10^{-5}$, where the error is the 1-sigma uncertainty. It is important to note that the uncertainties are now small compared with the large uncertainties which dogged the subject in the 1980s and 1990s and which are well-illustrated by the differing positions adopted by Hogan and Steigman at the 1996 Princeton meeting on *Critical Dialogues in Cosmology* (Hogan, 1997; Steigman, 1997).

Helium-3 (^3He). ^3He is observed in the oldest meteorites, the carbonaceous chondrites, with an abundance $(^3\text{He}/\text{H}) = (1.4 \pm 0.4) \times 10^{-5}$. This value is taken to be representative of the ^3He abundance about 4.6×10^9 years ago when the solar system formed. ^3He has also been observed at radio wavelengths through the equivalent of the 21-cm hyperfine line of neutral hydrogen and the abundances in interstellar clouds lie in the range $[^3\text{He}/\text{H}] = 1.2$ to 15×10^{-5} . ^3He is destroyed inside stars but it is a more robust isotope than deuterium. There are two important aspects to its cosmic abundance. First of all, when deuterium is burned, ^3He is one of the products. Second, when ^3He is destroyed, it creates ^4He which is then burned to form heavier elements. Thus, the interpretation of the ^3He abundance is more complicated than the deuterium abundance. In view of these complexities, Steigman suggests that the estimates of the primordial ^3He abundances provide a less reliable means of determining Ω_B . Rather, he proposes using his preferred value $(^3\text{He}/\text{H}) = (1.1 \pm 0.2) \times 10^{-5}$ as a consistency check.

Lithium-7 (^7Li). ^7Li is also a fragile element and so its primordial abundance can be depleted by circulation through the hot inner regions of stars. It can also, however, be enhanced by spallation collisions between cosmic ray protons and nuclei and the cold interstellar gas and by cosmic ray nucleosynthesis interactions in the interstellar medium. Therefore, the ^7Li abundance as a function of metallicity should reach a ‘plateau’ in metal-poor stars. In 1982, Spite and Spite made the first estimates of the ^7Li abundance for metal-poor halo stars and found that it converged at low metallicities (Spite and Spite, 1982). Steigman’s recent compilation of ^7Li abundances shows convincingly the ‘Spite plateau’ at metallicities $[\text{Fe}/\text{H}] \leq -2$ (Fig. 10.5). For larger values of $[\text{Fe}/\text{H}]$, a much wider spread in the lithium abundance is observed. This reflects the fact that high metallicities correspond to later stages in Galactic evolution. Steigman adopts a ^7Li abundance of $[^7\text{Li}] = 12 + \log(\text{Li}/\text{H}) = 2.1 \pm 0.1$. The absolute value may be slightly modified by the mixing of ^7Li between

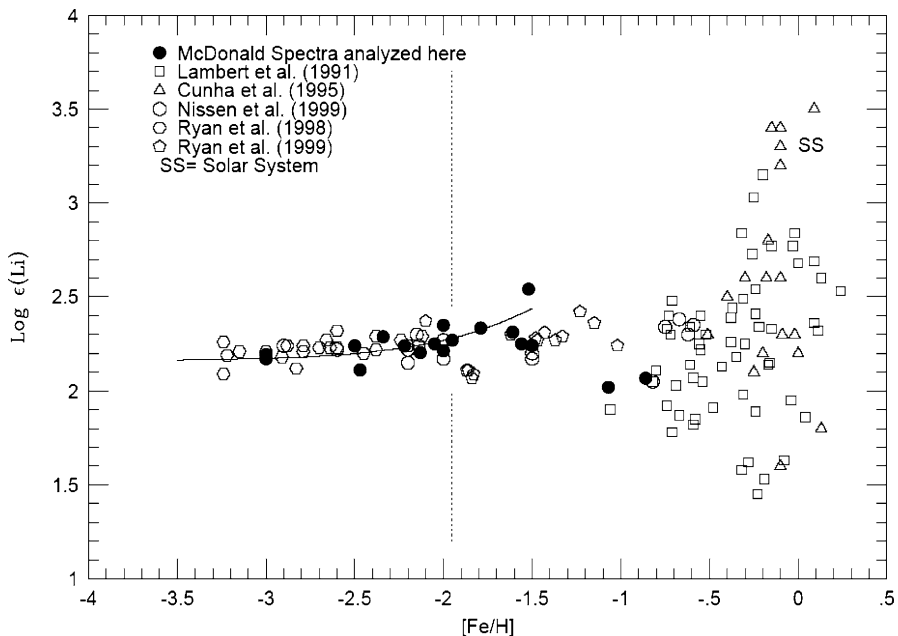


Fig. 10.5. A compilation of data on the cosmic lithium abundance from observations of metal-poor and metal-rich stars. $\varepsilon(\text{Li})$ is defined to be $10^{12}(\text{Li}/\text{H})$ and $[\text{Fe}/\text{H}]$ is the logarithmic metallicity relative to the standard solar value. The ‘Spite plateau’ in (Li/H) is observed at metallicities less than 100 times the solar value, $[\text{Fe}/\text{H}] \leq -2$ (Steigman, 2004)

the central and outer regions of old metal-poor stars, but the effect would be at the level of 0.1–0.3 dex in the above abundance.

10.4.2 Comparison of Theory and Observations

It is immediately apparent from the estimates of the primordial abundances of the light elements discussed in Sect. 10.4.1 and the predictions shown in Fig. 10.2 that there is an excellent match between the predictions and observations for values of $\eta \approx 6$. The facts that it is so difficult to account for the cosmic abundances of these elements by astrophysical processes occurring in stars and that they are created so naturally by primordial nucleosynthesis are compelling pieces of evidence that the standard Big Bang model must be along the correct lines. How well does the model survive quantitative scrutiny?

Steigman adopts the approach of using the deuterium abundance as the most sensitive probe of the baryon density parameter Ω_B , what he calls a *baryometer*, and then compares the predicted ${}^4\text{He}$, ${}^3\text{He}$ and ${}^7\text{Li}$ abundances with these. For $(\text{D}/\text{H}) = (2.6 \pm 0.4) \times 10^{-5}$, $\eta_{10} = 6.1_{-0.5}^{+0.7}$, corresponding to

$$\Omega_B h^2 = 0.022_{-0.002}^{+0.003}. \quad (10.14)$$

As we will discuss in Chap. 15, this value is in quite remarkable agreement with the entirely independent estimate of $\Omega_B h^2$ derived from analysis of the WMAP observations of the temperature fluctuation power spectrum of the Cosmic Microwave Background Radiation,

$$\Omega_B h^2 = 0.0224 \pm 0.0009 . \quad (10.15)$$

The expected value of $(^3\text{He}/\text{H})$ is $(1.0 \pm 0.1) \times 10^{-5}$, again in excellent agreement with the best estimate of the primordial ${}^3\text{He}$ abundance.

The agreement is somewhat less good for ${}^4\text{He}$ and ${}^7\text{Li}$. For ${}^4\text{He}$, the predicted mass fraction is $Y = 0.248 \pm 0.001$ compared with an adopted primordial abundance of $Y = 0.238 \pm 0.005$; for ${}^7\text{Li}$, the predicted fraction is $[\text{Li}] = 2.65^{+0.09}_{-0.11}$ compared with the observed value of 2.2 ± 0.1 . In both cases, the abundances are in agreement within the 2σ confidence levels. It is largely a matter of opinion how seriously one views these discrepancies. One might argue that, in view of the difficulty of extracting reliable information about the primordial abundances, it is extraordinary that everything hangs together at the 2σ level; it is a challenge to understand the magnitude of possible residual systematic errors still present in the best estimates of the primordial abundances.

There are ways of modifying the predictions if non-standard assumptions are built into the calculations of primordial nucleosynthesis. If the discrepancies proved to be significant, these might provide clues about physics beyond the standard model of particle physics. For example, suppose the expansion rate were greater than that of the standard radiation-dominated Universe during the crucial epochs when the neutrinos decoupled. This might be the case if, for example, the gravitational constant changed with time. The cosmic time-scale would also be speeded up if there were additional unknown neutrino species present during these epochs. In the latter case, the value of χ would be greater than that given by (10.9). Running through the same argument given in Sect. 10.2 to determine the dependence of the temperature at which the weak interaction time-scale is equal to the age of the Universe upon χ , it is found that the decoupling would take place at a higher temperature when the neutron-to-proton ratio would be greater than in the standard picture. As a result, a greater ${}^4\text{He}$ abundance would be predicted as compared with the standard model. This result goes entirely in the wrong direction in explaining the potential discrepancy between the observed and predicted ${}^4\text{He}$ abundance. Steigman shows that, leaving the number of neutrino species N_ν as a free parameter, the best-fitting value is $N_\nu = 2.3$, less than the known number of neutrino species $N_\nu = 3$, but this discrepancy is only at about the 1.5σ level. More than three neutrino species is, however, excluded at a high degree of significance. It is interesting that this limit to N_ν was derived from these cosmological arguments *before* the number was measured from the energy width of the decay products of the Z^0 boson by the Large Electron–Positron collider (LEP) at CERN (Opal Collaboration, 1990).

Another way of modifying the predictions of the standard picture would be to postulate an asymmetry between the number densities of electron neutrinos and antineutrinos. In this case, the excess would drive the weak interactions (10.5) one

way or another in favour of either neutrons or protons and so modify the predicted cosmic helium abundance. For the neutrino flavour i , the asymmetry is parameterised by the net lepton number L_i which can be related to the dimensionless degeneracy parameter $\xi_i = \mu_i/T$, where μ_i is the neutrino chemical potential. For values of $\xi_i \ll 1$, the net lepton number is

$$L_i = \frac{n_{v_i} - n_{\bar{v}_i}}{n_\gamma} \approx 0.684\xi_i . \quad (10.16)$$

Steigman finds a best-fitting value of ξ_i of about 0.05, but the null result $\xi_i = 0$ is within about 1.5σ of this estimate. The data are therefore not inconsistent with the value $\xi_i = 0$.

The upshot of this discussion is that the primordial abundances of the light elements are in remarkable agreement with the predictions of the standard model of Big Bang nucleosynthesis. Whilst it is right that the experts should continue to worry about the discrepancies highlighted above, in my view the successes of the theory far outweigh the relatively small uncertainties. Most striking is the fact that these studies have provided a very tight constraint on the baryon density parameter, as expressed by (10.14). Adopting our reference value of Hubble's constant $h = 0.7$, the density parameter in baryons is $\Omega_B = 0.045$. Hence, *there is insufficient baryonic matter to close the Universe*. Furthermore, since we have argued that the overall density parameter $\Omega_0 \approx 0.3$, it follows that the dark matter cannot be in the form of baryonic matter: *the matter content of the Universe must be dominated by non-baryonic dark matter*.

10.5 The Neutrino Background Temperature and the Value of χ

Another important piece of physics is associated with the determination of the temperature of the neutrino background radiation. We showed in Sect. 10.2 that the weak interactions maintained the equilibrium abundances of the neutrons and protons until the epoch at which $kT \approx 1$ MeV. Prior to this epoch, the photons, neutrinos, electrons and their antiparticles were the only relativistic species left and all had the same temperature. Just after neutrino decoupling, at an energy $kT \approx 0.5$ MeV, the electrons and positrons annihilated creating γ -ray photons. These high energy photons were rapidly thermalised by Compton scattering and so the temperature of the background electromagnetic radiation became greater than that of the neutrinos. The expansion was adiabatic and so the entropy per baryon was conserved during the expansion. Since the electrons and neutrinos were no longer coupled at $kT \approx 0.5$ MeV, the temperatures of the neutrinos and photons can be worked out assuming the entropy of the electrons and positrons was transferred to the radiation background.

As shown by Kolb and Turner, the entropy per unit comoving volume s is conserved as the Universe expands

$$ds = d \left[\frac{(\epsilon + p)R^3}{T} \right] = d \left[\sum_i g_i a T^3 R^3 \right] = 0 , \quad (10.17)$$

Table 10.1. The ratios of the energy densities and entropies of photons, electrons, positrons and neutrinos prior to the epoch of electron–positron annihilation

Energy density	ε_γ	$(\varepsilon_{e^-} + \varepsilon_{e^+})$	$(\varepsilon_\nu + \varepsilon_{\bar{\nu}})$	$(\varepsilon_{\nu_\mu} + \varepsilon_{\bar{\nu}_\mu})$	$(\varepsilon_{\nu_\tau} + \varepsilon_{\bar{\nu}_\tau})$
Entropy per baryon	s_γ	$(s_{e^-} + s_{e^+})$	$(s_\nu + s_{\bar{\nu}})$	$(s_{\nu_\mu} + s_{\bar{\nu}_\mu})$	$(s_{\nu_\tau} + s_{\bar{\nu}_\tau})$
$\sum_i g_i$	1	7/4	7/8	7/8	7/8

where ε and p are the equilibrium energy density and pressure respectively (Kolb and Turner, 1990). Before the epoch at which the electrons and positrons annihilated, the ratios of the energy densities ε and entropies s of the various equilibrium relativistic components had the values given in Table 10.1.

After annihilation, the energy and entropy of the electron–positron pairs were transferred to the radiation field and so the entropy of the radiation increased by a factor

$$\frac{s_\gamma + s_{e^+} + s_{e^-}}{s_\gamma} = \frac{11}{4}. \quad (10.18)$$

Therefore, since $\sum_i g_i T^{-3}$ is conserved and the neutrinos were decoupled from equilibrium, the temperature of the radiation was increased relative to that of the neutrinos by a factor $(11/4)^{1/3}$. This is the process which is responsible for the little ‘kink’ in the temperature history of the Big Bang illustrated in Fig. 9.3 at the epoch when the electrons and positrons annihilated.

Since the entropy per baryon is conserved throughout the subsequent evolution of the standard Big Bang, this ratio is also the ratio of the temperatures of the photons and neutrinos at the present day. Adopting $T_{\text{rad}} = 2.728$ K, the temperature of the neutrino background radiation is expected to be $T_\nu = (4/11)^{1/3} T_{\text{rad}} = 1.95$ K. This neutrino background was last scattered at the epoch when $kT \approx 1$ MeV, that is $t \approx 1$ s. Unfortunately, the detection of the neutrino background is far beyond the capabilities of the present generation of neutrino detectors.

Although they do not interact with matter, the neutrino background does affect the subsequent dynamics of the Universe. During the radiation-dominated phase, the dynamics of the expansion is determined by the total inertial mass density of massless particles. For massless particles, even when they are decoupled from the electrons, their energy density decreases as $\varepsilon_\nu \propto R^{-4}$, just like the radiation field, and so they still contribute to the total inertial mass density which retards the expansion of the Universe. The energy densities in photons and neutrinos after the epoch of annihilation of the electron–positron pairs are shown in Table 10.2.

Table 10.2. The energy densities of photons and neutrinos in units of aT_ν^4 after the epoch of electron–positron annihilation

Energy density	ε_γ	$(\varepsilon_\nu + \varepsilon_{\bar{\nu}})$	$(\varepsilon_{\nu_\mu} + \varepsilon_{\bar{\nu}_\mu})$	$(\varepsilon_{\nu_\tau} + \varepsilon_{\bar{\nu}_\tau})$
Contribution to energy density ε	$(11/4)^{4/3}$	7/8	7/8	7/8

Thus, the total energy density ε is

$$\begin{aligned}\varepsilon &= \left[\left(\frac{11}{4} \right)^{4/3} + \frac{21}{8} \right] aT_v^4 = 6.48 aT_v^4 \\ &= 6.48 \left(\frac{4}{11} \right)^{4/3} aT_{\text{rad}}^4 = 1.68 aT_{\text{rad}}^4.\end{aligned}\quad (10.19)$$

Thus, during the radiation-dominated era after electron–positron annihilation, we should use a value $\chi = 1.68$ in the expression for the dynamics of the Universe,

$$\varepsilon = \chi aT^4 = \frac{3c^2}{32\pi G} t^{-2}; \quad (10.20)$$

$$T = \left(\frac{3c^2}{32\pi G \chi a} \right)^{1/4} t^{-1/2} = 1.33 \times 10^{10} t^{-1/2} \text{ K}. \quad (10.21)$$

We can therefore rewrite the expression for the epoch at which the Universe changed from being ‘radiation-dominated’ to ‘matter-dominated’, in the sense that the dynamics changed from $R \propto t^{1/2}$ to $R \propto \Omega_0^{1/3} t^{2/3}$. Using (9.8) and (10.19), the ratio of energy densities of massless to non-relativistic matter becomes

$$\frac{\varrho_{\text{massless}}}{\varrho_{\text{matter}}} = \frac{1.68 aT_{\text{rad}}^4(z)}{\Omega_0 \varrho_c (1+z)^3 c^2} = \frac{4.2 \times 10^5 (1+z)}{\Omega_0 h^2}. \quad (10.22)$$

Therefore, the change-over in the dynamics took place at a redshift $z = 2.4 \times 10^4 \Omega_0 h^2$. Adopting our reference values of $\Omega_0 = 0.3$ and $h = 0.7$, the epoch of equality of the energy densities in matter and massless particles occurred at a redshift $z = 3530$.

10.6 Baryon-Symmetric Universes

The process of neutrino decoupling is similar in many ways to the more general issue of particle–antiparticle annihilation in the early Universe and the possible existence of significant fluxes of relic massive particles from these times. Let us consider the process of particle–antiparticle annihilation in a little more detail. The analyses of Zeldovich and Novikov and, in more detail, Kolb and Turner can be recommended (Zeldovich and Novikov, 1983; Kolb and Turner, 1990). It might be imagined that there would be negligible abundances of baryons and antibaryons in the Universe now if there were precisely equal numbers of baryons and antibaryons to begin with, but this is not correct. As discussed in Sect. 10.1, the equilibrium abundance of any species of mass m in thermal equilibrium at temperature T in the non-relativistic limit $kT \ll mc^2$ is

$$N = \bar{N} = g \left(\frac{mkT}{2\pi\hbar^2} \right)^{3/2} \exp \left(-\frac{mc^2}{kT} \right), \quad (10.23)$$

where for protons, antiprotons, neutrons and antineutrons $g = 2$. In the present case, m is the mass of the nucleon and so it might appear that, since $T = 2.728 \text{ K}$ at

the present day, the abundances of nucleons and antinucleons would be of the order $10^{-10^{12}}$. This is not correct, however, since the abundances ‘freeze out’ when the time-scale of the processes which maintain the nucleons and antinucleons in their equilibrium abundances become greater than the age of the Universe.

Zeldovich and Novikov presented a simple solution for the relic abundances of nucleons and antinucleons in baryon-symmetric Universes. The problem is to solve for the nucleon-to-photon ratio η in the non-relativistic regime. The annihilation cross-section for nucleons and antinucleons in the non-relativistic regime varies as $\sigma_{pp} = \sigma_0 c/v$ where $\sigma_0 \approx 2 \times 10^{-30} \text{ m}^2$ and so the probability of annihilation of one nucleon with an antinucleon per unit time is $\sigma_{pp} v N = \sigma_0 c N$. Therefore, the rate of change of the number density of nucleons is

$$\frac{dN}{dt} = -\sigma_0 c N^2 + \psi(t) - \frac{3N}{2t}, \quad (10.24)$$

where $\psi(t)$ is the pair creation rate and the term $-3N/2t$ describes the decrease in number density due to the expansion of the Universe in the radiation-dominated era. This rate of change of nucleons can be compared with the rate at which the number density of photons changes with time. The number of photons is conserved as the Universe expands during the relevant epochs and so

$$\frac{dN_\gamma}{dt} = -\frac{3N_\gamma}{2t}. \quad (10.25)$$

Therefore, since $\eta = N/N_\gamma$, differentiating N/N_γ , we find that

$$\frac{d\eta}{dt} = -\sigma_0 c \eta^2 + \frac{\psi(t)}{N_\gamma}. \quad (10.26)$$

As expected, if there were no annihilation or creation of proton–antiproton pairs, the right-hand side would be zero and this ratio would remain unchanged.

Following Zeldovich and Novikov, it is convenient to introduce the equilibrium value of $\eta = \eta_{\text{eq}}$ which would be found if the nucleons and antinucleons remained in equilibrium at all times. In their calculations, they considered the total numbers of baryons, antibaryons, neutrons and antineutrons. Then, η_{eq} would be given by the ratio of (10.4) to (10.2a),

$$\eta_{\text{eq}} = A\theta^{-3/2} \exp(-1/\theta), \quad (10.27)$$

where $\theta = kT/mc^2$ and A is a constant of order unity.

Now, in equilibrium, the rate of annihilations must equal the rate of pair production and so the right-hand side of (10.26) would be zero, that is

$$-\sigma_0 c \eta_{\text{eq}}^2 + \frac{\psi(t)}{N_\gamma} = 0. \quad (10.28)$$

Therefore, the equation for η can be written

$$\frac{d\eta}{dt} = -\sigma_0 c N_\gamma (\eta^2 - \eta_{\text{eq}}^2). \quad (10.29)$$

We are interested in finding the time at which the value of η began to depart from its equilibrium value and this occurred when $\eta - \eta_{\text{eq}} \approx \eta_{\text{eq}}$, that is, when

$$\frac{d\eta_{\text{eq}}}{dt} = -\sigma_0 c N_\gamma (\eta - \eta_{\text{eq}})(\eta + \eta_{\text{eq}}) \approx -2\sigma_0 c N_\gamma \eta_{\text{eq}}^2. \quad (10.30)$$

Therefore,

$$\frac{1}{\eta_{\text{eq}}} \frac{d\eta_{\text{eq}}}{dt} = \frac{d(\ln \eta_{\text{eq}})}{dt} \approx -2\sigma_0 c N_\gamma \eta_{\text{eq}}. \quad (10.31)$$

Now,

$$\ln \eta_{\text{eq}} = -\frac{3}{2} \ln \theta - \frac{1}{\theta} \quad (10.32)$$

and so, since we are well into the regime in which $\theta \ll 1$, we can approximate $\ln \eta_{\text{eq}} = -1/\theta$. Furthermore, during these radiation-dominated phases, $\theta \propto R^{-1} \propto t^{-1/2}$ and so

$$\frac{d(\ln \eta_{\text{eq}})}{dt} = \frac{d(\ln \eta_{\text{eq}})}{d\theta} \frac{d\theta}{dt} = \frac{1}{2\theta t} \approx -2\sigma_0 c N_\gamma \eta_{\text{eq}}. \quad (10.33)$$

Thus, the epoch at which decoupling took place is given by the solution of

$$4\sigma_0 c \eta_{\text{eq}} N_\gamma \theta t \approx 1 \quad \text{or} \quad 4\sigma_0 c t \theta^{-1/2} e^{-1/\theta} N_\gamma \approx 1. \quad (10.34)$$

Now, from (10.2a) and (10.10), the dependences of N_γ and θ as a function of cosmic time t are known,

$$N_\gamma = 0.244 \left(\frac{2\pi k T}{hc} \right)^3 = 2.6 \times 10^{46} \theta^3 \text{ m}^{-3}; \quad (10.35)$$

$$T = 10^{10} t^{-1/2} \text{ K}; \quad \theta = \frac{kT}{mc^2} = 10^{-3} t^{-1/2} \quad (10.36)$$

Substituting these values into (10.32), we find the critical value of $\theta = \theta_d$ is given by the solution of

$$e^{1/\theta_d} = 6.4 \times 10^{19} \theta_d^{1/2}. \quad (10.37)$$

The solution is found by repeated approximation, with the result

$$\theta_d = \frac{kT_d}{mc^2} \approx \frac{1}{44}; \quad t_d = 2.5 \times 10^{-3} \text{ s}; \quad \eta_d = 2 \times 10^{-18}. \quad (10.38)$$

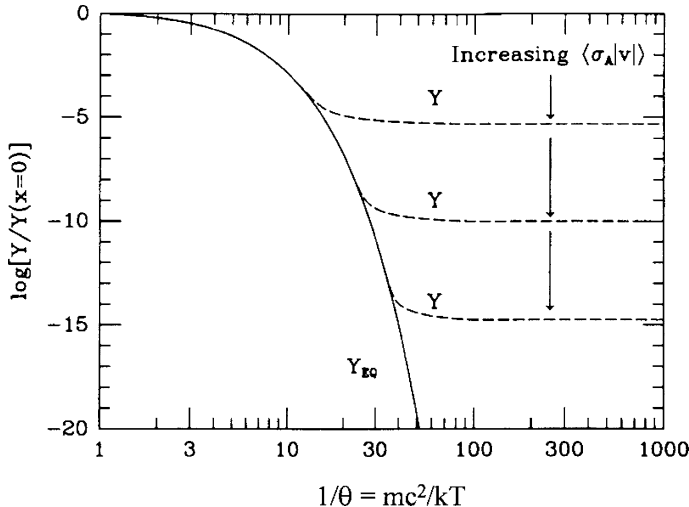


Fig. 10.6. Illustrating the freeze-out of massive species due to particle–antiparticle annihilation in the early Universe (Kolb and Turner, 1990). The parameter Y is the specific entropy of the particle, which is proportional to the number density of particles per unit comoving volume and so equivalent to the quantity η used in the text. The quantity plotted on the abscissa is $mc^2/kT = \theta^{-1}$. It can be seen that the freeze-out abundance for nucleon–nucleon annihilation, corresponding to $\theta^{-1} = 44$, agrees with the calculations presented in the text

Before this time, the particles and antiparticles were maintained in thermal equilibrium by the baryon–antibaryon annihilation and pair production mechanisms. At later times, the mean free path for $p\bar{p}$ collisions exceeded the horizon scale at that time as may be appreciated by evaluating the optical depth for these collisions $\tau_{p\bar{p}} = \sigma_0 N c t_d$. At that time the nucleon number density was $N \approx 6 \times 10^{23} \text{ m}^{-3}$ and so $\tau_{p\bar{p}} \approx 1$. Thus, at later times, there were insufficient interactions to maintain the equilibrium abundances.

We can now work out how the value of η changes after this epoch. Inspection of (10.25) shows that at later times η_{eq} decreases exponentially and so (10.27) for η reduces to

$$\frac{d\eta}{dt} = -\sigma_0 c N_\gamma \eta^2. \quad (10.39)$$

Taking the initial conditions to be given by (10.34), the solution is

$$\frac{\eta}{\eta_d} \approx \frac{1}{[1 + 10^{19} \eta_d (1 - \tau^{-1/2})]}, \quad (10.40)$$

where $\tau = t/t_d$. Thus, when $\tau \rightarrow \infty$,

$$\frac{\eta}{\eta_d} \approx \frac{1}{[1 + 10^{19} \eta_d]} \approx 0.05. \quad (10.41)$$

Therefore, from the time the nucleons decoupled, the value of η only decreased by a factor of about 20 and so the value of η at the present day should be about 10^{-19} , that is, about 10^9 times smaller than its observed value. This is the origin of the baryon asymmetry problem discussed in Sect. 9.6.

The reason for carrying out this calculation in some detail is that it gives physical insight into the decoupling of any type of massive particle in the early Universe, a subject dealt with in some detail by Kolb and Turner and to which we will return in Sect. 13.3 (Kolb and Turner, 1990). Figure 10.6 shows the results of calculations for the freeze-out of massive particle species in the early Universe for different values of the interaction cross-section $\langle\sigma v\rangle$. The solid line shows the equilibrium abundances and the dashed lines the actual abundances when account is taken of the decoupling of the particles from equilibrium. The physics behind these calculations is precisely the same as that involved in calculating the relic abundances of particles and their antiparticles. After decoupling takes place, the abundances freeze-out with more or less the value at decoupling. As the cross-section decreases, the freeze-out occurs at higher abundances of the massive species, as illustrated in Fig. 10.6.

11 The Evolution of Perturbations in the Standard Big Bang

At last, we can begin the study of the origin and formation of galaxies and the large-scale structure of the Universe. The first two parts of this book have presented the essential framework within which these problems have to be tackled. Much of this chapter, and indeed most of Part III, is concerned with understanding how the process of galaxy and structure formation began. What happened once these structures began to form is the subject of Part IV.

11.1 What the Theorists Are Trying to Do

As the discussions of Chaps. 3 and 4 have shown, galaxies and clusters of galaxies are complex systems, but the aim of the cosmologist is not to explain all their detailed features – that is the job of the astrophysicist. The cosmologist seeks to explain the origin of large-scale structures in the expanding Universe in the sense that, if $\delta\varrho$ is the enhancement in density of some region over the average background density ϱ , the *density contrast* $\Delta = \delta\varrho/\varrho$ reached amplitude $\Delta = \delta\varrho/\varrho \sim 1$ from initial conditions which must have been remarkably isotropic and homogeneous in the very early Universe. Once these perturbations have grown in amplitude to $\Delta = \delta\varrho/\varrho \sim 1$, their subsequent development becomes non-linear and they rapidly evolve towards bound structures in which star formation and other astrophysical process lead to the formation of galaxies and clusters of galaxies as we know them.

The cosmologist's objectives are therefore twofold: to understand how density perturbations evolve in the expanding Universe and then to derive and account for the initial conditions necessary for the formation of structure in the Universe. These may appear to be rather modest goals but they turn out to lead to some of the most profound problems of modern cosmology. As we will show, the origin of the fluctuations must lie in physical processes occurring in the very early Universe, well before the epochs to which we have ready access, meaning long before the epoch of nucleosynthesis discussed in Chap. 10. As a result, these studies offer the possibility of providing powerful tools for exploring physics under physical conditions which are not accessible in the laboratory. Indeed, they have undoubtedly expanded the scope of physical enquiry open to theorists and have the potential for constraining physical theories beyond the standard model of particle physics.

11.1.1 Why this Programme Is Feasible

Galaxies, clusters of galaxies and other large-scale features of our local Universe must have formed relatively late in the history of the Universe, as can be deduced from the following argument. As discussed in Sect. 8.7, the average density of matter in the Universe today corresponds to a density parameter $\Omega_0 \approx 0.3$. The analyses of Chaps. 3 and 4 show that the average densities of gravitationally bound systems such as galaxies and clusters of galaxies are much greater than this value, typically their densities being about 10^6 and 1000 times greater than the mean background density respectively. Superclusters, meaning unbound systems on scales greater than those of clusters of galaxies, have mean densities a few times the background density. Therefore, the density contrasts $\Delta = \delta\varrho/\varrho$ for galaxies, clusters of galaxies and superclusters at the present day are roughly 10^6 , 1000 and a few respectively. Since the average density of matter in the Universe ϱ changes as $(1+z)^3$, it follows that typical galaxies must have had $\Delta \sim 1$ at a redshift $z \approx 100$. They could not have separated out as discrete objects at greater redshifts, or else their mean densities would be much greater than those observed at the present epoch. The same argument applied to clusters and superclusters suggests that they could not have separated out from the expanding background at redshifts greater than $z \sim 10$ and 1 respectively. As we will discuss in more detail in Sect. 16.1.1, these are rather generous upper limits to the redshifts at which these objects could have formed.

We conclude that galaxies and larger-scale structures could only have attained density contrasts $\Delta \sim 1$ at redshifts significantly less than 100, in other words, long after the epoch of recombination at $z \approx 1000$ and well into the matter-dominated phase of the standard Big Bang. These are important conclusions since it means that the structures we observe today did not attain $\Delta \sim 1$ in the inaccessible remote past, but at redshifts which are in principle accessible by observation. It also means that these perturbations were certainly in the linear regime at redshifts $z > 100$ and this means the calculations of their evolution during the early evolution of the Universe can be carried out with real precision. This is why we can have some confidence in making the comparison between the predictions of theory and observations of large-scale structures. These considerations indicate why it is natural to begin this study with an analysis of how small density perturbations develop in the expanding Universe.

11.1.2 A Warning

It is important to issue the warning at the outset that the full analysis of the growth of perturbations in the standard Big Bang picture is far from trivial. A full general relativistic analysis is needed to tackle some of the trickier issues which arise and this can become quite complex. This goes far beyond the ambitions of this book which is to provide a non-technical guide to the physical content of the theory and its comparison with observation. Much of the analysis requires tools way beyond those contained in the standard course in physics and astrophysics and I will try to elucidate these in simple terms. But, it would be wrong to pretend that what I write

is other than a simple overview of many complex topics. The enthusiast has little alternative but than to make a head-on attack on general relativity and quantum field theory to gain deeper understanding.

Many books attempt to elucidate the physics of these processes. My own view is that understanding is best achieved by trying all of them and seeing which is most to the taste of the reader. I would regard the books by Peebles, Kolb and Turner, Peacock, Liddle and Lyth, Dodelson and Hobson, Efstathiou and Lasenby as an excellent set of texts from which the reader will undoubtedly gain considerable enlightenment (Peebles, 1993; Kolb and Turner, 1990; Peacock, 2000; Liddle and Lyth, 2000; Dodelson, 2003; Hobson et al., 2006). My objectives are much more modest, but may help in understanding the issues addressed in these more ambitious narratives.

11.2 The Non-Relativistic Wave Equation for the Growth of Small Perturbations in the Expanding Universe

Let us begin with the simplest case of the growth of gravitational instabilities in the non-relativistic regime for scales much less than the horizon scale, which for the moment we will take to be $l \approx ct$. Later, we will deal with the relativistic regime and superhorizon scales.

The analysis which follows is one of the classics of theoretical astrophysics. The problem of the growth of small perturbations under gravity dates back to the work of Jeans in the first decade of the twentieth century and then to a classic paper by Lifshitz of 1946 (Jeans, 1902; Lifshitz, 1946). We will carry out this analysis in some detail because of the general importance of the various differential equations which come out of this analysis.

The problem gets off to a very bad start. Let us first write down the equations of gas dynamics for a fluid in a gravitational field. These consist of three partial differential equations which describe (1) the conservation of mass, or the equation of continuity, (2) the equation of motion for an element of the fluid, *Euler's equation*, and (3) the equation for the gravitational potential in the presence of a density distribution ϱ , *Poisson's equation*.

$$\text{Equation of continuity:} \quad \frac{\partial \varrho}{\partial t} + \nabla \cdot (\varrho \mathbf{v}) = 0 ; \quad (11.1)$$

$$\text{Equation of motion:} \quad \frac{\partial \mathbf{v}}{\partial t} + (\mathbf{v} \cdot \nabla) \mathbf{v} = -\frac{1}{\varrho} \nabla p - \nabla \phi ; \quad (11.2)$$

$$\text{Gravitational potential:} \quad \nabla^2 \phi = 4\pi G \varrho . \quad (11.3)$$

Let us recall the meaning of these equations. They describe the dynamics of a fluid of density ϱ and pressure p in which the velocity distribution is \mathbf{v} . The gravitational potential ϕ at any point is given by Poisson's equation (11.3) in terms of the density distribution ϱ . In (11.1), (11.2) and (11.3), the partial derivatives describe the variations of these quantities *at a fixed point in space*. This description is often referred

to as an *Eulerian* system of coordinates. We can imagine setting up a fixed grid of points in space and then the Eulerian derivatives describe how the properties of the fluid at these fixed points on the grid change with time.

Another way of writing the equations of fluid dynamics is work in a coordinate system in which the motion of a particular fluid element is followed. These coordinates are known as *Lagrangian* coordinates.¹ I will write derivatives which follow a particular fluid element as total derivatives d/dt . It is straightforward to show that

$$\frac{d}{dt} = \frac{\partial}{\partial t} + (\mathbf{v} \cdot \nabla) . \quad (11.4)$$

Notice the significance of the operator $(\mathbf{v} \cdot \nabla)$. There is no ambiguity when this operator acts upon a scalar quantity. When it operates upon a vector quantity, it means that the derivative $v_x \partial/\partial x + v_y \partial/\partial y + v_z \partial/\partial z$ should be taken for each component of the vector. Using the identity $\nabla \cdot (\varrho \mathbf{v}) = \varrho \nabla \cdot \mathbf{v} + \mathbf{v} \cdot \nabla \varrho$, the equations of motion can be written in Lagrangian form,

$$\frac{d\varrho}{dt} = -\varrho \nabla \cdot \mathbf{v} ; \quad (11.5)$$

$$\frac{d\mathbf{v}}{dt} = -\frac{1}{\varrho} \nabla p - \nabla \phi ; \quad (11.6)$$

$$\nabla^2 \phi = 4\pi G \varrho . \quad (11.7)$$

The expression (11.6) describes the fact that the Lagrangian coordinate system is the natural system of coordinates in which to write down Newton's second law of motion since it describes the forces acting on a particular element of the fluid.

In the cases of *isotropic world models*, (11.5), (11.6) and (11.7) can be thought of as being written in comoving form, that is, the properties of a fluid element expanding uniformly with the Universe are followed, rather than what would be observed if we were located at a fixed point in space and watched the Universe expand past it. For such models, ∇p and $\nabla \phi$ are zero. Then, writing Hubble's law in the Eulerian frame as $\mathbf{v} = H\mathbf{r}$, (11.5) becomes

$$\frac{d\varrho}{dt} = -3H\varrho . \quad (11.8)$$

Then, since $H dt = (\dot{a}/a) dt$, $\varrho = \varrho_0 a^{-3}$ as expected. In the case we have to discuss here, however, there is an important distinction between the Lagrangian and comoving coordinate systems. The gradients in the gravitational potential and the pressure result in changes to the comoving distance coordinates of a particular fluid element; only in the uniform isotropic case do the points preserve the same comoving distance coordinates for all time.

The standard procedure is first to establish the solution for the unperturbed medium, that is, a uniform state in which ϱ and p are the same everywhere and

¹ I have discussed the relation between the Eulerian and Lagrangian systems of coordinates in the Appendix to Chap. 7 of my book *Theoretical Concepts in Physics* (Longair, 2003).

$\mathbf{v} = 0$. Unfortunately this solution does not exist for a stationary medium. Equations (11.5), (11.6) and (11.7) show that, in the uniform stationary state, the only solutions is $\varrho = 0$. This is a problem since it means that there is no static solution with finite density and pressure about which to perturb the medium. Fortunately, we need to treat the growth of fluctuations in a uniformly expanding medium and this eliminates the problem.

We first derive the unperturbed solutions for the velocity \mathbf{v}_0 , density ϱ_0 , pressure p_0 and gravitational potential ϕ_0 which satisfy (11.5), (11.6) and (11.7). Notice that we will use the subscripts 0 to refer to the properties of the unperturbed medium only in this section

$$\frac{d\varrho_0}{dt} = -\varrho_0 \nabla \cdot \mathbf{v}_0 ; \quad (11.9)$$

$$\frac{d\mathbf{v}_0}{dt} = -\frac{1}{\varrho_0} \nabla p_0 - \nabla \phi_0 ; \quad (11.10)$$

$$\nabla^2 \phi_0 = 4\pi G \varrho_0 . \quad (11.11)$$

Next, we write down the equations including first-order perturbations, that is,

$$\mathbf{v} = \mathbf{v}_0 + \delta\mathbf{v}, \quad \varrho = \varrho_0 + \delta\varrho, \quad p = p_0 + \delta p, \quad \phi = \phi_0 + \delta\phi . \quad (11.12)$$

These are substituted into (11.5), (11.6) and (11.7), which are expanded to first order in small quantities and then (11.9), (11.10) and (11.11) are subtracted from each of them in turn. From the subtraction of (11.9) from (11.5), we find

$$\frac{d}{dt} \left(\frac{\delta\varrho}{\varrho_0} \right) = \frac{d\Delta}{dt} = -\nabla \cdot \delta\mathbf{v} , \quad (11.13)$$

where $\Delta = \delta\varrho/\varrho_0$ is the density contrast. This is an important equation since it relates the rate at which the density contrast develops to the peculiar velocity $\delta\mathbf{v}$ associated with the collapse of the perturbation.

To make progress with (11.6), we expand $d\mathbf{v}/dt$ to first order in small quantities using (11.4).

$$\frac{d(\mathbf{v}_0 + \delta\mathbf{v})}{dt} = \frac{\partial \mathbf{v}_0}{\partial t} + (\mathbf{v}_0 \cdot \nabla) \mathbf{v}_0 + \frac{d(\delta\mathbf{v})}{dt} + (\delta\mathbf{v} \cdot \nabla) \mathbf{v}_0 . \quad (11.14)$$

In expanding the right-hand side of (11.10), we assume that the initial state is *homogeneous* and *isotropic* so that $\nabla p_0 = 0$ and $\nabla\varrho_0 = 0$. We then find, when we subtract (11.10) from (11.14), that

$$\frac{d(\delta\mathbf{v})}{dt} + (\delta\mathbf{v} \cdot \nabla) \mathbf{v}_0 = -\frac{1}{\varrho_0} \nabla \delta p - \nabla \delta\phi . \quad (11.15)$$

The third equation results from the subtraction of (11.11) from (11.7). Because of the linearity of Poisson's equation (11.7), we find

$$\nabla^2 \delta\phi = 4\pi G \delta\varrho . \quad (11.16)$$

Equations (11.13), (11.15) and (11.16) are the key differential equations in the present analysis.

In the cosmological case, the background is expanding uniformly and so it is convenient to introduce comoving coordinates by writing in the usual way $\mathbf{x} = a(t)\mathbf{r}$, where \mathbf{r} is comoving coordinate distance and $a(t)$ is the scale factor. Therefore,

$$\delta\mathbf{x} = \delta[a(t)\mathbf{r}] = \mathbf{r}\delta a(t) + a(t)\delta\mathbf{r}. \quad (11.17)$$

The velocity can therefore be written

$$\mathbf{v} = \frac{\delta\mathbf{x}}{\delta t} = \frac{da}{dt}\mathbf{r} + a(t)\frac{d\mathbf{r}}{dt}. \quad (11.18)$$

Thus, we can identify \mathbf{v}_0 with the Hubble expansion term $(da/dt)\mathbf{r}$ and the perturbation to the Hubble flow $\delta\mathbf{v}$ with the term $a(t)(d\mathbf{r}/dt)$. In other words, the second term is associated with the change in comoving distance coordinate under the influence of gravity and pressure gradients. It is convenient to write the perturbed velocity as $a(t)\mathbf{u}$ so that \mathbf{u} is the perturbed comoving velocity. Equation (11.15) then becomes

$$\frac{d}{dt}(a\mathbf{u}) + (a\mathbf{u} \cdot \nabla)\dot{a}\mathbf{r}_0 = -\frac{1}{\varrho_0}\nabla\delta p - \nabla\delta\phi. \quad (11.19)$$

It will prove convenient to write the derivatives with respect to the comoving coordinate \mathbf{r} rather than \mathbf{x} so that $d/dx = (1/a)d/dr$. Differentials with respect to comoving coordinates will be written ∇_c . Therefore, since $(a\mathbf{u} \cdot \nabla)\dot{a}\mathbf{r} = \mathbf{u}\dot{a}$, (11.19) becomes

$$\frac{d\mathbf{u}}{dt} + 2\left(\frac{\dot{a}}{a}\right)\mathbf{u} = -\frac{1}{\varrho_0 a^2}\nabla_c\delta p - \frac{1}{a^2}\nabla_c\delta\phi. \quad (11.20)$$

Now, let us consider *adiabatic perturbations* in which the perturbations in pressure and density are related to the adiabatic sound speed c_s^2 by $\partial p/\partial\varrho = c_s^2$. Thus, δp can be replaced by $c_s^2\delta\varrho$ in (11.20). We now combine (11.13) and (11.19) by taking the divergence in comoving coordinates of (11.20) and the time derivative of (11.13),

$$\nabla_c \cdot \dot{\mathbf{u}} + 2\left(\frac{\dot{a}}{a}\right)\nabla_c \cdot \mathbf{u} = -\frac{c_s^2}{\varrho_0 a^2}\nabla_c^2(\delta\varrho) - \frac{1}{a^2}\nabla_c^2(\delta\phi). \quad (11.21)$$

$$\frac{d^2}{dt^2}\left(\frac{\delta\varrho}{\varrho}\right) = -\nabla_c \cdot \dot{\mathbf{u}}. \quad (11.22)$$

Therefore,

$$\frac{d^2\Delta}{dt^2} + 2\left(\frac{\dot{a}}{a}\right)\frac{d\Delta}{dt} = \frac{c_s^2}{\varrho_0 a^2}\nabla_c^2\delta\varrho + 4\pi G\delta\varrho. \quad (11.23)$$

We now seek wave solutions for Δ of the form $\Delta \propto \exp i(\mathbf{k}_c \cdot \mathbf{r} - \omega t)$ and hence derive a wave equation for Δ .

$$\frac{d^2\Delta}{dt^2} + 2 \left(\frac{\dot{a}}{a} \right) \frac{d\Delta}{dt} = \Delta (4\pi G \varrho_0 - k^2 c_s^2), \quad (11.24)$$

where \mathbf{k}_c is the wavevector in comoving coordinates. The proper wavevector \mathbf{k} is related to \mathbf{k}_c by $\mathbf{k}_c = a\mathbf{k}$. Equation (11.24) is the result we have been seeking and a number of important conclusions follow from it. I make no apology for deriving (11.24) in somewhat gruesome detail because it is as important as any equation in astrophysical cosmology.

I have used cosmic time t as the time variable in this analysis but, in much of the technical literature, theorists prefer to use the *conformal time*, τ , which is introduced in Sect. 12.2. These times are related by $d\tau = dt/a$. It is a straightforward exercise to show that (11.24) becomes

$$\frac{d^2\Delta}{d\tau^2} + \left(\frac{\dot{a}}{a} \right) \frac{d\Delta}{d\tau} = \Delta (4\pi G \varrho_0 a^2 - k_c^2 c_s^2), \quad (11.25)$$

where k_c is the comoving wavenumber and the derivative \dot{a} is taken with respect to conformal time. We will use this result in Sect. 20.5.6.

11.3 The Jeans' Instability

Let us return first of all to the problem originally studied by Jeans (Jeans, 1902). The differential equation for gravitational instability in a static medium is obtained by setting $\dot{a} = 0$ in (11.24). Then, for waves of the form $\Delta = \Delta_0 \exp i(\mathbf{k} \cdot \mathbf{r} - \omega t)$, the *dispersion relation*,

$$\omega^2 = c_s^2 k^2 - 4\pi G \varrho, \quad (11.26)$$

is found. Note that we have dropped the subscript 0 on the density ϱ . This relation was first derived by Jeans in 1902. The corresponding equation for the electrostatic case was only derived after the discovery of plasma oscillations by Langmuir and Tonks in the 1920s, and describes the dispersion relation for longitudinal plasma oscillations, or Langmuir waves (Tonks and Langmuir, 1929):

$$\omega^2 = c_s^2 k^2 + \frac{N_e e^2}{m_e \epsilon_0}, \quad (11.27)$$

where N_e is the electron density and m_e is the mass of the electron. The formal similarity of the physics may be appreciated by comparing the attractive gravitational acceleration of a region of mass density ϱ and the repulsive electrostatic acceleration of a region of electric charge density $N_e e$. The equivalence of $-G\varrho m_e$ and $N_e e^2 / 4\pi \epsilon_0$ is apparent.

The dispersion relation (11.26) describes oscillations or instability depending upon the sign of its right-hand side:

- If $c_s^2 k^2 > 4\pi G \varrho$, the right-hand side is positive and the perturbations are oscillatory, that is, they are sound waves in which the pressure gradient is sufficient to provide support for the region. Writing the inequality in terms of wavelength, stable oscillations are found for wavelengths less than the critical *Jeans' wavelength* λ_J

$$\lambda_J = \frac{2\pi}{k_J} = c_s \left(\frac{\pi}{G \varrho} \right)^{1/2}. \quad (11.28)$$

- If $c_s^2 k^2 < 4\pi G \varrho$, the right-hand side of the dispersion relation (11.26) is negative, corresponding to unstable modes. The solutions can be written

$$\Delta = \Delta_0 \exp(\Gamma t + i\mathbf{k} \cdot \mathbf{r}), \quad (11.29)$$

where

$$\Gamma = \pm \left[4\pi G \varrho \left(1 - \frac{\lambda_J^2}{\lambda^2} \right) \right]^{1/2}. \quad (11.30)$$

The positive solution corresponds to exponentially growing modes. For wavelengths much greater than the Jeans' wavelength, $\lambda \gg \lambda_J$, the growth rate Γ becomes $(4\pi G \varrho)^{1/2}$. In this case, the characteristic growth time for the instability is,

$$\tau = \Gamma^{-1} = (4\pi G \varrho)^{-1/2} \sim (G \varrho)^{-1/2}. \quad (11.31)$$

This is the famous *Jeans' Instability* and the time-scale τ is the typical collapse time for a region of density ϱ .

The physics of this result is very simple. The instability is driven by the self-gravity of the region and the tendency to collapse is resisted by the internal pressure gradient. We can derive the Jeans' instability criterion by considering the pressure support of a region with pressure p , density ϱ and radius r . The equation of hydrostatic support for the region is

$$\frac{dp}{dr} = -\frac{G \varrho M(< r)}{r^2}. \quad (11.32)$$

The region becomes unstable when the self-gravity of the region on the right-hand side of (11.32) overwhelms the pressure forces on the left-hand side. To order of magnitude, we can write $dp/dr \sim -p/r$ and $M \sim \varrho r^3$. Therefore, since $c_s^2 \sim p/\varrho$, the region becomes unstable if $r > r_J \sim c_s/(G \varrho)^{1/2}$. Thus, the Jeans' length is the scale which is just stable against gravitational collapse. Notice that the expression for the Jeans' length is the distance a sound wave travels in a collapse time. The Jeans' instability is of central importance in understanding the process of star formation in giant molecular clouds.

11.4 The Jeans' Instability in an Expanding Medium

The results of this section are so important that three different versions of the Jeans' instability in an expanding medium are given, each illustrating different aspects of the same basic physical process.

11.4.1 Small Perturbation Analysis

We return first to the full version of (11.24) of

$$\frac{d^2\Delta}{dt^2} + 2\left(\frac{\dot{a}}{a}\right)\frac{d\Delta}{dt} = \Delta(4\pi G\varrho - k^2 c_s^2). \quad (11.24)$$

The second term $2(\dot{a}/a)(d\Delta/dt)$ modifies the classical Jeans' analysis in crucial ways. It is apparent from the right-hand side of (11.24) that the Jeans' instability criterion applies in this case also but the growth rate is significantly modified. Let us work out the growth rate of the instability in the long wavelength limit $\lambda \gg \lambda_J$, in which case we can neglect the pressure term $c_s^2 k^2$. We then have to solve the equation

$$\frac{d^2\Delta}{dt^2} + 2\left(\frac{\dot{a}}{a}\right)\frac{d\Delta}{dt} = 4\pi G\varrho\Delta. \quad (11.33)$$

Rather than deriving the general solution, let us first consider the special cases $\varOmega_0 = 1$ and $\varOmega_0 = 0$ for which the scale factor–cosmic time relations are $a = (\frac{3}{2}H_0 t)^{2/3}$ and $a = H_0 t$ respectively.

– *The Einstein–de Sitter critical model* $\varOmega_0 = 1$, $\varOmega_\Lambda = 0$. In this case,

$$4\pi G\varrho = \frac{2}{3t^2} \quad \text{and} \quad \frac{\dot{a}}{a} = \frac{2}{3t}. \quad (11.34)$$

Therefore,

$$\frac{d^2\Delta}{dt^2} + \frac{4}{3t}\frac{d\Delta}{dt} - \frac{2}{3t^2}\Delta = 0. \quad (11.35)$$

By inspection, it can be seen that there must exist power law solutions of (11.35) and so we seek solutions of the form $\Delta = at^n$. Substituting into (11.35), we find

$$n(n-1) + \frac{4}{3}n - \frac{2}{3} = 0, \quad (11.36)$$

which has solutions $n = 2/3$ and $n = -1$. The latter solution corresponds to a decaying mode. The $n = 2/3$ solution corresponds to the growing mode we are seeking, $\Delta \propto t^{2/3} \propto a = (1+z)^{-1}$. This is the key result

$$\Delta = \frac{\delta\varrho}{\varrho} \propto (1+z)^{-1}. \quad (11.37)$$

In contrast to the *exponential* growth found in the static case, the growth of the perturbation in the case of the critical Einstein–de Sitter universe is only *algebraic*. This is the origin of the problems of forming galaxies by gravitational collapse in the expanding Universe.

- *The empty, Milne model* $\Omega_0 = 0$, $\Omega_\Lambda = 0$. In this case,

$$\varrho = 0 \quad \text{and} \quad \frac{\dot{a}}{a} = \frac{1}{t}, \quad (11.38)$$

and hence

$$\frac{d^2\Delta}{dt^2} + \frac{2}{t} \frac{d\Delta}{dt} = 0. \quad (11.39)$$

Again, seeking power law solutions of the form $\Delta = at^n$, we find $n = 0$ and $n = -1$, that is, there is a decaying mode and one of constant amplitude $\Delta = \text{constant}$.

These simple results describe the evolution of small amplitude perturbations, $\Delta = \delta\varrho/\varrho \ll 1$ for models with $\Omega_\Lambda = 0$. In the early stages of the matter-dominated phase, the dynamics of the world models are approximately those of the Einstein–de Sitter model, $a \propto t^{2/3}$, and so the amplitude of the density contrast grows linearly with a . In the late stages of models with $\Omega_0 < 1$, $\Omega_\Lambda = 0$, the dynamics of the Universe become approximately those of the $\Omega_0 = 0$ model and then the amplitudes of the perturbations grow very slowly. In the limit $\Omega_0 = 0$, they do not grow at all.

There is another way of understanding this result. We can write Friedman’s equation in terms of the curvature of space, as in (7.19),

$$\dot{a}^2 = \frac{\Omega_0 H_0^2}{a} - \frac{c^2}{\mathfrak{R}^2} = \frac{\Omega_0 H_0^2}{a} - \kappa c^2. \quad (11.40)$$

κ is the space curvature at the present epoch and, in the $\Omega_\Lambda = 0$ models, is entirely determined by the density parameter Ω_0 ,

$$\kappa = \frac{1}{\mathfrak{R}^2} = \frac{(\Omega_0 - 1)}{(c^2/H_0^2)}. \quad (11.41)$$

We are only concerned with models with $\Omega_0 < 1$ and so we recover the results described in Sect. 7.2.3 that the models have finite velocities at infinity. But there is another way of thinking about this result. We can compare the gravitational deceleration with the curvature term in (11.40). When $\Omega_0 H_0^2/a \gg c^2/\mathfrak{R}^2$, we obtain the expression (7.29) which we found before. In the opposite case, in which $\Omega_0 H_0^2/a \ll c^2/\mathfrak{R}^2$, the dynamics become

$$\dot{a}^2 = -\frac{c^2}{\mathfrak{R}^2} = -\kappa c^2. \quad (11.42)$$

Because κ is negative, the spatial geometry of the Universe is hyperbolic and so the diverging geodesics counteract the attractive force of gravity. The transition between the two cases occurs at a redshift $\Omega_0 z \approx 1$.

11.4.2 Perturbing the Friedman Solutions

In our second approach, we investigate the behaviour of density perturbations from the perspective of the dynamics of the Friedman world models. We demonstrated in Sect. 7.2 how the dynamics of these models could be understood in terms of a simple Newtonian model. The development of a spherical perturbation in the expanding Universe can be modelled by embedding a spherical region of density $\varrho + \delta\varrho$ in an otherwise uniform Universe of density ϱ (Fig. 11.1). Using the same approach as in Sect. 7.2, the spherical region behaves dynamically like a Universe of slightly higher density. It is simplest to begin with the parametric solutions (7.25) and (7.26) for the dynamics of the world models

$$a = A(1 - \cos \theta) \quad t = B(\theta - \sin \theta); \quad (11.43)$$

$$A = \frac{\varOmega_0}{2(\varOmega_0 - 1)} \quad B = \frac{\varOmega_0}{2H_0(\varOmega_0 - 1)^{3/2}}. \quad (11.44)$$

First, we find the solutions for small values of θ , corresponding to early stages of the matter-dominated era. Expanding to third order in θ , $\cos \theta = 1 - \frac{1}{2}\theta^2$, $\sin \theta = \theta - \frac{1}{6}\theta^3$, we find the solution

$$a = \varOmega_0^{1/3} \left(\frac{3H_0 t}{2} \right)^{2/3}. \quad (11.45)$$

This solution is identical to (7.29) and shows that, in the early stages of matter-dominated models, their dynamics tend towards those of the Einstein–de Sitter

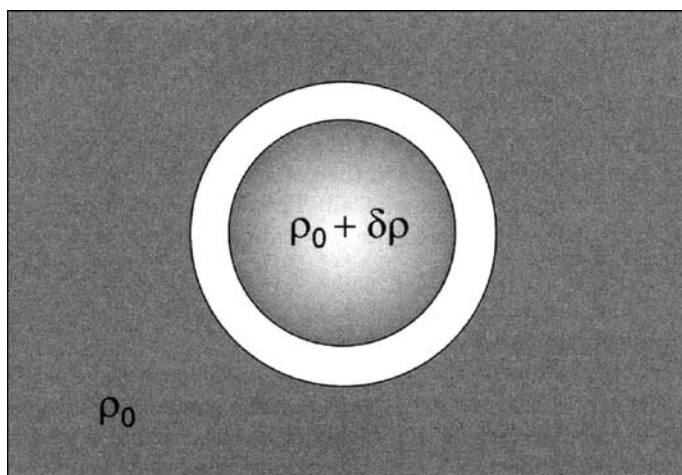


Fig. 11.1. Illustrating a spherical perturbation with slightly greater density than the average in a uniformly expanding Universe. The region with slightly greater density behaves dynamically exactly like a model Universe with density $\varrho + \delta\varrho$

model, $\Omega_0 = 1$, that is, $a = (3H_0t/2)^{2/3}$, but with a different constant of proportionality.

Now, consider a region of slightly greater density embedded within the background model. To derive the small amplitude behaviour of the perturbation, we expand the expressions for a and t to fifth order in θ , $\cos\theta = 1 - \frac{1}{2}\theta^2 + \frac{1}{24}\theta^4 \dots$, $\sin\theta = \theta - \frac{1}{6}\theta^3 + \frac{1}{120}\theta^5 \dots$. The solution follows in exactly the same manner as (11.45)

$$a = \Omega_0^{1/3} \left(\frac{3H_0t}{2} \right)^{2/3} \left[1 - \frac{1}{20} \left(\frac{6t}{B} \right)^{2/3} \right]. \quad (11.46)$$

We can now write down an expression for the change of density of the spherical perturbation with cosmic epoch

$$\varrho(a) = \varrho_0 a^{-3} \left[1 + \frac{3}{5} \frac{(\Omega_0 - 1)}{\Omega_0} a \right]. \quad (11.47)$$

The density perturbation may be considered to be a mini-Universe of slightly higher density than $\Omega_0 = 1$ embedded in an $\Omega_0 = 1$ model. Therefore, the density contrast changes with scale factor as

$$\Delta = \frac{\delta\varrho}{\varrho} = \frac{\varrho(a) - \varrho_0(a)}{\varrho_0(a)} = \frac{3}{5} \frac{(\Omega_0 - 1)}{\Omega_0} a. \quad (11.48)$$

This result illustrates why density perturbations grow only linearly with cosmic epoch. The instability corresponds to the slow divergence between the variations of the scale factors with cosmic epoch of the model with $\Omega_0 = 1$ and one with slightly greater density. This behaviour is illustrated in Fig. 11.2. This slow algebraic growth of density perturbations was at the heart of the arguments advanced by Tolman and Lemaître in the 1930s and more generally by Lifshitz in 1946 that there was not time for galaxies to have formed by gravitational collapse in the expanding Universe (Tolman, 1934; Lemaître, 1933).

Notice that, if $\Omega_0 = 1$, there is no growth of the perturbation. In order to form structures in a finite time, the perturbations on large scales have to have finite amplitudes which bring them onto the collapsing trajectory shown in Fig. 11.2. These cannot be simply statistical fluctuations in the numbers of particles on very large scales, which would be very small indeed.

11.4.3 Falling Poles

The third argument contains exactly the same physics. Consider a very long, thin pole of length l and mass m balanced on one end. We all know that the situation is unstable and that, if perturbed, the pole falls over. This is no more than a gravitational instability in which there is no restoring force to prevent collapse. We can work out the growth rate of the instability by conservation of energy in a uniform gravitational field. In Fig. 11.3, the pole is shown at an angle θ to the vertical and then, by

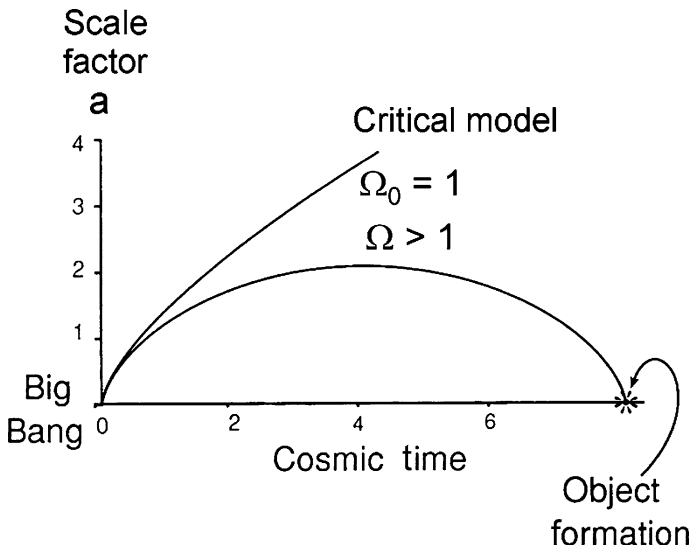
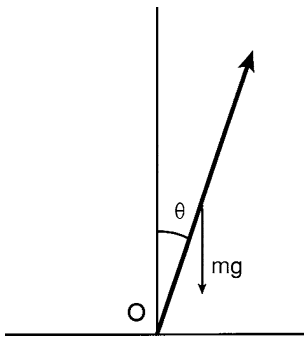


Fig. 11.2. Illustrating the growth of a spherical perturbation in the expanding Universe as the divergence between two Friedman models with slightly different densities

Fig. 11.3. Illustrating a falling pole



conservation of energy, the loss of gravitational potential energy $(gml/2)(1 - \cos \theta)$ must equal the increase in rotational energy $(1/2)I\omega^2$ about the bottom end of the pole O, where I is moment of inertia of the pole about O

$$\frac{gml}{2}(1 - \cos \theta) = \frac{1}{2}I\omega^2. \quad (11.49)$$

Since $I = \frac{1}{3}ml^2$ and $\omega = \dot{\theta}$, it follows that

$$\dot{\theta}^2 = 3\frac{g}{l}(1 - \cos \theta). \quad (11.50)$$

There is an exact non-linear solution for this equation, but let us deal only with the small angle approximation in which $\cos \theta = (1 - \theta^2/2 + \dots)$. Then, we obtain

a simple exponential equation for the collapse of the pole

$$\dot{\theta} = \left(\frac{3g}{2l} \right)^{1/2} \theta. \quad (11.51)$$

The solution $\theta = \theta_0 \exp(\Gamma t)$ with $\Gamma = (3g/2l)^{1/2}$ is the exact analogue of the equation for the growth of the Jeans' instability in the absence of pressure forces in a static medium.

To modify this result for the case of an expanding Universe, we recall that, in the absence of pressure gradients, the differential equation (11.24) for the growth rate of the instability is

$$\frac{d^2\Delta}{dt^2} + 2 \left(\frac{\dot{a}}{a} \right) \frac{d\Delta}{dt} = 4\pi G\varrho\Delta. \quad (11.52)$$

Notice that the force driving the instability on the right-hand side of this expression depends upon the product of the gravitational constant G and the density of the medium ϱ . Now, in the expanding Universe, $\varrho \propto a^{-3}$ and, for the critical model $\Omega_0 = 1$, $\Omega_A = 0$, $a \propto t^{2/3}$. Therefore, the driving force is proportional $G\varrho \propto t^{-2}$. To simulate this case for a collapsing pole, we can assume that the gravitational acceleration decreases as t^{-2} , in which case the equation of motion of the pole (11.48) becomes

$$\dot{\theta} \propto \frac{\theta}{t}. \quad (11.53)$$

Inspection of (11.50) shows that the solutions are of power law form, $\theta \propto t$, rather than exponentially growing solutions. This calculation illustrates the origin of the linear algebraic growth of the Jeans' instability in the expanding Universe. The gravitational driving force diminishes with time because the mean density of the Universe decreases as it expands.

11.4.4 The General Solution

The analyses of Sects. 11.4.1 to 11.4.3 give insight into the general solutions of (11.33). Following Heath, Carroll and his colleagues provide a general solution for the growth of the density contrast with scale factor for all pressure-free Friedman world models (Heath, 1977; Carroll et al., 1992). Equation (11.33) can be rewritten in terms of the density parameter Ω_0

$$\frac{d^2\Delta}{dt^2} + 2 \left(\frac{\dot{a}}{a} \right) \frac{d\Delta}{dt} = \frac{3\Omega_0 H_0^2}{2} a^{-3} \Delta, \quad (11.54)$$

where, in general,

$$\dot{a} = H_0 \left[\Omega_0 \left(\frac{1}{a} - 1 \right) + \Omega_A (a^2 - 1) + 1 \right]^{1/2}. \quad (11.55)$$

The solution for the growing mode can be written as follows:

$$\Delta(a) = \frac{5\Omega_0}{2} \left(\frac{1}{a} \frac{da}{dt} \right) \int_0^a \frac{da'}{\left(\frac{da'}{dt} \right)^3}, \quad (11.56)$$

where the constants have been chosen so that the density contrast for the critical world model, $\Omega_0 = 1$, $\Omega_\Lambda = 0$, has unit amplitude at the present epoch, $a = 1$. With this scaling, the density contrasts for all the examples considered below correspond to $\Delta = 10^{-3}$ at $a = 10^{-3}$. Solutions of this integral can be found in terms of elliptic functions, but it is simplest to carry out the calculations numerically for a representative sample of world models.

In Fig. 11.4, the development of density fluctuations from a scale factor $a = 1/1000$ to $a = 1$ is shown for a range of world models with $\Omega_\Lambda = 0$. These results are consistent with the calculations carried out in Sect. 11.4.1, in which it was argued that the amplitudes of the density perturbations vary as $\Delta \propto a$ so long as $\Omega_0 z \gg 1$, but the growth tends to zero at smaller redshifts.

Since the scale factor $a = 1/1000$ corresponds to the epoch of recombination, or the last scattering surface of the Cosmic Microwave Background Radiation, the density perturbations developed by relatively modest factors over an interval of cosmic time from about 300,000 to 10^{10} years after the origin of the Big Bang. For example, if $\Omega_0 = 1$, the increase is a factor of 10^3 , as expected from (11.37). In the case $\Omega_0 = 0.1$, the amplitudes of the fluctuations grow as $\Delta \propto a$ over the range of

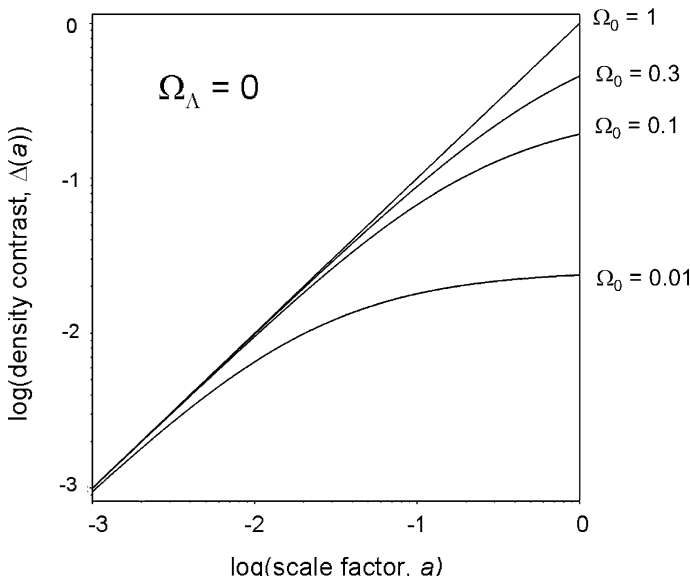


Fig. 11.4. The growth of density perturbations over the range of scale factors $a = 10^{-3}$ to 1 for world models with $\Omega_\Lambda = 0$ and density parameters $\Omega_0 = 0.01, 0.1, 0.3$ and 1

scale factors from $a = 10^{-3}$ to 10^{-1} , but grow only modestly from $a = 10^{-1}$ to 1. In this case, the growth of the density contrast is only by a factor of 190 from the epoch of recombination to the present epoch. If Ω_0 were 0.01, the growth of the density contrast would be even smaller, a factor of only 24.

Similar calculations can be carried out for the cases in which $\Omega_\Lambda \neq 0$. Those of the greatest interest are the flat models for which $(\Omega_0 + \Omega_\Lambda) = 1$. Figure 11.5 shows the development of the fluctuations over the range of scale factors from $a = 1/30$ to the present epoch $a = 1$, in all cases, the fluctuations having amplitude $\Delta = 10^{-3}$ at $a = 10^{-3}$. The growth of the density contrast is much greater in the cases $\Omega_0 = 0.1$ and 0.3 as compared with the corresponding cases with $\Omega_\Lambda = 0$. For example, in the case $\Omega_0 = 0.1$, the growth of the fluctuation from $a = 1/1000$ to 1 is 610. Inspection of Fig. 11.5 shows that the fluctuations continue to grow to greater values of the scale factor a , corresponding to smaller redshifts, as compared with the models with $\Omega_\Lambda = 0$.

The reason for the enhanced growth of the perturbations can be understood from the same line of reasoning presented in the discussion at the end of Sect. 11.4.1 Writing Friedman's equation with the curvature term shown explicitly, we find

$$\dot{a}^2 = \frac{\Omega_0 H_0^2}{a} + \Omega_\Lambda a^2 H_0^2 - \frac{c^2}{\mathfrak{R}^2} = \frac{\Omega_0 H_0^2}{a} + \Omega_\Lambda a^2 H_0^2 - \kappa c^2. \quad (11.57)$$

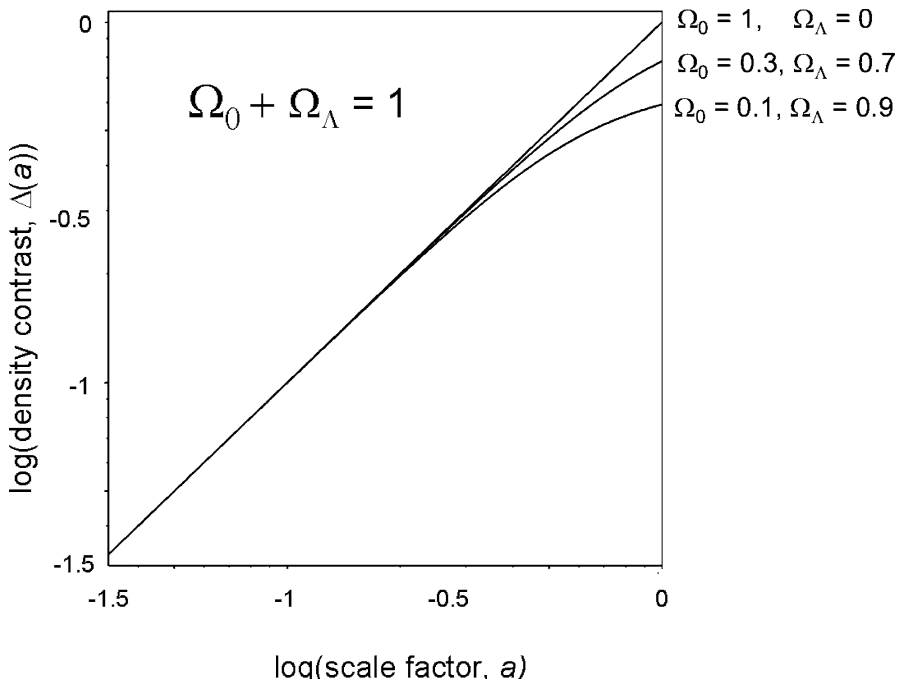


Fig. 11.5. The growth of density perturbations over the range of scale factors $a = 1/30$ to 1 for world models with $\Omega_0 + \Omega_\Lambda = 1$ and density parameters $\Omega_0 = 0.1, 0.3$ and 1

In the model with $\Omega_0 + \Omega_\Lambda = 1$, the curvature κ is zero, enforcing flat geometry. Thus, at small values of the scale factor, when the dark energy is less important than the gravitational influence of the matter, the dynamics of the Universe follow precisely

$$\dot{a}^2 = \frac{\Omega_0 H_0^2}{a}, \quad (11.58)$$

and so the growth of the instability continues, even if $\Omega_0 z \ll 1$. The continued growth of the instability can be attributed to the presence of the curvature term which ensures that the geometry is Euclidean during the expansion, rather than the hyperbolic geometry which would occur if $\Omega_\Lambda = 0$. Eventually, the repulsive effect of the dark energy becomes important when the dark energy term becomes greater than the gravitational term and the growth rate of the instability slows down. From (11.57), it can be seen that this occurs when $\Omega_0/a = \Omega_\Lambda a^2 = (1 - \Omega_0)a^2$, that is,

$$a \approx \left(\frac{\Omega_0}{1 - \Omega_0} \right)^{1/3} \quad \text{or} \quad (1 + z) \approx \Omega_0^{-1/3} \quad \text{if } \Omega_0 \ll 1. \quad (11.59)$$

These calculations explain the late declines in the growth rates of the instabilities seen in Fig. 11.5 as compared with those in Fig. 11.4. They also illustrate the importance of the curvature term in understanding the growth of instabilities in the expanding Universe.

We have considered only the cases of Friedman models with $\Omega_\Lambda = 0$ and flat cosmological models with $\Omega_0 + \Omega_\Lambda = 1$, but the space of conceivable world models is much greater than these cases. Their evolution can be either worked out numerically from (11.56) or, more crudely, from the physical arguments developed above.

11.5 The Evolution of Peculiar Velocities in the Expanding Universe

The development of velocity perturbations in the expanding Universe can be derived from (11.20). Let us investigate the case in which we neglect pressure gradients so that the velocity perturbations are only driven by the potential gradient $\delta\phi$

$$\frac{d\mathbf{u}}{dt} + 2 \left(\frac{\dot{a}}{a} \right) \mathbf{u} = -\frac{1}{a^2} \nabla_c \delta\phi. \quad (11.60)$$

We recall that \mathbf{u} is the perturbed *comoving* velocity. Let us split the velocity vector into components parallel and perpendicular to the gravitational potential gradient, $\mathbf{u} = \mathbf{u}_\parallel + \mathbf{u}_\perp$, where \mathbf{u}_\parallel is parallel to $\nabla_c \delta\phi$. The velocity associated with \mathbf{u}_\parallel is often referred to as *potential motion* since it is driven by the potential gradient. On the other hand, the perpendicular velocity component \mathbf{u}_\perp is not driven by potential gradients and corresponds to *vortex* or *rotational motions*. We consider the growth of the velocity perturbations as the gravitational instability develops.

Rotational velocities. Consider first the rotational component \mathbf{u}_\perp . Equation (11.60) reduces to

$$\frac{d\mathbf{u}_\perp}{dt} + 2 \left(\frac{\dot{a}}{a} \right) \mathbf{u}_\perp = 0. \quad (11.61)$$

The solution of this equation is straightforward $\mathbf{u}_\perp \propto a^{-2}$. Since \mathbf{u}_\perp is a comoving perturbed velocity, the proper velocity is $\delta\mathbf{v}_\perp = a\mathbf{u}_\perp \propto a^{-1}$. Thus, the rotational velocities decay as the Universe expands. This is no more than the conservation of angular momentum in an expanding medium, $mvr = \text{constant}$. This poses a grave problem for models of galaxy formation involving primordial turbulence. Rotational turbulent velocities decay and there must be sources of turbulent energy, if the rotational velocities are to be maintained.

Potential motions. The development of potential motions is most directly derived from (11.13)

$$\frac{d\Delta}{dt} = -\nabla \cdot \delta\mathbf{v}, \quad (11.62)$$

that is, the divergence of the peculiar velocity is proportional to minus the rate of growth of the density contrast. The peculiar velocity $\delta\mathbf{v}_\parallel$ is parallel to the wave vector of the perturbation $\Delta = \Delta_0 \exp i(\mathbf{k} \cdot \mathbf{x} - \omega t) = \Delta_0 \exp i(\mathbf{k}_c \cdot \mathbf{r} - \omega t)$ and so, using comoving derivatives, (11.13) can be rewritten

$$\frac{d\Delta}{dt} = -\frac{1}{a} \nabla_c \cdot (a\mathbf{u}) = -ik_c \cdot \mathbf{u}, \quad (11.63)$$

that is,

$$|\delta v_\parallel| = \frac{a}{k_c} \frac{d\Delta}{dt}. \quad (11.64)$$

Notice that we have written this expression in terms of the comoving wave vector k_c which means that this expression describes how the peculiar velocity associated with a particular perturbation changes with cosmic epoch. Let us consider separately the cases $\Omega_0 = 1$ and $\Omega_0 = 0$.

- $\Omega_0 = 1$. As shown above, $\Delta = \Delta_0(t/t_0)^{2/3}$ and $a = (3H_0t/2)^{2/3}$. Therefore,

$$|\delta v_\parallel| = |au| = \frac{H_0 a^{1/2}}{k} \left(\frac{\delta\varrho}{\varrho} \right)_0 = \frac{H_0}{k} \left(\frac{\delta\varrho}{\varrho} \right)_0 (1+z)^{-1/2}, \quad (11.65)$$

where $(\delta\varrho/\varrho)_0$ is the density contrast at the present epoch. This calculation shows how potential motions grow with cosmic time in the critical model, $\delta v_\parallel \propto t^{1/3}$. In addition, it can be seen that the peculiar velocities are driven by both the amplitude of the perturbation and its scale. Equation (11.65) shows that, if $\delta\varrho/\varrho$ is the same on all scales, the peculiar velocities are driven by the smallest values of k , that is, by the perturbations on the largest physical scales. Thus, local peculiar

velocities can be driven by density perturbations on the very largest scales, which is an important result for understanding the origin of the peculiar motion of the Galaxy with respect to the frame of reference in which the Microwave Background Radiation is 100% isotropic and of large-scale streaming velocities.

- $\Omega_0 = 0$. In this case, it is simplest to proceed from (11.20) in which there is no driving term in the equation

$$\frac{d\mathbf{u}}{dt} + 2 \left(\frac{\dot{a}}{a} \right) \mathbf{u} = 0. \quad (11.66)$$

The solution is the same as that for u_\perp given above, that is, $\delta v_\parallel \propto a^{-1}$ – the peculiar velocities decay with time. This is the same result deduced in Sect. 7.1.

- In the general case, we need the expression for $d\Delta/dt$ which is most simply derived from the numerical solutions of (11.56). There is, however, a useful approximation which is often used in the context of the cosmic virial theorem for the magnitude of the peculiar velocities induced by density perturbations, such as superclusters and other large-scale structures. Suppose we write $\Delta = \Delta_0 f(t)$, where Δ_0 is the amplitude of the density perturbation at the present epoch $t = t_0$. Then, we can write (11.64) as follows:

$$|\delta v_\parallel| = \frac{a}{k_c} \Delta_0 \frac{df}{dt} = \frac{a}{k_c} \Delta_0 \frac{df}{da} \frac{da}{dt}. \quad (11.67)$$

At the present epoch, $t = t_0$, $a = 1$, $da/dt = H_0$ and so the peculiar velocity is

$$|\delta v_\parallel| = \frac{\Delta_0 H_0}{k_c} \left(\frac{df}{da} \right)_0. \quad (11.68)$$

For the critical model $\Omega_0 = 1$, $f = a$ and we immediately recover (11.65) at $z = 0$. Thus, the amplitude of the peculiar velocities at the present epoch depends upon df/da . A common approximation for this function is $df/da = \Omega_0^{0.6}$, the result being exact for the case $\Omega_0 = 1$ (Gunn, 1978; Peebles, 1980); this is the origin of (8.33). As discussed in Sect. 8.7, a better analytic approximation, correct to second order in $\delta\rho/\rho$, has been derived by Lightman and Schechter for Friedman models with $\Omega_A = 0$ (Lightman and Schechter, 1990),

$$\frac{\Delta v}{v} = -\frac{1}{3} \Omega_0^{4/7} \left(\frac{\delta\rho}{\rho} \right)_0 + \frac{4}{63} \Omega_0^{13/21} \left(\frac{\delta\rho}{\rho} \right)_0^2. \quad (11.69)$$

It is straightforward to integrate (11.67) numerically using (11.56) and (11.57). These solutions are shown in Fig. 11.6 and, as expected, they mirror the behaviour of the density contrast with scale factor, because of (11.62). In the case of world models with $\Omega_A = 0$, the results found from the exact solutions above can account for the evolution of peculiar velocities with scale factor. So long as $\Omega_0 z \gg 1$, velocities driven by potential gradients grow as $a^{1/2} \propto t^{1/3}$, but at redshifts $\Omega_0 z \ll 1$, the velocities decrease as a^{-1} . For a given value of Ω_0 , there is a redshift at which the peculiar velocities of galaxies selected randomly from the general field have

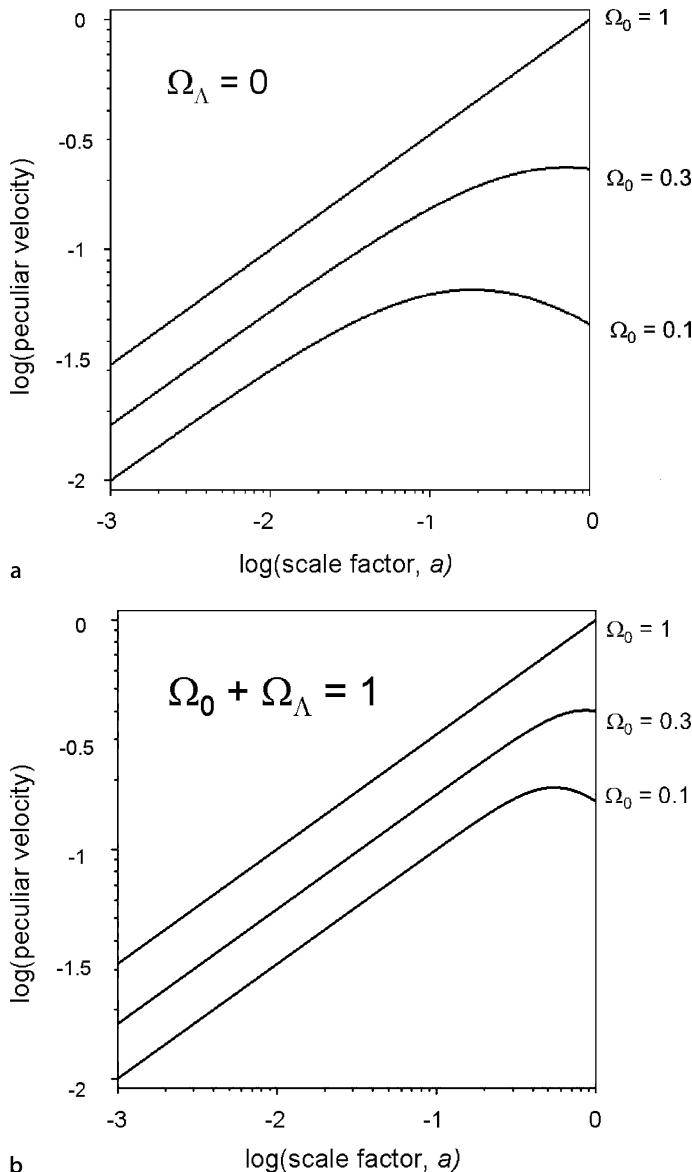


Fig. 11.6a,b. The growth of the peculiar velocities over the range of scale factors $a = 10^{-3}$ to 1 for: **a** world models with $\Omega_\Lambda = 0$ and density parameters $\Omega_0 = 0.1, 0.3$ and 1 and **b** for world models with $\Omega_0 + \Omega_\Lambda = 1$ and density parameters $\Omega_0 = 0.1, 0.3$ and 1. In both cases, the behaviour at small values of the scale factor is given by (11.67) in the limit $a \ll 1$ with $\Delta_0 H_0/k_c = 1$, $|\delta v_{\parallel}| \propto (a\Omega_0)^{1/2}$

a maximum value. A similar result is found for the models with $\Omega_0 + \Omega_A = 1$. Because the perturbations continue to grow in amplitude to larger values of the scale factor, the maximum peculiar velocities occur at a smaller redshifts. The maximum occurs at the redshift at which the dark energy term begins to dominate the dynamics, as given by (11.59).

11.6 The Relativistic Case

We investigate next the case of an ultrarelativistic or photon gas because, during the radiation-dominated era, the primordial perturbations are in a radiation-dominated plasma, for which the pressure can no longer be neglected and the relativistic equation of state $p = \frac{1}{3}\varepsilon$ is appropriate. Again, we consider only perturbations on scales much less than the horizon scale. We require the generalisations of (11.1), (11.2) and (11.3) for a relativistic gas. There is no simple way of demonstrating the appropriate forms of these equations except by using the energy-momentum tensor for a relativistic gas (Weinberg, 1972). Coles and Lucchin present the results of these calculations in a form similar to those of (11.1), (11.2) and (11.3) (Coles and Lucchin, 1995)

$$\frac{\partial \varrho}{\partial t} = -\nabla \cdot \left(\varrho + \frac{p}{c^2} \right) \mathbf{v}; \quad (11.70)$$

$$\left(\varrho + \frac{p}{c^2} \right) \left(\frac{\partial \mathbf{v}}{\partial t} + \mathbf{v} \cdot \nabla \mathbf{v} \right) = -\nabla p - \left(\varrho + \frac{p}{c^2} \right) \nabla \phi; \quad (11.71)$$

$$\nabla^2 \phi = 4\pi G \left(\varrho + \frac{3p}{c^2} \right). \quad (11.72)$$

We can recognise the presence of the pressure terms in the continuity equation, Euler's equation and Poisson's equation from the analyses which led to (7.6) and (7.12).

Substituting $p = \frac{1}{3}\varrho c^2$ into these equations and converting to Lagrangian derivatives, we find

$$\frac{d\varrho}{dt} = -\frac{4}{3}\varrho(\nabla \cdot \mathbf{v}); \quad (11.73)$$

$$\frac{d\mathbf{v}}{dt} = -\frac{1}{\frac{4}{3}\varrho} \nabla p - \nabla \phi; \quad (11.74)$$

$$\nabla^2 \phi = 8\pi G \varrho. \quad (11.75)$$

The net result is that the equations for the evolution of the perturbations in a relativistic gas are of similar mathematical form to the non-relativistic case (11.5), (11.6) and (11.7). The same type of analysis which was carried out in Sect. 11.2 leads to the following equation for the growth of density perturbations in the relativistic plasma:

$$\frac{d^2 \Delta}{dt^2} + 2 \left(\frac{\dot{a}}{a} \right) \frac{d\Delta}{dt} = \Delta \left(\frac{32\pi G \varrho}{3} - k^2 c_s^2 \right). \quad (11.76)$$

The only difference is that the constant in front of the gravitational driving term on the right-hand side is $32\pi/3$ instead of 4π . The relativistic expression for the Jeans' length is found by setting the right-hand side equal to zero,

$$\lambda_J = \frac{2\pi}{k_J} = c_s \left(\frac{3\pi}{8G\varrho} \right)^{1/2}, \quad (11.77)$$

where $c_s = c/\sqrt{3}$ is the relativistic sound speed. The result is similar to the standard expression (11.28) for the Jeans' length.

On scales much greater than the Jeans' length, the pressure gradient term in (11.74) can be neglected and then the following differential equation for the growth of the instability is obtained,

$$\frac{d^2\Delta}{dt^2} + 2\left(\frac{\dot{a}}{a}\right)\frac{d\Delta}{dt} = \frac{32\pi G\varrho}{3}\Delta. \quad (11.78)$$

This equation is the same as (11.33) but with a different constant on the right-hand side. Using the same approach as in Sect. 11.4.1, we seek solutions of the form $\Delta = at^n$, recalling that in the radiation-dominated phases, the scale factor–cosmic time relation is given by (9.7), $a \propto t^{1/2}$ and $\varrho \propto a^{-4}$. Going through precisely the same procedure as before, we find solutions $n = \pm 1$. Hence, for wavelengths $\lambda \gg \lambda_J$, the growing solution corresponds to

$$\Delta \propto t \propto a^2 \propto (1+z)^{-2}. \quad (11.79)$$

Thus, once again, the unstable mode grows only algebraically with cosmic time.

11.7 The Basic Problem

We will use the results derived above in the analysis of structure formation which follows. We have concentrated upon deriving a few exact results which will prove useful in understanding the more complete analyses found in the literature. Padmanabhan and Coles and Lucchin provide many useful solutions of the equations for the development of density perturbations in the expanding Universe and their analyses can be thoroughly recommended (Padmanabhan, 1993; Coles and Lucchin, 1995).

For the moment, let us note one of the most important conclusions of the above analysis. For the case of our reference cosmological model, $\Omega_0 = 0.3$, $\Omega_A = 0.7$, the growth of density perturbations depends upon scale factor, or redshift, more or less as

$$\Delta = \frac{\delta\varrho}{\varrho} \propto a = \frac{1}{1+z}, \quad (11.80)$$

throughout the post-recombinations era (Fig. 11.5). In the case of the models with $\Omega_A = 0$, the growth is significantly less, as can be seen from Fig. 11.4. At redshifts

less than $1/\Omega_0$, the instability grew very much more slowly and, in the limit $\Omega_0 = 0$, did not grow at all.

Since galaxies and astronomers certainly exist at the present day $a = 1$, $z = 0$, it follows that $\Delta \geq 1$ at $z = 0$ and so, at the last scattering surface, $z \sim 1000$, density fluctuations must have been present with amplitude at least $\Delta = \delta\varrho/\varrho \geq 10^{-3}$. These were certainly not infinitesimal perturbations.

We can look at the results of these calculations in two ways:

- On the one hand, the slow growth of density perturbations is the source of a fundamental problem in understanding the origin of galaxies – large-scale structures did not condense out of the primordial plasma by exponential collapse, in contrast to the formation of stars in dense interstellar clouds. As we will show, from the time the perturbations came through their horizon scales, these large-scale features grew by only a modest factor and so there must have been some mechanism for generating finite amplitude perturbations on large scales in the early Universe. This is one of the great problems of classical cosmology and was the reason that Tolman, Lemaître and Lifshitz concluded that galaxies could not have formed by gravitational collapse.
- On the other hand, because of the slow development of the density perturbations, we have the real possibility of learning about many aspects of the early Universe which would otherwise have been excluded. We have the opportunity of studying the processes of formation of structure on the last scattering surface at a redshift $z \sim 1000$ and, even more important, we can obtain crucial information about the spectrum of fluctuations which must have been present in the very early Universe. Thanks to the slow growth of the fluctuations, we have a direct probe of the physics of the early Universe.

12 More Tools and Problems

The central theme of the last chapter was the evolution of density perturbations under gravity in the expanding Universe. The attractive force of gravity and the opposing effect of the dark energy featured prominently in that analysis but we now need to add in many more physical processes in order to create physically acceptable models for the formation of structure. In this chapter, the emphasis is upon the role of baryonic matter. We will spend a little time understanding why purely baryonic models of the formation of cosmic structures fail to account for the observations, supporting the view that the dominant dark matter must be in some non-baryonic form. We will develop the dark matter models in much more detail in Chap. 13, using many of the tools developed in this chapter. First of all, we need to deal with a number of key issues concerning cosmological horizons and superhorizon perturbations which we have glossed over so far.

12.1 Horizons and the Horizon Problem

One of the important concepts in the theory of structure formation in the expanding Universe is that of *particle horizons*. At any epoch t , the particle horizon is defined to be the maximum distance over which causal communication could have taken place by that epoch. In other words, this is the distance a light signal could have travelled from the origin of the Big Bang at $t = 0$ by the epoch t . The Universe is expanding at a rate which varies with cosmic epoch and we take account of this by the same reasoning which led to the definition of comoving radial distance coordinate (Sect. 5.4). There, the problem was to define a distance at a single cosmic epoch, despite the fact that what we observe lies along our past light cone, which may span a wide range of cosmic epochs. The solution was to project increments of proper distance forward to a reference epoch t_0 , taken to be the present epoch. This projection takes account of the fact that the fundamental observers are separating as the Universe expands. The same procedure can be carried out for particle horizon scales as well. Now, we scale the comoving distance scale r back to the epoch t by multiplying by the scale factor $a(t)$ according to definition (5.27). These distances are defined to be *proper distances* at the epoch corresponding to the scale factor a .

The comoving radial distance r corresponding to the distance travelled by a light signal from the origin of the Big Bang to the epoch t is

$$r = \int_0^t \frac{c dt}{a(t)} = \int_0^t (1+z)c dt . \quad (12.1)$$

This integral is similar to that which led to the standard result (7.74), the difference being that the comoving radial distances in that case were integrated from redshifts 0 to z corresponding to $a = 1$ to a , whereas in the present case, the integral is from $z = \infty$ to z , or $a = 0$ to a . To find the proper horizon scale at the epoch corresponding to redshift z , we scale r in (12.1) by the factor $a(t) = (1+z)^{-1}$. Thus, the definition of the *particle horizon* $r_H(t)$ at the cosmic epoch t is

$$r_H(t) = a(t) \int_0^t \frac{c dt}{a(t)} = \frac{1}{1+z} \int_0^t (1+z)c dt = a(t) \int_0^a \frac{c da}{a\dot{a}} . \quad (12.2)$$

In the case of the standard Friedman models with $\Omega_A = 0$, we use (7.64) for dt so that, if $\Omega_0 > 1$, the integral is

$$\frac{c}{H_0} \int_{\infty}^z \frac{dz}{(1+z)(\Omega_0 z + 1)^{1/2}} = \frac{2c}{H_0(\Omega_0 - 1)^{1/2}} \left[\tan^{-1} \left(\frac{\Omega_0 z + 1}{\Omega_0 - 1} \right)^{1/2} \right]_{\infty}^z . \quad (12.3)$$

Putting in the limits to the integral and carrying out a little algebra, we find

$$r_H(t) = \frac{c}{H_0(\Omega_0 - 1)^{1/2}} a \cos^{-1} \left[1 - \frac{2(\Omega_0 - 1)}{\Omega_0} a \right] . \quad (12.4)$$

The corresponding result for $\Omega_0 < 1$ is

$$r_H(t) = \frac{c}{H_0(1 - \Omega_0)^{1/2}} a \cosh^{-1} \left[1 + \frac{2(1 - \Omega_0)}{\Omega_0} a \right] . \quad (12.5)$$

In the critical Einstein–de Sitter case, the particle horizon is

$$r_H(t) = \frac{2c}{H_0} a^{3/2}(t) = \frac{2c}{H_0} \frac{t}{t_0} = 3ct . \quad (12.6)$$

Notice that, at early times, corresponding to small values of a , both (12.4) and (12.5) reduce to

$$r_H(t) = \frac{2c}{H_0 \Omega_0^{1/2}} a^{3/2} , \quad (12.7)$$

similar to (12.6), but with a different constant. This is also true for models with a finite cosmological constant. For example, in the case of flat world models with

$\Omega_0 + \Omega_A = 1$, we can use (7.69) to determine r_H for this case:

$$r_H(t) = \frac{c}{H_0(1+z)} \int_{\infty}^z \frac{dz}{[\Omega_0(1+z)^3 + 1 - \Omega_0]^{1/2}}. \quad (12.8)$$

In the limit of large redshifts, the term in $(1+z)^3$ under the square root dominates and the result (12.7) is recovered. As already noted, at early times, all the Friedman models, including those with finite values of Ω_A , tend toward the dynamics of the critical model, but again with a different prefactor

$$a = \Omega_0^{1/3} \left(\frac{3H_0 t}{2} \right)^{2/3},$$

and so the particle horizon is $r_H(t) = 3ct$, the same result as (12.6). One might have expected that the distance which light could have travelled by epoch t to be of order ct . The factor 3 takes account of the fact that fundamental observers were closer together at early epochs and so greater distances could be causally connected than ct .

A similar calculation can be carried out for the radiation-dominated era at redshifts $z \gg 2.4 \times 10^4 \Omega_0 h^2 \approx 3530$, during which the dynamics of the expansion were described by $a \propto t^{1/2}$. Performing the integral (12.2) for this case, we find $r_H(t) = 2ct$. The factor of 2, rather than 3, reflects the difference between the early dynamics of the radiation-dominated and matter-dominated universes.

We can now use these results to illustrate the origin of the *horizon problem* for the standard Friedman models. Let us work out the angle θ_H which the particle horizon subtends on the last scattering surface according to an observer at the present epoch. At a redshift $z = 1000$, $\Omega_0 z \gg 1$ and so according to (7.77) for models with $\Omega_A = 0$, the distance measure D converges to the value $D = 2c/H_0\Omega_0$. Therefore, from (5.54) and (12.7) we find

$$\theta_H = \frac{r_H(t)(1+z)}{D} = \frac{\Omega_0^{1/2}}{(1+z)^{1/2}} = 1.8\Omega_0^{1/2} \text{ degrees}. \quad (12.9)$$

For our reference model, $\Omega_0 = 0.3$, $\Omega_A = 0.7$, θ_H is 2.1° . These results mean that, according to the standard Friedman picture, regions of the Universe separated by an angle of more than about a degree on the sky could not have been in causal contact on the last scattering surface at redshift $z \approx 1000$. Why then is the cosmic microwave background radiation so uniform over the whole sky to a precision of about one part in 10^5 ? In the standard picture, it has to be assumed that the remarkable isotropy of the Universe was part of its initial conditions. This is one of the major problems of classical cosmology.

This problem is circumvented in the inflationary model of the very early Universe because of the exponential expansion of the scale factor which ensures that opposite directions on the sky were in causal contact in the very distant past, although they are not today. To illustrate this, consider the de Sitter model (7.55), but now applied

to the very early Universe between scale factors a_1 and a_2 when the expansion was described by $a \propto \exp(\alpha t)$, where $\alpha = (\Lambda/3)^{1/2}$. Then, the particle horizon at scale factor a_2 was

$$r_H(a_2) = a_2 \int_{t_1}^{t_2} \frac{c dt}{a} = a_2 \int_{a_1}^{a_2} \frac{c da}{a \dot{a}}, \quad (12.10)$$

$$= \frac{c}{\alpha} [e^{\alpha(t_2-t_1)} - 1]. \quad (12.11)$$

For small time intervals, $\alpha(t_2-t_1) \ll 1$, the particle horizon reduces to $r_H = c(t_2-t_1)$, but for large time intervals, $\alpha(t_2-t_1) \gg 1$, r_H can become very much greater than $c(t_2-t_1)$. In the inflationary picture of the very early Universe described in Sect. 7.3.1, the value of $\alpha = (\Lambda/3)^{1/2}$ was quite enormous and so causal communication could have extended to distances vastly exceeding the scale ct by the epoch corresponding to a_2 .

To complete this discussion of horizons, we note that the term *event horizon*, introduced by Rindler, also appears in the cosmological literature (Rindler, 1956). The event horizon is the greatest distance an object can have at a particular cosmic epoch, if it is ever to be observable, however long the observer waits. Consider a light ray emitted at time t_1 which arrives at the observer at time t . Then, the comoving radial distance coordinate traversed by the light ray is

$$\int_{t_1}^t \frac{c dt}{a(t)}. \quad (12.12)$$

The question is whether or not this integral converges as $t \rightarrow \infty$ in the open models or as $t \rightarrow t_\infty$ for the collapsing closed models. The definition of the event horizon is therefore

$$r_E = \int_{t_1}^{t_\infty} \frac{c dt}{a(t)} = \int_{a_1}^{a_{\max}} \frac{c da}{a \dot{a}}. \quad (12.13)$$

In the standard world models with $\Omega_A = 0$, if $\Omega_0 \leq 1$, the integral (12.13) diverges, since $a \propto t^{2/3}$ for the $\Omega_0 = 1$ model and $a \propto t$ for $\Omega_0 = 0$. Therefore, it is eventually possible, in principle, to observe every particle there is in the Universe in these models. If $\Omega_0 > 1$, the integral (12.13) converges to a finite comoving radial distance coordinate. Using (7.22), we find $t_\infty = 2t_{\max} = \pi\Omega_0/H_0(\Omega_0 - 1)^{3/2}$. The integral is the same as (12.3) and, inserting the limits, we find

$$r_E = \frac{c}{H_0(\Omega_0 - 1)^{1/2}} \left\{ 2\pi - \cos^{-1} \left[1 - \frac{2(\Omega_0 - 1)}{\Omega_0} a(t_1) \right] \right\}. \quad (12.14)$$

As Weinberg pointed out, if $\Omega_0 = 2$, the most distant object we would ever be able to observe before the Big Crunch occurred has comoving radial distance coordinate $14,000 h^{-1} \approx 20,000$ Mpc at the present epoch (Weinberg, 1972).

In the case of models with finite values of Ω_A , which eventually expand to infinity, the integral (12.13) converges to a finite value because of the ultimate exponential growth of $a(t)$. We will encounter examples of this behaviour in the next section.

12.2 Pedagogical Interlude – Space–Time Diagrams for the Standard World Models

It is helpful to represent the various scales which we have introduced on space–time diagrams for the standard world models and to discuss some of their somewhat surprising features. This section has been inspired by the illuminating papers by Davis and Lineweaver (Davis and Lineweaver, 2004; Lineweaver, 2005).

12.2.1 Distance and Times

First, let us summarise the various times and distances introduced so far.

Comoving radial distance coordinate. The discussion of Sect. 5.4 indicated how careful one has to be about the definition of distances in the standard world models. We recall that to define a self-consistent distance at a specific epoch t , we projected the proper distances along our past light cone to that reference epoch which we took to be the present epoch t_0 . In terms of cosmic time and scale factor, the comoving radial distance coordinate r is defined to be

$$r = \int_t^{t_0} \frac{c dt}{a} = \int_a^1 \frac{c da}{a \dot{a}} . \quad (12.15)$$

Proper radial distance coordinate. We run up against the same problems we encountered in defining the comoving radial distance coordinate, in that it only makes sense to define distances at a particular cosmic epoch t . Therefore, we *define* the proper radial distance r_{prop} to be the comoving radial distance coordinate projected back to the epoch t . From (12.15) we find

$$r_{\text{prop}} = a \int_t^{t_0} \frac{c dt}{a} = a \int_a^1 \frac{c da}{a \dot{a}} . \quad (12.16)$$

Particle horizon. From the discussion of Sect. 12.1, we note the definition (12.2) of the particle horizon r_H as the maximum proper distance over which there can be causal communication at the epoch t

$$r_H = a \int_0^t \frac{c dt}{a} = a \int_0^a \frac{c da}{a \dot{a}} . \quad (12.17)$$

Event horizon. From the discussion of Sect. 12.1, we note the definition (12.13) of the event horizon r_E as the greatest proper radial distance an object can have if it is ever to be observable by an observer who observes the Universe at cosmic time t_1 .

$$r_E = a \int_{t_1}^{t_{\max}} \frac{c dt}{a(t)} = a \int_{a_1}^{a_{\max}} \frac{c da}{a \dot{a}} . \quad (12.18)$$

Cosmic time. Cosmic time t is defined as time measured by a fundamental observer who reads time on a standard clock.

$$t = \int_0^t dt = \int_0^a \frac{da}{\dot{a}} . \quad (12.19)$$

Conformal time. We have delayed introducing *conformal time* τ until now. There are similarities to the definition of comoving radial distance coordinate in that time intervals are projected forward to the present reference epoch using the definition

$$dt_{\text{conf}} = d\tau = \frac{dt}{a} . \quad (12.20)$$

Notice that, according to the cosmological time dilation formula (5.43), the interval of conformal time is what would be measured by a fundamental observer at the present epoch t_0 . Then, the Robertson–Walker metric (5.33) can be written in a form which makes both the space and time components of the metric change in the same way with cosmic epoch

$$ds^2 = a^2(t) \left\{ d\tau^2 - \frac{1}{c^2} [dr^2 + \mathfrak{R}^2 \sin^2(r/\mathfrak{R})(d\theta^2 + \sin^2 \theta d\phi^2)] \right\} . \quad (12.21)$$

At any epoch, the conformal time has value

$$\tau = \int_0^t \frac{dt}{a} = \int_0^a \frac{da}{a\dot{a}} . \quad (12.22)$$

It immediately follows from (12.17) and (12.22) that, in a space–time diagram in which the comoving radial distance coordinate is plotted against conformal time, the particle horizon is a straight line with slope equal to the speed of light.

Another attractive feature of using conformal time is that the growth of perturbations in the radiation- and matter-dominated eras have the same dependence upon τ .

$$\text{Radiation era: } \frac{\delta\varrho}{\varrho} \propto t ; \quad a \propto t^{1/2} ; \quad \tau \propto t^{1/2} ; \quad \frac{\delta\varrho}{\varrho} \propto \tau^2 , \quad (12.23)$$

$$\text{Matter era: } \frac{\delta\varrho}{\varrho} \propto t^{2/3} ; \quad a \propto t^{2/3} ; \quad \tau \propto t^{1/3} ; \quad \frac{\delta\varrho}{\varrho} \propto \tau^2 . \quad (12.24)$$

12.2.2 The Past Light Cone

This topic requires a little care because of the way in which the standard models are set up in order to satisfy the requirements of isotropy and homogeneity. As we showed in Sect. 5.4, these requirements result in the Robertson–Walker metric, even if we do not understand what determines the kinematics of the models, which are all subsumed into the variation of the scale factor $a(t)$ with the cosmic epoch.

Let us first demonstrate that, because of the assumptions of isotropy and homogeneity, Hubble’s linear relation $v = H_0 r$ applies at the present epoch *to recession speeds which exceed the speed of light*. Notice that r is the comoving radial distance coordinate. The reasoning of Sect. 5.4 shows that we can imagine measuring this distance by lining up a very large number of fundamental observers who measure increments of distance Δr at the present epoch t_0 and who are expanding apart at speed $H_0 \Delta r$. Thus, if we consider fundamental observers who are far enough apart,

this speed can exceed the speed of light. There is nothing in this argument which contradicts the special theory of relativity – it is simply a geometric result because of the requirements of isotropy and homogeneity.

To emphasise this important point, consider the familiar analogue for the expanding Universe of the surface of an expanding spherical balloon. As the balloon inflates, a linear velocity-distance relation is found on the surface of the sphere, not only about any point on the sphere, but also at arbitrarily large distances on its surface. Hence at very large distances, the speed of separation can be greater than the speed of light, but there is no causal connection between these points – they are simply partaking in the uniform expansion of what Bondi calls the substratum, the underlying space–time geometry of the Universe. This feature of the models is built into the Robertson–Walker metric.

Consider the proper distance between two fundamental observers at some epoch t

$$r_{\text{prop}} = a(t)r , \quad (12.25)$$

where r is the comoving radial distance. Differentiating with respect to cosmic time,

$$\frac{dr_{\text{prop}}}{dt} = \dot{a}r + a\frac{dr}{dt} . \quad (12.26)$$

The first term on the right-hand side represents the motion of the substratum and, at the present epoch, becomes $H_0 r$. Consider, for example, the case of a very distant object in the critical world model, $\Omega_0 = 1$, $\Omega_A = 0$. As a tends to zero, (7.75) and Fig. 7.6a show that the comoving radial distance coordinates tend to $r = 2c/H_0$. Therefore, the local rest frame of objects at these large distances moves at twice the speed of light relative to our local frame of reference *at the present epoch*. At the epoch at which the light signal was emitted along our past light cone, the recessional velocity of the local rest frame $v_{\text{rec}} = \dot{a}r$ was greater than this value, because $\dot{a} \propto a^{-1/2}$.

The second term on the right-hand side of (12.26) corresponds to the velocity of peculiar motions in the local rest frame at r , since it corresponds to changes of the comoving radial distance coordinate. The element of proper radial distance is $a dr$, and so if we consider a light wave travelling along our past light cone towards the observer at the origin, we find

$$v_{\text{tot}} = \dot{a}r - c . \quad (12.27)$$

This is the key result which defines the propagation of light from the source to the observer in space–time diagrams for the expanding Universe.

We can now plot the trajectories of light rays from their source to the observer at t_0 . The proper distance from the observer at $r = 0$ to the past light cone r_{PLC} is

$$r_{\text{PLC}} = \int_0^t v_{\text{tot}} dt = \int_0^a \frac{v_{\text{tot}} da}{\dot{a}} . \quad (12.28)$$

Notice that initially the light rays from distant objects are propagating away from the observer; this is because the local isotropic cosmological rest frame is moving away

from the observer at $r = 0$ at a speed greater than that of light. The light waves are propagated to the observer at the present epoch through local inertial frames which expand with progressively smaller velocities until they cross the *Hubble sphere* at which the recession velocity of the local frame of reference is the speed of light. The definition of the radius of the Hubble sphere r_{HS} at epoch t is thus given by

$$c = H(t) r_{\text{HS}} = \frac{\dot{a}}{a} r_{\text{HS}} \quad \text{or} \quad r_{\text{HS}} = \frac{ac}{\dot{a}}. \quad (12.29)$$

Note that r_{HS} is a proper radial distance. From this epoch onwards, propagation is towards the observer until, as $t \rightarrow t_0$, the speed of propagation towards the observer is the speed of light.

It is simplest to illustrate how the various scales change with time in specific examples of standard cosmological models. We consider first the critical world model and then our reference Λ model.

12.2.3 The Critical World Model $\Omega_0 = 1, \Omega_\Lambda = 0$

It is convenient to present the space–time diagrams with time measured in units of H_0^{-1} and distance in units of c/H_0 . The diagrams shown in Figs. 12.1 and 12.2 follow the attractive presentation by Davis and Lineweaver, but I have truncated the time axis at the present cosmological epoch (Davis and Lineweaver, 2004). The advantage of studying this simple case first is that there are simple analytic relations for all the distances which appear in Fig. 12.1. These are listed in Table 12.1.

Different versions of the space–time diagram for the critical world model are shown in Fig. 12.1a–c. In all three presentations, the world lines of galaxies having redshifts 0.5, 1, 2 and 3 are shown. When plotted against comoving radial distance coordinates in Figs. 12.1b and c, these are vertical lines. The Hubble sphere and particle horizon, as well as the past light cone, are shown in all three diagrams. There is no event horizon in this model.

Table 12.1. Dependence of various times and distances upon scale factor a and cosmic time t for the critical world model $\Omega_0 = 1, \Omega_\Lambda = 0$. The times and distances are measured in units of H_0^{-1} and c/H_0 respectively

Age of Universe at present epoch	$t_0 = 2/3$
Conformal time	$\tau = 2(t/t_0)^{1/3}$
Dynamics of world model	$a = (t/t_0)^{2/3}$
World lines of galaxies	$r_{\text{prop}} = r(t/t_0)^{2/3}$
Hubble sphere	$r_{\text{HS}} = (t/t_0)$
Past light cone	$r_{\text{PLC}} = 2(t/t_0)^{2/3} - 2(t/t_0)$
Particle horizon	$r_{\text{H}} = 3t$
Event horizon	There is no event horizon in this model.

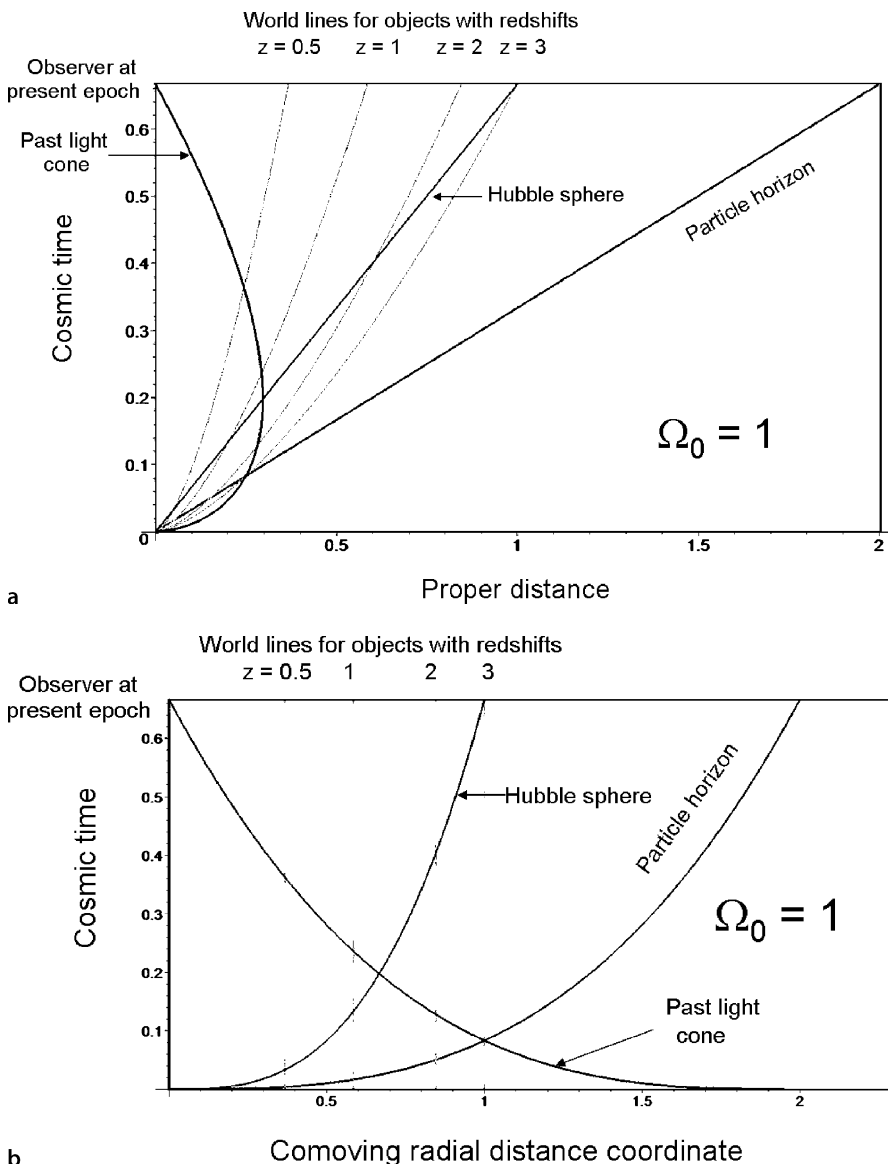


Fig. 12.1a–c. Space–time diagrams for the critical cosmological model, $\Omega_0 = 1$, $\Omega_\Lambda = 0$. The times and distances are measured in units of H_0^{-1} and c/H_0 respectively

These diagrams illustrate a number of interesting features.

- Fig. 12.1a is the most intuitive diagram. It illustrates clearly many of the points discussed above. For example, the Hubble sphere intersects the past light cone at the point where $v_{\text{tot}} = 0$ and the tangent to the past light cone is vertical.

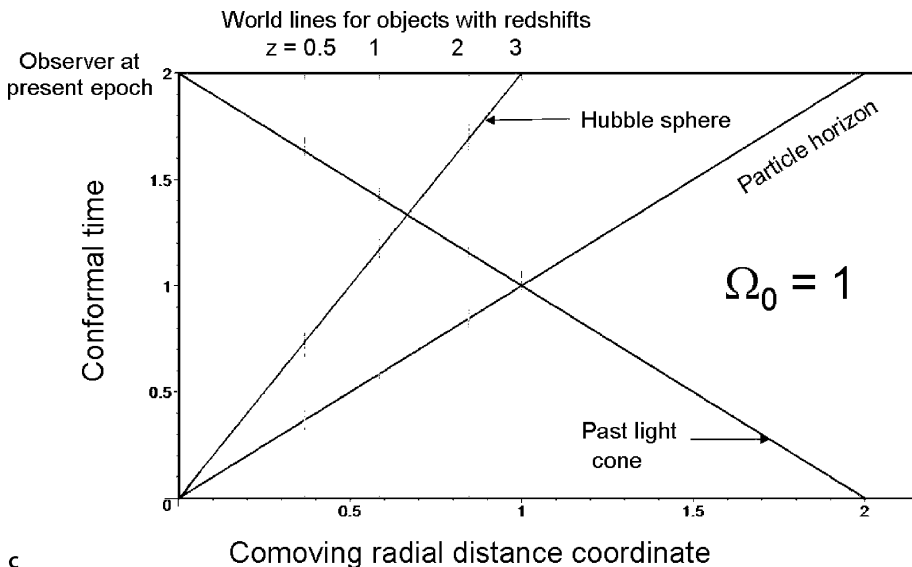


Fig. 12.1. (continued)

- In Fig. 12.1b and c, the initial singularity at $t = 0$ has been stretched out to become a singular line.
- Figure 12.1c is the simplest diagram in which cosmic time has been replaced by conformal time. In the critical model, the relations are particularly simple, the particle horizon, the past light cone and the Hubble sphere being given by

$$\begin{aligned} r_H(\text{comoving}) &= \tau , \\ r_{\text{PLC}}(\text{comoving}) &= 2 - \tau , \\ r_{\text{HS}}(\text{comoving}) &= \tau/2 . \end{aligned}$$

12.2.4 The Reference World Model $\Omega_0 = 0.3$, $\Omega_\Lambda = 0.7$

Having dealt with the simplest case of the critical model, we can appreciate the similarities and differences of the reference model with a finite cosmological constant. Specifically, with $\Omega_0 = 0.3$ and $\Omega_\Lambda = 0.7$, the rate of change of the scale factor with cosmic time in units in which $c = 1$ and $H_0 = 1$ is

$$\dot{a} = \left[\frac{0.3}{a} + 0.7(a^2 - 1) \right]^{1/2} . \quad (12.30)$$

The diagrams shown in Fig. 12.2a–c have many of the same general features as Fig. 12.1a–c, but there are significant differences, the most important of these being associated with the dominance of the dark energy term at late epochs.

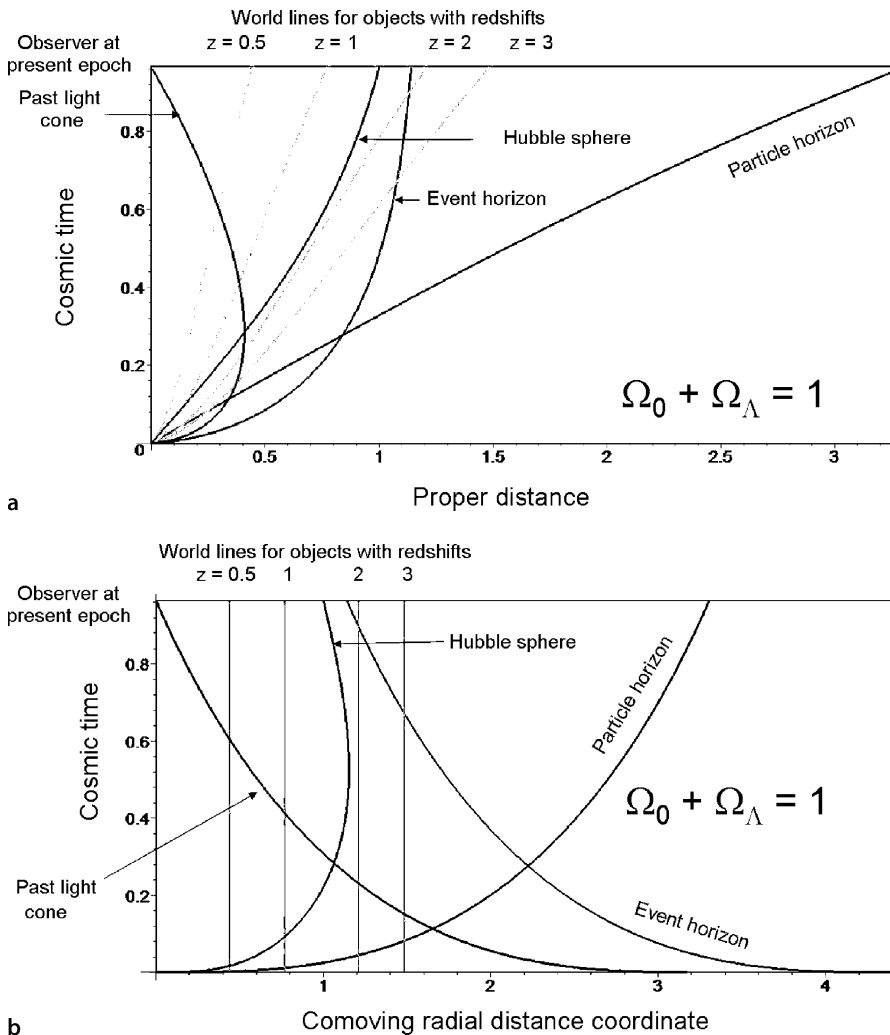


Fig. 12.2a–c. Space–time diagrams for the reference cosmological model, $\Omega_0 = 0.3$, $\Omega_\Lambda = 0.7$. The times and distances are measured in units of H_0^{-1} and c/H_0 respectively (Davis and Lineweaver, 2004)

- First, note that the cosmic timescale is stretched out relative to the critical model.
- The world lines of galaxies begin to diverge at the present epoch as the repulsive effect of the dark energy dominates over the attractive force of gravity.
- The Hubble sphere converges to a proper distance of 1.12 in units of c/H_0 . The reason for this is that the expansion becomes exponential in the future and Hubble’s constant tends to a constant value of $\Omega_\Lambda^{1/2}$.

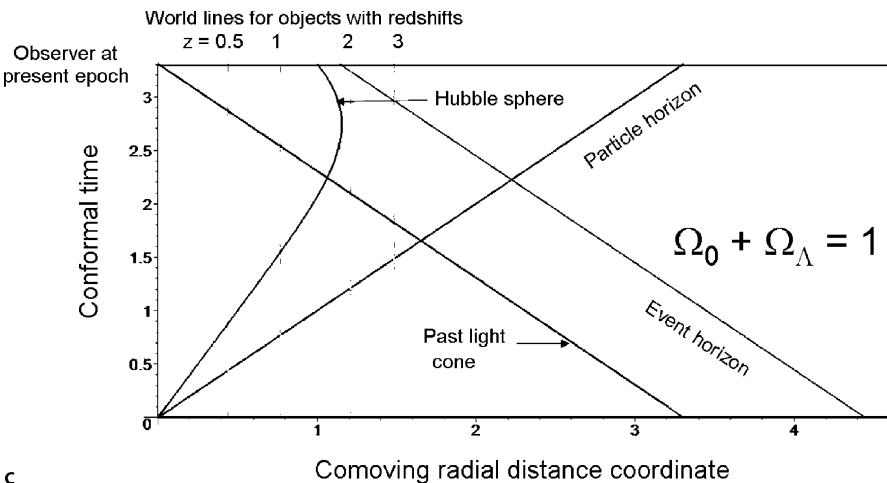


Fig. 12.2. (continued)

- Unlike the critical model, there is an event horizon in the reference model. The reason is that, although the geometry is flat, the exponential expansion drives galaxies beyond distances at which there could be causal communication with an observer at epoch t . It can be seen from Fig 12.2a that the event horizon tends towards the same asymptotic value of 1.12 in proper distance units as the Hubble sphere. To demonstrate this, we need to evaluate the integral

$$r_E = a \int_a^\infty \frac{da}{[0.3a + 0.7(a^4 - a^2)]^{1/2}}. \quad (12.31)$$

For large values of a , terms other than that in a^4 under the square root in the denominator can be neglected and the integral becomes $1/0.7^{1/2} = 1.12$, as found above for the Hubble sphere. In Fig. 12.2b and c, the comoving distance coordinates for the Hubble sphere and the event horizon tend to zero as $t \rightarrow \infty$ because, for example, (12.29) has to be divided by a to convert it to a comoving distance and $a \rightarrow \infty$.

- Just as in the case of the critical model, the simplest diagram is that in which conformal time is plotted against comoving radial distance coordinates. The relations for the particle horizon (12.14), the past light cone (12.26) and the event horizon (12.18) were all given in proper coordinates and so they have to be divided by a to convert to comoving coordinates. Using these definitions, it is a simple exercise to show that the various lines are:

$$\begin{aligned} r_H(\text{comoving}) &= \tau, \\ r_{PLC}(\text{comoving}) &= \tau_0 - \tau, \\ r_E(\text{comoving}) &= r_0 - \tau. \end{aligned} \quad (12.32)$$

where $\tau_0 = 3.305$ and $r_0 = 4.446$ for our reference cosmological model. These forms of the relations in terms of comoving distance coordinate and conformal time are true for all models.

The paper by Davis and Lineweaver repays close study (Davis and Lineweaver, 2004). Their remarkable Appendix B indicates how even some of the most distinguished cosmologists and astrophysicists can lead the newcomer to the subject astray.

12.3 Superhorizon Scales

The major diversion of Sect. 12.2 was partly stimulated by the need to demonstrate one of the key features of the cosmological models. The particle horizon shrinks to vanishingly small values as cosmic, or conformal, time tends to zero. In particular, it is clear from diagrams 12.2b and c, in which the horizon scale is plotted against the comoving radial distance coordinate, that at early enough epochs the horizon becomes smaller than the scales of galaxies, clusters of galaxies and other large-scale structures. This means that we cannot avoid tackling the problem of what happens to perturbations on scales greater than the particle horizon, what are called *superhorizon scales*.

We carried out the small perturbation analysis of Chap. 11 on the basis that the perturbations had a size much smaller than the particle horizon at all relevant epochs and so there was an unperturbed background which acts as a reference frame for the growth of small perturbations. We are also able to synchronise the clocks of all fundamental observers within the particle horizon by exchanging light signals. If, however, the scale of the perturbation exceeds the horizon scale, what do we mean by ‘the unperturbed background’? On superhorizon scales, we can think of each perturbation carrying its own standard clock, and the whole issue of the synchronisation of clocks and the selection of the appropriate reference frame provide real technical challenges.

The Newtonian small perturbation analysis carried out in Chap. 11 is inadequate to deal with these problems, and a full general relativistic treatment needs to be undertaken. Not surprisingly, this is highly non-trivial and raises complex technical issues in general relativity. The nature of the problem is compounded by the issue of choosing the most appropriate gauge within which to carry out the analysis. There is a good analogy with the use of the vector potential in electrodynamics. The vector potential \mathbf{A} only appears in classical electrodynamics as a tool for finding the magnetic flux density \mathbf{B} through the relation $\mathbf{B} = \text{curl } \mathbf{A}$, and so we can add to \mathbf{A} the gradient of any scalar function ϕ since it will disappear when the curl of $\mathbf{A} + \text{grad } \phi$ is taken. This is the procedure which results in, for example, the Coulomb and Lorentz gauges in classical electrodynamics. The different gauges have the same physical content, but some problems are easier to solve in one gauge than in another.

Exactly the same type of problem occurs in dealing with superhorizon scales in general relativity. Again, the same result should be found whichever gauge is

chosen, and some are easier to handle than others. It is best to summarise the results of these somewhat technical issues in the simple terms we have used throughout this book. I have found the books by Peacock, Dodelson and Liddle and Lyth helpful in understanding the issues involved (Peacock, 2000; Dodelson, 2003; Liddle and Lyth, 2000). Bertschinger has provided an accessible account of the issues involved, while Ellis and his colleagues provide insight into the physical meaning of the gauge-invariant variables (Bertschinger, 1996; Bruni et al., 1992).

The first important result is that scalar, vector and tensor perturbations can be separated out and considered independently. We are primarily concerned with the evolution of perturbations in the matter and radiation content of the Universe, and so we need only consider scalar perturbations for the moment. The vector perturbations correspond to vortex motions and the tensor perturbations to gravitational waves.

A second helpful result comes from writing down the most general form of the perturbed metric which can encompass the different ways in which the gauge can be selected. Following Peacock's presentation (Peacock, 2000), the metric can be written in the general form

$$ds^2 = a^2(\tau) \left\{ (1 + 2\phi) d\tau^2 + 2w_i d\tau dx^i - [(1 - 2\psi)\gamma_{ij} + 2h_{ij}] dx^i dx^j \right\}, \quad (12.33)$$

where γ_{ij} is the comoving spatial part of the Robertson–Walker metric. w_i is associated with the vector modes and h_{ij} with the tensor perturbations. τ is conformal time.

The gauge which bears the closest relation to the calculations in Chap. 11 is the *conformal Newtonian gauge* or *longitudinal gauge*. The vector and tensor components are set equal to zero, and so

$$ds^2 = a^2(\tau) [(1 + 2\phi)d\tau^2 - (1 - 2\psi)(dx^2 + dy^2 + dz^2)], \quad (12.34)$$

where it has been assumed that the geometry is flat; this will always be a good approximation in the early Universe. If this metric is inserted into the Einstein field equations and the energy-momentum tensor has no off-diagonal terms, meaning, for example, that we are dealing with a perfect fluid, then $\phi = \psi$ and the perturbations are described by the single scalar function ϕ , which is just the Newtonian gravitational potential. The metric then has the familiar form

$$ds^2 = a^2(\tau) [(1 + 2\phi)d\tau^2 - (1 - 2\phi)(dx^2 + dy^2 + dz^2)]. \quad (12.35)$$

The importance of this argument is that it demonstrates that the Newtonian gravitational potential provides an accurate description of cosmological perturbations on scales greater than the particle horizon.

There is considerable freedom in the choice of gauge. In an important paper, Bardeen demonstrated how it is possible to derive a set of gauge-invariant quantities for dealing with arbitrary perturbations on superhorizon scales, as well as the relations needed to transform from one gauge to another (Bardeen, 1980). An alternative gauge, which was used in many of the pioneering analyses before Bardeen's

paper, is the *synchronous gauge* in which the term $(1 + 2\phi)$ multiplying $d\tau^2$ is not present, with consequent changes of the other components of the metric. Following the presentation of Liddle and Lyth, the metric in the synchronous gauge can be written

$$ds^2 = a^2(\tau) \{d\tau^2 - [(1 + 2D)\delta_{ij} + 2E_{ij}] dx^i dx^j\}. \quad (12.36)$$

This different slicing through space–time illustrates the point that the appearance of the metric depends upon the choice of gauge, although all the metrics contain the same physics in the end. Which choice is used for calculations is largely a matter of convenience. For example, for computational purposes, it turns out to be easier to use the synchronous gauge rather than the conformal Newtonian gauge. Thus, although the metric may look very different in different gauges, for any well-defined physical model of the very early Universe and the origin of perturbations, they must all give the same physical results.

These issues are set out clearly by Ma and Bertschinger in an important paper in which they worked out in parallel the development of perturbations in both the conformal Newtonian gauge and the synchronous gauge (Ma and Bertschinger, 1995). An example of the difference the choice of gauge makes can be seen in Fig. 12.3 which shows the development of the same set of perturbations in the conformal Newtonian and synchronous gauges. These diagrams reinforce the point that the development of density perturbations can appear very different in the two gauges on superhorizon scales, because of the different slicings through space–time. It can be seen from these diagrams that, once the perturbations come through their particle horizons, the same evolution is found for all five components.

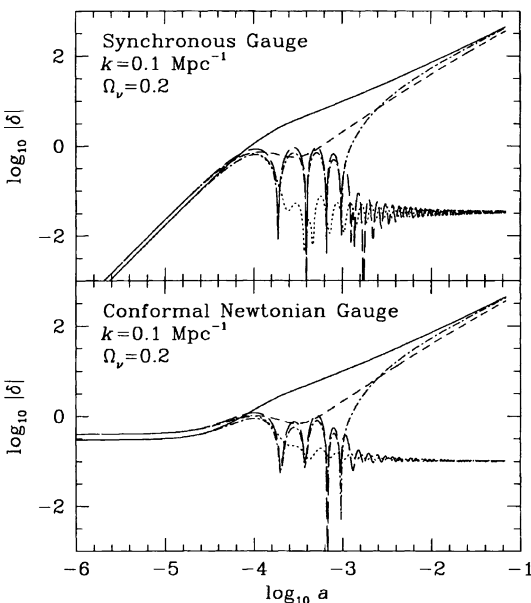


Fig. 12.3. Evolution of perturbations in conformal Newtonian and synchronous gauges (Ma and Bertschinger, 1995). These are mixed hot and cold dark matter models with $\Omega_v = 0.2$ and flat geometry. The different lines show the development of perturbations for cold dark matter (solid line), baryons (dot-dashed line), photons (long dashed line), massless neutrinos (dotted line) and massive neutrinos (short dashed lines). For $k = 0.1 \text{ Mpc}^{-1}$, the perturbations come through the horizon before the epoch of equality

Returning to the conformal Newtonian gauge (12.34), we can crudely estimate the form of the Newtonian gravitational potential which can be used on superhorizon scales in both the radiation and matter-dominated eras. According to (11.16) and (11.75), the perturbed part of the gravitational potential $\delta\phi$, which is the same as the ϕ which appears in (12.35), is

$$\text{Matter-dominated era: } \nabla^2 \delta\phi = 4\pi G \delta\varrho , \quad (12.37)$$

$$\text{Radiation-dominated era: } \nabla^2 \delta\phi = 8\pi G \delta\varrho . \quad (12.38)$$

These can be written in the approximate forms

$$\text{Matter era } \frac{\delta\phi}{L^2} = 4\pi G \varrho \Delta , \quad \text{Radiation era } \frac{\delta\phi}{L^2} = 8\pi G \varrho \Delta , \quad (12.39)$$

where $\Delta = \delta\varrho/\varrho$ and L is the scale of the perturbation. In the radiation-dominated era, $\Delta = \Delta_0 a^2$ and $\varrho = \varrho_0 a^{-4}$, while in the matter-dominated era, $\Delta = \Delta_0 a$ and $\varrho = \varrho_0 a^{-3}$. Referring the scale L to the comoving scale at the present epoch through the relation $L = aL_0$, we see that in the two cases

$$\delta\phi = 4\pi G \varrho_0 \Delta_0 L_0^2 \quad \text{and} \quad \delta\phi = 8\pi G \varrho_0 \Delta_0 L_0^2 , \quad (12.40)$$

for the radiation- and matter-dominated eras respectively. These are the key results we have been seeking. The perturbations in the gravitational potential are *independent of scale factor* in *both* the radiation- and matter-dominated eras. These are the potentials we need to insert into the metric (12.34) and they are ‘frozen in’ on superhorizon scales. This makes a lot of sense since there cannot be causal connection on the superhorizon scale L . Thus, from the point of view of understanding how the density contrasts Δ , rather than the gravitational potentials $\delta\phi$, evolves with cosmic epoch, we can use the results we have already derived for the development of the perturbations on superhorizon scales.

Notice that we have made no attempt to join together the radiation- and matter-dominated solutions. Dodelson provides a detailed analysis of how the potential $\delta\phi$ changes between the radiation- and matter-dominated eras for perturbations on superhorizon scales and finds that the magnitude of the potential, which he denotes Φ_0 , decreases by only about 10% as the perturbation evolves through the epoch of equality of matter and radiation energy densities (Dodelson, 2003).

12.4 The Adiabatic Baryonic Fluctuations in the Standard Big Bang

In the spirit of building up the tools we need to tackle the current favoured Λ CDM model of structure formation, let us first treat the case of baryonic models. These provided the most natural starting point for the pioneering studies of the 1960s and 1970s. During these years, the dark matter problem was well-established and it could not be excluded that the dark matter could have been in some baryonic form with

density parameter $\Omega_B \sim 0.1$ or greater. Many of the physical processes involved in the baryonic models reappear in the Λ CDM models in slightly different guises and so this analysis is far from wasted effort. It will also become apparent why the baryonic model, which might be thought of as the most natural model, fails – this failure in itself provides evidence that additional non-baryonic ingredients are needed to account for the observed large scale structure of our Universe.

The model is based upon the following results which we have already established.

- From (11.28) and (11.77) the *Jeans length* is the maximum scale on which density perturbations can be stabilised by their internal pressure gradients at any epoch,

$$\lambda_J = \frac{2\pi}{k_J} = c_s \left(\frac{\pi}{G\varrho} \right)^{1/2} \quad \text{or} \quad \lambda_J = c_s \left(\frac{3\pi}{8G\varrho} \right)^{1/2}, \quad (12.41)$$

in the non-relativistic and relativistic regimes respectively.

- For wavelengths smaller than the Jeans length, the perturbations are sound waves which evolve according to the solutions of (11.24) and (11.76) for propagating waves of the form $\Delta = \Delta_0 \exp i(\mathbf{k} \cdot \mathbf{r} - \omega t)$.
- For wavelengths greater than the Jeans wavelength, the perturbations are unstable and, for wavelengths $\lambda \gg \lambda_J$, the *growth rates* of the unstable modes are algebraic with epoch. In the matter-dominated phase, the perturbation grows as

$$\Delta = \frac{\delta\varrho}{\varrho} \propto a = (1+z)^{-1}, \quad (12.42)$$

so long as $\Omega_0 z \gg 1$ for models with $\Omega_A = 0$ and $(1+z) \geq \Omega_0^{-1/3}$ for flat models with finite Ω_A (see Sect. 11.4.4). The growth is much slower at smaller redshifts and becomes zero in the limit $\Omega_0 = 0$. In the radiation-dominated phases of the standard model, when all the inertial mass and pressure are associated with relativistic matter or radiation, the growth rate is algebraic with $\Delta \propto a^2 = (1+z)^{-2}$.

- The *horizon scale* is the maximum distance over which information can be communicated at cosmic epoch t and, as shown in Sect. 12.1, is $r_H(t) = 3ct$ in the matter-dominated era and $r_H(t) = 2ct$ in the radiation-dominated era.

Let us use these rules to study the evolution of perturbations of different masses in the standard baryonic model. We need to relate the wavelength of the perturbation λ_J to the mass of the baryonic object M_J which ultimately forms from it. The expectation is that this will comprise all the mass within a sphere of radius λ_J and so, for illustrative purposes, we adopt the definition of the *Jeans mass* as the mass contained within a region of diameter λ_J ,

$$M_J = (\pi\lambda_J^3/6)\varrho_B, \quad (12.43)$$

recalling that, in the present chapter, all the mass in the Universe is in baryonic form.

12.4.1 The Radiation-Dominated Era

Let us consider first the radiation-dominated phases, when the inertial mass density in the radiation and neutrinos was much greater than that in the baryons, $\varepsilon_{\text{rad}} \gg \varepsilon_B$. According to (9.34), the speed of sound to be included in the expression for the Jeans length is the ultrarelativistic sound speed $c/\sqrt{3}$. The Jeans length in the radiation-dominated phase is therefore

$$\lambda_J = \frac{c}{\sqrt{3}} \left(\frac{3\pi}{8G\varrho} \right)^{1/2}, \quad (12.44)$$

where ϱ is the total mass density including both photons and neutrinos, that is $\varrho = 4.7 \times 10^{-31} \chi (1+z)^4 \text{ kg m}^{-3}$, recalling that $\chi = 1.7$ when the neutrinos are taken into account.

During this era, essentially all the inertial mass of the perturbations was in the radiation, but the plasma was strongly coupled to it by Compton scattering, as discussed in Sect. 9.4. Although the Jeans length was determined by the energy density of radiation, we are interested in the mass of baryons within this scale, since this is the mass which eventually forms bound objects in the matter-dominated era. The mass density in baryons varied with redshift as $\varrho_B = 1.88 \times 10^{-26} \Omega_B h^2 a^{-3} \text{ kg m}^{-3}$, where Ω_B is the density parameter in baryons at the present epoch. Therefore, the mass within the Jeans length in baryons in the early stages of the radiation-dominated phase, $z \gg 2.4 \times 10^4 \Omega_0 h^2$, was

$$M_J = 8.5 \times 10^{28} a^3 \Omega_B h^2 M_\odot. \quad (12.45)$$

Several important conclusions can be drawn from this result. The first is that the baryonic mass within λ_J grew as $M_B \propto a^3$ during the radiation-dominated phases. Thus, for plausible values of Ω_B and h , M_B was one solar mass at a redshift $z \sim 3 \times 10^9$ and increased to the mass of a large galaxy $M = 10^{11} M_\odot$ at redshift $z \sim 10^6$. The second conclusion follows from a comparison of the Jeans length with the horizon scale $r_H = 2ct$. Using (9.7), the horizon scale can be written

$$r_H = 2ct = c \left(\frac{3}{8\pi G\varrho} \right)^{1/2} \quad \text{compared with} \quad \lambda_J = c \left(\frac{3\pi}{24G\varrho} \right)^{1/2}. \quad (12.46)$$

It is apparent that, during the radiation-dominated phases, the Jeans length was of the same order of magnitude as the horizon scale. This is a key result. Consider a perturbation containing a galactic mass of baryons, say $M = 10^{11} M_\odot$. In the very early stages of the radiation-dominated phases, its scale far exceeded the horizon scale and so the amplitudes of the perturbations grew as $\Delta \propto (1+z)^{-2}$. At a redshift $z \sim 10^6$, the perturbation entered the horizon and, at more or less the same time, the Jeans length became greater than the scale of the perturbation. The perturbations were therefore stabilised against gravitational collapse at later times and became sound waves. The variations with redshift of the Jeans mass and the baryonic mass within the horizon are shown schematically in Fig. 12.4.

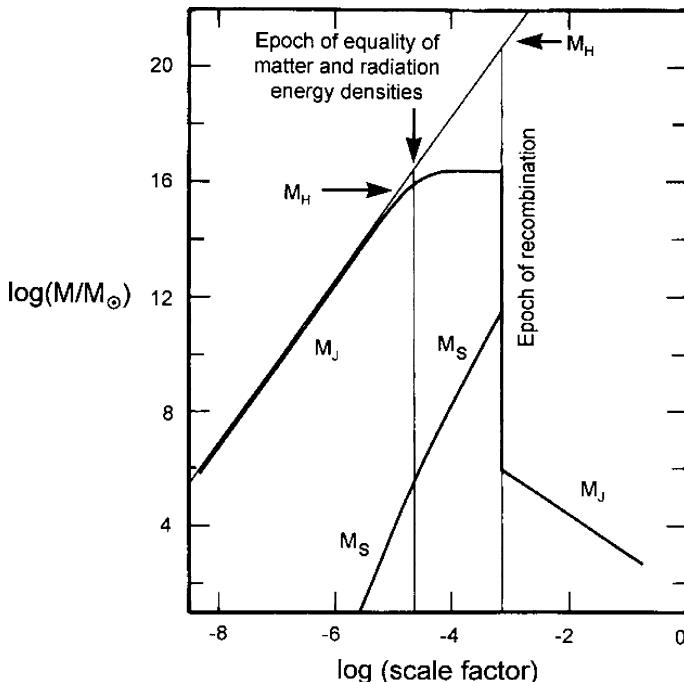


Fig. 12.4. Evolution of the baryonic Jeans mass M_J and baryonic mass within particle horizon M_H with scale factor. Also shown is the evolution of the Silk mass M_S , which was damped by photon diffusion, or Silk damping

12.4.2 The Matter-Dominated Era

After the epoch of equality of matter and radiation, that is at redshifts $z \ll 2.4 \times 10^4 \Omega_0 h^2$, the dynamics of the expansion were matter-dominated, but the matter and the radiation remained strongly thermally coupled so long as the diffuse cosmic plasma remained ionised. As discussed in Sects. 9.3 and 9.4, at a redshift $z \approx 1500$, the plasma was roughly 50% ionized, and at a redshift $z \approx 550 h^{2/5} \Omega_0^{1/5}$, the thermal coupling between matter and radiation ceased. These changes profoundly altered the variation of the Jeans mass with cosmic epoch.

Let us first work out the variation of the baryonic mass within the particle horizon as a function of scale factor during the matter-dominated era. Using (12.7) for the variation of the particle horizon with scale factor, the baryonic mass within the horizon was

$$M_B = \left(\frac{\pi r_H^3}{6} \right) \rho_B = \frac{3.0 \times 10^{22}}{(\Omega_0 h^2)^{1/2}} a^{3/2} M_\odot , \quad (12.47)$$

that is $M_B \propto a^{3/2} \propto t$. This relation is shown in Fig. 12.4.

To determine the Jeans length, we need to know the variation of the speed of sound with redshift. As the epoch of equality of the rest mass energies in matter and

radiation was approached, the sound speed became less than the relativistic sound speed $c/\sqrt{3}$ and is given by (9.32):

$$c_s^2 = \frac{c^2}{3} \frac{4\varrho_{\text{rad}}}{4\varrho_{\text{rad}} + 3\varrho_{\text{m}}} . \quad (12.48)$$

During this phase, the pressure within the perturbations was provided by the radiation but the inertial mass by the matter, and so the appropriate sound speed was

$$c_s = c \left(\frac{4\varrho_{\text{rad}}}{9\varrho_B} \right)^{1/2} = \frac{10^6(1+z)^{1/2}}{(\varOmega_B h^2)^{1/2}} \text{ m s}^{-1} . \quad (12.49)$$

Inserting this result into the expression for the Jeans mass, we find

$$M_J = \frac{3.75 \times 10^{15}}{(\varOmega_B h^2)^2} M_\odot , \quad (12.50)$$

that is, the Jeans mass was independent of scale factor during this era. Notice the important result that adiabatic perturbations with masses greater than the mass given by (12.50) grew according to the standard result for the matter-dominated era $\Delta \propto a$ from the time they came through the horizon. Since $\varOmega_0 h^2 \ll 1$, it follows that structures on scales much greater than those of a cluster of galaxies continued to grow in amplitude as $\Delta \propto a$ from the epoch when they came through their particle horizons.

Next, we need to study the development of the amplitudes of the oscillating perturbations on scales less than the Jeans mass. We recall that the expression for the development of the density contrast Δ is

$$\frac{d^2\Delta}{dt^2} + 2 \left(\frac{\dot{a}}{a} \right) \frac{d\Delta}{dt} = \Delta (4\pi G \varrho_0 - k^2 c_s^2) . \quad (12.51)$$

We need to solve this equation for oscillating solutions when the pressure, represented by the term $k^2 c_s^2$, provides the restoring force for the oscillations. The second term on the left-hand side of (12.51) is associated with the expansion of the substratum and has the form of a damping term which results in the adiabatic damping of the sound waves. These calculations have been carried out by Padmanabhan and by Coles and Lucchin (Padmanabhan, 1993; Coles and Lucchin, 1995), who established the following results:

- If the perturbations crossed the particle horizon during the radiation-dominated era, the sound speed is $c/\sqrt{3}$ and the sound waves in the relativistic gas propagated with constant amplitude, $\Delta = \text{constant}$, during that era.
- If the perturbations crossed the particle horizon during the matter-dominated era, or when subhorizon perturbations entered the matter-dominated era, the sound speed was given by (9.33) and the amplitudes of the oscillating perturbations decreased as $\Delta = \delta\varrho/\varrho \propto t^{-1/6}$. These authors show that this result can be interpreted as the adiabatic energy loss of the acoustic waves as the Universe expands.

The next crucial epoch was the epoch of recombination when the primordial plasma began to recombine and soon after the matter and radiation became decoupled thermally. The pressure within the perturbation was no longer provided by the radiation but by the thermal pressure of the baryonic matter. Because of the close coupling between the matter and radiation, the matter and radiation temperatures were more or less the same until a redshift $z = 550h^{2/5}\Omega_0^{1/5}$. Therefore, the appropriate sound speed to be included in the expression for the Jeans mass is the adiabatic sound speed for a gas at temperature 3000 K at a redshift of 1000. The sound speed is $c_s = (5kT/3m_H)^{1/2}$, and so the Jeans mass at the epoch of recombination was

$$M_J = \left(\frac{\pi\lambda_J^3}{6} \right) \rho_B = 1.6 \times 10^5 (\Omega_0 h^2)^{-1/2} M_\odot. \quad (12.52)$$

Thus, the Jeans mass decreased abruptly to masses much less than typical galactic masses. The consequence is that all perturbations with masses greater than about $10^5 M_\odot$ began to collapse and grew according to the standard growth rate $\Delta \propto a$. It is intriguing that the Jeans mass immediately following recombination corresponded roughly to the masses of globular clusters, the oldest stellar systems in our Galaxy.

The evolution of the Jeans mass following recombination depends upon the subsequent thermal history of the gas. If the gas continued to cool adiabatically as the Universe expanded, $T \propto a^{-2}$, $c_s \propto a^{-1}$, $\lambda_J \propto a^{-1/2}$, and so the Jeans mass would decrease as $M_J \propto a^{-3/2}$. This cannot, however, be the whole story. As we will discuss in Chap. 18, the intergalactic gas must have been very highly ionised at epochs corresponding to $z \leq 6$ because of the absence of Lyman- α absorption troughs in the spectra of distant quasars and so the gas must have been reheated and ionised at redshifts $z > 6$. The evolution of the various baryonic masses with scale factor is shown schematically in Fig. 12.4.

12.5 Dissipation Processes in the Pre-Recombination Era

To complete our discussion of the physics of adiabatic baryonic perturbations, we need to consider dissipative processes during the pre-recombination era. Although matter and radiation were closely coupled throughout this era, the coupling was not perfect and photons could diffuse out of the density perturbations. This was particularly important for perturbations with wavelengths less than the horizon scale since they were adiabatic sound waves. Radiation pressure provided the restoring force which maintained these oscillations, and so if the photons diffused out of the perturbations, the waves would have been damped out. This process was first described by Silk in 1968 and is often referred to as *Silk damping* (Silk, 1968).

Just as in the case of sound waves in an imperfect gas, the damping of the perturbations is associated with the finite viscosity and thermal conductivity of the medium through which the waves are propagated. In the present instance, energy and momentum are transported by the photons. Appropriate expressions for the coefficients of thermal conduction and shear viscosity are given by Weinberg, whose analysis can

be strongly recommended (Weinberg, 1972). We can obtain the essential results by somewhat cruder means by realising that the process which impedes the escape of radiation from the perturbations is Thomson scattering by free electrons in the plasma. An order-of-magnitude diffusion calculation illustrates the essence of the physics.

At any epoch, the mean free path for scattering of photons by electrons is $\lambda = (N_e \sigma_T)^{-1}$, where $\sigma_T = 6.665 \times 10^{-29} \text{ m}^2$ is the Thomson cross-section. As was shown in Sect. 9.4, the photons and electrons were in close thermal contact throughout the pre-recombination era. In addition, in a fully ionised plasma, the protons and electrons are closely coupled electrostatically and so the photons are closely coupled to the protons as well. To determine how far the photons can diffuse in time t , it is simplest to work out the diffusion coefficient D for photons which, according to kinetic theory, is related to their mean free path λ by $D = \frac{1}{3}\lambda c$, where c is the speed of light. Therefore, the radial distance over which the photons can diffuse is

$$r_S \approx (Dt)^{1/2} = \left(\frac{1}{3}\lambda ct\right)^{1/2}, \quad (12.53)$$

where t is cosmic time. The baryonic mass within this radius, $M_S = (4\pi/3)r_S^3 \Omega_B$, can therefore be evaluated during the pre-recombination era.

In the early pre-recombination phase, $z > 2.4 \times 10^4 \Omega_0 h^2$, the Universe was radiation-dominated and, from (9.7), the cosmic-time redshift relation was

$$t = \left(\frac{3c^2}{32\pi G \varepsilon}\right)^{1/2} = \left(\frac{3c^2}{32\pi G \chi a T_0^4}\right)^{1/2} \frac{1}{(1+z)^2} = \frac{2.4 \times 10^{19}}{(1+z)^2} \text{ s}, \quad (12.54)$$

where we have adopted $\chi = 1.68$ and taken the present temperature of the cosmic microwave background radiation to be $T_0 = 2.725 \text{ K}$. The number density of electrons varied as

$$N_e = \frac{\Omega_B \rho_c (1+z)^3}{m_p} = 11 \Omega_B h^2 (1+z)^3 \text{ m}^{-3}, \quad (12.55)$$

where m_p is the mass of the proton. Thus, the damping mass, sometimes referred to as the *Silk mass*, is

$$M_S = \frac{4\pi}{3} r_S^3 \rho_B = 2.4 \times 10^{26} (\Omega_B h^2)^{-1/2} (1+z)^{-9/2} M_\odot. \quad (12.56)$$

After the epoch of equality of the matter and radiation energy densities, the cosmic time-redshift relation is given by the matter-dominated relation

$$t = \frac{2}{3H_0 \Omega_0^{1/2}} \frac{1}{(1+z)^{3/2}} = \frac{2.06 \times 10^{17}}{(\Omega_0 h^2)^{1/2} (1+z)^{3/2}} \text{ s}. \quad (12.57)$$

In this case, we find

$$M_S = 2.0 \times 10^{23} (\Omega_B h^2)^{-5/4} (1+z)^{-15/4} M_\odot. \quad (12.58)$$

These variations of the damping mass M_S with scale factor are shown in Fig. 12.4. Damping of the perturbations continued until the epoch of recombination, when the electrons and protons began to recombine. By the redshift of the last scattering surface at $z = 1000$, the damping mass had reached the value $M_S = 10^{12} (\Omega_B h^2)^{-5/4} M_\odot$. Much more detailed calculations were carried out by Peebles, who took into account the details of the damping as the primordial plasma recombined and found the damping mass to be $M_S = 1.3 \times 10^{12} (\Omega_0 h^2)^{-3/2} M_\odot$ (Peebles, 1981). By the early 1980s, the value of $\Omega_B h^2$ was known to be significantly less than unity because of the constraints provided by the primordial nucleosynthesis of the light elements. The inference was that all masses less than those of very massive galaxies would have been damped out by the epoch of recombination. Adopting the estimate of the value of $\Omega_B h^2 = 0.022$ found in Sect. 10.4, all masses less than about $4 \times 10^{14} M_\odot$ would have been damped out.

The upshot of these calculations is that perturbations on scales up to those of groups and clusters of galaxies would have been damped out by the epoch of recombination. According to the theory of adiabatic baryonic perturbations, only perturbations on these scales and greater would have survived into the post-recombination era. The perturbations which could have resulted in stars, star clusters and normal galaxies such as our own were damped to exponentially small amplitudes. It therefore had to be assumed that structures on these scales were formed by the process of fragmentation of the large-scale structures which survived into the post-recombination era.

12.6 Isothermal Perturbations

In the above analysis of adiabatic perturbations, it was assumed that the density perturbations were associated with pressure perturbations according to the standard adiabatic relation

$$\frac{\delta p}{p} = \gamma \frac{\delta \varrho}{\varrho}, \quad (12.59)$$

where γ , the ratio of specific heats, is $5/3$ for a monatomic non-relativistic gas and $4/3$ for a relativistic gas. At the other extreme are the *isothermal perturbations*. During the radiation-dominated phase of the Big Bang model, these are fluctuations in the baryon density which take place against the uniform cosmic background radiation. The perturbations are isothermal in the sense that, since the matter is maintained at the same temperature as the radiation by Compton scattering and the radiation is assumed to be uniform, they cause no fluctuations in the background radiation temperature during the radiation-dominated phases. On the other hand, since the baryon density fluctuates from place to place, there are fluctuations in the entropy per baryon. This is in contrast to the case of adiabatic fluctuations, which, by definition, have constant entropy per baryon. In the case of perfect gases, any pressure and density distribution in the radiation-dominated phases can be represented as the superposition of a distribution of adiabatic and isothermal perturbations.

The evolution of the density contrast of the isothermal perturbations before the epoch of equality of mass densities in the matter and radiation is similar to that which will reappear in a different guise later – the density contrast is more or less frozen throughout this era. This problem was originally discussed by Mészáros for the case of perturbations associated with point masses during the radiation-dominated era (Mészáros, 1974).

This evolution of isothermal perturbations is pleasantly treated by Efstathiou and by Coles and Lucchin (Efstathiou, 1990; Coles and Lucchin, 1995). For simplicity, consider a spherical baryonic density perturbation in a smooth expanding background, similar to the little closed Universe discussed in Sect. 11.4.2. If the background were not expanding, the characteristic timescale for collapse would be given by (11.31), $\tau_g \approx (G\varrho_B)^{-1/2}$. This timescale can be compared with the characteristic timescale τ for expansion of the Universe during the radiation-dominated phase, which is readily derived from (9.6):

$$\tau = \frac{a}{da/dt} = \left(\frac{3c^2}{8\pi G \varepsilon_0} a^4 \right)^{1/2} = \left(\frac{3}{8\pi G \varrho_{\text{rad}}} \right)^{1/2} \approx (G\varrho_{\text{rad}})^{-1/2}. \quad (12.60)$$

Since $\varrho_{\text{rad}} \gg \varrho_B$ during the radiation-dominated phases, the expansion timescale is very much shorter than the collapse timescale and so, because the radiation is gravitationally dominant, the perturbation expands with the expanding substratum.

To illustrate this effect more quantitatively, we can adapt (11.24) to study the growth of the perturbation in the matter density, ϱ_B , embedded in a uniform radiation-dominated expanding substratum:

$$\frac{d^2 \Delta_B}{dt^2} + 2 \left(\frac{\dot{a}}{a} \right) \frac{d\Delta_B}{dt} = 4\pi G \varrho_B \Delta_B. \quad (12.61)$$

Notice that the perturbations are only present in the baryonic matter while the dynamical background remains uniform. Following Coles and Lucchin, we introduce the parameter $y = \varrho_B/\varrho_{\text{rad}} = a/a_{\text{eq}}$, where a_{eq} is the scale factor at which the matter and radiation energy densities were equal (Coles and Lucchin, 1995). From (7.2), the dynamics of the world model through the radiation- and matter-dominated eras can be written

$$\dot{a}^2 = \frac{8\pi G \varrho}{3} a^2 - \frac{c^2}{\mathfrak{H}^2} + \frac{1}{3} \Lambda a^2. \quad (12.62)$$

The last two terms of the right-hand side become very small during the early Universe, and so we can write

$$\dot{a}^2 = \frac{8\pi G \varrho}{3} a^2, \quad (12.63)$$

where the density ϱ is the sum of the radiation and matter densities which vary with scale factor as $\varrho_{\text{rad}} = \varrho_{0r} a^{-4}$ and $\varrho_{\text{mat}} = \varrho_{0m} a^{-3}$. Therefore,

$$\dot{a}^2 = \frac{8\pi G}{3} \left(\frac{\varrho_{0r}}{a^2} + \frac{\varrho_{0m}}{a} \right). \quad (12.64)$$

At the present epoch, the Universe is matter-dominated by a factor of over 1000, and so, adopting the critical model for the dynamics of the Universe at the present epoch, $8\pi G\varrho_{0m}/3H_0^2 = 1$. It is then straightforward to show that (12.64) can be written in terms of y as follows:

$$\dot{a} = \frac{H_0}{a_{\text{eq}}^{1/2}} \frac{(1+y)^{1/2}}{y}. \quad (12.65)$$

Changing variables from t to y , (12.61) reduces to

$$\frac{d^2\Delta_B}{dy^2} + \frac{2+3y}{2y(1+y)} \frac{d\Delta_B}{dy} - \frac{3\Delta_B}{2y(1+y)} = 0. \quad (12.66)$$

The growing solution is

$$\Delta_B \propto 1 + \frac{3y}{2}, \quad (12.67)$$

as can be verified by substitution into (12.66). Thus, in the very early Universe, $y \ll 1$, Δ_B was a constant – the perturbations were frozen into the expanding background. This important dynamical result is known as the *Mészáros effect* and will reappear in a different guise later (Mészáros, 1974). Thus, throughout the entire radiation-dominated era from $y = 0$ to $y = 1$, the initial perturbations grew by only a factor of 2.5 in amplitude. After the epoch of equality of the radiation and matter energy densities, $y \gg 1$, (12.67) shows that the density perturbations in the matter-dominated era. This is not the whole story, however, because we have neglected the interaction between the matter of the perturbation in the sea of photons. The above result would be correct if, for example, the matter component consisted of cold dark matter particles which do not interact with the radiation field. As we now show, the fact that the matter is baryonic and fully ionised changes the picture significantly.

We can illustrate the essential physics by the following order of magnitude calculation. The relation between the rate of growth of the perturbation and the velocity field \mathbf{v} induced by gravitational collapse is given by (11.13),

$$\frac{d}{dt} \left(\frac{\delta\varrho}{\varrho} \right) = \frac{d\Delta}{dt} = -\nabla \cdot \mathbf{v}. \quad (12.68)$$

Let us assume that we can ignore the photon field and estimate the velocity of collapse of the perturbation if it were to grow as $\Delta \propto a = (1+z)^{-1}$. Writing $\text{div } \mathbf{v} = v/\lambda$, we find

$$v \sim \frac{\lambda}{t} \left(\frac{\delta\varrho}{\varrho} \right). \quad (12.69)$$

The radiation force acting on an electron of the plasma moving at speed v through the isotropic background radiation is given by the first-order Compton scattering formula

$$f_{\text{rad}} = \frac{4}{3}\sigma_T \varepsilon_{\text{rad}} \frac{v}{c} = \frac{m_e v}{\tau}, \quad (12.70)$$

where τ is given by (9.22). This force is communicated to the protons through the strong electrostatic coupling between electrons and protons. We can compare this force with the typical gravitational force acting on a proton in the perturbation

$$f_g \approx \frac{Gm_p M_B}{\lambda^2} \sim Gm_p \lambda \varrho_B . \quad (12.71)$$

Therefore,

$$\frac{f_{\text{rad}}}{f_g} = \frac{m_e}{m_p} \frac{1}{Gt\tau\varrho_B} \left(\frac{\delta\varrho}{\varrho} \right) \quad (12.72)$$

$$= 3 \times 10^{-5} \left(\frac{\delta\varrho}{\varrho} \right) \frac{(1+z)^{5/2}}{(\Omega_0 h^2)^{1/2}} . \quad (12.73)$$

Because $\Delta = \delta\varrho/\varrho$ can at best grow as $(1+z)^{-1}$, the value of Δ must have been at least 10^{-3} at the last scattering surface at $z = 1000$. Thus, in the baryon-dominated picture of the formation of structure, even at the epoch of recombination, the radiation drag exceeded the gravitational force of attraction. The radiation drag therefore slowed up the collapse of the perturbation drastically and the net result was that the isothermal perturbations scarcely grew at all until after the epoch of recombination. Coles and Lucchin derive a similar result by including the damping force (12.70) in the equation for the evolution of the amplitude of the perturbations (11.61) and show that $\Delta_B \approx \text{constant}$. After the epoch of recombination, the amplitudes of the perturbations grew according to the standard formula $\Delta \propto a = (1+z)^{-1}$.

Thus, by the epoch of recombination, the spectrum of isothermal density perturbations on large mass scales ended up being not so different from that of adiabatic perturbations, but there are major differences for small masses. Since the background radiation is uniform, no Silk damping of the isothermal perturbations took place and so all mass scales survived to the epoch of recombination. As a result, after the isothermal perturbations evolved through the epoch of recombination and the Jeans mass decreased abruptly to the value $M = 1.6 \times 10^5 (\Omega_0 h^2)^{-1/2} M_\odot$, perturbations on all scales greater than this mass survived and began to collapse to form bound structures.

12.7 Baryonic Theories of Galaxy Formation

We can now put these ideas together to create baryonic theories of the origin of galaxies. This story brings back fond memories of the time I spent working with Zeldovich, Sunyaev, Doroshkevich and their colleagues in Moscow in 1968–69 when many of these ideas were being hammered out – it was an extraordinary experience. Zeldovich and his team studied both adiabatic and isothermal perturbations, but put most effort into the adiabatic scenario. In contrast, Peebles and his colleagues at Princeton favoured the isothermal picture. These baryonic models resulted in quite different pictures for the formation of galaxies and the large-scale structure of the

Universe. Although much of this discussion has been superseded by the Λ CDM models, it is of more than historical interest since the models contain many of the ideas which are built into the current picture of structure formation.

12.7.1 The Adiabatic Scenario

In the adiabatic picture developed by Zeldovich and his colleagues, it was assumed that a spectrum of small adiabatic perturbations was set up in the very early Universe and their evolution was then followed according to the physical rules developed above. Only large-scale perturbations with masses $M \geq M_S = 10^{12} (\Omega_B h^2)^{-5/4} M_\odot$ survived to the epoch of recombination, all fluctuations on smaller mass scales being damped out by photon diffusion, as discussed in Sect. 12.5. Perturbations with masses greater than the Jeans mass, $M_J = 3.75 \times 10^{15} / (\Omega_B h^2)^2 M_\odot$, continued to grow from the time they came through their particle horizons to the present epoch. Once they came through their particle horizons, those perturbations with masses less than the Jeans mass were sound waves which oscillated with a small decrease in amplitude until the epoch of recombination, when their internal pressure support vanished and the Jeans mass dropped abruptly to $M_J = 1.6 \times 10^5 (\Omega_0 h^2)^{-1/2} M_\odot$.

Zeldovich and his colleagues realised that there would be structure in the power spectrum of oscillations which survived to the epoch of recombination, as illustrated in Fig. 12.5a (Sunyaev and Zeldovich, 1970). Those fluctuations on a given mass scale, which would eventually develop into bound structures at late epochs, were those which had large positive amplitudes when they came through their particle horizons. Figure 12.5a shows perturbations on two different mass scales coming

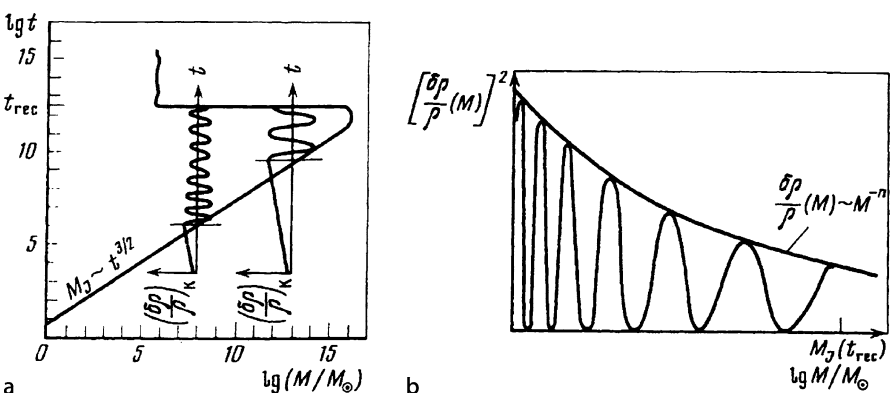


Fig. 12.5a,b. ‘Stability diagram’ of Sunyaev and Zeldovich (Sunyaev and Zeldovich, 1970). **a** The region of instability is to the right of the solid line. The two additional graphs illustrate the evolution of density perturbations of different masses as they come through the horizon up to the epoch of recombination. **b** Perturbations corresponding to different masses arrive at the epoch of recombination with different phases, resulting in a periodic dependence of the amplitude of the perturbations upon mass

through their particle horizons. The amplitude of the oscillations at the epoch of recombination depended upon the phase of the oscillation of the sound waves at that time. Those oscillations which completed an integral number of oscillations would be observed with maximum amplitude as they began to collapse freely once pressure support was removed. On the other hand, those which were $\pi/2$ out of phase with these would have zero amplitude at the epoch of recombination and so would not form objects at all. The predicted mass spectrum of objects formed is shown schematically in Fig. 12.5b.

Originally, it was thought that these oscillations might provide a means of creating a hierarchy of structures on the scales of galaxies, clusters and superclusters of galaxies. This work was carried out before the smoothness of the two-point correlation function for galaxies was established, as illustrated, for example, in Figs. 2.5 and 2.6. The spectrum of primordial oscillations as a function of angular scale at the epoch of recombination will reappear later as a crucial part of the favoured picture for the formation of large scale structures and for the determination of cosmological parameters. In fact, despite the smoothness of the two-point correlation functions in Figs. 2.5 and 2.6, evidence has been found for these oscillations at a low level in the two-point correlation functions derived from the large 2dF and SDSS Galaxy Surveys (Sect. 14.6). In contrast, the temperature fluctuations in the cosmic microwave background radiation are expected to be much larger and these provide a great deal of information about basic cosmological parameters (see also Sect. 15.9). These oscillations are often referred to as *acoustic oscillations*. Novikov has advocated referring to these as *Sakharov oscillations* in recognition of Sakharov's pioneering contributions in his paper of 1965, before the discovery of the cosmic microwave background radiation (Sakharov, 1965; Naselsky et al., 2006).

Following recombination, all the surviving perturbations grew in amplitude as $\Delta \propto (1+z)^{-1}$ until the epoch at which $\Omega_0 z \sim 1$. By the early 1970s, the density parameter in baryons Ω_B was known to be less than about $0.05h^{-2}$ from the constraints provided by primordial nucleosynthesis (Sect. 10.4) and so, even if $h = 0.5$, the perturbations would grow very slowly at redshifts $z \leq 5$. Therefore, the amplitudes of the perturbations must have attained $\Delta \sim 1$ by that epoch in order to ensure the formation of galaxies and larger-scale structures. This was an appealing result, since quasars were known to exist at redshifts greater than 2 and the number counts of quasars and radio sources indicated that these objects had flourished at these early epochs (see Sect. 17.2). Zeldovich and his colleagues inferred that galaxies and larger-scale structures formed at relatively late epochs, $z \sim 3 - 5$. Since the fluctuations had attained amplitude $\Delta \sim 1$ at $z \sim 5$ and $\Delta \propto (1+z)^{-1}$, the amplitude of the density perturbations at the epoch of recombination must have been at least $\Delta \geq 3 \times 10^{-3}$.

In the baryonic adiabatic scenario, only large-scale perturbations survived to $z \sim 5$ at which epoch their collapse became non-linear. We will deal with this topic in more detail in Chap. 16. For the moment, we note that the structures which survived on the scales of clusters and superclusters of galaxies were unlikely to be perfectly spherical and, in the simplest approximation, could be described by ellipsoids with three unequal axes. In 1970, Zeldovich derived an analytic solution for the non-linear

evolution of these structures and showed that such ellipsoids collapsed most rapidly along their shortest axis with the result that flattened structures, which Zeldovich called ‘pancakes’, were formed (Zeldovich, 1970). The density became large in the planes of the pancakes, and the infalling matter was heated to a high temperature as the matter collapsed into the pancakes, a process sometimes called the ‘burning of the pancakes’. Galaxies were assumed to form by fragmentation or thermal instabilities within the pancakes. In this picture, all galaxies formed late in the Universe, once the large-scale structures had collapsed. This baryonic pancake theory was developed in some detail by Zeldovich¹ and his colleagues in the 1970s and can be thought of as a ‘top-down’ scenario for galaxy formation (Sunyaev and Zeldovich, 1972). Among the successes of the theory was the fact that it accounted naturally for the large-scale structure in the distribution of galaxies. In three dimensions, the pancakes formed interconnected, flattened, stringy structures, not unlike the great holes and sheets of galaxies observed in the local Universe.

12.7.2 The Isothermal Scenario

In contrast, Peebles and his Princeton colleagues favoured the isothermal scenario in which perturbations on all scales greater than $M_J = 1.6 \times 10^5 (\Omega_0 h^2)^{-1/2} M_\odot$ survived to the epoch of recombination and began to collapse immediately thereafter. This scenario had the attractive feature that the first objects to form would have masses similar to those of globular clusters, which are the oldest known objects in our Galaxy. The process of galaxy and structure formation was ascribed to the hierarchical clustering of these small-scale structures under the influence of the power spectrum of density perturbations, which extended up to the largest scales. One of the attractive features of this picture was that there would be early enrichment of the chemical abundances of the elements as a result of nucleosynthesis in the first generations of massive stars. This process could account for the fact that, even in the largest redshift quasars, the abundances of the elements were not so different from those observed locally. Many of these ideas were developed by Peebles in his important monograph *The Large-Scale Structure of the Universe* (Peebles, 1980).

The process of structure formation by hierarchical clustering was put on a formal basis by Press and Schechter in 1974 in a remarkable paper which we will study in Sect. 16.3 (Press and Schechter, 1974). Throughout the 1970s, Peebles and his colleagues devoted an enormous effort to determining the correlation functions which describe the statistical properties of the clustering of galaxies (Sects. 2.2 and 14.1). As the power of digital computers increased, it became possible to carry out numerical simulations of the process of structure formation by hierarchical clustering, and one of the successes of that programme was the ability to account for the observed correlation functions for galaxies. We will return to this crucial topic in more detail in Chap. 14. In contrast to the adiabatic picture, the isothermal scenario

¹ Many of the most important papers by Zeldovich and his colleagues are contained in Volume 2 of Zeldovich’s selected works (Zeldovich, 1993).

is a ‘bottom-up’ picture, in which galaxies are built up out of smaller objects by clustering and coalescence.

12.8 What Went Wrong?

Despite some of their undoubted successes, there are major problems with both scenarios. The most important facts were that the dominant form of matter in the Universe is dark matter and that it is unlikely to be baryonic. The constraints from primordial nucleosynthesis of the light elements strongly suggested that the mean baryonic mass density of the Universe is about an order of magnitude less than the mean total mass density $\Omega_0 \approx 0.2\text{--}0.3$. Since the limits derived from primordial nucleosynthesis constrain the total amount of baryonic matter in the Universe, whatever its form, the difference between the baryonic mass density and the total mass density must be associated with some non-baryonic form of matter and it must be dynamically dominant throughout the matter-dominated era.

A major conceptual advance was made by Guth in 1981 when he proposed the concept of the inflationary expansion of the early Universe as a means of solving many of the fundamental problems of cosmology (Guth, 1981); we will discuss various aspects of his proposal throughout the remainder of this book. One of the immediate consequences of the proposal was that the Universe should have flat spatial geometry and so, if $\Omega_\Lambda = 0$, it follows that $\Omega_0 = 1$. In this case, there would be no question but that most of the mass in the Universe must be in some non-baryonic form.

From the perspective of observation, the most important conflict was with the expected amplitude of the temperature fluctuations in the cosmic microwave background radiation. During the epoch of recombination, both adiabatic and isothermal density perturbations began to collapse and, for masses on the scales of clusters of galaxies and greater, their behaviour was similar. The problem was that, in purely baryonic theories, these fluctuations had to have large amplitudes, $\Delta = \delta\varrho/\varrho \geq 3 \times 10^{-3}$ on the last scattering surface, and these would cause observable temperature fluctuations $\Delta T/T$ in the radiation temperature of the cosmic microwave background radiation. We will discuss the theory of these temperature fluctuations in some detail in Chap. 15, and so we simply summarise some of the key points here.

In 1968, Silk pointed out that adiabatic density perturbations would result in temperature fluctuations of the matter on the last scattering surface according to the adiabatic relation

$$\left(\frac{\delta T}{T} \right) = \frac{1}{3} \left(\frac{\delta\varrho}{\varrho} \right), \quad (12.74)$$

recalling that the matter and the radiation are strongly coupled through the recombination epoch (Silk, 1968). This calculation suggested that temperature fluctuations would be expected in the cosmic microwave background radiation at a level

$\delta T/T \geq 10^{-3}$, which could be excluded from the observational upper limits to the temperature fluctuations.

As we will show in Chap. 15, the processes by which fluctuations are imprinted on the background radiation are much more complex than this. The theory of these processes for both adiabatic and isothermal perturbations was worked out by Sunyaev and Zeldovich, who found that, for both types of perturbation, the root-mean-squared temperature fluctuations were predicted to be

$$\left\langle \left(\frac{\delta T}{T} \right)^2 \right\rangle^{1/2} = 2 \times 10^{-5} \left(\frac{M \Omega_0^{1/2}}{10^{15} M_\odot} \right)^{1/2} (1 + z_0), \quad (12.75)$$

for masses $M \geq 10^{15} \Omega_0^{-1/2} M_\odot$, where z_0 is the redshift at which $\delta \varrho/\varrho = 1$ (Sunyaev and Zeldovich, 1970). By the early 1980s, the upper limits of the intensity fluctuations in the cosmic background radiation were in conflict with the predictions of such purely baryonic theories (Partridge, 1980a,b).

It may seem remarkable that I have spent so much effort developing baryonic theories of structure formation which have ended up in serious conflict with the observations. There are two important reasons for this. The first is that we have developed many new tools and concepts which will be needed in the formulation of any acceptable theory of galaxy formation. The second is that we have presented the best that can be achieved assuming that all the matter in the Universe is in baryonic form. The fact that there are important conflicts with observation is in itself good reason for taking seriously the proposition that the Universe is dominated by some unknown form of non-baryonic dark matter.

To some, it may be disappointing that a theory of the origin of structure in the Universe, based entirely upon known forms of matter and radiation and their interactions, runs into insurmountable contradictions with the observations. We are faced with including an additional dominant constituent of the Universe, dark matter, the nature of which is unknown, as well as dark energy in Einstein's field equations. Thus, in compensation, there is the exciting prospect of gaining new insights into fundamental physical processes through the study of the origin of structure in the Universe. If this programme is successful, it would be yet one more example of astronomical problems leading to an understanding of fundamental physical processes which cannot as yet be studied in the laboratory.

This is the story we take up now.

13 Dark Matter and Galaxy Formation

13.1 Introduction

The discussion of Chap. 12 concerning the failure of purely baryonic models of galaxy formation and the compelling evidence presented in Sects. 4.7 and 8.7 that non-baryonic dark matter must be present in the Universe with density parameter $\Omega_0 \approx 0.3$ mean that we need to develop models in which dark matter is dominant dynamically in structure formation. This complicates the models of structure formation as illustrated in Fig. 13.1, which is adapted from Dodelson's highly recommendable analysis (Dodelson, 2003).

A number of useful points can be made about Fig. 13.1 before we tackle dark matter models of structure formation.

- The light grey circles indicate the components we have been principally concerned with so far. The protons and electrons were tightly coupled by Coulomb collisions during the pre-recombination era and so it is an excellent assumption that they had Maxwellian distributions at the same temperature. Likewise, the discussion of Sects. 9.3 and 9.4 showed that there was strong thermal coupling between the baryonic matter and the thermal background radiation throughout the pre-recombination era. Therefore, for most purposes, we could treat the pre-galactic material as a radiation-dominated plasma at a single temperature. We needed, however, to deal with non-equilibrium physics when the decoupling of various species occurred, for example, when the neutrinos decoupled and when the light elements were synthesised. The analysis of Sect. 10.6 showed how the transition to non-equilibrium physics could be treated.
- We touched only lightly upon the fact that the perturbations in the radiation-dominated plasma are coupled to perturbations in the metric and considered this issue only in our discussion of superhorizon scales (Sect. 12.3).
- We now need to include perturbations in both the dark matter and the neutrinos. The discovery that the neutrinos have finite rest mass needs to be included in the picture of structure formation. We argued in Sect. 4.7 that the masses of the electron, muon and tau neutrinos are too small to account for the dark matter in galaxies. Even if they cannot fulfill that role, the impact of a finite neutrino rest mass needs to be included in the analyses of structure formation.
- Most intriguing of all is that we need to include the dark matter perturbations without knowing their nature. Figure 13.1 makes the important point that for

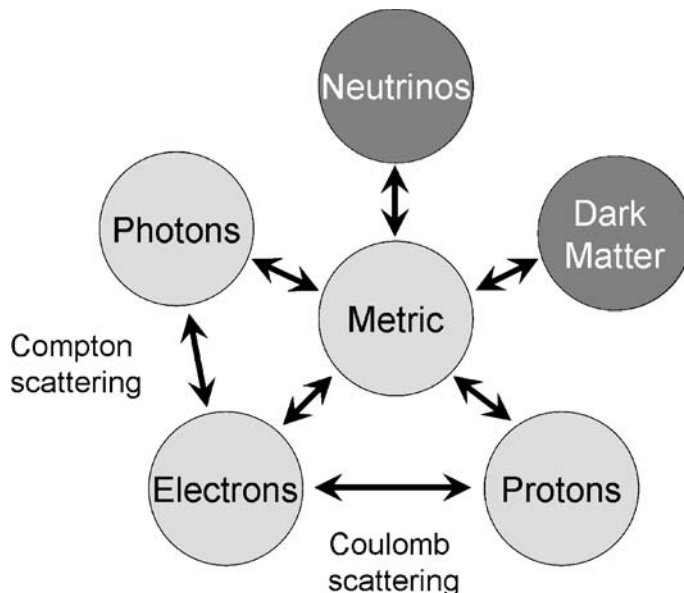


Fig. 13.1. Illustrating how the various components of the Universe interact with each other. Up till this chapter we have been concerned with baryonic perturbations in which there was strong coupling between the photons and baryonic matter. The failure of that picture and compelling evidence for dominance of dark matter mean that we need to include dark matter and neutrino perturbations in the picture (Dodelson, 2003)

much of the pre-recombination era, the neutrinos and dark matter particles were only coupled to the baryonic matter and the photons through their gravitational influence. As indicated on the diagram, it is best to think of the various components contributing to perturbations to the metric and then the strongly coupled radiation-dominated plasma responds to these metric perturbations.

- Whereas we could generally assume that the radiation-dominated plasma behaved like a perfect gas, the fact that the dark matter particles and neutrinos are ultra-weakly interacting means that in bulk they cannot be thought of as behaving like a thermal gas. Therefore, the Boltzmann equation, coupled to Einstein's equations of general relativity, needs to be adopted in a rigorous treatment.

The full analysis is complex and beyond the ambitions of this book. The introductions by Peacock and Dodelson give an excellent impression of what is involved (Peacock, 2000; Dodelson, 2003). More mathematical analyses are given by Mukhanov and by Naselsky, Novikov and Novikov (Mukhanov, 2005; Naselsky et al., 2006). Our modest aim in this chapter is to identify the key physical features which come out of the full analyses and carry out a number of simple calculations. Let us first return to the issue of the nature of the non-baryonic dark matter.

13.2 Forms of Non-Baryonic Dark Matter

We have already mentioned the three most popular suggestions for non-baryonic dark matter in Sect. 4.7.2 To recapitulate, these are:

1. *Axions.* The discussion by Kolb and Turner is recommended for the enthusiast who wishes to obtain insight into the motivation for the introduction of these particles into theories of elementary particles (Kolb and Turner, 1990). If these particles exist, they would have important astrophysical consequences which are discussed by Kolb and Turner. They show that, if the axions were produced in thermal equilibrium, they would have unacceptably large masses, which would result in conflict with observations of the Sun and the supernova SN1987A. Specifically, if the mass of the axion were greater than 1 eV, the rate of loss of energy by the emission of axions would exceed the rate at which energy is generated by nuclear reactions in the Sun and so its centre would need to be hotter, resulting in a shorter age than is acceptable and greater emission of high-energy neutrinos. In the case of SN1987A, the key observation was the duration of the neutrino pulse of about 12 s, consistent with the standard picture of neutrino emission. If the axions had masses in the range 10^{-3} to 2 eV, the cooling of the neutron star would be so rapid that a much shorter pulse of neutrinos would be expected. There is, however, another, non-equilibrium, route by which the axions could be created in the early Universe. In this variant, described by Kolb and Turner, the axions never acquired thermal velocities, as they were never in equilibrium. The acceptable range of rest mass energies of the axions is $10^{-2} - 10^{-5}$ eV. The axions remained ‘cold’ and, during the epochs we are interested in, behaved in bulk like the massive particles discussed below.
2. *Neutrinos.* The investigation into the role of massive neutrinos in the development of cosmological perturbations was stimulated by the report of Lyubimov and his colleagues in 1980 of a mass of 30 eV for the electron antineutrino (Lyubimov et al., 1980). Although subsequent experiments have not confirmed this result, the possibility that the rest mass energy of the neutrino was of the order of $\varepsilon_\nu \sim 10$ eV was of the greatest cosmological interest. As was shown in Sect. 4.7.2, if all types of relic neutrinos had this mass, they would be sufficient to close the Universe, $\Omega_0 = 1$. Furthermore, such neutrinos would have been highly relativistic when they decoupled from the electrons at $t \approx 1$ s, and so none of the predictions of standard primordial nucleosynthesis would be affected. As discussed in Sect. 4.7.2, the present upper limit to the mass of the electron antineutrino is $m_\nu \leq 2 - 3$ eV. Furthermore, the discovery of neutrino oscillations has provided a measurement of the mass difference between the μ and τ neutrinos of $\Delta m_\nu^2 \sim 3 \times 10^{-3}$, suggesting a rest mass of the order of 0.1 eV. Thus, although the neutrinos cannot play the role of the dark matter, their mass density may well be about 0.03 of that of the dark matter and so may still have observable consequences in studies of the power spectrum of fluctuations in the cosmic microwave background radiation.
3. *WIMPs.* A third possibility is that the dark matter is in some form of weakly interacting massive particle, or WIMP, with rest mass $\varepsilon \geq 1 - 10$ GeV. These

particles might be the gravitino, the supersymmetric partner of the graviton, or the photino, the supersymmetric partner of the photon, or some other type of massive neutrino-like particle as yet unknown. Let us investigate their properties in a little more detail.

13.3 WIMPs as Dark Matter Particles

We discussed limits to the masses of different candidates for the dark matter in Sect. 4.7.2. An important conclusion was that, if dark matter particles were as common as neutrinos and photons, their rest mass energies could not be much greater than 10 eV, or the present density of the Universe would exceed the critical mass density $\Omega_0 = 1$. Therefore, there would have to be some suppression mechanism to ensure that the massive particles were much less common than the photons and neutrinos at the present day.

There is a natural way in which this can occur if the decoupling of the WIMPs from thermal equilibrium took place after they had become non-relativistic, that is, the decoupling took place after the epoch at which $kT \sim m_X c^2$, where m_X is the mass of the WIMP. This argument is exactly the same as that used in Sect. 10.6 to estimate the number density of baryons and antibaryons which would survive to the present epoch. The relic abundances ‘froze out’ when the timescale for particle–antiparticle annihilation exceeded the age of the Universe. Repeating the key steps of the argument in Sect. 10.6, in the relativistic limit when all types of particle were maintained in thermal equilibrium, the number densities of the dark matter particles were given by

$$N_X = N_{\bar{X}} = \frac{4\pi g_X}{h^3} \int_0^\infty \frac{p^2 dp}{e^{E/kT} \pm 1}, \quad (13.1)$$

where g_X is the statistical weight of the particle, p its momentum and the \pm sign depends upon whether the particles are fermions (+) or bosons (−). When the particles became non-relativistic, $kT \ll m_X c^2$, but the species were maintained in thermal equilibrium by interactions between the particles, the non-relativistic limit of integral (13.1) gives the equilibrium number density

$$N_X = g_X \left(\frac{m_X kT}{h^2} \right)^{3/2} \exp \left(-\frac{m_X c^2}{kT} \right), \quad (13.2)$$

independent of whether they were fermions or bosons. Thus, once they became non-relativistic, the number densities decreased exponentially until the timescale of the interactions, which maintain the species in equilibrium, exceeded the expansion age of the Universe. At that point, provided they were stable, the abundances of the massive particles froze out. Taking the ratio of (13.2) and (13.1), the suppression factor of the species relative to its relativistic value is

$$\frac{N_X}{N_{\text{rel}}} \approx 0.04 \left(\frac{m_X c^2}{kT} \right)^{3/2} \exp \left(-\frac{m_X c^2}{kT} \right). \quad (13.3)$$

Decoupling took place when the timescale τ_X for the interaction of the particles became of the same order as the cosmological timescale, $t \sim \tau_X$, where $\tau_X = (\sigma_X Nv)^{-1}$, v being the thermal speed of the particles and σ_X the interaction cross-section of the WIMPs. We can use these results to estimate the value of the cross-section σ_X in order to create the observed density of dark matter particles at the present epoch, that is, that corresponding to a density parameter $\Omega_0 = 0.3$.

This calculation has been carried out by Dodelson. We can use the tools we have already developed to make a similar estimate. We use the result established in Sect. 10.6 that the final abundance is about 1/20 of the value when $t \sim \tau_X$. The present generation of particle colliders such as the LEP experiment at CERN have explored energies up to 100 GeV, and no evidence for WIMPs has been found. In a typical model for the production of dark matter particles, it is assumed that their rest masses must have been about 100 GeV or greater. This assumption immediately means that the decoupling of dark matter particles must have taken place in the early Universe before the epoch of annihilation of the primordial baryons and antibaryons which have masses of ~ 1 GeV.

The calculation is straightforward, but there are some important features which need to be built into the calculation. First of all, the number density of dark matter particles which survive from the very early Universe must result in a density parameter $\Omega_D = 0.3$ at the present epoch. Therefore, their number density must be $0.016/x \text{ m}^{-3}$ if the mass of dark matter particles is $100x \text{ GeV}$. This number density changes with scale factor as $0.016/a^3 x \text{ m}^{-3}$ back to the epoch when their abundance froze out.

Now, the particles must have become non-relativistic by the time the decoupling took place so that the suppression factor represented by (13.3) resulted in a number density of dark matter particles of $0.016/a^3 x \text{ m}^{-3}$ when freeze-out was complete. The number density of relativistic dark matter particles was

$$N_{\text{rel}} \approx 0.2 \left(\frac{2\pi kT}{hc} \right)^3 \text{ m}^{-3}. \quad (13.4)$$

This is where the first complication comes in. We cannot use the temperature-scale factor relation $T = T_0 a^{-1}$ because of the heating of the thermal background radiation by all the particle–antiparticle annihilations which must have taken place between the temperature corresponding to $kT = 100x \text{ GeV}$ and the present temperature of the cosmic microwave background radiation. In other words, we need to carry out a similar calculation to that of Sect. 10.5 to determine the relation between the thermal radiation temperature and the total energy density of particles at the early epochs before the annihilations have taken place. We need to determine χ in the relation $\varepsilon = \chi a T^4$ using the same types of arguments as in Sect. 10.5. We therefore need to guess the number of species present in the Universe at temperatures $kT = 100x \text{ GeV}$. Dodelson includes three generations of quarks and leptons, photons, gluons, weak bosons and ‘perhaps even the Higgs boson’. He estimates that χ might be of the order of 100, and this means that at $T \sim 100 \text{ GeV}$, the temperature would be lower by about a factor of $30^{1/3} \approx 3$ compared with $T \propto a^{-1}$. We follow

his recommendation and take $T = T_0/3a$ as the temperature of the background radiation during these early epochs, where T_0 is the present temperature of the cosmic microwave background radiation today.

WIMPs of rest mass $100x$ GeV were relativistic at a temperature $T = E/k = 10^{15}x$ K. At this temperature, the number density of WIMPs was given by (13.4). We can therefore determine the suppression factor by comparing $0.016/a^3x$ with (13.4)

$$\frac{N_X}{N_{\text{rel}}} = 20 \times \frac{8.7 \times 10^{-3}}{x} \left(\frac{hc}{kT_0} \right)^3 \approx \frac{2.5 \times 10^{-8}}{x}, \quad (13.5)$$

where the factor of 20 takes account of the further annihilations which took place after the epoch when $t \sim \tau_X$. Equating this number to (13.3), we find that the freeze-out had to begin when $T = T_{\text{rel}}/18.5$. All we need now is the scale factor and cosmic time at which this took place and we can find the interaction cross-section σ_X . The expression for the temperature–cosmic time relation (10.21) has to be modified to take account of the presence of large numbers of particle–antiparticle pairs, and so, as discussed above, we adopt the modified temperature history three times lower than that relation so that

$$T = 0.44 \times 10^{10} t^{-1/2}. \quad (13.6)$$

Therefore, the decoupling of the WIMPs began at an epoch when $T = 10^{15}x/18.5$ K, that is, when $t = 6.6 \times 10^{-9}$ s. This is the time which is now set equal to $(\sigma_X N_X v)^{-1}$. The scale factor at that temperature was $1.7 \times 10^{-14}/x$, and so $N_X = 3 \times 10^{39} \text{ m}^{-3}$. The thermal velocities of the particles were $\sim 10^8 \text{ m s}^{-1}$, and so we find $\sigma_X \approx 5 \times 10^{-40} \text{ m}^2$. Notice that the result is independent of x and so independent of the mass of the WIMP. This is the answer we have been seeking. It is not so different from the result quoted in the literature:

$$\langle \sigma_X v \rangle = (1 - 2) \times 10^{-32} \frac{\gamma}{4\Omega_X h^2} \text{ m}^3 \text{ s}^{-1}, \quad (13.7)$$

where γ is a constant of order unity (Primack et al., 1988). This can be approximated as

$$\Omega_X h^2 \approx \frac{3 \times 10^{-31}}{\langle \sigma_X v \rangle}. \quad (13.8)$$

There are clearly many rough approximations involved in the above estimates, which are only indicative of the results of more complete analyses. The important point is, however, that the predicted cross-section is very small and so there is no question but that these particles really must be weakly interacting massive particles.

The encouraging aspect of this analysis is that various theories of elementary particles beyond the standard model predict that the cross-section for such particles should be of this order. According to supersymmetric theories of elementary

particles, each type of fermion and boson has its supersymmetric counterpart and these must be very massive since they have not been detected in particle physics experiments. The particles have to be neutral since they must not interact with other particles nor can they emit photons. The particles must also be stable. Hence, they must be the lightest supersymmetric partners of one of the known neutral particles so that they cannot decay into any lighter particles. Possible candidates for the dark matter would therefore be the supersymmetric partners of the photon, the Higgs particles or the graviton. These supersymmetric neutral WIMPs are referred to as *neutralinos*.

As has been discussed in Sect. 4.7.2, according to particle theorists, almost all theories of physics beyond the standard model involve the existence of new particles at the TeV scale because of the symmetries which have to be introduced to avoid proton decay and violations of the precision tests of the electro-weak theory. These considerations lead to the expectation of new particles at the weak energy scale, and it is encouraging that the above calculations show that the types of cross-sections needed for the WIMPs are of the same order as those predicted by these theories.

Experiments are under way to search for different types of dark matter particles. These experiments have not found evidence for the elusive WIMPs, but the sensitivities of the searches are now reaching very impressive limits. The shaded areas in Fig. 13.2 show the range of possible masses and WIMP–nucleon cross-sections

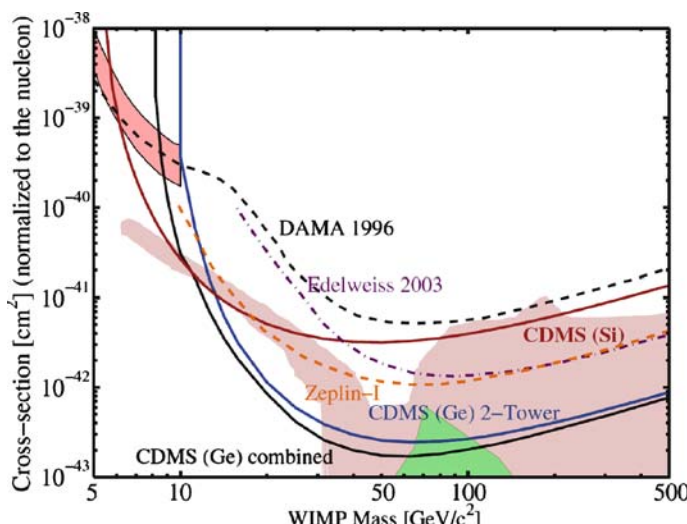


Fig. 13.2. WIMP–nucleon cross-section upper limits at 90% confidence limit plotted against WIMP mass. The *upper CDMS Ge curve* uses data from only a 74.5-d run in 2006; the *lower Ge curve* includes data from this experiment and previous runs. The *shaded regions* of the diagram show areas allowed by various supersymmetric models. The results of other dark matter experiments are also shown (Akerib et al., 2006). Notice that the WIMP–nucleon scattering cross-section is much smaller than the annihilation cross-section (13.8) (Primack et al., 1988)

predicted by various versions of supersymmetry theories. The figure also shows the limits obtained from the Cryogenic Dark Matter Search (CDMS II) at the Soudan Underground Laboratory. The experiment used both germanium and silicon detectors and was most sensitive to WIMPs with masses of $\sim 60 \text{ GeV}/c^2$. No WIMP signal exceeding the expected background was observed. The 90% confidence upper limit to the spin-independent WIMP–nucleon cross-section is $1.6 \times 10^{-47} \text{ m}^2$ from the germanium experiment and $3 \times 10^{-46} \text{ m}^2$ from the silicon experiment, both limits for WIMP masses of $60 \text{ GeV}/c^2$.

13.4 Metric Perturbations and Hot and Cold Dark Matter

Let us introduce some of the terminology used in the literature which describes the connections shown in Fig. 13.1. In the purely baryonic models of Chap. 12, we noted that the perturbations in the early Universe could be decomposed into isothermal and adiabatic modes. We now have to deal with perturbations in all the quantities shown in Fig. 13.1. In view of the fact that the terms ‘isothermal’ and ‘adiabatic’ are scarcely appropriate for systems containing collisionless dark matter particles and massive neutrinos, it is better to decompose the perturbations into *curvature* and *isocurvature* modes, which bear a number of similarities to the adiabatic and isothermal perturbations. These terms, however, explicitly indicate that perturbations in all the components shown in Fig. 13.1 contribute to perturbations in the metric, and in turn each component then responds to these metric perturbations. These different perturbation modes can be characterised as follows:

- The *curvature modes* are similar to the adiabatic modes in that, during the radiation-dominated era and before the epoch of equality of mass densities in the matter and radiation, the amplitudes of the perturbations in the radiation, the baryonic matter and the dark matter were similar and driven by gravitational potential perturbations in the metric. The relation between the density contrasts in the various mass-energies $\delta\varrho/\varrho$ is similar to the adiabatic law:

$$\frac{1}{3} \frac{\delta\varrho_B}{\varrho_B} = \frac{1}{3} \frac{\delta\varrho_D}{\varrho_D} = \frac{1}{4} \frac{\delta\varrho_{\text{rad}}}{\varrho_{\text{rad}}} = \frac{1}{4} \frac{\delta\varrho_\nu}{\varrho_\nu} = \left(\frac{1}{4} \frac{\delta\varrho_C}{\varrho_C} \right). \quad (13.9)$$

The subscripts have their obvious meanings: B = baryons, D = cold dark matter, rad = radiation and ν = neutrinos. The final term in large brackets is the total density contrast, which is determined by the curvature perturbations. Thus, there were variations in the local mass-energy density from point to point in the Universe, resulting in local perturbations to the curvature of space. The above relation is known as the *adiabatic condition* and the perturbations are often referred to as *adiabatic curvature perturbations*. One of the attractions of this picture is that these types of perturbation appear naturally in the inflationary picture of the origin of cosmological fluctuations, and one of the goals of that theory is to relate the curvature perturbations to quantum fluctuations associated with the inflation field.

- In the *isocurvature modes*, the total mass-energy density is constant, and so there are no perturbations of the spatial curvature of the background model, but there are fluctuations in the mass-energy density of each of the four components of (13.9) from point to point in the Universe.

As in the adiabatic and isothermal cases, any general distribution of perturbations can be decomposed into the sum of curvature and isocurvature modes. The adiabatic curvature modes have received the most attention because they are generated rather naturally in the inflationary model and so most attention has been devoted to them.

The considerations of Sects. 13.2 and 13.3 show that at least two different types of dark matter have been identified. We will consider the two most popular forms.

- A realisation of the *cold dark matter* model involves the WIMPs discussed in Sect. 13.3. These particles decoupled from other components in the very early Universe, when the Universe was about 10^{-14} s old, according to the calculation of Sect. 13.3. They decoupled when they were already non-relativistic, and this provided the powerful suppression mechanism which reduced their surviving number density to the value $\Omega_0 = 0.3$ at the present epoch. Although they no longer interacted with other particles, they cooled as part of the cosmological expansion to very low temperatures, and so the term *cold dark matter* seems entirely appropriate. According to Peebles, Richard Bond introduced the term cold dark matter in 1982 to encompass many of these exotic types of particle suggested by the particle physicists (Peebles, 1993). Notice that, once structures began to form gravitationally bound systems in the post-recombination era, cold dark matter was responsible for providing the gravitational potentials of the bound systems and the particles acquired velocities by the process of violent relaxation so that the systems satisfied the virial theorem.
- A realisation of the *hot dark matter* model would be one in which the known types of neutrinos have finite masses. The term ‘hot’ here refers to the fact that the particles were highly relativistic when they decoupled from the baryonic matter at $t \approx 1$ s. In the original hot dark matter model proposed by Zeldovich and his colleagues, the rest mass of the neutrino was taken to be about 10 eV. The neutrinos therefore became non-relativistic relatively late in the Universe and, when this transition took place, the neutrinos still had very large velocities with consequences which will be discussed in the next section. In fact, the likely rest mass of the neutrino is about 100 times smaller than this value, but it is important to study the physical consequences of the finite rest mass of the neutrino.

Let us develop some more of the tools needed to develop viable dark matter cosmologies.

13.5 Free Streaming and the Damping of Hot Dark Matter Perturbations

So long as dark matter particles were strongly coupled in the early Universe, they behaved no differently from ordinary relativistic or non-relativistic particles. If, how-

ever, the particles were relativistic at the epoch when they ‘froze-out’ as in the case of hot dark matter particles, they would continue to travel in ‘straight lines’ at the speed of light after this time. If the particles were the dominant source of mass-energy for the density perturbations, the relativistic dark matter particles would continue to stream freely when they came through the particle horizon, thereby rapidly damping out perturbations on the horizon scale. The process is similar to the phenomenon of Landau damping in a collisionless plasma where it is referred to as ‘phase-mixing’. The same occurs in this case – the unrestrained motion of the particles destroys the phase coherence of the density perturbation. This damping process was not important for cold dark matter perturbations since they were non-relativistic when they decoupled in the early Universe and were very cold by the time structures on the scales of galaxies and clusters came through the horizon.

For illustration, consider the case of neutrinos with masses of $m_\nu c^2 = 10 \text{ eV}$ in the standard critical model with $\Omega_0 = 1$. Then the epoch of equality of matter and radiation energy densities occurred at a redshift $z \approx 10^4$. For neutrinos of rest mass 10 eV, the particles become non-relativistic when $3kT_\nu \approx m_\nu c^2$. We recall that, in the standard Big Bang scenario, the temperatures of the neutrinos and the photons are related by $T_\nu = (4/11)^{1/3} T_r$, and so the redshift at which the neutrinos became non-relativistic was $z_{\text{NR}} = T_r/T_0 = 2 \times 10^4$. Thus, the neutrinos became non-relativistic at about the same time that the matter and radiation energy densities were the same. In the hot dark matter picture, this is not a coincidence. The reason is that the energy density in the neutrinos was more or less the same as the energy density in the photons so long as the neutrinos were relativistic. After the epoch when the neutrinos became non-relativistic, their inertial mass density decreased as a^{-3} , whereas that of the photons continued to decrease as a^{-4} . The neutrinos then became the dominant dark matter particles which make up Ω_0 at the present epoch.

Let us return to the damping of neutrino perturbations by free-streaming. The masses which were damped out depended upon how far the free-streaming particles could travel at a given epoch. Let us illustrate the result by the simple treatment of Kolb and Turner (Kolb and Turner, 1990). It will prove convenient to work in terms of comoving scales, and so the distance which a free-streaming particle can travel by the epoch t is

$$r_{\text{FS}} = \int_0^t \frac{v(t')}{a(t')} dt'. \quad (13.10)$$

Let us split the integral into two parts, the first from time $t = 0$ to the epoch when the particles became non-relativistic, $t = t_{\text{NR}}$ and the second from $t = t_{\text{NR}}$ to t_{eq} .

$$r_{\text{FS}} = \int_0^{t_{\text{NR}}} \frac{v(t')}{a(t')} dt' + \int_{t_{\text{NR}}}^{t_{\text{eq}}} \frac{v(t')}{a(t')} dt'. \quad (13.11)$$

The first part of the integral is just the horizon scale during the radiation-dominated phases while the particle was relativistic, expressed as a comoving coordinate distance. After the epoch when the particles became non-relativistic, the streaming

velocities of the particles decreased adiabatically as $v = (a_{\text{NR}}/a)c$, as shown in Sect. 7.1. Therefore,

$$r_{\text{FS}} = 2 \frac{ct_{\text{NR}}}{a_{\text{NR}}} + \int_{t_{\text{NR}}}^{t_{\text{eq}}} \frac{v(t')}{a(t')} dt'. \quad (13.12)$$

During the radiation-dominated era, the dynamics of the expansion were described by $a \propto t^{1/2}$ and so we can write $t = t_{\text{NR}}(a/a_{\text{NR}})^2$. Therefore,

$$r_{\text{FS}} = \left(\frac{ct_{\text{NR}}}{a_{\text{RN}}} \right) \left[2 + \ln \left(\frac{t_{\text{eq}}}{t_{\text{NR}}} \right) \right]. \quad (13.13)$$

In the logarithmic term in (13.13), $t_{\text{eq}}/t_{\text{NR}}$ is of order unity. Therefore, we can take the free-streaming scale r_{FS} to be the comoving particle horizon, $r_{\text{H}} = 2ct/a_{\text{eq}}$, at z_{NR} . Since we have worked in terms of comoving distances at the present epoch, the mass within this scale is

$$M_{\text{FS}} \sim \frac{\pi}{6} r_{\text{FS}}^3 \rho_0 = 2 \times 10^{15} M_{\odot}. \quad (13.14)$$

More detailed calculations show that the free-streaming damping mass is

$$M_{\text{FS}} \approx 4 \times 10^{15} \left(\frac{m_v}{30 \text{ eV}} \right)^{-2} M_{\odot}. \quad (13.15)$$

The key result is that all density perturbations on mass scales less than these very large masses were damped out as soon as they came through the horizon. Note that these masses are at least of the order of the most massive clusters of galaxies and so, in this picture, only structures on these very large scales and larger can survive after the epoch of equality of matter and radiation energy densities. This is a distinctive feature of the hot dark matter scenario and bears some resemblance to the baryonic adiabatic picture in which small masses were damped out by photon diffusion.

13.6 Instabilities in the Presence of Dark Matter

We need to reconsider the concept of the Jeans mass when dealing with weakly interacting particles. The equations of gas dynamics under gravity need to be replaced by the collisionless Boltzmann equation. This topic is dealt with by Coles and Lucchin, who show that the Jeans stability criterion also applies in the case of a collisionless gas, provided the sound speed c_s is replaced by the velocity v_* , where

$$v_*^{-2} = \frac{\int v^{-2} f(v) d^3v}{\int f(v) d^3v} \quad (13.16)$$

(Coles and Lucchin, 1995). $f(v)$ is the velocity distribution of the dark matter particles, which is assumed to be isotropic. In the case of a Maxwellian distribution of velocities, v_* is just the root-mean-squared velocity dispersion of the particles.

The physics of this result is straightforward. The issue is whether or not the gravitational pull of the dark matter particles within the perturbation is sufficient to prevent them escaping from it. Just as in the case of the Jeans analysis, on large enough scales the mass of the perturbation becomes more than enough to cause the collapse of the pressure-free, or dust, perturbation.

We need one result which is of particular importance once the matter and radiation decoupled after the epoch of recombination. As we will show, the baryonic perturbations were of much lower amplitude than those in the dark matter immediately after recombination, and so we need to understand how the baryonic perturbations behaved once they were coupled only by gravity to the larger-amplitude dark matter perturbations. Let us study the development of the gravitational instability in the dark and baryonic matter when the internal pressure can be neglected. Equation (11.24) can be written

$$\ddot{\Delta} + 2 \left(\frac{\dot{a}}{a} \right) \dot{\Delta} = A \varrho \Delta , \quad (13.17)$$

where $A = 4\pi G$ in the matter-dominated case. Let us write the density contrasts in the baryons and the dark matter as Δ_B and Δ_D respectively. We have to solve the coupled equations

$$\ddot{\Delta}_B + 2 \left(\frac{\dot{a}}{a} \right) \dot{\Delta}_B = A \varrho_B \Delta_B + A \varrho_D \Delta_D , \quad (13.18)$$

$$\ddot{\Delta}_D + 2 \left(\frac{\dot{a}}{a} \right) \dot{\Delta}_D = A \varrho_B \Delta_B + A \varrho_D \Delta_D , \quad (13.19)$$

where the gravitational driving terms on the right-hand side are the same for both components. Rather than find a general solution, let us find the solution for the case in which the dark matter has $\Omega_0 = 1$ and the baryon density and its perturbations can be taken to be negligible compared with those of the dark matter. Then (13.19) reduces to (13.17), for which we have already found the solution $\Delta_D = Ba$, where B is a constant. Therefore, the equation for the evolution of the baryon perturbations becomes

$$\ddot{\Delta}_B + 2 \left(\frac{\dot{a}}{a} \right) \dot{\Delta}_B = 4\pi G \varrho_D Ba . \quad (13.20)$$

The background model is the critical model for which $a = (3H_0 t/2)^{2/3}$ and $3H_0^2 = 8\pi G \varrho_D = 8\pi G \varrho_D(0)a^{-3}$, where $\varrho_D(0)$ is the critical density at the present epoch. Therefore, (13.20) simplifies to

$$a^{3/2} \frac{d}{da} \left(a^{-1/2} \frac{d\Delta}{da} \right) + 2 \frac{d\Delta}{da} = \frac{3}{2} B . \quad (13.21)$$

The solution, $\Delta = B(a - a_0)$, satisfies (13.21). This is a rather pleasant result because the perturbation can have $\Delta_B = 0$ at the epoch corresponding to $a = a_0$ and yet the

baryon perturbation grows under the influence of the growing perturbations in the dark matter. In terms of redshift, the growth of the perturbation can be written

$$\Delta_B = \Delta_D \left(1 - \frac{z}{z_0}\right). \quad (13.22)$$

Thus, the amplitude of the perturbations in the baryons grows rapidly to the same amplitude as that of the dark matter perturbations. To express this result more crudely, the baryons fall into the dark matter perturbations and, within a factor of two in redshift, have already grown in amplitude to half that of the dark matter perturbations.

Let us illustrate why this is an important calculation for understanding the formation of structure. Consider the case of adiabatic curvature perturbations. When they came through the particle horizon in the radiation-dominated era, the amplitudes of the perturbations in the four-component system were given by (13.9)

$$\frac{1}{3} \frac{\delta\varrho_B}{\varrho_B} = \frac{1}{3} \frac{\delta\varrho_D}{\varrho_D} = \frac{1}{4} \frac{\delta\varrho_{\text{rad}}}{\varrho_{\text{rad}}} = \frac{1}{4} \frac{\delta\varrho_v}{\varrho_v}. \quad (13.23)$$

The perturbations in the radiation-dominated plasma were quickly stabilised when they came through the horizon because the Jeans length was of the same order as the horizon scale and the radiation provided pressure support for the perturbations. The baryonic perturbations became sound waves which oscillated with more or less constant amplitude up to the epoch of recombination, when the decoupling of the matter and radiation took place. After the epoch of equality of the energy densities in the dark matter and the radiation, the dark matter perturbations grew independently of those in the radiation-dominated plasma.

We see now why the above calculation is of considerable importance. The baryon perturbations were stabilised from the redshift at which they entered the horizon to the epoch of recombination, but the amplitude of the perturbations in the dark matter grew from z_{eq} to the epoch of recombination as $\Delta_D \propto (1+z)^{-1}$. Therefore, the relative amplitudes of the fluctuations in the dark matter and the baryons was roughly $\Delta_B/\Delta_D \approx 1500/z_{\text{eq}}$, that is, the baryon perturbations were of much smaller amplitude than those in the dark matter at the epoch of recombination. This is a really important conclusion for studies of intensity fluctuations in the cosmic microwave background radiation. The perturbations in the radiation-dominated plasma were suppressed relative to those in the dark matter at the time the temperature perturbations were imprinted on the cosmic microwave background radiation. Once the matter was decoupled from the radiation, however, the baryons could collapse into the dark matter perturbations according to (13.20), thus restoring their amplitudes to those in the dark matter.

Perturbations on scales larger than those which came through the horizon at redshift z_{eq} have relatively smaller differences between Δ_D and Δ_B at the epoch of recombination. In the limit in which the perturbations came through the horizon at the epoch of recombination, the amplitudes of the fluctuations were of the same order of magnitude.

13.7 The Evolution of Hot and Cold Dark Matter Perturbations

Let us put these concepts together to outline how structure formation comes about in these rather different dark matter scenarios. We consider first the hot dark matter scenario which is to some extent of historical interest, but the presence of hot dark matter has observable consequences in the preferred cold dark matter scenario.

13.7.1 Hot Dark Matter Scenario

If the dark matter was in the form of known types of neutrino with rest masses of the order 10 eV, these particles became non-relativistic at an energy $m_\nu c^2 = 3kT$, which corresponds to a redshift of $z \approx 10^4$, assuming $\Omega_0 = 1$. As we have shown, the fact that the particles were highly relativistic when they decoupled means that this epoch also corresponded to the epoch at which the Universe changed from being radiation- to matter-dominated.

It is assumed that all perturbations of astrophysical interest were set up on a very wide range of scales which far exceeded their particle horizons in the very early Universe. These perturbations then grew according to the rules established in Sect. 13.5, until they came through their particle horizons. As we discussed in Sect. 13.5, if the neutrinos remained relativistic when they came through the horizon, the perturbations on these scales were rapidly damped out by free-streaming. This process continued until the epoch of equality of the matter and radiation energy densities at $z \approx 10^4$ and wiped out all perturbations in the dark matter with masses less than $M_{\text{FS}} = 4 \times 10^{15} (m_\nu / 30 \text{ eV})^{-2} M_\odot$.

At this epoch, the perturbations in the neutrinos, baryons and dark matter had more or less the same amplitude, but now the perturbations in the dark matter became dynamically dominant and, since they were not coupled to the radiation-dominated plasma, they continued to grow in amplitude as $\Delta_D \propto (1+z)^{-1}$. In contrast, when the perturbations in the radiation-dominated plasma came through the horizon, they were very quickly stabilised and oscillated with more or less constant amplitude between the epoch when they came through the horizon to the epoch of recombination. As discussed in the last section, the amplitudes of the perturbations in the dark matter became progressively greater than those in the plasma, and, by the epoch of recombination, the perturbations in the dark matter with masses $M \sim 4 \times 10^{15} (m_\nu / 30 \text{ eV})^{-2} M_\odot$ were greater than those in the plasma by a factor $\Delta_D / \Delta_B \approx (1+z_{\text{eq}}) / (1+z_{\text{rec}}) \approx 10$.

The perturbations in the plasma were subject to the dissipation processes discussed in Sect. 12.3, and so baryonic perturbations with masses up to about $10^{12} M_\odot$ were damped out, but this is not such an important feature of the hot dark matter scenario – the perturbations which determined the structures which form in the Universe now are those in the dark matter which survived to the epoch of equality of matter and radiation energy densities, that is, $M \geq 4 \times 10^{15} (m_\nu / 30 \text{ eV})^{-2} M_\odot$. After the epoch of recombination when the matter and radiation were decoupled, the baryonic matter collapsed into the dark matter perturbations. The density perturbations in the matter then grew rapidly to the same amplitude as those in the dark matter, which

continued to grow as $\Delta_D \propto (1+z)^{-1}$, until they became non-linear when $\Delta_D \sim 1$. At this point, the perturbations separated out as discrete entities and began to form the large-scale structures we observe today. The hot dark matter scenario avoids creating excessively large fluctuations in the cosmic background radiation because, at the last scattering surface, the amplitude of the perturbations in the plasma were significantly less than those in the dark matter.

A key prediction of the hot dark matter model is that the first structures to form are those on the largest scales in the Universe. It is assumed that smaller-scale structures such as galaxies and their contents formed by fragmentation and instabilities once the structures on the scales of clusters of galaxies and greater began to form. This picture was developed by Zeldovich and his colleagues in a remarkable series of papers in 1980, the most important of which are contained in Zeldovich's selected works (Zeldovich, 1993). A success of this picture was that it accounted naturally for the large-scale 'cellular' structure in the distribution of galaxies. Indeed, as we will discuss in the next chapter, the theory is too successful in producing structure on the very largest scales. The big problem with this scenario was that galaxies can only form once the large-scale structures have collapsed, and so it is inevitable that galaxies and their contents formed rather late in the Universe. This poses problems for topics such as the early heating and ionisation of the intergalactic gas and the early chemical enrichment of that gas.

13.7.2 Cold Dark Matter Scenario

The standard cold dark matter scenario has become the model of choice for studies of structure formation in the standard Big Bang. The cold dark matter particles decoupled early in the Universe after they had already become non-relativistic. Since the cold dark matter particles decoupled not too long after they became non-relativistic at $t \sim 10^{-9}$ s, the mass within the horizon at these times was very small, $M \ll M_\odot$. Free streaming was unimportant as soon as the particles became non-relativistic and so the cold dark matter scenario begins with the big advantage that dark matter perturbations on all scales of astrophysical interest survived from the early Universe.

Cold dark matter must be the dominant form of mass at the present epoch and, for our reference values of $\Omega_0 = 0.3$, $\Omega_A = 0.7$, $h = 0.7$, the epoch of equality of matter and radiation energy densities occurred at a redshift of $z = 2.4 \times 10^4 \Omega_0 h^2 \approx 3500$. Up till this epoch, the perturbations in the dark matter hardly grew at all because of the Mészáros effect. After this epoch, the dark matter became dynamically dominant and the perturbations in the dark matter grew independently of the behaviour of the perturbations in the radiation-dominated plasma. As in the standard baryonic picture, adiabatic baryonic fluctuations came through the horizon and were quickly stabilised by the pressure of the plasma. The diffusion of photons from these perturbations led to Silk damping of masses up to about $M_S = 10^{12} (\Omega_B h^2)^{-5/4} M_\odot \sim 10^{14} M_\odot$ by the epoch of recombination. Perturbations with greater masses survived as oscillating sound waves up to the epoch of recombination, when they imprinted their signature on the last scattering surface, just as in the case

of the hot dark matter and baryonic scenarios. However, because perturbations on all mass scales survived in the cold dark matter throughout these epochs, baryonic perturbations on all scales were regenerated by collapse into the cold dark matter perturbations very soon after the epoch of recombination when the coupling of matter and radiation ended. The appropriate Jeans mass for the baryons then corresponded to the standard Jeans mass for ordinary matter immediately after recombination, that is, $M_J = 10^6 (\Omega_B h^2)^{-1/2} M_\odot \approx 7 \times 10^6 M_\odot$, which is of the same order as the masses of globular clusters.

The evolution of the density perturbations in dark matter, baryonic matter and radiation for a mass $M = 10^{15} M_\odot$ is shown in Fig. 13.3, which contrasts the evolution of density perturbations in the purely baryonic picture discussed in Chap. 12 with the preferred cold dark matter scenario discussed here. This helpful diagram from the book by Coles and Lucchin displays many of the important features we have developed in the last three chapters (Coles and Lucchin, 1995). Notice in particular:

- The separate evolution of the perturbations in the cold dark matter and the coupled photon-baryon plasma from the epoch when the perturbations came through the horizon until after the epoch of recombination.
- The regeneration of large-amplitude perturbations in the baryons after the epoch of recombination.
- The decay of the perturbations in the photon gas after the epoch of recombination. This damping is associated with the fact that, as the primordial plasma recombined at a redshift of about 1000, the mean free path of the photons increased dramatically, and so they diffused out of the baryonic perturbations, resulting in strong damping of the perturbations in the radiation.
- The growth of the perturbations on superhorizon scales at $a < 3 \times 10^{-5}$. As shown in Sect. 12.3, although $\Delta = \delta\varrho/\varrho$ grew during these early epochs, they corresponded to gravitational potential perturbations of the metric which were ‘frozen-in’ on superhorizon scales.

Cold dark matter models for galaxy and structure formation have been studied in great detail by computer simulation. Once a spectrum of initial curvature perturbations has been adopted, their evolution can be followed rather precisely. The lowest-mass objects formed first soon after the epoch of recombination, and these then clustered and coalesced under the influence of the spectrum of perturbations on larger scales. Just like the baryonic isothermal model, this process can be thought of as a ‘bottom-up’ scenario in which small-scale structures formed first and subsequently clustered to form galaxies and clusters.

As we will see, the model is remarkably successful in accounting for the power spectrum of the spatial distribution of galaxies and for the spectrum of fluctuations in the cosmic microwave background radiation. Furthermore, the formation of stars and the other contents of galaxies can begin soon after the epoch of recombination, and so there is no problem in accounting for the early heating and reionisation of the intergalactic gas and the early chemical enrichment of the gas by the products of stellar nucleosynthesis. The success of the model in accounting for the large-scale distribution of galaxies has persuaded most theorists that this is the preferred

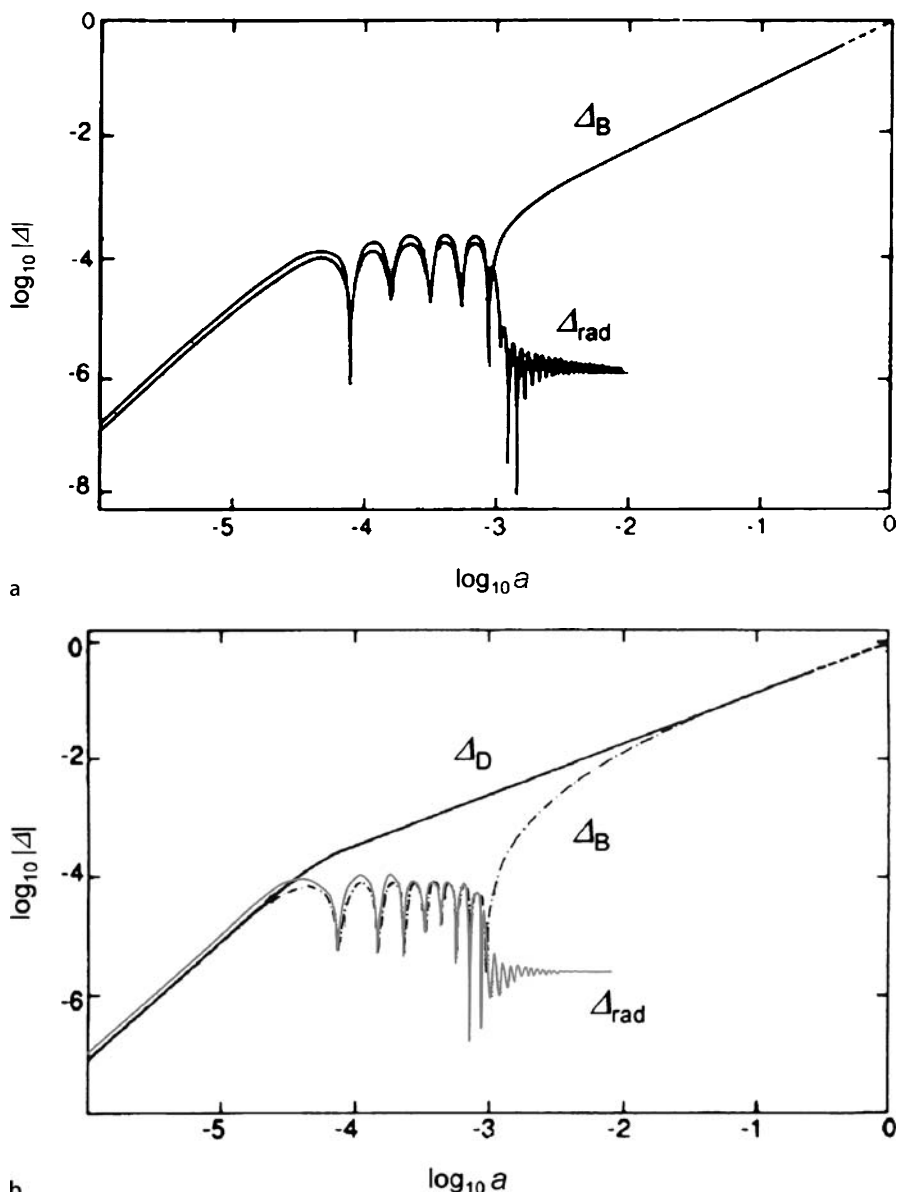


Fig. 13.3a,b. Illustrating the evolution of density perturbations in **a** baryonic matter Δ_B and radiation Δ_{rad} in the standard baryonic adiabatic model and **b** the baryonic matter Δ_B , the radiation Δ_{rad} and the dark matter Δ_D according to the cold dark matter scenario. In both cases, the mass of the perturbation is $M \sim 10^{15} M_\odot$ (Coles and Lucchin, 1995)

framework for studying the processes of galaxy formation. As we will see, although the model performs extremely well on the large scale, there remain problems in understanding how to create galaxies and clusters with all the properties we described in Chaps. 3 and 4. In addition, we have to tackle the difficult problems of the post-recombination era, what are often called the ‘dark ages’, between the epoch of recombination and the appearance of the first stars and galaxies.

13.8 Conclusion

We have now made considerable progress towards the development of physically self-consistent scenarios for galaxy formation. We now need to convert these scenarios into quantitative models for structure formation. To do this, we need to study the development of the spectrum of density fluctuations, and this is the subject of Chap. 14. Then, in Chap. 15, we confront these theories with observations of the temperature fluctuations in the cosmic microwave background radiation.

It is worthwhile stressing an important aspect of the discussion of the last two chapters. We have demonstrated how a purely baryonic picture of galaxy formation is difficult to reconcile with the observations and that these problems could be resolved by the introduction of non-baryonic dark matter. From the perspective of astrophysical cosmology, the incorporation of non-baryonic particles into the models is essential. This is a really momentous step, because these studies not only indicate that this new ingredient is present throughout the Universe, but also that we can use astrophysical arguments to constrain the nature of dark matter particles. The great interest of the particle physicists in these endeavours is understandable. The types of dark matter particles needed in the most promising scenarios may well be closely related to those predicted by theories of elementary particles but which have not yet been created in terrestrial accelerators.

14 Correlation Functions and the Spectrum of the Initial Fluctuations

To make a quantitative comparison between theories of galaxy and structure formation and the observed distribution of galaxies, we need to quantify the spectrum of density perturbations in the Universe and relate it to the spectrum of fluctuations from which these structures formed. So far, we have worked entirely in real space in our analysis of the structure, but the natural way of describing these distributions is in terms of their power spectra, in other words, working in Fourier, rather than in real, space. So, our first task is to relate the *correlation functions* for galaxies which were introduced in Chap. 2 to their associated *power spectra*. Then, we need to derive the power spectrum of initial fluctuations which must have been present in the very early Universe in order to create the structures we observe today.

The full analysis of these topics is non-trivial and, in the spirit of the present exposition, we will endeavour to emphasise the important aspects of the physics and then rely upon the results of supercomputer simulations to make detailed quantitative comparison between theory and observation. Let us first review the properties of the correlation function of galaxies at the present day, extending our introduction of Sect. 2.2. Then we will embark on the quantitative theory of structure formation through the use of power spectra which will provide the natural link to the resulting temperature fluctuation power spectra which are the subject of Chap. 15.

14.1 The Two-Point Correlation Function for Galaxies

The simplest quantitative description of the statistical distribution of galaxies on a large scale is provided by the *two-point correlation function*, which describes the excess probability of finding a galaxy at distance r from a galaxy selected at random over that expected in a uniform, random distribution. The spatial two-point correlation function $\xi(r)$ was introduced in Sect. 2.2 and describes the number of galaxies in the volume element dV at distance r from any galaxy in the form

$$dN(r) = N_0 [1 + \xi(r)] dV , \quad (14.1)$$

where N_0 is a suitably defined average background number density of galaxies. The function $\xi(r)$ can also be written in terms of the probability of finding pairs of galaxies separated by distance r :

$$dN_{\text{pair}} = N_0^2 [1 + \xi(r)] dV_1 dV_2 . \quad (14.2)$$

The two-point correlation function can be directly related to the *density contrast* $\Delta = \delta\varrho/\varrho_0$, which has dominated much of the discussion so far. We write $\varrho = \varrho_0[1 + \Delta(\mathbf{x})]$, and so the pairwise numbers of galaxies separated by distance \mathbf{r} , in the sense of (14.2), is

$$dN_{\text{pair}}(\mathbf{r}) = \varrho(\mathbf{x}) dV_1 \varrho(\mathbf{x} + \mathbf{r}) dV_2 . \quad (14.3)$$

Therefore,

$$dN_{\text{pair}}(\mathbf{r}) = \varrho_0^2 [1 + \Delta(\mathbf{x})] [1 + \Delta(\mathbf{x} + \mathbf{r})] dV_1 dV_2 . \quad (14.4)$$

Taking averages over a large number of volume elements, the mean value of Δ is zero by definition, and therefore the two-point correlation function becomes

$$dN_{\text{pair}}(r) = \varrho_0^2 [1 + \langle \Delta(\mathbf{x}) \Delta(\mathbf{x} + \mathbf{r}) \rangle] dV_1 dV_2 . \quad (14.5)$$

This calculation shows explicitly the relation between the density contrast $\Delta(r)$ on different scales r and the two-point correlation function for galaxies:

$$\xi(r) = \langle \Delta(\mathbf{x}) \Delta(\mathbf{x} + \mathbf{r}) \rangle . \quad (14.6)$$

As discussed in Sect. 2.2.1, observationally the *angular two-point correlation function* $w(\theta)$ is most readily derived from large galaxy surveys:

$$N(\theta) d\Omega = n_g [1 + w(\theta)] d\Omega . \quad (14.7)$$

$w(\theta)$ can be converted into a spatial two-point correlation function by the procedures described in Sect. 2.2.1. Thus, if $\xi(r)$ were of power-law form $\xi(r) \propto r^{-\gamma}$, then $w(\theta)$ would be proportional to $\theta^{-(\gamma-1)}$. The success of the scaling procedures described by (2.5), as applied to the Cambridge Southern Galaxy Survey and illustrated in Fig. 2.5, suggests that the derived form of $\xi(r)$ represents a stationary, random process. Although it might seem preferable to work directly with the three-dimensional correlation function $\xi(r)$, the very large statistics which can be obtained by simply counting galaxies has proved to be a very effective way of estimating $\xi(r)$.

The spatial two-point correlation function for galaxies is a rather sweeping, broad-brush description of their spatial distribution, in that it is assumed that, in taking the averages in (14.5), their distribution is spherically symmetric about any randomly selected galaxy. Inspection of Figs. 2.7 and 2.8 suggests that this is at best a rough approximation on large physical scales. Higher-order correlation functions such as the three- and four-point correlation functions can be defined which take into account more of the three-dimensional structure seen in the large-scale distribution of galaxies. These correlation functions have been treated in some detail by Peebles (Peebles, 1980, 1993). The most effort has, however, been devoted to deriving the predicted two-point correlation functions from large-scale computer simulations, and this is entirely reasonable in order to put some simple order into the massive amount of information contained in the data sets now available.

To recapitulate the results described in Sect. 2.2, the function $\xi(r)$ can be well represented by a power law of the form

$$\xi(r) = \left(\frac{r}{r_0}\right)^{-\gamma} \quad (14.8)$$

on physical scales from about $100 h^{-1}$ kpc to $10 h^{-1}$ Mpc with the scale $r_0 = 5h^{-1}$ Mpc and the exponent $\gamma = 1.8$. On scales greater than about $10h^{-1}$ Mpc, the two-point correlation function decreases more rapidly than the power law (14.8).

There are several points to be made about this correlation function.

1. Figure 2.5 shows that the correlation function for galaxies is quite smooth. There are no obvious preferred scales, say, on the scale of rich clusters or superclusters of galaxies. Of course, any such structures would have been very severely damped in the averaging process. We will find that there is now evidence for structure in the correlation function for galaxies at a low level on the largest scales which were causally connected at a redshift of $z = 1000$. Nonetheless the evidence of Fig. 2.5 is that perturbations on a very wide range of scales must have been present in the initial perturbation spectrum.
2. There is a characteristic scale $r_0 = 5h^{-1}$ Mpc which defines the scale at which the density of galaxies is greater than that of the background by a factor of two. This may be interpreted roughly as a measure of the scale on which the perturbations became non-linear, in the sense that all structures on smaller scales have $\xi(r) > 1$. This means that structures on the scales of groups and clusters of galaxies have certainly become strongly non-linear by the present epoch, entirely consistent with the formation of these virialised structures by the present epoch. This cannot be the whole story, however, since the cellular structure of the large-scale distribution of galaxies extends to scales very much greater than $5h^{-1}$ Mpc.
3. Of particular interest is the behaviour of the two-point correlation function on large physical scales. Although the amplitude of the two-point correlation function for galaxies in general is very much less than one, there is clustering on very large scales. Bahcall and her colleagues have found that Abell clusters, the richest clusters of galaxies, are correlated with a characteristic clustering scale of $r_0 \approx (15 - 25)h^{-1}$ Mpc (Bahcall, 1988, 1997). We described their clustering properties in Sect. 4.1.3. The 2dF and SDSS sky surveys have also provided a wealth of data on the correlation function of quasars on these very large scales. For example, Croom and his colleagues determined the two-point correlation function for quasi-stellar objects using over 20,000 objects from the final 2dF Quasar Redshift Survey (Croom et al., 2005). When averaged over the redshift range $0.3 \leq z \leq 2.2$, they found that $\xi(r)$ is somewhat flatter than (14.8) on small scales but steepens on scales greater than $25 h^{-1}$ Mpc. For a cosmology with $\Omega_0 = 0.27$, $\Omega_A = 0.73$, they found a best-fitting power law with $r_0 = 5.48h^{-1}$ Mpc and $\gamma = 1.20$ on scales from $r = (1 - 25)h^{-1}$ Mpc. Thus, there is no question about the reality of correlated

structures on these very large scales, although they are still in the linear stage of development.

14.2 The Perturbation Spectrum

Since we are dealing with a three-dimensional distribution of galaxies, we need to work in terms of three-dimensional Fourier transforms of $\Delta(\mathbf{r})$ so that the amplitude of the Fourier components with different wavelengths λ , or wavevectors $\mathbf{k} = (2\pi/\lambda)\mathbf{i}_k$, can be found. A number of simplifications can, however, be made since we aim to relate the spectrum of the fluctuations to the two-point correlation function, which is, by definition, spherically symmetric about each point.

14.2.1 The Relation Between $\xi(r)$ and the Power Spectrum of the Fluctuations

First of all, we define the Fourier transform pair for $\Delta(\mathbf{r})$

$$\Delta(\mathbf{r}) = \frac{V}{(2\pi)^3} \int \Delta_{\mathbf{k}} e^{-i\mathbf{k}\cdot\mathbf{r}} d^3 k ; \quad (14.9)$$

$$\Delta_{\mathbf{k}} = \frac{1}{V} \int \Delta(\mathbf{r}) e^{i\mathbf{k}\cdot\mathbf{r}} d^3 x , \quad (14.10)$$

where V is the volume within which $\Delta(\mathbf{r})$ is defined. We now use Parseval's theorem to relate the integrals of the squares of $\Delta(\mathbf{r})$ and its Fourier transform $\Delta_{\mathbf{k}}$:

$$\frac{1}{V} \int \Delta^2(\mathbf{r}) d^3 x = \frac{V}{(2\pi)^3} \int |\Delta_{\mathbf{k}}|^2 d^3 k . \quad (14.11)$$

The quantity on the left-hand side of (14.11) is the mean square amplitude of the fluctuation within the volume V , and $|\Delta_{\mathbf{k}}|^2$ is the *power spectrum* of the fluctuations, which is often written as $P(k)$. Therefore, we can write

$$\langle \Delta^2 \rangle = \frac{V}{(2\pi)^3} \int |\Delta_{\mathbf{k}}|^2 d^3 k = \frac{V}{(2\pi)^3} \int P(k) d^3 k . \quad (14.12)$$

Since the two-point correlation function is spherically symmetric, the element of \mathbf{k} -space can be written $d^3 k = 4\pi k^2 dk$, and so

$$\langle \Delta^2 \rangle = \frac{V}{2\pi^2} \int |\Delta_{\mathbf{k}}|^2 k^2 dk = \frac{V}{2\pi^2} \int P(k) k^2 dk . \quad (14.13)$$

The final step is to relate $\langle \Delta^2 \rangle$ to the two-point correlation function through (14.6). It is simplest to begin with a Fourier series and then transform the series

summation into a Fourier integral. We write $\Delta(\mathbf{x})$ as

$$\Delta(\mathbf{x}) = \sum_{\mathbf{k}} \Delta_{\mathbf{k}} e^{-i\mathbf{k}\cdot\mathbf{x}}. \quad (14.14)$$

$\Delta(\mathbf{x})$ is a real function, and therefore we can find $|\Delta(\mathbf{r})|^2$ by writing $|\Delta(\mathbf{r})|^2 = |\Delta(\mathbf{r})\Delta^*(\mathbf{r})|$, where $\Delta^*(\mathbf{r})$ is the complex conjugate of $\Delta(\mathbf{r})$. Taking the average value of the product of $\Delta(\mathbf{x})$ and $\Delta(\mathbf{x} + \mathbf{r})$ in order to find $\xi(r)$ in (14.6), we find

$$\xi(r) = \left\langle \sum_{\mathbf{k}} \sum_{\mathbf{k}'} \Delta_{\mathbf{k}} \Delta_{\mathbf{k}'}^* e^{-i(\mathbf{k}-\mathbf{k}')\cdot\mathbf{x}} e^{i\mathbf{k}'\cdot\mathbf{r}} \right\rangle. \quad (14.15)$$

When we multiply out the cross terms in this summation, they all vanish except for those for which $\mathbf{k} = \mathbf{k}'$. Therefore,

$$\xi(r) = \sum |\Delta_{\mathbf{k}}|^2 e^{i\mathbf{k}\cdot\mathbf{r}}. \quad (14.16)$$

We now convert this Fourier summation into a Fourier integral:

$$\xi(r) = \frac{V}{(2\pi)^3} \int |\Delta_{\mathbf{k}}|^2 e^{i\mathbf{k}\cdot\mathbf{r}} d^3k. \quad (14.17)$$

Finally, we note that $\xi(r)$ is a real function, and so we are only interested in the integral of the real part of $e^{i\mathbf{k}\cdot\mathbf{r}}$, that is, the integral over $\cos(\mathbf{k} \cdot \mathbf{r}) = \cos(kr \cos \theta)$. Because of the spherical symmetry of the two-point correlation function, we integrate over an isotropic probability distribution of angles θ on a sphere, that is, we integrate $\cos(kr \cos \theta)$ over $\frac{1}{2} \sin \theta d\theta$. Performing this integral, we obtain the final answer

$$\xi(r) = \frac{V}{2\pi^2} \int |\Delta_k|^2 \frac{\sin kr}{kr} k^2 dk = \frac{V}{2\pi^2} \int P(k) \frac{\sin kr}{kr} k^2 dk. \quad (14.18)$$

This is the relation between the two-point correlation function $\xi(r)$ and the power spectrum of the fluctuations $P(k) = |\Delta_k|^2$ we have been seeking. Notice what this procedure has achieved. The function $\sin kr / kr$ allows only wavenumbers $k \leq r^{-1}$ to contribute to the amplitude of the fluctuations on the scale r . Fluctuations with larger wavenumbers, corresponding to smaller scales, average out to zero on the scale r .

It is straightforward to write the power spectrum as an integral over the two-point correlation function $\xi(r)$ starting from (14.11). Following through the same procedure which led to (14.18), we find

$$P(k) = \frac{1}{V} \int_0^\infty \xi(r) \frac{\sin kr}{kr} 4\pi r^2 dr. \quad (14.19)$$

In some presentations of the power spectrum of the distribution of galaxies, $P(k)$, is written in an alternative dimensionless form by multiplying it by k^3 . The integral

(14.18) can then be written

$$\xi(r) = \frac{V}{2\pi^2} \int [k^3 P(k)] \frac{\sin kr}{kr} d(\ln k). \quad (14.20)$$

In the notation used by Peacock and others, the power spectrum can then be written

$$\Delta^2(k) = \frac{V}{(2\pi)^3} 4\pi k^3 P(k) = \frac{2}{\pi} k^3 \int_0^\infty \xi(r) \frac{\sin kr}{kr} r^2 dr. \quad (14.21)$$

This use of $\Delta(k)$ is not to be confused with our use of Δ to mean $\delta\varrho/\varrho$. Inspection of the integral in (14.21) shows that, because of the function $\sin kr/kr$, $\xi(r)$ is averaged over a volume of roughly k^{-3} , and so if the amplitude of $\xi(r)$ is of order unity, so also is $\Delta^2(k)$. This means that if $\Delta^2(k)$ is of order one, there are density fluctuations per unit logarithmic interval of k of order unity about the value k . Thus, although $\Delta^2(k)$ seems the more natural counterpart of $\xi(r)$, we will work with $P(k)$ since it is commonly used in the literature.

14.2.2 The Initial Power Spectrum

The observations described in Sect. 14.1 suggest that the spectrum of initial fluctuations must have been very broad with no preferred scales, and it is therefore natural to begin with a power spectrum of power-law form

$$P(k) = |\Delta_k|^2 \propto k^n. \quad (14.22)$$

According to (14.18), the correlation function $\xi(r)$ should then have the form

$$\xi(r) \propto \int \frac{\sin kr}{kr} k^{(n+2)} dk. \quad (14.23)$$

Because the function $\sin kr/kr$ has value unity for $kr \ll 1$ and decreases rapidly to zero when $kr \gg 1$, we can integrate k from 0 to $k_{\max} \approx 1/r$ to estimate the dependence of the amplitude of the correlation function on the scale r .

$$\xi(r) \propto r^{-(n+3)}. \quad (14.24)$$

Since the mass of the fluctuation is proportional to r^3 , this result can also be written in terms of the mass within the fluctuations on the scale r , $M \sim \varrho r^3$:

$$\xi(M) \propto M^{-(n+3)/3}. \quad (14.25)$$

Finally, to relate ξ to the root-mean-square density fluctuation on the mass scale M , $\Delta(M)$, we take the square root of ξ , that is,

$$\Delta(M) = \frac{\delta\varrho}{\varrho}(M) = \langle \Delta^2 \rangle^{1/2} \propto M^{-(n+3)/6}. \quad (14.26)$$

The above analysis illustrates the relations between the various ways of describing the density perturbations. To summarise, a power spectrum $P(k) = |\Delta_k|^2$ of power-law form $P(k) \propto k^n$ corresponds to a two-point correlation function $\xi(r) \propto r^{-(n+3)} \propto M^{-(n+3)/3}$ and to a spectrum of density perturbations $\Delta(M) \propto M^{-(n+3)/6}$. Power spectra and related functions appear in a variety of different forms in the literature. Sometimes $P(k)$ is plotted against k or M , sometimes $P(k)k^3$ against k or M , sometimes against λ , and so on. The above translations should help reconcile the different presentations. We will present the results of the analytic and computational calculations in terms of $P(k)$ and k .

One of the objectives of these studies is to determine the form of the initial power spectrum of fluctuations which must have been generated in the early phases of the Big Bang. We will study how the observed power spectrum of the distribution of galaxies can be related to the initial power spectrum, but first let us consider the important case of what is known as the *Harrison–Zeldovich* power spectrum.

14.2.3 The Harrison–Zeldovich Power Spectrum

The Harrison–Zeldovich power spectrum has $n = 1$ and results in a spectrum of density perturbations $\Delta(M) = \delta\varrho/\varrho(M)$ and two-point spatial correlation function of the forms

$$\Delta(M) \propto M^{-2/3} \quad \text{and} \quad \xi \propto r^{-4} \propto M^{-4/3}. \quad (14.27)$$

This spectrum has the important property that the density contrast $\Delta(M)$ had the same amplitude on all scales when the perturbations came through their particle horizons. Let us illustrate how this comes about.

Consider the early development of the perturbations on superhorizon scales before they came through their particle horizons and before the epoch of equality of matter and radiation energy densities. The density perturbations on these scales grew as $\Delta(M) \propto a^2$, as discussed in Sect. 12.3. Therefore, the development of the spectrum of density perturbations can be written

$$\Delta(M) \propto a^2 M^{-(n+3)/6}. \quad (14.28)$$

A perturbation of scale r came through the horizon when $r \approx ct$, and so the mass of dark matter within it was $M_D \approx \varrho_D(ct)^3$. During the radiation-dominated phases, $a \propto t^{1/2}$ and the number density of dark matter particles, which will eventually form bound structures at $z \sim 0$, varied as $N_D \propto a^{-3}$. Therefore, the horizon dark matter mass increased as $M_H \propto a^3$, or, $a \propto M_H^{1/3}$. We can insert this result into (14.28) in order to find the mass spectrum $\Delta(M)_H$ when the fluctuations came through the horizon at different cosmic epochs:

$$\Delta(M)_H \propto M^{2/3} M^{-(n+3)/6} = M^{-(n-1)/6}. \quad (14.29)$$

Thus, if $n = 1$, the density perturbations $\Delta(M) = \delta\varrho/\varrho(M)$ all had the same amplitude when they came through their particle horizons during the radiation-dominated era.

This rather special value, $n = 1$, is known as the *Harrison–Zeldovich spectrum* (Harrison, 1970; Zeldovich, 1972). The names of these authors are associated with this spectrum for slightly different reasons. Zeldovich stated in his paper:

‘One unique value (approximately 10^{-4}) of non-dimensional amplitude of metric perturbations, scale-independent, describes two different, most important properties of the Universe – its structure and its entropy.’

The scale independence of the perturbations was derived from the earlier analysis of Sunyaev and Zeldovich, who used a variety of constraints to derive the form of the initial power spectrum of density perturbations as they came through the horizon on mass scales from 10^5 to $10^{20} M_\odot$ (Sunyaev and Zeldovich, 1970).

Harrison’s paper addressed the issue of the form the primordial spectrum would have had to have in order to prevent the overproduction of excessively large-amplitude perturbations on small and large scales. We can understand this problem from the analysis carried out in Sect. 12.3. The perturbations on superhorizon scales corresponded to ‘frozen-in’ gravitational potential perturbations of the metric. The Harrison–Zeldovich spectrum has the property that these perturbations had the same ‘frozen-in’ amplitudes $\sim 10^{-4}$ *on all scales* when they crossed the horizon. If the spectral index were greater than $n = 1$, there would have been excessively large metric perturbations on very small scales in the early Universe, which would inevitably have resulted in their collapse to form black holes. The $n = 1$ spectrum also does not diverge on large physical scales and so is consistent with the observed large-scale isotropy of the Universe. It is intriguing that, if $n = 1$, the Universe is in a sense *fractal* – as the Universe expands, we always find density perturbations of the same amplitude coming through the horizon. One of the challenges for theory is to account for a value of the spectral index of the initial perturbations $n \approx 1$. Proponents of the inflationary picture of the early Universe find that fluctuations with the Harrison–Zeldovich spectrum occur rather naturally in that picture (see Sect. 20.5).

It is interesting to compare the Harrison–Zeldovich spectrum with that expected for Poisson noise. A natural model would be to consider the mass fluctuations to be associated with random statistical fluctuations in the numbers of particles N on the scale r . According to Poisson statistics, the fluctuations in the numbers of particles is $\delta N/N = 1/N^{1/2}$, or, in terms of mass fluctuations, $\Delta(M) = \delta M/M = 1/M^{1/2}$. It follows from the relation (14.26) that $n = 0$, in other words, a ‘white-noise’ power spectrum with equal power on all scales. The corresponding correlation functions would be $\xi(r) \propto r^{-3}$ and $\xi(M) \propto M^{-1}$.

We now need to tackle the issue of the linear and non-linear effects which must have dramatically modified the form of the initial power spectrum after the perturbations of different mass came through their particle horizons.

14.3 Evolution of the Initial Perturbation Spectrum – Transfer Functions

In Chaps. 12 and 13, we described a number of effects which significantly modify the initial perturbation spectrum. We now need to put these together to understand how the initial perturbation spectrum evolved to form the structures we observe in the Universe today. The first step is to introduce the *transfer function* $T(k)$, which describes how the shape of the initial power spectrum $\Delta_k(z)$ in the dark matter is modified by different physical processes through the relation

$$\Delta_k(z = 0) = T(k) f(z) \Delta_k(z). \quad (14.30)$$

$\Delta_k(z = 0)$ is the power spectrum at the present epoch and $f(z) \propto a \propto t^{2/3}$ is the linear growth factor between the scale factor at redshift z and the present epoch. Note that the wavenumbers k are comoving wavenumbers so that they follow the evolution of a perturbation of a particular dark matter mass. It is assumed that $\Delta_k(z)$ is defined at some early epoch before the perturbations came through their particle horizons and so has the shape of the initial perturbation spectrum. Notice that the functions in (14.30) refer to the density contrast in the dark matter and that there are corresponding perturbations in the radiation, which we take to include all forms of relativistic matter such as neutrinos. Let us give some examples of the expected forms of the function $T(k)$.

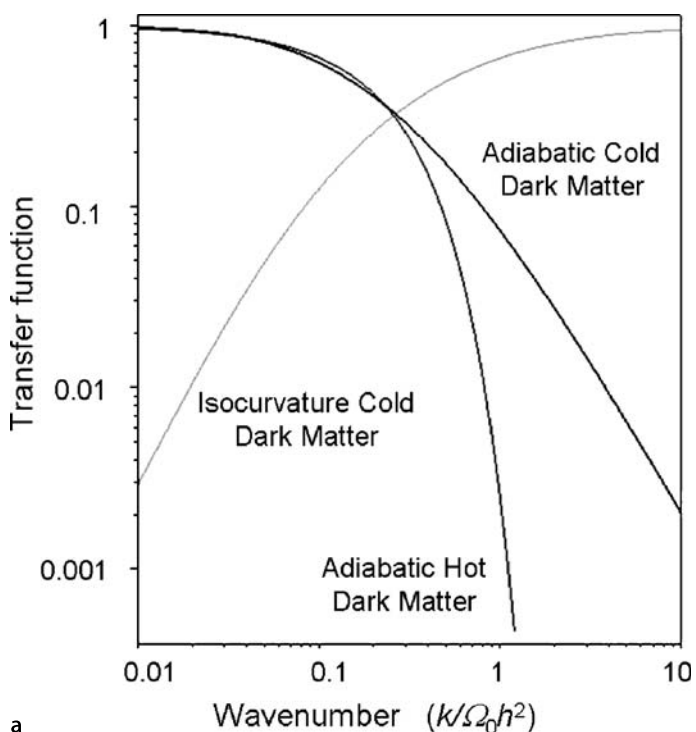
14.3.1 Adiabatic Cold Dark Matter

We adopt an initial power spectrum of standard power-law form

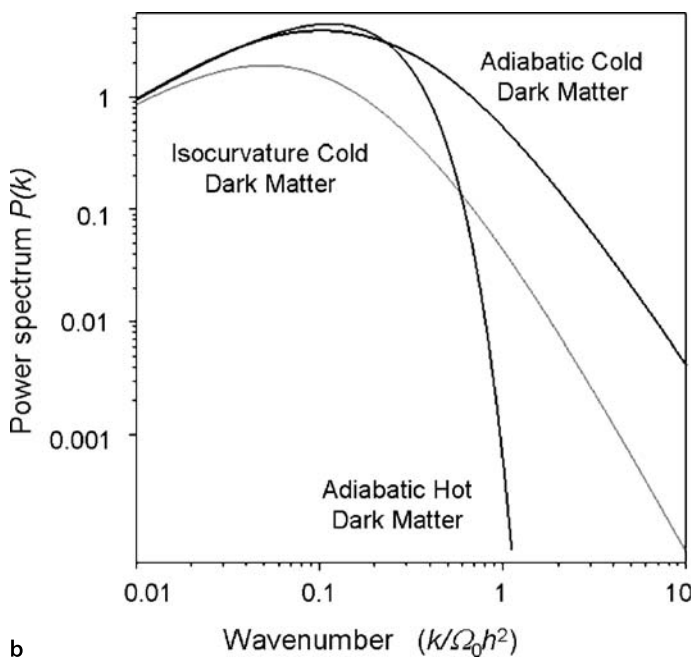
$$P(k) = |\Delta_k|^2 \propto k^n, \quad (14.31)$$

recalling that the Harrison–Zeldovich spectrum has $n = 1$. Before the perturbations entered the horizon during the radiation-dominated era, their density contrasts grew as $\Delta_k \propto a^2$ on all scales. If the perturbations came through the horizon during the radiation-dominated phase, the dark matter perturbations were gravitationally coupled to the radiation-dominated plasma and their amplitudes were stabilised by the Mészáros effect (Sect. 12.6). Thus, as soon as the perturbations came through the horizon, they ceased to grow until the epoch of equality of matter and radiation energy densities. After that time, all the perturbations grew as $\Delta_k \propto a$ until very late epochs. Thus, between crossing their particle horizons at scale factor a_H and the epoch of equality a_{eq} , the amplitudes of the perturbations were damped by a factor $(a_H/a_{\text{eq}})^2$ relative to the unmodified spectrum. This leads to a flattening of spectrum of density contrasts as

$$\Delta_k = \left(\frac{\delta \varrho}{\varrho} \right)_k \propto k^{n/2} \left(\frac{a_H}{a_{\text{eq}}} \right)^2. \quad (14.32)$$



a



b

Fig. 14.1. **a** Examples of the transfer functions $T(k)$ for different models of structure formation. These functions are those quoted by Peacock, which were taken from the paper by Bardeen and his colleagues (Peacock, 2000; Bardeen et al., 1986). **b** Predicted power spectra $P(k)$ for models shown in **a**. In the cases of the cold dark matter models, a Harrison–Zeldovich power spectrum, $n = 1$ has been assumed. In the case of the isocurvature model, the value $n = -3$ has been adopted. The scaling has been chosen so that the power spectra are the same at small wavenumbers, that is, on very large physical scales. In both cases, the wavenumbers are in Mpc^{-1}

Since $k \propto a_{\text{H}}^{-1}$, it follows that the transfer function $T(z)$ has the asymptotic forms

$$T_k = 1 \quad \text{for} \quad M \geq M_{\text{eq}}, \quad k \leq k_{\text{eq}} ; \quad (14.33)$$

$$T_k \propto k^{-2} \quad \text{for} \quad M \leq M_{\text{eq}}, \quad k \geq k_{\text{eq}} . \quad (14.34)$$

Thus, for small masses, the ‘processed’ power spectrum $P(k) \propto T_k^2$ is flatter than the input spectrum of perturbations by a power k^{-4} :

$$P(k) = |\Delta_k|^2 \propto k^{n-4} . \quad (14.35)$$

Running through the apparatus of Sect. 14.2.2, it follows that the amplitude of the spatial two-point correlation function is

$$\xi(r) \propto r^{-(n-1)} \quad \text{or} \quad \xi(M) \propto M^{-(n-1)/3} . \quad (14.36)$$

For the Harrison–Zeldovich spectrum with $n = 1$, the processed two-point correlation function is flat at small wavelengths.

It can be seen from transfer functions (14.33) and (14.34) that there is a large change in slope of the predicted power spectrum at the wavenumber k_{eq} or the mass M_{eq} , corresponding to the wavenumbers and masses of the horizon scale at the epoch of equality of matter and radiation energy densities. Representative values of these quantities are given in Table 14.1 for our reference model and for a cold dark matter model with $\Omega_0 = 1$, $\Omega_A = 0$, $h = 0.7$. These examples make the point that the location of the maximum of the power spectrum is sensitive to the parameters of the cosmological model. Notice that the turn-over in the spectrum is expected to occur on scales of the order of, or greater than, those of clusters of galaxies.

Detailed evaluations of the transfer functions using the full apparatus of the coupled Boltzmann and Einstein field equations have been carried out for different adiabatic cold dark matter models by a number of authors (Peebles, 1982; Davis et al., 1985). It is traditional to provide convenient analytic formulae which describe accurately the forms of the transfer functions. For the adiabatic cold dark matter model, the form adopted by Bardeen and his colleagues is

$$T_k = \frac{\ln(1 + 2.34q)}{2.34q} \left[1 + 3.89q + (16.1q)^2 + (5.46q)^3 + (6.71q)^4 \right]^{-1/4} , \quad (14.37)$$

where $q = k/(\Omega_0 h^2 \text{ Mpc}^{-1})$ (Bardeen et al., 1986).

Table 14.1. Properties of adiabatic cold dark matter perturbations which entered the particle horizon at the epoch of equality of matter and radiation energy densities

	$\Omega_0 = 0.3$	$\Omega_0 = 1$
World model	$\Omega_\Lambda = 0.7$	$\Omega_\Lambda = 0$
	$h = 0.7$	$h = 0.7$
z_{eq}	3,530	11,760
t_{eq}	47,500 years	4,277 years
Comoving horizon scale		
$r_{\text{eq}} = 2ct_{\text{eq}}/a_{\text{eq}}$	100 Mpc	26 Mpc
$M_{\text{eq}} = (\pi/6)r_{\text{eq}}^3 \rho_0$	$2.3 \times 10^{16} M_\odot$	$1.2 \times 10^{15} M_\odot$

It can be seen that the form of the spectrum is in agreement with the physical arguments presented above. The transfer function shown in Fig. 14.1a indicates that the curvature of the spectrum between the two asymptotic relations is very gradual, reflecting the rather slow change in the growth rate of the perturbations according to the Mészáros formula (12.67). Notice that primordial perturbations on all scales and masses survive into the post-recombination era in the cold dark matter picture.

This form of processed power spectrum is of particular importance and has dominated much of the discussion of structure formation. Part of the reason for this is the fact that the scale-invariant Harrison–Zeldovich spectrum appears rather naturally in the preferred inflationary scenario for the early Universe. Nonetheless, let us consider two other dark matter models which have already been mentioned.

14.3.2 Adiabatic Hot Dark Matter

In the case of the adiabatic hot dark matter model with massive neutrinos, small-scale perturbations are damped by the free-streaming of neutrinos as soon as they come through the horizon during the radiation-dominated era. The spectrum cuts off exponentially below the critical mass given by (13.15). An analytic expression for the transfer function $P(k)$ quoted by Peacock, following Bond and Szalay and Bardeen and his colleagues (Bond and Szalay, 1983; Bardeen et al., 1986) is

$$T_k = \exp(-3.9q - 2.1q^2), \quad (14.38)$$

where $q = k / (\Omega_0 h^2 \text{ Mpc}^{-1})$. Notice the exponential cut-off of the transfer function in Fig. 14.1a and the corresponding cut-off in the power spectrum in Fig. 14.1b. Again the power spectrum has a maximum on scales greater than those of clusters of galaxies, but all small-scale structure has been washed out by the free-streaming of the massive neutrinos.

14.3.3 Isocurvature Cold Dark Matter

The isocurvature modes behave quite differently from the adiabatic modes discussed above. As we asserted earlier, in the early radiation-dominated Universe when the

perturbations were on superhorizon scales, any perturbation could be decomposed into curvature and isocurvature modes. Therefore, although most current discussions of structure formation have concentrated upon the adiabatic curvature modes, the isocurvature modes may play a role. For these modes, the curvature must take the same value everywhere at a given epoch and so any perturbation in the dark matter must be compensated by the opposite perturbation in the radiation. These perturbations can be thought of as fluctuations in the local equation of state. Kolb and Turner express this in terms of fluctuations in the ratio of the number density of the dark matter species X to the entropy density s , that is, the inverse of the entropy per X particle. As noted in Sect. 10.5, the entropy per unit comoving volume is a conserved quantity as the Universe expands. For the isocurvature modes,

$$\delta(n_X/s) \neq 0 , \quad (14.39)$$

unlike the adiabatic modes for which $\delta(n_X/s) = 0$. Following Kolb and Turner, it is convenient to introduce the fractional fluctuation in (n_X/s) through the definition

$$(\delta_X)_i = \frac{\delta(n_X/s)}{(n_X/s)} . \quad (14.40)$$

Now $s \propto T^3$, and so we find

$$(\delta_X)_i = \frac{\delta n_X}{n_X} - 3 \frac{\delta T}{T} . \quad (14.41)$$

At the same time, the overall perturbation in the energy density must be zero so that there are no spatial variations of the curvature, that is,

$$\delta\varrho = \delta \left(m_X n_X + \frac{\chi a T^4}{c^2} \right) = 0 , \quad (14.42)$$

where m_X and n_X are the mass and number density of the dark matter species X. The resulting temperature perturbations are

$$\frac{\delta T}{T} = -\frac{1}{4} \frac{\varrho_X}{\varrho_{\text{rad}}} \frac{\delta n_X}{n_X} . \quad (14.43)$$

Combining (14.41) and (14.43), we find

$$\frac{\delta T}{T} = -\frac{(\delta_X)_i}{4} \left[\frac{\varrho_X/\varrho_{\text{rad}}}{1 + (3\varrho_X/4\varrho_{\text{rad}})} \right] , \quad (14.44)$$

$$\frac{\delta n_X}{n_X} = (\delta_X)_i + 3 \frac{\delta T}{T} . \quad (14.45)$$

In the very early radiation-dominated era, the inertial mass density in the radiation far exceeded that in the dark matter, and so (14.44) shows that only very small temperature perturbations were needed to provide the compensation for the

fluctuations in the cold dark matter. In other words, the perturbations were very closely isothermal. Equation (14.45) shows that the density contrast in the dark matter $\delta n_X/n_X$ was more or less constant with the primordial amplitude $(\delta_X)_i$.

As the epoch of equality was approached, however, the temperature perturbation increased according to (14.44) and so, in compensation, $\delta \varrho_X/\varrho_X$ had to decrease. Specifically, for $\varrho_X \gg \varrho_{\text{rad}}$, the temperature fluctuation tended to

$$\frac{\delta T}{T} \approx -\frac{(\delta_X)_i}{3}, \quad (14.46)$$

and the density contrast in the dark matter changed as

$$\frac{\delta n_X}{n_X} \approx \frac{4}{3} (\delta_X)_i \frac{\varrho_{\text{rad}}}{\varrho_X}. \quad (14.47)$$

These simple calculations enable us to estimate the transfer function for isocurvature perturbations. Let us first consider those perturbations which came through the horizon during the radiation era. Since $\varrho_{\text{rad}}/\varrho_X \gg 1$, these had more or less their primordial amplitudes. When they came through the horizon, the overdensity in the radiation streamed out of the density perturbations leaving density perturbations which then developed just as in the adiabatic cold dark matter perturbations. Because of the Mészáros effect, they scarcely grew until the epoch of equality of matter and radiation energy densities and then grew according to the standard growth function $f(z)$.

Perturbations with wavelengths greater than the horizon scale at the epoch of equality behaved somewhat differently. After the epoch of equality, the amplitude of the perturbations on large scales began to decline, but the temperature fluctuations had amplitude $\delta T/T \approx (\delta_X)_i/3$ and remained constant until the perturbation came through the horizon. Then, the pressure gradients associated with the entropy perturbations regenerated the perturbations in the cold dark matter until they had $\delta n_X/n_X \approx (\delta_X)_i$. As Peacock expresses it, as the photons disperse, the perturbation in the entropy density must be conserved, and so this must be transferred to the matter. After this time, they grew in amplitude just like the adiabatic cold dark matter perturbations.

The net result is that the large-scale perturbations lagged behind those on small scales by a factor of r_H/r_{eq} . The wavelength on the horizon scale is $\lambda = r_H = 3ct \propto a^{3/2}$, and so the comoving wavenumber $k = 2\pi/\lambda_0 = 2\pi/(r_H/a) \propto a^{-1/2}$. Therefore, the transfer function varied as $r_{\text{eq}}/r_H \propto a^{-1} \propto k^2$ for small k , that is, on large physical scales. It is conventional to normalise $T(k)$ to the constant value at large k , and so the transfer function $T(k)$ is the opposite of that found in the adiabatic cold dark matter model. The transfer function for this case is shown in Fig. 14.1a, which is taken from the analytic form presented by Efstathiou and Bond (Efstathiou and Bond, 1986):

$$T_k = (5.6q)^2 \left\{ 1 + \left[15.0q + (0.9q)^{3/2} + (5.6q)^2 \right]^{1.24} \right\}^{-1.24}. \quad (14.48)$$

To convert this into a power spectrum of perturbations at the present epoch, we need to multiply by the initial power spectrum. According to Efstathiou and Bond, scale-invariant entropy perturbations predicted by the theory of inflation have power spectrum $P_0(k) \propto k^{-3}$ and so, running through the apparatus of Sect. 14.2.2, we find that the power spectrum at the present epoch has slope $P(k) \propto T^2(k)P_0(k) \propto k$ on large physical scales, exactly the same result found in the case of adiabatic cold dark matter perturbations. The expected spectral shape is shown in Fig. 14.1b, normalised to have the same amplitude at small values of k , like the other curves. It can be seen that the power spectrum is expected to turn over at somewhat smaller wavenumbers than in the case of the adiabatic cold dark matter model.

14.3.4 The Subsequent Evolution

The processed power spectra of density perturbations in the dark matter shown in Fig. 14.1b developed according to relation (14.30) throughout the matter-dominated era. Linear growth of the spectrum continued until the perturbations became non-linear, $\Delta_D \sim 1$. Perturbations with the largest amplitudes attained $\Delta_D \sim 1$ first and then began to collapse to form bound systems. From the analyses of Sects. 14.2 and 14.3, the spectrum of density fluctuations was given by

$$\Delta_k \propto [k^3 P(k)]^{1/2}. \quad (14.49)$$

In the case of the *adiabatic* and *isocurvature cold dark matter* models, the processed power spectrum for large values of k was $P(k) \propto k^{n-4}$, and so for the Harrison–Zeldovich spectrum, $n = 1$, the spectrum of density fluctuations Δ_k was independent of wavelength and extended to very low masses. The spectra steepened for $k \leq 1$, meaning for larger physical scales and for very large masses they tended to $\Delta_k \propto k^2$. Thus, perturbations on small scales became non-linear first and collapsed to form low-mass bound systems.

Most of the mass of the perturbations was in the form of collisionless dark particles, and so dissipative processes, such as the release of energy by radiation or by friction and viscosity, were not important in the formation of gravitationally bound systems, which must satisfy the virial theorem (3.19). In order to achieve this, the collapsing dark matter perturbations had to lose internal kinetic energy and this could be achieved through the process of *violent relaxation*, which was first described by Lynden-Bell (Lynden-Bell, 1967). As the collapse of the dark matter perturbation got under way, large gravitational potential gradients developed, since the collapse was unlikely to be precisely spherically symmetric and there were equally significant perturbations on smaller scales, as shown by (14.49). The system relaxed under the influence of these potential gradients, and Lynden-Bell showed that the system rapidly evolved towards an equilibrium configuration in which all the masses attained the same velocity distribution. More details of this non-linear phase of structure formation are discussed in Sect. 16.1. Subsequently, energy exchange between the dark matter particles could take place by *dynamical friction*, the exchange of energy in gravitational encounters between particles, but this is a slow

process¹. According to the cold dark matter picture, these structures then began to be assembled into larger-scale systems by the processes of clustering and coalescence under the influence of perturbations on larger scales. This is the process by which the dark matter haloes of galaxies, groups and clusters were formed. The baryonic matter collapsed into these structures and, since it could lose energy by dissipative processes, stars and gas clouds began to form within the dark matter haloes.

The *hot dark matter* picture is quite different in that masses on scales less than the maximum of the processed spectra were damped out by the free-streaming of the massive neutrinos, the lowest-mass objects to form being those on the scale of clusters of galaxies or greater, as can be seen in Fig. 14.1b. As discussed in Sect. 13.7.1, non-linear asymmetric collapse led to the formation of flattened ‘pancake’ structures, into which the baryonic matter collapsed. Instabilities and fragmentation of the infalling baryonic matter led to the late formation of stars and other structures on small scales.

These models were the subject of an enormous amount of detailed computer simulation to determine how well they could reproduce the observed large-scale distribution of matter in the Universe. Beginning in the 1980s, the capabilities of large-scale computer simulation began to be realized, and it was soon appreciated that there were problems in reproducing what is observed in the sky. Figure 14.2 shows a sample of the results of some of the pioneering computer simulations of the hot and cold dark matter models carried out by Frenk and his colleagues (Frenk, 1986). The density parameter was taken to be $\Omega_0 = 0.2$ for the cold dark matter model and $\Omega_0 = 1$ for the hot dark matter model, both with $\Omega_A = 0$ reflecting the prejudices of the time. The problems with these models were as follows:

- In the *hot dark matter* picture, elongated and flattened structures were formed very effectively. The model was, in fact, too effective in producing highly clustered structures (Fig. 14.2b). Essentially everything collapsed into large clusters, and the observed Universe is not as highly structured as this (Fig. 14.2c). The baryonic matter formed pancakes within the large neutrino haloes and their evolution was similar to that of the adiabatic baryonic picture. The instabilities and fragmentation of the baryonic material in the pancakes, which resulted in the formation of galaxies and smaller structures, must have taken place rather late in this picture. It is therefore difficult to account for the early formation of stars and the subsequent early enrichment of the heavy element abundances in the interstellar media of distant galaxies and quasars.
- In the *cold dark matter* picture, large-scale structures such as galaxies and clusters of galaxies were assembled from their component parts by the dynamical processes discussed above. Figure 14.2a shows that large-scale structures indeed developed but were not as pronounced on the large scale as is observed in the local Universe. This is at least partly because gravitational clustering tends to make more symmetrical structures than the sheets and filaments of galaxies observed, for example, in the CfA survey (Fig. 14.2c). There were, however, important

¹ I have given a simple treatment of dynamical friction in astronomical systems as the gravitational analogue of the process of ionisation losses in the interactions of charged particles (Longair, 1997b).

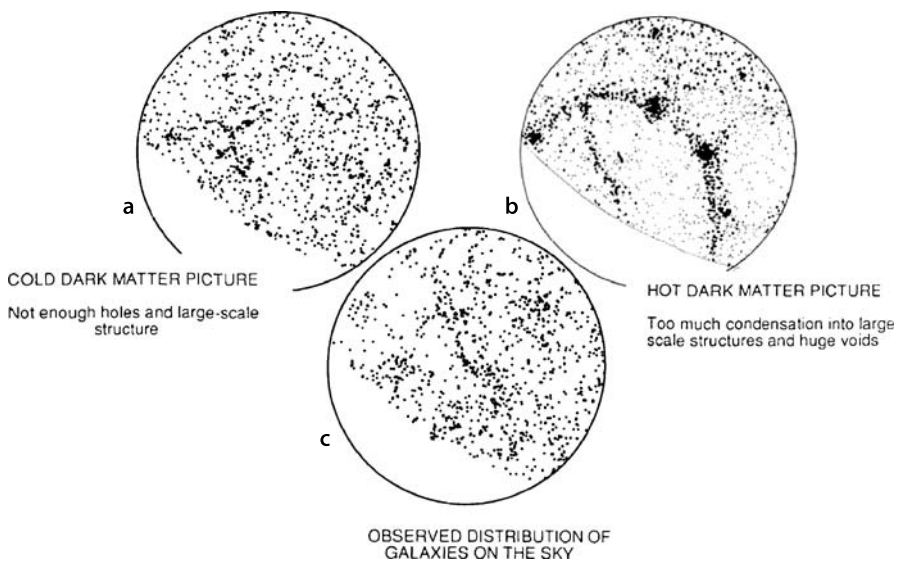


Fig. 14.2a–c. Simulations of the expectations of **a** the cold dark matter model with $\Omega_0 = 0.2$ and $\Omega_\Lambda = 0$ and **b** the hot dark matter model with $\Omega_0 = 1$ and $\Omega_\Lambda = 0$ for origin of large-scale structure of the Universe (Frenk, 1986). **c** These simulations can be compared with the large-scale distribution of galaxies observed in the Harvard-Smithsonian Center for Astrophysics Survey of Galaxies (Fig. 2.7). The unbiased cold dark matter model does not produce sufficient large-scale structure in the form of voids and filaments of galaxies, whereas the unbiased hot dark matter model produces too much clustering

successes for the cold dark matter picture. In particular, it could account for the observed two-point correlation function of galaxies $\xi(r) \propto r^{-1.8}$ over a wide range of physical scales. This form of correlation function resulted from further non-linear interactions once the perturbations had developed in amplitude to $\Delta_k > 1$. The cold dark matter picture was favoured by many of the investigators, but it was not without its problems. For example, in realisations of the cold dark matter model with $\Omega_0 = 1$, the velocity dispersion of galaxies chosen at random from the field was found to be too large (Efstathiou, 1990).

In both cases, the match to observation could be improved if it was assumed that the galaxies provided a biased view of the large-scale distribution of mass in the Universe, and this is the topic we have to tackle next.

14.4 Biasing

So far, it has been implicitly assumed that the visible parts of galaxies trace the distribution of dark matter, but one can imagine many reasons why this might not be so. The generic term for this phenomenon is *biasing*, meaning the preferential

formation of galaxies in certain regions of space rather than in others. Part of the motivation behind the introduction of biasing was to improve the agreement between the predictions of the cold dark matter scenario and the observed distribution of galaxies. In the hot dark matter picture, *anti-biasing* would be needed so that the formation of galaxies was not so highly structured.

Many possible biasing and anti-biasing mechanisms have been described by Dekel and Rees, who discuss how these can be tested by observations of the nearby Universe (Dekel, 1986; Dekel and Rees, 1987). Some biasing mechanisms come about rather naturally in the theory of the formation of galaxies, and we restrict attention to one or two of the more important of these. Kaiser realised that inherent in the description of the power spectrum of the perturbations in Sect. 14.2.1 is the assumption that the fluctuations are Gaussian with variance $\langle \Delta^2 \rangle$. Thus, the probability of encountering a density contrast Δ at some point in space is proportional to $\exp(-\Delta^2/\langle \Delta^2 \rangle)$ (Kaiser, 1984). Kaiser argued that galaxies are most likely to form in the highest peaks of the density distribution. Thus, if structures are only formed if the density contrast exceeds a certain value Δ_{crit} , galaxy formation would be biased towards the highest-density perturbations over the mean background density. This process could, for example, account for the fact that the clusters of galaxies are much more strongly clustered than galaxies in general, which is direct observational evidence for biasing (Sect. 4.1.2). As Kolb and Turner remark, the reason that all the highest mountains in the world are in the Himalayas is that they are superimposed upon the large-scale plateau, or long wavelength perturbation, caused by the plate supporting the Indian subcontinent crashing into the Asian plate (Kolb and Turner, 1990). This scenario has been worked out in detail by Peacock and Heavens and by Bardeen and his colleagues (Peacock and Heavens, 1985; Bardeen et al., 1986).

Another example of the type of astrophysics which might result in biasing involves galactic explosions which sweep gas away from the vicinity of a galaxy. This process could result in positive or negative biasing. A violent explosion can remove gas from the vicinity of the galaxy and heat it to too high a temperature for further star formation to occur in its vicinity. On the other hand, the swept-up gas may be highly compressed at the interface between the hot expanding sphere and the intergalactic gas. In the case of galactic supernova remnants, star formation can be stimulated by the passage of a strong shock wave and the same process might operate on a galactic scale (Ostriker and Cowie, 1981). This mechanism could also thicken pancakes in the hot dark matter picture.

Another biasing mechanism might be associated with gas in the voids between superclusters which might be so hot that stars and galaxies could not condense in these regions. It is evident from these examples that the understanding of biasing is an astrophysical problem and that star formation in the early phases of galaxy formation is of central importance in understanding the role it might play.

In a Gaussian model, Coles and Lucchin described how the spatial two-point correlation functions in the underlying dark matter $\xi_D(r)$ and the galaxies $\xi_{\text{gal}}(r)$ could be related by

$$\xi_{\text{gal}}(r) = b^2 \xi_D(r) , \quad (14.50)$$

where b is defined to be the *bias parameter* (Coles and Lucchin, 1995). There are a number of more-or-less equivalent definitions of the bias parameter b . From the relations between the two-point correlation function, the power spectrum and the density contrast, we see that

$$P_{\text{gal}}(k) = b^2 P_D(k) \quad \text{and} \quad \left(\frac{\delta \rho}{\rho} \right)_{\text{gal}} = b \left(\frac{\delta \rho}{\rho} \right)_D \quad \text{or} \quad \Delta_{\text{gal}} = b \Delta_D . \quad (14.51)$$

Another essentially equivalent definition often found in the literature is in terms of the variance in the counts of galaxies within a sphere of radius $8h^{-1}$ Mpc relative to the variance in the underlying mass distribution in the same sphere

$$b^2 = \frac{\sigma_8^2(\text{galaxies})}{\sigma_8^2(\text{mass})} . \quad (14.52)$$

The value $8h^{-1}$ Mpc has been chosen since that is the scale on which the two-point correlation function for galaxies has roughly unit amplitude, $\xi(r) \sim 1$.

The introduction of the bias parameter b brought with it a number of important advantages for the cold dark matter model. The numerical simulations described by Efstathiou illustrate how the density peaks of a Gaussian random field result in a much more highly structured distribution of galaxies as compared with the underlying mass distribution (Efstathiou, 1990). Furthermore, since galaxies form preferentially in peaks of the density distribution, their random velocities are smaller than those associated with the underlying dark matter distribution. Efstathiou showed how a cold dark matter model with $b = 2.5$ could be reconciled with a number of independent aspects of the large-scale distribution of galaxies, including the amplitude and slope of the two-point correlation function and the mean velocity dispersion of galaxies in the general field (Efstathiou, 1990).

The availability of large statistical samples of galaxies such as the 2dF Galaxy Redshift Survey has enabled bias parameters to be determined for galaxies in general and for those of different luminosities, types and colours. The advantage of the very large statistical samples of galaxies in the 2dF survey is that they contain information about both the mass distribution from the peculiar velocities of the galaxies and their spatial distribution. Verde and her colleagues have shown how the 2dF redshift survey can be used to estimate the bias to the second order in the bias parameter b from these data. In their analysis, the density contrast in the galaxies and dark matter are written to the second order as

$$\Delta_{\text{gal}} = b_1 \Delta_D + b_2 \Delta_D^2 . \quad (14.53)$$

Their procedure involves determining the bispectrum of the galaxy distribution, which is related to the Fourier transform of the three-point correlation function (Verde et al., 2002). The important result of their analysis is that the overall linear bias parameter b_1 is close to unity, specifically $b_1 = 1.04 \pm 0.11$, and the non-linear bias parameter consistent with zero, $b_2 = -0.054 \pm 0.08$. This analysis refers to the distribution of all galaxies on scales between roughly $5h^{-1}$ and $30h^{-1}$ Mpc. As

Verde and her colleagues remark, it is ironic that the linear bias parameter is so close to unity, which was the assumption used in early studies of structure formation and which was only brought into question as a result of the problems of reconciling the correlation function of galaxies with the predictions of the dark matter models.

Although the distribution of galaxies overall is unbiased on large scales, this does not exclude the possibility that there is bias on small scales or for different classes of galaxies, which is inevitably the case in, for example, accounting for the morphology-clustering relation described by Dressler (see Fig. 3.4) (Dressler, 1980). The analyses by Norberg and his colleagues have demonstrated how the bias parameter depends upon the luminosities and spectral types of the galaxies (Norberg et al., 2001, 2002). Figure 14.3a shows the dependence of the clustering scale r_0 , defined by the relation $\xi = (r/r_0)^\gamma$ as in (2.7) and (14.1), upon the absolute magnitudes, or luminosities, of the galaxies. There is a clear variation of the bias parameter b with absolute luminosity in the sense that the most luminous galaxies are more strongly correlated than galaxies in general (Norberg et al., 2001). The correlation can be described by the relation

$$b/b^* = 0.85 + 0.15 L/L^*. \quad (14.54)$$

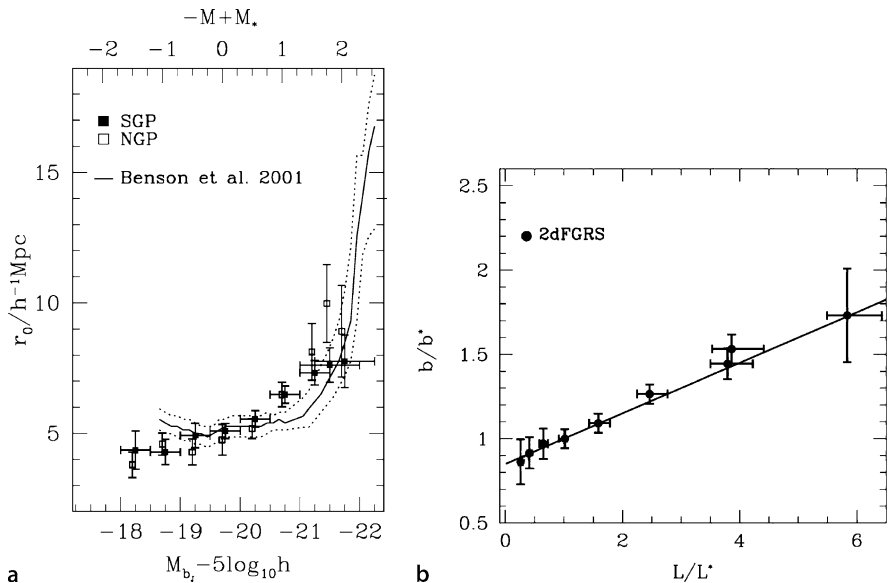


Fig. 14.3. **a** The characteristic correlation length r_0 for samples of galaxies of different luminosities selected from the 2dF Galaxy Redshift Survey (Norberg et al., 2001). The correlation scales for the Northern and Southern Galactic Pole regions are shown separately. Solid line: the predicted relation from simulations carried out by Benson and his colleagues (Benson et al., 2001). **b** Variation of the bias parameter b as a function of luminosity relative to the value b^* for galaxies with ‘break luminosity’ L^* . The dependence on luminosity can be described by $b/b^* = 0.85 + 0.15 L/L^*$ (solid line) (Norberg et al., 2001)

Norberg and his colleagues also examined the dependence of the bias parameter upon the spectral type of the galaxies. The sample was divided into galaxies with strong emission lines, which are associated with spiral, or late-type, galaxies and those without strong emission lines which are identified with elliptical, or early type, galaxies. Both classes of galaxy showed the same dependence of bias parameter upon luminosity as in Fig. 14.3b, although the amplitude of the correlation function was about 50% higher for the early types as compared with the late-type galaxies (Norberg et al., 2002).

It is interesting to compare these results with the earlier heroic analysis of Peacock and Dodds, who used eight separate data sets in their reconstruction of the power spectrum of galaxies at the present epoch (Peacock and Dodds, 1994). Their analysis was based upon the assumption that, despite the different amplitudes of the correlation and cross-correlation functions for galaxies and clusters of galaxies, these can be derived from a single smooth initial power spectrum which has been subject to different degrees of bias. Relative bias parameters were derived which produced a best fit to a smooth power spectrum; the following values were found:

$$b_A : b_R : b_O : b_I = 4.5 : 1.9 : 1.3 : 1, \quad (14.55)$$

where the subscripts refer to the bias parameters for Abell clusters (A), radio galaxies (R), optically selected galaxies (O) and IRAS galaxies (I). We recall that the amplitudes of the correlation functions are related by the square of the bias parameter (14.28), and so these values reflect well-known features of the relative clustering tendencies of these classes of object. Thus, the clusters of galaxies are much more strongly correlated than galaxies in general (Sect. 4.1.2), and radio galaxies tend to belong to groups and clusters of galaxies. The IRAS galaxies are strong dust emitters and so are preferentially associated with spiral and starburst galaxies. Since the spiral galaxies tend to avoid groups and clusters of galaxies, the IRAS sample displays the weakest clustering. These results are consistent with the trends found in the analysis of Norberg and his colleagues discussed above (Norberg et al., 2001).

14.5 Reconstructing the Processed Initial Power Spectrum

We are now in a position to attempt to invert the observational data to determine the form of the processed initial power spectrum which was the subject of Sect. 14.3 and compare it with the predictions of models such as those illustrated in Fig. 14.1. The remarkable results of the 2dF Galaxy Redshift Survey, or 2dF-GRS for short, are undoubtedly a landmark in these studies, and the major paper by Cole and his colleagues is essential reading (Cole et al., 2005). A large 2dF-GRS team of expert collaborators was involved in the analyses of the huge data set, which comprises 221,414 galaxies with measured redshifts. This meant that very thorough investigations could be made of these data and the analysis procedures. Here, there is only scope to highlight some of the important features of the analysis.

From the methodological point of view, a key factor in the analysis of the data was taking proper quantitative account of the many selection effects which

are inevitably present in such a data set and assessing their impact upon the final result. The 2dF-GRS team adopted the approach of first estimating all the selection functions and then understanding the effects of these upon mock catalogues which had similar clustering and other properties to the galaxies observed in the sample. This procedure enabled quantitative estimates of the magnitude of many potential biases to be estimated.

14.5.1 Redshift Biases

An example of the types of bias which had to be taken into account is the use of the galaxy redshift data. In the simplest picture, the redshifts provide estimates of the distances of the galaxies according to Hubble's law $r = cz/H_0$, but these distance estimates have to be corrected for the effects of *redshift bias*. This arises in two ways. First, the ‘fingers of God’ seen in large redshift surveys, such as the Harvard–CfA survey (Fig. 2.7), significantly alter the cosmological redshifts of the galaxies in clusters such that the galaxies would be shifted from their true spatial positions, reducing the amplitude of the correlation function.

The second effect is associated with the fact that large-scale density perturbations induce potential motions which can be approximated by the expression discussed in Sect. 11.5,

$$\delta v = H_0 r \Omega_0^{0.6} \left(\frac{\delta \varrho}{\varrho} \right) . \quad (14.56)$$

As a result, galaxies are expected to be observed ‘falling into’ large-scale density perturbations, and so the projected velocity component along the line of sight differs from that associated with its cosmological redshift. For large scales, on which the linear relation (14.56) is valid, Kaiser showed how this redshift bias could be estimated and eliminated from the inferred two-point correlation functions (Kaiser, 1987).

The 2dF data set has been used by Peacock and his collaborators both to measure the magnitude of redshift distortions and to make an independent estimate of the value of Ω_0 on scales greater than those of clusters of galaxies (Peacock et al., 2001). Two-dimensional correlation functions in the radial (π) and transverse (σ) directions are shown as a two-dimensional plot in Fig. 14.4 for a sample of 141,000 galaxies from the 2dF-Galaxy Redshift Survey. The stretching of the correlation function along the central vertical axis is due to the velocity dispersion of galaxies in groups and clusters, that is, the ‘fingers of God’. If there were no infall of galaxies into large-scale structures, the contours away from the vertical axis would be circular, meaning that the correlated structures have the same dimensions in the radial and transverse directions. It can be seen that the two-dimensional correlation function is flattened in the radial direction, and this is associated with the infall of galaxies on either side of the cluster in the radial direction. On the near side of the typical perturbation, the redshift is increased because of infall, whereas on the far side it is decreased for the same reason. This means that the distances derived from application of Hubble’s

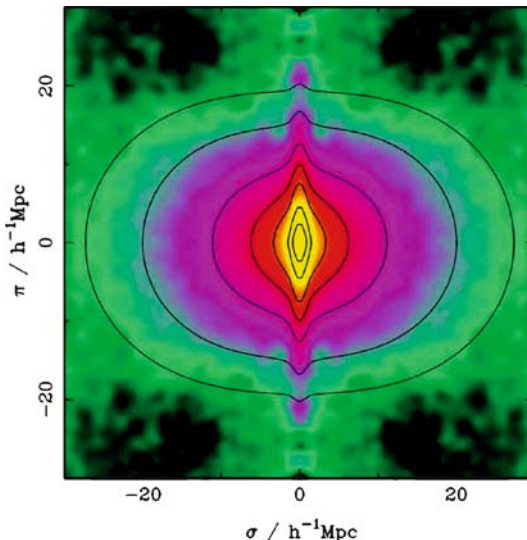


Fig. 14.4. The two-dimensional correlation function for galaxies selected from the 2dF Galaxy Redshift Survey, $\xi(\sigma, \pi)$, plotted as a function of the inferred transverse (σ) and radial (π) pair separation. To illustrate deviations from circular symmetry, the data from the first quadrant have been repeated with reflection in both axes. This plot shows clearly the redshift distortions associated with the ‘fingers of God’ elongations along the central vertical axis and the coherent Kaiser flattening of the correlation function in the radial direction at large radii (Peacock et al., 2001)

law decrease the actual dimension of the perturbation in the radial direction. From the observed flattening of the two-dimensional correlation function, Peacock and his colleagues concluded that

$$\Omega_0^{0.6}/b = 0.43 \pm 0.07 . \quad (14.57)$$

The analysis of Verde and her colleagues showed that for galaxies in general the bias parameter b is very close to unity (Verde et al., 2002) and so the dark matter density parameter can be found, $\Omega_0 = 0.25 \pm 0.06$, consistent with the estimates discussed in Sect. 8.7. This is undoubtedly among the most powerful pieces of evidence on the value of the density parameter Ω_0 because it refers to the distribution of gravitating mass on very large scales, typically $\sim 20h^{-1}$ Mpc, in which the perturbations are still in the linear regime.

14.5.2 Non-Linear Development of Density Perturbations

It is evident from the power-law form of the two-point correlation function $\xi(r) = (r/r_0)^{-1.8}$ that on scales much larger than the characteristic length scale r_0 , the perturbations are still in the linear stage of development and so provide directly information about the form of the processed initial power spectrum. On scales

$r \leq r_0$, the perturbations become non-linear and it might seem more difficult to recover information about the processed power spectrum on these scales. An important insight was provided by Hamilton and his colleagues who showed how it is possible to relate the observed spectrum of perturbations in the non-linear regime, $\xi(r) \geq 1$, to the processed initial spectrum in the linear regime (Hamilton et al., 1991).

The idea is that the evolution of the perturbations into the non-linear regime can be followed using the types of argument used in Sect. 11.4.2 and illustrated in Fig. 11.2. The perturbation behaves like a little closed universe which reaches maximum size at some epoch, known as the ‘turnround’ epoch, after which it collapses to form a bound structure. According to the arguments of Sect. 16.1, a bound structure which satisfies the virial theorem is formed when a perturbation has collapsed to half the dimension it achieved at the turnaround epoch. By the time the virialised structure has formed, the density contrast reaches values greater than 100.

Hamilton and his colleagues showed that the evolution from the linear to the non-linear regime closely follows a self-similar solution which can be found from the pioneering numerical computations of Efstathiou and his colleagues (Efstathiou et al., 1988). Figure 14.5a shows how the amplitude of the spatial two-point correlation function changes between the linear and non-linear regimes for different values of the index of the initial power spectrum. The form of the relations can be understood from the results already derived. In the linear regime $\delta\varrho/\varrho \propto a$, and

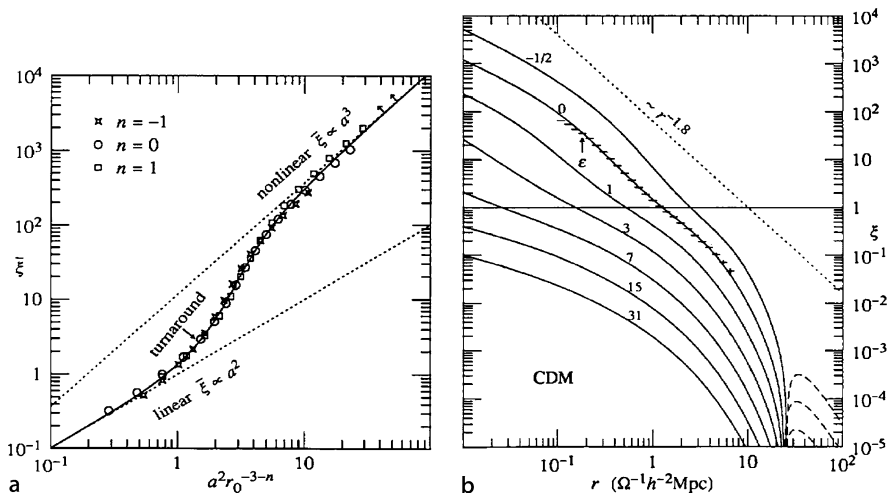


Fig. 14.5. **a** Variation of the spatial two-point correlation function with the square of the scale factor as perturbations evolve from linear to non-linear amplitudes. **b** Evolution of the spatial two-point correlation function as function of redshift. The function has been normalised to result in a correlation function which resembles the observed two-point correlation function for galaxies which has slope -1.8 . Non-linear clustering effects, as represented by the function shown in **a**, are responsible for steepening the processed initial power spectrum (Hamilton et al., 1991)

so, from (14.6) or (14.16), $\xi \propto a^2$. Once the perturbation is virialised, it forms a gravitationally bound system and so $\delta\varrho$ is a constant while the background density continues to decrease as $\varrho \propto a^{-3}$. Hence, once the system has virialised, $\delta\varrho/\varrho \propto a^3$. The self-similar solution of Fig. 14.5a shows the evolution between these two asymptotic solutions. Hamilton and his colleagues provided a convenient expression for the relation shown in Fig. 14.5a:

$$\xi = \frac{x + 0.358x^3 + 0.0236x^6}{1 + 0.0134x^3 + 0.00202x^{9/2}}, \quad \text{where } x = a^2\xi_0, \quad (14.58)$$

which has the asymptotic behaviour discussed above. The numerical simulations also showed that the assumption of virialisation when the perturbations had collapsed by a factor of two in radius from the turnaround epoch was a good one, the best-fit value corresponding to a factor of 1.8.

This formula can be used in conjunction with the expression for the evolution of the power spectrum (14.30) to work out the evolution of the two-point correlation function from its processed initial form to the present day. This is achieved by setting ξ_0 equal to the $T^2(k)P_0(k)$ in (14.58) and then evaluating ξ at different values of the scale factor a . The results presented by Hamilton and his colleagues are shown in Fig. 14.5b. This diagram shows rather beautifully the evolution of the processed initial power spectrum as a function of redshift. The horizontal line at $\xi = 1$ divides the linear from the non-linear evolution of the power spectrum. For values of ξ less than one, the evolution follows the expected linear growth on all scales, but once the perturbations become non-linear, the spectrum steepens. The example of the standard cold dark matter picture, with $\Omega_0 = 1$, has been chosen so that it reproduces the observed power spectrum of galaxies in the non-linear regime with spectral slope -1.8 .

Hamilton and his colleagues then showed how the procedure could be inverted to derive the processed initial mass function from the observed two-point correlation functions for different samples of galaxies. These authors considered only the critical world model $\Omega_0 = 1$, $\Omega_\Lambda = 0$. The procedures were extended by Peacock and Dodds for a wider range of world models with $\Omega_\Lambda = 0$ (Peacock and Dodds, 1994). Padmanabhan provides an analytic solution of this problem (Padmanabhan, 1997).

14.5.3 The Role of Baryon Perturbations

So far we have considered only the evolution of perturbations in the cold dark matter, but there are also perturbations in the baryons. Although we have argued that the baryons probably constitute only about 20% of the total mass density, they leave a perceptible imprint upon the galaxy power spectrum. The expected effects are conveniently illustrated by the analyses of Eisenstein and Hu, who provided prescriptions for the transfer functions and power spectra for models with mixed baryons and dark matter (Eisenstein and Hu, 1998).

Eisenstein and Hu's objective was to provide analytic fitting functions to the results of numerical solutions of the Boltzmann equation with a number of different

species. These simulations now agree within an accuracy of about 1% (Bond and Efstathiou, 1984; Holtzman, 1998; Hu et al., 1995b; Seljak and Zaldarriaga, 1996). It is best to consider first the case of baryon-only models, which were discussed and rejected in Sect. 12.7 since they gave rise to excessively large fluctuations in the cosmic microwave background radiation. The upper panels of Fig. 14.6 show the predicted transfer functions $T(k)$ for an open model with $\Omega_0 = 0.2$ and the critical model $\Omega_0 = 1$, in both cases with $\Omega_\Lambda = 0$. Translating into the language used in this chapter, it can be seen that the transfer function for small values of k is unity, but there are acoustic oscillations at larger wavenumbers, as illustrated schematically in Fig. 12.5. For comparison, these diagrams also show as dotted lines the cold dark matter transfer function with no baryons present. These diagrams illustrate many of the features we discussed in our analysis of the baryonic models, including the gradual damping of the oscillations between the epoch of equality and the epoch of recombination, and exponential Silk damping at large wavenumbers. Notice also the difference in the location of the wavenumber k_{eq} associated with the horizon scale at the epoch of equality, which is proportional to Ω_0 . It can be seen that the transfer functions for purely baryonic matter would result in very pronounced oscillations in the power spectrum of the distribution of galaxies at the present epoch.

The lower pair of diagrams in Fig. 14.6 shows the results of computations for mixed baryonic and cold dark matter models, again for $\Omega_0 = 0.2$ and the critical model $\Omega_0 = 1$ with $\Omega_\Lambda = 0$. In both cases, there are equal amounts of baryonic and dark matter. From the analysis of Sect. 13.7.2, the perturbations in the baryons had amplitudes much smaller than those in the cold dark matter immediately after recombination, but the acoustic oscillations were present in the baryonic component. After recombination, the perturbations in the baryons were amplified by the gravitational influence of the perturbations in the dark matter which have a smooth power spectrum with no acoustic oscillations. As a result, the amplitude of the acoustic oscillations as observed at the present day are significantly less pronounced than in the purely baryonic model because of the amplification of the perturbations on all scales by the perturbations in the dark matter. The acoustic oscillations are more prominent in the low-density model as compared with the critical model because the growth of the perturbations declines at redshift $z \sim \Omega_0^{-1}$, and so there was less time for the baryonic perturbations to be smoothed out by the growth on ‘null’ scales.

It may seem odd that we have devoted so much attention to models with no Λ -term, but this is because the models discussed above show most clearly the origin of the various features which are about to be encountered in the analysis of the 2dF Galaxy Redshift Survey power spectrum and the Sloan Digital Sky Survey. The considerations of this section make the important point that the detection of acoustic oscillations in the galaxy power spectrum is a crucial test of the standard picture of structure formation. They also are some indication of the problems of reconstructing the initial power spectrum from the observational data.

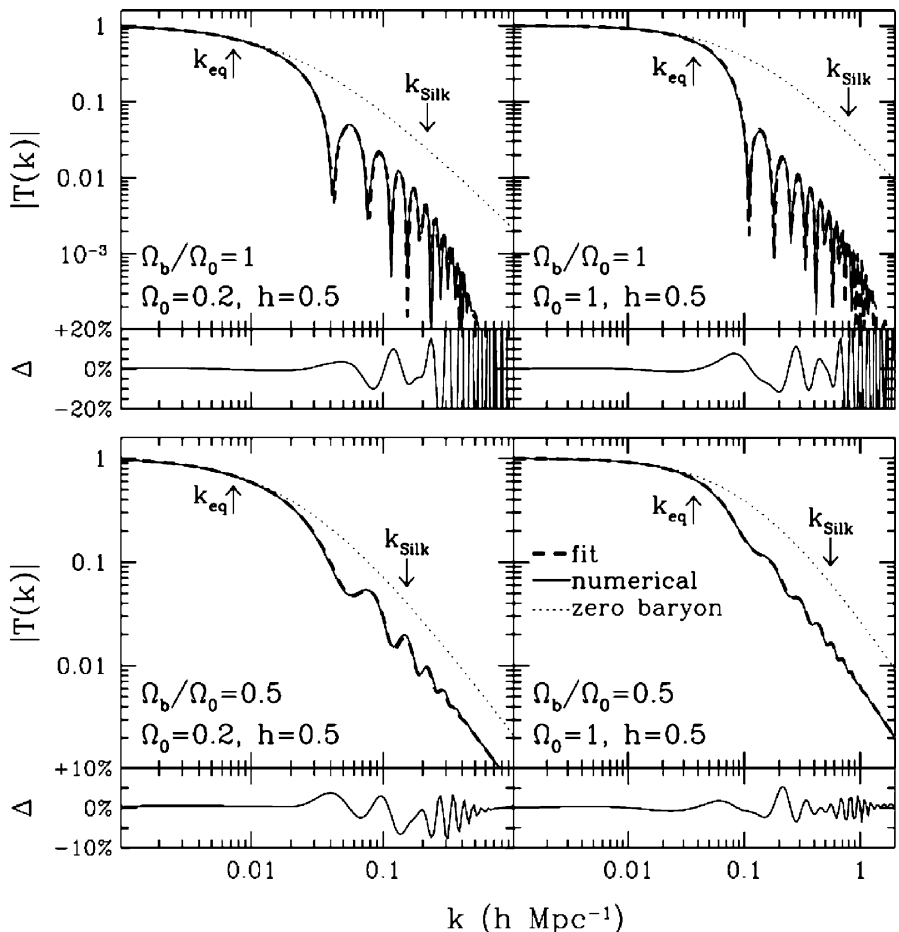


Fig. 14.6. Four examples of transfer functions for models of structure formation with baryons only (top pair of diagrams) and with mixed cold and baryonic models (bottom pair of diagrams) (Eisenstein and Hu, 1998). Eisenstein and Hu's primary objective was to present fitting functions to the transfer functions derived from numerical solutions to the Boltzmann equation for the development of mixed baryonic and cold dark matter perturbations. The numerical results are shown as solid lines and their fitting functions by dashed lines. The lower small boxes in each diagram show the percentage residuals to their fitting functions, which are always less than 10%

14.6 The Acoustic Peaks in the Power Spectrum of Galaxies

At last, we can tackle the power spectra of galaxies derived from the 2dF Galaxy Redshift Survey and the Sloan Digital Sky Survey. Before doing that, it is worthwhile paying tribute to the astrophysicists, engineers and technologists involved in both these very large undertakings. The Anglo-Australian Telescope Board was per-

suaded to make a very large investment in building the magnificent two-degree field secondary mirror structure and multi-object spectrograph for the Anglo-Australian telescope which enabled the huge numbers of redshifts of galaxies to be obtained over the 7 years of the survey from 1995 to 2002. The same remarks apply to the Sloan Digital Sky Survey, which has benefitted from the dedicated efforts of a large team of experts in all aspects of this very ambitious and successful project. Both projects have resulted in fundamental contributions to astrophysical cosmology which set the standard for what can be expected of the rigorous analysis of astronomical data and their interpretation at the beginning of the 21st century.

14.6.1 The 2dF Galaxy Redshift Survey

The analysis by Cole and his colleagues of the 2dF data set incorporates all aspects of the astrophysics which have been developed in this chapter (Cole et al., 2005). The paper is an impressive analysis of the data set of 221,414 galaxies, all with measured redshifts. The final version of the power spectrum and its uncertainties are displayed in Fig. 14.7. Corrections have been applied for the effects of biasing of different luminosities and galaxy types and for redshift bias. The overall shape of the power spectrum is similar to the form shown in Fig. 14.1b for the cold dark matter model, but it has to be somewhat modified to take account of the baryons, as illustrated by Fig. 14.6. Both the upper and lower panels show significant ‘ripples’, which are interpreted as the detection of the acoustic peaks in the power spectrum. They have the same characteristic form as those shown in the lower panels of Fig. 14.6.

In interpreting the power spectrum, the 2dF team compared the observed spectrum with the expectations of a range of cold dark matter models with different amounts of baryonic matter present. A key consideration is the degree to which the galaxies trace dark matter. In addition to the corrections for bias discussed above, semi-analytic models for the formation of galaxies of different types within the dark matter haloes have been used (Sect. 19.6). These models can account for the differences between the red and blue galaxy sequences and their associated correlations and have been thoroughly tested against the observed properties of different classes of galaxy (Benson et al., 2001). The resulting power spectrum is shown as a grey line in Fig. 14.7 and as a dark line when convolved with the window function for the survey. There is evidence that the first and second peaks of the baryon power spectrum have been detected at wavenumbers 0.06 and 0.12 respectively, corresponding to about $100h^{-1}$ and $60h^{-1}$ Mpc. Excellent agreement with the observations is obtained for the set of cosmological parameters listed in Table 14.2. The derived value of the density parameter is $\Omega_0 = 0.231 \pm 0.021$, somewhat lower than the reference value used throughout this book.

14.6.2 Sloan Digital Sky Survey

Equally impressive is the analysis of the power spectrum derived from a large sample of galaxies from the Sloan Digital Sky Survey by Eisenstein and his collaborators

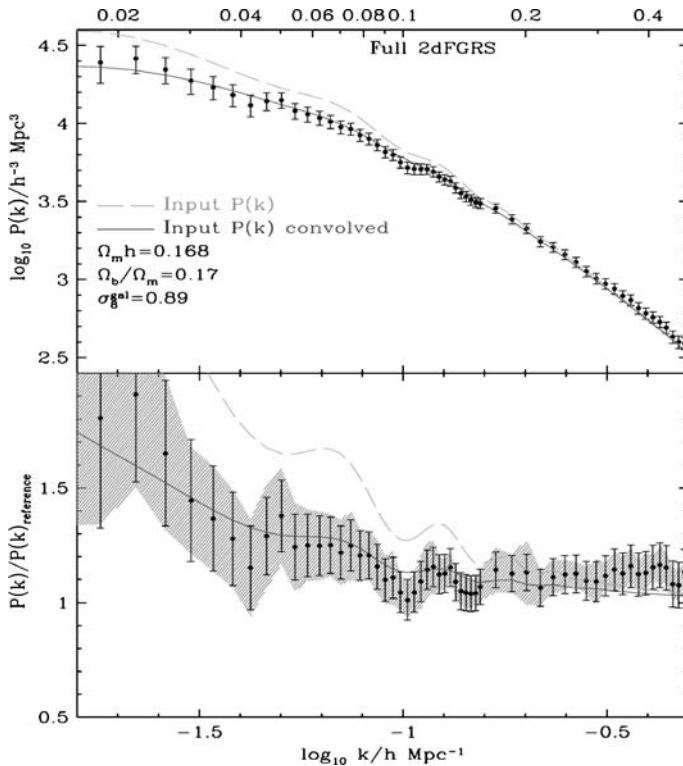


Fig. 14.7. The power spectrum of the three-dimensional distribution of galaxies in the 2dF Galaxy Redshift Survey. The points with *error bars* are the best estimates of the observed power spectrum once the biases and corrections for incompleteness are taken into account. In the *lower panel*, the data from the *upper panel* have been divided by a reference cold dark matter model, with $\Omega_D = 0.2$, $\Omega_\Lambda = 0$ and $\Omega_B = 0$, which has a smooth power spectrum. The *grey dashed line* is a best fitting model before convolution with the window function for the survey. The *solid line* shows the best fit once the model is convolved with the window function (Cole et al., 2005)

Table 14.2. Cosmological parameters derived from analysis of 2dF Galaxy Redshift Survey

Power spectrum spectral index	$n = 1$	assumed
Hubble's constant	$h = 0.72$	assumed
Neutrino masses	$m_\nu = 0$	assumed
Overall density parameter	$\Omega_0 h = 0.168 \pm 0.016$	derived
Baryon fraction	$\Omega_B / \Omega_0 = 0.185 \pm 0.046$	derived

(Eisenstein et al., 2005). In order to maximise the volume of space available for study, attention was restricted to a sample of 46,748 luminous red galaxies for which uniform selection criteria were adopted in the redshift range 0.16–0.47. The selection criteria and homogeneity of the sample were described by Hogg and his colleagues

(Hogg et al., 2005). The mean redshift of the sample was about 0.3 compared with 0.1 for the complete 2dF sample. Thus, although the statistics are smaller than in the 2dF sample, the restriction to luminous galaxies meant that better statistics were achieved over larger volumes, particularly in the crucial $50h^{-1}$ to $200h^{-1}$ Mpc range of scales.

The two-point correlation function is presented in Fig. 14.8 in the form $s^2\xi(s)$, where s is the separation of the galaxies. This form of presentation was adopted to highlight the curvature of the power spectrum on small physical scales. The clear maximum observed in the power spectrum at physical scale $100h^{-1}$ Mpc corresponds to the first acoustic peak in the power spectrum of primordial fluctuations. Its location is in good agreement with that inferred from the 2dF Galaxy Redshift Survey.

From the overall shape of the correlation function, the matter density was found to correspond to $\Omega_0 = 0.273 \pm 0.025$, if it is assumed that the dark energy is associated with the cosmological constant and the global geometry of the Universe is flat. If the scale of the acoustic peak is included in the estimates, the constraint on the spatial curvature was found to be $\Omega_k = (c/H_0)^2/\mathfrak{R}^2 = -0.010 \pm 0.009$. Notice that these conclusions are independent of the information derived from analyses of the fluctuations in the cosmic microwave background radiation.

Both the Sloan and 2dF teams recognised the central importance of the discovery of baryon oscillations in the power spectrum of galaxies. In conjunction with the very much larger amplitude perturbations observed in the cosmic microwave background

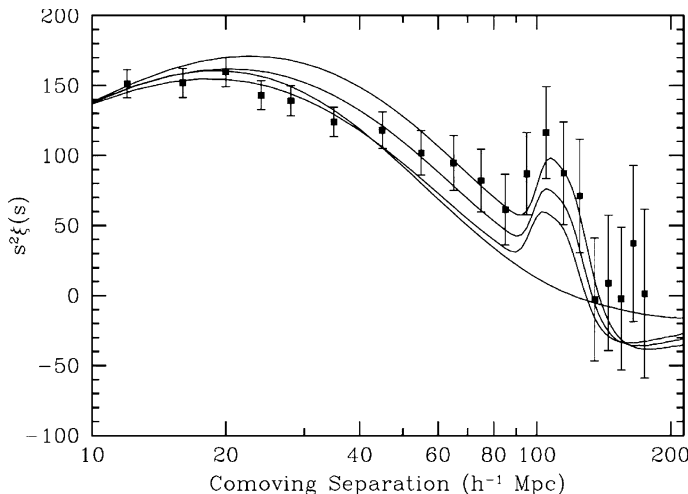


Fig. 14.8. The large-scale redshift-space correlation function of the Sloan Digital Sky Survey Luminous Red Galaxy sample plotted as the correlation function times s^2 . This presentation was chosen to show the curvature of the power spectrum at small physical scales. The models have $\Omega_0 h^2 = 0.12$ (top), 0.13 (middle) and 0.14 (bottom), all with $\Omega_B h^2 = 0.024$ and $n = 0.98$. The smooth line through the data with no acoustic peak is a pure cold dark matter model with $\Omega_0 h^2 = 0.105$ (Eisenstein et al., 2005)

radiation to be discussed in Chap. 15, they are convincing evidence for the grand design which is the central theme of this book, namely, that the structures we observe in the Universe today came about as a result of the gravitational collapse of small-amplitude perturbations generated in the early Universe.

14.7 Variations on a Theme of Cold Dark Matter

The results discussed above are remarkably compelling evidence that the standard Λ CDM model is in good agreement with the observations, even before we consider the evidence of the temperature fluctuations in the cosmic microwave background radiation. There might seem little point in developing alternative models of the formation of large-scale structure in the face of this success. The situation in 2007 is very different from 10 years ago when there was still uncertainty about whether or not the cosmological constant Λ was different from zero. Then, a number of alternative models were developed in order to account for the considerable discrepancies between the standard cold dark matter model with $\Omega_0 = 1$ and $\Omega_\Lambda = 0$ and the observations. The problems were sufficiently worrying for some experts that they published a paper in *Nature* entitled *The End of Cold Dark Matter?* (Davis et al., 1992a). A good impression of the controversial status of the subject during the 1990s is contained in the volume *Critical Dialogues in Cosmology* (Turok, 1997).

The problem facing the theorists is illustrated in Fig. 14.9, which compares the predictions of various models of structure formation with the power spectrum of galaxies estimated by Peacock and Dodds (Peacock and Dodds, 1994) and the normalisation of the power spectrum at very low wavenumbers provided by the temperature fluctuations in the cosmic microwave background radiation measured by the COBE satellite (Dodelson et al., 1996). The shape of the power spectra can be recognised from Fig. 14.2b. The best fit to the power spectrum of galaxies was provided by an open cosmology with $\Omega_0 \sim 0.2$ if the cosmological constant was zero. The problem with the favoured standard cold dark matter model with $\Omega_0 = 1$ was that it resulted in too much power at large wavenumbers. Much ingenuity was devoted to finding variants which produced a power spectrum of density perturbations similar to that of the open cold dark matter model but which retained the flat geometry favoured by proponents of the inflationary picture of the very early Universe.

The origin of the problem can be traced to the physics which determines the maximum in the power spectrum, namely the wavenumber which corresponds to the horizon scale at the epoch of equality. As shown in Sect. 10.5, the epoch of equality occurred at a redshift of

$$z_{\text{eq}} = \frac{3c^2 \Omega_0 H_0^2}{8\pi G \chi a T_0^4}, \quad (14.59)$$

while the particle horizon was $r_H = 2ct_{\text{eq}}$. Putting these together, Hu and Sugiyama found the comoving wavenumber corresponding to the maximum of the power

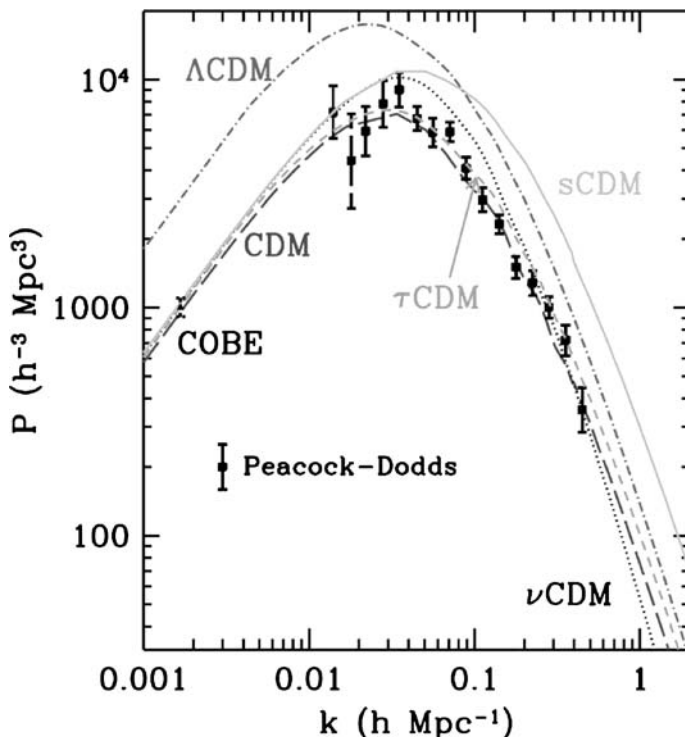


Fig. 14.9. Examples of the predicted power spectra of galaxies for different models of structure formation (Dodelson et al., 1996). The models shown involve standard cold dark matter (sCDM), open cold dark matter (CDM), cold dark matter with a finite cosmological constant (Λ CDM), cold dark matter with decaying neutrinos (τ CDM) and an alternative neutrino dark matter model (ν CDM) described by Dodelson and his colleagues. The models are compared with the power spectrum of galaxies derived by Peacock and Dodds (Peacock and Dodds, 1994) and the normalisation at small wavenumbers derived from the COBE observations of the temperature fluctuations in the cosmic microwave background radiation. The Λ CDM model has been shifted upwards for the sake of clarity. Notice that, in this presentation, the power spectrum $P(k)$ has dimensions Mpc^3 since the authors have not included the term V in the definition of the power spectrum (see (14.19))

spectrum to be

$$k_{\text{eq}} = \left(2\Omega_0 H_0^2 z_{\text{eq}}/c^2\right)^{1/2} = 7.3 \times 10^{-2} \Omega_0 h^2 \text{ Mpc}^{-1}, \quad (14.60)$$

where the temperature of the cosmic microwave background radiation has been assumed to be 2.728 K (Hu et al., 1997; Eisenstein and Hu, 1998). It can be seen that a value of $\Omega_0 = 1$ results in the maximum of the power spectrum being shifted to larger wavenumbers than the observed maximum and so to excess power on small scales. The trick is to find ways of moving the maximum, which (14.60) shows depends upon $\Omega_0 h^2$, to smaller wavenumbers. This is achieved in the open CDM

model with $\Omega_0 = 0.2$ and $h = 0.7$ and in the Λ CDM model, which also has $\Omega_0 = 0.2$ with the advantage that it includes the cosmological constant so that the geometry remains flat (CDM and Λ CDM models respectively in Fig. 14.9).

A range of these types of model was studied by Kauffmann and her collaborators (Kauffmann et al., 1999). The evolution of four of these examples is shown in Fig. 14.10, the initial perturbation spectrum being chosen to reproduce the same large-scale structure at the present epoch. It can be seen from the last column of images in Fig. 14.10 that this was successfully achieved. Notice that, although all four models result in similar large-scale structure at the present epoch, they make quite different predictions about the evolution of large-scale structure at earlier epochs.

Cold dark matter with a finite cosmological constant (Λ CDM). This model with $\Omega_0 \approx 0.25\text{--}0.3$, $\Omega_\Lambda \approx 0.7\text{--}0.75$, $n \approx 1$ has become the industry standard for the formation of large-scale structure and has been dealt with *in extenso* in the discussion earlier in this chapter.

Open cold dark matter (OCDM). As the second row of Fig. 14.10 shows, the open cold dark matter model with $\Omega_0 \approx 0.2$, $\Omega_\Lambda = 0$ has an evolutionary history very similar to that of the standard Λ CDM model. The reason for this is that there is not a great deal of difference in the dynamics of the underlying model as compared with the open cold dark matter model until late epochs. The concern with this picture was that proponents of the inflationary Universe much preferred the geometry of the Universe to be flat.

Standard cold dark matter (SCDM). The standard CDM model with $\Omega_0 = 1$, $\Omega_\Lambda = 0$ could only be made consistent with the present observed large-scale structure by adopting a low value of Hubble's constant, $h = 0.5$, so that a lower value of Ωh^2 is obtained, and a value of $\sigma_8 = 0.5$, lower than the present best estimates $\sigma_8 = 0.9$. Reducing σ_8 corresponds to increasing the bias parameter, as was found by Efstathiou in his reconciliation of the standard cold dark matter model with the power spectrum of galaxies. The last row of Fig. 14.9 shows that agreement with the observed large-scale structure at the present day could be achieved, but there is a very much more rapid evolution of the large-scale structure over the redshift range $3 > z > 0$ than in the Λ CDM or open models.

Cold dark matter with decaying neutrinos (τ CDM). In this scenario, the objective was to enhance the radiation to matter energy densities so that the epoch of equality of matter and radiation energy densities was shifted to lower redshifts as compared with the SCDM model, mimicking the case of the open cold dark matter picture. Light element formation by primordial nucleosynthesis should not be violated, and so there could not have been additional relativistic components present in the Universe during the epoch of nucleosynthesis or the expansion rate would have increased, resulting in the excessive formation of helium-4. The trick is to suppose that there existed massive neutrino-like particles which decayed into relativistic forms of matter after the epoch of nucleosynthesis (Bond and Efstathiou, 1991; McNally and Peacock, 1995). The result would be to enhance the relativistic energy density relative to the matter energy density and so delay the epoch of equality. The model has $\Omega_0 = 1$,

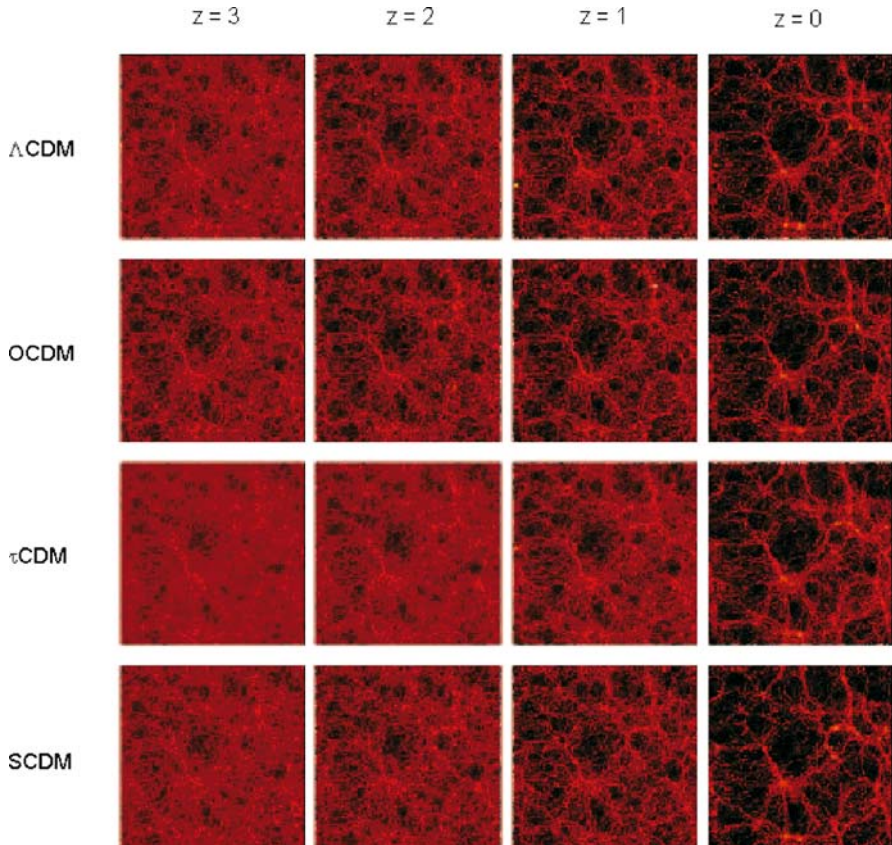


Fig. 14.10. Some examples of the predicted large-scale structure in the distribution of galaxies from supercomputer simulations by the Virgo consortium. Each panel has side $240h^{-1}\text{ Mpc}$ and the gravitational interactions of $256^3 = 1.7 \times 10^7$ particles were followed. The four models shown involve standard cold dark matter (SCDM), open cold dark matter (OCDM), cold dark matter with a finite cosmological constant (ΛCDM) and cold dark matter with decaying neutrinos (τCDM). The parameters of the models have been chosen to reproduce the observed large-scale structure in the distribution of galaxies at the present epoch (Kauffmann et al., 1999). More details of these computations can be found in the intermediate scale simulation at <http://www.mpa-garching.mpg.de/Virgo>

a low value of Hubble's constant, $h = 0.5$, and a low value of $\sigma_8 = 0.5$. The third row of Fig. 14.9 shows the resulting evolution of the large-scale structure. It is not surprising that the evolution is similar to the SCDM model with rapid evolution of the large-scale structure at small redshifts.

Besides the four models illustrated in Fig. 14.10, many other possibilities were considered. For example, a *mixed dark matter* (HCDM) model in which $\Omega_0 = 1$ and the dark matter was made up of a mixture of hot and cold dark matter could incorporate the positive features of both the hot and cold dark matter scenarios.

In the *tilted cold dark matter* model, the power spectrum of the initial fluctuations departed from the standard value $n = 1$ in order to reduce the power on small physical scales. In one variant on this scenario, there might be additional power on large physical scales, associated with primordial gravitational waves which would boost the fluctuations in the cosmic microwave radiation observed by COBE relative to the fluctuations associated with the galaxies on smaller physical scales. In the *broken-scale-invariant cold dark matter*, the initial power spectrum changed slope at the appropriate wave-number to reduce the power on small scales.

The consensus of astrophysical and cosmological opinion strongly favours the Λ CDM model as the model of choice for astrophysical cosmology. This change of perspective over the last decade has been driven by the discovery that the cosmological constant is non-zero and positive, by the considerations of large-scale structure formation discussed in this chapter and by the interpretation of spatial fluctuations in the cosmic microwave background radiation, which is the subject of the next chapter. The remaining discussion of this book will concentrate upon the Λ CDM model and its consequences.

Despite this change of perspective, it is salutary to bear in mind the lesson of Fig. 14.10. There is no limit to the ingenuity of astronomers and astrophysicists in finding ways of reconciling theory and observation. As more parameters are included in the models, the easier it will be to effect the reconciliation of theory with observation. The merit of the standard Λ CDM model is that it can account so successfully for so many different observations with a remarkably small number of cosmological parameters, which we will summarise at the end of the next chapter. We should not forget, however, that in doing so we are making prime application of Occam's razor to cosmology.

15 Fluctuations in the Cosmic Microwave Background Radiation

The power spectrum of angular fluctuations in the cosmic microwave background radiation and its polarisation properties provide a wealth of information of cosmological importance, both for the determination of cosmological parameters and for understanding the formation of structure in the Universe. This information is encoded in the intensity and polarisation maps obtained by ground-based and balloon experiments and by the outstandingly successful COBE and WMAP space observatories which were dedicated to these studies.

The objective of this chapter is to relate the models of structure formation discussed in Chap. 14 to the imprint they leave on the cosmic microwave background radiation. Observations of the background radiation are now of quite remarkable precision, and it is not without reason that these, in conjunction with observations of the large-scale distribution of galaxies discussed in the last chapter and the independent determination of cosmological parameters discussed in Chap. 8, have led to the concept of *precision cosmology*. To the amazement of astrophysicists of my generation, these observations have enabled cosmological parameters to be determined to better than 10%, in some cases with even better precision. There is every prospect that, with the next generation of space missions such as the Planck mission of ESA, the precision will approach the 1% level.

The remarkable accuracy now achieved and in prospect brings with it a number of problems of interpretation and of exposition of the physics involved. With a precision of a few percent or better, the cosmological models, the processes involved in structure formation and radiative transfer against a general relativistic background have to be understood with comparable accuracy. At the same time, observations of the cosmic microwave background radiation pose their own problems of interpretation, particularly in ensuring that foreground emissions are eliminated so that sensitivities at the microkelvin level can be achieved.

As a result, the theory of the origin of temperature fluctuations in the cosmic microwave background radiation has become a subject of considerable technical complexity. In this chapter, we address the issue of relating the fluctuations in the dark and baryonic matter at the epoch of recombination to the intensity fluctuations which they imprint upon the background radiation. The treatment will be at an introductory level. For more details of the many complexities involved in carry-

ing out a detailed analysis, the book *Modern Cosmology* by Dodelson provides an excellent introduction (Dodelson, 2003). Many reviews of these topics have been written, recent examples including those by Challinor, Hu and Dodelson, Subramanian and Zaldarriaga (Challinor, 2005; Hu and Dodelson, 2002; Subramanian, 2005; Zaldarriaga, 2004).

To obtain the accuracies required by present and future observations, the only feasible approach is to find numerical solutions of the coupled Einstein, Boltzmann and fluid dynamic equations. The fact that these computations now agree to a very high degree of precision is a tribute to a huge endeavour on the part of theorists and computational astrophysicists. One of the end results has been the creation of the CMBfast and CAMB computer codes which are publicly available and which allow the astronomer-in-the-street to study the predictions of their preferred model of structure formation.¹ Hu and Sugiyama made a valiant attempt to explain physically the origins of the many features of the analysis and gave analytic results which are accurate to 5 to 10%, and often to much better accuracy, on all angular scales (Hu and Sugiyama, 1995).

Of crucial importance in these calculations is the ionisation state of the intergalactic gas through the key epochs when it changed from being a fully ionised plasma to a neutral gas. These were the epochs when the primordial perturbations were imprinted on the background radiation. We have dealt with a number of aspects of the physics of this process in Sect. 9.3, but now we need to understand them in more detail.

15.1 The Ionisation of the Intergalactic Gas Through the Epoch of Recombination

An expression for the optical depth of fully ionised intergalactic gas due to Thomson scattering was derived in Sect. 9.3,

$$\tau = 0.035 \frac{\Omega_B}{\Omega_0^{1/2}} h z^{3/2}. \quad (15.1)$$

Using our reference values, $\Omega_0 = 0.3$, $\Omega_B = 0.05$ and $h = 0.7$, we find $\tau = 1.5 \times 10^{-3} z^{3/2}$, and so if the gas were fully ionised at redshifts $z \sim 10^3$, the optical depth would be very large. Any radiation originating at redshifts greater than the epoch of recombination was scattered many times before it could propagate unimpeded once the primordial plasma had recombined. The angular temperature fluctuations associated with primordial density perturbations originated in the rather narrow range of redshifts about that at which the optical depth of the partially ionised intergalactic gas was unity. This is not so different from the problem of radiative transfer in stellar atmospheres, the redshifts at which $\tau \sim 1$ corresponding to the stellar photosphere. To understand the properties of the fluctuations, we need to

¹ For details, see <http://www.cmbfast.org/> and <http://camb.info/>.

work out the range of redshifts from which the photons of the background radiation we observe today were last scattered. This probability distribution is given by the common expression

$$dp = e^{-\tau} d\tau \quad \text{or} \quad v(z) dz = e^{-\tau} \frac{d\tau}{dz} dz . \quad (15.2)$$

To determine the function $v(z)$, the *visibility function*, we need to know the ionisation history of the intergalactic gas through the epoch of recombination in some detail.

The problem, first analysed by Zeldovich, Kurt and Sunyaev and by Peebles, is that the recombination process was not instantaneous because the electrons could not cascade directly into the ground state of the hydrogen atom (Zeldovich et al., 1968; Peebles, 1968). There was a huge optical depth for the Lyman recombination transitions, particularly for the Lyman- α line and for Lyman continuum transitions to the ground state. Furthermore, fast reionisations took place out of excited states because of the huge reservoir of low-energy photons in the cosmic microwave background radiation. Any transition to the ground state resulted in the emission of a Lyman line or Lyman continuum photon, which immediately photoexcited or photoionised another atom in the ground state because there were very few Lyman photons in the cosmic microwave background radiation at its low temperature of less than 3000 K by this epoch. The only way the hydrogen atoms could reach the ground state was either by cosmologically redshifting the Lyman line photons or by means of the *two-photon process* in which two photons are liberated from the 2s state of hydrogen in a rare quadrupole transition. The spontaneous transition probability for this process is very small, $w = 8.23 \text{ sec}^{-1}$, but this turns out to be the dominant process which determined the rate at which the intergalactic gas recombined.

Since the pioneering studies by Zeldovich, Kurt and Sunyaev and by Peebles, more refined calculations of the degree of ionisation through the critical redshift range have been carried out (Jones and Wyse, 1985; Hu and Sugiyama, 1995; Seager et al., 2000; Chluba and Sunyaev, 2006). In the impressive paper by Seager and her colleagues, a detailed treatment of H, HeI and HeII recombination was carried out, following the populations of several hundred atomic energy levels for these species. Among the many refinements in their calculations, the researchers allowed the excited atomic level populations to depart from their equilibrium values. The results of calculations by Chluba and Sunyaev, which included corrections for induced two-photon decay, are shown in Fig. 15.1 for both the ionisation fraction and the visibility function. Figure 15.1a formalises the statement that the photons of the microwave background radiation were not last scattered at a single redshift. Rather, the maximum of the visibility function occurs at a redshift of $z = 1090$ and its half maxima lie at redshifts of $z = 1178$ and $z = 983$, corresponding to a redshift interval of $\Delta z = 195$. For our reference world model, the redshift of the maximum of the visibility function corresponded to an epoch $t = 370,000$ years from $t = 0$, and most of the photons were last scattered between the epochs $t = 320,000$ and $t = 440,000$ years.

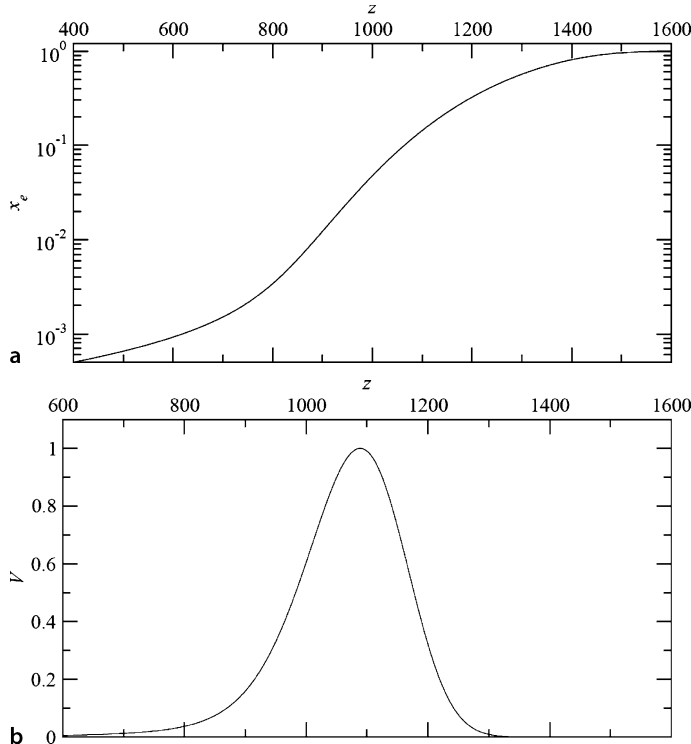


Fig. 15.1. **a** Ionisation fraction $x_e = N_e/N_H$ as a function of redshift z for the WMAP concordance values for cosmological parameters. **b** Visibility function $v(z) = e^{-\tau} d\tau/dz$ normalised to unity at maximum (Chluba and Sunyaev, 2006)

15.2 The Physical and Angular Scales of the Fluctuations

It is helpful to begin by listing the various scales and dimensions which will appear in the analysis which follows. For the sake of definiteness, we continue to use our reference set of parameters: $\Omega_0 = 0.3$, $\Omega_A = 0.7$, $\Omega_B = 0.05$, $h = 0.7$. Where necessary, we will use the spectral index $n = 1$ for the initial power spectrum. The element of comoving radial distance coordinate at redshift z during the matter-dominated era is given by (7.73):

$$dr = \frac{c dz}{H_0 [(1+z)^2(\Omega_0 z + 1) - \Omega_A z(z+2)]^{1/2}}, \quad (15.3)$$

which can be written

$$dr = \frac{c dz}{H_0 [\Omega_0(1+z)^3 + \Omega_A]^{1/2}}, \quad (15.4)$$

if $\Omega_0 + \Omega_A = 1$. Strictly speaking, we should also include in this formula the contribution of the energy density of photons and neutrinos at this redshift, $z = 1090$,

which is not much smaller than the redshift of the epoch of equality at $z = 3530$. However, because of the convergence of the comoving radial distance coordinate at very large redshifts (Fig. 7.6b), this is only a small change.²

The estimates which follow must be treated with caution. They are order-of-magnitude estimates, and some of them, for example the masses, are sensitive to factors of 2π in relating wavenumbers to physical scales. They also depend upon whether or not the relevant horizon scales are ct , $2ct$ or $3ct$, all of which are appropriate under different circumstances. The precise estimates of the dimensions and scales can only be derived by running an initial power spectrum of perturbations through numerical codes such as CMBfast. Nonetheless, the estimates discussed below reveal a number of interesting physical features of the numerical results.

15.2.1 The Last Scattering Layer

First of all, let us work out the increment of comoving radial distance coordinate corresponding to the thickness of the last scattering layer. At large redshifts, $\Omega_0 z \gg 1$, the term involving the cosmological constant can be neglected, and so

$$\Delta r = \frac{c}{H_0} \frac{\Delta z}{z^{3/2} \Omega_0^{1/2}}. \quad (15.5)$$

Taking the thickness of the last scattering layer to correspond to a redshift interval $\Delta z = 195$ at $z = 1090$, the corresponding comoving radial distance is

$$\Delta r = 16.2 (\Omega_0 h^2)^{-1/2} = 42 \text{ Mpc} \quad (15.6)$$

at the present epoch. The dark mass contained within this scale is roughly

$$M = \frac{\pi}{6} (\Delta r)^3 \rho_0 = 6.0 \times 10^{14} (\Omega_0 h^2)^{-1/2} M_\odot = 1.6 \times 10^{15} M_\odot, \quad (15.7)$$

corresponding roughly to the mass of a cluster of galaxies. The comoving scale $\Delta r = 16.2 (\Omega_0 h^2)^{-1/2}$ Mpc corresponds to a proper distance $\Delta r/(1+z)$ at redshift z and hence to an angular size

$$\theta = \frac{\Delta r}{D} = \frac{16.2 (\Omega_0 h^2)^{-1/2}}{r_{\text{Mpc}}} = 5.8 \Omega_0^{1/2} \text{ arcmin} = 3.2 \text{ arcmin}. \quad (15.8)$$

In this calculation, we have used the integral of (15.4) to estimate r_{Mpc} at $z = 1090$ and, since the geometry is flat, $D = r$.

On comoving scales less than $16.2 (\Omega_0 h^2)^{-1/2}$ Mpc = 42 Mpc at the present epoch, we expect a number of independent fluctuations to be present along the line

² The advanced version of the Cosmology Calculator developed by Dr. Edward Wright at <http://www.astro.ucla.edu/~wright/cosmolog.htm> is a useful tool for understanding the effects of changing the cosmological parameters upon distances and times.

of sight through the last scattering layer. Consequently, the random superposition of these perturbations leads to a statistical reduction in the amplitude of the observed intensity fluctuations by a factor of roughly $N^{-1/2}$, where N is the number of fluctuations along the line of sight.

We have already obtained the important result that, for primordial structures on scales greater than those of clusters of galaxies, we observe ‘slices’ through these on the last scattering layer.

15.2.2 The Silk Damping Scale

Next, we evaluate the comoving damping scale for baryonic perturbations at the epoch of recombination using (12.52) and (12.56) for the case in which the dynamics of the expansion were determined by the dark matter, $t = (2/3H_0)\Omega_0^{-1/2}z^{-1.5}$,

$$\lambda_S = \left(\frac{1}{3}\lambda ct\right)^{1/2} = \frac{0.867}{(\Omega_B h^2)^{1/2} (\Omega_0 h^2)^{1/4}} = 9.0 \text{ Mpc}. \quad (15.9)$$

This is a significant underestimate of the damping scale at recombination since it has not taken account of the dramatic increase in the mean free path of the photons as the recombination process gets under way. Hu and Sugiyama present a helpful diagram showing the impact of reionisation upon the Silk damping length (Fig. 15.2) (Hu and Sugiyama, 1995). Formally the damping scale becomes infinite, but Hu and Sugiyama convolve the damping scale with the visibility function so that the damping scale appropriate for baryonic density perturbations remains finite.

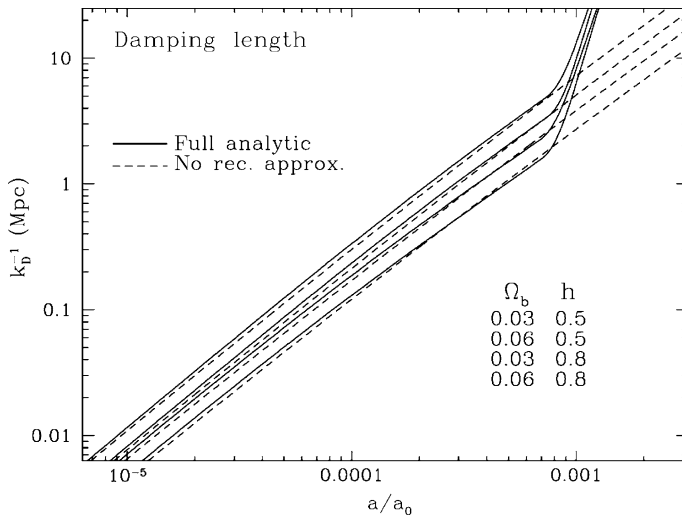


Fig. 15.2. Evolution of the Silk damping scale for primordial density perturbations. *Dashed lines*: the silk damping length without taking account of recombination. *Solid lines*: increase in the silk damping length as the process of recombination takes place at $z \approx 1090$ (Hu and Sugiyama, 1995)

15.2.3 The Sound Horizon at the Last Scattering Layer

The next key scale is the *sound horizon* at the last scattering layer, which is defined to be $\lambda_s = c_s t$, where c_s is the speed of sound and t the age of the Universe. This is the maximum distance which sound waves could travel and undergo coherent oscillations. The sound horizon therefore sets an upper limit to the wavelengths which acoustic waves could have at the epoch of recombination.

The sound speed is given by (9.34), which can be written as

$$c_s = \frac{c}{\sqrt{3}} \left(\frac{4\varrho_{\text{rad}}}{4\varrho_{\text{rad}} + 3\varrho_B} \right)^{1/2} = \frac{c}{\sqrt{3(1 + \mathcal{R})}} , \quad (15.10)$$

where $\mathcal{R} = 3\varrho_B/4\varrho_{\text{rad}}$. Comparing the inertial mass density in the baryonic matter and the radiation, we find

$$\mathcal{R} = \frac{3\varrho_B}{4\varrho_{\text{rad}}} = \frac{3\Omega_B \varrho_c c^3}{4a T_0^4 (1+z)} = 3.046 \times 10^4 \frac{\Omega_B h^2}{(1+z)} = 0.685 \quad (15.11)$$

for our reference set of cosmological parameters at redshift $z = 1090$ with $\Omega_B = 0.05$. In this case, the speed of sound on the last scattering layer was $c_s = 0.445c$.

The expression for the sound horizon therefore depends upon the values of Ω_0 and Ω_B . Using the matter-dominated dynamics of the world model for large redshifts (7.68), the dependence upon these parameters is

$$\lambda_s = c_s t = \frac{c}{\sqrt{3(1 + \mathcal{R})}} \frac{2z}{3H_0 \Omega_0^{1/2}} , \quad (15.12)$$

noting that there should be a small correction to (7.68) for the residual mass-energy of the radiation. For our reference set of parameters, including both the matter and the radiation mass-energy densities, the age of the Universe was 370,000 years at $z = 1090$ and the sound horizon had comoving distance scale $r_s = 56$ Mpc. The dark matter mass within a sphere of this diameter was

$$M = \frac{\pi}{6} r_s^3 \Omega_0 \varrho_c = 3.72 \times 10^{15} M_\odot . \quad (15.13)$$

There are two ways of thinking about the calculation we have just performed. It can be seen from (15.11) that the sound speed of the acoustic waves at $z = 1090$ is $c_s = 0.445c$, which is not so different from the sound speed of a fully relativistic plasma, $c_s = c/\sqrt{3} = 0.577c$. Thus, from the epoch when the perturbation came through the horizon to the epoch of recombination, the sound speed was of the order of $0.5c$, and then the wavelength $\lambda_s = c_s t$ corresponds to a single wavelength of oscillation between entry through the horizon and the epoch of recombination. The first maximum in the power spectrum of the temperature fluctuations is associated with this mode of oscillation. This is nicely illustrated by the schematic diagram published by Lineweaver (Fig. 15.3) (Lineweaver, 2005).

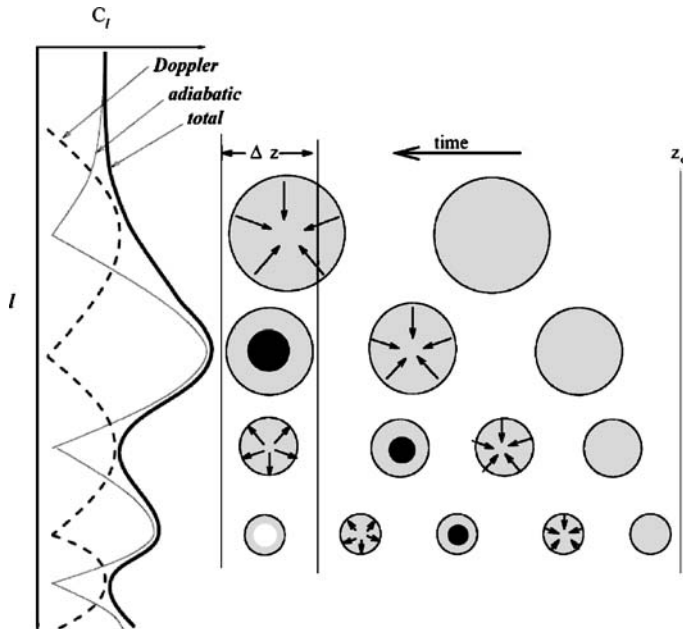


Fig. 15.3. Origin of the first few acoustic peaks in the power spectrum of the cosmic microwave background radiation. *Circles*: the response of the photon-baryon plasma to growing perturbations in cold dark matter potential wells (Lineweaver, 2005). *Dark filled circles*: maximum compression of the perturbations; *white filled circles*: maximum of rarefaction of the oscillations. z_{eq} is the epoch of equality and Δz is the thickness in redshift of the last scattering layer. Many more details of this diagram are discussed in Sects. 15.4 and 15.5

The second way of thinking about the sound horizon is that it is the maximum coherence length on the last scattering layer, and so we can work out the expected angular scale of this acoustic peak in the perturbation spectrum,

$$\theta_s \approx \frac{c_s t(1+z)}{D}. \quad (15.14)$$

For our reference set of cosmological parameters, this angular scale is 0.23° . In terms of the angular multipole l on the sky, which is introduced in the next section, there should be a maximum in the power spectrum at multipoles of $l \approx 250$, adopting the relation $l \approx \theta_s^{-1}$. Indeed, there is a very pronounced maximum in the power spectrum at this multipole (Fig. 15.4), but in view of the approximations made in this derivation, the agreement should be regarded as fortuitous.

The sound horizon is more important than the Jeans length in these studies, but the dispersion relation for baryonic perturbations during the period from the epoch of equality to the epoch of recombination is important. The interpretation of the Jeans length given in Sect. 11.3 was that it is the distance which sound waves can travel in the free-fall collapse time of the perturbation which is of order $\tau \sim (G\rho)^{-1/2}$. The difference between the sound horizon and the Jeans length in

the cosmological case is that the time scale associated with the expansion of the Universe is determined by the mass density in the dark matter, whereas the Jeans time scale for the collapse of the baryonic perturbations depends upon the mass density of the baryonic component. The acoustic oscillations, which are to play a key role in the discussion which follows, are supported by the pressure of the baryon–photon plasma within the larger-amplitude potential wells defined by the dark matter perturbations.

Inserting our reference baryon density into the expression for the baryonic Jeans length we find

$$\lambda_J = c_s \left(\frac{\pi}{G\varrho} \right)^{1/2} = \frac{c}{\sqrt{3(1+\mathcal{R})}} \left(\frac{\pi}{G\varrho} \right)^{1/2} = 2.6 \times 10^{22} \text{ m}, \quad (15.15)$$

corresponding to a comoving length scale of about 900 Mpc. The fact that the sound horizon λ_s is much less than the Jeans length λ_J means that we can use the short wavelength approximation for the dispersion relation of the acoustic waves, that is, we can write (11.26) in the form

$$\omega^2 = c_s^2 k^2 - 4\pi G\varrho = c_s^2 (k^2 - k_J^2) \approx c_s^2 k^2. \quad (15.16)$$

Thus, the waves were pure acoustic waves by the time they reached the epoch of recombination.

15.2.4 The Particle Horizon Scales

From (12.7), the proper *particle horizon scale* at the epoch of recombination in the matter-dominated limit was

$$r_H = 3ct = \frac{2c}{H_0\Omega_0^{1/2}} (1+z)^{-1.5} = 5.1 \times 10^{21} (\Omega_0 h^2)^{-1/2} = 1.34 \times 10^{22} \text{ m}, \quad (15.17)$$

corresponding to a comoving scale of about 500 Mpc. If account is taken of the radiation, this scale is reduced by 22%. Adopting a comoving scale of 500 Mpc, this subtends an angle of

$$\theta_H = \frac{r_H(1+z)}{D} = 2.1^\circ \quad (15.18)$$

at the present day for our reference parameter set, the same result we found in Sect. 12.1. As noted in that section, this means that regions of the microwave sky separated by angles greater than 2.1° could not have been in causal contact. As Figs. 2.2 and 2.3 show, despite this the COBE and WMAP experiments demonstrate that the Universe has the same appearance in all directions on this angular scale to a precision of better than one part in 10^5 .

Notice also that the baryonic Jeans length is of the same order as the horizon scale at the last scattering layer. This means that, as perturbations in the dark matter came

through the horizon, baryonic perturbations on the same scale began to oscillate as sound waves. Thus, all baryonic perturbations with wavelengths less than the horizon scale were *acoustic waves*.

Another useful figure is the particle horizon scale at the epoch of equality. For our reference values of the cosmological parameters and including the dynamics of both the matter and radiation, this occurred at an epoch 47,000 years after the initial singularity. Adopting a horizon scale of $2.5ct$ as a compromise between the values $2ct$ and $3ct$ in the radiation and matter-dominated eras, we find the comoving scale to be $\lambda_{\text{eq}} = 40 \text{ Mpc}$.

15.2.5 Summary

In a very real sense, we have been telling this story backwards because we ought to *derive* the values of the cosmological parameters from the observations rather than using the reference set to predict what we already know. My apologia for adopting this approach is that everyone knows what the denouement is going to be and doing the analysis in full generality would end up being a complicated and ultimately unnecessary exercise. The key pieces of information we obtain from this catalogue of physical and angular scales can be summarised as follows.

- The fluctuations in the cosmic microwave background radiation associated with primordial perturbations were imprinted at a redshift close to $z = 1090$ when the Universe had relatively recently entered the matter-dominated phase.
- Regions of the Universe on angular scales greater than 2° were not causally connected at the last scattering layer and so preserved information about the primordial perturbation spectrum.
- There is a wealth of structure due to different physical processes on the angular scales $0.01^\circ \leq \theta \leq 2^\circ$. These include the spectral imprint of the epoch of equality, the crucial acoustic oscillations on angular scales less than a degree, damping of the perturbations associated with Silk damping, and the finite thickness of the last scattering layer. The reason all this information is potentially available is because the baryonic perturbations were tightly coupled to the radiation but became sound waves as soon as they entered through their particle horizons. The amplitudes, phases and wavenumbers of these waves contain the wealth of information we need to reconstruct what the basic parameters of the Universe are and what must have happened in the very distant past.

A more detailed analysis of these phenomena can become formidably complicated, and it is not surprising that there is a strong temptation simply to gain insight by enjoying the remarkable powers of the CMBfast and CAMB programmes. Let us see how far we can get by simple physical arguments, relying on these programs to reinforce our intuition.

15.3 The Power Spectrum of Fluctuations in the Cosmic Microwave Background Radiation

15.3.1 The Statistical Description of the Temperature Fluctuations

Let us introduce the techniques and nomenclature used in making precise comparisons between theories and observations of temperature fluctuations in the cosmic microwave background radiation. We need to be able to deal with a continuous spectrum of temperature fluctuations, and the natural way of doing this is to take the Fourier transform of the intensity distribution. The temperature fluctuations are distributed over the surface of a sphere, and so we need the two-dimensional spherical polar equivalent of the relation between the density distribution and its power spectrum, which was given by (14.12) for the case of Fourier series in three Cartesian dimensions. For the surface of a sphere, the appropriate complete sets of orthonormal functions are the spherical harmonic functions. The first step is to make a spherical harmonic expansion of the temperature distribution over the whole sky.

$$\frac{\Delta T}{T}(\theta, \phi) = \frac{T(\theta, \phi) - T_0}{T_0} = \sum_{l=0}^{\infty} \sum_{m=-l}^{m=l} a_{lm} Y_{lm}(\theta, \phi), \quad (15.19)$$

where the normalised functions $Y_{lm}(\theta, \phi)$ are given by the expression

$$Y_{lm}(\theta, \phi) = \left[\frac{2l+1}{4\pi} \frac{(l-|m|)!}{(l+|m|)!} \right]^{1/2} P_{lm}(\cos \theta) e^{im\phi} \quad (15.20)$$

$$\times \begin{cases} (-1)^m & \text{for } m \geq 0 \\ 1 & \text{for } m < 0 \end{cases}. \quad (15.21)$$

$Y_{lm}(\theta, \phi)$ is called a spherical harmonic function of degree l and order m and $P_{lm}(\cos \theta)$ is an associated Legendre function. The polar angle, or colatitude, θ , falls in the range $0 \leq \theta \leq \pi$ and the longitude ϕ in the range $0 \leq \phi \leq 2\pi$. As can be seen from the double sum in (15.19), l takes integral values from 0 to infinity and m integral values in the range $-l \leq m \leq l$, in other words, $2l+1$ values for each degree l . With this normalisation, the orthogonality condition for the spherical harmonics is

$$\int_{4\pi} Y_{lm}^* Y_{l'm'} d\Omega = \delta_{ll'} \delta_{mm'}, \quad (15.22)$$

where the asterisk denotes the complex conjugate of the spherical harmonic and the integral is taken over the whole sky, that is, over $d\Omega = \sin \theta d\theta d\phi$, the element of a solid angle. The δ s are delta functions which take the value unity if $l = l'$ and $m = m'$, and are zero otherwise. From the orthogonality condition (15.22) the values of a_{lm} are found by multiplying the temperature distribution over the sphere by Y_{lm}^* and integrating over the sphere.

$$a_{lm} = \int_{4\pi} \frac{\Delta T}{T}(\theta, \phi) Y_{lm}^* d\Omega. \quad (15.23)$$

Peebles provides a physical interpretation of how the power on an angular scale θ is related to the power in the spherical harmonic l (Peebles, 1980). The zeros of the real and imaginary parts of Y_{lm} divide the sky into roughly rectangular cells, the minimum dimension of each cell at low latitude being close to π/l . Near the poles, the zeros of the azimuthal functions $\sin m\phi$ and $\cos m\phi$ are crowded together, but there the values of P_{lm} are close to zero. The net result is that each spherical harmonic corresponds to an angular resolution $\theta \approx \pi/l$. l is often referred to as the *multipole moment*.

In general, the temperature distribution over the sky need not be Gaussian. By this term, we mean that the phases of the waves which make up the spherical harmonic decomposition over the sky are random. As expressed by Kogut and his colleagues, the distribution of the coefficients a_{lm} should follow a Gaussian probability distribution with phases which are uniformly distributed between 0 and 2π (Kogut et al., 1996). Many theories predict that the fluctuations should obey Gaussian statistics. For example, in the inflation scenario of the early Universe, density perturbations arose from random quantum fluctuations in the inflationary era and so the perturbations should have random phases.

The temperature fluctuations on the sky might, however, display non-Gaussian features such as abrupt temperature discontinuities, intense hot spots, linear structures and so on. These types of features are predicted by theories in which large-scale structures are seeded by topological defects, cosmic strings or cosmic textures. These features would provide an important test of this class of theory. Non-Gaussian features would result in strongly correlated values of the coefficients a_{lm} rather than a Gaussian distribution of amplitudes. The analyses which have been made of the 4-year COBE data set found no evidence for non-Gaussian features over regions of sky away from the galactic plane (Kogut et al., 1996).

In what follows, it is assumed that the perturbations are Gaussian, an assumption which results in a number of simplifications in interpreting the angular power spectra. Specifically, if the fluctuations can be represented by a superposition of waves of random phase, each of the $(2l+1)$ coefficients a_{lm} provides an independent estimate of the amplitude of the temperature fluctuations associated with the multipole l . The *power spectrum* C_l is assumed to be circularly symmetric about each point on the sky, and so the mean value of $a_{lm}a_{lm}^*$, averaged over the whole sky, provides an estimate of the power associated with the multipole l .

$$C_l = \frac{1}{2l+1} \sum_m a_{lm}a_{lm}^* = \langle |a_{lm}|^2 \rangle . \quad (15.24)$$

Note that, because of the assumption that the fluctuations are Gaussian, the power spectrum C_l provides a *complete* statistical description of the temperature fluctuations.

Another way of presenting the results of these statistical analyses is to derive the *autocorrelation function* or *two-point correlation function* for the distribution of temperature over the sky in angular coordinates, the analogue of determining the

two-point correlation function for galaxies (Sect. 14.2.1):

$$C(\theta) = \left\langle \frac{\Delta T(\mathbf{i}_1)}{T} \frac{\Delta T(\mathbf{i}_2)}{T} \right\rangle, \quad (15.25)$$

where \mathbf{i}_1 and \mathbf{i}_2 are unit vectors in directions 1 and 2 and the average is taken over the sky with a fixed angular separation θ . Because of the orthogonality properties of the spherical harmonics, it follows that

$$C(\theta) = \frac{1}{4\pi} \sum_l (2l+1) C_l P_l(\cos \theta), \quad (15.26)$$

where $C_l = \langle |a_{lm}|^2 \rangle$ is the power spectrum of the temperature fluctuations on the sky as defined by (15.24). In deriving this result, we have used the addition theorem for spherical harmonics, namely, that

$$\sum_{lm} Y_{lm}^*(\mathbf{i}_1) Y_{lm}(\mathbf{i}_2) = \sum_l \frac{2l+1}{4\pi} P_l(\cos \theta), \quad (15.27)$$

where $P_l(\cos \theta)$ is the Legendre polynomial of degree l (Matthews and Walker, 1973). Expression (15.24) bears a close resemblance to the autocorrelation theorem in Fourier transform theory, namely, that if $f(x)$ has Fourier transform $F(s)$, then its autocorrelation function has Fourier transform $|F(s)|^2$ (Bracewell, 1986). The exponential has been replaced by the Legendre polynomial associated with multipole l . Note also the point emphasised by Bracewell that the autocorrelation theorem in Fourier theory wipes out all phase information (Bracewell, 1986). The same happens in (15.24) and (15.26), but we do not worry since the phases are assumed to be random and hence perfectly well-defined for our purposes. As Peebles points out, it is a matter of convenience whether one works with the angular two-point correlation function $C(\theta)$ or the power spectrum C_l (Peebles, 1993).

In presenting the angular correlation function, the quantity $l(l+1)C_l$ is commonly plotted, rather than C_l . This is a consequence of the form of the predicted temperature power spectrum for a Harrison–Zeldovich spectrum of density perturbations. As shown by Peebles and by White, Scott and Silk, if the power spectrum of the initial perturbations is of power-law form, $P(k) = Ak^n$, the values of C_l are given by

$$C_l = 2^n \pi^2 A \frac{\Gamma(3-n) \Gamma(l + \frac{n-1}{2})}{\Gamma^2(\frac{4-n}{2}) \Gamma(l + \frac{5-n}{2})}, \quad (15.28)$$

where the Γ s are Gamma-functions (Peebles, 1993; White et al., 1994). Recalling that $\Gamma(z+1) = z\Gamma(z)$, the values of C_l for the Harrison–Zeldovich spectrum, $n = 1$, are

$$C_l = \frac{8\pi A}{l(l+1)}. \quad (15.29)$$

Thus, the quantity $l(l + 1)C_l$ is expected to be independent of the multipole l for the Harrison–Zeldovich spectrum. We will derive this result by simpler means in Sect. 15.4.

Another way of expressing the amplitude of the temperature fluctuations has been used by the COBE investigators. They assume the perturbations have a flat spectrum and then work out the rms temperature fluctuation $Q_{\text{rms-ps}}$, which can be related to the best estimate of C_2 , the quadrupole component of the temperature power spectrum (White et al., 1994).

One important aspect of the above analysis is that it brings out clearly the problem of *cosmic variance*, which ultimately limits the precision with which the amplitude of the temperature fluctuations on any scale can be estimated. The spherical harmonic analysis shows that we obtain $(2l + 1)$ independent estimates of the value of C_l for a given multipole l . Thus, for small values of l , we obtain few independent samplings of the correlation function. Evidently, the precision with which value of C_l is known is proportional to $1/N^{1/2}$, where N is the number of individual estimates. Bennett and his colleagues quote an uncertainty in the values of C_l of

$$\frac{\sigma(C_l)}{C_l} \approx \left[\frac{2}{2l + 1} \right]^{1/2}. \quad (15.30)$$

(Bennett et al., 1996). According to their analysis of the 4-year COBE data set, the observations are cosmic-variance limited, rather than noise limited, for multipoles $l < 20$. Thus, there is limited prospect of improving the estimates of the power spectrum on large angular scales. For the WMAP experiment, the observations are cosmic-variance limited to multipole $l = 400$, because of the higher angular resolution of the experiment (Hinshaw et al., 2007).

15.3.2 The Power Spectrum of Fluctuations in the Intensity of the Cosmic Microwave Background Radiation

After this lengthy introduction, let us review the power spectrum of intensity fluctuations in the cosmic microwave background radiation as it was known in late 2006. In Fig. 15.4a, the power spectrum derived from the first 3 years of observation by the Wilkinson Microwave Anisotropy Probe (WMAP) is shown. The project was named after David Wilkinson, one of the pioneers of observations of the cosmic microwave background radiation. He was a key member of the project team but died before the WMAP mission came to fruition.

The power spectrum is shown in Fig. 15.4 in the form $l(l + 1)C_l/2\pi$ against multipole moment l . The WMAP results are extraordinarily impressive and have overshadowed the remarkable progress which had been made from ground- and balloon-based experiments³ before the release of the first-year data in 2003 (Bennett et al., 2003). There are many important points to be made about Fig. 15.4a. First of all, it can be

³ I have included a summary of the pre-WMAP experiments in my book *The Cosmic Century* (Longair, 2006).

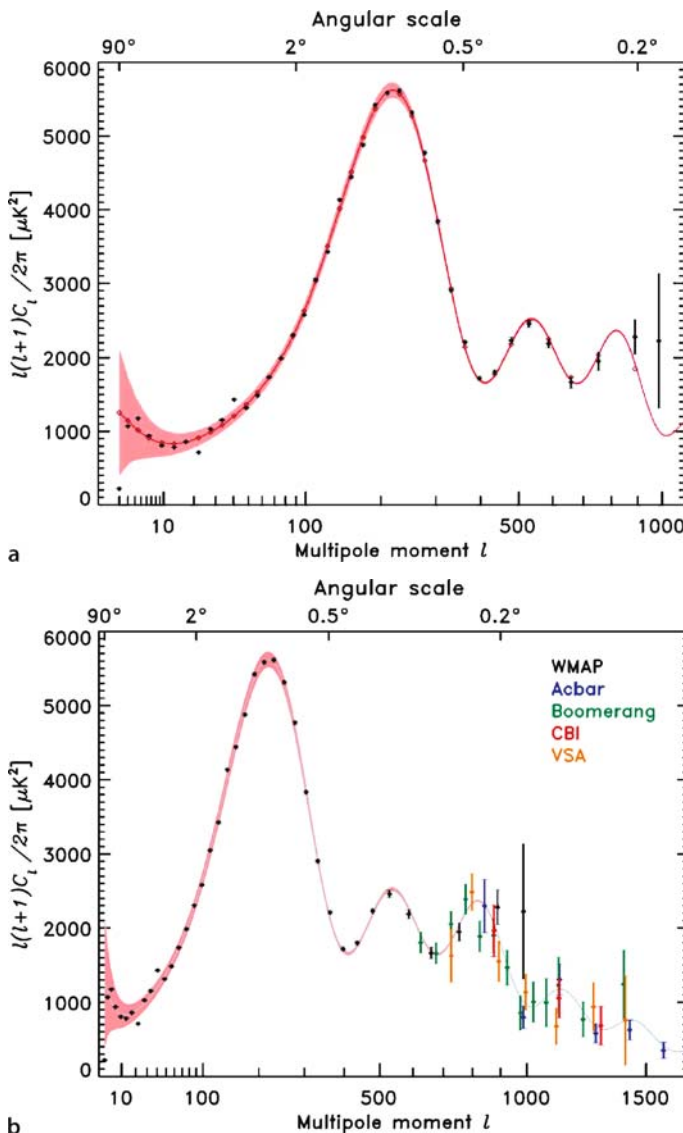


Fig. 15.4. **a** The binned 3-year angular power spectrum from the WMAP experiment (black symbols with $1 - \sigma$ noise error bars for $2 \leq l \leq 1000$). The grey band is the binned $1 - \sigma$ cosmic-variance uncertainty (Hinshaw et al., 2007). The curve is the best-fit Λ CDM model for the WMAP data alone (Spergel et al., 2007). The diamonds show the model points when binned in the same way as the data. **b** The WMAP 3-year power spectrum and other measurements of the angular power spectrum extending to larger multipoles (Hinshaw et al., 2007). The additional data, which have been restricted to those at large multipoles, are from the Boomerang (Jones et al., 2006), Acbar (Kuo et al., 2004), CBI (Readhead et al., 2004) and VSA (Dickinson et al., 2004) experiments. In both diagrams, note the variable logarithmic scale in multipole moment along the abscissa

seen that there is unambiguous evidence for the presence of acoustic oscillations in the power spectrum. The first and second peaks in the power spectrum are defined by the WMAP observations alone, whilst the third peak is also clearly detected when the WMAP observations are combined with the results of ground- and balloon-based experiments (Fig. 15.4b). The grey band represents the $1 - \sigma$ cosmic variance error. The WMAP team state that observations of the power spectrum are now variance limited to multipole moments $l = 400$ and so only marginal improvements in precision are possible over the first acoustic peak. It can be seen that the cosmic variance increases at small multipole moments and these are unlikely to decrease significantly in future.

We now need to take apart this remarkable power spectrum. We will deal separately with large, intermediate and small angular scales. Our aim is again modest – to give an impression of the wealth of astrophysics contained in these observations. The other daunting aspect of these observations is that the power spectrum is defined with such remarkable precision that theory has to attain a correspondingly high level of refinement so that effects at the 1 to 2% level are properly understood. This is a considerable theoretical challenge.

15.4 Large Angular Scales

By large angular scales we mean scales greater than about 2° . From the considerations of Sect. 15.2.4, the observed fluctuations on these scales exceeded their particle horizons at the last scattering layer and so contain unique information about the form of the unprocessed initial power spectrum. The data for angular scales greater than 2° are rather compressed in Fig. 15.4a, and so it is helpful to view them on a slightly expanded scale, as shown in Fig. 15.5. It can be seen that the power spectrum on these large angular scales is rather flat and would be consistent with the power spectrum in the form $l(l + 1)C_l$ being independent of multipole moment. It is apparent from both Figs. 15.4 and 15.5, however, that the observations are cosmic-variance limited, and so it is unlikely that we will obtain a significantly better estimate of the spectrum on these scales.

15.4.1 The Sachs–Wolfe Effect – Physical Arguments

On the very largest scales, the dominant source of intensity fluctuations results from the fact that the photons we observe originated from metric perturbations within the last scattering layer. These have dimensions greater than the thickness of the last scattering layer (Fig. 15.3). During their subsequent propagation to the Earth, although the photons pass through gravitational potential fluctuations, what they gain by falling into them is exactly compensated by the gravitational redshift coming out, so long as the perturbations continue to grow linearly with redshift, as we show below. Thus, it is the escape from density perturbations at the epoch of recombination which provides a first-order effect in the gravitational redshift. This phenomenon was first analysed by Sachs and Wolfe and is known as the *Sachs–Wolfe* effect (Sachs and Wolfe, 1967).

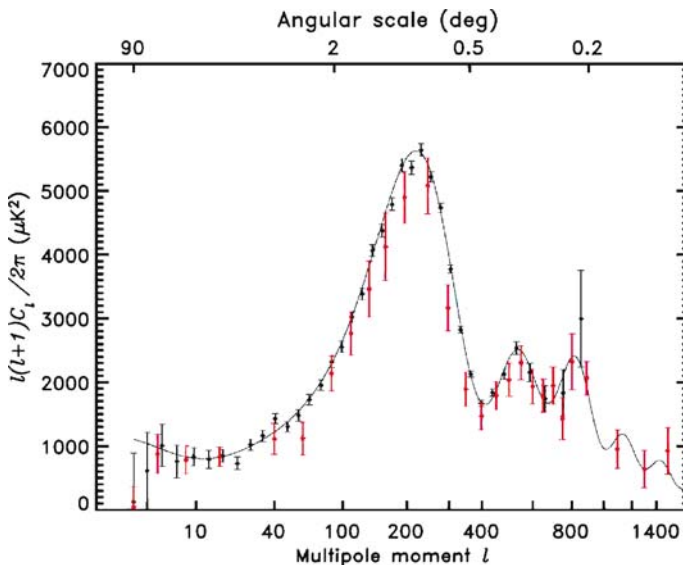


Fig. 15.5. The WMAP power spectrum from the first year of observation, compared with data published prior to WMAP, including COBE. The WMAP data are plotted with cosmic variance plus measurement uncertainties. The COBE and WMAP power spectra are in good agreement (Hinshaw et al., 2003)

The most straightforward way of approaching the problem is to use (13.9), which relates the curvature perturbations on superhorizon scales to the density contrasts in the baryonic matter, the cold dark matter and the radiation,

$$\frac{1}{3} \frac{\delta \varrho_B}{\varrho_B} = \frac{1}{3} \frac{\delta \varrho_D}{\varrho_D} = \frac{1}{4} \frac{\delta \varrho_{\text{rad}}}{\varrho_{\text{rad}}} . \quad (15.31)$$

Since $\varrho_{\text{rad}} = aT^4$, it follows that

$$\frac{\delta T}{T} = \frac{1}{3} \frac{\delta \varrho_D}{\varrho_D} . \quad (15.32)$$

We can illustrate the origin of this relation by a simple Newtonian argument which also shows how the issue of the choice of gauge enters the problem. According to the ‘Newtonian’ argument which led to (6.8), for small gravitational perturbations the frequency shift and the corresponding change in the thermodynamic temperature of the background radiation can be related to the gravitational redshift z_{grav}

$$\frac{\Delta v}{v} = \frac{\Delta T}{T} = z_{\text{grav}} = \frac{\Delta \phi}{c^2} . \quad (15.33)$$

This result is different from that found in a general relativistic treatment because we also need to take account of the time dilation of the radiation as it climbs out of

the density perturbation. This is another aspect of the problem of gauge choice in that on superhorizon scales we can choose to carry out the calculations in different gauges, as discussed in Sect. 12.3 and illustrated by (12.35) and (12.36). Because of the perturbation of the metric, the cosmic time, and hence the scale factor a , at which the fluctuations are observed, are shifted to slightly earlier cosmic times and hence to slightly hotter background temperatures. Temperature and scale factor change as $\Delta T/T = -\Delta a/a$. In the matter-dominated era $a \propto t^{2/3}$, and so the increment of cosmic time changes as $\Delta a/a = (2/3)\Delta t/t$. But $\Delta v/v = -\Delta t/t$ is the Newtonian gravitational redshift, with the result that there is a contribution to $\Delta T/T$ of $-(2/3)\Delta\phi/c^2$. The net temperature fluctuation is $\Delta T/T = \frac{1}{3}\Delta\phi/c^2$, recalling that $\Delta\phi$ is negative. The general relativistic analysis is discussed in some detail by Sachs and Wolfe, Hu, Padmanabhan and Dodelson (Sachs and Wolfe, 1967; Hu, 1996; Padmanabhan, 1993, 1996; Dodelson, 2003).

We can derive a number of important results by order-of-magnitude calculations using (14.12) and (14.13), which relate the power spectrum of the initial fluctuations to the mass spectrum. If the power spectrum of the fluctuations is taken to have the form $P(k) = |\Delta_k|^2 \propto k^n$, then the mass of an object of dimension $d \sim k^{-1}$ is proportional to k^{-3} , and so taking the integral (14.13) over wavenumber to be

$$\langle \Delta^2 \rangle \sim V |\Delta_k|^2 k^3 = V P(k) k^3 , \quad (15.34)$$

we find that

$$\langle \Delta^2 \rangle^{1/2} = \frac{\delta\varrho}{\varrho} = \frac{\delta M}{M} \propto k^{(n+3)/2} \propto M^{-(n+3)/6} . \quad (15.35)$$

Let us repeat the calculation performed in Sect. 12.3 to find the dependence of the fluctuation in the gravitational potential $\Delta\phi$ at the epoch of recombination in terms of the properties of the density perturbations observed at the present epoch. We assume that the perturbations remain small right up to the present epoch and that they developed linearly as $\Delta \propto (1+z)^{-1}$, as is appropriate for the critical $\Omega_0 = 1, \varOmega_A = 0$ model. The size of the perturbation d at redshift z corresponds to a physical size d_0 at the present epoch, such that $d(1+z) = d_0$. Therefore, the density perturbation $\Delta\varrho$ at redshift z was

$$\Delta\varrho = \frac{\Delta\varrho_0}{(1+z)} \frac{\varrho}{\varrho_0} = \Delta\varrho_0 (1+z)^2 . \quad (15.36)$$

Since $\Delta M \approx \Delta\varrho d^3$ and $d = d_0/(1+z)$, it follows that

$$\Delta\phi \approx \frac{G\Delta M}{d} \approx Gd^2\Delta\varrho \approx G\Delta\varrho_0 d_0^2 . \quad (15.37)$$

This is the first important result of this analysis – so long as the perturbations grow as $\delta\varrho/\varrho \propto (1+z)^{-1}$ to zero redshift, the perturbation of the gravitational potential is independent of the cosmic epoch, since all dependence upon redshift z

has disappeared from (15.37). This is the same result we derived in Sect. 12.3, which showed that the superhorizon potential fluctuations were frozen in on very large scales.

We now incorporate the mass spectrum into the calculation. Since $\delta\varrho_0 \propto \varrho_0 M^{-(n+3)/6}$, and $M \approx \varrho_0 d_0^3$, we find $\delta\varrho_0 \propto d_0^{-(n+3)/2}$, and hence

$$\Delta\phi \approx G\Delta\varrho_0 d_0^2 \propto d_0^{(1-n)/2}. \quad (15.38)$$

It follows from (15.32) and the expression relating the physical size d_0 of the perturbation at the present epoch to the angular size it would subtend at a large redshift, $d_0 = \theta D$, where $D = 2c/H_0\Omega_0$, that

$$\frac{\Delta T}{T} \approx \frac{1}{3} \frac{\Delta\phi}{c^2} \propto \theta^{(1-n)/2}. \quad (15.39)$$

This is the important result we have been seeking. The spectral index of the temperature fluctuations as a function of angular scale depends only upon the spectral index n of the initial power spectrum. In particular, the amplitude is independent of angular scale if $n = 1$, the spectral index of a Harrison–Zeldovich power spectrum. It is apparent from Figs. 15.4 and 15.5 that at small multipoles $l < 30$, the power spectrum is more or less independent of angular scale, consistent with the expectations of the Harrison–Zeldovich spectrum.

The power spectrum of temperature fluctuations in the cosmic microwave background radiation provides the best normalisation of the spectrum of density perturbations on very large physical scales. Perturbations on an angular scale of 10° correspond to physical dimensions of about 2400 Mpc at the present epoch, more than an order of magnitude greater than the large holes seen in the distribution of galaxies in Figs. 2.7 and 2.8 and greater than the angular scales over which the power spectra have been determined in Figs. 14.7 and 14.9. How this comparison is made is discussed in detail by Efstathiou, by Peebles and by Peacock and Dodds (Efstathiou, 1990; Peebles, 1993; Peacock and Dodds, 1994; Turner, 1997).

For the purposes of illustration, let us work out roughly the inferred galaxy power spectrum on very large scales at the present epoch using (15.33) and (15.37). On a scale of 10° , the temperature fluctuations are $\Delta T/T \approx 2 \times 10^{-5}$ and hence we can find the value of $\Delta\phi$ from (15.39). Inserting this value into (15.37) for a scale of 2400 Mpc, we can find $\delta\varrho_0$, which can be compared with the critical density $\varrho_c = 1.88 \times 10^{-26} h^2 \text{ kg m}^{-3}$. We find $\delta\varrho_0/\varrho_c = 1.7 \times 10^{-3}$ for our reference value $h = 0.7$. Then we can estimate the power spectrum on scale $d_0 = 2400 \text{ Mpc}$, or wavenumber $k \approx \pi/d_0 = 1.3 \times 10^{-3} \text{ Mpc}^{-1}$, using relation (15.34). In the definition of the units used in Fig. 14.9, the volume V is not included, and so, omitting that term from (15.34), the amplitude of the power spectrum becomes

$$P(k) \sim k^{-3} \langle \Delta^2 \rangle = k^{-3} \left(\frac{\delta\varrho_0}{\varrho_0} \right)^2 = 1300 \text{ Mpc}^3. \quad (15.40)$$

Inspection of Fig. 14.9 shows that our estimate is fortuitously close to the data point labelled ‘COBE’ presented by Dodelson and his colleagues (Dodelson et al., 1996). Obviously, a proper treatment needs to be carried out to relate the observed values of $l(l+1)C_l/2\pi$ presented in Figs. 15.4 and 15.5 to the power spectrum displayed in Fig. 14.7. The important point is that the COBE and WMAP experiments provide key information about the normalisation of the power spectrum of density perturbations on the very largest physical scales accessible to us. Furthermore, the spectrum of primordial density perturbations on the very largest scales, $k \sim 10^{-3} \text{ Mpc}^{-1}$, must be similar to those shown by the lines in Fig. 14.9 since they all have $n = 1$.

15.4.2 The Integrated Sachs–Wolfe and Rees–Sciama Effects

It will be noticed that the independence of the power spectrum upon multipole moment depends upon the assumption that the development of the perturbations is linear from the epoch of recombination to the present epoch. For models with $\Omega_0 \neq 1$ and in particular for the Λ CDM model, this is no longer true at small redshifts because the perturbations no longer grow as $\delta\rho/\rho \propto (1+z)^{-1}$, as can be seen from Figs. 11.4 and 11.5. For example, for the flat models with finite Ω_Λ , the growth rate becomes less than $\delta\rho/\rho \propto (1+z)^{-1}$ at redshifts less than $(1+z) \approx \Omega_0^{-1/3}$. In these cases, we need to integrate the Sachs–Wolfe effect over all redshifts back to the epoch of recombination. There is also a small residual effect at redshifts close to the last scattering layer since the dynamics of the Universe still contain a contribution from the inertial mass density of the radiation. These are quite small changes compared with the dominant role of the standard Sachs–Wolfe effect, but they need to be taken into account in the light of the high precision now attained by the observations of the background radiation.

Another effect which can result in additional contributions to the temperature fluctuations is the *Rees–Sciama effect*, which can be important on the very largest scales (Rees and Sciama, 1968). In this case, the depth of the gravitational potential wells increase during the time the background photons pass through the perturbations. As a result, there is not exact cancellation of the effects of infall and escape from the perturbation, causing a further contribution to the temperature power spectrum.

These effects are automatically taken into account in the numerical simulations such as CMBfast and CAMB which involve solving the coupled Einstein, Boltzmann and Euler equations.

15.4.3 Primordial Gravitational Waves

The inflationary paradigm for the very early evolution of the Universe has a number of appealing features, among which is the generic prediction that the spectrum of initial perturbations arose from quantum fluctuations of the field responsible for the inflationary expansion. As will be demonstrated in Sect. 20.5, the predicted

spectrum for the simplest model is exactly the Harrison–Zeldovich spectrum, which is an encouraging result. The importance of considering gravitational waves is that these too are likely to be generated as a result of quantum fluctuations in the inflation field. The gravitational waves only interact with matter through their quadrupole gravitational influence on the space–time through which they travel and so contain direct information about processes in the very early Universe. If these could be detected, they would provide compelling evidence in support of the inflationary paradigm. Gravitational waves behave like massless particles with equation of state $p = \frac{1}{3}\epsilon$, corresponding to a ratio of specific heats $\gamma = 4/3$. As a result, after they came through the horizon when $\lambda \sim r_H$, their energy density decreased as a^{-4} . Thus, unlike the scalar modes in the relativistic plasma, which were stabilised on coming through the horizon, the amplitudes of the tensor modes were damped adiabatically.

Just like the scalar perturbations, once the gravitational waves have been inflated to wavelengths greater than the horizon scale $\lambda \gg r_H$, they are frozen in and preserve their initial power spectrum until they re-enter their particle horizons at much later epochs. We are interested in the temperature fluctuations caused by the gravitational waves at the last scattering layer. It is simplest to think of the perturbations on superhorizon scales as gravitationally redshifting or blueshifting everything within the horizon and, as a result, they produce the same type of temperature perturbations on superhorizon scales as those produced by the Sachs–Wolfe effect. The simplest predictions of inflationary theory is that the spectrum of gravitational waves should be scale invariant with spectral index similar to that of the scalar perturbations $n \approx 1$. This is expected to be observed at multipoles less than about 100, or angular scales greater than $\theta \approx 2^\circ$, corresponding to the horizon scale at the epoch of recombination. For higher multipoles, the primordial gravitational waves decayed adiabatically from the epoch when they entered the horizon, and so the contribution of gravitational waves decreased as $\Delta_T/\Delta_s = a^{-1} \propto l^{-1}$ relative to the invariant Sachs–Wolfe power spectrum at multipoles greater than about 100.

Examples of the predicted temperature perturbation spectrum presented by Challinor are shown in Fig. 15.6 (Challinor, 2005). In this example, the ratio of tensor to scalar perturbations is taken to be one. It can be seen that the gravity wave contribution mimics that of the scalar perturbations at multipoles $l \leq 100$ and then decays at larger multipoles, the mean slope of the power spectrum reflecting the adiabatic decay of the gravity waves relative to the cold dark matter, $C_l(T)/C_l(s) \propto \Delta_T^2/\Delta_s^2 \propto l^{-2}$. Therefore, it is difficult to distinguish the contributions of scalar and tensor perturbations at multipoles $l \leq 100$ on the basis of their power spectra alone. Their polarisation signatures are, however, quite different, as we discuss in Sect. 15.8. The oscillations about the mean relation seen in Sect. 15.6 will be discussed in the next section.

Another way of seeking evidence for primordial gravitational waves is to make very precise measurements of the spectral index of the initial power spectrum. The relation between the power spectra in tensor and scalar perturbations depends

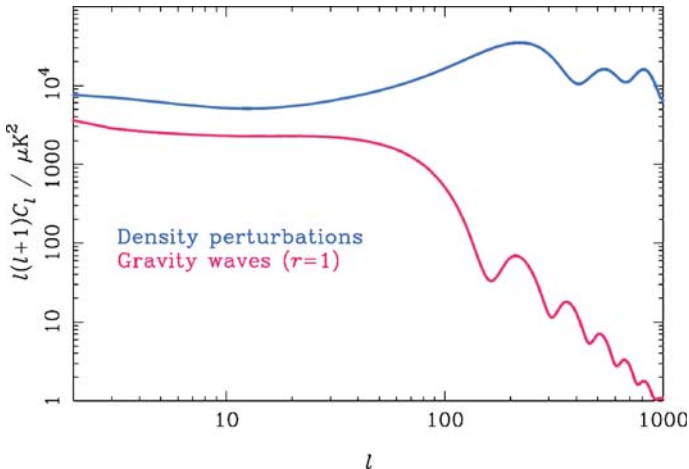


Fig. 15.6. The predicted power spectra of fluctuations in the cosmic microwave background radiation due to scalar perturbations (density perturbations; *top*) and tensor perturbations (gravity waves; *bottom*) for a tensor-to-scalar ratio $r = 1$ (Challinor, 2005)

upon the form of the inflationary potential (Starobinsky, 1985; Davis et al., 1992b; Crittenden et al., 1993). According to these theories, the ratio of the power spectra depends upon the spectral index of the scalar perturbations as

$$\frac{\Delta_T^2}{\Delta_s^2} \approx 6(1 - n), \quad (15.41)$$

where Δ_T^2 and Δ_s^2 are the density perturbations in the tensor and scalar modes respectively. Peacock provides an accessible introduction to this topic (Peacock, 2000). Thus, an important test of inflation is to measure the spectral index n of the scalar power spectrum with high precision, and this is now possible with the availability of the 3-year WMAP data set. To summarise the findings, which are dealt with in more detail in Sect. 15.9, the best-fit value of n to all the observational data is $n = 0.951^{+0.015}_{-0.019}$, suggesting that the predicted ‘tilt’ of the power spectrum may have been observed (Spergel et al., 2007).

We can set limits to the energy density of primordial gravitational waves at the present epoch from the observed power spectrum of the COBE fluctuations. As pointed out by Padmanabhan, gravitational waves at the present epoch with wavelength $\lambda \sim c/H_0$ would produce a quadrupole anisotropy in the cosmic microwave background radiation through the Sachs–Wolfe effect, and so the upper limit to the amplitude of these waves is the quadrupole anisotropy $h \sim \Delta T/T \approx 10^{-5}$ (Padmanabhan, 1993). Therefore, the upper limit to the energy density of these gravitational waves is

$$\varepsilon_G = \varrho_G c^2 \sim (32\pi G)^{-1} (\omega^2 h^2 c^2), \quad (15.42)$$

where ω is their angular frequency and h their amplitude. Setting $\omega^2 = c^2 k^2 = (4\pi^2 c^2 / \lambda^2) = 4\pi^2 H_0^2$, we find that

$$\Omega_G = \frac{8\pi G \rho}{3H_0^2} = \frac{\pi^2}{3} h^2. \quad (15.43)$$

Thus, the upper limit to gravitational waves on the scale of the horizon corresponds to $\Omega_G \leq 3 \times 10^{-10}$. This figure is far beyond the possibility of detection at the present time, and so we have to rely upon observations of the large-scale distribution of matter and radiation to advance these studies.

15.5 Intermediate Angular Scales – the Acoustic Peaks

We have already shown that oscillations in the power spectrum of temperature fluctuations are expected on scales less than the sound horizon at the last scattering layer. The pioneering papers by Sunyaev and Zeldovich and by Peebles and Yu involved only baryon cosmologies (Sunyaev and Zeldovich, 1970; Peebles and Yu, 1970). During the 1980s, corresponding results were developed for various dark matter cosmologies. Excellent surveys of the physics of temperature fluctuations in the cosmic microwave background radiation for dark matter models have been given by Hu, Sugiyama and Silk, by Efstathiou and by Dodelson (Hu and Sugiyama, 1995; Hu, 1996; Hu et al., 1997; Efstathiou, 1990; Dodelson, 2003). These authors give clear accounts of the physical origins of the various features of the predicted power spectra.

To begin with, let us ignore the presence of the dark matter perturbations, which continued to grow in amplitude once they entered the matter dominated era while perturbations in the radiation-dominated plasma became acoustic waves on the same scale once they passed through their particle horizons (Fig. 13.3b). As discussed in Sect. 15.2.3, the first acoustic peak is associated with perturbations on the scale of the sound horizon at the last scattering layer. Because of the assumption that the small perturbations are Gaussian, their probability distribution on a given mass scale is

$$p(\Delta) = \frac{1}{\sqrt{2\pi}\sigma(M)} \exp\left[-\frac{\Delta^2}{2\sigma^2(M)}\right]. \quad (15.44)$$

The perturbations in the baryonic matter which eventually collapsed to form bound structures had positive values of the density contrast Δ when the pressure support by the radiation disappeared after decoupling at the epoch of recombination. The amplitudes of these perturbations could, however, be positive or negative when they came through their particle horizons depending upon the number of wavelengths between that epoch and that of the last scattering layer. Thus, the amplitude of the baryonic perturbations at the last scattering layer depended upon the phase difference ϕ of the waves between these epochs,

$$\int d\phi = \int c_s dt. \quad (15.45)$$

The first peak in the temperature power spectrum corresponds to waves with half wavelength $\int d\phi = \pi$ between the particle horizon and the last scattering layer. We have already shown that the angular scale of the first peak is expected to occur at multipoles of order 250, and this feature has been spectacularly observed in the WMAP observations (Figs. 15.4 and 15.5).

As discussed in Sect. 15.2.3, expression (15.14)

$$\theta \approx \frac{c_s t(1+z)}{D}$$

provides a powerful tool for estimating cosmological parameters. The sound horizon on the last scattering surface is more or less a ‘rigid rod’ which depends only on the sound speed in the last scattering layer. There is a dependence upon the density parameter in the baryons Ω_B through the appearance of $\mathcal{R} = 3\varrho_B/4\varrho_{\text{rad}}$ in the expression for the sound speed, but, as we showed in Sect. 15.2.3, its value is expected to be close to $0.5c$. Then, the measured angular scale θ of the first acoustic peak provides an estimate of D , the distance parameter, at a known redshift z . Figures 7.6 and 7.7 show how D depends upon the values of the cosmological parameters. For precise estimates of the cosmological parameters, the dependence of the sound speed upon Ω_B needs to be included in the calculation. We will review the various ways in which the cosmological parameters influence the features of the power spectrum of fluctuations in the cosmic microwave background radiation in Sect. 15.9.

Let us label the wavenumber of the first acoustic peak k_1 . Then, oscillations which are $n\pi$ out of phase with the first acoustic peak also correspond to maxima in the temperature power spectrum at the epoch of recombination. There is, however, an important difference between the even and odd harmonics of k_1 . The odd harmonics correspond to the maximum compression of the waves and so to increases in the temperature, whereas the even harmonics correspond to rarefactions of the acoustic waves and so to temperature minima. Perturbations with phase differences $\pi(n + \frac{1}{2})$ relative to that of the first acoustic peak have zero amplitude at the last scattering layer and correspond to the minima in the power spectra, as discussed in Sect. 12.7.1. The acoustic peaks occur at wavenumbers corresponding to frequencies

$$\omega t_{\text{rec}} = n\pi . \quad (15.46)$$

Adopting the short wavelength dispersion relation (15.16), this condition becomes

$$c_s k_n t_{\text{rec}} = n\pi \quad k_n = \frac{n\pi}{\lambda_s} = nk_1 . \quad (15.47)$$

Thus, the acoustic peaks are expected to be evenly spaced in wavenumber in the short wavelength approximation. The separation between the acoustic peaks corresponds to $\Delta n = 1$, and so $\Delta k = \pi/\lambda_s$ provides a further estimate of the sound horizon λ_s .

The next task is to determine the amplitudes of the acoustic peaks in the power spectrum. Now, we need to take account of the fact that the acoustic oscillations take place in the presence of growing density perturbations in the dark matter, which have

greater amplitude than those in the acoustic oscillations. In dark matter scenarios, the acoustic waves are driven by the larger density perturbations in the dark matter with the same wavelength, that is, the perturbations are forced oscillations.

Let us develop the equation which describes these oscillations, neglecting the slow growth of the density perturbations in the dark matter and the time variation of the ratio of energy densities in the radiation and the matter. We begin with (11.24), but with the differences that oscillatory terms are associated with the photon-dominated plasma and the driving potential $4\pi G\varrho\Delta$ with the dark matter perturbations and that the expansion, or damping, term in $d\Delta/dt$ is neglected:

$$\frac{d^2\Delta_B}{dt^2} + \Delta_B k^2 c_s^2 = 4\pi G\varrho_D \Delta_D . \quad (15.48)$$

This procedure is similar to that which led to (13.20), but now we are interested in wave solutions rather than in growing solutions. The temperature fluctuations are related to the density perturbations by the standard adiabatic relation

$$\Theta_0 = \frac{\delta T}{T} = \frac{1}{3} \frac{\delta\varrho_B}{\varrho_B} = \frac{1}{3} \Delta_B , \quad (15.49)$$

and so

$$\frac{d^2\Theta_0}{dt^2} = \frac{4\pi G \Delta \varrho_D}{3} - k^2 c_s^2 \Theta_0 . \quad (15.50)$$

This equation can be compared with that presented by Hu⁴ (Hu, 1996):

$$\frac{d^2\Theta_0}{dt^2} = -\frac{1}{3} k^2 \Psi - k^2 c_s^2 \Theta_0 , \quad (15.51)$$

where Ψ is the gauge-invariant gravitational potential of the dark matter perturbations of wavenumber k . When anisotropic stresses are neglected, Ψ is the same as ψ in the conformal Newtonian metric (12.33) and is also equal to ϕ , which in our notation is the same as the $\Delta\phi$ used in Sect. 15.4.1. The equivalence of (15.50) and (15.51) is apparent if we write

$$-\Psi = -\Delta\phi \sim +\frac{G\Delta M}{d} \sim \frac{4\pi G d^2 \Delta \varrho_D}{3} \sim \frac{4\pi G \Delta \varrho_D}{3k^2} , \quad (15.52)$$

where $d \sim k^{-1}$ is the scale of the perturbation, recalling that Ψ and $\Delta\phi$ are negative quantities. Equation (15.51) is an approximation of the full equations for the evolution of the spectrum of acoustic oscillations which were derived by Peebles and Yu, by Hu and Sugiyama and by Dodelson (Peebles and Yu, 1970; Hu and Sugiyama, 1995; Dodelson, 2003). Notice that these authors carry out the analysis in terms of the evolution of the Fourier components of the acoustic oscillations.

⁴ Hu writes the derivatives with respect to conformal time rather than cosmic time, but this is not important since we have removed the expansion of the Universe from our illustrative calculation.

The solution of the forced-oscillator equation (15.51) is found by the usual procedure of adding the solution of the homogeneous equation

$$\frac{d^2\Theta_0}{dt^2} + k^2 c_s^2 \Theta_0 = 0 \quad (15.53)$$

to a particular integral of (15.51). By inspection, a particular integral of (15.51) is the constant value of Θ_0

$$\Theta_0 = -\frac{1}{3} \frac{\Psi}{c_s^2}. \quad (15.54)$$

Therefore, the complete solution is

$$\Theta_0(t) = A \cos \omega t + B \sin \omega t - \frac{1}{3} \frac{\Psi}{c_s^2}. \quad (15.55)$$

If $\Theta_0(0)$ and $\dot{\Theta}_0(0)$ are the amplitudes of the initial temperature fluctuation and its time derivative respectively, we can find the values of the constants A and B . Recalling that $c_s^2 = c/\sqrt{3(1+\mathcal{R})}$, we find

$$\Theta_0(t) = \left[\Theta_0(0) + \frac{(1+\mathcal{R})}{c^2} \Psi \right] \cos \omega t + \frac{1}{kc_s} \dot{\Theta}_0(0) \sin \omega t - \frac{(1+\mathcal{R})}{c^2} \Psi. \quad (15.56)$$

We require this solution at the epoch of recombination, $t = t_{\text{rec}}$, and then, setting $\omega t = kc_s t_{\text{rec}} = k\lambda_s$, we obtain the result

$$\Theta_0(t) = \left[\Theta_0(0) + \frac{(1+\mathcal{R})}{c^2} \Psi \right] \cos k\lambda_s + \frac{1}{kc_s} \dot{\Theta}_0(0) \sin k\lambda_s - \frac{(1+\mathcal{R})}{c^2} \Psi. \quad (15.57)$$

Expression (15.57) describes adiabatic temperature oscillations of the acoustic waves in the potential wells of the dark matter. Dodelson makes the important point that, because the oscillations are forced, they are not symmetrical about $\Theta_0 = 0$ but are displaced to a positive value because of the (negative) forcing term $(1+\mathcal{R})\Psi/c^2$.

In addition to the purely adiabatic effect, the matter of the perturbation must be in motion because of the continuity equation (11.13), which can be written

$$\frac{d}{dt} \left(\frac{\delta \rho_B}{\rho_B} \right) = \frac{d\Delta_B}{dt} = -\nabla \cdot \delta \mathbf{v} = -\mathbf{k} \cdot \delta \mathbf{v}. \quad (15.58)$$

The motion of the perturbations also gives rise to temperature fluctuations because of the Doppler effect such that $\Theta_1 = \delta T/T_0 = \delta v \cos \theta/c$. Therefore, (15.58) can be written in terms of the derivative of Θ_0 using (15.49):

$$3\dot{\Theta}_0(t) = -kc \Theta_1(t). \quad (15.59)$$

The temperature perturbations due to the Doppler motions at the last scattering surface are then found by differentiating (15.56) and evaluating it at $\omega t = k\lambda_s$:

$$\Theta_1(t) = \frac{3c_s}{c} \left[\Theta_0(0) + \frac{(1+\mathcal{R})}{c^2} \Psi \right] \sin k\lambda_s + \frac{3\dot{\Theta}_0(0)}{kc} \cos k\lambda_s . \quad (15.60)$$

The temperature perturbation $\Theta_0(t)$ is referred to as the ‘monopole’ contribution to the temperature fluctuation spectrum and $\Theta_1(t)$ as the ‘dipole’ term. Notice the important point that the monopole and dipole contributions are $\pi/2$ out of phase. This is illustrated schematically in Fig. 15.3.

As remarked by Hu, (15.57) and (15.60) are illuminating forms for the temperature fluctuation spectrum as a function of wavenumber k and describe ‘the main acoustic and redshift effects which dominate primary anisotropy formation’. The cosine term in (15.57) can be identified with the adiabatic modes since they had finite amplitudes when they came through the horizon at $t = 0$. In contrast, isocurvature modes had decayed to small amplitudes when they crossed the horizon, corresponding to the sine term in (15.60). As a result, the maxima of the two modes are $\pi/2$ out of phase.

Let us concentrate on the adiabatic modes, in other words, drop the sine term in (15.57) and the cosine term in (15.60). The pleasant aspect of (15.57) is that it enables us to compare the amplitude of the perturbations associated with the acoustic waves with those of the Sachs–Wolfe effect. Notice that we have not yet taken account of the gravitational redshifting of the temperature perturbations which originated within a gravitational potential well of depth Ψ . The temperature fluctuation observed by the distant observer is $\Theta_0(t) + \Psi/c^2$, recalling that Ψ is a negative quantity. As a result, what is observed is the quantity

$$\left(\frac{\Delta T}{T} \right)_{\text{eff}} = \Theta_0(t) + \frac{\Psi}{c^2} = \left[\Theta_0(0) + \frac{(1+\mathcal{R})}{c^2} \Psi \right] \cos \omega t - \frac{\mathcal{R}}{c^2} \Psi , \quad (15.61)$$

which Hu refers to as the *effective temperature perturbation*. We recall that the potential perturbation $\Psi = \Delta\phi$ is independent of cosmic epoch see (15.37). We can therefore relate the effective temperature perturbation to the amplitude of the corresponding Sachs–Wolfe perturbation when it came through the horizon at time $t = 0$. The monopole fluctuations must result in the Sachs–Wolfe temperature perturbation $(1/3)\Psi/c^2$. This enables us to relate the value of $\Theta_0(0)$ to Ψ/c^2 . Setting the effective temperature perturbation equal to $(1/3)\Psi/c^2$ at $t = 0$, we can eliminate $\Theta_0(0)$ and find that

$$\left(\frac{\Delta T}{T} \right)_{\text{eff}} = \frac{\Psi}{3c^2} (1 + 3\mathcal{R}) \cos k\lambda_s - \frac{\mathcal{R}}{c^2} \Psi . \quad (15.62)$$

This result illuminates a number of features of the complete solutions.

- First of all, in the limit $\mathcal{R} \rightarrow 0$, (15.62) reduces to

$$\left(\frac{\Delta T}{T} \right)_{\text{eff}} = \frac{\Psi}{3c^2} \cos k\lambda_s , \quad (15.63)$$

corresponding to acoustic oscillations in the photon-dominated plasma in the relativistic, or radiation-dominated, limit. There is no shift of the zero point of the oscillations since the baryonic mass is negligible compared with the inertial mass of the radiation.

- In the same limit, $\mathcal{R} \rightarrow 0$, the monopole oscillations are accompanied by dipole oscillations, the amplitude of these being given by the sine term in (15.60). In fact, we only observe a dipole temperature fluctuation of magnitude $\Theta_1/\sqrt{3}$ when averaged over the radial components of randomly oriented velocity vectors over the last scattering layer. Therefore, using (15.60) and recalling that $c_s = c/\sqrt{3}$ in the limit $\mathcal{R} \rightarrow 0$, we find

$$\left(\frac{\Delta T}{T} \right)_{\text{eff}} = \frac{\Psi}{3c^2} \sin k\lambda_s . \quad (15.64)$$

Thus, in the limit $\mathcal{R} \rightarrow 0$, the monopole and dipole temperature fluctuations are of the same amplitude, but are $\pi/2$ out of phase.

- When the inertia of the baryons can no longer be neglected, the monopole contribution becomes significantly greater than the dipole term. At maximum compression, $k\lambda_s = \pi$, the amplitude of the observed temperature fluctuation is $(1 + 6\mathcal{R})$ times that of the Sachs–Wolfe effect. Furthermore, the amplitudes of the oscillations are asymmetric if $\mathcal{R} \neq 0$, the temperature excursions varying between $-(\Psi/c^2)(1 + 6\mathcal{R})$ for $k\lambda_s = (2n + 1)\pi$ and (Ψ/c^2) for $k\lambda_s = 2n\pi$. The presence of the baryons causes extra compression of the photon–baryon fluid at maximum compression, thus enhancing the temperature excursions of the odd-numbered maxima over the even-numbered maxima, which are associated with the maximum rarefaction of the oscillations. These results can account for the observed asymmetry between the odd and even multipoles seen in Fig. 15.4.

This simplified discussion, which has closely followed the exposition of Hu, Sugiyama and Silk, is intended to give some flavour for the various physical phenomena which have to be taken into account in understanding the origin of the temperature perturbation spectrum on angular scales $\theta \leq 1^\circ$ (Hu et al., 1997). In the full analysis, many other features have to be taken into account. Specifically:

- The predicted spectrum has to be statistically averaged over a random distribution of acoustic waves and integrated over all wavenumbers.
- The Doppler (or dipole) contributions to the fluctuation spectrum have to be included as well as the monopole contributions.
- The acoustic waves evolve in an expanding substratum in which the speed of sound and the density perturbations in the dark matter vary with time.
- The coupled Boltzmann, Einstein and Euler equations need to be integrated through the last scattering layer. Hu and Sugiyama demonstrate how results accurate to better than 5% can be achieved by analytic procedures (Hu and Sugiyama, 1995), but for the high precision now needed to match the quality of the data, numerical integration of the equations is essential.

Some examples of the results of detailed predictions by Challinor are shown in Fig. 15.7, indicating how different features of the temperature anisotropy power spectrum are sensitive to variations of the cosmological parameters (Challinor, 2005). It is a useful exercise to study the power spectra in Fig. 15.7 in some detail and to use the results we have established in this section to understand the dependences upon cosmological parameters. For example, the left-hand plot of Fig. 15.7a shows clearly the strong enhancement of the first acoustic peak as the baryon density increases.

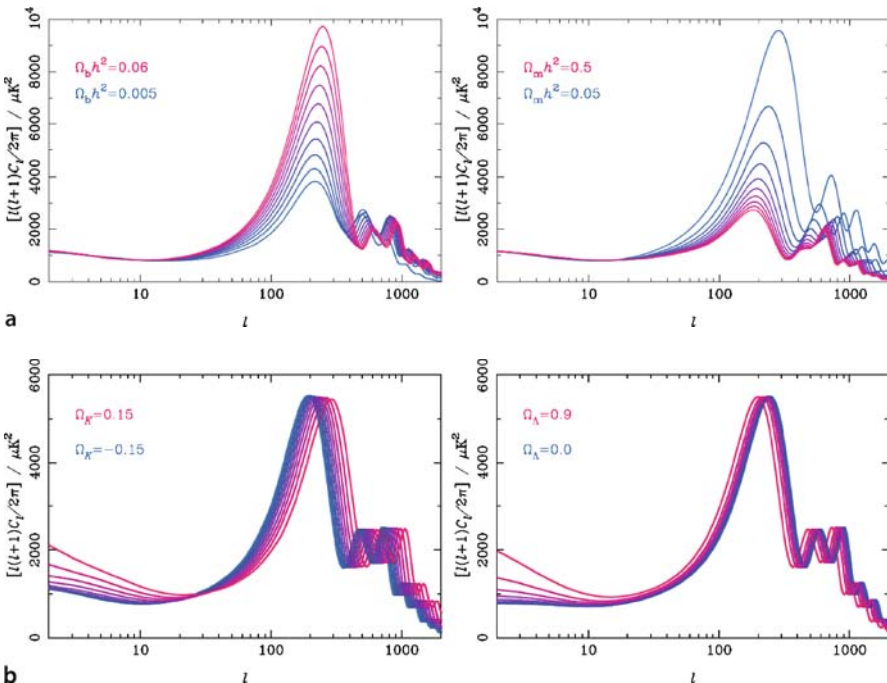


Fig. 15.7a,b. The dependence of the temperature-anisotropy power spectrum on different cosmological parameters (Challinor, 2005). In these examples, scale-invariant adiabatic initial perturbations are assumed. **a** Top pair of diagrams: dependence on the density parameter in baryons (left) and total matter density parameter Ω_0 (right). Top to bottom at first peak: the baryon density parameter varies linearly in the range $0.06 \geq \Omega_B h^2 \geq 0.005$ (left) and the matter density parameter in the range $0.05 \leq \Omega_m h^2 \leq 0.5$ (right). **b** Bottom pair of diagrams: The dependence on the curvature density parameter Ω_K (left) and the dark energy density parameter Ω_Λ (right). In both cases, the density parameters in baryons and matter were held constant, thus preserving the conditions on the last scattering layer. The curvature density parameter varies (left to right) in the range $-0.15 \leq \Omega_K \leq 0.15$ and the dark matter density parameter in the range $0.9 \geq \Omega_\Lambda \geq 0.0$

15.6 Small Angular Scales

15.6.1 Statistical and Silk Damping

On small angular scales, temperature fluctuations are damped by two effects. The first is the statistical reduction in the amplitude of the predicted perturbations when the dimension of the perturbation becomes less than the thickness of the last scattering layer. As discussed in Sect. 15.2.1, this leads to a reduction in the amplitude of the predicted fluctuation spectrum by a factor of order $N^{-1/2}$, where N is the average number of wavelengths through the last scattering layer.

The second effect is photon diffusion, or Silk damping, discussed in Sect. 12.5. A convenient way of describing the reduction in amplitude of the temperature perturbations is to modify (15.2) to take account of the effects of photon diffusion. The *suppression factor* for waves of wavenumber k can then be written

$$\int \frac{d\tau}{dz} e^{-\tau(z)} e^{-k/k_D(z)} dz , \quad (15.65)$$

where $k_D = 2\pi/\lambda_D$ and λ_D is given by (15.9). The predicted power spectra in Fig. 15.7 show clearly the effects of damping expected at large multipoles, $l \geq 500$. The effects of damping and the random superposition of the perturbations leads to a strong damping of all primordial temperature fluctuations with wavenumbers greater than about 2000, that is, on the scale of a few arcminutes. Despite the effects of damping, Fig. 15.7 shows that there is expected to be a wealth of structure in the temperature fluctuation power spectrum on angular scales $1^\circ > \theta > 1 \text{ arcmin}$.

15.6.2 The Sunyaev–Zeldovich Effect in Clusters of Galaxies

At the very high sensitivities expected to be achieved by experiments such as the Planck mission on small angular scales, it is important to take account of small effects which might contribute to the temperature fluctuations of the background radiation. One such effect which must be present on angular scales $\theta \sim 1 \text{ arcmin}$ is the Sunyaev–Zeldovich effect in the directions of clusters of galaxies which contain large quantities of hot gas. As shown in Sect. 4.5, the temperature fluctuation due to the passage of the cosmic microwave background radiation through a region of hot gas is

$$\frac{\Delta T}{T} = -2y = -2 \int \left(\frac{kT_e}{m_e c^2} \right) \sigma_T N_e dl , \quad (15.66)$$

in the Rayleigh–Jeans region of the spectrum. Observations of this effect in 12 clusters at redshifts in the range 0.1 to 0.8 are shown in Fig. 4.17 (Carlstrom et al., 2000). For these clusters of galaxies, the temperature decrements amount of $\Delta T/T \sim 10^{-4}$.

An analysis of the 3-year WMAP data found evidence for the Sunyaev–Zeldovich effect in the direction of the Coma cluster at a level $\Delta_{\text{SZ}} = -0.46 \pm 0.16 \text{ mK}$, consistent with the results of ground-based measurements (Hinshaw et al., 2007). The

team also carried out a statistical analysis of the background intensity in the direction of 242 X-ray emitting Abell clusters selected from the ROSAT All-Sky Survey and detected a mean decrement at the 2.5σ level. The WMAP team eliminated the possible contribution of this effect to the background fluctuations by excluding the regions about these clusters from the cosmological analysis. With its higher angular resolution, the effect may be more significant for the Planck experiment.

In addition to the above effect, known as the *thermal* Sunyaev–Zeldovich effect, there is also an effect associated with the peculiar motions of hot gas clouds with respect to the frame of reference in which the microwave background radiation is isotropic. For such a gas cloud, the background radiation appears anisotropic in their rest frames and those photons scattered by the hot electrons are redistributed isotropically in their moving frames. Sunyaev and Zeldovich showed that first order Thomson scattering of the background radiation results in temperature perturbations due to these peculiar motions,

$$\frac{\Delta T}{T} = \sigma_T \int N_e \frac{v_{\parallel}}{c} dl \quad (15.67)$$

(Sunyaev and Zeldovich, 1980b). This effect, known as the *kinematic* Sunyaev–Zeldovich effect, is independent of frequency. Inserting typical values for a hot gas cloud in a rich cluster of galaxies, $N_e = 3 \times 10^3 \text{ m}^{-3}$, $v_{\parallel} = 500 \text{ km s}^{-1}$ and taking the core radius of the cluster to be 0.4 Mpc , a temperature perturbation of about $30 \mu\text{K}$ is expected. This effect provides an important means of estimating the radial component of the peculiar velocities of clusters of galaxies. Sunyaev and Zeldovich also pointed out that the peculiar motion perpendicular to the line of sight could be measured from the polarisation of the temperature perturbation associated with the first-order Thomson scattering process.

15.6.3 Confusion Due to Discrete Sources

At some sensitivity level it is expected that discrete sources will eventually be the limiting factor in measuring the power spectrum of primordial temperature perturbations. The problem is that there are no deep all-sky surveys of radio sources in the crucial 40- to 100-GHz wavebands which are optimal for studies of temperature fluctuations in the cosmic microwave background radiation.

The analysis of the 3-year WMAP data by Hinshaw and his colleagues resulted in a catalogue of 323 point sources with flux densities 5σ or greater above the noise level of the survey (Hinshaw et al., 2007). The earlier analysis of the 1-year data resulted in a list of 208 sources. Of the sources for which simple decompositions of the radio spectra could be made, 40% of the 208 sources had flat and inverted radio spectra, 13% had GHz-peaked spectra, 8% were classical power-law sources and 7% had a classical low-frequency power law combined with a flat or inverted spectrum component. Reliable optical identifications have been found for 205 of the 208 sources, 141 being quasars, 29 galaxies, 19 active galactic nuclei, 19 BL Lac

objects and one planetary nebula, IC418 (Trushkin, 2003). This mix of sources is what might be expected and will enable projections to be made of the expected levels at which source confusion will limit the ability to measure the temperature power spectrum on small angular scales. Regions about these sources were excluded from the final cosmological analysis of the WMAP data.

A similar problem is present at submillimetre wavelengths. Thanks to the development of the submillimetre bolometer array receiver, SCUBA, for the James Clerk Maxwell Telescope, a population of intense submillimetre sources was discovered at 850 μm by Smail, Ivison and Blain (Smail et al., 1997). We will have much more to say about the number counts of these objects in Chap. 17. There is now reasonable agreement about the form of the number counts of these sources which are associated with star-forming galaxies, many of them being difficult to identify because of extinction by interstellar dust in the star forming galaxies themselves. The number counts of these sources are now in good agreement and, at a flux density of 1 mJy at 850 μm, their surface density amounts to about 10^4 degree^{-2} (Cowie et al., 2002) (Sect. 17.2.3). For the *Planck* mission, Blain and his colleagues found that the temperature fluctuations due to submillimetre sources are comparable to those of the specifications of the instrument itself at frequencies greater than 350 GHz (Blain et al., 1998).

15.7 The Reionised Intergalactic Gas

At some epoch well after the epoch of recombination, the intergalactic gas must have been heated and reionised, a topic which we deal with in much more detail in Chap. 19. From the perspective of the present chapter, the important issue is that there must therefore be a finite optical depth τ for Thomson scattering between the epoch of recombination and the present epoch. The effect of this scattering is to attenuate temperature fluctuations originating from the last scattering layer at a redshift of about 1000 by a factor $e^{-\tau}$. More detailed calculations of the effects of Thomson scattering are shown in Fig. 15.8 which were carried out by Challinor (Challinor, 2005). It can be seen from Fig. 15.8 that there is a general attenuation of the amplitude of the fluctuations, except at small multipoles where the integrated Sachs–Wolfe effect originating at small redshifts causes the predicted spectrum to increase with decreasing multipole.

The optical depth of the intergalactic gas to Thomson scattering was derived in Sect. 9.3 in the limit of large redshifts $\Omega_0 z \gg 1, z \gg 1$,

$$\tau \approx 0.035 \frac{\Omega_B}{\Omega_0^{1/2}} h z^{3/2}, \quad (15.68)$$

which is adequate for our present purposes. Adopting our reference values $\Omega_0 = 0.3$, $\Omega_B = 0.05$ and $h = 0.7$, the fully ionised intergalactic gas would have optical depth $\tau = 0.1$ and 0.2 if it extended out to a redshifts $z = 12$ and 20 respectively. These redshifts would then correspond to the epoch at which the intergalactic gas was

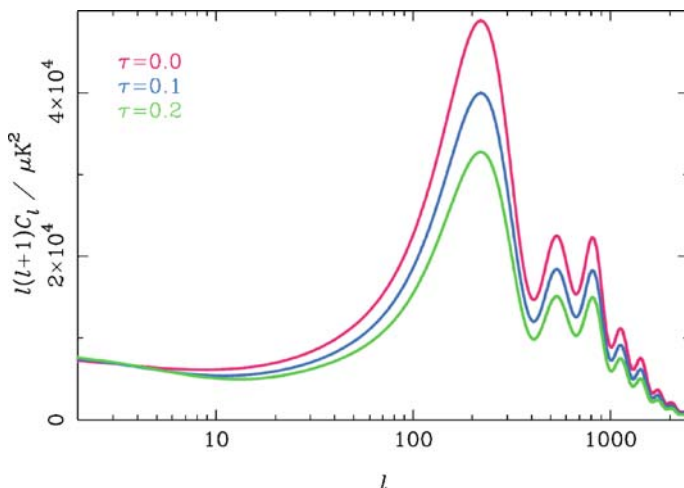


Fig. 15.8. The effect of reionisation on the temperature anisotropy power spectrum. The spectra are (*top to bottom*) for no reionisation, $\tau = 0.1$ and 0.2 . (Challinor, 2005)

reionised, presumably by the earliest generations of massive stars. These redshifts are not unreasonable values, as we will discuss in more detail in Chap. 18. The optical depth for Thomson scattering is one of the key cosmological parameters to be found from detailed analysis of the observed power spectrum of fluctuations in the cosmic microwave background radiation.

The formation of early generations of objects would necessarily give rise to significant velocity perturbations during the reionisation epoch, resulting in Doppler shifts of the background radiation, in exactly the same way that the dipole temperature perturbations were generated at the last scattering layer. The problem is that these effects are expected to be small, partly because the optical depth of the perturbations is small, and also because the random superposition of these perturbations leads to a statistical decrease of their amplitude. There is, however, a second-order effect discussed by Vishniac which does not lead to the statistical cancellation of the velocity perturbations (Vishniac, 1987). These perturbations are associated with second-order terms in $\delta n_e v$, where δn_e is the perturbation in the electron density and v the peculiar velocity associated with the motion of the perturbation. This effect only becomes significant on small angular scales at which the density perturbations are large. According to Vishniac's calculations, in the standard cold dark matter picture, these temperature fluctuations might amount to $\Delta T/T \sim 10^{-5}$ on the scale of 1 arcmin. Similar calculations have been carried out by Efstathiou with essentially the same result (Efstathiou, 1988). These are important conclusions since it is expected that all primordial perturbations on these scales would have been damped out by the processes discussed in Sect. 15.6.1.

15.8 The Polarisation of the Cosmic Microwave Background Radiation

The measurement of the power spectrum of temperature fluctuations in the cosmic microwave background radiation, as illustrated in Figs. 15.4 and 15.5, is a wonderful achievement. The information which can be derived from these observations has been the subject of the last four sections, and the implications for the determination of cosmological parameters will be summarised in the next section. Before that, however, we need to tackle the next great challenge facing theorists and experimenters – the polarisation of the cosmic microwave background radiation. This is an order of magnitude more difficult as compared with the study of temperature fluctuations, both theoretically and experimentally, but has the potential to produce unique information about the physics of the origin of structure formation. Even Dodelson in his admirable book admits that this is a ‘difficult subject’. Besides his book, the pedagogical review by Hu and White, and the more technical reviews by Zaldarriaga and by Challinor can be recommended as introductions to the subject (Hu and White, 1997; Zaldarriaga, 2004; Challinor, 2005).

15.8.1 The Polarisation Mechanism for the Cosmic Microwave Background Radiation

The mechanism for creating polarisation of the cosmic microwave background radiation is Thomson scattering of the radiation by free electrons. It is well known that Thomson scattering can create polarised emission from a beam of unpolarised radiation. A beam of unpolarised radiation incident upon a free electron causes it to oscillate in the plane perpendicular to the direction of the beam. The accelerated electron radiates with the standard dipole pattern so that the scattered radiation is 100% polarised when the electron is viewed perpendicular to the direction of propagation of the beam. In the case of the cosmic background radiation, however, the distribution of the radiation is highly isotropic and, in the case of complete isotropy, there would be exact cancellation of the polarised signals. Even in the case of a dipole distribution of the re-radiated field, which is the polar diagram for the scattered radiation, there is no net polarisation because of the dipole symmetry of the Thomson scattering process. The only way of creating a net polarised signal is if the radiation field incident upon the electron has a quadrupole anisotropic distribution of intensity.

This important point was clearly made in a perceptive paper by Zeldovich and Sunyaev in 1980 in which they argued that the detection of a polarised signal in the cosmic microwave background radiation would be evidence for a quadrupole component in its intensity (Zeldovich and Sunyaev, 1980). They gave the example of an incident radiation field

$$I = I_0 \left[1 + a\mu + b \left(\mu^2 - \frac{1}{3} \right) + \sum_{n=3}^{\infty} C_n P_n \right], \quad (15.69)$$

where $\mu = \cos \theta$. The term in a corresponds to a dipole field and that in b to a quadrupole field, the two terms being written as the first and second Legendre polynomials for a dipole and quadrupole respectively. The P_n s are higher-order Legendre polynomials. Integrating over all angles of incidence of the incoming radiation. Zeldovich and Sunyaev found that the fractional polarisation is

$$p = \frac{I_{\parallel} - I_{\perp}}{I_{\parallel} + I_{\perp}} = 0.1b\mu^2\tau, \quad (15.70)$$

where τ is the optical depth of the region for Thomson scattering. In the Rayleigh–Jeans region of the spectrum, a , b and C_n are independent of frequency. As Zeldovich and Sunyaev remarked:

Polarisation is a tensor quantity. Therefore, it is proportional to the quadrupole term but does not depend upon the dipole or higher terms in the intensity angular distribution.

15.8.2 Polarisation from the Last Scattering Layer

Let us consider first the polarisation arising from scattering in the last scattering layer. The radiation field seen by an electron in the last scattering layer is anisotropic because of the Doppler shifts associated with the dipole term Θ_1 in the expression for the power spectrum of temperature fluctuations (15.60). These result in first-order temperature perturbations $\Delta T/T = (v/c) \cos \theta$ and these are the source of the quadrupole intensity distribution. Figure 15.9 shows the predicted amplitude of the Doppler component compared with other contributions to the total power spectrum. The important points to note are as follows.

- The Doppler component is out of phase with the significantly larger monopole component, as discussed in the context of (15.57) and (15.60), and its power spectrum decreases in amplitude with decreasing multipole l . This decrease is associated with the fact that coherent oscillations cannot exist on scales greater than the sound horizon in the last scattering layer.
- The formation of the polarised signal involves two Thomson scattering events. The first created the quadrupolar field through scattering from motions caused by the oscillating baryon perturbations and the second by scattering of the quadrupolar field. Both of these events occurred within the last scattering layer.
- In consequence, the maximum of the polarised signal occurs at wavelengths which are of the same order as the mean free path of the photons in the last scattering layer.
- Notice that it is crucial that these processes take place in the last scattering layer. If there were many scatterings, the polarisation would be washed out, as takes place prior to the recombination epoch. It is the fact that the photons stream freely from the last scattering layer that results in the finite quadrupole anisotropy in the photon distribution.

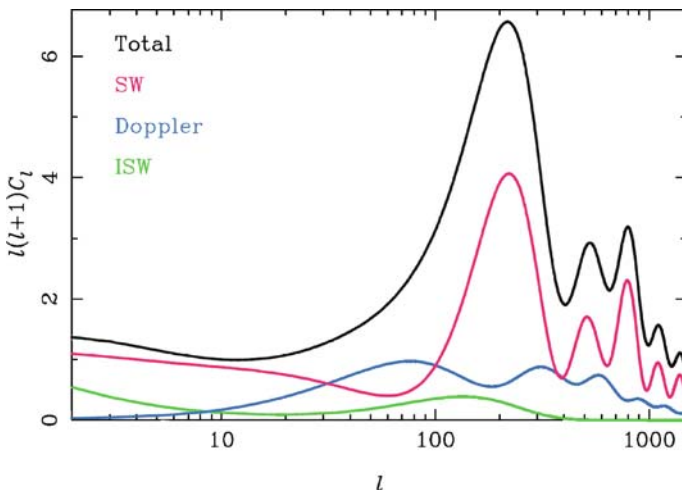


Fig. 15.9. Contributions of various terms to the temperature anisotropy power spectrum for adiabatic initial density perturbations. At large values of l , the contributions are, (top to bottom): total power; SW, the Sachs–Wolfe effect including the monopole anisotropy; the Doppler or dipole term; the integrated Sachs–Wolfe effect (Challinor, 2005)

As a result, the polarisation signal is expected to be much weaker than the intensity fluctuations. It is therefore a very considerable challenge to measure the polarisation signal experimentally, but this was first achieved by the ground-based Degree Angular Scale Interferometer (DASI) in 2002 (Leitch et al., 2002; Kovac et al., 2002). Subsequent ground-based experiments including the CBI (Readhead et al., 2004), the CAPMAP (Barkats et al., 2005) and Boomerang (Montroy et al., 2006) projects reported convincing detections of the polarised background signal.⁵ From space, the WMAP experiment detected a positive polarisation signal in the 1-year data (Bennett et al., 2003) and this was confirmed with improved signal-to-noise ratio in the 3-year data release (Page et al., 2007). It is simplest to summarise the results of these efforts using the 3-year WMAP polarisation data. It is again appropriate to pay tribute to the outstanding experimental and data analysis skills which have gone into these extremely demanding experiments. The extraction of the polarisation signal is particularly challenging because it has to be detected in the presence of the polarised Galactic radio emission, which has to be removed from the sky maps to reveal the polarisation associated with the primordial perturbations.

The total intensity fluctuations which were shown in Fig. 15.3 are displayed as filled dots at the top of Fig. 15.10 and are labelled TT. The polarisation power spectrum is labelled EE. The oscillating curve, which decreases towards small mul-

⁵ The reader by now will be aware of my preference to avoid acronyms but I have partially capitulated here: the translations are as follows: CBI = Cosmic Background Imager; CAPMAP = Cosmic Anisotropy Polarization Mapper; BOOMERanG = Balloon Observations Of Millimetric Extragalactic Radiation ANisotropy and Geophysics.

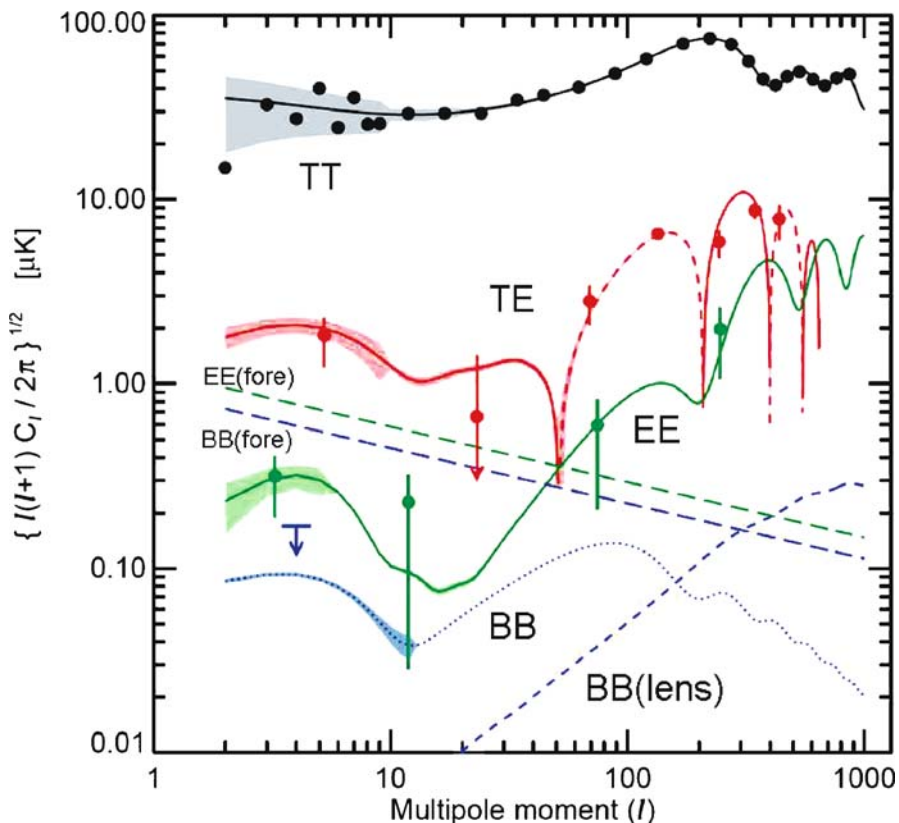


Fig. 15.10. The measured power spectrum of fluctuations in the intensity and polarisation of the cosmic microwave background radiation. Plots for the total intensity, the polarised intensity and the cross-correlation between the total intensity and the polarised intensity are labelled TT , EE and TE respectively. The best fitting model is shown by the corresponding lines. The dashed sections of the TE curve indicates multipoles in which the polarisation signal is anticorrelated with the total intensity. The model predictions are binned in l in the same way as the data. The binned EE polarisation data are divided into bins of $2 \leq l \leq 5$, $6 \leq l \leq 49$, $50 \leq l \leq 199$, and $200 \leq l \leq 799$. The dotted line labelled BB shows the expected power spectrum of B -mode gravitational waves if the primordial ratio of tensor to scalar perturbations was $r = \Delta_t^2/\Delta_s^2 = 0.3$. The WMAP experiment found only upper limits to this signal, the 1σ upper limit corresponding to $0.17 \mu\text{K}$ for the weighted average of multipoles $l = 2-10$. The B -mode signal due to gravitational lensing of the E -modes is shown as a dashed line labelled $BB(\text{lens})$. The upturn in the polarised signal at $l \leq 10$ is associated with polarisation originating during the reionisation era. The foreground model for galactic synchrotron radiation plus dust emission is shown as straight dashed lines labelled $EE(\text{fore})$ and $BB(\text{fore})$ for the scalar and tensor modes respectively, both being evaluated at $\nu = 65 \text{ GHz}$ (Page et al., 2007)

tipoles, shows the linear polarisation power spectrum predicted from the best fitting model, which can also account for the total intensity fluctuation power spectrum. The points and curve labelled TE are the cross-correlation power spectrum between the total intensity and the polarised intensity. Because the polarised intensity is closely associated with the dipole term in the total intensity spectrum, the dipole and polarisation signals are more strongly correlated than the EE signal on its own. The polarised component of the radiation is 90° out of phase with the dominant monopole temperature perturbations and so the cross-correlation power spectrum has twice as many minima as the either the TT or the EE spectra. The dashed lines in the predicted TE correlation function indicate the anti-correlated regions of the spectrum. The WMAP team noted the important point that the anticorrelated signal between multipoles 60 and 200 is the characteristic signature of primordial adiabatic perturbations. Notice that these remarks refer to multipoles greater than about 10 – for smaller values the increase in the polarised signal is associated with the reionisation of the intergalactic gas.

15.8.3 Polarisation from the Epoch of Reionisation

One of the exciting results of the 1-year WMAP data was the presence of strongly polarised signals in the TE cross-correlation power spectrum at small multipoles (Bennett et al., 2003). This signal is also present in the 3-year WMAP data, as can be seen in Fig. 15.10, but at a somewhat smaller amplitude than that reported in the analysis of the 1-year data. It was quickly realised that this was a signature of the epoch when the intergalactic gas was reheated and reionised, as had been predicted by Zaldarriaga (Zaldarriaga, 1997). The physics of the generation of linearly polarised emission during reionisation is exactly the same as that which resulted in the formation of polarisation in the last scattering layer. Once the intergalactic gas was reionised, any quadrupolar component of the background radiation created a linearly polarised signal. The strongest signal is again expected to occur at those multipoles for which the mean free path of the background photons is equal to the wavelength of the perturbations. It follows that, because a significant coherent polarised signal is observed at low multipoles, the scattering must occur on large physical scales at rather late epochs.

Zaldarriaga showed that, assuming the intergalactic gas is fully ionised out to redshift z_{ri} , the maximum polarisation occurs for wavenumbers $k(\tau_{\text{ri}} - \tau_{\text{re}}) \sim 2$, where τ_{ri} and τ_{re} are the conformal times corresponding to the epochs of reionisation (ri) and recombination (re) respectively (Zaldarriaga, 1997). The angular scale corresponding to the maximum multipole is $l \sim 2(\tau_0 - \tau_{\text{ri}})/(\tau_{\text{ri}} - \tau_{\text{re}}) \sim 2\sqrt{z_{\text{ri}}}$, where τ_0 is the conformal time corresponding to the present epoch and z_{ri} is the redshift of reionisation. Furthermore, the amplitude of the polarisation signal is determined by the optical depth τ of the intergalactic gas once it is reionised. At the same time, the amplitude of the acoustic peaks are damped by the factor $e^{-\tau}$. Zaldarriaga makes the point that the amplitude of the polarisation signal can be predicted rather precisely for adiabatic perturbations once the initial power spectrum is given. As described in Sect. 15.5, once the monopole term Θ_0 has been found, the dipole term Θ_1 is found

by differentiation and this is the cause of the quadrupole component responsible for the generation of the linearly polarised signal. This procedure is repeated for the late reionisation phases and accounts for the predicted linear polarisation ‘bump’ seen in the EE and TE power spectra in Fig. 15.10. Page and his colleagues point out that these polarisation observations provide entirely independent information about the optical depth for reionisation and consequently about the epoch at which it took place (Page et al., 2007).

15.8.4 Primordial Gravitational Waves

The considerations of Sect. 15.8.1 make it clear that gravitational waves can result in polarisation of the cosmic microwave background radiation. Because the force of gravity is always attractive, there are no dipole gravitational waves, only quadrupole waves.⁶ As a result, gravitational waves stretch and squeeze the geometry of space in orthogonal directions, the two independent modes of oscillation, h_+ and h_\times , being shown in Fig. 15.11 – they are oriented at 45° with respect to one another. There is, however, an important difference between the two modes in that they have opposite parity on making the translation $\mathbf{r} \rightarrow -\mathbf{r}$. The net result is that the polarisation signal can be uniquely decomposed into what are known as the electric E , or gradient, component associated with h_+ and a magnetic B , or curl, component with h_\times . These result in corresponding orthogonal patterns of polarisation on the sky. The importance of this decomposition is that, whereas the E components could be generated by either scalar or tensor perturbations, the B component is a signature of the presence of a pure curl component.

The importance of these considerations is that they provide another potential means of investigating physical processes in the very early Universe. Just as the spectrum of scalar perturbations can be associated with quantum fluctuations of the

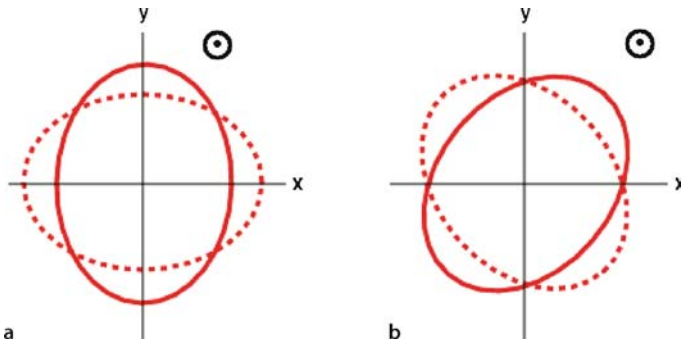


Fig. 15.11a,b. The two orthogonal polarisation modes, h_+ and h_\times , of gravitational radiation (Will, 2006)

⁶ For a simple introduction to gravitational radiation, see the review by Schutz (Schutz, 2001).

inflation field, so tensor perturbations can also be created with a similar power spectrum. The physics which relates the properties of the B -mode tensor perturbations to an observable polarisation power spectrum is the same as that which we described for the scalar perturbations. Specifically, the maximum B -mode signal is expected to be observed when the wavelength of the gravitational waves is equal to the mean free path of the photons in the last scattering layer. In addition, once the intergalactic gas has been reionised, the same physics enhances the detectability of the B modes on large angular scales. These features of the predicted BB power spectrum are shown by the dotted line labelled BB in Fig. 15.10. In that figure, it is assumed that the ratio of tensor to scalar power is $r = 0.3$. It can be seen that the expected signal is very weak and below the levels at which it would be detectable by the WMAP experiment. The best upper limits to primordial gravitational waves at the present time are obtained at low multipoles, the 1σ upper limit of $0.17 \mu\text{K}$ being found for the weighted average of multipoles in the range $l = 2\text{--}10$ (Page et al., 2007). From the full WMAP analysis, using both the intensity and polarisation data, the WMAP team quote a limit to the tensor to scalar ratio of $r < 0.55$ at the 95% confidence level, corresponding to an upper limit to the density parameter in gravitational waves of $\Omega_{\text{Gwh}}^2 < 10^{-12}$.

15.8.5 Weak Gravitational Lensing

Another source of polarisation of the cosmic microwave background radiation is weak gravitational lensing. The potential of this technique for providing information about the power spectrum of density perturbations was described in a pioneering paper by Kaiser (Kaiser, 1992). It was only realised observationally by a number of groups in the early years of the 21st century. An excellent introduction to the technique and the results of these observations is given in the review by Refregier (Refregier, 2003).

Gravitational lensing by mass concentrations was discussed in Sect. 4.6 and the types of distortions resulting from strong lensing were illustrated in Fig. 4.20. In the case of weak lensing, the images of background galaxies are slightly elongated and stretched, as illustrated in Fig. 15.12a. These distortions are described by a *distortion matrix* which Refrigier writes in the form

$$\Psi_{ij} \equiv \frac{\partial(\delta\theta_i)}{\partial\theta_j} \equiv \begin{pmatrix} \kappa + \gamma_1 & \gamma_2 \\ \gamma_2 & \kappa - \gamma_1 \end{pmatrix}, \quad (15.71)$$

where $\delta\theta_i$ is the deflection vector produced by weak gravitational lensing as observed on the sky. The convergence κ is proportional to the projected mass along the line of sight and describes overall dilations and contractions. The shear terms γ_1 and γ_2 describe stretches and compressions along and at 45° to the x -axis. Figure 15.12a illustrates the geometrical meaning of the shear components.

The big advantage of the weak gravitational lensing technique is that the lensing measures directly the distribution of mass rather than the light of galaxies. The problems of biasing in relating the observed distribution of galaxies to the underlying

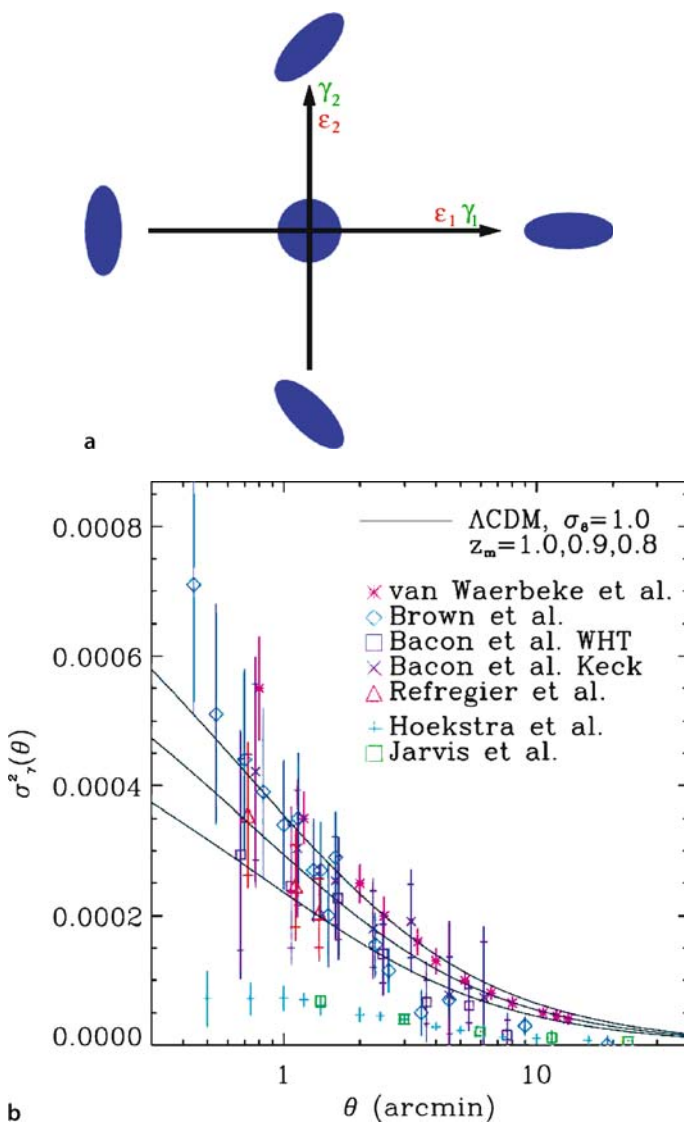


Fig. 15.12. **a** The significance of the shear components γ_1 and γ_2 of the distortion matrix in weak gravitational lensing. **b** A summary of estimates of the shear variance σ_γ^2 as a function of the radius θ of a circular cell (Refregier, 2003)

mass distribution are eliminated. These are, however, very demanding observations and require very careful understanding of the point spread function of the telescope optics to obtain convincing results. This has now been achieved, as illustrated by the shear variance distribution as a function of angular scale shown in Fig. 15.11b, which is taken from the summary by Refregier (Refregier, 2003). The results are

expressed in terms of the variance of the shear $\sigma_\gamma^2 \equiv \langle \bar{\gamma}^2 \rangle$ in randomly placed cells. σ_γ^2 is related to the shear power spectrum by

$$\sigma_\gamma^2 = \frac{1}{2\pi} \int_0^\infty dl l C_l |\tilde{W}_l|^2 , \quad (15.72)$$

where \tilde{W}_l is the Fourier transform of the cell aperture. In turn, the coefficients C_l can be related to the power spectrum of density perturbations in the mass distribution. Therefore, the observed distribution of σ_γ^2 can be compared with the expectations of the Λ CDM model and the standard primordial power spectrum of density perturbations with the results shown by different solid lines in Fig. 15.11b. z_m is the median redshift of the lensing galaxies. It can be seen that there is encouraging agreement between theory and observation.

The importance of this analysis for polarisation studies of the cosmic microwave background radiation is that weak lensing induces a polarisation signal because of the tensor character of the distortion matrix. As a result, there are quadrupole anisotropies in the radiation field which give rise to E -mode polarisation of the background radiation. In addition, gravitational lensing of the EE-mode polarisation results in

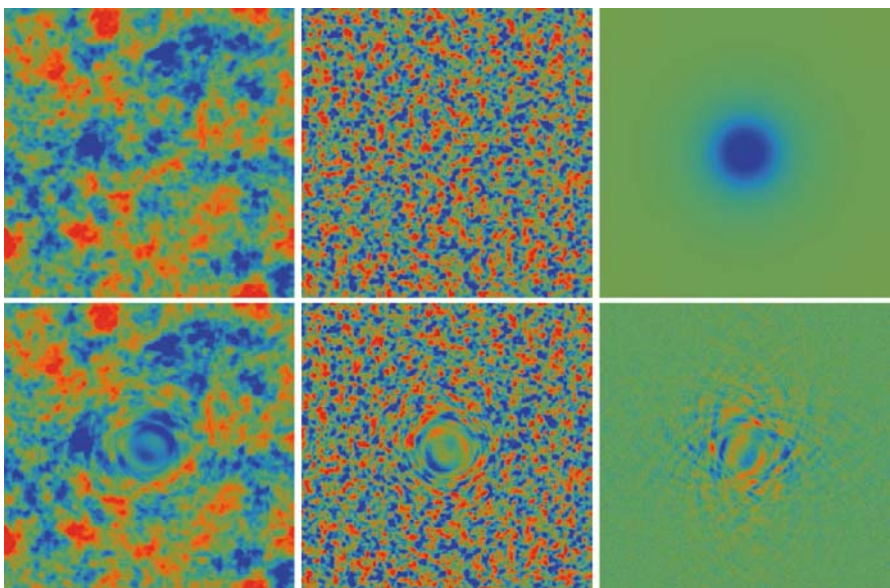


Fig. 15.13. The creation of BB-mode polarisation from EE modes by gravitational lensing. This diagram is an exaggerated example of the expected effect in a $10^\circ \times 10^\circ$ field in the computations of Hu and Okamoto (Hu and Okamoto, 2002). *Top row, left to right:* the unlensed temperature field, unlensed E-polarisation field and the spherically symmetric deflection field. *Bottom row, left to right:* the lensed temperature field, the lensed E-polarisation field and the lensed B-polarisation field. The intensity scale for the polarisation and temperature fields differ by a factor of 10

BB-mode polarisation. This effect is beautifully illustrated by the computations of Hu and Okamoto, an example of which is shown in Fig. 15.13 (Hu and Okamoto, 2002). In Fig. 15.10, the dashed line labelled BB(lens) shows an estimate of the B-mode polarisation power spectrum due to the effects of weak gravitational lensing (Page et al., 2007). It is clear that this is a very weak signal, but it is of the same amplitude as that expected due to gravitational waves, but on smaller angular scales. It can be seen that the gravitationally lensed BB-modes interfere with the detection of the BB signal due to gravitational waves at multipoles greater than about 100. Once the EE signal has been measured precisely, however, it is possible to remove the gravitationally lensed BB modes statistically from the total BB power spectrum.

15.9 Determination of Cosmological Parameters

Much of the discussion of this chapter has concerned understanding how various features of the power spectrum of fluctuations in the cosmic microwave background radiation enable cosmological parameters to be estimated. On their own, the WMAP observations provide important limits to many cosmological parameters, but they become even more impressive when taken in combination with independent data on the large-scale structure of the Universe. A detailed analysis of the cosmological implications of the WMAP data on their own and combined with other independent data sets has been provided by Spergel and his colleagues (Spergel et al., 2007).

The procedure involves first defining the range of parameters to be included in the simulations in order to reproduce the observed spatial correlation function for galaxies and the power spectra of the intensity and polarisation fluctuations in the cosmic background radiation. The original list of 13 parameters employed by Tegmark and his colleague (Tegmark et al., 2004) has been expanded to span a very wide range of possible models (Spergel et al., 2007); the list of parameters is shown in Table 15.1. Many of these parameters have been discussed in previous sections, for example, Ω_B , Ω_D , h , τ , Ω_Λ , w , Ω_k , n_s , r , b ; the definitions are summarised in Table 15.1. The additional parameters include f_ν – the ratio of mass densities in neutrinos to dark matter, N_ν – the effective number of relativistic neutrino species, $\Delta_{\mathcal{R}}^2$ – the amplitude of curvature perturbations, $\alpha = d(\ln n_s)/d(\ln k)$ – the curvature of the initial power spectrum, A_{SZ} – Sunyaev–Zeldovich marginalisation factor which takes account of the possible presence of Sunyaev–Zeldovich decrements and z_s – the weak lensing source redshift.

The standard analysis procedure is to use Bayesian statistical techniques and Monte Carlo Markov chain methods to make best estimates of the cosmological parameters, details of which are included in the papers by Tegmark and by Spergel and their colleagues (Tegmark et al., 2004; Spergel et al., 2007). First of all, it is interesting to note how much information can be derived from the 3-year intensity and polarisation data alone, before other microwave background experiments and completely independent data sets are included. The values shown in the third column of Table 15.1 are for a flat Λ CDM model with a single power-law initial power

Table 15.1. Parameters involved in the construction of cosmological models for the origin of structure in the Universe (Spergel et al., 2007). The estimates in the third column are for a flat Λ CDM model with power-law initial perturbation spectrum

Parameter	Definition	WMAP alone
$\omega_B = \Omega_B h^2$	Baryon density parameter	$0.0223^{+0.0007}_{-0.0009}$
$\omega_D = \Omega_D h^2$	Cold dark matter density parameter	$0.127^{+0.007}_{-0.013}$
h	Hubble's constant	$0.73^{+0.03}_{-0.03}$
n_s	Scalar spectral index ^a	$0.961^{+0.018}_{-0.019}$
τ	Reionisation optical depth	$0.09^{+0.03}_{-0.03}$
σ_8	Density variance in 8 Mpc spheres	$0.74^{+0.05}_{-0.06}$
Ω_Λ	Dark energy density parameter	
w	Dark energy equation of state	
Ω_k ^b	Space curvature	
$f_\nu = \Omega_\nu / \Omega_D$	Massive neutrino fraction	
N_ν	Number of relativistic neutrino species	
$\Delta_{\mathcal{R}}^2$	Amplitude of curvature perturbations	
r	Tensor-scalar ratio	
A_s	Amplitude of scalar power spectrum	
$\alpha = d \ln K / d \ln k$	Running of scalar spectral index	
A_{SZ}	SZ Marginalisation factor	
b	Bias factor	
z_s	Weak lensing source redshift	

^a $n_s = 1$ is the preferred value according to the standard inflation picture.

^b $\Omega_B + \Omega_D + \Omega_\Lambda + \Omega_k = 1$

spectrum. Blank entries in the table mean that they were set to zero or their values could be deduced from the first six quantities and the assumption of a flat Λ CDM model.

It is remarkable how closely these values agree with the completely independent estimates of these parameters which were discussed in Chap. 8. Particularly striking results are:

- The dark energy density parameter $\Omega_\Lambda \approx 0.7$ while the dark matter has density parameter $\Omega_D h^2 \approx 0.127$, both in excellent agreement with the estimates from Type 1A supernovae (Sect. 8.5.3) and from large-scale galaxy surveys (Sect. 8.7).
- The baryonic matter has density parameter $\Omega_B h^2 \approx 0.0223$, in excellent agreement with the results of primordial nucleosynthesis (Sect. 10.4.2).
- The inferred value of Hubble's constant is in excellent agreement with the results of the Hubble Space Telescope Key Project (Sect. 8.3).

- The spectral index of the primordial power spectrum is close to $n_s = 1$, but slightly less than the canonical value, as expected for inflation models of the early Universe.

Much of the independent information can be incorporated into the analysis, and then many of the assumptions involved in deriving the values shown in Table 15.1 can be relaxed. These data include the observations of the cosmic microwave background radiation to multipoles up to 1500 from other experiments, the two-point galaxy correlation functions from the SDSS and 2dF Galaxy redshift surveys, the redshift-distance relation for Type 1A supernovae and the independent determinations of Hubble’s constant. The many different ways in which these data can be combined and the resulting parameter estimates can be found at the WMAP website.⁷

It is helpful to quote some examples of how additional constraints can be obtained from these data from the summary provided by Spergel and his colleagues (Spergel et al., 2007). For example, assuming a power-law initial curvature spectrum, the WMAP data alone set an upper limit to the tensor-to-scalar ratio of $r < 0.55$ at the 95% confidence limit at wavenumber $k = 0.002 \text{ Mpc}^{-1}$. The combination of WMAP and the lensing-normalised SDSS galaxy survey results in an improved limit $r < 0.28$, again at the 95% confidence limit.

Models which suppress large-scale power through assuming a finite value of the running spectral index or a large-scale cut-off in the power spectrum provide a somewhat better fit to the WMAP and small-scale CMB data than the power-law Λ CDM model and would be consistent with a higher amplitude of gravitational waves.

In a flat universe, the combination of WMAP and the Supernova Legacy Survey data yields a significant constraint on the equation of state of the dark energy, $w = -0.97^{+0.07}_{-0.09}$. If it is assumed that $w = -1$, then the deviations from flat geometry with curvature density parameter $\Omega_k = 0$ are small: the combination of WMAP and the Supernova Legacy data imply $\Omega_k = -0.015^{+0.020}_{-0.016}$. The combination of WMAP 3-year data plus the HST key project constraint on H_0 implies $\Omega_k = -0.010^{+0.016}_{-0.009}$ and $\Omega_\Lambda = 0.72 \pm 0.04$. Even if we do not include the assumption that the universe is flat, by combining WMAP, large-scale-structure and supernova data, a strong constraint is still obtained for the dark energy equation of state, $w = -1.06^{+0.13}_{-0.08}$.

For a flat universe, the combination of WMAP and other astronomical data yield a constraint on the sum of the neutrino masses, $\sum m_\nu < 0.68 \text{ eV}$, at the 95% confidence level.

15.10 Other Sources of Primordial Fluctuations

The arguments presented above have been based upon the assumption that the spectrum of primordial fluctuations was a scale-invariant power law of roughly Harrison-Zeldovich form with random phases. These properties are naturally accounted for in the inflationary picture of the early Universe, the perturbations arising as quantum fluctuations during the inflationary phase. The success of the standard

⁷ http://lambda.gsfc.nasa.gov/product/map/dr2/parameters_info.cfm

Λ CDM model with adiabatic primordial curvature perturbations in accounting for so many different types of cosmological observation without any serious conflicts is quite remarkable. It is therefore not surprising that this model has become the model of choice for cosmological investigations.

It is worth cautioning, however, that there may well be more to the story than this. For example, an alternative picture for the origin of primordial density perturbations is that they are associated with symmetry breaking during phase transitions which took place during the inflationary era. The process of symmetry breaking can give rise to topological defects such as cosmic strings, monopoles and textures which could also seed the process of galaxy formation (Kibble, 1976; Turok, 1989).

An important difference between this class of theory and the standard picture is that the fluctuations are expected to have a non-Gaussian character. For example, cosmic strings would produce line-like discontinuities on the sky, and cosmic textures would produce distinct non-Gaussian hot and cold spots. A key test of this class of theory is therefore the presence of non-Gaussian features in the distribution of the radiation temperature over the sky. If the temperature fluctuations are Gaussian, the higher moments of the temperature distribution, such as its skewness and kurtosis, should be zero. If the fluctuations are non-Gaussian, these moments will be significantly different from zero. A variety of different tests for non-Gaussianity have been used to analyse the 3-year WMAP data sets but no significant departures from Gaussianity have been found (Spergel et al., 2007).

A second test is the power spectrum of temperature fluctuations, which is expected to be significantly different from the predictions of the standard Λ CDM model. The differences arise from the fact that topological defects give rise to isocurvature perturbations with non-random phases. The result is that the structure in the acoustic peaks predicted in the standard adiabatic picture are not present. Taken at face value, this form of spectrum is in poor agreement with the observations. Despite this, topological defects are a rather general feature of phase transitions during symmetry-breaking events in the very early Universe, and so there might well be a significant contribution from these to the temperature fluctuation spectrum at some level, which would complicate the interpretation of the observations.

15.11 Reflections

The spectacular results of these experiments and their analysis in the determination of cosmological parameters are quite remarkable for astrophysicists of my generation who were brought up to expect that if any cosmological parameter could be reliably determined within a factor of two, that was a real achievement. Now we are in the era of precision cosmology, with the values of cosmological parameters determined to better than 10%, and often significantly better than this. The fact that many different approaches to their determination result in concordant values is encouraging evidence that the standard model is the best framework for cosmological investigations. It would be wrong to pretend, however, that the problems are over. We will return to the many fundamental questions which this new understanding raises in Chap. 20.

In the meantime, there is great scope for advancing these studies with the next generation of experiments dedicated to studies of cosmic microwave background radiation. The first of these will be the ESA Planck mission, which aims to carry out definitive observations of the power spectrum of temperature fluctuations throughout the entire range of multipoles $2 \leq l \leq 2500$. The higher angular resolution and wider wavelength coverage as compared with the WMAP project mean that the observations are expected to be variance limited throughout this range of multipoles. The anticipated precision with which the power spectrum will be determined is illustrated in Fig. 15.14. The spacecraft will be launched in 2008.

A second class of experiments concerns the precision measurement of the polarisation of the background radiation and in particular the search for the elusive B -mode signals which could provide key information about the generation of gravitational waves during the inflationary phase of the expanding Universe. A number of projects are currently being developed and studied, but they are very demanding and need superb experimental and data analysis techniques to have any hope of success. This is a terrific challenge and one which I hope will be realised over the next decade.

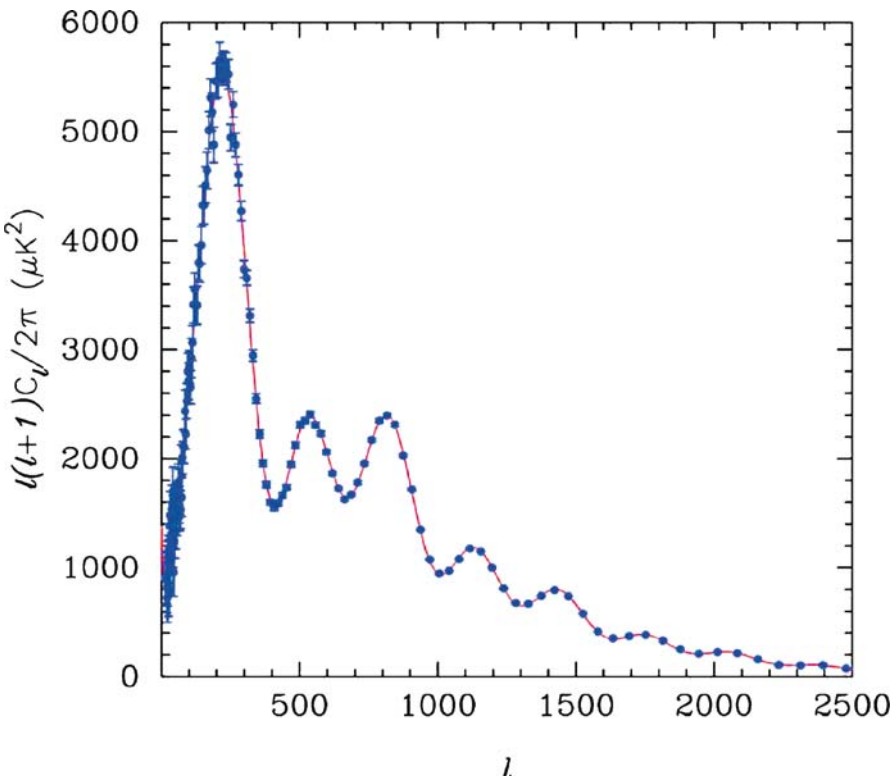


Fig. 15.14. The predicted performance of the *Planck Surveyor* mission of the European Space Agency. The *error bars* correspond to the total cosmic and experimental variances expected from 1 year of observation (Efstathiou et al., 2005)

Part IV

The Post-Recombination Universe

16 The Post-Recombination Era

In the final part of this book, we study the post-recombination Universe and the physical processes responsible for the formation of galaxies and clusters of galaxies as we know them today. This has been our objective from the beginning. This part of the story is, however, much more difficult intrinsically than the study of the pre-recombination era. This is because it necessarily involves the non-linear evolution of perturbations in the dark and baryonic matter, as well as a host of astrophysical phenomena associated with the formation and death of stars and the feedback mechanisms associated with the life cycles of stars and galaxies. In addition, we need to account for the formation and evolution of the supermassive black holes which are present in the nuclei of massive galaxies. It is therefore inevitable that this last part will be somewhat less structured and coherent than the very beautiful story of the linear evolution of small perturbations, which was the subject of Part III. That story took us up to epochs corresponding to roughly a redshift of 1000.

The *post-recombination era* spans the redshift interval from about 1000 to zero and can be divided rather naturally into two phases. The first corresponds to the epochs between the epoch of recombination at $z \sim 1000$ and the *epoch of reionisation* when the intergalactic gas was reionised, probably by the ultraviolet ionising radiation of the first generations of massive stars. This era is often referred to as the *dark ages* since it is very difficult to study observationally. Exactly when reionisation took place is a key issue for contemporary cosmology but it must have occurred at some epoch in the redshift interval $30 > z > 6$. There is no reason to suppose that the process of reionising the intergalactic gas took place at a single epoch, and one of the challenges for observational cosmology is to determine its reionisation history. There is compelling evidence that the intergalactic gas was more or less fully ionised by a redshift of 6–7, a topic which we take up in some detail in Chap. 18. There is therefore no doubt that the process of galaxy formation was well underway by these redshifts at the very latest.

The second phase corresponds to the redshift interval $0 < z < 6$ –7, what may be termed the *observable Universe of galaxies*. Thanks to the remarkable developments in detector and telescope technology over recent years, this is the range of redshifts over which luminous galaxies and quasars have now been observed. As we will show in Chap. 17, there is plentiful evidence that the populations of galaxies and quasars have evolved dramatically over the redshift interval $0 < z < 6$. The same technological revolution has also enabled the evolution of star formation activity in

galaxies and the associated evolving abundances of the heavy elements to be studied over a similar redshift interval. These topics are discussed in Chap. 19.

The great challenge is to synthesise this wealth of observational evidence into a convincing and coherent picture of galaxy formation. The intrinsically non-linear nature of the processes involved makes the subject an ideal challenge for large-scale computer simulations which can be used to obtain clues to the underlying astrophysics. Ideally, one might hope to study the problem by combining the preferred Λ CDM model of large-scale structure formation with hydrodynamic codes which follow the dynamical and thermal histories of the diffuse intergalactic gas. The latter have had considerable success in accounting for many of the properties of the intergalactic gas, as we discuss in Chap. 18. Unfortunately, key steps in the more ambitious programme to continue the simulations to form stars in galaxies as well are not sufficiently understood for this to be an attainable goal at the moment. An example of such a problem is the process of star formation. Understanding the physical processes involved in the formation of stars is not yet at a level at which it can be adequately built into large-scale hydrodynamical simulations. As a result, considerable efforts have been devoted to what are known as *semi-analytic models* for galaxy formation. These build upon the successes of the standard Λ CDM model and hydrodynamical simulations by including empirical rules for star formation, supernova rates, element enrichment and so on into very large-scale simulations. The hope is to be able to learn more about the non-linear processes which are needed to account for the observed properties of galaxies and clusters described in Chaps. 3 and 4. The results of these endeavours conclude Chap. 19.

Finally, in Chap. 20, we investigate the origins of the primordial perturbations which gave rise to the structures we observe in the Universe today. We also need to address the other fundamental problems of astrophysical cosmology which have been accumulating as our story has developed. As we will show, these provide very major challenges for the coming generations of theorists, particle physicists, astrophysicists and cosmologists.

To begin with, let us investigate what we can learn by extrapolation of the formalisms we have developed so far into the non-linear regime, as well as discussing physical processes such as the cooling of the baryonic matter in galaxies which must play a significant part in the story. We will also study the arguments first put forward by Press and Schechter concerning the evolution of the mass function of bound systems in hierarchical clustering models. These studies provide the astrophysical background to the more ambitious efforts which are the subject of the later chapters.

16.1 The Non-Linear Collapse of Density Perturbations

We discussed in Sect. 14.5.2 how the development of dark matter perturbations can be followed into the non-linear regime following the insights of Hamilton and his colleagues (Hamilton et al., 1991). There we demonstrated how non-linear effects resulted in steepening of the two-point correlation function of galaxies to roughly its observed form. Note that this is far from the end of the story since that analysis

referred to the correlation function of the dark matter perturbations, what might better be described as dark matter haloes, rather than to that of the baryonic component of galaxies, which is what is measured in large-scale galaxy surveys. Let us look at some aspects of this calculation in a little more detail.

16.1.1 Isotropic Top-Hat Collapse

One calculation, which can be carried out exactly, is the collapse of a uniform spherical density perturbation in an otherwise uniform Universe, a model sometimes referred to as ‘spherical top-hat collapse’. As discussed in Sect. 11.4.2, the dynamics of such a region are precisely the same as those of a closed Universe with $\Omega_0 > 1$. The variation of the ‘scale factor’, or relative size, of the perturbation a_p is cycloidal and given by the parametric solution (7.25) and (7.26)

$$\begin{aligned} a_p &= A(1 - \cos \theta) \quad t = B(\theta - \sin \theta) , \\ A &= \frac{\Omega_0}{2(\Omega_0 - 1)} \quad \text{and} \quad B = \frac{\Omega_0}{2H_0(\Omega_0 - 1)^{3/2}} . \end{aligned} \quad (16.1)$$

The perturbation reached maximum size at $\theta = \pi$, which is labelled ‘turnround’ in Fig. 14.5a, and then collapsed to infinite density at $\theta = 2\pi$, as illustrated in Fig. 11.2. To express this result in another way, the perturbation stopped expanding when $\dot{a}_p = 0$ at $\theta = \pi$ and so can be considered to have separated out of the expanding background. This occurred at scale factor

$$a_{\max} = 2A = \frac{\Omega_0}{\Omega_0 - 1} \quad \text{at time} \quad t_{\max} = \pi B = \frac{\pi\Omega_0}{2H_0(\Omega_0 - 1)^{3/2}} . \quad (16.2)$$

We can now work out the density of the perturbation at maximum scale factor ϱ_{\max} relative to that of the background ϱ_0 , which, for illustrative purposes, we take to be the critical model, $\Omega_0 = 1$, $\Omega_A = 0$. Recalling that the density within the perturbation was Ω_0 times that of the background model to begin with,

$$\frac{\varrho_{\max}}{\varrho_0} = \Omega_0 \left(\frac{a}{a_{\max}} \right)^3 = 9\pi^2/16 = 5.55 , \quad (16.3)$$

where the scale factor of the background model has been evaluated at cosmic time t_{\max} . Thus, by the time the perturbed sphere had stopped expanding, its density was already 5.55 times greater than that of the background density.

In the spherical top-hat model, the perturbation had no internal pressure and so it collapsed to infinite density at time $t = 2\pi B$, twice the time it took to reach maximum expansion. Since $a \propto t^{2/3}$, it follows that the relation between the redshift of maximum expansion z_{\max} and the redshift of collapse z_c is

$$1 + z_c = \frac{1 + z_{\max}}{2^{2/3}} . \quad (16.4)$$

This means that the collapse of the perturbation occurred very rapidly once the perturbation had separated out from the background. For example, if $z_{\max} = 20$, then $z_c = 12$, if $z_{\max} = 10$, then $z_c = 6$, and so on.

Interpreted literally, the spherical perturbed region would collapse to a black hole, but in practice, this does not happen. Because of the presence of dark matter density perturbations within the perturbation and the tidal effects of neighbouring perturbations, it fragmented into subunits which then came to a dynamical equilibrium under the influence of large-scale gravitational potential gradients, the process of *violent relaxation* described by Lynden-Bell (Lynden-Bell, 1967). In this process, the system ends up satisfying the Virial Theorem, in which the internal kinetic energy of the system is half its (negative) gravitational potential energy (Sect. 3.4.1).

We can work out the final dimensions of the virialised dark matter halo by the following argument. At z_{\max} , the sphere was stationary and all the energy of the system was in the form of gravitational potential energy. For a uniform sphere of radius r_{\max} , the gravitational potential energy is $-3GM^2/5r_{\max}$. If the system did not lose mass and collapsed to half this radius, its gravitational potential energy would be $-3GM^2/(5r_{\max}/2)$ and, by conservation of energy, the kinetic energy of collapse of the halo would be

$$\text{Kinetic Energy} = \frac{3GM^2}{5(r_{\max}/2)} - \frac{3GM^2}{5r_{\max}} = \frac{3GM^2}{5r_{\max}}. \quad (16.5)$$

Thus, by collapsing by a factor of two in radius from its maximum radius of expansion, the kinetic energy of collapse became half the negative gravitational potential energy. Once this energy was randomised by the process of violent relaxation, the condition for dynamical equilibrium according to the Virial Theorem was satisfied. Therefore, the density of the perturbation increased by a further factor of 8, while the background density continued to decrease. From (16.1), the scale factor of the perturbation reached the value $a_{\max}/2$ at time $t = (1.5 + \pi^{-1})t_{\max} = 1.81t_{\max}$, when the background density was a further factor of $(t/t_{\max})^2 = 3.3$ less than at maximum. The net result of these simple calculations is that, when the collapsing cloud became a bound virialised object, its density was $5.55 \times 8 \times 3.3 \approx 150$ times the background density at that time.

Although this is a highly idealised picture, similar results are found from N-body computer simulations of the process of formation of bound structures in the expanding Universe. According to Coles and Lucchin, these simulations suggest that the systems can be considered virialised after a few crossing times, $t \approx 3t_{\max}$, when the density contrast would be closer to 400 (Coles and Lucchin, 1995). This type of reasoning allowed the initial power spectrum of the density perturbations to be reconstructed well into the non-linear regime, as discussed in Sect. 14.5.2 (Hamilton et al., 1991; Peacock and Dodds, 1994). The general rule is that discrete objects such as galaxies and clusters of galaxies only became distinct gravitationally bound objects when their densities were at least 100 times the background density.

For illustration, let us see what this means for the redshifts at which galaxies and other large-scale systems could have separated out of the expanding background. The factor of order 100 derived above is the minimum enhancement in the density

of the bound object relative to the background. We can therefore state with some confidence that the density of the virialised object should be at least 100 times the background density, that is,

$$\varrho_{\text{vir}} \geq 100 \times \frac{3\Omega_0 H_0^2}{8\pi G} (1 + z_{\text{vir}})^3, \quad (16.6)$$

where z_{vir} is the redshift at which the system became virialised. We can make an estimate of ϱ_{vir} from the Virial Theorem. If M is the mass of the system and v^2 its velocity dispersion, the condition that the kinetic energy be half the gravitational potential energy is

$$\frac{1}{2} M v^2 = \frac{1}{2} \frac{GM^2}{R}, \quad (16.7)$$

where R is some suitably defined radius. Therefore,

$$\varrho_{\text{vir}} \approx \frac{M}{(4\pi/3)R^3} = \frac{v^6}{(4\pi/3)G^3 M^2}. \quad (16.8)$$

Inserting this value into (16.6), we can estimate the redshift at which the object became virialised:

$$(1 + z_{\text{vir}}) \leq 0.47 \left(\frac{v}{100 \text{ km s}^{-1}} \right)^2 \left(\frac{M}{10^{12} M_\odot} \right)^{-2/3} (\Omega_0 h^2)^{-1/3}. \quad (16.9)$$

What this calculation amounts to is an improved version of the simple estimate presented at the beginning of Chap. 11 concerning the relation between the mean densities of objects relative to the background density and when they first formed. Let us put in some representative figures. Adopting our reference values $\Omega_0 = 0.3$, $h = 0.7$, we find that, for galaxies having $v \sim 300 \text{ km s}^{-1}$ and $M \sim 10^{12} M_\odot$, the redshift of formation must have been less than about 7. For clusters of galaxies for which $v \sim 1000 \text{ km s}^{-1}$ and $M \sim 10^{15} M_\odot$, the redshift of formation cannot have been much greater than 1. This conclusion follows immediately from the rule that the density contrast of virialised objects should be at least 100 when they formed, which is not such a different factor from the ratio of the mean density of clusters of galaxies to typical cosmological densities at the present day. Thus, typically, clusters of galaxies must have formed in the relatively recent past.

16.1.2 The Zeldovich Approximation

One of the deficiencies of the top-hat model is the assumption that the perturbations were precisely spherically symmetric. The next best approximation is to assume that they were ellipsoidal with three unequal principal axes. Peacock and Heavens discussed the expected ellipticity distributions for perturbations arising from the superposition of random Gaussian fields (Peacock and Heavens, 1985). One of the general rules which comes out of the study of the collapse of ellipsoidal mass

distributions is that collapse takes place most rapidly along the shortest axis (Lin et al., 1965). For the case of primordial density fluctuations, Zeldovich showed in 1970 how the collapse could be followed into the non-linear regime in this more general case (Zeldovich, 1970).

In the *Zeldovich approximation*, the development of perturbations into the non-linear regime is followed in Lagrangian coordinates, the same procedure described in Sect. 11.2. In other words, rather than working out the development of the perturbation in some external Eulerian reference frame, the motion of particles in a comoving coordinate frame is followed. If \mathbf{x} and \mathbf{r} are the proper and comoving position vectors of the particles of the fluid, the Zeldovich approximation can be written

$$\mathbf{x} = a(t)\mathbf{r} + b(t)\mathbf{p}(\mathbf{r}) . \quad (16.10)$$

The first term on the right-hand side describes the uniform expansion of the background model and the second term the comoving deviations $\mathbf{p}(\mathbf{r})$ of the particles' positions relative to a fundamental observer located at comoving vector position \mathbf{r} . Zeldovich showed that, in the coordinate system of the principal axes of the ellipsoid, the motion of the particles in comoving coordinates is described by a 'deformation tensor' D :

$$D = \begin{bmatrix} a(t) - \alpha b(t) & 0 & 0 \\ 0 & a(t) - \beta b(t) & 0 \\ 0 & 0 & a(t) - \gamma b(t) \end{bmatrix} . \quad (16.11)$$

Because of conservation of mass, the density ϱ in the vicinity of any particle is

$$\varrho[a(t) - \alpha b(t)][a(t) - \beta b(t)][a(t) - \gamma b(t)] = \bar{\varrho}a^3(t) , \quad (16.12)$$

where $\bar{\varrho}$ is the mean density of matter in the Universe. The clever aspect of the Zeldovich approximation is that, although the constants α , β and γ vary from point to point in space depending upon the local density distribution, the functions $a(t)$ and $b(t)$ are the same for all particles. In the case of the critical model, $\Omega_0 = 1$,

$$a(t) = \frac{1}{1+z} = \left(\frac{t}{t_0}\right)^{2/3} \quad \text{and} \quad b(t) = \frac{2}{5} \frac{1}{(1+z)^2} = \frac{2}{5} \left(\frac{t}{t_0}\right)^{4/3} , \quad (16.13)$$

where $t_0 = 2/3H_0$. The function $b(t)$ has exactly the same dependence upon scale factor (or cosmic time) as was derived from perturbing the Friedman solutions in Sect. 11.4.2. This can be demonstrated by expanding (16.12) for small values of $b(t)$ for the case $\alpha = \beta = \gamma$ and comparing it with (11.47).

For the case $\alpha > \beta > \gamma$, collapse occurs most rapidly along the x -axis and the density becomes infinite when $a(t) - \alpha b(t) = 0$. At this point, the ellipsoid has collapsed to a 'pancake' and the solution breaks down at later times. Although the density becomes formally infinite in the pancake, the surface density remains finite, and so the solution still gives the correct result for the gravitational potential at points away from the caustic surface. Note that, in the Zeldovich approximation, the cold dark matter particles move purely under gravity and have no internal pressure.

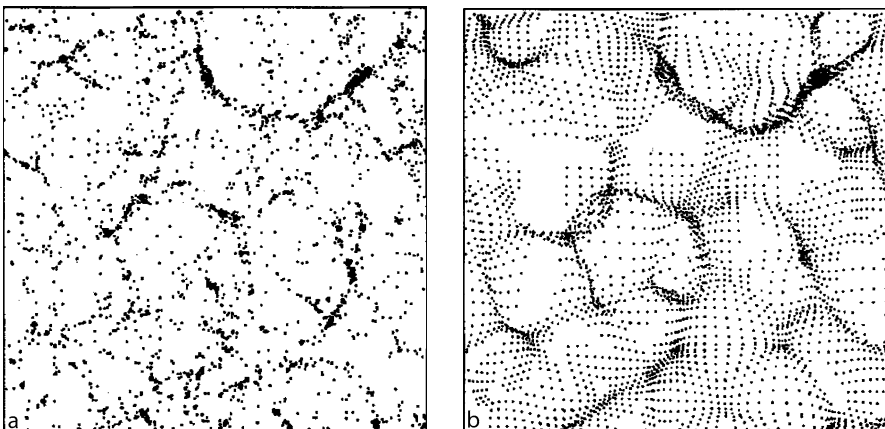


Fig. 16.1a,b. A comparison between the formation of large-scale structure according to a N-body simulations and **b** the Zeldovich approximation, which began with the same initial conditions, which were assumed to be Gaussian with power spectrum $P(k) \propto k^{-1}$ (Coles et al., 1993; Coles and Lucchin, 1995). The agreement between the two approaches is very good, particularly when highly non-linear Fourier modes with $k \geq k_{\text{nl}} = 8$ are truncated, as has been adopted in Fig. 16.1b

Consequently, collapse of the ellipsoids into pancakes does not give rise to strong shock waves, which would occur in purely baryonic models.

The results of numerical N-body simulations have shown that the Zeldovich approximation is quite remarkably effective in describing the non-linear evolution of large-scale structures up to the point at which caustics are formed. A comparison between the results of adopting the Zeldovich approximation and those of N-body simulations is shown in Fig. 16.1 (Coles et al., 1993; Coles and Lucchin, 1995). The two simulations began with the same Gaussian power spectrum with $P(k) \propto k^{-1}$. In the case of the Zeldovich approximation, the coefficients of the deformation tensor have to be evaluated at each point in space. Coles and his colleagues found that the Zeldovich approximation was extremely accurate quantitatively for power spectra characterized by $n = -1$ or less; when the approximation was ‘enhanced’ by truncating highly non-linear Fourier modes with $k \geq k_{\text{nl}}$, the approximation was found to be excellent even for $n = +1$ (Coles et al., 1993).

16.2 The Role of Dissipation

The analysis of the last section was primarily concerned with the non-linear dynamical evolution of dark matter perturbations. Their characteristic feature was that dark matter particles are collisionless and so are only detectable in bulk by their gravitational influence. In contrast, the baryonic component of galaxies is what makes them instantly recognisable optically, the emission being the integrated radiation of stars and interstellar material. This radiation is a sure sign that dissipative processes are

at work. The word dissipative is used in the sense that the baryonic matter can lose energy by a myriad of radiative processes, resulting in the loss of thermal energy from the system. It is certain that these processes take place and so the baryonic component of galaxies loses internal energy and shrinks within the dark matter haloes.

Once the gas within the system is stabilised by thermal pressure, loss of energy by radiation is an effective way of decreasing the internal pressure, allowing the region to contract and re-establish pressure equilibrium. If the radiation process is very effective in decreasing the thermal energy, and hence the pressure support, of the system, a runaway situation can result which is known as a *thermal instability*. This is the process which is responsible for the cooling flows observed in the hot intracluster gas in the central regions of rich clusters of galaxies (Sect. 4.4).

There are numerous ways in which dissipation plays an important role in galaxy formation. Undoubtedly star formation is an essential feature of the formation and evolution of galaxies, and we will study evidence on the cosmic star and heavy element formation rates in Chap. 19. In our own Galaxy, stars are formed within cool, dusty regions, most of the star formation occurring within giant molecular clouds, which pervade the disk of our Galaxy. The likely sequence of events is that a region within a cool dust cloud becomes unstable, either through the Jeans instability, described in Sect. 11.3, or the equivalent instability in a differentially rotating medium (expression (18.8)). The collapse of the gas cloud may also be stimulated by external influences, such as the passage of the gas cloud through a spiral arm, by compression of the gas by the blast wave of a supernova remnant or some other large-scale dynamical perturbation, such as the strong gravitational interactions, or collisions, of galaxies (see Sect. 3.3).

A star can only be formed if the collapsing protostellar cloud can get rid of its gravitational binding energy, and the most important means of achieving this is by radiation. This process continues until the cloud becomes optically thick to its own radiation. The loss of binding energy from the protostar is then mediated by the dust grains in the contracting gas cloud. The dust grains are heated to temperatures of about 60 to 100 K, and then energy can be radiated away at far-infrared wavelengths, at which the collapsing cloud is transparent to radiation. Observations of star-forming regions by the IRAS, ISO and Spitzer infrared space observatories and by ground-based millimetre and submillimetre telescopes make it wholly convincing that this is the process by which stars are formed at the present day in galaxies.

In the case of the very first generation of stars, there is the problem that there were no heavy elements present in the primordial gas out of which dust grains could be formed. In this case, star formation presumably had to take place in a gas of essentially pure molecular hydrogen. This suggests that the process of formation of the first generation of stars may well have been somewhat different from what we observe at the present day in our Galaxy. Once the first generation of massive stars had formed, however, the fraction of the heavy elements in the interstellar medium could build up rapidly, and it was out of this enriched gas that dust and subsequent generations of stars could form. Direct evidence of star formation in very large redshift objects has been obtained from millimetre and submillimetre observations of

molecular gas and dust emission in a variety of different types of galaxies, including quasars, Lyman-break galaxies, radio galaxies, ultraluminous infrared galaxies and radio-detected submillimetre galaxies (Omont, 1996; Ohta et al., 1996; Omont et al., 1996; Greve et al., 2005). Greve and his colleagues provide a convenient list of all the objects detected in the submillimetre lines of carbon monoxide (CO) with redshifts in the range $1 \leq z \leq 6$ up to 2005. Further direct evidence for on-going star formation out to the largest accessible redshifts is summarised by Bergeron in her survey of all classes of galaxy which can be observed out to redshift $z = 7$, and possibly greater redshifts (Bergeron, 2006). Of particular interest are studies of Lyman-break galaxies, many of which have been observed at redshifts of $z \geq 6$. These are convincingly associated with star-forming galaxies, as will be described in more detail in Chap. 19. There is therefore no doubt that there must have been considerable early enrichment of the interstellar media of galaxies.

Dissipative processes thus play a dominant role in the formation and evolution of stars, and this leads to the question of whether or not similar processes are important in the formation of larger-scale baryonic structures. The role of dissipative processes in galaxy formation was elegantly described by Rees and Ostriker, who considered the cooling of a primordial plasma with the primaeval abundances of hydrogen and helium (Rees and Ostriker, 1977). Silk and Wyse included in addition cooling by heavy elements at different levels of enrichment relative to the primordial values into their cooling curves (Silk and Wyse, 1993). The key relation is the energy loss rate of the plasma by radiation as a function of temperature (Fig. 16.2). The cooling rate is presented in the form $dE/dt = -N^2 \Lambda(T)$, where N is the number density of hydrogen ions. In the absence of heavy metals, the dominant loss mechanism at high temperatures, $T > 10^6$ K, is thermal bremsstrahlung, the energy loss rate being proportional to $N^2 T^{1/2}$. At lower temperatures, the main loss mechanisms are free-bound and bound-bound transitions of hydrogen at $T \approx 10^4$ K and of ionised helium at $T \approx 10^5$ K, corresponding to the two maxima in the primordial cooling curve of Fig. 16.2. As the abundance of the heavy elements increases, the overall energy loss rate can be more than an order of magnitude greater than that of the primordial plasma at temperatures $T \leq 10^6$.

For the case of a fully ionised plasma, the cooling time is defined to be the time it takes the plasma to radiate away its thermal energy

$$t_{\text{cool}} = \frac{E}{|dE/dt|} = \frac{3NkT}{N^2 \Lambda(T)}. \quad (16.14)$$

This timescale can be compared with the timescale for gravitational collapse, $t_{\text{dyn}} \approx (G\rho)^{-1/2} \propto N^{-1/2}$. The significance of these timescales is best appreciated by inspecting the locus of the equality $t_{\text{cool}} = t_{\text{dyn}}$ in a temperature-number density diagram (Fig. 16.3). The locus $t_{\text{cool}} = t_{\text{dyn}}$ is a mapping of the cooling curve of the hydrogen-helium plasma loss rate onto the $T - N$ plane. Inside this locus, the cooling time is shorter than the collapse time, and so it is expected that dissipative processes are more important than dynamical processes in determining the behaviour of the baryonic matter. Also shown on Fig. 16.3 are lines of constant mass, as well as loci corresponding to the radiation loss time being equal to the age of the Universe and to

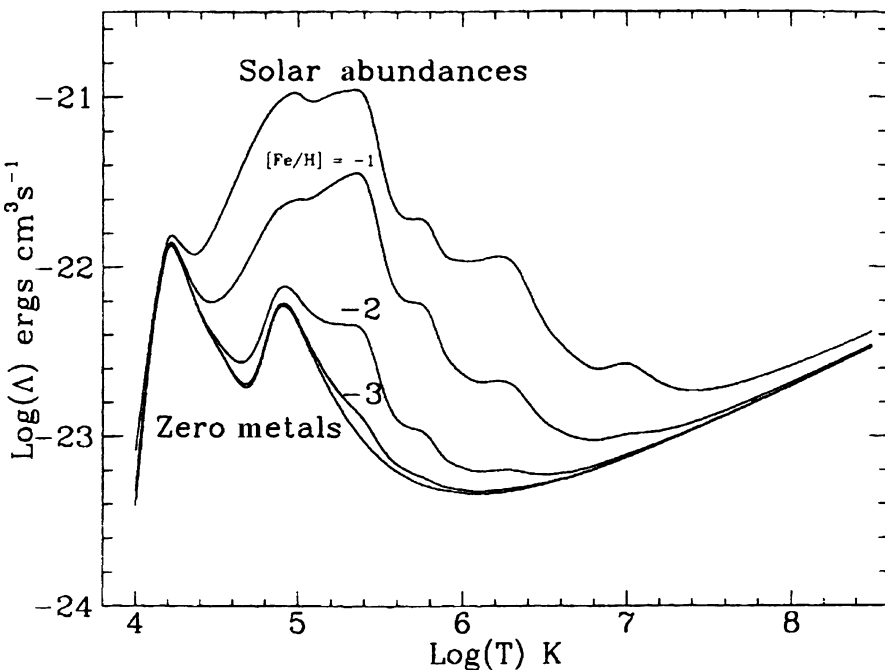


Fig. 16.2. The cooling rate per unit volume $\Lambda(T)$ of an astrophysical plasma of number density 1 nucleus cm^{-3} by radiation for different cosmic abundances of the heavy elements, ranging from zero metals to the present abundance of heavy elements as a function of temperature T (Silk and Wyse, 1993). In the zero metal case, the two maxima in the cooling curve are associated with the recombination of hydrogen ions and doubly ionised helium

the perturbations having such low density that they do not collapse gravitationally in 10^{10} years. It can be seen that the range of masses which lie within the critical locus, and which can cool in 10^{10} years, is $10^6 \leq M/M_\odot \leq 10^{12}$; this is the important conclusion of this analysis.

The fact that the masses lie naturally in the range of observed galaxy masses suggests that they are not only determined by the initial fluctuation spectrum, but also by dissipative astrophysical processes as well. It is intriguing that there is nothing in the spectrum of dark matter perturbations which would give rise naturally to the characteristic masses of galaxies being typically $M^* \sim 10^{10} M_\odot$ – the processed initial power spectrum is featureless at such masses. We will return to this issue in the next section.

This diagram can be used astrophysically in the following way. For any theory of the origin of large-scale structure, the density and temperature of the gas can be worked out as a function of cosmic epoch. Figure 16.3 can then be used to determine whether or not cooling by radiative processes is important. A good example was found in the various versions of the baryonic adiabatic pancake theory. When the gas cloud collapsed to form a pancake, the matter fell into a singular plane and, as

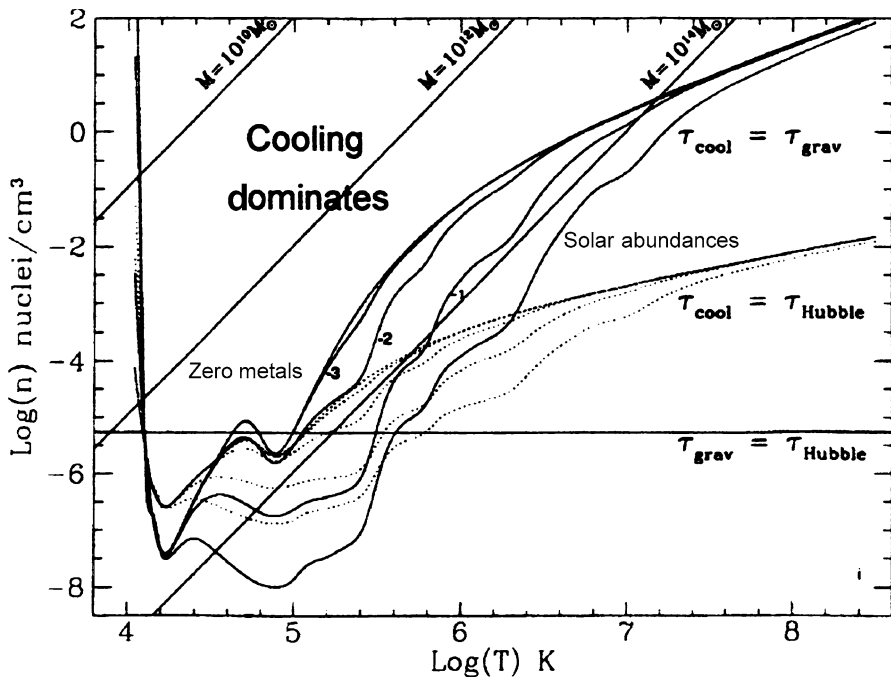


Fig. 16.3. A number density-temperature diagram showing the locus defined by the condition that the collapse time of a region t_{dyn} should be equal to the cooling time of the plasma by radiation t_{cool} for different abundances of the heavy elements (Silk and Wyse, 1993). Also shown are lines of constant mass, a cooling time of 10¹⁰ years (dotted lines), and the density at which the perturbations are of such low density that they do not collapse in the age of the Universe

a result, a shock wave passed out through the infalling matter, heating it to a high temperature. In this picture, galaxies could form by thermal instabilities in the heated gas. Inspection of Fig. 16.3 shows that, if the gas were heated above 10⁴ K, there would be no stable region for masses in the range 10⁹ to 10¹² M_{\odot} .

A second exercise carried out by Blumenthal and his colleagues was to plot the observed location of galaxies on a temperature-number density diagram similar to Fig. 16.3, but using velocity dispersion in place of temperature (Blumenthal et al., 1984). The effective temperature associated with the velocity dispersion of the stars in a galaxy or the galaxies in a cluster, $\frac{1}{2}kT_{\text{eff}} \approx \frac{1}{2}mv^2$, was plotted rather than the thermal temperature of the gas. The irregular galaxies fell well within the cooling locus and the spirals, S0 and elliptical galaxies all lay close to the critical line. On the other hand, the clusters of galaxies lay outside the cooling locus. Thus, cooling is expected to be an important factor in the formation of galaxies.

In the analysis of Rees and Ostriker, it was assumed that all the mass of galaxies was in the form of baryonic matter. Even at that time, this was a dubious assumption because of the problems of the large mass-to-luminosity ratios of large galaxies and

groups and clusters of galaxies. An important advance was made by White and Rees, who studied the more realistic case in which the galaxies and clusters are dominated by dark matter, the baryonic matter constituting only about 20% of the total mass (White and Rees, 1978). The dark haloes were assumed to form according to the scenario discussed in Sect. 16.1 and so provided the potential wells into which the baryonic matter could collapse and cool. They referred to this picture as a two-stage theory of galaxy formation, and it foreshadows the present favoured scenario. At that time, there were a number of problems with this picture, but these are best discussed in the context of the evolution of the mass function of the dark matter haloes; this leads naturally to the study of the Press–Schechter mass function.

16.3 The Press–Schechter Mass Function

According to the cold dark matter scenario for galaxy formation, galaxies and larger-scale structures were built up by the process of hierarchical clustering. An elegant description of this process was developed in 1974 in a remarkable paper by Press and Schechter (Press and Schechter, 1974). Their objective was to provide an analytic formalism for the process of structure formation once the density perturbations had reached such an amplitude that they could be considered to have formed bound objects. Press and Schechter were well aware of the limitations of their approach, but it has turned out that their mass function and its evolution with cosmic epoch are in remarkably good agreement with more detailed analyses and with the results of supercomputer simulations.

16.3.1 Exposition – Elementary Theory

The analysis begins with the assumption that the primordial density perturbations were *Gaussian fluctuations*. Thus, the phases of the waves which made up the density distribution were random and the probability distribution of the amplitudes of the perturbations could be described by a Gaussian function

$$p(\Delta) = \frac{1}{\sqrt{2\pi}\sigma(M)} \exp\left[-\frac{\Delta^2}{2\sigma^2(M)}\right], \quad (16.15)$$

where $\Delta = \delta\rho/\rho$ is the density contrast associated with perturbations of mass M . Being a Gaussian distribution, the mean value of the distribution is zero but its variance $\sigma^2(M)$, that is, the mean-squared fluctuation, is finite:

$$\langle \Delta^2 \rangle = \left\langle \left(\frac{\delta\rho}{\rho} \right)^2 \right\rangle = \sigma^2(M). \quad (16.16)$$

This is exactly the statistical description of the perturbations implicit in the analysis of Sect. 14.2, in particular the statistical average (14.12).

The Press–Schechter analysis begins with the assumption that, when the perturbations had developed to amplitude greater than some critical value Δ_c , they evolved rapidly into bound objects with mass M . Given the considerations of Sect. 16.1.1, this is an entirely plausible assumption, but it sweeps an enormous amount of detailed astrophysics under the carpet. Let us see where it leads. The problem is now completely defined since we can assume that the perturbations had a power-law power spectrum $P(k) = k^n$ and we know the rules which describe the growth of the perturbations with cosmic epoch. Press and Schechter assumed that the background world model was the critical Einstein–de Sitter model, $\Omega_0 = 1$, $\Omega_\Lambda = 0$, so that the perturbations developed as $\Delta \propto a \propto t^{2/3}$ right up to the present epoch. The analysis for the standard Λ CDM model is a straightforward extension of this argument.

For fluctuations of a given mass M , the fraction $F(M)$ of those which became bound at a particular epoch were those with amplitudes greater than Δ_c ,

$$F(M) = \frac{1}{\sqrt{2\pi}\sigma(M)} \int_{\Delta_c}^{\infty} \exp\left[-\frac{\Delta^2}{2\sigma^2(M)}\right] d\Delta = \frac{1}{2} [1 - \Phi(t_c)] , \quad (16.17)$$

where $t_c = \Delta_c/\sqrt{2}\sigma$ and $\Phi(x)$ is the probability integral defined by

$$\Phi(x) = \frac{2}{\sqrt{\pi}} \int_0^x e^{-t^2} dt . \quad (16.18)$$

Expression (14.26) can be used to relate the mean square density perturbation to the power spectrum of the perturbations.

$$\sigma^2(M) = \left\langle \left(\frac{\delta\rho}{\rho} \right)^2 \right\rangle = \langle \Delta^2 \rangle = A M^{-(3+n)/3} , \quad (16.19)$$

where A is a constant. We can now express t_c in terms of the mass distribution

$$t_c = \frac{\Delta_c}{\sqrt{2}\sigma(M)} = \frac{\Delta_c}{\sqrt{2}A^{1/2}} M^{(3+n)/6} = \left(\frac{M}{M^*} \right)^{(3+n)/6} , \quad (16.20)$$

where we have introduced a reference mass $M^* = (2A/\Delta_c^2)^{3/(3+n)}$.

Since the amplitude of the perturbation $\Delta(M)$ grew as $\Delta(M) \propto a \propto t^{2/3}$, it follows that $\sigma^2(M) = \Delta^2(M) \propto t^{4/3}$, that is, $A \propto t^{4/3}$. Therefore,

$$M^* \propto A^{3/(3+n)} \propto t^{4/(3+n)} , \quad (16.21)$$

which can be rewritten

$$M^* = M_0^* \left(\frac{t}{t_0} \right)^{4/(3+n)} , \quad (16.22)$$

where M_0^* is the value of M^* at the present epoch t_0 .

The fraction of perturbations with masses in the range M to $M + dM$ is $dF = (\partial F/\partial M) dM$. In the linear regime, the mass of the perturbation is $M = \bar{\rho}V$, where

$\bar{\rho}$ is the mean density of the background model. Once the perturbation became non-linear, collapse ensued and ultimately a bound object of mass M was formed. The space density $N(M) dM$ of these masses was V^{-1} , that is,

$$N(M) dM = \frac{1}{V} = -\frac{\bar{\rho}}{M} \frac{\partial F}{\partial M} dM , \quad (16.23)$$

the minus sign appearing because F is a decreasing function of increasing M .

We now have everything we need to determine the mass distribution and how it evolved with time from (16.17), (16.22) and (16.23). Noting that

$$\frac{d\Phi}{dx} = \frac{2}{\sqrt{\pi}} e^{-x^2} , \quad (16.24)$$

we find

$$N(M) = \frac{1}{2\sqrt{\pi}} \left(1 + \frac{n}{3}\right) \frac{\bar{\rho}}{M^2} \left(\frac{M}{M^*}\right)^{(3+n)/6} \exp\left[-\left(\frac{M}{M^*}\right)^{(3+n)/3}\right] , \quad (16.25)$$

in which all the time dependence of $N(M)$ has been absorbed into the variation of M^* with cosmic epoch (16.22).

This formalism results in only half the total mass density being condensed into bound objects because of the fact that, according to this simple analysis, only the positive density fluctuations of the symmetrical Gaussian distribution (16.15) developed into bound systems. The underlying cause of this factor of 2 discrepancy is the fact that the above analysis is based upon the linear theory of the growth of the perturbations. Once the perturbations developed to large amplitude, mass was accreted from the vicinity of the perturbation and N-body simulations show that most of the mass was indeed condensed into discrete structures. Press and Schechter were well aware of this problem and argued that the mass spectrum (16.25) should be multiplied by a factor of 2 to take account of the accretion of mass during the non-linear stages. Efstathiou showed how the problem of the evolution of the mass function can be formulated in such a way that all the mass is condensed into bound objects (Efstathiou, 1990).

Thus, the mass function can be written in the somewhat more compact form

$$N(M) = \frac{\bar{\rho}}{\sqrt{\pi}} \frac{\gamma}{M^2} \left(\frac{M}{M^*}\right)^{\gamma/2} \exp\left[-\left(\frac{M}{M^*}\right)^\gamma\right] , \quad (16.26)$$

where $\gamma = 1 + (n/3)$ and $M^* = M^*(t_0)(t/t_0)^{4/3\gamma}$. To illustrate how the mass function changes with cosmic epoch, we need to choose the value of spectral index n . We are interested in the range of small masses which eventually clustered hierarchically to form galaxies and clusters of galaxies and so we need the modified initial mass spectrum which is shown in Fig. 14.1b. As discussed in Sect. 14.3, the appropriate value of n is -3 if the unprocessed primordial mass spectrum was of Harrison-Zeldovich form. The variation of the Press-Schechter mass function with time for $n = -3$ is shown in Fig. 16.4.

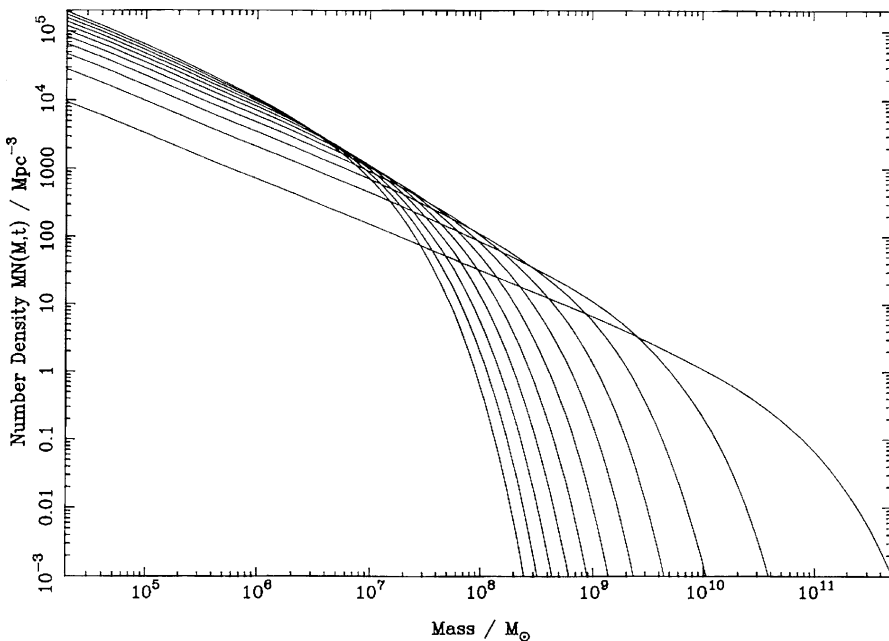


Fig. 16.4. Illustrating the variation of the form of the Press–Schechter mass function as a function of cosmic time for the processed Harrison–Zeldovich spectrum in the limit of small masses, that is, $n = -3$ (courtesy of Dr Andrew Blain). Note that the ordinate is plotted in units of $M N(M, t)$ and that the critical Einstein–de Sitter model is assumed

16.3.2 Development and Recapitulation

This remarkable argument has been the subject of a great deal of discussion and debate over the last 20 years (Monaco, 1998). Schechter has given an amusing and enlightening history and critique of the mass function which can be thoroughly recommended (Schechter, 2002). Press and Schechter were well aware of the limitations of the model, and a number of their assumptions turned out to be wrong – for example, their analysis assumed that all the matter in the Universe is baryonic and has the critical cosmological density. A pleasant assessment of the procedure was the statement by Monaco (Monaco, 1999):

There is a simple, effective and wrong way to describe the cosmological mass function. Wrong, of course, does not refer to the results, but to the whole procedure.

Monaco described numerous reasons why the calculation should not work. For example, there is the ‘peaks-within-peaks’ problem in the sense that a full treatment would take account of the fact that, in general, any perturbation of a particular wavenumber k is superimposed upon other longer wavelength perturbations. This issue has been the subject of intensive study (Bardeen et al., 1986; Efstathiou, 1990;

Kauffmann and White, 1993). Another problem is the assumption of spherical symmetry, which certainly breaks down, as discussed in Sect. 16.1.2 (Sheth et al., 2001). Monaco’s reasons why it should not work are perhaps most succinctly summarised in his statement that:

Once the “statistical” problem of achieving the correct normalization is solved, the worst defect of the Press–Schechter recipe is that it completely neglects the complexities of gravitational dynamics, which is treated just at the linear level.

Let us consider a few of the problems highlighted by Schechter in his critical assessment. He emphasised that the formalism describes the hierarchical clustering of smaller into larger masses, terminating with the formation of the mass spectrum of clusters of galaxies at the present epoch. A clear success of the theory is the prediction that the mass spectrum of clusters is of power-law form with an exponential cut-off at high masses, in good agreement with the observed mass function of clusters (Schechter, 2002). In the process of achieving this, however, it was implicitly assumed that smaller mass structures were wiped out as they coalesced to form more massive structures. Why then is there a mass, or luminosity, function for galaxies in clusters?

Early N-body simulations seemed to confirm the wiping out of all small-scale structures, but this now appears to have been the result of the lack of resolution and the necessity of softening the $1/r$ potential at small radii in the numerical simulations. The most recent massive N-body simulation, the *Millennium Simulation*, shows that there is indeed disruption of the coalescing dark matter haloes, but a significant fraction survives and can populate the haloes of giant clusters (Springel et al., 2005). In fact, there now appears to be the problem that the mass spectrum of what are referred to as ‘subhaloes’ has a power-law mass spectrum which results in too many low-mass systems and no exponential cut-off at high masses. These features differ from the observed *luminosity function* of galaxies, but of course the luminosities of galaxies are determined by their baryonic rather than their dark matter content. The formation of galaxies as we know them must involve the separation of the dark from the baryonic matter. Schechter argues that the dimensions of the baryonic component could be up to ten times smaller in size than the dark matter halo. He argues that the solution of these problems lies in the baryonic dissipative processes discussed by Ostriker, Rees and White, as well as feedback processes which can suppress the formation of baryonic structures within low-mass subhaloes. For large baryonic masses of low density, inspection of Fig. 16.3 shows that the cooling times can become of the order of the age of the Universe and this might be the cause of the exponential cut-off in the luminosity function of galaxies. We will discuss these issues in more detail in Chap. 19 in the context of semi-analytic models of galaxy formation.

For the moment, we are only interested in the evolution of the mass function of the dark matter haloes. Despite the concerns about the validity of the procedure by which it was derived, the most recent large-scale simulations for the standard Λ CDM model show that the Press–Schechter mass function is a remarkably effective description

of the form and evolution of the mass function of dark matter haloes with cosmic epoch. Figure 16.5 shows the results of the massive Millennium Simulation which involved following the evolution of more than 10^{10} particles. The symbols show the results of the computations of the differential mass function as a function of redshift. Notice that the ordinate is plotted as $(M^2/\bar{\rho}) dn/dM$ and so is one power of M ‘flatter’ than Fig. 16.4. $\bar{\rho}$ is the mean density of the background model. The solid lines show a parametric fit to the simulations and the faint dotted lines the predicted Press–Schechter function at redshifts $z = 10.07$ and $z = 0$. Although not perfect, the success of the Press–Schechter formalism is apparent. Springel and his colleagues caution that at the high-mass end where the ‘exponential’ cut-off occurs, the Press–Schechter function underpredicts the mass function by up to an order of magnitude, but, given the nature of exponentials, this is perhaps not too surprising. Notice also the flatness of the differential multiplicity function over a very wide range of low masses, of more or less exactly the same form expected from our analysis of the modified initial mass function.

One may ask why the formalism works so well in light of the concerns about the whole procedure. Monaco suggests that, because of the large number of dynamical effects to be considered, some form of ‘central limit theorem’ applies, meaning that the fluctuations on a given mass scale will end up being approximately Gaussian, whatever the input physics. Part of the success of the model can also be attributed to the fact that the perturbations do not become very non-linear before they are assumed to become bound systems. This assumption is made at all stages of the hierarchical clustering process.

The Press–Schechter formalism is therefore a useful tool for studying the development of galaxies and clusters of galaxies in hierarchical scenarios of galaxy formation. As an example of the use of the function, Efstathiou matched the Press–Schechter mass function to the results of N-body simulations of the development of galaxies and clusters within the context of the standard $\Omega_0 = 1$ cold dark matter model (Efstathiou, 1995). He then used that function to illustrate how the comoving number density of dark matter haloes with masses greater than a given value, $N(\geq M, z)$, changes with redshift (Fig. 16.6), which is just a different projection of Fig. 16.5 (Efstathiou, 1995; Efstathiou and Rees, 1988). The present number density of L^* galaxies is shown as a dotted line.

Although derived for the $\Omega_0 = 1$, $\Omega_\Lambda = 0$ model, the results are similar for the preferred Λ CDM model. Figure 16.6 illustrates a number of important aspects of hierarchical clustering models. First of all, it demonstrates vividly how the most massive systems formed rather late in the Universe. The considerations of Sect. 16.1.1 suggested that massive galaxies with $M = 10^{12} M_\odot$ could not have formed earlier than a redshift of 7 and giant clusters would only form late in the Universe. These conclusions are reinforced by the evolution of the mass function shown in Fig. 16.6.

Galaxies with masses $M \sim 10^{12} M_\odot$ only appear in substantial numbers at redshifts $z \leq 4$. Efstathiou and Rees used this result to suggest that there would necessarily be a rather dramatic cut-off to the distribution of quasars at redshifts $z \geq 4$ (Efstathiou and Rees, 1988). The basis of the argument was that supermassive

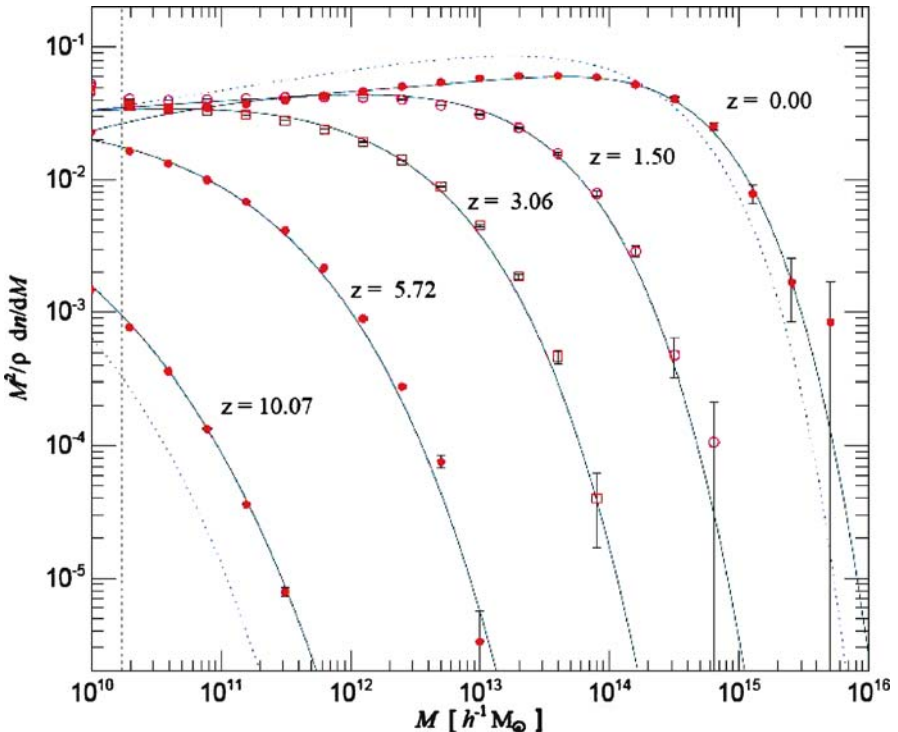


Fig. 16.5. Differential halo number density as a function of mass and redshift from the *Millennium Simulation* (Springel et al., 2005). The function $n(M, z)$ is the comoving number density of haloes with masses less than M . What is plotted is the differential halo multiplicity function in the form $(M^2/\bar{\rho}) dn/dM$, where $\bar{\rho}$ is the mean density of the Universe. Springel and his colleagues describe the procedures used to identify bound systems at each epoch. The *solid lines* represent an analytic fitting function, while the *dotted lines* show the Press–Schechter function at $z = 10.07$ and $z = 0$

black holes with $M \sim 10^9 M_\odot$ in the nuclei of galaxies are necessary to power the quasars observed at redshifts of $z \sim 4$ and these can only form from the baryonic component of the galaxy. Since the baryonic matter probably amounts to only about 10% of the mass of the dark matter halo, it follows that, to create a $10^9 M_\odot$ black hole, 1% of the baryonic mass would have to form a black hole in the nucleus of the galaxy. Among nearby galaxies at the present epoch, supermassive black hole masses are typically about 0.3% of their halo masses (Kormendy and Richstone, 1995; Magorrian et al., 1998), and so it would be feasible for $10^{12} M_\odot$ galaxies to contain massive enough black holes to power the most luminous quasars. The comoving number density of galaxies with masses $M = 10^{12} M_\odot$ decreases rapidly with increasing redshift beyond $z = 4$, and so the likelihood of observing quasars as luminous as those at $z \sim 3\text{--}4$ decreases dramatically, consistent with the decrease in their observed comoving space densities at large redshifts (see Sect. 17.5).

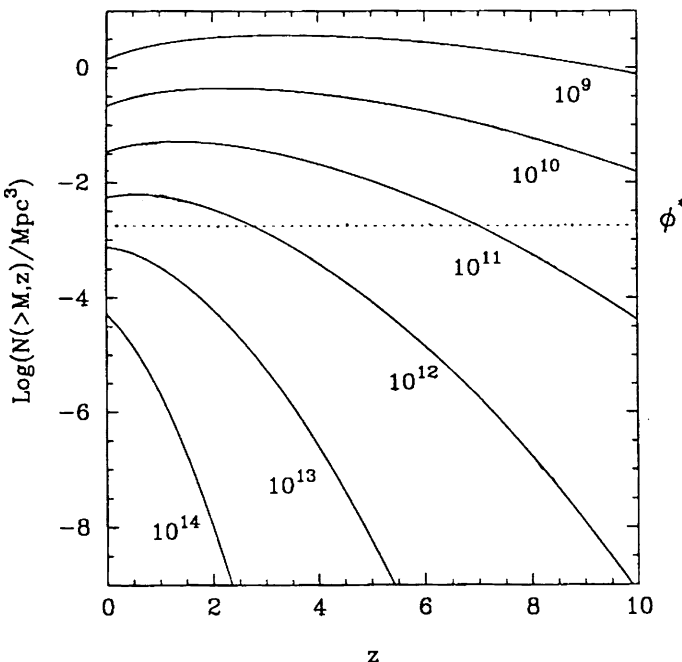


Fig. 16.6. The evolution of the comoving number density of dark matter haloes with masses greater than M as a function of redshift for a standard cold dark matter model with $\Omega_0 = 1$. The curves have been derived using the Press–Schechter form of evolution of the mass spectrum, which is a close fit to the results of N-body simulations. The dotted line labelled ϕ^* shows the present number density of L^* galaxies (Efstathiou, 1995)

Notice also the large number density of low-mass objects present throughout the redshift interval $0 < z < 10$. It is intriguing that, in her review of large redshift galaxies, Bergeron noted that the Lyman-limit galaxies detected at redshifts of $z \sim 6$ have a comoving luminosity function which is an order of magnitude lower than that at redshift $z \sim 2\text{--}3$.

These are persuasive arguments that the Press–Schechter formalism provides a convenient means of parameterising the process of formation of dark matter haloes through the entire post-recombination era from $z = 1000$ to the present epoch. The challenge is now to incorporate the baryonic matter as well; this will not prove so simple.

17 The Evolution of Galaxies and Active Galaxies with Cosmic Epoch

17.1 Introduction

Evidence for strong evolutionary changes of the populations of extragalactic objects with cosmic epoch was first found in surveys of extragalactic radio sources and quasars in the 1950s and 1960s. An excess of faint sources was discovered in radio source and quasar surveys as compared with the expectations of uniform world models. The inference was that these classes of objects were much more common at earlier cosmic epochs than they are at the present time. During the 1980s, the first deep counts of galaxies to very faint magnitudes became available thanks to the CCD revolution in optical detector technology. An excess of faint blue galaxies was discovered at faint apparent magnitudes and these studies were extended to extremely faint galaxies by Hubble Space Telescope observations of the Hubble Deep Field and the Hubble Ultra Deep Field.

This pattern of the discovery of excess numbers of faint objects at early cosmic epochs has been repeated in essentially all wavebands as deep surveys have become feasible. In the 1990s, the surveys of the X-ray sky carried out by the ROSAT X-ray Observatory provided evidence for an excess of faint X-ray sources, similar to that found for the extragalactic radio sources and quasars. These studies were extended to much fainter X-ray sources by observations with the Chandra and XMM-Newton X-ray Observatories. The IRAS survey of the mid- and far-infrared sky, although not extending to as large redshifts as the radio and X-ray surveys, provided evidence for an excess of faint sources. The deep mid- and far-infrared surveys carried out by the Spitzer Infrared Space Telescope have confirmed the large excess of faint infrared sources. Surveys became feasible in the submillimetre waveband in the late 1990s and a very large excess of faint submillimetre sources was discovered, the objects being associated with luminous dust-emitting galaxies.

Consequently, the study of the cosmological evolution of all classes of extragalactic object with cosmic epoch is now a major industry for those astrophysicists involved in understanding the origin and evolution of galaxies. These studies have been enormously advanced by the availability of the current generation of 8- to 10-m class ground-based optical-infrared telescopes, as well as the large-scale surveys of galaxies and quasars resulting from the AAT 2dF Survey and the Sloan Digital Sky Survey.

To generalise rather sweepingly, these studies of changes in source populations with cosmic epoch can be divided into two overlapping areas. The first is the evolution

of the stellar and gaseous components of galaxies with cosmic epoch. These studies include the evolution of the stellar populations and physical properties of galaxies, the changes in the numbers and chemical composition of the absorption line systems observed in the spectra of distant quasars, the evolution of the global star formation rate with cosmic epoch and so on.

The second concerns the evolution of the properties of systems with active galactic nuclei – the quasars, the Seyfert galaxies, the extragalactic radio and X-ray sources and their close relatives. These phenomena are associated with the presence of supermassive black holes in the nuclei of galaxies, and their defining characteristic is that their intense emission is dominated by non-thermal radiation processes such as synchrotron radiation and inverse Compton scattering of high-energy electrons. Undoubtedly, these two aspects of cosmic evolution will eventually converge into an understanding of the co-evolution of the stellar and black hole properties of galaxies, but at the moment exactly what that relation might be is not securely established, although the empirical evidence is accumulating in intriguing ways.

The primary data involved in both aspects of these studies are the availability of large complete samples of objects with accurately known flux densities or apparent magnitudes. The simplest way of analysing these data is simply to count the numbers of objects brighter than different flux density limits and compare these with the expectations of the standard world models. In itself, this procedure can provide global evidence for changes in source populations with cosmic epoch. Once redshifts and spectroscopic evidence become available for large samples of sources, the analysis can be greatly refined and the nature of the astrophysical changes with cosmic epoch determined in detail.

The plan of this chapter is to present an overview of what can be learned empirically from surveys of various classes of astrophysical object. This involves exploring number counts, redshift surveys and the background radiation and how these data can be used to constrain cosmological evolutionary changes. In Chap. 18, we investigate the physics of the intergalactic medium and in Chap. 19 the challenges of synthesising all these data into a convincing astrophysical picture for the origin and evolution of galaxies and the black holes in their nuclei.

17.2 Counts of Galaxies and Active Galaxies

In his earliest studies of galaxies as extragalactic systems, Hubble realised that the number counts of galaxies contain information about the large-scale structure of the Universe. In his famous monograph *The Realm of the Nebulae*, he used counts of galaxies to the limit of the Mount Wilson 100-inch telescope to demonstrate that, overall, their distribution is homogeneous on the large scale (Hubble, 1936). He also believed he had found evidence for deviations from the local Euclidean counts at faint apparent magnitudes, which he interpreted as being due to the non-Euclidean nature of space–time when galaxies are observed at large distances (Fig. 17.1). Hubble's argument concerning the homogeneity of the distribution of galaxies is

a powerful one and applies to objects studied in any waveband. It is worth repeating that argument as a preliminary to what follows.

17.2.1 Euclidean Source Counts

Suppose the sources have a luminosity function $N(L) dL$ and that they are uniformly distributed in Euclidean space. The numbers of sources with flux densities S greater than different limiting values in the solid angle Ω on the sky is denoted $N(\geq S)$. Consider first sources with luminosities in the range L to $L + dL$. In a survey to a limiting flux density S , these sources can be observed out to some limiting distance r , given by the inverse square law, $r = (L/4\pi S)^{1/2}$. The number of sources brighter than S is therefore that within distance r in the solid angle Ω ,

$$N(\geq S, L) dL = \frac{\Omega}{3} r^3 N(L) dL . \quad (17.1)$$

Substituting for r , the number of sources brighter than S is

$$N(\geq S, L) dL = \frac{\Omega}{3} \left(\frac{L}{4\pi S} \right)^{3/2} N(L) dL . \quad (17.2)$$

Integrating over the luminosity function of the sources,

$$N(\geq S) = \frac{\Omega}{3(4\pi)^{3/2}} S^{-3/2} \int L^{3/2} N(L) dL , \quad (17.3)$$

that is, $N(\geq S) \propto S^{-3/2}$, independent of the luminosity function $N(L)$. The result $N(\geq S) \propto S^{-3/2}$ is known as the *integral Euclidean source counts* for any class of extragalactic object. In terms of apparent magnitudes, $m = \text{constant} - 2.5 \log_{10} S$, the Euclidean source counts become

$$N(\leq m) \propto 10^{0.6m} \quad \text{or} \quad \log N(\leq m) = 0.6m + \text{constant} . \quad (17.4)$$

This was the homogeneity test carried out by Hubble with the results shown in Fig. 17.1.

The integral counts $N(\geq S)$ suffer from the disadvantage that the numbers of sources counted to different limiting flux densities are not independent since bright objects contribute to the counts at all lower flux densities. It is therefore statistically preferable to work in terms of *differential source counts* rather than integral counts, so that the numbers of sources counted in each flux density interval are independent. In this case,

$$dN(S) = N(S) dS \propto S^{-5/2} dS . \quad (17.5)$$

The corresponding expression in terms of apparent magnitudes is

$$dN(m) = N(m) dm \propto 10^{0.6m} dm . \quad (17.6)$$

These are useful reference relations and it is convenient to compare the observed counts and the expectations of various world models with them, as we illustrate below.

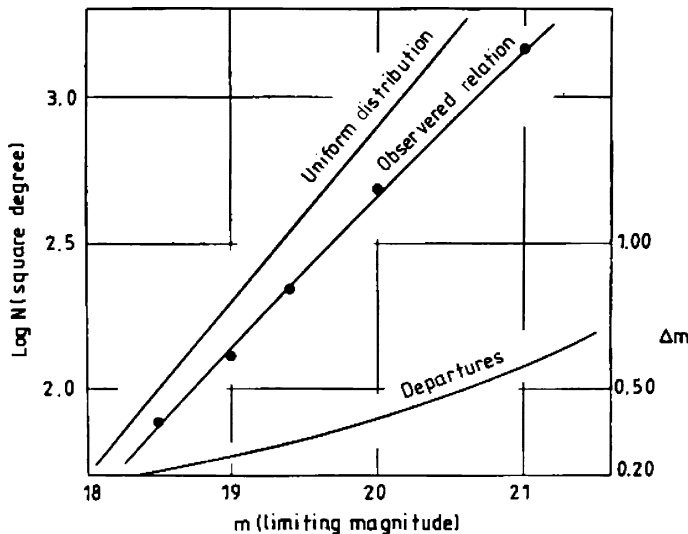


Fig. 17.1. Hubble's counts of galaxies (Hubble, 1936). The counts follow the Euclidean prediction at bright apparent magnitudes but depart from the prediction $\log N(\leq m) = 0.6m + \text{constant}$ towards the limit of the survey. Hubble interpreted this departure as evidence for the non-Euclidean nature of the space-time geometry of the Universe at large redshifts

17.2.2 Source Counts for the Standard World Models

We have developed all the tools necessary for predicting number counts and redshift distributions in Sect. 5.5. The two key relations are (5.64) and (5.73), which relate flux densities and number densities to redshift for isotropic world models. To repeat these relations,

$$S(v_0) = \frac{L(v_1)}{4\pi D^2(1+z)} ; \quad (17.7)$$

$$dN(z) = N(z) dz = \Omega D^2 N_0 dr , \quad (17.8)$$

where $v_0 = v_1/(1+z)$ is the frequency of observation at the present epoch, v_1 the emitted frequency and N_0 the local number density of sources. The formula relating the distance measure D to redshift z for world models with $\Omega_A = 0$ is given by (7.77). For models with $\Omega_A \neq 0$, (7.74) can be used to find the dependence of the comoving radial distance coordinate r upon redshift and then D found from $D = \mathfrak{N} \sin(r/\mathfrak{N})$, where \mathfrak{N} is given by (7.43).

A number of important differences as compared with the Euclidean formulae are immediately apparent.

- The observed flux density now depends upon the spectrum of the source because the radiation emitted at frequency ν_1 is observed at the redshifted frequency $\nu_0 = \nu_1/(1+z)$. For observations in the optical waveband, the differences between an inverse square law in luminosity distance and the predictions of the standard world models, when account is taken of the fact that a different region of the spectrum is observed, are often expressed in terms of K-corrections, as described by (5.70) and (5.71). Personally, I find it conceptually preferable to work directly with integrals over the emitted and observed frequency intervals.
- In the standard world models, the distance measure D tends to a finite limit as $z \rightarrow \infty$ (Figs. 7.6 and 7.7). Unless the spectrum is strongly inverted, as is the case for dust spectra in the submillimetre waveband, the effects of observing the source spectrum at a redshifted frequency generally result in the sources becoming fainter with increasing redshift. To put it another way, the effects of the K-correction compensate for the fact that D tends to a finite value as $z \rightarrow \infty$.
- The volume element per unit redshift interval changes from $dN(z) \propto z^2 dz$ at small redshifts, $z \ll 1$, to $dN(z) \propto z^{-3/2} dz$ at redshifts $\Omega_0 z \gg 1$. The volume elements become smaller and smaller with increasing redshift, resulting in a ‘cut-off’ to the source distribution at redshifts $\Omega_0 z \gg 1$.

It therefore becomes progressively more and more difficult to discover large redshift objects since they are discriminated against both in flux density and observable volume. For these reasons, the number counts of sources in the standard world models normally predict fewer sources as compared with the expectations of the Euclidean source counts if the source distribution extends to large redshifts. One of the great triumphs of observational cosmology has been that means have been found of overcoming these disadvantages. The study of discrete objects with redshifts up to $z \approx 6$ and beyond is unquestionably one of the most exciting areas of modern astrophysical cosmology.

For illustrative purposes, let us consider the case of a population of sources which have power-law spectra, $L(\nu) \propto \nu^{-\alpha}$, which is a good approximation for the spectra of extragalactic radio sources, X-ray sources and quasars, where $\alpha \approx 1$ is the spectral index. We adopt $\alpha = 1$ in the numerical examples given below, and this has the fortunate advantage that the results are then also exact for bolometric luminosities and flux densities, as can be seen by comparing (5.65) and (5.67). The flux density–redshift relation (17.7) then becomes

$$S(\nu_0) = \frac{L(\nu_0)}{4\pi D^2(1+z)^{1+\alpha}}. \quad (17.9)$$

Differentiating (17.9),

$$\frac{dS}{dz} = -\frac{L(\nu_0)}{4\pi D^2(1+z)^{1+\alpha}} \left[\frac{(1+\alpha)}{(1+z)} + \frac{2\left(\frac{dD}{dz}\right)}{D} \right]. \quad (17.10)$$

For a uniform population of sources of local space density $N_0(L)$, (17.8) becomes

$$dN = N(z) dz = \frac{c}{H_0} \frac{\Omega N_0(L) D^2}{[(1+z)^2(\Omega_0 z + 1) - \Omega_A z(z+2)]^{1/2}} dz . \quad (17.11)$$

Now, for a locally Euclidean population of sources, we expect

$$N_0(\geq S) = \frac{\Omega}{3} N_0(L) \left[\frac{L(v_0)}{4\pi S} \right]^{3/2} ; \quad dN_0 = -\frac{\Omega}{2} N_0(L) \left[\frac{L(v_0)}{4\pi} \right]^{3/2} S^{-5/2} dS . \quad (17.12)$$

Hence

$$\begin{aligned} \frac{dN}{dN_0} &= \frac{(dN/dS)}{(dN/dS)_0} \\ &= \frac{2c(1+z)^{-(3/2)(1+\alpha)}}{H_0 \left[(\Omega_0 z + 1) - \Omega_A \frac{z(z+2)}{(1+z)^2} \right]^{1/2} \left[D(1+\alpha) + 2(1+z) \left(\frac{dD}{dz} \right) \right]} . \end{aligned} \quad (17.13)$$

In general, this result for dN/dN_0 is cumbersome, but there is a simple solution for the Einstein-de Sitter world model, $\Omega_0 = 1$, $\Omega_A = 0$,

$$\frac{dN}{dN_0} = \frac{(1+z)^{-1.5(1+\alpha)}}{[(1+\alpha)(1+z)^{1/2} - \alpha]} . \quad (17.14)$$

To illustrate the expected behaviour of dN/dN_0 , (17.13) has been evaluated for some popular world models as a function of flux density and redshift in Fig. 17.2. The Euclidean prediction $dN/dN_0 = \text{constant}$ is represented by the abscissa, $\log_{10}(dN/dN_0) = 0$. Figure 17.2a shows the relations for world models with $\Omega_A = 0$ and Fig. 17.2b for models with $\Omega_0 + \Omega_A = 1$. The predicted differential counts depart rapidly from the Euclidean expectation even at relatively small redshifts. For example, for the case $\Omega_0 = 1$, the source counts at redshift $z = 0.5$ have differential slope -2.08 rather than -2.5 , corresponding to a slope of the integral source counts of -1.08 rather than -1.5 . Thus, the effects of redshift set in at much smaller redshifts than might be expected. Similar results are found for models with finite values of Ω_A which are shown in Fig. 17.2b. The three models have $\Omega_0 + \Omega_A = 1$ and $\Omega_0 = 1, 0.6$ and 0.3 ; the world model with $\Omega_0 = 0.3$ corresponds to our reference model. Note that some care needs to be taken in obtaining the correct relations for some models with finite values of Ω_A for the reasons explained in Sect. 17.2.4.

In practice, the source populations cannot be represented by a single luminosity, but rather, the differential counts shown in Fig. 17.2 should be convolved with the luminosity function $N_0(L)$ of the sources. It is evident, however, that because all the relations shown in Fig. 17.2 are monotonically decreasing functions of decreasing flux density, convolution with *any* function must also produce a monotonically decreasing function of decreasing flux density. In other words, in all viable world

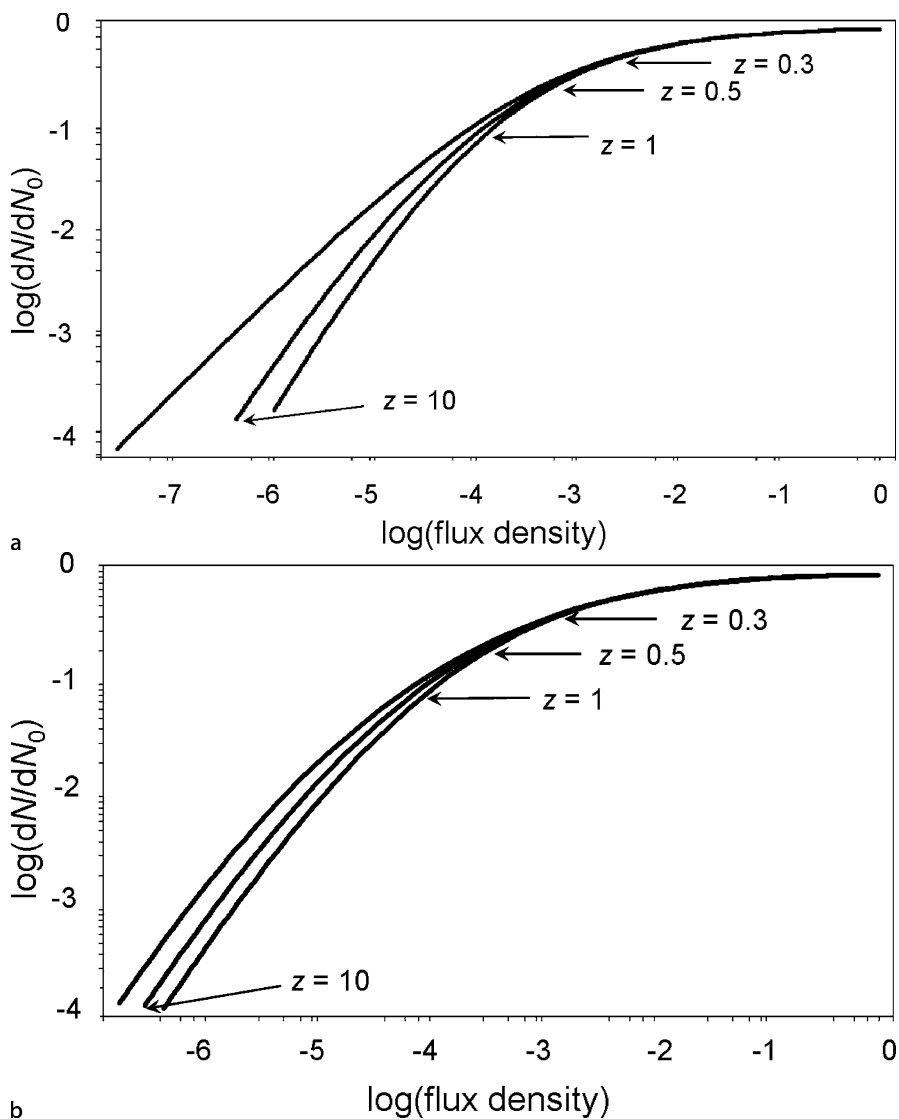


Fig. 17.2. **a** The predicted normalised differential source counts for a single luminosity class of source having spectral index $\alpha = 1$ for different values of the density parameter Ω_0 with $\Omega_A = 0$. Top to bottom: the differential counts are for models with $\Omega_0 = 0, 1$ and 2 (Longair, 1978). Arrows: redshifts at which the sources are observed. The integration was terminated at $z = 10$. **b** The same as **a** but for models with $\Omega_0 + \Omega_A = 1$ and spectral index $\alpha = 1$. Top to bottom: the differential counts are shown for models with $\Omega_0 = 0.3, 0.6$ and 1

models, the slope of the differential and integral source counts must be smaller than the Euclidean predictions, that is, if $N(\geq S) \propto S^{-\beta}$, $\beta < 1.5$.

Historically, this was an important result because the counts of extragalactic radio sources at high flux densities have integral slope $\beta = 1.8$, much steeper than that expected for any of the standard uniform world models (Fig. 17.9). In the 1960s, this was strong evidence that extragalactic radio sources were much more common at large redshifts than expected in uniform, isotropic models, indicating that the source population must have evolved strongly with cosmic epoch. The argument holds good for all models in which the flux densities of the sources decrease with increasing frequency, as is also the case for optically and X-ray selected quasars.

The same type of argument can be used in interpreting the number counts of γ -ray bursts which were defined by observations with the BATSE instrument of the Compton Gamma-ray Observatory. Their distribution is uniform over the sky and the slope of the number counts was found to be somewhat flatter than $\beta = 1.5$ (Paciesas et al., 1999). It is natural to assume that they are distant extragalactic objects, an inference subsequently confirmed by their optical identification through observations of their afterglows by the Beppo-SAX satellite (Costa et al., 1997; Sahu et al., 1997).

For galaxies observed in the optical waveband, the predicted number counts depend upon knowledge of their spectra in the ultraviolet waveband and this is sensitive to their star-formation histories. As an example, Fig. 17.3 shows the results of computations of the evolution with cosmic epoch of the spectral energy distribution of a model giant elliptical galaxy in its rest frame. The model involves the passive evolution of the stellar energy distribution in the sense that the stellar population was formed in an initial starburst of duration 10^8 years and the subsequent evolution followed using the stellar synthesis codes of Bruzual and Charlot (Bruzual and Charlot, 2003). There is a one-to-one relation between the mass of a star, its luminosity and the waveband in which it emits most of this luminosity and so stars radiating in the ultraviolet waveband are massive and have short lifetimes. This is reflected in the rapid decline of the spectral energy distribution in the ultraviolet regions of the spectrum with cosmic epoch. Consequently, the K-corrections to be used in the optical waveband are very sensitive to bursts of star-formation activity. Of course, if the spectrum of the galaxy is known throughout the ultraviolet, optical and infrared regions of the spectrum, there is no need to use empirical K-corrections – these can be found from the ratio $S[\nu_0/(1+z)]/S(\nu_0)$. This may not, however, be feasible if the galaxies are very faint and the redshifts are unknown.

The situation is somewhat better if the observations are carried out in the infrared waveband (Inskip et al., 2002). It can be seen from Fig. 17.3 that, if the observations are made at $2 \mu\text{m}$, for example, the corrections for the passive evolution of the stellar populations are much more stable and systematic as compared with the optical waveband since even at $z = 3$, the spectral energy distributions are much less influenced by star formation events. We will find that star-formation activity dominates the deep counts of galaxies in the optical waveband.

The form of evolution shown in Fig. 17.3 is known as the *passive evolution* of the galaxy spectral energy distribution, in that the stellar population was formed in

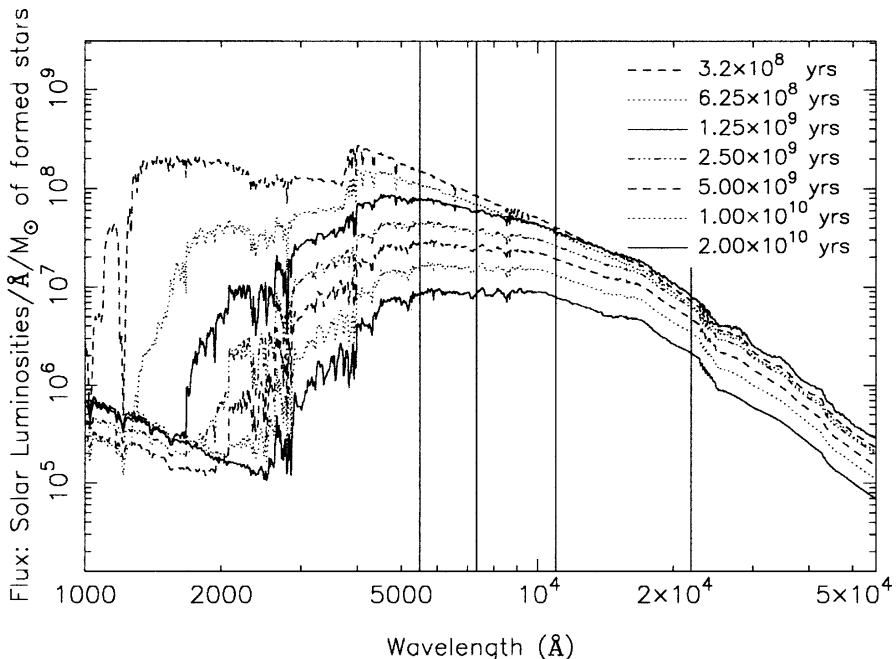


Fig. 17.3. Spectral evolution of a model giant elliptical galaxy in which the stellar population was formed in an initial starburst of duration 10^8 years. The computations used the stellar synthesis codes for the spectral energy distribution of galaxies developed by Bruzual and Charlot (Bruzual and Charlot, 2003). The predicted galaxy spectra are shown in equal logarithmic intervals of cosmic time up to the present day. The initial stellar population was chosen so that the observed spectrum of a giant elliptical galaxy at the present epoch was reproduced (Inskip et al., 2002). The vertical lines show the rest wavelengths which would be observed at redshifts $z = 0, 1, 2$ and 3 from right to left respectively if the galaxy were observed at a wavelength of $2.2\ \mu\text{m}$

an initial starburst and the resulting evolution is simply the ageing of that population. We can understand how the results for the infrared waveband come about by simple astrophysical arguments. As pointed out by Tinsley and Gunn, most of the infrared luminosity originates from stars on the red giant branch and their luminosities and colours are essentially independent of the masses of their main sequence progenitors (Tinsley and Gunn, 1976). The lifetimes of red giant stars are much shorter than the time their progenitors spend on the main sequence, and so the number of red giant stars is given by the product of the rate at which stars evolve off the main sequence onto the giant branch and the time they spend there. We need only know the rate of evolution of stars off the main sequence for quite a narrow range of masses, as can be understood from the following argument.

The mass-luminosity relation for stars on the main sequence is assumed to take the form $L/L_\odot = (M/M_\odot)^x$. Their main sequence lifetimes are determined by the time it takes the star to burn about 10% of its mass into helium, the well-

known *Schönberg–Chandrasekhar limit*. During evolution on the main sequence, the luminosities of stars of a given mass are remarkably constant (Kippenhahn and Weigert, 1990; Tayler, 1994). Since the available fuel is proportional to the mass of the star, it follows that the main sequence lifetime is $t = t_\odot(M/M_\odot)^{-(x-1)}$, where t_\odot is the main sequence lifetime of the Sun, which is about 10^{10} years. For stars with $M \sim M_\odot$, $x \sim 5$ and so the lifetimes of stars of mass $M = 2M_\odot$ is only 1/16 of the age of the Sun, that is, about 6×10^8 years. Thus, the range of masses of stars which contribute most of the light of the old stellar populations of galaxies lie in the range $1 < M_\odot < 2$ over the range of redshifts of interest.

Since the time stars spend on the giant branch, t_g , and their luminosities are relatively independent of their main-sequence masses, to find the change in luminosity of a galaxy with redshift, we need only determine the rate at which stars evolve off the main sequence onto the giant branch as a function of main-sequence mass (Gunn, 1978). It is assumed that all the stars were formed in an initial brief starburst and that the subsequent luminosity evolution of the galaxy is due to the stellar evolution of this population. Let us assume that the initial mass function of the stars was of Salpeter form, $dN = N(M) dM \propto M^{-y} dM$, where $y = 2.35$. It is a straightforward calculation to show that the number of stars on the giant branch N_g is

$$N_g = t_g \frac{dN}{dt} = t_g \left(\frac{dN}{dM} \right) \left(\frac{dM}{dt} \right). \quad (17.15)$$

Using the above relation between mass and main-sequence lifetime, $t = t_\odot(M/M_\odot)^{-(x-1)}$, we find

$$L(t) = L(t_0) t^{-(x-y)/(x-1)}. \quad (17.16)$$

Inserting the values $x = 5$ and $y = 2.35$, we find $L \propto t^{-0.66}$. For the case of the critical world model, $t/t_0 = (1+z)^{-3/2}$, and so, to an excellent approximation, $L \propto (1+z)$. Thus, at a redshift of 1, the old stellar populations of galaxies should be about twice as luminous as they are at the present epoch, and at redshift $z = 3$, four times as luminous. This accounts for the rather systematic behaviour of the decrease in infrared luminosity of galaxies seen in Fig. 17.3. Typically, if the galaxies evolved passively, they would only be about a magnitude more luminous at redshifts of $z \sim 1\text{--}2$ than they are at the present epoch.

17.2.3 Submillimetre Counts of Dusty Galaxies

The predictions shown in Fig. 17.2 are strongly modified for galaxies which are intense dust emitters if they are observed in the submillimetre waveband, $0.1 \leq \lambda \leq 1\text{ mm}$. Examples of the stellar energy distributions from submillimetre to ultraviolet wavelengths for a sample of infrared galaxies selected at $60\text{ }\mu\text{m}$ are shown in Fig. 17.4a (Sanders and Mirabel, 1996). The intense far-infrared and submillimetre emission is the radiation of heated dust grains, either because of intense star formation or because of heating by the ultraviolet radiation of an obscured

active galactic nucleus. The observed submillimetre spectra are similar to those of star-forming regions in our Galaxy and take the form of modified black-body spectra. The maximum intensity at 50 to 100 μm corresponds to the temperatures to which the dust grains are heated, which are about 30 to 60 K. To the long-wavelength side of this maximum, the dust clouds are optically thin and the spectral index of their thermal emission is typically $\alpha \approx -3$ to -4 . As can be seen from Fig. 17.4a, the ‘infrared galaxies’ can have luminosities in the far-infrared waveband which exceed those in the optical waveband and these types of galaxy are expected to be the dominant contributors to the counts of sources in the submillimetre waveband. These ‘inverted’ spectra strongly modify the predicted flux density–redshift relation and the predicted number counts in these wavebands.

Examples of the flux density–redshift relations at submillimetre wavelengths are shown in Fig. 17.4b. The relation flattens, or even inverts, at redshifts of $z \sim 1$ because of the very large negative K-corrections in these wavebands (Blain and Longair, 1993, 1996). From the flatness of the flux density–redshift relation at redshifts $z \geq 1$, it can be seen that, once these galaxies are observed at $z \sim 1$, the whole of the redshift range out to $z \sim 5 - 10$ becomes observable at about the same flux density. As a result, there is expected to be a dramatic increase in the numbers of sources at this flux density and the differential source counts are quite different from those shown in Fig. 17.2. In Fig. 17.4c, the predicted differential source counts are shown for a population of far-infrared sources with the far-infrared luminosity function of IRAS galaxies, which was determined at a wavelength of 60 μm (Saunders et al., 1990). When the source distribution extends to redshifts $z \geq 1$, the source counts are inverted with $\beta > 1.5$, even if there is no cosmological evolution of the source population.

17.2.4 Number Counts in Models with Finite Ω_Λ

Differential number counts for world models with $\Omega_\Lambda \neq 0$ were presented in Sect. 7.2.2 but they deserve a little more attention because of the stretching of the cosmological timescale associated with positive values of Ω_Λ . Let us consider the extreme case in which the Universe almost reached a stationary Eddington–Lemaître state at some redshift z_c (Fig. 7.3c). As discussed in Sect. 7.4.5, the flux density–redshift relation is strongly modified for those Lemaître models which differ only slightly from the static Eddington–Lemaître case. It can be seen from Fig. 7.10 and expression (7.79) that the strictly homogeneous models have an infinite flux density at those redshifts corresponding to the poles and antipoles in the relation between comoving radial distance coordinate and redshift.

It takes a little care to work out the number counts in these cases (Longair and Scheuer, 1970). The example shown in Fig. 17.5 is a Lemaître model which differs only slightly from an Eddington–Lemaître model, which would be stationary at redshift $z_c = 2$. The value of the dark energy density parameter is $\Omega_\Lambda = \Omega_{\Lambda c}(1 + \epsilon)$, where $\Omega_{\Lambda c}$ is the value of Ω_Λ for the stationary Eddington–Lemaître model and $\epsilon = 0.02$. The counts are shown as normalised *integral source counts* for a single luminosity class of source with spectral index $\alpha = 1$. The sharp peaks in these

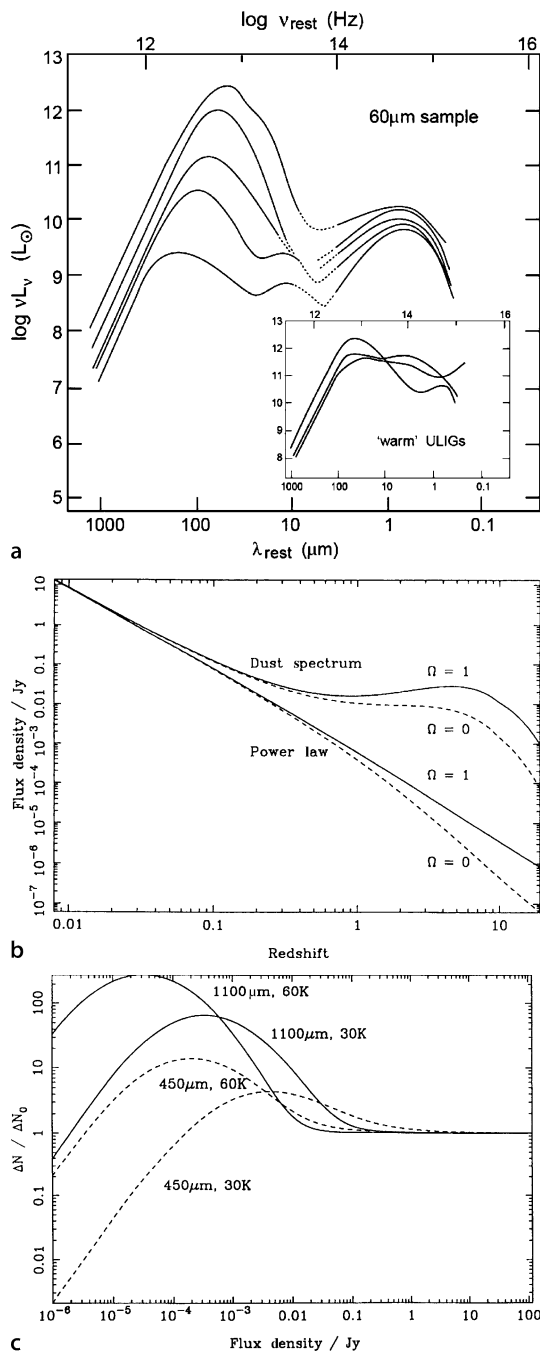


Fig. 17.4. **a** Examples of the stellar energy distributions from submillimetre to ultraviolet wavelengths for a sample of infrared galaxies selected at $60\text{ }\mu\text{m}$. The insert shows the energy distributions for ultraluminous infrared galaxies which have ‘warm’ infrared colours (Sanders and Mirabel, 1996). **b** The flux density–redshift relation in the submillimetre waveband for an infrared galaxy with the spectrum shown in **a**, assuming the source has far-infrared luminosity $10^{13} L_{\odot}$ for world models with $\Omega_0 = 1$ and 0. For comparison, the flux density–redshift relations for a population of sources with power-law spectra $S_v \propto v^{-1}$ are also shown. **c** The predicted differential normalised counts for a uniform distribution of sources at 450 and $1100\text{ }\mu\text{m}$ assuming the galaxies have spectra similar to those of Fig. 17.4a and that the far-infrared luminosity function at $60\text{ }\mu\text{m}$ is that of IRAS galaxies (Saunders et al., 1990). The predicted number counts at 450 and $1100\text{ }\mu\text{m}$ are shown for dust temperatures of 30 and 60 K (Blain and Longair, 1993)

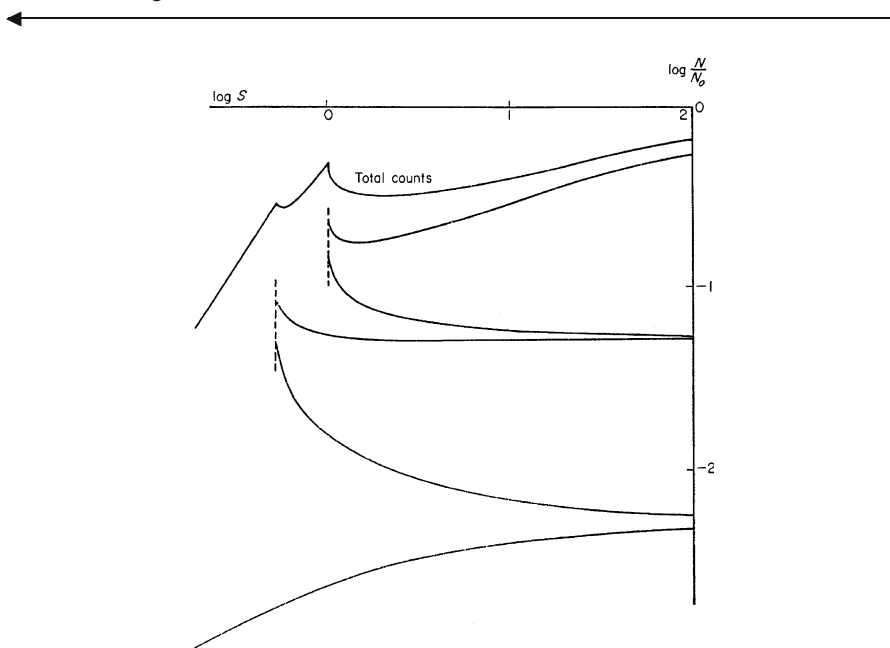


Fig. 17.5. The normalised integral source counts for a Lemaître model which differs only slightly from a static Eddington–Lemaître model. The value of the dark energy density parameter is $\Omega_A = \Omega_{A0}(1 + \epsilon)$, where Ω_{A0} is the value which would result in a static universe at redshift $z_c = 2$. In this example, $\epsilon = 0.02$ and the sources are assumed to have power-law spectra $S \propto v^{-1}$ (Longair and Scheuer, 1970). The vertical dashed lines indicate the flux densities corresponding to the pole and antipole in the flux density–redshift relation. The solid line labelled ‘Total counts’ is the integral source count found by summing the contributions from the ranges of r/\mathfrak{N} from 0 to $\pi/2$, $\pi/2$ to π and so on (Fig. 7.10)

relations correspond to the poles and antipoles in the flux density–redshift relation for this model. It can be seen that the source counts are flatter than the models with $\Omega_A = 0$ at high flux densities, but once observations extend to flux densities

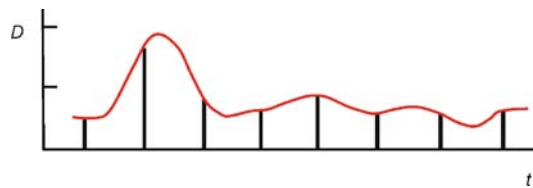


Fig. 17.6. Illustrating the fluctuations in the intensity of the background radiation due to the superposition of faint sources. The diagram represents a scan across a region of sky. The ‘noise’ is due to the superposition of faint sources within the telescope beam. In the $P(D)$ approach to estimating the number counts, individual sources are not identified, but the deflections D of the record are recorded at the Nyquist frequency, which corresponds to twice per telescope beam (after a diagram by Hewish (Hewish, 1961))

beyond the coasting phase at $z \approx z_c$, the counts converge dramatically. To work out a more realistic source count, the function displayed in Fig. 17.5 would have to be convolved with the luminosity function of the sources and this would wipe out the jagged structure in the counts, resulting in a monotonically decreasing function of decreasing flux density.

In reality, it is unlikely that the sharp maxima in the flux density–redshift relation would actually be observed. The existence of the poles and antipoles in the flux density–redshift relation depends upon the Universe being perfectly isotropic and homogeneous and so acting as a perfect lens for the focussing of the light rays from the distant source at the observer. As pointed out by Petrosian and Salpeter, if galaxies were present in the vicinity of the redshifts corresponding to the poles and antipoles, they would cause gravitational deflections of the light rays, resulting in the splitting up of background sources into a number of components, qualitatively similar to those shown in Fig. 4.20 (Petrosian and Salpeter, 1968). These gravitational deflections would have the effect of blurring the peaks in the predicted source counts. It is therefore unlikely that the predictions of the perfectly uniform model would be observed in the real Universe.

17.2.5 Fluctuations in the Background Radiation due to Discrete Sources

A topic of some importance directly related to the number counts of sources is the amplitude of *fluctuations* in the background radiation due to discrete sources. This problem was first solved by Scheuer, for the case of observations made with a radio interferometer and may be stated as follows (Scheuer, 1957) Suppose the sky is observed with a telescope of finite beamwidth θ and the integral number counts of sources are $N(\geq S) \propto S^{-\beta}$. If the survey extends to low enough flux densities, at some point there will be one source per beam area and then, at fainter flux densities, the yet more numerous faint sources cannot be detected individually – they simply add up incoherently within the beam of the telescope. In this circumstance, the noise level of the survey is determined by the random superposition of faint sources within the beam of the telescope, as illustrated schematically in Fig. 17.6. The problem

of detecting radio sources when the ‘noise’ is due to faint unresolved sources in the telescope beam is referred to as *confusion*. In a confusion-limited survey, the flux densities of sources are systematically overestimated because of the random presence of faint sources within each beam with a power-law intensity distribution. This problem afflicted the early 2C radio survey and is the reason the slope of the radio source counts was initially overestimated. Confusion may also limit the detection of fluctuations in the cosmic microwave background radiation on small angular scales (Longair and Sunyaev, 1969).

Subsequently, Scheuer solved the problem of interpreting the background fluctuations in a survey made with a single-beam telescope (Scheuer, 1974). In the $P(D)$ approach, we forget about detecting individual sources and deal directly with the probability distribution of intensity on the sky. If the map is sampled at the information rate, or Nyquist frequency, which corresponds to twice per beamwidth in a one-dimensional scan, a probability distribution $P(D)$ is found for the deflections D on the record measured from some zero level. The term ‘deflection’ D is used since the original radio astronomy surveys were recorded on strip charts and the ‘deflections’ really were the deflections of the recording pen.

Typical $P(D)$ distributions are shown in Fig. 17.7. The distributions are non-Gaussian with a power-law distribution at large values of D but, according to the central limit theorem, the noise level due to the fluctuations is given by the standard deviation of the probability distribution $P(D)$. Very large deflections are identified as discrete sources and so the $P(D)$ distribution tends asymptotically to the differential source count $P(D) dD \propto D^{-(\beta+1)} dD$ for large values of D . Some criterion for the reliable detection of discrete sources has to be established, for example, that the deflection D should exceed five times the standard deviation of the confusion noise, or equivalently restricting the identification of sources to one source per 20 or 30 beam areas.

Scheuer carried out a statistical analysis of the function $P(D)$ for sources selected randomly from the differential source count $dN(S) \propto S^{-(\beta+1)} dS$ and showed how the true slope of the source counts could be found without the need to identify individual sources. Figure 17.7 shows the normalised $P(D)$ distributions for different value of β . It can be seen that the *shape* of the $P(D)$ distribution provides a means of determining the slope of the source counts.

To make order-of-magnitude estimates of the fluctuations, the following argument can be used. The most probable value of $P(D)$ corresponds to the flux density at which the sources have a surface density of one source per beam area. This can be understood as follows. At higher flux densities, the sources are too rare to make a large contribution to the fluctuations in the background signal. At lower flux densities, many faint sources add up statistically and so contribute to the background intensity, but the fluctuations are dominated by the brightest source present in each beam. At roughly one source per beam area, the fluctuations can be thought of as arising from whether or not a source of that flux density is present by chance within the beam. Whereas reliable detection of individual sources can only be made at about five times the confusion noise level, statistical information about the source counts can be obtained to about one source per beam area,

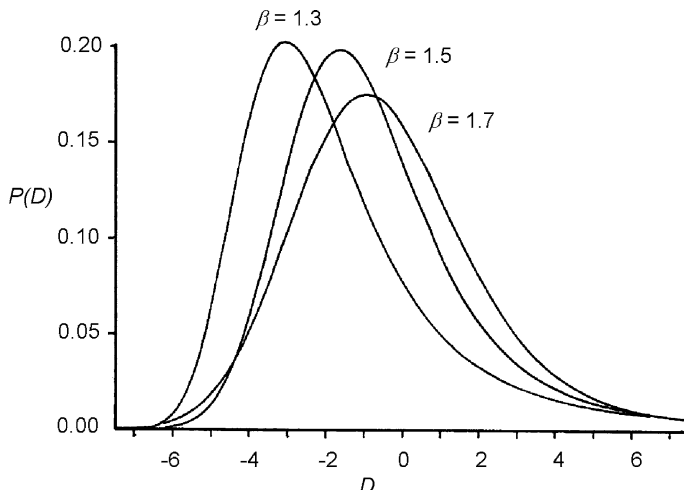


Fig. 17.7. Examples of the theoretical $P(D)$ distributions for observations made with a single-beam telescope for different assumed slopes of the differential source counts $dN(S) \propto S^{-(\beta+1)} dS$. The zero point of the abscissa is the mean amplitude \bar{D} and the areas under the probability distributions have been normalised to unity. The distributions tend asymptotically to $dN(D) \propto D^{-(\beta+1)} dD$ at large deflections D (Scheuer, 1974)

Scheuer's remarkable analysis of 1957 was entirely analytic, and somewhat forbidding. Nowadays, it is simpler to use Monte Carlo methods to work out the functions $P(D)$ for the assumed form of source count. The first study to use Monte Carlo modelling procedures was carried out by Hewish in his analysis of the original records of the Cambridge 4C survey (Hewish, 1961). His analysis made Scheuer's analytic approach more accessible and provided the first evidence for the convergence of the radio source counts at low flux densities. These procedures have been used to determine the radio source counts to the very faintest flux densities, for example, in the analyses of Fomalont and his colleagues and of Wall (Fig. 17.9) (Fomalont et al., 1988; Wall, 1996). They have also been successfully used in analysis of the deep ROSAT surveys by Hasinger and his colleagues (Fig. 17.16) (Hasinger et al., 1993).

A different approach to interpreting the fluctuations in the background radiation is to determine the spatial correlation function of the fluctuations. This has been carried out successfully in the optical waveband by Shectman, who found a clear signature corresponding to the two-point correlation function for galaxies (Shectman, 1974). The observed fluctuation spectrum is in quite remarkable agreement with the standard correlation function found in studies of large samples of galaxies.

Another application of this approach in the ultraviolet waveband was carried out by Martin and Bowyer. In a short rocket flight, they made a survey of a small region of sky and found a significant correlated signal among the spatial distribution of the counts (Martin and Bowyer, 1989). With a number of reasonable assumptions, they were able to show that they had detected the ultraviolet emission from galaxies.

Similar analyses have been carried out for the fluctuations in the X-ray background as observed by the HEAO1 A-2 experiment (Persic et al., 1989) and in five deep *Einstein* fields (Barcons and Fabian, 1989), but with negative results. The same type of fluctuation analysis has been carried out by Kashlinsky and his colleagues for the COBE diffuse background emission in the near-infrared region of the spectrum (Kashlinsky et al., 1996).

17.3 The V/V_{\max} or Luminosity-Volume Test

A more direct method of investigating the uniformity of a distribution of objects in space is to use what is known as the V/V_{\max} or *luminosity-volume test* (Schmidt, 1968; Rowan-Robinson, 1968). A sample of objects is selected which is known to be complete within well-defined flux density and apparent magnitude limits and for which complete redshift information is available. The essence of the test is to ask whether or not the distribution of objects is statistically uniform within the accessible region of space defined by the observational selection criteria. The test has been of particular value in the study of the space distribution of quasars and we begin by discussing it in that context.

Suppose a sample of quasars is *complete* in that all those having flux densities greater than some limiting value S_0 at a particular wavelength have been detected in some region of the sky. Assume also that redshifts have been measured for all of them and so distances can be found once a cosmological model has been adopted. Consider first quasars of a single luminosity L . For each quasar having flux density S , we can evaluate the quantity V/V_{\max} , where V is the volume of space enclosed by the redshift z of the quasar and V_{\max} is the volume of space within which this source could have been observed and still be included in the complete sample. The volume V_{\max} corresponds to the redshift z_{\max} at which a source of intrinsic luminosity L would have observed flux density S_0 . Thus,

$$\frac{V}{V_{\max}} = \frac{\int_0^r D^2 dr}{\int_0^{r_{\max}} D^2 dr}, \quad (17.17)$$

where D is the distance measure and r and r_{\max} are the comoving radial distance coordinates corresponding to z and z_{\max} respectively. Notice that the volumes used in the test are comoving coordinate volumes at the present epoch. Now suppose the distribution of quasars in space is uniform. The mean value of V/V_{\max} is then

$$\left\langle \frac{V}{V_{\max}} \right\rangle = \frac{\int_0^{r_0} \left(\frac{V}{V_{\max}} \right) D^2 dr}{\int_0^{r_0} D^2 dr}. \quad (17.18)$$

Setting

$$\int_0^r D^2 \, dr = X, \quad \frac{dX}{dr} = D^2, \quad (17.19)$$

and hence

$$\left\langle \frac{V}{V_{\max}} \right\rangle = \frac{\int_0^{r_0} X \left(\frac{dX}{dr} \right) dr}{X^2(r_0)} = \frac{1}{2}. \quad (17.20)$$

As is intuitively expected, for a uniform distribution of quasars, we observe sources on average half-way volume-wise to the limits of their observable volumes, independent of the luminosities of the sources.

Furthermore, the values of V/V_{\max} should be uniformly distributed between 0 and 1, if the source distribution is uniform, that is, if they have constant comoving number densities. In the original samples of extragalactic objects such as the 3CR quasars studied by Schmidt, the statistics of the complete samples were often limited and so it was normal practice to evaluate the quantity $\langle V/V_{\max} \rangle$ and compare this with the expected mean value of 0.5. The simplest statistical test for the significance of departures from the expected mean value of 0.5 can be developed as follows. For a uniform distribution of V/V_{\max} between 0 and 1, the standard deviation is $\sigma_0 = 1/\sqrt{12} = 0.288$. When the number of sources N is sufficiently large, the central limit theorem may be used and so the probability distribution of $\langle V/V_{\max} \rangle$ approaches a Gaussian distribution with standard deviation $N^{-1/2}$ of the original distribution, that is, $\sigma = \sigma_0/N^{1/2}$.

Sometimes, the samples of sources are only complete to certain radio and optical flux density limits – for example, in Schmidt's original sample of thirty-three 3CR quasars, the completeness criteria corresponded to a radio flux density limit at 178 MHz of $S_{178} = 9$ Jy and to a limiting optical visual magnitude of 18.4 (Schmidt, 1968). Thus, in some cases the limiting volume was determined by the radio flux density and in others by the optical apparent magnitude. The mean value of V/V_{\max} is, however, still expected to be 0.5 for a uniform distribution of sources, provided the larger of $(V/V_{\max})_{\text{radio}}$ and $(V/V_{\max})_{\text{optical}}$ is chosen for each source.

Thanks to the efforts of many astronomers, the redshifts of large complete samples of galaxies, quasars and active galaxies are now available. An instructive example is the V/V_{\max} distributions for 3CR radio galaxies and radio quasars shown in Fig. 17.8. These objects form complete samples of the brightest radio sources in the northern sky and they have similar redshift distributions, both of them extending to redshifts of $z \sim 2$ (Longair, 1997a). It can be seen that both distributions are biased towards values of V/V_{\max} greater than 0.5. The values of $\langle V/V_{\max} \rangle$ for the quasars and radio galaxies are $\langle V/V_{\max} \rangle = 0.686 \pm 0.042$ and 0.697 ± 0.031 respectively, showing that the objects in these samples were more common at large redshifts. Notice that this is exactly the same result inferred from the number counts of the radio sources and the root cause is the same – the steep source counts means that V/V_{\max} is greater than the mean. The additional information provided by the redshifts

strengthens the case considerably for the strong evolution of the comoving number densities of sources with redshift.

The V/V_{\max} procedure is a very powerful technique for determining the uniformity and space density of any class of object. For example, in Felten's determination of the luminosity function of galaxies, he took account of the effects of extinction by interstellar dust in our Galaxy upon the luminosities and observable volumes within which galaxies of different intrinsic luminosities could be observed (Felten, 1977). In this case, the observable volume is not spherically symmetric about the observer – the key point is that the samples of sources studied should be statistically complete within well-defined observational selection criteria.

Thus, generalising, we may say that the space density of any object can be written $N_i = 1/V_i$, where V_i is the volume of space within which the object could have been observed and still satisfy the selection criteria of the survey. By summing over all the objects in the complete sample, the luminosity function of the objects can be determined. The procedure can be further extended to consider the distribution of objects within a particular redshift interval, what is referred to as a *banded* V/V_{\max} test and this has been useful in studying whether or not there is a cut-off in the distribution of quasars at large redshifts (Waddington et al., 2001). These

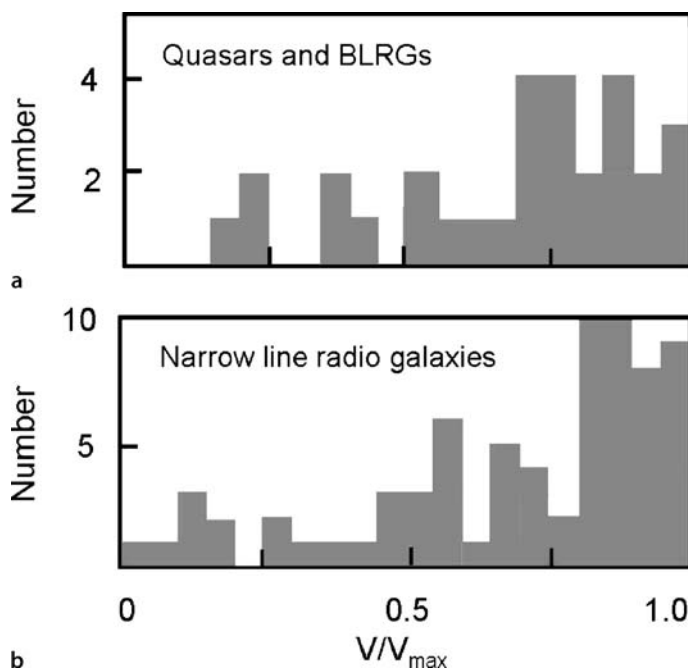


Fig. 17.8a,b. The V/V_{\max} distributions for **a** quasars and broad-line radio galaxies and **b** the narrow-line radio galaxies in a complete sample of extragalactic radio sources selected from the 3CR complete sample (Laing et al., 1983). Redshifts have been measured for all the objects in the sample, which is complete to a limiting radio flux density of 9.7 Jy at 178 MHz (Longair, 1997a)

calculations can be carried out for all objects in the sample within given redshift limits and so luminosity functions as a function of cosmic epoch derived directly from the samples. This type of analysis has been carried out with remarkable success for the 6000 optically selected quasars in the 2dF quasar survey (Fig. 17.14a).

17.4 Background Radiation

It is traditional to refer to the study of the background radiation as the ‘oldest problem in cosmology’. What is commonly called *Olbers’ paradox* revolves around the question

Why is the sky dark at night?

Olbers was one of many scientists who realised that the darkness of the night sky provides us with general information about the large-scale distribution of matter and radiation in the Universe. Harrison has written the history of Olbers’ paradox in his delightful book *Darkness at Night* (Harrison, 1987). In its modern guise, the observed integrated background emission from a population of extragalactic objects, or upper limits to it, can provide useful constraints on their spatial distribution and it is instructive to carry out some simple illustrative calculations which will be elaborated in the following sections.

17.4.1 Background Radiation and Source Counts

Let us first consider the relation between the observed source counts and the background radiation. The background radiation from a population of sources with differential source count $dN \propto S^{-(\beta+1)} dS$ is

$$I \propto \int_{S_{\min}}^{S_{\max}} S dN \propto \int_{S_{\min}}^{S_{\max}} S^{-\beta} dS = \frac{1}{1-\beta} [S^{(1-\beta)}]_{S_{\min}}^{S_{\max}}. \quad (17.21)$$

There is therefore a critical value $\beta = 1$ for the slope of the *integral* source counts. If the slope of the counts is steeper than $\beta = 1$, the background intensity $I_v \propto S_{\min}^{(1-\beta)}$; if the slope of the integral source counts is less than $\beta = 1$, the background intensity is proportional to $S_{\max}^{1-\beta}$. Thus, most of the background radiation originates from that region of the counts with slope $\beta = 1$. A uniform population of sources in Euclidean space has $\beta = 1.5$, but in real-world models the slope decreases with increasing redshift, as discussed in Sect. 17.2, where we showed that the slope of the integral counts is about 1 at a redshift $z \approx 0.5$. Thus, the bulk of the background radiation originates from redshifts $z \ll 1$. Let us carry out some more exact calculations.

17.4.2 Evaluating the Background due to Discrete Sources

For illustrative purposes, we assume that the sources have power-law spectra, $S \propto v^{-\alpha}$, and then the usual flux density-luminosity relation is

$$S(v_0) = \frac{L(v_0)}{4\pi D^2(1+z)^{1+\alpha}}. \quad (17.22)$$

The numbers of sources per steradian in the increment of comoving radial distance coordinate dr in the case of a uniform distribution of sources is

$$dN = N_0 D^2 dr . \quad (17.23)$$

Therefore, the background intensity $I(\nu_0)$ due to this uniform distribution of sources is

$$I(\nu_0) = \int S(\nu_0) dN = \int_0^\infty \frac{L(\nu_0)}{4\pi D^2(1+z)^{1+\alpha}} N_0 D^2 dr \quad (17.24)$$

$$= \frac{L(\nu_0) N_0}{4\pi} \int_0^\infty (1+z)^{-(1+\alpha)} dr . \quad (17.25)$$

For the Friedman world models,

$$dr = \frac{c dz}{H_0 [(\Omega_0 z + 1)(1+z)^2 - \Omega_A z(z+2)]^{1/2}} , \quad (17.26)$$

and so we obtain the result

$$I(\nu_0) = \frac{c}{H_0} \frac{L(\nu_0) N_0}{4\pi} \int_0^\infty \frac{dz}{[(\Omega_0 z + 1)(1+z)^2 - \Omega_A z(z+2)]^{1/2} (1+z)^{1+\alpha}} . \quad (17.27)$$

This result can be compared with the Newtonian version of the same calculation which, from the small redshift limit of (17.27), $z \rightarrow 0$, $r = cz/H_0$, becomes

$$I(\nu_0) = \frac{L(\nu_0) N_0}{4\pi} \int_0^\infty dr . \quad (17.28)$$

This is the standard exposition of *Olbers' paradox*, namely, that, in an isotropic, infinite, stationary Euclidean Universe, the background radiation diverges. This calculation has not taken account of the finite sizes of the sources, nor does it take account of thermodynamics, since in an infinite static Euclidean Universe all the matter must come into thermodynamic equilibrium at the same temperature.

Unlike the integral (17.28), (17.27) converges provided $\alpha > -1.5$. Even if the spectral index of the sources were more negative than this value, any realistic spectrum must eventually turn over at a high enough frequency, as can be seen in the spectra of dusty galaxies in Fig. 17.4a, and so a finite integral is always obtained. For example, the background intensity for world models with $\Omega_A = 0$, $\Omega_0 = 0$ and $\Omega_0 = 1$ are:

$$\Omega_0 = 0 \quad I(\nu_0) = \frac{c}{(1+\alpha)H_0} \frac{L(\nu_0) N_0}{4\pi} ; \quad (17.29)$$

$$\Omega_0 = 1 \quad I(\nu_0) = \frac{c}{(1.5+\alpha)H_0} \frac{L(\nu_0) N_0}{4\pi} . \quad (17.30)$$

Thus, for typical values of α , to order of magnitude, the background intensity is just that originating within a typical cosmological distance (c/H_0), that is,

$$I(v_0) \sim \frac{c}{H_0} \frac{L(v_0)N_0}{4\pi}. \quad (17.31)$$

A combination of factors leads to the convergence of the integral for the background intensity. Inspection of integral (17.27) shows that part of the convergence is due to the factor $(1+z)^{-(1+\alpha)}$, which is associated with the redshifting of the emitted spectrum of the sources. The second is the dependence of r and D upon redshift z . These relations are linear at small redshifts, $z \ll 1$, but, as shown in Figs. 7.6 and 7.7, r and D converge as $z \rightarrow \infty$. This convergence is associated with the fact that the Friedman models have finite ages and consequently there is a finite maximum radial distance from which electromagnetic waves can reach the Earth.

Let us look in a little more detail at the origin of the background radiation in the uniform models. For the critical model $\Omega_0 = 1$, $\Omega_\Lambda = 0$ with $\alpha = 1$, the background intensity out to redshift z is

$$I(v_0) = \frac{2c}{20\pi H_0} L(v_0) N_0 [1 - (1+z)^{-5/2}]. \quad (17.32)$$

Half of the background intensity therefore originates at redshifts $z \leq 0.31$. For the empty world model, $\Omega_0 = 0$, half the intensity originates from redshifts less than 0.42. Thus, although it might be thought that the background radiation would probe the very distant Universe, in fact, most of the radiation originates at redshifts $z \ll 1$. Furthermore, since half of the background is expected to originate at redshifts less than about 0.5, the principal contributors to the background radiation are not difficult to identify nowadays, provided their positions are accurately known. If the main sources of the background are associated with galaxies, there should be no difficulty in discovering the principal contributors to the background radiation, provided the sources are uniformly distributed in space. This statement is not correct, however, if the properties of the sources have evolved strongly with cosmic epoch.

17.4.3 The Effects of Evolution – the Case of the Radio Background Emission

If the luminosity function of the sources evolved with cosmic epoch, the background intensity is

$$I(v_0) = \frac{c}{H_0} \frac{L(v_0)N_0}{4\pi} \int_0^\infty \frac{f(L, z, \text{type}, \dots) dz}{[(\Omega_0 z + 1)(1+z)^2 - \Omega_\Lambda z(z+2)]^{1/2} (1+z)^{1+\alpha}}, \quad (17.33)$$

where the evolution of the comoving luminosity function is described by the function $f(L, z, \text{type}, \dots)$. For simplicity, let us consider one of the simplest forms of

evolution of the luminosity function which is a reasonable fit to the observed number counts and redshift data, ‘luminosity evolution’ of the form

$$\begin{aligned} L(z) &= L_0(1+z)^3 & 0 < z \leq 2; \\ L(z) &= 27L_0 & z > 2. \end{aligned}$$

The integrated background emission from a population of sources which locally has luminosity L_0 and space density N_0 is then

$$I(v_0) = \frac{c}{H_0} \frac{N_0}{4\pi} \int_0^\infty \frac{L(z) dz}{(1+z)^{7/2}}, \quad (17.34)$$

where we have assumed that the spectral index of the sources α is 1 and that $\Omega_0 = 1$, $\Omega_\Lambda = 0$. Performing the integral, we find

$$I(v_0) = \frac{c}{H_0} \left(\frac{N_0 L_0}{4\pi} \right) \left[\frac{12}{5} (1+z_m)^{1/2} - 2 \right]. \quad (17.35)$$

The contributions to the background from redshifts 0 to z_m and from z_m to infinity are in the ratio $5[1 - (1+z_m)^{-1/2}] : 1$.

In the *no-evolution* case, $L(z) = L_0$ for all redshifts and the background intensity is

$$I(v_0) = \frac{2}{5} \frac{c}{H_0} \left(\frac{N_0 L_0}{4\pi} \right). \quad (17.36)$$

In contrast, in the *evolution* case, adopting the simple example of luminosity evolution, the background intensity is $[6(1+z_m)^{1/2} - 5]$ times greater than in the no-evolution case. If we adopt $z_m = 2$, the background intensity is 5.4 times greater than in the case of no evolution.

This example agrees with what is found in interpreting the background radio emission at long radio wavelengths. If the effects of cosmological evolution were neglected, the background brightness temperature due to strong radio sources would amount to a brightness temperature only a few K at 178 MHz. Once the evolutionary effects are included in the calculation, however, a brightness temperature of 16–19 K is found for the strongly evolving component which gives better agreement with that of the isotropic radio background emission of about 23 K at 178 MHz, when the contribution of normal galaxies is included as well (Longair, 1966; Bridle, 1967).

This is a case in which the background emission *does* indeed originate from the distant Universe, the bulk of the background coming from redshifts of order 2, but this only occurs because of the *very* strong effects of cosmological evolution. The important point is that the evolution has to be very drastic if objects at redshifts $z \geq 1$ are to make a significant contribution to the intensity of the background emission.

17.5 The Evolution of Active Galaxies with Cosmic Epoch

17.5.1 Number Counts and V/V_{\max} Tests for Extragalactic Radio Sources

Historically, the number counts of extragalactic radio sources and the V/V_{\max} tests for quasars were among the first pieces of direct evidence for the evolution of certain classes of extragalactic object with cosmic epoch. The history of the early controversies over the counts of radio sources has been recounted by Scheuer and by Sullivan and more briefly, in the context of the development of astrophysical cosmology, in my history of astrophysics and cosmology (Scheuer, 1990; Sullivan, 1990; Longair, 2006). A compilation of counts of radio sources at a wide range of frequencies throughout the radio waveband is shown in Fig. 17.8 (Wall, 1996).

The cause of the controversies in the 1950s and early 1960s was the steepness of the radio source counts at high flux densities. These surveys were carried out at low radio frequencies, the counts at metre wavelengths (0.178 GHz) being the first to show the ‘inverted’ behaviour with $\beta = 1.8$ at high flux densities. The radio spectra of these sources have mean spectral index $\alpha \approx 0.8$ and so the arguments developed in Sect. 17.2.2, and illustrated in Fig. 17.2, show that there must be many more faint sources than are predicted according to all uniform world models. By the mid-1960s, it was known that the majority of these sources were at large redshifts and this led to the realisation that the source population had to evolve very strongly with cosmic epoch (Davidson and Davies, 1964; Longair, 1966).

When redshift data for complete samples of the radio quasars in the 3CR samples became available, Schmidt and Rowan-Robinson showed that these sources were concentrated towards the limits of their observable volumes, as illustrated in Fig. 17.8a (Rowan-Robinson, 1968; Schmidt, 1968). The radio galaxies in the 3CR sample were much more difficult to identify, but this was achieved thanks to the introduction of CCD cameras on the Palomar 5-metre telescope in the late 1970s which enabled optical identifications with galaxies to be made to about $V = 23.5$ (Gunn et al., 1981). Fortunately, many of these radio galaxies have strong narrow emission lines in their optical spectra and this enabled Spinrad. and his colleagues to measure their redshifts. The $\langle V/V_{\max} \rangle$ test for the 3CR radio galaxies gave almost exactly the same result as that for the radio quasars (Fig. 17.8b).

Since these pioneering days, radio source counts have been determined over the entire radio waveband from low radio frequencies to short centimetre wavelengths (Fig. 17.9). They all show the same overall features – a steep source count at high flux densities, a plateau at intermediate flux densities and convergence at low flux densities. At the very lowest flux densities, $S \leq 10^{-3}$ Jy, the source counts flatten again.

In interpreting the counts of sources, the objective is to find out how the luminosity function of the sources $N(L)$ has changed with cosmic epoch. The problem is that, to achieve this, it is necessary to measure the redshifts for large, complete samples of sources, spanning the range of flux densities shown in Fig. 17.9. This remains a time-consuming task since high-resolution radio maps are needed in order to make optical identifications of faint objects which typically have redshifts $z \geq 1$.

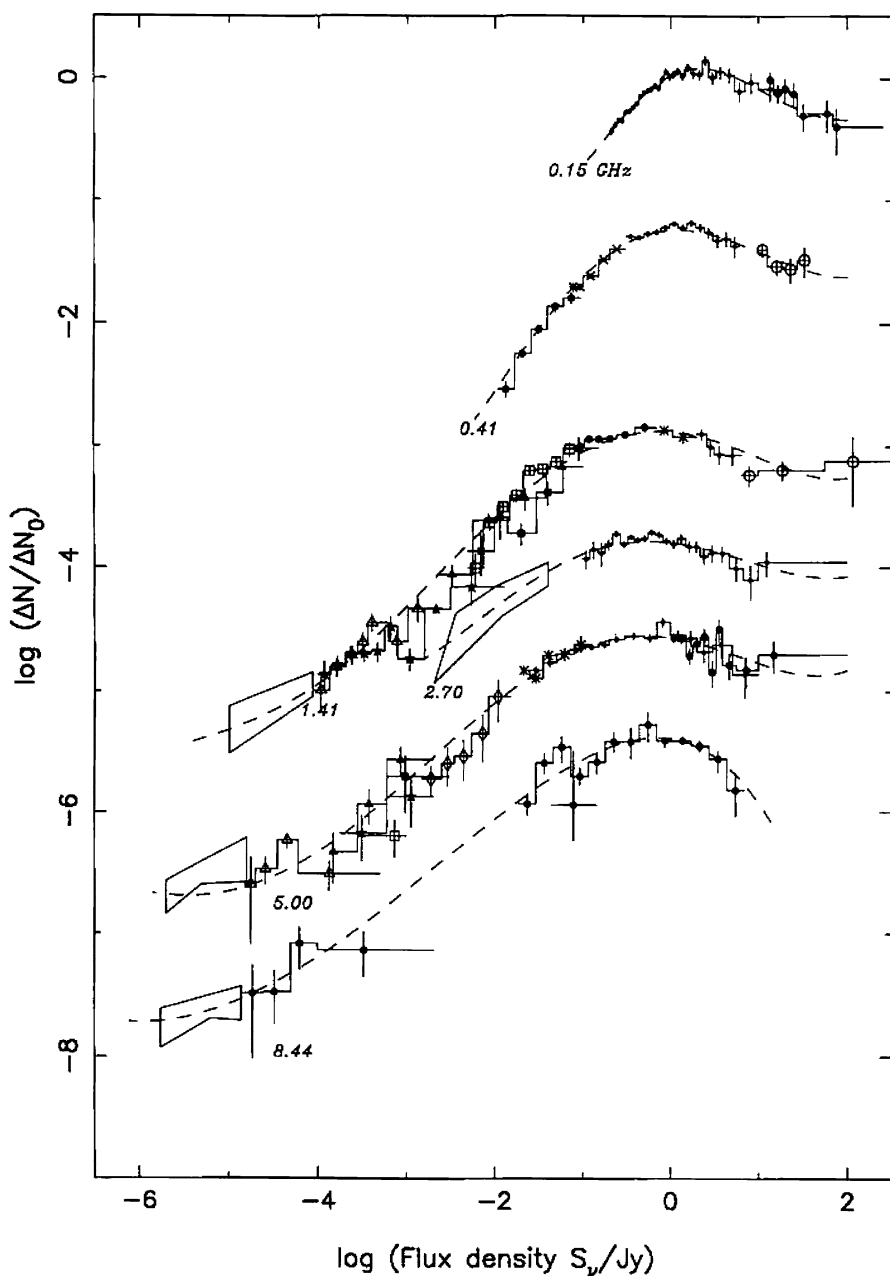


Fig. 17.9. The differential, normalised counts of extragalactic radio sources at a wide range of frequencies throughout the radio waveband. This compilation was kindly provided by Dr Jasper Wall (Wall, 1996). The *points* show the number counts derived from surveys of complete samples of radio sources. The *boxes* indicate extrapolations of the source counts to very low flux densities using the $P(D)$ technique described in Sect. 17.2.5

Then optical spectra and precise multiwavelength photometry are needed to obtain their redshifts and understand the evolutionary status of the host galaxies.

It is conventional to consider separately the radio sources with steep ($\alpha \sim 0.8$) and flat ($\alpha \sim 0$) radio spectra. The former are the extended double radio sources which are the dominant population at low radio frequencies, $\nu < 1$ GHz; the latter are the compact radio sources found in high-frequency samples, $\nu > 1$ GHz, and which often exhibit radio variability and superluminal motions. In order to define how the luminosity function of radio sources with steep and flat radio spectra have changed with cosmic epoch, free-form modelling techniques were developed by Peacock and extended by Dunlop and Peacock (Peacock, 1985; Dunlop and Peacock, 1990). All the available radio, infrared, optical and redshift data were used in constructing the models. The radio luminosity function was split into two populations, one consisting of intrinsically weak radio sources associated with normal and Seyfert galaxies and the other of the powerful extended and compact radio sources which typify the strong radio source phenomenon. Two examples of the types of model which were consistent with all the data available to Dunlop and Peacock are shown in Fig. 17.10. Both the steep- and flat-spectrum radio sources show the same forms of evolutionary behaviour.

In the mid-1990s, the changes in the radio luminosity function out to redshifts $z \approx 2$ could be simply described by what is termed *luminosity evolution*. In this form of evolution, the radio luminosity function of the powerful radio sources is shifted to greater radio luminosities with increasing redshift, whilst the normal galaxy radio luminosity function remains unchanged. These changes could be described by an increase in the radio luminosities of the strong radio sources with redshift as $L(z) = L_0(1 + z)^3$. It should be emphasised that this is simply a convenient way of parameterising the changes of the radio luminosity function to account for all the data. Inspection of Fig. 17.10 shows that, although the shift in luminosity amounts to a factor of 27 by a redshift of 2, the number density of sources of a given luminosity increases by a much greater factor. In the functions shown in Fig. 17.10, the comoving number density of sources of luminosity $10^{27} \text{ W Hz}^{-1} \text{ sr}^{-1}$ increases by a factor of about 1000, indicating how strongly the luminosity function of extragalactic radio sources has evolved with cosmic epoch. Note also that other parameterisations of the evolution of the luminosity function can account for the data equally well. Figure 17.10b shows what is referred to as luminosity-dependent density evolution, which is also a satisfactory fit to the data.

Both the models shown in Fig. 17.10 indicate that the dramatic changes in the luminosity function cannot continue to redshifts $z > 2$. For example, in Fig. 17.10a, the luminosity function at $z = 4$ has declined from the maximum at $z \approx 2 - 3$. If this decline at large redshifts did not take place, the observed convergence of the counts would not be reproduced and the radio background emission at low radio frequencies would be exceeded (see Sect. 17.4.3) (Longair, 1995).

To address this issue, complete samples of radio sources are needed at low radio flux densities, as was demonstrated by Dunlop (Dunlop, 1998). A suitable survey for these purposes was the Leiden–Berkeley Deep Survey (LBDS), which extended to flux densities about a factor of about 1000 fainter than the 3CRR sample. The radio

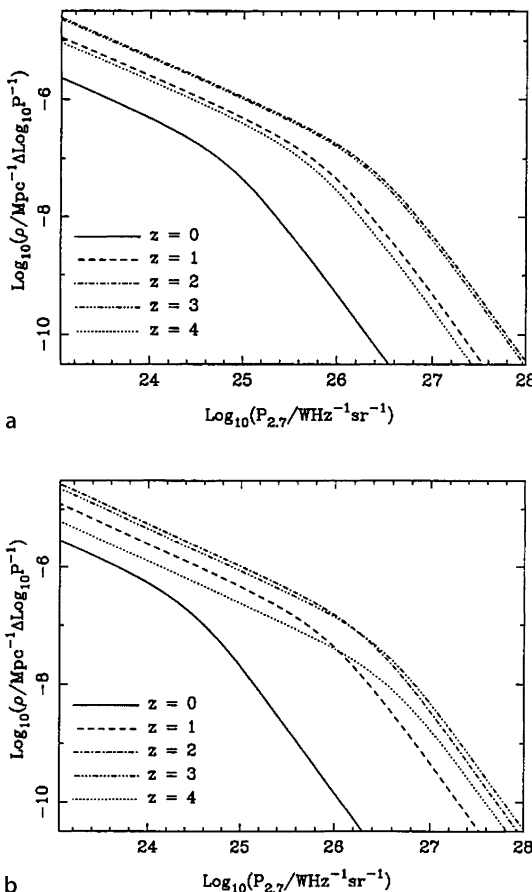


Fig. 17.10a,b. Two examples of the forms of evolving radio luminosity function which can account for the radio source counts and available redshift and identification data available in the mid-1990s (Dunlop, 1998). In model **a**, the change in the radio luminosity function is described by pure luminosity evolution. In model **b**, the changes in the radio luminosity function involve in addition negative density evolution at large redshifts. In both cases, the changes in the form of the radio luminosity function are described in terms of the number densities of sources per unit comoving volume (Dunlop, 1998)

luminosity–redshift diagram shown in Fig. 17.11 shows the flux density limits for the 3CRR and LBDS surveys, as well as the intermediate Parkes Selected Region (PSR) sample. The flux density limit for the LBDS survey is shown for flat-spectrum sources by a solid line and the flat spectrum sources in the survey by open circles; the steep-spectrum source limits are shown by a dashed line and the steep spectrum sources by solid circles (Waddington et al., 2001). There is a rather abrupt cut-off to the source distribution for both the flat- and steep-spectrum sources at $z \sim 2$ and this is not the result of observational selection or of the decrease in comoving volume per unit redshift. These results show convincingly that the radio source and associated black hole activity was at its greatest at redshifts $z \sim 2$ and that this activity decreased rather dramatically at earlier and later cosmological epochs. Waddington and his colleagues also showed that pure luminosity evolution was not a particularly good fit to the data when it was extended to low radio luminosities. Specifically, they found that there is a luminosity dependence of the high redshift cut-off – the lower luminosity sources with $P_{1.4\text{GHz}} \sim 10^{24} \text{ W Hz}^{-1} \text{ sr}^{-1}$ began to decline in comoving

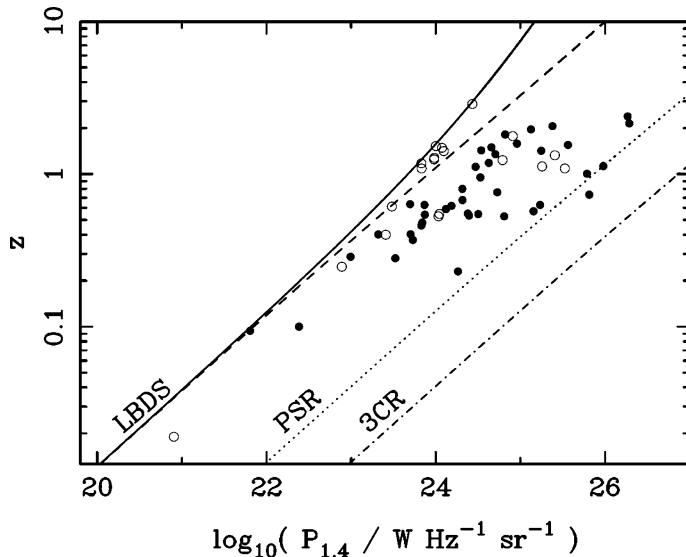


Fig. 17.11. The luminosity–redshift plane for radio sources with $S_{1.4} \geq 2$ mJy in the Leiden–Berkeley Deep Survey Hercules field. The flux density limits for the survey are shown for flat-spectrum (*solid line, open circles*) and steep-spectrum (*dashed line, solid circles*) sources, together with the limits for samples selected at higher flux densities, the PSR (*dotted line*) and 3CRR sample (*dot-dash line*) samples. Photometric redshifts have been adopted for those sources without spectroscopic redshifts (Waddington et al., 2001)

number density at redshifts of $z \approx 1\text{--}1.5$, while higher luminosity sources with $P_{1.4\text{GHz}} \sim 10^{25}\text{--}10^{26} \text{W Hz}^{-1} \text{sr}^{-1}$ were in decline in comoving number density beyond $z \approx 2\text{--}2.5$.

17.5.2 Radio Quiet Quasars

The quasars were discovered through their identification with extragalactic radio sources in the early 1960s. In 1965, the radio-quiet counterparts of the radio quasars were discovered by Sandage and these turned out to be about 50 to 100 times more common than the radio-loud variety (Sandage, 1965). It was soon established that they also had a steep source count and a value of $\langle V/V_{\max} \rangle$ much greater than 0.5 (Bracewell et al., 1970; Schmidt and Green, 1983). Subsequent studies have shown that the optically selected quasars exhibit evolutionary behaviour over cosmological time scales similar to that established for the radio-loud quasars.

The definition of complete samples of optically selected quasars is somewhat more complex than that of their radio counterparts because the optical spectra of quasars are much more complex and varied as compared with the simple power-law behaviour of the radio emission of radio quasars. Also, the optical emission of quasars is often found to be time-variable. A major methodological problem is that the radio-quiet quasars have to be identified in the presence of very large

numbers of stars belonging to our own Galaxy. Woltjer has given a concise summary of the relative merits of the different selection procedures for defining complete samples (Woltjer, 1990). The approaches which have been taken to the definition of statistically complete quasar samples can be summarised as follows.

- One of the most successful techniques for finding radio-quiet quasars has been the search for star-like objects which have ultraviolet excesses, one of the characteristics of the first samples of radio quasars. This technique relies upon the fact that the UV-optical continuum spectrum of quasars is, to a first approximation, a power law and so they are relatively more intense ultraviolet and infrared emitters than normal stars. The pioneering studies of Bracessi and his colleagues first demonstrated convincingly that the UV-excess objects have a much steeper number count than that expected in a uniform Euclidean world model (Bracessi et al., 1970). This technique is very successful for discovering quasars with redshifts $z \leq 2.2$. At this redshift, the Lyman- α emission line is redshifted into the B filter and so the quasars no longer exhibit ultraviolet excesses in the (U–B) colour index. At larger redshifts, absorption lines associated with the Lyman- α forest depress the ultraviolet emission beyond the Lyman- α line so that these quasars do not exhibit such a strong ultraviolet excess. The ultraviolet excess technique was exploited by Schmidt and Green, who derived a complete sample of 114 bright radio-quiet quasars with B, on average, less than 16.16 in a survey which covered about a quarter of the whole sky (Schmidt and Green, 1983). Interestingly, only 114 quasars were confirmed spectroscopically among the 1874 ultraviolet excess objects which satisfied the ultraviolet excess selection criteria. Most of 1874 objects were hot, hydrogen atmosphere subdwarf stars, the sdB stars, and white dwarfs.

The ultraviolet excess technique was exploited in the 2dF Quasar Redshift Survey carried out at the Anglo-Australian telescope. The ultraviolet excesses were defined from machine scans of plates taken by the UK Schmidt Telescope in the (u, b_J, r) wavebands. 25,000 quasars were discovered by this technique. The stacked spectra in the observer's rest frame are shown in Fig. 17.12. The observed wavelength is plotted on the abscissa and the redshift on the vertical axis. The plot shows the characteristic strong emission lines of MgII, CIII], CIV and Ly α seen in quasar spectra as they are redshifted through the optical waveband. At the largest redshifts, the Lyman- α line is redshifted into the optical window.

- The extension of this technique involved the use of multicolour photometry to longer optical wavelengths in order to distinguish objects with the typical spectra of large redshift quasars from stars. Koo and Kron used (U, J, F, N) photometry to find radio-quiet quasars with ultraviolet excesses to B = 23 (Koo and Kron, 1982) and found the first evidence for the convergence of the counts of radio-quiet quasars. The technique was extended by Warren and his colleagues to four-colour photometry using observations in the U, J, V, R and I wavebands, providing four colours (U–J, J–V, V–R, R–I) (Warren et al., 1987). Stars lie along a rather narrow locus in this four-dimensional colour space. By searching for objects which lay well away from that locus, Warren and his colleagues found

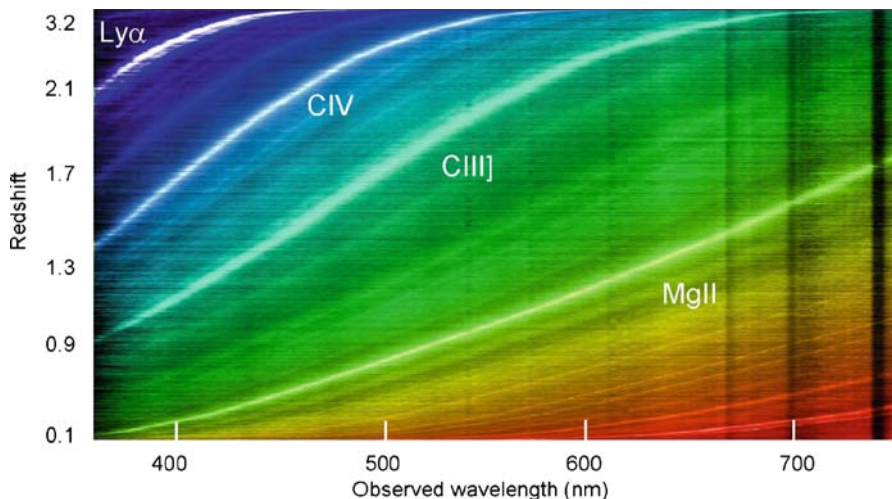


Fig. 17.12. The observed spectra of 20,000 quasars from the 2dF Quasar Redshift Survey. The spectra have been stacked in order of redshift from $z = 0.1$ to $z = 3.2$. The prominent emission lines seen in quasar spectra are labelled (courtesy of the 2dF Quasar Redshift (2QZ) team at www.2dfquasar.org)

the first quasar with a redshift $z > 4$. This technique for searching for quasars with redshifts greater than 4 was further refined by Irwin and his colleagues, who realised that they could be found by means of two-colour photometry from observations in the (B_J , R, I) wavebands (Irwin et al., 1991). The colours of these large redshift quasars are very different from those of stars because, at these very large redshifts, the redshifted Lyman- α forest enters the B_J waveband and so strongly depresses the redshifted continuum intensities of the quasars at blue wavelengths.

The largest sample of quasars to date has been found from images taken through the $ugriz$ filters as part of the Sloan Digital Sky Survey (Richards et al., 2006). The five filters spanned the complete optical spectrum between the sky cut-off at ultraviolet wavelengths to the cut-off wavelength of silicon CCD detectors at about $1.1\ \mu\text{m}$. These broadband filters were centred on the following wavelengths: $u - 350\ \text{nm}$, $g - 480\ \text{nm}$, $r - 625\ \text{nm}$, $i - 770\ \text{nm}$ and $z - 910\ \text{nm}$. From the third release of the SDSS data, 46,420 spectroscopically confirmed broad-line quasars were discovered, of which 15,343 formed a complete statistical sample which has been used to study the evolution of the luminosity function of optically selected quasars out to redshift $z = 5$.

- The extension of this colour-selection technique to even larger redshifts has been carried out using SDSS data by Fan and his colleagues (Fan et al., 2001, 2004). They searched for ‘ i -band drop-outs’, meaning that the i -band intensity was very significantly depressed relative to the z -band intensity. In these cases, the depression of the continuum intensity to the short-wavelength side of the

Lyman- α line is shifted to the extreme red end of the optical spectrum. They discovered nine quasars with redshifts $z > 5.7$, the maximum redshift being 6.28. These observations constrain the evolution of the luminosity function of the quasars at the very largest redshifts, as we discuss below.

- Another approach is to make use of the fact that the Lyman- α and CIV emission lines are always very strong in the spectra of quasars and are superimposed upon a roughly power-law continuum energy distribution (Fig. 17.12). The use of a dispersion prism, or grating, in conjunction with a wide-field telescope has proved to be a very powerful means of discovering quasars with redshifts $z > 2$, at which these lines are redshifted into the optical waveband. Pioneering studies were made by Osmer and his colleagues (Osmer, 1982). Perhaps the most remarkable use of this technique has been the survey of Schmidt and his colleagues (Schneider et al., 1991; Schmidt et al., 1995), who used the Palomar 5-metre telescope as a fixed transit instrument in conjunction with a grism and a large area CCD camera, which was clocked at the sidereal rate. In this way, six narrow bands across the sky were scanned both photometrically in the v and i wavebands, as well as spectroscopically, resulting in a total scanned area of 62 degree². Of 1660 candidate emission-line objects, 141 were found to be quasars in the redshift interval $2.0 < z < 4.7$ (Schneider et al., 1991; Schmidt et al., 1995).
- Finally, one of the most important characteristics of quasars is that they are variable over timescales which range from days to decades. If a sufficiently long baseline is used, say, of the order of 10 years, all quasars are found to be variable. Following the pioneering efforts of Hawkins, it has been confirmed that this is a successful approach in selecting complete samples of quasars (Hawkins, 1986). It is found that the degree of variability of a quasar is correlated with its luminosity, but not with redshift (Hook et al., 1991). In one variant of this approach, Majewski and his colleagues used a combination of variability and the lack of proper motions to estimate the completeness of various approaches to defining complete quasar samples (Majewski et al., 1991). They found the important result that the multicolour surveys miss at most up to 34% of the quasars and probably far less than this percentage.

The upshot of all these studies is that quasars display a steep number count which converges at faint magnitudes (Fig. 17.13). The changes of the optical luminosity function of optically selected quasars with cosmic epoch was derived by Boyle and his colleagues out to redshift $z \sim 2.3$ using a complete sample of 6,000 quasars from the AAT 2dF Quasar Redshift Survey (Fig. 17.14a) (Boyle et al., 2000). At zero redshift, the luminosity function of the overall quasar population joins smoothly on to that of the Seyfert galaxies, an important but natural continuity of the properties of these classes of active galactic nuclei. It is interesting that Schmidt and Green classified only 92 of their 114 ultraviolet excess objects as quasars since they had absolute magnitudes brighter than $M_B = -23$. The 22 lower-luminosity objects were either Seyfert 1 nuclei or what they termed low-luminosity quasars.

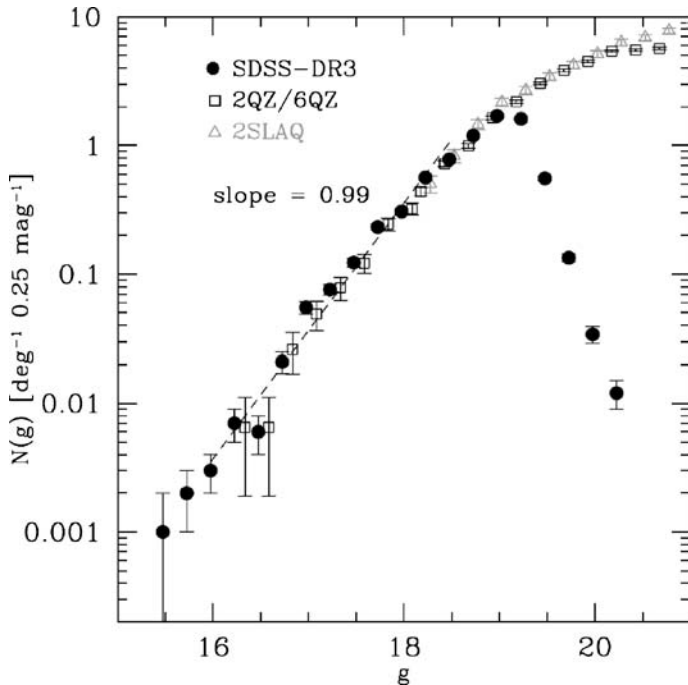
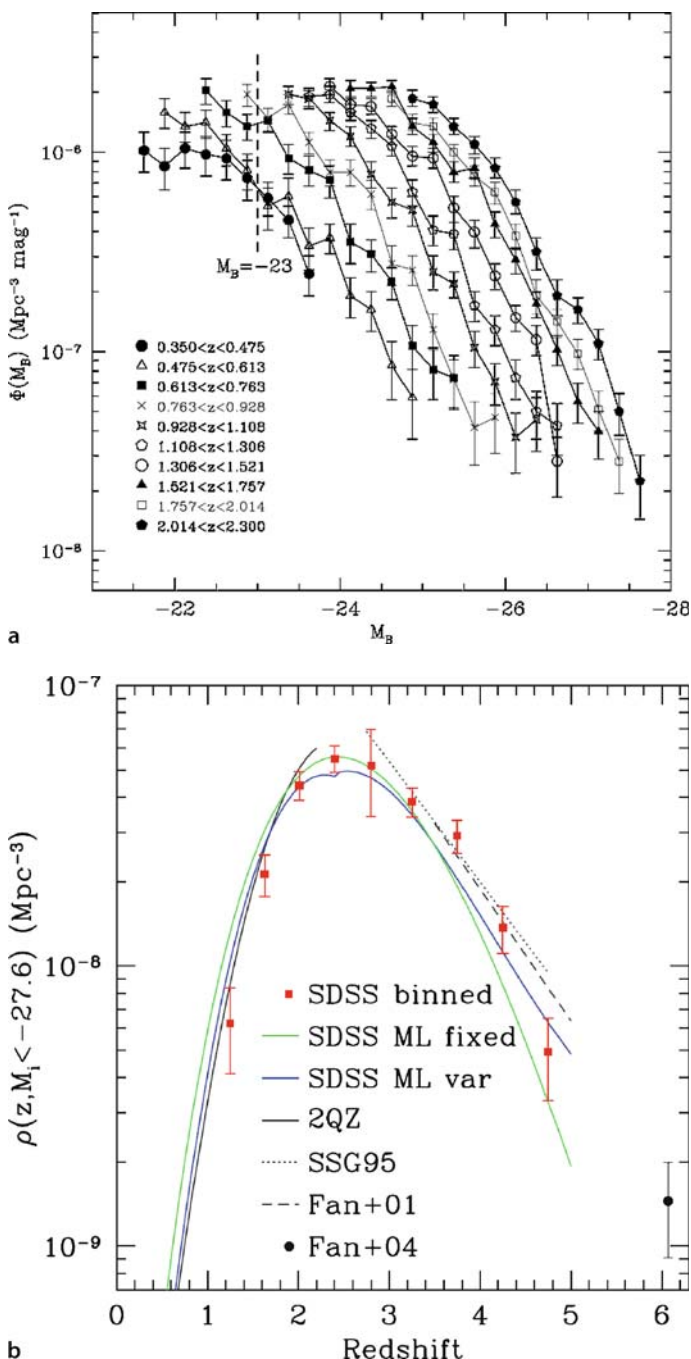


Fig. 17.13. Differential g -band number counts for quasars from the third data release of the Sloan Digital Sky Survey. The colour-selection criteria have been matched to those of the 2dF Quasar Redshift Survey. The cut-off at faint magnitudes in the SDSS sample is due to the i -band limiting magnitude of the survey. Also shown is a power-law fit to the bright end of the SDSS-DR3 sample; it has slope 0.99 ± 0.12 , compared with the Euclidean expectation of 0.6 (Richards et al., 2006)

With increasing redshift, there are many more quasars of a given luminosity per unit comoving volume than expected in uniform world models, as is dramatically illustrated in Fig. 17.14a. Over the redshift range $0 \leq z \leq 2.3$, the changes in the luminosity function can be described by ‘luminosity evolution’, of almost exactly the same form as that needed to account for the evolution of the radio luminosity

Fig. 17.14. a Evolution of the optical luminosity function for 6,000 optically selected quasars in the redshift range $0.35 \leq z \leq 2.3$ observed in the 2dF Quasar Redshift Survey carried out at the Anglo-Australian Telescope (Boyle et al., 2000). **b** Integrated i -band luminosity function for quasars more luminous than $M_i = -27.6$ (Richards et al., 2006). The solid black line terminating at $z \approx 2$ is from the 2dF Quasar Redshift Survey (Boyle et al., 2000). The dashed and dotted lines are from Fan and Schmidt and their colleagues (Fan et al., 2001; Schmidt et al., 1995) respectively. The point at $z \sim 6$ is the comoving space density estimated by Fan and his colleagues (Fan et al., 2004)



function for luminous extragalactic radio sources, namely, $L(z) \propto (1+z)^\beta$ out to $z = 2$ with $\beta = 3.5$.

Systematic surveys have been made to determine the large redshift evolution of the radio-quiet quasar population by a number of authors (Schmidt et al., 1995; Fan et al., 2001, 2004) and these provided evidence for a decrease in the comoving space density of quasars at redshifts greater than 2 to 3. The most recent evidence on the nature of the large redshift behaviour of the radio-quiet quasar population has been derived from the Sloan Digital Sky Survey. The use of the five-colour selection technique has enabled quasars up to $z = 5$ to be studied. There are, however, strong redshift-dependent selection effects at $z \geq 2.3$ which need to be understood in quantitative detail before the evolving luminosity function can be derived (Richards et al., 2006). Richards and his colleagues find that the number counts and luminosity functions agree well with the results of the Two-degree Field QSO Redshift Survey (2QZ) at redshifts where these data sets overlap in redshift and luminosity. At redshifts greater than 2, they find that the comoving number density of luminous quasars peaks between redshifts 2 and 3 and then converges rapidly at larger redshifts, in agreement with earlier studies (Fig. 17.14b). In addition, the slope of the luminosity function of quasars flattens at redshifts $z \geq 2.4$. They also included the results of Fan and his colleagues, who used the *i*-band drop-out technique to discover quasars with redshifts greater than $z = 5.7$ and showed that the decline in the comoving space density of luminous quasars continues out to redshift $z = 6$, as illustrated in Fig. 17.14b.

17.5.3 X-Ray Source Counts

One of the great surprises of the early history of X-ray astronomy was the remarkable brightness of the diffuse X-ray background emission. The objective of the pioneering rocket flight by Giacconi and his colleagues was to search for fluorescent X-ray emission from the Moon, but instead, the bright X-ray source Sco X-1 and the diffuse X-ray background were discovered (Giacconi et al., 1962). The brightness of the X-ray background is beautifully illustrated by the dramatic image of the Moon taken by the ROSAT X-ray Observatory (Fig. 17.15). The bright X-ray emission from the sunlit side of the Moon is the fluorescent emission which was the original objective of the 1962 rocket flight. In addition, the dark side of the Moon is seen in silhouette against the X-ray background radiation.

The history of the number counts of X-ray sources has been surveyed by Brandt and Hasinger (Brandt and Hasinger, 2005). The number counts for bright sources were derived from the surveys of the sky carried out by the UHURU, Ariel-V and HEAO-1 satellite observatories in the 1970s. These pioneering surveys were followed by the German-US-UK ROSAT mission which surveyed the whole sky in the X-ray energy band 0.1 to 2.4 keV. The survey contained about 60,000 sources and provided information about their X-ray spectra in four X-ray ‘colours’. The flux density limit of the ROSAT survey was about 100 times fainter than that of HEAO-1 survey. The number counts from the first deep ROSAT surveys were described by Hasinger and his colleagues (Hasinger et al., 1993). The next major advances were

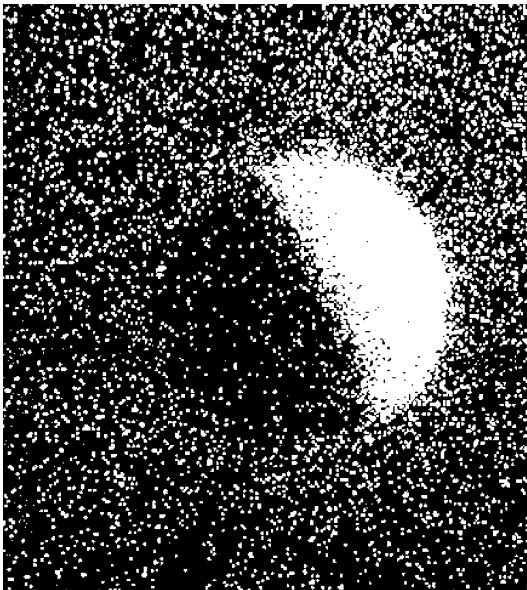
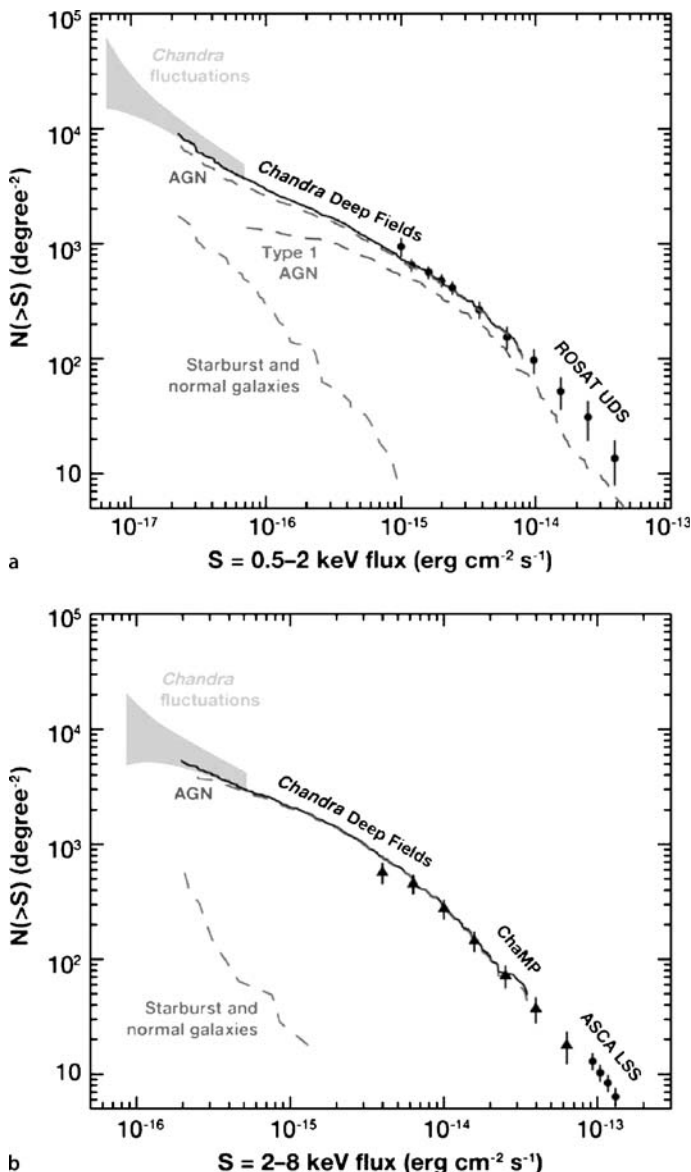


Fig. 17.15. An X-ray image of the Moon taken by the ROSAT Observatory showing the fluorescent emission from the sunlit side of the Moon. On the dark side, the Moon is seen occulting the diffuse X-ray background emission (courtesy Max Planck Institute for Extraterrestrial Physics, Garching)

made by the *Chandra* and *XMM-Newton* X-ray Observatories. Deep and wide-field surveys have been carried out with these telescopes with the results summarised by Brandt and Hasinger. They describe how number counts of X-ray sources have now been determined to faint X-ray flux densities throughout the 1 to 10 keV wavebands (Fig. 17.16). The counts have been extended to even lower flux densities using the $P(D)$ technique described in Sect. 17.2.5. Most recently, more detailed number counts, particularly for the hard X-ray energies, $\epsilon \sim 8$ keV, were described by Cappelluti and his colleagues (Cappelluti et al., 2007).

The interpretation of the X-ray source counts in the 0.5- to 10-keV waveband is more complex than is the case for the extragalactic radio sources and the optically selected quasars because the X-ray spectra of sources selected at, say, 1 and 10 keV can be quite different. To simplify what is undoubtedly a complex picture, Fig. 17.16a,b shows that the principal contributors to the number counts to the limits of the *Chandra* deep surveys are active galactic nuclei. Major efforts have been made to identify and obtain optical spectra for the X-ray sources in the *Chandra* surveys and these are sufficiently complete to enable estimates of the evolution of the comoving space density of sources of different X-ray luminosities in the 0.5- to 2-keV wavebands to be determined (Fig. 17.17a,b). These both show the characteristic feature of the evolution of the population of active galactic nuclei that the most luminous sources show the strongest cosmological evolution out to redshifts $z \approx 2$. The less luminous sources show much less dramatic evolution of their comoving space densities. Figure 17.17a,b shows marginal evidence for the decrease in comoving space densities beyond $z = 3$, but the statistics are quite limited.



What the functions displayed in Fig. 17.17 disguise is the fact that the X-ray spectral types change quite dramatically with X-ray energy. This is most easily illustrated by considering the types of source which make up the total X-ray background intensity from soft (~ 1 keV) and hard (~ 10 keV) X-ray energies. The spectrum of the X- and γ -ray background from 0.1 to 300 keV is shown in Fig. 17.18 from a multitude of experiments which are described by Gilli and his colleagues (Gilli et al., 2007).

Fig. 17.16. **a** Integral number counts of X-ray sources for the 0.5- to 2-keV band. The *data points* are derived from the ROSAT Lockman Hole field, the *solid black curve* from the Chandra Deep Fields and the *grey areas* from $P(D)$ analysis of the Chandra Deep Field-North. The *dashed curves* show number counts for all active galactic nuclei, type 1 active galactic nuclei and starburst and normal galaxies. **b** Integral number counts of X-ray sources in the 2- to 8-keV band. The *black circles* are from the ASCA Large Sky Survey, the *black triangles* from the ChaMP study, the *solid black curve* from the Chandra Deep Fields study and the *grey area* from a $P(D)$ analysis of the Chandra Deep Field-North. Details of the sources of these data are given in the review by Brandt and Hasinger from which these figures were taken (Brandt and Hasinger, 2005)

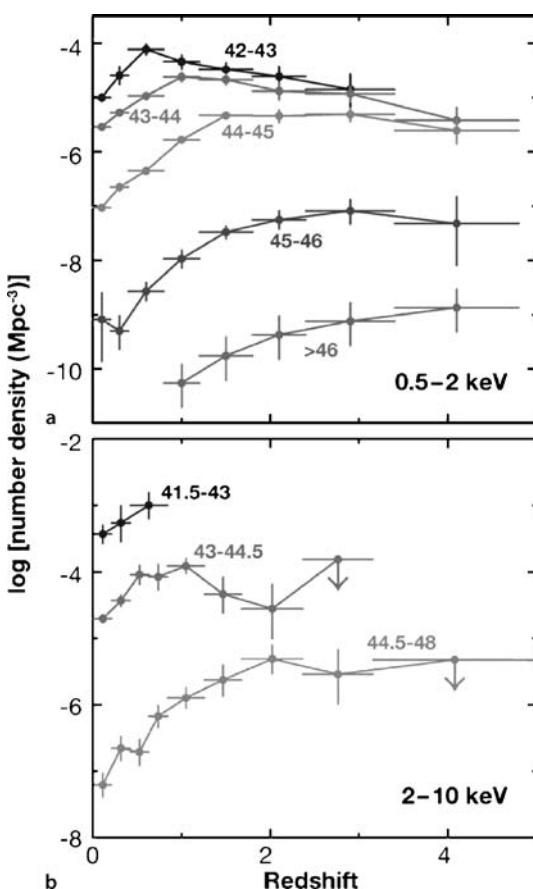


Fig. 17.17. **a** The comoving space density of X-ray selected active galactic nuclei in the 0.5–2 keV energy band as a function of redshift. Results are shown for five luminosity ranges which are labelled by the logarithm of the X-ray luminosity in erg s^{-1} . **b** The same relation for X-ray active galactic nuclei selected in the 2- to 10-keV energy band for three luminosity ranges (Brandt and Hasinger, 2005)

It is straightforward to determine how much of the X-ray background intensity in the 0.5- to 2-keV energy band can be attributed to discrete X-ray sources by integrating the number counts shown in Fig. 17.16a. There is general agreement that essentially all the background intensity in this waveband is associated with

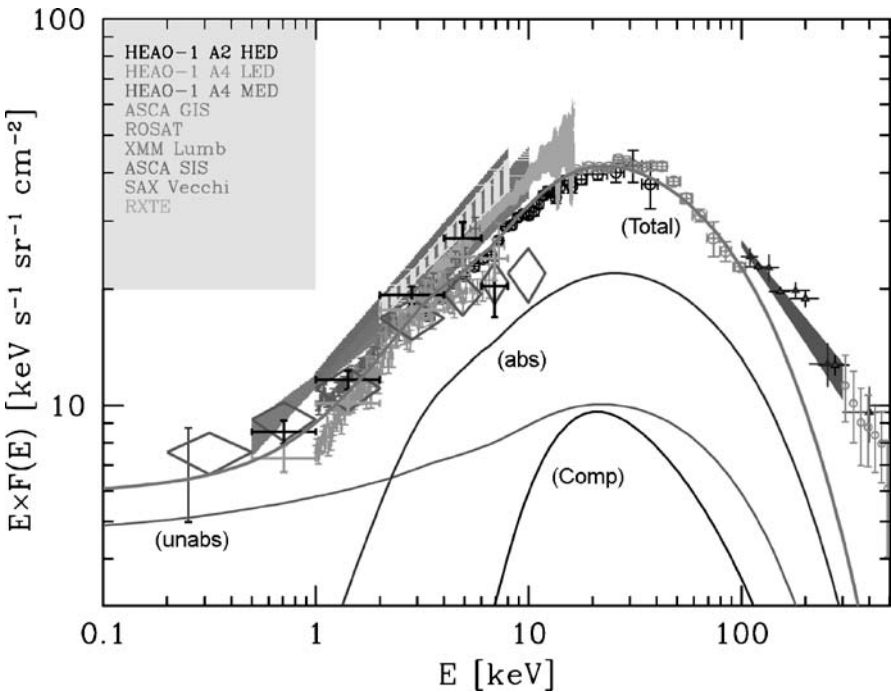


Fig. 17.18. The spectrum of the cosmic X-ray background emission compared with the predicted contributions from populations of Compton-thin and Compton-thick active galactic nuclei. The different estimates of the X-ray background intensity are explained by Gilli and his colleagues, the various instruments involved being listed in the *top left* of the diagram. *Solid lines* show the contributions of different types of active galactic nuclei according to the models of Gilli and his colleagues. These are: unobscured active galactic nuclei (*unabs*), obscured Compton-thin active galactic nuclei (*abs*), Compton-thick active galactic nuclei (*Comp*) and the sum of these three components, including the contribution of clusters of galaxies (*Total*). The *diamonds* (and some of the other *data points*) show estimates of the background intensity by counting sources to the limits of the deep surveys (Gilli et al., 2007)

discrete sources and that this population is dominated by active galactic nuclei. A major fraction of these sources are Type 1 active galactic nuclei in which the characteristic broad lines and continuum are observed. This means that the majority of contributors to the X-ray background at these energies are unobscured sources in which the nuclear regions of the active galaxies are observed directly. If attention is restricted only to the main contributors in this soft waveband, the typical photon number spectral index is about 1.9 with a dispersion of about 0.2 to 0.3 about this mean value. This immediately poses a problem since the spectral index of the background spectrum is significantly smaller than this value in the 1- to 10-keV waveband. This problem can be understood by comparing the observed background spectrum with the predicted spectrum due to unabsorbed sources which are labelled

(unabs) in Fig. 17.18. Therefore, the same population cannot explain the X-ray background intensity at harder X-ray energies.

Carrying out the same analysis at hard X-ray energies ($\epsilon \sim 10$ keV), at least 50% and probably more of the background is associated with the discrete sources already detected, but their spectral mix is somewhat different. The most important difference is that there is a major population of sources which are strongly absorbed at soft X-ray energies. Sources have now been observed in which photoelectric absorption strongly suppresses the soft X-ray flux density and so ‘hardens’ the X-ray spectra. The inferred column densities can be up to 10^{24} cm $^{-2}$ and greater. For column depths greater than 10^{24} cm $^{-2}$, the effects of Comptonisation need to be taken into account, and this process causes major distortions of the X-ray source spectra whatever the initial input photon spectrum. Gilli and his colleagues provide template spectra for this wide range of sources which also include the effects of iron lines and reflected X-ray components from the inner regions of the active galactic nucleus (Gilli et al., 2007).

At energies greater than 10 keV, the number count data are much sparser, but the background spectrum continues to be remarkably flat up to about 30 keV, beyond which it changes slope rather dramatically and continues more or less as a power law to γ -ray energies. It is assumed that Comptonised sources make a significant contribution to the background spectrum above 10 keV, as shown in Fig. 17.18. A detailed discussion of all these effects would take us far from the main thrust of this chapter. The interested reader should consult the paper by Gilli and his colleagues to obtain an appreciation of the types of source populations needed to account for the overall background spectrum (Gilli et al., 2007). Figure 17.18 shows their best estimate for the types of sources which make up the observed X-ray background spectrum. Whilst the solid lines are models for the various contributions to the background, they are also consistent with all the most recent data on the counts of X-ray sources in the 0.5- to 10-keV waveband reported by Cappelluti and his colleagues (Cappelluti et al., 2007). Notice also that, even taking account of the different types of known source, there must still be an additional component at γ -ray energies $E \geq 100$ keV to account for the observed γ -ray background spectrum. These might be further Compton-thick hard X-ray sources.

17.5.4 X-Ray Clusters of Galaxies

The total X-ray number counts include the clusters of galaxies which are strong X-ray emitters. They make a small but significant contribution to the counts at high flux densities, but their fractional contribution at lower flux densities decreases rapidly relative to that of the active galactic nuclei. Nonetheless, the counts of X-ray sources associated with clusters of galaxies provide a sensitive test of cosmological models. The observed number counts of X-ray clusters are shown in Fig. 17.19 in which they are fitted by a non-evolving X-ray luminosity function with the reference set of cosmological parameters (Rosati et al., 2002). The significance of this result can be appreciated in the context of simulations of the development of structure in different cosmological models.

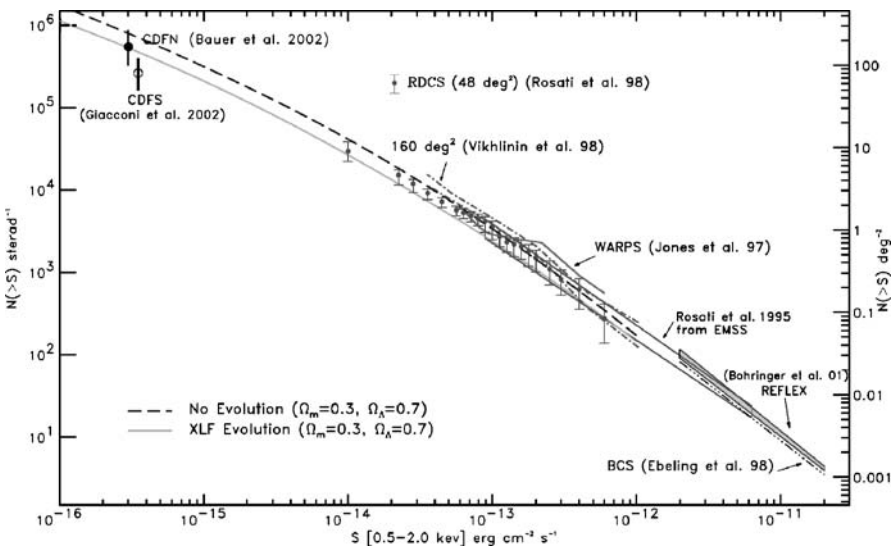
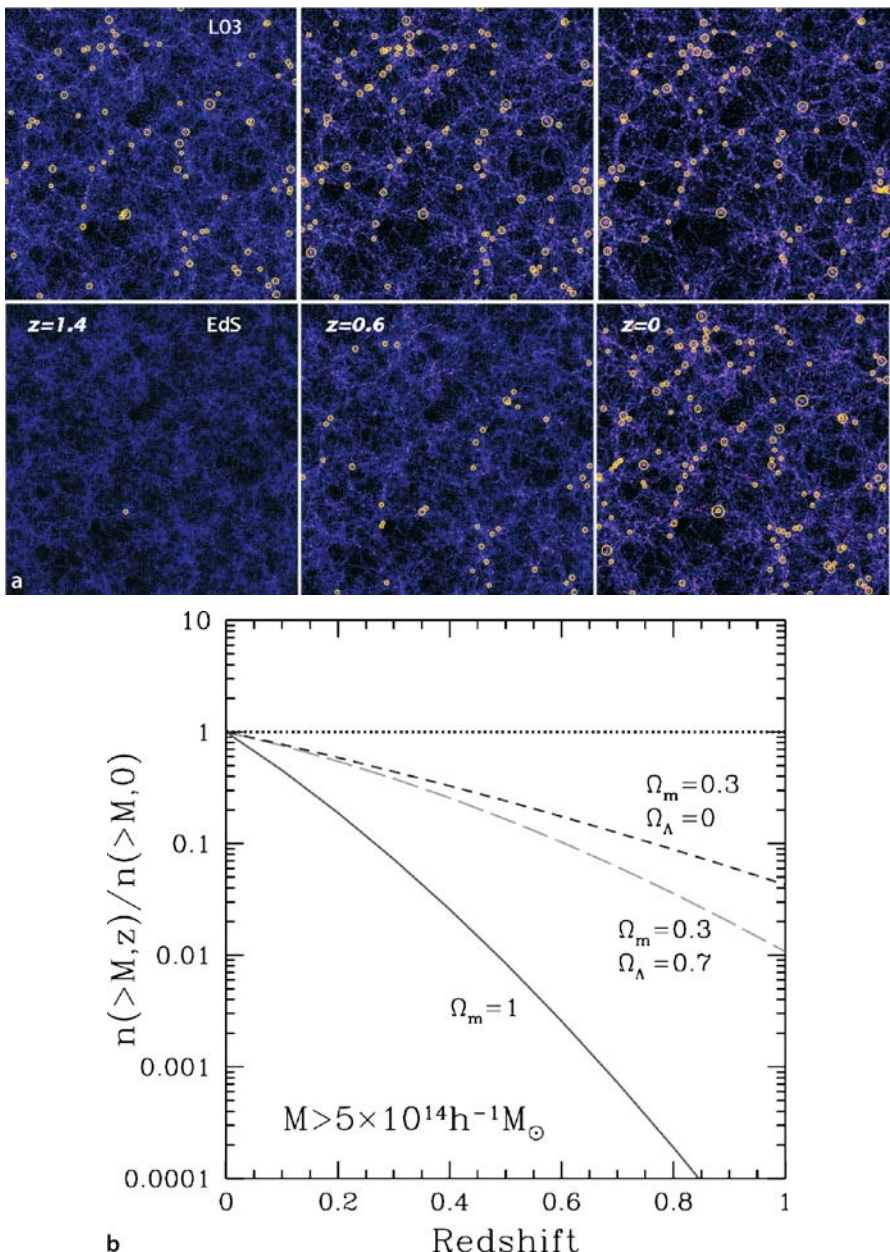


Fig. 17.19. The integral number counts for clusters of galaxies which are strong X-ray sources from a number of different X-ray surveys. The counts are compared with the numbers expected for a non-evolving distribution of sources for the reference world model with $\Omega_0 = 0.3$ and $\Omega_\Lambda = 0.7$

Fig. 17.20. a The evolution of gravitational clustering simulated using an N -body code for the standard CDM model ($\Omega_0 = 1$, $\Omega_\Lambda = 0$: EdS) and the Λ CDM model ($\Omega_0 = 0.3$, $\Omega_\Lambda = 0.7$: L03). The three redshift snapshots show a region $250 h^{-1}$ Mpc in size and $75 h^{-1}$ Mpc thick in comoving coordinates. In both cases the amplitude of the power spectrum is consistent with the number density of nearby galaxy clusters. The circles indicate dense regions where clusters of galaxies are formed and would be detectable as intense X-ray sources (Borgani and Guzzo, 2001). **b** The predicted evolution of the numbers of massive clusters $n(\geq M, z)$ for three representative world models, illustrating the strong dependence upon the cosmological model (Rosati et al., 2002)

Figure 14.10 shows how the development of the large-scale distribution of galaxies depends strongly on the matter-density parameter Ω_0 . The open and Λ CDM models predict rather mild evolution of large-scale structures over the redshift interval $0 < z < 2$, whereas the standard cold dark matter (SCDM) scenario with $\Omega_0 = 1$ shows a much more pronounced development of structure over the same redshift interval. This is entirely consistent with the considerations of Sect. 11.4.4 in which it was shown that the growth of the perturbations decreased at redshifts $z < \Omega_0^{-1}$ and similar results were found for the models with finite Ω_Λ . The simulations shown in Fig. 14.10 were designed to create the same large-scale structure at the present epoch. The numbers of massive clusters of galaxies formed at each epoch can be estimated from the N -body simulations, as has been most dramatically illustrated



by the simulations of Borgani and Guzzo shown in Fig. 17.20a (Borgani and Guzzo, 2001). A relatively modest decrease in numbers of massive clusters is expected with increasing redshift in the OCDM and Λ CDM models, whereas a much more rapid decline is expected in the standard CDM model with $\Omega_0 = 1$.

The predicted number density of massive clusters as a function of redshift for these world models is shown in Fig. 17.20b. This comparison with the observations is best carried out using X-ray selected clusters of galaxies since they extend to redshifts of $z \geq 1$. This comparison is not trivial since the temperature and mass of the gas in the clusters need to be well determined and various selection effects need to be taken into account. These issues are dealt with in some detail in the review by Rosati and his colleagues (Rosati et al., 2002). The upshot is, however, that the number density of massive clusters certainly does not decrease as dramatically with increasing redshift as is predicted by the standard CDM model. The reference model $\Omega_0 = 0.3$, $\Omega_A = 0.7$, however, provides a good account of the observed numbers of X-ray clusters of galaxies.

17.6 Infrared and Submillimetre Number Counts

In Sect. 17.5, the evolution with cosmic epoch of different populations of active galaxies was derived from number counts and their redshift distributions. The same approach can be adopted in the optical, infrared and submillimetre wavebands but now the evolution concerns various aspects of stellar populations of galaxies, rather than their active nuclei. In this section, we discuss the evolving properties of galaxies and sources selected in the mid-, far-infrared and submillimetre wavebands and deal with the optical number counts of galaxies in Sect. 17.7.

The IRAS Satellite carried out the first essentially complete sky survey of the infrared sky in those wavebands which are inaccessible from ground-based sites, namely, the wavebands between 12.5 and 100 μm . Among the many important discoveries of the mission was the realisation that many galaxies are intense far-infrared emitters, the most luminous of these being referred to as ultraluminous infrared galaxies, or ULIRGs. Examples of the spectra of some of these galaxies were presented in Fig. 17.4a. The far-infrared emission is the reradiation of heated dust grains, generally associated with intense bursts of star formation. The catalogue of IRAS galaxies was important cosmologically because complete samples of galaxies could be selected which are unaffected by obscuration by interstellar dust. As a result of a major effort by many astronomers, the redshifts of complete samples of IRAS galaxies were measured and their local luminosity function at 60 μm determined.

Counts of IRAS galaxies were made at 60 μm from the IRAS Point Source Catalogue, the IRAS Faint Source Survey and a survey in the region of the ecliptic poles (Oliver et al., 1992). The normalised differential counts showed that there were more faint IRAS galaxies than expected, in the same sense as the counts of radio sources, X-ray sources and quasars, although the range of redshifts sampled was very much smaller than those of the extragalactic radio sources and quasars. The normalised differential number counts with flux densities greater than 100 mJy in Fig. 17.21a were derived from the IRAS survey.

The successor to the IRAS survey was the Infrared Space Observatory (ISO) of the European Space Agency, which carried out deeper surveys in the mid- and far-infrared wavebands and confirmed the excesses of faint sources. Most recently,

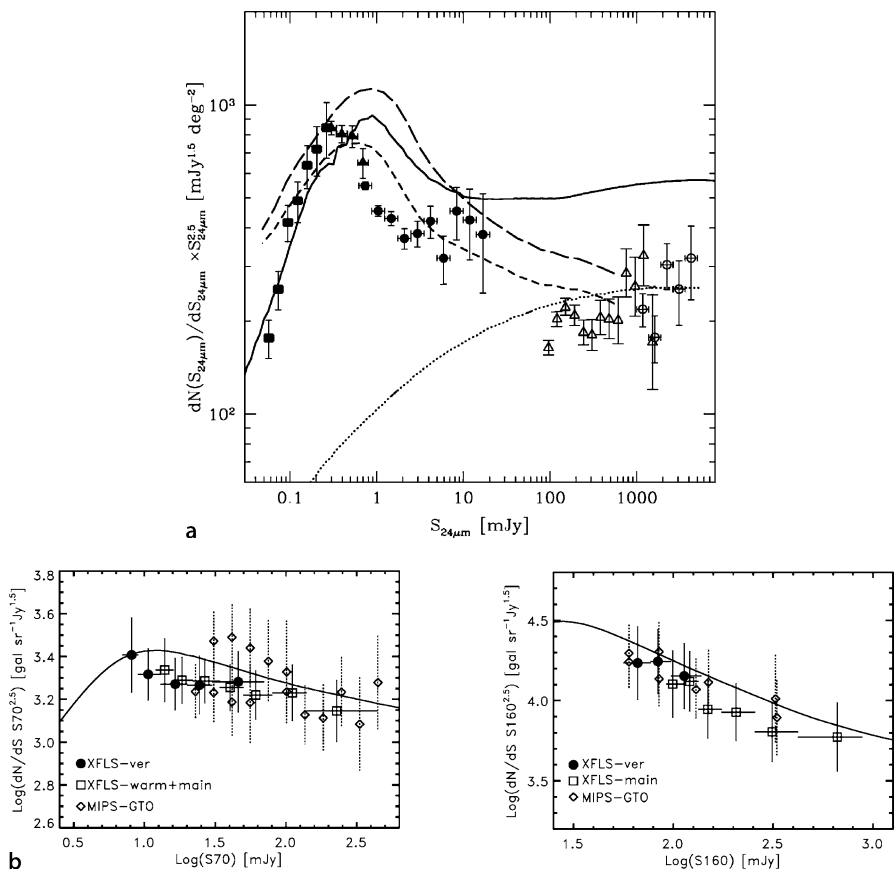


Fig. 17.21. **a** The differential extragalactic source counts at 24 μm from the Spitzer First Look Survey (filled circles), the verification strip (filled triangles) and the ELAIS-N1 survey (filled squares) normalised to the Euclidean prediction. The IRAS data points are shown as open symbols, transformed to 24-μm wavelength. The counts are compared to various predictions of the evolving luminosity function of galaxies in the mid-infrared waveband. The no-evolution model normalized to the IRAS counts is shown as a dotted line (Marleau et al., 2004). **b** The differential counts of extragalactic sources at 70 μm (left) and 160 μm (right) wavelength from the Spitzer Extragalactic First Look Survey (Frayer et al., 2006). The solid lines show an evolutionary model due to Lagache and his colleagues (Lagache et al., 2004)

number counts in these wavebands have been made by the NASA Spitzer Space Telescope, which is an 85-cm cryogenic telescope with three cryogenically cooled scientific instruments which provide imaging and spectroscopy capabilities in the 3.6- to 160-μm waveband. These instruments have produced number counts at 24 μm showing a clear excess of faint sources, as well as a rather dramatic cut-off at low flux densities (Fig. 17.21a). These observations are consistent with the findings of the ISO mission. Surveys have also been carried out at longer wavelengths, 70 and

170 μm , with the results shown in Fig. 17.21b. The now familiar pattern of an excess of faint sources is apparent in all the diagrams in Fig. 17.21.

Counts of sources have now been made in the submillimetre waveband in which it was expected that, even if there were no evolution of the population of sources with cosmic epoch, the normalised differential number counts would show an excess over the Euclidean prediction because of the ‘inverted’ spectra of dust-emitting sources in these wavebands, as discussed in Sect. 17.2.3. Counts in these wavebands became possible thanks to the availability of the SCUBA array detector on the James Clerk Maxwell Telescope, which resulted in the discovery of a very large population of submillimetre sources (Smail et al., 1997). Over the succeeding years a major effort was made to determine their number counts in detail, and this is summarised in Fig. 17.22, which is taken from the work of Cowie and his colleagues (Cowie et al., 2002). What Fig. 17.22 disguises is the fact that these number counts greatly exceed the numbers of sources expected on the basis of the local 60- μm luminosity function of luminous far-infrared galaxies determined by the IRAS survey. Indeed the numbers far exceeded the most extreme evolution models discussed by Blain and me in the early 1990s (Blain and Longair, 1993). The number counts of submillimetre galaxies must converge rapidly just below those flux densities shown in Fig. 17.22 or the submillimetre background intensity would be exceeded. The parametric fits to the counts shown by dashed and dotted lines in Fig. 17.22 converge to the submillimetre

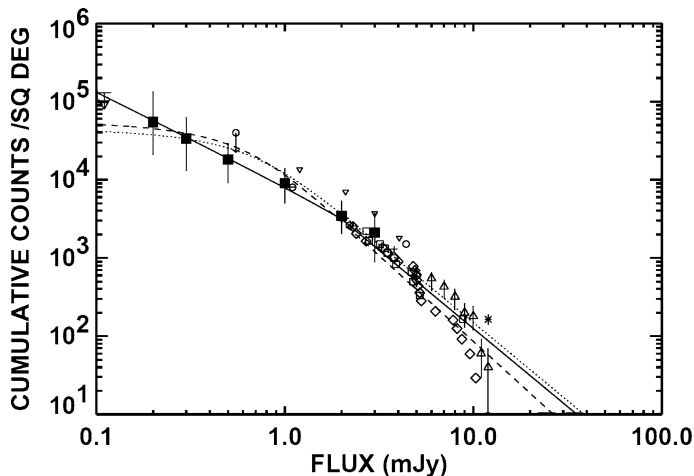


Fig. 17.22. The counts of submillimetre sources at 850 μm (Cowie et al., 2002). The sources of these data are discussed by Cowie and his colleagues. The *filled squares with error bars* have been derived from an analysis of submillimetre sources observed in the vicinity of clusters of galaxies, which enhances their flux densities because of gravitational lensing. The *points* with flux densities greater than about 2 Jy are derived from blank field surveys. The *dotted* and *dashed lines* show parametric fits to the counts which converge to the total extragalactic background emission observed in the submillimetre waveband

background intensity estimates by Puget, Hauser and their colleagues (Puget et al., 1996; Hauser et al., 1998; Hauser and Dwek, 2001).

The complications of interpreting the number counts of infrared galaxies is illustrated by the example of the spectral energy distribution of one of the luminous far-infrared galaxies, N1-015 (Sajina et al., 2006). Sajina and her collaborators showed that the spectrum can be decomposed into a number of components which are illustrated in Fig. 17.23. At the longest wavelengths, the submillimetre spectrum can be approximated by a grey-body spectrum, meaning a black-body spectrum with optically thin emissivity varying as $\nu^{1.5}$ (dotted line). In addition, to account for the gradual decline from the maximum of the black-body curve to shorter wavelengths, a warm power-law component is included, associated with dust grains of smaller size with decreasing wavelength (short-dashed line). In the 5- to 20- μm waveband the spectrum is dominated by the intense emission of polycyclic aromatic hydrocarbon molecules, PAHs, which can account for up to 20% of the total infrared luminosity (long-dashed line). At the shortest wavelengths, the stellar population of the galaxy

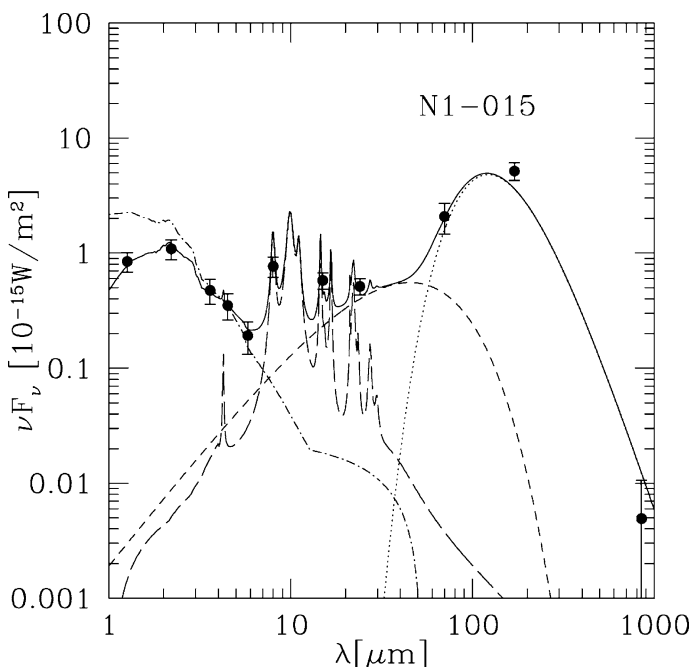


Fig. 17.23. An example of the spectral energy distribution of the luminous infrared galaxy N1-015 between 1 and 1000 μm (Sajina et al., 2006). The components include a grey-body spectrum in the submillimetre waveband (dotted line), a warm power law (short-dashed line), PAH emission (long-dashed line), and stellar emission (dot-dashed line) which suffers extinction $e^{-\tau_\nu}$, where τ_ν describes the extinction as a function of wavelength. The total spectrum is shown by the *continuous line* and the observed broad-band flux densities by *filled circles*

is dominant (dot-dashed line), but it suffers extinction as $e^{-\tau_\nu}$, where τ_ν describes the attenuation of the spectral energy distribution as a function of wavelength. The total spectrum is shown by the continuous line and the observed broadband flux densities by filled circles.

Thus, the interpretation of the number counts is non-trivial since the contributions of the various components in different classes of infrared galaxy need to be established. Various template-fitting procedures have been developed which enable estimates of the evolving luminosity function of galaxies in the infrared waveband to be established (Lagache et al., 2003, 2004; Babbedge et al., 2006). There is reasonable agreement about the features needed to account for the number counts throughout the infrared waveband.

First of all, the number counts in the infrared waveband are dominated by starburst activity. Babbedge and his colleagues use template fitting to study the evolution of active galactic nuclei in the SWIRE Legacy sample and find that they are far outnumbered by starburst galaxies (Babbedge et al., 2006). They find the same form of evolution in the infrared waveband for the active galactic nuclei as described in Sect. 17.4. There are certainly some far-infrared sources in which the energy source is likely to be an active galactic nucleus, but X-ray studies of far-infrared and submillimetre sources have shown that there are relatively few X-ray active galactic nuclei in the population of submillimetre sources compared with those which are assumed to be dominated by starbursts.

The phenomenological model of Lagache and his colleagues provides a simple picture for the evolutionary behaviour of the starburst population in the mid-infrared to submillimetre wavebands (Lagache et al., 2003, 2004). The population is split into two components, a population of normal galaxies which evolves passively with cosmic epoch and a strongly evolving starburst component which consists of all the highest luminosity far-infrared sources, $L \geq 3 \times 10^{11} L_\odot$. The infrared spectra are not very different from that shown in Fig. 17.23, although the far-infrared maximum is somewhat colder for the normal galaxies as compared with the luminous starbursts. The strong evolution is associated with this luminous starbursting component. The form of evolution is significantly different from that found for the population of active galaxies in that all the strong evolution takes place between redshifts 0 and 1 and then remains at roughly the same level from redshifts $1 \leq z \leq 5$. Specifically, the evolution of the luminosity function for the luminous star-forming galaxies can be described by luminosity evolution of the form $L \propto (1+z)^3$ from $z = 0$ to $z = 1.5$, beyond which the luminosity function remains constant out to redshift $z = 5$. This result is similar to that found by Babbedge and his colleagues from their larger dataset. The various evolutionary predictions are compared with the observations in Fig. 17.21, where it can be seen that the number counts throughout the mid-infrared to submillimetre wavebands are in reasonable agreement with this model, which can be tweaked to obtain better agreement with observation (Lagache et al., 2004). Lagache and his colleagues show that the abrupt convergence of the counts at low flux densities seen in Fig. 17.21a is accounted for in their models. The reason for this is that the strong evolution takes place over the redshift range $0 \leq z \leq 1$ and then the comoving space density of sources is constant. As a result, the differential

number counts change abruptly to the strong converging behaviour at $z \geq 1$ seen in Fig. 17.2.

It is important that this evolutionary behaviour is significantly different from that of the active galactic nuclei for which the evolving luminosity function has a maximum at $z \sim 2\text{--}3$. Notice also that the strong evolution all takes place between redshifts 0 and 1 and this explains the very large excess of sources observed in the submillimetre number counts. This evolutionary behaviour is reflected in the evolution of the star-formation history of the Universe, which will be a major theme of Chap. 19.

An interesting consequence of the evolution of the far-infrared galaxies results from the strong correlation between the radio emission of normal and starburst galaxies and their far-infrared emission (Helou et al., 1985). The proportionality extends over many orders of magnitude and can be written $S(60\,\mu\text{m}) = 90\,S(1.4\,\text{GHz})$, where both flux densities are measured in janskys. As a result, it is straightforward to predict the counts of starburst and normal galaxies in the radio waveband. It turns out that it is possible to account for the flattening of the radio source counts at radio flux densities $S \leq 10^{-3}$ Jy seen in Fig. 17.9 in terms of the evolution of the population of far-infrared galaxies (Rowan-Robinson et al., 1993). This conclusion is supported by the identification content of the millijansky radio sources, many of which are blue and have spectra similar to those of starburst galaxies (Windhorst et al., 1987, 1995).

17.7 Counts of Galaxies

Finally, we return to where we started, the counts of galaxies. It is intriguing that the emphasis has shifted away from counting the numbers of galaxies to much more targeted studies of physical quantities such as star formation rates, the different forms of luminosity functions for different classes or sequences of galaxies as a function of redshift and so on. The change in perspective on galaxy classification discussed in Chap. 3 has been reflected in the approach to the evolving populations of galaxies. Therefore, counting galaxies has become a somewhat outmoded approach to the study of galaxy evolution. Nonetheless, it is important in establishing a complete picture of the populations of evolving galaxies. The more physical approach will be dealt with in more detail in Chap. 19, where the emphasis is upon the role of star formation in the evolution of all types of galaxy.

Ellis has described clearly the complications in determining reliable galaxy counts and of their interpretation (Ellis, 1997). The reasons for these complications are manifold. First of all, galaxies are extended objects, often with complex brightness distributions, and care must be taken to ensure that the same types of object are compared at different magnitude limits and redshifts. Secondly, unlike the radio and X-ray sources, which are uniformly distributed over the sky, the distribution of galaxies is far from uniform on scales less than about $50\,h^{-1}\,\text{Mpc}$, as illustrated by the large voids and walls in the local distribution of galaxies (Figs. 2.7 and 2.8). Even at the faintest magnitudes, this ‘cellular’ structure in the distribution of galaxies

results in fluctuations in the number counts of galaxies which exceed the statistical fluctuations expected in a random distribution. Thirdly, Fig. 3.4 shows that the probability of finding galaxies of different morphological types or sequences depends upon the environment in which the galaxy is located.

A major complication concerns the K-corrections to be used for galaxies of different morphological types. In order to estimate the number counts of galaxies at large redshifts in the optical waveband, their spectra need to be known in the ultraviolet waveband, and these can only be observed from above the Earth's atmosphere. It turns out that there have been remarkably few systematic surveys of the ultraviolet spectra of normal galaxies. The problem is exacerbated by the fact that the ultraviolet spectra of galaxies can be dominated by bursts of star formation and these influence very strongly the observability of galaxies at large distances. As Ellis points out, this fact alone makes the comparison of the optical images of galaxies at the present epoch with those at redshifts of one and greater problematic.

Matters are somewhat improved if the counts of galaxies are determined in the infrared K waveband at $2.2\text{ }\mu\text{m}$. First of all, the galaxy counts in the K waveband are much less affected by dust extinction. Second, the light of the galaxies in the infrared waveband is dominated by the majority old, stellar populations in galaxies and so is not affected by bursts of star formation. Consequently, the K-corrections are much better known since, even at redshifts of $z \sim 3$, the observed light of the galaxies was emitted at 500 nm in the galaxies' rest frames, as was illustrated in Fig. 17.3.

These problems are clearly and carefully described in Ellis's excellent review. Granted these problems, Fig. 2.12 presented by Metcalfe and his colleagues still provides a very good impression of the overall counts of galaxies in the B(440 nm), I(800 nm) and K($2.2\text{ }\mu\text{m}$) wavebands (Metcalfe et al., 1996). These number counts were based upon a number of separate determinations by ground-based optical and infrared telescopes, as well as deep number counts in the Hubble Deep Field. The number counts of galaxies in the Hubble Deep Field join smoothly onto the ground-based counts. Furthermore, the Hubble Deep Field observations have enabled counts to be made in the I waveband, in which the background emission from the Earth's atmosphere becomes an increasingly important problem, and so to extend the counts by about a factor of 100 fainter than is possible from the ground. The lines labelled 'No evoln.' show the expectations of uniform world models and include appropriate K-corrections for the types of galaxy observed in bright galaxy samples.

These studies have been extended to even fainter magnitudes through Hubble Space Telescope observations of the Hubble Ultra Deep Field (HUDF), which made use of the wider field capabilities of the Advanced Camera for Surveys (ACS) (Beckwith et al., 2006). This project resulted in the deepest image ever taken of the sky and involved 400 orbits of HST observing time, or about a million seconds of exposure time (Fig. 17.24a). The integral number counts of galaxies were complete to magnitudes $z_{850} = 28.7$ and $i_{775} = 29.2$. These counts are compared with those derived from the Great Observatories Origins Deep Survey (GOODS), which were complete to $z_{850} = 26.5$ in Fig. 17.24b. Interestingly, the number counts in the HUDF are 10% lower than those in the GOODS field, reflecting the influence of the large-scale holes and walls of galaxies on the large scale.

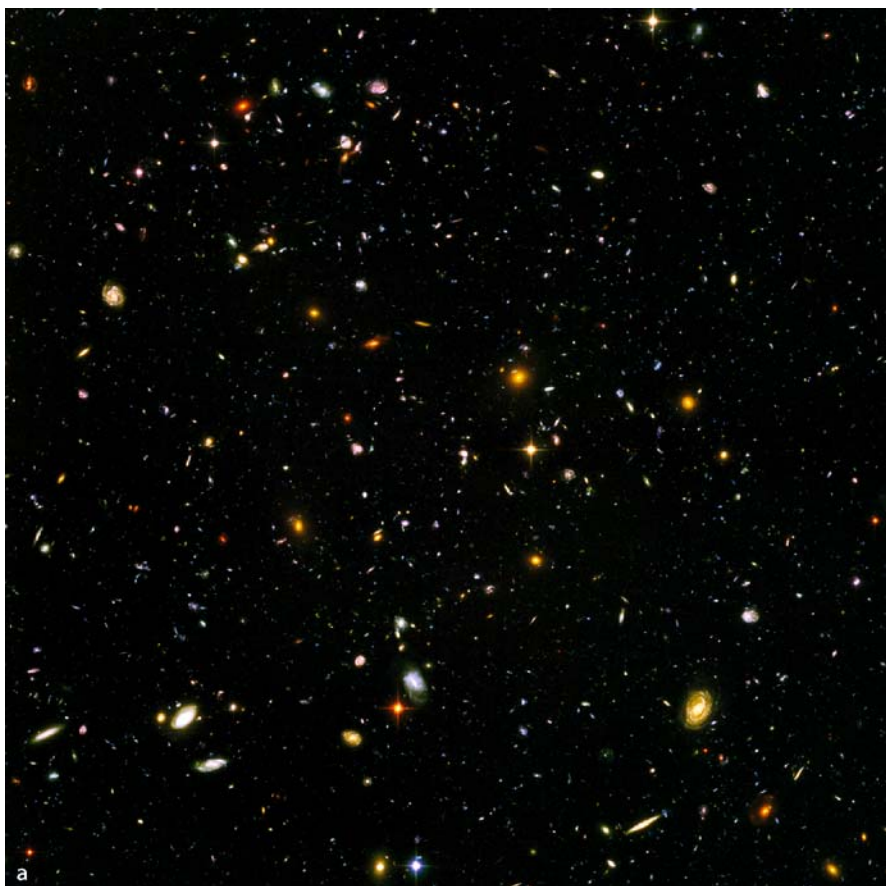


Fig. 17.24. a The Hubble Ultra Deep Field (Beckwith et al., 2006)

A convenient recent survey of a very large number of counts of galaxies has been presented by Ellis and Bland-Hawthorn (Ellis and Bland-Hawthorn, 2006). Their Appendix A provides a comprehensive list of galaxy counts in the U, B, R, I and K wavebands. Interestingly, their objective was not in the use of galaxy counts for cosmological purposes, but rather to provide reliable number counts and their standard deviations for use in projects which required the reliable subtraction of the numbers of background galaxies. Their paper is particularly valuable in providing a standardised set of number counts for these wavebands and also for providing estimates of the standard deviations in these numbers, taking account of both the statistical uncertainties and the variations due to the fact that the large-scale distribution of galaxies is highly correlated. As a result, the fluctuations in the number counts depend both upon the depth of the survey and angular scale over which the counts are made. Table 17.1, taken from their paper, can be recommended as illustrating both the number counts and the standard deviations of the numbers of

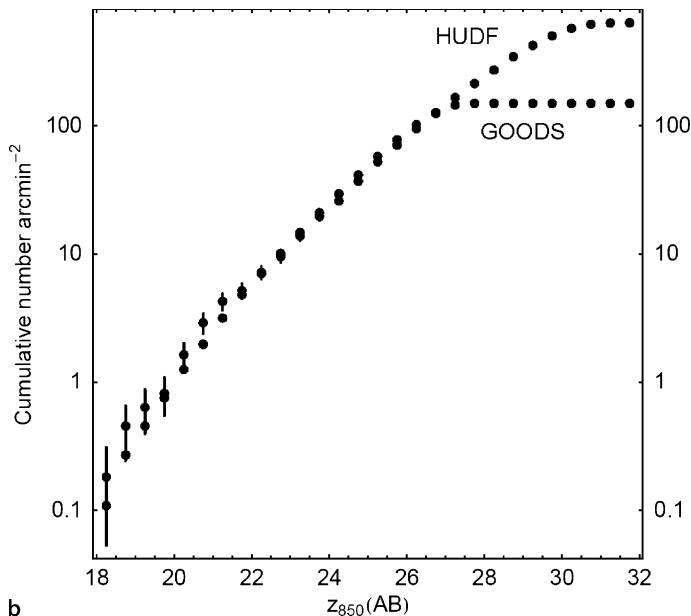


Fig. 17.24. (continued) **b** The integral counts of galaxies in the Hubble Ultra Deep Field compared with the number counts in the GOODS survey. The completeness limit of the GOODS survey is $z_{850} = 26.5$, whereas that of the HUDF is about $z_{850} = 30$

galaxies. For illustration, their number counts for observations made in a 15×15 arcmin² field are given in Table 17.1 and shown in Fig. 17.25. Because of the clustering tendencies of galaxies, it can be seen that the standard deviations are generally much greater than a $N^{1/2}$ estimate.

A number of general features of the galaxy counts are apparent from Figs. 2.12, 8.8 and 17.25. In the infrared K waveband ($2.2 \mu\text{m}$), the counts follow reasonably closely the expectations of uniform world models with $q_0 \sim 0 - 0.5$. This is perhaps not too unexpected since the old stellar populations of galaxies are the principal contributors to the luminosities of galaxies in these wavebands. Even corrections for the passive evolution of the galaxy population are quite small. In contrast, in the R, B and U wavebands, there is a large excess of faint galaxies, particularly in the shortest wavelength bands. The departure from the expectations of the uniform models sets in at about $B = 23$ and, at fainter magnitudes, there is a large excess of faint blue galaxies. The lines on Fig. 2.12 illustrate the results of various modelling exercises to account for the observed counts.

The nature of the excess of blue galaxies was soon elucidated by studies with the Hubble Space Telescope. The high-resolution images enabled the morphologies of galaxies to be classified into spheroidal/compact, spiral and irregular/peculiar/merger categories. The results of the pioneering analysis of Abraham and his colleagues are shown in Fig. 17.26 (Abraham et al., 1996). It is apparent that the spheroidal and spiral galaxies more or less follow the expectations of the uniform-world models,

Table 17.1. Galaxy counts N and their standard deviations σ for an area of sky 15×15 arcmin 2 in the U, B, R, I and K wavebands. The standard deviation depends upon the area of sky observed because of the strongly correlated distribution of galaxies (Ellis and Bland-Hawthorn, 2006). The numbers N quoted in the table are those between magnitudes m_{min} and m_{lim}

m_{lim}	$N(\text{U})$	σ_{U}	$N(\text{B})$	σ_{B}	$N(\text{R})$	σ_{R}	$N(\text{I})$	σ_{I}	$N(\text{K})$	σ_{K}
m_{min}	19		15		15		14		13	
15									11	5
16							2	2		
17			0	1	4	2			144	28
18							32	11		
19			6	4	40	10			993	87
20							248	37		
21	66	19	50	14	295	36			4890	230
22							1410	100		
23	688	76	408	47	1650	110			18,200	510
24							6410	270		
25	6020	310	4040	240	8930	360				
26							28,710	790		
27	27,210	780	20,940	710	39,390	1000				
28					74400	1600	101,500	1900		
29			63,400	1400						

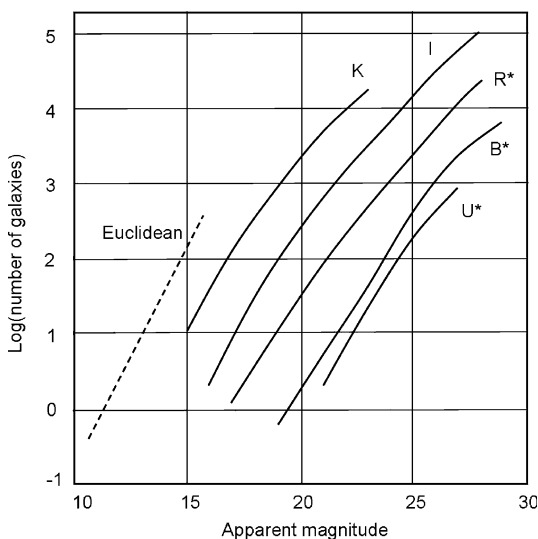


Fig. 17.25. Number counts of galaxies in the U, B, R, I and K wavebands from the survey of recent counts of galaxies for an area 15×15 arcmin 2 on the sky (Ellis and Bland-Hawthorn, 2006). The number counts and their standard deviations are given in Table 17.1. Note that, for the sake of clarity, the number counts in the I waveband have been displaced by -0.5 in $\log N$, the B-band number counts by -1 in $\log N$ and the I-band counts by -1.5 in $\log N$. For comparison, the Euclidean relation $N = 0.6m + \text{constant}$ is also shown

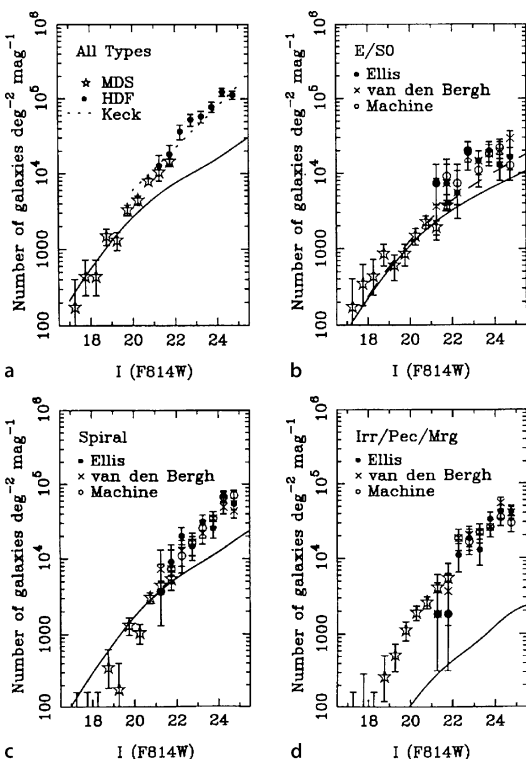


Fig. 17.26a–d. Number-magnitude relation for morphologically segregated samples of galaxies from the Medium Deep Survey (MDS) and the Hubble Deep Field (Abraham et al., 1996). The observations from the MDS survey are indicated by *stars*. The other *symbols* show the counts based upon morphological classifications carried out by Ellis, van den Bergh and by an automated machine-based classification algorithm. The *dotted line* in panel **a** shows the total counts of galaxies from a field observed by the Keck Telescope. The *solid lines* show the expected counts of the different morphological classes assuming their properties do not change with cosmic epoch (Glazebrook et al., 1995)

while the objects classified as irregular/peculiar/merger systems show a distinct excess relative to their numbers in bright galaxy samples, which amount to only about 1–2% of the galaxy population.

Part of the problem in understanding the nature of the faint blue galaxies is that, even with the present generation of 8- to 10-m optical-infrared telescopes, spectroscopic observations are limited to $m_B \leq 24$. According to Cowie and his colleagues, at this magnitude limit, the population of galaxies is composed of a mixture of normal galaxies at small redshifts plus galaxies undergoing rapid star formation from $z = 0.2$ to beyond $z = 1.7$ (Cowie et al., 1996). These results are in accord with the conclusions of Ellis that there is unquestionably an increase in the numbers of star-forming galaxies with increasing redshift. Equally intriguing, Cowie and his colleagues find that there is little change in the K-band luminosity function out to redshifts $z \approx 1$, suggesting that most of their stellar populations were already in place by a redshift of 1. The existence of old, red galaxies at redshifts up to almost $z = 2$ has been confirmed by the studies by Cimatti and his colleagues from studies of the K20 sample of galaxies (Cimatti et al., 2004).

The imaging evidence from the Hubble Deep Field and the HUDF is even more compelling. There is no question about the fact that most of the faint objects appearing in Fig. 17.24a bear little resemblance to the classical forms of galaxy.

This is particularly true if attention is restricted to the sample of galaxies which are certainly at large redshifts $z \geq 3.5$ through the observation of ‘drop-outs’ through the various filter bands. These are interpreted as star-forming galaxies in which the Lyman cut-off is redshifted into the optical waveband. The images in the paper by Beckwith and his colleagues illustrated many of the types of ‘drop-out’ galaxy observed in the HUDF (Fig. 19.5b). The galaxies are much smaller and much more irregular than those observed in the nearby Universe. Beckwith and his colleagues determined luminosity functions and size distributions for different types of drop-out galaxy. It is therefore apparent that a different approach is needed to the study of the evolution of galaxies in the optical waveband, and this is the subject of Chap. 19 – how can we put together this vast amount of data on the distant Universe into a consistent picture of galaxy formation and evolution?

17.8 Clusters of Galaxies

Butcher and Oemler first presented dramatic evidence for the evolution of galaxies in rich, regular clusters at relatively small redshifts (Butcher and Oemler, 1978, 1984). They found that the fraction of blue galaxies in such clusters increased from less than 5% in a nearby sample to percentages as large as 50% at redshift $z \sim 0.4$. The *Butcher–Oemler effect* has been the subject of a great deal of study and debate, the major observational problems concerning the contamination of the cluster populations by foreground and background galaxies, as well as by bias in the selection criteria according to which the clusters were selected for observation in the first place (Dressler, 1984).

Observations with the Hubble Space Telescope clarified a number of these issues (Dressler and Smail, 1997; Dressler et al., 1997; Dickinson, 1997). The colours of the spheroidal galaxies in clusters have been determined out to redshifts of $z = 0.5$ and these show remarkably little scatter about the relation expected for passively evolving elliptical galaxies (Ellis et al., 1997).

The inference is that these galaxies formed their stellar populations at large redshifts and that there has been little ongoing star formation. Perhaps the most remarkable result of these studies has been the change in the relative populations of galaxies of different types at $z \sim 0.5$ as compared with a nearby sample. Firstly, the fraction of spiral galaxies in the large redshift sample is very much greater at high galaxy densities than in the nearby sample. Secondly, the overall fraction of S0 galaxies is very much less at larger redshifts than in the local sample. At the same time, the fraction of spheroidal galaxies is at least as large as in the nearby sample, constituting further evidence that the population of elliptical galaxies was already fully formed at large redshifts. There is a correlation between galaxy type and galaxy density for the four highest-concentration, regular clusters in the sample but for the lower-concentration, irregular clusters, the correlation is not present.

These observations suggest that the elliptical galaxy population was already well formed at large redshifts and that it is unlikely that the bulk of the ellipticals were formed by mergers of spiral galaxies which were members of the cluster. On the

other hand, the population of S0 galaxies must have grown considerably over the redshift interval $0 < z < 1$. The likely origin of these population changes is the transformation of a significant fraction of the large abundance of spiral galaxies seen in the large redshift clusters into S0 galaxies. Dynamical interactions between galaxies, ram-pressure stripping, accretion of mass and collisions between spiral galaxies are possible means of enhancing the population of S0 galaxies relative to spiral galaxies. This picture would be consistent with the significant number of blue irregular, or merging systems observed in the clusters in the sample observed at $z \sim 0.5$.

In contrast to the passive evolution of the elliptical galaxies in rich clusters of galaxies, the redshift–K apparent magnitude relation for the brightest galaxies in clusters shows evidence for evolution of their total luminosities. Aragón-Salamanca and his colleagues showed that the observed relation is consistent with the expectations of standard world models in which their luminosities were unchanged with cosmic epoch (Aragón-Salamanca et al., 1993). This must be the result of a cosmic conspiracy since the stellar populations of the brightest cluster galaxies must have evolved at least passively with cosmic epoch, and so, according to the considerations of Sect. 17.2.2, the galaxies should be about one magnitude fainter at the present epoch as compared with their luminosities at $z \sim 1$. The obvious way of accounting for the constancy of the absolute magnitudes of these galaxies is to appeal to dynamical friction and galactic cannibalism, as described by Hausman and Ostriker in the context of explaining the small dispersion in the absolute magnitudes of the brightest galaxies in clusters (Hausman and Ostriker, 1977, 1978).

The argument can be understood from the following elementary considerations. The expression for the gravitational relaxation timescale τ_g for the exchange of kinetic energy between the masses M_1 and M_2 in a cluster of point masses has the form

$$\tau_g \propto \frac{v^3}{M_1 M_2} . \quad (17.37)$$

This process of *dynamical friction* leads to the exchange of kinetic energy between the point masses as they attempt to establish thermodynamic, as well as dynamical, equilibrium among the cluster members.¹ In the case of a cluster of galaxies, (17.37) shows that the most massive galaxies lose kinetic energy to less massive members most rapidly and so the former drift towards the dynamical centre of the cluster. Expression (17.37) also indicates that relaxation is most rapid among the more massive galaxies, leading to the most massive galaxies cannibalising the next most massive galaxies in the clusters. This might be an explanation for the Bautz–Morgan effect, discussed in Sect. 4.2.3. Obviously, the case of galaxies is much more complex than the case of point masses, but it can be appreciated that dynamical friction and cannibalism can naturally account for the increase in mass and luminosity of the brightest galaxies in clusters.

¹ I have given a simple derivation of this relation in the context of ionisation losses in a plasma (Longair, 1997b)

Simulations of the merging of galaxies in clusters have been carried out by Kauffmann and White within the context of the hierarchical scenario for cluster formation (Kauffmann and White, 1993). On the basis of these simulations, they have shown that the luminosity of the brightest galaxies in clusters can increase on average by a factor of between 3 and 5 between redshift $z \sim 1$ and the present epoch, which can account for the cosmic conspiracy which produces an apparently non-evolving redshift–K magnitude relation for the brightest galaxies in clusters.

It is of the greatest interest to extend these studies to redshifts $z \geq 1$. According to the considerations of Sect. 16.1.1, clusters of galaxies must have formed rather late in cosmic history and there should not be many fully formed clusters at large redshifts. Dickinson has given a list of possible associations of galaxies observed at redshifts $z > 2$, many of them being discovered as companion galaxies to active galaxies and quasars, while some of them have been found as clusters of Lyman- α absorbers (Dickinson, 1997). We will return to many of these issues when we attempt to put all the evidence on galaxy formation and evolution together in Chap. 19.

18 The Intergalactic Medium

Studies of the intergalactic medium have assumed a central role in astrophysical cosmology. Diffuse intergalactic gas is present in clusters of galaxies as indicated by the observation of intense X-ray bremsstrahlung at temperatures of $T \sim 10^8$ K (Sect. 4.4). In clusters such as the Coma and Perseus clusters, the mass of intergalactic gas is at least as great as the visible mass of the cluster galaxies. The observation of strong emission lines of highly ionised iron from the intergalactic gas shows that it has been enriched relative to its primordial abundance, but the heavy elements are underabundant relative to the cosmic abundances of the elements. The enrichment of the gas is inferred to be due to stellar nucleosynthesis within the galaxies of the cluster, followed by the expulsion of enriched gas into the intergalactic medium.

The study of the intergalactic medium between clusters of galaxies is more challenging, but the Lyman- α absorption line systems seen in the spectra of distant quasars show that gas clouds are certainly present in the space between galaxies. The densest of these absorption systems can be identified with the discs of protospiral galaxies, but there are many more clouds with much lower column densities which can be used to estimate the power spectrum of baryonic perturbations at low masses. The study of the chemical abundances in different types of absorption line systems is proving to be a powerful tool for studying metal production and feedback processes during galaxy formation, as well as the thermal and ionisation history of the Universe during and after the epoch of reionisation. Studies of the absorption line systems in quasar spectra have now been extended to redshifts greater than $z = 6$, at which evidence has been found for continuum absorption by the neutral diffuse intergalactic gas to the short-wavelength side of the redshifted Lyman- α line, the long-sought-after *Gunn–Peterson effect*. This is interpreted as evidence that the reionisation and heating of the neutral primordial intergalactic gas was nearing completion. This interpretation is consistent with the evidence of the optical depth of the intergalactic gas to Thomson scattering obtained from the 3-year WMAP observations (Sects. 15.7 and 15.8). These data suggest that the process of reionisation of the primordial intergalactic gas took place at epochs corresponding to $6 \leq z \leq 15$. Thus, studies of the intergalactic medium now inform many aspects of the processes of galaxy formation.

It should also be recalled that there is a ‘missing baryon’ problem in the sense that the most recent estimates of the mass density of the baryonic component of galaxies is only $\Omega_b h = (2 \pm 0.6) \times 10^{-3}$ (Bell et al., 2003), whereas the overall baryonic mass density inferred from primordial nucleosynthesis and the spectrum

of perturbations in the cosmic microwave background radiation is $\Omega_B h^2 = 0.0223$ (Sects. 15.7 and 15.9). Much of the remaining gas must be in the form of diffuse intergalactic gas in clusters of galaxies and in the medium between them.

Let us begin by deriving general expressions for the background emission of diffuse intergalactic gas and its optical depth for the absorption and scattering of the emission of background sources.

18.1 The Background Emission of and Absorption by the Intergalactic Gas

We can work out the expression for the background intensity of a uniform distribution of sources of luminosity $L(\nu_1, z)$ using (17.7) and (17.8). The background intensity in $\text{W m}^{-2} \text{Hz}^{-1} \text{sr}^{-1}$ is then

$$I(\nu_0) = \int S(\nu_0) dN = \frac{1}{4\pi} \int_0^\infty \frac{L(\nu_1, z) N_0}{(1+z)} dr , \quad (18.1)$$

where $\nu_0 = \nu_1/(1+z)$ is the frequency of observation at the present epoch. It is assumed that the comoving number density of sources N_0 is conserved, but their luminosities can change with cosmic epoch. To adapt this expression for the case of the emission of diffuse intergalactic gas, it is simplest to work in terms of the *proper* number density of objects at redshift z , $N(z) = N_0(1+z)^3$. Then, the luminosity per unit proper volume, that is the *emissivity* of the intergalactic medium, is $\varepsilon(\nu_1) = L(\nu_1, z)N(z)$, and the background intensity is

$$I(\nu_0) = \frac{1}{4\pi} \int_0^\infty \frac{\varepsilon(\nu_1)}{(1+z)^4} dr . \quad (18.2)$$

If we adopt the Friedman models with finite Ω_Λ , we find

$$I(\nu_0) = \frac{c}{4\pi H_0} \int_0^\infty \frac{\varepsilon(\nu_1)}{(1+z)^4[(1+z)^2(\Omega_0 z + 1) - \Omega_\Lambda z(z+2)]^{1/2}} dz . \quad (18.3)$$

In exactly the same way, we can work out the optical depth of the gas at an observed frequency ν_0 due to absorption by intergalactic matter along the line of sight to redshift z . If $\alpha(\nu_1)$ is the absorption coefficient for radiation at frequency ν_1 , then the increment of optical depth for the photons which are redshifted to frequency ν_0 by the time they reach the Earth is $d\tau(\nu_0) = \alpha(\nu_1) dl = \alpha(\nu_1)c dt$, where $c dt = dl$ is the element of proper distance at redshift z . Hence, integrating along the path of the photon, we find

$$\begin{aligned} \tau(\nu_0) &= \int \alpha(\nu_1) dl = \int \alpha(\nu_1) \frac{dr}{1+z} \\ &= \frac{c}{H_0} \int_0^z \frac{\alpha[\nu_0(1+z)] dz}{(1+z)[(\Omega_0 z + 1)(1+z)^2 - \Omega_\Lambda z(z+2)]^{1/2}} , \end{aligned} \quad (18.4)$$

where $\nu_0 = \nu_1/(1+z)$. Notice that, in the case of an absorption line, the function $\alpha(\nu_1)$ describes its line profile.

18.2 The Gunn–Peterson Test

One of the most important tests for the presence of diffuse intergalactic neutral hydrogen was described independently by Gunn and Peterson and by Scheuer, soon after the first quasar with redshift greater than 2, 3C9, was discovered (Gunn and Peterson, 1965; Scheuer, 1965). I am particularly fond of 3C9 since I made the optical identification of the quasar as almost my first task for Martin Ryle when I joined the Cambridge Radio Astronomy Group in 1963 (Ryle and Sandage, 1964; Longair, 1965). The particular feature of quasar spectra used in the test is the fact that their continuum emission is non-thermal and extends into the far ultraviolet and X-ray wavebands.

The Gunn–Peterson test makes use of the fact that the cross-section for scattering at the wavelength of Lyman- α photons, 121.6 nm, is very large indeed, and so when the ultraviolet continuum of distant quasars is shifted to the redshift at which it has wavelength 121.6 nm, the radiation is absorbed and re-emitted in some random direction many times. Therefore, if there is sufficient neutral hydrogen present at these redshifts, an absorption trough is observed to the short wavelength side of the redshifted Lyman- α line. Before the advent of space observatories with spectrographic capabilities in the ultraviolet waveband, only when quasars with redshifts of $z > 2$ were discovered was the Lyman- α wavelength redshifted into the observable visible waveband. Let us use (18.4) to work out the optical depth for Lyman- α scattering.

The photo-excitation cross-section of the Lyman- α transition is

$$\sigma(\nu) = \frac{e^2 f}{4\epsilon_0 m_e c} g(\nu - \nu_{\text{Ly}}), \quad (18.5)$$

where ν_{Ly} is the frequency of the Lyman- α transition, f is its oscillator strength, which is 0.416 for this transition, and the function $g(\nu - \nu_{\text{Ly}})$ describes the profile of the Lyman- α absorption line. In this form, the function $g(\nu)$ has been normalised so that $\int g(\nu) d\nu = 1$. Therefore, inserting $\alpha(\nu_1) = \sigma(\nu_1)N_{\text{H}}(z)$ into (18.4), the optical depth due to Lyman- α scattering is

$$\begin{aligned} \tau(\nu_0) &= \int_0^z \frac{\sigma(\nu_1)N_{\text{H}}(z) dr}{(1+z)} \\ &= \frac{e^2 f}{4\epsilon_0 m_e H_0} \int_{\nu_0}^{\nu_1} \frac{N_{\text{H}}(z)g[\nu_0(1+z) - \nu_{\text{Ly}}]}{\nu_0[(\Omega_0 z + 1)(1+z)^2 - \Omega_A z(z+2)]^{1/2}(1+z)} d[\nu_0(1+z)], \end{aligned}$$

where $\nu_1 = \nu_0(1+z_{\text{max}})$. Since $g(\nu)$ is very sharply peaked at the wavelength of the Lyman- α line, we can approximate it by a delta function, and then

$$\tau(\nu_0) = \frac{e^2 f}{4\epsilon_0 m_e H_0 \nu_{\text{Ly}}} \frac{N_{\text{H}}(z)}{[(\Omega_0 z + 1)(1+z)^2 - \Omega_A z(z+2)]^{1/2}}. \quad (18.6)$$

Inserting the values of the constants, we find

$$\tau(\nu_0) = 4 \times 10^4 h^{-1} \frac{N_{\text{H}}(z)}{[(\Omega_0 z + 1)(1+z)^2 - \Omega_A z(z+2)]^{1/2}}, \quad (18.7)$$

where $N_{\text{H}}(z)$ is measured in atoms m^{-3} . This continuum absorption trough has been searched for in those quasars which have such large redshifts that the Lyman- α line

is redshifted into the observable optical waveband, that is, quasars with redshifts $1 + z \geq (330 \text{ nm})/\lambda_{\text{Ly}}$, $z \geq 2$. There is no such redshift restriction for observations with the Hubble Space Telescope. The typical spectrum of a large redshift quasar is shown in Fig. 18.1 (Beaver et al., 1992). Although there are numerous narrow Lyman- α absorption lines present to the short-wavelength side of the Lyman- α line at 121.6 nm, there is no evidence for a depression of the continuum between these. Nor is there any depression to the short-wavelength side of the corresponding line of neutral helium, HeI, which has a rest wavelength of 58.4 nm. Searches have also been made for the Lyman- α trough in low redshift quasars, which can be observed beyond the redshifted Lyman- α line from space, by Davidsen and from the HST, but there is little evidence for any absorption at all (Davidsen, 1993).

Typically, the upper limit to the optical depth to the short-wavelength side of Lyman- α is $\tau(v_0) \leq 0.1$. Substituting this value into (18.7), we find that, for a quasar at a redshift of 3, the upper limit to the number density of neutral hydrogen atoms is $N_{\text{H}} \leq 10^{-5} \text{ m}^{-3}$. This is a very small value indeed compared to typical cosmological baryonic densities, which are about $10\Omega_{\text{B}}h^2(1+z)^3 \text{ m}^{-3} \approx 15 \text{ m}^{-3}$, assuming $z = 3$

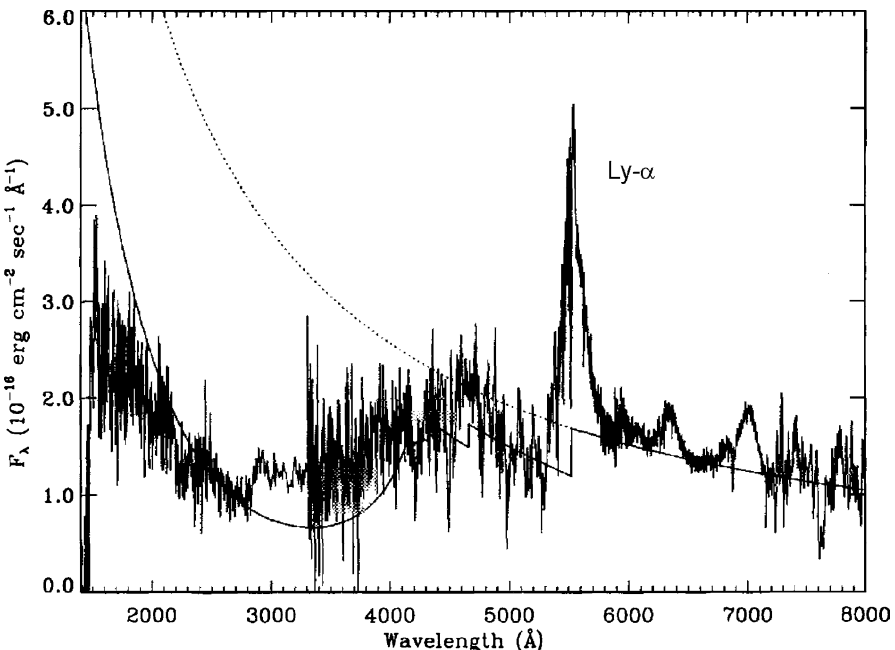


Fig. 18.1. The ultraviolet spectrum of the quasar OQ 172, which has a redshift $z = 3.544$, observed by the Faint Object Spectrograph of the Hubble Space Telescope and at the Lick Observatory (Beaver et al., 1992). Although there are absorption lines present associated with the Lyman- α forest, there is no depression of the continuum intensity to the short-wavelength side of either the Lyman- α line at 121.6 nm nor the HeI line at 58.4 nm. The *solid line* shows the expected absorption profile due to HI clouds along the line of sight to the quasar (Sect. 18.5 and Fig. 18.10a)

and $\Omega_B h^2 = 0.0223$. Thus, if there is a significant amount of hydrogen in the intergalactic medium, it must be very highly ionised.

Quasars with redshifts up to $z \sim 5$ have shown no evidence for neutral hydrogen absorption by diffuse intergalactic gas, although the continuum spectrum becomes more and more ravaged by Lyman- α absorption lines associated with the Lyman- α forest. At the very largest redshifts, however, a Gunn–Peterson trough has at last

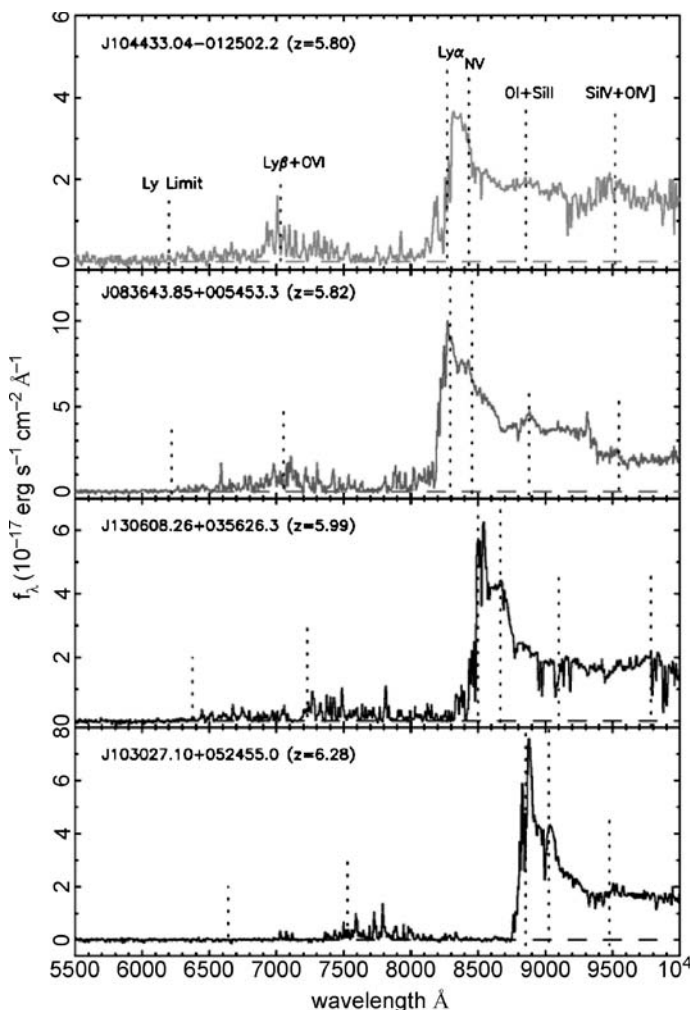


Fig. 18.2. Optical spectra of four very large redshift quasars ($z \geq 5.8$) observed with the Keck-2 telescope. In each spectrum, the wavelengths of prominent emission lines as well as the Lyman limit are indicated by *dashed vertical lines* (Becker et al., 2001). The key observation is the zero continuum flux to the short-wavelength side of the Lyman- α line in the spectrum of the largest redshift quasar, which can be contrasted with the residual Lyman- α forest in the lower redshift quasars

been discovered in the spectrum of the largest redshift quasar discovered as part of the Sloan Digital Sky Survey (Sect. 17.5.2). Four quasars with redshifts 5.80, 5.82 5.99 and 6.28, discovered by the technique of searching for *i*-band drop-outs, were observed by the Keck-2 telescope with the results shown in Fig. 18.2 (Becker et al., 2001).

The first three quasars show increasing absorption to the short-wavelength side of the redshifted Lyman- α line, as expected if the absorption were due to an increasing number of discrete absorbing clouds. At the very largest redshift $z = 6.28$, however, the continuum flux drops dramatically to zero to the short-wavelength side of the Lyman- α line. Becker and his colleagues interpreted this result as showing that the Gunn–Peterson trough had at last been observed, implying that the fractional abundance of diffuse neutral hydrogen began to increase with increasing redshift beyond $z \sim 6$. This result was reinforced by observations of the trough to the short-wavelength side of the Lyman- β line. In their words,

the Universe is approaching the reionisation epoch at $z \sim 6$.

The study of the Universe at redshifts $z \geq 6$, often referred to as the *dark ages*, is one of the great challenges for 21st-century astrophysical cosmology. The first generations of stars in galaxies must have formed between redshifts of $30 \geq z \geq 6$. The ultraviolet radiation of these newly formed stars and any black holes which had formed in the nuclei of galaxies must have resulted in heating and reionisation of the intergalactic gas. It is a great observational challenge to determine observationally the history of structure formation and the evolution of the intergalactic gas during these critical epochs.

18.3 The Lyman- α Absorption Clouds

The nature and properties of the Lyman- α absorption line systems seen in the spectra of large redshift quasars are vast subjects and, for more details, reference should be made to the volumes *QSO Absorption Lines* (Meylan, 1995), *The Hubble Space Telescope and the High Redshift Universe* (Tanvir et al., 1997) and *Probing Galaxies through Quasar Absorption Lines* (Williams et al., 2005). An excellent summary of the current state of understanding of absorption line systems and their rôle in astrophysical cosmology has been given by Srianand (Srianand, 2006).

18.3.1 The Properties of the Lyman- α Absorption Clouds

It is convenient to follow the standard classification of the types of absorption system seen in quasar spectra summarised by Srianand. There are three broad classes of absorption line system which are of direct importance for cosmological studies.

- By far the most common are those belonging to the *Lyman- α forest* which dominate the spectra of large redshift quasars, such as that illustrated in

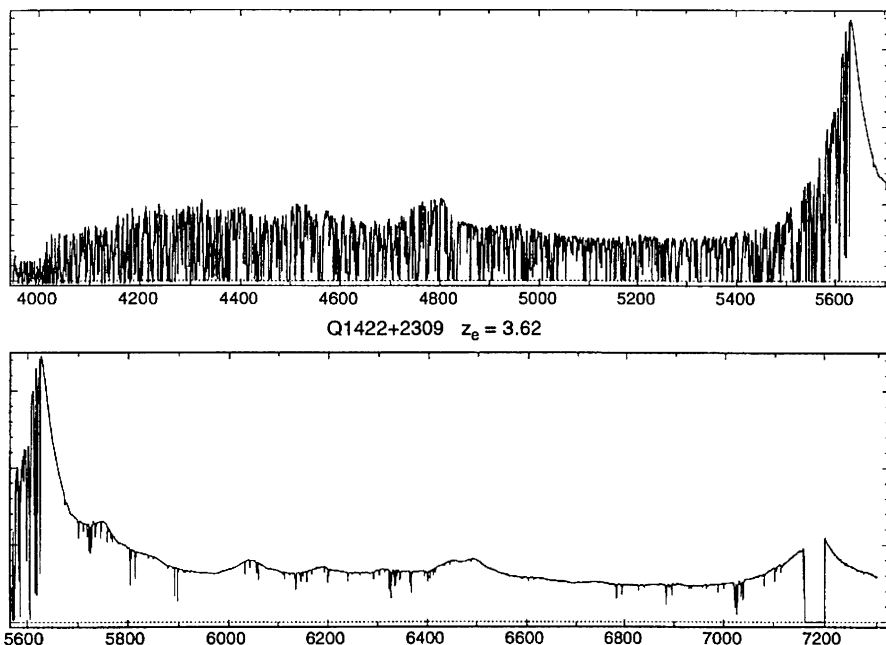


Fig. 18.3. The spectrum of the quasar Q1422+2309 at emission redshift $z = 3.62$ showing the remarkable ‘Lyman- α forest’ on the short-wavelength side of the strong redshifted Lyman- α emission line, which has an observed wavelength of 560 nm (courtesy Dr. W.L.W. Sargent (Boksenberg, 1997)). To the long-wavelength side of the Lyman- α line, the spectrum is very much smoother, only weak metal absorption lines being observed, most of them associated with the CIV absorption line

Fig. 18.3. These systems have neutral hydrogen column densities¹ in the range $N_{\text{HI}} \sim 10^{16}\text{--}10^{21} \text{ m}^{-2}$. In those systems with $N_{\text{HI}} \geq 10^{19} \text{ m}^{-2}$, evidence for low abundances of the heavy elements, corresponding to about 10^{-2} of the solar value, is usually found (Boksenberg, 1997). Systems with lower column densities do not possess detectable CIV lines, and so it is uncertain whether or not this is also true for all the weak Lyman- α absorbers. The absorbers responsible for the Lyman- α forest are interpreted as highly ionised intergalactic clouds, containing largely unprocessed primordial material. There must, however, be some means of mildly enriching these primordial clouds, the chemical abundances of which are similar to those of halo stars in our Galaxy.

- The very much rarer *Lyman-limit systems* have column densities in the range $N_{\text{HI}} \sim 10^{21}\text{--}2 \times 10^{24} \text{ m}^{-2}$. At these column densities, a continuum break is observed at the redshifted wavelength of the 91.2-nm Lyman limit, and absorption lines of the common elements are observed. The Lyman-limit systems can be

¹ Note that, for consistency, I express column densities in units of m^{-2} , although essentially all the literature uses units of cm^{-2} .

associated with the extended gaseous halos of galaxies in which the abundances of the heavy elements are less than 10% of their cosmic abundances (Bergeron, 1988). These properties are consistent with the inference that the halos are very extensive, $\sim 50\text{--}100$ kpc, and so the gas in these regions is not expected to be as enriched as the gas in the disc of a galaxy.

- The *damped Lyman- α* systems have the largest column densities, $N_{\text{HI}} \geq 2 \times 10^{24} \text{ m}^{-2}$ and are even rarer, comprising only about 10% of the Lyman-limit systems. They are so called because the optical depth of the Lyman- α line is so large that the continuum flux density of the quasar reaches essentially zero intensity at the line centre, and the profile of the absorption line can be fitted by a Voigt profile, characteristic of the natural broadening of an absorption line in the limit $\tau \gg 1$. These systems almost certainly contain most of the mass density of neutral gas in the Universe (Lanzetta et al., 1995). Wolfe showed that the damped Lyman- α systems can be convincingly associated with galactic discs, and in his pioneering paper he identified them with the progenitors of the stellar discs of present-day spiral galaxies (Wolfe, 1988). This interpretation was reinforced by the analysis of Kennicutt, who made detailed observations of a number of nearby spiral galaxies and showed that active star formation only takes place in their discs if the column density of neutral gas exceeds $2 \times 10^{24} \text{ m}^{-2}$ (Kennicutt, 1989). It is striking that this criterion is identical to the lower limit at which absorbers are identified as damped Lyman- α systems. Kennicutt argued that this criterion is consistent with the stability criterion for rotating thin gaseous discs, namely, that the disc becomes unstable if the surface density exceeds the critical value Σ_{crit} , where

$$\Sigma_{\text{crit}} = A \frac{\kappa c_s}{3.36G}. \quad (18.8)$$

κ is the epicyclic frequency, c_s is the sound speed in the disc and $A \sim 1$. Thus, the damped Lyman- α systems can provide key information about the chemical evolution of disc galaxies and their progenitors.

The observed number density distribution of Lyman- α absorbers follows closely a power-law distribution from the lowest detectable lines with $N_{\text{HI}} \sim 2 \times 10^{16} \text{ m}^{-2}$ to the high-density damped Lyman- α systems and can be described by the relation $N(N_{\text{HI}}) \propto H_{\text{HI}}^{-1.5}$ (Fig. 18.4).

18.3.2 The Nature of the Clouds in the Lyman- α Forest

The very low abundances of metals in the neutral hydrogen clouds of the Lyman- α forest strongly suggest that they consist of primordial material. Their *column densities* $\int N_{\text{H}} dl$ can be determined from the strength of the absorption lines, but there are only a few cases in which the number density of neutral hydrogen atoms can be found. A good example is the case of the Lyman- α absorbers observed in front of the double quasar 2345+007, in which the same clouds are observed along slightly different lines of sight to each quasar image. Knowing the extent of the clouds,

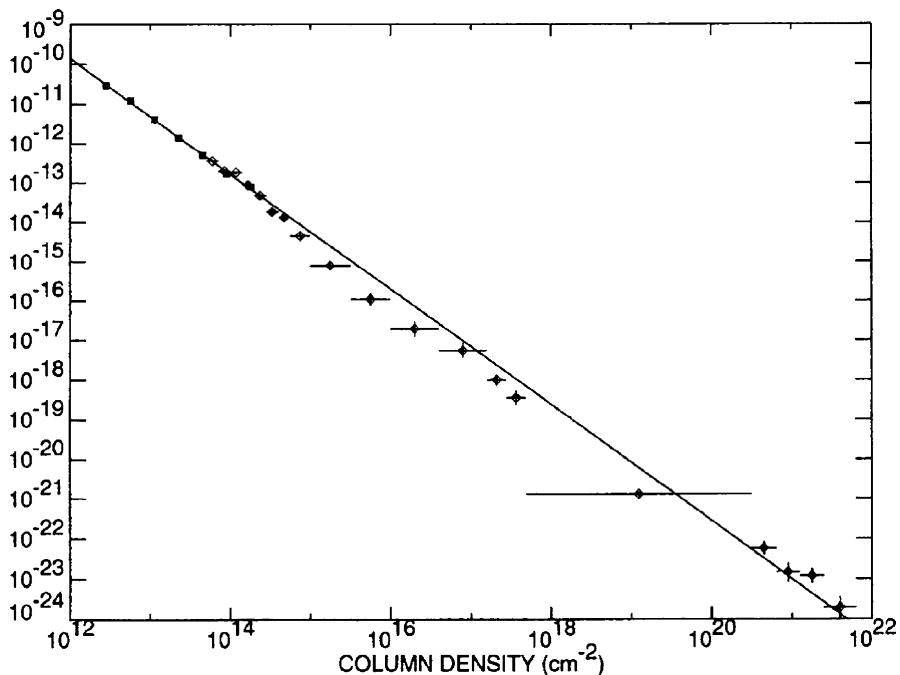


Fig. 18.4. Number density distribution of Lyman- α absorbing clouds as derived by Hu and her colleagues from Keck Telescope observations of large redshift quasars (Hu et al., 1995a)

a number density of neutral hydrogen atoms of about $3 \times 10^{-3} \text{ m}^{-3}$ has been found (Carswell, 1988). Knowing the intergalactic flux of ionising radiation, the number density of the ionised hydrogen atoms can be found by balancing the numbers of photoionisations by the number of the recombinations per second. Typically, the number density of ionised hydrogen amounts to about 10^2 m^{-3} , so that the neutral hydrogen fraction is of the order 3×10^{-5} , confirming the statement in Sect. 18.3.1 that the absorbers are associated with rather highly ionised gas clouds. The typical masses of the Lyman- α clouds are thought to lie in the range $10^6\text{--}10^9 M_\odot$.

The connection with the properties of the diffuse intergalactic gas arises from considerations of the means by which the clouds are confined. It should be emphasised that it is not at all certain how the clouds are held together. The most likely picture suggested by supercomputer simulations is that the Lyman- α clouds are in rough pressure balance with a ‘lukewarm’ intergalactic gas at a temperature of about $3 \times 10^4 \text{ K}$. The intergalactic flux of ionising radiation at a redshift of 2–4 is so intense that the clouds are almost completely ionised. To attain rough pressure balance, the intergalactic gas at redshifts $z \sim 2\text{--}4$ would have to be about 10^2 m^{-3} . At low redshifts, this would correspond to a density parameter in the intergalactic gas $\Omega_{\text{IGG}} \sim 0.1$.

The full treatment of this problem is quite complicated. A good example of the issues involved in these studies is provided by the papers by Ikeuchi and Ostriker

(Ostriker and Ikeuchi, 1983; Ikeuchi and Ostriker, 1986). A complete study involves consideration of the stability of the clouds, the role of evaporation, photoionisation balance within the clouds, and so on.

18.3.3 The Evolution of Lyman- α Absorption Clouds with Cosmic Epoch

The numbers of absorption systems per unit redshift interval for the Lyman- α forest and the Lyman-limit systems change with redshift. The variation of the number density of absorbers with redshift can be characterised by a power-law distribution

$$N(z) dz = A(1+z)^\gamma dz . \quad (18.9)$$

Typically, it is found that, for the Lyman- α forest systems, $A \approx 10$ and $\gamma = 2-3$ whereas, for the Lyman-limit systems $A \approx 1$ and $\gamma \sim 1$. These variations with redshift can be compared with the expected distribution if the properties of the absorbers were unchanging with cosmic epoch, that is, if the absorbers had the same proper cross-sections and constant *comoving* number density. The numbers of absorbers intercepted along any line of sight in the interval of *proper* length dr_{prop} is

$$N(z) dz = \sigma_A N_A(z) dr_{\text{prop}} , \quad (18.10)$$

where σ_A is the cross-section of each absorber and $N_A(z)$ is their proper number density at redshift z . Now, $N_A(z) = N_0(1+z)^3$, where N_0 is the comoving number density of absorbers, that is, the number density they would have at the present epoch, and

$$dr_{\text{prop}} = c dt = \frac{dr}{(1+z)} = \frac{c}{H_0} \frac{dz}{[(\Omega_0 z + 1)(1+z)^2 - \Omega_\Lambda z(z+2)]^{1/2}(1+z)} . \quad (18.11)$$

For simplicity, let us consider the case $\Omega_0 + \Omega_\Lambda = 1$, which we know is a very good approximation for the best fitting values of the cosmological parameters. Then,

$$N(z) dz = \sigma_A N_0 \frac{c}{H_0} \frac{(1+z)^2}{[(\Omega_0 z + 1)^3 - (1-\Omega_0)]^{1/2}} dz . \quad (18.12)$$

Since we are interested in redshifts $z > 2$, we can neglect the term in $(1-\Omega_0)$ in the denominator. Then, if Ω_0 were equal to 1, $N(z) \propto (1+z)^{1/2}$, and, if $\Omega_0 = 0.3$, $N(z)$ varies as a slightly higher power of $(1+z)$, although there is no simple closed form for this case. The significance of this calculation is that the observed number density of Lyman- α forest absorbers changes more rapidly with increasing redshift than expected according to the uniform absorber model. The sense of the evolution is that there were more Lyman- α forest systems at large redshifts as compared with low redshifts. On the other hand, the Lyman-limit systems seem to show a much more modest variation with redshift, almost as though their cross-sections and comoving number densities remained unchanged with cosmic epoch.

18.3.4 The Power Spectrum of the Lyman- α Forest

The statistics of absorbers in the Lyman- α forest are now very large thanks to the Sloan Digital Sky Survey (SDSS) and their two-point correlation functions and power spectra can be evaluated as a function of redshift. The importance of these observations is that they provide information about the distribution of baryonic perturbations in the redshift interval $2 \leq z \leq 4$ on physical scales roughly ($10h^{-1} \geq \lambda \geq h^{-1}$) Mpc. Since the systems are observed at large redshifts, the perturbations were significantly less non-linear than they are in the two-point correlation function for galaxies at the present epoch. What is observed is the distribution of baryonic absorbers which are presumed to be embedded in cold dark matter haloes. Therefore, assumptions need to be made to relate the two-point correlation function of the absorbers to the power spectrum of the underlying dark matter perturbations. This is where large-scale hydrodynamic simulations of the evolution of the intergalactic gas are important. We refer to the discussion of Sect. 18.6 in which the low column density absorbers are associated with a wide range of structures which have low density contrasts $\delta\varrho_B/\varrho_B$ and have not yet condensed into galaxies. It is therefore not unreasonable to suppose that there is a close relation between the two-point correlation function of low column depth absorbers and the initial power spectrum of perturbations on small scales.

The analysis of McDonald and his colleagues involved a sample of 3035 large redshift quasars from the SDSS, all of which displayed Lyman- α forest absorption systems (McDonald et al., 2006). The analysis of this very large data set is highly non-trivial, particularly in understanding the systematic effects which could bias the analysis. Some flavour of the challenges posed by these data is provided by the two-point correlation function in velocity space, which the authors warn should not be used for quantitative analyses (Fig. 18.5a). This diagram only uses data from the first six of the nine redshift bins listed in the caption to Fig. 18.5b. The correlation function is defined as in (14.6) by

$$\xi(r) = \langle \Delta(\mathbf{x})\Delta(\mathbf{x} + \mathbf{r}) \rangle , \quad (18.13)$$

but now \mathbf{x} and $\mathbf{x} + \mathbf{r}$ refer to the relative velocities of the absorption systems along the line of sight. In Fig. 18.5a, the amplitudes of the correlation functions in different redshift slices have been normalised to unity at $\delta v \equiv \mathbf{r} = 0$.

First of all, it can be seen that there is clearly a very strong correlated signal on scales less than about 1000 km s^{-1} , corresponding to a comoving scale of $10h^{-1} \text{ Mpc}$. Second, notice that the correlation functions have similar form in the six redshift intervals. Third, notice the ‘bump’ in the correlation function at 2271 km s^{-1} – this is associated with absorption lines of doubly-ionised silicon, SiIII, in the absorbing clouds. Corrections to the power spectra have to be made for these Lyman- α –SiIII correlated features.

The resulting power spectra for the Lyman- α forest in nine separate redshift intervals are shown in Fig. 18.5b. A different convention has been used for plotting the power spectra as compared with those of Chap. 14. On the abscissa, the wavenumber is given in inverse km s^{-1} – the translations to physical scales are $k = 0.001 \text{ km s}^{-1}$

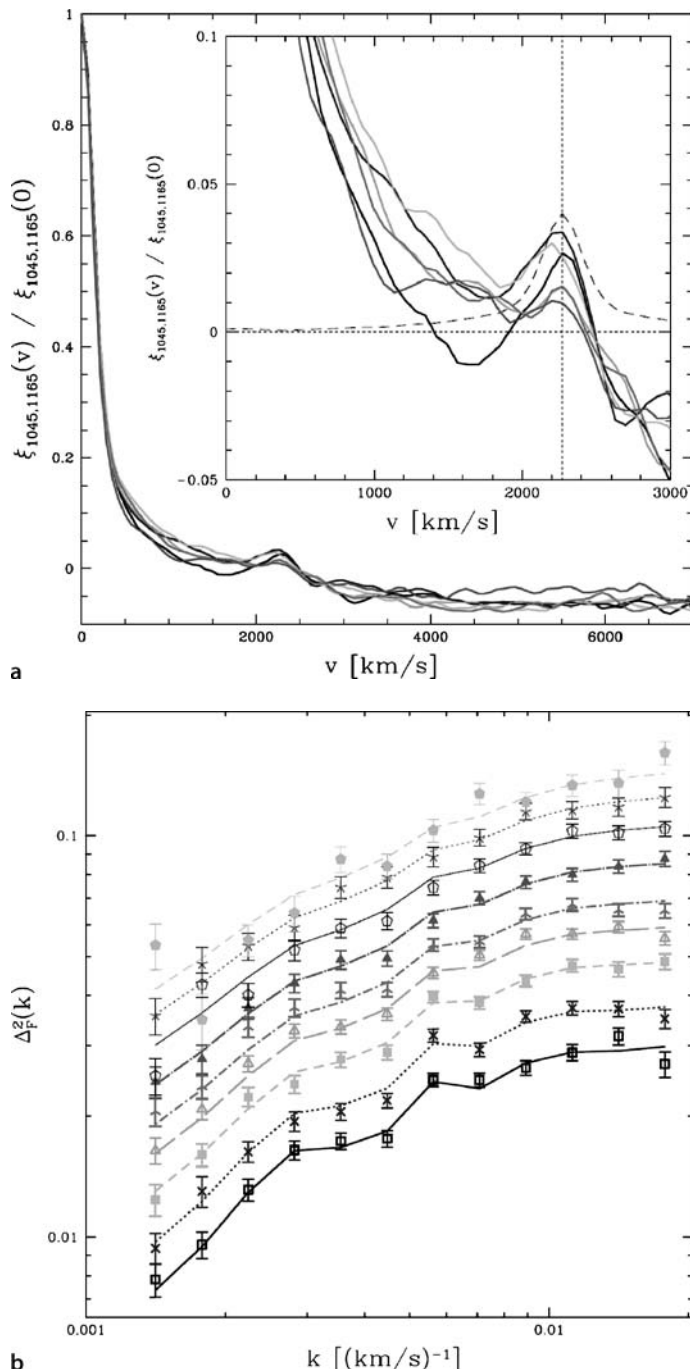


Fig. 18.5. **a** The two-point correlation function for the Lyman- α forest for six redshift intervals, uncorrected for resolution. The correlation functions have been normalised to unity at $\delta v = 0$. The ‘bump’ at 2271 km s^{-1} , and shown in more detail in the *inset*, is due to the presence of SiIII absorption lines associated with the Lyman- α clouds. Corrections have to be made for the presence of this absorber. The authors warn that this diagram should not be used for quantitative analyses. **b** The *points* with error bars show the observed power spectrum $P_F(k, z)$. The *lines* show the best fit once corrections for SiIII absorption are included. *Bottom to top*: the mean redshifts are $z = 2.2$ (*solid line, open square*), $z = 2.4$ (*dotted line, crosses*), $z = 2.6$ (*dashed line, filled squares*), $z = 2.8$ (*long-dashed line, open triangles*); $z = 3.0$ (*dot-dashed line, 3-point star*), $z = 3.2$ (*dot-long-dashed line, filled triangle*), $z = 3.4$ (*thin solid line, open pentagon*), $z = 3.6$ (*thin dotted line, 5-point star*) and $z = 3.8$ (*thin dashed line, filled pentagon*) (McDonald et al., 2006)

$\equiv 10h^{-1} \text{ Mpc}$ and $k = 0.01 \text{ km s}^{-1} \equiv 1h^{-1} \text{ Mpc}$. On the ordinate, the power spectra are plotted as $\Delta^2(k) \times k$ so that the plotted quantities are no longer per unit wavenumber but provide an estimate of the total power on a particular scale. To recover our version of the correlation functions per unit wavenumber, we should divide by k . Then, the power spectra shown in Fig. 18.5b would slope gently in the opposite direction.

It is important that Fig. 18.5b is free of interpretation and modelling of how the power spectra of the absorbers can be related to those of the dark matter perturbations in which they are embedded. The simplest interpretation is that the absorption lines trace the distribution of the dark matter. There are a number of striking features of Fig. 18.5b. First of all, although the amplitude of the power spectrum decreases with decreasing redshift, its shape remains essentially unchanged. Secondly, the spectral slope matches onto the power spectrum on larger physical scales and is consistent with the processed primordial power spectrum for the standard adiabatic cold dark matter model with initial power spectrum of Harrison-Zeldovich form. This continuity can be appreciated by comparing the predicted spectrum of Fig. 14.1b over the range of wavenumbers 1 to 10 Mpc^{-1} with Fig. 18.5b, recalling that the latter diagram should be divided by k to make this comparison.

Another way of illustrating how the power spectrum of the Lyman- α clouds fits rather naturally onto other determinations on larger physical scales and matches the expectations of the processed Harrison-Zeldovich spectrum is provided by the overall power spectrum presented by Tegmark (Fig. 18.6). The somewhat popular nature of Fig. 18.6 can be recognised and also the fact that a considerable amount of modelling and analysis has gone into its construction. The diagram is plotted as the total power $\Delta^2(k) \times k$ on the physical scale λ , in millions of light years rather than wavenumber.

A detailed analysis of these SDSS data combined with the 1-year WMAP temperature fluctuation data and the SDSS galaxy power spectrum has been carried out by Seljak and his colleagues (Seljak et al., 2005). The fact that the Lyman- α power spectrum extends to smaller linear scales than the other methods means that it is sensitive to physical processes which could distort the power spectrum

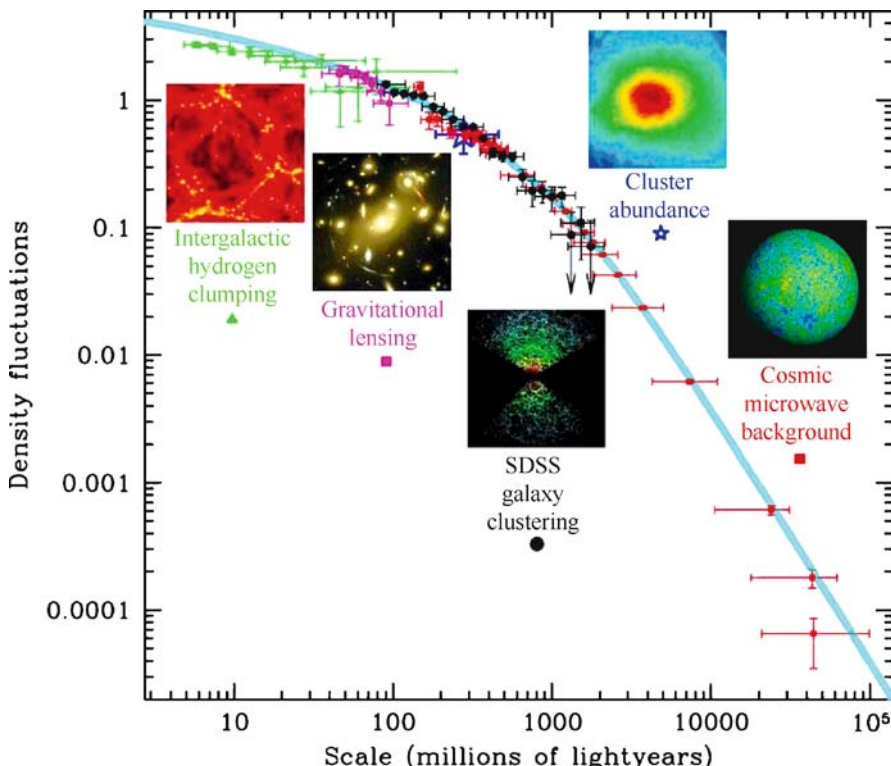


Fig. 18.6. A compilation of estimates of the power spectrum of density fluctuations showing how different samples of object provide information on the different physical scales. The agreement with a processed initial power spectrum of Harrison–Zeldovich form is subject to interpretation, but overall the agreement with this simple model is impressive (courtesy Dr. Max Tegmark)

on these scales. Examples include the damping effects which would be expected if the neutrinos had finite masses of order 1 eV or greater. The agreement of the observed power spectrum with that predicted by the standard concordance model means that the sum of the three massive neutrino families has to satisfy the relation $\sum m_\nu < 0.42 \text{ eV}$.

18.4 The Lukewarm Intergalactic Gas

The physical state of the diffuse intergalactic gas and the associated background ultraviolet ionising radiation field have been the subject of considerable study. It turns out that the likely temperature and density of the diffuse intergalactic gas make it very difficult to detect observationally, except by slightly indirect methods.

18.4.1 The X-Ray Background and a Cosmic Conspiracy

For a number of years, one possibility was that the isotropic X-ray background emission might be the X-ray bremsstrahlung of very hot intergalactic gas. Marshall and his colleagues pointed out that the spectrum of the X-ray background emission in the 1–50 keV energy band shown in Fig. 17.18 can be remarkably well described by the spectrum of thermal bremsstrahlung at a temperature of $kT = 40 \text{ keV}$ and baryon density parameter of $\Omega_B h^2 \geq 0.23$ (Marshall et al., 1980).

This simple picture cannot, however, be correct for a number of reasons. First of all, the considerations of Sect. 17.5.3 show that the X-ray background is due to the superposition of discrete sources throughout the X-ray waveband rather than to a diffuse component. The second major concern is that the large quantities of hot gas, $\Omega_B h^2 \geq 0.23$, needed to explain the intensity of the X-ray background exceed the best estimates of the baryon density parameter $\Omega_B h^2 = 0.0223$ from considerations of primordial nucleosynthesis and the 3-year WMAP data. A third problem is that hot diffuse gas at these high densities and temperatures would give rise to distortions of the Planck spectrum of the cosmic microwave background radiation. As discussed by Sunyaev and Zeldovich, Compton scattering of the photons of the background radiation leads to a characteristic distortion of the spectrum of the background radiation by redistributing the photon energies (Sect. 4.5). The perfect Planck spectrum of the background radiation as observed by COBE enabled Mather to set a powerful constraint to the Compton optical depth of hot diffuse intergalactic gas

$$y = \int \frac{kT_e(z)}{m_e c^2} \frac{\sigma_T N_e(z)}{(1+z)} dr \leq 2.5 \times 10^{-5} \quad (18.14)$$

(Mather, 1995). The most conservative estimate we can make is to assume that the hot gas fills the intergalactic medium at the present epoch, in which case we can make the approximation

$$y \approx \frac{c}{H_0} \sigma_T N_e(0) \frac{kT_e(0)}{m_e c^2}. \quad (18.15)$$

Assuming $\Omega_B = 0.23$ and $kT_e = 40 \text{ keV}$, we find $y = 5 \times 10^{-4}$, already in significant conflict with (18.14). If we adopt a more realistic picture, in which the heating took place at a large redshift, the value of y would increase roughly as $(1+z)^{2.5}$, resulting in even greater conflict with the observations. More detailed models of the heating of the intergalactic gas, which can account for the observed X-ray background spectrum, come to exactly the same conclusion (Taylor and Wright, 1989). Fabian and Barcons argued that, although the value of Ω_B could be reduced if the hot gas were clumped, the clumps would result in large fluctuations in the cosmic microwave background radiation because of the thermal Sunyaev–Zeldovich effect, when the background radiation passed through the clumps (Fabian and Barcons, 1992). They concluded that

the perfect bremsstrahlung shape of the X-ray background is just a cosmic conspiracy.

18.4.2 The Collisional Excitation of the Intergalactic Gas

The arguments of Sect. 18.4.1 rule out a high-temperature, high-density intergalactic gas, but it is possible that collisional excitation by shocks could be responsible for its heating and ionisation. If its temperature lay in the appropriate temperature range, the gas would be expected to be an emitter of collisionally excited HI and HeII Ly- α line emission at wavelengths $\lambda = 121.6$ nm and $\lambda = 30.4$ nm respectively. The observed intensity of the lines is given by (18.3), in which the emissivity of the Lyman- α line per unit frequency interval can be written

$$\varepsilon(\nu_1) = \varepsilon_{\text{Ly}}(z) g(\nu_1 - \nu_{\text{Ly}}) , \quad (18.16)$$

where $\varepsilon_{\text{Ly}}(z)$ is the emissivity of the Lyman- α line in W m^{-3} and $g(\nu_1 - \nu_{\text{Ly}})$ describes its line profile, normalised so that $\int g(\nu_1 - \nu_{\text{Ly}}) d\nu_1 = 1$. Therefore, the intensity of the line per unit bandwidth is $\varepsilon_{\text{Ly}}(z) g(\nu_1 - \nu_{\text{Ly}})$. The intensity of background radiation associated with the Lyman- α emission of the intergalactic gas is therefore

$$I(\nu_0) = \frac{c}{4\pi H_0} \int_0^\infty \frac{\varepsilon_{\text{Ly}}(z) g(\nu_1 - \nu_{\text{Ly}})}{(\Omega_0 z + 1)^{1/2}(1+z)^5} dz , \quad (18.17)$$

where $\nu_1 = \nu_{\text{Ly}} = \nu_0(1+z)$ and we have taken $\Omega_A = 0$ for simplicity. As in Sect. 18.2, we can take $g(\nu_1 - \nu_{\text{Ly}})$ to be a δ -function, in which case

$$\begin{aligned} I(\nu_0) &= \frac{c}{4\pi H_0} \int_0^\infty \frac{\varepsilon_{\text{Ly}}(z) \delta[\nu_0(1+z)]}{(\Omega_0 z + 1)^{1/2}(1+z)^5} dz \\ &= \frac{c}{4\pi H_0} \frac{\varepsilon_{\text{Ly}}(z)}{\nu_{\text{Ly}} (\Omega_0 z + 1)^{1/2}(1+z)^4} . \end{aligned} \quad (18.18)$$

Notice that, in this calculation, the intensities are in units of $\text{W m}^{-2} \text{Hz}^{-1} \text{sr}^{-1}$. In ultraviolet astronomy, it is common to quote intensities in terms of the numbers of photons $\text{s}^{-1} \text{m}^{-2} \text{Hz}^{-1} \text{sr}^{-1}$ or of photons $\text{s}^{-1} \text{m}^{-2} \text{nm}^{-1} \text{sr}^{-1}$. To transform (18.18) into these units, we note that $I(\nu_0) = h\nu_0 I_{\text{ph}}(\nu_0)$ and $\varepsilon_{\text{Ly}}(z) = h\nu_{\text{Ly}} N_{\text{Ly}}(z)$, where $I(\nu_0)$ is the observed intensity in photons per unit frequency interval and $N_{\text{Ly}}(z)$ is the emissivity of the intergalactic gas at redshift z in photons m^{-3} . It follows that

$$I_{\text{ph}}(\nu_0) = \frac{c}{4\pi H_0} \frac{N_{\text{Ly}}(z)}{\nu_{\text{Ly}} (\Omega_0 z + 1)^{1/2}(1+z)^3} . \quad (18.19)$$

Alternatively, in terms of photons per unit wavelength interval, we can write $I_{\text{ph}}(\lambda_0) = I_{\text{ph}}(\nu_0)(d\nu_0/d\lambda_0)$, and so, recalling that $\lambda_0 = \lambda_{\text{Ly}}(1+z)$, we find

$$I_{\text{ph}}(\lambda_0) = \frac{c}{4\pi H_0} \frac{N_{\text{Ly}}(z)}{\nu_{\text{Ly}} (\Omega_0 z + 1)^{1/2}(1+z)^5} . \quad (18.20)$$

The emissivity of the intergalactic gas can be written

$$N_{\text{Ly}}(z) = N_0^2 (1+z)^6 \gamma_{\text{Ly}}(T) , \quad (18.21)$$

where $N_0 = 7.8\Omega_B h^2 \text{ m}^{-3}$ is the number density of neutral hydrogen atoms at the present epoch and Ω_B is the baryon density parameter of the intergalactic gas (Jakobsen, 1995). γ_{Ly} is a suitably normalised emission coefficient. Figure 18.7a shows the variation of γ_{Ly} as a function of temperature for a standard mixture of hydrogen and helium in collisional and thermal equilibrium. It is apparent that collisionally excited HI and HeII Lyman- α lines are particularly intense at what are referred to as the ‘thermostat’ temperatures of $T \approx 2 \times 10^4 \text{ K}$ and $T \approx 8 \times 10^4 \text{ K}$, at which the ionisation state of the intergalactic gas changes from HI to HII and from HeII to HeIII respectively. These changes are illustrated by the change in ionisation state as a function of temperature in Fig. 18.7b. It is immediately apparent from Fig. 18.7b that, if the intergalactic gas were to be collisionally ionised, the temperature of the gas would have to be at least 10^5 K in order that $[N_{\text{HI}}/N_{\text{HII}}] \ll 10^{-5}$. These tools were used by a number of authors, including Kurt, Sunyaev and Weymann in the 1960s to show that the ultraviolet background radiation could be used to detect a ‘lukewarm’ intergalactic gas (Kurt and Sunyaev, 1967; Weymann, 1967).

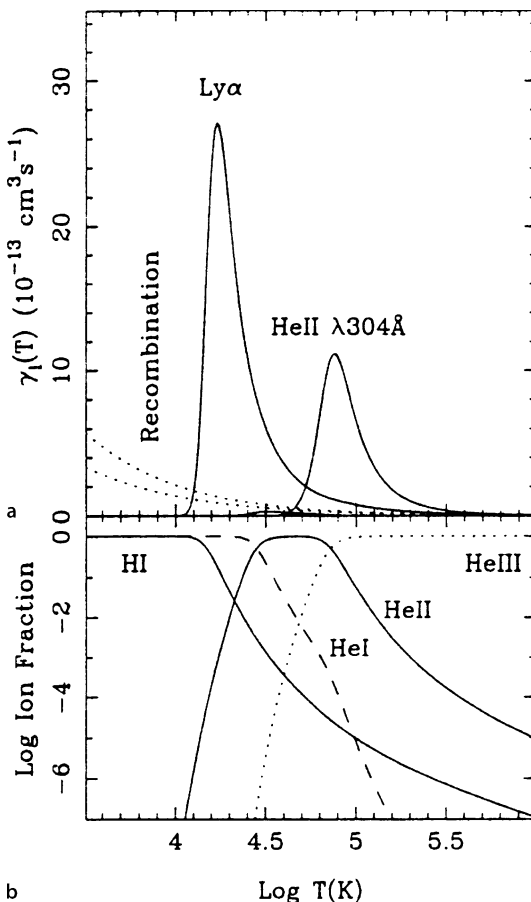


Fig. 18.7. **a** The emissivity per hydrogen atom of collisionally excited HI and HeII Ly- α emission. The dotted lines show the equivalent line emission due to recombination in a fully photoionised gas. **b** Ionisation structure of a cosmological mixture of hydrogen and helium in collisional equilibrium as a function of temperature. Emission from HeI is negligible compared with those of HI and HeII (Jakobsen, 1995)

18.4.3 The Emission and Absorption of Diffuse Lukewarm Intergalactic Gas

Jakobsen also addressed the question of whether or not the redshifted Lyman- α emission of lukewarm intergalactic gas would be detectable in the ultraviolet waveband (Jakobsen, 1995). The easiest case to consider is that in which the intergalactic gas is assumed to be kept more or less fully ionised by diffuse ultraviolet ionising background radiation. Jakobsen considered all the possible cases involving the photoionisation and shock heating of the intergalactic plasma. In the case of a pure photoionisation model, it is straightforward to show that the diffuse redshifted Lyman- α background observed at the present epoch would always be significantly less intense than the ionising background itself and make only a small contribution to the background radiation. The same conclusion was found for the case in which the intergalactic gas is heated by shocks. The basic reason that these backgrounds are so faint is twofold. First, the number density of neutral hydrogen atoms must be very low because of the null result of the Gunn–Peterson test for neutral hydrogen. Second, the constraints of primordial nucleosynthesis indicate that the density of the intergalactic gas is about 20 times less than the critical cosmological density.

An important diagnostic test for the ionisation state of the intergalactic gas is the search for He $^+$ continuum absorption, the equivalent of the Gunn–Peterson test but now for the redshifted He $^+$ Lyman- α line, which has rest wavelength 30.4 nm. If the intergalactic gas were photoionised by a diffuse intergalactic flux of ionising radiation with spectrum $I_\nu \propto \nu^{-0.5}$, the He $^+$ ion would be an order of magnitude more abundant than neutral hydrogen because of its higher ionisation potential and because it recombines more rapidly, and so the Gunn–Peterson decrement might be observable in large redshift quasars for which the 30.4-nm absorption line is redshifted into the observable ultraviolet waveband, that is, for quasars with redshifts greater than 3. The problem is that the 30.4-nm line falls below the Lyman-limit absorption edge of neutral hydrogen at 91.2 nm and so is attenuated by absorption in Lyman- α clouds and Lyman-limit systems which lie along the line of sight to the quasar.

HeII absorption troughs in the spectra of two large redshift quasars were discovered by Jakobsen, Davidsen and their colleagues (Jakobsen et al., 1994; Jakobsen, 1996; Davidsen et al., 1996). A remarkable set of observations was carried out by Jakobsen and his colleagues using the Faint Object Camera of the Hubble Space Telescope (HST). A survey was made of 25 large redshift quasars to discover the few examples in which the far-ultraviolet continuum radiation was not absorbed by intervening Lyman- α clouds. The only quasar which presented an unimpeded view of the wavebands shorter than HeII Lyman- α was the quasar Q0302–003 at a redshift $z = 3.286$. In the low-resolution spectrum shown in Fig. 18.8a, there is a break in the continuum intensity at precisely the wavelength of the redshifted HeII line at 30.4 nm. At shorter wavelengths, the continuum intensity falls below the noise level due to photon counting statistics. At the 90% confidence limit, the optical depth for HeII absorption was found to be $\tau_{\text{HeII}} \geq 1.7$. This limit corresponds to a lower bound to the diffuse intergalactic number density of HeII ions of $N_{\text{HeII}} \geq 1.5h \times 10^{-3} \text{ m}^{-3}$ at redshift $z = 3.29$. A similar result was found for the quasar PKS1935–692 at a redshift of $z = 3.185$ which was discovered in a similar spectroscopic survey carried

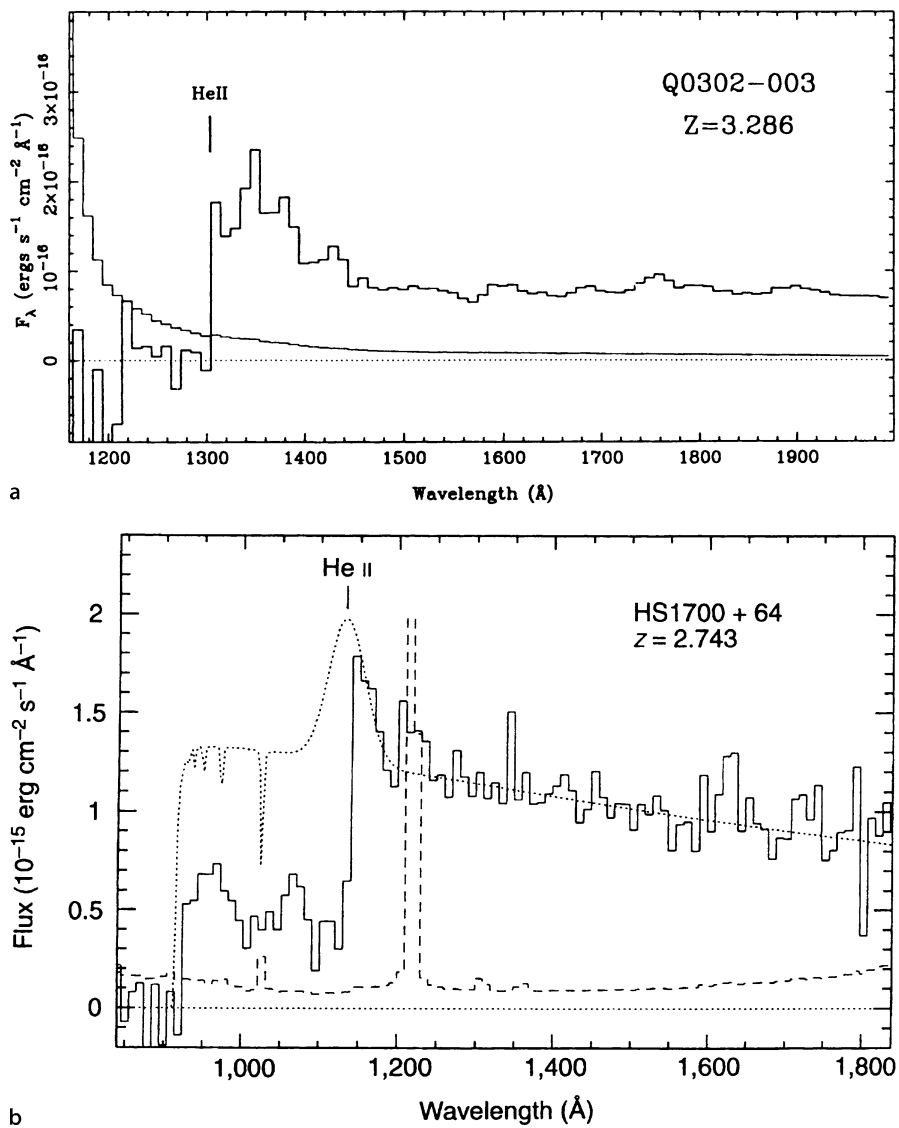


Fig. 18.8a,b. Evidence for absorption by He^+ ions at redshifts $z \sim 3$. **a** The ultraviolet spectrum of the quasar Q0302—003 observed by the Faint Object Camera of the Hubble Space Telescope. The *solid thin line* shows the 1σ uncertainty per wavelength bin of width $\Delta\lambda = 10 \text{ \AA}$, due to photon statistics. The position of the HeII line at 30.4 nm in the quasar rest frame is indicated (Jakobsen et al., 1994). **b** The far-ultraviolet spectrum of the quasar HS1700+64 observed by the Hopkins Ultraviolet Telescope as part of the Astro-2 mission of the Space Shuttle. The *dotted curve* shows an extrapolation of the power-law continuum spectrum beyond the redshifted HeII emission line. The *dashed line* shows the statistical error at each wavelength (Davidsen et al., 1996)

out by Tytler and his colleagues as discussed in the review by Jakobsen (Jakobsen, 1996). The two surveys discovered only two suitable candidates for this test from over 110 bright quasars with $z > 3$ observed by the Faint Object Camera because of the problems of intervening absorption by Lyman- α clouds. It is reassuring that these two observations have provided evidence for primordial helium in the intergalactic gas at large redshifts.

Jakobsen and his colleagues assumed that the absorption was associated with diffuse intergalactic gas (Jakobsen et al., 1994). In the meantime, observations of the Lyman- α forest for the same quasar Q0302–003 with the Keck 10-m Telescope by Cowie and his colleagues indicated that the column density distribution of Lyman- α clouds extended as a power-law $N(N_{\text{H}}) \propto N_{\text{H}}^{-1.5}$ to column densities as low as $2 \times 10^{16} \text{ m}^{-2}$, the limit at which line detection became confusion limited (Songaila et al., 1995; Hu et al., 1995b). Songaila and her colleagues showed that, instead of being associated with the diffuse intergalactic medium, the HeII absorption trough might be associated with the integrated effect of these Lyman- α clouds. This argument could be made in a remarkably model independent way by simply adopting a reasonable ratio for the optical depths for HeII and HI absorption.

The spectrum of the quasar HS1700+64 at redshift $z = 2.743$ was observed by Davidsen and his colleagues with the Hopkins Ultraviolet Telescope as part of the Astro-2 mission of the Space Shuttle programme in 1995 (Davidsen et al., 1996). This quasar is by far the brightest known quasar in the far-ultraviolet waveband at redshifts $z > 2$, being ten times brighter in these wavebands than Q0302–003 (Reimers et al., 1989; Vogel and Reimers, 1995). The remarkable spectrum obtained with the far-ultraviolet spectrograph in a 5.4-h exposure is shown in Fig. 18.8b. The wavelength response extended to the Lyman limit and so much more of the spectrum to the short-wavelength side of the redshifted HeII Lyman- α line was observable as compared with that of Q0302–003 and the spectral resolution was somewhat higher. There is an abrupt depression of the continuum intensity to the short-wavelength side of the redshifted HeII Lyman- α line, the optical depth for HeII absorption being $\tau_{\text{HeII}} = 1.00 \pm 0.07$. In addition, the flux density falls abruptly to zero at the Lyman limit, at which the interstellar gas in our Galaxy becomes opaque.

The resolution of the issue of the origin of the He $^+$ absorption in these quasars was provided by the high spectral resolution observations in the far-ultraviolet wavelength region $100 \leq \lambda \leq 119 \text{ nm}$ made by the Far Ultraviolet Spectroscopic Explorer (FUSE). These challenging observations reported by Kriss and his colleagues for the quasar HE 2347-4342, which has emission redshift $z = 2.885$, showed unambiguously that, in the redshift interval in which He $^+$ could be observed, most of the absorption is associated with the He $^+$ Lyman- α forest (Fig. 18.9) (Kriss et al., 2001). Many of the HeII absorption features could be associated with the HI absorption lines in the corresponding HI Lyman- α forest and so estimates could be made of the ratio of He $^+$ to H atoms, $\eta = N(\text{HeII})/N(\text{HI})$. The mean value of η was found to be about 80, but with a scatter ranging from 1 to greater than 1000. According to Davidsen and his colleagues, values of $\eta \sim 80$ are typically predicted for the ionisation of intergalactic gas clouds by the far-ultraviolet continuum spectra

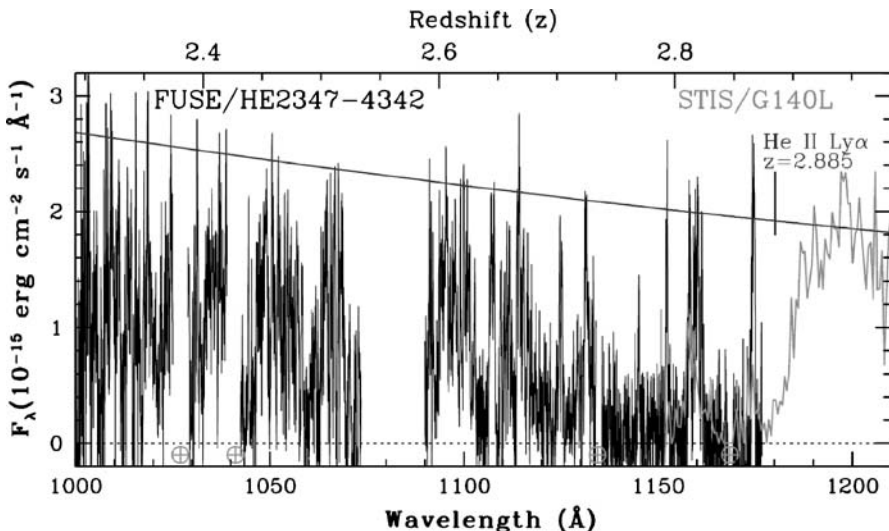


Fig. 18.9. The high-resolution spectrum of the quasar HE 2347-4342 obtained with the Far Ultraviolet Spectroscopic Explorer (FUSE) in the waveband $100 \leq \lambda \leq 119$ nm (Kriss et al., 2001). The near-ultraviolet spectrum obtain at the same time by the Space Telescope Imaging Spectrograph is shown in grey at wavelengths longer than 118 nm. The *straight line* shows the power-law continuum spectrum extrapolated from longer wavelengths, including corrections for dust extinction. The gap between 107.2 and 108.9 nm is due to gaps between the FUSE detector segments

of quasars (Davidson et al., 1996). There must, however, be variations in the UV ionising flux density to account for the range of values of $\eta \leq 100$. Furthermore, values of $\eta \geq 100$ require additional softer ionising photons to suppress the neutral hydrogen abundance. This emission could be associated with starburst galaxies or with strongly absorbed quasar spectra. The upper limit to diffuse He^+ absorption at redshift $z = 2.885$ corresponded to $\tau \leq 0.11\text{--}0.12$. Thus, helium must have been more or less fully ionised by this redshift.

Similar results were obtained in FUSE observations of the quasar HS1700+64 by Fechner and her colleagues, who demonstrated the importance of taking account of metal absorption lines in the H and He^+ Lyman- α forests (Fechner et al., 2006). The type of ionisation structure of the intergalactic gas implied by these observations is discussed and illustrated in Sect. 18.6.

18.4.4 The Proximity Effect and the Diffuse Ultraviolet Background Radiation at Large Redshifts

The Lyman- α forest can also be used to estimate the intensity of the ultraviolet background radiation through observation of the *proximity effect*. It was found that there is a deficit of Lyman- α absorbers with redshifts close to the emission line redshift of the

quasar relative to the expectations of formulae such as (18.9) (Carswell et al., 1982; Murdoch et al., 1986). As was shown in Sect. 18.3.2, the Lyman- α forest is interpreted as low density clouds which are almost fully ionised by the background of ultraviolet ionising radiation. Close to the quasar, however, the clouds are also ionised by the Lyman continuum radiation of the quasar itself. The ultraviolet intensity at any distance from the quasar can be estimated once its luminosity is known and so the distance at which the crossover takes place between ionisation predominantly due to the quasar and to the intergalactic continuum radiation can be estimated. Thus, the proximity effect enables estimates of the intensity of the intergalactic background ultraviolet radiation to be made. This approach was pioneered by Bajtlik and his colleagues who found that, if the background emission spectrum has the form $I(\nu) \propto \nu^{-0.5}$, the background intensity at the Lyman limit is roughly $10^{-24} \text{ W m}^{-2} \text{ Hz}^{-1} \text{ sr}^{-1}$ at redshift $z \sim 2\text{--}3$, corresponding to $\nu I_\nu \approx 3 \times 10^{-9} \text{ W m}^{-2} \text{ sr}^{-1}$ (Bajtlik et al., 1988). The corresponding photoionisation rate had to lie in the range $0.3 \leq \Gamma_{12} \leq 2$ at redshifts $z \approx 2\text{--}3$, where Γ_{12} is the HI photoionisation rate in units of 10^{-12} s^{-1} . More recently Scott and her colleagues surveyed values of Γ_{12} in the literature and found that at redshift $z = 3$, they varied by almost an order of magnitude, $1.5 \leq \Gamma_{12} \leq 9$ (Scott et al., 2000). The best fit value for $I(\nu)$ found by Scott and her colleagues was $7.0^{+3.4}_{-4.4} \times 10^{-25} \text{ W m}^{-2} \text{ Hz}^{-1} \text{ sr}^{-1}$ over the redshift range $1.7 \leq z \leq 3.8$. The best fit value for the HI ionisation rate was $\Gamma_{12} = 1.9^{+1.2}_{-1.0} \text{ s}^{-1}$.

The same technique can be used to estimate the flux of intergalactic ionising radiation at small redshifts from observations of low redshift quasars made with the Hubble Space Telescope. Kulkarni and Fall found tentative evidence for the proximity effect in a sample of 13 low redshift quasars observed by Bahcall and his colleagues as part of the Quasar Absorption Line key project (Kulkarni and Fall, 1993). They found a deficit of Lyman- α absorption clouds close to the redshifts of these quasars, their estimate of the intergalactic flux of ionising radiation at a typical redshift $z \sim 0.5$ lying in the range 4×10^{-26} to $2 \times 10^{-27} \text{ W m}^{-2} \text{ Hz}^{-1} \text{ sr}^{-1}$ with a best estimate of $6 \times 10^{-27} \text{ W m}^{-2} \text{ Hz}^{-1} \text{ sr}^{-1}$.

It is interesting to compare these values with other methods of estimating the local far-ultraviolet background radiation. H α emission has probably been detected from two high-velocity neutral hydrogen clouds in the halo of our Galaxy and this provides an upper limit to the local flux of ionising radiation of $I_\nu \leq 2 \times 10^{-25} \text{ W m}^{-2} \text{ Hz}^{-1} \text{ sr}^{-1}$ (Kutyrev and Reynolds, 1989; Songaila et al., 1989). In 1969, Sunyaev first proposed using the existence of neutral hydrogen in the peripheries of galaxies to set limits to the flux of intergalactic Lyman-continuum radiation (Sunyaev, 1969). The results depend somewhat upon the assumptions made about the spectrum of the ionising radiation and the thickness of the neutral hydrogen layer in galaxies. Bochkarev and Sunyaev, Corbelli and Salpeter and Maloney found values in the range $(1\text{--}10) \times 10^{-26} \text{ W m}^{-2} \text{ Hz}^{-1} \text{ sr}^{-1}$ (Bochkarev and Sunyaev, 1977; Corbelli and Salpeter, 1993; Maloney, 1993). Thus, the flux of ionising radiation at redshifts $z \sim 0.5$ may well be up to two orders of magnitude less than the intensity at redshifts $z \sim 2\text{--}3$.

An obvious source of ionising photons is the integrated emission of quasars which have non-thermal spectra which extend into the far-ultraviolet and X-ray wavebands. To account for the inferred background intensity of about $10^{-24} \text{ W m}^{-2} \text{ Hz}^{-1} \text{ sr}^{-1}$ at $z \sim 2\text{--}3$, there must be very strong evolution of the quasar population with cosmic epoch. Bajtlik and his colleagues were able to account for this background intensity as the integrated ultraviolet emission of the strongly evolving quasar population (Bajtlik et al., 1988). The same conclusion was reached by Scott and her colleagues for their larger sample of quasars for the redshift interval $1.7 \leq z \leq 3.8$. At low redshifts, the background flux density may well be two orders of magnitude less than that at large redshifts and so the problem of accounting for the background is somewhat less severe.

It is not so clear what the sources of the ionising background are at larger redshifts. The evolving population of luminous quasars at large redshifts seems to decline abruptly over the redshift interval $3 \leq z \leq 6$ (see Sect. 17.5.2). Another possibility is that the ionising radiation of star-forming galaxies or protogalaxies at large redshifts may make an important contribution. We will return to this issue in the context of the star formation rate in galaxies as a function of redshift in Chap. 19.

18.5 The Lyman Continuum Opacity of the Intergalactic Gas

As the redshift of the quasar increases, the Lyman- α forest depresses the continuum to the short-wavelength side of Lyman- α . As shown by Møller and Jakobsen, the effect increases dramatically with increasing redshift when account is taken of the evolution of the number of absorption systems per unit redshift (Møller and Jakobsen, 1990).

The low opacities for HI absorption found in the Gunn–Peterson test suggest that the diffuse intergalactic gas is remarkably transparent to far ultraviolet radiation. The cumulative effect of the Lyman- α forest and Lyman-limit systems, however, produces significant Lyman continuum absorption of the far ultraviolet radiation originating from large redshifts (Bechtold et al., 1987; Møller and Jakobsen, 1990). The facts that the number densities of both classes of absorption line systems, the range of column densities and their evolution with cosmic epoch are well characterised enabled estimates of the opacity of the Universe to far ultraviolet photons to be made.

Møller and Jakobsen evaluated the transmission of the intergalactic medium for large redshift quasars knowing the number density of absorption-line systems as a function of redshift $N(z)$ and the average absorption per absorber from the distribution function $N(N_{\text{H}})$ (Møller and Jakobsen, 1990). The absorption coefficient σ_{H} has the form $\sigma_0(v_{\text{H}}/\nu)^3$ for all frequencies greater than v_{H} , where v_{H} is the Lyman limit at 91.2 nm; for longer wavelengths, the absorption is taken to be zero. An example of the typical transmission as a function of observed wavelength for a quasar at emission redshift $z = 3.2$ is shown in Fig. 18.10a; the dashed lines show the $\pm 1\text{-}\sigma$ variations in transmission caused by the fluctuations in the numbers and

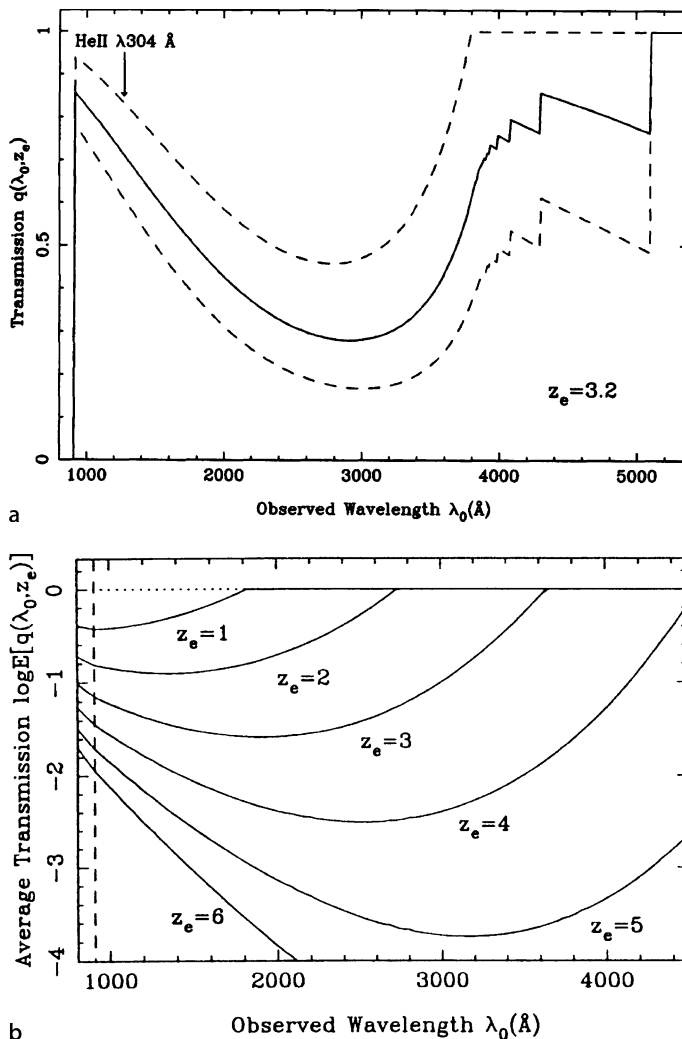


Fig. 18.10. **a** The average transmission of the spectrum of a quasar at redshift $z_e = 3.2$ due to line blanketing and continuum absorption associated with the Lyman- α forest. Line blanketing due to Lyman- α and 24 higher Lyman series lines are included. The dashed lines indicate the $\pm 1\sigma$ variations in transmission caused by the numbers and composition of absorbers along the line of sight (Møller and Jakobsen, 1990). **b** The average transmission of the ultraviolet universe out to large redshifts as a function of wavelength. The ‘Lyman valley’ shown in the figure includes the Lyman continuum opacity due to both the Lyman forest and to Lyman-limit systems (Jakobsen, 1995)

composition of absorbers along the line of sight. The impact of such a transmission function on the continuum spectrum is also shown in Fig. 18.1 for the quasar OQ 172 at a redshift of 3.544. Hence, the total optical depth on passing through a distribution

of clouds $N(z)$ dz is

$$\tau_{\text{tot}} = \int_0^{z_e} N(z)[1 - \exp(-\langle\tau\rangle)] dz , \quad (18.22)$$

and the fractional transmitted intensity is $E = \exp(-\tau_{\text{tot}})$.

This expression has been evaluated by Møller and Jakobsen and their results are displayed in Fig. 18.10b (Møller and Jakobsen, 1990). In the figure, z_e is the emission redshift and the ordinate shows the transmitted fraction of the radiation as observed at different ultraviolet wavelengths. The diagram can be interpreted as follows. Suppose we observe at a wavelength of 300 nm. Then, sources at redshifts of 2 or less do not suffer any Lyman continuum absorption because at a redshift of 2 the emission wavelength is 100 nm, which is greater than the wavelength of the Lyman limit. By a redshift of 3, however, the emission wavelength is 75 nm and there is strong absorption by the clouds in the redshift interval 3 to $z = (300/91.2) - 1 = 2.29$. It can be seen that the average transmission decreases very rapidly with increasing redshift and this has important consequences for the observability of sources at the very largest redshifts. For example, suppose we wished to observe the Gunn–Peterson decrement for He^+ at rest wavelength 30.4 nm or the HeII Lyman- α emission at the same wavelength at an observing wavelength of 160 nm. The radiation would then originate from redshift $z = (160/30.4) - 1 = 4.3$. Inspection of Fig. 18.10b shows that the intensity of such radiation would be attenuated by a factor of about 100, rendering its observation very difficult indeed. Empirically, this is confirmed by the fact that only two good examples out of over 110 quasars with $z > 3$ were found to be suitable for the HeII Lyman- α test. It is apparent that the far-ultraviolet Universe at large redshifts is likely to be heavily obscured. As Jakobsen expressed this result,

Even if the intergalactic medium did go through a phase of intense HeII emission during reheating, the resulting far-ultraviolet radiation will in all likelihood remain forever hidden from our view. (Jakobsen, 1995).

There is some relief from this conclusion in that the absorption is due to discrete clouds rather than to a diffuse medium and the strongest absorbers are the optically thick Lyman-limit systems. Therefore, along some lines of sight, there may be little absorption, which is what has allowed observations of the HeII absorption troughs in Q0302–003, PKS1935–692 and HS1700+64 to be made successfully. A further consequence is that any large redshift, far-ultraviolet diffuse emission should be patchy.

18.6 Modelling the Evolution of the Intergalactic Medium

It has been traditional to model the Lyman- α forest in terms of the properties of ‘clouds’, but simulations of the dynamics of the primordial intergalactic gas in dark matter models for galaxy formation provide a much more realistic picture of the types of structure which give rise to the absorption systems. Excellent examples of what can be achieved computationally are provided by the simulations of Hernquist,

Katz, Miralda-Escudé and their colleagues (Katz et al., 1996; Hernquist et al., 1996; Miranda-Escudé et al., 1996). The gas evolves dynamically under the gravitational influence of the large-scale distribution of the dark matter which can be realistically modelled by large-scale N -body simulations, as illustrated in Fig. 14.10. The dynamics of the gas is followed using single particle hydrodynamics codes. These codes include radiative cooling of the optically thin primordial gas which was discussed in Sect. 16.2. It is assumed that the gas is in ionisation equilibrium with the background ultraviolet radiation field, which can be specified by the investigator. A phenomenological description of the process of star formation is adopted according to which the cooling gas clouds which are unstable to the Jeans instability are gradually converted into stars. In addition, energy is returned to the surrounding medium by supernova explosions. The baryonic matter which collapses into dark matter potential wells dissipates its thermal energy and forms clumps with masses on a galactic scale. According to Katz and his colleagues, the results of their simulations are not sensitive to the assumptions made about the processes of star formation and supernova feedback. These are necessary features for the successful modelling of the structure of the intergalactic medium (Katz et al., 1996).

Of particular interest for this chapter are the resulting structures of intergalactic neutral hydrogen clouds, a good example being shown in Fig. 18.11, which is taken from the simulations of Hernquist and his colleagues (Hernquist et al., 1996). The underlying cosmology is a standard cold dark matter model with $\Omega_0 = 1$ and $h = 0.5$; the baryonic density parameter has been taken to be $\Omega_B = 0.05$. In this simulation, a background ionising radiation flux is assumed to be present which is consistent with the proximity effect observed in large redshift quasars (Sect. 18.4.4).

Figure 18.11 shows the resulting structure of neutral hydrogen clouds at redshift $z = 2$. The simulations result in a network of filaments with dense knots of neutral hydrogen forming in the vicinity of galaxies. Katz and his colleagues then worked out the column density distribution of Lyman- α absorption clouds which would be observed along any line of sight through this distribution to a distant quasar, taking into account the typical spectral resolution of modern spectrographs on large telescopes (Katz et al., 1996). Remarkably, the column densities found in these simulations span the range from about 10^{18} to 10^{26} m^{-2} , and their number density distribution follows closely the observed power-law relation $N(N_H) \propto N_H^{-1.5}$. Similar results have been obtained by Miralda-Escudé and his colleagues for simulations in the Λ cold dark matter model (Miralda-Escudé et al., 1996).

These are important results and suggest new ways of tackling the problems of the formation of galaxies and the hydrogen clouds associated with them. It is encouraging that the Lyman- α forest can develop rather naturally in the standard hierarchical picture for the origin of galaxies and larger scale structures. For our present purposes, the important consideration is the nature of the low column density systems. According to the simulations, the high column density knots, shown as white blobs in Fig. 18.11, arise from radiatively cooling gas associated with galaxies which form in dark matter potential wells. In contrast, the low-density systems are associated with a wide range of different types of structure. To quote Hernquist and his colleagues,

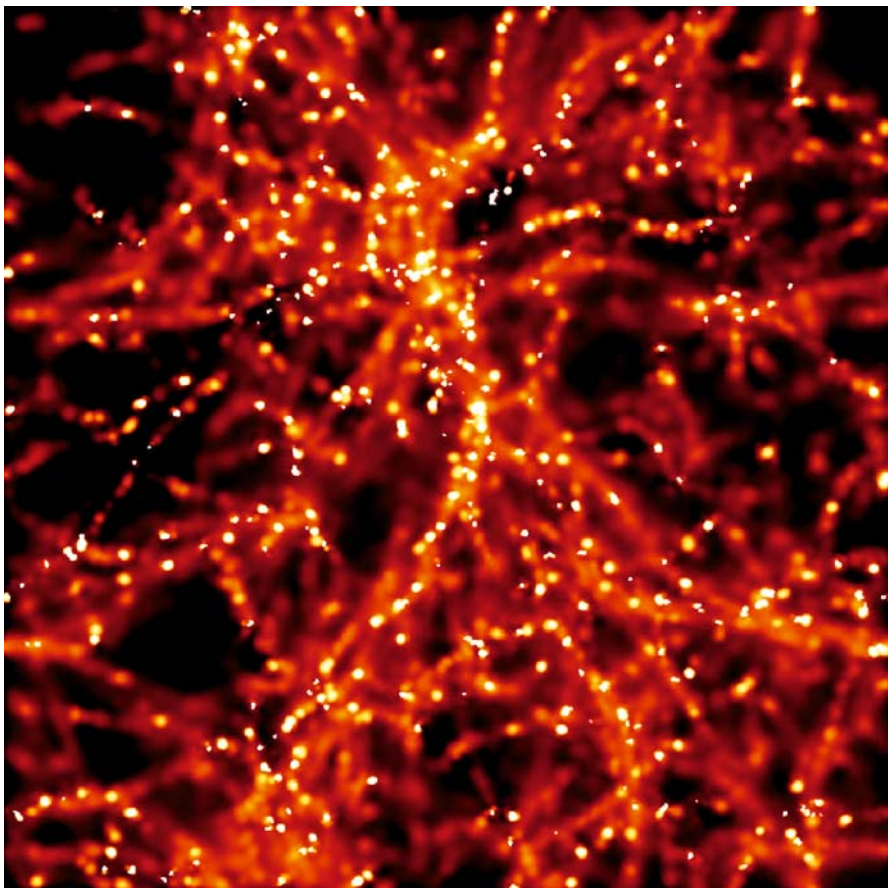


Fig. 18.11. A supercomputer simulation of the expected structure of neutral hydrogen in the intergalactic medium at a redshift $z = 2$ in a standard cold dark matter cosmology with $\Omega_0 = 1$. The size of the box corresponds to a comoving scale of 22.22 Mpc. The simulation includes self-shielding of the neutral hydrogen from the background ultraviolet ionising radiation. The greyscale is such that the white blobs correspond to column depths $N(HI) \geq 10^{20.5} \text{ m}^{-2}$. The faint filamentary structures correspond to column densities of $10^{19.5} \geq N(HI) \geq 10^{18.5} \text{ m}^{-2}$ and the black ‘voids’ to regions with $N(HI) \leq 10^{18.5} \text{ m}^{-2}$ (Katz et al., 1996)

... the low column density absorbers are physically diverse: they include filaments of warm gas; caustics in frequency space produced by converging velocity flows; high-density halos of hot collisionally ionised gas; layers of cool gas sandwiched between shocks; and modest local undulations in undistinguished regions of the intergalactic medium. Temperatures of the absorbing gas range from below 10^4 K to above 10^6 K. (Hernquist et al., 1996)

Of particular interest is the fact that most of the low column density absorbers are large, flattened structures in which the density contrast $\Delta_B = \delta\rho_B/\rho_B$ is low. These

are present throughout the ‘voids’ seen in Fig. 18.11. From this perspective, the distinction between the low column density absorbers of the Lyman- α forest and the continuum Gunn–Peterson effect may be largely academic.

18.7 The Epoch of Reionisation

The next great challenge is to tackle the astrophysical processes involved in the epoch of reionisation. Strong clues are already provided by the observation of the Gunn–Peterson decrement in quasars at redshift $z \geq 6$ (Sect. 18.2) and the optical depth $\tau = 0.09$ for Thomson scattering from the intensity and polarisation measurements of the cosmic microwave background radiation (Sects. 15.7 and 15.9).

The overall picture is well understood but the details are complex. As shown in Sect. 9.4, the matter and radiation finally decoupled at a redshift of $z \sim 375$, after which epoch the matter and radiation cooled separately and adiabatically until the first stars formed, probably at a redshift of $z \sim 30$. These stars were formed from pure primordial material and so were probably quite different from the stars we observe today. The absence of metals meant that they were much stronger sources of ultraviolet radiation than the stars we observe today. The massive stars would evolve rapidly, explode as supernovae and give rise to X-ray emission, both from the supernova remnant and from the compact dead stars formed in the collapse. Thus, in addition to the ultraviolet radiation of hot stars, there was very likely to be a contribution from X-rays as well. Once the first stars had completed their life cycles and returned processed material to the surrounding medium, the next generations of stars formed with properties progressively more and more similar to those of the types of star we observe in our Galaxy today. The ultraviolet radiation produced by the young stars and the X-rays emitted after the end of their lives as normal stars, as well as the ultraviolet emission of the black holes which began to form in the nuclei of protogalaxies, began the process of ionising the neutral hydrogen gas. Eventually, the ‘bubbles’ of hot ionised gas overlapped and the process of reionisation was completed by a redshift $z \approx 6$.

The range of redshifts from $z \sim 1000$ to $z \sim 6$ is often referred to as the *dark ages* since they are very difficult to observe in the optical waveband because of Lyman- α and Lyman continuum absorption. These redshifts are, however, accessible by observations of the highly redshifted 21-cm line of neutral hydrogen. Simulations of the expected distribution of neutral hydrogen through the reionisation epoch have been carried out by Furlanetto and his colleagues (Furlanetto et al., 2004). Some of the redshift slices through one of their simulations are shown in Fig. 18.12. At the largest redshift shown in Fig. 18.12, $z = 12.1$, most of the gas is still in the form of diffuse neutral hydrogen, although structure is present due to gas collapsing into the dark matter potential wells. The average predicted brightness temperature of the redshifted 21-cm line emission is about 25 mK, but there are also fluctuations about this value amounting to $\langle \delta T_b^2 \rangle^{1/2} \approx 10$ mK. This slice would be observed at a frequency of $1420/13.1 = 108$ MHz.

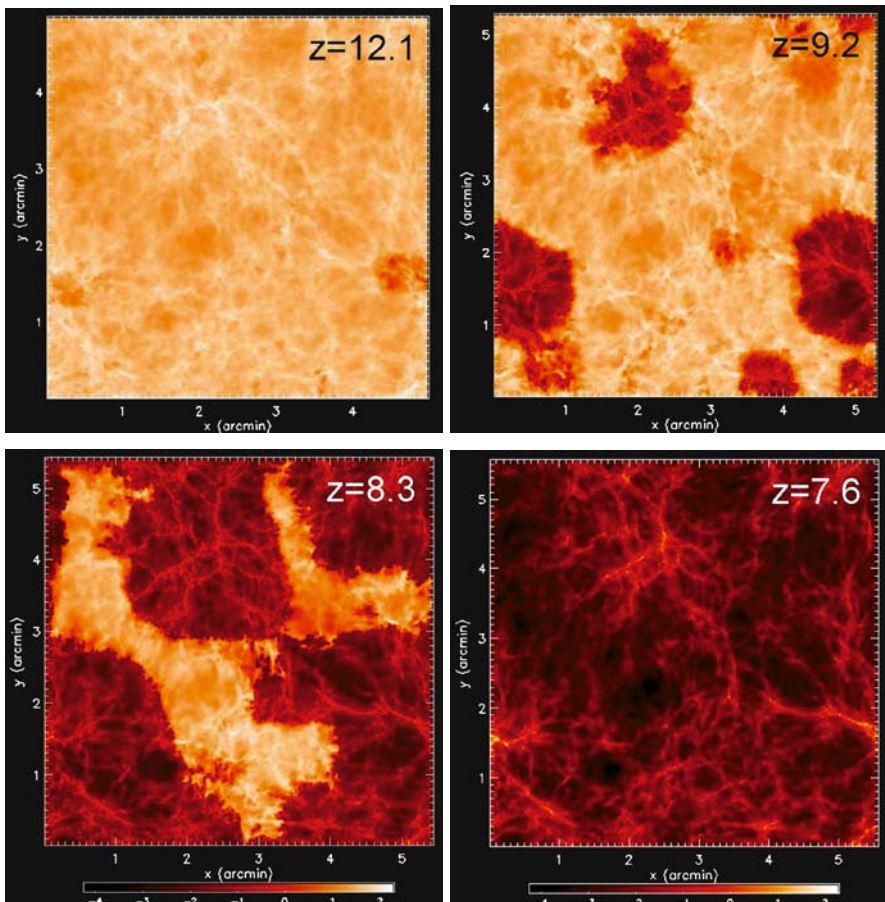


Fig. 18.12. A supercomputer simulation of the expected structure of neutral hydrogen in the intergalactic medium through the epoch of reionisation. The *colour scales* at the bottom of the *diagrams* show the brightness temperature of the 21-cm line at various redshifts as observed with a bandwidth $\Delta\nu = 0.1$ MHz spanning the range of brightness temperatures from 10^2 to 10^{-4} mK. Each *panel* corresponds to the same slice of the simulation of width $10h^{-1}$ comoving Mpc at redshifts $z = 12.1, 9.2, 8.3$ and 7.6 (Furlanetto et al., 2004)

As the first stars formed, they began to ‘burn holes’ in the neutral hydrogen distribution. The various feedback processes associated with the life cycle of the first generations of massive stars resulted in the expansion of these holes until they overlapped and the intergalactic gas was more or less fully ionised by a redshift $z = 7.6$, corresponding to a frequency of 165 MHz. By that redshift, the mean brightness temperature of the neutral hydrogen had dropped to 0.1 mK and the brightness temperature fluctuations to $\langle \delta T_b^2 \rangle^{1/2} \approx 0.1$ mK.

It is a very major experimental challenge to measure these changes by the observation of highly redshifted neutral hydrogen at long radio wavelengths. The

prediction is that there would be a change in the intensity of the radio background radiation in the frequency range of 50 to 150 MHz, but this is a very difficult observation in view of the very high brightness temperatures of the various foreground emissions in the low frequency radio wavebands. There are two features which make these challenging observations feasible. The first is that the foreground signals are all expected to be associated with continuum emission processes such as synchrotron radiation which have no spectral features. Therefore the search for a differential change in the continuum intensity of about 25 mK can be sought in the 50- to 150-MHz waveband. The second prediction is that there should be a corresponding decrease in the fluctuations about the mean brightness temperature as the neutral gas is reionised. These are the objectives of a number of current projects, including the LOFAR project in the Netherlands. Ultimately, the Square Kilometre Array (SKA) should be able to map the neutral hydrogen distribution over the sky through the reionisation era with high angular resolution and very high sensitivity.

There is now a large body of literature on the subject of the intensity and fluctuation power spectrum of the redshifted 21-cm line which is helpfully summarised by Pritchard and Furlanetto (Pritchard and Furlanetto, 2007). The physics involved in these studies is reflected in the expression for the brightness temperature T_b of the 21-cm line emission,

$$T_b = 27 x_{\text{HI}}(1 + \delta_B) \left(\frac{\Omega_B h^2}{0.023} \right) \left(\frac{0.15}{\Omega_0 h^2} \frac{1+z}{10} \right)^{1/2} \left(\frac{T_s - T_\gamma}{T_s} \right) \text{ mK}. \quad (18.23)$$

Taking each of the quantities in turn, x_{HI} is the neutral fraction of hydrogen and Ω_B is the overall baryonic density parameter, $\delta_B = \Delta \rho_B / \rho_B$ is the fractional overdensity in baryons, T_γ is the temperature of the cosmic microwave background radiation at redshift z and T_s is the spin temperature of the neutral hydrogen. The spin temperature describes the number densities of neutral hydrogen atoms in the 1S singlet and triplet states, n_0 and n_1 respectively, through the expression

$$\frac{n_1}{n_0} = \left(\frac{g_1}{g_0} \right) \exp(-T_{21}/T_s), \quad (18.24)$$

where $g_1/g_0 = 3$ is the ratio of spin degeneracies of the upper and lower levels of the transition and $T_{21} \equiv hc/k\lambda_{21} = 0.0628$ K. The spin temperature is determined by the different physical processes by which the levels of the hyperfine transition are populated and can be written

$$T_s^{-1} = \frac{T_\gamma^{-1} + x_\alpha T_\alpha^{-1} + x_c T_K^{-1}}{1 + x_\alpha + x_c}, \quad (18.25)$$

where T_α is the colour temperature of the Lyman- α radiation field at the Lyman- α frequency and is closely coupled to the kinetic temperature of the gas T_K by multiple scatterings. x_c is the collisional coupling coefficient and x_α is the coupling coefficient associated with the excitation of neutral hydrogen by the flux of Lyman- α photons, often referred to as the Wouthuysen-Field effect.

Pritchard and Furlanetto provide an illuminating discussion of the importance of different excitation conditions through the dark ages. While the radiation and

matter are strongly coupled at $z \geq 200$, $T_s = T_\gamma$, and so there is no 21-cm signal. Once the matter and radiation decouple, the kinetic temperature drops below the temperature of the background radiation $T_K < T_\gamma$ and so the 21-cm line would be observed in absorption against the background radiation. Notice that the fluctuations in the absorption signal would be associated with the baryon fluctuations δ_B and so the detection of this signal would provide one of the few ways of studying the redshift interval $30 < z < 150$. Once the first stars are formed, there is a competition between collisional and radiative excitation of the 21-cm line. There are a number of plausible scenarios for the subsequent thermal history of the gas. Suffice it to note that, once the heating of the neutral hydrogen elevated the temperature of the gas above that of the background radiation, the 21-cm line would be expected to be observed in emission.

As emphasised above, it is not only the mean intensity which is important astrophysically, but also the fluctuations about the mean background intensity. Furlanetto and his colleagues write the fluctuations as follows:

$$\delta_{T_b} = \beta\delta + \beta_x\delta_x + \beta_\alpha\delta_\alpha + \beta_T\delta_T - \delta_{\delta v}, \quad (18.26)$$

where δ is the fluctuation in the baryon density and can be assumed to be the same as the underlying density fluctuation in the dark matter; δ_x is the fluctuation in the neutral fraction and δ_α that in the Lyman- α coupling coefficient. δ_T is the fluctuation in the thermal temperature of the gas and $\delta_{\delta v}$ the line-of-sight peculiar velocity gradient. The expansion coefficients β are given by Pritchard and Furlanetto (Pritchard and Furlanetto, 2007).

These considerations present difficult challenges for experimental astrophysicists, but their importance lies in the fact that they provide one of the very few means of probing the dark ages and so of understanding how the process of galaxy formation really got under way.

18.8 The Origin of Magnetic Fields

So far, we have had very little to say about magnetic fields, but they are omnipresent in astronomy. Excellent surveys of the techniques by which magnetic flux densities can be measured in different astronomical environments, and the results of these studies can be found in the volume *Cosmical Magnetism* (Lynden-Bell, 1997) and the review by Vallée (Vallée, 1997).² The Bologna Conference on the *Origin and Evolution of Cosmic Magnetism* contained much recent information about cosmic magnetic fields (Beck et al., 2006).

Magnetic fields play a key role in the process of star-formation, in the dynamics of the interstellar medium and in many different aspects of high energy astrophysics. These topics are central to any study of the physics of galaxies and active galactic

² I have given derivations of many of the relevant aspects of the physics of astronomical magnetic field measurements in Chap. 17 of *High Energy Astrophysics, Vol. 2*. (Longair, 1997c).

nuclei. Some impression of the issues involved in understanding the origin of cosmic magnetic fields is provided by the surveys by Rees, Kulsrud and Parker (Rees, 1994, 1995, 2006; Kulsrud, 1997; Parker, 1997).

To summarise briefly, magnetic fields are present in all astronomical objects. In stars, the magnetic flux densities range from 10^8 T in the interiors of neutron stars, through values ~ 1 T in sunspots to about 10^{-7} T in protostellar objects.³ In the case of normal stars, it is probable that the origin and maintenance of their magnetic fields can be attributed to dynamo action in their interiors associated with the combination of convective motions and reconnection of the lines of force. The key point is that the timescale for the amplification of the magnetic field inside stars can be quite short and so there can be many e-folding times to create a finite magnetic field strength starting from a tiny seed field. There have been concerted efforts to study dynamo processes in the laboratory since it turns out that the various dimensionless parameters encountered in cosmic environments can be replicated in laboratory experiments. Recently, the first successful laboratory dynamo experiments were reported and involved the generation of magnetic fields by a strongly turbulent swirling flow of liquid sodium (Monchaux et al., 2007).

The situation is somewhat different in the case of the large-scale magnetic fields in the interstellar media in galaxies and in the intracluster medium. In our own Galaxy, the magnetic flux density in the interstellar medium consists of a large-scale ordered field of about 2×10^{-10} T superimposed upon which there is a random component of about one to two times this value (Taylor and Cordes, 1993). In the case of the intracluster medium in clusters of galaxies, evidence for large-scale fields is provided by the diffuse synchrotron radio emission observed in a number of clusters, as well as by the observation of depolarisation of the emission of extended extragalactic radio sources by the surrounding intracluster medium. Typical magnetic flux densities are $B \sim 10^{-10}$ T. In the case of the intergalactic medium between clusters of galaxies, there are only upper limits to the strengths of any large-scale magnetic fields from the lack of depolarisation of the emission of distant radio sources, typical limits corresponding to $B \leq 10^{-13}$ T.

In the case of the large-scale magnetic fields in galaxies and clusters, there is a problem in understanding their origin, since the characteristic timescales over which magnetic dynamos could operate are rather long. For example, in the case of the interstellar field in our own Galaxy, the period of rotation of the interstellar gas about the Galactic Centre is $\sim 2.5 \times 10^8$ years, and so there have been at most about 50 complete rotations of the gas about the centre. The differential rotation of the ionised gas in the interstellar medium results in the stretching and amplification of the magnetic field in the disc so that any primordial magnetic field would be tightly wound up. This is not sufficient, however, to produce an ordered uniform field since the winding up of the field lines would result in tightly wound tubes of magnetic flux running in opposite directions. There needs to be some way of reconnecting the lines of force to create a large-scale uniform field. The problems with this picture have

³ I use the SI unit of the tesla for magnetic flux densities. 1 tesla = 10^4 gauss; correspondingly, 1 nT = 10^{-5} gauss.

been discussed by Parker, who suggested that a solution may lie in the buoyancy of the interstellar cosmic ray gas which can inflate loops of magnetic fields which burst out of the plane of the Galactic disc, reconnect and snap off (Parker, 1997). Even if this process is effective, there is still the question of the origin of the seed field, which must be present to get the process going.

A process by which a very weak seed field can be generated was discovered by Biermann and is known as the *Biermann battery* (Biermann, 1950). The principles of operation of the primitive battery are clearly described by Kulsrud (Kulsrud, 1997, 2005). Initially, there was no magnetic field in the plasma, but it is supposed that there are fluctuations in the pressure of the electrons. The electrons flow to lower pressure regions, resulting in a charge imbalance in the plasma, which produces an electric field \mathbf{E} opposing the flow of electrons:

$$-n_e e \mathbf{E} = \nabla p_e . \quad (18.27)$$

As a result, the flow stops and an electromotive force (emf) is created in the plasma. This emf cannot drive a current, however, since the integral round any closed loop in the case of a linear gradient in electron density is zero. If, however, there are also variations in the electron density throughout the plasma, different emfs can be induced in different regions and then currents can flow in the plasma, as illustrated schematically in Fig. 18.13 (Kulsrud, 1997). Magnetic fields can then develop and are eventually limited by the self-inductance of the current loop itself. As Kulsrud shows, this process saturates when the magnetic flux density is only about 10^{-25} T, at least 10^{15} times less than the strength of the Galactic magnetic field. Thus, the challenge is to find a means of creating a large scale magnetic field from these

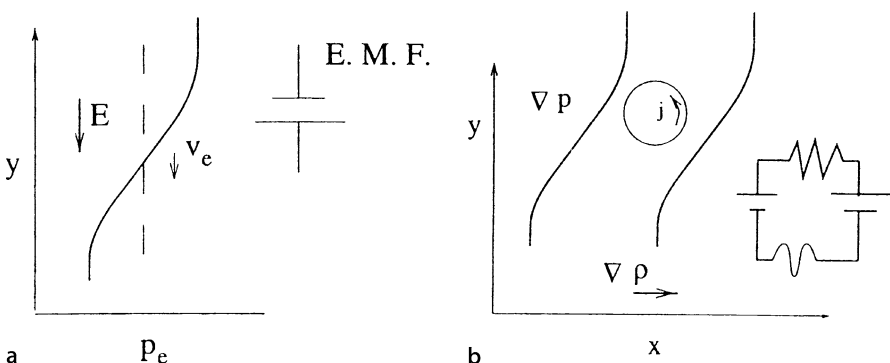


Fig. 18.13a,b. Illustrating the physics of the Biermann battery (Kulsrud, 1997). **a** In this case, there is a variation in electron pressure in the y direction which results in a drift of the electrons which is opposed by the electric field caused by the charge separation of the electrons from the protons. In this case, a static emf is created. **b** Expression (18.27) shows that, if the pressure gradient is fixed, the emf is proportional to n_e^{-1} . If the density of electrons is independent of y but varies in the x -direction, the emfs at different positions in the x -direction no longer balance and a current can flow, creating a small-scale seed magnetic field

tiny random seed fields, which are generated on the scale of the electron density fluctuations in the plasma. This is not a trivial problem.

In addition to the mechanism described by Parker, Kulsrud has discussed the amplification of the seed magnetic field in a turbulent medium, characterised by a Kolmogorov spectrum of turbulence. In a turbulent medium, energy is transferred from large-scale to small-scale eddies until the motions are dissipated by viscous forces on the smallest scales. This process has the advantage that, on small scales, the turnover time of the eddies is short and so effective amplification of the magnetic field can take place on small scales. The problem is to understand how such a strong chaotic small-scale field could result in a large-scale ordered field. Kulsrud argues that, once equipartition is established between the mean kinetic energy density of the turbulence and the magnetic field energy density, the dominant magnetic fields are those associated with the large-scale eddies, the smaller-scale structures being dissipated as energy is transferred to smaller and smaller scales.

There have been important advances in the observation of turbulent magnetic fields in the intergalactic medium in clusters of galaxies; many of these are summarised in the proceedings of the Bologna conference on the *Origin and Evolution of Cosmic Magnetic Fields*. On the observation side, de Bruyn described the development of rotation measure synthesis which enables information about the spectrum of magnetic turbulence in diffuse astronomical environments to be obtained (Brentjens and de Bruyn, 2006). Observations of the power spectrum of rotation measures in the intracluster medium and its comparison with the Kolmogorov spectrum of turbulence were reported by Govoni (Govoni, 2006).

Equally impressive has been the spectacular growth of studies of the predicted spectrum of turbulence by computer simulation, for example, the work of Ryu and his collaborators (O'Neill et al., 2006). While it is straightforward to derive the Kolmogorov spectrum of turbulence in a few lines of dimensional analysis, it is encouraging to find it coming directly out of large-scale cosmological simulations. There are, of course, variations in the exact spectrum, but the overall agreement with intuitive ideas about the turbulent growth of magnetic fields in clusters is compelling.

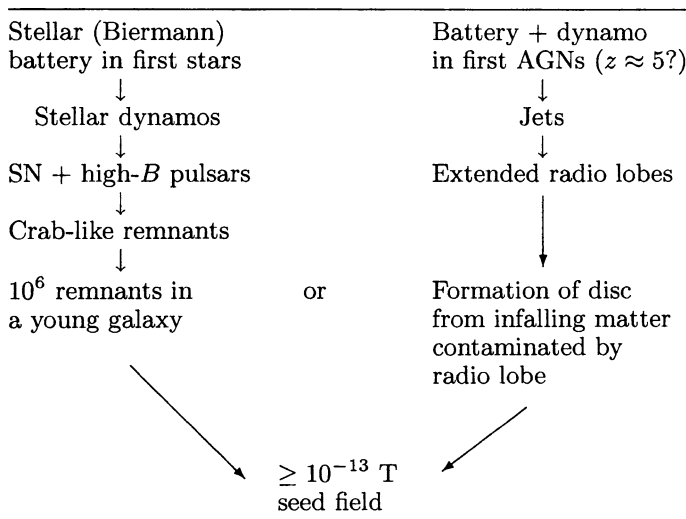
An alternative approach to the origin of magnetic fields has been suggested by Rees (Rees, 1994, 1995). The starting point is the observation that certain high energy astrophysical objects are undoubtedly capable of generating strong ordered magnetic fields over substantial scales. In the case of a supernova remnant such as the Crab Nebula, a convincing case can be made that the magnetic field in the Nebula, which has magnetic flux density about $10^{-7\text{--}8}$ T over scales of a few parsecs, originated in the rotating dipole field of the central pulsar, which was created in the collapse of the progenitor star of the neutron star. The origin of the intense magnetic field of the pulsar can be traced back to the collapse of the magnetic field present in the progenitor star which in turn can be attributed to some form of magnetic dynamo action within the star. The big advantage of this picture is that the timescales for the amplification of the magnetic field within the progenitor star can be very short and thus there is no problem in principle in generating strong magnetic fields.

The other convincing example of the formation of strong magnetic fields in high energy astrophysical objects concerns the extragalactic radio sources. The lobes

of these sources can extend to dimensions of 1 Mpc and greater and the fields within them are $B \sim 10^{-10}\text{--}10^{-9}$ T. The standard picture for the origin of these huge magnetic field energies involves the release of energy from the active galactic nucleus in the form of intense jets of high energy particles and magnetic field. Precisely how the fields are amplified is a matter of speculation, but there is no doubt that enormous energy fluxes are generated in active galactic nuclei and that these are sufficient to account for the total magnetic field energy requirements of the radio lobes. Again, it is assumed that, because the jets originate in the compact regions close to the active nucleus, there is no problem in principle in accounting for the amplification of the magnetic field because the timescales in these regions are very short. The presence of a supermassive rotating black hole in the nucleus can result in the generation of strong magnetic fields by electromagnetic induction if even a tiny magnetic field threads the black hole (Thorne et al., 1986).

Rees makes the point that these phenomena indicate how magnetic fields can be generated by high-energy astrophysical processes on the scales of supernova remnants, galaxies and clusters of galaxies. To fill the volume of a galaxy with magnetic flux due to supernova explosions, the process would have to be repeated many times in the early history of the galaxy and the net result could well be a seed field which could then be amplified by the processes discussed by Parker and Kulsrud. Notice that a key part of the process involves the smoothing out of the gross inhomogeneities in the field. In the same way, the magnetic field in clusters of galaxies might be the result of repeated radio source events. The magnetic fields created in the radio source events would diffuse through the intracluster plasma and repeated events would add to the total large scale magnetic flux within the cluster. Possible scenarios are indicated schematically in Table 18.1, which is taken from the reviews by Rees (Rees, 1994, 1995).

Table 18.1. The origin of magnetic fields (Rees, 1994, 1995)



There are good reasons why these issues should be taken rather seriously. One of the important means of discovering some of the most distant galaxies we know of is through the identification of extragalactic radio sources, the radio galaxy with the largest redshift being $z = 4.8$. The fact that the galaxy is a strong radio source means that there must already be a strong magnetic field within the galaxy. It seems plausible that magnetic fields were already present in galaxies and clusters at large redshifts. This will certainly have an influence upon many aspects of the formation of subsequent generations of stars and galaxies.

19 Making Real Galaxies

The final and, in many ways most difficult, part of the story is to put together the astrophysical concepts we have introduced so far in order to form galaxies as we know them at the present epoch. Many of the important processes were introduced in Chap. 16, but there we stopped short of considering, for example, the role of star formation and feedback mechanisms in accounting for the different Hubble types or equivalently, the red and blue sequences. The reason for this is simple – the formation of galaxies as we know them involves a large number of complex interlocking non-linear effects. Many key parts of the picture are poorly understood, for example, the appropriate rules for star formation and its dependence upon the physical conditions within the star-forming region, the role of supernova explosions in enhancing or inhibiting star formation, the role of the massive black holes which form in the centres of massive galaxies, and so on.

In many ways, progress is in the hands of the observers in defining empirically what must have occurred as a function of cosmic epoch. These endeavours are strongly supported by what is now possible computationally. The large-scale simulations can now include empirical rules about phenomena such as star formation and feedback mechanisms in order to find out the types of physics needed to form galaxies as we know them. This is the realm of *semi-analytic models* of galaxy formation and in many ways can be considered an experimental science in the sense that the numerical experiments provide guidance about the relevance of different physical processes in galaxy formation.

Central to all these considerations is the rôle of star formation in the evolution of galaxies, and that is where we begin.

19.1 Star and Element Formation in Galaxies

Some of the most important clues concerning the sequence of events which must have taken place as galaxies took up the forms they have today come from observations of the variation of the overall star-formation rate in galaxies with cosmic epoch. This story is closely related to studies of the rate at which the chemical elements were built up in the stars and in the interstellar media of galaxies – much of the chemical enrichment of the interstellar gas is associated with the formation of heavy elements in short-lived massive stars and their recirculation through the interstellar gas by supernova explosions. Star and element formation rates can be derived by a number

of independent methods and these help constrain scenarios for the evolution of galaxies.

- We can obtain limits to the total amount of element and star formation which could have taken place in galaxies from the intensity of the isotropic background radiation in the optical, infrared and submillimetre wavebands.
- The characteristic flat, blue spectra of regions of star formation can be observed over a wide range of redshifts, and these enable estimates to be made of the rates of star and element formation as a function of cosmic epoch. These estimates can be strongly influenced by the effects of dust in the star-forming regions and in the galaxy itself, but the absorbed energy is reradiated in the far-infrared and submillimetre wavebands, and so the overall production of heavy elements can be constrained by observations in these wavebands.
- The characteristic cut-off of the spectra of young stars beyond the Lyman limit at 91.2 nm has proved to be a very powerful method of detecting star-forming galaxies out to redshifts $z \approx 6$, thanks to the availability of the new generation of 8- to 10-m telescopes.
- Spectroscopic studies of absorption-line systems in the spectra of quasars provide estimates of the abundances of the elements in these gas clouds over a wide range of redshifts and, as we will show, provide direct evidence concerning the build-up of heavy elements in galaxies.

19.1.1 The Background Radiation and Element Formation

Heavy elements such as carbon and oxygen are formed in the central nuclear-burning regions of massive stars. In Fig. 19.1, the evolution of the internal chemical structure of a $5M_{\odot}$ star is shown, illustrating the synthesis of oxygen and carbon in its central regions (Kippenhahn and Weigert, 1990). The first step in the synthesis of these elements involves the burning of all the hydrogen into helium in the core of the star. The formation of carbon and oxygen only begins when the central regions have become sufficiently hot and dense for the triple- α reaction, $3^4\text{He} \rightarrow {}^{12}\text{C}$, to take place after about 6×10^7 years. By 8×10^7 years, the inner 20% by mass of the star has been converted into carbon and oxygen, which is recirculated through the interstellar gas following the demise of the star. During these brief terminal phases, the star evolves onto the red giant region of the Hertzsprung–Russell (H–R) diagram, as shown in the lower panel of Fig. 19.1.

Thus, the essential first step in the formation of the heavy elements during stellar evolution is the conversion of hydrogen into helium within the core of the star. Inspection of a table of the binding energies of the chemical elements shows that by far the most important source of energy generation during the processes of nucleosynthesis is the conversion of hydrogen into helium, in which 0.7% of the rest mass energy of the hydrogen atoms is liberated. Thus, to produce a given mass of heavy elements, the energy release during the main-sequence lifetime of a massive star is just the energy liberated in the hydrogen to helium conversion necessary to create that mass of heavy elements. In other words, to create a mass $M_Z = ZM$ of

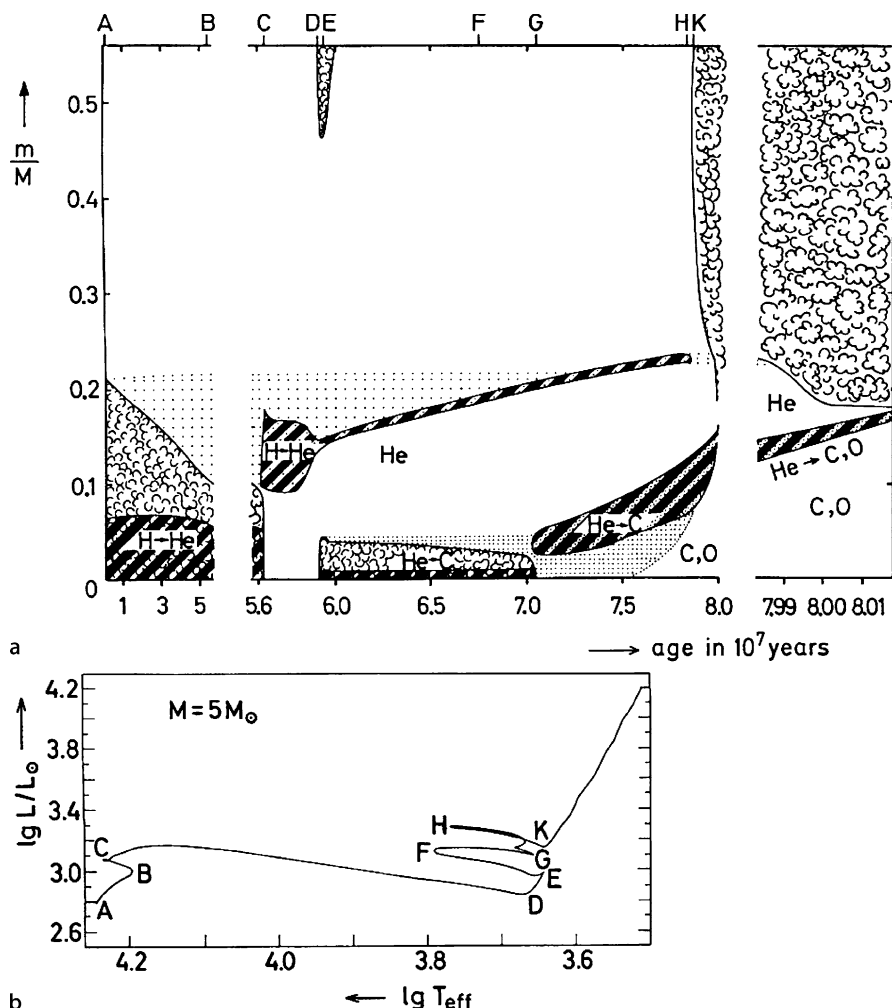


Fig. 19.1a,b. Evolution of the internal structure of a $5M_{\odot}$ star, illustrating the synthesis of carbon and oxygen in its central regions. The abscissa shows the age of the model star after the ignition of hydrogen in its core in units of 10^7 years. The ordinate shows the radial coordinate in terms of the mass m within a given radius relative to the total mass M of the star. The *cloudy regions* indicate convective zones. The corresponding positions of the star on an H-R diagram at each stage in its evolution are shown in the *lower panel* of the diagram (Kippenhahn and Weigert, 1990)

heavy elements, an energy $0.007ZMc^2$ must be liberated during the steady main-sequence hydrogen-burning phase of the star, where Z is the fraction of the total mass in the form of heavy elements, or metals, created by stellar nucleosynthesis. Therefore, taking averages over the lifetime of the star, if a mass of metals \dot{M}_Z is created per unit time, the average luminosity of the star during its main-sequence

phase is $0.007\dot{M}_Z c^2$, that is,

$$L = 0.007\dot{M}_Z c^2 . \quad (19.1)$$

Cowie has argued that this expression should be modified to take account of the fact that not all the heavy elements become available to be recycled through the interstellar gas and so incorporated into the next generation of stars (Cowie, 1988). Some of the mass is locked up in white dwarfs or neutron stars formed at the end of the star's lifetime and, if a black hole is formed, the infalling material is lost to us. If α_m is the fraction of the heavy elements which is recycled to the interstellar medium, which Cowie takes to be 0.67, a greater luminosity is required to create the observed interstellar abundance of the elements by a factor α_m^{-1} . Integrating over the lifetime of the galaxy, (19.1) can be written in terms of the total energy density of radiation ε which is built up in the process of creating a total mass density of heavy elements ϱ_m ,

$$\varepsilon = \frac{0.007\varrho_m c^2}{\alpha_m} , \quad (19.2)$$

where $\varrho_m = V^{-1} \int \dot{M}_Z dt$ and $\varepsilon = V^{-1} \int L dt$. If this energy was liberated at redshift z , (19.2) describes the energy density of radiation and the mean density of metals produced at that redshift. The energy density of radiation decreases with redshift as $(1+z)^{-4}$, whereas the average density of metals decreases as only $(1+z)^{-3}$. Writing the energy density of radiation in terms of the intensity, $I = \varepsilon c / 4\pi$, we find

$$I = \frac{0.007\varrho_m c^3}{4\pi\alpha_m(1+z)} . \quad (19.3)$$

This is the background radiation intensity which should be observed today if a mass density ϱ_m of heavy elements is observed at the present epoch.

Let us insert some plausible values into (19.3) to illustrate how the present abundance of the metals is constrained by the intensity of the background radiation. If the density parameter in baryons is Ω_B , $\varrho_m = Z\varrho_c\Omega_B$ and the intensity of the background radiation would be

$$I = 3.0 \times 10^{-4} \frac{Z\Omega_B h^2}{\alpha_m(1+z)} \text{ W m}^{-2} \text{ sr}^{-1} . \quad (19.4)$$

This estimate can be compared with various limits to the isotropic cosmic background radiation, which are shown in Figs. 9.1b and 9.2. These figures are plotted in units of $\nu I(\nu)$ and so represent the intensity of the radiation in the same units as (19.4). Taking as representative values $\Omega_B h^2 = 0.0223$, $Z = 0.01$ and $\alpha_m = 0.67$, we find $I = 10^{-7}/(1+z) \text{ W m}^{-2} \text{ sr}^{-1}$. If this radiation were due to the emission of stars, we would expect this to be the typical intensity emitted over roughly a decade in frequency. Clearly the result depends upon the redshift at which most of the metals were formed but it can be seen from Fig. 9.2 that this estimate lies close to the upper limits to the optical background radiation due to Toller, which is shown by

square boxes at roughly 440 nm (Toller, 1990). It is also not so different from the lower limit to the background light due to galaxies found by integrating the counts of faint galaxies, which is shown by the open boxes. Furthermore, the background is of the same order of magnitude as the upper limits to the optical-infrared background intensity inferred from analyses of the spectra of ultra-high-energy γ -ray sources in which the effects of $\gamma\gamma$ absorption attenuates the high energy spectrum (Aharonian et al., 2006). It is interesting that this rather crude estimate of the background radiation gives a result not too different from what might be expected from the observed abundances of heavy elements in the Universe today.

The background intensity in the optical waveband would be reduced if a significant fraction of the optical-UV emission of galaxies were absorbed by dust. Stars are formed in the coolest, dustiest regions of galaxies and much of the synthesis of the heavy elements may well have taken place when a much larger fraction of the baryonic mass of galaxies was in the form of interstellar gas than it is today. The very first generations of stars must have created a significant abundance of heavy elements, which would lead to the formation of interstellar dust. In turn, the presence of dust would facilitate the formation of subsequent generations of stars.

From our present perspective, the absorbed optical-UV radiation would be re-radiated in the submillimetre–far-infrared wavebands, in which case the same arguments which led to (19.4) can be used, but now applied to the background intensities in these wavebands which have been provided by the COBE experiment (Fig. 9.1b). At wavelengths longer than 0.5 mm, strong upper limits to the background intensity are provided by the lack of distortion of the spectrum of the cosmic background radiation (Fig. 2.1). At shorter wavelengths, the spectrum and intensity of the cosmic infrared background have been extracted from the COBE observations by Puget, Hauser and their colleagues. The results are shown schematically in Fig. 9.1b (Puget et al., 1996; Hauser et al., 1998; Hauser and Dwek, 2001). The background intensities in the cosmic infrared background are roughly the same as the upper limits and estimates in the optical waveband. These simple considerations make the important point that we need to include in our estimates of the cosmic star formation rate the optical, infrared and submillimetre intensities of star-forming galaxies.

19.1.2 The Global Star Formation Rate from Optical and Ultraviolet Observations of Star-Forming Galaxies

Lilly and Cowie first showed how the rate of formation of heavy elements could be inferred from the flat blue continuum spectra of star-forming galaxies and that these estimates are independent of the choice of cosmological model (Lilly and Cowie, 1987; Cowie, 1988). The analysis begins with the observation that a prolonged burst of star formation has a remarkably flat intensity spectrum at wavelengths longer than the Lyman limit at 91.2 nm. This is illustrated by the model starbursts presented by White from computations using the spectral synthesis codes of Bruzual for predicting the spectra of galaxies at different phases of their evolution (White, 1989). Figure 19.2 shows the spectrum of a starburst galaxy as observed at different ages, assuming

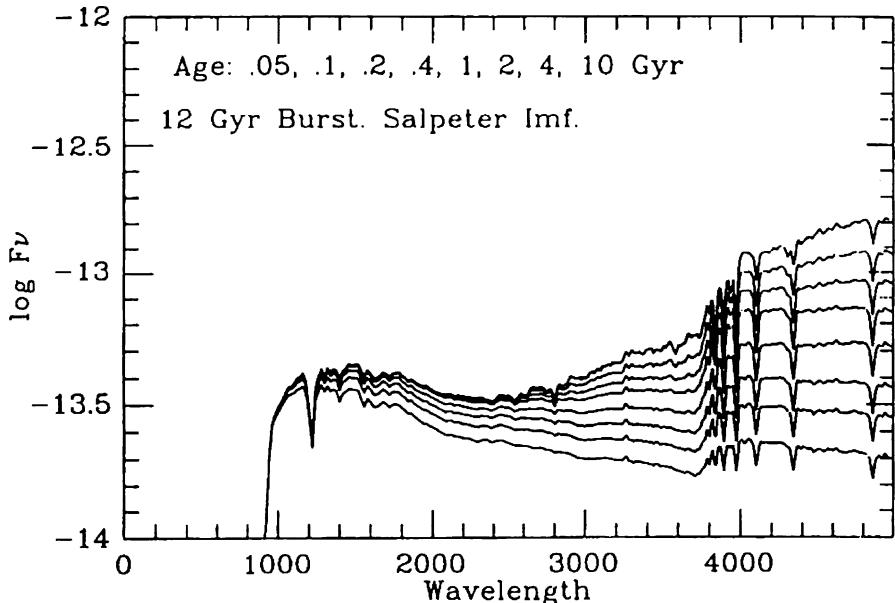


Fig. 19.2. Synthetic spectra for a starburst with constant star-formation rate as observed at the ages indicated. A Salpeter initial stellar mass function $N(M) dM \propto M^{-2.35} dM$ has been assumed with cut-offs at 75 and $0.08 M_{\odot}$. The spectra were generated by Bruzual using his evolutionary synthesis programmes (White, 1989)

that the star-formation rate is constant and that the stars are continuously formed with the same Salpeter initial mass function. The flatness of the spectrum is due to the fact that, although the most luminous blue stars have short lifetimes, these are constantly being replaced by new stars. To a good approximation, it can be assumed that the spectrum of the star-forming galaxy can be described by a power-law $I(\nu) \propto \nu^{-\alpha}$ with $\alpha = 0$ at wavelengths $\lambda > 91.2$ nm, and zero intensity at shorter wavelengths. Furthermore, the intensity of the flat part of the spectrum is directly proportional to the rate of formation of heavy elements in the starburst since, as discussed in Sect. 19.1.1, the conversion of hydrogen into helium is the essential first stage in the synthesis of the heavy elements in the central regions of massive stars.

The same assumptions made in Sect. 19.1.1 are adopted, namely that the total luminosity of the system is $0.007\dot{M}_Z c^2/\alpha_m$, where \dot{M}_Z is the rate at which heavy elements are synthesised and α_m is the fraction of the synthesised elements returned to the interstellar medium. We now use the result that this radiation has a flat intensity spectrum $\alpha = 0$ up to the Lyman limit ν_{Ly} , so that

$$\int L_\nu d\nu = L_\nu \nu_{Ly} = 0.007\dot{M}_Z c^2 / \alpha_m , \quad (19.5)$$

where L_ν is measured in W Hz^{-1} . This can be rewritten in the form

$$L_\nu = 2 \times 10^{22} \left(\frac{\dot{M}_Z/\alpha_m}{1 M_\odot \text{ year}^{-1}} \right) \text{ W Hz}^{-1} \quad (19.6)$$

for all wavelengths longer than the Lyman continuum limit at 91.2 nm. It is now a simple calculation to work out the background intensity of a cosmological distribution of such sources. The integral (17.33) can be used in the form

$$I(\nu_0) = \frac{1}{4\pi} \int_0^\infty \frac{L(\nu_0, z) N_0}{(1+z)^{1+\alpha}} dr , \quad (19.7)$$

where we have allowed the luminosity of the sources to be an arbitrary function of redshift and assumed that they all have the same spectral index α . Now $L(\nu_0, z) N_0$ is the *comoving* luminosity density per unit bandwidth due to the formation of heavy elements. From (19.5), this is just $0.007c^2 \dot{\varrho}_m / \alpha_m \nu_{Ly}$, where $\dot{\varrho}_m$ is the *comoving* rate of formation of heavy elements and the spectral index $\alpha = 0$. Therefore,

$$I(\nu_0) = \frac{0.007c^2}{4\pi\alpha_m \nu_{Ly}} \int_0^\infty \dot{\varrho}_m \frac{dr}{(1+z)} . \quad (19.8)$$

But $dr/(1+z) = c dt$, and so the background intensity is

$$I(\nu_0) = \frac{0.007c^3}{4\pi\alpha_m \nu_{Ly}} \int_0^\infty \dot{\varrho}_m dt = \frac{0.007c^3}{4\pi\alpha_m \nu_{Ly}} \int_0^\infty \frac{d\varrho_m}{dz} dz = \frac{0.007\varrho_m c^3}{4\pi\alpha_m \nu_{Ly}} , \quad (19.9)$$

provided the Lyman limit is not redshifted beyond the observing waveband. This is the remarkable result found by Cowie and Lilly – the background intensity due to star-forming galaxies as a function of redshift is directly related to the rate at which elements are formed and is *independent* of the cosmological model. Cowie recommended a correction factor of $\alpha_m = 0.67$ to take account of the fraction of metals which is not returned to the interstellar medium but is locked up in stellar remnants (Cowie, 1988). Inserting the values of the constants,

$$\Delta I_\nu(z) = 7 \times 10^{-25} \left[\frac{\Delta \varrho_m(z)}{10^{-31} \text{ kg m}^{-3}} \right] \text{ W m}^{-2} \text{ Hz}^{-1} \text{ sr}^{-1} . \quad (19.10)$$

Notice the pleasant result that $\Delta I_\nu(z)$ is the observed background intensity of flat spectrum star-forming galaxies in some redshift interval Δz and $\Delta \varrho_m(z)$ is the density of heavy elements observed at the present epoch which were created by these galaxies in that redshift interval. The reference density used in (19.10), $10^{-31} \text{ kg m}^{-3}$ of heavy elements, corresponds roughly to $Z = 0.01$ in a Universe in which the density parameter in baryons is $\Omega_B = 0.01$.

Cowie, Lilly and their colleagues undertook deep multicolour surveys to discover flat spectrum star-forming galaxies at large redshifts. Their survey was successful in finding such galaxies, which have roughly equal intensities in the U, B and V wavebands – the background due to such objects amounted to about

$10^{-24} \text{ W m}^{-2} \text{ Hz}^{-1} \text{ sr}^{-1}$. They interpreted this result as meaning that a significant fraction of the heavy elements, about $1.5 \times 10^{-31} \text{ kg m}^{-3}$, must have been synthesised at redshifts of about one (Cowie et al., 1988). This type of analysis has also been used to set limits to star-formation rates in the Canada-France Redshift Survey by Lilly and his colleagues and in the Hubble Deep Field by Madau and his colleagues (Lilly et al., 1995; Madau et al., 1996)

19.1.3 The Lyman-Break Galaxies

In a remarkable pioneering set of observations, Steidel and his colleagues extended the multicolour technique for finding star-forming galaxies to redshifts $z > 3$. The idea was similar to that developed by Cowie and Lilly, but now the objective was to search for star-forming galaxies in which the Lyman limit, clearly seen in the models of young galaxies shown in Fig. 19.2, is redshifted into the optical waveband. The technique is illustrated in Fig. 19.3a, in which the spectrum of a star-forming galaxy at redshift $z = 3.15$ is observed through carefully chosen filters in the ultraviolet, blue and red spectral regions. The signature of such a galaxy is that its image should be bright in the two longer wavebands but should not be present in the UV waveband. Steidel's original intention was to use this technique to identify the galaxies responsible for the Lyman-limit absorption systems in the spectra of distant quasars, and this programme turned out to be remarkably successful (Steidel and Hamilton, 1992). It was soon found that the technique was also a remarkably effective means of discovering star-forming galaxies in the general field at $z > 3$. Observations of the Hubble Deep and Ultra Deep Fields have proved to be ideal for exploiting this approach because, in addition to very precise photometry in four wavebands spanning the wavelength range $300 < \lambda < 900 \text{ nm}$, high-resolution optical images have enabled the morphologies of these galaxies to be studied. HST images in four wavebands of one of the Lyman-break galaxies in the Hubble Deep Field are shown in Fig. 19.3b.

The success of Steidel's programme is illustrated in Fig. 19.4, which shows the redshift distribution of 68 Lyman-break galaxies found in an area of only $9 \times 18 \text{ arcmin}^2$ for which spectroscopic redshifts were obtained with the Keck 10-m telescope. By 2000, he and his colleagues had accumulated large numbers of star-forming galaxies at redshifts $z \sim 3$ and showed that their luminosity function could be well-fitted by a Schechter luminosity function (Adelberger and Steidel, 2000).

19.1.4 The Hubble Deep and Ultra Deep Fields

Successive directors of the Hubble Space Telescope Science Institute, Drs. Robert Williams and Steven Beckwith, took the decision to devote large amounts of the director's discretionary time on the Telescope to very deep imaging of single fields with a view to studying galaxy populations in the very distant Universe. The regions to be observed were selected in consultation with the astronomical community and the data were made publically available very soon after they had been secured and

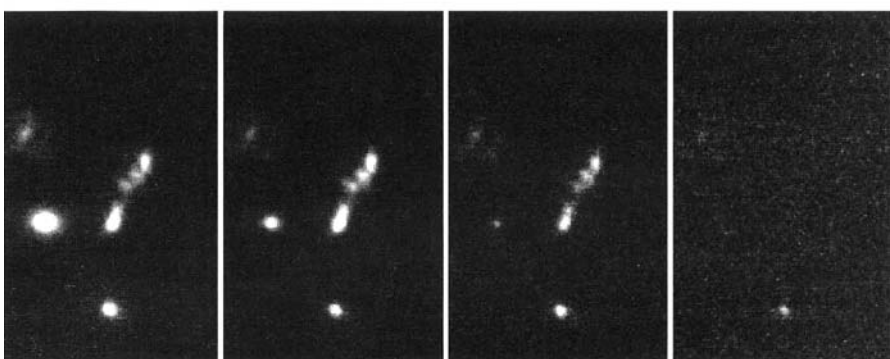
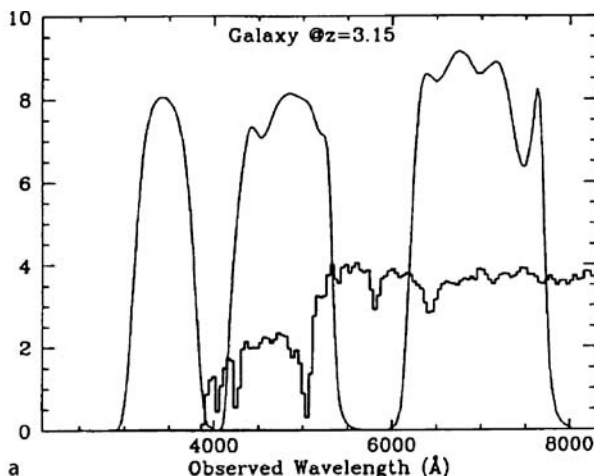
**b**

Fig. 19.3. **a** Illustrating how the use of multicolour photometry can be used to isolate star-forming galaxies at redshifts $z > 3$, at which the Lyman limit is redshifted into the optical region of the spectrum (Steidel, 1998). **b** Images of one of the distant star-forming galaxies appearing in the Hubble Deep Field. *Left to right:* the images were taken at red (I), green (V), blue (B) and ultraviolet (U) wavelengths. Because the Lyman limit has been redshifted beyond the U waveband, no image of the galaxy appears in the U image (reprinted from "Galaxies in the Young Universe", by F. Duccio Macchetto and Mark Dickinson, © 1997 by Scientific American, Inc. All rights reserved.)

calibrated (Ferguson et al., 2000; Beckwith et al., 2006). The Hubble Deep Field (HDF) was observed in four wavebands with the Wide Field Planetary Camera 2 in a 0.5-million-s exposure. The field of view was only 2.3 arcmin in angular size, but within that area there were about 3000 galaxies with apparent magnitudes $V \leq 29$ (Williams et al., 1996). The startling result of these observations was immediately apparent – there were vastly more blue galaxies than would be predicted by uniform world models and many of them had irregular and complex structures. The excess of faint blue galaxies was already known (Sect. 17.7), but the HDF observations with their very high sensitivity and high angular resolution in four wavebands enabled

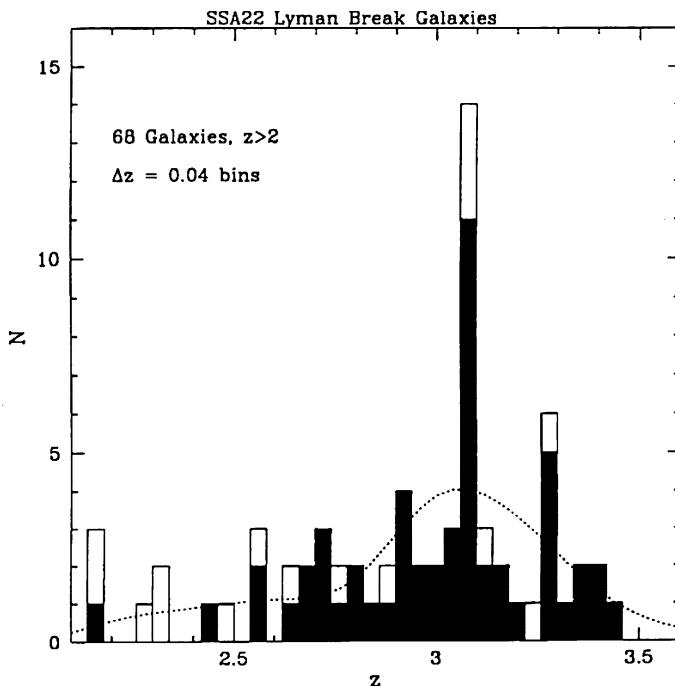


Fig. 19.4. The redshift distribution of Lyman-break galaxies in a single $9' \times 18'$ area of sky, all of which have spectroscopically confirmed redshifts. The differently shaded histograms reflect slightly different selection criteria. The dotted curve shows the expected redshift distribution defined by the colour selection criteria for the complete sample of objects. The ‘spike’ at $z = 3.09$ is significant at the 99.9% confidence level (Steidel, 1998)

the nature of the excess to be characterised in some detail and extended to fainter magnitudes.

The HDF was followed up by observations of a corresponding field in the Southern Hemisphere, the Hubble Deep Field South (HDFS) (Williams et al., 2000). The Advanced Camera for Surveys (ACS), which replaced the Faint Object Camera as part of the 2002 servicing mission, had a wider field of view and improved sensitivity compared with the WFPC2, and so the opportunity was taken to repeat the deep field imaging to fainter magnitudes, again in four wavebands. The image of the Hubble Ultra Deep Field (HUDF), shown in Fig. 17.24a, is the result of a 1-million-s exposure in four filters. These observations were complemented by those carried out as part of the Great Observatories Origins Deep Surveys (GOODS), which surveyed a wider field to a somewhat brighter limiting apparent magnitude (Fig. 17.24b). Giavalisco and his colleagues have summarised the objectives and the results of the GOODS project (Giavalisco et al., 2004b).

The community grasped the opportunities offered by these projects to carry out many important studies of the properties of galaxies at very large redshifts, many of these being summarised in the papers by Beckwith, Bouwens and their

colleagues (Beckwith et al., 2006; Bouwens et al., 2006). Of particular interest for the present study is the analysis of the properties of the ‘drop-out’ galaxies at progressively larger redshifts. The filters employed in the HUDF observations were carefully selected to enable Lyman drop-out galaxies to be observed at redshifts $z \sim 7$ (Fig. 19.5a). Beckwith and his colleagues reported that, of the 10,040 objects appearing in the catalogue in the i_{775} waveband, there were 504 B_{435} -drop-outs, 204- V_{204} drop-outs and 54 i_{775} -drop-outs, corresponding to galaxies with redshifts in the ranges $3.5 \leq z \leq 4.7$, $4.6 \leq z \leq 5.7$ and $5.7 \leq z \leq 7.4$ respectively.

A striking feature of the drop-out galaxies is immediately apparent from Fig. 19.5b, which shows images of the 24 brightest B_{435} -drop-out galaxies, as well as simulated images of what four typical nearby galaxies of different morphological types would look like at the mean redshift of B_{435} -drop-out galaxies, $z = 4.1$ (Lotz et al., 2006). The first three simulated galaxies are for early to late type galaxies and the fourth image is for a merger between two galaxies. It is apparent that most of the images resemble most closely the last simulation, but on a much more compact scale.

It is simplest to summarise the results of this comparison in the words of Beckwith and his colleagues:

Visual inspection of the drop-out sources . . . shows a large number of irregular structures, along with many compact objects. High-redshift galaxies appear much smaller and less regular than we see in the local universe, confirming similar findings from other deep surveys with the resolution of HST, notably the HDF. The majority of drop-out sources are compact, of order 1 kpc in extent. They often show multiple components and irregular structures. Few of the drop-out sources show the regular structures of local spiral or elliptical galaxies (Beckwith et al., 2006).

The change in physical size with redshift has been characterised by Bouwens and his colleagues who find that the half-light radius changes with redshift as $r_{\text{hl}} \propto (1 + z)^{-1.05}$ (Bouwens et al., 2004). At a redshift $z \sim 6$, the half-light radius is 1 kpc, corresponding to an angular size of 170 milliarcsec. The importance of the diffraction limited capability of the combination of the HST and the ACS is apparent.

The samples of drop-out galaxies have enabled estimates of the luminosity functions of these galaxies in the different redshift intervals to be determined. The three samples available from the HUDF can be described by Schechter luminosity functions but with different normalisations (Fig. 19.6) (Beckwith et al., 2006). According to these data, there is little change in the absolute magnitude M_* with increasing redshift, but the number density decreases very significantly between redshifts $z = 4$ and $z = 7$. These conclusions are somewhat different from those of Bouwens and his colleagues who found evidence that the value of M_* changed with redshift, in the sense that the typical luminosity increased as the Universe grew older (Bouwens et al., 2006). In her survey of the cosmic star-formation history as determined by these observations, Bergeron concluded that the statistics at the largest redshifts were too small to provide a definite resolution of this issue (Bergeron, 2006). Beckwith and

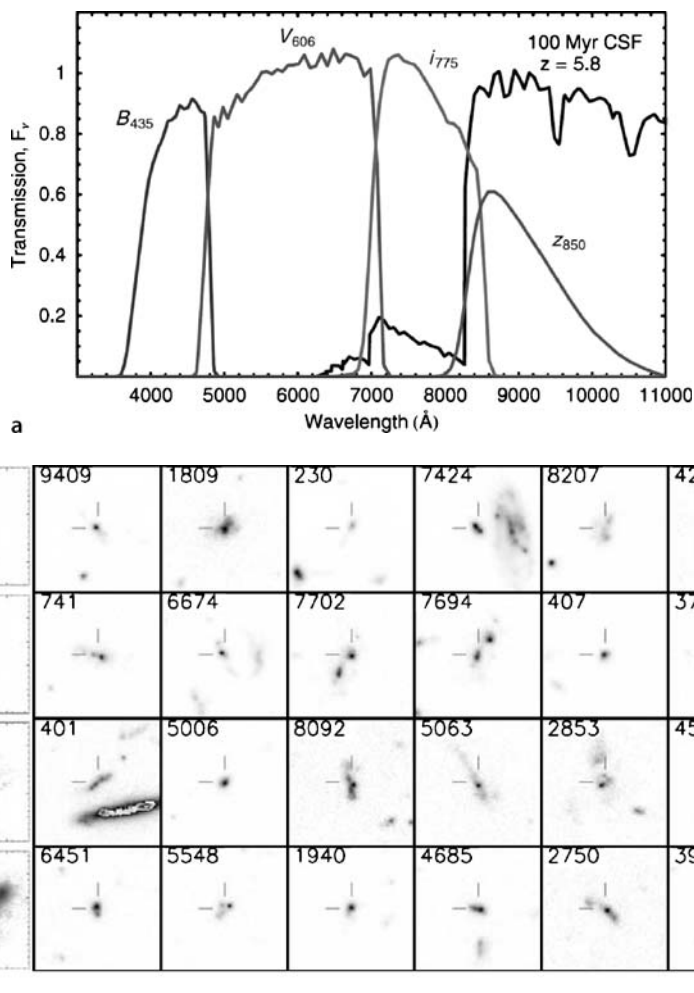


Fig. 19.5. **a** Filter transmission curves for the four bands used in HUDF survey. Also shown is the spectrum of a model star-forming galaxy at $z = 5.8$ from the models of Bruzual and Charlot assuming 0.4 solar metallicity and continuous star formation for 100 Myr (Beckwith et al., 2006). Intergalactic absorption due to intervening Lyman- α clouds has been incorporated into the predicted spectrum (Madau, 1995). **b** Comparison of simulated images of nearby galaxies (*four panels on left*) due to Lotz and her colleagues with images of the 24 brightest B435 drop-out sources on the *right* (Lotz et al., 2006). All the boxes have sizes corresponding to 21 kpc at $z = 4.1$. The drop-out sources are indicated by the *small lines* in the *centre* of each frame (Beckwith et al., 2006)

his colleagues emphasised how sensitive the derivation of the luminosity functions are to the details of the selection procedures and the reader should consult the papers cited here for many more details of the somewhat tricky issues involved. Despite this uncertainty, there is agreement that the luminosity density decreases by about

an order of magnitude between redshifts $z \sim 3$ and $z \sim 6$, as can be appreciated from the values of ϕ_* given in Fig. 19.6.

Returning to the topic which started this discussion, how does the UV luminosity density, and consequently the global star-formation rate, change with redshift? The results of the Subaru Deep Surveys, carried out making full use of the outstanding wide-field capability of the Japanese 8-m Subaru telescope have shown that, if attention is restricted to the luminous far-UV galaxies with $M_{\text{FUV}} \leq -21.3$, there is a factor of ten decrease in the far-UV luminosity density between redshifts $z \sim 3$ and $z \sim 6$ (Shimasaku et al., 2005). The less luminous sources, with $M_{\text{FUV}} \leq -19$, show very much less dramatic evolution, and in fact at the largest redshifts the less

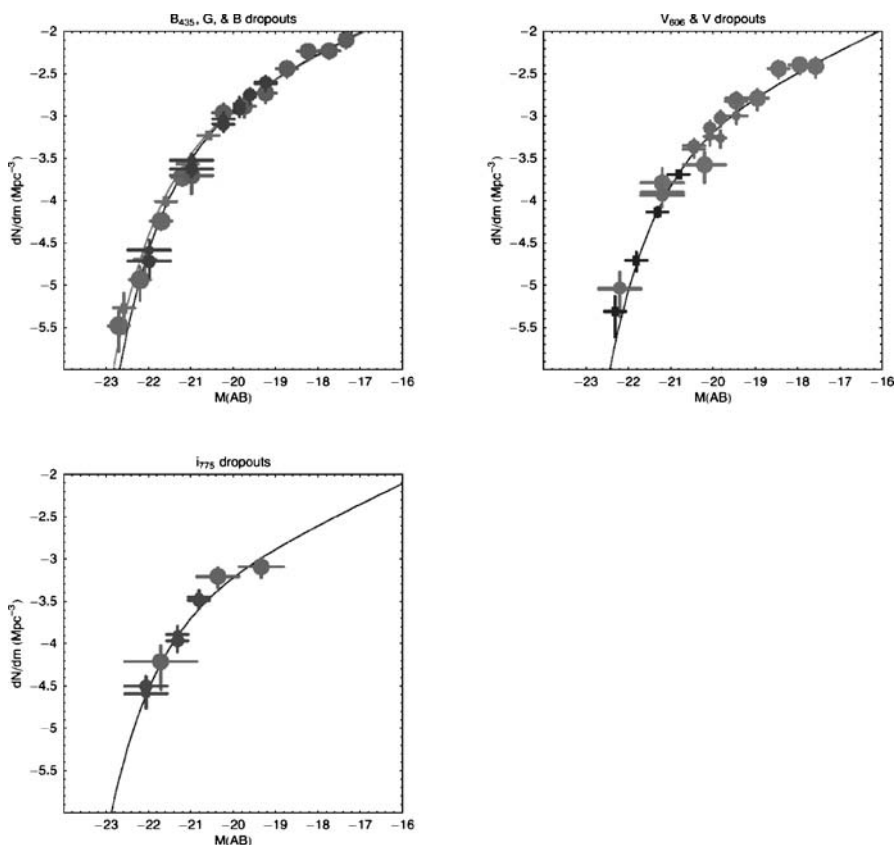


Fig. 19.6a–c. Luminosity functions for drop-out galaxies from the HUDF, GOODS, SAGDP99 (Steidel et al., 1999) and O04 (Ouchi et al., 2004) surveys. **a** B435 drop-outs ($3.5 \leq z \leq 4.7$). The lines are the best-fit Schechter functions. For the combined sample $M_* = 20.7$ and $\phi_* = 0.0013 \text{ Mpc}^{-3}$. **b** V606 drop-outs ($4.6 \leq z \leq 5.7$) from the HST samples together with V606 drop-outs from O04 (squares). The best-fit parameters are $M_* = 20.55$ and $\phi_* = 0.0009 \text{ Mpc}^{-3}$; **c** HST i775 drop-outs ($5.7 \leq z \leq 7.4$). The best-fit parameters are $M_* = 21.1$ and $\phi_* = 0.0005 \text{ Mpc}^{-3}$ (Beckwith et al., 2006)

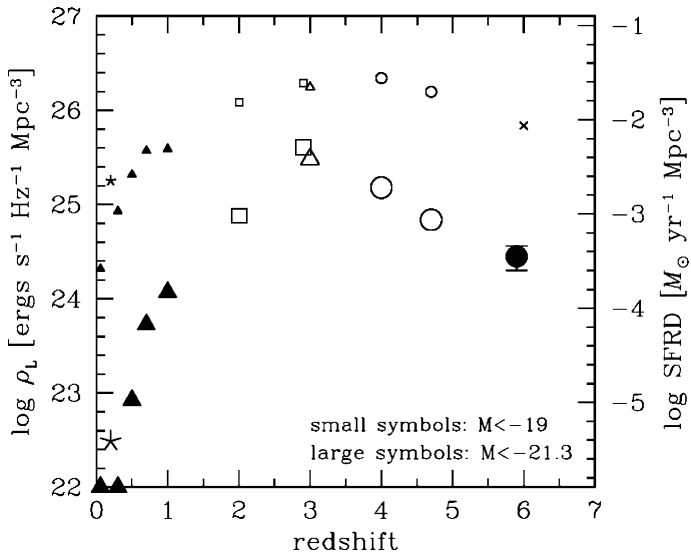


Fig. 19.7. Evolution of the far-UV luminosity density and the corresponding star-formation rates. The *large* and *small symbols* indicate the luminosity density of galaxies brighter than far-UV absolute magnitudes $M = -21.3$ and $M = -19.0$ respectively (Shimasaku et al., 2005)

luminous sources produce about 30 times more UV luminosity than the luminous galaxies (Fig. 19.7).

Similar results for the UV luminosity density were found from analyses of the data from the Hubble Ultra Deep Field, which suggest that it only decreased slightly from the values found at redshift $z \sim 2$ (Giavalisco et al., 2004a; Beckwith et al., 2006). Beckwith and his colleagues agree with the conclusion that the flatness of the intensity distribution with increasing redshift is largely associated with the intrinsically fainter galaxies in the samples. The consequence is that star formation was certainly well under way by the largest redshifts accessible by the HUDF survey, which just extend into the redshift range at which the reionisation of the intergalactic gas was more or less complete.

All researchers in these important areas emphasise the great care needed in converting the observational data into luminosity densities as a function of cosmic epoch. It is probably safest to keep an open mind about the exact value of the far-UV luminosity density at the largest redshifts $z \geq 4$. There is general agreement, however, that there is an order of magnitude decrease in the UV ionising radiation between redshifts $z \sim 1$ and the present epoch, one of the key results of the pioneering paper in this area by Madau and his colleagues (Madau et al., 1996).

19.1.5 Submillimetre Determinations of the Cosmic Star-Formation Rate

A concern about optical determinations of the cosmic star-formation rate is the extent to which the statistics are influenced by the effects of dust extinction. Galaxies

undergoing bursts of star formation are not only sources of intense UV continuum radiation but are also strong emitters in the far-infrared waveband because of the presence of dust in the star-forming regions. In a study of star-forming galaxies in the Markarian catalogues of UV-excess galaxies, Mazzarella and Balzano found that star-forming galaxies are on average stronger emitters in the far-infrared than in the UV waveband (Mazzarella and Balzano, 1986). Similarly, in a sample of star-forming galaxies studied by the International Ultraviolet Explorer, Weedman found that most of the galaxies emit much more of their luminosity in the far-infrared rather than in the UV region of the spectrum (Weedman, 1994). Thus, some star-forming galaxies may well be obscured by dust and so not be present in optical-UV multicolour surveys. Secondly, a significant fraction of the radiation associated with the formation of the heavy elements was not radiated in the UV-optical region of the spectrum, but at far-infrared wavelengths.

As discussed in Sect. 19.1.1, this issue can be addressed by making observations in the submillimetre waveband in which star-forming regions are intense emitters and the total millimetre/sub-millimetre luminosity of a galaxy also provides a measure of the star formation rate. The spectrum of dust is strongly ‘inverted’ in these spectral regions and so the K-corrections are large and negative. As a result, a typical star-forming galaxy is expected to have essentially the same flux density in the submillimetre waveband, whatever its redshift in the range $1 < z < 10$ (Fig. 17.4b) (Blain and Longair, 1993).

Such surveys could not be carried out until array detectors for the submillimetre waveband became available, specifically the SCUBA camera on the James Clerk Maxwell Telescope (JCMT). As discussed in Sect. 17.6, a large population of submillimetre sources was discovered by Smail and his colleagues (Smail et al., 1997), and this led to a number of intensive campaigns which resulted in the submillimetre number counts shown in Fig. 17.22. Reasonable extrapolations of the number counts can account for the total background radiation, but it is a much greater challenge to determine the redshift distribution of the sources. The problem is that the angular resolution of about 10 arcsec of the JCMT did not allow the identification of the submillimetre sources to be made with very faint galaxies. By observing spectroscopically all the candidates within the SCUBA error boxes, Barger and her colleagues achieved a success rate of about 25% for the bright SCUBA sources (Barger et al., 1999). Most of the fainter sources remained, however, unidentified.

Because of the strong far-infrared–radio correlation of star-forming galaxies, high-resolution radio observations with the Very Large Array could be used to provide improved positional accuracy for many of the SCUBA sources. For the sources with flux densities $S \geq 5$ mJy, the identification success rate increased to 60%. Spectroscopic observations of a sample of 70 identifications showed that the galaxies had redshifts in the expected range, $0.5 \leq z \leq 4$ with a mean redshift $z = 2.2$ (Chapman et al., 2005). These were very considerable achievements, but the sources with known redshifts at flux densities greater than 2 mJy accounted for only about 10% of the submillimetre background intensity.

To tackle this problem, Wang, Cowie and Barger used a stacking technique to correlate the near-infrared and X-ray flux densities of galaxies in the GOODS survey areas with their submillimetre flux densities (Wang et al., 2006). By this means they showed that active galactic nuclei could at most contribute 15% of the total background, whereas the sources present in the field at 1.6 and 3.6 μm could account for at least 60% of the 850- μm background intensity. Specifically, the submillimetre background intensity at 850 μm is about 31 to 42 Jy degree $^{-2}$, while the stacking of the infrared galaxies at 1.8 and 3.5 μm gave 24 Jy degree $^{-2}$. The remarkable result of their analysis was that most of the submillimetre background radiation was associated with Sb and Sc galaxies rather than with the Sd and irregular galaxies, many of the latter being the types of star-forming galaxy found in the deep optical-infrared surveys. The data can be converted into a plot of star-formation rate against redshift and it has a similar form to that derived from the optical-near-infrared studies, namely with increasing redshift the star-formation rate increases rapidly from zero to $z \approx 1$ and then remains roughly constant at redshifts up to four (Fig. 19.8).

The submillimetre star formation rates are similar to the estimates from the optical-UV continuum observations once appropriate extinction corrections are made, but the surprising result was that the blue star-forming galaxies did not contribute to the star-formation rates measured in the submillimetre waveband. This suggests that the extinction corrections must be greater for the galaxies which produce the bulk of the submillimetre background and lower in the blue star-forming galaxies (Wang et al., 2006). Notice also that the predicted total mass of stars formed by the present epoch is in good agreement with estimates of the total baryonic mass in stars today. Much more insight into these important issues will be obtained with observations to be carried out with the Atacama Large Millimetre Array (ALMA), which should be completed about 2012.

19.2 The Abundances of Elements in Lyman- α Absorption Systems

The cosmic star-formation rate is closely related to the rate at which the cosmic abundances of the elements are built up in the interstellar media of galaxies. Heavy elements are undoubtedly present in the most distant quasars observed but it is a complex issue to relate these to their cosmic abundances. More important are the element abundances observed in the Lyman- α absorption systems discussed in Sect. 18.3.

Fall has emphasised that one of the great attractions of using absorption lines in Lyman- α absorbers to estimate the relative abundances of any species along the line of sight to distant quasars is that, provided the absorbers are randomly oriented, average relative abundances can be found for different species, independent of the structures or clumpiness of the clouds (Fall, 1997). We can readily adapt (18.10) for the case in which the optical depth for absorption has been transformed into a column density \mathcal{N}_x for absorption by some species x along an arbitrary line of sight through a cloud. The subscript x might refer to hydrogen atoms ($x = \text{HI}$), metal

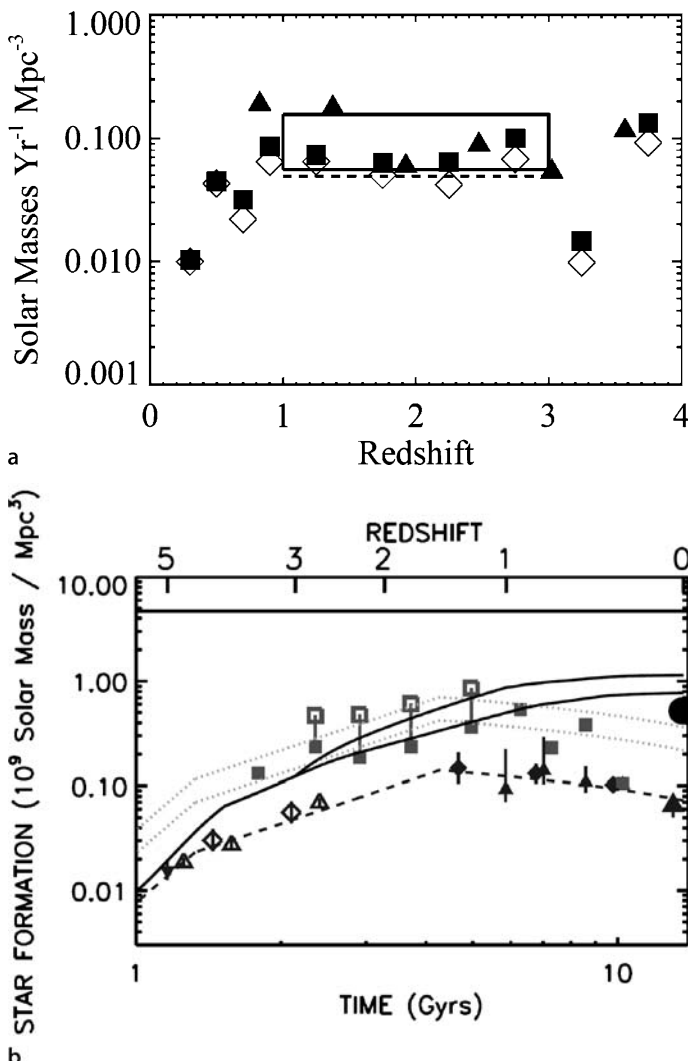


Fig. 19.8. **a** The star-formation rate density as a function of redshift derived from various submillimetre samples discussed in the text. The *dashed horizontal line* shows the rate assuming all the sources with $850\text{ }\mu\text{m}$ flux densities greater than 4 mJy lie at $1 \leq z \leq 3$. The *rectangular region* shows the density from the remaining submillimetre background that is not accounted for by the near-infrared observations, assuming that the sources lie in the redshift interval $1 \leq z \leq 3$ (Wang et al., 2006). **b** Comparison of optical-UV (triangles and diamonds) and submillimetre (filled squares) estimates of the amount of star formation as a function of epoch. The *ordinate* is the star-formation rate multiplied by the cosmic time scale at that epoch. The *open squares* joined to the *filled squares* show the maximum corrections for incompleteness of the submillimetre data. The *dotted lines* show the optical-UV data multiplied by factors of 3 and 5 to take account of the effects of dust extinction. The *solid lines* show the cumulative mass of stars formed by different epochs. The *filled circle* at $z = 0$ is an estimate of the present mass density in stars (Wang et al., 2006)

ions ($x = m$), or dust grains ($x = d$). Then, for a line of sight of proper length dr_{prop} through the cloud,

$$N(x)\sigma_x dr_{\text{prop}} = \sigma_x \mathcal{N}_x , \quad (19.11)$$

where $N(x)$ is the number density of species x in the cloud and σ_x is the absorption, or scattering, cross-section for species x , which is known from atomic physics. $\mathcal{N}_x = N(x) dr_{\text{prop}}$ is the column density of species x through the cloud. Thus, knowing the atomic cross-sections, the observations provide direct estimates of the column densities of each species in the clouds intercepted along a particular line of sight.

As illustrated in Fig. 18.4, there will generally be a distribution of column densities $N(\mathcal{N}_x) d\mathcal{N}_x$ for any species. This is expected to change with cosmic epoch as gas is condensed into stars and the interstellar gas in galaxies is enriched as a result of stellar nucleosynthesis and the recycling of processed material to the gas. We can estimate how the relative abundances of different species change with redshift by the following procedure. We relate the total column density of species x in the redshift interval z to $z + dz$ to the density parameter $\Omega_x(z)$ to which it would correspond at the present epoch. Notice that this will *not* be the density parameter of the species at that epoch – we adopt this procedure simply as a way of comparing abundances at different cosmic epochs in a self-consistent manner.

First of all, for species x , we define the function $N(\mathcal{N}_x, z) d\mathcal{N}_x dz$ to be the number of absorbers with column densities in the range \mathcal{N}_x to $\mathcal{N}_x + d\mathcal{N}_x$ and in the redshift interval z to $z + dz$. Then, the total column density of species x in the redshift interval dz is

$$\mathcal{N}_{\text{tot}}(x, z) dz = dz \int_0^\infty \mathcal{N}_x N(\mathcal{N}_x, z) d\mathcal{N}_x . \quad (19.12)$$

This column density can be related to the average *comoving* number density of species x at redshift z and the interval of proper length dr_{prop} by introducing the density parameter $\Omega_x(z)$ as follows:

$$\Omega_x(z) = \frac{8\pi G m_x N_x(z)}{3H_0^2(1+z)^3} \quad \text{where} \quad \mathcal{N}_{\text{tot}}(x, z) dz = N_x(z) dr_{\text{prop}} . \quad (19.13)$$

$N_x(z)$ is the average number density of species x at redshift z and m_x is the atomic, ionic or molecular mass of species x . Therefore, using (18.11) for the case $\Omega_\Lambda = 0$, which is a good approximation for large redshifts, we find

$$\Omega_x(z) = \frac{8\pi G m_x}{3H_0 c} \frac{(\Omega_0 z + 1)^{1/2}}{(1+z)} \mathcal{N}_{\text{tot}}(x, z) . \quad (19.14)$$

The beauty of this result is that, if we average over many lines of sight, the linearity of (19.12) and (19.13) means that we average over all systems in all orientations which contribute to $\Omega_x(z)$ at that redshift. Furthermore, we can determine how the global metallicity $Z = \Omega_m/\Omega_g$ and other relative abundances change with redshift by taking appropriate ratios.

The damped Lyman- α systems are of particular importance in understanding the evolution of neutral gas and the build-up of the heavy elements with cosmic epoch. As

discussed in Sect. 18.3.1, these are identified with the discs of the progenitors of spiral galaxies. The studies of Lanzetta, Storrie-Lombardi, Pettini and their colleagues are excellent examples of what could be achieved using the technologies of the 1990s (Lanzetta et al., 1995; Storrie-Lombardi et al., 1996; Pettini et al., 1997). The picture which emerged was that, at redshifts $z \sim 3$, the comoving density parameter in neutral hydrogen was $\Omega_{\text{HI}} \approx (1-2) \times 10^{-3} h^{-1}$, and this decreased with decreasing redshift until, at $z = 0$, its value was only about 2×10^{-4} , a value consistent with independent measures of the amount of neutral hydrogen present in galaxies and their environs at the present epoch (Fig. 19.9a). As Lanzetta and his colleagues remarked, although the comoving number density of damped Lyman- α systems does not change markedly with redshift, the column densities themselves are a strong function of redshift. Thus, all the systems at $z \sim 3.5$ have column densities greater than $N_{\text{HI}} = 10^{25} \text{ m}^{-2}$, whereas only 20% of them exceed this value at $z \approx 1$.

In Fig. 19.9a, the crosses with error bars show the estimates of Ω_{HI} in damped Lyman- α systems at different redshifts. These estimates have been corrected to take account of the effects of dust extinction (circles) and also for the presence of neutral hydrogen in systems with lower column densities (boxes). It is striking that the density parameter in neutral gas at a redshift of $z = 2.5$ is of the same order of magnitude as the density parameter corresponding to the mass of stars in galaxies at the present time, which is indicated by the hatched area in Fig. 19.9a.

The big advantage of studying the damped Lyman- α systems is that they have such large column densities that relatively rare species can be used to probe the chemical abundances of the elements. Pettini and his colleagues, for example, made observations of singly ionised zinc, Zn^+ or ZnII , which has a number of advantages as a tracer of the overall abundance of the heavy elements (Pettini et al., 1997, 1999). Zinc shows little affinity for dust and is predominantly in the form of Zn^+ in HI regions. As a result, observations of ZnII are likely to provide robust estimates of the total heavy element abundance as well as a means of determining the depletion of other elements such as iron into dust grains. Although zinc is a relatively rare species, the solar system value corresponding to $[\text{Zn}/\text{H}] = 3.8 \times 10^{-8}$, this has the advantage that the absorption lines are sufficiently weak for accurate column densities to be determined. Furthermore, zinc is probably synthesised by nuclear processes similar to those involved in the formation of iron and so provides a good tracer of the chemical history of the enrichment of the interstellar gas.

In Fig. 19.9b, the abundance of zinc relative to hydrogen is shown for a number of large-redshift-damped Lyman- α clouds with redshifts in the range $0.3 \leq z \leq 3.5$. Recalling that we need to take averages to obtain a mean element abundance as a function of redshift, it can be seen that the heavy element abundances were typically only about 10% of the present solar values throughout the redshift interval $0.3 \leq z \leq 3.5$. Intuitively, it might have been expected that there would be a steady increase in the heavy element abundance with decreasing redshift, but the build-up of these elements appears to be rather gradual.

A similar result was found by Kulkarni and his colleagues who used Hubble Space Telescope observations of low redshift absorption-line systems to measure the relative abundances of zinc and chromium using the ZnII and CrII lines in four

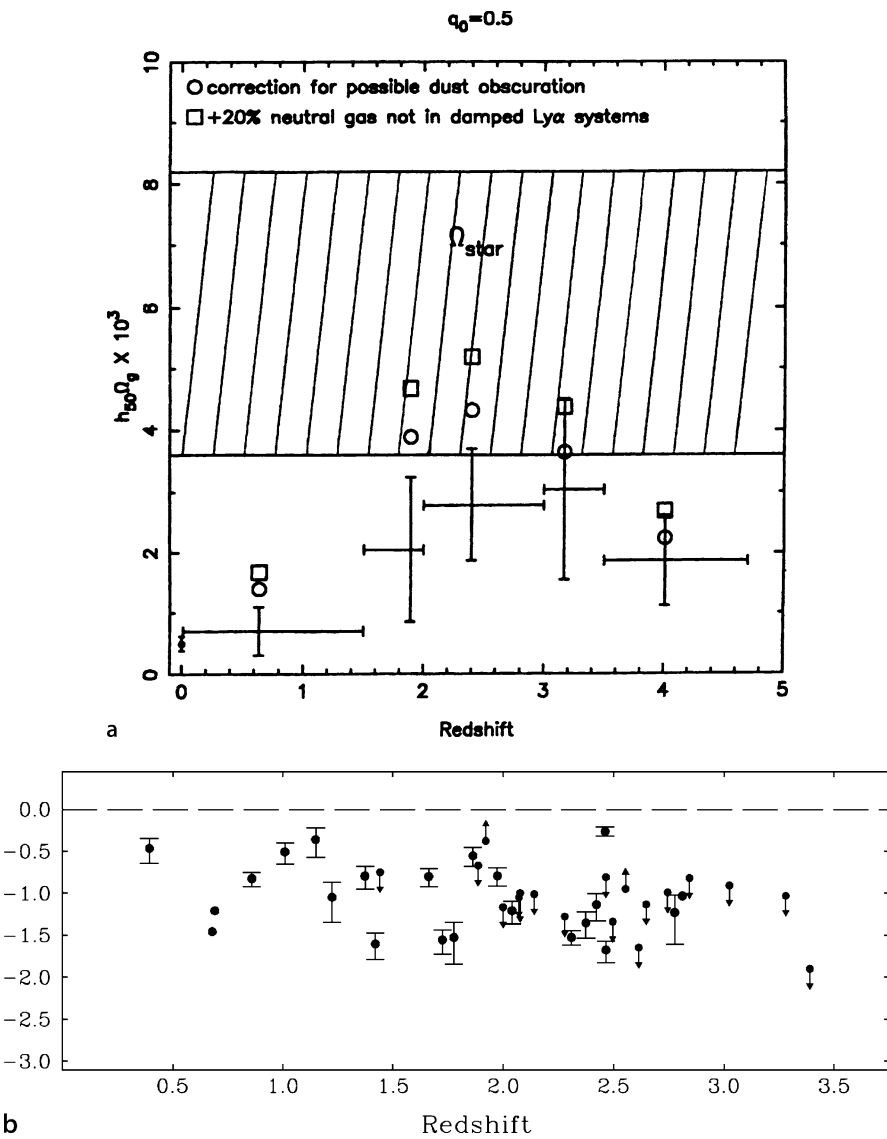


Fig. 19.9. **a** Evolution of the mass density of neutral gas as a function of redshift as determined by mass density of damped Lyman- α absorbers in the spectra of distant quasars (Storrie-Lombardi et al., 1996). Note that these authors use h_{50} rather than $h = h_{100}$. The circles show estimates of Ω_{HI} corrected for the effects of dust extinction and the boxes are corrected values which take account of neutral hydrogen not associated with damped Lyman- α systems. The shaded band indicates estimates of the density parameter in stars, that is, the mass associated with the visible light of galaxies, at the present day. **b** The [Zn/H] abundance determined by Pettini and his colleagues relative to the solar value, which is indicated by the dashed line (Pettini et al., 1997, 1999). The usual convention is adopted of plotting the logarithm of the abundance ratio [Zn/H] relative to its present cosmic value on the ordinate

damped Lyman- α systems with redshifts $0.09 < z < 0.52$ (Kulkarni et al., 2005). Metallicities much lower than the solar value were found, the extrapolated values at $z = 0$ corresponding to [Zn/H] in the range -0.7 to -0.75 , a similar result to that found by Pettini and his colleagues. Kulkarni and his colleagues suggested that their sample of low-redshift-damped Lyman- α systems may be dominated by dwarf or low-surface-brightness galaxies.

The advent of 8- to 10-m class telescopes has enabled the abundances of many elements in damped Lyman- α absorption systems to be studied in considerable detail. Excellent examples of the richness of these data sets are provided by the analyses of Prochaska and Wolfe and of Dessauges-Zavadsky and her colleagues (Prochaska and Wolfe, 2002; Dessauges-Zavadsky et al., 2006). An example of the results for the abundance of iron in the large uniform sample of damped Lyman- α systems studied by Prochaska, Wolfe and their colleagues is shown in Fig. 19.10. On averaging, it can be seen that the metal abundance increases quite gradually over the redshift interval $5 \geq z \geq 0.5$ (Prochaska et al., 2003). The high resolution and sensitivity provided by the 8- to 10-m class telescopes has meant that these studies could be extended to many more atomic and ionic species, for example, the observations of Dessauges-Zavadsky and her colleagues including abundances of 22 elements, B, C, N, O, Mg, Al, Si, P, S, Cl, Ar, Ti, Cr, Mn, Fe, Co, Ni, Cu, Zn, Ge,

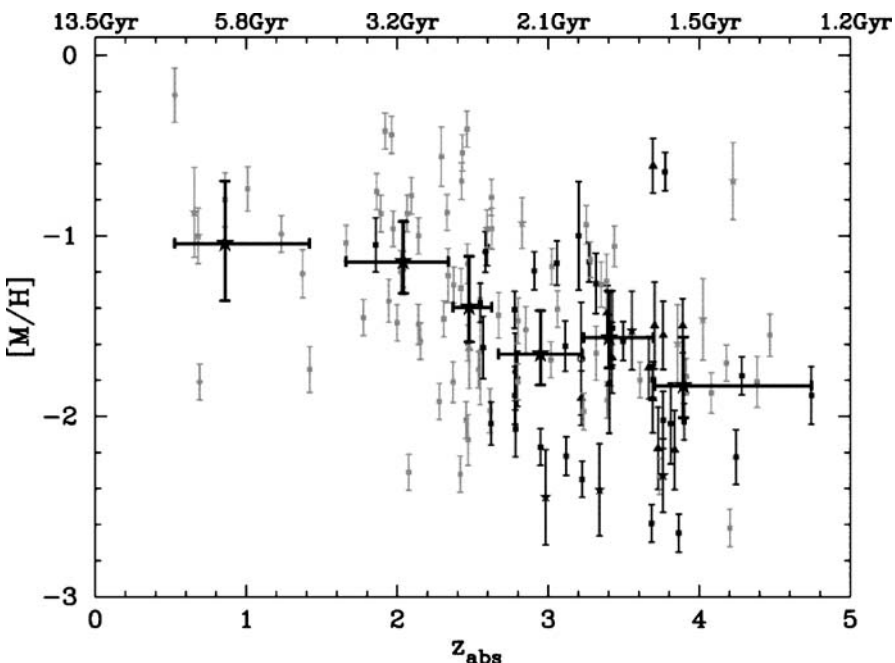


Fig. 19.10. The metal abundance relative to hydrogen [M/H] derived from 125 damped Lyman- α systems with redshifts $0.5 < z < 5$. The unweighted mean logarithmic metallicity in six bins is shown by the solid star with bold ‘error bars’, the vertical bar representing the 95% confidence limit (Prochaska et al., 2003)

As, Kr. The remarkable results of both papers is that there is little dispersion in the relative abundances of the elements, which are very similar to the solar abundances, but at much lower average metallicities. As Dessauges-Zavadsky and her colleagues remark:

This uniformity is remarkable given that the quasar sightlines cross gaseous regions with HI column densities spanning over one order of magnitude and metallicities ranging from 1/55 to 1/5 solar. The uniformity is also remarkable since damped Lyman- α systems are expected (and observed at low redshift) to be associated with a wide range of galaxy types. This implies the respective star formation histories seem to have conspired to yield one set of relative abundances.

Prochaska and Wolfe suggest that the mixing of the elements in these systems must have been remarkably efficient.

19.3 The Equations of Cosmic Chemical Evolution

It is useful to have analytic tools for understanding the relation between the cosmic star-formation rate and the rate at which the elements are built up in galaxies, and this has been provided by Fall and Pei (Fall and Pei, 1993; Pei and Fall, 1995). The formalism is based upon what they call the *equations of cosmic chemical evolution*, which are similar to those originally derived by Tinsley for the chemical evolution of galaxies (Tinsley, 1980). Pagel has given many more details of these types of calculation and of the physics of the chemical evolution of stars and galaxies (Pagel, 1997).

In the approach adopted by Fall and Pei, all mention of galaxies disappears, all that remains being the global averages of the density parameters for the major constituents of the Universe. At each stage, reasonable simplifications need to be made, but this is in the spirit of the approach, which is to provide a framework for star and metal formation in galaxies, viewed globally. The density parameter in stars Ω_s is zero when star formation begins and builds up to the mean value $\Omega_s(t_0) \approx (4\text{--}8) \times 10^{-3}$ by the present epoch. At the same time, the density parameter in gas Ω_g initially comprised 100% of the baryonic matter in galaxies and has decreased to only about 5% of its initial value by the present epoch. The density parameter in heavy elements Ω_m was initially zero and has built up to about 1% of the baryonic mass by the present epoch. Finally, dust was also formed as the abundance of the heavy elements built up. A typical figure would be that about 50% of the heavy elements in the interstellar media of galaxies is in the form of dust. Allowance can also be made for the infall of unprocessed material into galaxies from the intergalactic medium, and also for the expulsion of processed material from galaxies through supernova explosions and galactic winds.

The objective of the calculation is to relate the *absorption history*, which provides a series of snapshots of the values of the various density parameters at different epochs, to the *emission history*, which generally provides information about the

rates of formation of stars and heavy elements, that is, the derivatives of their density parameters with respect to cosmic time.

The first equation describes the conservation of mass

$$\frac{d}{dt} (\Omega_g + \Omega_s) = \dot{\Omega}_f , \quad (19.15)$$

where $\dot{\Omega}_f$ is the rate of infall into, or of the expulsion of baryonic matter from, galaxies. If this term is zero, then (19.15) states that $\dot{\Omega}_g = -\dot{\Omega}_s$, that is, the rate at which gas is depleted is equal to the rate at which mass is condensed into stars.

The second equation describes the rate at which the mass of heavy elements changes with time. The metallicity of the gas at any epoch is defined to be $Z = \Omega_m / \Omega_g$, and so we can write the rate of change of Ω_m as

$$\frac{d\Omega_m}{dt} = \frac{d}{dt} (Z\Omega_g) = y \frac{d\Omega_s}{dt} - Z \frac{d\Omega_s}{dt} + Z_f \dot{\Omega}_f . \quad (19.16)$$

The first term on the right-hand side, $y d\Omega_s/dt$, describes the rate of increase of the mass of heavy elements associated with the rate of star formation. The quantity y is called the *yield*. Written in this way, the term involves the assumption of *instantaneous recycling* of processed material to the interstellar medium. In reality, there is bound to be some delay between the formation of a generation of stars, the completion of their evolution and the recycling of processed material to the interstellar gas. The rationale behind the form of this term is that most of the heavy element formation is associated with massive stars, which have lifetimes that are short compared to the typical timescales over which the average abundances change significantly (Sect. 19.1.1). This term means that, in the time dt , a mass of stars $d\Omega_s$ is formed per unit comoving volume and these eventually return a mass of heavy elements $y d\Omega_s$ to the interstellar medium. In the spirit of this analysis, the yield y is assumed to be independent of cosmic epoch.

The second term on the right-hand side of (19.16) describes the loss of heavy elements because of the formation of stars from gas which has already attained a metallicity Z . In the time dt , the loss of heavy elements per unit comoving volume is $-d\Omega_m = -Z d\Omega_s$. The third term on the right-hand side represents the enhancement of the heavy element abundance by the infall of baryonic material from intergalactic space, assumed to have metallicity Z_f . This term can take account of the fact that the primordial gas might have been enriched by early generations of star formation. Pei and Fall give some simple illustrative examples of the solutions of (19.15) and (19.16) (Pei and Fall, 1995).

Closed Box Model. In this example, there is no infall of matter from intergalactic space, nor is gas expelled from the galaxies, $\dot{\Omega}_f = 0$. It is straightforward to show that

$$Z = -y \ln \left[\frac{\Omega_g(z)}{\Omega_g(\infty)} \right] , \quad (19.17)$$

where $\Omega_g(\infty)$ is the initial density parameter in baryons.

Inflow Model. In the simplest picture, the infalling matter consists of unenriched primordial gas, $Z_f = 0$. Some simplifying assumptions need to be made about $\dot{\Omega}_f$. Fall and Pei adopted a model in which $\dot{\Omega}_f = \nu \dot{\Omega}_s$, that is, the rate of infall of mass is regulated by the rate at which matter is being converted into stars. This is a plausible picture for the discs of spiral galaxies in which infall of intergalactic material replenishes gas which is continuously being converted into stars. Larson noted that, in the case of our own Galaxy, the rate of infall of mass is more or less the same as the rate at which mass is being converted into stars in regions of star formation in the disc of our Galaxy (Larson, 1972). This picture can account for the fact that the interstellar gas in the disc has not all been converted into stars. There is a simple analytic solution:

$$Z = \frac{y}{\nu} \left\{ 1 - \left[\frac{\Omega_g(z)}{\Omega_g(\infty)} \right]^{\nu/(1-\nu)} \right\}. \quad (19.18)$$

Outflow Model. The formalism employed in the infall model can be adapted to this case, the assumption being that the rate of loss of mass from a galaxy is proportional to the supernova rate, which, in the instantaneous recycling picture, is proportional to the rate at which stars are formed. The mathematical difference as compared with the inflow model is that, not only is mass lost from galaxies $\dot{\Omega}_f = -\nu \dot{\Omega}_s$, but also heavy elements are lost with $Z_f = Z$. This model also has a simple analytic solution:

$$Z = -\frac{y}{(1+\nu)} \ln \left[\frac{\Omega_g(z)}{\Omega_g(\infty)} \right]. \quad (19.19)$$

It should be emphasised that these are simply convenient analytic models for understanding the build-up of the heavy elements in galaxies. All three have the useful feature that the models are completely defined once the evolution of the gaseous content of galaxies as a function of cosmic epoch is prescribed. Fall and Pei used the formalism to indicate how sensitive the models are to corrections for dust extinction, particularly as it affects the selection of the quasars for absorption line studies (Pei and Fall, 1995). By including quite substantial corrections for the effects of dust in the selection of the samples for observation, they were able to relate successfully the evolution of the star-formation rate determined by Madau and his colleagues (Madau et al., 1996) to observations of the heavy element abundances in the damped Lyman- α systems at $z \sim 2$ as they were known in 1995.

Since that time, however, the picture has become more complicated. The problem is most easily appreciated by the comparison of the change of neutral hydrogen abundance with redshift (Fig. 19.9a) with the very modest changes in zinc abundance over the same range of redshifts (Fig. 19.9b). For example, for a simple closed box model, a linear change of neutral hydrogen abundance by a factor of 20 between redshifts 3 and 0 would result in an order of magnitude change in metallicity Z over the same redshift interval, in contradiction to the observations shown in Fig. 19.9b. There is a similar problem if the star-formation history derived from the optical-UV and submillimetre surveys are adopted. These suggest that the overall star-formation

rate was more or less constant over the redshift interval $1 \leq z \leq 4$. It would then be expected that there would be greater variation of the build-up in the heavy elements in galaxies than are displayed by the chemical abundances of the damped Lyman- α systems. These considerations suggest that the picture is more complicated than the simple chemical evolution models would predict and they may cast light on the rather subtle selection effects which go into the selection of complete samples of damped Lyman- α systems.

19.4 The Old Red Galaxies

The remarkable advances made in the study of Lyman-break or ‘drop-out’ galaxies out to redshifts $z \approx 6$ have provided key evidence about star-forming galaxies, but these are not the only populations of galaxies present at large redshifts. Various pieces of evidence indicate that some galaxies were already ‘old’ out to redshifts of at least $z = 2$ and so must have formed the bulk of their stellar populations at large redshifts. In addition, the most massive galaxies seem to have more or less the same maximum mass over the redshift interval $0 < z < 2$, contrary to what might have been expected if they had increased in mass and luminosity through the process of hierarchical clustering.

- The plot of stellar mass against redshift for the galaxies in the Gemini Deep Deep Survey and K20 Survey is shown in Fig. 19.11 (McCarthy, 2006). The galaxies were selected in the K ($2.2\text{ }\mu\text{m}$) waveband, and so the samples primarily selected the old stellar populations of galaxies, as indicated by Fig. 17.3. The stellar masses of the galaxies were derived by fitting the extensive multicolour photometric data from the above surveys to the stellar energy distributions provided by the galaxy evolution codes of Bruzual and Charlot (Bruzual and Charlot, 2003). This procedure automatically takes account of the stellar evolution of the populations of the galaxies. The importance of this type of survey was emphasised by McCarthy, who made the point that Fig. 19.11 represents the evolving stellar mass density which is the complement of the star-formation history discussed in Sect. 19.1 (McCarthy, 2006). The horizontal solid line at $\log(M/M_{\odot}) = 10.9$ is the present day value of the stellar mass corresponding to the ‘turnover’ luminosity L^* of the galaxy luminosity function and the dashed line represents the detection limit of the survey at $K = 20.6$. It is apparent that there is little evidence for any increase in the baryonic masses of the galaxies with decreasing redshift.

Glazebrook and his colleagues compared the data in Fig. 19.11 with the expected increase in mass according to the standard hierarchical clustering models of galaxy formation with decreasing redshift (Glazebrook et al., 2004). As expected from Fig. 16.6, the observations were inconsistent with these expectations. The inference is that these galaxies must have completed the formation of their stellar populations by a redshift $z \sim 2$.

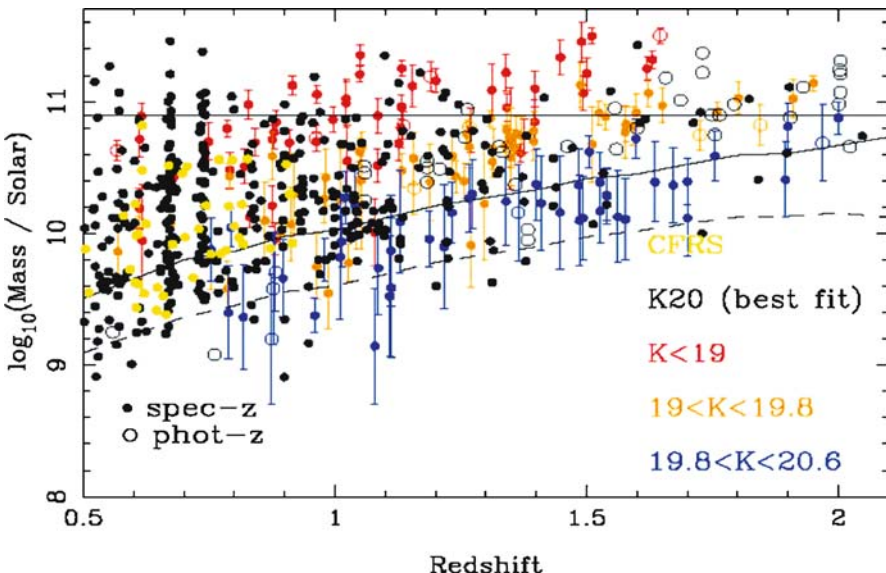


Fig. 19.11. A plot of stellar mass against redshift for galaxies selected from the Gemini Deep Deep Survey and K20 Survey (McCarthy, 2006). The galaxies were selected in the K ($2.2\text{ }\mu\text{m}$) waveband. The stellar masses were estimated by fitting the extensive multicolour data to the stellar energy distribution codes of Bruzual and Charlot (Bruzual and Charlot, 2003)

- In addition to photometry, 20 of the Gemini Deep Deep Survey galaxies with $z > 1.3$ were observed spectroscopically with very long exposures (McCarthy et al., 2004). Among objects with spectroscopic redshifts, 51% of the galaxies with $I - K > 3.5$ showed unambiguous evidence for old stellar components while the redder galaxies with $I - K > 4$ showed an even greater tendency for old stellar spectra. McCarthy and his colleagues concluded that for 50 to 80% of the red galaxies in the sample at $z \geq 1.3$ the optical-infrared emission is dominated by contributions from old stellar populations. Typically, the stellar populations must have formed by a redshift of 2.4 or greater for the reddest examples. As a result, the star-formation rates must have been very great during this initial ‘starburst’ phase, values of the order of $300\text{--}500 M_{\odot}\text{ year}^{-1}$ being found. They point out that these rates are much greater than those observed in the Lyman-limit drop-out systems but would be consistent with the observations of the strongly star-forming galaxies observed at large redshifts in the deep submillimetre surveys discussed in Sect. 19.1.5.
- Similar results have been reported by Cimatti and his colleagues from their analyses of the properties of four very red galaxies with redshifts in the range $1.6 \leq z \leq 1.9$ from the K20 sample (Cimatti et al., 2004). The spectroscopic and morphological properties of these galaxies indicated that they were ‘old, fully assembled, spheroidal galaxies’ with masses $M > 10^{11} M_{\odot}$. These objects are similar to the old red galaxies discussed above and again, comparing the numbers

of these galaxies with the expectations of the standard hierarchical clustering picture, Cimatti and his colleagues showed that the build-up of massive early-type galaxies must have been much faster in the early Universe than expected.

- Qualitatively similar conclusions can be derived from observations of the massive galaxies associated with the most powerful FR2 radio sources. Until the advent of the 8- to 10-m class telescopes, the identification of these rare classes of galaxy was one of the few methods for finding massive, old elliptical galaxies at large redshifts. The redshifts of the classical double 3CR radio galaxies span the redshift interval to $0.3 \leq z \leq 2$ and their mean stellar masses were found to be remarkably constant over this redshift interval (Best et al., 1998). These galaxies are among the most luminous known, with luminosities as great as those of the brightest galaxies in clusters at redshifts $z \sim 1$. Their stellar masses were estimated anew by the multicolour technique by McLure and his colleagues (Fig. 19.12), and their stellar masses were found to be $M \geq 3 \times 10^{11} M_{\odot}$, that is, greater than those of the most massive galaxies plotted in Fig. 19.11 (McLure et al., 2006). If account is taken of the dark matter present in these systems, their total masses are likely to be about ten times greater. This analysis again suggests that most of the star formation within these massive galaxies had been completed at some redshift $z \geq 2$.
- Evidence that the stellar populations of the large redshift radio galaxies are likely to be old was presented by Lilly for the radio galaxy 0902+34 at a redshift $z = 3.4$ and by Dunlop and his colleagues for the radio galaxy LBDS 53W091 at redshift 1.55 (Lilly, 1988; Dunlop et al., 1996). In the latter case, the age of its

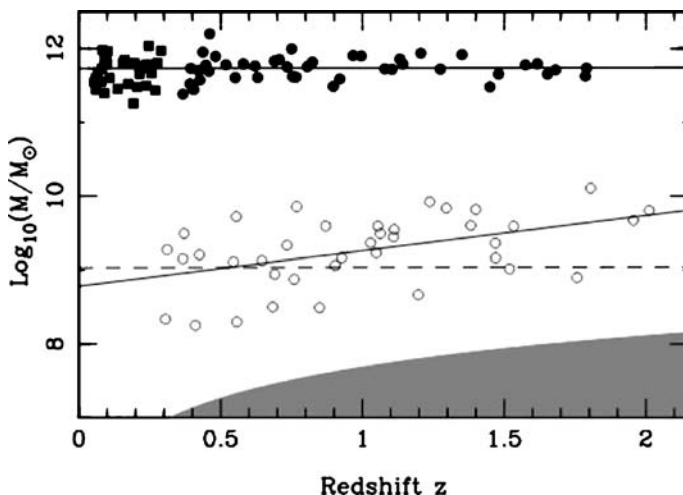


Fig. 19.12. The stellar masses of the 3CR radio galaxies (*black filled circles* and *squares*) and the black hole masses of the 3CR radio quasars (*open circles*), both drawn from the complete sample of 3CR radio sources, as a function of redshift (McLure et al., 2006). The galaxy stellar masses were deduced from their stellar energy distributions using the galaxy evolution codes of Bruzual and Charlot (Bruzual and Charlot, 2003)

stellar population was at least 3.5×10^9 years, so that these stars must have been formed at large redshifts. A similar result, namely an age of 4.5×10^9 years, was found for the radio galaxy LBDS 53W069 at a redshift of $z = 1.43$ (Dey, 1997). Radio galaxies with qualitatively the same stellar properties have been observed to redshifts of greater than 4 by Lacy, Spinrad and their colleagues (Lacy et al., 1994; Spinrad et al., 1995).

- Finally, as discussed in Sect. 17.5, the quasars were at the peak of activity in the redshift interval $2 < z < 3$. The evidence is compelling that there is a strong correlation between the mass of the black hole in the quasar nucleus and the mass of the spheroid of the host galaxy (Magorrian et al., 1998), the ratio of black hole mass M_{bh} to the mass of the spheroid M_{sph} being about 0.002. An example of this relation for the complete sample 3CR radio galaxies and quasars is shown in Fig. 19.12. Because of the success of unified schemes for radio galaxies and quasars in this sample, the ratio $M_{\text{bh}}/M_{\text{sph}}$ can be estimated from Fig. 19.12. The spheroid mass must be about ten times greater than the stellar mass to take account of the dark matter and so it can be seen that these data would be consistent with a ratio of $M_{\text{bh}}/M_{\text{sph}} \sim 0.002$. These data are naturally interpreted as evidence that the host galaxies of the quasars must have had masses $M \geq 10^{12} M_{\odot}$ and that their stellar populations must already have been assembled into galaxies, more or less as we know them today, by a redshift of 3.

It therefore seems that a significant fraction of all massive galaxies must have formed their stellar populations at large redshifts, $z \geq 2.5$, and that there was little subsequent increase in their masses through hierarchical clustering and subsequent star formation. This contrasts with the inference that the global star-formation rate was at its peak at redshifts $z \sim 1\text{--}2$. Most of the star formation must have taken place in less massive galaxies than those discussed in this section. This phenomenon, that the massive galaxies formed their stellar populations at early epochs and star formation continues for lower mass galaxies at much later epochs, is sometimes referred to as ‘downsizing’. These phenomena need to be built into an overall picture of galaxy evolution.

19.5 The Origin of Rotation

According to the standard picture of the development of density perturbations in the Friedman world models, rotational velocities are damped as the Universe expands. As shown in Sect. 11.5, rotational velocities decrease in amplitude as $\delta v_{\perp} \propto a^{-1}$, this result being no more than the conservation of angular momentum in a uniformly expanding medium. This consideration poses more or less insuperable problems for theories involving primordial turbulence (von Weizsächer, 1947), many of which have been discussed in some detail by Jones and Peebles (Jones and Peebles, 1972; Jones, 1973). As they point out, if the rotation of spiral galaxies at the present day were the relic of primordial turbulent eddies, these eddies would be highly supersonic at the epoch of recombination and so be dissipated by shocks.

The most natural explanation for the rotation of galaxies is that it is induced by tidal torques acting between perturbations during the linear stages of their development (Strömborg, 1934; Peebles, 1993). The perturbations associated with the superposition of random Gaussian waves are not spherical but, in the lowest approximation, are ellipsoidal and so pairs of ellipsoids experience the mutual effect of tidal torques. These torques lead to the build up of angular momentum in each of the bodies, whilst conserving angular momentum overall. This process can continue so long as the perturbations are in the linear regime. Once the perturbations reach amplitude $\Delta\varrho/\varrho \sim 1$, they rapidly become virialised and the final rotational state of the object is largely determined by the conservation of the angular momentum it acquired by the time $\Delta\varrho/\varrho \sim 1$.

The angular momentum J of a gravitationally bound object of mass M and gravitational binding energy E can be characterised by the dimensionless *spin parameter* λ , which is defined to be

$$\lambda = \frac{JE^{1/2}}{GM^{5/2}}. \quad (19.20)$$

As pointed out by Peebles, the quantity λ is a measure of the degree of rotational support of the galaxy (Peebles, 1993). The centripetal acceleration acting on unit mass at a typical radial distance r within the system is $a = v_\phi^2/r$ and the gravitational acceleration is $g \sim GM/r^2$. The angular momentum of the system is $J \sim Mrv_\phi$ and its gravitational binding energy GM^2/r . Therefore, eliminating v_ϕ and r from the ratio a/g , we find

$$\frac{a}{g} = \frac{v_\phi^2}{r} \frac{r^2}{GM} \sim \frac{J^2 E}{G^2 M^5} = \lambda^2. \quad (19.21)$$

Estimates of the typical value of the spin parameter induced by tidal torques during the growth of primordial density perturbations is best found from N -body simulations, the median value found from those of Barnes and Efstathiou being $\lambda = 0.05$ (Barnes and Efstathiou, 1987). The implication of (19.21) is that this amount of rotation is quite inadequate to provide rotational support for the system, which must be primarily supported by the random velocities of the stars and clouds within the system. This value of λ would, however, be consistent with the slow rotation of the spheroidal components of elliptical and spiral galaxies. If tidal torques are the origin of the angular momenta of spiral discs, it is essential that their baryonic components contract in the radial direction whilst conserving their angular momenta – in other words, the discs would have to lose gravitational binding energy at roughly constant angular momentum.

There is a pleasant solution to this problem within the context of models in which the spiral discs of galaxies form by dissipative contraction within dark matter haloes, as pointed out in a pioneering paper by White and Rees and by Fall and Efstathiou (White and Rees, 1978; Fall and Efstathiou, 1980). If the dark matter halo follows the density distribution of an isothermal gas sphere at large radii, $\varrho \propto r^{-2}$, then, as shown in Sects. 3.5.2 and 4.2.2, the rotation curve of a centrifugally supported disc

within this potential distribution is $v_c = \text{constant}$, consistent with the flat rotation curves of giant spiral galaxies. Let us assume that the material of the disc initially attains the same spin parameter due to tidal torques as the spheroidal component, $\lambda = 0.05$. Then, the initial rotational velocity of the disc v_ϕ can be found from (19.21),

$$v_\phi \sim \lambda v_c . \quad (19.22)$$

Now, in the dissipative contraction of the disc, the gravitational potential distribution is fixed by the mass distribution of the dark halo and so the disc can contract, conserving its angular momentum $v_\phi r = \text{constant}$ until it reaches the radius at which it is in centrifugal equilibrium, that is, when $v_\phi = v_c$. Thus, the final radius of the disc is λr_i . As pointed out by Peebles, this is an attractive scenario to account for the fact that the typical sizes of the discs of spiral galaxies are very much less than the inferred sizes of their dark matter haloes (Peebles, 1993). The typical scale length of the disc of a giant spiral galaxy, such as our own Galaxy, is $r \sim 4$ kpc, and, according to this scenario, this disc would have contracted from a halo of dimensions $4/\lambda \sim 100$ kpc, typical of the sizes of the spheroidal components of spiral galaxies inferred from analyses to the shear of background galaxies due to gravitational lensing (Sect. 4.6.4). This picture is consistent with the arguments developed by Ostriker and Peebles to account for the stability of the discs of spiral galaxies (Ostriker and Peebles, 1973).

This line of reasoning has been refined by Fall, who considered the role of both dissipation and tidal stripping to account for the rotational properties of the discs and spheroids of spiral and elliptical galaxies (Fall, 1983). His improved version of the above argument results in essentially the same answer, namely that dissipative contraction of the discs of spiral galaxies in dark matter haloes can account for their relative dimensions. In addition, he showed that, with reasonable assumptions, this picture could account for the approximate constancy of the central surface brightness distributions of spiral galaxies found by Freeman (Sect. 3.4.1) and the Tully–Fisher relation (Sect. 3.6.3). His conclusion was that this model for the formation of disc galaxies, involving the conservation of mass and angular momentum but the dissipation of the binding energy of the disc, can give a good account of the most important properties of disc galaxies.

There is, however, a problem with the elliptical galaxies. Since angular momentum is conserved in the formation of the disc, the specific angular momentum of the spiral galaxies, that is, the angular momentum per unit mass, should be the same for elliptical galaxies and the discs of spiral galaxies. This expectation is not consistent with his interpretation of the observations of Davies and his colleagues (Davies et al., 1983). Fall found that the specific angular momenta of spiral discs are about six times greater than those of elliptical galaxies, the comparison being made for galaxies of the same mass. He proposed various possible solutions to this problem. One might be that the tidal torques result in different values of the spin parameter λ in different galactic environments. For example, elliptical galaxies are found preferentially in regions of high galaxy density and so it might be that the value of λ is anticorrelated with the density of the large-scale environment in which the galaxy

is formed. Another possibility is that the outer regions of the collapsing galaxy in dense regions are stripped by tidal forces. Since most of the angular momentum is contained in the outer regions, it might be that some stripping of the protospheroid could reduce the specific angular momentum of the galaxies destined to become elliptical galaxies. The problem is to reduce the angular momentum by a sufficient factor without reducing the dimensions of the halo to unacceptably small values.

19.6 Putting It All Together – Semi-Analytic Models of Galaxy Formation

How well do all these separate pieces of evidence fit together to create a coherent and convincing picture of the formation and evolution of galaxies? The background Λ cold dark matter picture is undoubtedly a major triumph, and on the large scale there is little doubt that this is the correct framework within which the problems of the formation and evolution of galaxies should be addressed. The problems come about on much smaller scales and concern the role of astrophysical processes once galaxies begin their non-linear evolution. The preceding chapters of this last part of the text aimed to establish the relevant observations and astrophysics which must be part of the story.

Let us first summarise some of these problems and how they might be resolved.

- As N -body simulations of the development of structure improved in size and quality, an excess of low-mass dark matter haloes was found, which are presumed to be the potential wells within which low mass galaxies formed. This is the *excess of dwarf galaxies problem*. It might be thought that these low-mass dark matter haloes could be destroyed by tidal forces, but the Millennium Simulations have shown that they survive in the haloes of large galaxies. While a number of radical proposals have been made to resolve this problem, a popular view is that these systems are of too low mass to retain the gas out of which stars could have formed within their shallow gravitational potentials wells. The interstellar gas could be blown out of these potential wells by the cumulative effect of supernova explosions. Alternatively, the gas might be swept out of the galaxies by ram-pressure stripping by the intergalactic gas or in collisions between galaxies. There are evidently a number of plausible astrophysical mechanisms for resolving this problem.
- Another result of the high-resolution N -body simulations is that there should be pronounced dark matter cusps in the central regions of galaxies. This is not a trivial question to answer observationally since high-precision probes of the mass distribution within galaxies are needed, particularly in their central regions where the presence of supermassive black holes can complicate the analysis.
- Another puzzling result is that there is a positive correlation between the mass of a galaxy and its metallicity (Sect. 3.6.4). If massive galaxies resulted from the coalescence of less massive galaxies, there would have to be additional mechanisms for promoting the synthesis of the heavy elements in the more

massive galaxies. This might, for example, be associated with the mergers of the coalescing galaxies which undoubtedly leads to much enhanced star-formation rates, as observed in the ‘Antennae’ galaxies (Fig. 3.6b).

- The discussion of Sect. 19.4 indicates that the most massive elliptical galaxies must have formed their stellar populations at somewhat earlier epochs than those during which the bulk of star formation in galaxies took place. This problem of ‘downsizing’ suggests that there is unlikely to be a single simple picture for the formation of galaxies.
- We have not yet accounted for the various correlations between the properties of galaxies, for example, the Faber–Jackson relation, or equivalently the narrowness of the fundamental plane, for elliptical galaxies and the Tully–Fisher relation for spiral galaxies.

Because of the success of the Λ CDM model in accounting for the observed features of the Universe on large scales, the presupposition is that, to create a fully fledged theory of galaxy formation, many of these phenomena must be associated with the astrophysical processes by which the baryonic matter evolved within the dark matter haloes. This necessarily involves poorly understood processes such as the dependence of the star-formation rate upon the properties of the interstellar medium, the role of supernova explosions in sweeping matter away from star-forming regions and out of galaxies, the role of collisions between galaxies, the formation and growth of black holes in the nuclei of galaxies and so on. These involve non-linear processes and feedback mechanisms which can promote or suppress the formation of new stars and structures.

Computational astrophysics has made enormous contributions to understanding in considerable detail the origin and evolution of cosmic structures and the observational fingerprints these leave in the cosmic microwave background radiation. The elementary discussion of these topics in this book, or the much more sophisticated treatment given by Dodelson, are attempts to rationalise by physical arguments the essence of the physics which comes out of large-scale numerical simulations (Dodelson, 2003). But there is a limit to how far these analytic physical arguments can be used in the era of precision cosmology when it is essential to take account of the detailed coupling and decoupling of the various constituents of the Universe. To obtain the requisite precision, the numerical solutions of the coupled Boltzmann equations for each component within a framework of General Relativity are essential. It is our great good fortune, and not a coincidence, that the power of high-speed computers has enabled both vast observational data sets of very high quality to be obtained and the simulations of structure formation to be carried out with vast numbers of particles. The *Millennium Simulation* of the growth of dark matter perturbations under gravity involved following the evolution of over 10^{10} particles from a redshift $z = 127$ to the present epoch within a cubical region of comoving dimension $500h^{-1}$ Mpc (Springel et al., 2005). We have already made use of the results of these and similar simulations in comparing the observed distribution of gas and galaxies with the predictions of these models.

We described in Sect. 18.6 the success of the models in accounting for the distribution of Lyman- α absorbers when diffuse baryonic matter is included in the simulations. Rules had to be set up to describe the conversion of cooled gas into stars and the impact of subsequent supernova explosions which can strongly influence the distribution of the gas. In Sect. 18.7, similar simulations were used to predict the structure in the distribution of neutral hydrogen during the reionisation epoch. The success of these programmes is very striking and the question is how much further this type of modelling can be taken in order to address the astrophysical issues listed above. This is the domain of *semi-analytic models of galaxy formation*.

This approach to galaxy formation has been particularly promoted by the Virgo Consortium, a collaboration between British, German, Canadian and US astrophysicists who masterminded the Millennium Simulations. Excellent surveys of the procedures and what has been achieved are provided by the reviews by Springel and his colleagues and by Baugh (Springel et al., 2005; Baugh, 2006). The approach is based upon the success of large-scale computer simulations in understanding the distribution of dark matter in the Universe. The high-resolution and dynamic range of the Millennium Simulation enable the evolution of structures on a vast range of physical scales to be tracked over the full redshift range of the simulations. Whereas in the past the resultant ‘merger trees’ had to be simulated by Monte Carlo procedures, they can now be estimated directly from the Millennium Simulation. This provides the backdrop for the introduction of the baryonic component which reacts gravitationally on the growing network of dark matter potential wells.

In the semi-analytic approach, rules need to be set up to describe how the baryonic matter cools, forms stars and completes the full life cycle of stellar evolution. The supplementary information provided by Springel and his colleagues provides a very fair assessment of what needs to be done (Springel, 2005). To quote their words:

The term ‘semi-analytic’ conveys the notion that while in this approach the physics is parameterised in terms of simple analytic models, following the dark matter merger trees over time can only be carried out numerically. Semi-analytic models are hence best viewed as simplified simulations of the galaxy formation process.

In many ways, it is helpful to regard this approach as ‘experimental computational astrophysics’ in the sense that there are many possible realisations of these models and the aim is to constrain the necessary and essential physics on a trial-and-error basis. Only with the vast power of modern high-speed and parallel computing is this agenda feasible. To give some flavour of what is involved, it is useful to list some of the necessary ingredients of the most successful models and the reader can judge how much reliance can be placed upon the results. We follow the clear summary contained in the supplementary information provided by Springel and his colleagues.

- Central to the whole procedure are the processes of **radiative cooling and star formation**. It is assumed that initially the ratio of diffuse baryonic gas to cold dark matter has a constant ratio everywhere, consistent with the values found from the WMAP observations and from primordial nucleosynthesis arguments.

The equations of gas dynamics under the gravitational influence of the growing dark matter perturbations are solved and include cooling of the gas according to the recipes discussed in Sect. 16.2. Modified versions of the GADGET code described by Springel are used in these computations (Springel, 2005). Cold condensed gas accumulates in the central regions of the dark matter haloes and is identified with the interstellar medium of the protogalaxy. There is also a halo of hot gas which is heated by the background UV radiation field and by the supernova feedback mechanisms discussed below. The cool gas settles into a disc supported by rotation, the size of the disc being determined by the spin parameter of the dark matter halo. Once the surface gas density exceeds the critical density found from observational studies such as those of Kennicutt (Kennicutt, 1989), star formation is assumed to take place with an efficiency of 10% on the dynamical timescale of the disc. The parameters describing these processes are chosen to reproduce the phenomenological laws of star formation and the observed gas fractions in galaxies at small redshifts.

- The most massive stars formed have short lifetimes and explode as **supernovae**. Guided by observation, it is assumed that supernovae can blow gas out of star-forming discs and that the rate of mass ejection is proportional to the total mass of stars formed. The efficiency of mass ejection depends upon the depth of the gravitational potential wells – in small galaxies, supernovae may well blow away all the interstellar gas in a single starburst, whereas large galaxies can retain the heated gas.
- The **morphologies of the galaxies** are parameterised by their bulge-to-disc ratios, which are correlated with their Hubble types. There are two routes to the formation of bulges. The first is through secular instabilities in the rotating stellar disc which lead to the formation of bars, as in the case of barred spiral galaxies, or bulges in the case of normal spirals. As demonstrated by Ostriker and Peebles, the build-up of bulges or haloes is necessary to ensure the stability of the discs (Ostriker and Peebles, 1973). The second process is the merger of galaxies. These are classified as *major mergers* if the ratio of masses of the galaxies is greater than 0.3 and *minor mergers* if it is less than 0.3. In major mergers, the discs of both galaxies are destroyed and a common spheroid is formed – this is the process by which elliptical galaxies are created. In the minor mergers, the disc of the larger galaxy survives and the less massive galaxy is disrupted, its stars becoming part of the bulge population. Any surviving cold gas collapses to the nuclear regions of the galaxy where it gives rise to a nuclear starburst. The parameterisation of the latter process is derived from systematic studies of hydrodynamical simulations of galaxy collisions (Mihos and Hernquist, 1994, 1996).
- The models should also reproduce the observed spectra of galaxies at different stages of their evolution. The stellar population synthesis codes enable predictions to be made of the **spectrophotometric properties of galaxies** (Bruzual and Charlot, 2003). The bulge and disc components need to be treated separately. An important element of the spectral evolution of galaxies is the recycling of processed stellar material through the interstellar gas, both to the hot and cold

phases – the next generation of stars is formed in the cold phases. Dust extinction needs to be included, and this depends upon the enrichment of the interstellar gas with heavy elements and their condensation into dust grains.

- Finally, account needs to be taken of the **formation of massive black holes in the nuclei of galaxies**. It is assumed that the growth of these black holes takes place as a result of galaxy mergers during which cold gas is dragged into the central regions under the influence of tidal forces. This process creates a nuclear starburst as well as providing mass which is accreted into the black hole. The parameterisation of this process is chosen so that the observed relation between the mass of the central black hole and the mass of the bulge is obtained. The accretion process results in the huge luminosities of the quasars, so long as the supply of fuel lasts. The UV radiation of the quasars can contribute to the ionisation of the interstellar and intergalactic gas in their vicinity. In addition, the quasars are powerful sources of relativistic jets, and these have a profound influence upon the surrounding interstellar and intergalactic media, as illustrated in Fig. 4.15 for the case of the Perseus cluster. The effect of this heating is to inhibit the further accretion of baryonic mass onto the galaxy. In the modelling, it is assumed that the heating rate is proportional to the mass of the black hole and to $T^{3/2}$, where T is the temperature of the gas. This is the process which the modellers adopt to account for the fact that the central cluster galaxies do not grow indefinitely and so provides a cut-off at the high mass end of the luminosity function.

This list indicates the types of input physics which the semi-analytic modellers have to adopt in order to account for the observed properties of galaxies. It is an ambitious list, but it is hard to argue the proposition that these processes are not important in the evolution of galaxies. In a sense, all the models are doing is providing practical realisations of the many different physical processes we have discussed throughout this book in order to create a self-consistent picture of galaxy formation. The purist may argue that there are too many assumptions built into the modelling procedures and it is certainly true that the modellers have to keep a close eye on the observations and use a ‘trial and error’ approach to find the most plausible set of assumptions.

Let us give a few examples of the successes of the semi-analytic modelling procedure.

- Having incorporated all the baryonic physics into the Millennium dark matter simulations, the two-point correlation function for galaxies, rather than for dark matter haloes, can be determined. As can be seen from Fig. 19.13, the resulting two-point correlation function for galaxies is a much better fit to the observations than that of the dark matter haloes. The dashed line shows the correlation function for the dark haloes, very similar to the result shown in Fig. 14.5b. The effect of including the baryon physics has been to decrease the amplitude of the correlation function at small physical scale. In addition, the models can account for the galaxy two-point correlation function for galaxies of different luminosities and colours (Springel et al., 2005).

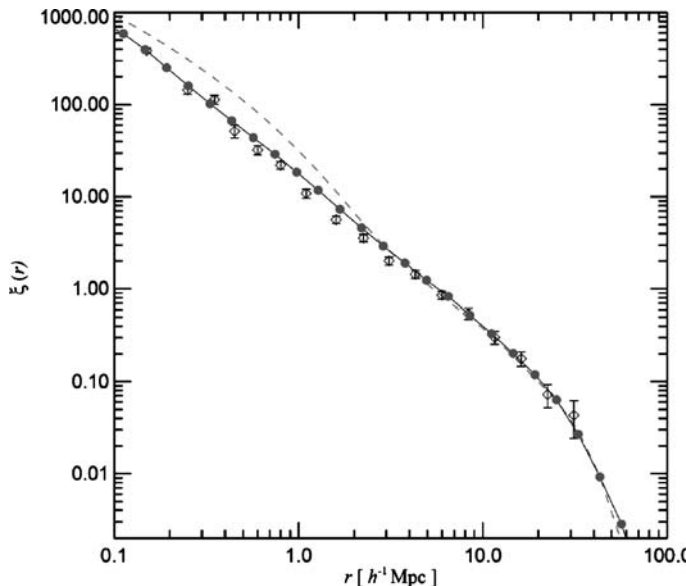
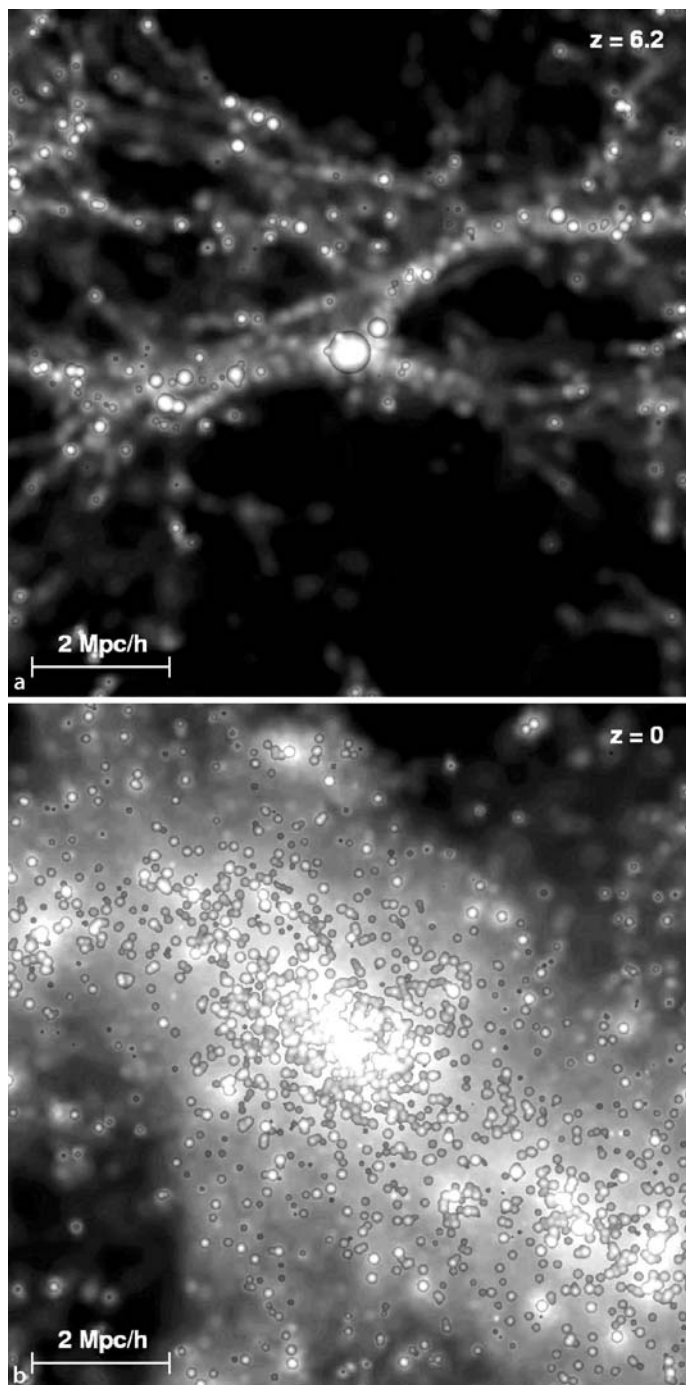


Fig. 19.13. The two-point correlation function for galaxies at the present epoch. *Filled circles* show estimates of the function for model galaxies brighter than $M_K = -23$ selected from the Millennium Simulation. The observed relation for the 2dF Galaxy Redshift Survey is shown as *diamonds with error bars*. Both the observational data and the simulated galaxies have correlation functions which are very close to power laws on scales $r \leq 20 h^{-1} \text{ Mpc}$. As in Fig. 14.5b, the correlation function for the dark matter alone, shown above by a *dashed line*, deviates significantly from a power law (Springel et al., 2005)

- The models can account for the formation of quasars at redshifts as large as $z = 6$, although there is only one such system in the simulation volume at this very large redshift. Figure 19.14a shows the region of the simulation containing a massive galaxy at redshift $z = 6.2$ as well as the developing cosmic web about it. The interesting point is that, although these high-density peaks are very rare, they do occur statistically and lead to the early formation of a galaxy massive enough to host a supermassive black hole. The same region can be tracked to the present epoch when it turns out that, not surprisingly, the overdense region has evolved into a rich cluster of galaxies with a massive galaxy at its centre

Fig. 19.14. a The environment of a ‘first quasar candidate’ in the Millennium Simulation at redshift $z = 6.2$ and **b** at the present epoch in a cube of comoving dimension $10 h^{-1} \text{ Mpc}$. The galaxies of the semi-analytic model are shown as *circles* overlaid on a greyscale image of the dark matter density distribution. The volume of the sphere representing each galaxy is proportional to its stellar mass. At $z = 6.2$, all the galaxies are blue because of ongoing star formation, whereas many of the galaxies which have been accreted into the rich cluster at $z = 0$ have evolved into red galaxies (Springel et al., 2005)



(Fig. 19.14b) (Springel et al., 2005). The simulations also indicate that the epoch of maximum quasar activity occurred at redshifts $z \sim 2\text{--}3$.

- In the discussion of the detection of the acoustic peaks in the large-scale galaxy distribution, it was remarked that the semi-analytic models had been used to convert the dark matter power-spectrum into the galaxy power-spectrum (Sect. 14.6.1). Besides resulting in excellent agreement with the cosmological parameter estimations from the WMAP 3-year data, the simulations have confirmed the observability of the acoustic oscillations in yet larger surveys of the distribution of galaxies.
- The models provide clear predictions about the evolution of the mass function of clusters of galaxies as a function of cosmic epoch, as was illustrated in Fig. 16.5.

There remain some stubborn problems. Examples include accounting for the zero-point of the Tully–Fisher relation and the details of the fundamental plane for elliptical galaxies.

From my personal perspective, the exciting thing about the semi-analytic approach is that it provides a powerful new tool for testing different hypotheses about the physical processes involved in galaxy formation. The simulations also provided strong motivations for future programmes of observation and theoretical analysis. One of the great challenges is to keep track of the non-linear physics involved in these remarkable simulations and make them an integral part of the toolkit of extragalactic astrophysics.

References

- Aaronson, M. and Mould, J. (1983). A distance scale from the infrared magnitude/H I velocity-width relation: IV. The morphological type dependence and scatter in the relation; the distances to nearby groups, *Astrophysical Journal*, **265**, 1–17.
- Abell, G.O. (1958). The distribution of rich clusters of galaxies, *Astrophysical Journal Supplement*, **3**, 221–288.
- Abell, G.O. (1962). Membership of clusters of galaxies, in *Problems of Extragalactic Research*, ed. McVittie, G.C., pp. 213–238. New York: Macmillan.
- Abell, G.O., Corwin Jr, H.G., and Olowin, R.P. (1989). A catalogue of rich clusters of galaxies, *Astrophysical Journal Supplement*, **70**, 1–138.
- Abraham, R.G., Tanvir, N.R., Santiago, B., Ellis, R.S., Glazebrook, K., and van den Bergh, S. (1996). Galaxy morphology to $I = 25$ mag in the Hubble Deep Field, *Monthly Notices of the Royal Astronomical Society*, **279**, L47–L52.
- Adelberger, K.L. and Steidel, C.C. (2000). Multiwavelength observations of dusty star formation at low and high redshift, *Astrophysical Journal*, **544**, 218–241.
- Afonso, C., Albert, J.N., and 40 authors (2003). Limits on galactic dark matter with 5 years of EROS SMC data, *Astronomy and Astrophysics*, **400**, 951–956.
- Aharonian, F., Akhperjanian, A.G., Bazer-Bachi, A.R., Beilicke, M., Benbow, W., Berge, D., Bernlöhr, K., Boisson, C., Bolz, O., Borrel, V., Braun, I., Breitling, F., Brown, A.M., Chadwick, P.M., Chounet, L.-M., Cornils, R., Costamante, L., Degrange, B., Dickinson, H.J., Djannati-Ataï, A., Drury, L.O., Dubus, G., Emmanoulopoulos, D., Espigat, P., Feinstein, F., Fontaine, G., Fuchs, Y., Funk, S., Gallant, Y.A., Giebels, B., Gillessen, S., Glicenstein, J.F., Goret, P., Hadjichristidis, C., Hauser, D., Hauser, M., Heinzelmann, G., Henri, G., Hermann, G., Hinton, J.A., Hofmann, W., Holleran, M., Horns, D., Jacholkowska, A., de Jager, O.C., Khélifi, B., Klages, S., Komin, N., Konopelko, A., Latham, I.J., Le Gallou, R., Lemière, A., Lemoine-Goumard, M., Leroy, N., Lohse, T., Martin, J.M., Martineau-Huynh, O., Marcowith, A., Masterson, C., McComb, T.J.L., de Naurois, M., Nolan, S.J., Noutsos, A., Orford, K.J., Osborne, J.L., Ouchrif, M., Panter, M., Pelletier, G., Pita, S., Pühlhofer, G., Punch, M., Raubenheimer, B.C., Raue, M., Raux, J., Rayner, S.M., Reimer, A., Reimer, O., Ripken, J., Rob, L., Rolland, L., Rowell, G., Sahakian, V., Saugé, L., Schlenker, S., Schlickeiser, R., Schuster, C., Schwanke, U., Siewert, M., Sol, H., Spangler, D., Steenkamp, R., Stegmann, C., Tavernet, J.-P., Terrier, R., Théoret, C.G., Tluczykont, M., van Eldik, C., Vasileiadis, G., Venter, C., Vincent, P., Völk, H.J., and Wagner, S.J.

- (2006). A low level of extragalactic background light as revealed by γ -rays from blazars, *Nature*, **440**, 1018–1021.
- Akerib, D.S., Attisha, M.J., Bailey, C.N., Baudis, L., Bauer, D.A., Brink, P.L., Brusov, P.P., Bunker, R., Cabrera, B., Caldwell, D.O., Chang, C.L., Cooley, J., Crisler, M.B., Cushman, P., Daal, M., Dixon, R., Dragowsky, M.R., Driscoll, D.D., Duong, L., Ferril, R., Filippini, J., Gaitskell, R.J., Golwala, S.R., Grant, D.R., Hennings-Yeomans, R., Holmgren, D., Huber, M.E., Kamat, S., Leclercq, S., Lu, A., Mahapatra, R., Mandic, V., Meunier, P., Mirabolfathi, N., Nelson, H., Nelson, R., Ogburn, R.W., Perera, T.A., Pyle, M., Ramberg, E., Rau, W., Reisetter, A., Ross, R.R., Sadoulet, B., Sander, J., Savage, C., Schnee, R.W., Seitz, D.N., Serfass, B., Sundqvist, K.M., Thompson, J.-P.F., Wang, G., Yellin, S., Yoo, J., and Young, B.A. (2006). Limits on spin-independent interactions of weakly interacting massive particles with nucleons from the two-tower run of the cryogenic dark matter search, *Physical Review Letters*, **96**, 011302–+.
- Albrecht, A. and Steinhardt, P. (1982). Cosmology for grand unified theories with radiatively induced symmetry breaking, *Physical Review Letters*, **48**, 1220–1223.
- Alcock, C., Akerlof, C.W., Allsman, R.A., Axelrod, T.S., Bennett, D.P., Chan, S., Cook, K.H., Freeman, K.C., Griest, K., Marshall, S.L., Park, H.-S., Perlmutter, S., Peterson, B.A., Pratt, M.R., Quinn, P.J., Rogers, A.W., Stubbs, C.W., and Sutherland, W. (1993a). Possible gravitational microlensing of a star in the Large Magellanic Cloud, *Nature*, **365**, 621–623.
- Alcock, C., Allsman, R.A., Axelrod, T.S., Bennett, D.P., Cook, K.H., Park, H.-S., Marshall, S.L., Stubbs, C.W., Griest, K., Perlmutter, S., Sutherland, W., Freeman, K.C., Peterson, B.A., Quinn, P.J., and Rogers, A.W. (1993b). The MACHO Project – a Search for the Dark Matter in the Milky-Way, in *Sky Surveys: Protostars to Protogalaxies*, ed. Soifer, T., pp. 291–296. San Francisco: Astronomical Society of the Pacific Conference Series.
- Alcock, C., Allsman, R.A., Alves, D.R., Axelrod, T.S., Becker, A.C., Bennett, D.P., Cook, K.H., Dalal, N., Drake, A.J., Freeman, K.C., Geha, M., Griest, K., Lehner, M.J., Marshall, S.L., Minniti, D., Nelson, C.A., Peterson, B.A., Popowski, P., Pratt, M.R., Quinn, P.J., Stubbs, C.W., Sutherland, W., Tomaney, A.B., Vandehei, T., and Welch, D. (2000). The MACHO Project: microlensing results from 5.7 years of Large Magellanic Cloud observations, *Astrophysical Journal*, **542**, 281–307.
- Aliu, E., Andringa, S., Aoki, S., and colleagues (2005). Evidence for muon neutrino oscillation in an accelerator-based experiment, *Physical Review Letters*, **94**(8), 081802–+.
- Alpher, R.A. and Herman, R.C. (1948). Evolution of the Universe, *Nature*, **162**, 774–775.
- Alpher, R.A. and Herman, R.C. (1950). Theory of the origin and relative distribution of the elements, *Reviews of Modern Physics*, **22**, 153–212.
- Anders, E. (1963). Meteorite ages, in *The Moon, Meteorites and Comets – The Solar System IV*, eds. Middelhurst, B.M. and Kuiper, G.P., pp. 402–495. Chicago: University of Chicago Press.

- Aragòn-Salamanca, A., Ellis, R.S., Couch, W.J., and Carter, D. (1993). Evidence for systematic evolution in the properties of galaxies in distant clusters, *Monthly Notices of the Royal Astronomical Society*, **262**, 764–794.
- Arp, H.C. (1966). *Atlas of Peculiar Galaxies*. Pasadena: California Institute of Technology.
- Arp, H.C., Madore, B.F., and Roberton, W.E. (1987). *A Catalogue of Southern Peculiar Galaxies and Associations*. Cambridge: Cambridge University Press.
- Baade, W. (1926). Über eine Möglichkeit, die Pulsationstheorie der δ -Cephei-Veränderlichen zu Prüfen (On a Possible Method of Testing the Pulsation Theory of the Variations of δ -Cephei), *Astronomische Nachrichten*, **228**, 359–362.
- Babbedge, T.S.R., Rowan-Robinson, M., Vaccari, M., Surace, J.A., Lonsdale, C.J., Clements, D.L., Fang, F., Farrah, D., Franceschini, A., Gonzalez-Solares, E., Hatziminaoglou, E., Lacey, C.G., Oliver, S., Onyett, N., Pérez-Fournon, I., Polletta, M., Pozzi, F., Rodighiero, G., Shupe, D.L., Siana, B., and Smith, H.E. (2006). Luminosity functions for galaxies and quasars in the Spitzer Wide-area Infrared Extragalactic Legacy Survey, *Monthly Notices of the Royal Astronomical Society*, **370**, 1159–1180.
- Bahcall, N. (1997). Dark matter, in *Critical Dialogues in Cosmology*, ed. Turok, N., pp. 221–232. Singapore: World Scientific.
- Bahcall, N.A. (1977). Clusters of galaxies, *Annual Review of Astronomy and Astrophysics*, **15**, 505–540.
- Bahcall, N.A. (1988). Large-scale structure in the Universe indicated by galaxy clusters, *Annual Review of Astronomy and Astrophysics*, **26**, 631–686.
- Bahcall, N.A. (2000). Clusters and cosmology, *Physics Reports*, **333**, 233–244.
- Bahcall, N.A., Dong, F., Hao, L., Bode, P., Annis, J., Gunn, J.E., and Schneider, D.P. (2003a). The richness-dependent cluster correlation function: early Sloan Digital Sky Survey Data, *Astrophysical Journal*, **599**, 814–819.
- Bahcall, N.A., McKay, T.A., Annis, J., Kim, R.S.J., Dong, F., Hansen, S., Goto, T., Gunn, J.E., Miller, C., Nichol, R.C., Postman, M., Schneider, D., Schroeder, J., Voges, W., Brinkmann, J., and Fukugita, M. (2003b). A merged catalog of clusters of galaxies from early Sloan Digital Sky Survey data, *Astrophysical Journal Supplement*, **148**, 243–274.
- Bajtlik, S., Duncan, R.C., and Ostriker, J.P. (1988). Quasar ionization of Lyman-alpha clouds – the proximity effect, a probe of the ultraviolet background at high redshift, *Astrophysical Journal*, **327**, 570–583.
- Baldry, I.K., Glazebrook, K., Brinkmann, J., Ivezić, Z., Lupton, R.H., Nichol, R.C., and Szalay, A. (2004). Quantifying the bimodal color-magnitude distribution of galaxies, *Astrophysical Journal*, **600**, 681–694.
- Baldry, I.K., Glazebrook, K., Budavári, T., Eisenstein, D.J., Annis, J., Bahcall, N.A., Blanton, M.R., Brinkmann, J., Csabai, I., Heckman, T.M., Lin, H., Loveday, J., Nichol, R.C., and Schneider, D.P. (2005). The Sloan Digital Sky Survey u-band Galaxy Survey: luminosity functions and evolution, *Monthly Notices of the Royal Astronomical Society*, **358**, 441–456.

- Barcons, X. and Fabian, A.C. (1989). The small-scale autocorrelation function of the X-ray background, *Monthly Notices of the Royal Astronomical Society*, **237**, 119–127.
- Bardeen, J.M. (1980). Gauge-invariant cosmological perturbations, *Physical Review D*, **22**, 1882–1905.
- Bardeen, J.M., Bond, J.R., Kaiser, N., and Szalay, A.S. (1986). The statistics of peaks in Gaussian random fields, *Astrophysical Journal*, **304**, 15–61.
- Barger, A.J., Cowie, L.L., Smail, I., Ivison, R.J., Blain, A.W., and Kneib, J.-P. (1999). Redshift distribution of the faint submillimeter galaxy population, *Astronomical Journal*, **117**, 2656–2665.
- Barkats, D., Bischoff, C., Farese, P., Fitzpatrick, L., Gaier, T., Gundersen, J.O., Hedman, M.M., Hyatt, L., McMahon, J.J., Samtleben, D., Staggs, S.T., Vandervlinde, K., and Winstein, B. (2005). First measurements of the polarization of the cosmic microwave background radiation at small angular scales from CAPMAP, *Astrophysical Journal Letters*, **619**, L127–L130.
- Barnes, J. and Efstathiou, G. (1987). Angular momentum from tidal torques, *Astrophysical Journal*, **319**, 575–600.
- Barnes, J. and Hernquist, L. (1996). Transformations of galaxies. II. Gasdynamics in merging disk galaxies, *Astrophysical Journal*, **471**, 115–142.
- Barrow, J. and Tipler, F. (1986). *The Anthropic Cosmological Principle*. Oxford: Oxford University Press.
- Batuski, D.J., Bahcall, N.A., Olowin, R.P., and Burns, J.O. (1989). The distribution of clusters in the Southern ACO Catalog, *Astrophysical Journal*, **341**, 599–610.
- Baugh, C.M. (2006). A primer on hierarchical galaxy formation: the semi-analytical approach, *Reports of Progress in Physics*, **69**, 3101–3156.
- Baumann, D. (2007). On the quantum origin of structure in the inflationary universe, See <http://www.princeton.edu/~dbaumann/inflation.pdf>.
- Bautz, L. and Morgan, W.W. (1970). On the classification of the forms of clusters of galaxies, *Astrophysical Journal Letters*, **162**, L149–L153.
- Beaver, E., Burbidge, M., Cohen, R., Junkkarinen, V., Lyons, R., and Rosenblatt, E. (1992). Spectroscopy of QSOs with the Faint Object Spectrograph, in *Science with the Hubble Space Telescope*, eds. Benvenuti, P. and Schreier, E.J., pp. 53–60.
- Bechtold, J., Weymann, R.J., Lin, Z., and Malkan, M.A. (1987). The integrated ultraviolet radiation field from QSOs, *Astrophysical Journal*, **315**, 180–197.
- Beck, R., Brunetti, G., and Feretti, L. (2006). The origin and evolution of cosmic magnetism, in *Astronomische Nachrichten*, eds. Beck, R., Brunetti, G., and Feretti, L., volume 327, pp. 385–639. Weinheim: Wiley Interscience.
- Becker, R., Fan, X., and 29 authors (2001). Evidence for reionisation at $Z \sim 6$: detection of a Gunn–Peterson trough in a $Z = 6.28$ quasar, *Astronomical Journal*, **122**, 2850–2857.
- Beckwith, S.V.W., Stiavelli, M., Koekemoer, A.M., Caldwell, J.A.R., Ferguson, H.C., Hook, R., Lucas, R.A., Bergeron, L.E., Corbin, M., Jogee, S., Panagia, N., Robberto, M., Royle, P., Somerville, R.S., and Sosey, M. (2006). The Hubble Ultra Deep Field, *Astronomical Journal*, **132**, 1729–1755.

- Bell, E.F., McIntosh, D.H., Katz, N., and Weinberg, M.D. (2003). The optical and near-infrared properties of galaxies: I. Luminosity and stellar mass functions, *Astrophysical Journal Supplement Series*, **149**, 289–312.
- Bender, R., Burstein, D., and Faber, S.M. (1993). Dynamically hot galaxies: II. Global stellar populations, *Astrophysical Journal*, **411**, 153–169.
- Bennett, C., Halpern, M., Hinshaw, G., Jarosik, N., Kogut, A., Limon, M., Meyer, S., Page, L., Spergel, D., Tucker, G., Wollack, E., Wright, E., Barnes, C., Greason, M., Hill, R., Komatsu, E., Nolta, M., Odegard, N., Peiris, H., Verde, L., and Weiland, J. (2003). First-year Wilkinson Microwave Anisotropy Probe (WMAP) observations: preliminary maps and basic results, *Astrophysical Journal Supplement Series*, **148**, 1–27.
- Bennett, C.L., Banday, A.J., Gorski, K.M., Hinshaw, G., Jackson, P., Koegstra, P., Kogut, A., Smoot, G.F., Wilkinson, D.T., and Wright, E.L. (1996). Four-year COBE DMR cosmic microwave background observations: maps and basic results, *Astrophysical Journal*, **464**, L1–L4.
- Benson, A.J., Frenk, C.S., Baugh, C.M., Cole, S., and Lacey, C.G. (2001). The clustering evolution of the galaxy distribution, *Monthly Notices of the Royal Astronomical Society*, **327**, 1041–1056.
- Benson, B.A., Church, S.E., Ade, P.A.R., Bock, J.J., Ganga, K.M., Henson, C.N., and Thompson, K.L. (2004). Measurements of Sunyaev–Zel'dovich effect scaling relations for clusters of galaxies, *Astrophysical Journal*, **617**, 829–846.
- Bergeron, J. (1988). Properties of the heavy-element absorption systems, in *QSO Absorption Lines: Probing the Universe*, eds. Blades, J., Turnshek, D., and Norman, C., pp. 127–143. Cambridge: Cambridge University Press.
- Bergeron, J. (2006). Cosmic star formation history: high redshift galaxies and black holes, in *Scientific Requirements for Extremely Large Telescopes: IAU Symposium No. 232*, eds. Whitelock, P., Dennefeld, M., and Leibundgut, B., pp. 159–170. Cambridge: Cambridge University Press.
- Bernstein, G., Fischer, P., Tyson, J.A., and Rhee, G. (1997). Improved parameters and new lensed features for Q0957+561 from WFPC2 imaging, *Astrophysical Journal*, **483**, L79–L82.
- Bernstein, J. and Feinberg, G. (1986). *Cosmological Constants: Papers in Modern Cosmology*. New York: Columbia University Press.
- Berry, M. (1989). *Principles of Cosmology and Gravitation*. Bristol: Adam Hilger.
- Bertola, F., Bettoni, D., Danziger, J., Sadler, E., Spark, L., and de Zeeuw, T. (1991). Testing the gravitational field in elliptical galaxies: NGC 5077, *Astrophysical Journal*, **373**, 369–390.
- Bertola, F. and Capaccioli, M. (1975). Dynamics of early type galaxies: I. The rotation curve of the elliptical galaxy NGC 4697, *Astrophysical Journal*, **200**, 439–445.
- Bertola, F. and Galletta, G. (1979). Ellipticity and twisting of isophotes in elliptical galaxies, *Astronomy and Astrophysics*, **77**, 363–365.
- Bertotti, B., Iess, L., and Tortora, P. (2003). A Test of general relativity using radio links with the Cassini spacecraft, *Nature*, **425**, 374–376.

- Bertschinger, E. (1996). Cosmological dynamics, in *Cosmology and Large Scale Structure: Proceedings of the “Les Houches Ecole d’Ete de Physique Theorique”*, eds. Schaeffer, R., Silk, J., Spiro, M., and Zinn-Justin, J., pp. 273–346. Amsterdam: Elsevier.
- Best, P.N., Longair, M.S., and Röttrung, H.J.A. (1996). Evolution of the aligned structures in $z \sim 1$ radio galaxies, *Monthly Notices of the Royal Astronomical Society*, **280**, L9–L12.
- Best, P.N., Longair, M.S., and Röttrung, H.J.A. (1998). HST, radio and infrared observations of 28 3CR radio galaxies at redshift z approximately equal to 1: II. Old stellar populations in central cluster galaxies, *Monthly Notices of the Royal Astronomical Society*, **295**, 549–567.
- Best, P.N., Longair, M.S., and Röttrung, H.J.A. (2000). Ionization, shocks and evolution of the emission-line gas of distant 3CR radio galaxies, *Monthly Notices of the Royal Astronomical Society*, **311**, 23–36.
- Biermann, L. (1950). On the Origin of Magnetic Fields on Stars and in Interstellar Space, *Zeitschrift für Naturforschung*, **5a**, 65–71.
- Binggeli, B., Sandage, A., and Tammann, A. (1988). The luminosity function of galaxies, *Annual Review of Astronomy and Astrophysics*, **26**, 509–560.
- Binggeli, B., Tammann, G.A., and Sandage, A. (1987). Studies of the Virgo Cluster: VI. Morphological and kinematical structure of the Virgo Cluster, *Astronomical Journal*, **94**, 251–277.
- Binney, J. and Merrifield, M. (1998). *Galactic Astronomy*. Princeton: Princeton University Press.
- Binney, J. and Tremaine, S. (1987). *Galactic Dynamics*. Princeton: Princeton University Press.
- Birkinshaw, M. (1990). Observations of the Sunyaev–Zeldovich effect, in *The Cosmic Microwave Background: 25 Years Later*, eds. Mandolesi, N. and Vittorio, N., pp. 77–94. Dordrecht: Kluwer.
- Blain, A.W., Ivison, R.J., and Smail, I. (1998). Observational limits to source confusion in the millimetre/submillimetre waveband, *Monthly Notices of the Royal Astronomical Society*, **296**, L29–L33.
- Blain, A.W. and Longair, M.S. (1993). Sub-millimetre cosmology, *Monthly Notices of the Royal Astronomical Society*, **264**, 509–521.
- Blain, A.W. and Longair, M.S. (1996). Observing strategies for blank-field surveys in the sub-millimetre waveband, *Monthly Notices of the Royal Astronomical Society*, **279**, 847–858.
- Blandford, R.D. and Narayan, R. (1992). Cosmological applications of gravitational lensing, *Annual Review of Astronomy and Astrophysics*, **30**, 311–358.
- Blanton, M., Hogg, D., Bahcall, N., Brinkmann, J., Britton, M., Connolly, A., Csabai, I., Fukugita, M., Loveday, J., Meiksin, A., Munn, J., Nichol, R., Okamura, S., Quinn, T., Schneider, D., Shimasaku, K., Strauss, M., Tegmark, M., Vogeley, M., and Weinberg, D. (2003). The galaxy luminosity function and luminosity density at redshift $z = 0.1$, *Astrophysical Journal*, **592**, 819–838.
- Blanton, M.R., Hogg, D.W., Bahcall, N.A., Baldry, I.K., Brinkmann, J., Csabai, I., Eisenstein, D., Fukugita, M., Gunn, J.E., Ivezić, Ž., Lamb, D.Q., Lupton, R.H.,

- Loveday, J., Munn, J.A., Nichol, R.C., Okamura, S., Schlegel, D.J., Shimasaku, K., Strauss, M.A., Vogeley, M.S., and Weinberg, D.H. (2003). The broadband optical properties of galaxies with redshifts $0.02 \leq z \leq 0.22$, *Astrophysical Journal*, **594**, 186–207.
- Blanton, M.R., Lupton, R.H., Schlegel, D.J., Strauss, M.A., Brinkmann, J., Fukugita, M., and Loveday, J. (2005). The properties and luminosity function of extremely low luminosity galaxies, *Astrophysical Journal*, **631**, 208–230.
- Bludman, S. and Ruderman, M. (1977). Induced cosmological constant expected above the phase transition restoring the broken symmetry, *Physical Review Letters*, **38**, 255–257.
- Blumenthal, G.R., Faber, S.M., Primack, J.R., and Rees, M.J. (1984). Formation of galaxies and large-scale structure with cold dark matter, *Nature*, **311**, 517–525.
- Bochkarev, N.G. and Sunyaev, R.A. (1977). Ionizing background radiation and the hydrogen at the periphery of galaxies, *Soviet Astronomy*, **21**, 542–547.
- Böhringer, H., Schuecker, P., Guzzo, L., Collins, C.A., Voges, W., Schindler, S., Neumann, D.M., Crudace, R.G., De Grandi, S., Chincarini, G., Edge, A.C., MacGillivray, H.T., and Shaver, P. (2001). The ROSAT-ESO flux limited X-ray (REFLEX) galaxy cluster survey. I. The construction of the cluster sample, *Astronomy and Astrophysics*, **369**, 826–850.
- Böhringer, H., Voges, W., Huchra, J.P., McLean, B., Giacconi, R., Rosati, P., Burg, R., Mader, J., Schuecker, P., Simić, D., Komossa, S., Reiprich, T.H., Retzlaff, J., and Trümper, J. (2000). The Northern ROSAT All-Sky (NORAS) Galaxy Cluster Survey: I. X-Ray properties of clusters detected as extended X-ray sources, *Astrophysical Journal Supplement*, **129**, 435–474.
- Boksenberg, A. (1997). Quasar absorption lines: reflections and views, in *The Hubble Space Telescope and the High Redshift Universe*, eds. Tanvir, N., Aragón-Salamanca, A., and Wall, J., pp. 283–294. Singapore: World Scientific.
- Bolte, M. (1997). Globular clusters: old, in *Critical Dialogues in Cosmology*, ed. Turok, N., pp. 156–168. Singapore: World Scientific.
- Bolyai, J. (1832). Appendix: Scientiam Spatii Absolute Veritam Exhibens (Appendix Explaining the Absolutely True Science of Space). published as an appendix to the essay by his father F. Bolyai, *An Attempt to Introduce Studious Youth to the Elements of Pure Mathematics*. Maros Vásárhely, Transylvania.
- Bonamente, M., Joy, M.K., LaRoque, S.J., Carlstrom, J.E., Reese, E.D., and Dawson, K.S. (2006). Determination of the cosmic distance scale from Sunyaev–Zel'dovich effect and Chandra X-ray measurements of high-redshift galaxy clusters, *Astrophysical Journal*, **647**, 25–54.
- Bond, J.R. and Efstathiou, G. (1984). Cosmic background radiation anisotropies in universes dominated by nonbaryonic dark matter, *Astrophysical Journal Letters*, **285**, L45–L48.
- Bond, J.R. and Efstathiou, G. (1991). The formation of cosmic structure with a 17 keV neutrino, *Physics Letters B*, **265**, 245–250.
- Bond, J.R. and Szalay, A.S. (1983). The collisionless damping of density fluctuations in the expanding Universe, *Astrophysical Journal*, **274**, 443–468.
- Bondi, H. (1960). *Cosmology*, 2nd edn. Cambridge: Cambridge University Press.

- Borgani, S. and Guzzo, L. (2001). X-ray clusters of galaxies as tracers of structure in the Universe, *Nature*, **409**, 39–45.
- Bosma, A. (1981). 21-cm line studies of spiral galaxies: II. The distribution and kinematics of neutral hydrogen in spiral galaxies of various morphological types, *Astronomical Journal*, **86**, 1825–1846.
- Bouwens, R.J., Illingworth, G.D., Blakeslee, J.P., (Broadhurst), T., and Franx, M. (2004). Galaxy size evolution at high redshift and surface brightness selection effects: constraints from the Hubble Ultra Deep Field, *Astrophysical Journal*, **611**, L1–L4.
- Bouwens, R.J., Illingworth, G.D., Blakeslee, J.P., and Franx, M. (2006). Galaxies at $z \sim 6$: the UV luminosity function and luminosity density from 506 HUDF, HUDF Parallel ACS Field, and GOODS i-Dropouts, *Astrophysical Journal*, **653**, 53–85.
- Boyle, B.J., Shanks, T., Croom, S.M., Smith, R.J., Miller, L., Loaring, N., and Heymans, C. (2000). The 2dF QSO Redshift Survey: I. The optical luminosity function of quasi-stellar objects, *Monthly Notices of the Royal Astronomical Society*, **317**, 1014–1022.
- Bracessi, A., Formiggini, L., and Gandolfi, E. (1970). Magnitudes, colours and coordinates of 175 ultraviolet excess objects in the field 13^{h} , $+36^{\circ}$, *Astronomy and Astrophysics*, **5**, 264–279. Erratum: *Astronomy and Astrophysics*, **23**, 159.
- Bracewell, R. (1986). *The Fourier Transform and Its Applications*. New York: McGraw-Hill.
- Brainerd, T.G., Blandford, R.D., and Smail, I. (1996). Weak gravitational lensing by galaxies, *Astrophysical Journal*, **466**, 623–637.
- Branch, D. and Patchett, B. (1973). Type I supernovae, *Monthly Notices of the Royal Astronomical Society*, **161**, 71–83.
- Branch, D. and Tammann, G.A. (1992). Type I supernovae as standard candles, *Annual Review of Astronomy and Astrophysics*, **30**, 359–389.
- Brandt, W.N. and Hasinger, G. (2005). Deep extragalactic X-ray surveys, *Annual Review of Astronomy and Astrophysics*, **43**, 827–859.
- Brentjens, M.A. and de Bruyn, A.G. (2006). RM-synthesis of the Perseus cluster, *Astronomische Nachrichten*, **327**, 545–551.
- Bridle, A.H. (1967). The spectrum of the radio background between 13 and 404 MHz, *Monthly Notices of the Royal Astronomical Society*, **136**, 219–240.
- Bruni, M., Dunsby, P.K.S., and Ellis, G.F.R. (1992). Cosmological perturbations and the physical meaning of gauge-invariant variables, *Astrophysical Journal*, **395**, 34–53.
- Bruzual, G. and Charlot, S. (2003). Stellar population synthesis at the resolution of 2003, *Monthly Notices of the Royal Astronomical Society*, **344**, 1000–1028.
- Burbidge, E., Burbidge, G., Fowler, W., and Hoyle, F. (1957). Synthesis of the elements in stars, *Reviews of Modern Physics*, **29**, 547–650.
- Butcher, H. and Oemler, Jr., A. (1978). The evolution of galaxies in clusters: I. ISIT Photometry of C1 0024+1654 and 3C 295, *Astrophysical Journal*, **219**, 18–30.
- Butcher, H. and Oemler, Jr., A. (1984). The evolution of galaxies in clusters: V. A study of populations since $z \approx 0.5$, *Astrophysical Journal*, **285**, 426–438.

- Cappelluti, N., Hasinger, G., Brusa, M., Comastri, A., Zamorani, G., Boehringer, H., Brunner, H., Civano, F., Finoguenov, A., Fiore, F., Gilli, R., Griffiths, R.E., Mainieri, V., Matute, I., Miyaji, T., and Silverman, J. (2007). The XMM-Newton wide-field survey in the COSMOS field II: X-ray data and the $\log N$ - $\log S$, *ArXiv Astrophysics e-prints*.
- Carlstrom, J.E., Joy, M.K., Grego, L., Holder, G.P., Holzapfel, W.L., Mohr, J.J., Patel, S., and Reese, E.D. (2000). Imaging the Sunyaev-Zel'dovich effect, in *Particle Physics and the Universe: Proceedings of Nobel Symposium 198*, eds. Bergström, L., Carlson, P., and Fransson, C., pp. 148–155. Stockholm: Physica Scripta.
- Carroll, S.M., Press, W.H., and Turner, E.L. (1992). The cosmological constant, *Annual Review of Astronomy and Astrophysics*, **30**, 499–542.
- Carswell, R.F. (1988). Properties of the Ly-alpha clouds, in *QSO Absorption Lines: Probing the Universe*, eds. Blades, J.C., Turnshek, D., and Norman, C.A., pp. 91–100. Cambridge: Cambridge University Press.
- Carswell, R.F., Whelan, J.A.J., Smith, M.G., Boksenberg, A., and Tytler, D. (1982). Observations of the spectra of Q0122-380 and Q1101-264, *Monthly Notices of the Royal Astronomical Society*, **198**, 91–110.
- Carter, B. (1974). Large number coincidences and the anthropic principle in cosmology, in *Confrontation of Cosmological Theories with Observational Data, IAU Symposium No. 63*, ed. Longair, M., pp. 291–298. Dordrecht: Reidel.
- Cavaliere, A. (1980). Models of X-ray Emission from Clusters of Galaxies, in *X-ray Astronomy*, eds. Giacconi, R. and Setti, G., pp. 217–237. Dordrecht: Reidel.
- Chaboyer, B. (1998). The age of the Universe, *Physics Reports*, **307**, 23–30.
- Chae, K.-H., Biggs, A.D., Blandford, R.D., Browne, I.W., de Bruyn, A.G., Fassnacht, C.D., Helbig, P., Jackson, N.J., King, L.J., Koopmans, L.V., Mao, S., Marlow, D.R., McKean, J.P., Myers, S.T., Norbury, M., Pearson, T.J., Phillips, P.M., Readhead, A.C., Rusin, D., Sykes, C.M., Wilkinson, P.N., Xanthopoulos, E., and York, T. (2002). Constraints on cosmological parameters from the analysis of the cosmic lens all sky survey radio-selected gravitational lens statistics, *Physical Review Letters*, **89**, 151301–.
- Challinor, A. (2005). Cosmic microwave background anisotropies, in *Lecture Notes in Physics Vol. 653: The Physics of the Early Universe*, ed. Tamvakis, K., vol. 653, pp. 71–+. Berlin: Springer.
- Challinor, A. and Lasenby, A. (1998). Relativistic corrections to the Sunyaev–Zeldovich effect, *Astrophysical Journal*, **499**, 1–6.
- Chambers, K.C., Miley, G.K., and van Breugel, W.J.M. (1987). Alignment of radio and optical orientations in high-redshift radio galaxies, *Nature*, **329**, 604–606.
- Chapman, S.C., Blain, A.W., Smail, I., and Ivison, R.J. (2005). A redshift survey of the submillimeter galaxy population, *Astrophysical Journal*, **622**, 772–796.
- Charlot, S. and Longhetti, M. (2001). Nebular emission from star-forming galaxies, *Monthly Notices of the Royal Astronomical Society*, **323**, 887–903.
- Chluba, J. and Sunyaev, R.A. (2006). Induced two-photon decay of the 2s level and the rate of cosmological hydrogen recombination, *Astronomy and Astrophysics*, **446**, 39–42.

- Chwolson, O. (1924). Über eine mögliche Form fiktiver Doppelsterne, *Astronomische Nachrichten*, **221**, 329–330.
- Cimatti, A., Daddi, E., Renzini, A., Cassata, P., Vanzella, E., Pozzetti, L., Cristiani, S., Fontana, A., Rodighiero, G., Mignoli, M., and Zamorani, G. (2004). Old galaxies in the young Universe, *Nature*, **430**, 184–187.
- Close, L.M., Hall, P.B., Liu, M.C., and Hege, E.K. (1995). Spectroscopic and morphological evidence that IRAS FSC 10214+4724 is a gravitational lens, *Astrophysical Journal*, **452**, L9–L12.
- Cole, S., Percival, W.J., Peacock, J.A., Norberg, P., Baugh, C.M., Frenk, C.S., Baldry, I., Bland-Hawthorn, J., Bridges, T., Cannon, R., Colless, M., Collins, C., Couch, W., Cross, N.J.G., Dalton, G., Eke, V.R., De Propris, R., Driver, S.P., Efstathiou, G., Ellis, R.S., Glazebrook, K., Jackson, C., Jenkins, A., Lahav, O., Lewis, I., Lumsden, S., Maddox, S., Madgwick, D., Peterson, B.A., Sutherland, W., and Taylor, K. (2005). The 2dF Galaxy Redshift Survey: power-spectrum analysis of the final data set and cosmological implications, *Monthly Notices of the Royal Astronomical Society*, **362**, 505–534.
- Coles, P. (2001). Einstein, Eddington and the 1919 Eclipse, in *Historical Development of Modern Cosmology*, eds. Martínez, V.J., Trimble, V., and Pons-Bordeña, M.J., pp. 21–41. San Francisco: ASP Conference Series, No. 252.
- Coles, P. and Lucchin, F. (1995). *Cosmology – the Origin and Evolution of Cosmic Structure*. Chichester: Wiley.
- Coles, P., Melott, A.L., and Shandarin, S.F. (1993). Testing approximations for non-linear gravitational clustering, *Monthly Notices of the Royal Astronomical Society*, **260**, 765–776.
- Colless, M., Dalton, G., Maddox, S., Sutherland, W., Norberg, P., Cole, S., Bland-Hawthorn, J., Bridges, T., Cannon, R., Collins, C., Couch, W., Cross, N., Deely, K., De Propris, R., Driver, S.P., Efstathiou, G., Ellis, R.S., Frenk, C.S., Glazebrook, K., Jackson, C., Lahav, O., Lewis, I., Lumsden, S., Madgwick, D., Peacock, J.A., Peterson, B.A., Price, I., Seaborne, M., and Taylor, K. (2001). The 2dF Galaxy Redshift Survey: spectra and redshifts, *Monthly Notices of the Royal Astronomical Society*, **328**, 1039–1063.
- Colless, M. and Dunn, A.M. (1996). Structure and dynamics of the Coma cluster, *Astrophysical Journal*, **458**, 435–454.
- Connolly, A., Scranton, R., Johnston, D., Dodelson, S., Eisenstein, D., Friedman, J., Gunn, J., Hui, L., Jain, B., Kent, S., Loveday, J., Nichol, R., O’Connell, L., Postman, M., Scoccimarro, R., Sheth, R., Stebbins, A., Strauss, M., Szalay, A., Szapudi, I., Tegmark, M., Vogeley, M., Zehavi, I., Annis, J., Bahcall, N., Brinkmann, J., Csabai, I., Doi, M., Fukugita, M., Hennessy, G., Hindsley, R., Ichikawa, T., Ivezić, Z., Kim, R., Knapp, G., Kunszt, P., Lamb, D., Lee, B., Lupton, R., McKay, T., Munn, J., Peoples, J., Pier, J., Rockosi, C., Schlegel, D., Stoughton, C., Tucker, D., Yanny, B., and York, D. (2002). The angular correlation function of galaxies from early Sloan Digital Sky Survey data, *Astrophysical Journal*, **579**, 42–47.
- Copi, C.J., Davis, A.N., and Krauss, L.M. (2004). New nucleosynthesis constraint on the variation of G, *Physical Review Letters*, **92**, 171301, 1–3.

- Corbelli, E. and Salpeter, E.E. (1993). Sharp HI edges in the outskirts of disk galaxies, *Astrophysical Journal*, **419**, 104–110.
- Costa, E., Frontera, F., Heise, J., Feroci, M., in 't Zand, J., Fiore, F., Cinti, M.N., dal Fiume, D., Nicastro, L., Orlandini, M., Palazzi, E., Rapisarda, M., Zavattini, G., Jager, R., Parmar, A., Owens, A., Molendi, S., Cusumano, G., Maccarone, M.C., Giarrusso, S., Coletta, A., Antonelli, L.A., Giommi, P., Muller, J.M., Piro, L., and Butler, R.C. (1997). Discovery of an X-ray afterglow associated with the gamma-ray burst of 28 February 1997, *Nature*, **387**, 783–785.
- Côté, P., McLaughlin, D.E., Cohen, J.G., and Blakeslee, J.P. (2003). Dynamics of the globular cluster system associated with M49 (NGC 4472): cluster orbital properties and the distribution of dark matter, *Astrophysical Journal*, **591**, 850–877.
- Côté, P., McLaughlin, D.E., Hanes, D.A., Bridges, T.J., Geisler, D., Merritt, D., Hesser, J.E., Harris, G.L.H., and Lee, M.G. (2001). Dynamics of the globular cluster system associated with M87 (NGC 4486): II. Analysis, *Astrophysical Journal*, **559**, 828–850.
- Cowan, J.J., Thielemann, F.K., and Truran, J.W. (1991). Radioactive dating of the elements, *Annual Review of Astronomy and Astrophysics*, **29**, 447–497.
- Cowie, L. (1988). Protogalaxies, in *The Post-Recombination Universe*, eds. Kaiser, N. and Lasenby, A.N., pp. 1–18. Dordrecht: Kluwer.
- Cowie, L., Lilly, S., Gardner, J., and McLean, I. (1988). A cosmologically significant population of galaxies dominated by very young star formation, *Astrophysical Journal*, **332**, L29–L32.
- Cowie, L.L., Barger, A.J., and Kneib, J.-P. (2002). Faint submillimeter counts from deep 850 micron observations of the lensing clusters A370, A851, and A2390, *Astronomical Journal*, **123**, 2197–2205.
- Cowie, L.L., Songaila, A., Hu, E.M., and Cohen, J.D. (1996). New insight on galaxy formation and evolution from Keck spectroscopy of the Hawaii deep fields, *Astronomical Journal*, **112**, 839–864.
- Cress, C., Helfand, D., Becker, R., Gregg, M., and White, R. (1996). The angular two-point correlation function for the FIRST Radio Survey, *Astrophysical Journal*, **473**, 7–14.
- Crittenden, R., Bond, R., Davis, R.L., Efstathiou, G., and Steinhardt, P.J. (1993). Imprint of gravitational waves on the cosmic microwave background, *Physical Review Letters*, **71**, 324–327.
- Croom, S.M., Boyle, B.J., Shanks, T., Smith, R.J., Miller, L., Outram, P.J., Loaring, N.S., Hoyle, F., and da Ângela, J. (2005). The 2dF QSO Redshift Survey: XIV. Structure and evolution from the two-point correlation function, *Monthly Notices of the Royal Astronomical Society*, **356**, 415–438.
- Croton, D.J., Farrar, G.R., Norberg, P., Colless, M., Peacock, J.A., Baldry, I.K., Baugh, C.M., Bland-Hawthorn, J., Bridges, T., Cannon, R., Cole, S., Collins, C., Couch, W., Dalton, G., De Propris, R., Driver, S.P., Efstathiou, G., Ellis, R.S., Frenk, C.S., Glazebrook, K., Jackson, C., Lahav, O., Lewis, I., Lumsden, S., Maddox, S., Madgwick, D., Peterson, B.A., Sutherland, W., and Taylor, K. (2005). The 2dF Galaxy Redshift Survey: luminosity functions by density environment

- and galaxy type, *Monthly Notices of the Royal Astronomical Society*, **356**, 1155–1167.
- Dashevsky, V.M. and Zeldovich, Y.B. (1964). Propagation of light in a nonhomogeneous non-flat Universe II, *Astronomicheskii Zhurnal*, **41**, 1071–1074. Translation: (1965), *Soviet Astronomy*, **8**, 854–856.
- Davidsen, A.F. (1993). Far-ultraviolet astronomy on the Astro-1 space shuttle mission, *Science*, **259**, 327–334.
- Davidsen, A.F., Kriss, G.A., and Zheng, W. (1996). Measurement of the opacity of ionized helium in the intergalactic medium, *Nature*, **380**, 47–49.
- Davidson, W. and Davies, M. (1964). Interpretation of the counts of radio sources in terms of a 4-parameter family of evolutionary universes, *Monthly Notices of the Royal Astronomical Society*, **127**, 241–255.
- Davies, R.L., Efstathiou, G., Fall, S.M., Illingworth, G., and Schechter, P.L. (1983). The kinematic properties of faint elliptical galaxies, *Astrophysical Journal*, **266**, 41–57.
- Davis, M., Efstathiou, G., Frenk, C., and White, S.D.M. (1985). The evolution of large-scale structure in a universe dominated by cold dark matter, *Astrophysical Journal*, **292**, 371–394.
- Davis, M., Efstathiou, G., Frenk, C., and White, S.D.M. (1992a). The end of cold dark matter?, *Nature*, **356**, 489–494.
- Davis, M., Geller, M.J., and Huchra, J. (1978). The local mean mass density of the Universe – new methods for studying galaxy clustering, *Astrophysical Journal*, **221**, 1–18.
- Davis, M. and Peebles, P.J.E. (1983). A survey of galaxy redshifts: V. The two-point position and velocity correlations, *Astrophysical Journal*, **267**, 465–482.
- Davis, R.L., Hodges, H.M., Smoot, G.F., Steinhardt, P.J., and Turner, M.S. (1992b). Cosmic microwave background probes models of inflation, *Physical Review Letters*, **69**, 1856–1859.
- Davis, T.M. and Lineweaver, C.H. (2004). Expanding confusion: common misconceptions of cosmological horizons and the superluminal expansion of the universe, *Publications of the Astronomical Society of Australia*, **21**, 97–109.
- de Plaa, J., Kaastra, J.S., Méndez, M., Tamura, T., Bleeker, J.A.M., Peterson, J.R., Paerels, F.B.S., Bonamente, M., and Lieu, R. (2005). The temperature structure in the core of Sérsic 159-03, *Advances in Space Research*, **36**, 601–604.
- de Sitter, W. (1917). On Einstein's theory of gravitation and its astronomical consequences, *Monthly Notices of the Royal Astronomical Society*, **78**, 3–28.
- de Vaucouleurs, G. (1948). Recherches sur les nébuleuses extragalactiques, *Annales d'Astrophysique*, **11**, 247–287.
- de Vaucouleurs, G. (1963). Revised classification of 1500 bright galaxies, *Astrophysical Journal Supplement*, **8**, 31–97.
- de Vaucouleurs, G. (1974). Structure, dynamics and statistical properties of galaxies (invited paper), in *The Formation and Dynamics of Galaxies*, IAU Symposium No. 58, ed. Shakeshaft, J.R., pp. 1–53. Dordrecht: Reidel.

- de Vaucouleurs, G., de Vaucouleurs, A., Corwin Jr., H.G., Buta, R.J., Paturel, G., and Fouque, P. (1991). *Third reference catalogue of bright galaxies: containing information on 23,024 galaxies with reference to papers published between 1913 and 1988*. Berlin: Springer.
- Dekel, A. (1986). Biased galaxy formation, *Comments on Astrophysics*, **11**, 235–256.
- Dekel, A., Burstein, D., and White, S. (1997). Measuring omega, in *Critical Dialogues in Cosmology*, ed. Turok, N., pp. 175–194. Singapore: World Scientific.
- Dekel, A. and Rees, M.J. (1987). Physical mechanisms for biased galaxy formation, *Nature*, **326**, 455–462.
- Dessauges-Zavadsky, M., Prochaska, J.X., DOdorico, S., Calura, F., and Matteucci, F. (2006). A new comprehensive set of elemental abundances in DLAs: II. Data analysis and chemical variation studies, *Astronomy and Astrophysics*, **445**, 93–113.
- Dey, A. (1997). The host galaxies of distant radio sources, in *The Hubble Space Telescope and the High Redshift Universe*, eds. Tanvir, N.R., Aragón-Salamanca, A., and Wall, J.V., pp. 373–376. Singapore: World Scientific.
- Dicke, R. (1961). Dirac's cosmology and Mach's principle, *Nature*, **192**, 440–441.
- Dicke, R. and Peebles, P. (1979). Big Bang cosmology – enigmas and nostrums, in *General Relativity: an Einstein Centenary Survey*, eds. Hawking, S. and Israel, W., pp. 504–517. Cambridge: Cambridge University Press.
- Dickinson, C., Battye, R.A., Carreira, P., Cleary, K., Davies, R.D., Davis, R.J., Genova-Santos, R., Grainge, K., Gutiérrez, C.M., Hafez, Y.A., Hobson, M.P., Jones, M.E., Kneissl, R., Lancaster, K., Lasenby, A., Leahy, J.P., Maisinger, K., Ödman, C., Pooley, G., Rajguru, N., Rebolo, R., Rubiño-Martin, J.A., Saunders, R.D.E., Savage, R.S., Scaife, A., Scott, P.F., Slosar, A., Sosa Molina, P., Taylor, A.C., Titterington, D., Waldram, E., Watson, R.A., and Wilkinson, A. (2004). High-sensitivity measurements of the cosmic microwave background power spectrum with the extended Very Small Array, *Monthly Notices of the Royal Astronomical Society*, **353**, 732–746.
- Dickinson, M. (1997). Clusters of galaxies at $z \geq 1$, in *The Hubble Space Telescope and the High Redshift Universe*, eds. Tanvir, N., Aragón-Salamanca, A., and Wall, J., pp. 207–218. Singapore: World Scientific.
- d'Inverno, R. (1992). *Introducing Einstein's Relativity*. Oxford: Clarendon.
- Disney, M.J. (1976). Visibility of galaxies, *Nature*, **263**, 573–575.
- Djorgovski, S.G. and Davis, M. (1987). Fundamental properties of elliptical galaxies, *Astrophysical Journal*, **313**, 59–68.
- Dodelson, S. (2003). *Modern Cosmolgy*. Amsterdam: Academic.
- Dodelson, S., Gates, E.I., and Turner, M.S. (1996). Cold dark matter, *Science*, **274**, 69–75.
- Doroshkevich, A., Sunyaev, R., and Zeldovich, Y. (1974). The formation of galaxies in Friedmannian universes, in *Confrontation of Cosmological Theories with Observational Data, (IAU Symposium No. 63)*, ed. Longair, M., pp. 213–225. Dordrecht: Reidel.
- Doroshkevich, A., Zeldovich, Y., Sunyaev, R., and Khlopov, M. (1980). Astrophysical Implications of the Neutrino Rest Mass: Part II. The density-perturbation

- spectrum and small-scale fluctuations in the microwave background, *Pis'ma v Astronomicheskii Zhurnal*, **6**, 457–464.
- Dressler, A. (1980). Galaxy morphology in rich clusters – implications for the formation and evolution of galaxies, *Astrophysical Journal*, **236**, 351–365.
- Dressler, A. (1984). The evolution of galaxies in clusters, *Annual Review of Astronomy and Astrophysics*, **22**, 185–222.
- Dressler, A., Lynden-Bell, D., Burstein, D., Davies, R.L., Faber, S.M., Terlevich, R., and Wegner, G. (1987). Spectroscopy and photometry of elliptical galaxies: I. A new distance estimator, *Astrophysical Journal*, **313**, 42–58.
- Dressler, A., Oemler, A.J., Couch, W.J., Smail, I., Ellis, R.G., Barger, A., Butcher, H., Poggianti, B.M., and Sharples, R.M. (1997). Evolution since $z = 0.5$ of the morphology-density relation for clusters of galaxies, *Astrophysical Journal*, **490**, 577–591.
- Dressler, A. and Smail, I. (1997). HST observations of distant clusters: implications for galaxy evolution, in *The Hubble Space Telescope and the High Redshift Universe*, eds. Tanvir, N., Aragón-Salamanca, A., and Wall, J., pp. 185–194. Singapore: World Scientific.
- Driver, S.P., Allen, P.D., Graham, A.W., Cameron, E., Liske, J., Ellis, S.C., Cross, N.J.G., De Propris, R., Phillipps, S., and Couch, W. (2006). The Millennium Galaxy Catalogue: morphological classification and bimodality in the colour-concentration plane, *Monthly Notices of the Royal Astronomical Society*, **368**, 414–434.
- Dunlop, J.S. (1998). Cosmic star-formation and radio source evolution, in *ASSL Vol. 226: Observational Cosmology with the New Radio Surveys*, eds. Bremer, M.N., Jackson, N., and Perez-Fournon, I., pp. 157–164. Dordrecht: Kluwer Academic Publishers.
- Dunlop, J.S. and Peacock, J.A. (1990). The redshift cut-off in the luminosity function of radio galaxies and quasars, *Monthly Notices of the Royal Astronomical Society*, **247**, 19–42.
- Dunlop, J.S., Peacock, J.A., Spinrad, H., Dey, A., Jimenez, R., Stern, D., and Windhorst, R. (1996). A 3.5-Gyr-old galaxy at redshift 1.55, *Nature*, **381**, 581–584.
- Dyer, C.C. and Roeder, R.C. (1972). The distance-redshift relation for universes with no intergalactic medium, *Astrophysical Journal Letters*, **174**, L115–L117.
- Dyer, C.C. and Roeder, R.C. (1973). Distance-redshift relations for universes with some intergalactic medium, *Astrophysical Journal Letters*, **180**, L31–L34.
- Eales, S.A., Rawlings, S., Law-Green, D., Cotter, G., and Lacy, M. (1997). A first sample of faint radio sources with virtually complete Redshifts: I. Infrared images, the Hubble diagram and the alignment effect, *Monthly Notices of the Royal Astronomical Society*, **291**, 593–615.
- Eastman, R.G. and Kirshner, R.P. (1989). Model atmospheres for SN 1987A and the distance to the Large Magellanic Cloud, *Astrophysical Journal*, **347**, 771–793.
- Eddington, A.S. (1916). The kinetic energy of a star cluster, *Monthly Notices of the Royal Astronomical Society*, **76**, 525–528.
- Eddington, A.S. (1926). Diffuse matter in interstellar space, *Proceedings of the Royal Society, A***111**, 424–456.

- Efstathiou, G. (1988). Effects of reionization on microwave background anisotropies, in *Large-scale Motions in the Universe*, eds. Rubin, V. and Coyne, G., pp. 299–319. Princeton: Princeton University Press.
- Efstathiou, G. (1990). Cosmological perturbations, in *Physics of the Early Universe*, eds. Peacock, J.A., Heavens, A.F., and Davies, A.T., pp. 361–463. Edinburgh: SUSSP.
- Efstathiou, G. (1995). High-redshift galaxies: problems and prospects, in *Galaxies in the Young Universe*, eds. Hippelein, H., Meissenheimer, K., and Röser, H.J., pp. 299–314. Berlin: Springer, Lecture Notes in Physics, Vol. 463.
- Efstathiou, G. and Bond, J.R. (1986). Isocurvature cold dark matter fluctuations, *Monthly Notices of the Royal Astronomical Society*, **218**, 103–121.
- Efstathiou, G., Frenk, C.S., White, S.D.M., and Davis, M. (1988). Gravitational clustering from scale-free initial conditions, *Monthly Notices of the Royal Astronomical Society*, **235**, 715–748.
- Efstathiou, G., Lawrence, C., and Tauber, J. (2005). *Planck: The Scientific Programme*. Noordwijk: European Space Agency Publications, ESA-SCI(2005)1.
- Efstathiou, G. and Rees, M.J. (1988). High-redshift quasars in the cold dark matter cosmogony, *Monthly Notices of the Royal Astronomical Society*, **230**, 5P–11P.
- Eguchi, K., Enomoto, S., and 97 authors (2003). First results from Kamland: evidence for reactor anti-neutrino disappearance, *Physical Review Letters*, **90**, id. 021802(1–6).
- Einstein, A. (1915). Die Feldgleichung der Gravitation (The field equations of gravitation), *Sitzungsberichte, Königlich Preussische Akademie der Wissenschaften (Berlin)*, **II**, 844–847.
- Einstein, A. (1916). Die Grundlage der Allgemeinen Relativitätstheorie (Foundation of the General Theory of Relativity), *Annalen der Physik*, **49**, 769–822.
- Einstein, A. (1917). Kosmologische Betrachtungen zur Allgemeinen Relativitätstheorie (Cosmological considerations in the General Theory of Relativity), *Sitzungsberichte, Königlich Preussische Akademie der Wissenschaften (Berlin)*, **I**, 142–152.
- Einstein, A. (1919). Spielen Gravitationsfelder im Aufbau der materiellen Elementarteilchen eine wesentliche Rolle? (Do gravitational fields play a significant role for the structure of elementary particles), *Sitzungsberichte, Königlich Preussische Akademie der Wissenschaften, Part 1*, 349–356.
- Einstein, A. (1922). Bemerkung zu der Arbeit von A. Friedmann “Ueber die Krümmung des Raumes” (Remark on the work of A. Friedmann “On the Curvature of Space”), *Zeitschrift für Physik*, **11**, 326.
- Einstein, A. (1923). Notiz zu der Arbeit von A. Friedmann “Über die Krümmung des Raumes” (A Note on the Work of A. Friedmann “On the Curvature of Space”), *Zeitschrift für Physik*, **16**, 228.
- Einstein, A. (1936). Lens-like action of a star by the deviation of light in the gravitational field, *Science*, **84**, 506–507.
- Eisenstein, D.J. and Hu, W. (1998). Baryonic features in the matter transfer function, *Astrophysical Journal*, **496**, 605–614.

- Eisenstein, D.J., Zehavi, I., Hogg, D.W., Scoccimarro, R., Blanton, M.R., Nichol, R.C., Scranton, R., Seo, H.-J., Tegmark, M., Zheng, Z., Anderson, S.F., Annis, J., Bahcall, N., Brinkmann, J., Burles, S., Castander, F.J., Connolly, A., Csabai, I., Doi, M., Fukugita, M., Frieman, J.A., Glazebrook, K., Gunn, J.E., Hendry, J.S., Hennessy, G., Ivezić, Z., Kent, S., Knapp, G.R., Lin, H., Loh, Y.-S., Lupton, R.H., Margon, B., McKay, T.A., Meiksin, A., Munn, J.A., Pope, A., Richmond, M.W., Schlegel, D., Schneider, D.P., Shimasaku, K., Stoughton, C., Strauss, M.A., SubbaRao, M., Szalay, A.S., Szapudi, I., Tucker, D.L., Yanny, B., and York, D.G. (2005). Detection of the baryon acoustic peak in the large-scale correlation function of SDSS luminous red galaxies, *Astrophysical Journal*, **633**, 560–574.
- Ellis, R.G. (1997). Faint blue galaxies, *Annual Review of Astronomy and Astrophysics*, **35**, 389–443.
- Ellis, R.G., Smail, I., Dressler, A., Couch, W.J., Oemler, A.J., Butcher, H., and Sharples, R.M. (1997). The homogeneity of spheroidal populations in distant clusters, *Astrophysical Journal*, **483**, 582–596.
- Ellis, S.C. and Bland-Hawthorn, J. (2006). GalaxyCount: a JAVA calculator of galaxy counts and variances in multiband wide-field surveys to 28 AB mag, *ArXiv Astrophysics e-prints*.
- Faber, S.M. (1973). Variations in spectral-energy distributions and absorption-line strengths among elliptical galaxies, *Astrophysical Journal*, **179**, 731–754.
- Faber, S.M. and Jackson, R.E. (1976). Velocity dispersions and mass-to-light ratios for elliptical galaxies, *Astrophysical Journal*, **204**, 668–683.
- Fabian, A.C. (1994). Cooling flows in clusters of galaxies, *Annual Review of Astronomy and Astrophysics*, **32**, 277–318.
- Fabian, A.C. and Barcons, X. (1992). The origin of the X-ray background, *Annual Review of Astronomy and Astrophysics*, **30**, 429–456.
- Fabian, A.C., Sanders, J.S., Ettori, S., Taylor, G.B., Allen, S.W., Crawford, C.S., Iwasawa, K., Johnstone, R.M., and Ogle, P.M. (2000). Chandra imaging of the complex X-ray core of the Perseus cluster, *Monthly Notices of the Royal Astronomical Society*, **318**, L65–L68.
- Fabian, A.C., Sanders, J.S., Taylor, G.B., Allen, S.W., Crawford, C.S., Johnstone, R.M., and Iwasawa, K. (2006). A very deep Chandra observation of the Perseus cluster: shocks, ripples and conduction, *Monthly Notices of the Royal Astronomical Society*, **366**, 417–428.
- Fabricant, D.G., Lecar, M., and Gorenstein, P. (1980). X-ray measurements of the mass of M87, *Astrophysical Journal*, **241**, 552–560.
- Fall, S. (1983). Galaxy formation – some comparisons between theory and observation, in *Internal Kinematics and Dynamics of Galaxies: IAU Symposium No. 100*, ed. Athanassoula, E., pp. 391–398. Dordrecht: Reidel.
- Fall, S. (1997). A global perspective on star formation, in *The Hubble Space Telescope and the High Redshift Universe*, eds. Tanvir, N., Aragón-Salamanca, A., and Wall, J., pp. 303–308. Singapore: World Scientific.
- Fall, S.M. and Efstathiou, G. (1980). Formation and rotation of disc galaxies with haloes, *Monthly Notices of the Royal Astronomical Society*, **193**, 189–206.

- Fall, S.M. and Pei, Y.C. (1993). Obscuration of quasars by dust in damped Lyman-alpha systems, *Astrophysical Journal*, **402**, 479–492.
- Fan, X., Hennawi, J.F., Richards, G.T., Strauss, M.A., Schneider, D.P., Donley, J.L., Young, J.E., Annis, J., Lin, H., Lampeitl, H., Lupton, R.H., Gunn, J.E., Knapp, G.R., Brandt, W.N., Anderson, S., Bahcall, N.A., Brinkmann, J., Brunner, R.J., Fukugita, M., Szalay, A.S., Szokoly, G.P., and York, D.G. (2004). A survey of $z \geq 5.7$ quasars in the Sloan Digital Sky Survey: III. Discovery of five additional quasars, *Astronomical Journal*, **128**, 515–522.
- Fan, X., Narayanan, V.K., Lupton, R.H., Strauss, M.A., Knapp, G.R., Becker, R.H., White, R.L., Pentericci, L., Leggett, S.K., Haiman, Z., Gunn, J.E., Ivezić, Ž., Schneider, D.P., Anderson, S.F., Brinkmann, J., Bahcall, N.A., Connolly, A.J., Csabai, I., Doi, M., Fukugita, M., Geballe, T., Grebel, E.K., Harbeck, D., Hennessy, G., Lamb, D.Q., Miknaitis, G., Munn, J.A., Nichol, R., Okamura, S., Pier, J.R., Prada, F., Richards, G.T., Szalay, A., and York, D.G. (2001). A survey of $z \geq 5.8$ quasars in the Sloan Digital Sky Survey: I. Discovery of three new quasars and the spatial density of luminous quasars at $z \sim 6$, *Astronomical Journal*, **122**, 2833–2849.
- Feast, M.W. and Catchpole, R.M. (1997). The cepheid period-luminosity zero-point from HIPPARCOS trigonometrical parallaxes, *Monthly Notices of the Royal Astronomical Society*, **286**, L1–L5.
- Fechner, C., Reimers, D., Kriss, G.A., Baade, R., Blair, W.P., Giroux, M.L., Green, R.F., Moos, H.W., Morton, D.C., Scott, J.E., Shull, J.M., Simcoe, R., Songaila, A., and Zheng, W. (2006). The UV spectrum of HS 1700+6416: II. FUSE observations of the HeII Lyman alpha forest, *Astrophysical Journal*, **455**, 91–106.
- Felten, J. (1977). Study of the luminosity function for field galaxies, *Astronomical Journal*, **82**, 861–878.
- Felten, J. (1985). Galaxy luminosity functions, M/L ratios, and closure of the Universe – numbers and problems, *Comments on Astrophysics*, **11**, 53–67.
- Ferguson, H.C., Dickinson, M., and Williams, R. (2000). The Hubble Deep Fields, *Annual Review of Astronomy and Astrophysics*, **38**, 667–715.
- Fixsen, D., Cheng, E., Gales, J., Mather, J., Shafer, R., and Wright, E. (1996). The cosmic microwave background spectrum from the full COBE FIRAS data set, *Astrophysical Journal*, **473**, 576–587.
- Foley, R.J., Filippenko, A.V., Leonard, D.C., Riess, A.G., Nugent, P., and Perlmutter, S. (2005). A definitive measurement of time dilation in the spectral evolution of the moderate-redshift type 1a Supernova 1997ex, *Astrophysical Journal Letters*, **626**, L11–L14.
- Fomalont, E.B., Kellermann, K.I., Anderson, M.C., Weistroop, D., Wall, J.V., Windhorst, R.A., and Kristian, J.A. (1988). New limits to fluctuations in the cosmic background radiation at 4.86 GHz between 12 and 60 arcsecond resolution, *Astrophysical Journal*, **96**, 1187–1191.
- Forman, W. and Jones, C. (1982). X-ray-imaging observations of clusters of galaxies, *Annual Review of Astronomy and Astrophysics*, **20**, 547–585.

- Fort, B. and Mellier, Y. (1994). Arc(let)s in clusters of galaxies, *Astronomy and Astrophysics Reviews*, **5**, 239–292.
- Frayer, D.T., Fadda, D., Yan, L., Marleau, F.R., Choi, P.I., Helou, G., Soifer, B.T., Appleton, P.N., Armus, L., Beck, R., Dole, H., Engelbracht, C.W., Fang, F., Gordon, K.D., Heinrichsen, I., Henderson, D., Hesselroth, T., Im, M., Kelly, D.M., Lacy, M., Laine, S., Latter, W.B., Mahoney, W., Makovoz, D., Masci, F.J., Morrison, J.E., Moshir, M., Noriega-Crespo, A., Padgett, D.L., Pesenson, M., Shupe, D.L., Squires, G.K., Storrie-Lombardi, L.J., Surace, J.A., Teplitz, H.I., and Wilson, G. (2006). Spitzer 70 and 160 μm observations of the extragalactic First Look Survey, *Astronomical Journal*, **131**, 250–260.
- Freedman, W.L., Madore, B.F., Gibson, B.K., Ferrarese, L., Kelson, D.D., Sakai, S., Mould, J.R., Kennicutt Jr., R.C., Ford, H.C., Graham, J.A., Huchra, J.P., Hughes, S.M.G., Illingworth, G.D., Macri, L.M., and Stetson, P.B. (2001). Final results from the Hubble Space Telescope key project to measure the Hubble constant, *Astrophysical Journal*, **533**, 47–72.
- Freeman, K.C. (1970). On the disks of spiral and S0 galaxies, *Astrophysical Journal*, **160**, 811–830.
- Frenk, C. (1986). Galaxy clustering and the dark-matter problem, *Philosophical Transactions of the Royal Astronomical Society*, **A320**, 517–541.
- Friedman, A.A. (1922). On the Curvature of Space, *Zeitschrift für Physik*, **10**, 377–386.
- Friedman, A.A. (1924). On the possibility of a world with constant negative curvature, *Zeitschrift für Physik*, **12**, 326–332.
- Fukugita, M., Futamase, T., Kasai, M., and Turner, E.L. (1992). Statistical properties of gravitational lenses with a nonzero cosmological constant, *Astrophysical Journal*, **393**, q3–21.
- Furlanetto, S.R., Sokasian, A., and Hernquist, L. (2004). Observing the reionization epoch through 21-centimetre radiation, *Monthly Notices of the Royal Astronomical Society*, **347**, 187–195.
- Gamow, G. (1970). *My World Line*. New York: Viking. The reference to Einstein's admission of 'the greatest blunder of my life' is on p. 44.
- Garnavich, P.M., Kirshner, R.P., Challis, P., Tonry, J., Gilliland, R.L., Smith, R.C., Clocchiatti, A., Diercks, A., Filippenko, A.V., Hamuy, M., Hogan, C.J., Leibundgut, B., Phillips, M.M., Riess, D., Riess, A.G., Schmidt, B.P., Schommer, R.A., Spyromilio, J., Stubbs, C., Suntzeff, N.B., and Wells, L. (1998). Constraints on cosmological models from Hubble Space Telescope observations of high-z supernovae, *Astrophysical Journal Letters*, **493**, L53–L58.
- Gavazzi, R., Treu, T., Rhodes, J.D., Koopmans, L.V.E., Bolton, A.S., Burles, S., Massey, R., and Moustakas, L.A. (2007). The Sloan Lens ACS Survey: IV. The mass density profile of early-type galaxies out to 100 effective radii, *ArXiv Astrophysics e-prints*.
- Ge, J., Bechtold, J., and Black, J. (1997). A new measurement of the cosmic microwave background radiation temperature at $Z = 1.97$, *Astrophysical Journal*, **474**, 67–73.
- Geller, M.J. and Huchra, J.P. (1989). Mapping the Universe, *Science*, **246**, 897–903.

- Geller, M.J. and Postman, M. (1983). First-ranked galaxies in groups, *Astrophysical Journal*, **274**, 31–38.
- Gershtein, S. and Zeldovich, Y. (1966). Rest mass of a muonic neutrino and cosmology, *Pisma v Zhurnal Eksperimentalnoi i Teoreticheskoi Fiziki*, **4**, 174–177.
- Giacconi, R., Gursky, H., Paolini, F.R., and Rossi, B.B. (1962). Evidence for X rays from sources outside the solar system, *Physical Review Letters*, **9**, 439–443.
- Giavalisco, M., Dickinson, M., Ferguson, H.C., Ravindranath, S., Kretchmer, C., Moustakas, L.A., Madau, P., Fall, S.M., Gardner, J.P., Livio, M., Papovich, C., Renzini, A., Spinrad, H., Stern, D., and Riess, A. (2004a). The rest-frame ultraviolet luminosity density of star-forming galaxies at redshifts $z \geq 3.5$, *Astrophysical Journal Letters*, **600**, L103–L106.
- Giavalisco, M., Ferguson, H.C., Koekemoer, A.M., Dickinson, M., Alexander, D.M., Bauer, F.E., Bergeron, J., Biagetti, C., Brandt, W.N., Casertano, S., Cesarsky, C., Chatzichristou, E., Conselice, C., Cristiani, S., Da Costa, L., Dahlen, T., de Mello, D., Eisenhardt, P., Erben, T., Fall, S.M., Fassnacht, C., Fosbury, R., Fruchter, A., Gardner, J.P., Grogin, N., Hook, R.N., Hornschemeier, A.E., Idzi, R., Jogee, S., Kretchmer, C., Laidler, V., Lee, K.S., Livio, M., Lucas, R., Madau, P., Mobasher, B., Moustakas, L.A., Nonino, M., Padovani, P., Papovich, C., Park, Y., Ravindranath, S., Renzini, A., Richardson, M., Riess, A., Rosati, P., Schirmer, M., Schreier, E., Somerville, R.S., Spinrad, H., Stern, D., Stiavelli, M., Strolger, L., Urry, C.M., Vandame, B., Williams, R., and Wolf, C. (2004b). The Great Observatories Origins Deep Survey: initial results from optical and near-infrared imaging, *Astrophysical Journal Letters*, **600**, L93–L98.
- eds. Gibbons, G., Shellard, E., and Rankin, S. (2003). *The Future of Theoretical Physics and Cosmology*. Cambridge: Cambridge University Press.
- Gibbons, G.W. and Hawking, S.W. (1977). Cosmological event horizons, thermodynamics, and particle creation, *Physical Review*, **D15**, 2738–2751.
- eds. Gibbons, G.W., Hawking, S.W., and Siklos, S.T.C. (1983). *The Very Early Universe: Proceedings of the Nuffield Workshop, Cambridge, UK, 21 June–9 July 1982*. Cambridge: Cambridge University Press.
- Gilli, R., Comastri, A., and Hasinger, G. (2007). The synthesis of the cosmic X-ray background in the Chandra and XMM-Newton era, *Astronomy and Astrophysics*, **463**, 79–96.
- Gilmore, G., King, I., and van der Kruit, P.C. (1989). *The Milky Way as a Galaxy: Proceedings of the 19th Advanced Course of the Swiss Society of Astronomy and Astrophysics (SSAA)*. Mill Valley, California: University Science Books. Van der Kruit's analyses of the surface brightness distributions in elliptical and spiral galaxies are contained in Sect. 5.2 (pp. 80–88) and Sect. 12.1 (pp. 257–267).
- Glazebrook, K., Abraham, R.G., McCarthy, P.J., Savaglio, S., Chen, H.-W., Crampton, D., Murowinski, R., Jørgensen, I., Roth, K., Hook, I., Marzke, R.O., and Carlberg, R.G. (2004). A high abundance of massive galaxies 3–6 billion years after the Big Bang, *Nature*, **430**, 181–184.
- Glazebrook, K., Ellis, R.S., Colless, M., Broadhurst, T.J., Allington-Smith, J.R., and Tanvir, N.R. (1995). The morphological identification of the rapidly evolving

- population of faint galaxies, *Monthly Notices of the Royal Astronomical Society*, **275**, L19–L22.
- Goldhaber, G., Groom, D.E., Kim, A., Aldering, G., Astier, P., Conley, A., Deustua, S.E., Ellis, R., Fabbro, S., Fruchter, A.S., Goobar, A., Hook, I., Irwin, M., Kim, M., Knop, R.A., Lidman, C., McMahon, R., Nugent, P.E., Pain, R., Panagia, N., Pennypacker, C.R., Perlmutter, S., Ruiz-Lapuente, P., Schaefer, B., Walton, N.A., and York, T. (2001). Timescale stretch parameterization of type 1a supernova B-band light curves, *Astrophysical Journal*, **558**, 359–368.
- Goobar, A. and Perlmutter, S. (1995). Feasibility of measuring the cosmological constant lambda and mass density omega using type IA supernovae, *Astrophysical Journal*, **450**, 14–18.
- Gott, J.R., Melott, A.L., and Dickinson, M. (1986). The sponge-like topology of large-scale structure in the Universe, *Astrophysical Journal*, **306**, 341–357.
- Govoni, F. (2006). Observations of magnetic fields in regular and irregular clusters, *Astronomische Nachrichten*, **327**, 539–544.
- Gregory, J. (1668). *Geometriae Pars Universalis*. Padua.
- Gregory, P. and Condon, J. (1991). The 87GB catalog of radio sources covering delta between 0 and +75 deg at 4.85 GHz, *Astrophysical Journal Supplement Series*, **75**, 1011–1291.
- Greve, T.R., Bertoldi, F., Smail, I., Neri, R., Chapman, S.C., Blain, A.W., Ivison, R.J., Genzel, R., Omont, A., Cox, P., Tacconi, L., and Kneib, J.-P. (2005). An interferometric CO survey of luminous submillimetre galaxies, *Monthly Notices of the Royal Astronomical Society*, **359**, 1165–1183.
- Gribben, J. and Rees, M. (1989). *Dark Matter, Mankind and Anthropic Cosmology*. New York: Bantam.
- Groth, E. and Peebles, P. (1977). Statistical Analysis of Catalogs of Extragalactic Objects. VII – Two- and Three-point correlation functions for the high-resolution Shane–Wirtanen catalog of galaxies, *Astrophysical Journal*, **217**, 385–405.
- Groth, E. and Peebles, P. (1986). The Shane–Wirtanen counts – observer and time-dependent effects, *Astrophysical Journal*, **310**, 507–517.
- Guenther, D.B., Krauss, L.M., and Demarque, P. (1998). Testing the constancy of the gravitational constant using helioseismology, *Astrophysical Journal*, **498**, 871–876.
- Gunn, J.E. (1978). The Friedmann models and optical observations in cosmology, in *Observational Cosmology: 8th Advanced Course, Swiss Society of Astronomy and Astrophysics, Saas-Fee 1978*, eds. Maeder, A., Martinet, L., and Tammann, G., pp. 1–121. Geneva: Geneva Observatory Publications.
- Gunn, J.E., Hoessel, J.G., Westphal, J.A., Perryman, M.A.C., and Longair, M.S. (1981). Investigations of the optical fields of 3CR radio sources to faint limiting magnitudes: IV. *Monthly Notices of the Royal Astronomical Society*, **194**, 111–123.
- Gunn, J.E. and Peterson, B.A. (1965). On the density of neutral hydrogen in intergalactic space, *Astrophysical Journal*, **142**, 1633–1636.
- Gurvits, L.I., Kellermann, K.I., and Frey, S. (1999). The “angular size – redshift” relation for compact radio structures in quasars and radio galaxies, *Astronomy and Astrophysics*, **342**, 378–388.

- Guth, A. (1981). Inflationary universe: a possible solution to the horizon and flatness problems, *Physical Review*, **D23**, 347–356.
- Guth, A.H. (1997). *The Inflationary Universe: The Quest for a New Theory of Cosmic Origins*. Reading, MA: Addison-Wesley.
- Guth, A.H. and Pi, S.-Y. (1982). Fluctuations in the new inflationary universe, *Physical Review Letters*, **49**, 1110–1113.
- Hamilton, A.J.S., Kumar, P., Lu, E., and Matthews, A. (1991). Reconstructing the primordial spectrum of fluctuations of the Universe from the observed nonlinear clustering of galaxies, *Astrophysical Journal*, **374**, L1–L4.
- Harrison, E. (1970). Fluctuations at the threshold of classical cosmology, *Physical Review*, **D1**, 2726–2730.
- Harrison, E.R. (1987). *Darkness at Night: A Riddle of the Universe*. Cambridge: Cambridge University Press.
- Hasinger, G., Burg, R., Giacconi, R., Hartner, G.D., Schmidt, M., Trümper, J., and Zamorani, G. (1993). A deep X-ray survey in the Lockman hole and the soft X-ray logN-logS, *Astronomy and Astrophysics*, **275**, 1–15.
- Hauser, M.G., Arendt, R.G., Kelsall, T., Dwek, E., Odegard, N., Weiland, J.L., Freudenreich, H.T., Reach, W.T., Silverberg, R.F., Moseley, S.H., Pei, Y.C., Lubin, P., Mather, J.C., Shafer, R.A., Smoot, G.F., Weiss, R., Wilkinson, D.T., and Wright, E.L. (1998). The COBE diffuse infrared background experiment search for the cosmic infrared background: I. Limits and detections, *Astrophysical Journal*, **508**, 25–43.
- Hauser, M.G. and Dwek, E. (2001). The cosmic infrared background: measurements and implications, *Annual Review of Astronomy and Astrophysics*, **39**, 249–307.
- Hausman, M.A. and Ostriker, J.P. (1977). Cannibalism among galaxies – dynamically produced evolution of cluster luminosity functions, *Astrophysical Journal*, **217**, L125–L129.
- Hausman, M.A. and Ostriker, J.P. (1978). Galactic cannibalism: III. The morphological evolution of galaxies and clusters, *Astrophysical Journal*, **224**, 320–336.
- Hawking, S.W. (1975). Particle creation by black holes, in *Quantum Gravity: Proceedings of the Oxford Symposium*, eds. Isham, C.J., Penrose, R., and Sciama, D.W., pp. 219–267. Oxford: Clarendon.
- Hawkins, M.R.S. (1986). On the nature of objects detected as faint long-term variables, *Monthly Notices of the Royal Astronomical Society*, **219**, 417–426.
- Heath, D.J. (1977). The growth of density perturbations in zero pressure Friedmann-Lemaître universes, *Monthly Notices of the Royal Astronomical Society*, **179**, 351–358.
- Helou, G., Soifer, B.T., and Rowan-Robinson, M. (1985). Thermal infrared and nonthermal radio – remarkable correlation in disks of galaxies, *Astrophysical Journal*, **298**, L7–L11.
- Hernquist, L., Katz, N., Weinberg, D.H., and Miralda-Escudé, J. (1996). The Lyman-alpha forest in the cold dark matter model, *Astrophysical Journal*, **457**, L51–L55.
- Herschel, W. (1785). On the construction of the heavens, *Philosophical Transactions of the Royal Society*, **75**, 213–268.

- Herschel, W. (1802). Catalogue of 500 new nebulae, nebulous stars, planetary nebulae, and clusters of stars; with remarks on the construction of the heavens, *Philosophical Transactions of the Royal Society*, **92**, 477–528.
- Hesser, J.E., Harris, W.E., VandenBerg, D.A., Allwright, J.W.B., Shott, P., and Stetson, P. (1987). A CCD color-magnitude study of 47 tucanae, *Publications of the Astronomical Society of the Pacific*, **99**, 739–808.
- Hewish, A. (1961). Extrapolation of the number-flux density relation of radio stars by Scheuer's statistical methods, *Monthly Notices of the Royal Astronomical Society*, **123**, 167–181.
- Hewitt, J.N., Turner, E.L., Burke, B.F., Lawrence, C.R., and Bennett, C.L. (1987). A VLA gravitational lens survey, in *Observational Cosmology: IAU Symposium No. 124*, eds. Hewitt, A., Burbidge, G., and Fang, L.Z., pp. 747–750. Dordrecht: Reidel.
- Higgs, P. (1964). Broken symmetries, massless particles and gauge fields, *Physics Letters*, **12**, 132–133.
- Hinshaw, G., Nolta, M.R., Bennett, C.L., Bean, R., Doré, O., Greason, M.R., Halpern, M., Hill, R.S., Jarosik, N., Kogut, A., Komatsu, E., Limon, M., Odegard, N., Meyer, S.S., Page, L., Peiris, H.V., Spergel, D.N., Tucker, G.S., Verde, L., Weiland, J.L., Wollack, E., and Wright, E.L. (2007). Three-year Wilkinson Microwave Anisotropy Probe (WMAP) observations: temperature analysis, *Astrophysical Journal Supplement*, **170**, 288–334.
- Hinshaw, G., Spergel, D.N., Verde, L., Hill, R.S., Meyer, S.S., Barnes, C., Bennett, C.L., Halpern, M., Jarosik, N., Kogut, A., Komatsu, E., Limon, M., Page, L., Tucker, G.S., Weiland, J.L., Wollack, E., and Wright, E.L. (2003). First-Year Wilkinson Microwave Anisotropy Probe (WMAP) observations: the angular power spectrum, *Astrophysical Journal Supplement*, **148**, 135–159.
- Hobson, M., Efstathiou, G., and Lasenby, A. (2006). *General Relativity: An Introduction for Physicists*. Cambridge: Cambridge University Press.
- Hoekstra, H., Yee, H.K.C., and Gladders, M.D. (2004). Properties of galaxy dark matter halos from weak lensing, *Astrophysical Journal*, **606**, 67–77.
- Hogan, C.J. (1997). Big Bang nucleosynthesis and the observed abundances of light elements, in *Critical Dialogues in Cosmology*, ed. Turok, N., pp. 50–62. Singapore: World Scientific.
- Hogg, D.W., Blanton, M.R., Brinchmann, J., Eisenstein, D.J., Schlegel, D.J., Gunn, J.E., McKay, T.A., Rix, H.-W., Bahcall, N.A., Brinkmann, J., and Meiksin, A. (2004). The dependence on environment of the color-magnitude relation of galaxies, *Astrophysical Journal*, **601**, L29–L32.
- Hogg, D.W., Eisenstein, D.J., Blanton, M.R., Bahcall, N.A., Brinkmann, J., Gunn, J.E., and Schneider, D.P. (2005). Cosmic homogeneity demonstrated with luminous red galaxies, *Astrophysical Journal*, **624**, 54–58.
- Holtzman, J.A. (1998). Microwave background anisotropies and large-scale structure in universes with cold dark matter, baryons, radiation and massive and massless neutrinos, *Astrophysical Journal Suppllement*, **71**, 1–24.
- Hook, I.M., McMahon, R.G., Boyle, B.J., and Irwin, M.J. (1991). The variability of a large sample of quasars, in *The Space Distribution of Quasars*, ed. Crampton, D.,

- vol. 21, pp. 67–75. San Francisco: Astronomical Society of the Pacific Conference Series.
- Hoskin, M.A. (1976). The ‘Great Debate’: what really happened, *Journal of the History of Astronomy*, **7**, 169–182.
- Hoyle, F. (1954). On nuclear reactions occurring in very hot stars: I. The synthesis of elements from carbon to nickel, *Astrophysical Journal Supplement*, **1**, 121–146.
- Hoyle, F. and Tayler, R. (1964). The mystery of the cosmic helium abundance, *Nature*, **203**, 1108–1110.
- Hoyle, F., Vogeley, M., and Gott III, J. (2002a). Two-dimensional topology of the Two-Degree Field Galaxy Redshift Survey, *Astrophysical Journal*, **570**, 44–53.
- Hoyle, F., Vogeley, M., Gott III, J., Blanton, M., Tegmark, M., Weinberg, D., Bahcall, N., Brinkmann, J., and York, D. (2002b). Two-dimensional topology of the Sloan Digital Sky Survey, *Astrophysical Journal*, **580**, 663–671.
- Hu, E.M., Kim, T.-S., Cowie, L.L., Songaila, A., and Rauch, M. (1995a). The distribution of column densities and B values in the Lyman-alpha forest, *Astronomical Journal*, **110**, 1526–1543.
- Hu, W. (1996). Concepts in CMB anisotropy formation, in *The Universe at High-z, Large-Scale Structure and the Cosmic Microwave Background*, eds. Martinez-Gonzales, E. and Sanz, J.L., pp. 207–240. Berlin: Springer.
- Hu, W. and Dodelson, S. (2002). Cosmic microwave background anisotropies, *Annual Review of Astronomy and Astrophysics*, **40**, 171–216.
- Hu, W. and Okamoto, T. (2002). Mass reconstruction with cosmic microwave background polarization, *Astrophysical Journal*, **574**, 566–574.
- Hu, W., Scott, D., Sugiyama, N., and White, M. (1995b). Effect of physical assumptions on the calculation of microwave background anisotropies, *Physical Review D*, **D52**, 5498–5515.
- Hu, W. and Sugiyama, N. (1995). Anisotropies in the cosmic microwave background: an analytic approach, *Astrophysical Journal*, **444**, 489–506.
- Hu, W., Sugiyama, N., and Silk, J. (1997). The physics of microwave background anisotropies, *Nature*, **386**, 37–43.
- Hu, W. and White, M. (1997). A CMB polarization primer, *New Astronomy*, **2**, 323–344.
- Hubble, E.P. (1926). Extra-galactic nebulae, *Astrophysical Journal*, **64**, 321–369.
- Hubble, E.P. (1929). A relation between distance and radial velocity among extra-galactic nebulae, *Proceedings of the National Academy of Sciences*, **15**, 168–173.
- Hubble, E.P. (1936). *The Realm of the Nebulae*. New Haven: Yale University Press.
- Hubble, E.P. and Humason, M. (1934). The velocity–distance relation among extra-galactic nebulae, *Astrophysical Journal*, **74**, 43–80.
- Hudson, M.J., Dekel, A., Courteau, S., Faber, S.M., and Willick, J.A. (1995). Ω and biasing from optical galaxies versus POTENT mass, *Monthly Notices of the Royal Astronomical Society*, **274**, 305–316.
- Huggins, W. and Miller, W.A. (1864). On the spectra of some of the nebulae; a supplement to the paper “On the Spectra of Some Fixed Stars”, *Philosophical Transactions of the Royal Society of London*, **154**, 437–444.

- Hulse, R.A. and Taylor, J.H. (1975). Discovery of a pulsar in a binary system, *Astrophysical Journal Letters*, **195**, L51–L53.
- Ikeuchi, S. and Ostriker, J.P. (1986). Evolution of the intergalactic medium – what happened during the epoch $Z = 3\text{--}10?$, *Astrophysical Journal*, **301**, 522–543.
- Illingworth, G. (1977). Rotation (?) in 13 elliptical galaxies, *Astrophysical Journal Letters*, **218**, L43–L47.
- Inskip, K.J., Best, P.N., Longair, M.S., and MacKay, D.J.C. (2002). Infrared magnitude-redshift relations for luminous radio galaxies, *Monthly Notices of the Royal Astronomical Society*, **329**, 277–289.
- Irwin, M., McMahon, R.G., and Hazard, C. (1991). APM optical surveys for high redshift quasars, in *ASP Conf. Ser. 21: The Space Distribution of Quasars*, ed. Crampton, D., pp. 117–126.
- Jakobsen, P. (1995). Ultraviolet background (theory), in *The Extragalactic Background Radiation*, eds. Calzetti, D., Livio, M., and Madau, P., pp. 75–101. Cambridge: Cambridge University Press.
- Jakobsen, P. (1996). Intergalactic helium absorption toward quasars, in *Science with the Hubble Space Telescope – II*, eds. Benvenuti, P., Macchetto, F.D., and Schreier, E.J., pp. 153–159. Paris: European Space Agency.
- Jakobsen, P., Boksenberg, A., Deharveng, J.M., Greenfield, P., Jedrzejewski, R., and Paresce, F. (1994). Detection of intergalactic ionized helium absorption in a high-redshift quasar, *Nature*, **370**, 35–39.
- Jeans, J. (1902). The stability of a spherical nebula, *Philosophical Transactions of the Royal Society of London*, **199**, 1–53.
- Jones, B.J.T. (1973). Cosmic turbulence and the origin of galaxies, *Astrophysical Journal*, **181**, 269–294.
- Jones, B.J.T. and Peebles, P.J.E. (1972). Chaos in cosmology, *Comments on Astrophysics and Space Physics*, **4**, 121–128.
- Jones, B.J.T. and Wyse, R.F.G. (1985). The ionisation of the primeval plasma at the time of recombination, *Astronomy and Astrophysics*, **149**, 144–150.
- Jones, W.C., Ade, P.A.R., Bock, J.J., Bond, J.R., Borrill, J., Boscaleri, A., Cabella, P., Contaldi, C.R., Crill, B.P., de Bernardis, P., De Gasperis, G., de Oliveira-Costa, A., De Troia, G., di Stefano, G., Hivon, E., Jaffe, A.H., Kisner, T.S., Lange, A.E., MacTavish, C.J., Masi, S., Mauskopf, P.D., Melchiorri, A., Montroy, T.E., Natoli, P., Netterfield, C.B., Pascale, E., Piacentini, F., Pogosyan, D., Polenta, G., Prunet, S., Ricciardi, S., Romeo, G., Ruhl, J.E., Santini, P., Tegmark, M., Veneziani, M., and Vittorio, N. (2006). A measurement of the angular power spectrum of the CMB temperature anisotropy from the 2003 flight of BOOMERANG, *Astrophysical Journal*, **647**, 823–832.
- Kaastra, J.S., Tamura, T., Peterson, J.R., Bleeker, J.A.M., Ferrigno, C., Kahn, S.M., Paerels, F.B.S., Piffaretti, R., Branduardi-Raymont, G., and Böhringer, H. (2004). Spatially resolved X-ray spectroscopy of cooling clusters of galaxies, *Astronomy and Astrophysics*, **413**, 415–439.
- Kaiser, N. (1984). On the spatial correlations of Abell clusters, *Astrophysical Journal*, **284**, L9–L12.

- Kaiser, N. (1987). Clustering in real space and in redshift space, *Monthly Notices of the Royal Astronomical Society*, **227**, 1–21.
- Kaiser, N. (1992). Weak gravitational lensing of distant galaxies, *Astrophysical Journal*, **388**, 272–286.
- Kapahi, V.K. (1987). The angular size-redshift relation as a cosmological tool, in *Observational Cosmology*, eds. Hewitt, A., Burbidge, G., and Fang, L.-Z., pp. 251–265. Dordrecht: Reidel.
- Kapteyn, J.C. (1922). First attempt at a theory of the arrangement and motion of the sidereal system, *Astrophysical Journal*, **55**, 302–328.
- Kashlinsky, A., Mather, J.C., Odenwald, S., and Hauser, M.G. (1996). Clustering of the diffuse infrared light from the COBE DIRBE maps: I. C(0) and limits on the near-infrared background, *Astrophysical Journal*, **470**, 681–705.
- Kaspi, V.M., Taylor, J.H., and Ryba, M.F. (1994). High-precision timing of millisecond pulsars: 3. Long-term monitoring of PSRs B1855+09 and B1937+21, *Astrophysical Journal*, **428**, 713–728.
- Kassiola, A., Kovner, I., and Blandford, R.D. (1991). Bounds on intergalactic compact objects from observations of compact radio sources, *Astrophysical Journal*, **381**, 6–13.
- Katz, N., Weinberg, D.H., Hernquist, L., and Miranda-Escudé, J. (1996). Damped Lyman-alpha and Lyman-limit absorbers in the cold dark matter model, *Astrophysical Journal*, **457**, L57–L60.
- Kauffmann, G., Heckman, T.M., White, S.D.M., Charlot, S., Tremonti, C., Peng, E.W., Seibert, M., Brinkmann, J., Nichol, R.C., SubbaRao, M., and York, D. (2003). The dependence of star formation history and internal structure on stellar mass for 10^5 low-redshift galaxies, *Monthly Notices of the Royal Astronomical Society*, **341**, 54–69.
- Kauffmann, G., J.M. Colberg, J.M., Diaferio, A., and White, S.D.M. (1999). Clustering of galaxies in a hierarchical universe: I. Methods and results at $z = 0$, *Monthly Notices of the Royal Astronomical Society*, **303**, 188–206.
- Kauffmann, G. and White, S.D. (1993). The merging history of dark matter haloes in a hierarchical universe, *Monthly Notices of the Royal Astronomical Society*, **261**, 921–928.
- Kellermann, K.I. (1993). The cosmological deceleration parameter estimated from the angular-size/redshift relation for compact radio sources, *Nature*, **361**, 134–136.
- Kennicutt, R. (1989). The star formation law in galactic discs, *Astrophysical Journal*, **344**, 685–703.
- Kennicutt, R.C., Edgar, B.K., and Hodge, P.W. (1989). Properties of H II region populations in galaxies: II. The H II region luminosity function, *Astrophysical Journal*, **337**, 761–781.
- Kent, S.M. and Gunn, J.E. (1982). The dynamics of rich clusters of galaxies: I. The Coma cluster, *Astronomical Journal*, **87**, 945–971.
- Kibble, T.W.B. (1976). Topology of cosmic domains and strings, *Journal of Physics A: Mathematical and General*, **9**, 1387–1398.

- King, I.R. (1966). The structure of star clusters: III. Some simple dynamical models, *Astronomical Journal*, **71**, 64–75.
- King, I.R. (1981). The dynamics of globular clusters, *Quarterly Journal of the Royal Astronomical Society*, **22**, 227–243.
- Kippenhahn, R. and Weigert, A. (1990). *Stellar Structure and Evolution*. Berlin and Heidelberg: Springer.
- Kirshner, R. and Kwan, J. (1974). Distances to extragalactic supernovae, *Astrophysical Journal*, **193**, 27–36.
- Kneib, J.P. (1993). *Ph.D. dissertation*. Université Paul Sabatier, Toulouse.
- Kneib, J.-P., Ellis, R.S., Smail, I., Couch, W.J., and Sharples, R.M. (1996). Hubble Space Telescope observations of the lensing cluster Abell 2218, *Astrophysical Journal*, **471**, 643–656.
- Knop, R., Aldering, G., Amanullah, R., Astier, P., Blanc, G., Burns, M., Conley, A., Deustua, S., Doi, M., Ellis, R., Fabbro, S., Folatelli, G., Fruchter, A., Garavini, G., Garmond, S., Garton, K., Gibbons, R., Goldhaber, G., Goobar, A., Groom, D., Hardin, D., Hook, I., Howell, D., Kim, A., Lee, B., Lidman, C., Mendez, J., Nobili, S., Nugent, P., Pain, R., Panagia, N., Pennypacker, C., Perlmutter, S., Quimby, R., Raux, J., Regnault, N., Ruiz-Lapuente, P., Sainton, G., Schaefer, B., Schahmaneche, K., Smith, E., Spadafora, A., Stanishev, V., Sullivan, M., Walton, N.A., Wang, L., Wood-Vasey, W.M., and Yasuda, N. (2003). New constraints on Ω_M , Ω_Λ , and w from an independent set of 11 high-redshift supernovae observed with the Hubble Space Telescope, *Astrophysical Journal*, **598**, 102–137.
- Kochanek, C. (1996). Is there a cosmological constant?, *Astrophysical Journal*, **466**, 638–659.
- Kogut, A., Banday, A.J., Bennett, C.L., Górski, K.M., Hinshaw, G., Smoot, G.F., and Wright, E.L. (1996). Tests for non-Gaussian statistics in the DMR four-year sky maps, *Astrophysical Journal*, **464**, L29–L33.
- Kolatt, T., Dekel, A., and Lahav, O. (1995). Large-scale mass distribution behind the galactic plane, *Monthly Notices of the Royal Astronomical Society*, **275**, 797–811.
- Kolb, E.W. and Turner, M.S. (1990). *The Early Universe*. Redwood City, CA: Addison-Wesley.
- Kompaneets, A. (1956). The establishment of thermal equilibrium between quanta and electrons, *Zhurnal Eksperimentalnoi i Teoreticheskoi Fiziki*, **31**, 876–885. (English translation: 1957 Soviet Physics, 4, 730–737).
- Koo, D.C. and Kron, R. (1982). QSO counts – a complete survey of stellar objects to $B = 23$, *Astronomy and Astrophysics*, **105**, 107–119.
- Kooiman, B.L., Burns, J.O., and Klypin, A.A. (1995). Two-point angular correlation function for the Green Bank 4.85 GHz Sky Survey, *Astrophysical Journal*, **448**, 500–509.
- Kormendy, J. (1982). Observations of galaxy structure and dynamics, in *Morphology and Dynamics of Galaxies: 12th Advanced Course of the Swiss Society of Astronomy and Astrophysics*, eds. Martinet, L. and Mayor, M., pp. 113–288. Sauverny, Switzerland: Geneva Observatory.

- Kormendy, J. and Richstone, D.O. (1995). Inward bound—the search for supermassive black holes in galactic nuclei, *Annual Review of Astronomy and Astrophysics*, **33**, 581–624.
- Kovac, J.M., Leitch, E.M., Pryke, C., Carlstrom, J.E., Halverson, N.W., and Holzapfel, W.L. (2002). Detection of polarization in the cosmic microwave background using DASI, *Nature*, **420**, 772–787.
- Kriss, G.A., Shull, J.M., Oegerle, W., Zheng, W., Davidsen, A.F., Songaila, A., Tumlinson, J., Cowie, L.L., Deharveng, J.-M., Friedman, S.D., Giroux, M.L., Green, R.F., Hutchings, J.B., Jenkins, E.B., Kruk, J.W., Moos, H.W., Morton, D.C., Sembach, K.R., and Tripp, T.M. (2001). Resolving the structure of ionized helium in the intergalactic medium with the far ultraviolet spectroscopic explorer, *Science*, **293**, 1112–1116.
- Kulkarni, V.P. and Fall, S.M. (1993). The proximity effect and the mean intensity of ionizing radiation at low redshifts, *Astrophysical Journal*, **413**, L63–L66.
- Kulkarni, V.P., Fall, S.M., Lauroesch, J.T., York, D.G., Welty, D.E., Khare, P., and Truran, J.W. (2005). Hubble space telescope observations of element abundances in low-redshift damped Ly α galaxies and implications for the global metallicity-redshift relation, *Astrophysical Journal*, **618**, 68–90.
- Kulsrud, R.M. (1997). Pregalactic model for cosmic magnetic fields, in *Critical Dialogues in Cosmology*, ed. Turok, N., pp. 328–342. Singapore: World Scientific.
- Kulsrud, R.M. (2005). *Plasma Physics for Astrophysics*. Princeton, NJ: Princeton University Press.
- Kundic, T., Turner, E.L., Colley, W.N., Gott III, J.R., Rhoads, J.E., Wang, Y., Bergeron, L.E., Gloria, K.A., Long, D.C., Malhotra, S., and Wambsganss, J. (1997). A robust determination of the time delay in 0957+561A, B and a measurement of the global value of Hubble's constant, *Astrophysical Journal*, **482**, 75–82.
- Kuo, C.L., Ade, P.A.R., Bock, J.J., Cantalupo, C., Daub, M.D., Goldstein, J., Holzapfel, W.L., Lange, A.E., Lueker, M., Newcomb, M., Peterson, J.B., Ruhl, J., Runyan, M.C., and Torbet, E. (2004). High-resolution observations of the cosmic microwave background power spectrum with ACBAR, *Astrophysical Journal*, **600**, 32–51.
- Kurt, V.G. and Sunyaev, R.A. (1967). Measurement of the ultraviolet and X-ray background outside the Earth's atmosphere and their role in the study of intergalactic gas, *Cosmical Research*, **5**, 496–512.
- Kutyrev, A.S. and Reynolds, R.J. (1989). Probable detection of H- α emission from a very high velocity cloud in Cetus, *Astrophysical Journal Letters*, **344**, L9–L11.
- Lacy, M., Miley, G., Rawlings, S., Saunders, R., Dickinson, M., Garrington, S., Maddox, S., Pooley, G., Steidel, C., Bremer, M.N., Cotter, G., van Oijk, R., Röttgering, H., and Warner, P. (1994). 8C 1435+635: a radio galaxy at $z = 4.25$, *Monthly Notices of the Royal Astronomical Society*, **271**, 504–512.
- Lagache, G., Dole, H., and Puget, J.-L. (2003). Modelling infrared galaxy evolution using a phenomenological approach, *Monthly Notices of the Royal Astronomical Society*, **338**, 555–571.
- Lagache, G., Dole, H., Puget, J.-L., Pérez-González, P.G., Le Floc'h, E., Rieke, G.H., Papovich, C., Egami, E., Alonso-Herrero, A., Engelbracht, C.W., Gordon, K.D.,

- Misselt, K.A., and Morrison, J.E. (2004). Polycyclic aromatic hydrocarbon contribution to the infrared output energy of the Universe at $z \cong 2$, *Astrophysical Journal Supplement*, **154**, 112–117.
- Laing, R.A., Riley, J.M., and Longair, M.S. (1983). Bright radio sources at 178 MHz – flux densities, optical identifications and the cosmological evolution of powerful radio galaxies, *Monthly Notices of the Royal Astronomical Society*, **204**, 151–187.
- Lanczos, K. (1922). Bemerkung zur die Sitterschen Welt (Remarks on de Sitter's World Model), *Physikalische Zeitschrift*, **23**, 539–543.
- Lanzetta, K., Wolfe, A., and Turnshek, D. (1995). The IUE Survey for damped Lyman- α and Lyman-limit absorption systems, *Astrophysical Journal*, **440**, 435–457.
- Larson, R.B. (1972). Infall of matter in the galaxies, *Nature*, **236**, 21–23.
- Larson, R.B. and Tinsley, B.M. (1978). Star formation rates in normal and peculiar galaxies, *Astrophysical Journal*, **219**, 46–59.
- Le Verrier, U.J.J. (1859). Sur la théorie de mercure et sur le mouvement du périhélie de cette planète (On the theory of mercury and the movement of the perihelion of this planet), *Comptes Rendus*, **49**, 379–383.
- Leavitt, H.S. (1912). Periods of 25 variable stars in the Small Magellanic Cloud, *Harvard College Observatory Circular*, No. **173**, 1–2.
- Ledoux, C., Petitjean, P., and Srianand, R. (2006). Molecular hydrogen in a damped Ly α system at $z_{\text{abs}} = 4.224$, *Astrophysical Journal*, **640**, L25–L28.
- Leitch, E.M., Kovac, J.M., Pryke, C., Carlstrom, J.E., Halverson, N.W., Holzapfel, W.L., Dragovan, M., Reddall, B., and Sandberg, E.S. (2002). Measurement of polarization with the Degree Angular Scale Interferometer, *Nature*, **420**, 763–771.
- Lemaître, G. (1927). A homogeneous universe of constant mass and increasing radius, accounting for the radial velocity of extra-galactic nebulae, *Annales de la Société Scientifique de Bruxelles*, **A47**, 29–39. Translation: (1931), *Monthly Notices of the Royal Astronomical Society*, **91**, 483–490.
- Lemaître, G. (1933). Spherical condensations in the expanding Universe, *Comptes Rendus de L'Academie des Sciences de Paris*, **196**, 903–904.
- Lequeux, J., Peimbert, M., Rayo, J.F., Serrano, A., and Torres-Peimbert, S. (1979). Chemical composition and evolution of irregular and blue compact galaxies, *Astronomy and Astrophysics*, **80**, 155–166.
- Liddle, A.R. and Lyth, D. (2000). *Cosmological Inflation and Large-Scale Structure*. Cambridge: Cambridge University Press.
- Lifshitz, E. (1946). On the gravitational stability of the expanding Universe, *Journal of Physics, Academy of Sciences of the USSR*, **10**, 116–129.
- Lightman, A.P. and Schechter, P.L. (1990). The omega dependence of peculiar velocities induced by spherical density perturbations, *Astrophysical Journal Supplement Series*, **74**, 831–832.
- Lilly, S. and Cowie, L. (1987). Deep infrared surveys, in *Infrared Astronomy with Arrays*, eds. Wynn-Williams, C. and Becklin, E., pp. 473–482. Honolulu: Institute for Astronomy, University of Hawaii Publications.

- Lilly, S.J. (1988). Discovery of a radio galaxy at a redshift of 3.395, *Astrophysical Journal*, **333**, L161–L167.
- Lilly, S.J. and Longair, M.S. (1984). Stellar populations in distant radio galaxies, *Monthly Notices of the Royal Astronomical Society*, **211**, 833–855.
- Lilly, S.J., Tresse, L., Hammer, F., Crampton, D., and LeFevre, O. (1995). The Canada–France Redshift Survey: VI. Evolution of the galaxy luminosity function to $z \sim 1$, *Astrophysical Journal*, **455**, 108–124.
- Lin, C.C., Mestel, L., and Shu, F. (1965). The gravitational collapse of a uniform spheroid, *Astrophysical Journal*, **142**, 1431–1446.
- Lin, H., Kirshner, R.P., Shectman, S.A., Landy, S.D., Oemler, A., and Tucker, D.L. (1996). The power spectrum of galaxy clustering in the Las Campanas Redshift Survey, *Astrophysical Journal*, **471**, 617–635.
- Linde, A. (1974). Is the Lee constant a cosmological constant?, *Zhurnal Experimentalnoi i Teoreticheskoi Fiziki (JETP) Letters*, **19**, 183–184.
- Linde, A. (1982). A new inflationary universe scenario: a possible solution of the horizon, flatness, homogeneity, isotropy and primordial monopole problems, *Physics Letters*, **108B**, 389–393.
- Linde, A. (1983). Chaotic inflation, *Physics Letters*, **129B**, 177–181.
- Lineweaver, C.H. (2005). Inflation and the cosmic microwave background, in *The New Cosmology*, ed. Colless, M., pp. 31–65.
- Linsky, J.L., Diplas, A., Savage, B., Andrusis, C., and Brown, A. (1994). Deuterium in the local interstellar medium: its cosmological Significance, in *Frontiers of Space and Ground-based Astronomy, 27th ESLAB Symposium*, eds. W. Wamsteker, W., Longair, M., and Kondo, Y., pp. 301–304.
- Lobachevsky, N.I. (1829). On the principles of geometry, *Kazanski Vestnik (Kazan Messenger)*.
- Lobachevsky, N.I. (1830). On the principles of geometry, *Kazanski Vestnik (Kazan Messenger)*.
- Longair, M. (1997a). Active galactic nuclei – the Redshift One 3CR galaxies, *Astronomy and Geophysics*, **38**, 10–15.
- Longair, M.S. (1965). Objects in the fields of 88 radio sources, *Monthly Notices of the Royal Astronomical Society*, **129**, 419–436.
- Longair, M.S. (1966). On the interpretation of radio source counts, *Monthly Notices of the Royal Astronomical Society*, **133**, 421–436.
- Longair, M.S. (1978). Radio astronomy and cosmology, in *Observational Cosmology: 8th Advanced Course, Swiss Society of Astronomy and Astrophysics, Saas-Fee 1978*, eds. Maeder, A., Martinet, L., and Tammann, G., pp. 125–257. Geneva: Geneva Observatory Publications.
- Longair, M.S. (1995). The physics of background radiation, in *The Deep Universe, by Sandage, A.R., Kron, R.G. and Longair, M.S.*, eds. Binggeli, B. and Buser, R., pp. 317–514.
- Longair, M.S. (1997b). *High Energy Astrophysics, Vol. 1 (revised 2nd edn.)*. Cambridge: Cambridge University Press.
- Longair, M.S. (1997c). *High Energy Astrophysics, Vol. 2 (revised 2nd edn.)*. Cambridge: Cambridge University Press.

- Longair, M.S. (2003). *Theoretical Concepts in Physics: An Alternative View of Theoretical Reasoning in Physics*. Cambridge: Cambridge University Press.
- Longair, M.S. (2006). *The Cosmic Century: A History of Astrophysics and Cosmology*. Cambridge: Cambridge University Press.
- Longair, M.S. and Scheuer, P.A.G. (1970). The luminosity-volume test for quasi-stellar objects, *Monthly Notices of the Royal Astronomical Society*, **151**, 45–63.
- Longair, M.S. and Sunyaev, R.A. (1969). Fluctuations in the microwave background radiation, *Nature*, **223**, 719–721.
- Longair, M.S. and Sunyaev, R.A. (1971). The electromagnetic background radiation of the Universe, *Uspekhi Fizicheskikh Nauk*, **105**, 41–96. English translation: *Soviet Physics Uspekhi*, **14**, 569–599, 1972.
- Lotz, J.M., Madau, P., Giavalisco, M., Primack, J., and Ferguson, H.C. (2006). The rest-frame far-ultraviolet morphologies of star-forming galaxies at $z \sim 1.5$ and 4, *Astrophysical Journal*, **636**, 592–609.
- Lynden-Bell, D. (1967). Statistical mechanics of violent relaxation in stellar systems, *Monthly Notices of the Royal Astronomical Society*, **136**, 101–121.
- ed. Lynden-Bell, D. (1997). *Cosmical magnetism*. Dordrecht: Kluwer.
- Lynds, R. and Petrosian, V. (1986). Giant luminous arcs in galaxy clusters, *Bulletin of the American Astronomical Society*, **18**, 1014.
- Lyne, A.G., Burgay, M., Kramer, M., Possenti, A., Manchester, R.N., Camilo, F., McLaughlin, M.A., Lorimer, D.R., D'Amico, N., Joshi, B.C., Reynolds, J., and Freire, P.C.C. (2004). A double-pulsar system: a rare laboratory for relativistic gravity and plasma physics, *Science*, **303**, 1153–1157.
- Lyubimov, V., Novikov, E., Nozik, V., Tretyakov, E., and Kozik, V. (1980). An estimate of the v_e mass from the β -spectrum of tritium in the valine molecule, *Physics Letters*, **138**, 30–56.
- Ma, C.-P. and Bertschinger, E. (1995). Cosmological perturbation theory in the synchronous and conformal Newtonian gauges, *Astrophysical Journal*, **455**, 7–25.
- Macchetto, F. and Dickinson, M. (1997). Galaxies in the young Universe, *Scientific American*, **276**, 66–73.
- Madau, P. (1995). Radiative transfer in a clumpy universe: the colors of high-redshift galaxies, *Astrophysical Journal*, **441**, 18–27.
- Madau, P., Ferguson, H., Dickinson, M., Giavalisco, M., Steidel, C., and Fruchter, A. (1996). High-redshift galaxies in the *Hubble Deep Field*: colour selection and star formation history to $z \sim 4$, *Monthly Notices of the Royal Astronomical Society*, **283**, 1388–1404.
- Maddox, S.J., Efstathiou, G., Sutherland, W.G., and Loveday, J. (1990). Galaxy correlations on large scales, *Monthly Notices of the Royal Astronomical Society*, **242**, 43P–47P.
- Maeder, A. (1994). A selection of 10 most topical stellar problems, in *Frontiers of Space and Ground-Based Astronomy*, eds. Wamsteker, W., Longair, M.S., and Kondo, Y., pp. 177–186. Dordrecht: Kluwer.
- Magorrian, J., Tremaine, S., Richstone, D., Bender, R., Bower, G., Dressler, A., Faber, S.M., Gebhardt, K., Green, R., Grillmair, C., Kormendy, J., and Lauer, T.

- (1998). The demography of massive dark objects in galaxy centers, *Astronomical Journal*, **115**, 2285–2305.
- Majewski, S.R., Munn, J.A., Kron, R.G., Bershadsky, M.A., Smetanka, J.J., and Koo, D.C. (1991). A proper motion and variability QSO survey to $B = 22.5$, in *The Space Distribution of Quasars*, ed. Crampton, D., volume 21, pp. 55–65. San Francisco: Astronomical Society of the Pacific Conference Series.
- Maloney, P. (1993). Sharp edges to neutral hydrogen disks in galaxies and the extragalactic radiation field, *Astrophysical Journal*, **414**, 41–56.
- Marleau, F.R., Fadda, D., Storrie-Lombardi, L.J., Helou, G., Makovoz, D., Frayer, D.T., Yan, L., Appleton, P.N., Armus, L., Chapman, S., Choi, P.I., Fang, F., Heinrichsen, I., Im, M., Lacy, M., Shupe, D., Soifer, B.T., Squires, G., Surace, J., Teplitz, H.I., and Wilson, G. (2004). Extragalactic source counts at 24 microns in the Spitzer First Look Survey, *Astrophysical Journal Supplement*, **154**, 66–69.
- Marshall, F.E., Boldt, E.A., Holt, S.S., Miller, R.B., Mushotzky, R.F., Rose, L.A., Rothschild, R.E., and Serlemitsos, P.J. (1980). The diffuse X-ray background spectrum from 3 to 50 keV, *Astrophysical Journal*, **235**, 4–10.
- Martin, C. and Bowyer, S. (1989). Evidence for an extragalactic component of the far-ultraviolet background and constraints on galaxy evolution for Z between 0.1 and 0.6, *Astrophysical Journal*, **338**, 677–706.
- Marx, G. and Szalay, A. (1972). Cosmological limit on neutretto mass. in *Neutrino '72*, vol. 1, pp. 191–195. Budapest: Technoinform.
- Mather, J. (1995). Microwave background radiation (observations), in *The Extragalactic Background Radiation*, eds. Calzetti, D., Livio, M., and Madau, P., pp. 169–190. Cambridge: Cambridge University Press.
- Matthews, J. and Walker, R.L. (1973). *Mathematical Methods of Physics*. New York: W.A. Benjamin.
- Mattig, W. (1959). Über den Zusammenhang Zwischen der Anzahl der Extragalaktischen Objekte und der Scheinbaren Helligkeit, *Astronomische Nachrichten*, **285**, 1–2.
- Mazzarella, J. and Balzano, V. (1986). A catalog of Markarian galaxies, *Astrophysical Journal Supplement Series*, **62**, 521–819.
- McCarthy, P.J. (2006). Galaxy formation and cosmology in the ELT era, in *Scientific Requirements for Extremely Large Telescopes: IAU Symposium No. 232*, eds. Whitelock, P., Dennefeld, M., and Leibundgut, B., pp. 119–129. Cambridge: Cambridge University Press.
- McCarthy, P.J., Le Borgne, D., Crampton, D., Chen, H.-W., Abraham, R.G., Glazebrook, K., Savaglio, S., Carlberg, R.G., Marzke, R.O., Roth, K., Jørgensen, I., Hook, I., Murowinski, R., and Juneau, S. (2004). Evolved galaxies at $z \geq 1.5$ from the Gemini Deep Deep Survey: the formation epoch of massive stellar systems, *Astrophysical Journal Letters*, **614**, L9–L12.
- McCarthy, P.J., van Breugel, W.J.M., Spinrad, H., and Djorgovski, G. (1987). A correlation between the radio and optical morphologies of distant 3CR radio galaxies, *Astrophysical Journal*, **321**, L29–L33.
- McCrea, W. (1970). A philosophy for Big Bang cosmology, *Nature*, **228**, 21–24.

- McDonald, P., Seljak, U., Burles, S., Schlegel, D.J., Weinberg, D.H., Cen, R., D., S., Schaye, J., Schneider, D.P., Bahcall, N.A., Briggs, J., Brinkmann, J., Brunner, R.J., Fukugita, M., Gunn, J.E., Ivezić, Z., Kent, S., Lupton, R.H., and Vanden Berk, D.E. (2006). The Ly- α forest power spectrum from the Sloan Digital Sky Survey, *Astrophysical Journal Supplement Series*, **163**, 80–109.
- McLure, R.J., Jarvis, M.J., Targett, T.A., Dunlop, J.S., and Best, P.N. (2006). On the evolution of the black hole: spheroid mass ratio, *Monthly Notices of the Royal Astronomical Society*, **368**, 1395–1403.
- McNally, S.J. and Peacock, J.A. (1995). The smallscale clustering power spectrum and relativistic decays, *Monthly Notices of the Royal Astronomical Society*, **277**, 143–151.
- Melott, A., Weinberg, D., and Gott, J. (1988). The topology of large-scale structure: II. Nonlinear evolution of Gaussian models, *Astrophysical Journal*, **328**, 50–68.
- Merritt, D. (1987). The distribution of dark matter in the Coma cluster, *Astrophysical Journal*, **313**, 121–135.
- Mészáros, P. (1974). The behaviour of point masses in an expanding cosmological substratum, *Astronomy and Astrophysics*, **37**, 225–228.
- Metcalfe, N., Shanks, T., Campos, A., Fong, R., and Gardner, J.P. (1996). Galaxy formation at high redshifts, *Nature*, **383**, 236–237.
- Metcalfe, N., Shanks, T., Weilbacher, P.M., McCracken, H.J., Fong, R., and Thompson, D. (2006). Galaxy number counts: VI. An H-band survey of the Herschel Deep Field, *Monthly Notices of the Royal Astronomical Society*, **370**, 1257–1273.
- ed. Meylan, G. (1995). *QSO Absorption Lines*. Berlin, Heidelberg: Springer.
- Michell, J. (1767). An inquiry into the probable parallax, and magnitude of the fixed stars, from the quantity of light which they afford us, and the particular circumstances of their situation, *Philosophical Transactions of the Royal Society*, **57**, 234–264.
- Mihos, J.C. and Hernquist, L. (1994). Triggering of starbursts in galaxies by minor mergers, *Astrophysical Journal*, **425**, L13–L16.
- Mihos, J.C. and Hernquist, L. (1996). Gasdynamics and starbursts in major mergers, *Astrophysical Journal*, **464**, 641–663.
- Miley, G.K. (1968). Variation of the angular sizes of quasars with red-shift, *Nature*, **218**, 933–934.
- Miley, G.K. (1971). The radio structure of quasars – a statistical investigation, *Monthly Notices of the Royal Astronomical Society*, **152**, 477–490.
- Milne, E.A. and McCrea, W.H. (1934a). Newtonian expanding universe, *Quarterly Journal of Mathematics*, **5**, 64–72.
- Milne, E.A. and McCrea, W.H. (1934b). Newtonian universes and the curvature of space, *Quarterly Journal of Mathematics*, **5**, 73–80.
- Miranda-Escudé, J., Cen, R., Ostriker, J.P., and Rauch, M. (1996). The Lyman alpha forest from gravitational collapse in the CDM + lambda model, *Astrophysical Journal*, **471**, 582–616.
- Mitchell, J.L., Keeton, C.R., Frieman, J.A., and Sheth, R.K. (2005). Improved cosmological constraints from gravitational lens statistics, *Astrophysical Journal*, **622**, 81–98.

- Mitchell, R.J., Culhane, J.L., Davison, P.J.N., and Ives, J.C. (1976). Ariel 5 observations of the X-ray spectrum of the Perseus cluster, *Monthly Notices of the Royal Astronomical Society*, **175**, 29P–34P.
- Møller, P. and Jakobsen, P. (1990). The Lyman continuum opacity at high redshifts – through the Lyman forest and beyond the Lyman valley, *Astronomy and Astrophysics*, **228**, 299–309.
- Monaco, P. (1998). The cosmological mass function, *Fundamentals of Cosmic Physics*, **19**, 157–317.
- Monaco, P. (1999). Dynamics in the cosmological mass function (or, why does the Press & Schechter work?), in *Observational Cosmology: The Development of Galaxy Systems*, eds. Giuricin, G., Mezzetti, M., and Salucci, P., pp. 186–197. San Francisco: Astronomical Society of the Pacific Conference Series No. 176.
- Monchaux, R., Berhanu, M., Bourgoin, M., Moulin, M., Odier, P., Pinton, J.-F., Volk, R., Fauve, S., Mordant, N., Pétrélis, F., Chiffaudel, A., Daviaud, F., Dubrulle, B., Gasquet, C., Marié, L., and Ravelet, F. (2007). Generation of a magnetic field by dynamo action in a turbulent flow of liquid sodium, *Physical Review Letters*, **98**(4), 044502.
- Montroy, T.E., Ade, P.A.R., Bock, J.J., Bond, J.R., Borrill, J., Boscaleri, A., Cambella, P., Contaldi, C.R., Crill, B.P., de Bernardis, P., De Gasperis, G., de Oliveira-Costa, A., De Troia, G., di Stefano, G., Hivon, E., Jaffe, A.H., Kisner, T.S., Jones, W.C., Lange, A.E., Masi, S., Mauskopf, P.D., MacTavish, C.J., Melchiorri, A., Natoli, P., Netterfield, C.B., Pascale, E., Piacentini, F., Pogosyan, D., Polenta, G., Prunet, S., Ricciardi, S., Romeo, G., Ruhl, J.E., Santini, P., Tegmark, M., Veneziani, M., and Vittorio, N. (2006). A measurement of the CMB (EE) spectrum from the 2003 flight of BOOMERANG, *Astrophysical Journal*, **647**, 813–822.
- Mukhanov, V. (2005). *Physical Foundations of Cosmology*. Cambridge: Cambridge University Press.
- Murdoch, H.S., Hunstead, R.W., Pettini, M., and Blades, J.C. (1986). Absorption spectrum of the $Z = 3.78$ QSO 2000-330: II. The redshift and equivalent width distributions of primordial hydrogen clouds, *Astrophysical Journal*, **309**, 19–32.
- Naselsky, P., Novikov, D., and Novikov, I. D. (2006). *The Physics of the Cosmic Microwave Background*. Cambridge: Cambridge University Press.
- Norberg, P., Baugh, C.M., Hawkins, E., Maddox, S., Madgwick, D., Lahav, O., Cole, S., Frenk, C.S., Baldry, I., Bland-Hawthorn, J., Bridges, T., Cannon, R., Colless, M., Collins, C., Couch, W., Dalton, G., De Propris, R., Driver, S.P., Efstathiou, G., Ellis, R.S., Glazebrook, K., Jackson, C., Lewis, I., Lumsden, S., Peacock, J.A., Peterson, B.A., Sutherland, W., and Taylor, K. (2002). The 2dF Galaxy Redshift Survey: the dependence of galaxy clustering on luminosity and spectral type, *Monthly Notices of the Royal Astronomical Society*, **332**, 827–838.
- Norberg, P., Baugh, C.M., Hawkins, E., Maddox, S., Peacock, J.A., Cole, S., Frenk, C.S., Bland-Hawthorn, J., Bridges, T., Cannon, R., Colless, M., Collins, C., Couch, W., Dalton, G., De Propris, R., Driver, S.P., Efstathiou, G., Ellis, R.S., Glazebrook, K., Jackson, C., Lahav, O., Lewis, I., Lumsden, S., Madgwick, D., Peterson, B.A., Sutherland, W., and Taylor, K. (2001). The 2dF Galaxy Redshift

- Survey: luminosity dependence of galaxy clustering, *Monthly Notices of the Royal Astronomical Society*, **328**, 64–70.
- Novikov, I. (1964). On the possibility of appearance of large scale inhomogeneities in the expanding Universe, *Journal of Experimental and Theoretical Physics*, **46**, 686–689.
- Oemler, A.J. (1974). The systematic properties of clusters of galaxies. Photometry of 15 clusters, *Astrophysical Journal*, **194**, 1–20.
- Oguri, M. (2007). Gravitational lens time delays: a statistical assessment of lens model dependences and implications for the global Hubble constant, *Astrophysical Journal*, **660**, 1–15.
- Ohta, K., Yamada, T., Nakanishi, K., Kohno, K., Akiyama, M., and Kawabe, R. (1996). Detection of molecular gas in the quasar BR1202-0725 at redshift $z = 4.69$, *Nature*, **382**, 426–428.
- Oliver, S.J., Rowan-Robinson, M., and Saunders, W. (1992). Infrared background constraints on the evolution of IRAS galaxies, *Monthly Notices of the Royal Astronomical Society*, **256**, 15P–22P.
- Omton, A. (1996). 1.3 mm detection and mapping of radioquiet QSOs at very high redshifts, in *Science with Large Millimetre Arrays*, ed. Shaver, P., pp. 82–85. Berlin: Springer.
- Omton, A., Petitjean, P., Guilloteau, S., McMahon, R.G., Solomon, P.M., and Pécontal, E. (1996). Molecular gas and dust around a radio-quiet quasar at redshift 4.69, *Nature*, **382**, 428–431.
- O'Neill, S.M., Jones, T.W., Tregillis, I.L., and Ryu, D. (2006). 3D MHD interactions of jets with cluster media, *Astronomische Nachrichten*, **327**, 535–536.
- Oort, J.H. (1958). Distribution of galaxies and density in the universe, in *Solvay Conference on The Structure and Evolution of the Universe*, pp. 163–181. Brussels: Institut International de Physique Solvay.
- Opal Collaboration (1990). A combined analysis of the hadronic and leptonic decays of the Z^0 , *Physics Letters*, **B240**, 497–512.
- Ortiz-Gil, A., Guzzo, L., Schuecker, P., Böhringer, H., and Collins, C.A. (2004). The X-ray luminosity-velocity dispersion relation in the REFLEX Cluster Survey, *Monthly Notices of the Royal Astronomical Society*, **348**, 325–332.
- Osmer, P.S. (1982). Evidence for a decrease in the space density of quasars at z more than about 3.5, *Astrophysical Journal*, **253**, 28–37.
- Ostriker, J.P. and Cowie, L. (1981). Galaxy formation in an intergalactic medium dominated by explosions, *Astrophysical Journal*, **243**, L127–L131.
- Ostriker, J.P. and Ikeuchi, S. (1983). Physical properties of the intergalactic medium and the Lyman-alpha absorbing clouds, *Astrophysical Journal Letters*, **268**, L63–L68.
- Ostriker, J.P. and Peebles, P.J.E. (1973). A numerical study of the stability of flattened galaxies: or, can cold galaxies survive?, *Astrophysical Journal*, **186**, 467–480.
- Oswalt, T.D., Smith, J.A., Wood, M.A., and Hintzen, P. (1996). A lower limit of 9.5 Gyr on the age of the galactic disk from the oldest white dwarf stars, *Nature*, **382**, 692–694.

- Ouchi, M., Shimasaku, K., Okamura, S., Furusawa, H., Kashikawa, N., Ota, K., Doi, M., Hamabe, M., Kimura, M., Komiyama, Y., Miyazaki, M., Miyazaki, S., Nakata, F., Sekiguchi, M., Yagi, M., and Yasuda, N. (2004). Subaru Deep Survey: V. A census of Lyman break galaxies at $z \sim 4$ and 5 in the Subaru Deep Fields: photometric properties, *Astrophysical Journal*, **611**, 660–684.
- Paciesas, W.S., Meegan, C.A., Pendleton, G.N., Briggs, M.S., Kouveliotou, C., Koshut, T.M., Lestrade, J.P., McCollough, M.L., Brainerd, J.J., Hakkila, J., Henze, W., Preece, R.D., Connaughton, V., Kippen, R.M., Mallozzi, R.S., Fishman, G.J., Richardson, G.A., and Sahi, M. (1999). The 4th BATSE Gamma-Ray Burst Catalog (revised), *Astrophysical Journal Supplement Series*, **122**, 465–495.
- Padmanabhan, T. (1993). *Structure Formation in the Universe*. Cambridge: Cambridge University Press.
- Padmanabhan, T. (1996). *Cosmology and Astrophysics through Problems*. Cambridge: Cambridge University Press. See pp. 437–440.
- Padmanabhan, T. (1997). Nonlinear gravitational clustering in the expanding Universe, in *Gravitation and Cosmology: Proc. ICGC-95 Conference, Pune*, eds. Dhurandhar, S. and Padmanabhan, T., pp. 37–52. Dordrecht: Kluwer Academic Publishers.
- Page, L. (1997). Review of observations of the cosmic microwave background, in *Critical Dialogues in Cosmology*, ed. Turok, N., pp. 343–362. Singapore: World Scientific.
- Page, L., Hinshaw, G., Komatsu, E., Nolta, M.R., Spergel, D.N., Bennett, C.L., Barnes, C., Bean, R., Doré, O., Dunkley, J., Halpern, M., Hill, R.S., Jarosik, N., Kogut, A., Limon, M., Meyer, S.S., Odegard, N., Peiris, H.V., Tucker, G.S., Verde, L., Weiland, J.L., Wollack, E., and Wright, E.L. (2007). Three-year Wilkinson Microwave Anisotropy Probe (WMAP) observations: polarization analysis, *Astrophysical Journal Supplement*, **170**, 335–376.
- Pagel, B. (1997). *Nucleosynthesis and Chemical Evolution of Galaxies*. Cambridge: Cambridge University Press.
- Pais, A. (1982). *Subtle is the Lord . . . : the Science and Life of Albert Einstein*. Oxford: Oxford University Press.
- Panagia, N., Gilmozzi, R., Macchetto, F., Adorf, H.-M., and Kirshner, R.P. (1991). Properties of the SN 1987A circumstellar ring and the distance to the Large Magellanic Cloud, *Astrophysical Journal*, **380**, L23–L26.
- Parker, E.N. (1997). Galactic dynamos and other questions on the origins of magnetic fields, in *Critical Dialogues in Cosmology*, ed. Turok, N., pp. 309–327. Singapore: World Scientific.
- Partridge, R. (1980a). Fluctuations in the cosmic microwave background radiation at small angular scales, *Physica Scripta*, **21**, 624–629.
- Partridge, R. (1980b). New limits on small-scale angular fluctuations in the cosmic microwave background, *Astrophysical Journal*, **235**, 681–687.
- Peacock, J. (2000). *Cosmological Physics*. Cambridge: Cambridge University Press.
- Peacock, J.A. (1985). The high-redshift evolution of radio galaxies and quasars, *Monthly Notices of the Royal Astronomical Society*, **217**, 601–631.

- Peacock, J.A., Cole, S., Norberg, P., Baugh, C.M., Bland-Hawthorn, J., Bridges, T., Cannon, R.D., Colless, M., Collins, C., Couch, W., Dalton, G., Deeley, K., De Propris, R., Driver, S.P., Efstathiou, G., Ellis, R.S., Frenk, C.S., Glazebrook, K., Jackson, C., Lahav, O., Lewis, I., Lumsden, S., Maddox, S., Percival, W.J., Peterson, B.A., Price, I., Sutherland, W., and Taylor, K. (2001). A measurement of the cosmological mass density from clustering in the 2dF Galaxy Redshift Survey, *Nature*, **410**, 169–173.
- Peacock, J.A. and Dodds, S.J. (1994). Reconstructing the linear power spectrum of cosmological mass fluctuations, *Monthly Notices of the Royal Astronomical Society*, **267**, 1020–1034.
- Peacock, J.A. and Heavens, A.F. (1985). The statistics of maxima in primordial density perturbations, *Monthly Notices of the Royal Astronomical Society*, **217**, 805–820.
- Peebles, P. (1981). Primeval adiabatic perturbations – constraints from the mass distribution, *Astrophysical Journal*, **248**, 885–897.
- Peebles, P. (1982). Large-scale background temperature and mass fluctuations due to scale-invariant primeval perturbations, *Astrophysical Journal*, **263**, L1–L5.
- Peebles, P.J.E. (1968). Recombination of the primeval plasma, *Astrophysical Journal*, **153**, 1–11.
- Peebles, P.J.E. (1976). A cosmic virial theorem, *Astrophysics and Space Science*, **45**, 3–19.
- Peebles, P.J.E. (1980). *The Large-Scale Structure of the Universe*. Princeton: Princeton University Press.
- Peebles, P.J.E. (1993). *Principles of Physical Cosmology*. Princeton: Princeton University Press.
- Peebles, P.J.E. and Yu, J.T. (1970). Primeval adiabatic perturbation in an expanding Universe, *Astrophysical Journal*, **162**, 815–836.
- Pei, Y. and Fall, S. (1995). Cosmic chemical evolution, *Astrophysical Journal*, **454**, 69–76.
- Penrose, R. (1997). *The Large, the Small and the Human Mind*. Cambridge: Cambridge University Press.
- Penzias, A.A. and Wilson, R.W. (1965). A measurement of excess antenna temperature at 4080 MHz, *Astrophysical Journal*, **142**, 419–421.
- Perlmutter, S., Aldering, G., della Valle, M., Deustua, S., Ellis, R.S., Fabbro, S., Fruchter, A., Goldhaber, G., Groom, D.E., Hook, I.M., Kim, A.G., Kim, M.Y., Knop, R.A., Lidman, C., McMahon, R.G., Nugent, P., Pain, R., Panagia, N., Pennypacker, C.R., Ruiz-Lapuente, P., Schaefer, B., and Walton, N. (1998). Discovery of a supernova explosion at half the age of the universe, *Nature*, **391**, 51–54.
- Perlmutter, S., Boyle, B., Bunclark, P., Carter, D., Couch, W., Deustua, S., Dopita, M., Ellis, R., Filippenko, A.V., Gabi, S., Glazebrook, K., Goldhaber, G., Goobar, A., Groom, D., Hook, I., Irwin, M., Kim, A., Kim, M., Lee, J., Matheson, T., McMahon, R., Newberg, H., Pain, R., Pennypacker, C., and Small, I. (1996). High-redshift supernova discoveries on demand: first results from a new tool for cosmology and bounds on q_0 , *Nuclear Physics B*, **51**, 20–29.

- Perlmutter, S., Gabi, S., Goldhaber, G., Goobar, A., Groom, D.E., Hook, I.M., Kim, A.G., Kim, M.Y., Lee, J.C., Pain, R., Pennypacker, C.R., Small, I.A., Ellis, R.S., McMahon, R.G., Boyle, B.J., Bunclark, P.S., Carter, D., Irwin, M.J., Glazebrook, K., Newberg, H.J.M., Filippenko, A.V., Matheson, T., Dopita, M., and Couch, W.J. (1997). Measurements of the cosmological parameters omega and lambda from the first seven supernovae at $z > 0.35$, *Astrophysical Journal*, **483**, 565–581.
- Persic, M., de Zotti, G., Boldt, E.A., Marshall, F.E., Danese, L., Franceschini, A., and Palumbo, G.G.C. (1989). The autocorrelation properties of fluctuations in the cosmic X-ray background, *Astrophysical Journal Letters*, **336**, L47–L50.
- Petrosian, V. and Salpeter, E.E. (1968). Ghost images in inhomogeneous Friedmann universes, *Astrophysical Journal*, **151**, 411–429.
- Pettini, M., Ellison, S.L., Steidel, C.C., and Bowen, D.V. (1999). Metal abundances at $z \leq 1.5$: fresh clues to the chemical enrichment history of damped Lyman- α systems, *Astrophysical Journal*, **510**, 576–589.
- Pettini, M., King, D.L., Smith, L.J., and Hunstead, R.W. (1997). The metallicity of high-redshift galaxies: the abundance of zinc in 34 damped Ly- α systems from $z = 0.7$ to 3.4, *Astrophysical Journal*, **486**, 665–680.
- Phillips, M.M. (1993). The absolute magnitudes of Type IA supernovae, *Astrophysical Journal*, **413**, L105–L108.
- Pound, R. and Rebka, G. (1960). Apparent weight of photons, *Physical Review Letters*, **4**, 337–341.
- Pound, R. and Snider, J. (1965). Effect of gravity on gamma radiation, *Physical Review*, **140**, B788–B803.
- Pozdnyakov, L.A., Sobol, I.M., and Sunyaev, R.A. (1983). Comptonization and the shaping of X-ray source spectra – Monte Carlo calculations, *Soviet Scientific Reviews, Section E: Astrophysics and Space Physics Reviews*, **2**, 189–331.
- Pratt, G.W. and Arnaud, M. (2002). The mass profile of A1413 observed with XMM-Newton: implications for the M-T relation, *Astronomy and Astrophysics*, **394**, 375–393.
- Press, W. and Schechter, P. (1974). Formation of galaxies and clusters of galaxies by self-similar gravitational condensation, *Astrophysical Journal*, **187**, 425–438.
- Primack, J.R., Seckel, D., and Sadoulet, B. (1988). Detection of cosmic dark matter, *Annual Review of Nuclear and Particle Science*, **38**, 751–807.
- Pritchard, J.R. and Furlanetto, S.R. (2007). 21-cm Fluctuations from inhomogeneous X-ray heating before reionisation, *Monthly Notices of the Royal Astronomical Society*, **376**, 1680–1694.
- Prochaska, J.X. and Wolfe, A.M. (2002). The UCSD HIRES/Keck I damped Ly α abundance database: II. The implications, *Astrophysical Journal*, **566**, 68–92.
- Prochaska, J.X., Gawiser, E., Wolfe, A.M., Castro, S. and Djorgovski, S.G. (2003). The Age-Metallicity Relation of the Universe in Neutral Gas: The First 100 Damped Ly α Systems, *Astrophysical Journal Letters*, **595**, L9–L12.
- Puget, J.-L., Abergel, A., Bernard, J.-P., Boulanger, F., Burton, W.B., Desert, F.-X., and Hartmann, D. (1996). Tentative detection of a cosmic far-infrared background with COBE, *Astronomy and Astrophysics*, **308**, L5–L8.

- Readhead, A.C.S., Mason, B.S., Contaldi, C.R., Pearson, T.J., Bond, J.R., Myers, S.T., Padin, S., Sievers, J.L., Cartwright, J.K., Shepherd, M.C., Pogosyan, D., Prunet, S., Altamirano, P., Bustos, R., Bronfman, L., Casassus, S., Holzapfel, W.L., May, J., Pen, U.-L., Torres, S., and Udomprasert, P.S. (2004). Extended mosaic observations with the cosmic background imager, *Astrophysical Journal*, **609**, 498–512.
- Rees, M.J. (1994). Origin of the seed magnetic field for a galactic dynamo, in *Cosmical Magnetism*, ed. Lynden-Bell, D., pp. 155–160. Dordrecht: Kluwer.
- Rees, M.J. (1995). *Perspectives in Astrophysical Cosmology*. Cambridge: Cambridge University Press.
- Rees, M.J. (2006). Origin of cosmic magnetic fields, *Astronomische Nachrichten*, **327**, 395–398.
- Rees, M.J. and Ostriker, J.P. (1977). Cooling, dynamics and fragmentation of massive gas clouds – clues to the masses and radii of galaxies and clusters, *Monthly Notices of the Royal Astronomical Society*, **179**, 541–559.
- Rees, M.J. and Sciama, D.W. (1968). Large-scale density inhomogeneities in the Universe, *Nature*, **217**, 511–516.
- Refregier, A. (2003). Weak gravitational lensing by large-scale structure, *Annual Review of Astronomy and Astrophysics*, **41**, 645–668.
- Reimers, D., Clavel, J., Groote, D., Engels, D., Hagen, H.J., Naylor, T., Wamsteker, W., and Hopp, U. (1989). The luminous Quasar HS1700+6416 and the shape of the ‘Big Bump’ below 500 Å, *Astronomy and Astrophysics*, **218**, 71–77.
- Reiprich, T.H. and Böhringer, H. (2002). The mass function of an X-Ray Flux-limited sample of galaxy clusters, *Astrophysical Journal*, **567**, 716–740.
- Richards, G.T., Strauss, M.A., Fan, X., Hall, P.B., Jester, S., Schneider, D.P., Vanden Berk, D.E., Stoughton, C., Anderson, S.F., Brunner, R.J., Gray, J., Gunn, J.E., Ivezić, Ž., Kirkland, M.K., Knapp, G.R., Loveday, J., Meiksin, A., Pope, A., Szalay, A.S., Thakar, A.R., Yanny, B., York, D.G., Barentine, J.C., Brewington, H.J., Brinkmann, J., Fukugita, M., Harvanek, M., Kent, S.M., Kleinman, S.J., Krzesiński, J., Long, D.C., Lupton, R.H., Nash, T., Neilsen, Jr., E.H., Nitta, A., Schlegel, D.J., and Snedden, S.A. (2006). The Sloan Digital Sky Survey Quasar Survey: quasar luminosity function from data release 3, *Astronomical Journal*, **131**, 2766–2787.
- Rindler, W. (1956). Visual horizons in world models, *Monthly Notices of the Royal Astronomical Society*, **116**, 662–677.
- Rindler, W. (2001). *Relativity: Special, General and Cosmological*. Oxford: Oxford University Press.
- Roberts, M.S. and Haynes, M.P. (1994). Physical parameters along the Hubble Sequence, *Annual Review of Astronomy and Astrophysics*, **26**, 115–152.
- Robertson, H.P. (1935). Kinematics and world structure, *Astrophysical Journal*, **82**, 284–301.
- Rosati, P., Borgani, S., and Norman, C. (2002). The evolution of X-ray clusters of galaxies, *Annual Review of Astronomy and Astrophysics*, **40**, 539–577.

- Rowan-Robinson, M. (1968). The determination of the evolutionary properties of quasars by means of the luminosity-volume test, *Monthly Notices of the Royal Astronomical Society*, **141**, 445–458.
- Rowan-Robinson, M. (1985). *The Cosmological Distance Ladder*. New York: Freeman.
- Rowan-Robinson, M. (1988). The extragalactic distance scale, *Space Science Reviews*, **48**, 1–71.
- Rowan-Robinson, M., Benn, C.R., Lawrence, A., McMahon, R.G., and Broadhurst, T.J. (1993). The evolution of faint radio sources, *Monthly Notices of the Royal Astronomical Society*, **263**, 123–130.
- Rutherford, E. (1907). Some cosmical aspects of radioactivity, *Journal of the Royal Astronomical Society of Canada*, **1**, 145–165.
- Ryle, M. (1955). Radio stars and their cosmological significance, *The Observatory*, **75**, 137–147.
- Ryle, M. (1958). The nature of the cosmic radio sources, *Proceedings of the Royal Society*, **A248**, 289–308.
- Ryle, M. and Sandage, A.R. (1964). The optical identification of three new radio objects of the 3C 48 class, *Astrophysical Journal*, **139**, 419–421.
- Sachs, R. and Wolfe, A. (1967). Perturbations of a cosmological model and angular variations in the microwave background, *Astrophysical Journal*, **147**, 73–90.
- Sahu, K.C., Livio, M., Petro, L., Macchetto, F.D., van Paradijs, J., Kouveliotou, C., Fishman, G.J., Meegan, C.A., Groot, P.J., and Galama, T. (1997). The optical counterpart to gamma-ray burst GRB 970228 observed using the Hubble Space Telescope, *Nature*, **387**, 476–478.
- Sajina, A., Scott, D., Dennefeld, M., Dole, H., Lacy, M., and Lagache, G. (2006). The 1–1000 μm spectral energy distributions of far-infrared galaxies, *Monthly Notices of the Royal Astronomical Society*, **369**, 939–957.
- Sakharov, A. (1965). The initial stage of an expanding universe and the appearance of a nonuniform distribution of matter, *Zhurnal Eksperimentalnoi i Teoreticheskoi Fiziki*, **49**, 345–358. [English translation: *Soviet Physics JETP*, **22**, 241–249, 1966.]
- Sakharov, A. (1967). Violation of CP invariance, C asymmetry, and baryon asymmetry of the Universe, *Zhurnal Experimentalnoi i Teoreticheskikh Fizika (JETP) Letters*, **5**, 32–35.
- Sandage, A.R. (1961a). The ability of the 200-inch telescope to discriminate between selected world models, *Astrophysical Journal*, **133**, 355–392.
- Sandage, A.R. (1961b). *The Hubble Atlas of Galaxies*. Washington D.C.: Carnegie Institution of Washington. Publication 618.
- Sandage, A.R. (1965). The existence of a major new constituent of the Universe: the quasistellar galaxies, *Astrophysical Journal*, **141**, 1560–1578.
- Sandage, A.R. (1968). Observational cosmology, *The Observatory*, **88**, 91–106.
- Sandage, A.R. (1975). Classification and stellar content of galaxies obtained from direct photography, in *Stars and Stellar Systems*, **9. Galaxies and the Universe**, eds. A.R. Sandage, M.S. and Kristian, J., pp. 1–35. Chicago: Chicago University Press.

- Sandage, A.R. (1988). Observational tests of world models, *Annual Review of Astronomy and Astrophysics*, **26**, 561–630.
- Sandage, A.R. (1995). Practical cosmology: inventing the past, in *The Deep Universe*, by Sandage, A.R., Kron, R.G. and Longair, M.S., eds. Binggeli, B. and Buser, R., pp. 1–232. Berlin: Springer-Verlag.
- Sandage, A.R. and Hardy, E. (1973). The redshift-distance relation: VII. Absolute magnitudes of the first three ranked cluster galaxies as function of cluster richness and Bautz–Morgan cluster type: the effect on q_0 , *Astrophysical Journal*, **183**, 743–758.
- Sandage, A.R. and Schwarzschild, M. (1952). Inhomogeneous stellar models: II. Models with exhausted cores in gravitational contraction, *Astrophysical Journal*, **116**, 463–476.
- Sanders, D.B. and Mirabel, I.F. (1996). Luminous infrared galaxies, *Annual Review of Astronomy and Astrophysics*, **34**, 749–792.
- Saunders, W., Rowan-Robinson, M., Lawrence, A., Efstathiou, G., Kaiser, N., Ellis, R.S., and Frenk, C.S. (1990). The 60-micron and far-infrared luminosity functions of IRAS galaxies, *Monthly Notices of the Royal Astronomical Society*, **242**, 318–337.
- Savaglio, S., Glazebrook, K., Le Borgne, D., Juneau, S., Abraham, R.G., Chen, H.-W., Crampton, D., McCarthy, P.J., Carlberg, R.G., Marzke, R.O., Roth, K., Jørgensen, I., and Murowinski, R. (2005). The Gemini Deep Deep Survey: VII. The redshift evolution of the mass-metallicity relation, *Astrophysical Journal*, **635**, 260–279.
- Schechter, P. (1976). An analytic expression for the luminosity function of galaxies, *Astrophysical Journal*, **203**, 297–306.
- Schechter, P.L. (2002). Tales within tales and cutoffs within cutoffs: what sets the mass scale for galaxies?, in *Lighthouses of the Universe: The Most Luminous Objects and Their Use for Cosmology*, eds. Gilfanov, M., Sunyeav, R., and Churazov, E., pp. 3–12. Berlin: Springer.
- Scheuer, P.A.G. (1957). A statistical method for analysing observations of faint radio stars, *Proceedings of the Cambridge Philosophical Society*, **53**, 764–773.
- Scheuer, P.A.G. (1965). A sensitive test for the presence of atomic hydrogen in intergalactic space, *Nature*, **207**, 963.
- Scheuer, P.A.G. (1974). Fluctuations in the X-ray background, *Monthly Notices of the Royal Astronomical Society*, **166**, 329–338.
- Scheuer, P.A.G. (1990). Radio source counts, in *Modern Cosmology in Retrospect*, eds Bertotti, B., Balbinot, R., Bergia, S., and Messina, A., pp. 331–346. Cambridge: Cambridge University Press.
- Schindler, S., Binggeli, B., and Böhringer, H. (1999). Morphology of the Virgo cluster: gas versus galaxies, *Astronomy and Astrophysics*, **343**, 420–438.
- Schmidt, B.P., Kirshner, R.P., and Eastman, R.G. (1992). Expanding photospheres of type II supernovae and the extragalactic distance scale, *Astrophysical Journal*, **395**, 366–386.
- Schmidt, M. (1968). Space distribution and luminosity functions of quasi-stellar sources, *Astrophysical Journal*, **151**, 393–409.

- Schmidt, M. and Green, R.F. (1983). Quasar evolution derived from the Palomar Bright Quasar Survey and other complete quasar surveys, *Astrophysical Journal*, **269**, 352–374.
- Schmidt, M., Schneider, D.P., and Gunn, J.E. (1995). Spectroscopic CCD Surveys for Quasars at Large Redshift. IV. Evolution of the luminosity function from quasars detected by their Lyman-alpha emission, *Astronomical Journal*, **110**, 68–77.
- Schneider, D., Schmidt, M., and Gunn, J.E. (1991). PC 1247 + 3406 - an optically selected quasar with a redshift of 4.897, *Astronomical Journal*, **102**, 837–840.
- Schneider, P., Kochanek, C.S., and Wambsganss, J. (2006). *Gravitational Lensing: Strong, Weak and Micro*. Berlin: Springer. Saas-Fee Advanced Course 33: eds. Meylan, G. and Jetzer, P. and North, P.
- Schramm, D.N. (1997). The age of the Universe, in *Critical Dialogues in Cosmology*, ed. Turok, N., pp. 81–91. Singapore: World Scientific.
- Schramm, D.N. and Wasserburg, G.T. (1970). Nucleochronologies and the mean age of the elements, *Astrophysical Journal*, **162**, 57–69.
- Schutz, B. (2001). Gravitational radiation, in *Encyclopaedia of Astronomy and Astrophysics*, ed. P. M., volume 2, pp. 1030–1042. Bristol and Philadelphia: Institute of Physics Publishing and London: Nature Publishing Group.
- Schwarzchild, M. (1979). A numerical model for a triaxial stellar system in dynamical equilibrium, *Astrophysical Journal*, **232**, 236–228.
- Scott, J., Bechtold, J., Dobrzycki, A., and Kulkarni, V.P. (2000). A uniform analysis of the Ly α forest at $z = 0 – 5$: II. Measuring the mean intensity of the extragalactic ionizing background using the proximity effect, *Astrophysical Journal Supplement*, **130**, 67–89.
- Scranton, R., Johnston, D., Dodelson, S., Frieman, J., Connolly, A., Eisenstein, D., Gunn, J., Hui, L., Jain, B., Kent, S., Loveday, J., Narayanan, V., Nichol, R., O’Connell, L., Scoccimarro, R., Sheth, R., Stebbins, A., Strauss, M., Szalay, A., Szapudi, I., Tegmark, M., Vogeley, M., Zehavi, I., Annis, J., Bahcall, N., Brinkman, J., Csabai, I., Hindsley, R., Ivezić, Z., Kim, R., Knapp, G., Lamb, D., Lee, B., Lupton, R., McKay, T., Munn, J., Peoples, J., Pier, J., Richards, G., Rockosi, C., Schlegel, D., Schneider, D., Stoughton, C., Tucker, D., Yanny, B., and York, D. (2002). Analysis of systematic effects and statistical uncertainties in angular clustering of galaxies from early Sloan Digital Sky Survey Data, *Astrophysical Journal*, **579**, 48–75.
- Seager, S., Sasselov, D.D., and Scott, D. (2000). How exactly did the Universe become neutral?, *Astrophysical Journal Supplement*, **128**, 407–430.
- Seldner, M. and Peebles, P.J.E. (1977). Statistical analysis of catalogs of extragalactic objects: VIII. Cross-correlation of the Abell and the 10-arcmin Shane–Wirtanen catalogs, *Astrophysical Journal*, **215**, 703–716.
- Seljak, U., Makarov, A., McDonald, P., Anderson, S.F., Bahcall, N.A., Brinkmann, J., Burles, S., Cen, R., Doi, M., Gunn, J.E., Ivezić, Ž., Kent, S., Loveday, J., Lupton, R.H., Munn, J.A., Nichol, R.C., Ostriker, J.P., Schlegel, D.J., Schneider, D.P., Tegmark, M., Berk, D.E., Weinberg, D.H., and York, D.G. (2005). Cosmological parameter analysis including SDSS Ly α forest and galaxy bias: constraints on the

- primordial spectrum of fluctuations, Neutrino Mass, and Dark Energy, *Physical Review D*, **71**, 103515.
- Seljak, U. and Zaldarriaga, M. (1996). A line-of-sight integration approach to cosmic microwave background anisotropies, *Astrophysical Journal*, **469**, 437–444.
- Sérsic, J.L. (1968). *Atlas de galaxias australes*. Cordoba, Argentina: Observatorio Astronomico.
- Shapiro, I. (1990). Solar system tests of General Relativity: recent results and present plans, in *General Relativity and Gravitation*, eds. Ashby, N., Bartlett, D.F., and Wyss, W., pp. 313–330. Cambridge: Cambridge University Press.
- Shapiro, I.I. (1964). Fourth test of General Relativity, *Physical Review Letters*, **13**, 789–791.
- Shapiro, S.S., Davis, J.L., Lebach, D.E., and Gregory, J.S. (2004). Measurement of the solar gravitational deflection of radio waves using geodetic very-long-baseline interferometry data, 1979–1999, *Physical Review Letters*, **92**, 121101.
- Shapley, H. (1918). Studies Based on the Colors and Magnitudes in Stellar Clusters. VII. The distances, distribution in space, and dimensions of 60 globular clusters, *Astrophysical Journal*, **48**, 154–181.
- Shectman, S.A. (1974). The small scale anisotropy of the cosmic light, *Astrophysical Journal*, **188**, 233–242.
- Shellard, P. (2003). The future of cosmology: observational and computational prospects, in *The Future of Theoretical Physics and Cosmology*, eds. Gibbons, G., Shellard, E., and Rankin, S., pp. 755–780. Cambridge: Cambridge University Press.
- Sheth, R.K., Mo, H.J., and Tormen, G. (2001). Ellipsoidal collapse and an improved model for the number and spatial distribution of dark matter haloes, *Monthly Notices of the Royal Astronomical Society*, **323**, 1–12.
- Shimasaku, K., Ouchi, M., Furusawa, H., Yoshida, M., Kashikawa, N., and Okamura, S. (2005). Number density of bright Lyman-break galaxies at $z \sim 6$ in the Subaru Deep Field, *Publications of the Astronomical Society of Japan*, **57**, 447–458.
- Silk, J. (1968). Cosmic black-body radiation and galaxy formation, *Astrophysical Journal*, **151**, 459–471.
- Silk, J. and Wyse, R.F.G. (1993). Galaxy formation and Hubble sequence, *Physics Reports*, **231**, 293–365.
- Simon, P., Hetterscheidt, M., Schirmer, M., Erben, T., Schneider, P., Wolf, C., and Meisenheimer, K. (2007). GaBoDS: The Garching–Bonn Deep Survey: VI. Probing galaxy bias using weak gravitational lensing, *Astronomy and Astrophysics*, **461**, 861–879.
- Smail, I., Ivison, R.J., and Blain, A.W. (1997). A deep sub-millimeter survey of lensing clusters: a new window on galaxy formation and evolution, *Astrophysical Journal Letters*, **490**, L5–L8.
- Smith, R.W. (1982). *The Expanding Universe: Astronomy's 'Great Debate' 1900–1931*. Cambridge: Cambridge University Press.
- Smoot, G., Bennett, C., Kogut, A., Wright, E., Aymon, J., Boggess, N., Cheng, E., de Amici, G., Gulkis, S., Hauser, M., Hinshaw, G., Jackson, P., Janssen, M.,

- Kaita, E., Kelsall, T., Keegstra, P., Lineweaver, C., Loewenstein, K., Lubin, P., Mather, J., Meyer, S., Moseley, S., Murdock, T., Rokke, L., Silverberg, R., Tenorio, L., Weiss, R., and Wilkinson, D. (1992). Structure in the COBE differential microwave radiometer first-year maps, *Astrophysical Journal*, **396**, L1–L5.
- Sneden, C., McWilliam, A., Preston, G.W., Cowan, J.J., Burris, D.L., and Armosky, B.J. (1992). The ultra-metal-poor, neutron-capture-rich giant star CS 22892-052, *Astrophysical Journal*, **467**, 819–840.
- Songaila, A., Bryant, W., and Cowie, L.L. (1989). Limits on the galactic and cosmic ionizing fluxes from measurements of H- α emission from the high-velocity neutral hydrogen clouds, *Astrophysical Journal Letters*, **345**, L71–L73.
- Songaila, A., Cowie, L.L., Vogt, S., Keane, M., Wolfe, A.M., Hu, E.M., Oren, A.L., Tytler, D.R., and Lanzetta, K.M. (1994). Measurement of the microwave background temperature at a redshift of 1.776, *Nature*, **371**, 43–45.
- Songaila, A., Hu, E.M., and Cowie, L.L. (1995). A population of very diffuse Lyman- α clouds as the origin of the He $^+$ absorption signal in the intergalactic medium, *Nature*, **375**, 124–126.
- Soucail, G., Fort, B., Mellier, Y., and Picat, J.P. (1987). A blue ring-like structure, in the center of the A370 cluster of galaxies, *Astronomy and Astrophysics*, **172**, L14–L16.
- Sparke, L. and Gallagher, J. (2000). *Galaxies in the Universe: an Introduction*. Cambridge: Cambridge University Press.
- Spergel, D.N., Bean, R., Doré, O., Nolta, M.R., Bennett, C.L., Dunkley, J., Hinshaw, G., Jarosik, N., Komatsu, E., Page, L., Peiris, H.V., Verde, L., Halpern, M., Hill, R.S., Kogut, A., Limon, M., Meyer, S.S., Odegard, N., Tucker, G.S., Weiland, J.L., Wollack, E., and Wright, E.L. (2007). Three-year Wilkinson Microwave Anisotropy Probe (WMAP) observations: implications for cosmology, *Astrophysical Journal Supplement*, **170**, 377–408.
- Spinrad, H., Dey, A., and Graham, J.R. (1995). Keck observations of the most distant galaxy: 8C 1435+63 at $z = 4.25$, *Astrophysical Journal*, **438**, L51–L54.
- Spite, F. and Spite, M. (1982). Abundance of lithium in unevolved halo stars and old disk stars – interpretation and consequences, *Astronomy and Astrophysics*, **115**, 357–366.
- Springel, V. (2005). The cosmological simulation code GADGET-2, *Monthly Notices of the Royal Astronomical Society*, **364**, 1105–1134. For access to his simulations, see <http://www.mpa-garching.mpg.de/gadget/right.html>.
- Springel, V., White, S.D.M., Jenkins, A., Frenk, C.S., Yoshida, N., Gao, L., Navarro, J., Thacker, R., Croton, D., Helly, J., Peacock, J.A., Cole, S., Thomas, P., Couchman, H., Evrard, A., Colberg, J., and Pearce, F. (2005). Simulations of the formation, evolution and clustering of galaxies and quasars, *Nature*, **435**, 629–636.
- Srianand, R. (2006). Intergalactic medium, in *The Scientific Requirements for Extremely Large Telescopes: IAU Symposium No. 232*, eds. Whitelock, P., Dennefeld, M., and Leibundgut, B., pp. 130–139.
- Starobinsky, A.A. (1985). Cosmic background anisotropy induced by isotropic flat-spectrum gravitational-wave perturbations, *Soviet Astronomy Letters*, **11**, 133–137. In Russian: 1985, *Pis'ma v Astronomicheskii Zhurnal*, **11**, 323–330.

- Steidel, C. (1998). Galaxy evolution: has the “epoch of galaxy formation” been found?, in *Eighteenth Texas Symposium on Relativistic Astrophysics and Cosmology*, eds. Olinto, A., Frieman, J., and Schramm, D., pp. 124–135. River Edge, NJ: World Scientific.
- Steidel, C. and Hamilton, D. (1992). Deep imaging of high redshift QSO fields below the Lyman limit: I. The field of Q0000-263 and galaxies at $Z = 3.4$, *Astronomical Journal*, **104**, 941–949.
- Steidel, C.C., Adelberger, K.L., Giavalisco, M., Dickinson, M., and Pettini, M. (1999). Lyman-break galaxies at $z \geq 4$ and the evolution of the ultraviolet luminosity density at high redshift, *Astrophysical Journal*, **519**, 1–17.
- Steigman, G. (1997). The crisis confronting standard Big Bang nucleosynthesis, in *Critical Dialogues in Cosmology*, ed. Turok, N., pp. 63–80. Singapore: World Scientific.
- Steigman, G. (2004). Big Bang nucleosynthesis: probing the first 20 minutes, in *Measuring and Modeling the Universe*, ed. Freedman, W.L., pp. 169–195. Cambridge: Cambridge University Press.
- Steigman, G. (2006). Primordial nucleosynthesis: successes and challenges, *International Journal of Modern Physics E*, **15**, 1–35.
- Steigman, G. (2007). Primordial nucleosynthesis, *Annual Review of Nuclear and Particle Science*, **57**, (in press).
- Storrie-Lombardi, L., McMahon, R., and Irwin, M. (1996). Evolution of neutral gas at high redshift: implications for the epoch of galaxy formation, *Monthly Notices of the Royal Astronomical Society*, **283**, L79–L83.
- Stoughton, D., Lupton, R.H., and 191 authors (2002). Sloan Digital Sky Survey: early data release, *Astronomical Journal*, **123**, 485–548.
- Strömborg, G. (1934). The origin of the galactic rotation and of the connection between physical properties of the stars and their motions, *Astrophysical Journal*, **79**, 460–474.
- Subramanian, K. (2005). The physics of CMBR anisotropies, *Current Science*, **88**, 1068–1087.
- Sullivan, III, W.T. (1990). The entry of radio astronomy into cosmology: radio stars and Martin Ryle’s 2C survey, in *Modern Cosmology in Retrospect*, eds. Bertotti, B., Balbinot, R., Bergia, S., and Messina, A., pp. 309–330. Cambridge: Cambridge University Press.
- Sunyaev, R. and Zeldovich, Y. (1970). Small-scale fluctuations of relic radiation, *Astrophysics and Space Science*, **7**, 3–19.
- Sunyaev, R.A. (1969). The interaction of the metagalactic ultraviolet background radiation with galaxies and the limit on the density of the intergalactic gas, *Astrophysical Letters*, **3**, 33–38.
- Sunyaev, R.A. and Zeldovich, Y.B. (1972). Formation of clusters of galaxies; protocluster fragmentation and intergalactic gas heating, *Astronomy and Astrophysics*, **20**, 189–200.
- Sunyaev, R.A. and Zeldovich, Y.B. (1980a). Microwave background radiation as a probe of the contemporary structure and history of the Universe, *Annual Review of Astronomy and Astrophysics*, **18**, 537–560.

- Sunyaev, R.A. and Zeldovich, Y.B. (1980b). The velocity of clusters of galaxies relative to the microwave background – the possibility of its measurement, *Monthly Notices of the Royal Astronomical Society*, **190**, 413–420.
- eds. Tanvir, N.R., Aragon-Salamanca, A., and Wall, J.V. (1997). *The Hubble Space Telescope and the High Redshift Universe*. Singapore: World Scientific.
- Taylor, R.J. (1994). *The Stars: Their Structure and Evolution*. Cambridge: Cambridge University Press.
- Taylor, G.B. and Wright, E.L. (1989). Effects of a hot intergalactic medium, *Astrophysical Journal*, **339**, 619–628.
- Taylor, J.H. (1992). Pulsar timing and relativistic gravity, *Philosophical Transactions of the Royal Society*, **341**, 117–134.
- Taylor, J.H. and Cordes, J.M. (1993). Pulsar distances and the galactic distribution of free electrons, *Astrophysical Journal*, **411**, 674–684.
- Tegmark, M., Strauss, M., and 66 authors (2004). Cosmological parameters from SDSS and WMAP, *Physical Review D*, **69**, 103501 (1–28).
- Thorne, K., Price, R., and Macdonald, D. (1986). *Black Holes: The Membrane Paradigm*. New Haven: Yale University Press.
- Tinsley, B.M. (1980). Evolution of the stars and gas in galaxies, *Fundamentals of Cosmic Physics*, **5**, 287–388.
- Tinsley, B.M. and Gunn, J.E. (1976). Luminosity functions and the evolution of low-mass population: I. Giants, *Astrophysical Journal*, **206**, 525–535.
- Toller, G.N. (1990). Optical observations of galactic and extragalactic light – implications for galactic structure, in *The Galactic and Extragalactic Background Radiation*, eds. Bowyer, S. and Leinert, C., IAU Symposium No. 139, pp. 21–34. Dordrecht: Kluwer.
- Tolman, R. (1934). Effect of inhomogeneity on cosmological models, *Proceedings of the National Academy of Sciences*, **20**, 169–176.
- Tonks, L. and Langmuir, I. (1929). Oscillations in ionized gases, *Physical Review*, **33**, 195–210.
- Tonry, J., Schmidt, B., Barris, B., Candia, P., Challis, P., Clocchiatti, A., Coil, A., Filippenko, A., Garnavich, P., Hogan, C., Holland, S., Jha, S., Kirshner, R., Krisciunas, K., Leibundgut, B., Li, W., Matheson, T., Phillips, M., Riess, A., Schommer, R., Smith, R., Sollerman, J., Spyromilio, J., Stubbs, C., and Suntzeff, N. (2003). Cosmological results from high-z supernovae, *Astrophysical Journal*, **594**, 1–24.
- Toomre, A. (1974). Gravitational interactions between galaxies, in *IAU Symposium No. 58: The Formation and Dynamics of Galaxies*, ed. Shakeshaft, J., pp. 347–365. Dordrecht: D. Reidel Publishing Company
- Toomre, A. and Toomre, J. (1972). Galactic bridges and tails, *Astrophysical Journal*, **178**, 623–666.
- Tremaine, S. and Gunn, J. (1979). Dynamical role of light neutral leptons in cosmology, *Physical Review Letters*, **42**, 407–410.
- Tremaine, S. and Richstone, D.O. (1977). A test of a statistical model for the luminosities of bright cluster galaxies, *Astrophysical Journal*, **212**, 311–316.

- Tremonti, C.A., Heckman, T.M., Kauffmann, G., Brinchmann, J., Charlot, S., White, S.D.M., Seibert, M., Peng, E.W., Schlegel, D.J., Uomoto, A., Fukugita, M., and Brinkmann, J. (2004). The origin of the mass-metallicity relation: insights from 53,000 star-forming galaxies in the Sloan Digital Sky Survey, *Astrophysical Journal*, **613**, 898–913.
- Trimble, V. (1995). The 1920 Shapley–Curtis discussion: background, issues, and aftermath, *Publications of the Astronomical Society of the Pacific*, **107**, 1133–1144.
- Trodden, M. (2006). Physics of the very early Universe: what can we learn from particle collider experiments?, *Proceedings of Science*, **CMB2006**, 1–9. This electronic publication can be found at <http://pos.sissa.it/archive/conferences/027/003/CMB2006-003.pdf>.
- Tropp, E., Frenkel, V., and Chernin, A. (1993). *Alexander A. Friedmann: the Man who Made the Universe Expand*. Cambridge: Cambridge University Press.
- Trushkin, S.A. (2003). Radio spectra of the WMAP catalog sources, *Bulletin of the Special Astrophysical Observatory*, **55**, 90–132.
- Tully, R.B. and Fisher, J.R. (1977). A new method of determining distances to galaxies, *Astronomy and Astrophysics*, **54**, 661–673.
- Turner, M. (1997). Inflationary cosmology, in *Relativistic Astrophysics*, eds Jones, B.J.T. and Markovic, D., pp. 83–102. Cambridge: Cambridge University Press.
- Turok, N. (1989). Global texture as the origin of cosmic structure, *Physical Review Letters*, **63**, 2625–2628.
- ed. Turok, N. (1997). *Critical Dialogues in Cosmology*. Singapore: World Scientific.
- Tyson, J.A., Kochanski, G.P., and dell’Antonio, I.P. (1998). Detailed mass map of CL 0024+1654 from strong lensing, *Astrophysical Journal Letters*, **498**, L107–L110.
- Vallée, J.P. (1997). Observations of the magnetic fields inside and outside the Milky Way, starting with globules (~ 1 parsec), filaments, clouds, superbubbles, spiral arms, galaxies, superclusters, and ending with the cosmological Universe’s background surface (at ~ 8 teraparsecs), *Fundamentals of Cosmic Physics*, **19**, 1–89.
- van den Bergh, S. (1998). *Galaxy Morphology and Classification*. Cambridge: Cambridge University Press.
- Verde, L., Heavens, A.F., Percival, W.J., Matarrese, S., Baugh, C.M., Bland-Hawthorn, J., Bridges, T., Cannon, R., Cole, S., Colless, M., Collins, C., Couch, W., Dalton, G., De Propris, R., Driver, S.P., Efstathiou, G., Ellis, R.S., Frenk, C.S., Glazebrook, K., Jackson, C., Lahav, O., Lewis, I., Lumsden, S., Maddox, S., Madgwick, D., Norberg, P., Peacock, J.A., Peterson, B.A., Sutherland, W., and Taylor, K. (2002). The 2dF Galaxy Redshift Survey: the bias of galaxies and the density of the Universe, *Monthly Notices of the Royal Astronomical Society*, **335**, 432–440.
- Vishniac, E.T. (1987). Reionization and small-scale fluctuations in the microwave background, *Astrophysical Journal*, **322**, 597–604.

- Visvanathan, N. and Sandage, A.R. (1977). The color-absolute magnitude relation for E and S0 galaxies: I. Calibration and tests for universality using Virgo and eight other nearby clusters, *Astrophysical Journal*, **216**, 214–226.
- Vogel, S. and Reimers, D. (1995). The ultraviolet absorption spectrum of the $Z = 2.72$ QSO HS 1700+6416: 1. Results on heavy-element absorption systems, *Astronomy and Astrophysics*, **294**, 377–410.
- von Weizsächer, C.F. (1947). Zur Kosmogonie, *Zeitschrift für Astrophysik*, **24**, 181–206.
- Waddington, I., Dunlop, J.S., Peacock, J.A., and Windhorst, R.A. (2001). The LBDS Hercules sample of mJy radio sources at 1.4 GHz – II. Redshift distribution, radio luminosity function, and the high-redshift cut-off, *Monthly Notices of the Royal Astronomical Society*, **328**, 882–896.
- Wagoner, R., Fowler, W., and Hoyle, F. (1967). On the synthesis of elements at very high temperatures, *Astrophysical Journal*, **148**, 3–49.
- Wagoner, R.V. (1973). Big-Bang nucleosynthesis revisited, *Astrophysical Journal*, **179**, 343–360.
- Walker, A.G. (1936). On Milne's theory of world structure, *Proceedings of the London Mathematical Society, Series 2*, **42**, 90–127.
- Wall, J.V. (1996). Space distribution of radio source populations, in *Extragalactic Radio Sources, IAU Symposium No. 175*, eds. Ekers, R., Fanti, C., and Padrielli, L., pp. 547–552. Dordrecht: Kluwer.
- Walsh, D., Carswell, R.F., and Weymann, R.J. (1979). 0957+561A, B – twin quasistellar objects or gravitational lens, *Nature*, **279**, 381–384.
- Wambsganss, J. (1998). Gravitational lensing in astronomy, *Living Review in Relativity*, **1**. Online article: accepted 28 August 1998; last amended 31 August 2001 <http://www.livingreviews.org/lrr-1998-12>.
- Wang, W.-H., Cowie, L.L., and Barger, A.J. (2006). A near-infrared analysis of the submillimeter background and the cosmic star-formation history, *Astrophysical Journal*, **647**, 74–85.
- Warren, S.J., Hewett, P.C., Irwin, M.J., McMahon, R.G., and Bridgeland, M.T. (1987). First observation of a quasar with a redshift of 4, *Nature*, **325**, 131–133.
- Weedman, D. (1994). Starburst galaxies at high redshift, in *First Stromlo Symposium: Physics of Active Galactic Nuclei*, eds. Bicknell, G., Dopita, M., and Quinn, P., pp. 409–415. San Francisco: Astronomical Society of the Pacific Conference Series, Vol. 34.
- Weinberg, S. (1972). *Gravitation and Cosmology*. New York: Wiley.
- Weinberg, S. (1989). The cosmological constant problem, *Reviews of Modern Physics*, **61**, 1–23.
- Weinberg, S. (1997). Theories of the cosmological constant, in *Critical Dialogues in Cosmology*, ed. Turok, N., pp. 195–203. Singapore: World Scientific.
- Weinheimer, C. (2001). Neutrino mass from tritium β -Decay, in *Dark Matter in Astro- and Particle Physics, Proceedings of the International Conference DARK 2000*, ed. Klapdor-Kleingrothaus, H.V., pp. 513–519. Berlin: Springer-Verlag.
- Weiss, R. (1980). Measurements of the cosmic background radiation, *Annual Review of Astronomy and Astrophysics*, **18**, 489–535.

- Wesselink, A.J. (1947). The Observations of Brightness, Colour and Radial Velocity of δ -Cephei and the pulsation hypothesis, *Bulletin of the Astronomical Institutes of the Netherlands*, **10**, 91–99. Errata, **10**, 258 and 310.
- Weyl, H. (1923). Zur allgemeinen Relativitätstheorie (On the Theory of General Relativity), *Physikalische Zeitschrift*, **29**, 230–232.
- Weymann, R. (1966). The energy spectrum of radiation in the expanding Universe, *Astrophysical Journal*, **145**, 560–571.
- Weymann, R. (1967). Possible thermal histories of intergalactic gas, *Astrophysical Journal*, **147**, 887–900.
- Wheeler, J. (1977). Genesis and observership, in *Foundational Problems in the Special Science*, eds. Butts, R. and Hintikka, J., pp. 3–33. Dordrecht: Reidel.
- White, D.A., Fabian, A.C., Allen, S.W., Edge, A.C., Crawford, C.S., Johnstone, R.M., Stewart, G.C., and Voges, W. (1994). A ROSAT HRI observation of the ABELL:478 cluster of galaxies, *Monthly Notices of the Royal Astronomical Society*, **269**, 589–606.
- White, S.D. (1989). Observable signatures of young galaxies, in *The Epoch of Galaxy Formation*, eds. Frenk, C.S., Ellis, R.S., Shanks, T., Heavens, A.F., and Peacock, J.A., pp. 15–30. Dordrecht: Kluwer.
- White, S.D.M. (1990). Physical cosmology, in *Physics of the Early Universe*, eds Peacock, J.A., Heavens, A.F., and Davies, A.T., pp. 1–62. Edinburgh: SUSSP.
- White, S.D.M. and Rees, M.J. (1978). Core condensation in heavy halos – a two-stage theory for galaxy formation and clustering, *Monthly Notices of the Royal Astronomical Society*, **183**, 341–358.
- Wilkinson, P.N., Henstock, D.R., Browne, I.W., Polatidis, A.G., Augusto, P., Readhead, A.C., Pearson, T.J., Xu, W., Taylor, G.B., and Vermeulen, R.C. (2001). Limits on the cosmological abundance of supermassive compact objects from a search for multiple imaging in compact radio sources, *Physical Review Letters*, **86**, 584–587.
- Will, C. (1993). *Theory and Experiment in Gravitational Physics*. Cambridge: Cambridge University Press.
- Will, C.M. (2006). The confrontation between General Relativity and experiment, *Living Reviews in Relativity*, **9**. Online article: cited on 21 June 2006 <http://www.livingreviews.org/lrr-2006-3>.
- Williams, J.G., Turyshev, S.G., and Boggs, D.H. (2004). Progress in lunar laser ranging tests of relativistic gravity, *Physical Review Letters*, **93**, 261101, 1–4.
- eds. Williams, P., Shu, C.-G., and Ménard, B. (2005). *Probing Galaxies through Quasar Absorption Lines*. Cambridge: Cambridge University Press.
- Williams, R.E., Baum, S., Bergeron, L.E., Bernstein, N., Blacker, B.S., Boyle, B.J., Brown, T.M., Carollo, C.M., Casertano, S., Covarrubias, R., de Mello, D.F., Dickinson, M.E., Espey, B.R., Ferguson, H.C., Fruchter, A., Gardner, J.P., Gonnella, A., Hayes, J., Hewett, P.C., Heyer, I., Hook, R., Irwin, M., Jones, D., Kaiser, M.E., Levay, Z., Lubenow, A., Lucas, R.A., Mack, J., MacKenty, J.W., Madau, P., Makidon, R.B., Martin, C.L., Mazzuca, L., Mutchler, M., Norris, R.P., Perriello, B., Phillips, M.M., Postman, M., Royle, P., Sahu, K., Savaglio, S., Sherwin, A., Smith, T.E., Stiavelli, M., Suntzeff, N.B., Teplitz, H.I., van der

- Marel, R.P., Walker, A.R., Weymann, R.J., Wiggs, M.S., Williger, G.M., Wilson, J., Zacharias, N., and Zurek, D.R. (2000). The Hubble Deep Field South: formulation of the observing campaign, *Astronomical Journal*, **120**, 2735–2746.
- Williams, R.E., Blacker, B., Dickenson, M., Dixon, W.V.D., Ferguson, H.C., Fruchter, A.S., Giavalisco, M., Gilliland, R.L., Heyer, I., Katsanis, R., Levay, Z., Lucas, R.A., McElroy, D.B., Petro, L., Postman, M., Adorf, H.M., and Hook, R.N. (1996). The Hubble Deep Field: observations, data reduction, and galaxy photometry, *Astronomical Journal*, **112**, 1335–1389.
- Windhorst, R.A., Dressler, A., and Koo, D.A. (1987). Ultradeep optical identifications and spectroscopy of faint radio sources, in *Observational Cosmology*, eds. Hewitt, A., Burbidge, G., and Fang, L.-Z., pp. 573–576. Dordrecht: Reidel.
- Windhorst, R.A., Fomalont, E.B., Kellermann, K.I., Partridge, R.B., Richards, E., Franklin, B.E., Pascerelle, S.M., and Griffiths, R.E. (1995). Identification of faint radio sources with optically luminous interacting disk galaxies, *Nature*, **375**, 471–474.
- Wolfe, A. (1988). Damped Ly- α absorption systems, in *QSO Absorption Lines: Probing the Universe*, eds. Blades, J., Turnshek, D., and Norman, C., pp. 306–317. Cambridge: Cambridge University Press.
- Woltjer, L. (1990). Phenomenology of active galactic nuclei, in *Saas-Fee Advanced Course 20. Active Galactic Nuclei*, eds. Courvoisier, T.J.-L. and Mayor, M., pp. 1–55. Berlin: Springer-Verlag.
- Wood-Vasey, W.M., Miknaitis, G., Stubbs, C.W., Jha, S., Riess, A.G., Garnavich, P.M., Kirshner, R.P., Aguilera, C., Becker, A.C., Blackman, J.W., Blondin, S., Challis, P., Clocchiatti, A., Conley, A., Covarrubias, R., Davis, T.M., Filippenko, A.V., Foley, R.J., Garg, A., Hicken, M., Krisciunas, K., Leibundgut, B., Li, W., Matheson, T., Miceli, A., Narayan, G., Pignata, G., Prieto, J.L., Rest, A., Salvo, M.E., Schmidt, B.P., Smith, R.C., Sollerman, J., Spyromilio, J., Tonry, J.L., Suntzeff, N.B., and Zenteno, A. (2007). Observational constraints on the nature of the dark energy: first cosmological results from the ESSENCE Supernova Survey, *Astrophysical Journal*, **666**, 294–715.
- Zaldarriaga, M. (1997). Polarization of the microwave background in reionized models, *Physical Review*, **D55**, 1822–1829.
- Zaldarriaga, M. (2004). The polarization of the cosmic microwave background, in *Measuring and Modeling the Universe*, ed. Freedman, W.L., pp. 309–329. Cambridge: Cambridge University Press.
- Zaritsky, D., Kennicutt, R.C., and Huchra, J.P. (1994). H II regions and the abundance properties of spiral galaxies, *Astrophysical Journal*, **420**, 87–109.
- Zekser, K.C., White, R.L., Broadhurst, T.J., Benítez, N., Ford, H.C., Illingworth, G.D., Blakeslee, J.P., Postman, M., Jee, M.J., and Coe, D.A. (2006). Mass modeling of Abell 1689 Advanced Camera for surveys observations with a perturbed Navarro-Frenk-White model, *Astrophysical Journal*, **640**, 639–661.
- Zeldovich, Y. (1965). Survey of modern cosmology, *Advances of Astronomy and Astrophysics*, **3**, 241–379.
- Zeldovich, Y. (1970). Gravitational instability: an approximate theory for large density perturbations, *Astronomy and Astrophysics*, **5**, 84–89.

- Zeldovich, Y. (1972). A hypothesis, unifying the structure and the entropy of the universe, *Monthly Notices of the Royal Astronomical Society*, **160**, 1P–3P.
- Zeldovich, Y. (1986). Cosmological field theory for observational astronomers, *Astrophysics and Space Physics Reviews*, **5**, 1–37.
- Zeldovich, Y. and Sunyaev, R. (1969). The interaction of matter and radiation in a hot-model universe, *Astrophysics and Space Science*, **4**, 301–316.
- Zeldovich, Y.B. (1964). Observations in a Universe homogeneous in the mean, *Astronomicheskii Zhurnal*, **41**, 19–24. [Translation: (1964), *Soviet Astronomy*, **8**, 13–16].
- Zeldovich, Y.B. (1968). The cosmological constant and the theory of elementary particles, *Uspekhi Fizicheskikh Nauk*, **95**, 209–230. [Translation: (1968) *Soviet Physics – Uspekhi*, **11**, 381–393.]
- Zeldovich, Y.B. (1993). Particles, nuclei and the Universe, in *Selected Works of Yakov Borisovich Zeldovich*, Vol. 2., eds. Ostriker, J., Barenblatt, G., and Sunyaev, R. Princeton: Princeton University Press.
- Zeldovich, Y.B., Kurt, D., and Sunyaev, R.A. (1968). Recombination of hydrogen in the hot model of the Universe, *Zhurnal Eksperimentalnoi i Teoreticheskoi Fiziki*, **55**, 278–286. Translation: (1969), *Soviet Physics – JETP*, **28**, 146–150.
- Zeldovich, Y.B. and Novikov, I.D. (1983). *Relativistic astrophysics*, Vol. 2. Chicago: Chicago University Press.
- Zeldovich, Y.B. and Sunyaev, R.A. (1980). The angular distribution of the microwave background, and its intensity in the direction of galaxy clusters, *Soviet Astronomy Letters*, **6**, 285–286.
- Zwicky, F. (1937). On the masses of nebulae and of clusters of nebulae, *Astrophysical Journal*, **86**, 217–246.

Name Index

- Aaronson, Marc 246
Abell, George 81, 95, 101, 102
Abraham, Robert 540
Adams, Walter 177, 178
Albrecht, Andreas 24, 629
Alpher, Ralph 14
Aragón-Salamanca, Alfonso 253, 544
Arnaud, Monique 117
Arp, Halton 56
- Baade, Walter 13, 248
Babbage, Thomas 536
Bahcall, John 568
Bahcall, Neta 99, 100, 108, 267, 387
Bajtlik, Stanislaw 568, 569
Balzano, Vicki 597
Barcons, Xavier 561
Bardeen, James 348, 349, 394–396, 402
Barger, Amy 597, 598
Barnes, Joshua 611
Barrow, John 625
Baugh, Carlton 615
Baumann, Daniel 630, 631, 634, 636–638, 640
Bautz, Laura 109
Becker, Robert 552
Beckwith, Steven 543, 590, 592, 593, 596
Benson, Bradford 404
Bentley, Richard 4
Bergeron, Jacqueline 479, 489, 593
Berkeley, Bishop 11
Bertschinger, Edmund 348, 349, 638
Bessel, Friedrich 5
Biermann, Ludwig 579
Binggeli, Bruno 78, 82, 116
Binney, James 108
Blain, Andrew 452, 534
Bland-Hawthorn, Jonathan 539
- Blandford, Roger 228, 229
Bludman, Sydney 24, 626
Blumenthal, George 481
Bolte, Michael 250, 251
Bolyai, János 11, 151
Bond, Richard 20, 375, 396, 398, 399
Bondi, Hermann 149, 150, 341
Borgani, Stefano 531
Bouwens, Rychard 592, 593
Bowyer, Stuart 506
Boyle, Brian 521
Boyle, Robert 4
Bracessi, Alessandro 519
Bracewell, Ronald 433
Braginsky, Vladimir 174
Brahe, Tycho 3
Brainerd, Tereasa 138
Branch, David 248
Brandt, W. Niel 524, 525, 527
Bruzual, Gustavo 498, 499, 587, 588, 594, 607–609
Burbidge, Geoffrey 14
Burbidge, Margaret 14
Burstein, David 269
Butcher, Harvey 543
- Cappelluti, Nico 529
Carroll, Sean 265, 324
Carswell, Robert 249
Carter, Brandon 625
Cayley, Arthur 11, 151
Chaboyer, Brian 250, 251
Challinor, Anthony 126, 422, 441, 449, 452, 454
Chambers, Kenneth 254
Charlot, Stéphane 498, 499, 594, 607–609
Chluba, Jens 423
Chwolson, Orest 128

- Cimatti, Andrea 542, 608, 609
 Clausius, Rudolph 64
 Clifford, William 11, 151
 Cole, Shaun 405
 Coles, Peter 331, 332, 354, 358, 360, 377,
 382, 402, 474
 Colless, Matthew 113
 Corbelli, Edvige 568
 Cowan, John 252
 Cowie, Lennox 272, 534, 542, 566, 586,
 587, 589, 590, 598
 Crommelin, Andrew 190
 Croom, Scott 387
- Dashevsky, Vladimir 233
 Davidsen, Arthur 550, 564, 566
 Davies, Roger 612
 Davis, Tamara 339, 342, 347
 de Bruyn, Ger 580
 de Sitter, Willem 12, 149
 de Vaucouleurs, Gérard 49, 51, 54, 246
 Dekel, Avni 268, 269, 402
 Descartes, René 5
 Dessauges-Zavadsky, Miroslava 603, 604
 Dicke, Robert 174, 621, 622
 Dickinson, Mark 545
 Disney, Michael 62
 Dodds, Stephen 405, 409, 415, 416, 439
 Dodelson, Scott 348, 350, 367, 368, 371,
 416, 422, 438, 440, 443, 445, 446,
 454, 614
 Doroshkevich, Andrei 18, 360
 Dressler, Alan 56, 102, 108, 404
 Dreyer, John 7
 Dunlop, James 516, 609
 Dunn, Andrew 113
 Dyer, Charles 233–235
- Eales, Stephen 255
 Eastman, Ronald 248
 Eddington, Arthur 13, 177, 178, 190
 Efstathiou, George 143, 173, 184, 313,
 358, 398, 399, 403, 408, 417, 439,
 443, 453, 484, 487, 611
 Einstein, Albert 11, 12, 128, 149, 151,
 173, 174, 181, 182, 184, 188, 199,
 204, 207
 Eisenstein, Daniel 409, 411, 412
 Ellis, George 348
- Ellis, Richard 130, 253, 259, 537, 538,
 542
 Ellis, Simon 539
 Eötvös, Lóránd 174
- Faber, Sandra 74
 Fabian, Andrew 122–124, 561
 Fabricant, Donald 115
 Fall, Michael 568, 598, 604–606, 611, 612
 Fan, Xiaohui 522, 524
 Faulkner, John 14
 Fechner, Cora 567
 Felten, James 77, 78, 509
 Fisher, Richard 73
 Fomalont, Edward 506
 Fort, Bernard 134, 136
 Fowler, William 14, 293
 Freedman, Wendy 247, 250
 Freeman, Kenneth 62, 612
 Frenk, Carlos 400, 401
 Friedman, Aleksander 12, 13, 149, 202,
 204
 Furlanetto, Steven 574, 576, 577
- Galilei, Galileo 5
 Gamow, George 13, 14
 Garnavich, Peter 257
 Gauss, Carl Friedrich 11, 151, 156
 Gavazzi, Raphaël 138
 Ge, Jian 273
 Geller, Margaret 109
 Gerling, Christian 11
 Gershtein, Semion 19
 Giacconi, Riccardo 524
 Giavalisco, Mauro 592
 Gibbons, Gary 25
 Gilli, Roberto 526, 528, 529
 Glazebrook, Karl 607
 Goobar, Ariel 257
 Gorenstein, Paul 115
 Gott, Richard 41, 42
 Govoni, Federica 580
 Green, Richard 519, 521
 Gregory, James 4
 Greve, Thomas 479
 Gribben, John 625
 Grossmann, Marcel 181, 182
 Groth, Edward 35

- Gunn, James 20, 111–113, 144, 267, 268,
499, 549
- Gurvits, Leonid 263
- Guth, Alan 24, 364, 626, 627, 639
- Guzzo, Luigi 531
- Hale, George Ellery 9
- Hamilton, Andrew 408, 409, 472
- Hardy, Eduardo 253
- Harrison, Edward 17, 392, 510
- Hasinger, Günther 506, 524, 525, 527
- Hauser, Michael 535, 587
- Hausman, Marc 544
- Hawking, Stephen 25, 643, 644
- Hawkins, Michael 521
- Haynes, Martha 84
- Heath, D. 324
- Heavens, Alan 402, 475
- Helfand, David 42
- Herman, Robert 14
- Hernquist, Lars 572
- Herschel, Caroline 7
- Herschel, John 7
- Herschel, William 5–7
- Hewish, Antony 504, 506
- Hewitt, Jacqueline 140
- Hinshaw, Gary 451
- Hogan, Craig 298
- Hoyle, Fiona 42
- Hoyle, Fred 14, 293
- Hu, Esther 555
- Hu, Wayne 409, 411, 415, 422, 426, 438,
443, 445, 447, 448, 454, 462, 463
- Hubble, Edwin 8–10, 44–46, 162, 267,
492–494
- Huggins, William 7
- Humason, Milton 9, 45
- Huygens, Christiaan 11
- Ikeuchi, Satoru 555
- Ivison, Robert 452
- Jakobsen, Peter 564, 566, 569, 571
- Jeans, James 4, 16, 313, 317
- Jones, Bernard 610
- Kaiser, Nicholas 136, 235, 402, 406, 407,
460
- Kant, Immanuel 5
- Kapahi, Vijay 261
- Kapteyn, Jacobus 7, 8
- Kashlinsky, Alexander 507
- Katz, Neal 572
- Kauffmann, Guinevere 417, 545
- Kellermann, Kenneth 263
- Kennicutt, Robert 87, 554, 616
- Kent, Stephen 111–113
- Kepler, Johannes 3
- Kibble, Thomas 628
- King, Ivan 107
- Kirshner, Robert 248
- Kneib, Jean-Pierre 130
- Kochanek, Christopher 130, 138
- Kogut, Alan 432
- Kolb, Rocky 143, 301, 303, 307, 369, 376,
397, 402, 642
- Kompaneets, Aleksander 17
- Koo, David 519
- Kooiman, Brian 42
- Kormendy, John 49, 51
- Kriss, Gerard 566
- Kron, Richard 519
- Kulkarni, Varsha 568, 601, 603
- Kulsrud, Russell 578–581
- Kundic, Tomislav 249
- Kurt, Vladimir 423, 563
- Kwan, John 248
- Lacy, Mark 610
- Lagache, Guilane 533, 536
- Lambert, Johann 5, 11, 150
- Lanczos, Cornelius 149
- Langmuir, Irving 317
- Lanzetta, Kenneth 601
- Larson, Richard 606
- Lasenby, Anthony 126
- Le Verrier, Urbain 189
- Leavitt, Henrietta 7, 8
- Lecar, Myron 115
- Ledoux, Cédric 273
- Lemaître, Georges 4, 13, 16, 204, 207,
322, 333
- Liddle, Andrew 25, 348, 349, 629, 630
- Lifshitz, Evgenii 4, 16, 313, 322, 333
- Lightman, Alan 268, 329
- Lilly, Simon 254, 587, 589, 590, 609
- Linde, Andrei 24, 626, 629

- Lineweaver, Charles 339, 342, 347, 427, 626
 Lobachevsky, Nikolai 11, 151
 Longair, Malcolm 534
 Lotz, Jennifer 594
 Lucchin, Francesco 331, 332, 354, 358, 360, 377, 382, 402, 474
 Lynden-Bell, Donald 399, 474
 Lynds, Roger 130
 Lyth, David 25, 348, 349, 629, 630
 Lyubimov, Valentin 19, 369
- Ma, Chung-Pei 349
 Mach, Ernst 11
 Madau, Piero 590, 596, 606
 Maeder, André 250
 Majewski, Steven 521
 Maloney, Philip 568
 Marshall, Francis 561
 Martin, Christopher 506
 Marx, Györgi 19
 Mather, John 561
 Mazzarella, Joseph 597
 McCarthy, Patrick 254, 607, 608
 McCrea, William 202, 624
 McDonald, Patrick 557
 Mellier, Yannick 134, 136
 Merritt, David 111–113
 Messier, Charles 7
 Metcalfe, Nigel 538
 Michell, John 5, 6
 Miley, George 254, 261
 Milne, Ernest 202
 Miralda-Escudé, Jordi 572
 Monaco, Pierluigi 485–487
 Morgan, William 109
 Mould, Jeremy 246
 Mukhanov, Vyechislav 368
 Møller, Palle 569, 571
- Narajan, Ramesh 228, 229
 Naselsky, Pavel 368
 Newton, Isaac 4, 174
 Norberg, Peder 404, 405
 Novikov, Dmitry 368
 Novikov, Igor 17, 303, 304, 362, 368
- Oemler, Augustus 102, 543
 Okamoto, Takemi 462, 463
- Olbers, Heinrich 510
 Oort, Jan 267
 Osmer, Patrick 521
 Ostriker, Jeremiah 69, 479, 481, 486, 544, 556, 612, 616
- Padmanabhan, Thanu 332, 354, 409, 438, 442
 Page, Lyman 29, 459
 Pagel, Bernard 604
 Pais, Abraham 184
 Panagia, Nino 248
 Parker, Eugene 578–581
 Partridge, Bruce 19
 Patchett, Bruce 248
 Payne, Cecilia 14
 Peacock, John 269, 348, 368, 390, 396, 398, 402, 405–407, 409, 415, 416, 439, 442, 475, 516
 Peebles, James 17, 20, 35, 37, 69, 100, 283, 357, 360, 363, 375, 386, 423, 432, 433, 439, 443, 445, 610–612, 616, 622
 Pei, Yichuan 604–606
 Penrose, Roger 644
 Penzias, Arno 15, 27
 Perlmutter, Saul 257
 Peterson, Bruce 549
 Petrosian, Vahe 130, 504
 Pettini, Max 601–603
 Pi, So-Young 639
 Postman, Marc 109
 Pound, Robert 178
 Pozdnyakov, Lev 281
 Pratt, Gabriel 117
 Press, William 363, 472, 482–485
 Pritchard, Jonathan 576, 577
 Prochaska, Jason 603, 604
 Puget, Jean-Loup 535, 587
- Rawlings, Stephen 255
 Rebka, Glen 178
 Rees, Martin 402, 479, 481, 482, 486, 487, 578, 580, 581, 611, 625
 Refregier, Alexandre 460
 Richards, Gordon 524
 Richstone, Douglas 82, 109
 Riemann, Bernhard 11, 151
 Roberts, Morton 84

- Robertson, Howard 4, 149
 Roeder, Robert 233–235
 Rosati, Piero 532
 Rowan-Robinson, Michael 246, 514
 Ruderman, Malvin 24, 626
 Rutherford, Ernest 251
 Ryle, Martin 549
 Ryu, Dongsu 580
- Saccheri, Girolamo 11, 150
 Sachs, Rainer 436, 438
 Sajina, Anna 535
 Sakharov, Andrei 24, 641
 Salpeter, Edwin 504, 568
 Sandage, Allan 13, 49, 51, 78, 109, 116,
 246, 250, 251, 253, 259, 518
 Sargent, Wallace 553
 Schechter, Paul 77, 268, 329, 363, 472,
 482–486
 Scheuer, Peter 151, 504–506, 514, 549
 Schmidt, Brian 248
 Schmidt, Maarten 508, 514, 519, 521, 522
 Schneider, Peter 130, 133, 138
 Schramm, David 252
 Schutz, Bernard 459
 Schwarzschild, Martin 250
 Scott, Douglas 433
 Scott, Jennifer 568, 569
 Seager, Sara 423
 Seldner, Michael 100
 Seljak, Uros 559
 Shapiro, Irwin 189, 191
 Shapley, Harlow 7, 9
 Shectman, Stephen 506
 Shellard, Paul 629
 Silk, Joseph 17, 364, 433, 443, 448, 479
 Smail, Ian 452, 597
 Smoot, George 21
 Sneden, Christopher 252
 Snider, Joseph 178
 Songaila, Antoinette 566
 Soucail, Geneviève 130
 Spergel, David 463, 465
 Spinrad, Hyron 254, 514, 610
 Spite, François 298
 Spite, Monique 298
 Springel, Volker 487, 615, 616
 Srianand, Raghunathan 552
 Steidel, Charles 590
- Steigman, Gary 140, 294, 296, 298–301
 Steinhardt, Paul 24, 629
 Storrie-Lombardi, Lisa 601
 Subramanian, Kandaswamy 422
 Sugiyama, Naoshi 415, 422, 426, 443,
 445, 448
 Sullivan, Woodruff 514
 Sunyaev, Rashid XI, XII, 17, 18, 21, 28,
 29, 125, 281, 360, 365, 392, 423, 443,
 451, 454, 455, 561, 563, 568
 Szalay, Alex 19, 396
- Tammann, Gustav 78, 116, 246
 Tayler, Roger 14
 Taylor, Joseph 192
 Tegmark, Max 463, 559
 Tinsley, Beatrice 499, 604
 Tipler, Frank 625
 Toller, Gary 586
 Tolman, Richard 16, 322, 333
 Tonks, Lewi 317
 Toomre, Alar 57, 58
 Toomre, Juri 57, 58
 Tremaine, Scott 20, 82, 108, 109, 144
 Trodden, Mark 144
 Tully, Brent 73
 Turner, Michael 143, 301, 303, 307, 369,
 376, 397, 402, 642
 Tyson, Anthony 136
 Tytler, David 566
- Vallée, Jacques 577
 van den Bergh, Sidney 49, 51, 542
 van der Kruit, Piet 62
 Vandenberg, Donald 251
 Verde, Licia 403, 404, 407
 Vishniac, Ethan 453
 Vogeley, Michael 42
- Waddington, Ian 517
 Wagoner, Robert 15, 292, 294
 Walker, Arthur 149
 Wall, Jasper 506, 515
 Walsh, Dennis 249
 Wambsganss, Joachim 129, 130, 138
 Wang, Wei-Hao 598
 Warren, Stephen 519
 Weedman, Daniel 597
 Weinberg, Steven 338, 355, 626

- Wesselink, Adriaan 248
Weyl, Hermann 149, 150
Weymann, Raymond 17, 249, 281, 563
Wheeler, John 625
White, Martin 433, 454
White, Simon 200, 269, 482, 486, 545,
 587
Wilkinson, David 434
Wilkinson, Peter 140
Will, Clifford 173, 174, 189, 190, 192,
 195, 196
Williams, Robert 590
Wilson, Robert 15, 27
Wolfe, Arthur 436, 438, 554, 603, 604
Woltjer, Lodewijk 519
Wright, Thomas 5
Wyse, Rosemary 479
Yu, Jer Tsang 443, 445
Zaldarriaga, Matias 422, 454, 458
Zeldovich, Yakov 13, 17–21, 24, 28, 29,
 125, 208, 231, 233, 281, 303, 304,
 360–363, 365, 375, 381, 392, 423,
 443, 451, 454, 455, 476, 561, 626

Index

Major topics and their principal references are highlighted in **bold-face** type.

- Abell 194 110
Abell 478 122, 123
Abell 1228 110
Abell 1413 117, 118
Abell 1656 *see* Coma cluster of galaxies
Abell 2199 109, 110
Abell 2218 96, 130, 131, 136
Abell Catalogues of rich clusters of galaxies 96–98
comparison with clusters selected from the Sloan Digital Sky Survey 98–99
complete statistical sample 97
selection criteria for inclusion in 96
compactness criterion 97
distance criterion 97
richness criterion and richness classes 96, 97
space density of clusters in 98
Abell clusters and the large-scale distribution of galaxies 99–100
superclustering of galaxies about 100
absolute luminosities of galaxies 77
absorption history of the Universe 604
abundances of elements in Lyman- α absorption systems 598–604
absorption, or scattering, cross-sections and 600
advantages of determining zinc abundance 601, 602, 606
chemical history of the interstellar gas and 601
depletion of heavy elements and 601
in redshift interval $0.3 \leq z \leq 3.5$ 601
density parameter $\Omega_{\text{HI}}(z)$ for neutral hydrogen 601, 606
corrected for dust extinction and systems with low column densities 601
density parameter $\Omega_x(z)$ for species x and 600, 601
determination of average 598
global metallicity ratios and 600
iron abundance in redshift interval $1.7 \leq z \leq 4.6$ 603
uniformity of relative 604
variation of neutral hydrogen abundance with redshift 602
Acbar experiment 435
acoustic oscillations in galaxy power spectrum 362, 410–415
Sloan Digital Sky Survey (SDSS) 412–415
first peak and 414
2dF galaxy redshift survey 412–413
cosmological parameters from 413
first and second peaks and 412
acoustic oscillations in the power spectrum of the cosmic microwave background radiation
as forced oscillations 446
estimation of cosmological parameters and 449
acoustic oscillations in the power spectrum of the cosmic microwave background radiation 428–430, 436, 443–449
adiabatic temperature oscillations of 446, 447
amplitudes of 444
as forced oscillations 445, 446

- 'dipole' contributions to 447, 448, 455, 456, 459
- Doppler fluctuations associated with 446, 447
- effective temperature perturbation of 447
- estimation of cosmological parameters and 444, 449
- even and odd harmonics of 444
- first maximum of 427, 443, 444, 449
- gravitational redshifting of 447
- isocurvature modes and 447
- 'monopole' contributions to 447, 448, 456, 459
- relation to adiabatic density perturbations 445
- temperature excursions of 448
- wavenumbers of maxima of 444
- active galactic nuclei 51
 - ratio of black hole to spheroid masses 610, 617
 - Type 1 528
 - unobscured 528
- active gravitational mass density 201
- adiabatic baryonic perturbations in the standard Big Bang 350–357, 361–363**
 - as a 'top-down' process 363
 - 'burning of pancakes' 363
 - formation of 'pancakes' 363
 - matter-dominated era 353–355
 - radiation-dominated era 352
- adiabatic damping of neutrino velocities 377
- adiabatic damping of the sound waves 354
- adiabatic expansion of a photon gas 272, 281
- adiabatic expansion of a thermal gas 281
- adiabatic hot dark matter 396
- adiabatic model of structure formation 18
- adiabatic sound speed 316
- Advanced Camera for Surveys (ACS) 136, 138, 538, 592
- age of the Earth 251
- age of the Universe T_0 13, 16, 242
 - globular clusters and 250, 251
 - nucleocosmochronology and 252
 - white dwarf cooling ages and 251
- alignment effect in radio galaxies 254, 256
 - shock-excitation and 255
- Andromeda Nebula 8
- Anglo-Australian Telescope 2dF Survey 22, 519
- angular diameter distance 130, 157, 264
- angular diameter distances between any two redshifts 228–230**
 - gravitational lens formulae and 229
 - models with $\Omega_A = 0$ 228–229
 - models with $\Omega_A \neq 0$ 230
 - reciprocity theorem 229
- angular two-point correlation function 34–36, 386
 - for extragalactic radio sources 42
- Antennae galaxies 57–60, 614
- anthropic cosmological principle 624–626
 - existence of sentient beings and 625
 - strong form of 625
- APM galaxy survey 33–36
- APM survey of clusters of galaxies 95
- Arecibo radio telescope 192
- Ariel-V satellite 115, 524
- ASCA Large Sky Survey 525
- Astro-2 mission 565, 566
- astroparticle physics 145
- Atacama Large Millimetre Array (ALMA) 598
- Atlas of Peculiar Galaxies (Arp) 56
- Auger cosmic ray air-shower array 625
- autocorrelation function 432, 433
- Baade–Wesselink method 261
- background radiation 510–513**
 - discrete source contribution to 510–512
 - effects of evolution 512–513
 - 'luminosity evolution' 513
 - integrated emission of galaxies and 587
 - Lyman- α emission of the intergalactic gas 562
 - origin of, in standard world models 512
 - radio emission at long radio wavelengths 513
 - source counts and 510
 - starburst galaxies and 589
 - independence of cosmological model 589
- submillimetre and far-infrared 597
- COBE observations of 587

- contribution of active galactic nuclei 598
 main contributors to 598
 metal formation and 587
ultraviolet
 decrease at large redshifts 595, 596
 decrease in intensity from $z = 1$ to present epoch 596
 from the proximity effect 568–569
 from the proximity effect at small redshifts 568
 global star formation rate and 595
 integrated emission of quasars and 569
 integrated emission of star-forming galaxies at large redshifts 569
 neutral hydrogen in the peripheries of galaxies and 568
 ultraviolet, optical and near-infrared 586
 effects of dust 587
 from spectra of ultra-high-energy γ -ray sources 587
baising
 antibiasing 402
 galactic explosions and 402
Balloon Observations Of Millimetric Extragalactic Radiation ANisotropy and Geophysics (Boomerang) 456
bar instability in differentially rotating discs 69
 barred spiral galaxies 51, 54
baryogenesis 641–642
 baryon number violation of primordial X, \overline{X} bosons 642
 baryon-asymmetry problem 641
 Sakharov's rules 641
 baryon number violation 641
 C and CP violation 641
 non-equilibrium conditions 641
 unification of quarks and leptons and 642
 baryon asymmetry problem 23, 286, 307, 622
 baryon number violation
 generic feature of grand unified theories 641
 baryon perturbations in cold dark matter models 409–410
 baryon–antibaryon pair production 23, 622
baryonic theories of galaxy formation 360–364, 383
 what went wrong 364–365
 Bautz–Morgan classification of clusters of galaxies 109, 110
 Bautz–Morgan effect 253, 254, 544
 Bayesian statistical techniques 463
 Bell Telephone Laboratories 27
bending of light rays 179–181
 by ‘negative mass’ in inhomogeneous Universe 232, 233
 dependence upon the gravitational potential 181
 Beppo-SAX satellite 498
 bias parameter 137
 gravitational lensing and 138
 biasing 21, 401–405
 bias parameter 269, 403, 404, 407, 417
 bispectrum of galaxy distribution and 403
 dependence of luminosity and spectral type 404, 405
 for different classes of galaxy 405
 two-point correlation function for galaxies and 403, 405
 Gaussian fluctuations and 402
 hot gas in voids 402
 mechanisms for 402
 non-linear bias parameter 403
 Biermann battery 579, 581
Big Bang model of the Universe, history of 14–16
 big crunch 205, 338
big problems of cosmology 466, 621–624
 BIMA Millimetre Array 126, 127, 249
 black holes 140, 586
 formation in early Universe 392
 supermassive 140, 471, 488, 492
 epoch of maximum quasar activity 517
 non-thermal radiation processes and 492
 ratio of mass to spheroid mass 488
 Bohr's theory of the hydrogen atom 623
 Boltzmann equation 368, 377, 395, 409, 411, 422, 440, 448, 614
 Boomerang experiment 435

- Bose–Einstein spectrum 29, 284
 Boulby Underground Laboratory 146
 bremsstrahlung 95, 115, 128, 248, 547,
 561
 bolometric luminosity of 119
 cooling rate 121, 479
 emissivity of 128
 spectral emissivity of 115
 spectrum of 116, 128, 248
 thermal 561
 brightest galaxies in clusters 44, 45
 brightest members of rich clusters of
 galaxies
 absolute magnitudes of 109
 brown dwarfs 139–141
 Butcher–Oemler effect 253, 543–544
 changing fractions of galaxy types with
 redshift and 543
 passive evolution of spheroidal galaxies
 and 543
 selection criteria and 543
- C and CP violation
 in decay of neutral K^0 and \bar{K}^0 mesons
 641
- Calán-Tololo supernova project 164–166
 CalTech Submillimetre Observatory 126
 CAMB computer code 422, 430, 440
 Cambridge 4C survey 506
 Cambridge APM galaxy survey 269, 386
 Canada-France Redshift Survey 590
 Cartesian coordinates 155
 Cartwheel galaxy 56, 58
 Cassini spacecraft 191, 192
 CBI experiment 435
 cD clusters of galaxies 102–103
 cD galaxies 51, 82, 96, 102, 103, 109
 in small groups 103
 central bulge of lenticular galaxies 53
 central bulge of spiral galaxies 51
 central limit theorem 487, 505, 508
 Cepheid variables 7, 246, 247
 period–luminosity relation for 7, 8, 246
 CfA galaxy survey 38, 39, 41, 400, 401,
 406
 ChaMP study 525
 Chandra Deep Fields 525
 Chandra X-ray Observatory 116, 124,
 125, 249, 491, 525
- chemical potential 284
 Chwolson ring 129
 Cl 0024+1654 235
 classification of galaxies 59
 cluster Cl 0024+1654 136, 137
clusters of galaxies 37, 42, 43, **95–146**
 Butcher–Oemler effect 543–544
 central mass density of 107
 core radius 103, 105
 counts of X-ray clusters 529–532
distribution of galaxies in **101–110**
 galaxy content and spatial distribution
 of galaxies in 101–103
dynamical estimates of masses of
110–114
gravitational lensing by *see* gravitational
 lensing by galaxies and clusters
 of galaxies
hot gas in *see* hot gas in clusters of
 galaxies
isothermal gas spheres and *see*
 isothermal gas spheres, **103–108**
large-scale distribution of **95–100**
luminosity function for galaxies in
108–110
 mass–luminosity ratios of 99, 117
 on a temperature-number density diagram
 481
 segregation by galaxy type 102
 segregation by mass 103
summary of properties of **109–110**
Sunyaev–Zeldovich effect in hot intra-
 cluster gas *see* Sunyaev–Zeldovich
 effect in hot intracluster gas
 two-point correlation functions for 100,
 101, 387, 402
 velocity dispersions of 99
 CMBfast computer code 422, 425, 430,
 440
 cold dark matter 19–21, 359, 374, 375,
 381, 382, 398, 441, 464, 476, 615
 perturbations in 367, 374, 376, 380,
 382, 396, 437, 557
 WIMPs and 375
cold dark matter model of galaxy
 formation 20, 21, 349, 380–383,
 393–395, 399, 401–403, 409–412,
 414, 415, 418, 428, 482, 487, 489
 adiabatic 395, 396, 399, 412

- as a ‘bottom-up’ picture for structure formation 382
 broken-scale-invariant 419
 concerns about 415
 hierarchical clustering in 382
 isocurvature 396, 398, 400
 mixed hot and 418
 open 400, 401, 410, 413, 416–418
 standard 401, 409, 415–418, 530, 532, 559, 572, 573
 tilted 419
 with decaying neutrinos 416–418
 with finite cosmological constant 416–418, 572, 613
 collisions between galaxies 478, 544, 613
 Coma cluster of galaxies 42, 64, 102, 109–114, 547
 core radius of 108
 mass of 111
 mass–luminosity ratio of 111, 113, 267
 Sunyaev–Zeldovich effect in 450
 X-ray image of 114
 comoving angular diameter distance 161
 comoving luminosity density 589
comoving radial distance coordinate
 159, 160, 161, 168, 170, 172, 203, 218, 219, 221, 226, 228, 232, 243, 244, 316, 336, 339, 341, 342, 424, 425, 494, 501, 507, 511, 631–633
 definition of 164
 comoving volume 171
 variation with redshift 495
 Compton double scattering 284
 Compton Gamma-ray Observatory
 BATSE instrument 498
 Compton optical depth of hot diffuse intergalactic gas 561
 Compton scattering 17, 28, 29, 125, 248, 281–284, 301, 352, 357, 359, 561
 exchange of energy between photons and electrons by 281–284
 induced 17
 inverse 492
 Compton scattering in post-recombination Universe 282, 284
 Compton scattering in radiation-dominated Universe 281–284
 Compton scattering optical depth 29, 125, 283, 284
 computer simulations
 galaxy formation and 472
 hydrodynamic, of intergalactic gas 557, 571–574
 at redshift $z = 2$ 573
 cold dark matter models and 572
 feedback processes and 572
 predicted column density distribution of Lyman- α absorption clouds 572, 615
 predicted structures of neutral hydrogen clouds and 572, 615
 Single Particle Hydrodynamics 572
 star formation and 572
 supernova explosions and 572
 hydrodynamical simulations of galaxy collisions 616
 large-scale structure and 400, 474, 477, 484, 486, 487, 489, 530
 excess of dwarf satellites 486
 Press–Schechter mass function 487, 488
 large-scale structure formation 613
 origin and evolution of cosmic structures and 614
 origin of intracluster magnetic fields by turbulence 580
 predicted spin parameter λ 611
 reionisation era 574, 575
 semi-analytic models of galaxy formation 583
 concentration index C 91, 92
 concordance Λ CDM world model 22, 37, 42, 241, 424, 560, 621, 623, 625
 conformal diagram 631
 including inflation 632
 passing through and re-entering the Hubble sphere 633
 conformal Newtonian gauge 348, 349, 445
 conformal time 317, 340, 342, 344, 346–348, 445, 458, 631–634, 637
 extension to negative values before end of inflationary era 631
 confusion 505
 confusion-limited survey 505
 systematic overestimation of flux densities in 505
 convergence κ 460

- cooling rate of astrophysical plasma 479, 480
 cooling time of astrophysical plasma 479, 481, 486
 Copernicus satellite 297
 core radius of brightness distribution 61
correlation functions and the spectrum of the initial fluctuations 385–419
 acoustic peaks in the power spectrum of galaxies 411–415
 2dF galaxy redshift survey 412–413
 Sloan digital sky survey 412–415
 biasing 401–405
 evolution of the initial perturbation spectrum – transfer functions 393–401
 adiabatic cold dark matter 393–396
 adiabatic hot dark matter 396
 isocurvature cold dark matter 396–399
 subsequent evolution 399–401
 power spectrum
 origin of maximum of 415
 reconstructing the processed initial power spectrum 405–410
 non-linear development of the density fluctuations 407–409
 redshift biases 406–407
 role of baryon perturbations 409–410
 the perturbation spectrum 388–392
 Harrison–Zeldovich power spectrum 391–392
 initial power spectrum 390–391
 relation between $\xi(r)$ and the power spectrum of the fluctuations 388–390
 two-point correlation function for galaxies 385–388
 variation on a theme of cold dark matter 415
 correlation functions for galaxies 363, 405
 correlation lengths 404
 higher order 386
 three-point correlation function 403
 Cosmic Anisotropy Polarization Mapper (CAPMAP) 456
 Cosmic Background Explorer (COBE) 15, 21, 27–33, 284, 415, 416, 419, 421, 429, 432, 434, 437, 440, 442, 507, 561, 587
 Cosmic Background Imager (CBI) 456
The Cosmic Century: A History of Astrophysics and Cosmology (Longair) 3, 149, 193, 434, 514
 cosmic chemical evolution, equations of 604–607
 closed box model 605, 606
 conservation of mass 605
 infall of material from intergalactic medium 604–607
 inflow model 606
 instantaneous recycling approximation 605
 loss of heavy elements due to star formation 605
 outflow due to supernova explosions 606
 outflow model 606
 outflow of processed material 604–607
 rate of change of mass of heavy elements 605
 rate of infall or outflow $\dot{\Omega}_f$ 605
 rate of star formation 605
 role of dust 604, 606
 yield y 605
 Cosmic Lens All Sky Survey (CLASS) 266
cosmic microwave background radiation 15, 16, 18, 22, 27–33, 241, 275, 467, 624
 dipole component of 30, 31
 discovery of 17, 362
 distortions from a perfect black-body spectrum 283–284
 causes of 283
 distortions from a perfect black-body spectrum 28, 29
 energy density of 276
 epoch of recombination and 277, 279
 estimation of cosmological parameters from 250, 252, 259, 269, 270, 300
 fluctuations in the *see* fluctuations in the cosmic microwave background radiation
 horizon problem and 621
isotropy of 29–33, 41, 42, 149, 150, 337
 last scattering surface of 325, 631
 neutrinos and 369

- number density of photons in 277, 423
 polarisation of *see* polarisation of the cosmic microwave background radiation
 prediction of 14
 specific entropy per baryon of 277
spectrum of 28–29
 Sunyaev–Zeldovich distortions of 125, 126, 561
 temperature fluctuations in the *see* fluctuations in the cosmic microwave background radiation
 temperature of 143, 356, 371, 416, 576
 observations of the variation with redshift 272, 273
 variation with redshift 272
 temperature of at epoch of recombination 279
 thermal history of 278
cosmic star-formation rate
 advantages of submillimetre waveband 597
 cosmic abundances of the elements and 598–607
 maximum at redshifts $z \sim 1\text{--}2$ 610
 optical–UV determinations of 606
 problem of dust extinction 596, 598
 problems with the simple models 606
 submillimetre determinations of 596–598, 606
 as a function of redshift 598, 599
cosmic time 150, 158–160, 161, 163, 207, 217, 231, 237–239, 252, 317, 339, 344, 438, 445
 cosmic variance 434–436, 467
 cosmic virial theorem 268, 329
Cosmical Magnetism (ed. Lynden–Bell) 577
 cosmological constant Λ 13, 21, 202, 208, 212, 214, 215, 242, 265, 267, 273, 336, 344, 414–418, 425, 630
 ‘repulsive force of a vacuum’ and 208, 209
 dark energy and 23, 24, 207, 208, 210, 626
 evidence for finite value of 257
 history of 12, 13, 24, 188, 199, 207, 623
 zero-point fluctuations of vacuum and 626
Cosmological Constants (Bernstein and Feinberg) 202
Cosmological Inflation and Large-Scale Structure (Liddle and Lyth) 313, 629
cosmological parameters, determination of 241–270, 463–465
 Ω_A and the statistics of gravitational lenses 263–267
 age of the Universe T_0 *see* age of the Universe T_0 , 250–252
 angular diameter–redshift test 261–263
 deceleration parameter q_0 *see* deceleration parameter q_0 , 252–263
 density parameter Ω_0 267–270
 Hubble’s constant H_0 *see* Hubble’s constant, 246–250
 number counts of galaxies 259–261
 infrared H waveband 260
 problems of using to determine q_0 259, 260
 parameters to be determined 463–465
 relative lensing probabilities Ω_A and the statistics of gravitational lenses 265
 relative lensing probabilities 265
see density parameter Ω_0 267
 testing the Friedman models 242–245
 the parameters and relations between them 241–242
 three-year WMAP data and 463–465
Cosmological Physics (Peacock) 209, 313
cosmological principle 149–150, 158, 199, 204, 237, 238, 625
 Cosmology Calculator of Dr. Edward Wright 425
 COSMOS survey of clusters of galaxies 95
 counts of γ -ray bursts 498
 counts of active galaxies evolution in infrared waveband 536
 counts of extragalactic radio sources 498, 508, 514–516
 excess of faint radio sources 514
 evidence for strong cosmological evolution 514
 counts of far-infrared and submillimetre sources 597
counts of galaxies 537–543
 advantages of infrared K waveband 538

- evidence for homogeneity of Universe 493
- excess of faint blue galaxies 47, 261, 540
- and starburst galaxies 542, 543
- nature of 540–543
- fluctuations in, due to large-scale clustering 538–541
- for irregular/peculiar/merger systems 542
- for spheroidal and spiral galaxies 540, 542
- Hubble's 494
- in infrared K band 540
- in infrared K waveband 542
- in U, B, R, I and K wavebands 541
- problems of determining 537–538
- counts of galaxies and active galaxies, predicted** 492–507
- at submillimetre wavelengths 500–501, 534
- normalised differential counts 501, 503
- Euclidean 493
- differential 493
- integral 493
- for standard world models 494–500
- comparison with Euclidean counts 495
- for bolometric luminosities and flux densities 495
- for sources with power-law spectra 495–496
- normalised, differential 495–496
- optical counts for galaxies 498–500
- slopes of integral and differential 496, 498
- models with finite Ω_A 501–504
- counts of infrared and submillimetre sources** 532–537
- convergence of, at mid-infrared wavelengths 537
- far-infrared wavelengths 533, 534
- IRAS galaxies 532, 533
- excess of faint sources 532
- Spitzer First Look Survey 533
- excess of faint sources 533
- submillimetre wavelengths 534
- excess of faint sources 534
- counts of radio-quiet quasars 518, 521, 522
- counts of X-ray clusters of galaxies 529–532
- counts of X-ray sources** 524–532
- evidence for evolution of the source populations 525
- hard X-ray energies, 2–10 keV 525, 527, 529
- history of 524
- problems of interpretation 525
- soft X-ray energies, 0.5–2 keV 527
- and the integrated X-ray background emission 527
- soft X-ray energies, 0.5–2 keV and 2–10 keV 525
- coupling of dark and baryonic matter by gravity 378
- coupling of electrons and protons by Coulomb collisions 367
- coupling of matter and radiation in the expanding Universe 17, 353, 355, 367
- CP violation in decays of K^0 mesons 287
- Crab Nebula
- origin of magnetic field of 580
- critical surface density for star formation in spiral galaxies 554
- critical cosmological density** 139, 145, 204
- in neutrinos with finite mass 143
- critical density 439
- critical density for star formation 616
- Critical Dialogues in Cosmology* (ed. Turok) 269, 298, 415
- crossing time 111, 474
- definition of 63
- for a cluster of galaxies 43
- Cryogenic Dark Matter Search (CDMS) 146
- Cryogenic Dark Matter Search (CDMS II) 373, 374
- curvature of space κ** 154, 156, 157, 171, 231, 242, 243, 320, 627, 638
- condition for flat Euclidean space 210, 211, 364
- effect of hyperbolic space on growth of perturbations 320, 326, 327

- radius of, at the present epoch \mathfrak{N} 161, 199, 210, 228, 239
 relation between Ω_0 , Ω_A and 210
 variation with scale factor a 160
 curvature of space–time 181
 curvature perturbations 437
 amplitude of 463
 cusp catastrophe 135
 61 Cygni 5
- damped Lyman- α systems in quasar spectra 272, 600–604, 606, 607
 dark ages 384, 471, 552, 574, 576
 observability through fluctuations in the neutral hydrogen intensity 577
dark energy 207–211, 216, 230, 243, 245, 327, 331, 335, 344, 345, 414, 623, 634
 density parameter Ω_A of the 21–23, 242, 449, 501, 503, 623
equation of state of 210–211, 267, 465, 630
 problem of the 23, 24, 365, 623
dark matter 139–146, 241, 268, 269, 367
astrophysical and experimental limits
144–146
 axions and 142, 369
baryonic 139–142
 black holes and 140, 141
 limits to mass density from gravitational lensing 140
 very low mass 141
 brown dwarfs and baryonic 140
 clusters of galaxies and 95, 112, 113, 115
 density parameter Ω_D in the 205, 214
 distribution of 235
forms of 139–146
 gravitational coupling to baryonic matter 368
 gravitational lensing and 130, 136, 137
 in clusters of galaxies 113, 117, 119, 136, 137, 267
 in early-type galaxies 138
 in elliptical galaxies 69
 in galaxies 267, 367, 368
 in spiral galaxies 69
 MACHOs and 141, 142
- gravitational microlensing and 141, 142
 masses of dark matter particles 145
 nature of 24, 301, 625
 neutrinos with finite rest mass and 143, 369
non-baryonic 142–144, 301, 335, 364, 365, 367
 nature of 368, 369
 searches for dark matter particles 145, 146
 standard bricks and 139
 structure of 137
 WIMPs and 143, 144
- dark matter and galaxy formation**
367–384, 400
 evolution of hot and cold dark matter perturbations 380–384
 cold dark matter scenario 381–384
 hot dark matter scenario 380–381
 forms of non-baryonic dark matter 369–370
 free-streaming and damping of hot dark matter perturbations 375–377
 instabilities in the presence of dark matter 377–379
 metric perturbations and hot and cold dark matter 374–375
 adiabatic curvature modes 374, 379
 curvature modes 374
 isocurvature modes 374, 375
 WIMPs as dark matter particles 370–374
- dark matter haloes
 formation according to Press-Schechter formalism 489
 dark matter haloes of galaxies and clusters 137
- dark matter particles
 collisionless 399
 nature of 384
 ultraweakly interacting 368
 dark matter problem 350, 365
Darkness at Night (Harrison) 510
 de Sitter solution 149, 213
 de Sitter world model 337, 626, 639
 de Vaucouleurs $r^{1/4}$ law for surface brightness 61, 62, 108
 de Vaucouleurs radius 70

- de Vaucouleurs' classification of galaxies 54, 55, 93
- deceleration parameter q_0 216, 241
- angular diameter-redshift test 261–263
- for compact radio sources 262, 263
 - for double radio sources 261, 262
- number counts of galaxies 259–261
- redshift-magnitude relation for brightest galaxies in clusters 252–254
- effects of stellar evolution on 253
- infrared 544–545
- problems of interpreting at large redshifts 253
- redshift-magnitude relation for radio galaxies 254–255
- advantages of determining in the K waveband 254, 255
- and the alignment effect 254, 256
- corrections for effects of stellar evolution 254
- redshift-magnitude relation for Type 1a supernovae 256–259, 464
- evidence for non-zero cosmological constant 257
- relation with Ω_0 and Ω_A 243
- decoupling of matter and radiation in the post-recombination Universe 283
- deflection D 505
- deformation tensor in Zeldovich approximation 476, 477
- Degree Angular Scale Interferometer (DASI) 456
- density contrast 268, 269, 311, 312, 315, 325, 328, 354, 358, 378, 391, 393, 402, 408, 443, 482, 573
- for curvature modes in early Universe 374
- growth of 393
- density parameter** Ω_0 204, 241, 243, 267–270, 412, 414
- cosmic virial theorem and 268
- defined at any epoch 230
- infall of galaxies into large-scale structures and 268, 269, 406, 407, 464
- density parameter in baryons** Ω_B 269, 289, 352, 362, 364, 444, 548, 561, 563, 564, 576, 586, 622
- from primordial nucleosynthesis 293, 299, 301, 357
- from WMAP power spectrum 300, 464
- density parameter in gas Ω_g 604–607
- density parameter in heavy elements Ω_m 604–607
- density parameter in intergalactic gas Ω_{IGG} 555
- density parameter in neutral hydrogen Ω_{HI} 554
- density parameter in stars Ω_s 547, 598, 604–607
- density parameter of the dark energy** Ω_A 21, 23, 209, 210, 242, 449, 464, 501, 503, 623, 626
- density parameter of the dark matter** Ω_D 464
- deuterium D
- abundance in Lyman- α absorbers 297
 - observed primordial abundance 297–298
 - as a ‘baryometer’ 299
 - solar abundance 297
- deuteron, binding energy of 292
- Differential Microwave Radiometers of COBE 30
- disc component of spiral galaxies 51
- disc scale length for spiral galaxies 62
- discs of spiral galaxies
- stability of 612
- dissipation processes and galaxy formation** 477–482
- radiative processes 478
 - star formation and 478–479
 - first generation of stars 478
 - in very large redshift objects 479
 - thermal instabilities 478, 481
- distance indicators 246, 247
- distance measure D 494, 495
- distance of the stars 4
- distortion matrix 462
- shear components of 460, 461
- Doppler shift
- Newtonian 162, 176
 - special relativistic 162
 - ‘downsizing’ 614
- ‘drop-out’ galaxies 543, 593, 594, 607
- decrease in luminosity density at large redshifts 595

- luminosity functions for 595
- properties of 593
- dust emission and star formation 478, 501
- dust extinction 538
- dust extinction of galaxy spectral energy distribution 535, 536
- dwarf elliptical galaxies 51
- dwarf galaxies 51
- dynamical equilibrium 63
- dynamical friction 399, 544

- early history of cosmology 3–5**
- early history of galaxies and the structure of our Galaxy 5–9**
- The Early Universe* (Kolb and Turner) 313
- early-type galaxies 50
 - mass distribution is 138
- eclipse expeditions of 1919 190
- Einstein angle 130, 132, 136
- Einstein radius 129, 132, 134, 264
- Einstein ring 130
- Einstein X-ray Observatory 116, 123, 507
- Einstein's field equations** 12, 13, 149,
 - 188, 199–202, 208, 243, 273, 348, 365, 368, 395, 422, 440, 448
 - conservation of energy for relativistic and non-relativistic gases 201
 - equation of conservation of mass and 200
 - first law of thermodynamics and 200, 201
 - monatomic gases and 201
 - ultrarelativistic gases and 201
- Einstein's static model of the Universe 8, 12, 149, 151, 188, 199, 214
- Einstein-de Sitter world model 205, 231–235, 265, 266, 319, 320, 322, 336, 483, 485, 496, 500
 - as only ‘stable’ model 622
- electron–positron annihilation 301
- electron–positron pair production 23, 622
- elliptical galaxies 50, 51
 - formation at large redshifts 543
- elliptical galaxies as triaxial systems 71–73**
 - linear programming techniques for 73
- ellipticities of elliptical galaxies 51
- emission history of the Universe 604

- energies of the photon and neutrino backgrounds 302
- energy density of the Cosmic Microwave Background Radiation 33
- entropies of the photon and neutrino backgrounds 301, 302
- entropy per baryon
 - fluctuations in, in isothermal picture of structure formation 357
- Eötvös experiment 173
- Eöt-Wash experiment 174, 175
- Eötvös ratio 174, 175
- epicyclic frequency 554
- epoch of baryon–antibaryon pair production 286
- epoch of decoupling of matter and radiation 574
- epoch of electron-positron pair production 286
- epoch of equality of radiation and matter
 - energy densities 17, 277, 285, 354, 358, 359, 376, 381, 393, 395, 396, 398, 410, 425, 430
 - including neutrinos 303
- epoch of formation of first stars 574
- epoch of formation of galaxies, clusters and superclusters 312, 474, 487
- epoch of maximum quasar activity 362
- epoch of nucleosynthesis 286
- epoch of recombination 17, 33, 277–281, 285, 312, 325, 355, 357, 362, 364, 378–381, 410, 440, 446
- epoch of recombination for helium 279
- epoch of reheating of the intergalactic gas 286
- epoch of reionisation of the intergalactic gas 33, 355, 452, 471, 547, 552, 574–577
- role of black holes in nuclei of galaxies 574
- equation of continuity 313
 - relativistic case 331
- equation of state
 - for photons, massless particles and ultrarelativistic gas 271, 331
- equivalence principle *see* principle of equivalence
- EROS project 141
- ESO catalogue of galaxies 44
- ESSENCE supernova project 257, 258

- Euclid's fifth postulate 150
 Euler's equation 313, 440, 448
 relativistic case 331
 Eulerian coordinate system 314, 476
 event horizon 338, 339, 342, 346, 634
 definition of 338
evolution of active galaxies with cosmic epoch 514–532, 569
 extragalactic radio sources 514–518
 ‘luminosity evolution’ 516
 cut-off of strong evolution beyond redshift $z \sim 2$ –3 516, 517
 for sources with steep and flat radio spectra 516, 517
 luminosity-dependent density evolution 516, 518
 radio-quiet quasars 518–524
evolution of galaxies and active galaxies with cosmic epoch 471, 491–545
 active galaxies 492, 514–532
 extragalactic radio sources 514–518
 radio-quiet quasars 518–524
 X-ray clusters of galaxies 529–532
 X-ray sources 524–529
 background radiation
 source counts and 510
 background radiation and 510–513
 effects of evolution and the radio background emission 512–513
 evaluation of 510–512
 brief history of evidence for 491–492
 clusters of galaxies 543–545
 co-evolution of stellar and black hole properties of galaxies 492
 counts of galaxies 537–543
 counts of galaxies and active galaxies 492–507
 euclidean source counts 493
 fluctuations in the background radiation
 due to discrete sources 504–507
 for standard world models 500
 models with finite Ω_A 501–504
 submillimetre counts of dusty galaxies 500–501
 counts of galaxies and active galaxies, predicted
 for standard world models 494
 infrared and submillimetre number counts 532–537
 stellar and gaseous components of galaxies 492
 V/V_{\max} or luminosity-volume test 507–510
 excess dwarf galaxy problem
 solution by sweeping out gas by astrophysical processes 613
 excess of faint blue galaxies 46, 591
 irregular nature of 593, 594
 extragalactic background radiation
 due to discrete sources 275
 due to galaxies 275
 energy density of, in different wavebands 275
 in the ultraviolet, optical and infrared wavebands 275, 276
 limits from $\gamma\gamma$ absorption in spectra of γ -ray sources 275
 number density of photons in different wavebands 275, 277
 spectrum of 273–277
 plotted as vI_v 275
 plotted as I_v 275, 276
 extragalactic radio sources 578
 depolarisation of 578
 luminosity function of
 evolution with cosmic epoch 514–518
 origin of magnetic fields of 580, 581
 active galactic nuclei and 581
 supermassive black holes in nuclei of 581
Faber–Jackson Relation for elliptical galaxies 70–71
 Faint Object Camera 564–566, 592
 Far Infrared Absolute Spectrophotometer (FIRAS) of COBE 28
 Far Ultraviolet Spectroscopic Explorer (FUSE) 566, 567
 feedback mechanisms in galaxy formation 471
 field galaxies 56
 fifth force, search for 174, 175
 fine-tuning problem 23, 622
 ‘fingers of God’ 39, 406, 407
 FIRST deep VLA survey of radio sources 42
 first generation of stars 552
 formation of interstellar dust 587

- properties of 574
 ultraviolet and X-ray emission of 574
- first law of thermodynamics 200, 201
- flat two-space, isotropic 154
- flatness problem** 23, 24, 230–231, 622
- fluctuations in the background radiation due to discrete sources 504–507
 spatial correlation technique 506
- fluctuations in the cosmic microwave background radiation 18, 19, 21, 30, 32, 33, 167, 281, 362, 364, 379, 382, 384, 410, 414–416, 419, 421–467, 614, 640
- acoustic peaks *see* acoustic oscillations in the power spectrum of the cosmic microwave background radiation
- discrete source confusion and 451, 505
- epoch of recombination and 430
- ionisation of the intergalactic gas through the epoch of recombination 422–423
- physical and angular scales of 424–430
 last scattering layer 425–426
 particle horizon scales 429–430
 Silk damping scale 426
 sound horizon at the last scattering layer 427–429
- physics of 443
- power spectrum of 13, 431–436, 439, 465
 cosmological parameters from 444, 463–465, 548
 observations of 434–436
 other sources of 465–466
 statistical description of 431–434
- power spectrum on intermediate scales – acoustic peaks 443–449
- power spectrum on large angular scales 436–443
- integrated Sachs–Wolfe and Rees–Sciama effects 440
- primordial gravitational waves 440–443
- Sachs–Wolfe effect – physical arguments 436–440
- power spectrum on small angular scales 450–452
- confusion due to discrete sources 451–452
- confusion due to submillimetre sources 452
- statistical and Silk damping 426, 450
- Sunyaev–Zeldovich effect in clusters of galaxies 450–451
- quadrupole anisotropy of 442
- reionised intergalactic gas 452–453
- Sunyaev–Zeldovich effect and 450
 detection of statistical effect from X-ray Abell clusters by WMAP 451
- Thomson scattering optical depth and 453, 574
- Fokker–Planck equation for stars in clusters 107
- fold catastrophe 135
- four-tensors in relativity 184–187**
- curvature scalar 188
 - differentiation of 188
 - electromagnetic field tensor 186
 - energy–momentum tensor 188
 - for dust 186
 - including pressure 186
 - Maxwell’s equations 186, 187
 - Ricci tensor 188
 - Riemann–Christoffel tensor 188
 - energy–momentum tensor
 - for dust 185
 - four-vectors 185
 - examples of 185
 - velocity 185
 - Fourier integral 389
 - Fourier series 389, 431
 - Fourier transformations 431, 462
 - autocorrelation theorem for 433
 - of acoustic oscillations in cosmic microwave background radiation 445
 - three-dimensional 388
 - FR2 3CR radio sources 609
 - fractal Universe 392
 - free-bound and bound-bound transitions of hydrogen 479
 - free-streaming of neutrinos 19
 - Freeman’s law 62, 74, 612
 - ‘freeze-out’ of hot dark matter particles by free-streaming 376
 - ‘freeze-out’ of massive particle species in the early Universe 307

- frequencies of galaxies of different types
 54, 56, 541
 in different galactic environments 56,
 57, 404, 538
- Friedman world models** 12, 13, 16, 151,
 199–239, 621, 624
- Friedman world models with $\Lambda = 0$**
202–207
- closed, spherical geometries 205
 - critical world model 205
 - curvature–density parameter relation
 205
 - dust models 202
 - dynamics of 205–207
 - flat Einstein–de Sitter model 205
 - Newtonian analogue for 202–204
 - problems of boundary conditions 203
 - open, hyperbolic geometries 205
 - parametric solutions for 207, 321
- Friedman world models with $\Lambda \neq 0$**
207–215
- bouncing models 212–214
 - classification of 215
 - dust models 208, 209
 - dynamics of 211–216
 - Eddington–Lemaître models 213, 214,
 223, 501
 - antipodal points of 225, 501, 503, 504
 - effects of gravitational lensing at
 antipodal points 504
 - number counts in 501, 503
 - redshift–flux density relation for 501
 - stationary redshift 214, 223
 - Lemaître models 214, 501, 503
 - ghost images in 226
 - loitering models 214, 223, 226
 - minimum rate of expansion of 212
- Friedman’s equation 199, 200, 320, 326,
 638
- Friedman: the man who made the Universe expand* (Tropp, Frenkel and Chernin)
 204
- fundamental observer 150, 158–161, 164,
 168, 204, 207, 237, 238, 335, 337,
 339–341, 347
- fundamental plane for elliptical galaxies**
70–71
- The Future of Theoretical Physics* (eds.
 Gibbons, Shellard and Rankin) 643
- GADGET computer code 616
- GAIA mission, prospects for light deflection
 observations 191
- Galactic ‘cirrus’ 30
- Galactic Astronomy* (Binney and Merrifield)
 49
- Galactic bulge 141
- galactic cannibalism 253, 544
- Galactic Dynamics* (Binney and Tremaine)
 49
- galactic extinction law 77
- Galactic synchrotron radiation 30
- galaxies 49
 - characteristic masses of 480
 - dependence of types upon environment
 613
 - mean luminosity of 84
 - mean space density of 84
 - on a temperature-number density diagram
 481
 - passive evolution of 498, 499
 - importance of red giant branch 499
 - starbursts and evolution of 499
- Galaxies in the Universe: an Introduction*
 (Sparke and Gallagher) 49, 64
- galaxies, correlations along the**
Hubblesequence 84–88
- colour–colour diagram and 87, 88
 - integrated colour 87
 - luminosity function of HII regions 87
 - masses and luminosities 84
 - neutral hydrogen 86
 - star formation rates and 87
 - total surface density and surface density
 of neutral hydrogen 87
- galaxies, old red 542
- galaxies, properties of 8, 49
- galaxies, red and blue sequences of** 63,
88–94, 412
 - colour–absolute magnitude relation
 89–90
 - colour–Sérsic index relation 91
 - definitions of 89
 - effect of the galaxy environment 92–93
 - mean stellar age–concentration index
 relation 91
- Galaxy
 age of 64

- disc scale length of 62
- luminosity of 84
- structure of 7–9
- galaxy and structure formation, history of 16–19**
- galaxy formation 583–620**
 - background radiation and element formation 584–587
 - energy density of background radiation and density of metals formed 586
 - intensity of background radiation and density of metals formed 586
 - processes of element formation 584, 585
 - collisions between galaxies and 614
 - ‘downsizing’ 610
 - feedback mechanisms and 486, 583, 614
 - growth of supermassive black holes and 614
 - Lyman-break galaxies 590
 - in the general field 590
 - multicolour technique for discovering 590, 591
 - observed global star formation rate 587–590
 - as a function of redshift 583, 589
 - star-forming galaxies and 587
 - starburst galaxies at large redshift 589
- star and element formation and 583–598
 - build-up of heavy elements in galaxies 583
 - numbers of ‘drop-out’ galaxies and 584
 - numbers of blue star-forming galaxies and 584
 - numbers of far-infrared and submillimetre galaxies and 584
 - quasar absorption line systems and 584
- star formation and 614
- two-stage theory of 482, 611
 - final radius of disc 612
- γ -ray background emission
 - Comptonisation and 529
 - spectrum of 526
- Garching-Bonn Deep Survey 138
- gas dynamics
 - equations of 313
 - in Lagrangian form 314
 - Newton’s second law in 314
 - relativistic case 331, 332
 - relativistic case in Lagrangian coordinates 331
- gauge choices
 - in electrodynamics 347
 - Lorentz and Coulomb gauges 347
 - superhorizon scales and 347, 437, 438
 - gauge-invariant gravitational potential 445
 - gauge-invariant variables 348
- Gaunt factor 116, 121
- Gauss’s theorem for Newton’s law of gravity 67, 133, 202
- Gauss, Carl Friedrich
 - theory of surfaces 181
- Gaussian curvature *see* curvature
- Gaussian fluctuations 402, 432, 443, 475, 477, 482, 484, 487
- Gaussian perturbations with random phases 41, 42
- Gemini Deep Deep Survey 607, 608
- general relativity 11, 48, 149, 151**
 - introduction to 173–198**
 - further complications 181–184
 - what Einstein did 187–188
 - route to 184–188**
 - superhorizon scales and 347–350
 - general relativity, experimental and observational tests of 189–197**
 - four tests of general relativity 189–192
 - advance of perihelion of Mercury 189
 - deflection of light and radio waves by the Sun 190, 191
 - gravitational redshift 189
 - time delay in Sun’s gravitational field 191, 192
 - parameterised post-Newtonian (PPN)
 - formulation of 175, 195
 - limits to values of the parameters 197
 - metric potentials in 196
 - physical significance of 176
 - pulsars and 192–194
 - xparameterised post-Newtonian (PPN)
 - formulation of 197
 - General Relativity: An Introduction for Physicists* (Hobson, Efstathiou and Lasenby) 173, 184, 313

- general theory of relativity *see* general relativity, 614
- geodesic distance 157
- geodesics 149–153, 158, 320
- giant molecular clouds 478
- globular cluster 47 Tucanae 250, 251
- globular clusters 250, 355
- Gran Sasso underground laboratory 146
- Gravitation and Cosmology* (Weinberg) 184
- gravitational collapse
- timescale of 479
- gravitational constant, variation with cosmic epoch 197–198**
- helioseismology and 198
 - limits to 197
 - lunar laser ranging and 197
 - primordial nucleosynthesis and 198
 - pulsar timing and 197
- gravitational deflection of light rays 134
- by the Sun 128
 - collision parameter for 128
- gravitational lensing by galaxies and clusters of galaxies 128–139**
- necessary conditions for 133
 - astrophysics of galaxies and 136–139
 - basic theory of 128–131
 - caustics and cusps in 135, 136
 - cluster masses from 134
 - critical surface density for 133
 - dark matter and 130, 136, 137
 - distortion of background images by 136
 - extended deflectors and 133–136
 - galaxy-galaxy imaging and 138
 - magnification of images by 130–132
 - mirror inversion of images in 132
 - time variations of intensities of images 139
- gravitational lensing, strong 138, 235
- case of the galaxy IRAS F10214+4724 235
 - complete sample of radio sources and quasars 266
 - magnification of intensities by 235
 - probability of 264, 266
- gravitational lensing, weak 138, 235, 460–463
- and cosmic shear 235
 - shear variance distribution of 461
- power spectrum of density perturbations in the mass distribution and 462
- Gravitational Lensing: Strong, Weak and Micro* (Schneider, Kochanek and Wambsganss) 130, 138
- gravitational mass 173, 174
- gravitational potential, Newtonian limit 179
- gravitational redshift 176–179**
- dependence upon gravitational potential 177
 - in general relativity 183
 - in the Newtonian limit 177
 - incompatibility with special relativity 178
 - time dilation in a gravitational field and 178
- gravitational relaxation timescale 544
- gravitational waves 625
- and tilt of spectrum of scalar perturbations 442
 - dependence upon inflationary potential 442
 - limits to energy density of primordial 442, 460
 - polarisation signature of primordial 441
 - primordial
 - detection of as the ‘smoking gun’ for inflationary cosmologies 640
 - spectral index of primordial 441, 640
 - from WMAP power spectrum 640
 - temperature power spectrum of 441, 442 - tensor to scalar ratio of primordial 442, 460, 640
 - limits to 460
- gravitons 373
- ‘Great Attractor’ 268
- ‘Great Debate’ 7
- Great Observatories Origins Deep Survey (GOODS) 538, 540, 592, 595, 598
- ‘Great Wall’ 38
- Greenbank Catalogue of radio sources at 6 cm 42, 43
- grey-body spectrum 535
- GUT era, new physics at 643
- GUT phase transition 628
- half-light radius of light distribution 61

- Harrison–Zeldovich initial power spectrum** 18, 21, 25, **391–392**, 393–396, 399, 433, 439, 441, 465, 484, 485, 559, 560, 624, 630, 640
- Hawking radiation 141
- He^+ Lyman- α absorption clouds in intergalactic medium 566
- HEAO-1 X-ray Observatory 524
- HEAO1 A-2 experiment 507
- Heaviside–Lorentz units 187
- Heisenberg’s uncertainty principle 636
- helium abundance
- as a thermometer of the early Universe 293
- helium-3 He^3
- observed by radio hyperfine transition line 298
 - observed primordial abundance 298
- helium-4 He^4
- observed primordial abundance 296
 - in low metallicity, extragalactic HII regions 296
- Hercules cluster of galaxies 102
- Hertzsprung–Russell (H–R) diagram 250, 251, 584, 585
- main sequence termination point 250
- hierarchical clustering 18, 59
- hierarchical model of the Universe 5
- hierarchical models of galaxy formation
- old red galaxies and 607
- hierarchical scenario for cluster formation 545
- Higgs fields and Higgs particles 24, 208, 373, 623, 626, 643
- High Energy Astrophysics Vol. 1* (Longair) 126, 544
- High Energy Astrophysics, Vol. 2* (Longair) 577
- Himalayas 402
- Hipparcos* astrometric satellite 247, 251
- Hipparcos* measurements of light deflection by the Sun 191
- Hopkins Ultraviolet Telescope 565, 566
- horizon mass 352, 353, 391, 395
- horizon problem** 22, 24, 337, 631
- last scattering surface and 337
 - solution of in inflationary model of the early Universe 337, 626, 627, 631
- horizon scale 17, 204, 441, 627
- horizons and the horizon problem** 335–338, 621
- hot and cold dark matter model of galaxy formation 335, 418
- hot and cold dark matter, history of** 19–22
- hot dark matter model of galaxy formation 19–21, 375–377, 380–381, 400–402
- formation of galaxies by fragmentation of large-scale structures 381
- late formation of structure in 400
- hot gas in clusters of galaxies** 114–124
- absence of cool gas in 123
 - associated with heating by radio lobes 124
 - models to explain the 123
 - abundance of iron 118
 - characteristic cooling time for 121
 - cooling flows in 122, 478
 - enthalpy of 123
 - mass inflow rates of 123
 - cooling time of 122
 - iron line FeXXVI from 115
 - sound waves in 125
- Hubble Deep and Ultra-Deep Fields 261
- Hubble Deep Field 491, 538, 542, 590–593
- Hubble Deep Field South (HDFS) 592
- Hubble diagram 44
- Hubble sequence of galaxies 50
- Hubble Space Telescope 58, 59, 130, 131, 138, 249, 254, 257, 297, 464, 491, 538, 540, 543, 550, 552, 564, 565, 568, 590, 593, 595, 601
- The Hubble Space Telescope and the High Redshift Universe* (ed. Tanvir) 552
- Hubble Space Telescope Science Institute 590
- Hubble sphere 342–346, 632–634, 638
- definition of 342
 - distinction between particle horizon and 631
 - shrinking of 631, 633, 634
- Hubble Ultra Deep Field (HUDF) 491, 538, 540, 542, 543, 590, 592, 594–596
- filter transmission curves for 594
- Hubble’s constant 9, 13, 46, 241
- Baade–Wesselink method and 248
 - brightest stars in galaxies and 246

- Cepheid variables and 246, 247
 controversy over value of 246
 cosmological distance ladder and 246,
 247
 defined at any epoch 166, 230
 from Sunyaev–Zeldovich effect 128
 globular clusters and 246
 Hubble Space Telescope Key project and
 246, 247
 final result of 248, 464
 present expansion rate of the Universe
 and 167
 redshift–magnitude relation for brightest
 cluster galaxies and 246
 Sunyaev–Zeldovich effect and 248
 Tully–Fisher relation and 246
 Type 1a supernovae and 246
 written as $H_0 = 100h \text{ km s}^{-1} \text{ Mpc}^{-1}$
 204
- Hubble's law 9, 10, 44–46, 150, 165, 314,
 407
 comoving radial distance coordinates and
 340
 discovery of 150
 gravitational lensing and 249
 recession velocities exceeding the speed
 of light in 341
- Hubble's law and the expansion of the
 Universe 44–48, 165**
- Hubble's law for surface brightness 61
 hydrostatic equilibrium 104, 115
 hydrostatic support, equation of 318
 hyperbolic two-space, isotropic 154, 155
- i*-band drop-outs 552
 I0 galaxies 54
 inertial mass 173, 174, 181
 inflationary model of the early Universe
 24, 25, 364, 392, 621, 624
 accelerated expansion 634
 chaotic inflation 626
 exponential expansion and 626, 627,
 629
 role of scalar fields 629
 straightening of geometry 627
 violation of strong energy condition and
 630
- historical background 626–629
- formation of ‘bubbles’ in original Guth
 picture 628
 lack of physical realisation of
 inflationary picture 629
 monopole problem 628
 new inflationary model of Linde,
 Albrecht and Steinhardt 629
 slow rollover model 629
 symmetry breaking in Grand Unified
 Theories 627
 transition from false to true vacuum in
 original Guth picture 627
- necessary conditions for many e-folding
 times 635
- necessary tools from theoretical and
 particle physics 630
 release of ‘latent heat’ 627
 scale factor-temperature relation 628
 shrinking of Hubble sphere 634
 three equivalent conditions 634
 violation of the strong energy condition
 634
 transition to standard radiation-dominated
 model 627
- inflaton potential 24, 629
- infrared luminosity function of galaxies
 evolution of 536
 comparison with evolution of active
 galaxies 537
- Infrared Space Observatory (ISO) 532,
 533
- inhomogeneous world models 231–235**
- initial mass function
 modified 487
- initial power spectrum
 curvature of 463
 modifications of 409
 modified 484
 reconstruction of 474
- interacting galaxies 57, 60, 478
 fraction of 59
- intergalactic gas, optical depth for Thomson
 scattering of 280, 281
- intergalactic medium 547–582**
- absorption by 548
 absorption coefficient of 548
 background emission of 548
 emissivity of 548
 epoch of reionisation of 574–577

- Gunn–Peterson test for ionised helium in 564–567, 571
due to integrated effect of Lyman- α clouds 566–567
feasibility of, for large redshift quasars 564
Gunn–Peterson test for neutral hydrogen in 547, 549–552, 569, 574
positive detection at $z \geq 6$ 551, 552, 564, 574
upper limits to neutral hydrogen number density from 550
lukewarm gas in 555, 560–569
collisional excitation of 562–563
diffuse ultraviolet radiation at large redshifts and 567–569
emission and absorption of 564–567
proximity effect and 567–569
Lyman continuum opacity of 569–571, 574
Lyman- α absorption clouds in 547, 552–560
evolution of, with cosmic epoch 556
nature of 554–556
power spectrum of forest of 557–560
predicted evolution of, with cosmic epoch 556
properties of 552–554
modelling the evolution of 571–574
neutral hydrogen at large redshifts 574
fluctuations in observed intensity 574–577
intensity of 576
ionsation by first generation of massive stars 575
observational challenge of detecting 575
predicted brightness temperature of 576
problem of synchrotron radiation foregrounds 576
optical depth of 548
origin of magnetic fields 577–582
ultraviolet opacity of 569–571
X-ray background and a cosmic conspiracy 561
International Linear Collider (ILC) 144
International Ultraviolet Explorer (IUE) 248, 597
intrinsic curvature *see* curvature
Introducing Einstein's Relativity (d'Inverno) 184
ionisation fraction through epoch of recombination 423, 424
ionisation of intergalactic gas through the epoch of recombination 422–423
IRAS F10214+4724 235
IRAS Faint Source Survey 532
IRAS galaxies 501, 503
catalogue of 532
complete samples of 532
correlation functions for 405
ultraluminous 58
IRAS infrared observatory 478, 491, 532
IRAS Point Source Catalogue 532
Irr II galaxies 54
irregular clusters of galaxies 102–103
irregular galaxies 53
island universes 5
ISO infrared space observatory 478
isocurvature cold dark matter 396–399
fluctuations in local equation of state and 397
isophotal angular diameters 223
isothermal baryonic perturbations in the standard Big Bang 357–360
isothermal gas spheres 103–108, 134, 264, 611
projected 105, 106
singular 134
tidal radius of 107
truncated 107
isothermal model of structure formation 18, 357–360, 363–364
‘bottom-up’ picture of galaxy formation 364
‘freezing in’ of perturbations 358, 359
early enrichment of heavy elements 363
early formation of globular clusters and 363
hierarchical clustering and 363
radiation drag, effects of 359, 360
isotropic curved spaces 150–154, 159
radius of curvature of 155
three-dimensional 156, 157
two-dimensional 155, 156
isotropic two-space flat 157

- hyperbolic 157
- spherical 154, 157
- isotropy of the distribution of extragalactic radio sources 42
- isotropy of Universe on a large scale 32
- J0737-3039 (binary pulsar) 193
- Jagellonian field 35
- James Clerk Maxwell Telescope (JCMT) 452, 534, 597
- Jeans' analysis of damped harmonic oscillator 638
- Jeans' criterion in an expanding Universe 16, 319
- Jeans' instability 318, 324, 478
 - growth rate of 324, 358
 - physical nature of 318
- Jeans' instability criterion 16, 378
 - for collisionless gas 377
- Jeans' length 16, 17, 318, 332, 351–353, 379, 428, 429
 - in baryons 352
 - relativistic case 332
- Jeans' mass 17, 18, 351–355, 360, 361, 377
- Jeans' wavelength 318
- Jupiter 4, 5
- K-correction 170, 253, 495, 498, 538
 - in infrared K waveband 538
 - submillimetre 597
 - uncertainties in ultraviolet wavebands due to starbursts 538
- K20 sample of galaxies 542
- K20 Survey 607, 608
 - very red galaxies in 608
- Keck 10-metre telescope 272, 542, 555, 566, 590
- Keck-2 telescope 551, 552
- Kelvin-Helmholtz picture of stellar evolution 251
- Kepler's laws of planetary motion 3
 - third law 4, 67
- King profiles for mass distribution in clusters 107, 111
- Kolmogorov spectrum of turbulence 580
- Kompaneets equation 126
- Lagrangian and comoving coordinate systems, difference between 314
- Lagrangian coordinate system 314, 476
- Λ CDM model of galaxy and structure formation** 22, 59, 435, 440, 462, 463, 466, 472, 483, 486, 487, 530, 532, **613–620**
- problems with 613–614
 - accounting for Faber–Jackson relation and Tully–Fisher relation 614, 620
 - 'downsizing' problem 614
 - excess dwarf galaxy problem 613
 - mass-metallicity correlation 613
 - predicted cusps in central regions of galaxies 613
- Landau damping 376
- Lane–Emden equation 104
- Langmuir waves 317
- Large Electron–Positron collider (LEP) 300, 371
- Large Hadron Collider (LHC) 144, 208, 643
- Large Magellanic Cloud (LMC) 54, 141
 - distance of 248
- large-scale distribution of galaxies 33–44**
- large-scale structure of the Universe 27–48**
- The Large-Scale Structure of the Universe* (Peebles) 363
- Las Campanas redshift survey 41
- last scattering layer 444
- last scattering layer at $z = 1000$ 621
- last scattering surface 33, 333, 357
 - for neutrinos 292
- last scattering surface at the epoch of recombination 631, 632
- last scattering surface for electromagnetic radiation 624
- late-type galaxies 50
- laws of conservation of momentum and energy in relativity 186
- Legendre function
 - associated 431
- Legendre polynomials 433, 455
- Leiden–Berkeley Deep Survey (LBDS) 516, 518
- lens equation 132
- lenticular galaxies 52, 55
- lepton number L_i 301

- Lick counts of galaxies 35, 36
 Lick Observatory 550
light distribution in galaxies 59–63
 in elliptical galaxies 61
 in spiral and lenticular galaxies 61
 in spiral galaxies 68
 putting the light distributions together
 62
 light elements, primordial nucleosynthesis
 of *see* nucleosynthesis, primordial
 lightest supersymmetric particle 643
 limits of observation in cosmology
 624–625
 fundamental limitations 624
 limitations due to cosmic variance 624
 lithium ^7Li
 observed primordial abundance 298,
 299
 local group of galaxies 51
 local supercluster of galaxies 43, 44, 78
 Lockman Hole survey field 525
 LOFAR project (Netherlands) 576
 longitudinal gauge 348
 longitudinal plasma oscillations 317
 Lorentz invariance 184, 196
 form-invariance 184
 Lorentz transformations 185, 187, 207,
 238, 239
 lukewarm intergalactic gas 560–569
 collisional excitation of 562–563
 ‘thermostat’ temperatures of 563
 by shock waves 562
 emissivity of 562, 563
 HI and HeII Ly- α line emission due to
 562
 ionisation state of 563
 diffuse ultraviolet radiation at large
 redshifts and 567–569
 emission and absorption of 564–567
 detectability of redshifted Lyman- α
 emission 564
 photoexcitation and 564
 shock excitation and 564
 proximity effect and 567–569, 572
luminosity function of galaxies 77–84,
 509
luminosity–metallicity relations for
 galaxies 74–76
 luminous infrared galaxies
 evolution of 536
 luminous infrared galaxy N1-015
 spectral energy distribution of 535
 lunar laser ranging 175
 Lyman limit 588, 589, 591
 ‘Lyman valley’ 570
Lyman- α absorption clouds in in-
 tergalactic medium 545, 550,
 552–560
 confinement of 555
 evolution of, with cosmic epoch 556,
 569
 nature of 554–556
 according to large-scale hydrodynamic
 simulations 573
 observed number density distribution of
 554, 555, 566, 600
 power spectrum of forest of 557–560
 properties of 552–554
 column densities of 554
 damped Lyman- α systems 554
 fractional ionisation of 555
 Lyman- α forest 552–554, 556–558,
 566–572, 574
 Lyman-limit systems 553, 554, 556,
 564, 569–571, 590
 masses of 555
 origin of damped Lyman- α systems
 572
 two-point correlation function of 557,
 558
 dark matter perturbations and 559
 SiIII absorption features and 557, 558
 Lyman- α emission of the intergalactic gas
 562
 Lyman- α radiation field, colour temperature
 of 576
 Lyman- α scattering, optical depth for 549
 Lyman- α transition
 oscillator strength for 549
 photo-excitation cross-section for 549
 Lyman-break galaxies 479, 607
 redshift distribution of 590, 592
 Lyman-limit galaxies, decreasing comoving
 density at large redshifts 489
 α Lyrae 5
 M31
 luminosity of 84

- rotation curve of 67
- M49 (NGC 4472) 69, 116
 - velocity dispersion of 70
- M51 (NGC 5194) 52
- M82 54
- M86 116
- M87 (NGC 4486) 52, 55, 69, 116
- Mössbauer effect 178, 189
- Mach's principle 11, 12, 199
- MACHO project 141, 142
- MACHOs 141
 - mean mass of 141
- Magellanic Clouds 7, 54, 141
- Magellanic irregular galaxies 54
- magnetic fields
 - in stars 578
 - in the interstellar and intergalactic medium 578
 - origin of 577–582
 - amplification mechanisms and 578
 - amplification of seed field by turbulence 580
 - dynamo action and 578, 580
 - emf created by Biermann battery 579
 - extragalactic radio sources and 581
 - extragalactic radio sources at large redshifts 582
 - laboratory demonstration of dynamo action 578
 - magnetic reconnection and 578
 - problems of dynamo action on large scales 578
 - seed field created by Biermann battery 579
 - seed fields 579
- power spectrum of magnetic turbulence 580
- predicted power spectrum from magnetic turbulence 580
- role in astrophysics 577
- rotation measure synthesis and 580
- making real galaxies 583–620**
 - abundances of elements in Lyman- α absorption systems 598–604
 - equations of cosmic chemical evolution 604–607
 - old red galaxies 607–610
 - origin of rotation 610–613
- putting it all together – semi-analytic models of galaxy formation 613–620
- star and element formation 583–598
 - background radiation and element formation 584–587
- Hubble Deep and Ultra Deep Fields 590–596
- Lyman-break galaxies 590
- observed global star formation rate 587–590
- submillimetre determinations of cosmic star-formation rate 596–598
- Malmquist bias 246
- Markarian ultraviolet-excess galaxies 597
- mass density of the Universe
 - in stars at the present epoch 84
- mass–luminosity ratio
 - early-type galaxies 138
 - for clusters of galaxies 267
 - for galaxies and clusters 482
 - for Universe as a whole 83, 267
 - of elliptical galaxies 69, 84
 - of spiral galaxies 68, 84
- mass–luminosity relation for stars 499
- mass–metallicity relations for galaxies at large redshifts 76
- mass–energy relation $E = mc^2$ 181
- masses of galaxies 63–70**
- massive galaxies in clusters 617
- massive ultra-weakly interacting particles 643
- matter-dominated Universe 276
- Mattig's formula 219
- MCG catalogue of galaxies 44
- 'meatball' topology 41
- Medium Deep Survey of galaxies (MDS) 542
- Mercury, advance of perihelion of 189
 - radar ranging and 189
- 'merger trees', hierarchical clustering and 615
- mergers of coalescing galaxies 614
- MERLIN long baseline interferometer 266
- Mészáros effect 358–359, 381, 393, 396, 398
- metallicity Z 74, 600, 605, 606
- metric angular diameters 221, 253

- between any two redshifts 228
- metric of isotropic two-space 155
- metric perturbations 368, 374, 392, 436
- metric tensor 155, 186–188
 - components of as gravitational potentials 187
- microlensing, gravitational 132
- Millennium Galaxy Catalogue 62, 63, 83
- Millennium Simulation 486–488, 613–615, 617–619
 - first quasar candidate 619
- Milne empty world model 207, 237
- Minkowski metric 158, 179, 181, 187, 188, 195
 - ‘missing baryon’ problem 547
- Modern Cosmology* (Dodelson) 313, 422
- Monte Carlo Markov chain methods 463
- Monte Carlo methods 506
- Moon, fluorescent X-rays from 524, 525
- morphologies of galaxies 49, 50
- Mount Wilson 100-inch telescope 492
- multipole moment 432, 433

- N galaxies 51
- nebulae
 - cataloguing of 7
 - nature of 6, 7
- ‘negative mass’ in inhomogeneous Universe 233
- negative pressure equation of state 208, 623, 630, 644
 - speed of sound for 638
- neutralinos 373
- neutrino astrophysics 625
- neutrino background temperature 301–303
- neutrino barrier 286, 292
- neutrino chemical potential 301
- neutrino interaction cross-sections 291
- neutrino oscillations 143
- neutrino perturbation
 - damping by free-streaming 376
 - free-streaming damping mass 377, 380, 381
- neutrinos
 - astrophysical limits to masses of 20
 - cosmological limits to masses of 560
 - cosmological limits to number of species of 463
 - cosmological mass density in 463, 465
- decoupling of 367
- equilibrium number density of 143, 301
- free-streaming of 380, 400
- laboratory limits to the masses of 143
- laboratory limits to the number of species of 145
- massive decaying 417
- neutrino background temperature 376
 - their role in primordial nucleosynthesis
- see* nucleosynthesis, primordial
- time-scale for interaction in the early Universe 291
- with finite rest mass 19, 367, 375, 376, 380
- neutrinos, free-streaming of 396
- neutron decay 292, 294
- neutron stars 586
- Newton’s law of gravity 4
- Newtonian gravitational potential 348, 350, 438
- NGC 1300 53, 54
- NGC 2787 55
- NGC 3077 54
- NGC 4486 52
- NGC 4839 114
- NGC 4874 111, 114
- NGC 4889 111, 114
- NGC 5194 52
- NGC 5195 52
- NGC 520 54
- NICMOS infrared camera of Hubble Space Telescope 140
- non-Euclidean geometries 11, 150–152, 173, 492
- non-Gaussian fluctuations 432, 466
 - examples of 432
 - skewness and kurtosis 466
- non-linear collapse of spherical density perturbations 472–477
 - spherical top-hat collapse 473–475
 - maximum scale-factor for 473
 - redshift of collapse of 473
 - turn-around epoch 473
 - violent relaxation and 474
- non-linear development of density fluctuations 407–409
- self-similar solution for 408
- two-point correlation function 407–409

- NORAS catalogue of X-ray clusters of galaxies 116
- normalised impact parameter 132
- nuclear reactions in the Sun 279
- nucleocosmochronology 13, 252
- nucleosynthesis in stars 14
- nucleosynthesis, primordial** 14–16, 140, 289, 289–307, 417
- baryon-symmetric Universes 303–307
- ‘freeze-out’ of abundances in 304, 306
- equilibrium abundances in the early Universe 289–290
- equilibrium energy densities 290
- in the non-relativistic limit 290, 303
- neutron–proton ratio 290
- relativistic statistical mechanics and 289
- evolution of abundances during 293, 294
- light elements, abundances of 295–301
- comparison of theory and observation 299–301
- observations of 296–299
- massive neutrinos and 369
- neutrino background temperature 301–303
- neutrinos, decoupling of 290–292
- ‘freezing out’ of the n/p ratio and 291
- non-standard assumptions concerning 300
- lepton asymmetry 300
- limits to the number of unknown neutrino species 300
- varying gravitational constant 300
- synthesis of the light elements 292–295
- dependence upon photon-baryon ratio 294
- deuterium formation 292, 293
- epoch of nucleosynthesis 292
- helium formation 292, 293
- lithium formation 293, 294
- neutron fraction 292
- nuclear reactions involved in 292
- number counts of galaxies 46
- number counts of submillimetre sources 452
- Nyquist frequency 504, 505
- O04 survey 595
- observable Universe of galaxies 471
- observations in cosmology** 162–171
- age of the Universe** T_0 171
- angular diameter distance 167, 172
- angular diameters** 167
- apparent intensities** 168–170
- for bolometric luminosities and flux densities 169
- K-corrections 170, 223
- cosmological redshift and time dilation** 162–166
- the meaning of redshift in cosmology 164
- distance measure D 167, 172, 218, 243
- independence of Ω_0 at small redshifts 245
- Hubble’s law** 165–167
- luminosity distance 169, 172
- number densities** 170–171, 172
- comoving number density 171
- comoving volume 170
- reciprocity theorem 169
- observations in cosmology for Friedman world models** 215–228
- angular diameter–redshift relations 221–223
- for inhomogeneous Friedman world models 233, 234
- for models with $\Omega_A = 0$ 221
- for models with $\Omega_A \neq 0$ 223
- for partially inhomogeneous Friedman world models 235
- comoving volume within redshift z 226–228
- models with $\Omega_A = 0$ 226
- models with $\Omega_A \neq 0$ 228, 263
- cosmic time–redshift relation 217–218, 280
- age of Universe for flat world models with $\Omega_A \neq 0$ 218
- age of Universe for models with $\Omega_A = 0$ 217
- for flat world models with $\Omega_A \neq 0$ 218
- for models with $\Omega_A = 0$ 217
- for models with $\Omega_A \neq 0$ 218
- deceleration parameter 216
- relation to Ω_0 and Ω_A 216

- distance measures as a function of redshift 218–219
 for Milne's empty world model 219
 for models with $\Omega_A = 0$ 219
 for models with $\Omega_A \neq 0$ 219
 Mattig's formula 219
- flux density–redshift relations 223–226
 for inhomogeneous Friedman world models 235
 for starburst galaxies in the submillimetre waveband 501, 503
 ghost images 223
- Occam's razor 419
- Ohio State University 295
- Olbers' paradox 510
 in an infinite, static, Euclidean Universe 511
- resolution of, in standard world models 511, 512
- old red galaxies 607–610
 constancy of masses with redshift 607
 early formation of stellar populations of 610
 evidence for old stellar populations in 608
 evolving stellar mass density and 607
 massive 607–610
 need for early starbursts 608, 609
 selected in the K waveband 607
 star-forming galaxies at large redshift and 608
 stellar masses as a function of redshift 608
- On the Principles of Geometry* (Lobachevsky) 11, 151
- optical depth for intergalactic HeII absorption 564
- optical jet in M87 52
- The Origin and Evolution of Cosmic Magnetism* (ed. Beck, Brunetti, and Feretti) 577, 580
- origin of the spectrum of primordial perturbations 629–640**
 duration of the inflationary phase 630–631
 necessary number of e-folding times 631
 equation of state 630
- freezing of perturbations on passing through Hubble sphere 634
 shrinking Hubble sphere 631–634
- OVRO Millimetre Array 126, 127, 249
- P(D)* distribution 504–506, 514, 525
 asymptotic slope of 505
 in infrared waveband 507
 in ultraviolet waveband 506
 in X-ray waveband 507
 non-Gaussian statistics and 505
 physical meaning of 505
 shape of 505
- Palomar 200-inch telescope 514, 521
- Palomar 48-inch Schmidt telescope 96
- Palomar 48-inch Telescope Sky Survey 96
- pancakes 20, 363, 400, 402, 476, 477, 480
- parallel transport, or parallel displacement 151–153
- Parkes Selected Region (PSR) sample 517, 518
- Parseval's theorem 388
- particle horizon** 22, 335–340, 342, 344, 346–349, 351–354, 361, 362, 376, 377, 379, 380, 391–393, 415, 429, 430, 436, 441, 443, 444, 626–629, 631
 definition of 336
 radiation-dominated Universe and 337
- particle physics and cosmology 624, 625
- particle–antiparticle annihilation in the early Universe 278, 303
- collision time exceeds expansion age 306
- cross-sections for 304
- epoch of decoupling of particles and antiparticles 305
- equilibrium number densities 304
- Particles, Nuclei and the Universe, Selected Works of Yakov Borisovich Zeldovich, Vol. 2.* (Zeldovich) 381
- past light cone 159, 335, 339–344, 346, 631–633
- Pauli exclusion principle 144
- Pavo cluster of galaxies 42
- peculiar and interacting galaxies 56–59**
- peculiar velocities
 from polarisation measurements of the cosmic microwave background radiation 451

- in the local Universe 268
 of galaxies 201
 of perturbations 315, 453
 Perseus cluster of galaxies 124, 125, 547,
 617
perturbations, evolution of, in the standard cosmological models 311–333
 acoustic oscillation and 361–362
 conservation of angular momentum and 328
 for models with $\Omega_A = 0$ 325
 for models with $\Omega_A \neq 0$ 326
 in terms of conformal time τ 340
 Jeans' instability 317–318
 dispersion relation for, in a static medium 317
 growth rate for, in static medium 318
 Jeans' instability in an expanding Universe 319–327
 Einstein-de Sitter case 319
 empty Milne world model 320
 falling poles 322–324
 general solution 324–327
 linear growth of 319–327, 332, 351,
 354
 necessity of finite initial amplitudes 322, 333
 perturbing the Friedman solutions 321–323, 476
 small perturbation analysis 319–320
 spherical perturbations in standard Friedman models 321
 linear 312
 non-relativistic wave equation for 313–317
 adiabatic perturbations 316
 first-order solutions for 315
 in terms of conformal time 317
 in terms of cosmic time 317
 unperturbed solutions for 315
 peculiar velocities in the expanding Universe 327–331
 decay of in $\Omega_0 = 0$ case 329
 evolution of 329, 330
 growth of in $\Omega_0 = 1$ case 328
 potential motions 327, 328, 406
 primordial turbulence and 328
 rotational motions 328
 relativistic case 331–332
 growth rate in radiation-dominated case 332
 the basic problem 332–333
 what the theorists are trying to do 311–313
 Petrosian r-band luminosity 91
 photon barrier 280
 photon diffusion 355
 coefficients of thermal conduction and shear viscosity 355, 356
 photon-to-baryon number ratio 23, 277,
 622
 physics beyond the standard model 372
 Planck energy scale 209
 Planck era 287, 631, 642–644
 need for quantum theory of gravity 642
 new physics before reaching 643
 Planck mass 209
 Planck mission of ESA 421, 450–452,
 467, 625
 Planck spectral energy distribution
 Rayleigh-Jeans region of 455
 variation with redshift z 272
 Wien region of 278, 279
 fraction of photons in 278
 Planck time 642
 planetary nebula IC418 452
 Pleiades star cluster 5
 Plummer model for elliptical galaxies 108
 Poisson noise 392
 Poisson's equation for gravity 108, 187,
 268, 313
 linearity of 315
 relativistic case 331
 polar coordinates 155
polarisation of the cosmic microwave background radiation 454–463, 625
 anticorrelated TE cross correlation power spectrum of as evidence of adiabatic perturbations 458
 B-modes and 457, 467
 B-modes due to gravitational lensing 457
 BB power spectrum and 457
 EE power spectrum of 456, 457, 459
 from the epoch of reionisation 458–459

- angular scale of strongest polarised signal 458
- from the last scattering layer 455–458
- physics of 454–455
- necessity of quadrupole intensity distribution 455, 458
- polarised galactic radio emission and 456, 457
- primordial gravitational waves and 459–460
- B-modes 459, 460
 - E-modes 459
 - origin in the early Universe 460
 - polarisation modes of 459
 - predicted BB power spectrum of 460
- TE cross correlation power spectrum of 457–459
- TT intensity power spectrum and 456, 457
- weak gravitational lensing and 460–463
- BB-mode polarisation due to lensing of
 - EE-mode polarisation 462, 463
 - distortion matrix 460
 - E-mode polarisation due to 462
- polycyclic aromatic hydrocarbon (PAH) molecules 535
- post-recombination era** 384, 471–489
- non-linear collapse of density perturbations 472–477
 - isotropic top-hat collapse 473–475
 - Zeldovich approximation 475–477
- Press–Schechter mass function 482–489
- development and recapitulation 485–489
 - exposition – elementary theory 482–484
 - role of dissipation 477–482
- POTENT reconstruction procedures 269
- power spectrum of cosmic microwave background radiation 434, 436
- power spectrum of fluctuations 388–392
- relations between different descriptions of 391
- power spectrum of initial fluctuations 17, 390–392, 405, 438
- modifications of 393–401
- power spectrum of temperature fluctuations 432, 433
- for non-Gaussian fluctuations 466
 - precision cosmology 421, 466, 614, 621
- Press–Schechter mass function** 20, 363, 482, 482–489
- ‘peaks-within-peaks’ problem 485
 - critical density contrast for structure formation 483
 - evolution of number density of dark matter haloes with redshift 487, 489
 - hierarchical clustering and 486, 487, 489
- mass function of clusters and 486
- problems with simple derivation 485, 486
- time evolution of 484, 485
- primordial fluctuation problem 23, 25, 472, 623
- Harrison–Zeldovich spectrum and 623
- primordial gravitational waves 440–443
- equation of state of 441
 - on superhorizon scales 441
 - quadrupole nature of 441
 - quantum origin in the early Universe 441
 - tensor to scalar ratio 441
- primordial nucleosynthesis of the light elements *see* nucleosynthesis, primordial
- Principia Mathematica* (Newton) 10
- principle of covariance 184
- principle of equivalence** 173–176, 176, 177, 179–181, 184, 196
- Einstein’s 174, 175, 196
 - local Lorentz invariance (LLI) 175
 - local position invariance (LPI) 175
 - free-fall 174, 179
 - weak 174, 175
- Principles of Physical Cosmology* (Peebles) 313
- probability integral 483
- Probing Galaxies through Quasar Absorption Lines* (eds. Williams, Shu and Ménard) 552
- problem of the values of the cosmological parameters 23
- prograde orbits 57
- projected surface brightness 116
- proper radial distance coordinate 339

- properties of spiral and elliptical galaxies** **70–76**
- proton decay
 - avoidance of 373
 - PSR 1913+16 192–195
 - pulsars and general relativity 192–194
 - emission of gravitational waves 193, 194
 - acceleration of binary pulsar due to 194, 195
 - masses of neutron stars 193, 194
 - QSO Absorption Lines* (ed. Meylan) 552
 - quadrupole component of the temperature power spectrum 434
 - quantised harmonic oscillator 635–637
 - angular frequency of 636
 - carrying out a proper calculation 637
 - energy levels of 635
 - Hermite polynomials and 636
 - Schrödinger's equation for 635
 - wavefunctions for 635
 - zero-point energy of 636
 - zero-point fluctuations of 636
 - quantum theory of gravity 644
 - quasar 0957+561 (double quasar) 249
 - quasar 2345+007 (double quasar) 554
 - Quasar Absorption Line key project 568
 - quasar HE 2347-4342 566, 567
 - quasar HS1700+64 566, 567, 571
 - quasar OQ 172 570
 - ultraviolet spectrum of 550
 - quasar PKS1935–692 564, 571
 - quasar PSS J1443+2724 273
 - quasar Q0302–003 564, 566, 571
 - quasar Q1331+170 272
 - quasar Q1422+2309 553
 - quasar Q2237+0305 139
 - quasar QSO 0013–004 273
 - quasar spectra
 - Lyman- α emission line 519, 520
 - prominent emission lines in 520
 - quasars
 - 3CR sample of radio 508, 509
 - cut-off at large redshifts 487, 488
 - early formation of supermassive black holes in 610
 - low-luminosity 521
 - most luminous 488
 - radio-quiet *see* radio-quiet quasars
 - ratio of black hole to spheroid masses 610, 617
 - unification scheme with radio galaxies 610
 - radiation-dominated universe 14, 276
 - Compton scattering in 281–284
 - dynamics of 271–273
 - including neutrinos 302, 303
 - maintenance of photons and matter at the same temperature by Compton scattering 282
 - time-scale for expansion of 291
 - total energy density of relativistic species 291
 - radio galaxies 51, 479
 - 3CR sample of 508, 509
 - evidence for old stellar populations in 609
 - radio galaxy 0902+34 609
 - radio galaxy LBDS 53W069 610
 - radio galaxy LBDS 53W091 609
 - radio-far-infrared correlation for galaxies 597
 - flattening of radio source counts and 537
 - radio-quiet quasars
 - counts of 521, 522
 - cut-off at large redshifts 519, 524, 569
 - definition of complete samples of 518–521
 - completeness of 521
 - dispersion prism-grating techniques 521
 - multicolour photometric technique 519–520
 - searches for '*i*-band drop-outs' 520–521, 524
 - searches for Lyman- α and CIV emission lines 521
 - searches for variability of 521
 - ultraviolet excess technique 519
 - discovery of 518
 - evolution of, with cosmic epoch 518, 520, 521, 610
 - luminosity function of
 - 'luminosity evolution' of 522
 - evolution of 521, 522

- ram-pressure stripping 544, 613
 Rayleigh–Jeans region of Planck spectrum 455
 Rayleigh–Jeans spectrum 27, 29, 30
The Realm of the Nebulae (Hubble) 50, 492
 reciprocity theorem 229
 reconstruction of local mass distribution 268, 269
 red and blue sequences of galaxies *see* galaxies, red and blue sequences of Red-Sequence Cluster Survey 138
 redshift biases 406–407
 redshift, definition of 45, 162
 redshift–apparent magnitude relation 44
 redshift–magnitude relation for brightest galaxies in clusters
 infrared 544–545
 cosmic conspiracy and 544, 545
 galactic cannibalism and 545
 passive evolution and 544
 reduced deflection angle 130
 Rees–Sciama effect 440
 REFLEX catalogue of X-ray clusters of galaxies 116, 120, 121
 regular clusters of galaxies 102–103
 reionisation of the intergalactic gas 382
 relation between angular and spatial two-point correlation functions 37, 38
 relativistic binary stars 192
relativistic gravity, introduction to 173–198
 non-linearity of 181, 182
 relativistic jets, heating of the interstellar gas by 617
 relativity of simultaneity 238
Relativity: Special, General, and Cosmological (Rindler) 184
revised Hubble sequence for galaxies 50–56
 Riemannian geometries 151, 182, 184
 Riemannian metric 187
 ring galaxies 56, 58
Robertson–Walker metric 149, 150, 158–162, 163, 167, 168, 340, 341
 for an empty Milne Universe 237–239
 for the critical world model 231
 invariant interval ds^2 161
 ROSAT X-ray Observatory 116, 117, 119, 120, 122, 451, 491, 506, 524, 525
 rotation curve of a centrifugally supported disc in isothermal gas sphere 612
rotation curves of spiral galaxies 66–69
 rotation of galaxies, origin of 610–613
 damping of primordial rotational velocities 610
 dissipative contraction within dark matter haloes 611
 problem of specific angular momenta 612
 problems of theories of primordial turbulence 610
 role of tidal stripping 613
 roles of dissipation and tidal stripping 612
 tidal torques 611, 612
 during linear growth of perturbations 611
 slow rotation of the spheroidal components of elliptical and spiral galaxies and 611
 Rutherford scattering 190
 S0 galaxies 52
 Sérsic 159–03 123, 124
 Sérsic index 91
 Sa galaxies 51
Sachs–Wolfe effect 18, 21, 441, 447, 456
 dependence upon angular scale 439
 gravitational redshift and 436, 437
 integrated 452, 456
 physical arguments 436–440
 SAGDP99 survey 595
 Sakharov oscillations 21, 362
 Salpeter initial mass function 500, 588
 Sb galaxies 51
 Sc galaxies 52
 scalar fields 208, 623, 629, 634–635
 density and pressure of 634
 Einstein’s field equations and 635
 fluctuations in 635
 negative pressure equation of state and 634
 not yet detected experimentally 634
 properties of 634–635
 slow-roll parameters 635, 640
 string theory and 634

- theories beyond the standard model of particle physics and 634
- scale factor** $a(t)$ 160, 161, 162, 164, 167, 171, 172
- scale factor-redshift relation** 164, 201, 271
- scaling test for homogeneity of clustering of galaxies 35–37
- Schönberg–Chandrasekhar limit 500
- Schechter luminosity function for galaxies 77, 79, 82, 108, 109, 590, 593, 595
- break absolute magnitude M^* of 78, 81
- break luminosity L^* of 77, 78, 81
- brightest galaxies in clusters 82
- dependence upon galactic environment 79, 81
- evolution with redshift 82
- for low luminosity galaxies 82
- in voids 80, 81
- L^* as a standard candle 80
- turnover luminosity L^* 607
- Schwarzschild metric 183, 187
- coordinate time in 183
- proper time in 183
- Schwarzschild radius r_g 184
- Sco X-1 524
- SCUBA submillimetre bolometer array 534, 597
- Sd galaxies 52
- secular instabilities in rotating stellar discs 616
- self-similar model for cluster formation 118, 119
- semi-analytic models of galaxy formation** 412, 472, 486, 583, 613–620
- acoustic peaks in the large-scale galaxy distribution and 620
- as ‘experimental computational astrophysics’ 615
- dust extinction and 617
- evolution of mass function of galaxies and 620
- formation of supermassive black holes and 617, 618
- in centres of rich clusters 620
- heating of the intergalactic gas in clusters and 617
- mergers of galaxies and 616
- major 616
- minor 616
- morphologies of galaxies and 616
- nuclear starbursts and 616, 617
- objectives of 615
- quasars at large redshifts and 618, 619
- radiative cooling and star formation 615
- spectrophotometric properties of galaxies and 616
- supernova explosions and 616
- the epoch of maximum quasar activity and 620
- ‘trial and error’ approach to 617
- two-point correlation function for galaxies and 617, 618
- for different luminosities and colours 617
- Sérsic index 63
- Sérsic’s law 62
- Seyfert galaxies 51, 516, 521
- counts of 521
- Shane–Wirtanen catalogue of galaxies 100
- Sidereus Nuncius or the Starry Messenger* (Galileo) 5
- σ_8
- definition of 403
- two-point correlation function and 403
- Silk damping 353, 355, 357, 360, 361, 381, 410, 426, 430, 450
- Silk mass 17, 353, 356, 357
- singularity theorems of Penrose and Hawking 644
- Sirius 5
- Sirius B 177
- 6C radio galaxies 255
- Sloan Digital Sky Survey (SDSS) 22, 35, 36, 40–42, 49, 50, 75, 76, 78, 79, 82–84, 87–91, 93, 95, 99–101, 110, 111, 245, 362, 387, 410–412, 414, 465, 491, 520, 522, 524, 552, 557, 559
- power spectrum of galaxies in 412–415
- Small Magellanic Cloud 8
- Smoluchowski’s envelope 105
- Soudan Underground Laboratory 146, 374
- sound horizon 443, 444
- sound horizon at the last scattering layer 427–429
- Space Telescope Imaging Spectrograph 567

- space–time diagram
 for an empty Universe 237
 for the expanding Universe 170
- space–time diagrams for standard world models 339–347**
- critical world model $\Omega_0 = 1, \Omega_A = 0$ 342–344
 distances and times 339–340
 past light cone 340
 reference world model
 $\Omega_0 = 0.3, \Omega_A = 0.7$ 344–347
- space–time metric for isotropic curved spaces 155–158**
- ‘spaghetti’ topology 41
 spatial two-point correlation function 37, 38, 385, 386
 special theory of relativity 183, 184, 186
 spectral energy distribution of galaxies
 evolution of 498–500
 in far infrared and submillimetre
 wavebands 500, 503
 spectrum of primordial perturbations
 spectrum of primordial gravitational waves and 640
 spectrum of primordial perturbations in the scalar field 637–640
 constant noise-power on horizon scale 639
 damping on superhorizon scales 638
 decay of scalar field at end of inflationary era 639
 growth of potential fluctuations in inflationary expansion 638
 applicability on superhorizon scales 638
 as an equation of damped harmonic oscillator 638
 damping on superhorizon scales 638
 growth of vacuum fluctuations in inflationary expansion 637
 comparison with growth of non-relativistic density perturbations 637
 differential equation for 637
 growth of zero point fluctuations 638
 relation to perturbations in post-inflationary relativistic plasma 639
- time-delay formalism for 639
 zero point fluctuations in the ground state 638
- speed of sound as a function of cosmic epoch 285–286, 354, 427, 444
 at constant entropy 285
- speed of sound, relativistic 332, 352
- spherical harmonic functions 431, 433
 addition theorem for 433
- spheroidal component of spiral galaxies 51
- spin parameter λ 611, 612, 616
 as a measure of rotational support of a galaxy 611
- spin temperature of neutral hydrogen 576
- spiral galaxies 50, 51
 rotation curves of 66
 types of 51
- spiral-poor clusters of galaxies 102–103
- spiral-rich clusters of galaxies 102–103
- Spite plateau 298, 299
- Spitzer First Look Survey 533
- Spitzer infrared space observatory 478, 491, 533
- ‘sponge’ topology 41, 42
- Square Kilometre Array (SKA) 576
- stability diagram for adiabatic baryon perturbations 361
- standard cold dark matter model of galaxy formation 403
- star formation in galaxies 472
- star-forming galaxies 452
 at redshifts $z > 3$ 591
 dust extinction and 597
 spectrum of 594
- starburst galaxies 54, 536, 537
 ultraviolet spectra of 587, 588
 rate of formation of heavy elements and 588
- statistical equilibrium 65
- statistical methods into astronomy 5
- statistical weight g 289
- Stefan–Boltzmann law 272
- stellar evolution and element formation 584, 585
 energy generation in the conversion of hydrogen into helium 584, 585
 mean stellar luminosity during main sequence evolution 586

- stellar parallaxes 5
 stellar populations, ages of 91
 structural index, or structural length 105
 sub-dwarf (sdB) stars 519
 Subaru 8-metre telescope 595
 Subaru Deep Surveys 595
 submillimetre background radiation 534
 submillimetre bolometer array (SCUBA)
 452
 submillimetre galaxies
 problems of redshift determinations 597
 redshifts measurements in CO line 479
 substratum 149, 150, 341, 354, 358
Subtle is the Lord . . . (Pais) 184
 Sun, quadrupole moment of 189
 measured by helioseismology 190
Sunyaev–Zeldovich effect in hot
 intracluster gas 95, 125–128, 261
 distance estimates using 128
 fluctuations in the cosmic microwave
 background radiation and 450–451
 in the Rayleigh–Jeans limit 126
 kinematic 451
 spectral shape of distortions 126
 SuZIE experiment and measurement of
 spectral shape of distortions 126
 Sunyaev–Zeldovich marginalisation factor
 463
 superCDMS experiment 146
 superclusters of galaxies 43
 supergalactic plane 44, 269
superhorizon scales 347–350, 367, 379,
 382, 391, 392, 397, 437
 freezing of potential fluctuations on 439
 Supernova Cosmology Program 164–166,
 258, 259
 Supernova Legacy Survey 257, 258, 465
 supernova SN1987A 369
 distance of Large Magellanic Cloud and
 248
 supernovae of Type Ia 165, 166, 252
 ESSENCE project 165
 luminosity–width correlation 164, 165,
 256, 257
 redshift–apparent magnitude relation for
 256–259
 stretch factor 166
 white dwarfs in binary systems and 256,
 257
 supersymmetric particles 373
 suppression factor 450
 SWIRE Legacy sample 536
 ‘swiss-cheese’ topology 41
 symmetry breaking 24
 fluctuations associated with 466
 synchronous gauge 349
 synchrotron radiation 492
 synchrotron radio emission in clusters of
 galaxies 578
 temperature fluctuation on the last scattering
 surface
 adiabatic 364, 365
 temperature of formation of light elements
 279
 temperature of regions of ionised hydrogen
 279
 temperature-scale factor relation in the very
 early Universe 371, 372
 temperatures of the photon and neutrino
 backgrounds 301–303
 tensor perturbations and gravitational waves
 348
 tensor virial theorem 64
*The Inflationary Universe: The Quest for
 a New Theory of Cosmic Origins*
 (Guth) 626
Theoretical Concepts in Physics (Longair)
 173, 184, 314
*Theory and Experiment in Gravitational
 Physics* (Will) 189
**theory of the expanding Universe, history
 of** 10–13
thermal history of the Universe 17, 32,
 271–287
 early epochs 286–287
 epoch of recombination 277–281
 matter and radiation content of the
 Universe 273–277
 radiation-dominated era 271–273,
 281–284
 speed of sound as a function of cosmic
 epoch 285–286
*Third Reference Catalogue of Bright
 Galaxies* (de Vaucouleurs et al) 84
 Thomson optical depth for reionisation
 459

- Thomson scattering 33, 279, 356, 422, 451–454
 conditions for creation of polarised radiation by 454, 455, 458
 cross-section 29, 356
 optical depth of intergalactic gas for 452
3CR quasars 610
 black holes masses of 609
3CR radio galaxies 254–256, 514, 609, 610
 early formation of bulk of stellar population 609
 increase in luminosity with redshift 255
 stellar masses of large redshift 609
3CR radio sources 514, 516, 518
 tidal forces 613
 tidal forces and relativistic gravity 182, 183
 tidal radius 137, 138
 tidal radius of cluster of galaxies 105
 time dilation
 cosmological 163
 test of 164–166
 in a gravitational field 178, 438
 in special relativity 163
 topological defects
 cosmic strings, monopoles and textures 466, 628, 640
 isocurvature perturbations and 466
 phase transitions in the early Universe and 466
 topology of the distribution of galaxies 41, 42
 transfer function 393
 adiabatic cold dark matter 393–396
 adiabatic hot dark matter 394, 396
 isocurvature cold dark matter 394, 396–399
 subsequent evolution of different modified power spectra 399–401
 transfer functions
 for baryons 410, 411
 triaxial velocity distribution in galaxies 69
 triple- α reaction 293, 584
 tritium, half-life of 293
Tully–Fisher relation for spiral galaxies
73–74, 612
 in the infrared waveband 74
 ‘tuning-fork’ diagram 50
 turnaround epoch 408, 409
 2C radio survey 505
 Two Micron All Sky Survey (2MASS) 84, 140
2dF galaxy redshift survey 40–42, 49, 50, 78–83, 87, 88, 93, 245, 266, 269, 362, 387, 403–407, 410–414, 465, 491, 519, 618
 final power spectrum of 412–413
2dF quasar redshift survey 387, 510, 519–522, 524
 two-dimensional isotropic curved geometry 151, 152
 two-photon process 423
 two-point correlation function 432
 angular 433
two-point correlation function for galaxies
22, 34–38, 150, 268, 362, **385–388**, 433
 features of 387–388
 relation to the density contrast 386
 relation to the power spectrum of density fluctuations 389
Type Ia supernovae 13, 21
 types of topology of the distribution of galaxies 41
 UGC catalogue of galaxies 44
 UHURU X-ray Observatory 114, 524
 UK Schmidt telescope 33, 519
 ultraluminous infrared galaxies (ULIRGs) 479, 503, 532
 spectra of 532
 ultrametal-poor star CS 22892-052
 thrium abundance in 252
 ultraviolet astronomy
 unit used in 562
 ultraviolet opacity of the intergalactic medium 569
 V/V_{\max} or luminosity-volume test
 507–510
 banded 509
 for radio galaxies 514
 for radio quasars 514
 for radio-quiet quasars 518
 space distribution of galaxies, quasars
 active galaxies 507–510

- vacuum energy density** 207, 208–211, 625
 estimate from quantum field theory 209
 problem of the magnitude of 209, 623
 values of the cosmological parameters
 problems of 623
 vector perturbations and vortex motions 348
- velocity dispersions of elliptical galaxies** 69–70
 velocity of Solar System through the Cosmic Microwave Background Radiation 30
 velocity–distance relation for galaxies 44–46, 48
 in an expanding universe 46, 47
- very early Universe** 621–644
 anthropic cosmological principle 625–626
 baryogenesis 641–642
 big problems of cosmology 621–624
 baryon-asymmetry problem 622
 flatness problem 622
 horizon problem 621
 primordial fluctuation problem 623
 values of the cosmological parameters 623
 way ahead 624
- inflationary Universe – historical background 22–25, 626–629
 limits of observation 624–625
 origin of the spectrum of primordial perturbations 629–640
 duration of the inflationary phase 630–631
 equation of state 630
 fluctuations in the scalar field and 637–640
 quantised harmonic oscillator 635–637
 scalar fields 634–635
 shrinking Hubble sphere 631–634
 Planck era 642–644
- Very Large Array (VLA) 140, 266, 597
 Very Long Baseline Array (VLBA) 266
Viking spacecraft 191, 192
 violent relaxation 399
 Virgo Cluster Catalogue 117
 Virgo cluster of galaxies 43, 52, 102, 110, 116, 117, 246, 248
 Virgo consortium 418, 615
 Virgo supercluster 268
 virial of Clausius 64
virial theorem 63–66, 103, 110, 119, 243, 375, 399, 408, 409, 474, 475
 applied to clusters of galaxies 66
 problems of applying 66
 Vishniac effect 453
 visibility function 423, 424, 426
 visible matter in the Universe
 integrated luminosity of 83
 mean mass–luminosity ratio of 83
 VLBI measurements of deflection of radio waves by the Sun 190, 191
 voids in the distribution of galaxies 41, 381, 439, 537
 Voigt profile 554
 VSA experiment 435
- walls and voids in the distribution of galaxies** 38–44
 weak gravitational lensing 136
 Weyl's postulate 149, 150, 158, 199
 white dwarfs 519, 586
 cooling times for 251
 gravitational redshift and 189
- Wide Field Planetary Camera 2 591, 592
 Wilkinson Microwave Anisotropy Probe (WMAP) 21, 32, 33, 231, 300, 421, 429, 434–437, 440, 442, 444, 450, 451, 456–458, 460, 463, 465–467, 547, 559, 561, 615, 620, 624, 625
 point sources detected in the WMAP survey 451
 nature of 452
- William Herschel's model of the Galaxy 5
 WIMPs
 abundance of 289
 as dark matter particles 370–374
 astrophysical limits to the masses of 144
 candidates for 143
 decoupling from thermal equilibrium 370
 in very early Universe 371
 epoch of decoupling of 372
 equilibrium abundances of 370

- 'freezing out' of abundances of 370, 371
- interaction cross-section for 371–373
 - experimental limits for 374
- laboratory detection of 145
- laboratory limits to the masses of 145
- suppression mechanisms for 145, 370–372, 375
- world lines 199, 237
 - of galaxies 342, 345
- Wouthuysen-Field effect 576
- W^\pm and Z^0 bosons 145, 208
- X-ray background emission 524
 - at hard X-ray energies
 - nature of sources contributing to 529
 - at soft X-ray energies
 - nature of sources contributing to 527, 529
 - a cosmic conspiracy and 561
 - contributions of different classes of source to 528
 - spectrum of 526
- X-ray clusters of galaxies
 - number counts as a test of cosmological models 532
- tests of cosmological models and 529–532
- X-ray emission of intracluster gas 95
- X-ray luminosity–mass relation for clusters of galaxies 119, 120
- X-ray luminosity–velocity dispersion relation for clusters of galaxies 120
- X-ray sources
 - Comptonisation and 529
 - evolution of luminosity function of, with cosmic epoch 527
 - populations at soft and hard X-ray energies 526, 528
 - strongly absorbed 529
 - template spectra for strongly absorbed sources 529
- XMM-Newton X-ray Observatory 114, 116–118, 123, 124, 491, 525
- Z^0 boson, energy width of 300
- Zeldovich solution for non-linear collapse under gravity 20, 363
 - formation of caustics 477
- zinc abundance 601, 602
- Zwicky catalogue of galaxies 35



ASTRONOMY AND ASTROPHYSICS LIBRARY

Series Editors:

G. Börner · A. Burkert · W. B. Burton · M. A. Dopita
A. Eckart · T. Encrenaz · E. K. Grebel · B. Leibundgut
J. Lequeux · A. Maeder · V. Trimble

The Stars By E. L. Schatzman and F. Praderie

Modern Astrometry 2nd Edition

By J. Kovalevsky

The Physics and Dynamics of Planetary Nebulae By G. A. Gurzadyan

Galaxies and Cosmology By F. Combes,
P. Boissé, A. Mazure and A. Blanchard

Observational Astrophysics 2nd Edition
By P. Léna, F. Lebrun and F. Mignard

Physics of Planetary Rings Celestial Mechanics of Continuous Media
By A. M. Fridman and N. N. Gorkavyi

Tools of Radio Astronomy 4th Edition,
Corr. 2nd printing
By K. Rohlfs and T. L. Wilson

Tools of Radio Astronomy Problems and Solutions 1st Edition, Corr. 2nd printing
By T. L. Wilson and S. Hüttemeister

Astrophysical Formulae 3rd Edition
(2 volumes)

Volume I: Radiation, Gas Processes and High Energy Astrophysics
Volume II: Space, Time, Matter and Cosmology
By K. R. Lang

Galaxy Formation 2nd Edition

By M. S. Longair

Astrophysical Concepts 4th Edition
By M. Harwit

Astrometry of Fundamental Catalogues
The Evolution from Optical to Radio Reference Frames

By H. G. Walter and O. J. Sovers

Compact Stars. Nuclear Physics, Particle Physics and General Relativity 2nd Edition
By N. K. Glendenning

The Sun from Space By K. R. Lang

Stellar Physics (2 volumes)

Volume 1: Fundamental Concepts and Stellar Equilibrium
By G. S. Bisnovatyi-Kogan

Stellar Physics (2 volumes)

Volume 2: Stellar Evolution and Stability
By G. S. Bisnovatyi-Kogan

Theory of Orbits (2 volumes)

Volume 1: Integrable Systems and Non-perturbative Methods
Volume 2: Perturbative and Geometrical Methods
By D. Boccaletti and G. Pucacco

Black Hole Gravitohydromagnetics

By B. Punsly

Stellar Structure and Evolution

By R. Kippenhahn and A. Weigert

Gravitational Lenses By P. Schneider,
J. Ehlers and E. E. Falco

Reflecting Telescope Optics (2 volumes)

Volume I: Basic Design Theory and its Historical Development. 2nd Edition
Volume II: Manufacture, Testing, Alignment, Modern Techniques
By R. N. Wilson

Interplanetary Dust

By E. Grün, B. Å. S. Gustafson, S. Dermott and H. Fechtig (Eds.)

The Universe in Gamma Rays

By V. Schönfelder

Astrophysics. A New Approach 2nd Edition

By W. Kundt

Cosmic Ray Astrophysics

By R. Schlickeiser

Astrophysics of the Diffuse Universe

By M. A. Dopita and R. S. Sutherland

The Sun An Introduction. 2nd Edition

By M. Stix

Order and Chaos in Dynamical Astronomy

By G. J. Contopoulos

Astronomical Image and Data Analysis

2nd Edition By J.-L. Starck and F. Murtagh

The Early Universe Facts and Fiction

4th Edition By G. Börner



ASTRONOMY AND ASTROPHYSICS LIBRARY

Series Editors:

G. Börner · A. Burkert · W. B. Burton · M. A. Dopita
A. Eckart · T. Encrenaz · E. K. Grebel · B. Leibundgut
J. Lequeux · A. Maeder · V. Trimble

The Design and Construction of Large Optical Telescopes By P. Y. Bely

The Solar System 4th Edition
By T. Encrenaz, J.-P. Bibring, M. Blanc,
M. A. Barucci, F. Roques, Ph. Zarka

General Relativity, Astrophysics, and Cosmology By A. K. Raychaudhuri,
S. Banerji, and A. Banerjee

Stellar Interiors Physical Principles,
Structure, and Evolution 2nd Edition
By C. J. Hansen, S. D. Kawaler, and V. Trimble

Asymptotic Giant Branch Stars
By H. J. Habing and H. Olofsson

The Interstellar Medium
By J. Lequeux

Methods of Celestial Mechanics (2 volumes)
Volume I: Physical, Mathematical, and
Numerical Principles
Volume II: Application to Planetary System,
Geodynamics and Satellite Geodesy
By G. Beutler

Solar-Type Activity in Main-Sequence Stars
By R. E. Gershberg

Relativistic Astrophysics and Cosmology
A Primer By P. Hoang

Magneto-Fluid Dynamics
Fundamentals and Case Studies
By P. Lorrain

Compact Objects in Astrophysics
White Dwarfs, Neutron Stars and Black Holes
By Max Camenzind

Special and General Relativity
With Applications to White Dwarfs, Neutron
Stars and Black Holes
By Norman K. Glendenning



ASTRONOMY AND ASTROPHYSICS LIBRARY

Series Editors:

- G. Börner, Garching, Germany
A. Burkert, München, Germany
W. B. Burton, Charlottesville, VA, USA and
Leiden, The Netherlands
M. A. Dopita, Canberra, Australia
A. Eckart, Köln, Germany
T. Encrenaz, Meudon, France
E. K. Grebel, Heidelberg, Germany
B. Leibundgut, Garching, Germany
J. Lequeux, Paris, France
A. Maeder, Sauverny, Switzerland
V. Trimble, College Park, MD, and Irvine, CA, USA

Malcolm S. Longair

Galaxy Formation

Second Edition

With 202 Figures and 20 Tables



Springer

Malcolm S. Longair

Jacksonian Professor of Natural Philosophy
Cavendish Laboratory
J. J. Thomson Avenue
Cambridge CH3 0HE
England, UK
e-mail: msl1000@cam.ac.uk

Cover image: Galaxies NGC 2207 and IC 2163. Credit: NASA and The Hubble Heritage Team (STScI); Hubble Space Telescope WFPC2; STScI-PRC99-41; Source: <http://heritage.stsci.edu/1999/41/index.html>

Library of Congress Control Number: 2007935444

ISSN 0941-7834

ISBN 978-3-540-73477-2 Springer Berlin Heidelberg New York

This work is subject to copyright. All rights are reserved, whether the whole or part of the material is concerned, specifically the rights of translation, reprinting, reuse of illustrations, recitation, broadcasting, reproduction on microfilm or in any other way, and storage in data banks. Duplication of this publication or parts thereof is permitted only under the provisions of the German Copyright Law of September 9, 1965, in its current version, and permission for use must always be obtained from Springer. Violations are liable to prosecution under the German Copyright Law.

Springer is a part of Springer Science+Business Media

springer.com

© Springer-Verlag Berlin Heidelberg 1998, 2008

The use of general descriptive names, registered names, trademarks, etc. in this publication does not imply, even in the absence of a specific statement, that such names are exempt from the relevant protective laws and regulations and therefore free for general use.

Typesetting and production: LE-TeX Jelonek, Schmidt & Vöckler GbR, Leipzig, Germany
Cover design: eStudio Calamar S.L., F. Steinen-Broo, Girona, Spain

SPIN: 11394105 55/3180/YL - 5 4 3 2 1 0 Printed on acid-free paper

For Deborah, Mark and Sarah

Preface

This is the second edition of my book *Galaxy Formation*. Many people liked the first edition which appeared in 1998, just before the explosion of magnificent new data which have completely changed the face of astrophysical cosmology. Many of the agonies which had to be gone through in the first edition have disappeared and, to many people's amazement, including mine, there is now a *concordance model* for cosmology, the cosmologist's equivalent of the particle physicist's *standard model*. Just like the standard model, however, the concordance model creates as many problems as it solves. This is not a cause for concern, but rather one for celebration because we are now able to ask much better and deeper questions than in the past. These questions indicate clearly the need for physics and astrophysics 'Beyond the Concordance Model'.

The object of this new edition is to bring this amazing story up-to-date, very much in the spirit of the first edition. To recapitulate some of the points made in the previous preface about the origin of the book, I was asked by Springer-Verlag to expand the set of lecture notes that I prepared in 1988 for the First Astrophysics School organised by the European Astrophysics Doctoral Network into a full-length book. The set of notes was entitled *Galaxy Formation* and was published as a chapter of the volume *Evolution of Galaxies: Astronomical Observations* (eds. I. Appenzeller, H.J. Habing and P. Lena, pages 1 to 93, Springer-Verlag Berlin, Heidelberg, 1989). In that chapter, I attempted to bridge the gap between elementary cosmology and the technical papers appearing in the literature which can seem quite daunting on first encounter. The objective was to present the physical ideas and key results as clearly as possible as an introduction and guide to the technical literature.

In 1993, more lecture notes on *The Physics of Background Radiation* were prepared for the 23rd Advanced Course of the Swiss Society of Astrophysics and Astronomy, the topic being *The Deep Universe* (A.R. Sandage, R.G. Kron and M.S. Longair, Springer-Verlag Berlin, Heidelberg, 1995). Then, also in 1993, I completed a history of twentieth century astrophysics and cosmology, which was published as Chap. 23 of a three-volume work entitled *Twentieth Century Physics* (eds. L.M. Brown, A. Pais and A.B. Pippard, IOP Publications, AIP Press Bristol, and New York 1995). A much enlarged full-length book on this topic entitled *The Cosmic Century: A History of Astrophysics and Cosmology* was published by Cambridge University Press in 2006. That book brought the story of the origin of

galaxies and the large-scale structure of the Universe up-to-date as of October 2005 and it has been further updated and expanded in the present book. Just as in the first edition, the present volume is much more than a recycled and concatenated version of previously published works. I have rewritten and rethought the original versions, expanded some parts, brought everything up-to-date and included new material.

I often find that I understand things best, and present them most clearly, when I have to prepare them for students, at either the undergraduate or the post-graduate level, and so I have adopted the same form of presentation here. I have intentionally presented the material in an informal, pedagogical manner, and attempted to avoid getting bogged down in formalities and technicalities. If the material becomes too difficult, I simply summarise the key points, give some appropriate references and pass on. My approach is to reduce the problems to their simplest form and rationalise from these examples the results of more complete analyses. Wherever it is feasible without excessive effort, we will attempt to derive exact results. The level of presentation is intended to be appropriate for a final-year undergraduate or first-year post-graduate course of lectures. In other words, it is assumed that the reader has a good grasp of basic physics but does not necessarily have the appropriate background in astronomy, astrophysics or cosmology. My aim has been to write a user-friendly book, taking particular care to expound carefully areas where I have found students have difficulty.

When I wrote the original set of lecture notes on galaxy formation, my objective was to tell the story of modern astrophysical cosmology from the perspective of one of its most important and fundamental problems of cosmology – how did the galaxies come about? I enjoy this approach to the exposition of modern cosmology because, to do the problem justice, it is essential to introduce the whole of what I call *classical cosmology*, as the framework for the discussion. This approach has, for me, the great advantage of concentrating upon a crucial problem of astrophysical cosmology rather than regarding the objective of cosmology as being simply the delineation of a preferred cosmological model, however interesting that is in its own right. As we will show, the origin of galaxies and larger-scale structures in the Universe is one of the great cosmological problems and has provided us with unique and direct information about the physics of the very early Universe.

This new understanding brings with it the question of whether or not the old structure of the book is really appropriate – do we really need to grind through all the old story in order to understand the problems raised by the concordance model? My decision has been to maintain much of the original structure of the book, largely because the approach was very strongly physics-motivated and the old story reveals much of the essential physics of the concordance model.

One final warning is in order. I make no claim that this presentation is complete, unbiased or objective. You should regard the book as my own impressions and opinions of what I consider to be the important issues of modern astrophysical cosmology. Others would tell the story in a completely different way and put

emphasis upon different parts of what is unquestionably a multi-dimensional story. I will endeavour to include as wide a spectrum of ideas and opinions as possible, but the text will inevitably be incomplete. I do not worry about this – it should encourage you to read as widely as possible in order to neutralise my prejudices and biases.

Good Luck!

Venice and Cambridge,
July 2007

Malcolm Longair

Acknowledgements

Many people have contributed directly, or indirectly, to my understanding of the contents of this book. Perhaps the most important influence has been the late Peter Scheuer, who first introduced me to the physics of astrophysical cosmology. His approach and methods have very strongly influenced the way I have understood and taught this material over the years. I am very grateful to Immo Appenzeller, Harm Habing and Pierre Lena for the opportunity to give the lecture course in Les Houches in 1988. In preparing that set of lecture notes, I greatly benefitted from the advice of John Peacock and Alan Heavens who read parts of the typescript of the first edition and offered very helpful comments. John Peacock very kindly allowed me to use part of his lecture notes in preparing some of the material for the original chapter. John has now written up his notes in his book *Cosmological Physics* (Cambridge University Press, 2000). In my view, John's book is a brilliant achievement and I urge all interested readers to become familiar with his deep insights. Some of the text of the present book is based upon joint work with Rashid Sunyaev, which dates from the period 1968 to 1980. I fully acknowledge Rashid's contributions to clarifying my own understanding.

The invitation to deliver the 1993 course of lectures on the background radiation, as part of the 23rd Course of the Swiss Society of Astrophysics and Astronomy, came from Gustav Tammann, Bruno Binggeli and Hermann Buser and I am grateful for their kindness and hospitality at Les Diablerets. My history of twentieth century astrophysics and cosmology was commissioned by Brian Pippard on behalf of the editors of *Twentieth Century Physics* and I am grateful to him for his perceptive comments on that article.

I am particularly grateful to Bob Williams and his colleagues at the Space Telescope Science Institute at Baltimore, where I was a Visiting Fellow from September to December 1997. Without that sabbatical term at the Institute, the completion of the first edition would have been impossible. Special thanks are due to the staff, graduate students and research fellows at the Institute and at Johns Hopkins University, who kindly acted as guinea pigs on whom I 'battle-tested' portions of the book. Many of the research workers at the Institute gave generously of their time in discussing many of the topics in the book; the discussions with Ron Allen, Michael Fall, Harry Ferguson, Mario Livio, Duccio Macchetto and Piero Madau were especially helpful. The writing was enormously aided by access to the excellent library facilities at the Institute. Martin Harwit kindly read the first edition of the book very carefully and made a number of helpful suggestions.

Since the first edition was published, many colleagues have pointed out minor errors and suggested further topics for discussion. The preparation of the present edition began in December 2005, at the beginning of a two-year period of sabbatical leave kindly granted by the University of Cambridge. So much had changed in the matter of just a few years that essentially everything had to be rewritten in the light of this new understanding.

From February to May 2006, I was Adjunct Professor of Astronomy at the Astronomy Department of the University of Massachusetts at Amherst. I am most grateful to Ronald Snell and his colleagues for their warm welcome and the many helpful discussions we had about galaxies. Martin Weinberg, Neal Katz and Hou-Jun Mo were very stimulating colleagues. A special thank you goes to Dan McIntosh who introduced me to the red and blue sequences of galaxies and showed how our perception of what galaxies are has changed.

From October to December 2006, I was Visiting Professor at the Max Planck Institute for Astrophysics at Garching at the invitation of Rashid Sunyaev. The discussions with Rashid, Simon White and their colleagues were very helpful indeed in sharpening my understanding of many of the issues of astrophysical cosmology. I was back in Garching from February to April 2007 at the invitation of Catherine Cesarsky as a Visiting Scientist at the European Southern Observatory. This also proved to be a very stimulating visit. The wealth of expertise at ESO and the nearby Institutes made Garching a ideal haven in which to complete much of the final chapters of the new edition. I am most grateful to Bruno Leibundgut and all the staff members, visitors, post-docs and graduate students on whom I tried out some of the new sections of the book. The very final sections of the book were completed while I was a guest at the Osservatorio Astrofisico di Arcetri in Florence. I am most grateful to Francesco Palla and his colleagues for their kindness and hospitality.

Four colleagues are worthy of special thanks. Paul Schechter used the first edition of the book as a text for his courses on cosmology and kindly set up a web-site with corrections to it. He also made helpful suggestions for the present edition. Megan Donahue also used the first edition as a class text and provided a very helpful list of corrections and suggested improvements. She then ‘battle-tested’ Parts 2 and 3 of the new edition on her students and made helpful comments. I am most grateful to Megan and her students for this invaluable help which will undoubtedly have improved the book. Luigi Guzzo kindly read a number of sections of the book very careful and provided helpful suggestions and corrections. Peter Schneider reviewed the draft text at the invitation of Springer-Verlag and suggested a number of very helpful improvements.

Finally, the book is dedicated to my family, Deborah, Mark and Sarah, whose constant love, support and patience have made it possible.

Contents

Part I Preliminaries

1	A Brief History of Cosmology and Galaxy Formation	3
1.1	Pre-History	3
1.2	The Galaxies and the Structure of our Galaxy	5
1.3	The Theory of the Expanding Universe	10
1.4	The Big Bang	14
1.5	Galaxy and Structure Formation	16
1.6	Hot and Cold Dark Matter	19
1.7	The Very Early Universe	22
2	The Large-Scale Structure of the Universe	27
2.1	The Spectrum and Isotropy of the Cosmic Microwave Background Radiation	27
2.1.1	The Spectrum of the Cosmic Microwave Background Radiation	28
2.1.2	The Isotropy of the Cosmic Microwave Background Radiation	29
2.2	The Large-Scale Distribution of Galaxies	33
2.2.1	Two-Point Correlation Functions	34
2.2.2	Walls and Voids in the Distribution of Galaxies on Large Scales	38
2.3	Hubble's Law and the Expansion of the Universe	44
2.4	Conclusion	48
3	Galaxies	49
3.1	Introduction	49
3.2	The Revised Hubble Sequence for Galaxies	50
3.3	Peculiar and Interacting Galaxies	56
3.4	The Light Distribution in Galaxies	59
3.4.1	Elliptical Galaxies	61
3.4.2	Spiral and Lenticular Galaxies	61
3.4.3	Putting the Light Distributions Together	62
3.5	The Masses of Galaxies	63

3.5.1	The Virial Theorem for Clusters of Stars, Galaxies and Clusters of Galaxies	63
3.5.2	The Rotation Curves of Spiral Galaxies	66
3.5.3	The Velocity Dispersions of Elliptical Galaxies	69
3.6	The Properties of Spiral and Elliptical Galaxies.....	70
3.6.1	The Faber–Jackson Relation and the Fundamental Plane ...	70
3.6.2	Ellipticals Galaxies as Triaxial Systems.....	71
3.6.3	The Tully–Fisher Relation for Spiral Galaxies	73
3.6.4	Luminosity–Metallicity Relations.....	74
3.7	The Luminosity Function of Galaxies	77
3.7.1	Aspects of the Luminosity Function of Galaxies	79
3.7.2	The Integrated Luminosity and the Mean Mass-to-Luminosity Ratio for Visible Matter in the Universe	83
3.8	The Properties of Galaxies: Correlations Along the Hubble Sequence	84
3.9	The Red and Blue Sequences	88
3.9.1	Colour Versus Absolute Magnitude	89
3.9.2	Sérsic Index and Colour	91
3.9.3	Mean Stellar Age and Concentration Index C	91
3.9.4	The Effect of the Galaxy Environment	92
3.9.5	The New Perspective	93
3.10	Concluding Remark.....	94
4	Clusters of Galaxies	95
4.1	The Large-Scale Distribution of Clusters of Galaxies	95
4.1.1	The Abell Catalogues of Rich Clusters of Galaxies	96
4.1.2	Comparison with Clusters Selected from the Sloan Digital Sky Survey	98
4.1.3	Abell Clusters and the Large-Scale Distribution of Galaxies	99
4.2	The Distribution of Galaxies in Clusters of Galaxies.....	101
4.2.1	The Galaxy Content and Spatial Distribution of Galaxies in Clusters	101
4.2.2	Clusters of Galaxies and Isothermal Gas Spheres	103
4.2.3	The Luminosity Function for Cluster Galaxies	108
4.2.4	Summary of the Properties of Rich Clusters of Galaxies ...	109
4.3	Dynamical Estimates of the Masses of Clusters of Galaxies	110
4.4	X-Ray Observations of Hot Gas in Clusters of Galaxies	114
4.5	The Sunyaev–Zeldovich Effect in Hot Intracluster Gas	125
4.6	Gravitational Lensing by Galaxies and Clusters of Galaxies	128
4.6.1	Basic Theory of Gravitational Deflections	128
4.6.2	Magnification of Images by Gravitational Lensing	130
4.6.3	Extended Deflectors	133
4.6.4	Gravitational Lensing and the Astrophysics of Galaxies ...	136
4.7	Forms of Dark Matter	139

4.7.1	Baryonic Dark Matter	139
4.7.2	Non-Baryonic Dark Matter	142
4.7.3	Astrophysical and Experimental Limits	144

Part II The Basic Framework

5	The Theoretical Framework	149
5.1	The Cosmological Principle	149
5.2	Isotropic Curved Spaces	150
5.3	The Space–Time Metric for Isotropic Curved Spaces	155
5.4	The Robertson–Walker Metric	158
5.5	Observations in Cosmology	162
5.5.1	The Cosmological Redshift	162
5.5.2	Hubble’s Law	165
5.5.3	Angular Diameters	167
5.5.4	Apparent Intensities	168
5.5.5	Number Densities	170
5.5.6	The Age of the Universe	171
5.6	Summary	171
6	An Introduction to Relativistic Gravity	173
6.1	The Principle of Equivalence	173
6.2	The Gravitational Redshift	176
6.3	The Bending of Light Rays	179
6.4	Further Complications	181
6.5	The Route to General Relativity	184
6.5.1	Four-Tensors in Relativity	184
6.5.2	What Einstein Did	187
6.6	Experimental and Observational Tests of General Relativity	189
6.6.1	The Four Tests of General Relativity	189
6.6.2	Pulsars and General Relativity	192
6.6.3	Parameterised Post-Newtonian Models	195
6.6.4	Variation of the Gravitational Constant with Cosmic Epoch	197
6.7	Summary	198
7	The Friedman World Models	199
7.1	Einstein’s Field Equations	199
7.2	The Standard Friedman World Models with $\Lambda = 0$	202
7.2.1	The Newtonian Analogue of the Friedman World Models ..	202
7.2.2	The Critical Density and the Density Parameter	204
7.2.3	The Dynamics of the Friedman Models with $\Lambda = 0$..	205
7.3	Friedman Models with Non-Zero Cosmological Constant	207
7.3.1	The Cosmological Constant and the Vacuum Energy Density	208

7.3.2	Varying the Equation of State of the Vacuum Energy	210
7.3.3	The Dynamics of World Models with $\Lambda \neq 0$: General Considerations	211
7.4	Observations in Cosmology	215
7.4.1	The Deceleration Parameter	216
7.4.2	The Cosmic Time–Redshift Relation	217
7.4.3	Distance Measures as a Function of Redshift	218
7.4.4	Angular Diameter–Redshift Relations	221
7.4.5	Flux Density–Redshift Relations	223
7.4.6	The Comoving Volume Within Redshift z	226
7.5	Angular Diameter Distances Between Any Two Redshifts	228
7.6	The Flatness Problem	230
7.7	Inhomogeneous World Models	231
A7	The Robertson–Walker Metric for an Empty Universe	237
8	The Determination of Cosmological Parameters	241
8.1	The Cosmological Parameters	241
8.2	Testing the Friedman Models	242
8.3	Hubble’s Constant H_0	246
8.4	The Age of the Universe T_0	250
8.5	The Deceleration Parameter q_0	252
8.5.1	The Redshift–Magnitude Relation for the Brightest Galaxies in Clusters	252
8.5.2	The Redshift–Magnitude Relation for Radio Galaxies	254
8.5.3	The Redshift–Magnitude Relation for Type 1a Supernovae .	256
8.5.4	The Number Counts of Galaxies	259
8.5.5	The Angular Diameter–Redshift Test	261
8.6	Ω_A and the Statistics of Gravitational Lenses	263
8.7	The Density Parameter Ω_0	267
8.8	Summary	270
9	The Thermal History of the Universe	271
9.1	Radiation-Dominated Universes	271
9.2	The Matter and Radiation Content of the Universe	273
9.3	The Epoch of Recombination	277
9.4	The Radiation-Dominated Era	281
9.5	The Speed of Sound as a Function of Cosmic Epoch	285
9.6	Early Epochs	286
10	Nucleosynthesis in the Early Universe	289
10.1	Equilibrium Abundances in the Early Universe	289
10.2	The Decoupling of Neutrinos and the Neutrino Barrier	290
10.3	The Synthesis of the Light Elements	292
10.4	The Abundances of the Light Elements	295

10.4.1	Determinations of the Observed Abundances of the Light Elements	296
10.4.2	Comparison of Theory and Observations	299
10.5	The Neutrino Background Temperature and the Value of χ	301
10.6	Baryon-Symmetric Universes	303

Part III The Development of Primordial Fluctuations Under Gravity

11	The Evolution of Perturbations in the Standard Big Bang	311
11.1	What the Theorists Are Trying to Do	311
11.1.1	Why this Programme Is Feasible	312
11.1.2	A Warning	312
11.2	The Non-Relativistic Wave Equation for the Growth of Small Perturbations in the Expanding Universe	313
11.3	The Jeans' Instability	317
11.4	The Jeans' Instability in an Expanding Medium	319
11.4.1	Small Perturbation Analysis	319
11.4.2	Perturbing the Friedman Solutions	321
11.4.3	Falling Poles	322
11.4.4	The General Solution	324
11.5	The Evolution of Peculiar Velocities in the Expanding Universe	327
11.6	The Relativistic Case	331
11.7	The Basic Problem	332
12	More Tools and Problems	335
12.1	Horizons and the Horizon Problem	335
12.2	Pedagogical Interlude – Space–Time Diagrams for the Standard World Models	339
12.2.1	Distance and Times	339
12.2.2	The Past Light Cone	340
12.2.3	The Critical World Model $\Omega_0 = 1, \Omega_A = 0$	342
12.2.4	The Reference World Model $\Omega_0 = 0.3, \Omega_A = 0.7$	344
12.3	Superhorizon Scales	347
12.4	The Adiabatic Baryonic Fluctuations in the Standard Big Bang	350
12.4.1	The Radiation-Dominated Era	352
12.4.2	The Matter-Dominated Era	353
12.5	Dissipation Processes in the Pre-Recombination Era	355
12.6	Isothermal Perturbations	357
12.7	Baryonic Theories of Galaxy Formation	360
12.7.1	The Adiabatic Scenario	361
12.7.2	The Isothermal Scenario	363
12.8	What Went Wrong?	364

13 Dark Matter and Galaxy Formation	367
13.1 Introduction	367
13.2 Forms of Non-Baryonic Dark Matter	369
13.3 WIMPs as Dark Matter Particles	370
13.4 Metric Perturbations and Hot and Cold Dark Matter	374
13.5 Free Streaming and the Damping of Hot Dark Matter Perturbations	375
13.6 Instabilities in the Presence of Dark Matter	377
13.7 The Evolution of Hot and Cold Dark Matter Perturbations	380
13.7.1 Hot Dark Matter Scenario	380
13.7.2 Cold Dark Matter Scenario	381
13.8 Conclusion	384
14 Correlation Functions and the Spectrum of the Initial Fluctuations	385
14.1 The Two-Point Correlation Function for Galaxies	385
14.2 The Perturbation Spectrum	388
14.2.1 The Relation Between $\xi(r)$ and the Power Spectrum of the Fluctuations	388
14.2.2 The Initial Power Spectrum	390
14.2.3 The Harrison–Zeldovich Power Spectrum	391
14.3 Evolution of the Initial Perturbation Spectrum – Transfer Functions	393
14.3.1 Adiabatic Cold Dark Matter	393
14.3.2 Adiabatic Hot Dark Matter	396
14.3.3 Isocurvature Cold Dark Matter	396
14.3.4 The Subsequent Evolution	399
14.4 Biasing	401
14.5 Reconstructing the Processed Initial Power Spectrum	405
14.5.1 Redshift Biases	406
14.5.2 Non-Linear Development of Density Perturbations	407
14.5.3 The Role of Baryon Perturbations	409
14.6 The Acoustic Peaks in the Power Spectrum of Galaxies	411
14.6.1 The 2dF Galaxy Redshift Survey	412
14.6.2 Sloan Digital Sky Survey	412
14.7 Variations on a Theme of Cold Dark Matter	415
15 Fluctuations in the Cosmic Microwave Background Radiation	421
15.1 The Ionisation of the Intergalactic Gas Through the Epoch of Recombination	422
15.2 The Physical and Angular Scales of the Fluctuations	424
15.2.1 The Last Scattering Layer	425
15.2.2 The Silk Damping Scale	426
15.2.3 The Sound Horizon at the Last Scattering Layer	427
15.2.4 The Particle Horizon Scales	429
15.2.5 Summary	430
15.3 The Power Spectrum of Fluctuations in the Cosmic Microwave Background Radiation	431

15.3.1	The Statistical Description of the Temperature Fluctuations	431
15.3.2	The Power Spectrum of Fluctuations in the Intensity of the Cosmic Microwave Background Radiation	434
15.4	Large Angular Scales	436
15.4.1	The Sachs–Wolfe Effect – Physical Arguments	436
15.4.2	The Integrated Sachs–Wolfe and Rees–Sciama Effects	440
15.4.3	Primordial Gravitational Waves	440
15.5	Intermediate Angular Scales – the Acoustic Peaks	443
15.6	Small Angular Scales	450
15.6.1	Statistical and Silk Damping	450
15.6.2	The Sunyaev–Zeldovich Effect in Clusters of Galaxies	450
15.6.3	Confusion Due to Discrete Sources	451
15.7	The Reionised Intergalactic Gas	452
15.8	The Polarisation of the Cosmic Microwave Background Radiation	454
15.8.1	The Polarisation Mechanism for the Cosmic Microwave Background Radiation	454
15.8.2	Polarisation from the Last Scattering Layer	455
15.8.3	Polarisation from the Epoch of Reionisation	458
15.8.4	Primordial Gravitational Waves	459
15.8.5	Weak Gravitational Lensing	460
15.9	Determination of Cosmological Parameters	463
15.10	Other Sources of Primordial Fluctuations	465
15.11	Reflections	466

Part IV The Post-Recombination Universe

16	The Post-Recombination Era	471
16.1	The Non-Linear Collapse of Density Perturbations	472
16.1.1	Isotropic Top-Hat Collapse	473
16.1.2	The Zeldovich Approximation	475
16.2	The Role of Dissipation	477
16.3	The Press–Schechter Mass Function	482
16.3.1	Exposition – Elementary Theory	482
16.3.2	Development and Recapitulation	485
17	The Evolution of Galaxies and Active Galaxies with Cosmic Epoch	491
17.1	Introduction	491
17.2	Counts of Galaxies and Active Galaxies	492
17.2.1	Euclidean Source Counts	493
17.2.2	Source Counts for the Standard World Models	494
17.2.3	Submillimetre Counts of Dusty Galaxies	500
17.2.4	Number Counts in Models with Finite Ω_A	501
17.2.5	Fluctuations in the Background Radiation due to Discrete Sources	504

17.3	The V/V_{\max} or Luminosity-Volume Test	507
17.4	Background Radiation	510
17.4.1	Background Radiation and Source Counts	510
17.4.2	Evaluating the Background due to Discrete Sources	510
17.4.3	The Effects of Evolution – the Case of the Radio Background Emission	512
17.5	The Evolution of Active Galaxies with Cosmic Epoch	514
17.5.1	Number Counts and V/V_{\max} Tests for Extragalactic Radio Sources	514
17.5.2	Radio Quiet Quasars	518
17.5.3	X-Ray Source Counts	524
17.5.4	X-Ray Clusters of Galaxies	529
17.6	Infrared and Submillimetre Number Counts	532
17.7	Counts of Galaxies	537
17.8	Clusters of Galaxies	543
18	The Intergalactic Medium	547
18.1	The Background Emission of and Absorption by the Intergalactic Gas	548
18.2	The Gunn–Peterson Test	549
18.3	The Lyman- α Absorption Clouds	552
18.3.1	The Properties of the Lyman- α Absorption Clouds	552
18.3.2	The Nature of the Clouds in the Lyman- α Forest	554
18.3.3	The Evolution of Lyman- α Absorption Clouds with Cosmic Epoch	556
18.3.4	The Power Spectrum of the Lyman- α Forest	557
18.4	The Lukewarm Intergalactic Gas	560
18.4.1	The X-Ray Background and a Cosmic Conspiracy	561
18.4.2	The Collisional Excitation of the Intergalactic Gas	562
18.4.3	The Emission and Absorption of Diffuse Lukewarm Intergalactic Gas	564
18.4.4	The Proximity Effect and the Diffuse Ultraviolet Background Radiation at Large Redshifts	567
18.5	The Lyman Continuum Opacity of the Intergalactic Gas	569
18.6	Modelling the Evolution of the Intergalactic Medium	571
18.7	The Epoch of Reionisation	574
18.8	The Origin of Magnetic Fields	577
19	Making Real Galaxies	583
19.1	Star and Element Formation in Galaxies	583
19.1.1	The Background Radiation and Element Formation	584
19.1.2	The Global Star Formation Rate from Optical and Ultraviolet Observations of Star-Forming Galaxies	587
19.1.3	The Lyman-Break Galaxies	590
19.1.4	The Hubble Deep and Ultra Deep Fields	590

19.1.5 Submillimetre Determinations of the Cosmic Star-Formation Rate	596
19.2 The Abundances of Elements in Lyman- α Absorption Systems	598
19.3 The Equations of Cosmic Chemical Evolution	604
19.4 The Old Red Galaxies	607
19.5 The Origin of Rotation	610
19.6 Putting It All Together – Semi-Analytic Models of Galaxy Formation	613
20 The Very Early Universe	621
20.1 The Big Problems	621
20.1.1 The Horizon Problem	621
20.1.2 The Flatness Problem	622
20.1.3 The Baryon-Asymmetry Problem	622
20.1.4 The Primordial Fluctuation Problem	623
20.1.5 The Values of the Cosmological Parameters	623
20.1.6 The Way Ahead	624
20.2 The Limits of Observation	624
20.3 The Anthropic Cosmological Principle	625
20.4 The Inflationary Universe – Historical Background	626
20.5 The Origin of the Spectrum of Primordial Perturbations	629
20.5.1 The Equation of State	630
20.5.2 The Duration of the Inflationary Phase	630
20.5.3 The Shrinking Hubble Sphere	631
20.5.4 Scalar Fields	634
20.5.5 The Quantised Harmonic Oscillator	635
20.5.6 The Spectrum of Fluctuations in the Scalar Field	637
20.6 Baryogenesis	641
20.7 The Planck Era	642
References	645
Name Index	695
Index	701

Part IV

The Post-Recombination Universe

20 The Very Early Universe

20.1 The Big Problems

The developments in astrophysical and geometrical cosmology described in this book represent quite extraordinary progress in understanding the origins and evolution of our Universe and its contents. The contrast between the apparently insuperable problems of determining precise values of cosmological parameters up till the 1990s and the era of *precision cosmology* of the early years of the 21st century is startling.

The concordance model is undoubtedly remarkably successful, but, like all good theories, it raises as many new problems as it solves. The picture is incomplete in the sense that, within the context of the standard Friedman world models, the initial conditions described by the parameters listed in Table 15.1 have to be put in by hand in order to create the Universe as we observe it today. How did these initial conditions arise? As the quality of the observations has improved, a number of fundamental issues for astrophysical cosmology have become apparent. The resolution of these problems will undoubtedly give insight into the laws of physics under physical conditions which at the moment can only be studied by cosmological observations.

Let us review the basic problems which have appeared at various points in the development.

20.1.1 The Horizon Problem

This problem, clearly recognised by Dicke in 1961 and discussed in Sect. 12.1, can be restated: ‘Why is the Universe so isotropic?’ (Dicke, 1961). At earlier cosmological epochs, the particle horizon $r \sim ct$ encompassed less and less mass and so the scale over which particles could be causally connected became smaller and smaller. We can illustrate this by working out how far light could have travelled along the last scattering layer at $z = 1000$ since the Big Bang. In matter-dominated models, this distance is $r = 3ct$, corresponding to an angle $\theta_H \approx 2^\circ$ on the sky. Thus, regions of the sky separated by greater angular distances could not have been in causal communication. Why then is the cosmic microwave background radiation so isotropic? How did causally separated regions ‘know’ that they had to have the same temperature to better than one part in 10^5 ? As we showed in Sect. 12.1, an early period of exponential growth of the scale factor with cosmic time, the inflationary era, can overcome this problem. We will illustrate this process from a different perspective in Sect. 20.5.3.

20.1.2 The Flatness Problem

Why is the Universe geometrically flat, $\Omega_k \approx 0$ (Sect. 7.6)? The flatness problem was also recognised by Dicke in 1961 and reiterated by Dicke and Peebles in 1979 for standard world models with $\Omega_A = 0$ (Dicke, 1961; Dicke and Peebles, 1979). In its original version, the problem arises from the fact that, according to the standard world models, if the Universe were set up with a value of the density parameter differing even slightly from the critical value $\Omega = 1$, it would diverge very rapidly from this value at later epochs. As shown in Sect. 7.6, if the Universe has density parameter Ω_0 today, at redshift z , $\Omega(z)$ would have been

$$\left[1 - \frac{1}{\Omega(z)}\right] = f(z) \left[1 - \frac{1}{\Omega_0}\right], \quad (20.1)$$

where $f(z) = (1+z)^{-1}$ for the matter-dominated era and $f(z) \propto (1+z)^{-2}$ during the radiation-dominated era. Thus, since $\Omega_0 \sim 1$ at the present epoch, it must have been extremely close to the critical value in the remote past. Alternatively, if $\Omega(z)$ had departed from $\Omega(z) = 1$ at a very large redshift, Ω_0 would be very far from $\Omega_0 = 1$ today. Thus, the only ‘stable’ value of Ω_0 is $\Omega_0 = 1$. There is nothing in the standard world models that would lead us to prefer any particular value of Ω_0 . This is sometimes referred to as the *fine-tuning problem*.

20.1.3 The Baryon-Asymmetry Problem

The baryon-asymmetry problem arises from the fact that the photon-to-baryon ratio today is

$$\frac{N_\gamma}{N_B} = \frac{4 \times 10^7}{\Omega_B h^2} = 1.6 \times 10^9, \quad (20.2)$$

where Ω_B is the density parameter in baryons and the values of Ω_B and h have been taken from Table 15.1. If photons are neither created nor destroyed, this ratio is conserved as the Universe expands. At temperature $T \approx 10^{10}$ K, electron–positron pair production takes place from the photon field. At a correspondingly higher temperature, baryon–antibaryon pair production takes place with the result that there must have been a very small asymmetry in the baryon–antibaryon ratio in the very early Universe if we are to end up with the correct photon-to-baryon ratio at the present day. As explained in Sect. 10.6, at these very early epochs, there must have been roughly $10^9 + 1$ baryons for every 10^9 antibaryons to guarantee the observed ratio at the present epoch. If the Universe had been symmetric with respect to matter and antimatter, we showed in Sect. 10.6 that the photon-to-baryon ratio would now be about 10^{18} , in gross contradiction with the observed value (Zeldovich, 1965). Therefore, there must have been some mechanism in the early Universe which resulted in a slight asymmetry between matter and antimatter.

20.1.4 The Primordial Fluctuation Problem

What was the origin of the density fluctuations from which galaxies and large-scale structures formed? According to the analyses of Part III, the amplitudes of the density perturbations when they came through the horizon had to be of finite amplitude, $\delta\varrho/\varrho \sim 10^{-5}$, on a very wide range of mass scales. These cannot have originated as statistical fluctuations in the numbers of particles on, say, the scales of superclusters of galaxies. There must have been some physical mechanism which generated finite amplitude perturbations with a power spectrum close to $P(k) \propto k$ in the early Universe.

20.1.5 The Values of the Cosmological Parameters

The horizon and flatness problems were recognised before compelling evidence was found for the finite value of the cosmological constant, or the density parameter in the vacuum fields ϱ_A , but these problems remain unchanged. The concordance values for the cosmological parameters create their own problems. The Universe is very close to being geometrically flat, $\Omega_k = 0$, and so the sum of the density parameters in the matter and the dark energy must sum to unity, $\Omega_A + \Omega_0 = 0.72 + 0.28 = 1$. Even if the sum of these two parameters were not precisely unity, it is a surprise that they are of the same order of magnitude at the present epoch. The matter density evolves with redshift as $(1+z)^3$, while the dark energy density is unchanging with cosmic epoch. Why then do we live at an epoch when they have more or less the same values?

The strange history of the cosmological constant and its modern interpretation was discussed in Sect. 7.3.1. A key insight resulted from the introduction of Higgs fields into the theory of weak interactions (Higgs, 1964). The Higgs fields are *scalar* fields which have negative pressure equations of state, $p = -\varrho c^2$. We also discussed how the theoretical value of ϱ_A could be estimated from quantum field theory and found $\varrho_v = 10^{95} \text{ kg m}^{-3}$, about 10^{120} times greater than the value of ϱ_A at the present epoch, which corresponds to $\varrho_A \approx 10^{-27} \text{ kg m}^{-3}$ (Carroll et al., 1992). This is quite a problem.

As if these problems were not serious enough, they are compounded by the fact that the nature of the dark matter and the dark energy is unknown. Thus, one of the consequences of precision cosmology is the remarkable result that we do not understand the nature of about 95% of the material which drives the large-scale dynamics of the Universe. The concordance values for the cosmological parameters listed in Table 15.1 really are extraordinary – many of my colleagues regard them as crazy. Rather than being causes for despair, however, these problems should be seen as the great challenges for the astrophysicists and cosmologists of the 21st century. It is not too far-fetched to see an analogy with Bohr’s theory of the hydrogen atom, which was an uncomfortable mix of classical and primitive quantum ideas but which was ultimately to lead to completely new and deep insights with the development of quantum mechanics.

20.1.6 The Way Ahead

In the standard Friedman models, the problems are solved by assuming that the Universe was endowed with appropriate initial conditions in its very early phases. It is postulated that our Universe evolved from an initial state which was isotropic with flat geometry, was slightly matter-antimatter asymmetric, contained fluctuations with roughly a Harrison-Zeldovich spectrum and had initial values of Ω_0 and Ω_A such that they ended up being roughly equal at the present day. To put it crudely, we get out at the end what we put in at the beginning. In a truly physical picture of our Universe, we should be able to do better than this.

I have suggested five possible approaches to solving these problems (Longair, 1997a).

- That is just how the Universe is – the initial conditions were set up that way.
- There are only certain classes of Universe in which intelligent life could have evolved. The Universe has to have the appropriate initial conditions and the fundamental constants of nature should not be too different from their measured values or else there would be no chance of life forming as we know it. This approach involves the *Anthropic Cosmological Principle* according to which it is asserted that the Universe is as it is because we are here to observe it.
- The inflationary scenario for the early Universe.
- Seek clues from particle physics and extrapolate that understanding beyond what has been confirmed by experiment to the earliest phases of the Universe.
- Something else we have not yet thought of. This would certainly involve new physical concepts.

Let us consider each of these approaches.

20.2 The Limits of Observation

Even the first, somewhat defeatist, approach might be the only way forward if it turned out to be just too difficult to disentangle convincingly the physics responsible for setting up the initial conditions from which our Universe evolved. In 1970, McCrea considered the fundamental limitations involved in asking questions about the very early Universe, his conclusion being that we can obtain less and less information the further back in time one asks questions about the early Universe (McCrea, 1970). A modern version of this argument would be framed in terms of the limitations imposed by the existence of a last scattering surface for electromagnetic radiation at $z \approx 1000$ and those imposed on the accuracy of observations of the cosmic microwave background radiation and the large-scale structure of the Universe because of their cosmic variances. It is an interesting challenge to review McCrea's arguments in the light of present understanding of the cosmological models.

In the case of the cosmic microwave background radiation, the observations made by the WMAP experiment are already cosmic variance limited for multipoles $l \leq 354$ – we will never be able to learn much more than we know already about

the amplitude of the power spectrum on these scales. Observations by the Planck Satellite will provide independent validation of the results of WMAP for these multipoles and extend the cosmic variance limit to $l \approx 2000$. In these studies, the search for new physics will depend upon the discovering discrepancies between the standard concordance model and future observations. The optimists, of whom the present author is one, would argue that the advances will come through extending our technological capabilities so that new classes of observation become cosmic variance limited. For example, the detection of primordial gravitational waves through their polarisation signature at small multipoles in the cosmic microwave background radiation, the nature of dark matter particles and even the nature of the vacuum energy are the cutting edge of fundamental issues for astrophysical cosmology in the 21st century. These approaches will be accompanied by discoveries in particle physics with the coming generations of ultra-high-energy particle experiments. There will undoubtedly be surprises which open up completely new ways of tackling problems which seem to be intractable today – for example, what will be discovered in ultra-high-energy cosmic ray experiments, such as those to be carried out with the Auger array? What will neutrino astrophysics tell us of cosmological importance?

It is folly to attempt to predict what will be discovered over the coming years, but we might run out of luck. How would we then be able to check that the theoretical ideas proposed to account for the properties of the very early Universe are correct? Can we do better than bootstrapped self-consistency? The great achievement of modern observational and theoretical cosmology has been that we have made enormous strides in defining a convincing framework for astrophysical cosmology and the basic problems identified above can now be addressed as areas of genuine physical enquiry.

20.3 The Anthropic Cosmological Principle

There is certainly some truth in the fact that our ability to ask questions about the origin of the Universe says something about the sort of Universe we live in. The Cosmological Principle asserts that we do not live at any special location in the Universe, and yet we are certainly privileged in being able to make this statement at all. In this line of reasoning, there are only certain types of Universe in which life as we know it could have formed. For example, the stars must live long enough for there to be time for biological life to form and evolve into sentient beings. This line of reasoning is embodied in the *Anthropic Cosmological Principle*, first expounded by Carter in 1974 (Carter, 1974) and dealt with *in extenso* in the books by Barrow and Tipler and by Gribbin and Rees (Barrow and Tipler, 1986; Gribbin and Rees, 1989). Part of the problem stems from the fact that we have only one Universe to study – we cannot go out and investigate other Universes to see if they have evolved in the same way as ours. There are a number of versions of the Principle, some of them stronger than others. In extreme interpretations, it leads to statements such as the strong form of the Principle enunciated by Wheeler (Wheeler, 1977),

Observers are necessary to bring the Universe into being.

It is a matter of taste how seriously one wishes to take this line of reasoning. To many cosmologists, it is not particularly appealing because it suggests that it will never be possible to find physical reasons for the initial conditions from which the Universe evolved or for the values of the fundamental constants of nature. But some of these problems are really hard. Weinberg, for example, found it such a puzzle that the vacuum energy density Ω_Λ is so very much smaller than the values expected according to current theories of elementary particles that he invoked anthropic reasoning to account for its smallness (Weinberg, 1989, 1997). Another manifestation of this type of reasoning is to invoke the range of possible initial conditions which might come out of the picture of chaotic inflation (Linde, 1983) and argue that, if there were at least 10^{120} of them, then we live in one of the few which has the right conditions for life to develop as we know it. Again, I leave it to the reader how seriously these ideas should be taken. I worry about the issue of observational validation of these ideas. I prefer to regard the Anthropic Cosmological Principle as the very last resort if all other physical approaches fail.

20.4 The Inflationary Universe – Historical Background

The most important conceptual development for studies of the very early Universe can be dated to 1980 and the proposal by Guth of the *inflationary model* for the very early Universe (Guth, 1981). There had been earlier suggestions foreshadowing his proposal. Zeldovich had noted in 1968 that there is a physical interpretation of the cosmological constant Λ in terms of the zero-point fluctuations in a vacuum (Zeldovich, 1968). Linde in 1974 and Bludman and Ruderman in 1977 had shown that the scalar Higgs fields of particle physics have similar properties to those which would result in a positive cosmological constant (Linde, 1974; Bludman and Ruderman, 1977). A popular account of the history of the development of ideas about the inflation picture of the early Universe is contained in Guth's book *The Inflationary Universe: The Quest for a New Theory of Cosmic Origins* (Guth, 1997). The pedagogical review by Lineweaver can also be recommended. He adopts a somewhat sceptical attitude to the concept of inflation and our ability to test inflationary models through confrontation with observations (Lineweaver, 2005). Nonetheless, for good reasons, this model dominates much of present-day cosmological thinking.

Guth realised that, if there were an early phase of exponential expansion of the Universe, this could solve the horizon problem and drive the Universe towards a flat spatial geometry, thus solving the flatness problem at the same time. Suppose the scale factor, a , increased exponentially with time as $a \propto e^{t/T}$. Such exponentially expanding models were found in some of the earliest solutions of the Friedman equations, in the guise of empty de Sitter models driven by what is now termed the vacuum energy density Ω_Λ (Sect. 7.3.3) (Lanczos, 1922). Consider a tiny region of the early Universe expanding under the influence of the exponential expansion. Particles within the region were initially very close together and in causal communication with each other. Before the inflationary expansion began, the region had physical scale less than the particle horizon, and so there was time for it to attain a uniform,

homogeneous state. The region then expanded exponentially so that neighbouring points were driven to such large distances that they could no longer communicate by light signals – the causally connected regions were swept beyond their particle horizons by the inflationary expansion. At the end of the inflationary epoch, the Universe transformed into the standard radiation-dominated Universe and the inflated region continued to expand as $a \propto t^{1/2}$. More formal demonstrations of how the exponential expansion can resolve the problem of the particle horizon are given in Sects. 12.1 and 20.5.3.

In Guth's original inflationary scenario, the exponential expansion was associated with the symmetry breaking of grand unified theories of elementary particles at very high energies through a first-order phase transition, only about 10^{-34} s after the Big Bang. Although this picture was soon demonstrated not to work, let us demonstrate to order of magnitude how the argument runs. The timescale 10^{-34} s is taken to be the characteristic e-folding time for the exponential expansion. Over the interval from 10^{-34} s to 10^{-32} s, the radius of curvature of the Universe increased exponentially by a factor of about $e^{100} \approx 10^{43}$. The horizon scale at the beginning of this period was only $r \approx ct \approx 3 \times 10^{-26}$ m and this was inflated to a dimension of 3×10^{17} m by the end of the inflationary era. This dimension then scaled as $t^{1/2}$, as in the standard radiation-dominated Universe, so that the region would have expanded to a size of 3×10^{42} m by the present day; this dimension far exceeds the present particle horizon $r \approx cT_0$ of the Universe, which is about 10^{26} m. Thus, our present Universe would have arisen from a tiny region in the very early Universe which was much smaller than the horizon scale at that time. This guaranteed that our present Universe would be isotropic on the large scale, resolving the horizon problem. At the end of the inflationary era, there was an enormous release of energy associated with the ‘latent heat’ of the phase transition and this reheated the Universe to a very high temperature indeed (Fig. 20.1).

The exponential expansion also had the effect of straightening out the geometry of the early Universe, however complicated it may have been to begin with. Suppose the tiny region of the early Universe had some complex geometry. The radius of curvature of the geometry $R_c(t)$ scales as $R_c(t) = \mathfrak{R}a(t)$, where \mathfrak{R} is its value at the present epoch t_0 , and so the radius of curvature of the geometry is inflated to dimensions vastly greater than the present size of the Universe, driving the geometry of the inflated region towards flat Euclidean geometry, $\Omega_\kappa = 0$, and consequently the Universe must have $\Omega_0 + \Omega_\Lambda = 1$. It is important to note that these two aspects of the case for the inflationary picture can be made independently of a detailed understanding of the physics of the inflation. There is also considerable freedom about the exact time when the inflationary expansion could have occurred, provided there are sufficient e-folding times to isotropise our observable Universe and flatten its geometry.

In Guth's original proposal, the Universe was in a symmetric state, referred to as a false vacuum state, at a very high temperature before the inflationary phase took place. As the temperature fell, spontaneous symmetry breaking took place through the process of barrier penetration from the false vacuum state and the Universe attained a lower energy state, the true vacuum. At the end of this period

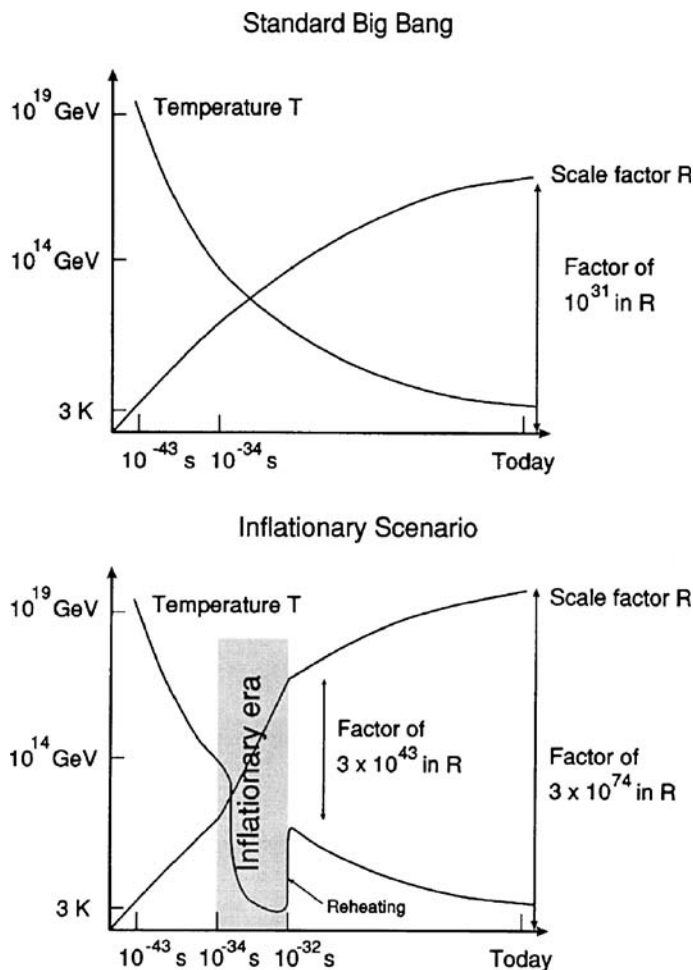


Fig. 20.1. Comparison of the evolution of the scale factor and temperature in the standard Big Bang and inflationary cosmologies

of exponential expansion, the phase transition took place, releasing a huge amount of energy. The problem with this realisation was that it predicted ‘bubbles’ of true vacuum embedded in the false vacuum, with the result that huge inhomogeneities were predicted. Another concern about the original proposal was that an excessive number of monopoles were created during the GUT phase transition. Kibble showed that when this phase transition took place, topological defects were likely created, including point defects (or monopoles), line defects (or cosmic strings) and sheet defects (or domain walls) (Kibble, 1976). Kibble showed that one monopole is created for each correlation scale at that epoch. Since that scale cannot be greater than the particle horizon at the GUT phase transition, it is expected that huge

numbers of monopoles are created. According to the simplest picture of the GUT phase transition, the mass density in these monopoles in the standard Big Bang picture would vastly exceed $\Omega_0 = 1$ at the present epoch (Kolb and Turner, 1990).

The model was revised in 1982 by Linde and by Albrecht and Steinhardt, who proposed instead that, rather than through the process of barrier penetration, the transition took place through a second-order phase transition which did not result in the formation of ‘bubbles’ and, hence, excessive inhomogeneities (Linde, 1982, 1983; Albrecht and Steinhardt, 1982). This picture, often referred to as *new inflation*, also eliminated the monopole problem since the likelihood of even one being present in the observable Universe was very small.

The original hope that a physical realisation for the inflationary expansion could be found within the context of particle physics beyond the standard model has not been achieved, but the underlying concepts of the inflationary picture have been used to define the necessary properties of the *inflaton potential* needed to create the Universe as we know it. The successful realisations are similar to those involved in the new inflationary picture. Once the inflationary expansion began at some stage in the early Universe, the change from the false to the true vacuum state took place through a process of *slow rollover*, meaning that the inflationary expansion took place over many e-folding times before the huge energy release took place. An excellent introduction to these concepts and the changing perspective on the inflationary picture of the early Universe is contained in the book *Cosmological Inflation and Large-Scale Structure* by Liddle and Lyth (Liddle and Lyth, 2000). Many different versions of the inflationary picture of the early Universe have emerged, an amusing table of over 100 possibilities being presented by Shellard (Shellard, 2003).

As a result, it cannot be claimed that there is a physical theory of the inflationary Universe, but its basic concept resolves some of the basic problems listed in Sect. 20.1. What it also does, and which gives it considerable appeal, is to suggest an origin for the spectrum of initial density perturbations as quantum perturbations on the scale of the particle horizon, and that is the topic we deal with next.

20.5 The Origin of the Spectrum of Primordial Perturbations

In many ways, the story of inflation up to this point has been remarkably physics free. All that has been stated is that an early period of rapid exponential expansion can overcome a number of the fundamental problems of cosmology. The next step involves real physics, but it is not the type of physics familiar to most astrophysical cosmologists. The key role is played by *scalar fields*, which have quite different properties from the vector and tensor fields familiar in electrodynamics and general relativity. These fields are, however, common in theories of particle physics and so the particle theorists are well prepared to take on the problem of putting real physics into the inflationary paradigm.

The reason these ideas have to be taken seriously is that they suggest a remarkably natural origin for the spectrum of primordial perturbations with a spectrum

close to the Harrison–Zeldovich spectrum. The theory also makes quantitative predictions about the intensity and spectrum of primordial gravitational waves which are accessible to experimental validation. According to Liddle and Lyth:

Although introduced to resolve problems associated with the initial conditions needed for the Big Bang cosmology, inflation's lasting prominence is owed to a property discovered soon after its introduction: It provides a possible explanation for the initial inhomogeneities in the Universe that are believed to have led to all the structures we see, from the earliest objects formed to the clustering of galaxies to the observed irregularities in the microwave background.

There are now several recommendable books on this subject (Liddle and Lyth, 2000; Dodelson, 2003; Mukhanov, 2005). For the standard ‘cosmologist in the street’, these do not make for particularly easy reading, largely because the reader must feel comfortable with many aspects of theoretical physics which lie outside the standard tools of the observational cosmologist. They may once have been understood as examination requirements in theoretical physics, but they rarely appear in the standard astrophysical literature – ladder operators, quantum field theory, zero-point fluctuations in quantum fields, all of these developed within the framework of general relativity. Having battled with various degrees of success with the above books and many others, I found the essay by Baumann to be the most straightforward and accessible account of the physical content of the theory (Baumann, 2007); what follows is a ‘vulgarisation’ of his presentation. Developing the theory of the quantum origin of density perturbations in detail cannot be carried out with modest effort and is far beyond the ambitions of the present exposition. There is no question, however, that these remarkable developments are at the cutting edge of cosmological research and have the potential to reveal new physics.

Let us list some of the clues about the formulation of a successful theory.

20.5.1 The Equation of State

We know from our analysis of the physical significance of the cosmological constant Λ in Sect. 7.3 that exponential growth of the scale factor is found if the dark energy has a negative pressure equation of state $p = -\varrho c^2$. More generally, inspection of (7.1) shows that exponential growth of the scale factor is found provided the strong energy condition is violated, that is, if $p < -\frac{1}{3}\varrho c^2$. To be effective in the very early Universe, the mass density of the scalar field has to be vastly greater than the value of ϱ_Λ we measure today.

20.5.2 The Duration of the Inflationary Phase

In the example of the inflationary expansion given in Sect. 20.4, we arbitrarily assumed that 100 e-folding times would take place during the inflationary expansion. A more careful calculation shows that there must have been at least 60 e-folding

times and these took place in the very early Universe, much earlier than those which have been explored experimentally by particle physics experiments. It is customary to assume that inflation got seriously under way not long after the Planck era, but there is quite a bit of room for manoeuvre.

20.5.3 The Shrinking Hubble Sphere

If these precepts are accepted, there is a natural way of understanding how fluctuations can be generated from processes in the very early Universe. It is helpful to visit again the conformal diagrams for world models which were discussed in Sect. 12.2, in particular Fig. 12.2c. Recall that these diagrams are exact in the sense that the comoving radial distance coordinate and conformal time are worked out for the reference model with $\Omega_0 = 0.3$ and $\Omega_A = 0.7$, the abscissa being in units of c/H_0 and the ordinate in units of H_0^{-1} . The effect of using conformal time is to stretch out time in the past and shrink it into the future. Notice that, because of the use of linear scales in the ordinate, the radiation-dominated phase of the standard Big Bang is scarcely visible.

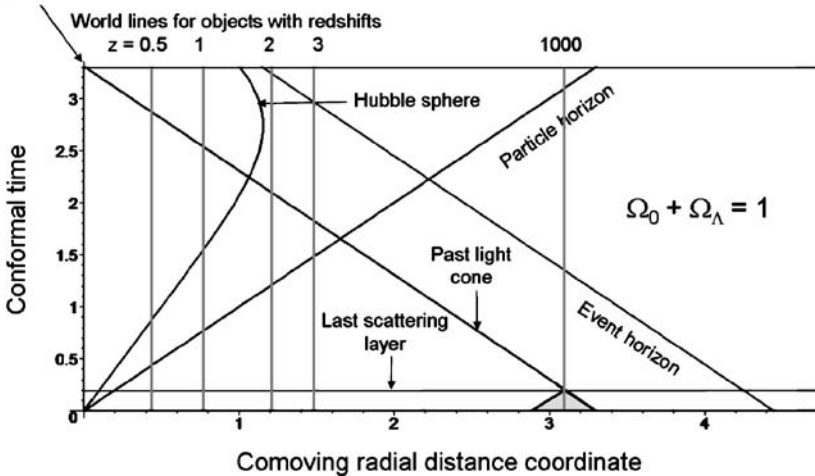
There are two additions to Fig. 12.2c in Fig. 20.2a. The redshift of 1000 is shown corresponding to the last scattering surface of the cosmic microwave background radiation. The intersection with our past light cone is shown and then a past light cone from the last scattering surface to the singularity at conformal time $\tau = 0$ is shown as a shaded triangle. This is another way of demonstrating the *horizon problem* – the region of causal contact is very small compared with moving an angle of 180° over the sky, which would correspond to twice the distance between the origin and the comoving radial distance coordinate at 3.09.

Let us now add the inflationary era to Fig. 20.2a. Baumann's insights are helpful in constructing Fig. 20.2b. He makes the important point that it is useful to regard the end of the inflation era as the zero of time for the standard Big Bang and then to extend the diagram back to negative conformal times. In other words, we shift the zero of conformal time very slightly to, say, 10^{-32} s, and then we can extend the light cones back through the entire inflationary era.

This construction provides another way of understanding how the inflationary picture resolves the causality problem. The light cones have unit slope in the conformal diagram, and so we draw light cones from the ends of the element of comoving radial distance at $\tau = 0$ from the last scattering surface. These are shown in the diagram, and it can be seen that projecting far enough back in time, the light cones from opposite directions on the sky overlap, represented by the dark grey shaded area in Fig. 20.2b. This is another way of understanding how the inflationary picture results in causal contact in the early Universe.

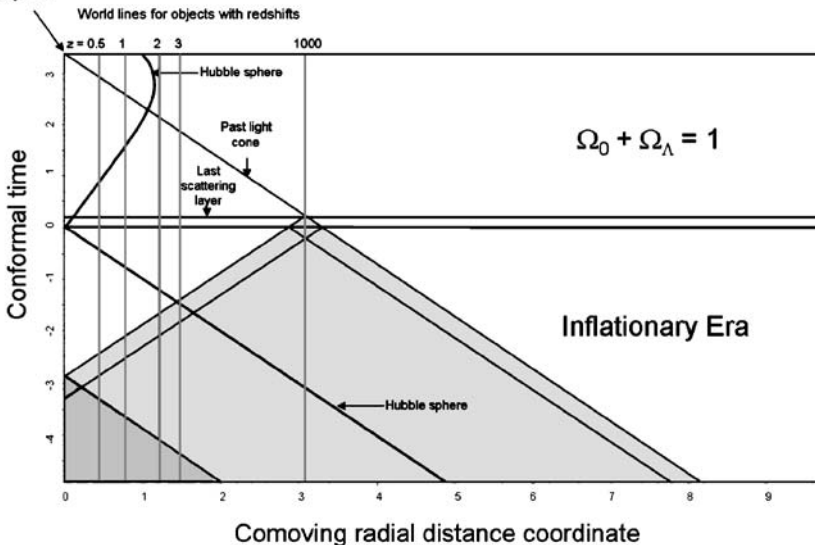
There is, however, an even better way of understanding what is going on. We were at pains to distinguish between the Hubble sphere and the particle horizon in Sect. 12.2, but now this distinction becomes important. The particle horizon is defined as the maximum distance over which causal contact could have been made from the time of the singularity to a given epoch. In other words, it is not just what happened at a particular epoch which is important, but the history along the past light

Observer at present epoch



a

Observer at present epoch



b

Fig. 20.2. **a** A repeat of conformal diagram Fig. 12.2c in which conformal time is plotted against comoving radial distance coordinate. Now, the last scattering surface at the epoch of recombination is shown as well as the past light cone from the point at which our past light cone intersects the last scattering surface. **b** An extended conformal diagram now showing the inflationary era. The time coordinate is set to zero at the end of the inflationary era and evolution of the Hubble sphere and the past light cone at recombination extrapolated back to the inflationary era

cone. In contrast, the Hubble radius is the distance of causal contact *at a particular epoch*. It is the distance at which the velocity in the velocity-distance relation at that epoch is equal to the speed of light. As shown in (12.29), the Hubble sphere has proper radius

$$r_{\text{HS}} = \frac{c}{H(z)} = \frac{ac}{\dot{a}} . \quad (20.3)$$

Writing the exponential inflationary expansion of the scale factor as $a = a_0 \exp[H(t - t_i)]$, where a_0 is the scale factor when the inflationary expansion began at t_i , $r_{\text{HS}} = c/H$ and the comoving Hubble sphere has radius $r_{\text{HS}}(\text{com}) = c/(Ha)$. Since H is a constant throughout most of the inflationary era, it follows that the comoving Hubble sphere *decreases* as the inflationary expansion proceeds.

We now need to join this evolution of the comoving Hubble sphere onto its behaviour after the end of inflation, that is, join it onto Fig. 20.2a. The expression for conformal time during the inflationary era is

$$\tau = \int \frac{da}{a\dot{a}} , \quad (20.4)$$

and so, integrating and using the expression for $r_{\text{HS}}(\text{com})$, we find

$$\tau = \text{constant} - \frac{r_{\text{HS}}(\text{com})}{c} . \quad (20.5)$$

This solution for $r_{\text{HS}}(\text{com})$ is joined on to the standard result at the end of the inflationary epoch, as illustrated in Fig. 20.2b. The complete evolution of the Hubble sphere is indicated by the heavy line labelled ‘Hubble sphere’ in that diagram.

Figure 20.2b illustrates very beautifully how the inflationary paradigm solves the horizon problem. It will be noticed that the point at which the Hubble sphere crosses the comoving radial distance coordinate of the last scattering surface corresponds exactly to the time when the past light cones from opposite directions on the sky touch at conformal time -3 . This is not a coincidence – they are different ways of stating that opposite regions of the cosmic microwave background were in causal contact at conformal time $t = -3$.

But we learn a lot more. Because any object preserves its comoving radial distance coordinate for all time, as represented by the vertical lines in Fig. 20.2b, it can be seen that, in the early Universe, objects lie within the Hubble sphere, but during the inflationary expansion, they pass through it and remain outside it for the rest of the inflationary expansion. Only when the Universe transforms back into the standard Friedman model does the Hubble sphere begin to expand again and objects can then ‘re-enter the horizon’. Consider, for example, the region of the Universe out to redshift $z = 0.5$, which corresponds to one of the comoving coordinate lines in Fig. 20.2b. It remained within the Hubble sphere during the inflationary era until conformal time $\tau = -0.4$, after which it was outside the horizon. It then re-entered the Hubble sphere at conformal time $\tau = 0.8$. This behaviour occurs for all scales and masses of interest in understanding the origin of structure in the present Universe.

Since causal connection is not possible on scales greater than the Hubble sphere, it follows that objects ‘freeze out’ when they pass through the Hubble sphere during the inflationary era, but they come back in again and regain causal contact when they recross the Hubble sphere. This is one of the key ideas behind the idea that the perturbations from which galaxies formed were created in the early Universe, froze out on crossing the Hubble sphere and then grew again on re-entering it at conformal times $\tau > 0$.

Notice that, at the present epoch, we are entering a phase of evolution of the Universe when the comoving Hubble sphere about us has begun to shrink again. This can be seen in the upper part of Fig. 20.2b and is entirely due to the fact that the dark energy is now dominating the expansion and its dynamics are precisely another exponential expansion. In fact, the Hubble sphere tends asymptotically to the line labelled ‘event horizon’ in Fig. 20.2a.

20.5.4 Scalar Fields

As Baumann notes, there are three equivalent conditions necessary to produce an inflationary expansion (Baumann, 2007):

- The decreasing of the Hubble sphere during the early expansion of the Universe;
- An accelerated expansion;
- Violation of the strong energy condition, specifically, $p < -\varrho c^2/3$.

How can this be achieved physically? It is simplest to quote Baumann’s words:

Answer: scalar field with special dynamics! Although no fundamental scalar field has yet been detected in experiments, there are fortunately plenty of such fields in theories beyond the standard model of particle physics. In fact, in string theory for example there are numerous scalar fields (moduli), but it proves very challenging to find just one with the right characteristics to serve as an inflaton candidate.

At this point, I simply quote the results of calculations of the properties of the scalar field $\phi(t)$ which is assumed to be homogeneous at a given epoch. There is a kinetic energy $\dot{\phi}^2/2$ and a potential energy, or self-interaction energy, $V(\phi)$ associated with the field. Putting these through the machinery of field theory results in expressions for the density and pressure of the scalar field:

$$\varrho_\phi = \frac{1}{2}\dot{\phi}^2 + V(\phi) \quad (20.6)$$

$$p_\phi = \frac{1}{2}\dot{\phi}^2 - V(\phi). \quad (20.7)$$

Clearly the scalar field can result in a negative pressure equation of state, provided the potential energy of the field is very much greater than its kinetic energy. In the limit in which the kinetic energy is neglected, we obtain the equation of state

$p = -\varrho c^2$, where I have restored the c^2 , which is set equal to one by professional field theorists.

To find the time evolution of the scalar field, we need to combine properties (20.6) and (20.7) with the Einstein equations. The results are

$$H^2 = \frac{1}{3} \left(\frac{1}{2} \dot{\phi}^2 + V(\phi) \right) \quad (20.8)$$

$$\ddot{\phi} + 3H\dot{\phi} + V_{,\phi}(\phi) = 0 , \quad (20.9)$$

where $V_{,\phi}$ means the derivative of $V(\phi)$ with respect to ϕ . Thus, to obtain the inflationary expansion over many e-folding times, the kinetic energy term must be very small compared with the potential energy and the potential energy term must be very slowly varying with time. This is formalised by requiring the two *slow-roll parameters* $\epsilon(\phi)$ and $\eta(\phi)$ to be very small during the inflationary expansion. These parameters set constraints upon the dependence of the potential energy function upon the field ϕ and are formally written as follows:

$$\epsilon(\phi) \equiv \frac{1}{2} \left(\frac{V_{,\phi}}{V} \right)^2 ; \quad \eta(\phi) \equiv \frac{V_{,\phi\phi}}{V} \quad \text{with} \quad \epsilon(\phi), |\eta(\phi)| \ll 1 , \quad (20.10)$$

where $V_{,\phi\phi}$ means the second derivative of $V(\phi)$ with respect to ϕ . Under these conditions, we obtain what we need for inflation, namely,

$$H^2 = \frac{1}{3} V(\phi) = \text{constant} \quad \text{and} \quad a(t) \propto e^{Ht} . \quad (20.11)$$

At this stage, it may appear that we have not really made much progress since we have adjusted the theory of the scalar field to produce what we know we need. The bonus comes when we consider fluctuations in the scalar field and their role in the formation of the spectrum of primordial perturbations.

20.5.5 The Quantised Harmonic Oscillator

The key result can be derived from the elementary quantum mechanics of a harmonic oscillator. The solutions of Schrödinger's equation for a harmonic potential have quantised energy levels

$$E = \left(n + \frac{1}{2} \right) \hbar\omega \quad (20.12)$$

and the wavefunctions of these stationary states are

$$\psi_n = H_n(\xi) \exp \left(-\frac{1}{2} \xi^2 \right) , \quad (20.13)$$

where $H_n(\xi)$ is the Hermite polynomial of order n and $\xi = \sqrt{\beta}x$. For the simple harmonic oscillator, $\beta^2 = am/\hbar^2$, where a is the constant in the expression for the harmonic potential $V = \frac{1}{2}ax^2$ and m is the reduced mass of the oscillator. Then, the angular frequency $\omega = \sqrt{a/m}$ is exactly the same as is found for the classical harmonic oscillator.

We are interested in fluctuations about the zero-point energy, that is, the stationary state with $n = 0$. The zero-point energy and Hermite polynomial of order $n = 0$ are

$$E = \frac{1}{2}\hbar\omega \quad \text{and} \quad H_0(\xi) = \text{constant}. \quad (20.14)$$

The first expression is the well-known result that the oscillator has to have finite kinetic energy in the ground state. The underlying cause of this is the need to satisfy Heisenberg's uncertainty principle.

Part of the package of quantum mechanics is that there must be quantum fluctuations in the stationary states, again because of the need to satisfy Heisenberg's uncertainty principle. It is straightforward to work out the variance of the position coordinate x of the oscillator. First, we need to normalise the wavefunction so that

$$\int_{-\infty}^{+\infty} \psi\psi^* dx = 1. \quad (20.15)$$

Since (20.13) is real, it is straightforward to show that

$$\psi = \left(\frac{am}{\hbar^2\pi^2} \right)^{1/8} \exp\left(-\frac{1}{2}\xi^2\right). \quad (20.16)$$

To find the variance of the position coordinate of the oscillator, we form the quantity

$$\langle x^2 \rangle = \int_{-\infty}^{+\infty} \psi\psi^* x^2 dx. \quad (20.17)$$

Carrying out this integral, we find the important result

$$\langle x^2 \rangle = \frac{\hbar}{2\sqrt{am}} = \frac{\hbar}{2\omega m}. \quad (20.18)$$

This result is identical to that derived by Baumann, who sets the particle mass $m = 1$ 'for convenience'. The reason for this is that the analogy with the next part of the calculation is clearest for the case of an oscillator with this mass. In this case, we find

$$\langle x^2 \rangle = \frac{\hbar}{2\omega}. \quad (20.19)$$

These are the fluctuations which must necessarily accompany the zero-point energy of the vacuum fields.

This elementary calculation sweeps an enormous number of technical issues under the carpet. Baumann's clear presentation of the proper calculation, which involves the definition of the action, the introduction of canonical quantisation and of creation and annihilation operators and so on, as well as worrying about the issues of applying the formalism in curved space–time, can be warmly recommended. It is reassuring that his final answer agrees exactly with the results (20.12) and (20.19) for the one-dimensional harmonic oscillator.

20.5.6 The Spectrum of Fluctuations in the Scalar Field

We have almost gone as far as is reasonable without becoming involved in seriously heavy calculation. We need only one more equation – the expression for the evolution of the vacuum fluctuations in the inflationary expansion. The inflaton field is decomposed into a uniform homogeneous background and a perturbed component $\delta\phi$, which is the analogue of the deviation x of the zero-point oscillations of the harmonic oscillator. We need to work out the spectrum of these fluctuations, and so we consider the amplitude of the perturbation associated with a particular wavenumber k , $\delta\phi_k$. If k is taken to be the comoving wavenumber and λ_0 the wavelength at the present epoch, the proper wavelength of the perturbation is $\lambda = a\lambda_0 \sim a/k$ and the proper wavenumber at scale factor a is $k_{\text{prop}} = k/a$. Then the evolution of $\delta\phi_k$ is given by the differential equation

$$\ddot{\delta\phi}_k + 3H\dot{\delta\phi}_k + \frac{k^2}{a^2}\delta\phi_k = 0, \quad (20.20)$$

where $H = \dot{a}/a$. The derivation of this equation is outlined by Baumann, who also warns of the many technical complexities which need to be dealt with in a rigorous treatment.

We can understand the form of (20.20) starting from (11.24) and (11.76) for the density contrast Δ of non-relativistic and relativistic material respectively in the standard world models. For simplicity, let us consider the non-relativistic case (11.24) which is

$$\frac{d^2\Delta}{dt^2} + 2\left(\frac{\dot{a}}{a}\right)\frac{d\Delta}{dt} = \Delta(4\pi G\rho_0 - k^2c_s^2), \quad (20.21)$$

where k is the proper wavenumber and c_s is the speed of sound. The first step is to convert (20.21) into a differential equation with respect to conformal time τ rather than cosmic time t . From (11.25) we find

$$\frac{d^2\Delta}{d\tau^2} + \left(\frac{\dot{a}}{a}\right)\frac{d\Delta}{d\tau} = \Delta(4\pi G\rho_0a^2 - k_c^2c_s^2). \quad (20.22)$$

The next step is to change (20.22) from an equation for Δ into an equation for the perturbation of the gravitational potential $\delta\phi_k$ using (11.16) written in comoving

coordinates:

$$\nabla_c^2 \delta\phi_k = 4\pi G \varrho a^2 \Delta . \quad (20.23)$$

It is a piece of straightforward manipulation, which is given in Bertschinger's excellent review, to show that (20.22) and (20.23), combined with Friedman's equation and its derivative, reduce to the equation

$$\ddot{\delta\phi}_k + 3 \left(\frac{\dot{a}}{a} \right) \delta\dot{\phi}_k + (k_c^2 c_s^2 - 2\kappa) \delta\phi_k = 0 , \quad (20.24)$$

where κ is the curvature of space at the present epoch (Bertschinger, 1996). Since we are interested in flat space solutions, $\kappa = 0$. Furthermore, for matter with equation of state $p = -\varrho c^2$, the speed of sound is the speed of light, which according to Baumann's conventions is set equal to unity, and so we obtain an equation of the form (20.20). A big advantage of Baumann's proper derivation of (20.20) is that it can be applied on superhorizon scales as well as for those within the horizon.

We recognise that (20.20) is the equation of motion for a damped harmonic oscillator. If the 'damping term' $3H\delta\dot{\phi}_k$ is set equal to zero, we find harmonic oscillations, just as in the case of the Jeans analysis of Sect. 11.3. On the other hand, for scales much greater than the radius of the Hubble sphere, $\lambda \gg c/H$, an order of magnitude calculation shows that the damping term dominates and the velocity $\delta\dot{\phi}_k$ tends exponentially to zero, corresponding to the 'freezing' of the fluctuations on superhorizon scales.

We now use the results of Sect. 20.5.5. Both x and $\delta\phi_k$ have zero-point fluctuations in the ground state. In the case of the harmonic oscillator, we found $\langle x^2 \rangle \propto \omega^{-1}$. In exactly the same way, we expect the fluctuations in $\delta\phi_k$ to be inversely proportional to the 'angular frequency' in (20.20), that is,

$$\langle (\delta\phi_k)^2 \rangle \propto \frac{1}{k/a} \propto \lambda , \quad (20.25)$$

recalling that λ is the proper wavelength. Since $\lambda \propto a$, the 'noise-power' $\langle (\delta\phi_k)^2 \rangle$ increases linearly proportional to the scale factor until the wavelength is equal to the dimensions of the Hubble sphere when the noise-power stops growing. Therefore, the power spectrum is given by the power within the horizon when $\lambda = c/H$, that is, when $k = a_* H_*$ where a_* and H_* are the values of the scale factor and Hubble's constant when the wavelength is equal to the radius of the Hubble sphere. Therefore, per unit volume, the primordial power spectrum on superhorizon scales is expected to have the form

$$\langle (\delta\phi_k)^2 \rangle \propto \frac{1}{a_*^3 (k/a_*)} \propto \frac{H_*^2}{k^3} . \quad (20.26)$$

In the simplest approximation, $H_* = H = \text{constant}$ throughout the inflationary era. Now, (20.26) is the power spectrum in Fourier space, and so to convert it into a real space power spectrum, we perform the same type of Fourier inversion as in (14.17)

and (14.18). This amounts to multiplying (20.26) by k^3 :

$$\langle (\delta\phi)^2 \rangle \propto \int \langle (\delta\phi_k)^2 \rangle e^{ik \cdot r} k^2 dk = \int \langle (\delta\phi_k)^2 \rangle \left(\frac{\sin kr}{kr} \right) k^2 dk \approx \langle (\delta\phi_k)^2 \rangle k^3. \quad (20.27)$$

Thus, we obtain the important result

$$\langle (\delta\phi)^2 \rangle \propto H^2. \quad (20.28)$$

At the end of the inflationary expansion, the scalar field is assumed to decay into the types of particles which dominate our Universe at the present epoch, releasing a vast amount of energy which reheats the contents of the Universe to a very high temperature, as illustrated schematically in Fig. 20.1. The final step in the calculation is to relate the fluctuations $\delta\phi$ to the density perturbations in the highly relativistic plasma in the post-inflation era. In the simplest picture, we can think of this transition as occurring abruptly between the era when $p = -\varrho c^2$ and the scale factor increases exponentially with time, as in the de Sitter metric, to that in which the standard relativistic equation of state $p = \frac{1}{3}\varrho c^2$ applies with associated variation of the inertial mass density with cosmic time $\varrho \propto H^2 \propto t^{-2}$ (see (9.7)). Guth and Pi introduced what is known as the time-delay formalism which enables the density perturbations to be related to the perturbations of the inflation potential (Guth and Pi, 1982).

The idea is that the presence of the perturbation in the scalar field $\delta\phi$ results in a time delay

$$\delta t = \frac{\delta\phi}{\dot{\phi}}. \quad (20.29)$$

This should be evaluated at the time the fluctuation in ϕ is frozen in at horizon crossing. At the end of the inflationary era, this time delay translates into a perturbation in the density in the radiation-dominated era. Since $\varrho \propto t^{-2}$ and $H \propto t^{-1}$,

$$\frac{\delta\varrho}{\varrho} \propto H \delta t. \quad (20.30)$$

Since Hubble's constant must be continuous across the discontinuity at the end of the inflationary era and must have roughly the same value at horizon crossing, it follows that

$$\frac{\delta\varrho}{\varrho} \propto \frac{H_*^2}{\dot{\phi}_*}. \quad (20.31)$$

This order of magnitude calculation illustrates how quantum fluctuations in the scalar field ϕ can result in density fluctuations in the matter which all have the same amplitude when they passed through the horizon in the very early Universe. They then remained frozen in until they re-entered the horizon much later in the radiation-dominated era, as illustrated in Fig. 20.2b.

This schematic calculation is only intended to illustrate why the inflationary paradigm is taken so seriously by theorists. It results remarkably naturally in the Harrison–Zeldovich spectrum for the spectrum of primordial perturbations. The above calculation is a gross simplification of the many complexities involved in the full calculation, and these are nicely presented by Baumann (Baumann, 2007).

In the full theory of the origin of the perturbations, the values of the small parameters ϵ and η defined by (20.10) cannot be neglected, and they have important consequences for the spectrum of the perturbations and the existence of primordial gravitational waves. Specifically, the spectral index of the perturbations on entering the horizon is predicted to be

$$n_S - 1 = 2\eta - 6\epsilon . \quad (20.32)$$

Furthermore, tensor perturbations, corresponding to gravitational waves, are also expected to be excited during the inflationary era, and their spectral index is predicted to be

$$n_T - 1 = -2\epsilon , \quad (20.33)$$

where scale invariance corresponds to $n_T = 0$. The tensor-to-scalar ratio is defined as

$$r = \frac{\Delta_T^2}{\Delta_S^2} = 16\epsilon , \quad (20.34)$$

where Δ_T^2 and Δ_S^2 are the power spectra of tensor and scalar perturbations respectively.

These results illustrate why the deviations of the spectral index of the observed perturbations from the value $n_S = 1$ are so important. The fact that the best fit value $n_S = 0.961x_{-0.019}^{+0.018}$ is slightly, but significantly, less than one suggests that there may well be a background of primordial gravitational waves, as was discussed in Sects. 15.4.3 and 15.8.4. These are really very great observational challenges, but they provide a remarkably direct link to processes which may have occurred during the inflationary epoch. To many cosmologists, this would be the ‘smoking gun’ which sets the seal on the inflationary model of the early Universe.

Whilst the above calculation is a considerable triumph for the inflationary scenario, we should remember that there is as yet no physical realisation of the scalar field. Although the scale-invariant spectrum is a remarkable prediction, the amplitude of the perturbation spectrum is model dependent. There are literally hundreds of possible inflationary models depending upon the particular choice of the inflationary potential. We should also not neglect the possibility that there are other sources of perturbations which could have resulted from various types of topological defect, such as cosmic strings, domain walls, textures and so on (Shellard, 2003). Granted all these caveats, the startling success of the inflationary model in accounting for the observed spectrum of fluctuations in the cosmic microwave background radiation has made it the model of choice for studies of the early Universe.

20.6 Baryogenesis

A key contribution of particle physics to studies of the early Universe concerns the baryon-asymmetry problem, a subject referred to as *baryogenesis*. In a prescient paper of 1967, Sakharov enunciated the three conditions necessary to account for the baryon–antibaryon asymmetry of the Universe (Sakharov, 1967). *Sakharov's rules* for the creation of non-zero baryon number from an initially baryon symmetric state are:

- The *baryon number* must be violated;
- C (charge conjugation) and CP (charge conjugation combined with parity) must be violated;
- The asymmetry must be created under *non-equilibrium conditions*.

The reasons for these rules can be readily appreciated from simple arguments (Kolb and Turner, 1990). Concerning the first rule, it is evident that, if the baryon asymmetry developed from a symmetric high temperature state, the baryon number must have been violated at some stage – otherwise, the baryon asymmetry would have to be built into the model from the very beginning. The second rule is necessary in order to ensure that a net baryon number is created, even in the presence of interactions which violate baryon conservation. The third rule is necessary because baryons and antibaryons have the same mass and so, thermodynamically, they would have the same abundances in thermodynamic equilibrium, despite the violation of baryon number and C and CP invariance.

There is evidence that all three rules can be satisfied in the early Universe from a combination of theoretical ideas and experimental evidence from particle physics. Thus, baryon number violation is a generic feature of grand unified theories which unify the strong and electroweak interactions – the same process is responsible for the predicted instability of the proton. C and CP violation have been observed in the decay of the neutral K^0 and \bar{K}^0 mesons. The K^0 meson should decay symmetrically into equal numbers of particles and antiparticles but, in fact, there is a slight preference for matter over antimatter, at the level of 10^{-3} , very much greater than the degree of asymmetry necessary for baryogenesis, $\sim 10^{-8}$. The need for departure from thermal equilibrium follows from the same type of reasoning which led to the primordial synthesis of the light elements (Sects. 10.3 and 10.6). As in that case, so long as the timescales of the interactions which maintained the various constituents in thermal equilibrium were less than the expansion timescale, the number densities of particles and antiparticles of the same mass would be the same. In thermodynamic equilibrium, the number densities of different species did not depend upon the cross-sections for the interactions which maintain the equilibrium. It is only after decoupling, when non-equilibrium abundances were established, that the number densities depended upon the specific values of the cross-sections for the production of different species.

In a typical baryogenesis scenario, the asymmetry is associated with some very massive boson and its antiparticle, X, \bar{X} , which are involved in the unification of the strong and electroweak forces and which can decay into final states which

have different baryon numbers. Kolb and Turner provided a clear description of the principles by which the observed baryon asymmetry can be generated at about the epoch of grand unification or soon afterwards, when the very massive bosons can no longer be maintained in equilibrium (Kolb and Turner, 1990). Although the principles of the calculations are well defined, the details are not understood, partly because the energies at which they are likely to be important are not attainable in laboratory experiments, and partly because predicted effects, such as the decay of the proton, have not been observed. Thus, although there is no definitive evidence that this line of reasoning is secure, well-understood physical processes of the type necessary for the creation of the baryon–antibaryon asymmetry exist. The importance of these studies goes well beyond their immediate significance for astrophysical cosmology. As Kolb and Turner remark,

... in the absence of direct evidence for proton decay, baryogenesis may provide the strongest, albeit indirect, evidence for some kind of unification of the quarks and the leptons.

20.7 The Planck Era

Enormous progress has been made in understanding the types of physical processes necessary to resolve the basic problems of cosmology, but it is not clear how independent evidence for them can be found. The methodological problem with these ideas is that they are based upon extrapolations to energies vastly exceeding those which can be tested in terrestrial laboratories. Cosmology and particle physics come together in the early Universe and they bootstrap their way to a self-consistent solution. This may be the best that we can hope for, but it would be preferable to have independent constraints upon the theories.

A representation of the evolution of the Universe from the Planck era to the present day is shown in Fig. 20.3. The *Planck era* is that time in the very remote past when the energy densities were so great that a quantum theory of gravity is needed. On dimensional grounds, this era must have occurred when the Universe was only about $t_{\text{Pl}} \sim (hG/c^5)^{1/2} \sim 10^{-43}$ s old. Despite enormous efforts on the part of theorists, there is no quantum theory of gravity and so we can only speculate about the physics of these extraordinary eras.

Being drawn on a logarithmic scale, Fig. 20.2 encompasses the evolution of the whole of the Universe, from the Planck area at $t \sim 10^{-43}$ s to the present age of the Universe which is about 4×10^{17} s or 13.5×10^9 years old. Halfway up the diagram, from the time when the Universe was only about 1 ms old to the present epoch, we can be reasonably confident that the Big Bang scenario is the most convincing framework for astrophysical cosmology.

At times earlier than about 1 ms, we quickly run out of known physics. This has not discouraged theorists from making bold extrapolations across the huge gap from 10^{-3} s to 10^{-43} s using the current understanding of particle physics and concepts from string theories. Some impression of the types of thinking involved in these

studies can be found in the ideas expounded in the excellent volume *The Future of Theoretical Physics*, celebrating the 60th birthday of Stephen Hawking (Gibbons et al., 2003). Maybe many of these ideas will turn out to be correct, but there must be some concern that some fundamentally new physics will emerge at higher and higher energies before we reach the GUT era at $t \sim 10^{-36}$ s and the Planck era at $t \sim 10^{-43}$ s. This is why the particle physics experiments to be carried with the Large Hadron Collider at CERN are of such importance for astrophysics and cosmology, as well as for particle physics. It is fully expected that definite evidence will be found for the Higgs' boson. In addition, there is the possibility of discovering new types of particles, such as the lightest supersymmetric particle or new massive ultra-weakly interacting particles, as the accessible range of particle energies increases from about 100 GeV to 1 TeV. These experiments should provide clues to the nature of physics beyond the standard model of particle physics and will undoubtedly feed back into understanding of the physics of the early Universe.

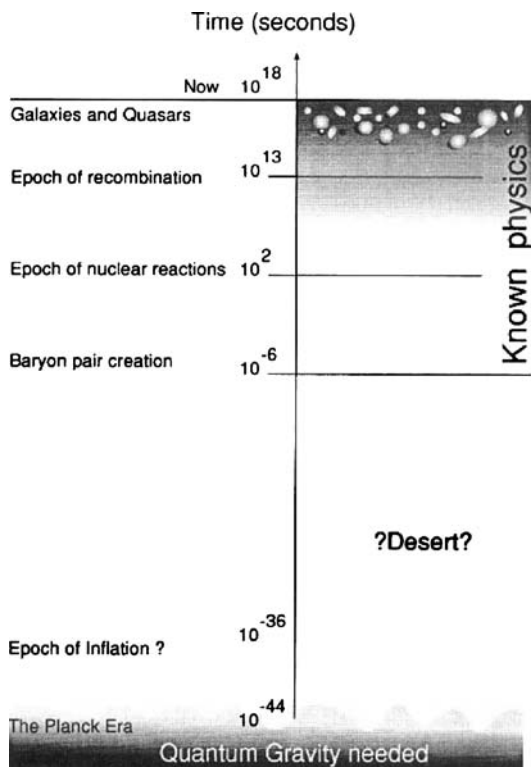


Fig. 20.3. Schematic diagram illustrating the evolution of the Universe from the Planck era to the present time. The shaded area to the right of the diagram indicates the regions of known physics

It is certain that at some stage a quantum theory of gravity is needed which may help resolve the problems of singularities in the early Universe. The singularity theorems of Penrose and Hawking show that, according to classical theories of gravity under very general conditions, there is inevitably a physical singularity at the origin of the Big Bang, that is, as $t \rightarrow 0$, the energy density of the Universe tends to infinity. However, it is not clear that the actual Universe satisfies the various energy conditions required by the singularity theorems, particularly if the negative pressure equation of state $p = -\rho c^2$ holds true in the very early Universe. All these considerations show that new physics is needed if we are to develop a convincing physical picture of the very early Universe.

References

- Aaronson, M. and Mould, J. (1983). A distance scale from the infrared magnitude/H I velocity-width relation: IV. The morphological type dependence and scatter in the relation; the distances to nearby groups, *Astrophysical Journal*, **265**, 1–17.
- Abell, G.O. (1958). The distribution of rich clusters of galaxies, *Astrophysical Journal Supplement*, **3**, 221–288.
- Abell, G.O. (1962). Membership of clusters of galaxies, in *Problems of Extragalactic Research*, ed. McVittie, G.C., pp. 213–238. New York: Macmillan.
- Abell, G.O., Corwin Jr, H.G., and Olowin, R.P. (1989). A catalogue of rich clusters of galaxies, *Astrophysical Journal Supplement*, **70**, 1–138.
- Abraham, R.G., Tanvir, N.R., Santiago, B., Ellis, R.S., Glazebrook, K., and van den Bergh, S. (1996). Galaxy morphology to $I = 25$ mag in the Hubble Deep Field, *Monthly Notices of the Royal Astronomical Society*, **279**, L47–L52.
- Adelberger, K.L. and Steidel, C.C. (2000). Multiwavelength observations of dusty star formation at low and high redshift, *Astrophysical Journal*, **544**, 218–241.
- Afonso, C., Albert, J.N., and 40 authors (2003). Limits on galactic dark matter with 5 years of EROS SMC data, *Astronomy and Astrophysics*, **400**, 951–956.
- Aharonian, F., Akhperjanian, A.G., Bazer-Bachi, A.R., Beilicke, M., Benbow, W., Berge, D., Bernlöhr, K., Boisson, C., Bolz, O., Borrel, V., Braun, I., Breitling, F., Brown, A.M., Chadwick, P.M., Chounet, L.-M., Cornils, R., Costamante, L., Degrange, B., Dickinson, H.J., Djannati-Ataï, A., Drury, L.O., Dubus, G., Emmanoulopoulos, D., Espigat, P., Feinstein, F., Fontaine, G., Fuchs, Y., Funk, S., Gallant, Y.A., Giebels, B., Gillessen, S., Glicenstein, J.F., Goret, P., Hadjichristidis, C., Hauser, D., Hauser, M., Heinzelmann, G., Henri, G., Hermann, G., Hinton, J.A., Hofmann, W., Holleran, M., Horns, D., Jacholkowska, A., de Jager, O.C., Khélifi, B., Klages, S., Komin, N., Konopelko, A., Latham, I.J., Le Gallou, R., Lemière, A., Lemoine-Goumard, M., Leroy, N., Lohse, T., Martin, J.M., Martineau-Huynh, O., Marcowith, A., Masterson, C., McComb, T.J.L., de Naurois, M., Nolan, S.J., Noutsos, A., Orford, K.J., Osborne, J.L., Ouchrif, M., Panter, M., Pelletier, G., Pita, S., Pühlhofer, G., Punch, M., Raubenheimer, B.C., Raue, M., Raux, J., Rayner, S.M., Reimer, A., Reimer, O., Ripken, J., Rob, L., Rolland, L., Rowell, G., Sahakian, V., Saugé, L., Schlenker, S., Schlickeiser, R., Schuster, C., Schwanke, U., Siewert, M., Sol, H., Spangler, D., Steenkamp, R., Stegmann, C., Tavernet, J.-P., Terrier, R., Théoret, C.G., Tluczykont, M., van Eldik, C., Vasileiadis, G., Venter, C., Vincent, P., Völk, H.J., and Wagner, S.J.

- (2006). A low level of extragalactic background light as revealed by γ -rays from blazars, *Nature*, **440**, 1018–1021.
- Akerib, D.S., Attisha, M.J., Bailey, C.N., Baudis, L., Bauer, D.A., Brink, P.L., Brusov, P.P., Bunker, R., Cabrera, B., Caldwell, D.O., Chang, C.L., Cooley, J., Crisler, M.B., Cushman, P., Daal, M., Dixon, R., Dragowsky, M.R., Driscoll, D.D., Duong, L., Ferril, R., Filippini, J., Gaitskell, R.J., Golwala, S.R., Grant, D.R., Hennings-Yeomans, R., Holmgren, D., Huber, M.E., Kamat, S., Leclercq, S., Lu, A., Mahapatra, R., Mandic, V., Meunier, P., Mirabolfathi, N., Nelson, H., Nelson, R., Ogburn, R.W., Perera, T.A., Pyle, M., Ramberg, E., Rau, W., Reisetter, A., Ross, R.R., Sadoulet, B., Sander, J., Savage, C., Schnee, R.W., Seitz, D.N., Serfass, B., Sundqvist, K.M., Thompson, J.-P.F., Wang, G., Yellin, S., Yoo, J., and Young, B.A. (2006). Limits on spin-independent interactions of weakly interacting massive particles with nucleons from the two-tower run of the cryogenic dark matter search, *Physical Review Letters*, **96**, 011302–+.
- Albrecht, A. and Steinhardt, P. (1982). Cosmology for grand unified theories with radiatively induced symmetry breaking, *Physical Review Letters*, **48**, 1220–1223.
- Alcock, C., Akerlof, C.W., Allsman, R.A., Axelrod, T.S., Bennett, D.P., Chan, S., Cook, K.H., Freeman, K.C., Griest, K., Marshall, S.L., Park, H.-S., Perlmutter, S., Peterson, B.A., Pratt, M.R., Quinn, P.J., Rogers, A.W., Stubbs, C.W., and Sutherland, W. (1993a). Possible gravitational microlensing of a star in the Large Magellanic Cloud, *Nature*, **365**, 621–623.
- Alcock, C., Allsman, R.A., Axelrod, T.S., Bennett, D.P., Cook, K.H., Park, H.-S., Marshall, S.L., Stubbs, C.W., Griest, K., Perlmutter, S., Sutherland, W., Freeman, K.C., Peterson, B.A., Quinn, P.J., and Rogers, A.W. (1993b). The MACHO Project – a Search for the Dark Matter in the Milky-Way, in *Sky Surveys: Protostars to Protogalaxies*, ed. Soifer, T., pp. 291–296. San Francisco: Astronomical Society of the Pacific Conference Series.
- Alcock, C., Allsman, R.A., Alves, D.R., Axelrod, T.S., Becker, A.C., Bennett, D.P., Cook, K.H., Dalal, N., Drake, A.J., Freeman, K.C., Geha, M., Griest, K., Lehner, M.J., Marshall, S.L., Minniti, D., Nelson, C.A., Peterson, B.A., Popowski, P., Pratt, M.R., Quinn, P.J., Stubbs, C.W., Sutherland, W., Tomaney, A.B., Vandehei, T., and Welch, D. (2000). The MACHO Project: microlensing results from 5.7 years of Large Magellanic Cloud observations, *Astrophysical Journal*, **542**, 281–307.
- Aliu, E., Andringa, S., Aoki, S., and colleagues (2005). Evidence for muon neutrino oscillation in an accelerator-based experiment, *Physical Review Letters*, **94**(8), 081802–+.
- Alpher, R.A. and Herman, R.C. (1948). Evolution of the Universe, *Nature*, **162**, 774–775.
- Alpher, R.A. and Herman, R.C. (1950). Theory of the origin and relative distribution of the elements, *Reviews of Modern Physics*, **22**, 153–212.
- Anders, E. (1963). Meteorite ages, in *The Moon, Meteorites and Comets – The Solar System IV*, eds. Middelhurst, B.M. and Kuiper, G.P., pp. 402–495. Chicago: University of Chicago Press.

- Aragòn-Salamanca, A., Ellis, R.S., Couch, W.J., and Carter, D. (1993). Evidence for systematic evolution in the properties of galaxies in distant clusters, *Monthly Notices of the Royal Astronomical Society*, **262**, 764–794.
- Arp, H.C. (1966). *Atlas of Peculiar Galaxies*. Pasadena: California Institute of Technology.
- Arp, H.C., Madore, B.F., and Roberton, W.E. (1987). *A Catalogue of Southern Peculiar Galaxies and Associations*. Cambridge: Cambridge University Press.
- Baade, W. (1926). Über eine Möglichkeit, die Pulsationstheorie der δ -Cephei-Veränderlichen zu Prüfen (On a Possible Method of Testing the Pulsation Theory of the Variations of δ -Cephei), *Astronomische Nachrichten*, **228**, 359–362.
- Babbedge, T.S.R., Rowan-Robinson, M., Vaccari, M., Surace, J.A., Lonsdale, C.J., Clements, D.L., Fang, F., Farrah, D., Franceschini, A., Gonzalez-Solares, E., Hatziminaoglou, E., Lacey, C.G., Oliver, S., Onyett, N., Pérez-Fournon, I., Polletta, M., Pozzi, F., Rodighiero, G., Shupe, D.L., Siana, B., and Smith, H.E. (2006). Luminosity functions for galaxies and quasars in the Spitzer Wide-area Infrared Extragalactic Legacy Survey, *Monthly Notices of the Royal Astronomical Society*, **370**, 1159–1180.
- Bahcall, N. (1997). Dark matter, in *Critical Dialogues in Cosmology*, ed. Turok, N., pp. 221–232. Singapore: World Scientific.
- Bahcall, N.A. (1977). Clusters of galaxies, *Annual Review of Astronomy and Astrophysics*, **15**, 505–540.
- Bahcall, N.A. (1988). Large-scale structure in the Universe indicated by galaxy clusters, *Annual Review of Astronomy and Astrophysics*, **26**, 631–686.
- Bahcall, N.A. (2000). Clusters and cosmology, *Physics Reports*, **333**, 233–244.
- Bahcall, N.A., Dong, F., Hao, L., Bode, P., Annis, J., Gunn, J.E., and Schneider, D.P. (2003a). The richness-dependent cluster correlation function: early Sloan Digital Sky Survey Data, *Astrophysical Journal*, **599**, 814–819.
- Bahcall, N.A., McKay, T.A., Annis, J., Kim, R.S.J., Dong, F., Hansen, S., Goto, T., Gunn, J.E., Miller, C., Nichol, R.C., Postman, M., Schneider, D., Schroeder, J., Voges, W., Brinkmann, J., and Fukugita, M. (2003b). A merged catalog of clusters of galaxies from early Sloan Digital Sky Survey data, *Astrophysical Journal Supplement*, **148**, 243–274.
- Bajtlik, S., Duncan, R.C., and Ostriker, J.P. (1988). Quasar ionization of Lyman-alpha clouds – the proximity effect, a probe of the ultraviolet background at high redshift, *Astrophysical Journal*, **327**, 570–583.
- Baldry, I.K., Glazebrook, K., Brinkmann, J., Ivezić, Z., Lupton, R.H., Nichol, R.C., and Szalay, A. (2004). Quantifying the bimodal color-magnitude distribution of galaxies, *Astrophysical Journal*, **600**, 681–694.
- Baldry, I.K., Glazebrook, K., Budavári, T., Eisenstein, D.J., Annis, J., Bahcall, N.A., Blanton, M.R., Brinkmann, J., Csabai, I., Heckman, T.M., Lin, H., Loveday, J., Nichol, R.C., and Schneider, D.P. (2005). The Sloan Digital Sky Survey u-band Galaxy Survey: luminosity functions and evolution, *Monthly Notices of the Royal Astronomical Society*, **358**, 441–456.

- Barcons, X. and Fabian, A.C. (1989). The small-scale autocorrelation function of the X-ray background, *Monthly Notices of the Royal Astronomical Society*, **237**, 119–127.
- Bardeen, J.M. (1980). Gauge-invariant cosmological perturbations, *Physical Review D*, **22**, 1882–1905.
- Bardeen, J.M., Bond, J.R., Kaiser, N., and Szalay, A.S. (1986). The statistics of peaks in Gaussian random fields, *Astrophysical Journal*, **304**, 15–61.
- Barger, A.J., Cowie, L.L., Smail, I., Ivison, R.J., Blain, A.W., and Kneib, J.-P. (1999). Redshift distribution of the faint submillimeter galaxy population, *Astronomical Journal*, **117**, 2656–2665.
- Barkats, D., Bischoff, C., Farese, P., Fitzpatrick, L., Gaier, T., Gundersen, J.O., Hedman, M.M., Hyatt, L., McMahon, J.J., Samtleben, D., Staggs, S.T., Vandervlinde, K., and Winstein, B. (2005). First measurements of the polarization of the cosmic microwave background radiation at small angular scales from CAPMAP, *Astrophysical Journal Letters*, **619**, L127–L130.
- Barnes, J. and Efstathiou, G. (1987). Angular momentum from tidal torques, *Astrophysical Journal*, **319**, 575–600.
- Barnes, J. and Hernquist, L. (1996). Transformations of galaxies. II. Gasdynamics in merging disk galaxies, *Astrophysical Journal*, **471**, 115–142.
- Barrow, J. and Tipler, F. (1986). *The Anthropic Cosmological Principle*. Oxford: Oxford University Press.
- Batuski, D.J., Bahcall, N.A., Olowin, R.P., and Burns, J.O. (1989). The distribution of clusters in the Southern ACO Catalog, *Astrophysical Journal*, **341**, 599–610.
- Baugh, C.M. (2006). A primer on hierarchical galaxy formation: the semi-analytical approach, *Reports of Progress in Physics*, **69**, 3101–3156.
- Baumann, D. (2007). On the quantum origin of structure in the inflationary universe, See <http://www.princeton.edu/~dbaumann/inflation.pdf>.
- Bautz, L. and Morgan, W.W. (1970). On the classification of the forms of clusters of galaxies, *Astrophysical Journal Letters*, **162**, L149–L153.
- Beaver, E., Burbidge, M., Cohen, R., Junkkarinen, V., Lyons, R., and Rosenblatt, E. (1992). Spectroscopy of QSOs with the Faint Object Spectrograph, in *Science with the Hubble Space Telescope*, eds. Benvenuti, P. and Schreier, E.J., pp. 53–60.
- Bechtold, J., Weymann, R.J., Lin, Z., and Malkan, M.A. (1987). The integrated ultraviolet radiation field from QSOs, *Astrophysical Journal*, **315**, 180–197.
- Beck, R., Brunetti, G., and Feretti, L. (2006). The origin and evolution of cosmic magnetism, in *Astronomische Nachrichten*, eds. Beck, R., Brunetti, G., and Feretti, L., volume 327, pp. 385–639. Weinheim: Wiley Interscience.
- Becker, R., Fan, X., and 29 authors (2001). Evidence for reionisation at $Z \sim 6$: detection of a Gunn–Peterson trough in a $Z = 6.28$ quasar, *Astronomical Journal*, **122**, 2850–2857.
- Beckwith, S.V.W., Stiavelli, M., Koekemoer, A.M., Caldwell, J.A.R., Ferguson, H.C., Hook, R., Lucas, R.A., Bergeron, L.E., Corbin, M., Jogee, S., Panagia, N., Robberto, M., Royle, P., Somerville, R.S., and Sosey, M. (2006). The Hubble Ultra Deep Field, *Astronomical Journal*, **132**, 1729–1755.

- Bell, E.F., McIntosh, D.H., Katz, N., and Weinberg, M.D. (2003). The optical and near-infrared properties of galaxies: I. Luminosity and stellar mass functions, *Astrophysical Journal Supplement Series*, **149**, 289–312.
- Bender, R., Burstein, D., and Faber, S.M. (1993). Dynamically hot galaxies: II. Global stellar populations, *Astrophysical Journal*, **411**, 153–169.
- Bennett, C., Halpern, M., Hinshaw, G., Jarosik, N., Kogut, A., Limon, M., Meyer, S., Page, L., Spergel, D., Tucker, G., Wollack, E., Wright, E., Barnes, C., Greason, M., Hill, R., Komatsu, E., Nolta, M., Odegard, N., Peiris, H., Verde, L., and Weiland, J. (2003). First-year Wilkinson Microwave Anisotropy Probe (WMAP) observations: preliminary maps and basic results, *Astrophysical Journal Supplement Series*, **148**, 1–27.
- Bennett, C.L., Banday, A.J., Gorski, K.M., Hinshaw, G., Jackson, P., Koegstra, P., Kogut, A., Smoot, G.F., Wilkinson, D.T., and Wright, E.L. (1996). Four-year COBE DMR cosmic microwave background observations: maps and basic results, *Astrophysical Journal*, **464**, L1–L4.
- Benson, A.J., Frenk, C.S., Baugh, C.M., Cole, S., and Lacey, C.G. (2001). The clustering evolution of the galaxy distribution, *Monthly Notices of the Royal Astronomical Society*, **327**, 1041–1056.
- Benson, B.A., Church, S.E., Ade, P.A.R., Bock, J.J., Ganga, K.M., Henson, C.N., and Thompson, K.L. (2004). Measurements of Sunyaev–Zel'dovich effect scaling relations for clusters of galaxies, *Astrophysical Journal*, **617**, 829–846.
- Bergeron, J. (1988). Properties of the heavy-element absorption systems, in *QSO Absorption Lines: Probing the Universe*, eds. Blades, J., Turnshek, D., and Norman, C., pp. 127–143. Cambridge: Cambridge University Press.
- Bergeron, J. (2006). Cosmic star formation history: high redshift galaxies and black holes, in *Scientific Requirements for Extremely Large Telescopes: IAU Symposium No. 232*, eds. Whitelock, P., Dennefeld, M., and Leibundgut, B., pp. 159–170. Cambridge: Cambridge University Press.
- Bernstein, G., Fischer, P., Tyson, J.A., and Rhee, G. (1997). Improved parameters and new lensed features for Q0957+561 from WFPC2 imaging, *Astrophysical Journal*, **483**, L79–L82.
- Bernstein, J. and Feinberg, G. (1986). *Cosmological Constants: Papers in Modern Cosmology*. New York: Columbia University Press.
- Berry, M. (1989). *Principles of Cosmology and Gravitation*. Bristol: Adam Hilger.
- Bertola, F., Bettoni, D., Danziger, J., Sadler, E., Spark, L., and de Zeeuw, T. (1991). Testing the gravitational field in elliptical galaxies: NGC 5077, *Astrophysical Journal*, **373**, 369–390.
- Bertola, F. and Capaccioli, M. (1975). Dynamics of early type galaxies: I. The rotation curve of the elliptical galaxy NGC 4697, *Astrophysical Journal*, **200**, 439–445.
- Bertola, F. and Galletta, G. (1979). Ellipticity and twisting of isophotes in elliptical galaxies, *Astronomy and Astrophysics*, **77**, 363–365.
- Bertotti, B., Iess, L., and Tortora, P. (2003). A Test of general relativity using radio links with the Cassini spacecraft, *Nature*, **425**, 374–376.

- Bertschinger, E. (1996). Cosmological dynamics, in *Cosmology and Large Scale Structure: Proceedings of the “Les Houches Ecole d’Ete de Physique Theorique”*, eds. Schaeffer, R., Silk, J., Spiro, M., and Zinn-Justin, J., pp. 273–346. Amsterdam: Elsevier.
- Best, P.N., Longair, M.S., and Röttrung, H.J.A. (1996). Evolution of the aligned structures in $z \sim 1$ radio galaxies, *Monthly Notices of the Royal Astronomical Society*, **280**, L9–L12.
- Best, P.N., Longair, M.S., and Röttrung, H.J.A. (1998). HST, radio and infrared observations of 28 3CR radio galaxies at redshift z approximately equal to 1: II. Old stellar populations in central cluster galaxies, *Monthly Notices of the Royal Astronomical Society*, **295**, 549–567.
- Best, P.N., Longair, M.S., and Röttrung, H.J.A. (2000). Ionization, shocks and evolution of the emission-line gas of distant 3CR radio galaxies, *Monthly Notices of the Royal Astronomical Society*, **311**, 23–36.
- Biermann, L. (1950). On the Origin of Magnetic Fields on Stars and in Interstellar Space, *Zeitschrift für Naturforschung*, **5a**, 65–71.
- Binggeli, B., Sandage, A., and Tammann, A. (1988). The luminosity function of galaxies, *Annual Review of Astronomy and Astrophysics*, **26**, 509–560.
- Binggeli, B., Tammann, G.A., and Sandage, A. (1987). Studies of the Virgo Cluster: VI. Morphological and kinematical structure of the Virgo Cluster, *Astronomical Journal*, **94**, 251–277.
- Binney, J. and Merrifield, M. (1998). *Galactic Astronomy*. Princeton: Princeton University Press.
- Binney, J. and Tremaine, S. (1987). *Galactic Dynamics*. Princeton: Princeton University Press.
- Birkinshaw, M. (1990). Observations of the Sunyaev–Zeldovich effect, in *The Cosmic Microwave Background: 25 Years Later*, eds. Mandolesi, N. and Vittorio, N., pp. 77–94. Dordrecht: Kluwer.
- Blain, A.W., Ivison, R.J., and Smail, I. (1998). Observational limits to source confusion in the millimetre/submillimetre waveband, *Monthly Notices of the Royal Astronomical Society*, **296**, L29–L33.
- Blain, A.W. and Longair, M.S. (1993). Sub-millimetre cosmology, *Monthly Notices of the Royal Astronomical Society*, **264**, 509–521.
- Blain, A.W. and Longair, M.S. (1996). Observing strategies for blank-field surveys in the sub-millimetre waveband, *Monthly Notices of the Royal Astronomical Society*, **279**, 847–858.
- Blandford, R.D. and Narayan, R. (1992). Cosmological applications of gravitational lensing, *Annual Review of Astronomy and Astrophysics*, **30**, 311–358.
- Blanton, M., Hogg, D., Bahcall, N., Brinkmann, J., Britton, M., Connolly, A., Csabai, I., Fukugita, M., Loveday, J., Meiksin, A., Munn, J., Nichol, R., Okamura, S., Quinn, T., Schneider, D., Shimasaku, K., Strauss, M., Tegmark, M., Vogeley, M., and Weinberg, D. (2003). The galaxy luminosity function and luminosity density at redshift $z = 0.1$, *Astrophysical Journal*, **592**, 819–838.
- Blanton, M.R., Hogg, D.W., Bahcall, N.A., Baldry, I.K., Brinkmann, J., Csabai, I., Eisenstein, D., Fukugita, M., Gunn, J.E., Ivezić, Ž., Lamb, D.Q., Lupton, R.H.,

- Loveday, J., Munn, J.A., Nichol, R.C., Okamura, S., Schlegel, D.J., Shimasaku, K., Strauss, M.A., Vogeley, M.S., and Weinberg, D.H. (2003). The broadband optical properties of galaxies with redshifts $0.02 \leq z \leq 0.22$, *Astrophysical Journal*, **594**, 186–207.
- Blanton, M.R., Lupton, R.H., Schlegel, D.J., Strauss, M.A., Brinkmann, J., Fukugita, M., and Loveday, J. (2005). The properties and luminosity function of extremely low luminosity galaxies, *Astrophysical Journal*, **631**, 208–230.
- Bludman, S. and Ruderman, M. (1977). Induced cosmological constant expected above the phase transition restoring the broken symmetry, *Physical Review Letters*, **38**, 255–257.
- Blumenthal, G.R., Faber, S.M., Primack, J.R., and Rees, M.J. (1984). Formation of galaxies and large-scale structure with cold dark matter, *Nature*, **311**, 517–525.
- Bochkarev, N.G. and Sunyaev, R.A. (1977). Ionizing background radiation and the hydrogen at the periphery of galaxies, *Soviet Astronomy*, **21**, 542–547.
- Böhringer, H., Schuecker, P., Guzzo, L., Collins, C.A., Voges, W., Schindler, S., Neumann, D.M., Crudace, R.G., De Grandi, S., Chincarini, G., Edge, A.C., MacGillivray, H.T., and Shaver, P. (2001). The ROSAT-ESO flux limited X-ray (REFLEX) galaxy cluster survey. I. The construction of the cluster sample, *Astronomy and Astrophysics*, **369**, 826–850.
- Böhringer, H., Voges, W., Huchra, J.P., McLean, B., Giacconi, R., Rosati, P., Burg, R., Mader, J., Schuecker, P., Simić, D., Komossa, S., Reiprich, T.H., Retzlaff, J., and Trümper, J. (2000). The Northern ROSAT All-Sky (NORAS) Galaxy Cluster Survey: I. X-Ray properties of clusters detected as extended X-ray sources, *Astrophysical Journal Supplement*, **129**, 435–474.
- Boksenberg, A. (1997). Quasar absorption lines: reflections and views, in *The Hubble Space Telescope and the High Redshift Universe*, eds. Tanvir, N., Aragón-Salamanca, A., and Wall, J., pp. 283–294. Singapore: World Scientific.
- Bolte, M. (1997). Globular clusters: old, in *Critical Dialogues in Cosmology*, ed. Turok, N., pp. 156–168. Singapore: World Scientific.
- Bolyai, J. (1832). Appendix: Scientiam Spatii Absolute Veritam Exhibens (Appendix Explaining the Absolutely True Science of Space). published as an appendix to the essay by his father F. Bolyai, *An Attempt to Introduce Studious Youth to the Elements of Pure Mathematics*. Maros Vásárhely, Transylvania.
- Bonamente, M., Joy, M.K., LaRoque, S.J., Carlstrom, J.E., Reese, E.D., and Dawson, K.S. (2006). Determination of the cosmic distance scale from Sunyaev–Zel'dovich effect and Chandra X-ray measurements of high-redshift galaxy clusters, *Astrophysical Journal*, **647**, 25–54.
- Bond, J.R. and Efstathiou, G. (1984). Cosmic background radiation anisotropies in universes dominated by nonbaryonic dark matter, *Astrophysical Journal Letters*, **285**, L45–L48.
- Bond, J.R. and Efstathiou, G. (1991). The formation of cosmic structure with a 17 keV neutrino, *Physics Letters B*, **265**, 245–250.
- Bond, J.R. and Szalay, A.S. (1983). The collisionless damping of density fluctuations in the expanding Universe, *Astrophysical Journal*, **274**, 443–468.
- Bondi, H. (1960). *Cosmology*, 2nd edn. Cambridge: Cambridge University Press.

- Borgani, S. and Guzzo, L. (2001). X-ray clusters of galaxies as tracers of structure in the Universe, *Nature*, **409**, 39–45.
- Bosma, A. (1981). 21-cm line studies of spiral galaxies: II. The distribution and kinematics of neutral hydrogen in spiral galaxies of various morphological types, *Astronomical Journal*, **86**, 1825–1846.
- Bouwens, R.J., Illingworth, G.D., Blakeslee, J.P., (Broadhurst), T., and Franx, M. (2004). Galaxy size evolution at high redshift and surface brightness selection effects: constraints from the Hubble Ultra Deep Field, *Astrophysical Journal*, **611**, L1–L4.
- Bouwens, R.J., Illingworth, G.D., Blakeslee, J.P., and Franx, M. (2006). Galaxies at $z \sim 6$: the UV luminosity function and luminosity density from 506 HUDF, HUDF Parallel ACS Field, and GOODS i-Dropouts, *Astrophysical Journal*, **653**, 53–85.
- Boyle, B.J., Shanks, T., Croom, S.M., Smith, R.J., Miller, L., Loaring, N., and Heymans, C. (2000). The 2dF QSO Redshift Survey: I. The optical luminosity function of quasi-stellar objects, *Monthly Notices of the Royal Astronomical Society*, **317**, 1014–1022.
- Bracessi, A., Formiggini, L., and Gandolfi, E. (1970). Magnitudes, colours and coordinates of 175 ultraviolet excess objects in the field 13^{h} , $+36^{\circ}$, *Astronomy and Astrophysics*, **5**, 264–279. Erratum: *Astronomy and Astrophysics*, **23**, 159.
- Bracewell, R. (1986). *The Fourier Transform and Its Applications*. New York: McGraw-Hill.
- Brainerd, T.G., Blandford, R.D., and Smail, I. (1996). Weak gravitational lensing by galaxies, *Astrophysical Journal*, **466**, 623–637.
- Branch, D. and Patchett, B. (1973). Type I supernovae, *Monthly Notices of the Royal Astronomical Society*, **161**, 71–83.
- Branch, D. and Tammann, G.A. (1992). Type I supernovae as standard candles, *Annual Review of Astronomy and Astrophysics*, **30**, 359–389.
- Brandt, W.N. and Hasinger, G. (2005). Deep extragalactic X-ray surveys, *Annual Review of Astronomy and Astrophysics*, **43**, 827–859.
- Brentjens, M.A. and de Bruyn, A.G. (2006). RM-synthesis of the Perseus cluster, *Astronomische Nachrichten*, **327**, 545–551.
- Bridle, A.H. (1967). The spectrum of the radio background between 13 and 404 MHz, *Monthly Notices of the Royal Astronomical Society*, **136**, 219–240.
- Bruni, M., Dunsby, P.K.S., and Ellis, G.F.R. (1992). Cosmological perturbations and the physical meaning of gauge-invariant variables, *Astrophysical Journal*, **395**, 34–53.
- Bruzual, G. and Charlot, S. (2003). Stellar population synthesis at the resolution of 2003, *Monthly Notices of the Royal Astronomical Society*, **344**, 1000–1028.
- Burbidge, E., Burbidge, G., Fowler, W., and Hoyle, F. (1957). Synthesis of the elements in stars, *Reviews of Modern Physics*, **29**, 547–650.
- Butcher, H. and Oemler, Jr., A. (1978). The evolution of galaxies in clusters: I. ISIT Photometry of C1 0024+1654 and 3C 295, *Astrophysical Journal*, **219**, 18–30.
- Butcher, H. and Oemler, Jr., A. (1984). The evolution of galaxies in clusters: V. A study of populations since $z \approx 0.5$, *Astrophysical Journal*, **285**, 426–438.

- Cappelluti, N., Hasinger, G., Brusa, M., Comastri, A., Zamorani, G., Boehringer, H., Brunner, H., Civano, F., Finoguenov, A., Fiore, F., Gilli, R., Griffiths, R.E., Mainieri, V., Matute, I., Miyaji, T., and Silverman, J. (2007). The XMM-Newton wide-field survey in the COSMOS field II: X-ray data and the $\log N$ - $\log S$, *ArXiv Astrophysics e-prints*.
- Carlstrom, J.E., Joy, M.K., Grego, L., Holder, G.P., Holzapfel, W.L., Mohr, J.J., Patel, S., and Reese, E.D. (2000). Imaging the Sunyaev-Zel'dovich effect, in *Particle Physics and the Universe: Proceedings of Nobel Symposium 198*, eds. Bergström, L., Carlson, P., and Fransson, C., pp. 148–155. Stockholm: Physica Scripta.
- Carroll, S.M., Press, W.H., and Turner, E.L. (1992). The cosmological constant, *Annual Review of Astronomy and Astrophysics*, **30**, 499–542.
- Carswell, R.F. (1988). Properties of the Ly-alpha clouds, in *QSO Absorption Lines: Probing the Universe*, eds. Blades, J.C., Turnshek, D., and Norman, C.A., pp. 91–100. Cambridge: Cambridge University Press.
- Carswell, R.F., Whelan, J.A.J., Smith, M.G., Boksenberg, A., and Tytler, D. (1982). Observations of the spectra of Q0122-380 and Q1101-264, *Monthly Notices of the Royal Astronomical Society*, **198**, 91–110.
- Carter, B. (1974). Large number coincidences and the anthropic principle in cosmology, in *Confrontation of Cosmological Theories with Observational Data, IAU Symposium No. 63*, ed. Longair, M., pp. 291–298. Dordrecht: Reidel.
- Cavaliere, A. (1980). Models of X-ray Emission from Clusters of Galaxies, in *X-ray Astronomy*, eds. Giacconi, R. and Setti, G., pp. 217–237. Dordrecht: Reidel.
- Chaboyer, B. (1998). The age of the Universe, *Physics Reports*, **307**, 23–30.
- Chae, K.-H., Biggs, A.D., Blandford, R.D., Browne, I.W., de Bruyn, A.G., Fassnacht, C.D., Helbig, P., Jackson, N.J., King, L.J., Koopmans, L.V., Mao, S., Marlow, D.R., McKean, J.P., Myers, S.T., Norbury, M., Pearson, T.J., Phillips, P.M., Readhead, A.C., Rusin, D., Sykes, C.M., Wilkinson, P.N., Xanthopoulos, E., and York, T. (2002). Constraints on cosmological parameters from the analysis of the cosmic lens all sky survey radio-selected gravitational lens statistics, *Physical Review Letters*, **89**, 151301–.
- Challinor, A. (2005). Cosmic microwave background anisotropies, in *Lecture Notes in Physics Vol. 653: The Physics of the Early Universe*, ed. Tamvakis, K., vol. 653, pp. 71–+. Berlin: Springer.
- Challinor, A. and Lasenby, A. (1998). Relativistic corrections to the Sunyaev–Zeldovich effect, *Astrophysical Journal*, **499**, 1–6.
- Chambers, K.C., Miley, G.K., and van Breugel, W.J.M. (1987). Alignment of radio and optical orientations in high-redshift radio galaxies, *Nature*, **329**, 604–606.
- Chapman, S.C., Blain, A.W., Smail, I., and Ivison, R.J. (2005). A redshift survey of the submillimeter galaxy population, *Astrophysical Journal*, **622**, 772–796.
- Charlot, S. and Longhetti, M. (2001). Nebular emission from star-forming galaxies, *Monthly Notices of the Royal Astronomical Society*, **323**, 887–903.
- Chluba, J. and Sunyaev, R.A. (2006). Induced two-photon decay of the 2s level and the rate of cosmological hydrogen recombination, *Astronomy and Astrophysics*, **446**, 39–42.

- Chwolson, O. (1924). Über eine mögliche Form fiktiver Doppelsterne, *Astronomische Nachrichten*, **221**, 329–330.
- Cimatti, A., Daddi, E., Renzini, A., Cassata, P., Vanzella, E., Pozzetti, L., Cristiani, S., Fontana, A., Rodighiero, G., Mignoli, M., and Zamorani, G. (2004). Old galaxies in the young Universe, *Nature*, **430**, 184–187.
- Close, L.M., Hall, P.B., Liu, M.C., and Hege, E.K. (1995). Spectroscopic and morphological evidence that IRAS FSC 10214+4724 is a gravitational lens, *Astrophysical Journal*, **452**, L9–L12.
- Cole, S., Percival, W.J., Peacock, J.A., Norberg, P., Baugh, C.M., Frenk, C.S., Baldry, I., Bland-Hawthorn, J., Bridges, T., Cannon, R., Colless, M., Collins, C., Couch, W., Cross, N.J.G., Dalton, G., Eke, V.R., De Propris, R., Driver, S.P., Efstathiou, G., Ellis, R.S., Glazebrook, K., Jackson, C., Jenkins, A., Lahav, O., Lewis, I., Lumsden, S., Maddox, S., Madgwick, D., Peterson, B.A., Sutherland, W., and Taylor, K. (2005). The 2dF Galaxy Redshift Survey: power-spectrum analysis of the final data set and cosmological implications, *Monthly Notices of the Royal Astronomical Society*, **362**, 505–534.
- Coles, P. (2001). Einstein, Eddington and the 1919 Eclipse, in *Historical Development of Modern Cosmology*, eds. Martínez, V.J., Trimble, V., and Pons-Bordeña, M.J., pp. 21–41. San Francisco: ASP Conference Series, No. 252.
- Coles, P. and Lucchin, F. (1995). *Cosmology – the Origin and Evolution of Cosmic Structure*. Chichester: Wiley.
- Coles, P., Melott, A.L., and Shandarin, S.F. (1993). Testing approximations for non-linear gravitational clustering, *Monthly Notices of the Royal Astronomical Society*, **260**, 765–776.
- Colless, M., Dalton, G., Maddox, S., Sutherland, W., Norberg, P., Cole, S., Bland-Hawthorn, J., Bridges, T., Cannon, R., Collins, C., Couch, W., Cross, N., Deely, K., De Propris, R., Driver, S.P., Efstathiou, G., Ellis, R.S., Frenk, C.S., Glazebrook, K., Jackson, C., Lahav, O., Lewis, I., Lumsden, S., Madgwick, D., Peacock, J.A., Peterson, B.A., Price, I., Seaborne, M., and Taylor, K. (2001). The 2dF Galaxy Redshift Survey: spectra and redshifts, *Monthly Notices of the Royal Astronomical Society*, **328**, 1039–1063.
- Colless, M. and Dunn, A.M. (1996). Structure and dynamics of the Coma cluster, *Astrophysical Journal*, **458**, 435–454.
- Connolly, A., Scranton, R., Johnston, D., Dodelson, S., Eisenstein, D., Friedman, J., Gunn, J., Hui, L., Jain, B., Kent, S., Loveday, J., Nichol, R., O’Connell, L., Postman, M., Scoccimarro, R., Sheth, R., Stebbins, A., Strauss, M., Szalay, A., Szapudi, I., Tegmark, M., Vogeley, M., Zehavi, I., Annis, J., Bahcall, N., Brinkmann, J., Csabai, I., Doi, M., Fukugita, M., Hennessy, G., Hindsley, R., Ichikawa, T., Ivezić, Z., Kim, R., Knapp, G., Kunszt, P., Lamb, D., Lee, B., Lupton, R., McKay, T., Munn, J., Peoples, J., Pier, J., Rockosi, C., Schlegel, D., Stoughton, C., Tucker, D., Yanny, B., and York, D. (2002). The angular correlation function of galaxies from early Sloan Digital Sky Survey data, *Astrophysical Journal*, **579**, 42–47.
- Copi, C.J., Davis, A.N., and Krauss, L.M. (2004). New nucleosynthesis constraint on the variation of G, *Physical Review Letters*, **92**, 171301, 1–3.

- Corbelli, E. and Salpeter, E.E. (1993). Sharp HI edges in the outskirts of disk galaxies, *Astrophysical Journal*, **419**, 104–110.
- Costa, E., Frontera, F., Heise, J., Feroci, M., in 't Zand, J., Fiore, F., Cinti, M.N., dal Fiume, D., Nicastro, L., Orlandini, M., Palazzi, E., Rapisarda, M., Zavattini, G., Jager, R., Parmar, A., Owens, A., Molendi, S., Cusumano, G., Maccarone, M.C., Giarrusso, S., Coletta, A., Antonelli, L.A., Giommi, P., Muller, J.M., Piro, L., and Butler, R.C. (1997). Discovery of an X-ray afterglow associated with the gamma-ray burst of 28 February 1997, *Nature*, **387**, 783–785.
- Côté, P., McLaughlin, D.E., Cohen, J.G., and Blakeslee, J.P. (2003). Dynamics of the globular cluster system associated with M49 (NGC 4472): cluster orbital properties and the distribution of dark matter, *Astrophysical Journal*, **591**, 850–877.
- Côté, P., McLaughlin, D.E., Hanes, D.A., Bridges, T.J., Geisler, D., Merritt, D., Hesser, J.E., Harris, G.L.H., and Lee, M.G. (2001). Dynamics of the globular cluster system associated with M87 (NGC 4486): II. Analysis, *Astrophysical Journal*, **559**, 828–850.
- Cowan, J.J., Thielemann, F.K., and Truran, J.W. (1991). Radioactive dating of the elements, *Annual Review of Astronomy and Astrophysics*, **29**, 447–497.
- Cowie, L. (1988). Protogalaxies, in *The Post-Recombination Universe*, eds. Kaiser, N. and Lasenby, A.N., pp. 1–18. Dordrecht: Kluwer.
- Cowie, L., Lilly, S., Gardner, J., and McLean, I. (1988). A cosmologically significant population of galaxies dominated by very young star formation, *Astrophysical Journal*, **332**, L29–L32.
- Cowie, L.L., Barger, A.J., and Kneib, J.-P. (2002). Faint submillimeter counts from deep 850 micron observations of the lensing clusters A370, A851, and A2390, *Astronomical Journal*, **123**, 2197–2205.
- Cowie, L.L., Songaila, A., Hu, E.M., and Cohen, J.D. (1996). New insight on galaxy formation and evolution from Keck spectroscopy of the Hawaii deep fields, *Astronomical Journal*, **112**, 839–864.
- Cress, C., Helfand, D., Becker, R., Gregg, M., and White, R. (1996). The angular two-point correlation function for the FIRST Radio Survey, *Astrophysical Journal*, **473**, 7–14.
- Crittenden, R., Bond, R., Davis, R.L., Efstathiou, G., and Steinhardt, P.J. (1993). Imprint of gravitational waves on the cosmic microwave background, *Physical Review Letters*, **71**, 324–327.
- Croom, S.M., Boyle, B.J., Shanks, T., Smith, R.J., Miller, L., Outram, P.J., Loaring, N.S., Hoyle, F., and da Ângela, J. (2005). The 2dF QSO Redshift Survey: XIV. Structure and evolution from the two-point correlation function, *Monthly Notices of the Royal Astronomical Society*, **356**, 415–438.
- Croton, D.J., Farrar, G.R., Norberg, P., Colless, M., Peacock, J.A., Baldry, I.K., Baugh, C.M., Bland-Hawthorn, J., Bridges, T., Cannon, R., Cole, S., Collins, C., Couch, W., Dalton, G., De Propris, R., Driver, S.P., Efstathiou, G., Ellis, R.S., Frenk, C.S., Glazebrook, K., Jackson, C., Lahav, O., Lewis, I., Lumsden, S., Maddox, S., Madgwick, D., Peterson, B.A., Sutherland, W., and Taylor, K. (2005). The 2dF Galaxy Redshift Survey: luminosity functions by density environment

- and galaxy type, *Monthly Notices of the Royal Astronomical Society*, **356**, 1155–1167.
- Dashevsky, V.M. and Zeldovich, Y.B. (1964). Propagation of light in a nonhomogeneous non-flat Universe II, *Astronomicheskii Zhurnal*, **41**, 1071–1074. Translation: (1965), *Soviet Astronomy*, **8**, 854–856.
- Davidsen, A.F. (1993). Far-ultraviolet astronomy on the Astro-1 space shuttle mission, *Science*, **259**, 327–334.
- Davidsen, A.F., Kriss, G.A., and Zheng, W. (1996). Measurement of the opacity of ionized helium in the intergalactic medium, *Nature*, **380**, 47–49.
- Davidson, W. and Davies, M. (1964). Interpretation of the counts of radio sources in terms of a 4-parameter family of evolutionary universes, *Monthly Notices of the Royal Astronomical Society*, **127**, 241–255.
- Davies, R.L., Efstathiou, G., Fall, S.M., Illingworth, G., and Schechter, P.L. (1983). The kinematic properties of faint elliptical galaxies, *Astrophysical Journal*, **266**, 41–57.
- Davis, M., Efstathiou, G., Frenk, C., and White, S.D.M. (1985). The evolution of large-scale structure in a universe dominated by cold dark matter, *Astrophysical Journal*, **292**, 371–394.
- Davis, M., Efstathiou, G., Frenk, C., and White, S.D.M. (1992a). The end of cold dark matter?, *Nature*, **356**, 489–494.
- Davis, M., Geller, M.J., and Huchra, J. (1978). The local mean mass density of the Universe – new methods for studying galaxy clustering, *Astrophysical Journal*, **221**, 1–18.
- Davis, M. and Peebles, P.J.E. (1983). A survey of galaxy redshifts: V. The two-point position and velocity correlations, *Astrophysical Journal*, **267**, 465–482.
- Davis, R.L., Hodges, H.M., Smoot, G.F., Steinhardt, P.J., and Turner, M.S. (1992b). Cosmic microwave background probes models of inflation, *Physical Review Letters*, **69**, 1856–1859.
- Davis, T.M. and Lineweaver, C.H. (2004). Expanding confusion: common misconceptions of cosmological horizons and the superluminal expansion of the universe, *Publications of the Astronomical Society of Australia*, **21**, 97–109.
- de Plaa, J., Kaastra, J.S., Méndez, M., Tamura, T., Bleeker, J.A.M., Peterson, J.R., Paerels, F.B.S., Bonamente, M., and Lieu, R. (2005). The temperature structure in the core of Sérsic 159-03, *Advances in Space Research*, **36**, 601–604.
- de Sitter, W. (1917). On Einstein's theory of gravitation and its astronomical consequences, *Monthly Notices of the Royal Astronomical Society*, **78**, 3–28.
- de Vaucouleurs, G. (1948). Recherches sur les nébuleuses extragalactiques, *Annales d'Astrophysique*, **11**, 247–287.
- de Vaucouleurs, G. (1963). Revised classification of 1500 bright galaxies, *Astrophysical Journal Supplement*, **8**, 31–97.
- de Vaucouleurs, G. (1974). Structure, dynamics and statistical properties of galaxies (invited paper), in *The Formation and Dynamics of Galaxies*, IAU Symposium No. 58, ed. Shakeshaft, J.R., pp. 1–53. Dordrecht: Reidel.

- de Vaucouleurs, G., de Vaucouleurs, A., Corwin Jr., H.G., Buta, R.J., Paturel, G., and Fouque, P. (1991). *Third reference catalogue of bright galaxies: containing information on 23,024 galaxies with reference to papers published between 1913 and 1988*. Berlin: Springer.
- Dekel, A. (1986). Biased galaxy formation, *Comments on Astrophysics*, **11**, 235–256.
- Dekel, A., Burstein, D., and White, S. (1997). Measuring omega, in *Critical Dialogues in Cosmology*, ed. Turok, N., pp. 175–194. Singapore: World Scientific.
- Dekel, A. and Rees, M.J. (1987). Physical mechanisms for biased galaxy formation, *Nature*, **326**, 455–462.
- Dessauges-Zavadsky, M., Prochaska, J.X., DOdorico, S., Calura, F., and Matteucci, F. (2006). A new comprehensive set of elemental abundances in DLAs: II. Data analysis and chemical variation studies, *Astronomy and Astrophysics*, **445**, 93–113.
- Dey, A. (1997). The host galaxies of distant radio sources, in *The Hubble Space Telescope and the High Redshift Universe*, eds. Tanvir, N.R., Aragón-Salamanca, A., and Wall, J.V., pp. 373–376. Singapore: World Scientific.
- Dicke, R. (1961). Dirac's cosmology and Mach's principle, *Nature*, **192**, 440–441.
- Dicke, R. and Peebles, P. (1979). Big Bang cosmology – enigmas and nostrums, in *General Relativity: an Einstein Centenary Survey*, eds. Hawking, S. and Israel, W., pp. 504–517. Cambridge: Cambridge University Press.
- Dickinson, C., Battye, R.A., Carreira, P., Cleary, K., Davies, R.D., Davis, R.J., Genova-Santos, R., Grainge, K., Gutiérrez, C.M., Hafez, Y.A., Hobson, M.P., Jones, M.E., Kneissl, R., Lancaster, K., Lasenby, A., Leahy, J.P., Maisinger, K., Ödman, C., Pooley, G., Rajguru, N., Rebolo, R., Rubiño-Martin, J.A., Saunders, R.D.E., Savage, R.S., Scaife, A., Scott, P.F., Slosar, A., Sosa Molina, P., Taylor, A.C., Titterington, D., Waldram, E., Watson, R.A., and Wilkinson, A. (2004). High-sensitivity measurements of the cosmic microwave background power spectrum with the extended Very Small Array, *Monthly Notices of the Royal Astronomical Society*, **353**, 732–746.
- Dickinson, M. (1997). Clusters of galaxies at $z \geq 1$, in *The Hubble Space Telescope and the High Redshift Universe*, eds. Tanvir, N., Aragón-Salamanca, A., and Wall, J., pp. 207–218. Singapore: World Scientific.
- d'Inverno, R. (1992). *Introducing Einstein's Relativity*. Oxford: Clarendon.
- Disney, M.J. (1976). Visibility of galaxies, *Nature*, **263**, 573–575.
- Djorgovski, S.G. and Davis, M. (1987). Fundamental properties of elliptical galaxies, *Astrophysical Journal*, **313**, 59–68.
- Dodelson, S. (2003). *Modern Cosmolgy*. Amsterdam: Academic.
- Dodelson, S., Gates, E.I., and Turner, M.S. (1996). Cold dark matter, *Science*, **274**, 69–75.
- Doroshkevich, A., Sunyaev, R., and Zeldovich, Y. (1974). The formation of galaxies in Friedmannian universes, in *Confrontation of Cosmological Theories with Observational Data, (IAU Symposium No. 63)*, ed. Longair, M., pp. 213–225. Dordrecht: Reidel.
- Doroshkevich, A., Zeldovich, Y., Sunyaev, R., and Khlopov, M. (1980). Astrophysical Implications of the Neutrino Rest Mass: Part II. The density-perturbation

- spectrum and small-scale fluctuations in the microwave background, *Pis'ma v Astronomicheskii Zhurnal*, **6**, 457–464.
- Dressler, A. (1980). Galaxy morphology in rich clusters – implications for the formation and evolution of galaxies, *Astrophysical Journal*, **236**, 351–365.
- Dressler, A. (1984). The evolution of galaxies in clusters, *Annual Review of Astronomy and Astrophysics*, **22**, 185–222.
- Dressler, A., Lynden-Bell, D., Burstein, D., Davies, R.L., Faber, S.M., Terlevich, R., and Wegner, G. (1987). Spectroscopy and photometry of elliptical galaxies: I. A new distance estimator, *Astrophysical Journal*, **313**, 42–58.
- Dressler, A., Oemler, A.J., Couch, W.J., Smail, I., Ellis, R.G., Barger, A., Butcher, H., Poggianti, B.M., and Sharples, R.M. (1997). Evolution since $z = 0.5$ of the morphology-density relation for clusters of galaxies, *Astrophysical Journal*, **490**, 577–591.
- Dressler, A. and Smail, I. (1997). HST observations of distant clusters: implications for galaxy evolution, in *The Hubble Space Telescope and the High Redshift Universe*, eds. Tanvir, N., Aragón-Salamanca, A., and Wall, J., pp. 185–194. Singapore: World Scientific.
- Driver, S.P., Allen, P.D., Graham, A.W., Cameron, E., Liske, J., Ellis, S.C., Cross, N.J.G., De Propris, R., Phillipps, S., and Couch, W. (2006). The Millennium Galaxy Catalogue: morphological classification and bimodality in the colour-concentration plane, *Monthly Notices of the Royal Astronomical Society*, **368**, 414–434.
- Dunlop, J.S. (1998). Cosmic star-formation and radio source evolution, in *ASSL Vol. 226: Observational Cosmology with the New Radio Surveys*, eds. Bremer, M.N., Jackson, N., and Perez-Fournon, I., pp. 157–164. Dordrecht: Kluwer Academic Publishers.
- Dunlop, J.S. and Peacock, J.A. (1990). The redshift cut-off in the luminosity function of radio galaxies and quasars, *Monthly Notices of the Royal Astronomical Society*, **247**, 19–42.
- Dunlop, J.S., Peacock, J.A., Spinrad, H., Dey, A., Jimenez, R., Stern, D., and Windhorst, R. (1996). A 3.5-Gyr-old galaxy at redshift 1.55, *Nature*, **381**, 581–584.
- Dyer, C.C. and Roeder, R.C. (1972). The distance-redshift relation for universes with no intergalactic medium, *Astrophysical Journal Letters*, **174**, L115–L117.
- Dyer, C.C. and Roeder, R.C. (1973). Distance-redshift relations for universes with some intergalactic medium, *Astrophysical Journal Letters*, **180**, L31–L34.
- Eales, S.A., Rawlings, S., Law-Green, D., Cotter, G., and Lacy, M. (1997). A first sample of faint radio sources with virtually complete Redshifts: I. Infrared images, the Hubble diagram and the alignment effect, *Monthly Notices of the Royal Astronomical Society*, **291**, 593–615.
- Eastman, R.G. and Kirshner, R.P. (1989). Model atmospheres for SN 1987A and the distance to the Large Magellanic Cloud, *Astrophysical Journal*, **347**, 771–793.
- Eddington, A.S. (1916). The kinetic energy of a star cluster, *Monthly Notices of the Royal Astronomical Society*, **76**, 525–528.
- Eddington, A.S. (1926). Diffuse matter in interstellar space, *Proceedings of the Royal Society, A***111**, 424–456.

- Efstathiou, G. (1988). Effects of reionization on microwave background anisotropies, in *Large-scale Motions in the Universe*, eds. Rubin, V. and Coyne, G., pp. 299–319. Princeton: Princeton University Press.
- Efstathiou, G. (1990). Cosmological perturbations, in *Physics of the Early Universe*, eds. Peacock, J.A., Heavens, A.F., and Davies, A.T., pp. 361–463. Edinburgh: SUSSP.
- Efstathiou, G. (1995). High-redshift galaxies: problems and prospects, in *Galaxies in the Young Universe*, eds. Hippelein, H., Meissenheimer, K., and Röser, H.J., pp. 299–314. Berlin: Springer, Lecture Notes in Physics, Vol. 463.
- Efstathiou, G. and Bond, J.R. (1986). Isocurvature cold dark matter fluctuations, *Monthly Notices of the Royal Astronomical Society*, **218**, 103–121.
- Efstathiou, G., Frenk, C.S., White, S.D.M., and Davis, M. (1988). Gravitational clustering from scale-free initial conditions, *Monthly Notices of the Royal Astronomical Society*, **235**, 715–748.
- Efstathiou, G., Lawrence, C., and Tauber, J. (2005). *Planck: The Scientific Programme*. Noordwijk: European Space Agency Publications, ESA-SCI(2005)1.
- Efstathiou, G. and Rees, M.J. (1988). High-redshift quasars in the cold dark matter cosmogony, *Monthly Notices of the Royal Astronomical Society*, **230**, 5P–11P.
- Eguchi, K., Enomoto, S., and 97 authors (2003). First results from Kamland: evidence for reactor anti-neutrino disappearance, *Physical Review Letters*, **90**, id. 021802(1–6).
- Einstein, A. (1915). Die Feldgleichung der Gravitation (The field equations of gravitation), *Sitzungsberichte, Königlich Preussische Akademie der Wissenschaften (Berlin)*, **II**, 844–847.
- Einstein, A. (1916). Die Grundlage der Allgemeinen Relativitätstheorie (Foundation of the General Theory of Relativity), *Annalen der Physik*, **49**, 769–822.
- Einstein, A. (1917). Kosmologische Betrachtungen zur Allgemeinen Relativitätstheorie (Cosmological considerations in the General Theory of Relativity), *Sitzungsberichte, Königlich Preussische Akademie der Wissenschaften (Berlin)*, **I**, 142–152.
- Einstein, A. (1919). Spielen Gravitationsfelder im Aufbau der materiellen Elementarteilchen eine wesentliche Rolle? (Do gravitational fields play a significant role for the structure of elementary particles), *Sitzungsberichte, Königlich Preussische Akademie der Wissenschaften, Part 1*, 349–356.
- Einstein, A. (1922). Bemerkung zu der Arbeit von A. Friedmann “Ueber die Krümmung des Raumes” (Remark on the work of A. Friedmann “On the Curvature of Space”), *Zeitschrift für Physik*, **11**, 326.
- Einstein, A. (1923). Notiz zu der Arbeit von A. Friedmann “Über die Krümmung des Raumes” (A Note on the Work of A. Friedmann “On the Curvature of Space”), *Zeitschrift für Physik*, **16**, 228.
- Einstein, A. (1936). Lens-like action of a star by the deviation of light in the gravitational field, *Science*, **84**, 506–507.
- Eisenstein, D.J. and Hu, W. (1998). Baryonic features in the matter transfer function, *Astrophysical Journal*, **496**, 605–614.

- Eisenstein, D.J., Zehavi, I., Hogg, D.W., Scoccimarro, R., Blanton, M.R., Nichol, R.C., Scranton, R., Seo, H.-J., Tegmark, M., Zheng, Z., Anderson, S.F., Annis, J., Bahcall, N., Brinkmann, J., Burles, S., Castander, F.J., Connolly, A., Csabai, I., Doi, M., Fukugita, M., Frieman, J.A., Glazebrook, K., Gunn, J.E., Hendry, J.S., Hennessy, G., Ivezić, Z., Kent, S., Knapp, G.R., Lin, H., Loh, Y.-S., Lupton, R.H., Margon, B., McKay, T.A., Meiksin, A., Munn, J.A., Pope, A., Richmond, M.W., Schlegel, D., Schneider, D.P., Shimasaku, K., Stoughton, C., Strauss, M.A., SubbaRao, M., Szalay, A.S., Szapudi, I., Tucker, D.L., Yanny, B., and York, D.G. (2005). Detection of the baryon acoustic peak in the large-scale correlation function of SDSS luminous red galaxies, *Astrophysical Journal*, **633**, 560–574.
- Ellis, R.G. (1997). Faint blue galaxies, *Annual Review of Astronomy and Astrophysics*, **35**, 389–443.
- Ellis, R.G., Smail, I., Dressler, A., Couch, W.J., Oemler, A.J., Butcher, H., and Sharples, R.M. (1997). The homogeneity of spheroidal populations in distant clusters, *Astrophysical Journal*, **483**, 582–596.
- Ellis, S.C. and Bland-Hawthorn, J. (2006). GalaxyCount: a JAVA calculator of galaxy counts and variances in multiband wide-field surveys to 28 AB mag, *ArXiv Astrophysics e-prints*.
- Faber, S.M. (1973). Variations in spectral-energy distributions and absorption-line strengths among elliptical galaxies, *Astrophysical Journal*, **179**, 731–754.
- Faber, S.M. and Jackson, R.E. (1976). Velocity dispersions and mass-to-light ratios for elliptical galaxies, *Astrophysical Journal*, **204**, 668–683.
- Fabian, A.C. (1994). Cooling flows in clusters of galaxies, *Annual Review of Astronomy and Astrophysics*, **32**, 277–318.
- Fabian, A.C. and Barcons, X. (1992). The origin of the X-ray background, *Annual Review of Astronomy and Astrophysics*, **30**, 429–456.
- Fabian, A.C., Sanders, J.S., Ettori, S., Taylor, G.B., Allen, S.W., Crawford, C.S., Iwasawa, K., Johnstone, R.M., and Ogle, P.M. (2000). Chandra imaging of the complex X-ray core of the Perseus cluster, *Monthly Notices of the Royal Astronomical Society*, **318**, L65–L68.
- Fabian, A.C., Sanders, J.S., Taylor, G.B., Allen, S.W., Crawford, C.S., Johnstone, R.M., and Iwasawa, K. (2006). A very deep Chandra observation of the Perseus cluster: shocks, ripples and conduction, *Monthly Notices of the Royal Astronomical Society*, **366**, 417–428.
- Fabricant, D.G., Lecar, M., and Gorenstein, P. (1980). X-ray measurements of the mass of M87, *Astrophysical Journal*, **241**, 552–560.
- Fall, S. (1983). Galaxy formation – some comparisons between theory and observation, in *Internal Kinematics and Dynamics of Galaxies: IAU Symposium No. 100*, ed. Athanassoula, E., pp. 391–398. Dordrecht: Reidel.
- Fall, S. (1997). A global perspective on star formation, in *The Hubble Space Telescope and the High Redshift Universe*, eds. Tanvir, N., Aragón-Salamanca, A., and Wall, J., pp. 303–308. Singapore: World Scientific.
- Fall, S.M. and Efstathiou, G. (1980). Formation and rotation of disc galaxies with haloes, *Monthly Notices of the Royal Astronomical Society*, **193**, 189–206.

- Fall, S.M. and Pei, Y.C. (1993). Obscuration of quasars by dust in damped Lyman-alpha systems, *Astrophysical Journal*, **402**, 479–492.
- Fan, X., Hennawi, J.F., Richards, G.T., Strauss, M.A., Schneider, D.P., Donley, J.L., Young, J.E., Annis, J., Lin, H., Lampeitl, H., Lupton, R.H., Gunn, J.E., Knapp, G.R., Brandt, W.N., Anderson, S., Bahcall, N.A., Brinkmann, J., Brunner, R.J., Fukugita, M., Szalay, A.S., Szokoly, G.P., and York, D.G. (2004). A survey of $z \geq 5.7$ quasars in the Sloan Digital Sky Survey: III. Discovery of five additional quasars, *Astronomical Journal*, **128**, 515–522.
- Fan, X., Narayanan, V.K., Lupton, R.H., Strauss, M.A., Knapp, G.R., Becker, R.H., White, R.L., Pentericci, L., Leggett, S.K., Haiman, Z., Gunn, J.E., Ivezić, Ž., Schneider, D.P., Anderson, S.F., Brinkmann, J., Bahcall, N.A., Connolly, A.J., Csabai, I., Doi, M., Fukugita, M., Geballe, T., Grebel, E.K., Harbeck, D., Hennessy, G., Lamb, D.Q., Miknaitis, G., Munn, J.A., Nichol, R., Okamura, S., Pier, J.R., Prada, F., Richards, G.T., Szalay, A., and York, D.G. (2001). A survey of $z \geq 5.8$ quasars in the Sloan Digital Sky Survey: I. Discovery of three new quasars and the spatial density of luminous quasars at $z \sim 6$, *Astronomical Journal*, **122**, 2833–2849.
- Feast, M.W. and Catchpole, R.M. (1997). The cepheid period-luminosity zero-point from HIPPARCOS trigonometrical parallaxes, *Monthly Notices of the Royal Astronomical Society*, **286**, L1–L5.
- Fechner, C., Reimers, D., Kriss, G.A., Baade, R., Blair, W.P., Giroux, M.L., Green, R.F., Moos, H.W., Morton, D.C., Scott, J.E., Shull, J.M., Simcoe, R., Songaila, A., and Zheng, W. (2006). The UV spectrum of HS 1700+6416: II. FUSE observations of the HeII Lyman alpha forest, *Astrophysical Journal*, **455**, 91–106.
- Felten, J. (1977). Study of the luminosity function for field galaxies, *Astronomical Journal*, **82**, 861–878.
- Felten, J. (1985). Galaxy luminosity functions, M/L ratios, and closure of the Universe – numbers and problems, *Comments on Astrophysics*, **11**, 53–67.
- Ferguson, H.C., Dickinson, M., and Williams, R. (2000). The Hubble Deep Fields, *Annual Review of Astronomy and Astrophysics*, **38**, 667–715.
- Fixsen, D., Cheng, E., Gales, J., Mather, J., Shafer, R., and Wright, E. (1996). The cosmic microwave background spectrum from the full COBE FIRAS data set, *Astrophysical Journal*, **473**, 576–587.
- Foley, R.J., Filippenko, A.V., Leonard, D.C., Riess, A.G., Nugent, P., and Perlmutter, S. (2005). A definitive measurement of time dilation in the spectral evolution of the moderate-redshift type 1a Supernova 1997ex, *Astrophysical Journal Letters*, **626**, L11–L14.
- Fomalont, E.B., Kellermann, K.I., Anderson, M.C., Weistroop, D., Wall, J.V., Windhorst, R.A., and Kristian, J.A. (1988). New limits to fluctuations in the cosmic background radiation at 4.86 GHz between 12 and 60 arcsecond resolution, *Astrophysical Journal*, **96**, 1187–1191.
- Forman, W. and Jones, C. (1982). X-ray-imaging observations of clusters of galaxies, *Annual Review of Astronomy and Astrophysics*, **20**, 547–585.

- Fort, B. and Mellier, Y. (1994). Arc(let)s in clusters of galaxies, *Astronomy and Astrophysics Reviews*, **5**, 239–292.
- Frayer, D.T., Fadda, D., Yan, L., Marleau, F.R., Choi, P.I., Helou, G., Soifer, B.T., Appleton, P.N., Armus, L., Beck, R., Dole, H., Engelbracht, C.W., Fang, F., Gordon, K.D., Heinrichsen, I., Henderson, D., Hesselroth, T., Im, M., Kelly, D.M., Lacy, M., Laine, S., Latter, W.B., Mahoney, W., Makovoz, D., Masci, F.J., Morrison, J.E., Moshir, M., Noriega-Crespo, A., Padgett, D.L., Pesenson, M., Shupe, D.L., Squires, G.K., Storrie-Lombardi, L.J., Surace, J.A., Teplitz, H.I., and Wilson, G. (2006). Spitzer 70 and 160 μm observations of the extragalactic First Look Survey, *Astronomical Journal*, **131**, 250–260.
- Freedman, W.L., Madore, B.F., Gibson, B.K., Ferrarese, L., Kelson, D.D., Sakai, S., Mould, J.R., Kennicutt Jr., R.C., Ford, H.C., Graham, J.A., Huchra, J.P., Hughes, S.M.G., Illingworth, G.D., Macri, L.M., and Stetson, P.B. (2001). Final results from the Hubble Space Telescope key project to measure the Hubble constant, *Astrophysical Journal*, **533**, 47–72.
- Freeman, K.C. (1970). On the disks of spiral and S0 galaxies, *Astrophysical Journal*, **160**, 811–830.
- Frenk, C. (1986). Galaxy clustering and the dark-matter problem, *Philosophical Transactions of the Royal Astronomical Society*, **A320**, 517–541.
- Friedman, A.A. (1922). On the Curvature of Space, *Zeitschrift für Physik*, **10**, 377–386.
- Friedman, A.A. (1924). On the possibility of a world with constant negative curvature, *Zeitschrift für Physik*, **12**, 326–332.
- Fukugita, M., Futamase, T., Kasai, M., and Turner, E.L. (1992). Statistical properties of gravitational lenses with a nonzero cosmological constant, *Astrophysical Journal*, **393**, q3–21.
- Furlanetto, S.R., Sokasian, A., and Hernquist, L. (2004). Observing the reionization epoch through 21-centimetre radiation, *Monthly Notices of the Royal Astronomical Society*, **347**, 187–195.
- Gamow, G. (1970). *My World Line*. New York: Viking. The reference to Einstein's admission of 'the greatest blunder of my life' is on p. 44.
- Garnavich, P.M., Kirshner, R.P., Challis, P., Tonry, J., Gilliland, R.L., Smith, R.C., Clocchiatti, A., Diercks, A., Filippenko, A.V., Hamuy, M., Hogan, C.J., Leibundgut, B., Phillips, M.M., Riess, D., Riess, A.G., Schmidt, B.P., Schommer, R.A., Spyromilio, J., Stubbs, C., Suntzeff, N.B., and Wells, L. (1998). Constraints on cosmological models from Hubble Space Telescope observations of high-z supernovae, *Astrophysical Journal Letters*, **493**, L53–L58.
- Gavazzi, R., Treu, T., Rhodes, J.D., Koopmans, L.V.E., Bolton, A.S., Burles, S., Massey, R., and Moustakas, L.A. (2007). The Sloan Lens ACS Survey: IV. The mass density profile of early-type galaxies out to 100 effective radii, *ArXiv Astrophysics e-prints*.
- Ge, J., Bechtold, J., and Black, J. (1997). A new measurement of the cosmic microwave background radiation temperature at $Z = 1.97$, *Astrophysical Journal*, **474**, 67–73.
- Geller, M.J. and Huchra, J.P. (1989). Mapping the Universe, *Science*, **246**, 897–903.

- Geller, M.J. and Postman, M. (1983). First-ranked galaxies in groups, *Astrophysical Journal*, **274**, 31–38.
- Gershtein, S. and Zeldovich, Y. (1966). Rest mass of a muonic neutrino and cosmology, *Pisma v Zhurnal Eksperimentalnoi i Teoreticheskoi Fiziki*, **4**, 174–177.
- Giacconi, R., Gursky, H., Paolini, F.R., and Rossi, B.B. (1962). Evidence for X rays from sources outside the solar system, *Physical Review Letters*, **9**, 439–443.
- Giavalisco, M., Dickinson, M., Ferguson, H.C., Ravindranath, S., Kretchmer, C., Moustakas, L.A., Madau, P., Fall, S.M., Gardner, J.P., Livio, M., Papovich, C., Renzini, A., Spinrad, H., Stern, D., and Riess, A. (2004a). The rest-frame ultraviolet luminosity density of star-forming galaxies at redshifts $z \geq 3.5$, *Astrophysical Journal Letters*, **600**, L103–L106.
- Giavalisco, M., Ferguson, H.C., Koekemoer, A.M., Dickinson, M., Alexander, D.M., Bauer, F.E., Bergeron, J., Biagetti, C., Brandt, W.N., Casertano, S., Cesarsky, C., Chatzichristou, E., Conselice, C., Cristiani, S., Da Costa, L., Dahlen, T., de Mello, D., Eisenhardt, P., Erben, T., Fall, S.M., Fassnacht, C., Fosbury, R., Fruchter, A., Gardner, J.P., Grogin, N., Hook, R.N., Hornschemeier, A.E., Idzi, R., Jogee, S., Kretchmer, C., Laidler, V., Lee, K.S., Livio, M., Lucas, R., Madau, P., Mobasher, B., Moustakas, L.A., Nonino, M., Padovani, P., Papovich, C., Park, Y., Ravindranath, S., Renzini, A., Richardson, M., Riess, A., Rosati, P., Schirmer, M., Schreier, E., Somerville, R.S., Spinrad, H., Stern, D., Stiavelli, M., Strolger, L., Urry, C.M., Vandame, B., Williams, R., and Wolf, C. (2004b). The Great Observatories Origins Deep Survey: initial results from optical and near-infrared imaging, *Astrophysical Journal Letters*, **600**, L93–L98.
- eds. Gibbons, G., Shellard, E., and Rankin, S. (2003). *The Future of Theoretical Physics and Cosmology*. Cambridge: Cambridge University Press.
- Gibbons, G.W. and Hawking, S.W. (1977). Cosmological event horizons, thermodynamics, and particle creation, *Physical Review*, **D15**, 2738–2751.
- eds. Gibbons, G.W., Hawking, S.W., and Siklos, S.T.C. (1983). *The Very Early Universe: Proceedings of the Nuffield Workshop, Cambridge, UK, 21 June–9 July 1982*. Cambridge: Cambridge University Press.
- Gilli, R., Comastri, A., and Hasinger, G. (2007). The synthesis of the cosmic X-ray background in the Chandra and XMM-Newton era, *Astronomy and Astrophysics*, **463**, 79–96.
- Gilmore, G., King, I., and van der Kruit, P.C. (1989). *The Milky Way as a Galaxy: Proceedings of the 19th Advanced Course of the Swiss Society of Astronomy and Astrophysics (SSAA)*. Mill Valley, California: University Science Books. Van der Kruit's analyses of the surface brightness distributions in elliptical and spiral galaxies are contained in Sect. 5.2 (pp. 80–88) and Sect. 12.1 (pp. 257–267).
- Glazebrook, K., Abraham, R.G., McCarthy, P.J., Savaglio, S., Chen, H.-W., Crampton, D., Murowinski, R., Jørgensen, I., Roth, K., Hook, I., Marzke, R.O., and Carlberg, R.G. (2004). A high abundance of massive galaxies 3–6 billion years after the Big Bang, *Nature*, **430**, 181–184.
- Glazebrook, K., Ellis, R.S., Colless, M., Broadhurst, T.J., Allington-Smith, J.R., and Tanvir, N.R. (1995). The morphological identification of the rapidly evolving

- population of faint galaxies, *Monthly Notices of the Royal Astronomical Society*, **275**, L19–L22.
- Goldhaber, G., Groom, D.E., Kim, A., Aldering, G., Astier, P., Conley, A., Deustua, S.E., Ellis, R., Fabbro, S., Fruchter, A.S., Goobar, A., Hook, I., Irwin, M., Kim, M., Knop, R.A., Lidman, C., McMahon, R., Nugent, P.E., Pain, R., Panagia, N., Pennypacker, C.R., Perlmutter, S., Ruiz-Lapuente, P., Schaefer, B., Walton, N.A., and York, T. (2001). Timescale stretch parameterization of type 1a supernova B-band light curves, *Astrophysical Journal*, **558**, 359–368.
- Goobar, A. and Perlmutter, S. (1995). Feasibility of measuring the cosmological constant lambda and mass density omega using type IA supernovae, *Astrophysical Journal*, **450**, 14–18.
- Gott, J.R., Melott, A.L., and Dickinson, M. (1986). The sponge-like topology of large-scale structure in the Universe, *Astrophysical Journal*, **306**, 341–357.
- Govoni, F. (2006). Observations of magnetic fields in regular and irregular clusters, *Astronomische Nachrichten*, **327**, 539–544.
- Gregory, J. (1668). *Geometriae Pars Universalis*. Padua.
- Gregory, P. and Condon, J. (1991). The 87GB catalog of radio sources covering delta between 0 and +75 deg at 4.85 GHz, *Astrophysical Journal Supplement Series*, **75**, 1011–1291.
- Greve, T.R., Bertoldi, F., Smail, I., Neri, R., Chapman, S.C., Blain, A.W., Ivison, R.J., Genzel, R., Omont, A., Cox, P., Tacconi, L., and Kneib, J.-P. (2005). An interferometric CO survey of luminous submillimetre galaxies, *Monthly Notices of the Royal Astronomical Society*, **359**, 1165–1183.
- Gribben, J. and Rees, M. (1989). *Dark Matter, Mankind and Anthropic Cosmology*. New York: Bantam.
- Groth, E. and Peebles, P. (1977). Statistical Analysis of Catalogs of Extragalactic Objects. VII – Two- and Three-point correlation functions for the high-resolution Shane–Wirtanen catalog of galaxies, *Astrophysical Journal*, **217**, 385–405.
- Groth, E. and Peebles, P. (1986). The Shane–Wirtanen counts – observer and time-dependent effects, *Astrophysical Journal*, **310**, 507–517.
- Guenther, D.B., Krauss, L.M., and Demarque, P. (1998). Testing the constancy of the gravitational constant using helioseismology, *Astrophysical Journal*, **498**, 871–876.
- Gunn, J.E. (1978). The Friedmann models and optical observations in cosmology, in *Observational Cosmology: 8th Advanced Course, Swiss Society of Astronomy and Astrophysics, Saas-Fee 1978*, eds. Maeder, A., Martinet, L., and Tammann, G., pp. 1–121. Geneva: Geneva Observatory Publications.
- Gunn, J.E., Hoessel, J.G., Westphal, J.A., Perryman, M.A.C., and Longair, M.S. (1981). Investigations of the optical fields of 3CR radio sources to faint limiting magnitudes: IV. *Monthly Notices of the Royal Astronomical Society*, **194**, 111–123.
- Gunn, J.E. and Peterson, B.A. (1965). On the density of neutral hydrogen in intergalactic space, *Astrophysical Journal*, **142**, 1633–1636.
- Gurvits, L.I., Kellermann, K.I., and Frey, S. (1999). The “angular size – redshift” relation for compact radio structures in quasars and radio galaxies, *Astronomy and Astrophysics*, **342**, 378–388.

- Guth, A. (1981). Inflationary universe: a possible solution to the horizon and flatness problems, *Physical Review*, **D23**, 347–356.
- Guth, A.H. (1997). *The Inflationary Universe: The Quest for a New Theory of Cosmic Origins*. Reading, MA: Addison-Wesley.
- Guth, A.H. and Pi, S.-Y. (1982). Fluctuations in the new inflationary universe, *Physical Review Letters*, **49**, 1110–1113.
- Hamilton, A.J.S., Kumar, P., Lu, E., and Matthews, A. (1991). Reconstructing the primordial spectrum of fluctuations of the Universe from the observed nonlinear clustering of galaxies, *Astrophysical Journal*, **374**, L1–L4.
- Harrison, E. (1970). Fluctuations at the threshold of classical cosmology, *Physical Review*, **D1**, 2726–2730.
- Harrison, E.R. (1987). *Darkness at Night: A Riddle of the Universe*. Cambridge: Cambridge University Press.
- Hasinger, G., Burg, R., Giacconi, R., Hartner, G.D., Schmidt, M., Trümper, J., and Zamorani, G. (1993). A deep X-ray survey in the Lockman hole and the soft X-ray logN-logS, *Astronomy and Astrophysics*, **275**, 1–15.
- Hauser, M.G., Arendt, R.G., Kelsall, T., Dwek, E., Odegard, N., Weiland, J.L., Freudenreich, H.T., Reach, W.T., Silverberg, R.F., Moseley, S.H., Pei, Y.C., Lubin, P., Mather, J.C., Shafer, R.A., Smoot, G.F., Weiss, R., Wilkinson, D.T., and Wright, E.L. (1998). The COBE diffuse infrared background experiment search for the cosmic infrared background: I. Limits and detections, *Astrophysical Journal*, **508**, 25–43.
- Hauser, M.G. and Dwek, E. (2001). The cosmic infrared background: measurements and implications, *Annual Review of Astronomy and Astrophysics*, **39**, 249–307.
- Hausman, M.A. and Ostriker, J.P. (1977). Cannibalism among galaxies – dynamically produced evolution of cluster luminosity functions, *Astrophysical Journal*, **217**, L125–L129.
- Hausman, M.A. and Ostriker, J.P. (1978). Galactic cannibalism: III. The morphological evolution of galaxies and clusters, *Astrophysical Journal*, **224**, 320–336.
- Hawking, S.W. (1975). Particle creation by black holes, in *Quantum Gravity: Proceedings of the Oxford Symposium*, eds. Isham, C.J., Penrose, R., and Sciama, D.W., pp. 219–267. Oxford: Clarendon.
- Hawkins, M.R.S. (1986). On the nature of objects detected as faint long-term variables, *Monthly Notices of the Royal Astronomical Society*, **219**, 417–426.
- Heath, D.J. (1977). The growth of density perturbations in zero pressure Friedmann-Lemaître universes, *Monthly Notices of the Royal Astronomical Society*, **179**, 351–358.
- Helou, G., Soifer, B.T., and Rowan-Robinson, M. (1985). Thermal infrared and nonthermal radio – remarkable correlation in disks of galaxies, *Astrophysical Journal*, **298**, L7–L11.
- Hernquist, L., Katz, N., Weinberg, D.H., and Miralda-Escudé, J. (1996). The Lyman-alpha forest in the cold dark matter model, *Astrophysical Journal*, **457**, L51–L55.
- Herschel, W. (1785). On the construction of the heavens, *Philosophical Transactions of the Royal Society*, **75**, 213–268.

- Herschel, W. (1802). Catalogue of 500 new nebulae, nebulous stars, planetary nebulae, and clusters of stars; with remarks on the construction of the heavens, *Philosophical Transactions of the Royal Society*, **92**, 477–528.
- Hesser, J.E., Harris, W.E., VandenBerg, D.A., Allwright, J.W.B., Shott, P., and Stetson, P. (1987). A CCD color-magnitude study of 47 tucanae, *Publications of the Astronomical Society of the Pacific*, **99**, 739–808.
- Hewish, A. (1961). Extrapolation of the number-flux density relation of radio stars by Scheuer's statistical methods, *Monthly Notices of the Royal Astronomical Society*, **123**, 167–181.
- Hewitt, J.N., Turner, E.L., Burke, B.F., Lawrence, C.R., and Bennett, C.L. (1987). A VLA gravitational lens survey, in *Observational Cosmology: IAU Symposium No. 124*, eds. Hewitt, A., Burbidge, G., and Fang, L.Z., pp. 747–750. Dordrecht: Reidel.
- Higgs, P. (1964). Broken symmetries, massless particles and gauge fields, *Physics Letters*, **12**, 132–133.
- Hinshaw, G., Nolta, M.R., Bennett, C.L., Bean, R., Doré, O., Greason, M.R., Halpern, M., Hill, R.S., Jarosik, N., Kogut, A., Komatsu, E., Limon, M., Odegard, N., Meyer, S.S., Page, L., Peiris, H.V., Spergel, D.N., Tucker, G.S., Verde, L., Weiland, J.L., Wollack, E., and Wright, E.L. (2007). Three-year Wilkinson Microwave Anisotropy Probe (WMAP) observations: temperature analysis, *Astrophysical Journal Supplement*, **170**, 288–334.
- Hinshaw, G., Spergel, D.N., Verde, L., Hill, R.S., Meyer, S.S., Barnes, C., Bennett, C.L., Halpern, M., Jarosik, N., Kogut, A., Komatsu, E., Limon, M., Page, L., Tucker, G.S., Weiland, J.L., Wollack, E., and Wright, E.L. (2003). First-Year Wilkinson Microwave Anisotropy Probe (WMAP) observations: the angular power spectrum, *Astrophysical Journal Supplement*, **148**, 135–159.
- Hobson, M., Efstathiou, G., and Lasenby, A. (2006). *General Relativity: An Introduction for Physicists*. Cambridge: Cambridge University Press.
- Hoekstra, H., Yee, H.K.C., and Gladders, M.D. (2004). Properties of galaxy dark matter halos from weak lensing, *Astrophysical Journal*, **606**, 67–77.
- Hogan, C.J. (1997). Big Bang nucleosynthesis and the observed abundances of light elements, in *Critical Dialogues in Cosmology*, ed. Turok, N., pp. 50–62. Singapore: World Scientific.
- Hogg, D.W., Blanton, M.R., Brinchmann, J., Eisenstein, D.J., Schlegel, D.J., Gunn, J.E., McKay, T.A., Rix, H.-W., Bahcall, N.A., Brinkmann, J., and Meiksin, A. (2004). The dependence on environment of the color-magnitude relation of galaxies, *Astrophysical Journal*, **601**, L29–L32.
- Hogg, D.W., Eisenstein, D.J., Blanton, M.R., Bahcall, N.A., Brinkmann, J., Gunn, J.E., and Schneider, D.P. (2005). Cosmic homogeneity demonstrated with luminous red galaxies, *Astrophysical Journal*, **624**, 54–58.
- Holtzman, J.A. (1998). Microwave background anisotropies and large-scale structure in universes with cold dark matter, baryons, radiation and massive and massless neutrinos, *Astrophysical Journal Suppllement*, **71**, 1–24.
- Hook, I.M., McMahon, R.G., Boyle, B.J., and Irwin, M.J. (1991). The variability of a large sample of quasars, in *The Space Distribution of Quasars*, ed. Crampton, D.,

- vol. 21, pp. 67–75. San Francisco: Astronomical Society of the Pacific Conference Series.
- Hoskin, M.A. (1976). The ‘Great Debate’: what really happened, *Journal of the History of Astronomy*, **7**, 169–182.
- Hoyle, F. (1954). On nuclear reactions occurring in very hot stars: I. The synthesis of elements from carbon to nickel, *Astrophysical Journal Supplement*, **1**, 121–146.
- Hoyle, F. and Tayler, R. (1964). The mystery of the cosmic helium abundance, *Nature*, **203**, 1108–1110.
- Hoyle, F., Vogeley, M., and Gott III, J. (2002a). Two-dimensional topology of the Two-Degree Field Galaxy Redshift Survey, *Astrophysical Journal*, **570**, 44–53.
- Hoyle, F., Vogeley, M., Gott III, J., Blanton, M., Tegmark, M., Weinberg, D., Bahcall, N., Brinkmann, J., and York, D. (2002b). Two-dimensional topology of the Sloan Digital Sky Survey, *Astrophysical Journal*, **580**, 663–671.
- Hu, E.M., Kim, T.-S., Cowie, L.L., Songaila, A., and Rauch, M. (1995a). The distribution of column densities and B values in the Lyman-alpha forest, *Astronomical Journal*, **110**, 1526–1543.
- Hu, W. (1996). Concepts in CMB anisotropy formation, in *The Universe at High-z, Large-Scale Structure and the Cosmic Microwave Background*, eds. Martinez-Gonzales, E. and Sanz, J.L., pp. 207–240. Berlin: Springer.
- Hu, W. and Dodelson, S. (2002). Cosmic microwave background anisotropies, *Annual Review of Astronomy and Astrophysics*, **40**, 171–216.
- Hu, W. and Okamoto, T. (2002). Mass reconstruction with cosmic microwave background polarization, *Astrophysical Journal*, **574**, 566–574.
- Hu, W., Scott, D., Sugiyama, N., and White, M. (1995b). Effect of physical assumptions on the calculation of microwave background anisotropies, *Physical Review D*, **D52**, 5498–5515.
- Hu, W. and Sugiyama, N. (1995). Anisotropies in the cosmic microwave background: an analytic approach, *Astrophysical Journal*, **444**, 489–506.
- Hu, W., Sugiyama, N., and Silk, J. (1997). The physics of microwave background anisotropies, *Nature*, **386**, 37–43.
- Hu, W. and White, M. (1997). A CMB polarization primer, *New Astronomy*, **2**, 323–344.
- Hubble, E.P. (1926). Extra-galactic nebulae, *Astrophysical Journal*, **64**, 321–369.
- Hubble, E.P. (1929). A relation between distance and radial velocity among extra-galactic nebulae, *Proceedings of the National Academy of Sciences*, **15**, 168–173.
- Hubble, E.P. (1936). *The Realm of the Nebulae*. New Haven: Yale University Press.
- Hubble, E.P. and Humason, M. (1934). The velocity–distance relation among extra-galactic nebulae, *Astrophysical Journal*, **74**, 43–80.
- Hudson, M.J., Dekel, A., Courteau, S., Faber, S.M., and Willick, J.A. (1995). Ω and biasing from optical galaxies versus POTENT mass, *Monthly Notices of the Royal Astronomical Society*, **274**, 305–316.
- Huggins, W. and Miller, W.A. (1864). On the spectra of some of the nebulae; a supplement to the paper “On the Spectra of Some Fixed Stars”, *Philosophical Transactions of the Royal Society of London*, **154**, 437–444.

- Hulse, R.A. and Taylor, J.H. (1975). Discovery of a pulsar in a binary system, *Astrophysical Journal Letters*, **195**, L51–L53.
- Ikeuchi, S. and Ostriker, J.P. (1986). Evolution of the intergalactic medium – what happened during the epoch $Z = 3\text{--}10?$, *Astrophysical Journal*, **301**, 522–543.
- Illingworth, G. (1977). Rotation (?) in 13 elliptical galaxies, *Astrophysical Journal Letters*, **218**, L43–L47.
- Inskip, K.J., Best, P.N., Longair, M.S., and MacKay, D.J.C. (2002). Infrared magnitude-redshift relations for luminous radio galaxies, *Monthly Notices of the Royal Astronomical Society*, **329**, 277–289.
- Irwin, M., McMahon, R.G., and Hazard, C. (1991). APM optical surveys for high redshift quasars, in *ASP Conf. Ser. 21: The Space Distribution of Quasars*, ed. Crampton, D., pp. 117–126.
- Jakobsen, P. (1995). Ultraviolet background (theory), in *The Extragalactic Background Radiation*, eds. Calzetti, D., Livio, M., and Madau, P., pp. 75–101. Cambridge: Cambridge University Press.
- Jakobsen, P. (1996). Intergalactic helium absorption toward quasars, in *Science with the Hubble Space Telescope – II*, eds. Benvenuti, P., Macchetto, F.D., and Schreier, E.J., pp. 153–159. Paris: European Space Agency.
- Jakobsen, P., Boksenberg, A., Deharveng, J.M., Greenfield, P., Jedrzejewski, R., and Paresce, F. (1994). Detection of intergalactic ionized helium absorption in a high-redshift quasar, *Nature*, **370**, 35–39.
- Jeans, J. (1902). The stability of a spherical nebula, *Philosophical Transactions of the Royal Society of London*, **199**, 1–53.
- Jones, B.J.T. (1973). Cosmic turbulence and the origin of galaxies, *Astrophysical Journal*, **181**, 269–294.
- Jones, B.J.T. and Peebles, P.J.E. (1972). Chaos in cosmology, *Comments on Astrophysics and Space Physics*, **4**, 121–128.
- Jones, B.J.T. and Wyse, R.F.G. (1985). The ionisation of the primeval plasma at the time of recombination, *Astronomy and Astrophysics*, **149**, 144–150.
- Jones, W.C., Ade, P.A.R., Bock, J.J., Bond, J.R., Borrill, J., Boscaleri, A., Cabella, P., Contaldi, C.R., Crill, B.P., de Bernardis, P., De Gasperis, G., de Oliveira-Costa, A., De Troia, G., di Stefano, G., Hivon, E., Jaffe, A.H., Kisner, T.S., Lange, A.E., MacTavish, C.J., Masi, S., Mauskopf, P.D., Melchiorri, A., Montroy, T.E., Natoli, P., Netterfield, C.B., Pascale, E., Piacentini, F., Pogosyan, D., Polenta, G., Prunet, S., Ricciardi, S., Romeo, G., Ruhl, J.E., Santini, P., Tegmark, M., Veneziani, M., and Vittorio, N. (2006). A measurement of the angular power spectrum of the CMB temperature anisotropy from the 2003 flight of BOOMERANG, *Astrophysical Journal*, **647**, 823–832.
- Kaastra, J.S., Tamura, T., Peterson, J.R., Bleeker, J.A.M., Ferrigno, C., Kahn, S.M., Paerels, F.B.S., Piffaretti, R., Branduardi-Raymont, G., and Böhringer, H. (2004). Spatially resolved X-ray spectroscopy of cooling clusters of galaxies, *Astronomy and Astrophysics*, **413**, 415–439.
- Kaiser, N. (1984). On the spatial correlations of Abell clusters, *Astrophysical Journal*, **284**, L9–L12.

- Kaiser, N. (1987). Clustering in real space and in redshift space, *Monthly Notices of the Royal Astronomical Society*, **227**, 1–21.
- Kaiser, N. (1992). Weak gravitational lensing of distant galaxies, *Astrophysical Journal*, **388**, 272–286.
- Kapahi, V.K. (1987). The angular size-redshift relation as a cosmological tool, in *Observational Cosmology*, eds. Hewitt, A., Burbidge, G., and Fang, L.-Z., pp. 251–265. Dordrecht: Reidel.
- Kapteyn, J.C. (1922). First attempt at a theory of the arrangement and motion of the sidereal system, *Astrophysical Journal*, **55**, 302–328.
- Kashlinsky, A., Mather, J.C., Odenwald, S., and Hauser, M.G. (1996). Clustering of the diffuse infrared light from the COBE DIRBE maps: I. C(0) and limits on the near-infrared background, *Astrophysical Journal*, **470**, 681–705.
- Kaspi, V.M., Taylor, J.H., and Ryba, M.F. (1994). High-precision timing of millisecond pulsars: 3. Long-term monitoring of PSRs B1855+09 and B1937+21, *Astrophysical Journal*, **428**, 713–728.
- Kassiola, A., Kovner, I., and Blandford, R.D. (1991). Bounds on intergalactic compact objects from observations of compact radio sources, *Astrophysical Journal*, **381**, 6–13.
- Katz, N., Weinberg, D.H., Hernquist, L., and Miranda-Escudé, J. (1996). Damped Lyman-alpha and Lyman-limit absorbers in the cold dark matter model, *Astrophysical Journal*, **457**, L57–L60.
- Kauffmann, G., Heckman, T.M., White, S.D.M., Charlot, S., Tremonti, C., Peng, E.W., Seibert, M., Brinkmann, J., Nichol, R.C., SubbaRao, M., and York, D. (2003). The dependence of star formation history and internal structure on stellar mass for 10^5 low-redshift galaxies, *Monthly Notices of the Royal Astronomical Society*, **341**, 54–69.
- Kauffmann, G., J.M. Colberg, J.M., Diaferio, A., and White, S.D.M. (1999). Clustering of galaxies in a hierarchical universe: I. Methods and results at $z = 0$, *Monthly Notices of the Royal Astronomical Society*, **303**, 188–206.
- Kauffmann, G. and White, S.D. (1993). The merging history of dark matter haloes in a hierarchical universe, *Monthly Notices of the Royal Astronomical Society*, **261**, 921–928.
- Kellermann, K.I. (1993). The cosmological deceleration parameter estimated from the angular-size/redshift relation for compact radio sources, *Nature*, **361**, 134–136.
- Kennicutt, R. (1989). The star formation law in galactic discs, *Astrophysical Journal*, **344**, 685–703.
- Kennicutt, R.C., Edgar, B.K., and Hodge, P.W. (1989). Properties of H II region populations in galaxies: II. The H II region luminosity function, *Astrophysical Journal*, **337**, 761–781.
- Kent, S.M. and Gunn, J.E. (1982). The dynamics of rich clusters of galaxies: I. The Coma cluster, *Astronomical Journal*, **87**, 945–971.
- Kibble, T.W.B. (1976). Topology of cosmic domains and strings, *Journal of Physics A: Mathematical and General*, **9**, 1387–1398.

- King, I.R. (1966). The structure of star clusters: III. Some simple dynamical models, *Astronomical Journal*, **71**, 64–75.
- King, I.R. (1981). The dynamics of globular clusters, *Quarterly Journal of the Royal Astronomical Society*, **22**, 227–243.
- Kippenhahn, R. and Weigert, A. (1990). *Stellar Structure and Evolution*. Berlin and Heidelberg: Springer.
- Kirshner, R. and Kwan, J. (1974). Distances to extragalactic supernovae, *Astrophysical Journal*, **193**, 27–36.
- Kneib, J.P. (1993). *Ph.D. dissertation*. Université Paul Sabatier, Toulouse.
- Kneib, J.-P., Ellis, R.S., Smail, I., Couch, W.J., and Sharples, R.M. (1996). Hubble Space Telescope observations of the lensing cluster Abell 2218, *Astrophysical Journal*, **471**, 643–656.
- Knop, R., Aldering, G., Amanullah, R., Astier, P., Blanc, G., Burns, M., Conley, A., Deustua, S., Doi, M., Ellis, R., Fabbro, S., Folatelli, G., Fruchter, A., Garavini, G., Garmond, S., Garton, K., Gibbons, R., Goldhaber, G., Goobar, A., Groom, D., Hardin, D., Hook, I., Howell, D., Kim, A., Lee, B., Lidman, C., Mendez, J., Nobili, S., Nugent, P., Pain, R., Panagia, N., Pennypacker, C., Perlmutter, S., Quimby, R., Raux, J., Regnault, N., Ruiz-Lapuente, P., Sainton, G., Schaefer, B., Schahmaneche, K., Smith, E., Spadafora, A., Stanishev, V., Sullivan, M., Walton, N.A., Wang, L., Wood-Vasey, W.M., and Yasuda, N. (2003). New constraints on Ω_M , Ω_Λ , and w from an independent set of 11 high-redshift supernovae observed with the Hubble Space Telescope, *Astrophysical Journal*, **598**, 102–137.
- Kochanek, C. (1996). Is there a cosmological constant?, *Astrophysical Journal*, **466**, 638–659.
- Kogut, A., Banday, A.J., Bennett, C.L., Górski, K.M., Hinshaw, G., Smoot, G.F., and Wright, E.L. (1996). Tests for non-Gaussian statistics in the DMR four-year sky maps, *Astrophysical Journal*, **464**, L29–L33.
- Kolatt, T., Dekel, A., and Lahav, O. (1995). Large-scale mass distribution behind the galactic plane, *Monthly Notices of the Royal Astronomical Society*, **275**, 797–811.
- Kolb, E.W. and Turner, M.S. (1990). *The Early Universe*. Redwood City, CA: Addison-Wesley.
- Kompaneets, A. (1956). The establishment of thermal equilibrium between quanta and electrons, *Zhurnal Eksperimentalnoi i Teoreticheskoi Fiziki*, **31**, 876–885. (English translation: 1957 Soviet Physics, 4, 730–737).
- Koo, D.C. and Kron, R. (1982). QSO counts – a complete survey of stellar objects to $B = 23$, *Astronomy and Astrophysics*, **105**, 107–119.
- Kooiman, B.L., Burns, J.O., and Klypin, A.A. (1995). Two-point angular correlation function for the Green Bank 4.85 GHz Sky Survey, *Astrophysical Journal*, **448**, 500–509.
- Kormendy, J. (1982). Observations of galaxy structure and dynamics, in *Morphology and Dynamics of Galaxies: 12th Advanced Course of the Swiss Society of Astronomy and Astrophysics*, eds. Martinet, L. and Mayor, M., pp. 113–288. Sauverny, Switzerland: Geneva Observatory.

- Kormendy, J. and Richstone, D.O. (1995). Inward bound—the search for supermassive black holes in galactic nuclei, *Annual Review of Astronomy and Astrophysics*, **33**, 581–624.
- Kovac, J.M., Leitch, E.M., Pryke, C., Carlstrom, J.E., Halverson, N.W., and Holzapfel, W.L. (2002). Detection of polarization in the cosmic microwave background using DASI, *Nature*, **420**, 772–787.
- Kriss, G.A., Shull, J.M., Oegerle, W., Zheng, W., Davidsen, A.F., Songaila, A., Tumlinson, J., Cowie, L.L., Deharveng, J.-M., Friedman, S.D., Giroux, M.L., Green, R.F., Hutchings, J.B., Jenkins, E.B., Kruk, J.W., Moos, H.W., Morton, D.C., Sembach, K.R., and Tripp, T.M. (2001). Resolving the structure of ionized helium in the intergalactic medium with the far ultraviolet spectroscopic explorer, *Science*, **293**, 1112–1116.
- Kulkarni, V.P. and Fall, S.M. (1993). The proximity effect and the mean intensity of ionizing radiation at low redshifts, *Astrophysical Journal*, **413**, L63–L66.
- Kulkarni, V.P., Fall, S.M., Lauroesch, J.T., York, D.G., Welty, D.E., Khare, P., and Truran, J.W. (2005). Hubble space telescope observations of element abundances in low-redshift damped Ly α galaxies and implications for the global metallicity-redshift relation, *Astrophysical Journal*, **618**, 68–90.
- Kulsrud, R.M. (1997). Pregalactic model for cosmic magnetic fields, in *Critical Dialogues in Cosmology*, ed. Turok, N., pp. 328–342. Singapore: World Scientific.
- Kulsrud, R.M. (2005). *Plasma Physics for Astrophysics*. Princeton, NJ: Princeton University Press.
- Kundic, T., Turner, E.L., Colley, W.N., Gott III, J.R., Rhoads, J.E., Wang, Y., Bergeron, L.E., Gloria, K.A., Long, D.C., Malhotra, S., and Wambsganss, J. (1997). A robust determination of the time delay in 0957+561A, B and a measurement of the global value of Hubble's constant, *Astrophysical Journal*, **482**, 75–82.
- Kuo, C.L., Ade, P.A.R., Bock, J.J., Cantalupo, C., Daub, M.D., Goldstein, J., Holzapfel, W.L., Lange, A.E., Lueker, M., Newcomb, M., Peterson, J.B., Ruhl, J., Runyan, M.C., and Torbet, E. (2004). High-resolution observations of the cosmic microwave background power spectrum with ACBAR, *Astrophysical Journal*, **600**, 32–51.
- Kurt, V.G. and Sunyaev, R.A. (1967). Measurement of the ultraviolet and X-ray background outside the Earth's atmosphere and their role in the study of intergalactic gas, *Cosmical Research*, **5**, 496–512.
- Kutyrev, A.S. and Reynolds, R.J. (1989). Probable detection of H- α emission from a very high velocity cloud in Cetus, *Astrophysical Journal Letters*, **344**, L9–L11.
- Lacy, M., Miley, G., Rawlings, S., Saunders, R., Dickinson, M., Garrington, S., Maddox, S., Pooley, G., Steidel, C., Bremer, M.N., Cotter, G., van Oijk, R., Röttgering, H., and Warner, P. (1994). 8C 1435+635: a radio galaxy at $z = 4.25$, *Monthly Notices of the Royal Astronomical Society*, **271**, 504–512.
- Lagache, G., Dole, H., and Puget, J.-L. (2003). Modelling infrared galaxy evolution using a phenomenological approach, *Monthly Notices of the Royal Astronomical Society*, **338**, 555–571.
- Lagache, G., Dole, H., Puget, J.-L., Pérez-González, P.G., Le Floc'h, E., Rieke, G.H., Papovich, C., Egami, E., Alonso-Herrero, A., Engelbracht, C.W., Gordon, K.D.,

- Misselt, K.A., and Morrison, J.E. (2004). Polycyclic aromatic hydrocarbon contribution to the infrared output energy of the Universe at $z \cong 2$, *Astrophysical Journal Supplement*, **154**, 112–117.
- Laing, R.A., Riley, J.M., and Longair, M.S. (1983). Bright radio sources at 178 MHz – flux densities, optical identifications and the cosmological evolution of powerful radio galaxies, *Monthly Notices of the Royal Astronomical Society*, **204**, 151–187.
- Lanczos, K. (1922). Bemerkung zur die Sitterschen Welt (Remarks on de Sitter's World Model), *Physikalische Zeitschrift*, **23**, 539–543.
- Lanzetta, K., Wolfe, A., and Turnshek, D. (1995). The IUE Survey for damped Lyman- α and Lyman-limit absorption systems, *Astrophysical Journal*, **440**, 435–457.
- Larson, R.B. (1972). Infall of matter in the galaxies, *Nature*, **236**, 21–23.
- Larson, R.B. and Tinsley, B.M. (1978). Star formation rates in normal and peculiar galaxies, *Astrophysical Journal*, **219**, 46–59.
- Le Verrier, U.J.J. (1859). Sur la théorie de mercure et sur le mouvement du périhélie de cette planète (On the theory of mercury and the movement of the perihelion of this planet), *Comptes Rendus*, **49**, 379–383.
- Leavitt, H.S. (1912). Periods of 25 variable stars in the Small Magellanic Cloud, *Harvard College Observatory Circular*, No. **173**, 1–2.
- Ledoux, C., Petitjean, P., and Srianand, R. (2006). Molecular hydrogen in a damped Ly α system at $z_{\text{abs}} = 4.224$, *Astrophysical Journal*, **640**, L25–L28.
- Leitch, E.M., Kovac, J.M., Pryke, C., Carlstrom, J.E., Halverson, N.W., Holzapfel, W.L., Dragovan, M., Reddall, B., and Sandberg, E.S. (2002). Measurement of polarization with the Degree Angular Scale Interferometer, *Nature*, **420**, 763–771.
- Lemaître, G. (1927). A homogeneous universe of constant mass and increasing radius, accounting for the radial velocity of extra-galactic nebulae, *Annales de la Société Scientifique de Bruxelles*, **A47**, 29–39. Translation: (1931), *Monthly Notices of the Royal Astronomical Society*, **91**, 483–490.
- Lemaître, G. (1933). Spherical condensations in the expanding Universe, *Comptes Rendus de L'Academie des Sciences de Paris*, **196**, 903–904.
- Lequeux, J., Peimbert, M., Rayo, J.F., Serrano, A., and Torres-Peimbert, S. (1979). Chemical composition and evolution of irregular and blue compact galaxies, *Astronomy and Astrophysics*, **80**, 155–166.
- Liddle, A.R. and Lyth, D. (2000). *Cosmological Inflation and Large-Scale Structure*. Cambridge: Cambridge University Press.
- Lifshitz, E. (1946). On the gravitational stability of the expanding Universe, *Journal of Physics, Academy of Sciences of the USSR*, **10**, 116–129.
- Lightman, A.P. and Schechter, P.L. (1990). The omega dependence of peculiar velocities induced by spherical density perturbations, *Astrophysical Journal Supplement Series*, **74**, 831–832.
- Lilly, S. and Cowie, L. (1987). Deep infrared surveys, in *Infrared Astronomy with Arrays*, eds. Wynn-Williams, C. and Becklin, E., pp. 473–482. Honolulu: Institute for Astronomy, University of Hawaii Publications.

- Lilly, S.J. (1988). Discovery of a radio galaxy at a redshift of 3.395, *Astrophysical Journal*, **333**, L161–L167.
- Lilly, S.J. and Longair, M.S. (1984). Stellar populations in distant radio galaxies, *Monthly Notices of the Royal Astronomical Society*, **211**, 833–855.
- Lilly, S.J., Tresse, L., Hammer, F., Crampton, D., and LeFevre, O. (1995). The Canada–France Redshift Survey: VI. Evolution of the galaxy luminosity function to $z \sim 1$, *Astrophysical Journal*, **455**, 108–124.
- Lin, C.C., Mestel, L., and Shu, F. (1965). The gravitational collapse of a uniform spheroid, *Astrophysical Journal*, **142**, 1431–1446.
- Lin, H., Kirshner, R.P., Shectman, S.A., Landy, S.D., Oemler, A., and Tucker, D.L. (1996). The power spectrum of galaxy clustering in the Las Campanas Redshift Survey, *Astrophysical Journal*, **471**, 617–635.
- Linde, A. (1974). Is the Lee constant a cosmological constant?, *Zhurnal Experimentalnoi i Teoreticheskoi Fiziki (JETP) Letters*, **19**, 183–184.
- Linde, A. (1982). A new inflationary universe scenario: a possible solution of the horizon, flatness, homogeneity, isotropy and primordial monopole problems, *Physics Letters*, **108B**, 389–393.
- Linde, A. (1983). Chaotic inflation, *Physics Letters*, **129B**, 177–181.
- Lineweaver, C.H. (2005). Inflation and the cosmic microwave background, in *The New Cosmology*, ed. Colless, M., pp. 31–65.
- Linsky, J.L., Diplas, A., Savage, B., Andrusis, C., and Brown, A. (1994). Deuterium in the local interstellar medium: its cosmological Significance, in *Frontiers of Space and Ground-based Astronomy, 27th ESLAB Symposium*, eds. W. Wamsteker, W., Longair, M., and Kondo, Y., pp. 301–304.
- Lobachevsky, N.I. (1829). On the principles of geometry, *Kazanski Vestnik (Kazan Messenger)*.
- Lobachevsky, N.I. (1830). On the principles of geometry, *Kazanski Vestnik (Kazan Messenger)*.
- Longair, M. (1997a). Active galactic nuclei – the Redshift One 3CR galaxies, *Astronomy and Geophysics*, **38**, 10–15.
- Longair, M.S. (1965). Objects in the fields of 88 radio sources, *Monthly Notices of the Royal Astronomical Society*, **129**, 419–436.
- Longair, M.S. (1966). On the interpretation of radio source counts, *Monthly Notices of the Royal Astronomical Society*, **133**, 421–436.
- Longair, M.S. (1978). Radio astronomy and cosmology, in *Observational Cosmology: 8th Advanced Course, Swiss Society of Astronomy and Astrophysics, Saas-Fee 1978*, eds. Maeder, A., Martinet, L., and Tammann, G., pp. 125–257. Geneva: Geneva Observatory Publications.
- Longair, M.S. (1995). The physics of background radiation, in *The Deep Universe, by Sandage, A.R., Kron, R.G. and Longair, M.S.*, eds. Binggeli, B. and Buser, R., pp. 317–514.
- Longair, M.S. (1997b). *High Energy Astrophysics, Vol. 1 (revised 2nd edn.)*. Cambridge: Cambridge University Press.
- Longair, M.S. (1997c). *High Energy Astrophysics, Vol. 2 (revised 2nd edn.)*. Cambridge: Cambridge University Press.

- Longair, M.S. (2003). *Theoretical Concepts in Physics: An Alternative View of Theoretical Reasoning in Physics*. Cambridge: Cambridge University Press.
- Longair, M.S. (2006). *The Cosmic Century: A History of Astrophysics and Cosmology*. Cambridge: Cambridge University Press.
- Longair, M.S. and Scheuer, P.A.G. (1970). The luminosity-volume test for quasi-stellar objects, *Monthly Notices of the Royal Astronomical Society*, **151**, 45–63.
- Longair, M.S. and Sunyaev, R.A. (1969). Fluctuations in the microwave background radiation, *Nature*, **223**, 719–721.
- Longair, M.S. and Sunyaev, R.A. (1971). The electromagnetic background radiation of the Universe, *Uspekhi Fizicheskikh Nauk*, **105**, 41–96. English translation: *Soviet Physics Uspekhi*, **14**, 569–599, 1972.
- Lotz, J.M., Madau, P., Giavalisco, M., Primack, J., and Ferguson, H.C. (2006). The rest-frame far-ultraviolet morphologies of star-forming galaxies at $z \sim 1.5$ and 4, *Astrophysical Journal*, **636**, 592–609.
- Lynden-Bell, D. (1967). Statistical mechanics of violent relaxation in stellar systems, *Monthly Notices of the Royal Astronomical Society*, **136**, 101–121.
- ed. Lynden-Bell, D. (1997). *Cosmical magnetism*. Dordrecht: Kluwer.
- Lynds, R. and Petrosian, V. (1986). Giant luminous arcs in galaxy clusters, *Bulletin of the American Astronomical Society*, **18**, 1014.
- Lyne, A.G., Burgay, M., Kramer, M., Possenti, A., Manchester, R.N., Camilo, F., McLaughlin, M.A., Lorimer, D.R., D'Amico, N., Joshi, B.C., Reynolds, J., and Freire, P.C.C. (2004). A double-pulsar system: a rare laboratory for relativistic gravity and plasma physics, *Science*, **303**, 1153–1157.
- Lyubimov, V., Novikov, E., Nozik, V., Tretyakov, E., and Kozik, V. (1980). An estimate of the v_e mass from the β -spectrum of tritium in the valine molecule, *Physics Letters*, **138**, 30–56.
- Ma, C.-P. and Bertschinger, E. (1995). Cosmological perturbation theory in the synchronous and conformal Newtonian gauges, *Astrophysical Journal*, **455**, 7–25.
- Macchetto, F. and Dickinson, M. (1997). Galaxies in the young Universe, *Scientific American*, **276**, 66–73.
- Madau, P. (1995). Radiative transfer in a clumpy universe: the colors of high-redshift galaxies, *Astrophysical Journal*, **441**, 18–27.
- Madau, P., Ferguson, H., Dickinson, M., Giavalisco, M., Steidel, C., and Fruchter, A. (1996). High-redshift galaxies in the *Hubble Deep Field*: colour selection and star formation history to $z \sim 4$, *Monthly Notices of the Royal Astronomical Society*, **283**, 1388–1404.
- Maddox, S.J., Efstathiou, G., Sutherland, W.G., and Loveday, J. (1990). Galaxy correlations on large scales, *Monthly Notices of the Royal Astronomical Society*, **242**, 43P–47P.
- Maeder, A. (1994). A selection of 10 most topical stellar problems, in *Frontiers of Space and Ground-Based Astronomy*, eds. Wamsteker, W., Longair, M.S., and Kondo, Y., pp. 177–186. Dordrecht: Kluwer.
- Magorrian, J., Tremaine, S., Richstone, D., Bender, R., Bower, G., Dressler, A., Faber, S.M., Gebhardt, K., Green, R., Grillmair, C., Kormendy, J., and Lauer, T.

- (1998). The demography of massive dark objects in galaxy centers, *Astronomical Journal*, **115**, 2285–2305.
- Majewski, S.R., Munn, J.A., Kron, R.G., Bershadsky, M.A., Smetanka, J.J., and Koo, D.C. (1991). A proper motion and variability QSO survey to $B = 22.5$, in *The Space Distribution of Quasars*, ed. Crampton, D., volume 21, pp. 55–65. San Francisco: Astronomical Society of the Pacific Conference Series.
- Maloney, P. (1993). Sharp edges to neutral hydrogen disks in galaxies and the extragalactic radiation field, *Astrophysical Journal*, **414**, 41–56.
- Marleau, F.R., Fadda, D., Storrie-Lombardi, L.J., Helou, G., Makovoz, D., Frayer, D.T., Yan, L., Appleton, P.N., Armus, L., Chapman, S., Choi, P.I., Fang, F., Heinrichsen, I., Im, M., Lacy, M., Shupe, D., Soifer, B.T., Squires, G., Surace, J., Teplitz, H.I., and Wilson, G. (2004). Extragalactic source counts at 24 microns in the Spitzer First Look Survey, *Astrophysical Journal Supplement*, **154**, 66–69.
- Marshall, F.E., Boldt, E.A., Holt, S.S., Miller, R.B., Mushotzky, R.F., Rose, L.A., Rothschild, R.E., and Serlemitsos, P.J. (1980). The diffuse X-ray background spectrum from 3 to 50 keV, *Astrophysical Journal*, **235**, 4–10.
- Martin, C. and Bowyer, S. (1989). Evidence for an extragalactic component of the far-ultraviolet background and constraints on galaxy evolution for Z between 0.1 and 0.6, *Astrophysical Journal*, **338**, 677–706.
- Marx, G. and Szalay, A. (1972). Cosmological limit on neutretto mass. in *Neutrino '72*, vol. 1, pp. 191–195. Budapest: Technoinform.
- Mather, J. (1995). Microwave background radiation (observations), in *The Extragalactic Background Radiation*, eds. Calzetti, D., Livio, M., and Madau, P., pp. 169–190. Cambridge: Cambridge University Press.
- Matthews, J. and Walker, R.L. (1973). *Mathematical Methods of Physics*. New York: W.A. Benjamin.
- Mattig, W. (1959). Über den Zusammenhang Zwischen der Anzahl der Extragalaktischen Objekte und der Scheinbaren Helligkeit, *Astronomische Nachrichten*, **285**, 1–2.
- Mazzarella, J. and Balzano, V. (1986). A catalog of Markarian galaxies, *Astrophysical Journal Supplement Series*, **62**, 521–819.
- McCarthy, P.J. (2006). Galaxy formation and cosmology in the ELT era, in *Scientific Requirements for Extremely Large Telescopes: IAU Symposium No. 232*, eds. Whitelock, P., Dennefeld, M., and Leibundgut, B., pp. 119–129. Cambridge: Cambridge University Press.
- McCarthy, P.J., Le Borgne, D., Crampton, D., Chen, H.-W., Abraham, R.G., Glazebrook, K., Savaglio, S., Carlberg, R.G., Marzke, R.O., Roth, K., Jørgensen, I., Hook, I., Murowinski, R., and Juneau, S. (2004). Evolved galaxies at $z \geq 1.5$ from the Gemini Deep Deep Survey: the formation epoch of massive stellar systems, *Astrophysical Journal Letters*, **614**, L9–L12.
- McCarthy, P.J., van Breugel, W.J.M., Spinrad, H., and Djorgovski, G. (1987). A correlation between the radio and optical morphologies of distant 3CR radio galaxies, *Astrophysical Journal*, **321**, L29–L33.
- McCrea, W. (1970). A philosophy for Big Bang cosmology, *Nature*, **228**, 21–24.

- McDonald, P., Seljak, U., Burles, S., Schlegel, D.J., Weinberg, D.H., Cen, R., D., S., Schaye, J., Schneider, D.P., Bahcall, N.A., Briggs, J., Brinkmann, J., Brunner, R.J., Fukugita, M., Gunn, J.E., Ivezić, Z., Kent, S., Lupton, R.H., and Vanden Berk, D.E. (2006). The Ly- α forest power spectrum from the Sloan Digital Sky Survey, *Astrophysical Journal Supplement Series*, **163**, 80–109.
- McLure, R.J., Jarvis, M.J., Targett, T.A., Dunlop, J.S., and Best, P.N. (2006). On the evolution of the black hole: spheroid mass ratio, *Monthly Notices of the Royal Astronomical Society*, **368**, 1395–1403.
- McNally, S.J. and Peacock, J.A. (1995). The smallscale clustering power spectrum and relativistic decays, *Monthly Notices of the Royal Astronomical Society*, **277**, 143–151.
- Melott, A., Weinberg, D., and Gott, J. (1988). The topology of large-scale structure: II. Nonlinear evolution of Gaussian models, *Astrophysical Journal*, **328**, 50–68.
- Merritt, D. (1987). The distribution of dark matter in the Coma cluster, *Astrophysical Journal*, **313**, 121–135.
- Mészáros, P. (1974). The behaviour of point masses in an expanding cosmological substratum, *Astronomy and Astrophysics*, **37**, 225–228.
- Metcalfe, N., Shanks, T., Campos, A., Fong, R., and Gardner, J.P. (1996). Galaxy formation at high redshifts, *Nature*, **383**, 236–237.
- Metcalfe, N., Shanks, T., Weilbacher, P.M., McCracken, H.J., Fong, R., and Thompson, D. (2006). Galaxy number counts: VI. An H-band survey of the Herschel Deep Field, *Monthly Notices of the Royal Astronomical Society*, **370**, 1257–1273.
- ed. Meylan, G. (1995). *QSO Absorption Lines*. Berlin, Heidelberg: Springer.
- Michell, J. (1767). An inquiry into the probable parallax, and magnitude of the fixed stars, from the quantity of light which they afford us, and the particular circumstances of their situation, *Philosophical Transactions of the Royal Society*, **57**, 234–264.
- Mihos, J.C. and Hernquist, L. (1994). Triggering of starbursts in galaxies by minor mergers, *Astrophysical Journal*, **425**, L13–L16.
- Mihos, J.C. and Hernquist, L. (1996). Gasdynamics and starbursts in major mergers, *Astrophysical Journal*, **464**, 641–663.
- Miley, G.K. (1968). Variation of the angular sizes of quasars with red-shift, *Nature*, **218**, 933–934.
- Miley, G.K. (1971). The radio structure of quasars – a statistical investigation, *Monthly Notices of the Royal Astronomical Society*, **152**, 477–490.
- Milne, E.A. and McCrea, W.H. (1934a). Newtonian expanding universe, *Quarterly Journal of Mathematics*, **5**, 64–72.
- Milne, E.A. and McCrea, W.H. (1934b). Newtonian universes and the curvature of space, *Quarterly Journal of Mathematics*, **5**, 73–80.
- Miranda-Escudé, J., Cen, R., Ostriker, J.P., and Rauch, M. (1996). The Lyman alpha forest from gravitational collapse in the CDM + lambda model, *Astrophysical Journal*, **471**, 582–616.
- Mitchell, J.L., Keeton, C.R., Frieman, J.A., and Sheth, R.K. (2005). Improved cosmological constraints from gravitational lens statistics, *Astrophysical Journal*, **622**, 81–98.

- Mitchell, R.J., Culhane, J.L., Davison, P.J.N., and Ives, J.C. (1976). Ariel 5 observations of the X-ray spectrum of the Perseus cluster, *Monthly Notices of the Royal Astronomical Society*, **175**, 29P–34P.
- Møller, P. and Jakobsen, P. (1990). The Lyman continuum opacity at high redshifts – through the Lyman forest and beyond the Lyman valley, *Astronomy and Astrophysics*, **228**, 299–309.
- Monaco, P. (1998). The cosmological mass function, *Fundamentals of Cosmic Physics*, **19**, 157–317.
- Monaco, P. (1999). Dynamics in the cosmological mass function (or, why does the Press & Schechter work?), in *Observational Cosmology: The Development of Galaxy Systems*, eds. Giuricin, G., Mezzetti, M., and Salucci, P., pp. 186–197. San Francisco: Astronomical Society of the Pacific Conference Series No. 176.
- Monchaux, R., Berhanu, M., Bourgoin, M., Moulin, M., Odier, P., Pinton, J.-F., Volk, R., Fauve, S., Mordant, N., Pétrélis, F., Chiffaudel, A., Daviaud, F., Dubrulle, B., Gasquet, C., Marié, L., and Ravelet, F. (2007). Generation of a magnetic field by dynamo action in a turbulent flow of liquid sodium, *Physical Review Letters*, **98**(4), 044502.
- Montroy, T.E., Ade, P.A.R., Bock, J.J., Bond, J.R., Borrill, J., Boscaleri, A., Cambella, P., Contaldi, C.R., Crill, B.P., de Bernardis, P., De Gasperis, G., de Oliveira-Costa, A., De Troia, G., di Stefano, G., Hivon, E., Jaffe, A.H., Kisner, T.S., Jones, W.C., Lange, A.E., Masi, S., Mauskopf, P.D., MacTavish, C.J., Melchiorri, A., Natoli, P., Netterfield, C.B., Pascale, E., Piacentini, F., Pogosyan, D., Polenta, G., Prunet, S., Ricciardi, S., Romeo, G., Ruhl, J.E., Santini, P., Tegmark, M., Veneziani, M., and Vittorio, N. (2006). A measurement of the CMB (EE) spectrum from the 2003 flight of BOOMERANG, *Astrophysical Journal*, **647**, 813–822.
- Mukhanov, V. (2005). *Physical Foundations of Cosmology*. Cambridge: Cambridge University Press.
- Murdoch, H.S., Hunstead, R.W., Pettini, M., and Blades, J.C. (1986). Absorption spectrum of the $Z = 3.78$ QSO 2000-330: II. The redshift and equivalent width distributions of primordial hydrogen clouds, *Astrophysical Journal*, **309**, 19–32.
- Naselsky, P., Novikov, D., and Novikov, I. D. (2006). *The Physics of the Cosmic Microwave Background*. Cambridge: Cambridge University Press.
- Norberg, P., Baugh, C.M., Hawkins, E., Maddox, S., Madgwick, D., Lahav, O., Cole, S., Frenk, C.S., Baldry, I., Bland-Hawthorn, J., Bridges, T., Cannon, R., Colless, M., Collins, C., Couch, W., Dalton, G., De Propris, R., Driver, S.P., Efstathiou, G., Ellis, R.S., Glazebrook, K., Jackson, C., Lewis, I., Lumsden, S., Peacock, J.A., Peterson, B.A., Sutherland, W., and Taylor, K. (2002). The 2dF Galaxy Redshift Survey: the dependence of galaxy clustering on luminosity and spectral type, *Monthly Notices of the Royal Astronomical Society*, **332**, 827–838.
- Norberg, P., Baugh, C.M., Hawkins, E., Maddox, S., Peacock, J.A., Cole, S., Frenk, C.S., Bland-Hawthorn, J., Bridges, T., Cannon, R., Colless, M., Collins, C., Couch, W., Dalton, G., De Propris, R., Driver, S.P., Efstathiou, G., Ellis, R.S., Glazebrook, K., Jackson, C., Lahav, O., Lewis, I., Lumsden, S., Madgwick, D., Peterson, B.A., Sutherland, W., and Taylor, K. (2001). The 2dF Galaxy Redshift

- Survey: luminosity dependence of galaxy clustering, *Monthly Notices of the Royal Astronomical Society*, **328**, 64–70.
- Novikov, I. (1964). On the possibility of appearance of large scale inhomogeneities in the expanding Universe, *Journal of Experimental and Theoretical Physics*, **46**, 686–689.
- Oemler, A.J. (1974). The systematic properties of clusters of galaxies. Photometry of 15 clusters, *Astrophysical Journal*, **194**, 1–20.
- Oguri, M. (2007). Gravitational lens time delays: a statistical assessment of lens model dependences and implications for the global Hubble constant, *Astrophysical Journal*, **660**, 1–15.
- Ohta, K., Yamada, T., Nakanishi, K., Kohno, K., Akiyama, M., and Kawabe, R. (1996). Detection of molecular gas in the quasar BR1202-0725 at redshift $z = 4.69$, *Nature*, **382**, 426–428.
- Oliver, S.J., Rowan-Robinson, M., and Saunders, W. (1992). Infrared background constraints on the evolution of IRAS galaxies, *Monthly Notices of the Royal Astronomical Society*, **256**, 15P–22P.
- Omton, A. (1996). 1.3 mm detection and mapping of radioquiet QSOs at very high redshifts, in *Science with Large Millimetre Arrays*, ed. Shaver, P., pp. 82–85. Berlin: Springer.
- Omton, A., Petitjean, P., Guilloteau, S., McMahon, R.G., Solomon, P.M., and Pécontal, E. (1996). Molecular gas and dust around a radio-quiet quasar at redshift 4.69, *Nature*, **382**, 428–431.
- O'Neill, S.M., Jones, T.W., Tregillis, I.L., and Ryu, D. (2006). 3D MHD interactions of jets with cluster media, *Astronomische Nachrichten*, **327**, 535–536.
- Oort, J.H. (1958). Distribution of galaxies and density in the universe, in *Solvay Conference on The Structure and Evolution of the Universe*, pp. 163–181. Brussels: Institut International de Physique Solvay.
- Opal Collaboration (1990). A combined analysis of the hadronic and leptonic decays of the Z^0 , *Physics Letters*, **B240**, 497–512.
- Ortiz-Gil, A., Guzzo, L., Schuecker, P., Böhringer, H., and Collins, C.A. (2004). The X-ray luminosity-velocity dispersion relation in the REFLEX Cluster Survey, *Monthly Notices of the Royal Astronomical Society*, **348**, 325–332.
- Osmer, P.S. (1982). Evidence for a decrease in the space density of quasars at z more than about 3.5, *Astrophysical Journal*, **253**, 28–37.
- Ostriker, J.P. and Cowie, L. (1981). Galaxy formation in an intergalactic medium dominated by explosions, *Astrophysical Journal*, **243**, L127–L131.
- Ostriker, J.P. and Ikeuchi, S. (1983). Physical properties of the intergalactic medium and the Lyman-alpha absorbing clouds, *Astrophysical Journal Letters*, **268**, L63–L68.
- Ostriker, J.P. and Peebles, P.J.E. (1973). A numerical study of the stability of flattened galaxies: or, can cold galaxies survive?, *Astrophysical Journal*, **186**, 467–480.
- Oswalt, T.D., Smith, J.A., Wood, M.A., and Hintzen, P. (1996). A lower limit of 9.5 Gyr on the age of the galactic disk from the oldest white dwarf stars, *Nature*, **382**, 692–694.

- Ouchi, M., Shimasaku, K., Okamura, S., Furusawa, H., Kashikawa, N., Ota, K., Doi, M., Hamabe, M., Kimura, M., Komiyama, Y., Miyazaki, M., Miyazaki, S., Nakata, F., Sekiguchi, M., Yagi, M., and Yasuda, N. (2004). Subaru Deep Survey: V. A census of Lyman break galaxies at $z \sim 4$ and 5 in the Subaru Deep Fields: photometric properties, *Astrophysical Journal*, **611**, 660–684.
- Paciesas, W.S., Meegan, C.A., Pendleton, G.N., Briggs, M.S., Kouveliotou, C., Koshut, T.M., Lestrade, J.P., McCollough, M.L., Brainerd, J.J., Hakkila, J., Henze, W., Preece, R.D., Connaughton, V., Kippen, R.M., Mallozzi, R.S., Fishman, G.J., Richardson, G.A., and Sahi, M. (1999). The 4th BATSE Gamma-Ray Burst Catalog (revised), *Astrophysical Journal Supplement Series*, **122**, 465–495.
- Padmanabhan, T. (1993). *Structure Formation in the Universe*. Cambridge: Cambridge University Press.
- Padmanabhan, T. (1996). *Cosmology and Astrophysics through Problems*. Cambridge: Cambridge University Press. See pp. 437–440.
- Padmanabhan, T. (1997). Nonlinear gravitational clustering in the expanding Universe, in *Gravitation and Cosmology: Proc. ICGC-95 Conference, Pune*, eds. Dhurandhar, S. and Padmanabhan, T., pp. 37–52. Dordrecht: Kluwer Academic Publishers.
- Page, L. (1997). Review of observations of the cosmic microwave background, in *Critical Dialogues in Cosmology*, ed. Turok, N., pp. 343–362. Singapore: World Scientific.
- Page, L., Hinshaw, G., Komatsu, E., Nolta, M.R., Spergel, D.N., Bennett, C.L., Barnes, C., Bean, R., Doré, O., Dunkley, J., Halpern, M., Hill, R.S., Jarosik, N., Kogut, A., Limon, M., Meyer, S.S., Odegard, N., Peiris, H.V., Tucker, G.S., Verde, L., Weiland, J.L., Wollack, E., and Wright, E.L. (2007). Three-year Wilkinson Microwave Anisotropy Probe (WMAP) observations: polarization analysis, *Astrophysical Journal Supplement*, **170**, 335–376.
- Pagel, B. (1997). *Nucleosynthesis and Chemical Evolution of Galaxies*. Cambridge: Cambridge University Press.
- Pais, A. (1982). *Subtle is the Lord . . . : the Science and Life of Albert Einstein*. Oxford: Oxford University Press.
- Panagia, N., Gilmozzi, R., Macchetto, F., Adorf, H.-M., and Kirshner, R.P. (1991). Properties of the SN 1987A circumstellar ring and the distance to the Large Magellanic Cloud, *Astrophysical Journal*, **380**, L23–L26.
- Parker, E.N. (1997). Galactic dynamos and other questions on the origins of magnetic fields, in *Critical Dialogues in Cosmology*, ed. Turok, N., pp. 309–327. Singapore: World Scientific.
- Partridge, R. (1980a). Fluctuations in the cosmic microwave background radiation at small angular scales, *Physica Scripta*, **21**, 624–629.
- Partridge, R. (1980b). New limits on small-scale angular fluctuations in the cosmic microwave background, *Astrophysical Journal*, **235**, 681–687.
- Peacock, J. (2000). *Cosmological Physics*. Cambridge: Cambridge University Press.
- Peacock, J.A. (1985). The high-redshift evolution of radio galaxies and quasars, *Monthly Notices of the Royal Astronomical Society*, **217**, 601–631.

- Peacock, J.A., Cole, S., Norberg, P., Baugh, C.M., Bland-Hawthorn, J., Bridges, T., Cannon, R.D., Colless, M., Collins, C., Couch, W., Dalton, G., Deeley, K., De Propris, R., Driver, S.P., Efstathiou, G., Ellis, R.S., Frenk, C.S., Glazebrook, K., Jackson, C., Lahav, O., Lewis, I., Lumsden, S., Maddox, S., Percival, W.J., Peterson, B.A., Price, I., Sutherland, W., and Taylor, K. (2001). A measurement of the cosmological mass density from clustering in the 2dF Galaxy Redshift Survey, *Nature*, **410**, 169–173.
- Peacock, J.A. and Dodds, S.J. (1994). Reconstructing the linear power spectrum of cosmological mass fluctuations, *Monthly Notices of the Royal Astronomical Society*, **267**, 1020–1034.
- Peacock, J.A. and Heavens, A.F. (1985). The statistics of maxima in primordial density perturbations, *Monthly Notices of the Royal Astronomical Society*, **217**, 805–820.
- Peebles, P. (1981). Primeval adiabatic perturbations – constraints from the mass distribution, *Astrophysical Journal*, **248**, 885–897.
- Peebles, P. (1982). Large-scale background temperature and mass fluctuations due to scale-invariant primeval perturbations, *Astrophysical Journal*, **263**, L1–L5.
- Peebles, P.J.E. (1968). Recombination of the primeval plasma, *Astrophysical Journal*, **153**, 1–11.
- Peebles, P.J.E. (1976). A cosmic virial theorem, *Astrophysics and Space Science*, **45**, 3–19.
- Peebles, P.J.E. (1980). *The Large-Scale Structure of the Universe*. Princeton: Princeton University Press.
- Peebles, P.J.E. (1993). *Principles of Physical Cosmology*. Princeton: Princeton University Press.
- Peebles, P.J.E. and Yu, J.T. (1970). Primeval adiabatic perturbation in an expanding Universe, *Astrophysical Journal*, **162**, 815–836.
- Pei, Y. and Fall, S. (1995). Cosmic chemical evolution, *Astrophysical Journal*, **454**, 69–76.
- Penrose, R. (1997). *The Large, the Small and the Human Mind*. Cambridge: Cambridge University Press.
- Penzias, A.A. and Wilson, R.W. (1965). A measurement of excess antenna temperature at 4080 MHz, *Astrophysical Journal*, **142**, 419–421.
- Perlmutter, S., Aldering, G., della Valle, M., Deustua, S., Ellis, R.S., Fabbro, S., Fruchter, A., Goldhaber, G., Groom, D.E., Hook, I.M., Kim, A.G., Kim, M.Y., Knop, R.A., Lidman, C., McMahon, R.G., Nugent, P., Pain, R., Panagia, N., Pennypacker, C.R., Ruiz-Lapuente, P., Schaefer, B., and Walton, N. (1998). Discovery of a supernova explosion at half the age of the universe, *Nature*, **391**, 51–54.
- Perlmutter, S., Boyle, B., Bunclark, P., Carter, D., Couch, W., Deustua, S., Dopita, M., Ellis, R., Filippenko, A.V., Gabi, S., Glazebrook, K., Goldhaber, G., Goobar, A., Groom, D., Hook, I., Irwin, M., Kim, A., Kim, M., Lee, J., Matheson, T., McMahon, R., Newberg, H., Pain, R., Pennypacker, C., and Small, I. (1996). High-redshift supernova discoveries on demand: first results from a new tool for cosmology and bounds on q_0 , *Nuclear Physics B*, **51**, 20–29.

- Perlmutter, S., Gabi, S., Goldhaber, G., Goobar, A., Groom, D.E., Hook, I.M., Kim, A.G., Kim, M.Y., Lee, J.C., Pain, R., Pennypacker, C.R., Small, I.A., Ellis, R.S., McMahon, R.G., Boyle, B.J., Bunclark, P.S., Carter, D., Irwin, M.J., Glazebrook, K., Newberg, H.J.M., Filippenko, A.V., Matheson, T., Dopita, M., and Couch, W.J. (1997). Measurements of the cosmological parameters omega and lambda from the first seven supernovae at $z > 0.35$, *Astrophysical Journal*, **483**, 565–581.
- Persic, M., de Zotti, G., Boldt, E.A., Marshall, F.E., Danese, L., Franceschini, A., and Palumbo, G.G.C. (1989). The autocorrelation properties of fluctuations in the cosmic X-ray background, *Astrophysical Journal Letters*, **336**, L47–L50.
- Petrosian, V. and Salpeter, E.E. (1968). Ghost images in inhomogeneous Friedmann universes, *Astrophysical Journal*, **151**, 411–429.
- Pettini, M., Ellison, S.L., Steidel, C.C., and Bowen, D.V. (1999). Metal abundances at $z \leq 1.5$: fresh clues to the chemical enrichment history of damped Lyman- α systems, *Astrophysical Journal*, **510**, 576–589.
- Pettini, M., King, D.L., Smith, L.J., and Hunstead, R.W. (1997). The metallicity of high-redshift galaxies: the abundance of zinc in 34 damped Ly- α systems from $z = 0.7$ to 3.4, *Astrophysical Journal*, **486**, 665–680.
- Phillips, M.M. (1993). The absolute magnitudes of Type IA supernovae, *Astrophysical Journal*, **413**, L105–L108.
- Pound, R. and Rebka, G. (1960). Apparent weight of photons, *Physical Review Letters*, **4**, 337–341.
- Pound, R. and Snider, J. (1965). Effect of gravity on gamma radiation, *Physical Review*, **140**, B788–B803.
- Pozdnyakov, L.A., Sobol, I.M., and Sunyaev, R.A. (1983). Comptonization and the shaping of X-ray source spectra – Monte Carlo calculations, *Soviet Scientific Reviews, Section E: Astrophysics and Space Physics Reviews*, **2**, 189–331.
- Pratt, G.W. and Arnaud, M. (2002). The mass profile of A1413 observed with XMM-Newton: implications for the M-T relation, *Astronomy and Astrophysics*, **394**, 375–393.
- Press, W. and Schechter, P. (1974). Formation of galaxies and clusters of galaxies by self-similar gravitational condensation, *Astrophysical Journal*, **187**, 425–438.
- Primack, J.R., Seckel, D., and Sadoulet, B. (1988). Detection of cosmic dark matter, *Annual Review of Nuclear and Particle Science*, **38**, 751–807.
- Pritchard, J.R. and Furlanetto, S.R. (2007). 21-cm Fluctuations from inhomogeneous X-ray heating before reionisation, *Monthly Notices of the Royal Astronomical Society*, **376**, 1680–1694.
- Prochaska, J.X. and Wolfe, A.M. (2002). The UCSD HIRES/Keck I damped Ly α abundance database: II. The implications, *Astrophysical Journal*, **566**, 68–92.
- Prochaska, J.X., Gawiser, E., Wolfe, A.M., Castro, S. and Djorgovski, S.G. (2003). The Age-Metallicity Relation of the Universe in Neutral Gas: The First 100 Damped Ly α Systems, *Astrophysical Journal Letters*, **595**, L9–L12.
- Puget, J.-L., Abergel, A., Bernard, J.-P., Boulanger, F., Burton, W.B., Desert, F.-X., and Hartmann, D. (1996). Tentative detection of a cosmic far-infrared background with COBE, *Astronomy and Astrophysics*, **308**, L5–L8.

- Readhead, A.C.S., Mason, B.S., Contaldi, C.R., Pearson, T.J., Bond, J.R., Myers, S.T., Padin, S., Sievers, J.L., Cartwright, J.K., Shepherd, M.C., Pogosyan, D., Prunet, S., Altamirano, P., Bustos, R., Bronfman, L., Casassus, S., Holzapfel, W.L., May, J., Pen, U.-L., Torres, S., and Udomprasert, P.S. (2004). Extended mosaic observations with the cosmic background imager, *Astrophysical Journal*, **609**, 498–512.
- Rees, M.J. (1994). Origin of the seed magnetic field for a galactic dynamo, in *Cosmical Magnetism*, ed. Lynden-Bell, D., pp. 155–160. Dordrecht: Kluwer.
- Rees, M.J. (1995). *Perspectives in Astrophysical Cosmology*. Cambridge: Cambridge University Press.
- Rees, M.J. (2006). Origin of cosmic magnetic fields, *Astronomische Nachrichten*, **327**, 395–398.
- Rees, M.J. and Ostriker, J.P. (1977). Cooling, dynamics and fragmentation of massive gas clouds – clues to the masses and radii of galaxies and clusters, *Monthly Notices of the Royal Astronomical Society*, **179**, 541–559.
- Rees, M.J. and Sciama, D.W. (1968). Large-scale density inhomogeneities in the Universe, *Nature*, **217**, 511–516.
- Refregier, A. (2003). Weak gravitational lensing by large-scale structure, *Annual Review of Astronomy and Astrophysics*, **41**, 645–668.
- Reimers, D., Clavel, J., Groote, D., Engels, D., Hagen, H.J., Naylor, T., Wamsteker, W., and Hopp, U. (1989). The luminous Quasar HS1700+6416 and the shape of the ‘Big Bump’ below 500 Å, *Astronomy and Astrophysics*, **218**, 71–77.
- Reiprich, T.H. and Böhringer, H. (2002). The mass function of an X-Ray Flux-limited sample of galaxy clusters, *Astrophysical Journal*, **567**, 716–740.
- Richards, G.T., Strauss, M.A., Fan, X., Hall, P.B., Jester, S., Schneider, D.P., Vanden Berk, D.E., Stoughton, C., Anderson, S.F., Brunner, R.J., Gray, J., Gunn, J.E., Ivezić, Ž., Kirkland, M.K., Knapp, G.R., Loveday, J., Meiksin, A., Pope, A., Szalay, A.S., Thakar, A.R., Yanny, B., York, D.G., Barentine, J.C., Brewington, H.J., Brinkmann, J., Fukugita, M., Harvanek, M., Kent, S.M., Kleinman, S.J., Krzesiński, J., Long, D.C., Lupton, R.H., Nash, T., Neilsen, Jr., E.H., Nitta, A., Schlegel, D.J., and Snedden, S.A. (2006). The Sloan Digital Sky Survey Quasar Survey: quasar luminosity function from data release 3, *Astronomical Journal*, **131**, 2766–2787.
- Rindler, W. (1956). Visual horizons in world models, *Monthly Notices of the Royal Astronomical Society*, **116**, 662–677.
- Rindler, W. (2001). *Relativity: Special, General and Cosmological*. Oxford: Oxford University Press.
- Roberts, M.S. and Haynes, M.P. (1994). Physical parameters along the Hubble Sequence, *Annual Review of Astronomy and Astrophysics*, **26**, 115–152.
- Robertson, H.P. (1935). Kinematics and world structure, *Astrophysical Journal*, **82**, 284–301.
- Rosati, P., Borgani, S., and Norman, C. (2002). The evolution of X-ray clusters of galaxies, *Annual Review of Astronomy and Astrophysics*, **40**, 539–577.

- Rowan-Robinson, M. (1968). The determination of the evolutionary properties of quasars by means of the luminosity-volume test, *Monthly Notices of the Royal Astronomical Society*, **141**, 445–458.
- Rowan-Robinson, M. (1985). *The Cosmological Distance Ladder*. New York: Freeman.
- Rowan-Robinson, M. (1988). The extragalactic distance scale, *Space Science Reviews*, **48**, 1–71.
- Rowan-Robinson, M., Benn, C.R., Lawrence, A., McMahon, R.G., and Broadhurst, T.J. (1993). The evolution of faint radio sources, *Monthly Notices of the Royal Astronomical Society*, **263**, 123–130.
- Rutherford, E. (1907). Some cosmical aspects of radioactivity, *Journal of the Royal Astronomical Society of Canada*, **1**, 145–165.
- Ryle, M. (1955). Radio stars and their cosmological significance, *The Observatory*, **75**, 137–147.
- Ryle, M. (1958). The nature of the cosmic radio sources, *Proceedings of the Royal Society*, **A248**, 289–308.
- Ryle, M. and Sandage, A.R. (1964). The optical identification of three new radio objects of the 3C 48 class, *Astrophysical Journal*, **139**, 419–421.
- Sachs, R. and Wolfe, A. (1967). Perturbations of a cosmological model and angular variations in the microwave background, *Astrophysical Journal*, **147**, 73–90.
- Sahu, K.C., Livio, M., Petro, L., Macchetto, F.D., van Paradijs, J., Kouveliotou, C., Fishman, G.J., Meegan, C.A., Groot, P.J., and Galama, T. (1997). The optical counterpart to gamma-ray burst GRB 970228 observed using the Hubble Space Telescope, *Nature*, **387**, 476–478.
- Sajina, A., Scott, D., Dennefeld, M., Dole, H., Lacy, M., and Lagache, G. (2006). The 1–1000 μm spectral energy distributions of far-infrared galaxies, *Monthly Notices of the Royal Astronomical Society*, **369**, 939–957.
- Sakharov, A. (1965). The initial stage of an expanding universe and the appearance of a nonuniform distribution of matter, *Zhurnal Eksperimentalnoi i Teoreticheskoi Fiziki*, **49**, 345–358. [English translation: *Soviet Physics JETP*, **22**, 241–249, 1966.]
- Sakharov, A. (1967). Violation of CP invariance, C asymmetry, and baryon asymmetry of the Universe, *Zhurnal Experimentalnoi i Teoreticheskikh Fizika (JETP) Letters*, **5**, 32–35.
- Sandage, A.R. (1961a). The ability of the 200-inch telescope to discriminate between selected world models, *Astrophysical Journal*, **133**, 355–392.
- Sandage, A.R. (1961b). *The Hubble Atlas of Galaxies*. Washington D.C.: Carnegie Institution of Washington. Publication 618.
- Sandage, A.R. (1965). The existence of a major new constituent of the Universe: the quasistellar galaxies, *Astrophysical Journal*, **141**, 1560–1578.
- Sandage, A.R. (1968). Observational cosmology, *The Observatory*, **88**, 91–106.
- Sandage, A.R. (1975). Classification and stellar content of galaxies obtained from direct photography, in *Stars and Stellar Systems*, **9. Galaxies and the Universe**, eds. A.R. Sandage, M.S. and Kristian, J., pp. 1–35. Chicago: Chicago University Press.

- Sandage, A.R. (1988). Observational tests of world models, *Annual Review of Astronomy and Astrophysics*, **26**, 561–630.
- Sandage, A.R. (1995). Practical cosmology: inventing the past, in *The Deep Universe*, by Sandage, A.R., Kron, R.G. and Longair, M.S., eds. Binggeli, B. and Buser, R., pp. 1–232. Berlin: Springer-Verlag.
- Sandage, A.R. and Hardy, E. (1973). The redshift-distance relation: VII. Absolute magnitudes of the first three ranked cluster galaxies as function of cluster richness and Bautz–Morgan cluster type: the effect on q_0 , *Astrophysical Journal*, **183**, 743–758.
- Sandage, A.R. and Schwarzschild, M. (1952). Inhomogeneous stellar models: II. Models with exhausted cores in gravitational contraction, *Astrophysical Journal*, **116**, 463–476.
- Sanders, D.B. and Mirabel, I.F. (1996). Luminous infrared galaxies, *Annual Review of Astronomy and Astrophysics*, **34**, 749–792.
- Saunders, W., Rowan-Robinson, M., Lawrence, A., Efstathiou, G., Kaiser, N., Ellis, R.S., and Frenk, C.S. (1990). The 60-micron and far-infrared luminosity functions of IRAS galaxies, *Monthly Notices of the Royal Astronomical Society*, **242**, 318–337.
- Savaglio, S., Glazebrook, K., Le Borgne, D., Juneau, S., Abraham, R.G., Chen, H.-W., Crampton, D., McCarthy, P.J., Carlberg, R.G., Marzke, R.O., Roth, K., Jørgensen, I., and Murowinski, R. (2005). The Gemini Deep Deep Survey: VII. The redshift evolution of the mass-metallicity relation, *Astrophysical Journal*, **635**, 260–279.
- Schechter, P. (1976). An analytic expression for the luminosity function of galaxies, *Astrophysical Journal*, **203**, 297–306.
- Schechter, P.L. (2002). Tales within tales and cutoffs within cutoffs: what sets the mass scale for galaxies?, in *Lighthouses of the Universe: The Most Luminous Objects and Their Use for Cosmology*, eds. Gilfanov, M., Sunyeav, R., and Churazov, E., pp. 3–12. Berlin: Springer.
- Scheuer, P.A.G. (1957). A statistical method for analysing observations of faint radio stars, *Proceedings of the Cambridge Philosophical Society*, **53**, 764–773.
- Scheuer, P.A.G. (1965). A sensitive test for the presence of atomic hydrogen in intergalactic space, *Nature*, **207**, 963.
- Scheuer, P.A.G. (1974). Fluctuations in the X-ray background, *Monthly Notices of the Royal Astronomical Society*, **166**, 329–338.
- Scheuer, P.A.G. (1990). Radio source counts, in *Modern Cosmology in Retrospect*, eds Bertotti, B., Balbinot, R., Bergia, S., and Messina, A., pp. 331–346. Cambridge: Cambridge University Press.
- Schindler, S., Binggeli, B., and Böhringer, H. (1999). Morphology of the Virgo cluster: gas versus galaxies, *Astronomy and Astrophysics*, **343**, 420–438.
- Schmidt, B.P., Kirshner, R.P., and Eastman, R.G. (1992). Expanding photospheres of type II supernovae and the extragalactic distance scale, *Astrophysical Journal*, **395**, 366–386.
- Schmidt, M. (1968). Space distribution and luminosity functions of quasi-stellar sources, *Astrophysical Journal*, **151**, 393–409.

- Schmidt, M. and Green, R.F. (1983). Quasar evolution derived from the Palomar Bright Quasar Survey and other complete quasar surveys, *Astrophysical Journal*, **269**, 352–374.
- Schmidt, M., Schneider, D.P., and Gunn, J.E. (1995). Spectroscopic CCD Surveys for Quasars at Large Redshift. IV. Evolution of the luminosity function from quasars detected by their Lyman-alpha emission, *Astronomical Journal*, **110**, 68–77.
- Schneider, D., Schmidt, M., and Gunn, J.E. (1991). PC 1247 + 3406 - an optically selected quasar with a redshift of 4.897, *Astronomical Journal*, **102**, 837–840.
- Schneider, P., Kochanek, C.S., and Wambsganss, J. (2006). *Gravitational Lensing: Strong, Weak and Micro*. Berlin: Springer. Saas-Fee Advanced Course 33: eds. Meylan, G. and Jetzer, P. and North, P.
- Schramm, D.N. (1997). The age of the Universe, in *Critical Dialogues in Cosmology*, ed. Turok, N., pp. 81–91. Singapore: World Scientific.
- Schramm, D.N. and Wasserburg, G.T. (1970). Nucleochronologies and the mean age of the elements, *Astrophysical Journal*, **162**, 57–69.
- Schutz, B. (2001). Gravitational radiation, in *Encyclopaedia of Astronomy and Astrophysics*, ed. P. M., volume 2, pp. 1030–1042. Bristol and Philadelphia: Institute of Physics Publishing and London: Nature Publishing Group.
- Schwarzchild, M. (1979). A numerical model for a triaxial stellar system in dynamical equilibrium, *Astrophysical Journal*, **232**, 236–228.
- Scott, J., Bechtold, J., Dobrzycki, A., and Kulkarni, V.P. (2000). A uniform analysis of the Ly α forest at $z = 0 – 5$: II. Measuring the mean intensity of the extragalactic ionizing background using the proximity effect, *Astrophysical Journal Supplement*, **130**, 67–89.
- Scranton, R., Johnston, D., Dodelson, S., Frieman, J., Connolly, A., Eisenstein, D., Gunn, J., Hui, L., Jain, B., Kent, S., Loveday, J., Narayanan, V., Nichol, R., O’Connell, L., Scoccimarro, R., Sheth, R., Stebbins, A., Strauss, M., Szalay, A., Szapudi, I., Tegmark, M., Vogeley, M., Zehavi, I., Annis, J., Bahcall, N., Brinkman, J., Csabai, I., Hindsley, R., Ivezić, Z., Kim, R., Knapp, G., Lamb, D., Lee, B., Lupton, R., McKay, T., Munn, J., Peoples, J., Pier, J., Richards, G., Rockosi, C., Schlegel, D., Schneider, D., Stoughton, C., Tucker, D., Yanny, B., and York, D. (2002). Analysis of systematic effects and statistical uncertainties in angular clustering of galaxies from early Sloan Digital Sky Survey Data, *Astrophysical Journal*, **579**, 48–75.
- Seager, S., Sasselov, D.D., and Scott, D. (2000). How exactly did the Universe become neutral?, *Astrophysical Journal Supplement*, **128**, 407–430.
- Seldner, M. and Peebles, P.J.E. (1977). Statistical analysis of catalogs of extragalactic objects: VIII. Cross-correlation of the Abell and the 10-arcmin Shane–Wirtanen catalogs, *Astrophysical Journal*, **215**, 703–716.
- Seljak, U., Makarov, A., McDonald, P., Anderson, S.F., Bahcall, N.A., Brinkmann, J., Burles, S., Cen, R., Doi, M., Gunn, J.E., Ivezić, Ž., Kent, S., Loveday, J., Lupton, R.H., Munn, J.A., Nichol, R.C., Ostriker, J.P., Schlegel, D.J., Schneider, D.P., Tegmark, M., Berk, D.E., Weinberg, D.H., and York, D.G. (2005). Cosmological parameter analysis including SDSS Ly α forest and galaxy bias: constraints on the

- primordial spectrum of fluctuations, Neutrino Mass, and Dark Energy, *Physical Review D*, **71**, 103515.
- Seljak, U. and Zaldarriaga, M. (1996). A line-of-sight integration approach to cosmic microwave background anisotropies, *Astrophysical Journal*, **469**, 437–444.
- Sérsic, J.L. (1968). *Atlas de galaxias australes*. Cordoba, Argentina: Observatorio Astronomico.
- Shapiro, I. (1990). Solar system tests of General Relativity: recent results and present plans, in *General Relativity and Gravitation*, eds. Ashby, N., Bartlett, D.F., and Wyss, W., pp. 313–330. Cambridge: Cambridge University Press.
- Shapiro, I.I. (1964). Fourth test of General Relativity, *Physical Review Letters*, **13**, 789–791.
- Shapiro, S.S., Davis, J.L., Lebach, D.E., and Gregory, J.S. (2004). Measurement of the solar gravitational deflection of radio waves using geodetic very-long-baseline interferometry data, 1979–1999, *Physical Review Letters*, **92**, 121101.
- Shapley, H. (1918). Studies Based on the Colors and Magnitudes in Stellar Clusters. VII. The distances, distribution in space, and dimensions of 60 globular clusters, *Astrophysical Journal*, **48**, 154–181.
- Shectman, S.A. (1974). The small scale anisotropy of the cosmic light, *Astrophysical Journal*, **188**, 233–242.
- Shellard, P. (2003). The future of cosmology: observational and computational prospects, in *The Future of Theoretical Physics and Cosmology*, eds. Gibbons, G., Shellard, E., and Rankin, S., pp. 755–780. Cambridge: Cambridge University Press.
- Sheth, R.K., Mo, H.J., and Tormen, G. (2001). Ellipsoidal collapse and an improved model for the number and spatial distribution of dark matter haloes, *Monthly Notices of the Royal Astronomical Society*, **323**, 1–12.
- Shimasaku, K., Ouchi, M., Furusawa, H., Yoshida, M., Kashikawa, N., and Okamura, S. (2005). Number density of bright Lyman-break galaxies at $z \sim 6$ in the Subaru Deep Field, *Publications of the Astronomical Society of Japan*, **57**, 447–458.
- Silk, J. (1968). Cosmic black-body radiation and galaxy formation, *Astrophysical Journal*, **151**, 459–471.
- Silk, J. and Wyse, R.F.G. (1993). Galaxy formation and Hubble sequence, *Physics Reports*, **231**, 293–365.
- Simon, P., Hetterscheidt, M., Schirmer, M., Erben, T., Schneider, P., Wolf, C., and Meisenheimer, K. (2007). GaBoDS: The Garching–Bonn Deep Survey: VI. Probing galaxy bias using weak gravitational lensing, *Astronomy and Astrophysics*, **461**, 861–879.
- Smail, I., Ivison, R.J., and Blain, A.W. (1997). A deep sub-millimeter survey of lensing clusters: a new window on galaxy formation and evolution, *Astrophysical Journal Letters*, **490**, L5–L8.
- Smith, R.W. (1982). *The Expanding Universe: Astronomy's 'Great Debate' 1900–1931*. Cambridge: Cambridge University Press.
- Smoot, G., Bennett, C., Kogut, A., Wright, E., Aymon, J., Boggess, N., Cheng, E., de Amici, G., Gulkis, S., Hauser, M., Hinshaw, G., Jackson, P., Janssen, M.,

- Kaita, E., Kelsall, T., Keegstra, P., Lineweaver, C., Loewenstein, K., Lubin, P., Mather, J., Meyer, S., Moseley, S., Murdock, T., Rokke, L., Silverberg, R., Tenorio, L., Weiss, R., and Wilkinson, D. (1992). Structure in the COBE differential microwave radiometer first-year maps, *Astrophysical Journal*, **396**, L1–L5.
- Sneden, C., McWilliam, A., Preston, G.W., Cowan, J.J., Burris, D.L., and Armosky, B.J. (1992). The ultra-metal-poor, neutron-capture-rich giant star CS 22892-052, *Astrophysical Journal*, **467**, 819–840.
- Songaila, A., Bryant, W., and Cowie, L.L. (1989). Limits on the galactic and cosmic ionizing fluxes from measurements of H- α emission from the high-velocity neutral hydrogen clouds, *Astrophysical Journal Letters*, **345**, L71–L73.
- Songaila, A., Cowie, L.L., Vogt, S., Keane, M., Wolfe, A.M., Hu, E.M., Oren, A.L., Tytler, D.R., and Lanzetta, K.M. (1994). Measurement of the microwave background temperature at a redshift of 1.776, *Nature*, **371**, 43–45.
- Songaila, A., Hu, E.M., and Cowie, L.L. (1995). A population of very diffuse Lyman- α clouds as the origin of the He $^+$ absorption signal in the intergalactic medium, *Nature*, **375**, 124–126.
- Soucail, G., Fort, B., Mellier, Y., and Picat, J.P. (1987). A blue ring-like structure, in the center of the A370 cluster of galaxies, *Astronomy and Astrophysics*, **172**, L14–L16.
- Sparke, L. and Gallagher, J. (2000). *Galaxies in the Universe: an Introduction*. Cambridge: Cambridge University Press.
- Spergel, D.N., Bean, R., Doré, O., Nolta, M.R., Bennett, C.L., Dunkley, J., Hinshaw, G., Jarosik, N., Komatsu, E., Page, L., Peiris, H.V., Verde, L., Halpern, M., Hill, R.S., Kogut, A., Limon, M., Meyer, S.S., Odegard, N., Tucker, G.S., Weiland, J.L., Wollack, E., and Wright, E.L. (2007). Three-year Wilkinson Microwave Anisotropy Probe (WMAP) observations: implications for cosmology, *Astrophysical Journal Supplement*, **170**, 377–408.
- Spinrad, H., Dey, A., and Graham, J.R. (1995). Keck observations of the most distant galaxy: 8C 1435+63 at $z = 4.25$, *Astrophysical Journal*, **438**, L51–L54.
- Spite, F. and Spite, M. (1982). Abundance of lithium in unevolved halo stars and old disk stars – interpretation and consequences, *Astronomy and Astrophysics*, **115**, 357–366.
- Springel, V. (2005). The cosmological simulation code GADGET-2, *Monthly Notices of the Royal Astronomical Society*, **364**, 1105–1134. For access to his simulations, see <http://www.mpa-garching.mpg.de/gadget/right.html>.
- Springel, V., White, S.D.M., Jenkins, A., Frenk, C.S., Yoshida, N., Gao, L., Navarro, J., Thacker, R., Croton, D., Helly, J., Peacock, J.A., Cole, S., Thomas, P., Couchman, H., Evrard, A., Colberg, J., and Pearce, F. (2005). Simulations of the formation, evolution and clustering of galaxies and quasars, *Nature*, **435**, 629–636.
- Srianand, R. (2006). Intergalactic medium, in *The Scientific Requirements for Extremely Large Telescopes: IAU Symposium No. 232*, eds. Whitelock, P., Dennefeld, M., and Leibundgut, B., pp. 130–139.
- Starobinsky, A.A. (1985). Cosmic background anisotropy induced by isotropic flat-spectrum gravitational-wave perturbations, *Soviet Astronomy Letters*, **11**, 133–137. In Russian: 1985, *Pis'ma v Astronomicheskii Zhurnal*, **11**, 323–330.

- Steidel, C. (1998). Galaxy evolution: has the “epoch of galaxy formation” been found?, in *Eighteenth Texas Symposium on Relativistic Astrophysics and Cosmology*, eds. Olinto, A., Frieman, J., and Schramm, D., pp. 124–135. River Edge, NJ: World Scientific.
- Steidel, C. and Hamilton, D. (1992). Deep imaging of high redshift QSO fields below the Lyman limit: I. The field of Q0000-263 and galaxies at $Z = 3.4$, *Astronomical Journal*, **104**, 941–949.
- Steidel, C.C., Adelberger, K.L., Giavalisco, M., Dickinson, M., and Pettini, M. (1999). Lyman-break galaxies at $z \geq 4$ and the evolution of the ultraviolet luminosity density at high redshift, *Astrophysical Journal*, **519**, 1–17.
- Steigman, G. (1997). The crisis confronting standard Big Bang nucleosynthesis, in *Critical Dialogues in Cosmology*, ed. Turok, N., pp. 63–80. Singapore: World Scientific.
- Steigman, G. (2004). Big Bang nucleosynthesis: probing the first 20 minutes, in *Measuring and Modeling the Universe*, ed. Freedman, W.L., pp. 169–195. Cambridge: Cambridge University Press.
- Steigman, G. (2006). Primordial nucleosynthesis: successes and challenges, *International Journal of Modern Physics E*, **15**, 1–35.
- Steigman, G. (2007). Primordial nucleosynthesis, *Annual Review of Nuclear and Particle Science*, **57**, (in press).
- Storrie-Lombardi, L., McMahon, R., and Irwin, M. (1996). Evolution of neutral gas at high redshift: implications for the epoch of galaxy formation, *Monthly Notices of the Royal Astronomical Society*, **283**, L79–L83.
- Stoughton, D., Lupton, R.H., and 191 authors (2002). Sloan Digital Sky Survey: early data release, *Astronomical Journal*, **123**, 485–548.
- Strömborg, G. (1934). The origin of the galactic rotation and of the connection between physical properties of the stars and their motions, *Astrophysical Journal*, **79**, 460–474.
- Subramanian, K. (2005). The physics of CMBR anisotropies, *Current Science*, **88**, 1068–1087.
- Sullivan, III, W.T. (1990). The entry of radio astronomy into cosmology: radio stars and Martin Ryle’s 2C survey, in *Modern Cosmology in Retrospect*, eds. Bertotti, B., Balbinot, R., Bergia, S., and Messina, A., pp. 309–330. Cambridge: Cambridge University Press.
- Sunyaev, R. and Zeldovich, Y. (1970). Small-scale fluctuations of relic radiation, *Astrophysics and Space Science*, **7**, 3–19.
- Sunyaev, R.A. (1969). The interaction of the metagalactic ultraviolet background radiation with galaxies and the limit on the density of the intergalactic gas, *Astrophysical Letters*, **3**, 33–38.
- Sunyaev, R.A. and Zeldovich, Y.B. (1972). Formation of clusters of galaxies; protocluster fragmentation and intergalactic gas heating, *Astronomy and Astrophysics*, **20**, 189–200.
- Sunyaev, R.A. and Zeldovich, Y.B. (1980a). Microwave background radiation as a probe of the contemporary structure and history of the Universe, *Annual Review of Astronomy and Astrophysics*, **18**, 537–560.

- Sunyaev, R.A. and Zeldovich, Y.B. (1980b). The velocity of clusters of galaxies relative to the microwave background – the possibility of its measurement, *Monthly Notices of the Royal Astronomical Society*, **190**, 413–420.
- eds. Tanvir, N.R., Aragon-Salamanca, A., and Wall, J.V. (1997). *The Hubble Space Telescope and the High Redshift Universe*. Singapore: World Scientific.
- Taylor, R.J. (1994). *The Stars: Their Structure and Evolution*. Cambridge: Cambridge University Press.
- Taylor, G.B. and Wright, E.L. (1989). Effects of a hot intergalactic medium, *Astrophysical Journal*, **339**, 619–628.
- Taylor, J.H. (1992). Pulsar timing and relativistic gravity, *Philosophical Transactions of the Royal Society*, **341**, 117–134.
- Taylor, J.H. and Cordes, J.M. (1993). Pulsar distances and the galactic distribution of free electrons, *Astrophysical Journal*, **411**, 674–684.
- Tegmark, M., Strauss, M., and 66 authors (2004). Cosmological parameters from SDSS and WMAP, *Physical Review D*, **69**, 103501 (1–28).
- Thorne, K., Price, R., and Macdonald, D. (1986). *Black Holes: The Membrane Paradigm*. New Haven: Yale University Press.
- Tinsley, B.M. (1980). Evolution of the stars and gas in galaxies, *Fundamentals of Cosmic Physics*, **5**, 287–388.
- Tinsley, B.M. and Gunn, J.E. (1976). Luminosity functions and the evolution of low-mass population: I. Giants, *Astrophysical Journal*, **206**, 525–535.
- Toller, G.N. (1990). Optical observations of galactic and extragalactic light – implications for galactic structure, in *The Galactic and Extragalactic Background Radiation*, eds. Bowyer, S. and Leinert, C., IAU Symposium No. 139, pp. 21–34. Dordrecht: Kluwer.
- Tolman, R. (1934). Effect of inhomogeneity on cosmological models, *Proceedings of the National Academy of Sciences*, **20**, 169–176.
- Tonks, L. and Langmuir, I. (1929). Oscillations in ionized gases, *Physical Review*, **33**, 195–210.
- Tonry, J., Schmidt, B., Barris, B., Candia, P., Challis, P., Clocchiatti, A., Coil, A., Filippenko, A., Garnavich, P., Hogan, C., Holland, S., Jha, S., Kirshner, R., Krisciunas, K., Leibundgut, B., Li, W., Matheson, T., Phillips, M., Riess, A., Schommer, R., Smith, R., Sollerman, J., Spyromilio, J., Stubbs, C., and Suntzeff, N. (2003). Cosmological results from high-z supernovae, *Astrophysical Journal*, **594**, 1–24.
- Toomre, A. (1974). Gravitational interactions between galaxies, in *IAU Symposium No. 58: The Formation and Dynamics of Galaxies*, ed. Shakeshaft, J., pp. 347–365. Dordrecht: D. Reidel Publishing Company
- Toomre, A. and Toomre, J. (1972). Galactic bridges and tails, *Astrophysical Journal*, **178**, 623–666.
- Tremaine, S. and Gunn, J. (1979). Dynamical role of light neutral leptons in cosmology, *Physical Review Letters*, **42**, 407–410.
- Tremaine, S. and Richstone, D.O. (1977). A test of a statistical model for the luminosities of bright cluster galaxies, *Astrophysical Journal*, **212**, 311–316.

- Tremonti, C.A., Heckman, T.M., Kauffmann, G., Brinchmann, J., Charlot, S., White, S.D.M., Seibert, M., Peng, E.W., Schlegel, D.J., Uomoto, A., Fukugita, M., and Brinkmann, J. (2004). The origin of the mass-metallicity relation: insights from 53,000 star-forming galaxies in the Sloan Digital Sky Survey, *Astrophysical Journal*, **613**, 898–913.
- Trimble, V. (1995). The 1920 Shapley–Curtis discussion: background, issues, and aftermath, *Publications of the Astronomical Society of the Pacific*, **107**, 1133–1144.
- Trodden, M. (2006). Physics of the very early Universe: what can we learn from particle collider experiments?, *Proceedings of Science*, **CMB2006**, 1–9. This electronic publication can be found at <http://pos.sissa.it/archive/conferences/027/003/CMB2006-003.pdf>.
- Tropp, E., Frenkel, V., and Chernin, A. (1993). *Alexander A. Friedmann: the Man who Made the Universe Expand*. Cambridge: Cambridge University Press.
- Trushkin, S.A. (2003). Radio spectra of the WMAP catalog sources, *Bulletin of the Special Astrophysical Observatory*, **55**, 90–132.
- Tully, R.B. and Fisher, J.R. (1977). A new method of determining distances to galaxies, *Astronomy and Astrophysics*, **54**, 661–673.
- Turner, M. (1997). Inflationary cosmology, in *Relativistic Astrophysics*, eds Jones, B.J.T. and Markovic, D., pp. 83–102. Cambridge: Cambridge University Press.
- Turok, N. (1989). Global texture as the origin of cosmic structure, *Physical Review Letters*, **63**, 2625–2628.
- ed. Turok, N. (1997). *Critical Dialogues in Cosmology*. Singapore: World Scientific.
- Tyson, J.A., Kochanski, G.P., and dell’Antonio, I.P. (1998). Detailed mass map of CL 0024+1654 from strong lensing, *Astrophysical Journal Letters*, **498**, L107–L110.
- Vallée, J.P. (1997). Observations of the magnetic fields inside and outside the Milky Way, starting with globules (~ 1 parsec), filaments, clouds, superbubbles, spiral arms, galaxies, superclusters, and ending with the cosmological Universe’s background surface (at ~ 8 teraparsecs), *Fundamentals of Cosmic Physics*, **19**, 1–89.
- van den Bergh, S. (1998). *Galaxy Morphology and Classification*. Cambridge: Cambridge University Press.
- Verde, L., Heavens, A.F., Percival, W.J., Matarrese, S., Baugh, C.M., Bland-Hawthorn, J., Bridges, T., Cannon, R., Cole, S., Colless, M., Collins, C., Couch, W., Dalton, G., De Propris, R., Driver, S.P., Efstathiou, G., Ellis, R.S., Frenk, C.S., Glazebrook, K., Jackson, C., Lahav, O., Lewis, I., Lumsden, S., Maddox, S., Madgwick, D., Norberg, P., Peacock, J.A., Peterson, B.A., Sutherland, W., and Taylor, K. (2002). The 2dF Galaxy Redshift Survey: the bias of galaxies and the density of the Universe, *Monthly Notices of the Royal Astronomical Society*, **335**, 432–440.
- Vishniac, E.T. (1987). Reionization and small-scale fluctuations in the microwave background, *Astrophysical Journal*, **322**, 597–604.

- Visvanathan, N. and Sandage, A.R. (1977). The color-absolute magnitude relation for E and S0 galaxies: I. Calibration and tests for universality using Virgo and eight other nearby clusters, *Astrophysical Journal*, **216**, 214–226.
- Vogel, S. and Reimers, D. (1995). The ultraviolet absorption spectrum of the $Z = 2.72$ QSO HS 1700+6416: 1. Results on heavy-element absorption systems, *Astronomy and Astrophysics*, **294**, 377–410.
- von Weizsächer, C.F. (1947). Zur Kosmogonie, *Zeitschrift für Astrophysik*, **24**, 181–206.
- Waddington, I., Dunlop, J.S., Peacock, J.A., and Windhorst, R.A. (2001). The LBDS Hercules sample of mJy radio sources at 1.4 GHz – II. Redshift distribution, radio luminosity function, and the high-redshift cut-off, *Monthly Notices of the Royal Astronomical Society*, **328**, 882–896.
- Wagoner, R., Fowler, W., and Hoyle, F. (1967). On the synthesis of elements at very high temperatures, *Astrophysical Journal*, **148**, 3–49.
- Wagoner, R.V. (1973). Big-Bang nucleosynthesis revisited, *Astrophysical Journal*, **179**, 343–360.
- Walker, A.G. (1936). On Milne's theory of world structure, *Proceedings of the London Mathematical Society, Series 2*, **42**, 90–127.
- Wall, J.V. (1996). Space distribution of radio source populations, in *Extragalactic Radio Sources, IAU Symposium No. 175*, eds. Ekers, R., Fanti, C., and Padrielli, L., pp. 547–552. Dordrecht: Kluwer.
- Walsh, D., Carswell, R.F., and Weymann, R.J. (1979). 0957+561A, B – twin quasistellar objects or gravitational lens, *Nature*, **279**, 381–384.
- Wambsganss, J. (1998). Gravitational lensing in astronomy, *Living Review in Relativity*, **1**. Online article: accepted 28 August 1998; last amended 31 August 2001 <http://www.livingreviews.org/lrr-1998-12>.
- Wang, W.-H., Cowie, L.L., and Barger, A.J. (2006). A near-infrared analysis of the submillimeter background and the cosmic star-formation history, *Astrophysical Journal*, **647**, 74–85.
- Warren, S.J., Hewett, P.C., Irwin, M.J., McMahon, R.G., and Bridgeland, M.T. (1987). First observation of a quasar with a redshift of 4, *Nature*, **325**, 131–133.
- Weedman, D. (1994). Starburst galaxies at high redshift, in *First Stromlo Symposium: Physics of Active Galactic Nuclei*, eds. Bicknell, G., Dopita, M., and Quinn, P., pp. 409–415. San Francisco: Astronomical Society of the Pacific Conference Series, Vol. 34.
- Weinberg, S. (1972). *Gravitation and Cosmology*. New York: Wiley.
- Weinberg, S. (1989). The cosmological constant problem, *Reviews of Modern Physics*, **61**, 1–23.
- Weinberg, S. (1997). Theories of the cosmological constant, in *Critical Dialogues in Cosmology*, ed. Turok, N., pp. 195–203. Singapore: World Scientific.
- Weinheimer, C. (2001). Neutrino mass from tritium β -Decay, in *Dark Matter in Astro- and Particle Physics, Proceedings of the International Conference DARK 2000*, ed. Klapdor-Kleingrothaus, H.V., pp. 513–519. Berlin: Springer-Verlag.
- Weiss, R. (1980). Measurements of the cosmic background radiation, *Annual Review of Astronomy and Astrophysics*, **18**, 489–535.

- Wesselink, A.J. (1947). The Observations of Brightness, Colour and Radial Velocity of δ -Cephei and the pulsation hypothesis, *Bulletin of the Astronomical Institutes of the Netherlands*, **10**, 91–99. Errata, **10**, 258 and 310.
- Weyl, H. (1923). Zur allgemeinen Relativitätstheorie (On the Theory of General Relativity), *Physikalische Zeitschrift*, **29**, 230–232.
- Weymann, R. (1966). The energy spectrum of radiation in the expanding Universe, *Astrophysical Journal*, **145**, 560–571.
- Weymann, R. (1967). Possible thermal histories of intergalactic gas, *Astrophysical Journal*, **147**, 887–900.
- Wheeler, J. (1977). Genesis and observership, in *Foundational Problems in the Special Science*, eds. Butts, R. and Hintikka, J., pp. 3–33. Dordrecht: Reidel.
- White, D.A., Fabian, A.C., Allen, S.W., Edge, A.C., Crawford, C.S., Johnstone, R.M., Stewart, G.C., and Voges, W. (1994). A ROSAT HRI observation of the ABELL:478 cluster of galaxies, *Monthly Notices of the Royal Astronomical Society*, **269**, 589–606.
- White, S.D. (1989). Observable signatures of young galaxies, in *The Epoch of Galaxy Formation*, eds. Frenk, C.S., Ellis, R.S., Shanks, T., Heavens, A.F., and Peacock, J.A., pp. 15–30. Dordrecht: Kluwer.
- White, S.D.M. (1990). Physical cosmology, in *Physics of the Early Universe*, eds Peacock, J.A., Heavens, A.F., and Davies, A.T., pp. 1–62. Edinburgh: SUSSP.
- White, S.D.M. and Rees, M.J. (1978). Core condensation in heavy halos – a two-stage theory for galaxy formation and clustering, *Monthly Notices of the Royal Astronomical Society*, **183**, 341–358.
- Wilkinson, P.N., Henstock, D.R., Browne, I.W., Polatidis, A.G., Augusto, P., Readhead, A.C., Pearson, T.J., Xu, W., Taylor, G.B., and Vermeulen, R.C. (2001). Limits on the cosmological abundance of supermassive compact objects from a search for multiple imaging in compact radio sources, *Physical Review Letters*, **86**, 584–587.
- Will, C. (1993). *Theory and Experiment in Gravitational Physics*. Cambridge: Cambridge University Press.
- Will, C.M. (2006). The confrontation between General Relativity and experiment, *Living Reviews in Relativity*, **9**. Online article: cited on 21 June 2006 <http://www.livingreviews.org/lrr-2006-3>.
- Williams, J.G., Turyshev, S.G., and Boggs, D.H. (2004). Progress in lunar laser ranging tests of relativistic gravity, *Physical Review Letters*, **93**, 261101, 1–4.
- eds. Williams, P., Shu, C.-G., and Ménard, B. (2005). *Probing Galaxies through Quasar Absorption Lines*. Cambridge: Cambridge University Press.
- Williams, R.E., Baum, S., Bergeron, L.E., Bernstein, N., Blacker, B.S., Boyle, B.J., Brown, T.M., Carollo, C.M., Casertano, S., Covarrubias, R., de Mello, D.F., Dickinson, M.E., Espey, B.R., Ferguson, H.C., Fruchter, A., Gardner, J.P., Gonnella, A., Hayes, J., Hewett, P.C., Heyer, I., Hook, R., Irwin, M., Jones, D., Kaiser, M.E., Levay, Z., Lubenow, A., Lucas, R.A., Mack, J., MacKenty, J.W., Madau, P., Makidon, R.B., Martin, C.L., Mazzuca, L., Mutchler, M., Norris, R.P., Perriello, B., Phillips, M.M., Postman, M., Royle, P., Sahu, K., Savaglio, S., Sherwin, A., Smith, T.E., Stiavelli, M., Suntzeff, N.B., Teplitz, H.I., van der

- Marel, R.P., Walker, A.R., Weymann, R.J., Wiggs, M.S., Williger, G.M., Wilson, J., Zacharias, N., and Zurek, D.R. (2000). The Hubble Deep Field South: formulation of the observing campaign, *Astronomical Journal*, **120**, 2735–2746.
- Williams, R.E., Blacker, B., Dickenson, M., Dixon, W.V.D., Ferguson, H.C., Fruchter, A.S., Giavalisco, M., Gilliland, R.L., Heyer, I., Katsanis, R., Levay, Z., Lucas, R.A., McElroy, D.B., Petro, L., Postman, M., Adorf, H.M., and Hook, R.N. (1996). The Hubble Deep Field: observations, data reduction, and galaxy photometry, *Astronomical Journal*, **112**, 1335–1389.
- Windhorst, R.A., Dressler, A., and Koo, D.A. (1987). Ultradeep optical identifications and spectroscopy of faint radio sources, in *Observational Cosmology*, eds. Hewitt, A., Burbidge, G., and Fang, L.-Z., pp. 573–576. Dordrecht: Reidel.
- Windhorst, R.A., Fomalont, E.B., Kellermann, K.I., Partridge, R.B., Richards, E., Franklin, B.E., Pascerelle, S.M., and Griffiths, R.E. (1995). Identification of faint radio sources with optically luminous interacting disk galaxies, *Nature*, **375**, 471–474.
- Wolfe, A. (1988). Damped Ly- α absorption systems, in *QSO Absorption Lines: Probing the Universe*, eds. Blades, J., Turnshek, D., and Norman, C., pp. 306–317. Cambridge: Cambridge University Press.
- Woltjer, L. (1990). Phenomenology of active galactic nuclei, in *Saas-Fee Advanced Course 20. Active Galactic Nuclei*, eds. Courvoisier, T.J.-L. and Mayor, M., pp. 1–55. Berlin: Springer-Verlag.
- Wood-Vasey, W.M., Miknaitis, G., Stubbs, C.W., Jha, S., Riess, A.G., Garnavich, P.M., Kirshner, R.P., Aguilera, C., Becker, A.C., Blackman, J.W., Blondin, S., Challis, P., Clocchiatti, A., Conley, A., Covarrubias, R., Davis, T.M., Filippenko, A.V., Foley, R.J., Garg, A., Hicken, M., Krisciunas, K., Leibundgut, B., Li, W., Matheson, T., Miceli, A., Narayan, G., Pignata, G., Prieto, J.L., Rest, A., Salvo, M.E., Schmidt, B.P., Smith, R.C., Sollerman, J., Spyromilio, J., Tonry, J.L., Suntzeff, N.B., and Zenteno, A. (2007). Observational constraints on the nature of the dark energy: first cosmological results from the ESSENCE Supernova Survey, *Astrophysical Journal*, **666**, 294–715.
- Zaldarriaga, M. (1997). Polarization of the microwave background in reionized models, *Physical Review*, **D55**, 1822–1829.
- Zaldarriaga, M. (2004). The polarization of the cosmic microwave background, in *Measuring and Modeling the Universe*, ed. Freedman, W.L., pp. 309–329. Cambridge: Cambridge University Press.
- Zaritsky, D., Kennicutt, R.C., and Huchra, J.P. (1994). H II regions and the abundance properties of spiral galaxies, *Astrophysical Journal*, **420**, 87–109.
- Zekser, K.C., White, R.L., Broadhurst, T.J., Benítez, N., Ford, H.C., Illingworth, G.D., Blakeslee, J.P., Postman, M., Jee, M.J., and Coe, D.A. (2006). Mass modeling of Abell 1689 Advanced Camera for surveys observations with a perturbed Navarro-Frenk-White model, *Astrophysical Journal*, **640**, 639–661.
- Zeldovich, Y. (1965). Survey of modern cosmology, *Advances of Astronomy and Astrophysics*, **3**, 241–379.
- Zeldovich, Y. (1970). Gravitational instability: an approximate theory for large density perturbations, *Astronomy and Astrophysics*, **5**, 84–89.

- Zeldovich, Y. (1972). A hypothesis, unifying the structure and the entropy of the universe, *Monthly Notices of the Royal Astronomical Society*, **160**, 1P–3P.
- Zeldovich, Y. (1986). Cosmological field theory for observational astronomers, *Astrophysics and Space Physics Reviews*, **5**, 1–37.
- Zeldovich, Y. and Sunyaev, R. (1969). The interaction of matter and radiation in a hot-model universe, *Astrophysics and Space Science*, **4**, 301–316.
- Zeldovich, Y.B. (1964). Observations in a Universe homogeneous in the mean, *Astronomicheskii Zhurnal*, **41**, 19–24. [Translation: (1964), *Soviet Astronomy*, **8**, 13–16].
- Zeldovich, Y.B. (1968). The cosmological constant and the theory of elementary particles, *Uspekhi Fizicheskikh Nauk*, **95**, 209–230. [Translation: (1968) *Soviet Physics – Uspekhi*, **11**, 381–393.]
- Zeldovich, Y.B. (1993). Particles, nuclei and the Universe, in *Selected Works of Yakov Borisovich Zeldovich*, Vol. 2., eds. Ostriker, J., Barenblatt, G., and Sunyaev, R. Princeton: Princeton University Press.
- Zeldovich, Y.B., Kurt, D., and Sunyaev, R.A. (1968). Recombination of hydrogen in the hot model of the Universe, *Zhurnal Eksperimentalnoi i Teoreticheskoi Fiziki*, **55**, 278–286. Translation: (1969), *Soviet Physics – JETP*, **28**, 146–150.
- Zeldovich, Y.B. and Novikov, I.D. (1983). *Relativistic astrophysics*, Vol. 2. Chicago: Chicago University Press.
- Zeldovich, Y.B. and Sunyaev, R.A. (1980). The angular distribution of the microwave background, and its intensity in the direction of galaxy clusters, *Soviet Astronomy Letters*, **6**, 285–286.
- Zwicky, F. (1937). On the masses of nebulae and of clusters of nebulae, *Astrophysical Journal*, **86**, 217–246.

Name Index

- Aaronson, Marc 246
Abell, George 81, 95, 101, 102
Abraham, Robert 540
Adams, Walter 177, 178
Albrecht, Andreas 24, 629
Alpher, Ralph 14
Aragón-Salamanca, Alfonso 253, 544
Arnaud, Monique 117
Arp, Halton 56
- Baade, Walter 13, 248
Babbage, Thomas 536
Bahcall, John 568
Bahcall, Neta 99, 100, 108, 267, 387
Bajtlik, Stanislaw 568, 569
Balzano, Vicki 597
Barcons, Xavier 561
Bardeen, James 348, 349, 394–396, 402
Barger, Amy 597, 598
Barnes, Joshua 611
Barrow, John 625
Baugh, Carlton 615
Baumann, Daniel 630, 631, 634, 636–638, 640
Bautz, Laura 109
Becker, Robert 552
Beckwith, Steven 543, 590, 592, 593, 596
Benson, Bradford 404
Bentley, Richard 4
Bergeron, Jacqueline 479, 489, 593
Berkeley, Bishop 11
Bertschinger, Edmund 348, 349, 638
Bessel, Friedrich 5
Biermann, Ludwig 579
Binggeli, Bruno 78, 82, 116
Binney, James 108
Blain, Andrew 452, 534
Bland-Hawthorn, Jonathan 539
- Blandford, Roger 228, 229
Bludman, Sydney 24, 626
Blumenthal, George 481
Bolte, Michael 250, 251
Bolyai, János 11, 151
Bond, Richard 20, 375, 396, 398, 399
Bondi, Hermann 149, 150, 341
Borgani, Stefano 531
Bouwens, Rychard 592, 593
Bowyer, Stuart 506
Boyle, Brian 521
Boyle, Robert 4
Bracessi, Alessandro 519
Bracewell, Ronald 433
Braginsky, Vladimir 174
Brahe, Tycho 3
Brainerd, Tereasa 138
Branch, David 248
Brandt, W. Niel 524, 525, 527
Bruzual, Gustavo 498, 499, 587, 588, 594, 607–609
Burbidge, Geoffrey 14
Burbidge, Margaret 14
Burstein, David 269
Butcher, Harvey 543
- Cappelluti, Nico 529
Carroll, Sean 265, 324
Carswell, Robert 249
Carter, Brandon 625
Cayley, Arthur 11, 151
Chaboyer, Brian 250, 251
Challinor, Anthony 126, 422, 441, 449, 452, 454
Chambers, Kenneth 254
Charlot, Stéphane 498, 499, 594, 607–609
Chluba, Jens 423
Chwolson, Orest 128

- Cimatti, Andrea 542, 608, 609
 Clausius, Rudolph 64
 Clifford, William 11, 151
 Cole, Shaun 405
 Coles, Peter 331, 332, 354, 358, 360, 377,
 382, 402, 474
 Colless, Matthew 113
 Corbelli, Edvige 568
 Cowan, John 252
 Cowie, Lennox 272, 534, 542, 566, 586,
 587, 589, 590, 598
 Crommelin, Andrew 190
 Croom, Scott 387
- Dashevsky, Vladimir 233
 Davidsen, Arthur 550, 564, 566
 Davies, Roger 612
 Davis, Tamara 339, 342, 347
 de Bruyn, Ger 580
 de Sitter, Willem 12, 149
 de Vaucouleurs, Gérard 49, 51, 54, 246
 Dekel, Avni 268, 269, 402
 Descartes, René 5
 Dessauges-Zavadsky, Miroslava 603, 604
 Dicke, Robert 174, 621, 622
 Dickinson, Mark 545
 Disney, Michael 62
 Dodds, Stephen 405, 409, 415, 416, 439
 Dodelson, Scott 348, 350, 367, 368, 371,
 416, 422, 438, 440, 443, 445, 446,
 454, 614
 Doroshkevich, Andrei 18, 360
 Dressler, Alan 56, 102, 108, 404
 Dreyer, John 7
 Dunlop, James 516, 609
 Dunn, Andrew 113
 Dyer, Charles 233–235
- Eales, Stephen 255
 Eastman, Ronald 248
 Eddington, Arthur 13, 177, 178, 190
 Efstathiou, George 143, 173, 184, 313,
 358, 398, 399, 403, 408, 417, 439,
 443, 453, 484, 487, 611
 Einstein, Albert 11, 12, 128, 149, 151,
 173, 174, 181, 182, 184, 188, 199,
 204, 207
 Eisenstein, Daniel 409, 411, 412
 Ellis, George 348
- Ellis, Richard 130, 253, 259, 537, 538,
 542
 Ellis, Simon 539
 Eötvös, Lóránd 174
- Faber, Sandra 74
 Fabian, Andrew 122–124, 561
 Fabricant, Donald 115
 Fall, Michael 568, 598, 604–606, 611, 612
 Fan, Xiaohui 522, 524
 Faulkner, John 14
 Fechner, Cora 567
 Felten, James 77, 78, 509
 Fisher, Richard 73
 Fomalont, Edward 506
 Fort, Bernard 134, 136
 Fowler, William 14, 293
 Freedman, Wendy 247, 250
 Freeman, Kenneth 62, 612
 Frenk, Carlos 400, 401
 Friedman, Aleksander 12, 13, 149, 202,
 204
 Furlanetto, Steven 574, 576, 577
- Galilei, Galileo 5
 Gamow, George 13, 14
 Garnavich, Peter 257
 Gauss, Carl Friedrich 11, 151, 156
 Gavazzi, Raphaël 138
 Ge, Jian 273
 Geller, Margaret 109
 Gerling, Christian 11
 Gershtein, Semion 19
 Giacconi, Riccardo 524
 Giavalisco, Mauro 592
 Gibbons, Gary 25
 Gilli, Roberto 526, 528, 529
 Glazebrook, Karl 607
 Goobar, Ariel 257
 Gorenstein, Paul 115
 Gott, Richard 41, 42
 Govoni, Federica 580
 Green, Richard 519, 521
 Gregory, James 4
 Greve, Thomas 479
 Gribben, John 625
 Grossmann, Marcel 181, 182
 Groth, Edward 35

- Gunn, James 20, 111–113, 144, 267, 268,
499, 549
- Gurvits, Leonid 263
- Guth, Alan 24, 364, 626, 627, 639
- Guzzo, Luigi 531
- Hale, George Ellery 9
- Hamilton, Andrew 408, 409, 472
- Hardy, Eduardo 253
- Harrison, Edward 17, 392, 510
- Hasinger, Günther 506, 524, 525, 527
- Hauser, Michael 535, 587
- Hausman, Marc 544
- Hawking, Stephen 25, 643, 644
- Hawkins, Michael 521
- Haynes, Martha 84
- Heath, D. 324
- Heavens, Alan 402, 475
- Helfand, David 42
- Herman, Robert 14
- Hernquist, Lars 572
- Herschel, Caroline 7
- Herschel, John 7
- Herschel, William 5–7
- Hewish, Antony 504, 506
- Hewitt, Jacqueline 140
- Hinshaw, Gary 451
- Hogan, Craig 298
- Hoyle, Fiona 42
- Hoyle, Fred 14, 293
- Hu, Esther 555
- Hu, Wayne 409, 411, 415, 422, 426, 438,
443, 445, 447, 448, 454, 462, 463
- Hubble, Edwin 8–10, 44–46, 162, 267,
492–494
- Huggins, William 7
- Humason, Milton 9, 45
- Huygens, Christiaan 11
- Ikeuchi, Satoru 555
- Ivison, Robert 452
- Jakobsen, Peter 564, 566, 569, 571
- Jeans, James 4, 16, 313, 317
- Jones, Bernard 610
- Kaiser, Nicholas 136, 235, 402, 406, 407,
460
- Kant, Immanuel 5
- Kapahi, Vijay 261
- Kapteyn, Jacobus 7, 8
- Kashlinsky, Alexander 507
- Katz, Neal 572
- Kauffmann, Guinevere 417, 545
- Kellermann, Kenneth 263
- Kennicutt, Robert 87, 554, 616
- Kent, Stephen 111–113
- Kepler, Johannes 3
- Kibble, Thomas 628
- King, Ivan 107
- Kirshner, Robert 248
- Kneib, Jean-Pierre 130
- Kochanek, Christopher 130, 138
- Kogut, Alan 432
- Kolb, Rocky 143, 301, 303, 307, 369, 376,
397, 402, 642
- Kompaneets, Aleksander 17
- Koo, David 519
- Kooiman, Brian 42
- Kormendy, John 49, 51
- Kriss, Gerard 566
- Kron, Richard 519
- Kulkarni, Varsha 568, 601, 603
- Kulsrud, Russell 578–581
- Kundic, Tomislav 249
- Kurt, Vladimir 423, 563
- Kwan, John 248
- Lacy, Mark 610
- Lagache, Guilane 533, 536
- Lambert, Johann 5, 11, 150
- Lanczos, Cornelius 149
- Langmuir, Irving 317
- Lanzetta, Kenneth 601
- Larson, Richard 606
- Lasenby, Anthony 126
- Le Verrier, Urbain 189
- Leavitt, Henrietta 7, 8
- Lecar, Myron 115
- Ledoux, Cédric 273
- Lemaître, Georges 4, 13, 16, 204, 207,
322, 333
- Liddle, Andrew 25, 348, 349, 629, 630
- Lifshitz, Evgenii 4, 16, 313, 322, 333
- Lightman, Alan 268, 329
- Lilly, Simon 254, 587, 589, 590, 609
- Linde, Andrei 24, 626, 629

- Lineweaver, Charles 339, 342, 347, 427, 626
 Lobachevsky, Nikolai 11, 151
 Longair, Malcolm 534
 Lotz, Jennifer 594
 Lucchin, Francesco 331, 332, 354, 358, 360, 377, 382, 402, 474
 Lynden-Bell, Donald 399, 474
 Lynds, Roger 130
 Lyth, David 25, 348, 349, 629, 630
 Lyubimov, Valentin 19, 369
- Ma, Chung-Pei 349
 Mach, Ernst 11
 Madau, Piero 590, 596, 606
 Maeder, André 250
 Majewski, Steven 521
 Maloney, Philip 568
 Marshall, Francis 561
 Martin, Christopher 506
 Marx, Györgi 19
 Mather, John 561
 Mazzarella, Joseph 597
 McCarthy, Patrick 254, 607, 608
 McCrea, William 202, 624
 McDonald, Patrick 557
 Mellier, Yannick 134, 136
 Merritt, David 111–113
 Messier, Charles 7
 Metcalfe, Nigel 538
 Michell, John 5, 6
 Miley, George 254, 261
 Milne, Ernest 202
 Miralda-Escudé, Jordi 572
 Monaco, Pierluigi 485–487
 Morgan, William 109
 Mould, Jeremy 246
 Mukhanov, Vyechislav 368
 Møller, Palle 569, 571
- Narajan, Ramesh 228, 229
 Naselsky, Pavel 368
 Newton, Isaac 4, 174
 Norberg, Peder 404, 405
 Novikov, Dmitry 368
 Novikov, Igor 17, 303, 304, 362, 368
 Oemler, Augustus 102, 543
 Okamoto, Takemi 462, 463
- Olbers, Heinrich 510
 Oort, Jan 267
 Osmer, Patrick 521
 Ostriker, Jeremiah 69, 479, 481, 486, 544, 556, 612, 616
- Padmanabhan, Thanu 332, 354, 409, 438, 442
 Page, Lyman 29, 459
 Pagel, Bernard 604
 Pais, Abraham 184
 Panagia, Nino 248
 Parker, Eugene 578–581
 Partridge, Bruce 19
 Patchett, Bruce 248
 Payne, Cecilia 14
 Peacock, John 269, 348, 368, 390, 396, 398, 402, 405–407, 409, 415, 416, 439, 442, 475, 516
 Peebles, James 17, 20, 35, 37, 69, 100, 283, 357, 360, 363, 375, 386, 423, 432, 433, 439, 443, 445, 610–612, 616, 622
 Pei, Yichuan 604–606
 Penrose, Roger 644
 Penzias, Arno 15, 27
 Perlmutter, Saul 257
 Peterson, Bruce 549
 Petrosian, Vahe 130, 504
 Pettini, Max 601–603
 Pi, So-Young 639
 Postman, Marc 109
 Pound, Robert 178
 Pozdnyakov, Lev 281
 Pratt, Gabriel 117
 Press, William 363, 472, 482–485
 Pritchard, Jonathan 576, 577
 Prochaska, Jason 603, 604
 Puget, Jean-Loup 535, 587
- Rawlings, Stephen 255
 Rebka, Glen 178
 Rees, Martin 402, 479, 481, 482, 486, 487, 578, 580, 581, 611, 625
 Refregier, Alexandre 460
 Richards, Gordon 524
 Richstone, Douglas 82, 109
 Riemann, Bernhard 11, 151
 Roberts, Morton 84

- Robertson, Howard 4, 149
 Roeder, Robert 233–235
 Rosati, Piero 532
 Rowan-Robinson, Michael 246, 514
 Ruderman, Malvin 24, 626
 Rutherford, Ernest 251
 Ryle, Martin 549
 Ryu, Dongsu 580
- Saccheri, Girolamo 11, 150
 Sachs, Rainer 436, 438
 Sajina, Anna 535
 Sakharov, Andrei 24, 641
 Salpeter, Edwin 504, 568
 Sandage, Allan 13, 49, 51, 78, 109, 116,
 246, 250, 251, 253, 259, 518
 Sargent, Wallace 553
 Schechter, Paul 77, 268, 329, 363, 472,
 482–486
 Scheuer, Peter 151, 504–506, 514, 549
 Schmidt, Brian 248
 Schmidt, Maarten 508, 514, 519, 521, 522
 Schneider, Peter 130, 133, 138
 Schramm, David 252
 Schutz, Bernard 459
 Schwarzschild, Martin 250
 Scott, Douglas 433
 Scott, Jennifer 568, 569
 Seager, Sara 423
 Seldner, Michael 100
 Seljak, Uros 559
 Shapiro, Irwin 189, 191
 Shapley, Harlow 7, 9
 Shectman, Stephen 506
 Shellard, Paul 629
 Silk, Joseph 17, 364, 433, 443, 448, 479
 Smail, Ian 452, 597
 Smoot, George 21
 Sneden, Christopher 252
 Snider, Joseph 178
 Songaila, Antoinette 566
 Soucail, Geneviève 130
 Spergel, David 463, 465
 Spinrad, Hyron 254, 514, 610
 Spite, François 298
 Spite, Monique 298
 Springel, Volker 487, 615, 616
 Srianand, Raghunathan 552
 Steidel, Charles 590
- Steigman, Gary 140, 294, 296, 298–301
 Steinhardt, Paul 24, 629
 Storrie-Lombardi, Lisa 601
 Subramanian, Kandaswamy 422
 Sugiyama, Naoshi 415, 422, 426, 443,
 445, 448
 Sullivan, Woodruff 514
 Sunyaev, Rashid XI, XII, 17, 18, 21, 28,
 29, 125, 281, 360, 365, 392, 423, 443,
 451, 454, 455, 561, 563, 568
 Szalay, Alex 19, 396
- Tammann, Gustav 78, 116, 246
 Tayler, Roger 14
 Taylor, Joseph 192
 Tegmark, Max 463, 559
 Tinsley, Beatrice 499, 604
 Tipler, Frank 625
 Toller, Gary 586
 Tolman, Richard 16, 322, 333
 Tonks, Lewi 317
 Toomre, Alar 57, 58
 Toomre, Juri 57, 58
 Tremaine, Scott 20, 82, 108, 109, 144
 Trodden, Mark 144
 Tully, Brent 73
 Turner, Michael 143, 301, 303, 307, 369,
 376, 397, 402, 642
 Tyson, Anthony 136
 Tytler, David 566
- Vallée, Jacques 577
 van den Bergh, Sidney 49, 51, 542
 van der Kruit, Piet 62
 Vandenberg, Donald 251
 Verde, Licia 403, 404, 407
 Vishniac, Ethan 453
 Vogeley, Michael 42
- Waddington, Ian 517
 Wagoner, Robert 15, 292, 294
 Walker, Arthur 149
 Wall, Jasper 506, 515
 Walsh, Dennis 249
 Wambsganss, Joachim 129, 130, 138
 Wang, Wei-Hao 598
 Warren, Stephen 519
 Weedman, Daniel 597
 Weinberg, Steven 338, 355, 626

- Wesselink, Adriaan 248
Weyl, Hermann 149, 150
Weymann, Raymond 17, 249, 281, 563
Wheeler, John 625
White, Martin 433, 454
White, Simon 200, 269, 482, 486, 545,
 587
Wilkinson, David 434
Wilkinson, Peter 140
Will, Clifford 173, 174, 189, 190, 192,
 195, 196
Williams, Robert 590
Wilson, Robert 15, 27
Wolfe, Arthur 436, 438, 554, 603, 604
Woltjer, Lodewijk 519
Wright, Thomas 5
Wyse, Rosemary 479
Yu, Jer Tsang 443, 445
Zaldarriaga, Matias 422, 454, 458
Zeldovich, Yakov 13, 17–21, 24, 28, 29,
 125, 208, 231, 233, 281, 303, 304,
 360–363, 365, 375, 381, 392, 423,
 443, 451, 454, 455, 476, 561, 626

Index

Major topics and their principal references are highlighted in **bold-face** type.

- Abell 194 110
Abell 478 122, 123
Abell 1228 110
Abell 1413 117, 118
Abell 1656 *see* Coma cluster of galaxies
Abell 2199 109, 110
Abell 2218 96, 130, 131, 136
Abell Catalogues of rich clusters of galaxies 96–98
comparison with clusters selected from the Sloan Digital Sky Survey 98–99
complete statistical sample 97
selection criteria for inclusion in 96
compactness criterion 97
distance criterion 97
richness criterion and richness classes 96, 97
space density of clusters in 98
Abell clusters and the large-scale distribution of galaxies 99–100
superclustering of galaxies about 100
absolute luminosities of galaxies 77
absorption history of the Universe 604
abundances of elements in Lyman- α absorption systems 598–604
absorption, or scattering, cross-sections and 600
advantages of determining zinc abundance 601, 602, 606
chemical history of the interstellar gas and 601
depletion of heavy elements and 601
in redshift interval $0.3 \leq z \leq 3.5$ 601
density parameter $\Omega_{\text{HI}}(z)$ for neutral hydrogen 601, 606
corrected for dust extinction and systems with low column densities 601
density parameter $\Omega_x(z)$ for species x and 600, 601
determination of average 598
global metallicity ratios and 600
iron abundance in redshift interval $1.7 \leq z \leq 4.6$ 603
uniformity of relative 604
variation of neutral hydrogen abundance with redshift 602
Acbar experiment 435
acoustic oscillations in galaxy power spectrum 362, 410–415
Sloan Digital Sky Survey (SDSS) 412–415
first peak and 414
2dF galaxy redshift survey 412–413
cosmological parameters from 413
first and second peaks and 412
acoustic oscillations in the power spectrum of the cosmic microwave background radiation
as forced oscillations 446
estimation of cosmological parameters and 449
acoustic oscillations in the power spectrum of the cosmic microwave background radiation 428–430, 436, 443–449
adiabatic temperature oscillations of 446, 447
amplitudes of 444
as forced oscillations 445, 446

- 'dipole' contributions to 447, 448, 455, 456, 459
- Doppler fluctuations associated with 446, 447
- effective temperature perturbation of 447
- estimation of cosmological parameters and 444, 449
- even and odd harmonics of 444
- first maximum of 427, 443, 444, 449
- gravitational redshifting of 447
- isocurvature modes and 447
- 'monopole' contributions to 447, 448, 456, 459
- relation to adiabatic density perturbations 445
- temperature excursions of 448
- wavenumbers of maxima of 444
- active galactic nuclei 51
 - ratio of black hole to spheroid masses 610, 617
 - Type 1 528
 - unobscured 528
- active gravitational mass density 201
- adiabatic baryonic perturbations in the standard Big Bang 350–357, 361–363**
 - as a 'top-down' process 363
 - 'burning of pancakes' 363
 - formation of 'pancakes' 363
 - matter-dominated era 353–355
 - radiation-dominated era 352
- adiabatic damping of neutrino velocities 377
- adiabatic damping of the sound waves 354
- adiabatic expansion of a photon gas 272, 281
- adiabatic expansion of a thermal gas 281
- adiabatic hot dark matter 396
- adiabatic model of structure formation 18
- adiabatic sound speed 316
- Advanced Camera for Surveys (ACS) 136, 138, 538, 592
- age of the Earth 251
- age of the Universe T_0 13, 16, 242
 - globular clusters and 250, 251
 - nucleocosmochronology and 252
 - white dwarf cooling ages and 251
- alignment effect in radio galaxies 254, 256
 - shock-excitation and 255
- Andromeda Nebula 8
- Anglo-Australian Telescope 2dF Survey 22, 519
- angular diameter distance 130, 157, 264
- angular diameter distances between any two redshifts 228–230**
 - gravitational lens formulae and 229
 - models with $\Omega_A = 0$ 228–229
 - models with $\Omega_A \neq 0$ 230
 - reciprocity theorem 229
- angular two-point correlation function 34–36, 386
 - for extragalactic radio sources 42
- Antennae galaxies 57–60, 614
- anthropic cosmological principle 624–626
 - existence of sentient beings and 625
 - strong form of 625
- APM galaxy survey 33–36
- APM survey of clusters of galaxies 95
- Arecibo radio telescope 192
- Ariel-V satellite 115, 524
- ASCA Large Sky Survey 525
- Astro-2 mission 565, 566
- astroparticle physics 145
- Atacama Large Millimetre Array (ALMA) 598
- Atlas of Peculiar Galaxies (Arp) 56
- Auger cosmic ray air-shower array 625
- autocorrelation function 432, 433
- Baade–Wesselink method 261
- background radiation 510–513**
 - discrete source contribution to 510–512
 - effects of evolution 512–513
 - 'luminosity evolution' 513
 - integrated emission of galaxies and 587
 - Lyman- α emission of the intergalactic gas 562
 - origin of, in standard world models 512
 - radio emission at long radio wavelengths 513
 - source counts and 510
 - starburst galaxies and 589
 - independence of cosmological model 589
- submillimetre and far-infrared 597
- COBE observations of 587

- contribution of active galactic nuclei 598
 main contributors to 598
 metal formation and 587
ultraviolet
 decrease at large redshifts 595, 596
 decrease in intensity from $z = 1$ to present epoch 596
 from the proximity effect 568–569
 from the proximity effect at small redshifts 568
 global star formation rate and 595
 integrated emission of quasars and 569
 integrated emission of star-forming galaxies at large redshifts 569
 neutral hydrogen in the peripheries of galaxies and 568
 ultraviolet, optical and near-infrared 586
 effects of dust 587
 from spectra of ultra-high-energy γ -ray sources 587
baising
 antibiasing 402
 galactic explosions and 402
Balloon Observations Of Millimetric Extragalactic Radiation ANisotropy and Geophysics (Boomerang) 456
bar instability in differentially rotating discs 69
 barred spiral galaxies 51, 54
baryogenesis 641–642
 baryon number violation of primordial X, \overline{X} bosons 642
 baryon-asymmetry problem 641
 Sakharov's rules 641
 baryon number violation 641
 C and CP violation 641
 non-equilibrium conditions 641
 unification of quarks and leptons and 642
 baryon asymmetry problem 23, 286, 307, 622
 baryon number violation
 generic feature of grand unified theories 641
 baryon perturbations in cold dark matter models 409–410
 baryon–antibaryon pair production 23, 622
baryonic theories of galaxy formation 360–364, 383
 what went wrong 364–365
 Bautz–Morgan classification of clusters of galaxies 109, 110
 Bautz–Morgan effect 253, 254, 544
 Bayesian statistical techniques 463
 Bell Telephone Laboratories 27
bending of light rays 179–181
 by ‘negative mass’ in inhomogeneous Universe 232, 233
 dependence upon the gravitational potential 181
 Beppo-SAX satellite 498
 bias parameter 137
 gravitational lensing and 138
 biasing 21, 401–405
 bias parameter 269, 403, 404, 407, 417
 bispectrum of galaxy distribution and 403
 dependence of luminosity and spectral type 404, 405
 for different classes of galaxy 405
 two-point correlation function for galaxies and 403, 405
 Gaussian fluctuations and 402
 hot gas in voids 402
 mechanisms for 402
 non-linear bias parameter 403
 Biermann battery 579, 581
Big Bang model of the Universe, history of 14–16
 big crunch 205, 338
big problems of cosmology 466, 621–624
 BIMA Millimetre Array 126, 127, 249
 black holes 140, 586
 formation in early Universe 392
 supermassive 140, 471, 488, 492
 epoch of maximum quasar activity 517
 non-thermal radiation processes and 492
 ratio of mass to spheroid mass 488
 Bohr's theory of the hydrogen atom 623
 Boltzmann equation 368, 377, 395, 409, 411, 422, 440, 448, 614
 Boomerang experiment 435

- Bose–Einstein spectrum 29, 284
 Boulby Underground Laboratory 146
 bremsstrahlung 95, 115, 128, 248, 547,
 561
 bolometric luminosity of 119
 cooling rate 121, 479
 emissivity of 128
 spectral emissivity of 115
 spectrum of 116, 128, 248
 thermal 561
 brightest galaxies in clusters 44, 45
 brightest members of rich clusters of
 galaxies
 absolute magnitudes of 109
 brown dwarfs 139–141
 Butcher–Oemler effect 253, 543–544
 changing fractions of galaxy types with
 redshift and 543
 passive evolution of spheroidal galaxies
 and 543
 selection criteria and 543
- C and CP violation
 in decay of neutral K^0 and \bar{K}^0 mesons
 641
- Calán-Tololo supernova project 164–166
 CalTech Submillimetre Observatory 126
 CAMB computer code 422, 430, 440
 Cambridge 4C survey 506
 Cambridge APM galaxy survey 269, 386
 Canada-France Redshift Survey 590
 Cartesian coordinates 155
 Cartwheel galaxy 56, 58
 Cassini spacecraft 191, 192
 CBI experiment 435
 cD clusters of galaxies 102–103
 cD galaxies 51, 82, 96, 102, 103, 109
 in small groups 103
 central bulge of lenticular galaxies 53
 central bulge of spiral galaxies 51
 central limit theorem 487, 505, 508
 Cepheid variables 7, 246, 247
 period–luminosity relation for 7, 8, 246
 CfA galaxy survey 38, 39, 41, 400, 401,
 406
 ChaMP study 525
 Chandra Deep Fields 525
 Chandra X-ray Observatory 116, 124,
 125, 249, 491, 525
- chemical potential 284
 Chwolson ring 129
 Cl 0024+1654 235
 classification of galaxies 59
 cluster Cl 0024+1654 136, 137
clusters of galaxies 37, 42, 43, **95–146**
 Butcher–Oemler effect 543–544
 central mass density of 107
 core radius 103, 105
 counts of X-ray clusters 529–532
distribution of galaxies in **101–110**
 galaxy content and spatial distribution
 of galaxies in 101–103
dynamical estimates of masses of
110–114
gravitational lensing by *see* gravitational
 lensing by galaxies and clusters
 of galaxies
hot gas in *see* hot gas in clusters of
 galaxies
isothermal gas spheres and *see*
 isothermal gas spheres, **103–108**
large-scale distribution of **95–100**
luminosity function for galaxies in
108–110
 mass–luminosity ratios of 99, 117
 on a temperature-number density diagram
 481
 segregation by galaxy type 102
 segregation by mass 103
summary of properties of **109–110**
Sunyaev–Zeldovich effect in hot intra-
 cluster gas *see* Sunyaev–Zeldovich
 effect in hot intracluster gas
 two-point correlation functions for 100,
 101, 387, 402
 velocity dispersions of 99
 CMBfast computer code 422, 425, 430,
 440
 cold dark matter 19–21, 359, 374, 375,
 381, 382, 398, 441, 464, 476, 615
 perturbations in 367, 374, 376, 380,
 382, 396, 437, 557
 WIMPs and 375
cold dark matter model of galaxy
 formation 20, 21, 349, 380–383,
 393–395, 399, 401–403, 409–412,
 414, 415, 418, 428, 482, 487, 489
 adiabatic 395, 396, 399, 412

- as a ‘bottom-up’ picture for structure formation 382
 broken-scale-invariant 419
 concerns about 415
 hierarchical clustering in 382
 isocurvature 396, 398, 400
 mixed hot and 418
 open 400, 401, 410, 413, 416–418
 standard 401, 409, 415–418, 530, 532, 559, 572, 573
 tilted 419
 with decaying neutrinos 416–418
 with finite cosmological constant 416–418, 572, 613
 collisions between galaxies 478, 544, 613
 Coma cluster of galaxies 42, 64, 102, 109–114, 547
 core radius of 108
 mass of 111
 mass–luminosity ratio of 111, 113, 267
 Sunyaev–Zeldovich effect in 450
 X-ray image of 114
 comoving angular diameter distance 161
 comoving luminosity density 589
comoving radial distance coordinate
 159, 160, 161, 168, 170, 172, 203, 218, 219, 221, 226, 228, 232, 243, 244, 316, 336, 339, 341, 342, 424, 425, 494, 501, 507, 511, 631–633
 definition of 164
 comoving volume 171
 variation with redshift 495
 Compton double scattering 284
 Compton Gamma-ray Observatory
 BATSE instrument 498
 Compton optical depth of hot diffuse intergalactic gas 561
 Compton scattering 17, 28, 29, 125, 248, 281–284, 301, 352, 357, 359, 561
 exchange of energy between photons and electrons by 281–284
 induced 17
 inverse 492
 Compton scattering in post-recombination Universe 282, 284
 Compton scattering in radiation-dominated Universe 281–284
 Compton scattering optical depth 29, 125, 283, 284
 computer simulations
 galaxy formation and 472
 hydrodynamic, of intergalactic gas 557, 571–574
 at redshift $z = 2$ 573
 cold dark matter models and 572
 feedback processes and 572
 predicted column density distribution of Lyman- α absorption clouds 572, 615
 predicted structures of neutral hydrogen clouds and 572, 615
 Single Particle Hydrodynamics 572
 star formation and 572
 supernova explosions and 572
 hydrodynamical simulations of galaxy collisions 616
 large-scale structure and 400, 474, 477, 484, 486, 487, 489, 530
 excess of dwarf satellites 486
 Press–Schechter mass function 487, 488
 large-scale structure formation 613
 origin and evolution of cosmic structures and 614
 origin of intracluster magnetic fields by turbulence 580
 predicted spin parameter λ 611
 reionisation era 574, 575
 semi-analytic models of galaxy formation 583
 concentration index C 91, 92
 concordance Λ CDM world model 22, 37, 42, 241, 424, 560, 621, 623, 625
 conformal diagram 631
 including inflation 632
 passing through and re-entering the Hubble sphere 633
 conformal Newtonian gauge 348, 349, 445
 conformal time 317, 340, 342, 344, 346–348, 445, 458, 631–634, 637
 extension to negative values before end of inflationary era 631
 confusion 505
 confusion-limited survey 505
 systematic overestimation of flux densities in 505
 convergence κ 460

- cooling rate of astrophysical plasma 479, 480
 cooling time of astrophysical plasma 479, 481, 486
 Copernicus satellite 297
 core radius of brightness distribution 61
correlation functions and the spectrum of the initial fluctuations 385–419
 acoustic peaks in the power spectrum of galaxies 411–415
 2dF galaxy redshift survey 412–413
 Sloan digital sky survey 412–415
 biasing 401–405
 evolution of the initial perturbation spectrum – transfer functions 393–401
 adiabatic cold dark matter 393–396
 adiabatic hot dark matter 396
 isocurvature cold dark matter 396–399
 subsequent evolution 399–401
 power spectrum
 origin of maximum of 415
 reconstructing the processed initial power spectrum 405–410
 non-linear development of the density fluctuations 407–409
 redshift biases 406–407
 role of baryon perturbations 409–410
 the perturbation spectrum 388–392
 Harrison–Zeldovich power spectrum 391–392
 initial power spectrum 390–391
 relation between $\xi(r)$ and the power spectrum of the fluctuations 388–390
 two-point correlation function for galaxies 385–388
 variation on a theme of cold dark matter 415
 correlation functions for galaxies 363, 405
 correlation lengths 404
 higher order 386
 three-point correlation function 403
 Cosmic Anisotropy Polarization Mapper (CAPMAP) 456
 Cosmic Background Explorer (COBE) 15, 21, 27–33, 284, 415, 416, 419, 421, 429, 432, 434, 437, 440, 442, 507, 561, 587
 Cosmic Background Imager (CBI) 456
The Cosmic Century: A History of Astrophysics and Cosmology (Longair) 3, 149, 193, 434, 514
 cosmic chemical evolution, equations of 604–607
 closed box model 605, 606
 conservation of mass 605
 infall of material from intergalactic medium 604–607
 inflow model 606
 instantaneous recycling approximation 605
 loss of heavy elements due to star formation 605
 outflow due to supernova explosions 606
 outflow model 606
 outflow of processed material 604–607
 rate of change of mass of heavy elements 605
 rate of infall or outflow $\dot{\Omega}_f$ 605
 rate of star formation 605
 role of dust 604, 606
 yield y 605
 Cosmic Lens All Sky Survey (CLASS) 266
cosmic microwave background radiation 15, 16, 18, 22, 27–33, 241, 275, 467, 624
 dipole component of 30, 31
 discovery of 17, 362
 distortions from a perfect black-body spectrum 283–284
 causes of 283
 distortions from a perfect black-body spectrum 28, 29
 energy density of 276
 epoch of recombination and 277, 279
 estimation of cosmological parameters from 250, 252, 259, 269, 270, 300
 fluctuations in the *see* fluctuations in the cosmic microwave background radiation
 horizon problem and 621
isotropy of 29–33, 41, 42, 149, 150, 337
 last scattering surface of 325, 631
 neutrinos and 369

- number density of photons in 277, 423
 polarisation of *see* polarisation of the cosmic microwave background radiation
 prediction of 14
 specific entropy per baryon of 277
spectrum of 28–29
 Sunyaev–Zeldovich distortions of 125, 126, 561
 temperature fluctuations in the *see* fluctuations in the cosmic microwave background radiation
 temperature of 143, 356, 371, 416, 576
 observations of the variation with redshift 272, 273
 variation with redshift 272
 temperature of at epoch of recombination 279
 thermal history of 278
cosmic star-formation rate
 advantages of submillimetre waveband 597
 cosmic abundances of the elements and 598–607
 maximum at redshifts $z \sim 1\text{--}2$ 610
 optical–UV determinations of 606
 problem of dust extinction 596, 598
 problems with the simple models 606
 submillimetre determinations of 596–598, 606
 as a function of redshift 598, 599
cosmic time 150, 158–160, 161, 163, 207, 217, 231, 237–239, 252, 317, 339, 344, 438, 445
 cosmic variance 434–436, 467
 cosmic virial theorem 268, 329
Cosmical Magnetism (ed. Lynden–Bell) 577
 cosmological constant Λ 13, 21, 202, 208, 212, 214, 215, 242, 265, 267, 273, 336, 344, 414–418, 425, 630
 ‘repulsive force of a vacuum’ and 208, 209
 dark energy and 23, 24, 207, 208, 210, 626
 evidence for finite value of 257
 history of 12, 13, 24, 188, 199, 207, 623
 zero-point fluctuations of vacuum and 626
Cosmological Constants (Bernstein and Feinberg) 202
Cosmological Inflation and Large-Scale Structure (Liddle and Lyth) 313, 629
cosmological parameters, determination of 241–270, 463–465
 Ω_A and the statistics of gravitational lenses 263–267
 age of the Universe T_0 *see* age of the Universe T_0 , 250–252
 angular diameter–redshift test 261–263
 deceleration parameter q_0 *see* deceleration parameter q_0 , 252–263
 density parameter Ω_0 267–270
 Hubble’s constant H_0 *see* Hubble’s constant, 246–250
 number counts of galaxies 259–261
 infrared H waveband 260
 problems of using to determine q_0 259, 260
 parameters to be determined 463–465
 relative lensing probabilities Ω_A and the statistics of gravitational lenses 265
 relative lensing probabilities 265
see density parameter Ω_0 267
 testing the Friedman models 242–245
 the parameters and relations between them 241–242
 three-year WMAP data and 463–465
Cosmological Physics (Peacock) 209, 313
cosmological principle 149–150, 158, 199, 204, 237, 238, 625
 Cosmology Calculator of Dr. Edward Wright 425
 COSMOS survey of clusters of galaxies 95
 counts of γ -ray bursts 498
 counts of active galaxies evolution in infrared waveband 536
 counts of extragalactic radio sources 498, 508, 514–516
 excess of faint radio sources 514
 evidence for strong cosmological evolution 514
 counts of far-infrared and submillimetre sources 597
counts of galaxies 537–543
 advantages of infrared K waveband 538

- evidence for homogeneity of Universe 493
- excess of faint blue galaxies 47, 261, 540
- and starburst galaxies 542, 543
- nature of 540–543
- fluctuations in, due to large-scale clustering 538–541
- for irregular/peculiar/merger systems 542
- for spheroidal and spiral galaxies 540, 542
- Hubble's 494
- in infrared K band 540
- in infrared K waveband 542
- in U, B, R, I and K wavebands 541
- problems of determining 537–538
- counts of galaxies and active galaxies, predicted** 492–507
- at submillimetre wavelengths 500–501, 534
- normalised differential counts 501, 503
- Euclidean 493
- differential 493
- integral 493
- for standard world models 494–500
- comparison with Euclidean counts 495
- for bolometric luminosities and flux densities 495
- for sources with power-law spectra 495–496
- normalised, differential 495–496
- optical counts for galaxies 498–500
- slopes of integral and differential 496, 498
- models with finite Ω_A 501–504
- counts of infrared and submillimetre sources** 532–537
- convergence of, at mid-infrared wavelengths 537
- far-infrared wavelengths 533, 534
- IRAS galaxies 532, 533
- excess of faint sources 532
- Spitzer First Look Survey 533
- excess of faint sources 533
- submillimetre wavelengths 534
- excess of faint sources 534
- counts of radio-quiet quasars 518, 521, 522
- counts of X-ray clusters of galaxies 529–532
- counts of X-ray sources** 524–532
- evidence for evolution of the source populations 525
- hard X-ray energies, 2–10 keV 525, 527, 529
- history of 524
- problems of interpretation 525
- soft X-ray energies, 0.5–2 keV 527
- and the integrated X-ray background emission 527
- soft X-ray energies, 0.5–2 keV and 2–10 keV 525
- coupling of dark and baryonic matter by gravity 378
- coupling of electrons and protons by Coulomb collisions 367
- coupling of matter and radiation in the expanding Universe 17, 353, 355, 367
- CP violation in decays of K^0 mesons 287
- Crab Nebula
- origin of magnetic field of 580
- critical surface density for star formation in spiral galaxies 554
- critical cosmological density** 139, 145, 204
- in neutrinos with finite mass 143
- critical density 439
- critical density for star formation 616
- Critical Dialogues in Cosmology* (ed. Turok) 269, 298, 415
- crossing time 111, 474
- definition of 63
- for a cluster of galaxies 43
- Cryogenic Dark Matter Search (CDMS) 146
- Cryogenic Dark Matter Search (CDMS II) 373, 374
- curvature of space κ** 154, 156, 157, 171, 231, 242, 243, 320, 627, 638
- condition for flat Euclidean space 210, 211, 364
- effect of hyperbolic space on growth of perturbations 320, 326, 327

- radius of, at the present epoch \mathfrak{N} 161, 199, 210, 228, 239
 relation between Ω_0 , Ω_A and 210
 variation with scale factor a 160
 curvature of space–time 181
 curvature perturbations 437
 amplitude of 463
 cusp catastrophe 135
 61 Cygni 5
- damped Lyman- α systems in quasar spectra 272, 600–604, 606, 607
 dark ages 384, 471, 552, 574, 576
 observability through fluctuations in the neutral hydrogen intensity 577
dark energy 207–211, 216, 230, 243, 245, 327, 331, 335, 344, 345, 414, 623, 634
 density parameter Ω_A of the 21–23, 242, 449, 501, 503, 623
equation of state of 210–211, 267, 465, 630
 problem of the 23, 24, 365, 623
dark matter 139–146, 241, 268, 269, 367
astrophysical and experimental limits
144–146
 axions and 142, 369
baryonic 139–142
 black holes and 140, 141
 limits to mass density from gravitational lensing 140
 very low mass 141
 brown dwarfs and baryonic 140
 clusters of galaxies and 95, 112, 113, 115
 density parameter Ω_D in the 205, 214
 distribution of 235
forms of 139–146
 gravitational coupling to baryonic matter 368
 gravitational lensing and 130, 136, 137
 in clusters of galaxies 113, 117, 119, 136, 137, 267
 in early-type galaxies 138
 in elliptical galaxies 69
 in galaxies 267, 367, 368
 in spiral galaxies 69
 MACHOs and 141, 142
- gravitational microlensing and 141, 142
 masses of dark matter particles 145
 nature of 24, 301, 625
 neutrinos with finite rest mass and 143, 369
non-baryonic 142–144, 301, 335, 364, 365, 367
 nature of 368, 369
 searches for dark matter particles 145, 146
 standard bricks and 139
 structure of 137
 WIMPs and 143, 144
- dark matter and galaxy formation**
367–384, 400
 evolution of hot and cold dark matter perturbations 380–384
 cold dark matter scenario 381–384
 hot dark matter scenario 380–381
 forms of non-baryonic dark matter 369–370
 free-streaming and damping of hot dark matter perturbations 375–377
 instabilities in the presence of dark matter 377–379
 metric perturbations and hot and cold dark matter 374–375
 adiabatic curvature modes 374, 379
 curvature modes 374
 isocurvature modes 374, 375
 WIMPs as dark matter particles 370–374
- dark matter haloes
 formation according to Press-Schechter formalism 489
 dark matter haloes of galaxies and clusters 137
- dark matter particles
 collisionless 399
 nature of 384
 ultraweakly interacting 368
 dark matter problem 350, 365
Darkness at Night (Harrison) 510
 de Sitter solution 149, 213
 de Sitter world model 337, 626, 639
 de Vaucouleurs $r^{1/4}$ law for surface brightness 61, 62, 108
 de Vaucouleurs radius 70

- de Vaucouleurs' classification of galaxies 54, 55, 93
- deceleration parameter q_0 216, 241
- angular diameter-redshift test 261–263
- for compact radio sources 262, 263
 - for double radio sources 261, 262
- number counts of galaxies 259–261
- redshift-magnitude relation for brightest galaxies in clusters 252–254
- effects of stellar evolution on 253
- infrared 544–545
- problems of interpreting at large redshifts 253
- redshift-magnitude relation for radio galaxies 254–255
- advantages of determining in the K waveband 254, 255
- and the alignment effect 254, 256
- corrections for effects of stellar evolution 254
- redshift-magnitude relation for Type 1a supernovae 256–259, 464
- evidence for non-zero cosmological constant 257
- relation with Ω_0 and Ω_A 243
- decoupling of matter and radiation in the post-recombination Universe 283
- deflection D 505
- deformation tensor in Zeldovich approximation 476, 477
- Degree Angular Scale Interferometer (DASI) 456
- density contrast 268, 269, 311, 312, 315, 325, 328, 354, 358, 378, 391, 393, 402, 408, 443, 482, 573
- for curvature modes in early Universe 374
- growth of 393
- density parameter** Ω_0 204, 241, 243, 267–270, 412, 414
- cosmic virial theorem and 268
- defined at any epoch 230
- infall of galaxies into large-scale structures and 268, 269, 406, 407, 464
- density parameter in baryons** Ω_B 269, 289, 352, 362, 364, 444, 548, 561, 563, 564, 576, 586, 622
- from primordial nucleosynthesis 293, 299, 301, 357
- from WMAP power spectrum 300, 464
- density parameter in gas Ω_g 604–607
- density parameter in heavy elements Ω_m 604–607
- density parameter in intergalactic gas Ω_{IGG} 555
- density parameter in neutral hydrogen Ω_{HI} 554
- density parameter in stars Ω_s 547, 598, 604–607
- density parameter of the dark energy** Ω_A 21, 23, 209, 210, 242, 449, 464, 501, 503, 623, 626
- density parameter of the dark matter** Ω_D 464
- deuterium D
- abundance in Lyman- α absorbers 297
 - observed primordial abundance 297–298
 - as a ‘baryometer’ 299
 - solar abundance 297
- deuteron, binding energy of 292
- Differential Microwave Radiometers of COBE 30
- disc component of spiral galaxies 51
- disc scale length for spiral galaxies 62
- discs of spiral galaxies
- stability of 612
- dissipation processes and galaxy formation** 477–482
- radiative processes 478
 - star formation and 478–479
 - first generation of stars 478
 - in very large redshift objects 479
 - thermal instabilities 478, 481
- distance indicators 246, 247
- distance measure D 494, 495
- distance of the stars 4
- distortion matrix 462
- shear components of 460, 461
- Doppler shift
- Newtonian 162, 176
 - special relativistic 162
 - ‘downsizing’ 614
- ‘drop-out’ galaxies 543, 593, 594, 607
- decrease in luminosity density at large redshifts 595

- luminosity functions for 595
- properties of 593
- dust emission and star formation 478, 501
- dust extinction 538
- dust extinction of galaxy spectral energy distribution 535, 536
- dwarf elliptical galaxies 51
- dwarf galaxies 51
- dynamical equilibrium 63
- dynamical friction 399, 544

- early history of cosmology 3–5**
- early history of galaxies and the structure of our Galaxy 5–9**
- The Early Universe* (Kolb and Turner) 313
- early-type galaxies 50
 - mass distribution is 138
- eclipse expeditions of 1919 190
- Einstein angle 130, 132, 136
- Einstein radius 129, 132, 134, 264
- Einstein ring 130
- Einstein X-ray Observatory 116, 123, 507
- Einstein's field equations** 12, 13, 149,
 - 188, 199–202, 208, 243, 273, 348, 365, 368, 395, 422, 440, 448
 - conservation of energy for relativistic and non-relativistic gases 201
 - equation of conservation of mass and 200
 - first law of thermodynamics and 200, 201
 - monatomic gases and 201
 - ultrarelativistic gases and 201
- Einstein's static model of the Universe 8, 12, 149, 151, 188, 199, 214
- Einstein-de Sitter world model 205, 231–235, 265, 266, 319, 320, 322, 336, 483, 485, 496, 500
 - as only ‘stable’ model 622
- electron–positron annihilation 301
- electron–positron pair production 23, 622
- elliptical galaxies 50, 51
 - formation at large redshifts 543
- elliptical galaxies as triaxial systems 71–73**
 - linear programming techniques for 73
- ellipticities of elliptical galaxies 51
- emission history of the Universe 604

- energies of the photon and neutrino backgrounds 302
- energy density of the Cosmic Microwave Background Radiation 33
- entropies of the photon and neutrino backgrounds 301, 302
- entropy per baryon
 - fluctuations in, in isothermal picture of structure formation 357
- Eötvös experiment 173
- Eöt-Wash experiment 174, 175
- Eötvös ratio 174, 175
- epicyclic frequency 554
- epoch of baryon–antibaryon pair production 286
- epoch of decoupling of matter and radiation 574
- epoch of electron-positron pair production 286
- epoch of equality of radiation and matter
 - energy densities 17, 277, 285, 354, 358, 359, 376, 381, 393, 395, 396, 398, 410, 425, 430
 - including neutrinos 303
- epoch of formation of first stars 574
- epoch of formation of galaxies, clusters and superclusters 312, 474, 487
- epoch of maximum quasar activity 362
- epoch of nucleosynthesis 286
- epoch of recombination 17, 33, 277–281, 285, 312, 325, 355, 357, 362, 364, 378–381, 410, 440, 446
- epoch of recombination for helium 279
- epoch of reheating of the intergalactic gas 286
- epoch of reionisation of the intergalactic gas 33, 355, 452, 471, 547, 552, 574–577
- role of black holes in nuclei of galaxies 574
- equation of continuity 313
 - relativistic case 331
- equation of state
 - for photons, massless particles and ultrarelativistic gas 271, 331
- equivalence principle *see* principle of equivalence
- EROS project 141
- ESO catalogue of galaxies 44
- ESSENCE supernova project 257, 258

- Euclid's fifth postulate 150
 Euler's equation 313, 440, 448
 relativistic case 331
 Eulerian coordinate system 314, 476
 event horizon 338, 339, 342, 346, 634
 definition of 338
evolution of active galaxies with cosmic epoch 514–532, 569
 extragalactic radio sources 514–518
 ‘luminosity evolution’ 516
 cut-off of strong evolution beyond redshift $z \sim 2$ –3 516, 517
 for sources with steep and flat radio spectra 516, 517
 luminosity-dependent density evolution 516, 518
 radio-quiet quasars 518–524
evolution of galaxies and active galaxies with cosmic epoch 471, 491–545
 active galaxies 492, 514–532
 extragalactic radio sources 514–518
 radio-quiet quasars 518–524
 X-ray clusters of galaxies 529–532
 X-ray sources 524–529
 background radiation
 source counts and 510
 background radiation and 510–513
 effects of evolution and the radio background emission 512–513
 evaluation of 510–512
 brief history of evidence for 491–492
 clusters of galaxies 543–545
 co-evolution of stellar and black hole properties of galaxies 492
 counts of galaxies 537–543
 counts of galaxies and active galaxies 492–507
 euclidean source counts 493
 fluctuations in the background radiation
 due to discrete sources 504–507
 for standard world models 500
 models with finite Ω_A 501–504
 submillimetre counts of dusty galaxies 500–501
 counts of galaxies and active galaxies, predicted
 for standard world models 494
 infrared and submillimetre number counts 532–537
 stellar and gaseous components of galaxies 492
 V/V_{\max} or luminosity-volume test 507–510
 excess dwarf galaxy problem
 solution by sweeping out gas by astrophysical processes 613
 excess of faint blue galaxies 46, 591
 irregular nature of 593, 594
 extragalactic background radiation
 due to discrete sources 275
 due to galaxies 275
 energy density of, in different wavebands 275
 in the ultraviolet, optical and infrared wavebands 275, 276
 limits from $\gamma\gamma$ absorption in spectra of γ -ray sources 275
 number density of photons in different wavebands 275, 277
 spectrum of 273–277
 plotted as vI_v 275
 plotted as I_v 275, 276
 extragalactic radio sources 578
 depolarisation of 578
 luminosity function of
 evolution with cosmic epoch 514–518
 origin of magnetic fields of 580, 581
 active galactic nuclei and 581
 supermassive black holes in nuclei of 581
Faber–Jackson Relation for elliptical galaxies 70–71
 Faint Object Camera 564–566, 592
 Far Infrared Absolute Spectrophotometer (FIRAS) of COBE 28
 Far Ultraviolet Spectroscopic Explorer (FUSE) 566, 567
 feedback mechanisms in galaxy formation 471
 field galaxies 56
 fifth force, search for 174, 175
 fine-tuning problem 23, 622
 ‘fingers of God’ 39, 406, 407
 FIRST deep VLA survey of radio sources 42
 first generation of stars 552
 formation of interstellar dust 587

- properties of 574
 ultraviolet and X-ray emission of 574
- first law of thermodynamics 200, 201
- flat two-space, isotropic 154
- flatness problem** 23, 24, 230–231, 622
- fluctuations in the background radiation due to discrete sources 504–507
 spatial correlation technique 506
- fluctuations in the cosmic microwave background radiation 18, 19, 21, 30, 32, 33, 167, 281, 362, 364, 379, 382, 384, 410, 414–416, 419, 421–467, 614, 640
- acoustic peaks *see* acoustic oscillations in the power spectrum of the cosmic microwave background radiation
- discrete source confusion and 451, 505
- epoch of recombination and 430
- ionisation of the intergalactic gas through the epoch of recombination 422–423
- physical and angular scales of 424–430
 last scattering layer 425–426
 particle horizon scales 429–430
 Silk damping scale 426
 sound horizon at the last scattering layer 427–429
- physics of 443
- power spectrum of 13, 431–436, 439, 465
 cosmological parameters from 444, 463–465, 548
 observations of 434–436
 other sources of 465–466
 statistical description of 431–434
- power spectrum on intermediate scales – acoustic peaks 443–449
- power spectrum on large angular scales 436–443
- integrated Sachs–Wolfe and Rees–Sciama effects 440
- primordial gravitational waves 440–443
- Sachs–Wolfe effect – physical arguments 436–440
- power spectrum on small angular scales 450–452
- confusion due to discrete sources 451–452
- confusion due to submillimetre sources 452
- statistical and Silk damping 426, 450
- Sunyaev–Zeldovich effect in clusters of galaxies 450–451
- quadrupole anisotropy of 442
- reionised intergalactic gas 452–453
- Sunyaev–Zeldovich effect and 450
 detection of statistical effect from X-ray Abell clusters by WMAP 451
- Thomson scattering optical depth and 453, 574
- Fokker–Planck equation for stars in clusters 107
- fold catastrophe 135
- four-tensors in relativity 184–187**
- curvature scalar 188
 - differentiation of 188
 - electromagnetic field tensor 186
 - energy–momentum tensor 188
 - for dust 186
 - including pressure 186
 - Maxwell’s equations 186, 187
 - Ricci tensor 188
 - Riemann–Christoffel tensor 188
 - energy–momentum tensor
 - for dust 185
 - four-vectors 185
 - examples of 185
 - velocity 185
- Fourier integral 389
- Fourier series 389, 431
- Fourier transformations 431, 462
 autocorrelation theorem for 433
 of acoustic oscillations in cosmic microwave background radiation 445
- three-dimensional 388
- FR2 3CR radio sources 609
- fractal Universe 392
- free-bound and bound-bound transitions of hydrogen 479
- free-streaming of neutrinos 19
- Freeman’s law 62, 74, 612
- ‘freeze-out’ of hot dark matter particles by free-streaming 376
- ‘freeze-out’ of massive particle species in the early Universe 307

- frequencies of galaxies of different types
 54, 56, 541
 in different galactic environments 56,
 57, 404, 538
- Friedman world models** 12, 13, 16, 151,
 199–239, 621, 624
- Friedman world models with $\Lambda = 0$**
202–207
- closed, spherical geometries 205
 - critical world model 205
 - curvature–density parameter relation
 205
 - dust models 202
 - dynamics of 205–207
 - flat Einstein–de Sitter model 205
 - Newtonian analogue for 202–204
 - problems of boundary conditions 203
 - open, hyperbolic geometries 205
 - parametric solutions for 207, 321
- Friedman world models with $\Lambda \neq 0$**
207–215
- bouncing models 212–214
 - classification of 215
 - dust models 208, 209
 - dynamics of 211–216
 - Eddington–Lemaître models 213, 214,
 223, 501
 - antipodal points of 225, 501, 503, 504
 - effects of gravitational lensing at
 antipodal points 504
 - number counts in 501, 503
 - redshift–flux density relation for 501
 - stationary redshift 214, 223
 - Lemaître models 214, 501, 503
 - ghost images in 226
 - loitering models 214, 223, 226
 - minimum rate of expansion of 212
- Friedman’s equation 199, 200, 320, 326,
 638
- Friedman: the man who made the Universe expand* (Tropp, Frenkel and Chernin)
 204
- fundamental observer 150, 158–161, 164,
 168, 204, 207, 237, 238, 335, 337,
 339–341, 347
- fundamental plane for elliptical galaxies**
70–71
- The Future of Theoretical Physics* (eds.
 Gibbons, Shellard and Rankin) 643
- GADGET computer code 616
- GAIA mission, prospects for light deflection
 observations 191
- Galactic ‘cirrus’ 30
- Galactic Astronomy* (Binney and Merrifield)
 49
- Galactic bulge 141
- galactic cannibalism 253, 544
- Galactic Dynamics* (Binney and Tremaine)
 49
- galactic extinction law 77
- Galactic synchrotron radiation 30
- galaxies 49
 - characteristic masses of 480
 - dependence of types upon environment
 613
 - mean luminosity of 84
 - mean space density of 84
 - on a temperature-number density diagram
 481
 - passive evolution of 498, 499
 - importance of red giant branch 499
 - starbursts and evolution of 499
- Galaxies in the Universe: an Introduction*
 (Sparke and Gallagher) 49, 64
- galaxies, correlations along the**
Hubblesequence 84–88
- colour–colour diagram and 87, 88
 - integrated colour 87
 - luminosity function of HII regions 87
 - masses and luminosities 84
 - neutral hydrogen 86
 - star formation rates and 87
 - total surface density and surface density
 of neutral hydrogen 87
- galaxies, old red 542
- galaxies, properties of 8, 49
- galaxies, red and blue sequences of** 63,
88–94, 412
 - colour–absolute magnitude relation
 89–90
 - colour–Sérsic index relation 91
 - definitions of 89
 - effect of the galaxy environment 92–93
 - mean stellar age–concentration index
 relation 91
- Galaxy
 age of 64

- disc scale length of 62
- luminosity of 84
- structure of 7–9
- galaxy and structure formation, history of 16–19**
- galaxy formation 583–620**
 - background radiation and element formation 584–587
 - energy density of background radiation and density of metals formed 586
 - intensity of background radiation and density of metals formed 586
 - processes of element formation 584, 585
 - collisions between galaxies and 614
 - ‘downsizing’ 610
 - feedback mechanisms and 486, 583, 614
 - growth of supermassive black holes and 614
 - Lyman-break galaxies 590
 - in the general field 590
 - multicolour technique for discovering 590, 591
 - observed global star formation rate 587–590
 - as a function of redshift 583, 589
 - star-forming galaxies and 587
 - starburst galaxies at large redshift 589
- star and element formation and 583–598
 - build-up of heavy elements in galaxies 583
 - numbers of ‘drop-out’ galaxies and 584
 - numbers of blue star-forming galaxies and 584
 - numbers of far-infrared and submillimetre galaxies and 584
 - quasar absorption line systems and 584
- star formation and 614
- two-stage theory of 482, 611
 - final radius of disc 612
- γ -ray background emission
 - Comptonisation and 529
 - spectrum of 526
- Garching-Bonn Deep Survey 138
- gas dynamics
 - equations of 313
 - in Lagrangian form 314
 - Newton’s second law in 314
 - relativistic case 331, 332
 - relativistic case in Lagrangian coordinates 331
- gauge choices
 - in electrodynamics 347
 - Lorentz and Coulomb gauges 347
 - superhorizon scales and 347, 437, 438
 - gauge-invariant gravitational potential 445
 - gauge-invariant variables 348
- Gaunt factor 116, 121
- Gauss’s theorem for Newton’s law of gravity 67, 133, 202
- Gauss, Carl Friedrich
 - theory of surfaces 181
- Gaussian curvature *see* curvature
- Gaussian fluctuations 402, 432, 443, 475, 477, 482, 484, 487
- Gaussian perturbations with random phases 41, 42
- Gemini Deep Deep Survey 607, 608
- general relativity 11, 48, 149, 151**
 - introduction to 173–198**
 - further complications 181–184
 - what Einstein did 187–188
 - route to 184–188**
 - superhorizon scales and 347–350
 - general relativity, experimental and observational tests of 189–197**
 - four tests of general relativity 189–192
 - advance of perihelion of Mercury 189
 - deflection of light and radio waves by the Sun 190, 191
 - gravitational redshift 189
 - time delay in Sun’s gravitational field 191, 192
 - parameterised post-Newtonian (PPN)
 - formulation of 175, 195
 - limits to values of the parameters 197
 - metric potentials in 196
 - physical significance of 176
 - pulsars and 192–194
 - xparameterised post-Newtonian (PPN)
 - formulation of 197
 - General Relativity: An Introduction for Physicists* (Hobson, Efstathiou and Lasenby) 173, 184, 313

- general theory of relativity *see* general relativity, 614
- geodesic distance 157
- geodesics 149–153, 158, 320
- giant molecular clouds 478
- globular cluster 47 Tucanae 250, 251
- globular clusters 250, 355
- Gran Sasso underground laboratory 146
- Gravitation and Cosmology* (Weinberg) 184
- gravitational collapse
- timescale of 479
- gravitational constant, variation with cosmic epoch 197–198**
- helioseismology and 198
 - limits to 197
 - lunar laser ranging and 197
 - primordial nucleosynthesis and 198
 - pulsar timing and 197
- gravitational deflection of light rays 134
- by the Sun 128
 - collision parameter for 128
- gravitational lensing by galaxies and clusters of galaxies 128–139**
- necessary conditions for 133
 - astrophysics of galaxies and 136–139
 - basic theory of 128–131
 - caustics and cusps in 135, 136
 - cluster masses from 134
 - critical surface density for 133
 - dark matter and 130, 136, 137
 - distortion of background images by 136
 - extended deflectors and 133–136
 - galaxy-galaxy imaging and 138
 - magnification of images by 130–132
 - mirror inversion of images in 132
 - time variations of intensities of images 139
- gravitational lensing, strong 138, 235
- case of the galaxy IRAS F10214+4724 235
 - complete sample of radio sources and quasars 266
 - magnification of intensities by 235
 - probability of 264, 266
- gravitational lensing, weak 138, 235, 460–463
- and cosmic shear 235
 - shear variance distribution of 461
- power spectrum of density perturbations in the mass distribution and 462
- Gravitational Lensing: Strong, Weak and Micro* (Schneider, Kochanek and Wambsganss) 130, 138
- gravitational mass 173, 174
- gravitational potential, Newtonian limit 179
- gravitational redshift 176–179**
- dependence upon gravitational potential 177
 - in general relativity 183
 - in the Newtonian limit 177
 - incompatibility with special relativity 178
 - time dilation in a gravitational field and 178
- gravitational relaxation timescale 544
- gravitational waves 625
- and tilt of spectrum of scalar perturbations 442
 - dependence upon inflationary potential 442
 - limits to energy density of primordial 442, 460
 - polarisation signature of primordial 441
 - primordial
 - detection of as the ‘smoking gun’ for inflationary cosmologies 640
 - spectral index of primordial 441, 640
 - from WMAP power spectrum 640
 - temperature power spectrum of 441, 442 - tensor to scalar ratio of primordial 442, 460, 640
 - limits to 460
- gravitons 373
- ‘Great Attractor’ 268
- ‘Great Debate’ 7
- Great Observatories Origins Deep Survey (GOODS) 538, 540, 592, 595, 598
- ‘Great Wall’ 38
- Greenbank Catalogue of radio sources at 6 cm 42, 43
- grey-body spectrum 535
- GUT era, new physics at 643
- GUT phase transition 628
- half-light radius of light distribution 61

- Harrison–Zeldovich initial power spectrum** 18, 21, 25, **391–392**, 393–396, 399, 433, 439, 441, 465, 484, 485, 559, 560, 624, 630, 640
- Hawking radiation 141
- He^+ Lyman- α absorption clouds in intergalactic medium 566
- HEAO-1 X-ray Observatory 524
- HEAO1 A-2 experiment 507
- Heaviside–Lorentz units 187
- Heisenberg’s uncertainty principle 636
- helium abundance
- as a thermometer of the early Universe 293
- helium-3 He^3
- observed by radio hyperfine transition line 298
 - observed primordial abundance 298
- helium-4 He^4
- observed primordial abundance 296
 - in low metallicity, extragalactic HII regions 296
- Hercules cluster of galaxies 102
- Hertzsprung–Russell (H–R) diagram 250, 251, 584, 585
- main sequence termination point 250
- hierarchical clustering 18, 59
- hierarchical model of the Universe 5
- hierarchical models of galaxy formation
- old red galaxies and 607
- hierarchical scenario for cluster formation 545
- Higgs fields and Higgs particles 24, 208, 373, 623, 626, 643
- High Energy Astrophysics Vol. 1* (Longair) 126, 544
- High Energy Astrophysics, Vol. 2* (Longair) 577
- Himalayas 402
- Hipparcos* astrometric satellite 247, 251
- Hipparcos* measurements of light deflection by the Sun 191
- Hopkins Ultraviolet Telescope 565, 566
- horizon mass 352, 353, 391, 395
- horizon problem** 22, 24, 337, 631
- last scattering surface and 337
 - solution of in inflationary model of the early Universe 337, 626, 627, 631
- horizon scale 17, 204, 441, 627
- horizons and the horizon problem** 335–338, 621
- hot and cold dark matter model of galaxy formation 335, 418
- hot and cold dark matter, history of** 19–22
- hot dark matter model of galaxy formation 19–21, 375–377, 380–381, 400–402
- formation of galaxies by fragmentation of large-scale structures 381
- late formation of structure in 400
- hot gas in clusters of galaxies** 114–124
- absence of cool gas in 123
 - associated with heating by radio lobes 124
 - models to explain the 123
 - abundance of iron 118
 - characteristic cooling time for 121
 - cooling flows in 122, 478
 - enthalpy of 123
 - mass inflow rates of 123
 - cooling time of 122
 - iron line FeXXVI from 115
 - sound waves in 125
- Hubble Deep and Ultra-Deep Fields 261
- Hubble Deep Field 491, 538, 542, 590–593
- Hubble Deep Field South (HDFS) 592
- Hubble diagram 44
- Hubble sequence of galaxies 50
- Hubble Space Telescope 58, 59, 130, 131, 138, 249, 254, 257, 297, 464, 491, 538, 540, 543, 550, 552, 564, 565, 568, 590, 593, 595, 601
- The Hubble Space Telescope and the High Redshift Universe* (ed. Tanvir) 552
- Hubble Space Telescope Science Institute 590
- Hubble sphere 342–346, 632–634, 638
- definition of 342
 - distinction between particle horizon and 631
 - shrinking of 631, 633, 634
- Hubble Ultra Deep Field (HUDF) 491, 538, 540, 542, 543, 590, 592, 594–596
- filter transmission curves for 594
- Hubble’s constant 9, 13, 46, 241
- Baade–Wesselink method and 248
 - brightest stars in galaxies and 246

- Cepheid variables and 246, 247
 controversy over value of 246
 cosmological distance ladder and 246,
 247
 defined at any epoch 166, 230
 from Sunyaev–Zeldovich effect 128
 globular clusters and 246
 Hubble Space Telescope Key project and
 246, 247
 final result of 248, 464
 present expansion rate of the Universe
 and 167
 redshift–magnitude relation for brightest
 cluster galaxies and 246
 Sunyaev–Zeldovich effect and 248
 Tully–Fisher relation and 246
 Type 1a supernovae and 246
 written as $H_0 = 100h \text{ km s}^{-1} \text{ Mpc}^{-1}$
 204
- Hubble's law 9, 10, 44–46, 150, 165, 314,
 407
 comoving radial distance coordinates and
 340
 discovery of 150
 gravitational lensing and 249
 recession velocities exceeding the speed
 of light in 341
- Hubble's law and the expansion of the
 Universe 44–48, 165**
- Hubble's law for surface brightness 61
 hydrostatic equilibrium 104, 115
 hydrostatic support, equation of 318
 hyperbolic two-space, isotropic 154, 155
- i*-band drop-outs 552
 I0 galaxies 54
 inertial mass 173, 174, 181
 inflationary model of the early Universe
 24, 25, 364, 392, 621, 624
 accelerated expansion 634
 chaotic inflation 626
 exponential expansion and 626, 627,
 629
 role of scalar fields 629
 straightening of geometry 627
 violation of strong energy condition and
 630
- historical background 626–629
- formation of ‘bubbles’ in original Guth
 picture 628
 lack of physical realisation of
 inflationary picture 629
 monopole problem 628
 new inflationary model of Linde,
 Albrecht and Steinhardt 629
 slow rollover model 629
 symmetry breaking in Grand Unified
 Theories 627
 transition from false to true vacuum in
 original Guth picture 627
- necessary conditions for many e-folding
 times 635
- necessary tools from theoretical and
 particle physics 630
 release of ‘latent heat’ 627
 scale factor-temperature relation 628
 shrinking of Hubble sphere 634
 three equivalent conditions 634
 violation of the strong energy condition
 634
 transition to standard radiation-dominated
 model 627
- inflaton potential 24, 629
- infrared luminosity function of galaxies
 evolution of 536
 comparison with evolution of active
 galaxies 537
- Infrared Space Observatory (ISO) 532,
 533
- inhomogeneous world models 231–235**
- initial mass function
 modified 487
- initial power spectrum
 curvature of 463
 modifications of 409
 modified 484
 reconstruction of 474
- interacting galaxies 57, 60, 478
 fraction of 59
- intergalactic gas, optical depth for Thomson
 scattering of 280, 281
- intergalactic medium 547–582**
- absorption by 548
 absorption coefficient of 548
 background emission of 548
 emissivity of 548
 epoch of reionisation of 574–577

- Gunn–Peterson test for ionised helium in 564–567, 571
due to integrated effect of Lyman- α clouds 566–567
feasibility of, for large redshift quasars 564
Gunn–Peterson test for neutral hydrogen in 547, 549–552, 569, 574
positive detection at $z \geq 6$ 551, 552, 564, 574
upper limits to neutral hydrogen number density from 550
lukewarm gas in 555, 560–569
collisional excitation of 562–563
diffuse ultraviolet radiation at large redshifts and 567–569
emission and absorption of 564–567
proximity effect and 567–569
Lyman continuum opacity of 569–571, 574
Lyman- α absorption clouds in 547, 552–560
evolution of, with cosmic epoch 556
nature of 554–556
power spectrum of forest of 557–560
predicted evolution of, with cosmic epoch 556
properties of 552–554
modelling the evolution of 571–574
neutral hydrogen at large redshifts 574
fluctuations in observed intensity 574–577
intensity of 576
ionsation by first generation of massive stars 575
observational challenge of detecting 575
predicted brightness temperature of 576
problem of synchrotron radiation foregrounds 576
optical depth of 548
origin of magnetic fields 577–582
ultraviolet opacity of 569–571
X-ray background and a cosmic conspiracy 561
International Linear Collider (ILC) 144
International Ultraviolet Explorer (IUE) 248, 597
intrinsic curvature *see* curvature
Introducing Einstein's Relativity (d'Inverno) 184
ionisation fraction through epoch of recombination 423, 424
ionisation of intergalactic gas through the epoch of recombination 422–423
IRAS F10214+4724 235
IRAS Faint Source Survey 532
IRAS galaxies 501, 503
catalogue of 532
complete samples of 532
correlation functions for 405
ultraluminous 58
IRAS infrared observatory 478, 491, 532
IRAS Point Source Catalogue 532
Irr II galaxies 54
irregular clusters of galaxies 102–103
irregular galaxies 53
island universes 5
ISO infrared space observatory 478
isocurvature cold dark matter 396–399
fluctuations in local equation of state and 397
isophotal angular diameters 223
isothermal baryonic perturbations in the standard Big Bang 357–360
isothermal gas spheres 103–108, 134, 264, 611
projected 105, 106
singular 134
tidal radius of 107
truncated 107
isothermal model of structure formation 18, 357–360, 363–364
‘bottom-up’ picture of galaxy formation 364
‘freezing in’ of perturbations 358, 359
early enrichment of heavy elements 363
early formation of globular clusters and 363
hierarchical clustering and 363
radiation drag, effects of 359, 360
isotropic curved spaces 150–154, 159
radius of curvature of 155
three-dimensional 156, 157
two-dimensional 155, 156
isotropic two-space flat 157

- hyperbolic 157
- spherical 154, 157
- isotropy of the distribution of extragalactic radio sources 42
- isotropy of Universe on a large scale 32
- J0737-3039 (binary pulsar) 193
- Jagellonian field 35
- James Clerk Maxwell Telescope (JCMT) 452, 534, 597
- Jeans' analysis of damped harmonic oscillator 638
- Jeans' criterion in an expanding Universe 16, 319
- Jeans' instability 318, 324, 478
 - growth rate of 324, 358
 - physical nature of 318
- Jeans' instability criterion 16, 378
 - for collisionless gas 377
- Jeans' length 16, 17, 318, 332, 351–353, 379, 428, 429
 - in baryons 352
 - relativistic case 332
- Jeans' mass 17, 18, 351–355, 360, 361, 377
- Jeans' wavelength 318
- Jupiter 4, 5
- K-correction 170, 253, 495, 498, 538
 - in infrared K waveband 538
 - submillimetre 597
 - uncertainties in ultraviolet wavebands due to starbursts 538
- K20 sample of galaxies 542
- K20 Survey 607, 608
 - very red galaxies in 608
- Keck 10-metre telescope 272, 542, 555, 566, 590
- Keck-2 telescope 551, 552
- Kelvin-Helmholtz picture of stellar evolution 251
- Kepler's laws of planetary motion 3
 - third law 4, 67
- King profiles for mass distribution in clusters 107, 111
- Kolmogorov spectrum of turbulence 580
- Kompaneets equation 126
- Lagrangian and comoving coordinate systems, difference between 314
- Lagrangian coordinate system 314, 476
- Λ CDM model of galaxy and structure formation** 22, 59, 435, 440, 462, 463, 466, 472, 483, 486, 487, 530, 532, **613–620**
- problems with 613–614
 - accounting for Faber–Jackson relation and Tully–Fisher relation 614, 620
 - 'downsizing' problem 614
 - excess dwarf galaxy problem 613
 - mass-metallicity correlation 613
 - predicted cusps in central regions of galaxies 613
- Landau damping 376
- Lane–Emden equation 104
- Langmuir waves 317
- Large Electron–Positron collider (LEP) 300, 371
- Large Hadron Collider (LHC) 144, 208, 643
- Large Magellanic Cloud (LMC) 54, 141
 - distance of 248
- large-scale distribution of galaxies 33–44**
- large-scale structure of the Universe 27–48**
- The Large-Scale Structure of the Universe* (Peebles) 363
- Las Campanas redshift survey 41
- last scattering layer 444
- last scattering layer at $z = 1000$ 621
- last scattering surface 33, 333, 357
 - for neutrinos 292
- last scattering surface at the epoch of recombination 631, 632
- last scattering surface for electromagnetic radiation 624
- late-type galaxies 50
- laws of conservation of momentum and energy in relativity 186
- Legendre function
 - associated 431
- Legendre polynomials 433, 455
- Leiden–Berkeley Deep Survey (LBDS) 516, 518
- lens equation 132
- lenticular galaxies 52, 55
- lepton number L_i 301

- Lick counts of galaxies 35, 36
 Lick Observatory 550
light distribution in galaxies 59–63
 in elliptical galaxies 61
 in spiral and lenticular galaxies 61
 in spiral galaxies 68
 putting the light distributions together
 62
 light elements, primordial nucleosynthesis
 of *see* nucleosynthesis, primordial
 lightest supersymmetric particle 643
 limits of observation in cosmology
 624–625
 fundamental limitations 624
 limitations due to cosmic variance 624
 lithium ^7Li
 observed primordial abundance 298,
 299
 local group of galaxies 51
 local supercluster of galaxies 43, 44, 78
 Lockman Hole survey field 525
 LOFAR project (Netherlands) 576
 longitudinal gauge 348
 longitudinal plasma oscillations 317
 Lorentz invariance 184, 196
 form-invariance 184
 Lorentz transformations 185, 187, 207,
 238, 239
 lukewarm intergalactic gas 560–569
 collisional excitation of 562–563
 ‘thermostat’ temperatures of 563
 by shock waves 562
 emissivity of 562, 563
 HI and HeII Ly- α line emission due to
 562
 ionisation state of 563
 diffuse ultraviolet radiation at large
 redshifts and 567–569
 emission and absorption of 564–567
 detectability of redshifted Lyman- α
 emission 564
 photoexcitation and 564
 shock excitation and 564
 proximity effect and 567–569, 572
luminosity function of galaxies 77–84,
 509
luminosity–metallicity relations for
 galaxies 74–76
 luminous infrared galaxies
 evolution of 536
 luminous infrared galaxy N1-015
 spectral energy distribution of 535
 lunar laser ranging 175
 Lyman limit 588, 589, 591
 ‘Lyman valley’ 570
Lyman- α absorption clouds in in-
 tergalactic medium 545, 550,
 552–560
 confinement of 555
 evolution of, with cosmic epoch 556,
 569
 nature of 554–556
 according to large-scale hydrodynamic
 simulations 573
 observed number density distribution of
 554, 555, 566, 600
 power spectrum of forest of 557–560
 properties of 552–554
 column densities of 554
 damped Lyman- α systems 554
 fractional ionisation of 555
 Lyman- α forest 552–554, 556–558,
 566–572, 574
 Lyman-limit systems 553, 554, 556,
 564, 569–571, 590
 masses of 555
 origin of damped Lyman- α systems
 572
 two-point correlation function of 557,
 558
 dark matter perturbations and 559
 SiIII absorption features and 557, 558
 Lyman- α emission of the intergalactic gas
 562
 Lyman- α radiation field, colour temperature
 of 576
 Lyman- α scattering, optical depth for 549
 Lyman- α transition
 oscillator strength for 549
 photo-excitation cross-section for 549
 Lyman-break galaxies 479, 607
 redshift distribution of 590, 592
 Lyman-limit galaxies, decreasing comoving
 density at large redshifts 489
 α Lyrae 5
 M31
 luminosity of 84

- rotation curve of 67
- M49 (NGC 4472) 69, 116
 - velocity dispersion of 70
- M51 (NGC 5194) 52
- M82 54
- M86 116
- M87 (NGC 4486) 52, 55, 69, 116
- Mössbauer effect 178, 189
- Mach's principle 11, 12, 199
- MACHO project 141, 142
- MACHOs 141
 - mean mass of 141
- Magellanic Clouds 7, 54, 141
- Magellanic irregular galaxies 54
- magnetic fields
 - in stars 578
 - in the interstellar and intergalactic medium 578
 - origin of 577–582
 - amplification mechanisms and 578
 - amplification of seed field by turbulence 580
 - dynamo action and 578, 580
 - emf created by Biermann battery 579
 - extragalactic radio sources and 581
 - extragalactic radio sources at large redshifts 582
 - laboratory demonstration of dynamo action 578
 - magnetic reconnection and 578
 - problems of dynamo action on large scales 578
 - seed field created by Biermann battery 579
 - seed fields 579
- power spectrum of magnetic turbulence 580
- predicted power spectrum from magnetic turbulence 580
- role in astrophysics 577
- rotation measure synthesis and 580
- making real galaxies 583–620**
 - abundances of elements in Lyman- α absorption systems 598–604
 - equations of cosmic chemical evolution 604–607
 - old red galaxies 607–610
 - origin of rotation 610–613
- putting it all together – semi-analytic models of galaxy formation 613–620
- star and element formation 583–598
 - background radiation and element formation 584–587
- Hubble Deep and Ultra Deep Fields 590–596
- Lyman-break galaxies 590
- observed global star formation rate 587–590
- submillimetre determinations of cosmic star-formation rate 596–598
- Malmquist bias 246
- Markarian ultraviolet-excess galaxies 597
- mass density of the Universe
 - in stars at the present epoch 84
- mass–luminosity ratio
 - early-type galaxies 138
 - for clusters of galaxies 267
 - for galaxies and clusters 482
 - for Universe as a whole 83, 267
 - of elliptical galaxies 69, 84
 - of spiral galaxies 68, 84
- mass–luminosity relation for stars 499
- mass–metallicity relations for galaxies at large redshifts 76
- mass–energy relation $E = mc^2$ 181
- masses of galaxies 63–70**
- massive galaxies in clusters 617
- massive ultra-weakly interacting particles 643
- matter-dominated Universe 276
- Mattig's formula 219
- MCG catalogue of galaxies 44
- 'meatball' topology 41
- Medium Deep Survey of galaxies (MDS) 542
- Mercury, advance of perihelion of 189
 - radar ranging and 189
- 'merger trees', hierarchical clustering and 615
- mergers of coalescing galaxies 614
- MERLIN long baseline interferometer 266
- Mészáros effect 358–359, 381, 393, 396, 398
- metallicity Z 74, 600, 605, 606
- metric angular diameters 221, 253

- between any two redshifts 228
- metric of isotropic two-space 155
- metric perturbations 368, 374, 392, 436
- metric tensor 155, 186–188
 - components of as gravitational potentials 187
- microlensing, gravitational 132
- Millennium Galaxy Catalogue 62, 63, 83
- Millennium Simulation 486–488, 613–615, 617–619
 - first quasar candidate 619
- Milne empty world model 207, 237
- Minkowski metric 158, 179, 181, 187, 188, 195
 - ‘missing baryon’ problem 547
- Modern Cosmology* (Dodelson) 313, 422
- Monte Carlo Markov chain methods 463
- Monte Carlo methods 506
- Moon, fluorescent X-rays from 524, 525
- morphologies of galaxies 49, 50
- Mount Wilson 100-inch telescope 492
- multipole moment 432, 433

- N galaxies 51
- nebulae
 - cataloguing of 7
 - nature of 6, 7
- ‘negative mass’ in inhomogeneous Universe 233
- negative pressure equation of state 208, 623, 630, 644
 - speed of sound for 638
- neutralinos 373
- neutrino astrophysics 625
- neutrino background temperature 301–303
- neutrino barrier 286, 292
- neutrino chemical potential 301
- neutrino interaction cross-sections 291
- neutrino oscillations 143
- neutrino perturbation
 - damping by free-streaming 376
 - free-streaming damping mass 377, 380, 381
- neutrinos
 - astrophysical limits to masses of 20
 - cosmological limits to masses of 560
 - cosmological limits to number of species of 463
 - cosmological mass density in 463, 465
- decoupling of 367
- equilibrium number density of 143, 301
- free-streaming of 380, 400
- laboratory limits to the masses of 143
- laboratory limits to the number of species of 145
- massive decaying 417
- neutrino background temperature 376
 - their role in primordial nucleosynthesis
 - see* nucleosynthesis, primordial
- time-scale for interaction in the early Universe 291
- with finite rest mass 19, 367, 375, 376, 380
- neutrinos, free-streaming of 396
- neutron decay 292, 294
- neutron stars 586
- Newton’s law of gravity 4
- Newtonian gravitational potential 348, 350, 438
- NGC 1300 53, 54
- NGC 2787 55
- NGC 3077 54
- NGC 4486 52
- NGC 4839 114
- NGC 4874 111, 114
- NGC 4889 111, 114
- NGC 5194 52
- NGC 5195 52
- NGC 520 54
- NICMOS infrared camera of Hubble Space Telescope 140
- non-Euclidean geometries 11, 150–152, 173, 492
- non-Gaussian fluctuations 432, 466
 - examples of 432
 - skewness and kurtosis 466
- non-linear collapse of spherical density perturbations 472–477
 - spherical top-hat collapse 473–475
 - maximum scale-factor for 473
 - redshift of collapse of 473
 - turn-around epoch 473
 - violent relaxation and 474
- non-linear development of density fluctuations 407–409
- self-similar solution for 408
- two-point correlation function 407–409

- NORAS catalogue of X-ray clusters of galaxies 116
- normalised impact parameter 132
- nuclear reactions in the Sun 279
- nucleocosmochronology 13, 252
- nucleosynthesis in stars 14
- nucleosynthesis, primordial** 14–16, 140, 289, 289–307, 417
- baryon-symmetric Universes 303–307
- ‘freeze-out’ of abundances in 304, 306
- equilibrium abundances in the early Universe 289–290
- equilibrium energy densities 290
- in the non-relativistic limit 290, 303
- neutron–proton ratio 290
- relativistic statistical mechanics and 289
- evolution of abundances during 293, 294
- light elements, abundances of 295–301
- comparison of theory and observation 299–301
- observations of 296–299
- massive neutrinos and 369
- neutrino background temperature 301–303
- neutrinos, decoupling of 290–292
- ‘freezing out’ of the n/p ratio and 291
- non-standard assumptions concerning 300
- lepton asymmetry 300
- limits to the number of unknown neutrino species 300
- varying gravitational constant 300
- synthesis of the light elements 292–295
- dependence upon photon-baryon ratio 294
- deuterium formation 292, 293
- epoch of nucleosynthesis 292
- helium formation 292, 293
- lithium formation 293, 294
- neutron fraction 292
- nuclear reactions involved in 292
- number counts of galaxies 46
- number counts of submillimetre sources 452
- Nyquist frequency 504, 505
- O04 survey 595
- observable Universe of galaxies 471
- observations in cosmology** 162–171
- age of the Universe** T_0 171
- angular diameter distance 167, 172
- angular diameters** 167
- apparent intensities** 168–170
- for bolometric luminosities and flux densities 169
- K-corrections 170, 223
- cosmological redshift and time dilation** 162–166
- the meaning of redshift in cosmology 164
- distance measure D 167, 172, 218, 243
- independence of Ω_0 at small redshifts 245
- Hubble’s law** 165–167
- luminosity distance 169, 172
- number densities** 170–171, 172
- comoving number density 171
- comoving volume 170
- reciprocity theorem 169
- observations in cosmology for Friedman world models** 215–228
- angular diameter–redshift relations 221–223
- for inhomogeneous Friedman world models 233, 234
- for models with $\Omega_A = 0$ 221
- for models with $\Omega_A \neq 0$ 223
- for partially inhomogeneous Friedman world models 235
- comoving volume within redshift z 226–228
- models with $\Omega_A = 0$ 226
- models with $\Omega_A \neq 0$ 228, 263
- cosmic time–redshift relation 217–218, 280
- age of Universe for flat world models with $\Omega_A \neq 0$ 218
- age of Universe for models with $\Omega_A = 0$ 217
- for flat world models with $\Omega_A \neq 0$ 218
- for models with $\Omega_A = 0$ 217
- for models with $\Omega_A \neq 0$ 218
- deceleration parameter 216
- relation to Ω_0 and Ω_A 216

- distance measures as a function of redshift 218–219
 for Milne's empty world model 219
 for models with $\Omega_A = 0$ 219
 for models with $\Omega_A \neq 0$ 219
 Mattig's formula 219
- flux density–redshift relations 223–226
 for inhomogeneous Friedman world models 235
 for starburst galaxies in the submillimetre waveband 501, 503
 ghost images 223
- Occam's razor 419
- Ohio State University 295
- Olbers' paradox 510
 in an infinite, static, Euclidean Universe 511
- resolution of, in standard world models 511, 512
- old red galaxies 607–610
 constancy of masses with redshift 607
 early formation of stellar populations of 610
 evidence for old stellar populations in 608
 evolving stellar mass density and 607
 massive 607–610
 need for early starbursts 608, 609
 selected in the K waveband 607
 star-forming galaxies at large redshift and 608
 stellar masses as a function of redshift 608
- On the Principles of Geometry* (Lobachevsky) 11, 151
- optical depth for intergalactic HeII absorption 564
- optical jet in M87 52
- The Origin and Evolution of Cosmic Magnetism* (ed. Beck, Brunetti, and Feretti) 577, 580
- origin of the spectrum of primordial perturbations 629–640**
 duration of the inflationary phase 630–631
 necessary number of e-folding times 631
 equation of state 630
- freezing of perturbations on passing through Hubble sphere 634
 shrinking Hubble sphere 631–634
- OVRO Millimetre Array 126, 127, 249
- P(D)* distribution 504–506, 514, 525
 asymptotic slope of 505
 in infrared waveband 507
 in ultraviolet waveband 506
 in X-ray waveband 507
 non-Gaussian statistics and 505
 physical meaning of 505
 shape of 505
- Palomar 200-inch telescope 514, 521
- Palomar 48-inch Schmidt telescope 96
- Palomar 48-inch Telescope Sky Survey 96
- pancakes 20, 363, 400, 402, 476, 477, 480
- parallel transport, or parallel displacement 151–153
- Parkes Selected Region (PSR) sample 517, 518
- Parseval's theorem 388
- particle horizon** 22, 335–340, 342, 344, 346–349, 351–354, 361, 362, 376, 377, 379, 380, 391–393, 415, 429, 430, 436, 441, 443, 444, 626–629, 631
 definition of 336
 radiation-dominated Universe and 337
- particle physics and cosmology 624, 625
- particle–antiparticle annihilation in the early Universe 278, 303
- collision time exceeds expansion age 306
- cross-sections for 304
- epoch of decoupling of particles and antiparticles 305
- equilibrium number densities 304
- Particles, Nuclei and the Universe, Selected Works of Yakov Borisovich Zeldovich, Vol. 2.* (Zeldovich) 381
- past light cone 159, 335, 339–344, 346, 631–633
- Pauli exclusion principle 144
- Pavo cluster of galaxies 42
- peculiar and interacting galaxies 56–59**
- peculiar velocities
 from polarisation measurements of the cosmic microwave background radiation 451

- in the local Universe 268
 of galaxies 201
 of perturbations 315, 453
 Perseus cluster of galaxies 124, 125, 547,
 617
perturbations, evolution of, in the standard cosmological models 311–333
 acoustic oscillation and 361–362
 conservation of angular momentum and 328
 for models with $\Omega_A = 0$ 325
 for models with $\Omega_A \neq 0$ 326
 in terms of conformal time τ 340
 Jeans' instability 317–318
 dispersion relation for, in a static medium 317
 growth rate for, in static medium 318
 Jeans' instability in an expanding Universe 319–327
 Einstein-de Sitter case 319
 empty Milne world model 320
 falling poles 322–324
 general solution 324–327
 linear growth of 319–327, 332, 351,
 354
 necessity of finite initial amplitudes 322, 333
 perturbing the Friedman solutions 321–323, 476
 small perturbation analysis 319–320
 spherical perturbations in standard Friedman models 321
 linear 312
 non-relativistic wave equation for 313–317
 adiabatic perturbations 316
 first-order solutions for 315
 in terms of conformal time 317
 in terms of cosmic time 317
 unperturbed solutions for 315
 peculiar velocities in the expanding Universe 327–331
 decay of in $\Omega_0 = 0$ case 329
 evolution of 329, 330
 growth of in $\Omega_0 = 1$ case 328
 potential motions 327, 328, 406
 primordial turbulence and 328
 rotational motions 328
 relativistic case 331–332
 growth rate in radiation-dominated case 332
 the basic problem 332–333
 what the theorists are trying to do 311–313
 Petrosian r-band luminosity 91
 photon barrier 280
 photon diffusion 355
 coefficients of thermal conduction and shear viscosity 355, 356
 photon-to-baryon number ratio 23, 277,
 622
 physics beyond the standard model 372
 Planck energy scale 209
 Planck era 287, 631, 642–644
 need for quantum theory of gravity 642
 new physics before reaching 643
 Planck mass 209
 Planck mission of ESA 421, 450–452,
 467, 625
 Planck spectral energy distribution
 Rayleigh-Jeans region of 455
 variation with redshift z 272
 Wien region of 278, 279
 fraction of photons in 278
 Planck time 642
 planetary nebula IC418 452
 Pleiades star cluster 5
 Plummer model for elliptical galaxies 108
 Poisson noise 392
 Poisson's equation for gravity 108, 187,
 268, 313
 linearity of 315
 relativistic case 331
 polar coordinates 155
polarisation of the cosmic microwave background radiation 454–463, 625
 anticorrelated TE cross correlation power spectrum of as evidence of adiabatic perturbations 458
 B-modes and 457, 467
 B-modes due to gravitational lensing 457
 BB power spectrum and 457
 EE power spectrum of 456, 457, 459
 from the epoch of reionisation 458–459

- angular scale of strongest polarised signal 458
- from the last scattering layer 455–458
- physics of 454–455
- necessity of quadrupole intensity distribution 455, 458
- polarised galactic radio emission and 456, 457
- primordial gravitational waves and 459–460
- B-modes 459, 460
 - E-modes 459
 - origin in the early Universe 460
 - polarisation modes of 459
 - predicted BB power spectrum of 460
- TE cross correlation power spectrum of 457–459
- TT intensity power spectrum and 456, 457
- weak gravitational lensing and 460–463
- BB-mode polarisation due to lensing of
 - EE-mode polarisation 462, 463
 - distortion matrix 460
 - E-mode polarisation due to 462
- polycyclic aromatic hydrocarbon (PAH) molecules 535
- post-recombination era** 384, 471–489
- non-linear collapse of density perturbations 472–477
 - isotropic top-hat collapse 473–475
 - Zeldovich approximation 475–477
- Press–Schechter mass function 482–489
- development and recapitulation 485–489
 - exposition – elementary theory 482–484
 - role of dissipation 477–482
- POTENT reconstruction procedures 269
- power spectrum of cosmic microwave background radiation 434, 436
- power spectrum of fluctuations 388–392
- relations between different descriptions of 391
- power spectrum of initial fluctuations 17, 390–392, 405, 438
- modifications of 393–401
- power spectrum of temperature fluctuations 432, 433
- for non-Gaussian fluctuations 466
 - precision cosmology 421, 466, 614, 621
- Press–Schechter mass function** 20, 363, 482, 482–489
- ‘peaks-within-peaks’ problem 485
 - critical density contrast for structure formation 483
 - evolution of number density of dark matter haloes with redshift 487, 489
 - hierarchical clustering and 486, 487, 489
- mass function of clusters and 486
- problems with simple derivation 485, 486
- time evolution of 484, 485
- primordial fluctuation problem 23, 25, 472, 623
- Harrison–Zeldovich spectrum and 623
- primordial gravitational waves 440–443
- equation of state of 441
 - on superhorizon scales 441
 - quadrupole nature of 441
 - quantum origin in the early Universe 441
 - tensor to scalar ratio 441
- primordial nucleosynthesis of the light elements *see* nucleosynthesis, primordial
- Principia Mathematica* (Newton) 10
- principle of covariance 184
- principle of equivalence** 173–176, 176, 177, 179–181, 184, 196
- Einstein’s 174, 175, 196
 - local Lorentz invariance (LLI) 175
 - local position invariance (LPI) 175
 - free-fall 174, 179
 - weak 174, 175
- Principles of Physical Cosmology* (Peebles) 313
- probability integral 483
- Probing Galaxies through Quasar Absorption Lines* (eds. Williams, Shu and Ménard) 552
- problem of the values of the cosmological parameters 23
- prograde orbits 57
- projected surface brightness 116
- proper radial distance coordinate 339

- properties of spiral and elliptical galaxies** **70–76**
- proton decay
 - avoidance of 373
 - PSR 1913+16 192–195
 - pulsars and general relativity 192–194
 - emission of gravitational waves 193, 194
 - acceleration of binary pulsar due to 194, 195
 - masses of neutron stars 193, 194
- QSO Absorption Lines* (ed. Meylan) 552
- quadrupole component of the temperature power spectrum 434
 - quantised harmonic oscillator 635–637
 - angular frequency of 636
 - carrying out a proper calculation 637
 - energy levels of 635
 - Hermite polynomials and 636
 - Schrödinger's equation for 635
 - wavefunctions for 635
 - zero-point energy of 636
 - zero-point fluctuations of 636
 - quantum theory of gravity 644
 - quasar 0957+561 (double quasar) 249
 - quasar 2345+007 (double quasar) 554
 - Quasar Absorption Line key project 568
 - quasar HE 2347-4342 566, 567
 - quasar HS1700+64 566, 567, 571
 - quasar OQ 172 570
 - ultraviolet spectrum of 550
 - quasar PKS1935–692 564, 571
 - quasar PSS J1443+2724 273
 - quasar Q0302–003 564, 566, 571
 - quasar Q1331+170 272
 - quasar Q1422+2309 553
 - quasar Q2237+0305 139
 - quasar QSO 0013–004 273
 - quasar spectra
 - Lyman- α emission line 519, 520
 - prominent emission lines in 520
 - quasars
 - 3CR sample of radio 508, 509
 - cut-off at large redshifts 487, 488
 - early formation of supermassive black holes in 610
 - low-luminosity 521
 - most luminous 488
 - radio-quiet *see* radio-quiet quasars
 - ratio of black hole to spheroid masses 610, 617
 - unification scheme with radio galaxies 610
- radiation-dominated universe 14, 276
- Compton scattering in 281–284
 - dynamics of 271–273
 - including neutrinos 302, 303
 - maintenance of photons and matter at the same temperature by Compton scattering 282
 - time-scale for expansion of 291
 - total energy density of relativistic species 291
- radio galaxies 51, 479
- 3CR sample of 508, 509
 - evidence for old stellar populations in 609
 - radio galaxy 0902+34 609
 - radio galaxy LBDS 53W069 610
 - radio galaxy LBDS 53W091 609
 - radio-far-infrared correlation for galaxies 597
 - flattening of radio source counts and 537
- radio-quiet quasars
- counts of 521, 522
 - cut-off at large redshifts 519, 524, 569
 - definition of complete samples of 518–521
 - completeness of 521
 - dispersion prism-grating techniques 521
 - multicolour photometric technique 519–520
 - searches for '*i*-band drop-outs' 520–521, 524
 - searches for Lyman- α and CIV emission lines 521
 - searches for variability of 521
 - ultraviolet excess technique 519
 - discovery of 518
 - evolution of, with cosmic epoch 518, 520, 521, 610
 - luminosity function of
 - 'luminosity evolution' of 522
 - evolution of 521, 522

- ram-pressure stripping 544, 613
 Rayleigh–Jeans region of Planck spectrum 455
 Rayleigh–Jeans spectrum 27, 29, 30
The Realm of the Nebulae (Hubble) 50, 492
 reciprocity theorem 229
 reconstruction of local mass distribution 268, 269
 red and blue sequences of galaxies *see* galaxies, red and blue sequences of Red-Sequence Cluster Survey 138
 redshift biases 406–407
 redshift, definition of 45, 162
 redshift–apparent magnitude relation 44
 redshift–magnitude relation for brightest galaxies in clusters
 infrared 544–545
 cosmic conspiracy and 544, 545
 galactic cannibalism and 545
 passive evolution and 544
 reduced deflection angle 130
 Rees–Sciama effect 440
 REFLEX catalogue of X-ray clusters of galaxies 116, 120, 121
 regular clusters of galaxies 102–103
 reionisation of the intergalactic gas 382
 relation between angular and spatial two-point correlation functions 37, 38
 relativistic binary stars 192
relativistic gravity, introduction to 173–198
 non-linearity of 181, 182
 relativistic jets, heating of the interstellar gas by 617
 relativity of simultaneity 238
Relativity: Special, General, and Cosmological (Rindler) 184
revised Hubble sequence for galaxies 50–56
 Riemannian geometries 151, 182, 184
 Riemannian metric 187
 ring galaxies 56, 58
Robertson–Walker metric 149, 150, 158–162, 163, 167, 168, 340, 341
 for an empty Milne Universe 237–239
 for the critical world model 231
 invariant interval ds^2 161
 ROSAT X-ray Observatory 116, 117, 119, 120, 122, 451, 491, 506, 524, 525
 rotation curve of a centrifugally supported disc in isothermal gas sphere 612
rotation curves of spiral galaxies 66–69
 rotation of galaxies, origin of 610–613
 damping of primordial rotational velocities 610
 dissipative contraction within dark matter haloes 611
 problem of specific angular momenta 612
 problems of theories of primordial turbulence 610
 role of tidal stripping 613
 roles of dissipation and tidal stripping 612
 tidal torques 611, 612
 during linear growth of perturbations 611
 slow rotation of the spheroidal components of elliptical and spiral galaxies and 611
 Rutherford scattering 190
 S0 galaxies 52
 Sérsic 159–03 123, 124
 Sérsic index 91
 Sa galaxies 51
Sachs–Wolfe effect 18, 21, 441, 447, 456
 dependence upon angular scale 439
 gravitational redshift and 436, 437
 integrated 452, 456
 physical arguments 436–440
 SAGDP99 survey 595
 Sakharov oscillations 21, 362
 Salpeter initial mass function 500, 588
 Sb galaxies 51
 Sc galaxies 52
 scalar fields 208, 623, 629, 634–635
 density and pressure of 634
 Einstein’s field equations and 635
 fluctuations in 635
 negative pressure equation of state and 634
 not yet detected experimentally 634
 properties of 634–635
 slow-roll parameters 635, 640
 string theory and 634

- theories beyond the standard model of particle physics and 634
- scale factor** $a(t)$ 160, 161, 162, 164, 167, 171, 172
- scale factor-redshift relation** 164, 201, 271
- scaling test for homogeneity of clustering of galaxies 35–37
- Schönberg–Chandrasekhar limit 500
- Schechter luminosity function for galaxies 77, 79, 82, 108, 109, 590, 593, 595
- break absolute magnitude M^* of 78, 81
- break luminosity L^* of 77, 78, 81
- brightest galaxies in clusters 82
- dependence upon galactic environment 79, 81
- evolution with redshift 82
- for low luminosity galaxies 82
- in voids 80, 81
- L^* as a standard candle 80
- turnover luminosity L^* 607
- Schwarzschild metric 183, 187
- coordinate time in 183
- proper time in 183
- Schwarzschild radius r_g 184
- Sco X-1 524
- SCUBA submillimetre bolometer array 534, 597
- Sd galaxies 52
- secular instabilities in rotating stellar discs 616
- self-similar model for cluster formation 118, 119
- semi-analytic models of galaxy formation** 412, 472, 486, 583, 613–620
- acoustic peaks in the large-scale galaxy distribution and 620
- as ‘experimental computational astrophysics’ 615
- dust extinction and 617
- evolution of mass function of galaxies and 620
- formation of supermassive black holes and 617, 618
- in centres of rich clusters 620
- heating of the intergalactic gas in clusters and 617
- mergers of galaxies and 616
- major 616
- minor 616
- morphologies of galaxies and 616
- nuclear starbursts and 616, 617
- objectives of 615
- quasars at large redshifts and 618, 619
- radiative cooling and star formation 615
- spectrophotometric properties of galaxies and 616
- supernova explosions and 616
- the epoch of maximum quasar activity and 620
- ‘trial and error’ approach to 617
- two-point correlation function for galaxies and 617, 618
- for different luminosities and colours 617
- Sérsic index 63
- Sérsic’s law 62
- Seyfert galaxies 51, 516, 521
- counts of 521
- Shane–Wirtanen catalogue of galaxies 100
- Sidereus Nuncius or the Starry Messenger* (Galileo) 5
- σ_8
- definition of 403
- two-point correlation function and 403
- Silk damping 353, 355, 357, 360, 361, 381, 410, 426, 430, 450
- Silk mass 17, 353, 356, 357
- singularity theorems of Penrose and Hawking 644
- Sirius 5
- Sirius B 177
- 6C radio galaxies 255
- Sloan Digital Sky Survey (SDSS) 22, 35, 36, 40–42, 49, 50, 75, 76, 78, 79, 82–84, 87–91, 93, 95, 99–101, 110, 111, 245, 362, 387, 410–412, 414, 465, 491, 520, 522, 524, 552, 557, 559
- power spectrum of galaxies in 412–415
- Small Magellanic Cloud 8
- Smoluchowski’s envelope 105
- Soudan Underground Laboratory 146, 374
- sound horizon 443, 444
- sound horizon at the last scattering layer 427–429
- Space Telescope Imaging Spectrograph 567

- space–time diagram
 for an empty Universe 237
 for the expanding Universe 170
- space–time diagrams for standard world models 339–347**
- critical world model $\Omega_0 = 1, \Omega_A = 0$ 342–344
 distances and times 339–340
 past light cone 340
 reference world model
 $\Omega_0 = 0.3, \Omega_A = 0.7$ 344–347
- space–time metric for isotropic curved spaces 155–158**
- ‘spaghetti’ topology 41
 spatial two-point correlation function 37, 38, 385, 386
 special theory of relativity 183, 184, 186
 spectral energy distribution of galaxies
 evolution of 498–500
 in far infrared and submillimetre
 wavebands 500, 503
 spectrum of primordial perturbations
 spectrum of primordial gravitational waves and 640
 spectrum of primordial perturbations in the scalar field 637–640
 constant noise-power on horizon scale 639
 damping on superhorizon scales 638
 decay of scalar field at end of inflationary era 639
 growth of potential fluctuations in inflationary expansion 638
 applicability on superhorizon scales 638
 as an equation of damped harmonic oscillator 638
 damping on superhorizon scales 638
 growth of vacuum fluctuations in inflationary expansion 637
 comparison with growth of non-relativistic density perturbations 637
 differential equation for 637
 growth of zero point fluctuations 638
 relation to perturbations in post-inflationary relativistic plasma 639
- time-delay formalism for 639
 zero point fluctuations in the ground state 638
- speed of sound as a function of cosmic epoch 285–286, 354, 427, 444
 at constant entropy 285
- speed of sound, relativistic 332, 352
- spherical harmonic functions 431, 433
 addition theorem for 433
- spheroidal component of spiral galaxies 51
- spin parameter λ 611, 612, 616
 as a measure of rotational support of a galaxy 611
- spin temperature of neutral hydrogen 576
- spiral galaxies 50, 51
 rotation curves of 66
 types of 51
- spiral-poor clusters of galaxies 102–103
- spiral-rich clusters of galaxies 102–103
- Spite plateau 298, 299
- Spitzer First Look Survey 533
- Spitzer infrared space observatory 478, 491, 533
- ‘sponge’ topology 41, 42
- Square Kilometre Array (SKA) 576
- stability diagram for adiabatic baryon perturbations 361
- standard cold dark matter model of galaxy formation 403
- star formation in galaxies 472
- star-forming galaxies 452
 at redshifts $z > 3$ 591
 dust extinction and 597
 spectrum of 594
- starburst galaxies 54, 536, 537
 ultraviolet spectra of 587, 588
 rate of formation of heavy elements and 588
- statistical equilibrium 65
- statistical methods into astronomy 5
- statistical weight g 289
- Stefan–Boltzmann law 272
- stellar evolution and element formation 584, 585
 energy generation in the conversion of hydrogen into helium 584, 585
 mean stellar luminosity during main sequence evolution 586

- stellar parallaxes 5
 stellar populations, ages of 91
 structural index, or structural length 105
 sub-dwarf (sdB) stars 519
 Subaru 8-metre telescope 595
 Subaru Deep Surveys 595
 submillimetre background radiation 534
 submillimetre bolometer array (SCUBA)
 452
 submillimetre galaxies
 problems of redshift determinations 597
 redshifts measurements in CO line 479
 substratum 149, 150, 341, 354, 358
Subtle is the Lord . . . (Pais) 184
 Sun, quadrupole moment of 189
 measured by helioseismology 190
Sunyaev–Zeldovich effect in hot
 intracluster gas 95, 125–128, 261
 distance estimates using 128
 fluctuations in the cosmic microwave
 background radiation and 450–451
 in the Rayleigh–Jeans limit 126
 kinematic 451
 spectral shape of distortions 126
 SuZIE experiment and measurement of
 spectral shape of distortions 126
 Sunyaev–Zeldovich marginalisation factor
 463
 superCDMS experiment 146
 superclusters of galaxies 43
 supergalactic plane 44, 269
superhorizon scales 347–350, 367, 379,
 382, 391, 392, 397, 437
 freezing of potential fluctuations on 439
 Supernova Cosmology Program 164–166,
 258, 259
 Supernova Legacy Survey 257, 258, 465
 supernova SN1987A 369
 distance of Large Magellanic Cloud and
 248
 supernovae of Type Ia 165, 166, 252
 ESSENCE project 165
 luminosity–width correlation 164, 165,
 256, 257
 redshift–apparent magnitude relation for
 256–259
 stretch factor 166
 white dwarfs in binary systems and 256,
 257
 supersymmetric particles 373
 suppression factor 450
 SWIRE Legacy sample 536
 ‘swiss-cheese’ topology 41
 symmetry breaking 24
 fluctuations associated with 466
 synchronous gauge 349
 synchrotron radiation 492
 synchrotron radio emission in clusters of
 galaxies 578
 temperature fluctuation on the last scattering
 surface
 adiabatic 364, 365
 temperature of formation of light elements
 279
 temperature of regions of ionised hydrogen
 279
 temperature-scale factor relation in the very
 early Universe 371, 372
 temperatures of the photon and neutrino
 backgrounds 301–303
 tensor perturbations and gravitational waves
 348
 tensor virial theorem 64
*The Inflationary Universe: The Quest for
 a New Theory of Cosmic Origins*
 (Guth) 626
Theoretical Concepts in Physics (Longair)
 173, 184, 314
*Theory and Experiment in Gravitational
 Physics* (Will) 189
**theory of the expanding Universe, history
 of** 10–13
thermal history of the Universe 17, 32,
 271–287
 early epochs 286–287
 epoch of recombination 277–281
 matter and radiation content of the
 Universe 273–277
 radiation-dominated era 271–273,
 281–284
 speed of sound as a function of cosmic
 epoch 285–286
*Third Reference Catalogue of Bright
 Galaxies* (de Vaucouleurs et al) 84
 Thomson optical depth for reionisation
 459

- Thomson scattering 33, 279, 356, 422, 451–454
 conditions for creation of polarised radiation by 454, 455, 458
 cross-section 29, 356
 optical depth of intergalactic gas for 452
3CR quasars 610
 black holes masses of 609
3CR radio galaxies 254–256, 514, 609, 610
 early formation of bulk of stellar population 609
 increase in luminosity with redshift 255
 stellar masses of large redshift 609
3CR radio sources 514, 516, 518
 tidal forces 613
 tidal forces and relativistic gravity 182, 183
 tidal radius 137, 138
 tidal radius of cluster of galaxies 105
 time dilation
 cosmological 163
 test of 164–166
 in a gravitational field 178, 438
 in special relativity 163
 topological defects
 cosmic strings, monopoles and textures 466, 628, 640
 isocurvature perturbations and 466
 phase transitions in the early Universe and 466
 topology of the distribution of galaxies 41, 42
 transfer function 393
 adiabatic cold dark matter 393–396
 adiabatic hot dark matter 394, 396
 isocurvature cold dark matter 394, 396–399
 subsequent evolution of different modified power spectra 399–401
 transfer functions
 for baryons 410, 411
 triaxial velocity distribution in galaxies 69
 triple- α reaction 293, 584
 tritium, half-life of 293
Tully–Fisher relation for spiral galaxies
73–74, 612
 in the infrared waveband 74
 ‘tuning-fork’ diagram 50
 turnaround epoch 408, 409
 2C radio survey 505
 Two Micron All Sky Survey (2MASS) 84, 140
2dF galaxy redshift survey 40–42, 49, 50, 78–83, 87, 88, 93, 245, 266, 269, 362, 387, 403–407, 410–414, 465, 491, 519, 618
 final power spectrum of 412–413
2dF quasar redshift survey 387, 510, 519–522, 524
 two-dimensional isotropic curved geometry 151, 152
 two-photon process 423
 two-point correlation function 432
 angular 433
two-point correlation function for galaxies
22, 34–38, 150, 268, 362, **385–388**, 433
 features of 387–388
 relation to the density contrast 386
 relation to the power spectrum of density fluctuations 389
Type Ia supernovae 13, 21
 types of topology of the distribution of galaxies 41
 UGC catalogue of galaxies 44
 UHURU X-ray Observatory 114, 524
 UK Schmidt telescope 33, 519
 ultraluminous infrared galaxies (ULIRGs) 479, 503, 532
 spectra of 532
 ultrametal-poor star CS 22892-052
 thrium abundance in 252
 ultraviolet astronomy
 unit used in 562
 ultraviolet opacity of the intergalactic medium 569
 V/V_{\max} or luminosity-volume test
 507–510
 banded 509
 for radio galaxies 514
 for radio quasars 514
 for radio-quiet quasars 518
 space distribution of galaxies, quasars
 active galaxies 507–510

- vacuum energy density** 207, 208–211, 625
 estimate from quantum field theory 209
 problem of the magnitude of 209, 623
 values of the cosmological parameters
 problems of 623
 vector perturbations and vortex motions 348
- velocity dispersions of elliptical galaxies** 69–70
 velocity of Solar System through the Cosmic Microwave Background Radiation 30
 velocity–distance relation for galaxies 44–46, 48
 in an expanding universe 46, 47
- very early Universe** 621–644
 anthropic cosmological principle 625–626
 baryogenesis 641–642
 big problems of cosmology 621–624
 baryon-asymmetry problem 622
 flatness problem 622
 horizon problem 621
 primordial fluctuation problem 623
 values of the cosmological parameters 623
 way ahead 624
- inflationary Universe – historical background 22–25, 626–629
 limits of observation 624–625
 origin of the spectrum of primordial perturbations 629–640
 duration of the inflationary phase 630–631
 equation of state 630
 fluctuations in the scalar field and 637–640
 quantised harmonic oscillator 635–637
 scalar fields 634–635
 shrinking Hubble sphere 631–634
 Planck era 642–644
- Very Large Array (VLA) 140, 266, 597
 Very Long Baseline Array (VLBA) 266
Viking spacecraft 191, 192
 violent relaxation 399
 Virgo Cluster Catalogue 117
 Virgo cluster of galaxies 43, 52, 102, 110, 116, 117, 246, 248
 Virgo consortium 418, 615
 Virgo supercluster 268
 virial of Clausius 64
virial theorem 63–66, 103, 110, 119, 243, 375, 399, 408, 409, 474, 475
 applied to clusters of galaxies 66
 problems of applying 66
 Vishniac effect 453
 visibility function 423, 424, 426
 visible matter in the Universe
 integrated luminosity of 83
 mean mass–luminosity ratio of 83
 VLBI measurements of deflection of radio waves by the Sun 190, 191
 voids in the distribution of galaxies 41, 381, 439, 537
 Voigt profile 554
 VSA experiment 435
- walls and voids in the distribution of galaxies** 38–44
 weak gravitational lensing 136
 Weyl's postulate 149, 150, 158, 199
 white dwarfs 519, 586
 cooling times for 251
 gravitational redshift and 189
- Wide Field Planetary Camera 2 591, 592
 Wilkinson Microwave Anisotropy Probe (WMAP) 21, 32, 33, 231, 300, 421, 429, 434–437, 440, 442, 444, 450, 451, 456–458, 460, 463, 465–467, 547, 559, 561, 615, 620, 624, 625
 point sources detected in the WMAP survey 451
 nature of 452
- William Herschel's model of the Galaxy 5
 WIMPs
 abundance of 289
 as dark matter particles 370–374
 astrophysical limits to the masses of 144
 candidates for 143
 decoupling from thermal equilibrium 370
 in very early Universe 371
 epoch of decoupling of 372
 equilibrium abundances of 370

- 'freezing out' of abundances of 370, 371
- interaction cross-section for 371–373
 - experimental limits for 374
- laboratory detection of 145
- laboratory limits to the masses of 145
- suppression mechanisms for 145, 370–372, 375
- world lines 199, 237
 - of galaxies 342, 345
- Wouthuysen-Field effect 576
- W^\pm and Z^0 bosons 145, 208
- X-ray background emission 524
 - at hard X-ray energies
 - nature of sources contributing to 529
 - at soft X-ray energies
 - nature of sources contributing to 527, 529
 - a cosmic conspiracy and 561
 - contributions of different classes of source to 528
 - spectrum of 526
- X-ray clusters of galaxies
 - number counts as a test of cosmological models 532
- tests of cosmological models and 529–532
- X-ray emission of intracluster gas 95
- X-ray luminosity–mass relation for clusters of galaxies 119, 120
- X-ray luminosity–velocity dispersion relation for clusters of galaxies 120
- X-ray sources
 - Comptonisation and 529
 - evolution of luminosity function of, with cosmic epoch 527
 - populations at soft and hard X-ray energies 526, 528
 - strongly absorbed 529
 - template spectra for strongly absorbed sources 529
- XMM-Newton X-ray Observatory 114, 116–118, 123, 124, 491, 525
- Z^0 boson, energy width of 300
- Zeldovich solution for non-linear collapse under gravity 20, 363
 - formation of caustics 477
- zinc abundance 601, 602
- Zwicky catalogue of galaxies 35



ASTRONOMY AND ASTROPHYSICS LIBRARY

Series Editors:

G. Börner · A. Burkert · W. B. Burton · M. A. Dopita
A. Eckart · T. Encrenaz · E. K. Grebel · B. Leibundgut
J. Lequeux · A. Maeder · V. Trimble

The Stars By E. L. Schatzman and F. Praderie

Modern Astrometry 2nd Edition

By J. Kovalevsky

The Physics and Dynamics of Planetary Nebulae By G. A. Gurzadyan

Galaxies and Cosmology By F. Combes,
P. Boissé, A. Mazure and A. Blanchard

Observational Astrophysics 2nd Edition
By P. Léna, F. Lebrun and F. Mignard

Physics of Planetary Rings Celestial Mechanics of Continuous Media
By A. M. Fridman and N. N. Gorkavyi

Tools of Radio Astronomy 4th Edition,
Corr. 2nd printing
By K. Rohlfs and T. L. Wilson

Tools of Radio Astronomy Problems and Solutions 1st Edition, Corr. 2nd printing
By T. L. Wilson and S. Hüttemeister

Astrophysical Formulae 3rd Edition
(2 volumes)

Volume I: Radiation, Gas Processes and High Energy Astrophysics
Volume II: Space, Time, Matter and Cosmology
By K. R. Lang

Galaxy Formation 2nd Edition

By M. S. Longair

Astrophysical Concepts 4th Edition
By M. Harwit

Astrometry of Fundamental Catalogues
The Evolution from Optical to Radio Reference Frames

By H. G. Walter and O. J. Sovers

Compact Stars. Nuclear Physics, Particle Physics and General Relativity 2nd Edition
By N. K. Glendenning

The Sun from Space By K. R. Lang

Stellar Physics (2 volumes)

Volume 1: Fundamental Concepts and Stellar Equilibrium
By G. S. Bisnovatyi-Kogan

Stellar Physics (2 volumes)

Volume 2: Stellar Evolution and Stability
By G. S. Bisnovatyi-Kogan

Theory of Orbits (2 volumes)

Volume 1: Integrable Systems and Non-perturbative Methods
Volume 2: Perturbative and Geometrical Methods
By D. Boccaletti and G. Pucacco

Black Hole Gravitohydromagnetics

By B. Punsly

Stellar Structure and Evolution

By R. Kippenhahn and A. Weigert

Gravitational Lenses By P. Schneider,
J. Ehlers and E. E. Falco

Reflecting Telescope Optics (2 volumes)

Volume I: Basic Design Theory and its Historical Development. 2nd Edition
Volume II: Manufacture, Testing, Alignment, Modern Techniques
By R. N. Wilson

Interplanetary Dust

By E. Grün, B. Å. S. Gustafson, S. Dermott and H. Fechtig (Eds.)

The Universe in Gamma Rays

By V. Schönfelder

Astrophysics. A New Approach 2nd Edition

By W. Kundt

Cosmic Ray Astrophysics

By R. Schlickeiser

Astrophysics of the Diffuse Universe

By M. A. Dopita and R. S. Sutherland

The Sun An Introduction. 2nd Edition

By M. Stix

Order and Chaos in Dynamical Astronomy

By G. J. Contopoulos

Astronomical Image and Data Analysis

2nd Edition By J.-L. Starck and F. Murtagh

The Early Universe Facts and Fiction

4th Edition By G. Börner



ASTRONOMY AND ASTROPHYSICS LIBRARY

Series Editors:

G. Börner · A. Burkert · W. B. Burton · M. A. Dopita
A. Eckart · T. Encrenaz · E. K. Grebel · B. Leibundgut
J. Lequeux · A. Maeder · V. Trimble

The Design and Construction of Large Optical Telescopes By P. Y. Bely

The Solar System 4th Edition
By T. Encrenaz, J.-P. Bibring, M. Blanc,
M. A. Barucci, F. Roques, Ph. Zarka

General Relativity, Astrophysics, and Cosmology By A. K. Raychaudhuri,
S. Banerji, and A. Banerjee

Stellar Interiors Physical Principles,
Structure, and Evolution 2nd Edition
By C. J. Hansen, S. D. Kawaler, and V. Trimble

Asymptotic Giant Branch Stars
By H. J. Habing and H. Olofsson

The Interstellar Medium
By J. Lequeux

Methods of Celestial Mechanics (2 volumes)
Volume I: Physical, Mathematical, and
Numerical Principles
Volume II: Application to Planetary System,
Geodynamics and Satellite Geodesy
By G. Beutler

Solar-Type Activity in Main-Sequence Stars
By R. E. Gershberg

Relativistic Astrophysics and Cosmology
A Primer By P. Hoang

Magneto-Fluid Dynamics
Fundamentals and Case Studies
By P. Lorrain

Compact Objects in Astrophysics
White Dwarfs, Neutron Stars and Black Holes
By Max Camenzind

Special and General Relativity
With Applications to White Dwarfs, Neutron
Stars and Black Holes
By Norman K. Glendenning